

# Developments in high-temperature corrosion and protection of materials

Edited by Wei Gao and Zhengwei Li



WP

@Seismicisolation

# Developments in high-temperature corrosion and protection of materials

## Related titles:

### *Creep-resistant steels*

(ISBN 978-1-84569-178-3)

Creep-resistant steels must be reliable over very long periods of time, at high temperatures and in severe environments. Their microstructures have to be very stable, in both the wrought and the welded states. Creep, especially long-term creep behaviour, of these materials is a vital property and it is necessary to evaluate and estimate long-term creep strength accurately for safe operation of plant and equipment. The first part of the book describes the specifications and manufacture of creep-resistant steels. Part II covers the behaviour of creep-resistant steels and a final group of chapters analyses applications.

### *Industrial gas turbines: Performance and operability*

(ISBN 978-1-84569-205-6)

This important book provides operators of industrial gas turbines with a review of the principles of gas turbine operation and how they can be used to predict and improve turbine performance. The book is accompanied by a CD which allows readers to simulate such aspects of performance as emissions, changes in pressure and power augmentation.

### *Fundamentals of metallurgy*

(ISBN 978-1-85573-927-7)

As product specifications become more demanding, manufacturers require steel with ever more specific functional properties. As a result, there has been a wealth of research on how those properties emerge during steelmaking. *Fundamentals of metallurgy* summarises this research and its implications for manufacturers.

Details of these and other Woodhead Publishing materials books, as well as materials books from Maney Publishing, can be obtained by:

- visiting our website at [www.woodheadpublishing.com](http://www.woodheadpublishing.com)
- contacting Customer Services (e-mail: [sales@woodhead-publishing.com](mailto:sales@woodhead-publishing.com); fax: +44 (0) 1223 893694; tel.: +44 (0) 1223 891358 ext.130; address: Woodhead Publishing Ltd, Abington Hall, Abington, Cambridge CB21 6AH, England)

If you would like to receive information on forthcoming titles, please send your address details to: Francis Dodds (address, tel. and fax as above; e-mail: [francisd@woodhead-publishing.com](mailto:francisd@woodhead-publishing.com)). Please confirm which subject areas you are interested in.

Maney currently publishes 16 peer-reviewed materials science and engineering journals. For further information visit [www.maney.co.uk/journals](http://www.maney.co.uk/journals)

# Developments in high-temperature corrosion and protection of materials

---

Edited by  
Wei Gao and Zhengwei Li

Woodhead Publishing and Maney Publishing  
on behalf of  
The Institute of Materials, Minerals & Mining

WPNL2204

CRC Press  
Boca Raton Boston New York Washington, DC

WOODHEAD PUBLISHING LIMITED  
Cambridge England

@Seismicisolation  
WPNL2204

Woodhead Publishing Limited and Maney Publishing Limited on behalf of  
The Institute of Materials, Minerals & Mining

Woodhead Publishing Limited, Abington Hall, Abington  
Cambridge CB21 6AH, England  
[www.woodheadpublishing.com](http://www.woodheadpublishing.com)

Published in North America by CRC Press LLC, 6000 Broken Sound Parkway, NW,  
Suite 300, Boca Raton, FL 33487, USA

First published 2008, Woodhead Publishing Limited and CRC Press LLC  
© 2008, Woodhead Publishing Limited  
The authors have asserted their moral rights.

This book contains information obtained from authentic and highly regarded sources.  
Reprinted material is quoted with permission, and sources are indicated. Reasonable  
efforts have been made to publish reliable data and information, but the authors and the  
publishers cannot assume responsibility for the validity of all materials. Neither the  
authors nor the publishers, nor anyone else associated with this publication, shall be  
liable for any loss, damage or liability directly or indirectly caused or alleged to be  
caused by this book.

Neither this book nor any part may be reproduced or transmitted in any form or by  
any means, electronic or mechanical, including photocopying, microfilming and  
recording, or by any information storage or retrieval system, without permission in  
writing from Woodhead Publishing Limited.

The consent of Woodhead Publishing Limited does not extend to copying for general  
distribution, for promotion, for creating new works, or for resale. Specific permission  
must be obtained in writing from Woodhead Publishing Limited for such copying.

Trademark notice: Product or corporate names may be trademarks or registered  
trademarks, and are used only for identification and explanation, without intent to  
infringe.

British Library Cataloguing in Publication Data  
A catalogue record for this book is available from the British Library.

Library of Congress Cataloging in Publication Data  
A catalog record for this book is available from the Library of Congress.

Woodhead Publishing ISBN 978-1-84569-219-3 (book)  
Woodhead Publishing ISBN 978-1-84569-425-8 (e-book)  
CRC Press ISBN 978-1-4200-7208-2  
CRC Press order number: WP7208

The publishers' policy is to use permanent paper from mills that operate a  
sustainable forestry policy, and which has been manufactured from pulp  
which is processed using acid-free and elementary chlorine-free practices.  
Furthermore, the publishers ensure that the text paper and cover board used  
have met acceptable environmental accreditation standards.

Project managed by Macfarlane Production Services, Dunstable, Bedfordshire, England  
(e-mail:[macfarl@aol.com](mailto:macfarl@aol.com))

Typeset by Replika Press Pvt. Ltd. India  
Printed by TJ International Limited, Padstow, Cornwall, England

## Contents

---

	<i>Contributor contact details</i>	<i>xiii</i>
1	Introduction	1
	W GAO and Z LI, The University of Auckland, New Zealand	
 <b>Part I Developments in high temperature corrosion</b>		
2	Diffusion and solid state reactions	9
	B PIERAGGI, ENSIACET, France	
2.1	Introduction	9
2.2	The Kirkendall effect and interface actions in poly-phased systems	11
2.3	Application to the role of oxide/metal interface during oxide scale growth	16
2.4	Elementary interface reactions, interface structure and interface actions	20
2.5	Growth stresses and interfacial processes	28
2.6	Conclusions and future trends	32
2.7	Acknowledgement	33
2.8	References	33
3	Transition between external and internal oxidation of alloys	36
	Y HE, University of Science and Technology Beijing, China and Z LI and W GAO, The University of Auckland, New Zealand	
3.1	Introduction	36
3.2	Thermodynamics of alloy oxidation	40
3.3	Model for the transition from external to internal oxidation of alloys	43
3.4	Summary	56

3.5	Acknowledgements	56
3.6	References	57
4	Modern analytical techniques in high temperature oxidation and corrosion	59
	M J GRAHAM, National Research Council of Canada, Canada	
4.1	Introduction	59
4.2	Metals and alloys	61
4.3	Semiconductors	71
4.4	Concluding remarks	75
4.5	Acknowledgements	76
4.6	References	77
5	Metal dusting corrosion of metals and alloys	80
	T A RAMANARAYANAN, Princeton University, USA and C M CHUN, Exxon Mobil, USA	
5.1	Introduction	80
5.2	Background	81
5.3	Nature of the metal dusting environment	83
5.4	Metal dusting of pure metals	85
5.5	Metal dusting of alloys	92
5.6	Control of metal dusting	103
5.7	Future trends	110
5.8	Sources of further information and advice	113
5.9	References	113
6	Tribological degradation at elevated temperature	117
	M ROY, Defence Metallurgical Research Laboratory, India	
6.1	Introduction	117
6.2	High temperature wear test facilities	118
6.3	Important features of elevated temperature tribological degradation: sliding wear	126
6.4	Important features of elevated temperature erosive wear	137
6.5	Important features of elevated temperature abrasive wear	146
6.6	Recent developments	149
6.7	Future trends	158
6.8	Concluding remarks	159
6.9	Acknowledgement	161
6.10	References	161

7	Hot corrosion of alloys and coatings	164
	S PRAKASH, Indian Institute of Technology Roorkee, India	
7.1	What is hot corrosion?	164
7.2	Types of hot corrosion	165
7.3	Chemistry of hot corrosion	166
7.4	Salt fluxing	168
7.5	Salt chemistry	171
7.6	Hot corrosion of Fe, Ni and Co based alloys	172
7.7	How to avoid hot corrosion	179
7.8	High temperature coatings	182
7.9	References and further reading	187
8	Oxide scales on hot-rolled steel strips	192
	R Y CHEN and W Y D YUEN, BlueScope Steel, Australia	
8.1	Introduction	192
8.2	Long-term oxidation of iron and steel	198
8.3	Short-time oxidation of iron and steel	221
8.4	Deformation and failure of oxide scale during hot rolling	226
8.5	Electron backscatter diffraction (EBSD) analyses of oxide scale structure	239
8.6	Conclusions	243
8.7	References	244

## **Part II Developments in protective oxide scales and coatings**

9	High-temperature corrosion mechanism of layered ternary ceramics	255
	Z J LIN, M S LI and Y C ZHOU, Institute of Metal Research, Chinese Academy of Sciences, China	
9.1	Introduction	255
9.2	Microstructure and synthesis of layered ternary ceramics (LTCs)	256
9.3	High-temperature oxidation mechanism of layered ternary ceramics	263
9.4	Hot corrosion mechanism of layered ternary ceramics	279
9.5	Summary and future trends	283
9.6	Acknowledgements	285
9.7	References	285

10	Formation and growth of protective alumina scales S CHEVALIER, University of Bourgogne, France	290
10.1	Introduction	290
10.2	Alumina scales: growth and properties	291
10.3	Influence of minor element addition	301
10.4	Recent developments in alumina-forming materials: intermetallics	313
10.5	References	319
11	Oxidation of Ti-Al intermetallic compounds S TANIGUCHI, formerly Osaka University, Japan	329
11.1	Introduction	329
11.2	Oxidation characteristics of TiAl-base alloys	334
11.3	Oxidation characteristics of $Ti_3Al$ and $Ti_3Al-Nb$ alloys	353
11.4	Oxidation characteristics of $TiAl_3$ -base alloys	357
11.5	Future trends	358
11.6	Acknowledgements	358
11.7	References	359
12	Oxidation of metal matrix composites Z LI and W GAO, The University of Auckland, New Zealand	365
12.1	Introduction	365
12.2	Classification of metal matrix composites	365
12.3	Reinforcing phase	366
12.4	Matrix	367
12.5	Fabrication	368
12.6	Mechanical properties	368
12.7	Corrosion of metal matrix composites	369
12.8	Titanium alloys, titanium aluminides and composites	369
12.9	Oxidation of titanium matrix composites	371
12.10	Oxidation of iron aluminide based composites	382
12.11	Oxidation of nickel aluminide based composites	383
12.12	Oxidation of niobium silicide-based in-situ composites	386
12.13	Concluding remarks	388
12.14	References	389
13	Design strategies for new oxidation-resistant high temperature alloys B A PINT, Oak Ridge National Laboratory, USA	398
13.1	Introduction	398

13.2	Chromia-forming alloys	398
13.3	Alumina-forming alloys	403
13.4	Reactive element (RE) optimization	410
13.5	Strategies for increasing lifetime	416
13.6	'Fantasy' high temperature materials	421
13.7	Future trends	423
13.8	Summary	424
13.9	Sources of further information and advice	424
13.10	Acknowledgments	425
13.11	References	425
14	Oxidation behavior of chemical vapor deposited silicon carbide	433
	T Goto, Tohoku University, Japan	
14.1	Introduction	433
14.2	Synthesis of chemical vapor deposited (CVD) silicon carbide (SiC) thick plates	434
14.3	Passive oxidation of silicon carbide	437
14.4	Active oxidation of silicon carbide	444
14.5	Bubble formation of silicon carbide	449
14.6	Summary	452
14.7	References	453
15	Oxidation-resistant nanocrystalline coatings	456
	X PENG and F WANG, Chinese Academy of Sciences, China	
15.1	Nanocrystalline materials and coatings	456
15.2	Oxidation-resistant coatings	457
15.3	Oxidation-resistant nanocrystalline coatings	459
15.4	Concluding remarks	470
15.5	Acknowledgement	471
15.6	References	471
16	Thermal barrier coatings	476
	H Xu, H Guo and S GONG, Beijing University of Aeronautics and Astronautics, China	
16.1	Introduction	476
16.2	Manufacture of thermal barrier coatings (TBCs)	477
16.3	Thermal barrier coating materials	479
16.4	Failure of thermal barrier coatings	487
16.5	Future trends	488
16.6	References	489

**Part III Case studies**

17	High temperature corrosion problems in the petrochemical industry	495
	Y HE and Z NING, University of Science and Technology Beijing, China and W. GAO, The University of Auckland, New Zealand	
17.1	Introduction	495
17.2	High temperature sulfidation	498
17.3	High temperature naphthenic acid corrosion	504
17.4	Case studies in high temperature naphthenic acid corrosion	507
17.5	High temperature corrosion of furnace radiant tubes	513
17.6	References	519
18	Oxidation processing of electronic materials	521
	Z LI and W GAO, The University of Auckland, New Zealand	
18.1	Introduction	521
18.2	Oxidation processing in semiconductors	522
18.3	Oxidation of precursors for preparation of superconductors	528
18.4	Preparation of zinc oxide (ZnO) films and nanostructures by oxidation	530
18.5	Concluding remarks	548
18.6	References	549
19	Corrosion in modern incinerators	557
	Y KAWAHARA, Mitsubishi Heavy Industries Ltd, Japan	
19.1	Introduction	557
19.2	Recent tends in waste-to-energy plants and materials	557
19.3	Corrosion environment of waste-to-energy boilers	558
19.4	Progress of high temperature corrosion-resistant materials for superheaters	561
19.5	Corrosion mechanisms of materials	569
19.6	Progress of corrosion-resistant coatings for waterwall tubes	572
19.7	Deterioration mechanisms of spray coatings	577
19.8	Corrosion testing and environmental monitoring methods	577
19.9	Corrosion lifetime evaluation of materials	592
19.10	Summary	594
19.11	References	595

20	Sulfidation of metallic materials	599
	Z GRZESIK and K PRZYBYLSKI, AGH University of Science and Technology, Poland	
20.1	Introduction	599
20.2	Physicochemical properties of metal sulfides	600
20.3	Sulfidation of pure metals – a short review	608
20.4	Sulfidation of selected alloys	609
20.5	Concluding remarks	634
20.6	Acknowledgement	634
20.7	References	634
	<i>Index</i>	639



## Contributor contact details

---

(\* = main contact)

### Chapter 1

Wei Gao and Zhengwei Li  
Department of Chemical and  
Materials Engineering  
The University of Auckland  
Private Bag 92019  
Auckland  
New Zealand

E-mail: [w.gao@auckland.ac.nz](mailto:w.gao@auckland.ac.nz)  
[zw.li@auckland.ac.nz](mailto:zw.li@auckland.ac.nz)

### Chapter 2

Professor Bernard Pieraggi  
ENSIACET  
118 route de Narbonne  
F-31077 Toulouse cedex 04  
France

E-mail: [Bernard.Pieraggi@ensiacet.fr](mailto:Bernard.Pieraggi@ensiacet.fr)

### Chapter 3

Yedong He  
Beijing Key Laboratory for  
Corrosion, Erosion and Surface  
Technology  
University of Science and  
Technology Beijing  
100083 Beijing  
China

E-mail: [htgroup@mater.ustb.edu.cn](mailto:htgroup@mater.ustb.edu.cn)

Wei Gao\* and Zhengwei Li  
Department of Chemical and  
Materials Engineering  
The University of Auckland  
Private Bag 92019  
Auckland  
New Zealand

E-mail: [w.gao@auckland.ac.nz](mailto:w.gao@auckland.ac.nz)  
[zw.li@auckland.ac.nz](mailto:zw.li@auckland.ac.nz)

## Chapter 4

Mike Graham  
Institute for Microstructural Sciences  
Bldg M 50  
National Research Council of Canada  
Ottawa  
Canada K1A 0R6

E-mail: mike.graham@nrc-cnrc.gc.ca

## Chapter 7

Dr Satya Prakash  
Metallurgical & Materials Engineering Department  
Indian Institute of Technology Roorkee  
Roorkee 247 667 (UA)  
India

E-mail: truthfmt@iitr.ernet.in

## Chapter 5

Dr Trikur A. Ramanarayanan\*  
Frick Laboratory  
Department of Chemistry  
Princeton University  
Princeton, NJ 08544-1009  
USA

E-mail: trikur@princeton.edu

Dr ChangMin Chun  
Exxon Mobil Research and Engineering Company  
Corporate Strategic Research  
Annandale, NJ 08801  
USA

E-mail:  
changmin.chun@exxonmobil.com

## Chapter 8

R. Y. Chen\*  
BlueScope Steel – Western Port Works  
Private Bag No. 1  
Hastings  
Victoria 3915  
Australia

E-mail: rex.chen@bluescopesteel.com

W. Y. D. Yuen  
BlueScope Steel Research  
PO Box 202  
Port Kembla  
New South Wales 2505  
Australia

E-mail:  
daniel.yuen@bluescopesteel.com

## Chapter 6

Manish Roy  
Defence Metallurgical Research Laboratory  
PO Kanchanbagh  
Hyderabad 500 058  
India

E-mail: rmanish64@rediffmail.com

**Chapter 9**

Zhijun Lin, Meishuan Li\* and  
 Yanchun Zhou  
 High-performance Ceramic  
 Division  
 Shenyang National Laboratory for  
 Materials Science  
 Institute of Metal Research  
 Chinese Academy of Sciences  
 72 Wenhua Road  
 Shenyang 110016  
 China

E-mail: [zjlin6@gmail.com](mailto:zjlin6@gmail.com)  
[mshli@imr.ac.cn](mailto:mshli@imr.ac.cn)  
[yczhou@imr.ac.cn](mailto:yczhou@imr.ac.cn)

**Chapter 10**

Professor Sebastien Chevalier  
 University of Bourgogne  
 Institut Carnot of Bourgogne  
 UMR 5209 CNRS  
 9 avenue Savary  
 BP 47870  
 21078 Dijon  
 France

E-mail:  
[sebastien.chevalier@u-bourgogne.fr](mailto:sebastien.chevalier@u-bourgogne.fr)

**Chapter 11**

Shigeji Taniguchi  
 Division of Materials Science and  
 Manufacturing Engineering  
 Graduate School of Engineering  
 Osaka University  
 2-1 Yamadaoka  
 Suita 565-0871  
 Osaka  
 Japan

E-mail:  
[taniguchiphms@oboe.ocn.ne.jp](mailto:taniguchiphms@oboe.ocn.ne.jp)

Visiting Professor  
 Center for Advanced Research  
 of Energy Conversion Materials  
 Hokkaido University  
 North 13, West 8  
 Kita-ku  
 Sapporo 060-8628  
 Japan

E-mail: [s-tanigu@eng.hokudai.ac.jp](mailto:s-tanigu@eng.hokudai.ac.jp)

**Chapter 12**

Zhengwei Li and Wei Gao\*  
 Department of Chemical and  
 Materials Engineering  
 The University of Auckland  
 Private Bag 92019  
 Auckland  
 New Zealand

E-mail: [w.gao@auckland.ac.nz](mailto:w.gao@auckland.ac.nz) and  
[zw.li@auckland.ac.nz](mailto:zw.li@auckland.ac.nz)

**Chapter 13**

Bruce A. Pint  
 Corrosion Science and Technology  
 Group  
 Materials Science and Technology  
 Division  
 Oak Ridge National Laboratory  
 (ORNL)  
 1 Bethel Valley Road  
 MS 6156  
 Oak Ridge, TN 37831-6156  
 USA

E-mail: [pintba@ornl.gov](mailto:pintba@ornl.gov)

## Chapter 14

Takashi Goto  
Institute for Materials Research  
Tohoku University  
2-1-1 Katahira  
Aoba-ku  
Sendai 980-8577  
Japan

E-mail: goto@imr.tohoku.ac.jp

## Chapter 15

Xiao Peng\* and Fuhui Wang  
State Key Laboratory for Corrosion  
and Protection  
Institute of Metal Research  
Chinese Academy of Sciences  
62 Wencui Road  
Shenyang 110016  
China

E-mail: xpeng@imr.ac.cn

## Chapter 16

Huibin Xu,\* Hongbo Guo,  
Shengkai Gong  
Beijing University of Aeronautics  
and Astronautics (BUAA)  
No. 37 Xueyuan Road  
Beijing 100083  
China

E-mail: xuhb@buaa.edu.cn  
guo.hongbo@buaa.edu.cn  
hbkuotbc@yahoo.com

## Chapter 17

Yedong He and Zhaohui Ning  
Beijing Key Laboratory for  
Corrosion, Erosion and Surface  
Technology  
University of Science and  
Technology Beijing  
100083 Beijing  
China

E-mail:  
(He) htgroup@mater.ustb.edu.cn

Wei Gao\*  
Department of Chemical and  
Materials Engineering  
The University of Auckland  
Private Bag 92019  
Auckland  
New Zealand

E-mail: w.gao@auckland.ac.nz

## Chapter 18

Zhengwei Li and Wei Gao\*  
Department of Chemical and  
Materials Engineering  
The University of Auckland  
Private Bag 92019  
Auckland  
New Zealand

E-mail: zw.li@auckland.ac.nz  
w.gao@auckland.ac.nz

## Chapter 19

Yuuzou Kawahara  
Yokohama R&D Center  
Mitsubishi Heavy Industries, Ltd  
1-8-1, Sachiura  
Kanazawa-ku  
Yokohama 236-8515  
Japan

E-mail: [yuuzou\\_kawahara@mhi.co.jp](mailto:yuuzou_kawahara@mhi.co.jp)

## Chapter 20

Z. Grzesik and K. Przybylski\*  
AGH University of Science and  
Technology  
Faculty of Materials Science and  
Ceramics  
Department of Solid State  
Chemistry  
Al. Mickiewicza 30  
30-059 Cracow  
Poland

E-mail: [kaz@agh.edu.pl](mailto:kaz@agh.edu.pl)



## Introduction

---

W GAO and Z LI, The University of Auckland,  
New Zealand

High-temperature corrosion is one of the most important issues for materials selection, structure design and service life prediction of engineering parts which are exposed to high-temperature environments. The formation of corrosion products such as oxides (the most common form), carbides, nitrides, sulfides, or their mixtures, in general leads to the loss of load-bearing cross-section, decreases the reliability and stability, and finally shortens the service lifetime of the engineering components. Inward diffusion of oxygen, nitrogen, sulfur or carbon may also result in undesired precipitation of compounds which are normally brittle in nature. High-temperature corrosion therefore deteriorates materials and thus degrades the performance of engineering parts. Directly or indirectly, high-temperature corrosion processes also have an impact on environmental problems such as air pollution and global warming.

Studies of high-temperature corrosion of metals have a long history. The basis for high-temperature corrosion and oxidation was established in the 1920s and 1930s. The focus at that time was mainly on kinetics (Tammann), mechanical property of oxide scale (Pilling–Bedworth ratio), and stress measurement (Evans). Carl Wagner made significant contributions towards the defect structure of oxides and diffusion processes during oxide growth. His theoretical analyses using oxidation models of single-phase alloys, growth and development of stable oxide scales, and especially the modelling of the transition of internal and external oxidation, still influence and provide guidance to modern oxidation studies. From the 1950s to the 1970s an integrated, multidisciplinary approach was developed to study the oxidation of binary alloys and, more generally, commercial alloys. These research activities, supported by powerful modern analytical tools such as scanning electron microscopy, transmission electron microscopy, electron probe microanalysis, X-ray diffraction, X-ray photoelectron spectroscopy, Auger spectroscopy, secondary ion mass spectroscopy, etc., were focused on scaling kinetics, scale morphology, and microstructural and compositional characterizations. This phase of research lasted for a long period with a varying emphasis on

defect structure, transportation mechanism, minor element additions and their effects on the growth and mechanical properties of oxide scales.

The last 20 years have seen a fast and steady increase of research into high-temperature corrosion. A quick survey with SCOPUS using the keywords ‘high temperature corrosion’ or ‘high temperature oxidation’ gave the following results: in 1985, 972 papers were published and 7756 patents applied for; in 1995, the figures increased to 1190 and 13,158, whilst in 2005 they increased to 3956 and 45,562 respectively. This is a direct result of the many investigations into high-performance structural materials for aerospace, energy and automobile applications, and also long-life corrosion-resistant bulk and coating materials for engineering components working in complex environments, such as oxidizing, sulfidizing, carburizing or chloridizing environments with or without additional mechanical action of solid particles on the material surface. Metals and alloys must be effectively protected against these corrosive environments through the formation of protective oxide layers with the characteristics of slow growth, high resistance to cracking and spallation, and strong re-healing ability. The prevention of high-temperature corrosive attacks on materials plays a critical role in aspects such as reliability, quality, safety and profitability of any industrial sector associated with high-temperature processes.

Two excellent books, *High Temperature Corrosion* by Professor P. Kofstad (1988), and *Introduction to the High Temperature Oxidation of Metals* by Professors N. Birks, G.H. Meier and F.S. Pettit (1983, 2006), described the high-temperature corrosion processes of metals and alloys at elevated temperatures, providing an expert treatment of the fundamental mechanisms involved in various high-temperature corrosion processes. To summarize the experimental developments achieved in this active area, many excellent review-type papers have also been published. They provide detailed information on defect structure and transport, selective oxidation, the reactive element effect, high-performance coatings, corrosion in molten salt, metal dusting, high-temperature erosion-corrosion, alloy and coating design strategy, and analytical technique.

The present book, *Developments in High-temperature Corrosion and Protection of Materials*, is intended to be a showcase for the current state of research activity in high-temperature corrosion of various materials. A number of leading researchers within universities, institutes and industries from Australia, Canada, China, France, India, Japan, New Zealand, Poland and the USA have contributed to this book, bringing together a wide range of studies within a single volume.

This book is divided into three parts: developments in high-temperature corrosion theories and processes, oxide scales and coatings, and practical case studies. In the second chapter, Professor Pieraggi describes the role of diffusion and mass transport processes in scale growth, and in particular, the potential influences of interfacial reactions and structures on the mechanical

properties of oxide scales and oxidation behaviours of components. In Chapter 3, Professor He and his colleagues study the oxide nucleation and growth behaviour of typical single-phase binary alloys under low oxygen partial pressure, and propose a model describing the transition between the internal and external oxidation processes. The progress of high-temperature corrosion studies is heavily dependent on the characterization of microstructure, composition and phase structure of oxide scales and bulk materials. In Chapter 4, the applications of modern analytical techniques in oxidation and corrosion research are reviewed by Professor Graham with his extensive studies of metals, alloys and semiconductors.

High-temperature corrosion in atmospheres containing gases other than oxygen is reviewed in the following chapters. Professor Ramanarayanan and Dr Chun report on the metal dusting corrosion of Fe, Co and Ni and selected Fe-based, Fe-Ni-based and Ni-based alloys, and have formulated some general principles governing the metal dusting process. Engineering components used in the nuclear industry, power generation and the transport industry may be subjected to mechanical degradation due to wear. This situation becomes worse with a synergistic interaction of oxidation and wear at elevated temperatures. In Chapter 6, Dr Roy describes typical high-temperature tribological degradation processes including sliding wear, erosive wear and abrasive wear. Hot corrosion is a complex phenomenon leading to serious problems in engines burning fuels containing sulfur, potassium, sodium, vanadium, etc., or exposed to various salts. In Chapter 7, Professor Prakash reviews the chemistry of hot corrosion and summarizes the methods used to prevent this type of accelerated attack. Oxidation is also a problem in the steelmaking industry, since the formation of oxide scale on sheet or strip steels both leads to material loss and affects the rolling process. Drs Chen and Yuen from BlueScope Steel (Australia) summarize current understanding of the long- and short-term oxidation behaviour of steel in air and oxygen, and in reheat furnace atmospheres, and review recent studies of the mechanical properties of oxide scales and their deformation and fracture behaviour.

The high-temperature oxidation and hot corrosion mechanisms of layered ternary ceramics, such as  $Ti_3SiC_2$ ,  $Ti_3AlC_2$  and  $Ti_2AlC$ , are reported by Drs Lin, Li and Zhou in Chapter 9. Their unique crystal structure and microstructure have strong influences on the scaling behaviour of these materials, and make them promising candidates for high-temperature structural applications. The development and maintenance of a protective oxide scale are determined by many chemical and mechanical factors. Dr Chevalier discusses the formation and growth of protective alumina scales in relation to growth kinetics and mechanisms, phase transformations and reactive element effects in Chapter 10. Ti-Al based intermetallic compounds are receiving more and more attention recently due to their high mechanical strength at elevated temperatures and low density. However, their high-temperature oxidation resistance is inadequate,

though they have a relatively high Al content in comparison with Ni-based superalloys. Why is the protective alumina scale hard to form on these materials? The reasons can be found in Professor Taniguchi's Chapter 11 which reviews the oxidation behaviour of Ti-Al alloys. Methods commonly used to enhance the oxidation resistance of TiAl, such as microstructure control, composition optimization and surface treatment, are also presented.

Incorporation of particulate or fibre shaped reinforcements into metal matrices can significantly change their response to mechanical loads. The presence of reinforcing phases, however, may not always be advantageous to the oxidation resistance of composites, since the enhancement of high-temperature corrosion resistance is often not the main concern of composite design. This is particularly true for long fibre-reinforced composite materials without special treatments to the fibre-matrix interface. A comprehensive summary of the literature on the general oxidation properties of metal matrix composites is given in Chapter 12 by Drs Li and Gao. This chapter also discusses the development of Ti-based in-situ composites. It has been found that incorporation of alumina particles into the Ti-Al matrix through in-situ reactions has improved the mechanical stability of thermally grown oxide scales, thereby increasing oxidation resistance significantly. In Chapter 13, Dr Pint of Oak Ridge National Laboratory USA reports on the valuable experience gained on design strategies for oxidation-resistant high-temperature alloys. In particular, he discusses how to develop a protective alumina scale on NiCr and FeNiCr alloys without sacrificing their mechanical properties.

Coating is a common way to prevent high-temperature corrosive attacks while maintaining the mechanical properties of bulk materials for structural applications. In the next group of chapters Professor Goto reports that SiC coatings are finding practical applications for engineering parts working in harsh environments. While a better understanding of the intrinsic oxidation behaviour of SiC, i.e., passive oxidation, active oxidation and bubble formation, is still needed, he believes that high-purity SiC derived by chemical vapour deposition might be a suitable candidate. Surface micro-crystallization or nano-crystallization has also become a 'hot' topic since it has been found that reduction of grain size can promote the formation of protective oxide layers through enhanced grain boundary diffusion. In Chapter 15, Drs Peng and Wang review the oxidation of nano-crystalline coatings in relation to the formation, growth and mechanical response of oxide scales, while in the following chapter, as an important type of coating, Professors Xu, Guo and Gong summarize the developments in materials, process and failure of thermal barrier coatings for advanced gas-turbine engines with higher efficiency and improved durability.

High-temperature corrosion phenomena and their related failures are widely found in the chemical, electrical, energy and transportation industries. The corrosion processes in real situations may have a quite different character in

comparison with laboratory experiments. Corrosion studies in service conditions are therefore necessary to define the nature of the attacks in order to design materials and structures with better performance. In Chapter 17, Professors He, Ning and Gao introduce the main corrosion problems commonly found in the petrochemical industry. The main effort in high-temperature oxidation research is to protect materials from attack. However, controllable growth of oxide may find important applications in areas such as the semiconductor industry. Thermal growth of native oxide,  $\text{SiO}_2$ , on Si through dry or wet oxidation has long been used to establish surface passivation layers and functional dielectrics as summarized in Chapter 18 by Drs Li and Gao. Syntheses of superconducting composites, oxide thin films such as  $\text{ZnO}$  and low-dimensional nanostructures are reported, together with some results showing the effects of the oxidation conditions on the photoluminescence property of thermally grown  $\text{ZnO}$  films. Dr Kawahara, in Chapter 19, reports on developments in materials and coatings used in waste-to-energy incineration plants and the testing and monitoring methods employed to acquire information for a greater understanding of corrosion mechanisms.

From the contents it can be seen that this book seeks to reflect current developments in high-temperature corrosion science, to chart progress in the design of new materials and new methods, and to achieve a balance of theory and practice. The contributions from industrial experts in this respect are very welcome. The Editors would like to thank all contributors for the energy and time spent in the preparation of chapters and their willingness to share their results and understanding. Finally, the Editors would also like to thank the Publications Coordinators at Woodhead Publishing, Ian Borthwick and Beatrice Bertram, the Project Editor Laura Pugh, the Commissioning Editor Rob Sitton, and the Editorial Director Francis Dodds, for their very effective work in developing the book and in organizing the delivery of each of its constituent chapters.



# **Part I**

Developments in high temperature  
corrosion

---



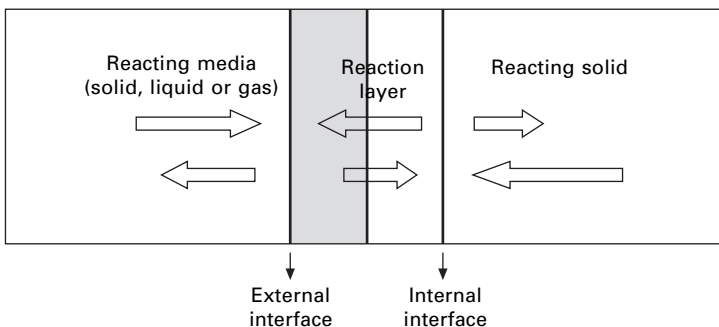
## Diffusion and solid state reactions

B PIERAGGI, ENSIACET, France

### 2.1 Introduction

As schematized by Fig. 2.1, the growth of intermediate phases between two reacting phases is a more or less complex combination of interfacial reactions and diffusion processes. Figure 2.1 shows a reaction zone formed of two sublayers that can be of different microstructure and/or different composition. For both cases, the role of external and internal interfaces delimiting these two sublayers and separating them from the two reacting phases has to be considered, and the reactions occurring at these interfaces cannot be neglected in the analysis of reaction mechanisms.

However, for a growing oxide layer, the main constraints on the reactions occurring at the external interface separating the oxide layer from the oxidant phase are linked to the fluxes of reactive species towards this interface or the counter-fluxes of volatile or dissolved reaction products; their influence on scale growth processes and rates can often be neglected and are not considered here. There are, on the contrary, many examples of solid-state reactions for which solid/solid interfaces and interfacial reactions play a major role (Dybkov,



2.1 Schematic representation of the growth of a reaction layer separating one reacting medium from a reacting solid and involving mass transport and interface reactions.

2002). In the field of high-temperature oxidation, one well-known example is the oxidation of silicon (Bauza, 2001). Molecular oxygen diffusing through the thin silica layer reacts with the silicon substrate at the silica/silicon interface. This interface reaction is likely to be the controlling step for the growth of the very thin silica layers now required in the manufacture of integrated circuits.

Thus, the growth of an external oxide scale by the reaction between a pure metal or a metallic alloy and a gaseous or liquid oxidant phase at high temperature is also a combination of diffusion processes and interfacial reactions, and Fig. 2.1 also applies to such corrosion processes that are formally similar to solid-state reactions in poly-phase and multi-constituent systems. Such a similarity will be considered to extend the treatment of the Kirkendall effect for two-phase diffusion couples to the growth of an oxide scale on a pure metal or on an alloy. The roles of interfaces will be analysed more particularly in relation to some specific topics related to oxide scaling processes such as interface displacement, growth stresses and injection of point defects (vacancy or interstitial).

As the question of vacancy generation/annihilation is of prime importance for oxidation of metals and alloys, the second section of this chapter, following this first short introductory section, is devoted to a reminder of the Kirkendall effect in mono- and poly-phase diffusion couples. Some general statements about the interface actions required to maintain the reacting system in local equilibrium are deduced from this analysis. After an illustration of the similarity between the growth of oxide scales and intermediate phases, the goal of the third section is to show that the proposed discussion of the Kirkendall effect in two-phase systems can be applied to the growth of an oxide scale on pure metals or disordered solid solutions. Section 2.4 is then devoted to a description of the general structure of the scale–substrate interface, the nature and role of interfacial defects and the elementary interfacial reactions in combination with scale growth mechanisms. These elements permit the introduction of a general discussion of growth stresses and interfacial processes that is developed in the fifth section. The final part of this section treats the specific topic of vacancy injection in the oxidized substrate and its relation to growth stresses and the role of external stresses.

Finally, Section 2.6, after some concluding remarks, proposes some ideas for future work that particularly concern the high-temperature oxidation of intermetallic compounds that are not considered in the present overview. Contrary to the case of pure metals or disordered solid solutions, vacancies in intermetallic compounds cannot be considered as non-conservative species. Indeed, their equilibrium molar fraction depends not only on temperature and stress state but also on the local chemical composition, which corresponds to a situation drastically different from that of a pure metal or a disordered solid solutions.

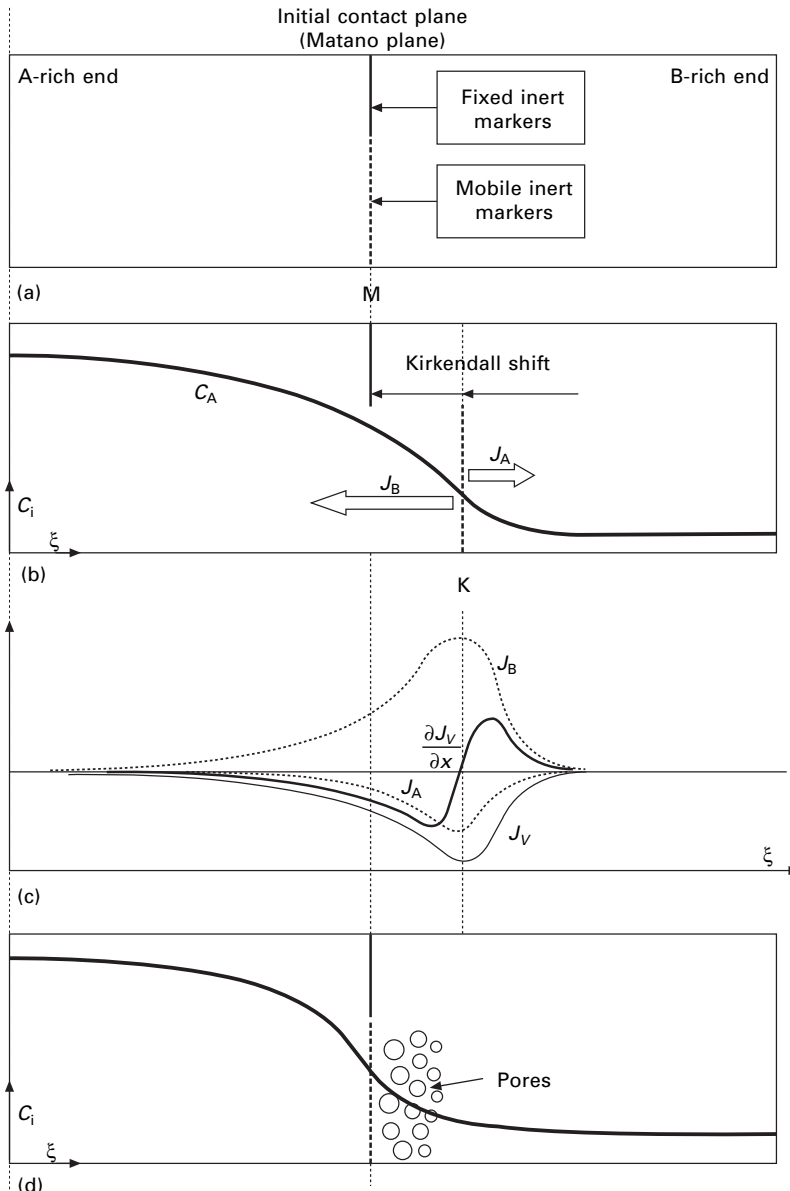
## 2.2 The Kirkendall effect and interface actions in poly-phased systems

### 2.2.1 Basis of the Kirkendall effect

The Kirkendall effect is a well-known phenomenon resulting from the difference in intrinsic diffusivities of chemical constituents of substitution solid solutions (non-reciprocal diffusion). Many textbooks provide a detailed and quantitative treatment of this important phenomenon (Philibert, 1991) schematized in Fig. 2.2 for a homogeneous diffusion couple of constituents A and B forming a continuous substitutional solid solution. In Fig. 2.2a, the initial position of the contact surface is marked by fixed inert markers that define the origin, also named the Matano plane (M), of the reference frame centred on the mass or the number of moles; this reference frame is commonly used to define interdiffusion processes and the unique interdiffusion coefficient that permits the characterization of the transport of A and B. Moving inert markers determine the actual position of the initial contact surface (Fig. 2.2b) and therefore visualize the drift of lattice planes within the diffusion zone. They mark the origin, also named the Kirkendall plane, of the lattice-fixed frame of reference that permits the definition of the different intrinsic diffusion coefficients of the A and B constituents. Relative to the Matano plane, this drift of lattice planes is equivalent to a translation of the diffusion couple without apparent deformation and without the action of any externally applied stress or, in other words, to a rigid body translation of the phase lattice.

The simplest and classical treatment of the Kirkendall effect in binary homogeneous systems assumes that the differences between the intrinsic diffusion fluxes of the two substitutional constituents are compensated by the action of local vacancy sinks and sources that maintains the system in local equilibrium, i.e. in states that can be completely defined by the knowledge of appropriate state variables to permit the calculation of pertinent state functions such as, for example, the chemical potential of system constituents. The drift of lattice planes is one important characteristic of the Kirkendall effect in stress-free homogeneous systems and is a consequence of the action of these vacancy sources and/or sinks distributed along the diffusion zone. As the system remains in local equilibrium by the action of vacancy sinks and sources, the vacancy concentration or molar fraction remains constant and equal to its equilibrium value within the entire diffusion couple. Therefore, no effective gradient of vacancy concentration is established in the diffusion zone. However, the local action of vacancy sinks or sources along the diffusion direction is formally equivalent to a vacancy flux  $J_V$  related to the required local density of vacancy sources or sinks  $\rho_S$  equal to the flux divergence,

$\rho_S = \frac{\partial J_V}{\partial x}$  (Fig. 2.2c). For conservative species such as chemical elements, a Fickian diffusion flux is always the consequence of a gradient of chemical



2.2 Kirkendall effect in a homogeneous binary diffusion couple.  
 (a) Initial stage showing the position of fixed and mobile inert markers.  
 (b) Relative displacement of inert markers resulting from difference in intrinsic diffusion coefficient of A and B species.  
 (c) Variation along the diffusion zone of intrinsic fluxes of A and B species, density of vacancy sinks/sources and equivalent vacancy flux.  
 (d) Pore formation resulting from the blocking of relative displacement of lattice planes within the diffusion zone.

potential or concentration, but such a gradient is not required for the apparent migration of non-conservative species such as vacancies that can be annihilated at sinks and created elsewhere at sources and vice-versa.

If, within the diffusion zone, there is no active vacancy source or sink, then no drift of lattice planes could occur and the difference in the diffusion fluxes of substitutional chemical species would result in vacancy supersaturation and build-up of local stress states within the diffusion zone. Return to local equilibrium in a stress-free state could be achieved by the nucleation of pores leading to the well-known Kirkendall porosity (Fig. 2.2d). All intermediate situations are possible depending on local stress states and the density, distribution and efficiency of vacancy sources or sinks. However, it should be emphasized that complete Kirkendall shift would occur only in stress-free systems in local equilibrium. Therefore, all obstacles to the free relative displacement of lattice planes would lead to local non-equilibrium. Such a situation corresponds to the build-up of stress states that modify the conditions of local equilibrium and the action of vacancy sources or sinks; these stress states must therefore be taken into account to define and analyse these local conditions and their spatial and temporal evolutions.

One possible origin of local stresses for a diffusion couple is linked to localized variation of volume associated with the variation of composition within the diffusion zone. Indeed, the total volume of a homogeneous diffusion couple would remain constant only if its constituents form an ideal solid solution. Therefore, interdiffusion is often accompanied by localized volume changes and any constraint on the extent and location of these volume changes could also be a source of stress. Such volume changes may also interact with lattice plane shifts associated with the Kirkendall effect, so that the nature, density and distribution of vacancy sinks or sources can have a marked influence on the magnitude of volume change and the build-up of local stress (Boettinger *et al.*, 2005). This influence would also depend on the size and geometry of the diffusion couple and diffusion zone. Thus, a better understanding and interpretation of diffusion processes must consider the interactions between lattice plane shift, volume changes, stress state, geometry and size of the diffusion zone, etc.

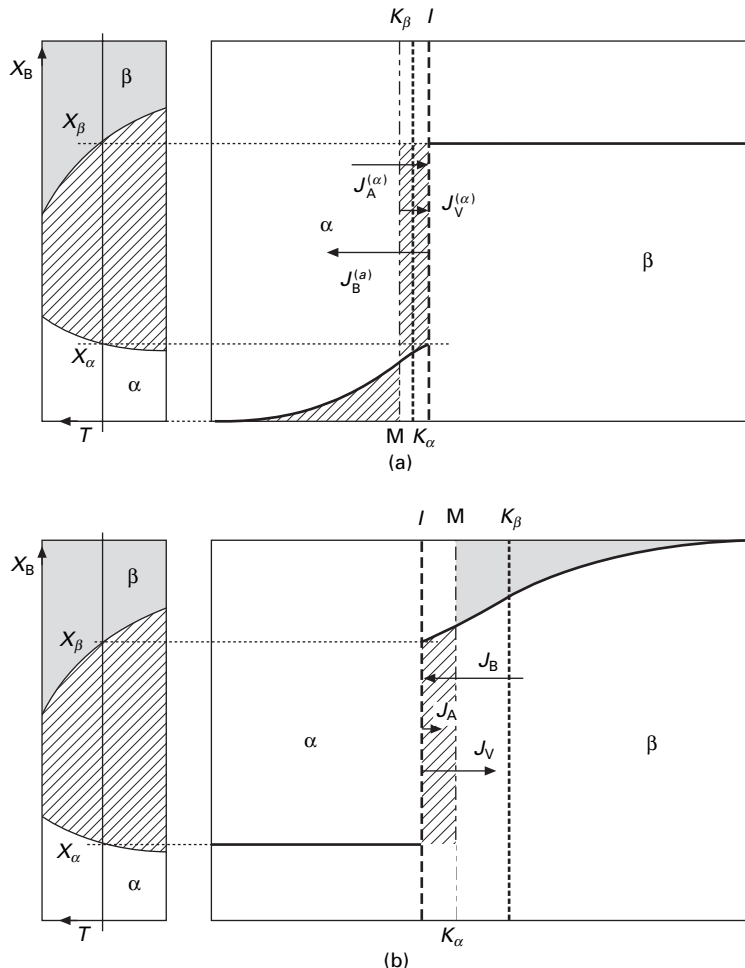
### 2.2.2 Specificity of the Kirkendall effect in two-phase diffusion couples

For a diffusion couple involving two homogeneous phases,  $\alpha$  and  $\beta$ , of a binary A-B system, interdiffusion of A and B constituents may lead to the migration of the interface separating these two phases, i.e. one phase is growing while the other one is receding. The sense and magnitude of the interface migration is determined only by the initial composition of the two contacting phases.

For such a two-phase diffusion couple, the Matano plane can be determined, as for a homogeneous couple, by the position of fixed inert markers. The situation is more complex for mobile inert markers that are linked to the displacement of lattice planes. In a two-phase diffusion couple, the displacement of lattice planes is different in both phases. Therefore, the displacements of lattice planes in both phases cannot be referred to a unique frame of reference; each phase requires one specific lattice-fixed frame of reference, as proposed by van Loo *et al.* (1990) in a general analysis of the growth or recession of one phase in diffusion-driven phase transformations. This analysis was confirmed by the splitting of mobile inert markers sometimes observed in several poly-phased binary diffusion couples (Paul *et al.*, 2004); the different locations of the mobile inert markers define the origins of different lattice-fixed frames of reference, i.e. the position of the Kirkendall plane associated with each phase of the diffusion couple. But, for a phase receding during a phase transformation, it may happen that the Kirkendall plane of the receding phase does not belong to that phase but corresponds to a virtual plane located in another adjacent phase (van Loo *et al.*, 1990).

For a binary A-B system and a general  $\alpha/\beta$  interface migrating by diffusion control, via a vacancy mechanism, the differences in intrinsic diffusivity within both the  $\alpha$  and  $\beta$  phases requires, as for a homogeneous diffusion couple, the action of a vacancy sinks sources distributed within the volume of  $\alpha$  and  $\beta$  phases (van Loo *et al.*, 1990). The differences in the distribution of vacancy sources and sinks in each phase, particularly along the interface surface, require that any given  $\alpha/\beta$  interface must be able to either create or annihilate vacancies depending upon the intrinsic diffusion coefficients and the initial compositions of  $\alpha$  and  $\beta$  phases. The diffusion profiles of Figs 2.3a and 2.3b were calculated for two different initial compositions of hypothetical binary diffusion couples of which the two constituents A and B have limited mutual solubility; the partial molar volumes of A and B were assumed constant and equal in this calculation (van Loo *et al.*, 1990). As shown by Figs 2.3a and 2.3b, the interface acts as a vacancy source for initial  $\alpha$  and  $\beta$  phases consisting of saturated  $\alpha$  and pure B, but the same interface acts as a vacancy sink for a diffusion couple made of pure A and saturated  $\beta$ . Therefore, vacancy creation or annihilation must be considered as an inherent interfacial activity in any diffusion-driven phase transformation involving substitutional solid solutions or ordered compounds with diffusion via vacancies (van Loo *et al.*, 1990).

The above statements remain valid in the case of mixed growth processes combining diffusion processes and interface reactions. However, such a mixed process implies that the interface is out of equilibrium while the two contacting phases remain in local equilibrium. Thus, the action of the interface would depend on its departure from equilibrium and its time evolution.



2.3 Concentration profiles calculated for interdiffusion between two solid solutions  $\alpha$  and  $\beta$  to illustrate the reversible role of a given interface as a vacancy source or sink: (a) interdiffusion between pure A constituent and saturated  $\beta$  solid solution; (b) interdiffusion between saturated  $\alpha$  solid solution and pure B constituent (van Loo, 1990).

### 2.2.3 Role of the interface in phase transformations

For a phase transformation totally or partially driven by diffusion, the role of the interface is not limited to the creation or annihilation of vacancies involved in the diffusion process but the interface has several other roles to play. Indeed, for one phase growing at the expense of another, phase, the interface needs to satisfy several interrelated requirements to accommodate:

- the change in chemical composition and eventually in chemical bonding;
- the mismatch in crystal structure and molar volume;
- the difference in phase growth or recession rate and interface displacement rate by annihilating or creating the point defects involved in the diffusion processes.

If one of these requirements is not realized by the interface, then the interface and the reacting phases could not be in a state of local equilibrium. Additional constraints must be considered and therefore additional state variables must be introduced to describe and quantify the properties of contacting phases and the evolution of the system. These constraints can be local stresses or constraints related to interface reactions, mass transport and interface movement.

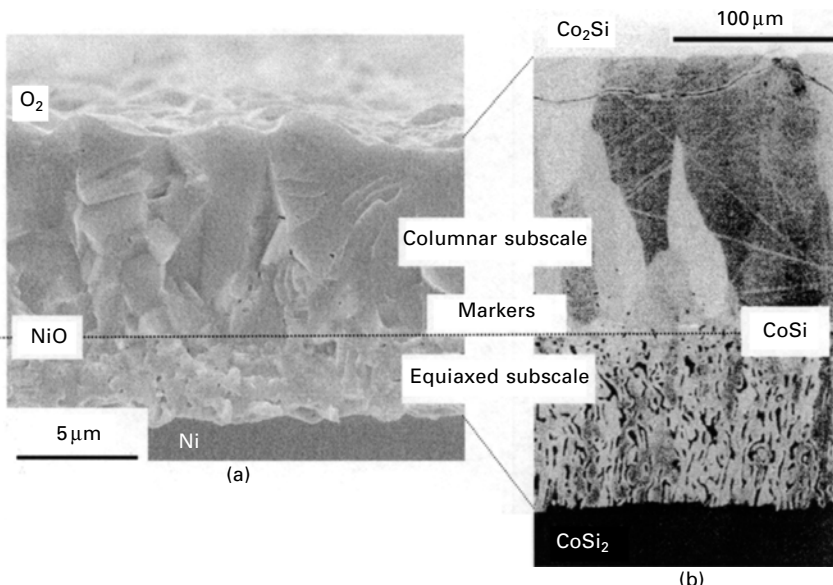
Therefore, the first step, in trying to analyse the origin and role of these constraints linked to the role of the interface, is to define the ideal case for the growth or recession of the contacting phases when the interface acts to effect all the previous requirements, i.e. such that no constraint interacts with the growth or recession processes. After such a description and analysis, the nature and role of constraints linked to the movement of the interface and to the accommodation of volume change can be considered and analysed.

## **2.3 Application to the role of the oxide/metal interface during oxide scale growth**

### **2.3.1 Similarity between the growth of oxide scales and intermediate phases**

The growth of an oxide scale on a pure metal or an alloy fits into the general category of diffusion-driven phase transformation, as illustrated by Fig. 2.4 showing the microstructure of a NiO scale grown at 800°C on high-purity Ni (Peraldi *et al.*, 2002) and of a CoSi layer formed in a Co<sub>2</sub>Si/CoSi<sub>2</sub> diffusion couple (Paul *et al.*, 2004). These micrographs reveal the very similar microstructures of the NiO scale and the CoSi layer that are both duplex and formed of two sublayers of equiaxed and columnar microstructure respectively. The growth of duplex NiO scales and that of CoSi layers both involve the diffusion of their two chemical constituents.

The growth of a columnar CoSi sublayer combines the diffusion of Si from CoSi<sub>2</sub> towards Co<sub>2</sub>Si and its reaction at the Co<sub>2</sub>Si/CoSi interface. Simultaneously, the counter-diffusion of Co and its reaction at the CoSi/CoSi<sub>2</sub> interface leads to the growth of the equiaxed CoSi sublayer. Inert markers, initially located at the Co<sub>2</sub>Si/CoSi<sub>2</sub> interface, are always located along the internal interface separating the columnar and equiaxed sublayers and define the location of the Kirkendall plane of the CoSi phase.



**2.4 Similarity of the microstructure of a NiO scale grown on a high-purity nickel (Peraldi *et al.*, 2002) and of a CoSi layer grown between CoSi<sub>2</sub> and Co<sub>2</sub>Si (Paul *et al.*, 2004).**

Such a duplex microstructure is commonly observed for NiO scales grown at a temperature lower than 1000°C (Peraldi *et al.*, 2002; Haugsrud, 2003). For such duplex scales, inert marker location, <sup>18</sup>O experiments and careful analysis of NiO scale microstructure show that the growth of the external columnar subscale is associated with the outward diffusion of Ni cations and occurs at the scale–gas interface, while the inward diffusion of oxygen is involved in the growth of the inner equiaxed subscale. Therefore, the internal interface between the equiaxed and columnar sublayers marks the initial location of the Ni surface before the formation and growth of NiO scales.

These two examples clearly show that similar growth processes lead to similar microstructures. The microstructure of a growing phase appears to depend directly on the nature of diffusing species and on the localization of growth reactions as observed in many examples of solid state and solid–gas reactions (Dybkov, 2002; van Loo, 1990).

### 2.3.2 Ideal stress-free growth of oxide scales

The similarity illustrated by Fig. 2.4 shows that the preceding description of diffusion-driven phase transformations can be applied to the growth of an oxide scale. This description permits one to define the conditions required for the ideal case of scale growth process in a situation such that neither local

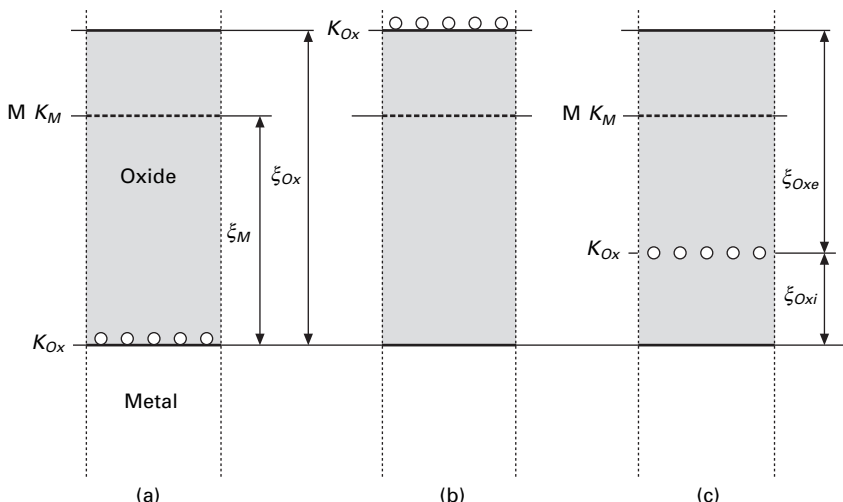
stresses nor lateral deformations are generated during scale growth at the surface of a 3D metallic substrate of large size with respect to the usual range of oxide scale thickness.

In that case, the first requirement is that the scale/substrate interface acts as a source or a sink for the point defects involved in the mass transport within the oxide scale and/or the metallic substrate. This action must be combined with the action of defect sinks/sources within the oxide scale and its substrate to maintain the system in local equilibrium. The second requirement is the absence of any obstacle to the free displacement of that interface and, if required, to the free relative displacements of lattice planes in the oxide scale and the metallic substrate.

However, for the oxidation of metals or alloys a difficulty arises because of the large volume change usually induced by the transformation of a metal into its oxide. This volume change is characterized by the well-known Pilling–Bedworth ratio (PBR)  $\phi$ . For the growth of the oxide  $MO_v$ , this ratio is given by  $\phi = v_{MO_v}/\bar{v}_M$ , where  $v_{MO_v}$  is the molar volume of the growing oxide and  $\bar{v}_M$  the partial molar volume of metal M at the oxide/metal interface.

This volume change must be accommodated by additional displacements parallel to the growth direction. Figure 2.5 schematizes, for the oxidation of a pure metal, the three different situations that can be observed for the ideal stress-free growth of an oxide scale depending on the location of the reactions leading to oxide lattice growth; for these three cases, the recession of metal lattice obviously occurs at the oxide/metal interface. On Fig. 2.5, M defines the position of the Matano plane, i.e. the initial position of the metal surface before starting oxide growth;  $K_M$  and  $K_{Ox}$  define the positions of the Kirkendall planes associated with the metal and oxide lattice respectively. The thickness of the oxidized metal is denoted as  $\xi_M$  and corresponds to a thickness  $\xi_{Ox}$  of the oxide scale such that the ratio  $\xi_{Ox}/\xi_M$  is equal to the PBR  $\phi$ . This simple relation is implicitly assumed when a parabolic rate constant  $k'_p$ , expressed in  $\text{cm}^2\text{s}^{-1}$ , is calculated from experimental values of  $k_p$  derived from mass gain measurements and expressed in  $\text{mg}^2\text{cm}^{-4}\text{s}^{-1}$  (Birks *et al.*, 2006; Kofstad, 1988). But its validity has rarely been checked, although any departure from this relation would give a strong indication of deviation from ideal stress-free growth.

Figure 2.5a shows the relative location of these specific planes for the ideal growth of a scale of p-type oxide such as NiO; in that case, oxide lattice growth occurs only at the gas/oxide interface. Figure 2.5b defines the same location for an ideally grown scale of n-type oxide such as  $\text{ZrO}_2$  for which oxide lattice growth and metal lattice recession occur simultaneously along the oxide/metal interface. Figure 2.5c corresponds to a mixed case whereby oxide lattice growth occurs simultaneously at both the gas/oxide and oxide/metal interfaces. The oxide scale fraction growing at the external gas/oxide interface has a thickness  $\xi_{Oxe}$  and the fraction growing at the internal oxide/



2.5 Relative positions of  $M$ ,  $K_M$  and  $K_{Ox}$  reference planes during the growth of an oxide scale by oxidation of a pure metal: (a) scale growth occurring only at the external gas/oxide interface; (b) scale growth occurring only at the internal oxide/metal interface; (c) scale growth occurring at both interfaces.

metal interface a thickness  $\xi_{Oxi}$ . For ideal diffusion-controlled scale growth, the relative magnitudes of  $\xi_{Oxe}$  and  $\xi_{Oxi}$  are directly proportional to the relative magnitude of intrinsic diffusivity of species involved in the growth process, as observed in many examples of solid state reactions (van Loo, 1990).

The theoretical locations of the reference planes  $M$ ,  $K_M$  and  $K_{Ox}$  can be easily calculated from only the knowledge of the PBR and relative diffusivities. Many experimental methods permit a determination of the position of the reference plane  $K_{Ox}$ . The use of inert markers, illustrated by Fig. 2.5, is commonly employed in oxidation studies. However, as the microstructure of a growing phase differs at both sides of its Kirkendall plane (van Loo, 1990), metallographic examinations also provide an easy way to determine the location of  $K_{Ox}$ . For a pure metal, the position of planes  $M$  and  $K_M$  always coincide with the position of the initially non-oxidized metallic surface. Therefore, after the growth of an oxide scale, the positions of these reference planes can be accurately determined from a fixed reference plane previously defined, such as, for example, the specimen mid-plane or any marked plane far enough from the scale/metal interface to be supposed fixed and not affected by the lattice movements that could be induced by scale growth. These displacements can be rationalized by a factor  $T$  that defines the displacement  $\xi$  of any reference plane of the oxide scale as a function of the thickness of oxidized metal  $\xi_m$ :  $\xi = T\xi_m$  (Manning, 1979); the factor  $T$  is defined as positive for outward displacement. For the general case of

simultaneous growth at the external gas/scale interface and at the internal scale/substrate interface, the factor  $T$  is given by:

$$T = \phi(1 - f_C) - 1 \quad 2.1$$

The term  $f_C$  in relation [2.1] is the fraction of cationic scale growth occurring at the external interface;  $f_C$  is equal to the ratio of intrinsic diffusivity of cations and anions and, for the considered ideal case, is also equal to the ratio  $\xi_{Oxe}/\xi_{Oxi}$ . Relation [2.1] can be easily checked from the displacement of the  $K_{Ox}$  plane for pure cationic (Fig. 2.5a) or pure anionic (Fig. 2.5b) growth.

Thus, if sufficiently accurate measurements can be performed on oxidized specimens, comparison between the theoretical and actual positions of these reference planes would provide a quantitative evaluation of the departure from ideal stress-free scale growth and would permit an evaluation of the effective role and the action of scale/substrate interface during scale growth and to interpret it in terms of local strains and stresses within both the oxide scale and its underlying substrate close to the scale/metal interface could become possible.

The schematization of Fig. 2.5 and relation [2.1] remain valid for the selective oxidation of ideal disordered solid solutions. Indeed, the total volume of such an ideal solid solution does not depend on the spatial distribution of its constituents, as the partial molar volume of each constituent is equal to its molar volume. Therefore, there is no difference between the pure metal and an ideal solid solution regarding the definition and location of planes  $M$  and  $K_M$ . In relation [2.1], the value of  $\phi$  is then that of the selectively oxidized constituent.

The situation is more complex for non-ideal solid solutions because the partial molar volume of each constituent varies as a function of composition. Selective oxidation of one constituent of a solid solution results in concentration gradients for all constituents in the alloy underlying the oxide scale. Therefore, local variations of partial molar volumes result in local volume changes that must be accommodated by an additional displacement field parallel to the growth and diffusion direction to maintain the system in a stress-free state. An accurate evaluation of such a volume change and the related displacement field requires many data, often not available, to determine or calculate concentration profiles and partial molar volumes. However, the assumption of ideal solution behaviour would often provide estimated values of a sufficient accuracy.

## 2.4 Elementary interface reactions, interface structure and interface actions

As shown in the previous section, stress-free growth of an oxide scale on a metallic substrate can occur only if there is no obstacle to the free migration

of the scale/substrate interface, to the free relative displacements of oxide and metal lattice planes and to the complete accommodation of local volume changes by displacements parallel to the growth and/or diffusion direction. Thus, a detailed knowledge of interfacial processes is required to determine how the interface acts and moves to maintain the reacting gas/scale/substrate system in stress-free local equilibrium states.

This condition of local equilibrium implies that point defects associated with mass transport within an oxide scale must be created and/or annihilated at gas/scale and/or scale/substrate interfaces. Therefore, the interface reactions must be expressed to account for this required interface action of point defect creation/annihilation. But this interface action depends also on the structure of the interface. A description of the interface structure is thus needed before considering how interface action and interface structure interact to simultaneously achieve, or fail to achieve, the relative displacement of the metal and/or oxide lattices and the migration of the scale/substrate interface.

#### 2.4.1 Elementary interface reactions

At high temperature, the interface reactions involving only the gas phase and occurring at the external gas/oxide interface, such as, for example, the adsorption and/or dissociation reactions of oxidant species, are usually fast enough to be considered at equilibrium if no specific constraint limits the flux and circulation of the gas phase in the vicinity of the oxidized material. Therefore, only the elementary interfacial reactions associated with the growth of the oxide lattice and to the recession of the metal lattice are considered. These reactions occur at the gas/scale and scale/substrate interfaces and depend on the nature of predominant point defects of the growing oxide. In the following, only the classical cases of p-type oxides with predominant cation vacancies ( $\text{NiO}$ , for example) and of n-type oxides with predominant anion vacancies ( $\text{ZrO}_2$ , for example) are considered, but this analysis can be applied to interstitial defects. For the sake of simplicity, the equilibria associated with the ionization of these vacancies are also not considered and all these vacancies are assumed to be fully ionized. The Kröger–Vink notation is used in the writing of interface reactions, the underlined symbols representing species belonging to the metallic substrate.

##### Cationic growth

For a p-type oxide  $MO_v$  with predominant cation vacancies, the growth of the oxide lattice occurs at the gas/scale interface and the consumption of the metal lattice at the scale/substrate interface. The growth of the oxide lattice can be expressed by the following interface reaction:



Reaction [2.2] expresses the formation of one neutral structure unit of oxide lattice from adsorbed oxygen species by the subsequent formation of one cation vacancy per  $v$  atoms of absorbed oxygen.

The consumption of the metal lattice occurs at the scale/substrate interface and can be described by reaction [2.3]:



This reaction involves three steps: (1) the jump of a metal atom from the metal towards the oxide lattice; (2) its ionization to occupy a cation vacancy, and (3) the simultaneous displacement of the scale/substrate interface. Indeed, in its present form, reaction [2.3] implicitly assumes that all the cation vacancies created at the external gas/scale interface and arriving at the internal scale/substrate interface are annihilated at the internal interface. Therefore, reaction [2.3] also means that the scale/substrate interface is free to migrate and therefore acts as a perfect sink for all the incoming cation vacancies. In other terms, the simultaneous rigid body translation of the oxide lattice to maintain the contact between the oxide and metal lattices so that the origin of metal and oxide Kirkendall frames remains located at their normal position as shown in Fig. 2.5a. Therefore, the actual distance between  $K_M$  and  $K_{Ox}$  is directly related to oxide scale thickness and to PBR value. However, as oxide growth occurs at the gas/oxide interface, no constraint hinders the volume change associated with the formation of new oxide structure units.

### Anionic growth

As illustrated by Fig. 2.5b, the growth of an anion-diffusing scale leads to an apparently simpler situation than for a cationic oxide. Indeed, the growth of the oxide lattice and the correlated consumption (recession) of the metal lattice both take place at the internal scale/substrate interface and can be expressed by the following reaction:



Reaction [2.4] expresses the formation of a new structure unit of oxide upon the oxidation of one metal atom. The anion vacancies created from reaction [2.4] are annihilated at the external gas/scale interface according to reaction [2.5]:



There is no constraint on reaction [2.5] so that the system remains in local equilibrium. The situation is more complex for reaction [2.4], although the

formation of the oxide lattice apparently results only in a translation of the scale/substrate interface and does not involve any displacement of metal lattice planes, which can be considered as spatially fixed. Therefore, for a hypothetical oxide of molar volume identical to the metal molar volume, the planes  $K_M$  and  $K_{Ox}$  would coincide with the oxide scale surface and the initial metal surface. But, as seen in Fig. 2.5b, for anionic scales, the main problem is related to the usually large volume change associated with oxide formation, i.e. the usually high value of PBR for common n-type oxides such as  $ZrO_2$  ( $\phi = 1.56$ ). This volume change is localized along the scale/substrate interface and must be transformed in a displacement parallel to the growth direction to maintain the system in a stress-free state.

#### 2.4.2 Interface structure

Independent of the nature of the reacting metallic substrate, i.e. pure metal or disordered alloy, the reactions at internal metal/scale interfaces correspond to the ionization of metal atoms and their transfer, by jumps or interface migration, from the metal lattice to the oxide lattice. To be possible and energetically favourable, these jumps from the metal to oxide lattices must be as short as possible and thus the metal and oxide lattices must be as close as possible. Therefore, the two lattices must be mutually oriented to minimize the distance between metal lattice sites and cation lattice sites of the oxide lattice. Similarly, interface migration implies parallelism of metal and oxide lattice planes if it does not involve atomic jumps. Both requirements usually lead to the parallelism of high-density lattice planes and lattice directions of both lattices, i.e. to specific mutual orientation relationships, or epitaxial relationships, between the metal and oxide lattices that usually correspond to an interface structure of low energy. Therefore, as observed for many metal–oxide interfaces (Ernst, 1995), metal and oxide lattices are expected to share more or less complex mutual epitaxial orientation relationships.

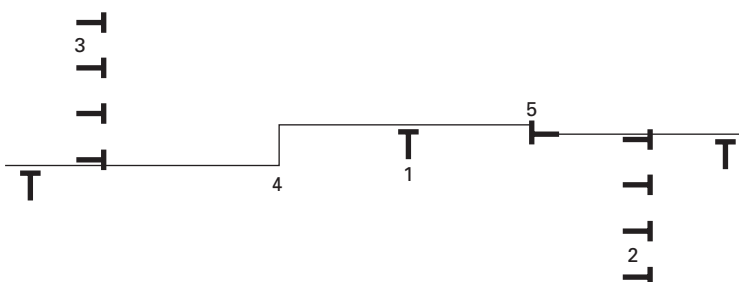
However, most of the works on the crystallographic structure of metal/oxide interfaces deal with static and non-reacting metal/oxide systems (Ernst, 1995). Only a few studies have been devoted to the crystallographic characterization, by means of TEM cross-sections, of the oxide/metal interface in the case of growing oxide scales involving interface migration; the most commonly studied interface is also the simplest one, i.e.  $NiO/Ni$  (Hobbs *et al.*, 1983; Leseur and Pieraggi, 1985). These TEM examinations reported excellent contact between  $NiO$  scales and  $Ni$  substrate along their interface, and simple epitaxial orientation relationships between lattices of metal and oxide grains leading to interfacial dislocation structure of both extrinsic and secondary dislocations while  $NiO$  grains farther into the scale can adopt other texture orientations. TEM characterizations of the interface structure of more complex systems such as  $HfO_2/Hf$  (Pieraggi and Dabosi, 1980) and

$\text{Al}_2\text{O}_3/\text{MCrAlY}$  (Rhouta and Pieraggi, 2001) confirmed the existence of mutual orientation relationships between oxide and metal lattices at the interface. The observed mutual lattice orientation relationships were consistent with a classical modelling of the interface structure (Bollmann, 1970).

The structure of a semi-coherent interface resulting from any epitaxial relationship between two crystal lattices can be described by the combination of several sets of line and/or surface defects. For a semi-coherent oxide/metal interface, these defects can be classified into two main categories:

- Defects permitting the accommodation of the size difference of metal and oxide lattices i.e. the difference in molar volume of oxide and the equivalent partial molar volume of metal, as characterized by the PBR (Pieraggi and Rapp, 1988; Hirth, 1991; Pieraggi *et al.*, 1995).
- Defects permitting the accommodation of the departure of the actual orientation of the metal and oxide lattices from an ideal mutual orientation relationship (Hirth *et al.*, 1995; Pieraggi *et al.*, 1995).

Figure 2.6 illustrates these different types of defects for a semi-coherent metal–oxide interface. The accommodation of lattice size difference can be achieved by regular networks of misfit dislocations, denoted as 1 on Fig. 2.6. Misfit dislocations are edge dislocations of Burgers vector parallel to the interface plane; their spacing is determined by the relative size of metal and oxide lattice cells in the interface plane; the spacing of misfit dislocations can be easily adjusted by their glide along the interface. Consistent with PBR values higher than 1, the spacing of metal lattice planes is usually smaller than the spacing of oxide lattice planes; thus, misfit dislocations have their extra reticular planes on the metal side so that the climb out of the interface of such misfit dislocations leads to dislocations of the metal lattice (Pieraggi and Rapp, 1988). But the ratio between reticular distances of metal



2.6 Interfacial line defects at a semi-coherent interface: 1, misfit dislocation; 2, misorientation dislocation with an extra half-plane in the metal lattice; 3, misorientation dislocation with an extra half-plane in the oxide lattice; 4, ledge; 5, disconnection.

and oxide lattice planes is not usually a rational number, so that the formation of a semi-coherent interface always involves homogeneous elastic straining of the metal and oxide lattices. But for a semi-infinite substrate, only the oxide scale only is elastically strained. The elastic strain so imposed on the scale depends on temperature as the thermal expansion coefficients of scale and substrate are usually different (Pieraggi, 1983).

Networks of misorientation dislocations of Burgers vector normal to the interface surface permit the accommodation of departures from an ideal orientation relationship; they are denoted as 2 and 3 on Fig. 2.6. These misorientation dislocations may have their extra half-plane in the metal lattice (metal misorientation dislocation denoted as 2) or in the oxide lattice (oxide misorientation dislocation, denoted as 3). Misorientation dislocations are not inherent to the interface structure; therefore, as schematized in Fig. 2.6, dislocation sources are needed to maintain the mutual orientation of both lattices upon climbing of these misorientation dislocations in a direction parallel to the interface plane.

More complex defects such as ledges and kinks, denoted as 4 on Fig. 2.6, further allow for the accommodation of both volume change and lattice misorientation. The height or width of these ledges or kinks is fixed by the spacing of metal and oxide planes parallel to the interface and intersecting these ledges or kinks (Hirth *et al.*, 1995). One additional linear defect, called disconnection, is denoted as 5 on Fig. 2.6 and is symbolized by an asymmetric dislocation symbol. Disconnections are defects specific to an heterogeneous interface (Pond and Hirth, 1994); they participate in lattice misorientation. These defects have part dislocation character and part ledge character and are formed at the junction of two half-planes of the same orientation belonging respectively to the metal and oxide lattices; in scaling reactions, the dislocation part has a Burgers vector normal to the interface plane (Hirth *et al.*, 1995). Therefore, the transformation of a metal into its oxide at the scale/substrate interface can only be achieved only by the translation of such disconnections along planes parallel to the interface, as long as the required reacting species can be transported towards these moving defects (Pieraggi *et al.*, 1995).

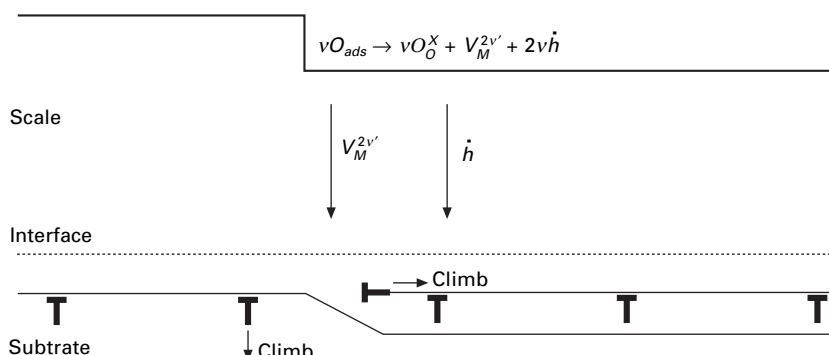
#### 2.4.3 Combined effects of interface reactions and interface structure

Interface reactions depend on interface structure and vice-versa. The combined effects of these two elements of phase transformations involving the diffusion of reacting species results in interface dynamics as analysed the general case of diffusion-driven phase transformations (Pieraggi *et al.*, 1990). The proposed models can be adapted to the growth of an oxide scale in distinguishing cationic and anionic scale growth.

### Cationic growing scales

Figure 2.7 proposes, for a cationic growing scale, a schematic representation of growth dynamics and processes compatible with interface reactions and interface structure. As shown by reactions [2.2] and [2.3], the growth of such an oxide scale occurs at the gas/scale interface by the formation of a  $MO_v$  structure unit associating  $v$  anions and one cation vacancy. Such a growth process can be schematized by the movement of ledges and kinks along the scale surface (Rapp, 1985). There is usually no strong obstacle to such an advance of kinks and ledges at a clean gas/solid interface. The situation is more complex at the internal scale/substrate interface that must permit the annihilation of incoming cation vacancies, the recession of the metal lattice and the rigid body translation of the oxide scale. Furthermore, the difficulty of these processes increases greatly at substrate edges and corners. Among the interface defects described in the previous section, the climb of misorientation dislocations having their extra half-plane lying on the oxide side and the displacement of disconnections are not permitted, as the displacements of these defects necessarily involve the transport of anions or anion vacancies, which is not compatible with the very low concentration of anionic defects in cationic oxides.

However, the required interface action can be accomplished by the climb of dislocations belonging to the metal lattice, i.e. metal misorientation dislocations or misfit dislocations. Indeed, the jump of one metal atom from these dislocations towards one cation vacancy at the scale/substrate interface simultaneously achieves two interface requirements: the consumption of the metal lattice and the annihilation of incoming cation vacancies by the climb of misorientation and/or misfit dislocations. As schematically shown in Fig. 2.7, the climb of misorientation dislocations would, in addition to cation vacancy annihilation, permit the required rigid body translation of the oxide lattice. However, the density of misfit dislocations usually greatly exceeds

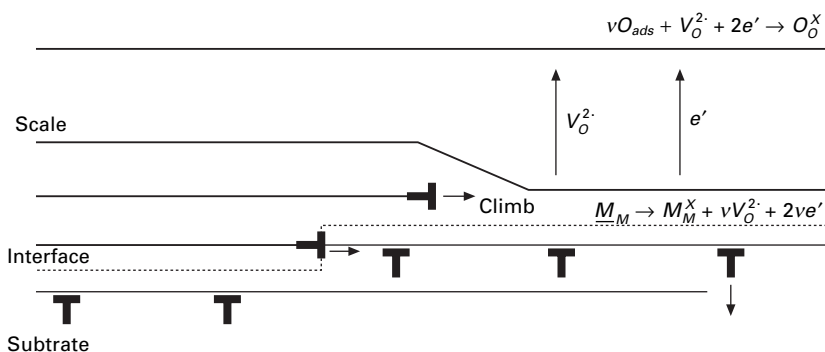


2.7 Interfacial defects active in the growth of a cationic scale.

that of misorientation dislocations. Therefore, as proposed by Pieraggi and Rapp (1988), the climb of these misfit dislocations must be favoured. The climb of misfit dislocations out of the interface plane induces local interfacial strains, but these strains are minimized by the continuous adjustment of the spacing of misfit dislocation and by their return glide to the interface after climbing. This process of climb and return glide satisfies all the interface requirements; it is equivalent to a Bardeen–Herring mill that continuously resupplies the interface with misfit dislocations and, on average, maintains the interface in a stress-free state. Such a process probably occurs during the oxidation of pure nickel at temperatures higher than 1000°C, leading to the formation of compact and adherent NiO scales on flat substrate without apparent deformation of the oxidized specimens and without pore formation in the nickel substrate.

#### Anionic growing scales

The possible interfacial processes for anionic growing scales are schematized in Fig. 2.8. The annihilation of anion vacancies at the gas/scale interface requires no specific feature, so that there is no important constraint exerted on this interface. This is not the case for the scale/substrate interface where the formation of new structural units of oxide lattice occurs. Such a growth process could be realized by the movement of ledges and kinks along the scale/substrate interface. But, because of the usually high PBR value of anionic oxides, monoatomic ledges are energetically unfavourable. The formation of polyatomic ledges minimizing interface stress would correspond to a highly stepped interface (Hirth, 1991), but such a stepped interface has not been reported from TEM cross-section examinations of an ZrO<sub>2</sub>/Zr alloy interface (Hobbs *et al.*, 2005). Therefore, the most likely growth processes are, as shown in Fig. 2.8, either the climb of oxide misorientation dislocations or the displacement of disconnections.



2.8 Interfacial defects active in the growth of an anionic scale.

The disconnection translation is a conservative movement but the misfit dislocations must be maintained along the scale/substrate interface to avoid the build-up of large interfacial stresses. Because of PBR values higher than 1, the growth of one molecular layer of semi-coherent oxide at the scale/substrate interface involves fewer cations than the corresponding number of metal atoms in the substrate reticular plane in contact with the scale. Therefore, the translation of disconnections cannot be the only scale growth process as it would not permit the minimization of interface stresses and the maintenance of the interface in a stress-free state. Disconnection translation needs to be assisted by the climb of oxide misorientation dislocations and/or by the climb of misfit and misorientation dislocations on the metal side. Climb of oxide misorientation dislocations would result in an expansion of the oxide lattice normal to the interface, while the climb of metal dislocations would result in a recession of the metal lattice.

If there is no obstacle to dislocation activity along the scale/substrate interface and a sufficient density of active dislocation sources, the climb of oxide misorientation dislocation would likely be predominant as it permits more easily the maintainance of the interface structure. Such a growth process probably occurs at high temperatures as shown by the oxidation behaviour of pure zirconium. Zirconia ( $\text{ZrO}_2$ ) is characteristic of anionic oxide and forms compact and adherent oxide scales upon high-temperature oxidation, i.e. higher than 800°C then, for pure zirconium oxidised in dry oxygen. The corresponding microstructural features of  $\text{ZrO}_2/\text{Zr}$  systems are in agreement with the schematic representation of Fig. 2.5b (Kofstad, 1988).

## 2.5 Growth stresses and interfacial processes

The question of the origin of stress accompanying the isothermal formation and growth of oxide scales is an old but important topic because of its noticeable influence on the mechanical stability of oxide scales. Three main causes of stress generation during scaling are commonly considered (Birks *et al.*, 2006; Kofstad, 1988; Stringer, 1970):

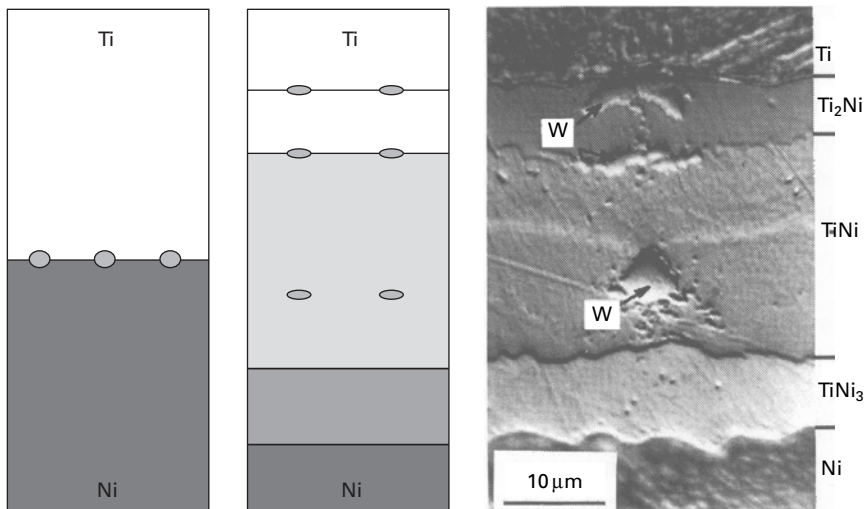
- Volume change associated to PBR values usually higher than 1.
- Elastic straining of oxide scale resulting from epitaxial relationships between the oxide and metal lattices.
- Formation of new oxide within growing oxide scale by counter-diffusion of cations and anions along oxide grain boundaries normal to the scale/substrate interface.

This latter cause of stress generation was extended to the climb, in the bulk of the oxide scale, of edge dislocations with a Burgers vector parallel to the interface (Clarke, 2003). All these causes of stress generation have been

treated by considering that the established stress state is biaxial and that the stress normal to the interface plane is negligibly small. However, from the preceding description of the ideal case of stress-free growth of an oxide scale, other possible causes of stress generation can be associated with the complete or partial blocking of one of the required actions of the scale/substrate interface.

### 2.5.1 Experimental evidence of stresses associated with interdiffusion processes

One specific aspect of the Kirkendall effect in two-phase systems, emphasized in Section 2.2.2, resides in the need to define one Kirkendall plane, i.e. one lattice-fixed frame of reference, for both phases of such a system. For a diffusion couple between two constituents forming one or several compounds, the Kirkendall planes of all the phases, the reacting phases as well as the product phases, coincide with the initial contact surface at  $t = 0$ . These planes tend to separate as the product phases grow and the reacting phases recede. Thus, the behaviour of inert markers located at the initial contact surface is difficult to determine as they can be attached to each of these possible Kirkendall planes. Figure 2.9 shows that 10  $\mu\text{m}$  tungsten wires used as inert markers in a Ti–Ni diffusion couple were broken longitudinally and split in several pieces that mark the Kirkendall planes of the different phases (Bastin and Rieck, 1974). This observation provides an impressive illustration



2.9 Interdiffusion in Ni-Ti system: splitting of inert markers to mark the Kirkendall frame of reference of each phase formed (Bastin and Rieck, 1974).

of the chemical forces acting during interdiffusion. This observation also shows that any obstacles to the free displacement of lattice planes and of the scale/substrate interface must result in large stresses applied in a direction normal to the interface plane. Therefore, the assumption of a non-moving interface, often proposed in the interpretation of pore formation within the substrate or along the scale/substrate interface, appears to be rather unrealistic.

### 2.5.2 Interfacial processes and growth stresses in scale growth

As shown in preceding sections, hindrance of interface migration and/or lattice plane displacements must result from strong chemical, geometrical and/or mechanical constraints. A common example of the effect of such constraints can be observed at specimen edges and corners of parallelepiped specimens where oxide scale features such as thickness and microstructure usually differ from those observed along specimen faces (Rapp, 1985). This observation can be generalized by considering the influence of interface curvature on oxidation processes that can be deduced from the knowledge of the translation factor  $T$  introduced in relation [2.1]. Indeed, for an interface of curvature radius  $R$ , defined as positive for a concave surface, an increase  $d\xi$  of oxide scale thickness induces a tangential strain  $d\epsilon_t$  such that (Manning, 1979):

$$d\epsilon_t = \frac{T}{R} d\xi \quad 2.6$$

Relation [2.6] defines the magnitude and sign of  $d\epsilon_t$  and the sign of resulting radial and tangential stresses. This tangential strain  $\epsilon_t$  results in a two-component, radial and tangential, stress state of the oxide scale that would then depend on its ability to creep to relax these stresses.

This kind of interface hindrance is purely geometrical; its magnitude, as shown by relation [2.6], depends on the interface curvature and vanishes for a planar interface. However, there is much experimental evidence for the generation of stresses during the growth of an oxide scale on planar surfaces (Stringer, 1970). For example, in the case of cationic growth, the oxide scale is free to grow at the external interface but interface migration depends on dislocation activity at the interface and in the underlying substrate. Therefore, any obstacle to this dislocation activity could partially or entirely block the interface migration. Such an interface blocking can result from interfacial segregation of impurities, high dislocation density, selective oxidation along grain boundaries, internal oxide precipitates, specimen microstructure, specimen size, and so on. The festooned scale/substrate interface of oxidized Ni-20Cr specimens (Calvarin *et al.*, 2000) is an example of the effect of intergranular oxidation. In the case of anionic scales, dislocation activities in both the

oxide and metal lattices are involved and similar phenomena can contribute to interface blocking. Unfortunately, no specific rule applies to this problem; each situation must be considered specifically to determine the possible causes that hinder the movement of the scale/substrate interface or lattice planes and promote build-up of growth stress.

### 2.5.3 Vacancy injection

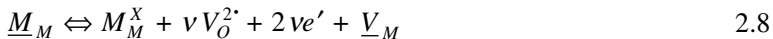
Vacancy injection, a phenomenon usually considered to be characteristic of cationic scale growth, was a rather popular topic after the mid-1990s. This phenomenon is again often invoked to explain the formation of pores and cavities within the metallic substrate beneath an oxide scale such as NiO or FeO and, more recently, Al<sub>2</sub>O<sub>3</sub> for the oxidation of intermetallic aluminides. In that case, the metal–oxide interface is assumed to be unable to move freely to follow the recession of the metal lattice. Reaction [2.3] must then be replaced by the following reaction:



In relation [2.7],  $\underline{V}_M$  represents a vacancy of the metal lattice. One important question then concerns the fate of such ‘injected’ vacancies. Many authors assume that these vacancies are able to diffuse within the substrate (Bobeth *et al.*, 1998), up to their annihilation at the unoxidized specimen’s back face (Francis and Lees, 1989) or to voids formed close to the specimen mid-plane (Perusin *et al.*, 2004). In addition to the assumption of a non-moving interface, such a mechanism implies that a gradient in molar fraction of so-injected vacancies must be established in the substrate underlying the oxide scale. However, for pure metals or disordered solid solutions, the equilibrium molar fraction of vacancies depends on temperature only. Therefore, the assumption of local equilibrium cannot apply to a substrate, having a vacancy gradient which does not allow defining the chemical potential of substrate constituents and vacancy and consequently their mobility or diffusivity. In fact, this question of vacancy injection cannot be separated from the build-up of a more or less complex stress state within the oxide scale and its substrate, because an immovable scale/substrate interface obviously leads to stress in the substrate with a tensile component normal to the interface. Therefore, the knowledge of the local stress state is required for a complete analysis of scale growth processes and kinetics, because the molar fraction and behaviour of vacancies depends on this stress state (Aziz, 1997). Indeed, the local stress tensor defines an additional intensive property that permits a complete description of the conditions of local equilibrium, within the oxide scale and its substrate, compatible with the existence of a vacancy gradient.

This phenomenon of vacancy injection is commonly considered to be restricted to cationic growing scales. However, vacancy injection could also

accompany the growth of an anionic growing scale if, for any reason, the scale/substrate interface is unable to move. In that case, relation [2.4] must be written:



Relation [2.8] describes the jumps of metal atoms to ledges or oxide misorientation dislocations while leaving metal vacancies  $\underline{V}_M$  behind them. Such jumps and vacancy creations within the metal lattice even have the advantage of providing some available space to accommodate the local volume increase associated with the formation of new oxide lattice sites along the scale/substrate interface. Therefore, for the specific question of vacancy injection, no real distinction has to be made between cationic and anionic growth because the origin of this phenomenon, when it could occur, is only linked to the blocking of interface displacement, not to the growth mode.

## 2.6 Conclusions and future trends

The major role of diffusion and related mass transport processes in scale growth is well recognized and proven. The validity and interest of Wagner's theory of oxidation was again demonstrated by the recent work of Mrowec for the oxidation of pure nickel at temperatures higher than 1100°C (Mrowec and Grzesik, 2004). However, there are still some controversial questions and problems such as, for example, the deviations from Wagner's theory that are commonly observed in the oxidation behaviour of many metallic materials. Growth stresses, vacancy injection and the reactive element effect are among the many questions that still need to be investigated for a better understanding and modelling of scale growth processes and kinetics.

A better knowledge of the role of the scale/substrate interface may help in the solving of some of these pending questions. Indeed, as illustrated in Section 2.3.1, there is a clear similarity between oxide scale growth and growth of a reaction layer in a diffusion couple. Therefore, the usual approach of interdiffusion processes, particularly the distinction between the mass-centred frame of reference and lattice-fixed frame of reference and its origin, can be quite useful for analysing the scale growth processes. This approach was used in Section 2.3.2 to define the conditions, valid for pure metals or ideal solid solutions, for stress-free growth of oxide scales. The extension of this analysis of scale growth to non-ideal solid solution or intermetallic compounds is possible, and could be quite useful, if required data such as partial molar volume of all constituents, and their variation with composition, are known. However, the distinct nature of vacancies in a disordered solid solution (thermal point defects) and in an ordered intermetallic compounds (structural point defects) needs to be carefully considered.

In addition, the development of experimental techniques and methods

permitting an accurate determination of the relative translation of  $M$ ,  $K_M$  and  $K_{Ox}$  planes would be of great help in the determination of growth stress sources and in the modelling of the corresponding stress state.

One important point is the combined action and effect of interface structure and interface reactions. The development of this kind of model could lead to a new approach to questions linked to the effect of impurities and their segregation, to the effect of reactive elements or to the coupling between mechanical and oxidation behaviour, which could be of major importance in the determination of service lifetime for high-temperature components.

All these possible developments could permit a better understanding of the dynamic behaviour of the scale/substrate interface during scale growth. Such an understanding could, in addition, introduce new opportunities to control the oxidation behaviour of high temperature materials and to improve their oxidation resistance.

## 2.7 Acknowledgement

I am greatly indebted to Professor Robert A. Rapp from The Ohio State University for the many years of common work and collaboration that led to most of the topics and ideas presented here.

## 2.8 References

- Aziz M J (1997), ‘Thermodynamics of diffusion under pressure and stress: relation to point defect mechanisms’, *Appl Phys Lett*, 70(21), 2810–2812.
- Bastin G F and Rieck G D (1974), ‘Diffusion in the titanium–nickel system. Part 1’, *Met Trans A*, 5A, 1817–1826.
- Bauza D (2001), ‘Thermal oxidation of silicon and Si-SiO<sub>2</sub> interface morphology, structure and localised states’, in Nalwa H S, *Handbook of Surfaces and Interfaces of Materials*, San Diego, CA, Academic Press, 1, 115–216.
- Birks N, Meier G H and Pettit F S (2006), *Introduction to the High Temperature Oxidation of Metals*, Cambridge, Cambridge University Press.
- Bobeth M, Gutkin M, Pompe W and Romanov A E (1998), ‘Modelling of vacancy diffusion and pore formation during parabolic oxide growth’, *Phys Stat Sol (a)*, 165, 165–184.
- Boettinger W J, McFadden G B, Corriel S R, Sekerka R F and Warren J A (2005), ‘Lateral deformation of diffusion couples’, *Acta Mater*, 53, 1995–2008.
- Bollmann W (1970), *Crystal Defects and Crystalline Interfaces*, Berlin, Springer.
- Calvarin G, Molins R and Huntz A M (2000), ‘Oxidation mechanism of Ni-20Cr foils and relation with the oxide microstructure’, *Oxid Met*, 53(1/2), 25–48.
- Clarke D R (2003), ‘The lateral growth strain accompanying the formation of a thermally grown oxide’, *Acta Mater*, 51, 1393–1407.
- Dybkov V I (2002), *Reaction-diffusion and Solid-state Chemical Kinetics*, Kiev, Ukraine, IPMS Publications.
- Ernst F (1995), ‘Metal–oxide interfaces’, *Mat Sci Eng Rep*, R14(3), 97–156.

- Francis R and Lees D G (1989), 'Evidence for vacancy injection during the oxidation of iron', *Mat Sci Eng A*, 120–121, 97–99.
- Haugsrud R (2003), 'On the high temperature oxidation of nickel', *Corr Sci*, 45, 211–235.
- Hirth J P (1991), 'Interface dislocations and ledges in oxidation and diffusional phase transformations', *Met Trans A*, 22A(6), 1331–1339.
- Hirth J P, Pieraggi B and Rapp R A (1995), 'The role of interface dislocations and ledges as sources/sinks for point defects in scaling reactions', *Acta Metall Mater*, 43(3), 1065–1073.
- Hobbs L W, Sawhill H T and Tinker M T (1983), 'Defect microstructures in nickel monoxide scales and nickel/nickel monoxide interfaces', *Radiation Effects*, 74(1–4), 291–297.
- Hobbs L W, Rosen Benezra V, Mangin S P, Treska M and Hunter G (2005), 'Oxidation microstructures and interfaces in the oxidized zirconium', *Int J Appl Ceram Techn*, 2(3), 221–246.
- Kofstad P (1988), *High Temperature Corrosion*, London, Elsevier.
- Leseur M and Pieraggi B (1985), 'Structure of metal–oxide interfaces', *J Phys*, 46(C4), 135–142.
- Manning M I (1979), 'Geometrical effects on oxide scale integrity', *Corr Sci*, 21(4), 301–316.
- Mrowec S and Grzesik Z (2004), 'Oxidation of nickel and transport properties of nickel oxide', *J Phys Chem Sol*, 65, 1651–1657.
- Paul A, van Dal M J H, Kodentsov A A and van Loo F J J (2004), 'The Kirkendall effect in multiphase diffusion', *Acta Mater*, 52, 623–630.
- Peraldi R, Monceau D and Pieraggi B (2002), 'Correlations between growth kinetics and microstructure for scales formed by high-temperature oxidation of pure nickel. I. Morphologies and microstructures', *Oxid Met*, 58(3/4), 249–273.
- Perusin S, Viguier B, Monceau D, Ressier L and Andrieu E (2004), 'Injection of vacancies at metal grain boundaries during the oxidation of nickel', *Acta Mater*, 52, 5375–5380.
- Philibert J (1991), *Atom Movements: Diffusion and Mass Transport in Solids*, Les Ulis, France, Editions de Physique.
- Pieraggi B (1983), 'Geometrical approach of the structure of metal–oxide interfaces', in Yan M F and Heuer A H, *Advances in Ceramics*, 6, *Character of Grain Boundaries*, Columbus, OH, The American Ceramic Society, 117–128.
- Pieraggi B and Dabosi F (1980), 'Structure of metal–oxide interfaces', *J Mic Spect Elec*, 5(4), 489–498.
- Pieraggi B and Rapp R A (1988), 'Stress generation and vacancy annihilation during scale growth limited by cation-vacancy diffusion', *Acta Metall*, 36(5), 1281–1289.
- Pieraggi B, Rapp R A, van Loo F J J and Hirth J P (1990), 'Interfacial dynamics in diffusion-driven phase transformations', *Acta Metall Mater*, 38(9), 1781–1788.
- Pieraggi B, Rapp R A and Hirth J P (1995), 'Role of interface structure and interfacial defects in oxide scale growth', *Oxid Met*, 44(1/2), 63–79.
- Pond R C and Hirth J P (1994), 'Defects at surfaces and interfaces', *Sol Stat Phys*, 47, 287–365.
- Rapp R A (1985), 'The high temperature oxidation of metals forming cation-diffusing scales', *Met Trans A*, 15A(5), 765–782.
- Rhouta B and Pieraggi B (2001), 'Microstructural characterisation of the oxide scale grown at the interface between PSZ top coat and MCRAIY bond coat', *Mat Sci Forum*, 369–372(2), 687–694.

- Stringer J (1970), 'Stress generation and relief in growing oxide films', *Corr Sci*, 10(5), 513–543.
- van Loo F J J (1990), 'Multiphase diffusion in binary and ternary solid-state systems', *Prog Sol State Chem*, 20(1), 47–99.
- van Loo F J J, Pieraggi B and Rapp R A (1990), 'Interface migration and the Kirkendall effect in diffusion-driven phase transformations', *Acta Metall Mater*, 38(9), 1769–1779.

# 3

## Transition between external and internal oxidation of alloys

---

Y HE, University of Science and Technology Beijing, China, and  
Z LI and W GAO, The University of Auckland, New Zealand

### 3.1 Introduction

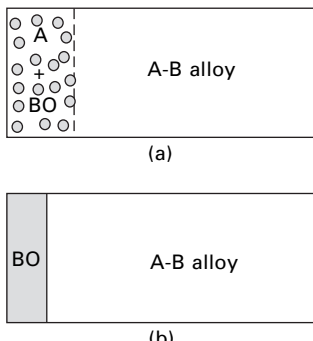
High temperature oxidation of alloys is a much more complex phenomenon compared with the oxidation of pure metals. Because the components of an alloy have different affinities for oxygen, and the reacting atoms do not diffuse at the same rates in the oxides or in the alloy substrates, various kinds of oxides may form on or in the alloys, and the oxides formed on the alloy surface or in the alloy substrate will not contain the same relative amounts of the alloy constituents. When oxygen and metal atoms diffuse and react at the surface of an alloy, a continuous or discontinuous external oxide scale may form on the surface. This process is termed ‘external oxidation’. When oxygen dissolves and diffuses into the alloy substrate during exposure at high temperatures, the less noble components may react with oxygen to form oxide particles within the alloy matrix. This process is called ‘internal oxidation’. Similar processes also occur when the oxidant is sulfur, carbon or nitrogen [1].

The resistance to high temperature oxidation of alloys is determined mainly by the formation of external oxide scales. Therefore, oxidation-resistant alloys should have the ability to form a stable and slow-growing oxide scale such as  $\text{Al}_2\text{O}_3$ ,  $\text{Cr}_2\text{O}_3$  or  $\text{SiO}_2$  on the outer surfaces to prevent their substrates from further oxidation. It is generally observed that when the solute concentration in an alloy is greater than a critical value, selective external oxidation will take place. Otherwise, oxygen could dissolve and diffuse into the alloy and react with the solute metal, forming internal oxides and causing deterioration of the mechanical properties of the alloy. The aim of studies on the internal oxidation behaviours of high temperature oxidation-resistant alloys is to avoid this oxidation process or to prevent undesirable internal oxidation, which is related to the transition between internal and external oxidation of alloys. This transition is normally called ‘the transition from internal to external oxidation’ [2,3]. On the other hand, internal oxidation of alloys is a well-known process that can be used advantageously to generate oxide

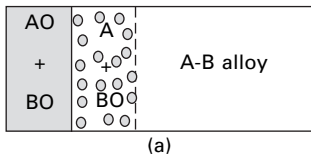
dispersion strengthened (ODS) materials [4,5]. For this purpose, a suitable condition is required to maintain the progress of internal oxidation in the alloy substrate. This is also related to the transition between internal and external oxidation of alloys. But in this case, this transition should be called ‘the transition from external to internal oxidation’, compared with the former case.

The transition phenomena between external and internal oxidation of alloys are very complex. For simplification, such transitions can be divided into two main types according to the composition of the oxides formed on or in the alloys [6]. In the first type of transition, the external oxide scale and the internal oxide particle have the same composition, as shown in Fig. 3.1. This type of transition takes place between the growth processes of internal oxide particles in the alloy substrate (Fig. 3.1a) and an exclusive oxide scale on the alloy surface (Fig. 3.1b), under the condition that only the solute metal in the alloy can oxidize. In the second type of transition, the external oxide scale has a composite structure, as shown in Figs 3.2a and 3.2b. The composite oxide scale (AO + BO) represents mixtures, compounds or layers of AO and BO under different oxidizing conditions. This type of transition takes place between the formations of the internal oxide particles beneath the composite oxide scale (Fig. 3.2a) and a composite oxide scale on the alloy surface (Fig. 3.2b), under the condition that oxidation of all elements in the alloy can occur. In addition, there is a possibility of another type of transition between the growth processes of a composite oxide scale (Fig. 3.2b) and an exclusive oxide scale on the alloy surface (Fig. 3.2c) [7].

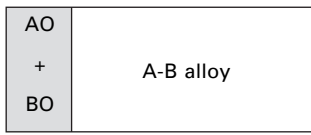
The principal features and theoretical models for the transitions between external and internal oxidation of alloys have been studied under relatively simple oxidation conditions. Wagner [2] was the first to develop a theoretical



3.1 Wagner’s model of the transition from internal to external oxidation of alloy A-B under the condition where only B can be oxidized: (a)  $N_B$  is less than the critical content for the transition; (b)  $N_B$  is higher than the critical content for the transition.



(a)



(b)



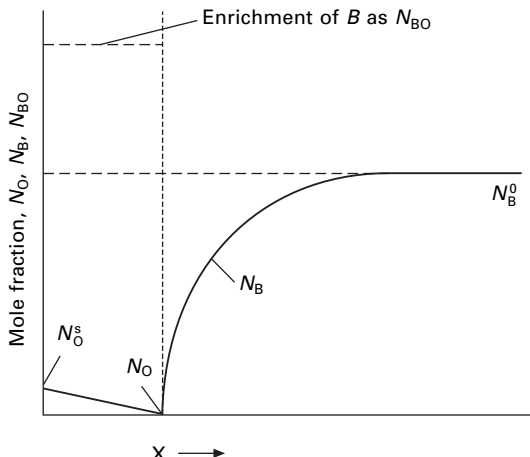
(c)

**3.2 Models of transitions under the condition that all elements in the alloy can oxidize:** transition from internal oxide particles (a) to external composite oxide scale (b); and transition from external composite oxide scale (b) to external exclusive oxide scale (c).

analysis for the transition from internal to external oxidation of a binary alloy in which the base metal *A* is noble and the solute metal *B* can be oxidized, as the first type of transition shown in Fig. 3.1. In Wagner's model (as shown in Fig. 3.3), the oxidation process on the alloy surface was not considered, and the internal oxidation was solely controlled by lattice diffusion. It was assumed that this transition was caused by blocking the inward diffusion of oxygen upon the formation of internal oxides with a critical volume fraction in the alloy substrate. According to Wagner's theory, the critical volume fraction of the internal oxide ( $g^*$ ) and the critical concentration of the solute metal *B* in the alloy *A-B* needed for the transition from internal to external oxidation,  $N_{B^+}^0$ , follows the equation:

$$N_{B^+}^0 = \left( \frac{\pi g^* N_O^s D_O V_M}{2 D_B V_{OX}} \right)^{\frac{1}{2}} \quad 3.1$$

where  $N_O^s$  is the atomic oxygen concentration on the alloy surface,  $D_O$  and  $D_B$  are the diffusivities of oxygen and solute *B* in the alloy, and  $V_M$  and  $V_{OX}$  are the molar volumes of the alloy and the oxide, respectively. This theory was further developed by Smeltzer and Whittle [8]. Rapp [3,9] tested the validity of this theory with Ag-In alloys and his experimental results agreed well with Eq. (3.1).



3.3 Concentration profiles of O and B atoms for an enrichment of *B* as BO in the internal oxidation zone of *A-B* alloy.

However, it should be noted that Eq. (3.1) describes an extreme condition of the internal oxidation process, i.e., the extent to which the internal oxidation can develop under the critical condition of the transition. When a stable exclusive external oxide scale forms, internal oxides might not have formed in the alloy at all. Therefore, the formation of internal oxides might not be necessary for the formation of an external oxide scale. In other words, the internal oxidation process can be completely avoided by the formation of an external oxide scale.

It is interesting to note that in another theoretical analysis for the selective oxidation of alloys, Wagner did not consider the internal oxidation process at all, and derived the critical concentration of solute *B* required to maintain the growth of an external *BO* scale on the alloy *A-B*, or to avoid the formation of internal *BO* particles in the alloy *A-B* substrate, as the following [10]:

$$N_B^0 = \frac{V_M}{16z_B} \left( \frac{\pi k_p}{D_B} \right)^{\frac{1}{2}} \quad 3.2$$

where  $k_p$  is the parabolic rate constant for the growth of the oxide scale, and  $z_B$  is the valence of *B*. From Eq. (3.2), it can be seen that the formation of an external oxide scale is not related to the parameters of internal oxidation used in Eq. (3.1), e.g., the critical volume fraction of oxide ( $g^*$ ) and the diffusivity of oxygen in the alloy.

For the second type of transition shown in Fig. 3.2, Eq. (3.2) gives the criterion for the transition between the states shown in Figs 3.2b and 3.2c, but Eq. (3.1) cannot be used directly as a criterion for the transition between the states shown in Figs 3.2a and 3.2b. Therefore, quantitative analysis on

this type of transition is needed. Rhines *et al.* [11] and Maak [12] developed analytic solutions for the kinetics of internal oxidation combined with external scale formation, while Wang *et al.* [13] proposed a rigorous analysis on the competing scale formation by considering both thermodynamic and kinetic requirements. The criterion developed by Wang *et al.* provided a better approximation for the actual value of the minimum solute concentration for the exclusive formation of its oxide scale. The model could be extended in a semi-quantitative manner to provide a criterion for the minimum solute concentration in the alloy required for the transition from internal to external scale formation, implying that the two theories developed by Wagner could be combined together. Recently, Zhang *et al.* [7] discussed the criteria for the transition from the internal oxidation of solute metal beneath an external composite oxide scale to the formation of an external composite oxide scale, and for the transition from the formation of an external composite oxide scale to the formation of an exclusive oxide scale. However, the concept of internal to external scale formation was still used in these analyses, which is the key point to be discussed in this chapter.

He and his co-workers [14–19] studied the oxidation behaviours of Ag-In, Co-Cr, Ni-Al and Ni-Cr binary alloys under ultra-low oxygen pressure atmospheres in which the solvent in the alloys does not oxidize. They found that continuous external oxide scales could form on all alloy surfaces, especially for the specimens after a short exposure. More importantly, the formation and growth of external oxide scales may or may not be accompanied by the formation of internal oxides in the alloy matrix. Based on these experimental results, they proposed that the transition between the oxidation models of an alloy should be from external to internal oxidation [18,19]. In this chapter, their works on this subject will be summarized and discussed briefly to get a better understanding of the transition between external and internal oxidation of alloys.

## 3.2 Thermodynamics of alloy oxidation

### 3.2.1 Thermodynamics of chemical reactions in alloy oxidation

Excellent reviews on the thermodynamics of alloy oxidation have been given by Whittle [20] and Douglass [21]. In this chapter, we will refer mainly to the analyses proposed by Wang *et al.* [13] in discussing the thermodynamics of oxidation for binary alloys.

Considering an alloy *A-B* with *B* having a greater affinity to oxygen than *A*, the oxidation reactions for all the alloy constituents can be expressed simply as



for  $A$ , and



for  $B$ . To simplify the analysis, it is assumed that  $AO$  and  $BO$  are insoluble in each other. The formation of a mixed phase such as a spinel phase  $A_{1+x}B_{2-x}O_4$  ( $A$  = Co, Ni or Fe;  $B$  = Cr or Al) will not be considered. When reactions (3.3) and (3.4) are at equilibrium, their equilibrium constants,  $K_1$  and  $K_2$ , can be expressed as

$$K_1 = \frac{a_A P_{\text{O}_2}^{1/2}}{a_{AO}} \quad 3.5$$

$$K_2 = \frac{a_B P_{\text{O}_2}^{1/2}}{a_{BO}} \quad 3.6$$

where  $a$  is the thermodynamic activity of either the alloying element or the oxide.

The activity of the oxide is assumed to be 1. The activities of the alloying constituents  $A$  and  $B$  are proportional to their atomic fractions,  $N_i$ , so that  $a_i = \gamma_i N_i$ , where  $\gamma_i$  is the activity coefficient, and  $N_A + N_B = 1$ . Thus, the equilibrium exists between  $AO$ ,  $BO$  and alloy  $A-B$  at

$$P_{\text{O}_2}^{e,o} = \left( \frac{K_1}{\gamma_A} + \frac{K_2}{\gamma_B} \right)^2 \quad 3.7$$

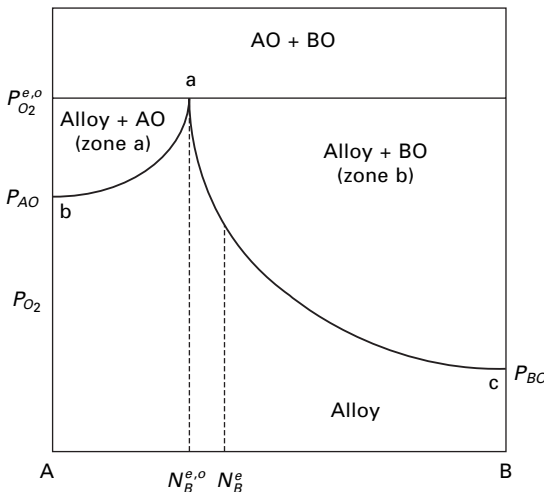
and

$$N_B^{e,o} = \frac{1}{(K_1/K_2)(\gamma_B/\gamma_A) + 1} \quad 3.8$$

This is shown schematically in Fig. 3.4, in which  $P_{AO}$  and  $P_{BO}$  are the dissociation pressures of  $AO$  and  $BO$ , respectively. For a given binary alloy system at a particular temperature,  $N_B^{e,o}$  is a constant. Therefore, alloys with a composition of  $N_B < N_B^{e,o}$ , in zone a, will form  $AO$  preferentially, whereas alloys with a composition of  $N_B > N_B^{e,o}$ , in zone b, will form  $BO$  preferentially. However, from the thermodynamic diagram shown in Fig. 3.4, it is impossible to determine such oxidation processes as being internal or external.

### 3.2.2 Thermodynamics of oxide nucleation at the alloy surface and in the alloy substrate

The oxidation of alloys is not only a chemical process, but also a physical process – the formation of new phases. The thermodynamics of these two processes therefore should be considered equally. According to the classical



3.4 Schematic diagram showing the stability of an *A-B-O* system.

nucleation theory, the free energy change,  $\Delta G$ , for the formation of a nucleus is [22]:

$$\Delta G = \Delta G_V V_{\text{nul}} + \sigma S + \varepsilon V_{\text{nul}} \quad 3.9$$

where  $\Delta G_V$  is the free energy change for the formation of oxide per unit volume,  $\sigma$  is the surface energy,  $\varepsilon$  is the strain energy,  $S$  is the surface area of an oxide nucleus and  $V_{\text{nul}}$  is its volume.

The nuclei with a radius larger than the critical radius,  $r^*$ , will grow spontaneously. The total free energy change,  $\Delta G^*$ , for the formation of an oxide nucleus with the critical radius is the activation barrier to nucleation, which is given by:

$$\Delta G^* = \frac{16\pi\sigma^3}{3(\Delta G_V + \varepsilon)^2} \quad 3.10$$

Then, from the absolute reaction rate theory, the nucleation rate,  $J_{\text{nul}}$ , can be expressed as:

$$J_{\text{nul}} = n v \exp\left(\frac{-E}{RT}\right) \exp\left(\frac{-\Delta G^*}{RT}\right) \quad 3.11$$

where  $n$  is the atom number per unit volume,  $v$  is the vibration frequency of the atom and  $E$  is the diffusion activation energy of the atom. From Eqs (3.9)–(3.11), it can be seen that  $\Delta G_V$  is the real driving force while  $\sigma$  and  $\varepsilon$  are the resistant forces for the formation of an oxide nucleus.

It is reasonable to deduce that it should be easier for oxide nucleation to take place on the surface than in the substrate of an alloy. There are several

reasons. Firstly, the value of  $\Delta G_V$  for the formation of an oxide nucleus at the gas/alloy interface should be more negative than that in the alloy substrate, since the activities of oxygen and solute  $B$  at the gas/alloy interface are higher than at the internal oxidation front, especially at the initial oxidation stage. Secondly, the surface energy  $\sigma$  for the formation of the heterogeneous oxide nuclei at the gas/alloy interface is generally lower than that of the homogeneous oxide nuclei in the alloy, since Douglass [23] pointed out that the interfacial energies in the internal oxidation systems were high. Finally, the Pilling–Bedworth ratios for many protective oxides are greater than 1; compressive stresses will be generated in the alloy substrate [24]. When oxide nuclei form at the gas/alloy interface, the stresses can be effectively released and therefore the strain,  $\varepsilon$ , is low. When oxide nuclei form inside the alloy, the volume expansion will be constrained and therefore  $\varepsilon$  is high. Taking all these factors into account, we may conclude that oxide nuclei form more easily at the gas/alloy interface than in the alloy substrate.

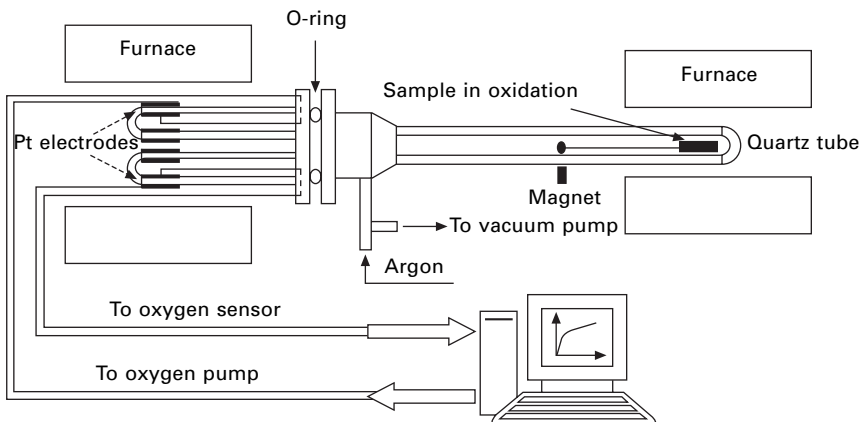
### **3.3 Model for the transition from external to internal oxidation of alloys**

Comparing the two important theories developed by Wagner, it can be found that, for the first type of transition, these two theories actually describe the same criterion, i.e. the criterion for such a transition is equal to the criterion for the formation of a stable external oxide scale. However, these two theories are established on different bases. The first is based on the nucleation and growth of oxides in the alloy substrate, and the second is based on the growth of oxides on the alloy surface. Therefore, in order to obtain a better understanding of these two theories and the oxidation transition behaviour of an alloy, a theory describing the transition between external and internal oxidation of alloys should be established. This model should be based on full consideration of the nucleation and growth of oxides both on the alloy surface and in the alloy substrate.

#### **3.3.1 Experimental observations**

Ni-Cr and Co-Cr alloys are typical single-phase binary alloys. Ni-6Cr, Ni-8Cr, Co-5Cr and Co-10Cr alloys were selected to study the first type of transition between external and internal oxidation under atmospheres with ultra-low oxygen partial pressures  $P_{O_2}$  in which the solvent Ni or Co in the alloys does not oxidize [14,19].

The experimental apparatus is shown schematically in Fig. 3.5. This system uses a solid-state electrochemical oxygen sensor and an oxygen pump to measure and control the oxygen partial pressure in an enclosed reaction system. Our previous results showed that this system can be used to control



3.5 Schematic diagram of the ultra-low oxygen partial pressure controlling system.

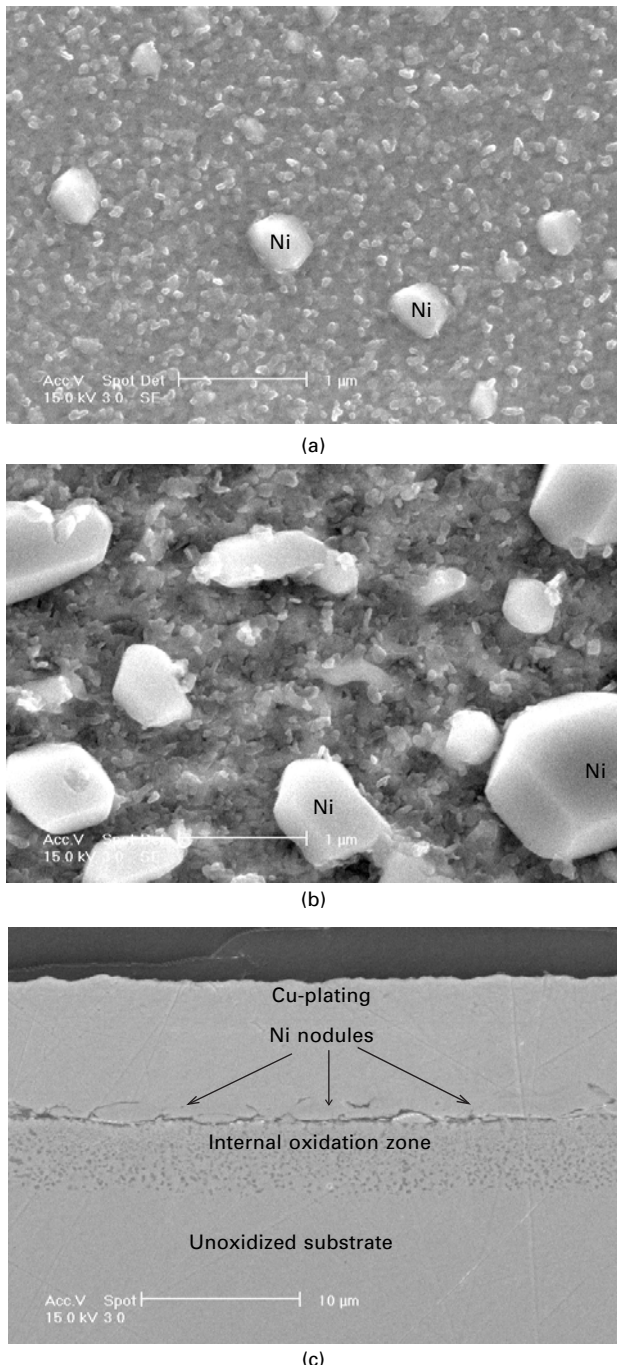
and maintain the oxygen partial pressure in a typical range of  $10^{-23}$  to 5 atm [14,19,25–27]. In these studies, the oxygen partial pressure was lower than the dissociation pressure of NiO/Ni or CoO/Co at the oxidation temperature, so that oxidation of Ni or Co could be completely prevented during exposure. After the  $P_{O_2}$  reached the pre-set value and was stabilized for 2–3 hours, the specimen was pushed into the hot zone of the reaction chamber to start oxidation. After each oxidation run, the specimen was pulled out from the hot zone and cooled down to ambient temperature under an environment of Ar with a low  $P_{O_2}$ . The specimen was then characterized by high resolution scanning microscopy, energy dispersive X-ray spectroscopy, X-ray diffractometry and X-ray photoelectron spectroscopy.

#### *Oxidation of Ni-6Cr alloy*

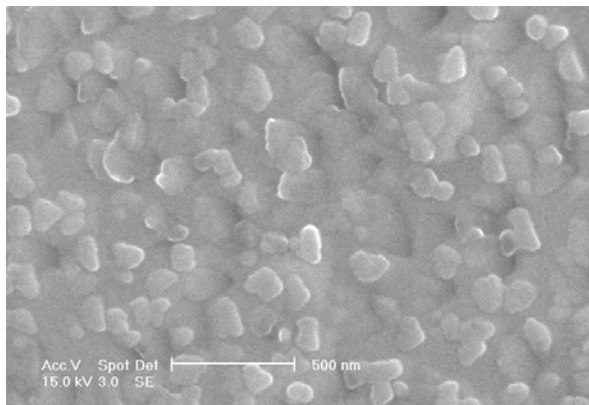
Figure 3.6 shows the surface and cross-section morphologies of the Ni-6Cr alloy after oxidation at 900°C under an oxygen partial pressure of  $10^{-9}$  Pa for 2 min (Fig. 3.6a),  $10^{-11}$  Pa for 40 hr (b) and  $10^{-9}$  Pa for 40 hr (c). It can be seen that after both 2 min and 40 hr oxidation, oxide scales with small particles and big metal nodules appeared on the surfaces (Figs 3.6a and 3.6b); an internal oxidation zone can be seen in the cross-sectional image as well (Fig. 3.6c).

#### *Oxidation of Ni-8Cr alloy*

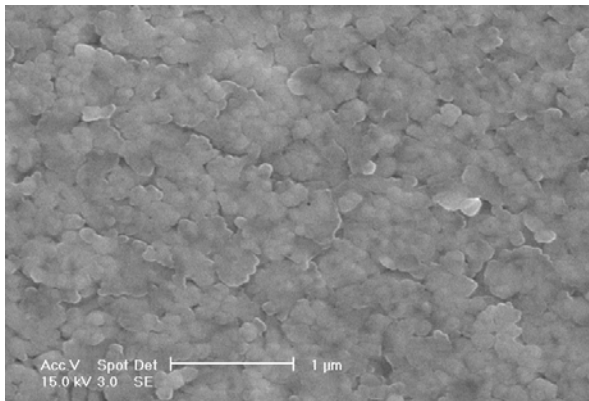
Figure 3.7 shows the surface and cross-section morphologies of the Ni-8Cr alloy after oxidation at 900°C under an oxygen partial pressure of  $10^{-13}$  Pa



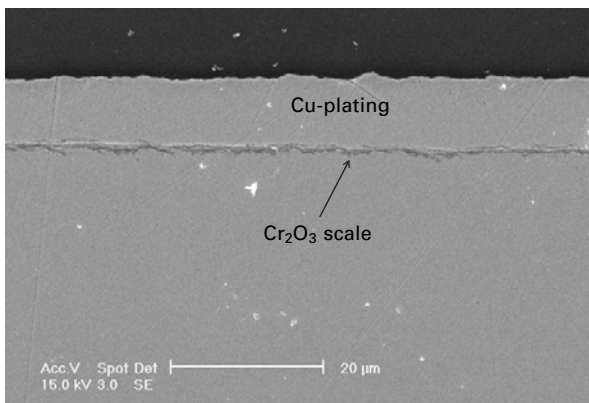
3.6 Surface and cross-section morphologies of Ni-6Cr alloy after oxidation at 900°C under different conditions: (a)  $P_{O_2} = 10^{-9}$  Pa, 2 min; (b)  $P_{O_2} = 10^{-11}$  Pa, 40 hr, and (c)  $P_{O_2} = 10^{-9}$  Pa, 40 hr.



(a)



(b)



(c)

3.7 Surface and cross-section morphologies of Ni-8Cr alloy after oxidation at 900°C under different conditions: (a)  $P_{O_2} = 10^{-13}$  Pa, 2 min; (b) and (c)  $P_{O_2} = 10^{-15}$  Pa, 40 hr.

for 2 min (Fig. 3.7a) and  $10^{-15}$  Pa for 40 hr (b and c). A thin and continuous oxide scale formed on the surface of this alloy.

#### *Oxidation of Co-5Cr alloy*

Figure 3.8 shows the surface and cross-section morphologies of the cast Co-5Cr alloy after oxidation at  $1000^{\circ}\text{C}$  under an oxygen partial pressure of  $10^{-10}$  Pa for 15 min (Fig. 3.8a) and 25 hr (b) and (c). It can be seen that after both 15 min and 25 hr oxidation, oxide scales with small particles and big metal nodules can be observed on their surfaces (Figs 3.8a and 3.8b). An internal oxidation zone can be found in the alloy substrate (Fig. 3.8c), which is similar to the features shown in Fig. 3.6.

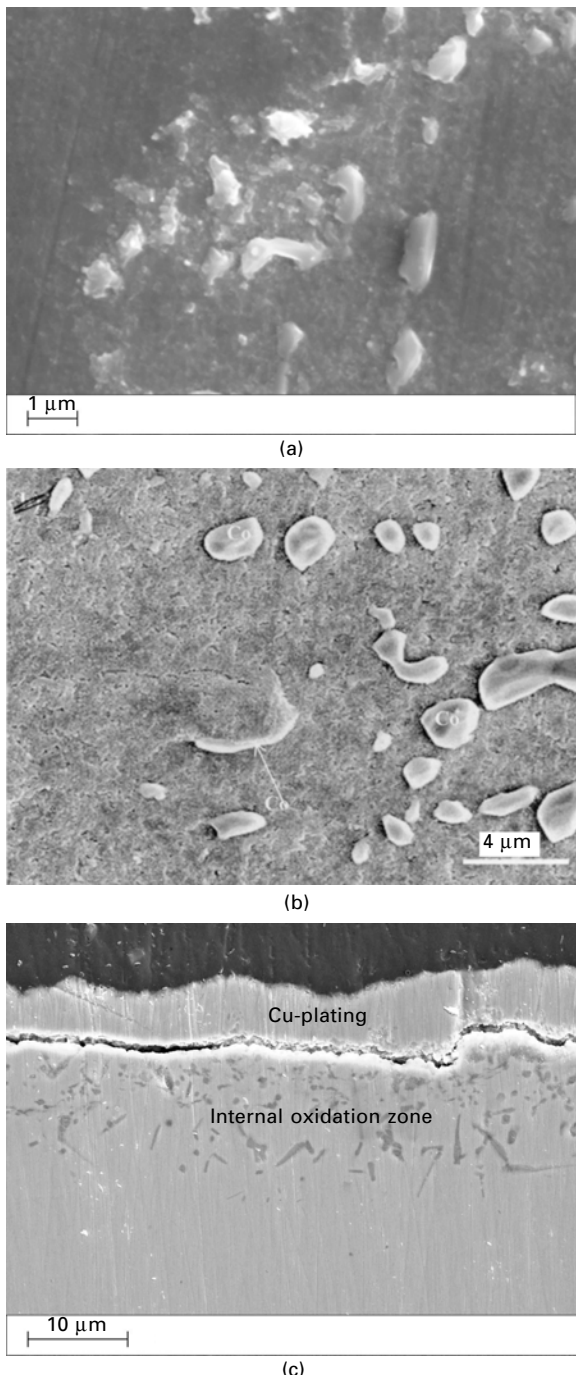
#### *Oxidation of Co-10Cr alloy*

Figure 3.9 shows the surface and cross-section morphologies of the cast Co-10Cr alloy after oxidation at  $1000^{\circ}\text{C}$  under an oxygen partial pressure of  $10^{-10}$  Pa for 15 min (Fig. 3.9a) and 25 hr (b) and (c). It can be seen that a thin and continuous oxide scale formed on the alloy surface.

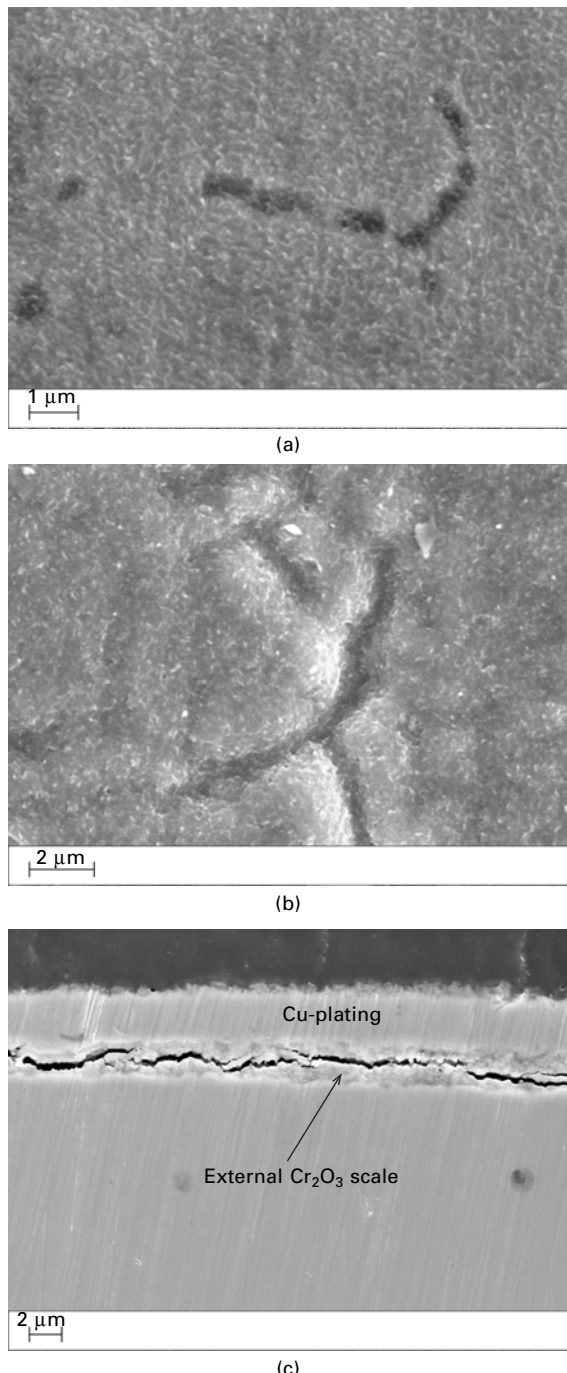
Because these oxidation experiments were performed with an oxygen partial pressure under which Ni and Co could not be oxidized, the oxides formed were only from oxidation of Cr, so the oxides were  $\text{Cr}_2\text{O}_3$ . As a special feature of the internal oxidation of dilute alloys, metal nodules formed on the surfaces, which were Ni and Co for Ni-Cr and Co-Cr alloys, respectively. The compositions and phases of these modules were confirmed by analyses using energy dispersive X-ray spectroscopy (EDS), X-ray diffraction and X-ray photoelectron energy spectroscopy [14,19].

From these experimental results, it can be clearly seen that continuous external  $\text{Cr}_2\text{O}_3$  scales could form on the surfaces of the M-Cr alloys oxidized under all conditions. The formation of these external oxide scales may or may not be accompanied by the formation of internal  $\text{Cr}_2\text{O}_3$  particles in the alloy substrate. In other words, the oxidation started on the alloy surface to form an external  $\text{Cr}_2\text{O}_3$  scale, and then it could proceed into the alloy substrate to form internal  $\text{Cr}_2\text{O}_3$  particles if the Cr concentrations were not high enough. When the Cr content in the M-Cr alloys is higher than the critical value, a protective external  $\text{Cr}_2\text{O}_3$  scale forms on the alloy surface, and the formation of the internal  $\text{Cr}_2\text{O}_3$  particles would then be completely avoided.

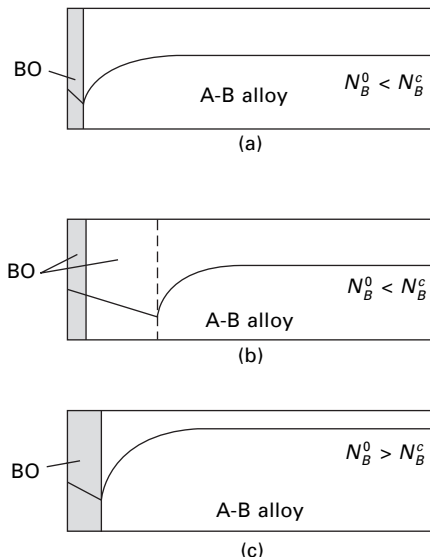
Here, it is necessary to distinguish two concepts: (1) the transition from temporary external oxidation to internal oxidation, i.e., the external oxide scale forms on the alloy surface during the initial oxidation stage (Fig. 3.10a), then oxides form in the alloy within a longer exposure time (Fig. 3.10b); and (2) the transition from permanent external oxidation to internal oxidation, i.e., an external oxide scale forms on the alloy surface without any internal



3.8 Surface and cross-section morphologies of the cast Co-5Cr alloy after oxidation at 1000°C under an oxygen partial pressure of  $10^{-10}$  Pa: (a) for 15 min; (b) and (c) for 25 hr.



3.9 Surface and cross-section morphologies of the cast Co-10Cr alloy after oxidation at 1000°C under an oxygen partial pressure of  $10^{-10}$  Pa: (a) for 15 min; (b) and (c) for 25 hr.



**3.10** Transition models from external to internal oxidation of a binary alloy A-B: the transition from temporary external oxidation (a) to internal oxidation (b), and the transition from permanent external oxidation (c) to internal oxidation (b).

oxide (Fig. 3.10c), only when the oxidizing condition is changed, a transition takes place (from Figs 3.10c to 3.10b). Therefore, transition (1) takes place under a fixed condition, such as a fixed alloy composition or a fixed oxygen partial pressure; while transition (2) takes place since the oxidation conditions, such as the alloy compositions or the oxygen partial pressures, are changed during exposure. Obviously, these new concepts/processes are quite different from the traditional consideration of the transition from internal to external oxidation [18,19].

### 3.3.2 Criterion for the transition from permanent external oxidation to internal oxidation

From the experimental results, it can be found that when only the solute B in the alloy A-B can oxidize, there is a critical bulk composition,  $N_B^c$ , of the alloy, over which an exclusive BO scale can permanently form on the alloy surface. Otherwise the transition from external to internal oxidation will occur. Such a critical bulk composition,  $N_B^c$ , is related not only to the thermodynamic conditions at the oxide scale/alloy interface, but also to the kinetic factors of both the oxide scale and the alloy substrate.

It should be pointed out that kinetically, an equilibrium is rarely achieved during oxidation. The interdiffusion within the A-B alloy is always slower

than that in the oxide scale at the initial oxidation stage, therefore the supply of *B* to the oxide scale/alloy interface is slower than the consumption of *B* for the scale growth. Thus *B* will deplete locally at this interfacial area. It is suggested that when the transition from external to internal oxidation takes place, the interface of oxide scale/alloy should be under an equilibrium state. The equilibrium composition,  $N_B^e$ , of the alloy *A-B* at the oxide scale/alloy interface is a function of the oxygen partial pressure as the line *a-c* in Fig. 3.4, which can be expressed as:

$$N_B^e = f(P_{O_2}) \quad 3.12$$

Based on Wang's analysis [13], the diffusion equation and its boundary conditions can be established for the exclusive formation of *BO* as:

$$\frac{\partial N_B}{\partial x} = D \frac{\partial^2 N_B}{\partial x^2} \quad 3.13$$

$$D \frac{\partial C_B}{\partial x} \Big|_{x=\chi} + C_B(x=\chi) \frac{d\chi}{dt} = \frac{1}{V_{AB}} \frac{d\chi}{dt} \quad 3.14$$

$$N_B(x=\infty) = N_B(t=0) = N_B^0 \quad 3.15$$

where *D* is the interdiffusion coefficient of the alloy, which is assumed to be independent of composition;  $N_B^0$  is the original composition of *B* in the alloy;  $C_B = N_B/V_{AB}$ ,  $V_{AB}$  being the equivalent molar volume of the alloy; and  $\chi$  is the position of the oxide scale/alloy interface with reference to the original alloy interface (i.e.,  $x=0$ ). Obviously  $\chi$  is the depth of the metal consumption zone (MCZ), which is related to the parabolic rate constant for the growth of *BO* by:

$$\chi = \frac{V_{AB}}{V_{BO}} \sqrt{2k_p(P_{O_2})t} \quad 3.16$$

where  $V_{BO}$  is the equivalent molar volumes of *BO*, and  $k_p(P_{O_2})$  is the parabolic rate constant for the growth of *BO*, which is a function of  $P_{O_2}$ . The physical model represented by the above equations is shown schematically in Fig. 3.11.

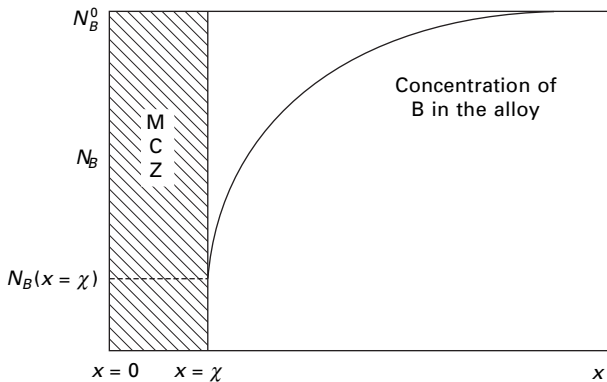
The general solution to this equation group can be expressed as [28]:

$$N_B(x > 0) = C_1 + C_2 \operatorname{erfc} \left( \frac{x}{2\sqrt{Dt}} \right) \quad 3.17$$

where  $C_1$  and  $C_2$  are constants determined by the boundary conditions. Letting  $x \rightarrow \infty$  or  $t \rightarrow 0$ ,  $C_1$  and  $C_2$  can be derived as:

$$C_1 = N_B^0$$

$$C_2 = -[1 - N_B(x=\chi)] \left( \frac{\pi k_p}{2D} \right)^{1/2} \frac{V_{AB}}{V_{BO}} \exp \left( \frac{V_{AB}^2}{V_{BO}^2} \frac{k_p(P_{O_2})}{2D} \right) \quad 3.18$$



3.11 Schematic diagram of the coordinate system used to solve for the concentration of *B* in alloy *A-B*.

Substituting Eqs (3.17) and (3.18) into (3.14), the concentration of *B* in the alloy can be solved as:

$$N_B(x \geq \chi) = N_B^0 - \left( \frac{\pi k_p(P_{O_2})}{2D} \right)^{1/2} \frac{V_{AB}}{V_{BO}} \exp \left( \frac{V_{AB}^2}{V_{BO}^2} \frac{k_p(P_{O_2})}{2D} \right) \operatorname{erfc} \left( \frac{x}{2\sqrt{Dt}} \right) \quad 3.19$$

Thus, at  $x = \chi$  and using Eq. (3.16), the concentration of *B* at the oxide scale/alloy interface can be expressed as:

$$N_B(x = \chi) = N_B^0 - [1 - N_B(x = \chi)]F(u) \quad 3.20$$

where

$$F(u) = \sqrt{\pi u} \exp(u^2) \operatorname{erfc}(u) \quad 3.21$$

with

$$u = \frac{V_{AB}}{V_{BO}} \sqrt{\frac{k_p(P_{O_2})}{2D}} \quad 3.22$$

The  $F(u)$  function is the auxiliary function used by Wagner [29], and can be expressed as follows:

$$F(u) = \sqrt{\pi}u - 2u^2 + \sqrt{\pi}u^3 - 2u^4 + \dots \quad \text{if } u \ll 1 \quad 3.23$$

$$F(u) = 1 - \frac{1}{2}u^{-2} + \frac{3}{4}u^{-4} - \frac{5}{8}u^{-6} + \dots \quad \text{if } u \gg 1 \quad 3.24$$

As discussed above, when *BO* forms on the alloy surface exclusively, the minimum concentration of *B* at the oxide scale/alloy interface must have

$$N_B(x = \chi) = N_B^e \quad 3.25$$

Substituting Eq. (3.25) into (3.20), the critical concentration,  $N_B^0 = N_B^c$ , of the alloy A-B for the exclusive formation of BO on the alloy surface can be expressed as:

$$N_B^c = N_B^e + [1 - N_B^e]F(u) \quad 3.26$$

Because  $D$  is much larger than  $k_p$  for oxidation of alloy A-B,  $u$  is very small and the above equation can be simplified to:

$$N_B^c = N_B^e + [1 - N_B^e] \frac{\sqrt{\pi} V_{AB}}{V_{BO}} \sqrt{\frac{k_p(P_{O_2})}{2D}} \quad 3.27$$

It should be noted that the method used for the derivation of Eq. (3.27) is very similar to Wang's analysis [13]. The meaning, however, is quite different. In Wang's analysis [13],  $N_B^e$  stands for just one point,  $N_B^e = N_B^{e,o}$ , while in the present study  $N_B^e$  is a function of the oxygen pressure as indicated by the line **a-c** in Fig. 3.4. The concentration of solute B at the oxide scale/alloy interface,  $N_B^e$ , is very small, so Eq. (3.27) can be simplified to:

$$N_B^c = \frac{\sqrt{\pi} V_{AB}}{V_{BO}} \sqrt{\frac{k_p(P_{O_2})}{2D}} \quad 3.28$$

If  $N_B^0 \geq N_B^c$ , then

$$N_B^0 \geq \frac{\sqrt{\pi} V_{AB}}{V_{BO}} \sqrt{\frac{k_p(P_{O_2})}{2D}} \quad 3.29$$

Exclusive BO scales can form on the surface of the alloy A-B under the conditions of  $P_{BO} < P_{O_2} \leq P_{O_2}^{e,o}$  and  $P_{O_2} \leq P_{O_2}^{e,o}$ , as shown in Figs 3.1b and 3.2c. Therefore, Eq. (3.29) is a modified Wagner criterion for the formation of an exclusive BO scale, and is similar to Eq. (3.2). If  $N_B^0 < N_B^c$ , Eq. (3.28) gives

$$N_B^0 < \frac{\sqrt{\pi} V_{AB}}{V_{BO}} \sqrt{\frac{k_p(P_{O_2})}{2D}} \quad 3.30$$

Different types of oxides can form. Under the conditions of  $P_{O_2} \geq P_{O_2}^{e,o}$  and Eq. (3.30), a composite oxide scale can form on the alloy surface, as shown in Fig. 3.2b. Under the conditions of  $P_{BO} < P_{O_2} \leq P_{O_2}^{e,o}$  and Eq. (3.30), a transition from temporary external oxidation to internal oxidation can take place (Fig. 3.10b). Under the conditions described by Eq. (3.29), however, this is the transition from permanent external to internal oxidation (Figs 3.10c to 3.10b). Therefore, under the condition of  $P_{O_2} \geq P_{O_2}^{e,o}$ , Eq. (3.28) can be used as the criterion for the transition between the growth processes of an exclusive oxide scale and a composite oxide scale; while under the conditions of  $P_{BO} < P_{O_2} \leq P_{O_2}^{e,o}$ , it can be used as the criterion for the transition from permanent external to internal oxidation of the A-B alloy.

Comparing the present analysis with Wagner's theory on the transition from internal to external oxidation of alloys [2], it can be seen that there are several important differences. Firstly, in Wagner's theory, the formation of an external oxide scale is related to the oxygen diffusion in the alloy, while in the present model it is not, since the transition actually takes place from external oxidation to internal oxidation. The diffusion of oxygen in the alloy substrate has no influence on the transition before it occurs. Only after the transition does the diffusion of oxygen affect the internal oxidation rate.

Secondly, in Wagner's theory, a critical volume fraction,  $g^*$ , of the internal oxides is needed for the transition from internal to external oxidation. In the present model,  $g^*$  is no longer needed. However, it gives a better understanding on why, under the critical condition for this transition, there is a critical volume fraction of oxide ( $g^*$ ) formed in the internal oxidation zone. The reason is that the characteristics of nucleation and growth of oxides on the alloy surface and in the alloy substrate are quite different. The nucleation and growth of oxides on the surface of an alloy are easier than inside the alloy: the oxide volume fraction of a continuous  $BO$  scale formed on the alloy surface must be 1, while the internal oxide volume fraction must be less than 1. For the transition from temporary external oxidation to internal oxidation of alloys, the internal oxide volume fraction must be changed with the alloy composition, since the transition from permanent external oxidation to internal oxidation is an extreme case of the transition from temporary external oxidation to internal oxidation, and occurs under a special condition, i.e., with a certain alloy composition, and the internal oxide volume fraction must be a constant,  $g^*$ , which is smaller than 1.

Thirdly, in Wagner's theory, there are no factors representing the growth of an oxide scale, while in the present model, as shown in Eq. (3.28), this is considered by introducing the parabolic rate constant,  $k_p$ , of the oxide scale. Therefore, all factors influencing  $k_p$  will also affect the transition from permanent external oxidation to internal oxidation of alloys. For example,  $k_p$  is a function of  $P_{O_2}$  and decreases with a decrease of  $P_{O_2}$  [30], thus, the critical concentration,  $N_B^c$ , should also decrease with a decrease of  $P_{O_2}$ . Then the gettering effect in multi-component alloys can be explained. When the Cr content is sufficiently high in the Ni-Cr-Al alloy, a continuous layer of  $Cr_2O_3$  can form on the alloy surface. The oxygen partial pressure at the oxide scale/alloy interface decreases to a low level, so the  $k_p$  of the  $Al_2O_3$  scale formed beneath the  $Cr_2O_3$  layer decreases, and the critical content of Al for the formation of  $Al_2O_3$  scale also decreases.

The reactive element effects on the transition can also be explained by the present model. Application of reactive elements or their oxides onto the alloy surface or into the alloy substrate can change the growth mechanisms of oxide scales [12]. For undoped M-Cr alloys, the growth of  $Cr_2O_3$  scales is sustained mainly by the outward diffusion of  $Cr^{+3}$  ions, resulting in the

formation of pores at the oxide scale/alloy interface, and the oxide forms at the outer surface of the scale. For M-Cr alloys with reactive elements or their oxides, the oxide scale growth is maintained by the inward diffusion of oxygen along the grain boundaries. New oxides, therefore, form at the oxide scale/alloy interface, leading to a stronger adhesion between the oxide scale and the alloy. Since the diffusivity of oxygen is several orders of magnitude smaller than that of Cr in the  $\text{Cr}_2\text{O}_3$  scale, the growth rate of the  $\text{Cr}_2\text{O}_3$  scale decreases markedly, resulting in a reduced parabolic rate constant,  $k_p$ . According to Eq. (3.28), this will also reduce the critical concentration,  $N_B^c$ , for the transition from permanent external oxidation to internal oxidation of the alloy.

Finally, although the critical concentrations of  $B$  in the alloy  $A-B$  for both transition models are inversely proportional to  $D^{1/2}$ , where  $D$  is the diffusivity of  $B$  in the alloy, their physical meanings are quite different. In Wagner's theory, the diffusion boundary for  $B$  is at the internal oxidation front; an increase of  $D$  can increase the internal oxide volume fraction in the alloy substrate. On the other hand, in the present analysis, the diffusion boundary for  $B$  is at the oxide scale/alloy interface; an increase of  $D$  increases the formation of external oxide scale on the alloy surface. For example, surface micro- or nano-crystallization of M-Cr alloys can increase the outward diffusion of Cr along grain boundaries with a higher density, thus the diffusivity in Eq. (3.28) increases, which decreases  $N_B^c$  and promotes the formation of permanent  $\text{Cr}_2\text{O}_3$  scale on M-Cr alloys [31,32].

### 3.3.3 Formation of pure solvent metal nodules during the transition from external to internal oxidation of alloys

As described above, nodules of pure solvent metals, Ni and Co, form on the surface of M-Cr alloys. Guruswamy *et al.* [33] established a model to explain this phenomenon. Douglass [23] summarized the mechanisms for the nodule formation and suggested that the high stresses generated by the internal oxide precipitation in the alloy substrate caused extrusion of the solvent element through dislocation pipes, leading to extensive nodule formation, either on grain boundaries or on the grains, depending on the alloy and oxidizing conditions.

Since a continuous oxide scale can form on the alloy surface before the formation of internal oxide precipitates, it is reasonable to suggest that the external oxide scale is another important factor in determining the formation of solvent metal nodules. When the internal oxide precipitation forms in the alloy substrate, stresses are generated, volume expansion occurs and the position of the alloy surface moves outward correspondingly. This volume expansion should be constrained by the oxide scale formed on the alloy

surface, thus a tensile stress is generated on the oxide scale. Meanwhile, the oxide scales with structural defects are easy to crack under the tensile stress. Consequently, the solvent element could be extruded out at these weak locations to form nodules on the alloy surface, as shown in Figs 3.6a, 3.6b, 3.8a and 3.8b.

### 3.4 Summary

Extensive experimental observations demonstrate that on a binary *A-B* alloy oxidized in an atmosphere with a low oxygen partial pressure (*A* will not be oxidized), a continuous external *BO* scale always forms on the alloy surface after a short exposure. The formation of this external oxide scale may or may not be accompanied by the formation of internal oxides in the alloy substrate. In other words, the oxidation process starts on the alloy surface to form an external *BO* scale, and then it may or may not proceed into the alloy substrate to develop internal *BO* particles, depending on the alloy composition and the oxidation condition. When the content of *B* in the *A-B* alloy is higher than a critical value, a protective external *BO* scale can form and stay on the alloy surface, and the formation of internal *BO* particles in the alloy substrate can be completely avoided.

It is proposed that the transition of oxidation models for alloys should be from external oxidation to internal oxidation. There are two types of transition: (1) the transition from temporary external oxidation to internal oxidation; and (2) the transition from permanent external oxidation to internal oxidation. The second transition is an extreme case of the first transition process.

The criterion for the minimum solute concentration,  $N_B^c$ , of a binary *A-B* alloy required for the second transition process has been derived based on thermodynamic and kinetic analyses. Using this equation the effects of oxygen partial pressure, addition of rare earth elements, surface micro-crystallization, and the gettering effects on the transition between external and internal oxidations can be explained.

The formation of an external oxide scale is also an important factor in determining the formation of pure solvent metal nodules on the alloy surface during oxidation. The stresses generated by the internal oxide precipitation in the alloy are the driving force for the formation of these nodules. Under the constraint of the external oxide scale, solvent metal could be pushed out at the weak locations of the oxide scale to form nodules on the surface.

### 3.5 Acknowledgements

The work is supported by the Foundation for PhD Research from the Education Ministry of China (Grant No. 2000000815) and New Zealand Asia 2000 Foundations.

### 3.6 References

1. Kofstad P, *High Temperature Corrosion*, London and New York, Elsevier Applied Science, 1988.
2. Wagner C, 'Reaktionstypen bei der Oxydation von Legierungen', *Z. Elektrochem.*, 1959 **63**, 772–782.
3. Rapp R A, 'Kinetics, microstructures and mechanism of internal oxidation, its effect and prevention in high temperature alloy oxidation', *Corrosion*, 1965 **21**, 382–401.
4. Bronsted P and Toftsorensen O, 'Preparation of dispersion-hardened copper by internal oxidation', *J. Mater. Sci.*, 1978 **13**, 1224–1228.
5. Li G B, Sun J B, Guo Q M and Wang R, 'Fabrication of the nanometer Al<sub>2</sub>O<sub>3</sub>/Cu composite by internal oxidation', *J. Mater. Process. Technol.*, 2005 **170**, 336–340.
6. Meier G H, 'A review of advances in high-temperature corrosion', *Mater. Sci. Eng.*, 1989 **A120**, 1–11.
7. Zhang Z G, Gesmundon F, Hou P Y and Niu Y, 'Criteria for the formation of protective Al<sub>2</sub>O<sub>3</sub> scales on Fe-Al and Fe-Cr-Al alloys', *Corr. Sci.*, 2006 **48**, 741–765.
8. Smeltzer W W and Whittle D P, 'The criterion for the onset of internal oxidation beneath the external scales on binary alloys', *J. Electrochem. Soc.*, 1978 **125**, 1116.
9. Rapp R A, 'The transition from internal to external oxidation and the formation of interruption bands in silver-indium alloys', *Acta Metall.*, 1961 **9**, 730–741.
10. Wagner C, 'Theoretical analysis of the diffusion processes determining the oxidation rate of alloys', *J. Electrochem. Soc.*, 1952 **99**, 369–380.
11. Rhines F N, Johnson W A and Anderson W A, 'Rates of high temperature oxidation of dilute copper alloys', *Trans. Metal. Soc. AIME*, 1942 **147**, 205–221.
12. Maak F, 'Zur Auswertung von Messungen der Schichtdicken binärer Legierungen mit innerer Oxydation bei gleichzeitiger äußerer Oxydation', *Z. Metallkd.*, 1961 **52**, 545–546.
13. Wang G, Glesson B and Douglass D L, 'An extension of Wagner's analysis of competing scale formation', *Corr. Sci.*, 1991 **35**, 317–332.
14. He Y D, Li Z W and Gao W, 'Transition from external to internal oxidation of Ni-Cr alloys', *Mater. High Temp.*, 2000 **18S**, 17–22.
15. Gao W, Li Z W and He Y D, 'Solid-state oxygen pump and its application in oxidation studies', *Mater. High Temp.*, 2000 **18S**, 23–30.
16. Wang D R, He Y D, Li S and Gao W, 'Oxidation phenomenon of Ag-In alloys under different oxygen pressures', *J. Chin. Soc. Corr. Protect.*, 2002 **22**(2), 79–83.
17. Gao W, Li Z W, Wu Z, Li S and He Y D, 'Oxidation behavior of Ni<sub>3</sub>Al and FeAl intermetallics under low oxygen partial pressures', *Intermetallics*, 2002 **10**, 263–270.
18. He Y D, Ma J, Li Z W and Gao W, 'Transition from external to internal oxidation of single phase binary alloys', *Mater. Sci. Forum*, 2006 **522–523**, 45–52.
19. He Y D, Ma J, Li Z W and Gao W, 'Transition from external to internal oxidation of Co-Cr alloys', *Mater. Res. Innov.*, 2005 **9**(4), 106–108.
20. Whittle D P, 'Oxidation mechanism for alloys in single oxidant gases', in *High-Temperature Corrosion*, NACE-6, edited by Rapp R A, Houston, TX, NACE, 1983, 171.
21. Douglass D L, in *Selected Topics in High Temperature Chemistry – Defect Chemistry of Solids*, edited by Johannessen Ø and Anderson A G, Amsterdam, Elsevier, 1989.
22. He Y D, Li Z W, Qi H B and Gao W, 'Standard free energy change of formation per unit volume: A new parameter for evaluating nucleation and growth of oxides, sulphides, carbides and nitrides', *Mater. Res. Innov.*, 1997 **1**, 157.

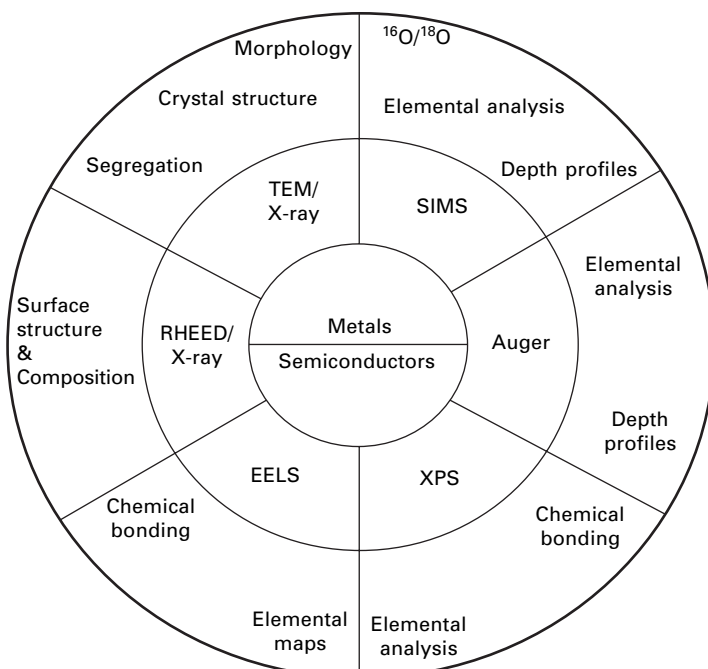
23. Douglass D L, 'A critique of internal oxidation in alloys during the post-Wagner era', *Oxid. Met.*, 1995 **44**(1/2), 81–111.
24. Stott F H and Wood G C, 'Internal oxidation', *Mater. Sci. Technol.*, 1988 **4**, 1072–1078.
25. He Y D, Yao H Y, Li Z W, Qi H B and Stott F H, 'A system for measurement of oxidation kinetics of metals based on solid-state electrochemistry', *Oxid. Met.*, 2000 **53**(3/4), 323–339.
26. Li Z W, He Y D and Gao W, 'Use of a solid-state oxygen pump to study oxidation kinetics of Cr and Mo', *Oxid. Met.*, 2000 **53**(5/6), 577–596.
27. Li Z W, He Y D and Gao W, 'An ultralow oxygen partial pressure-controlling system and its application to oxidation studies', *Oxid. Met.*, 2000 **54**(1/2), 47–62.
28. Carslaw H S and Jaeger J C, *Conduction of Heat in Solids*, 2nd edn, Oxford, Clarendon Press, 1959.
29. Wagner C, 'Theoretical analysis of the diffusion processes determining the oxidation rate of alloys', *J. Electrochem. Soc.*, 1952 **99**, 369–380.
30. Kofstad P, *Nonstoichiometry, Diffusion and Electrical Conductivity in Binary Metal Oxides*, New York, Wiley, 1972.
31. He Y D, Huang Z F, Qi H B, Wang D R, Li Z W and Gao W, 'Oxidation behaviour of micro-crystallized Ni-20Cr-Y<sub>2</sub>O<sub>3</sub> ODS alloy coatings', *Mater. Lett.*, 2000 **45**, 75–85.
32. He Y D, Qi H B, Bai X, Wang D R, Li Z W, Xu C H and Gao W, 'Synergistic effects of surface micro-crystallisation and Ce addition on selective oxidation of Ni-20Cr alloy', *High Temp. Mater. Process.*, 2000 **19**(2), 71–77.
33. Guruswamy S, Park S M, Hirth J P and Rapp R A, 'Internal oxidation of Ag-In alloys: Stress relief and the influence of imposed strain', *Oxid. Met.*, 1986 **26**, 77–100.

# Modern analytical techniques in high temperature oxidation and corrosion

M J GRAHAM, National Research Council of Canada,  
Canada

## 4.1 Introduction

Modern analytical techniques can provide useful information regarding the nature and composition of oxide films and transport processes in oxide scales grown at high temperature. Figure 4.1 illustrates the principal techniques that have been used at the National Research Council of Canada (NRC) and elsewhere in oxidation studies, together with information they provide. Auger electron spectroscopy (AES) provides oxide composition as a function of



4.1 Modern analytical techniques.

depth with a depth resolution of ~2 nm and a spatial resolution ~10 nm. AES is an electron spectroscopy and is closely related to X-ray photoelectron spectroscopy (XPS), each possessing high surface sensitivity from the limited mean free path in solids of the emergent signal. In AES, a finely focused electron beam is used to excite an analytical signal of Auger electrons, whereas in XPS a less damaging X-ray beam is used to excite photoelectrons. The advantages of AES include high spatial resolution, imaging and mapping capabilities, and good depth resolution in composition-depth profiling. There may be severe charging problems and mapping is slow. Although some chemical information is available, AES is largely a technique for elemental analysis only. XPS provides chemical composition, chemical bonding information from the deconvolution of high resolution spectra, mapping capabilities, angle-resolved spectra, depth profiling and charge neutralization to examine insulating oxides. It does not have as good a spatial resolution as Auger, but involves minimal sample charging. Both AES and XPS have rapid data collection, quantification (within 3% using standards), good reproducibility, a narrow sensitivity range (within a factor of 20), detection of ~0.1 at% of an element, large user bases and support data.

Secondary ion mass spectrometry (SIMS) is the mass spectrometric detection of ions emitted from a surface during its bombardment with a beam of positive or negative ions. It provides oxide composition and the use of  $^{16}\text{O}/^{18}\text{O}$  sequential oxidation can be used to evaluate oxide growth mechanisms. Other advantages of SIMS include chemical information from the detection of sputtered molecular fragments of oxides, high sensitivity (ppm range), high spatial resolution using liquid metal ion guns, rapid imaging and mapping, good depth resolution and rapid data collection. SIMS spectra are complex, but quantification can be achieved using standards.

While the spatial resolution of AES, XPS and SIMS continues to improve, atomic scale analysis can only be obtained by transmission electron microscopy (TEM), combined with energy dispersive X-ray spectroscopy (EDX) or electron energy loss spectroscopy (EELS). EDX detects X-rays characteristic of the elements present and EELS probes electrons which lose energy due to their interaction with the specimen. The energy losses are characteristic of both the elements present and their chemistry. Reflection high-energy electron diffraction (RHEED) provides information on surface structure and crystallinity. Further details of the principles of AES, XPS, SIMS and other techniques can be found in a recent publication [1]. This chapter includes the use of AES, XPS, SIMS, RHEED and TEM to study the composition of oxides on nickel, chromia and alumina formers, silicon, gallium arsenide, indium phosphide and indium aluminum phosphide. Details of the instrumentation can be found in previous reviews [2–4].

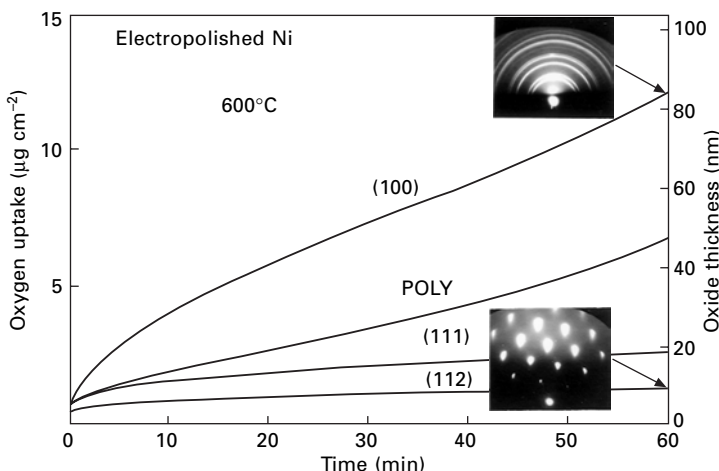
## 4.2 Metals and alloys

This section considers the growth of oxide on nickel and chromium, chromia and alumina forming alloys and intermetallics.

### 4.2.1 Nickel

RHEED, in combination with X-ray emission analysis (XRE), has been used to study the initial stages of oxidation of nickel at low temperatures (e.g. room temperature to 200°C) [5,6]. The RHEED/XRE facility developed at NRC yields structural information comparable to the LEED (low energy electron diffraction) technique and elemental and chemical information about the surface similar to AES. For nickel single crystals the rates of oxidation vary considerably with substrate orientation, but three stages of oxidation, viz. chemisorption, nucleation and lateral growth, and oxide thickening, are always observed.

For thicker films of NiO formed at higher temperatures (e.g. 600°C), ex-situ RHEED is useful to examine the structure of the oxide which forms [7]. Figure 4.2 compares the oxidation of electropolished (112), (111) and (100) monocrystals with electropolished polycrystalline nickel at 600°C. Only ~10 nm of oxide has formed on (112)Ni after 1 h; from RHEED, the single orientation prior oxide [(111) antiparallel NiO on (111) steps of the (112) macrosurface] persists during oxidation. The lower growth rate is the result of formation of oxide by lattice diffusion only. The increased rate of oxidation

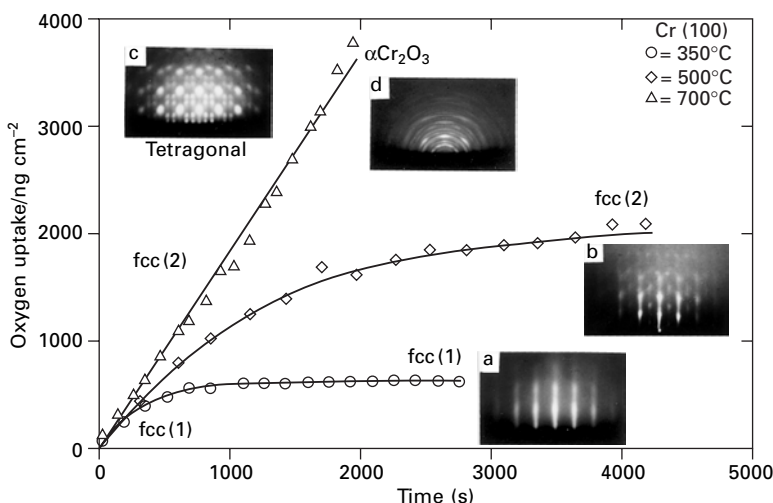


4.2 Oxygen uptake by electropolished (100), (111), (112) and polycrystalline nickel at 600°C. As seen by RHEED, oxidation of (112) nickel produces a singly oriented growth whereas a polycrystalline oxide is propagated on (100) nickel. (From Graham *et al.* [7].)

of (100), (111) and polycrystalline EP Ni can be explained by a modification in the structure of the growing oxide film. Oxide on (111)Ni comprises twin related orientations [7] and the oxidation rate is found to be somewhat faster than (112)Ni because of the presence of incoherent twin boundary leakage paths. (100)Ni oxidizes faster initially (Fig. 4.2) because two sets of twin related oxides provide a greater density of incoherent boundaries and hence more rapid nickel transport. The increase in oxidation rate after about 30 min for both (100) and polycrystalline nickel (Fig. 4.2) most likely results from a recrystallization of the oxide, probably to relieve stress due to epitaxial strain, resulting in the production of mismatch boundaries which provide a greater outward nickel flux. After 1 h the outer oxide on (100)Ni has, in fact, become polycrystalline (Fig. 4.2). SIMS, in conjunction with  $^{16}\text{O}_2/^{18}\text{O}_2$  experiments, has been used to confirm that NiO grows as a result of outward nickel diffusion [8].

#### 4.2.2 Chromium

RHEED/XRD has also been used to study the early stages of oxidation of chromium [9]. Figure 4.3 shows oxidation kinetics and RHEED patterns of Cr(100) after oxidation at temperatures between 350°C and 700°C in  $4.7 \times 10^{-8}$  torr oxygen.

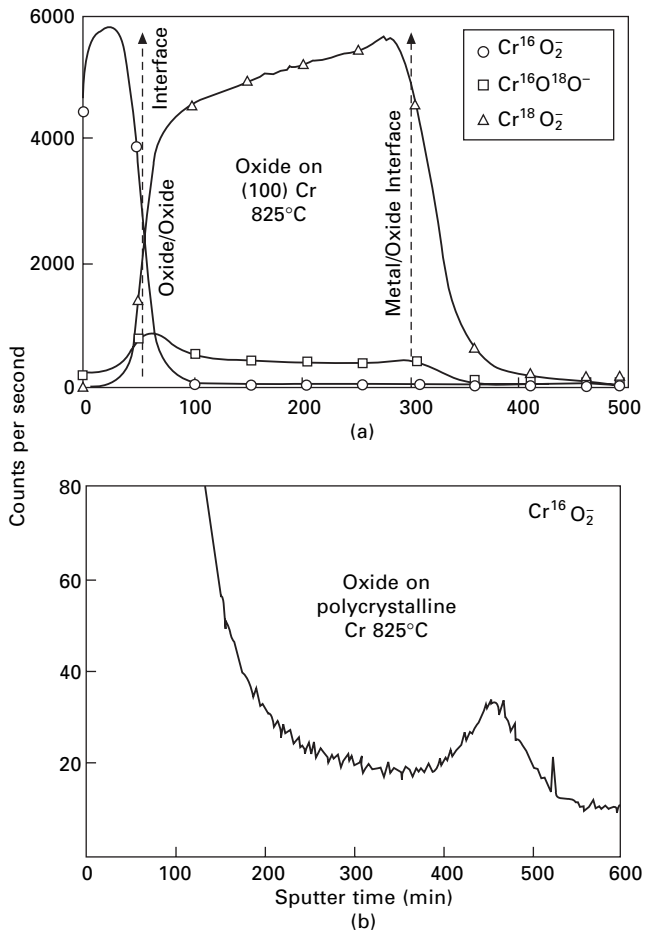


4.3 Oxygen uptake by (100) chromium as a function of time at a pressure of  $4.7 \times 10^{-8}$  torr oxygen at 350, 500 and 700°C. Indicated on the kinetic curves are the temperature/mass regions over which the various oxide phases are observed. The RHEED patterns correspond to (a) fcc (1) oxide, (b) fcc (2) oxide, (c) tetragonal oxide and (d)  $\alpha\text{-Cr}_2\text{O}_3$ . (From Arlow *et al.* [9].)

$10^{-8}$  torr oxygen. The first oxide formed is an fcc phase ( $a_0 = 0.42$  nm), denoted as fcc (1), and is observed at all temperatures up to an oxygen uptake of  $\sim 0.5 \mu\text{g.cm}^{-2}$ . The additional RHEED patterns in Fig. 4.3 show the other oxides which are stable over the temperature/thickness ranges indicated by the oxygen uptake curves. The fcc (2) structure is fundamentally identical to fcc (1) except that the oxygen sublattice now has an  $a_0$  of 1.18 nm. The tetragonal oxide has an  $a_0$  of 0.87 nm and probably corresponds to  $\text{Cr}_3\text{O}_4$ . At the highest temperatures, rings of  $\alpha\text{-Cr}_2\text{O}_3$  are observed. All the oxides (except  $\alpha\text{-Cr}_2\text{O}_3$ ) are well epitaxed to the substrate, observing the epitaxial relationships:  $\text{Cr}(100)/\text{CrO}_x(100)$  and  $\text{Cr}[011]/\text{CrO}_x[010]$ . The fcc and tetragonal structures are thought to arise from the formation of different chromium vacancy superlattices due to oxygen incorporation, which leads eventually to the precipitation of  $\alpha\text{-Cr}_2\text{O}_3$ .  $^{18}\text{O}/\text{SIMS}$  experiments show that the initial stage of oxide formation ( $T < 300^\circ\text{C}$ ) is dominated by oxygen transport. At higher temperatures cation transport begins to dominate.

Considering transport in  $\alpha\text{-Cr}_2\text{O}_3$  at higher temperatures, Fig. 4.4(a) shows a typical SIMS profile for (100)Cr oxidized at  $825^\circ\text{C}$  first in  $^{18}\text{O}_2$  and then in  $^{16}\text{O}_2$ . The  $\text{Cr}^{16}\text{O}_2^-$  and  $\text{Cr}^{18}\text{O}_2^-$  profiles show that the  $^{16}\text{O}$ -oxide exists as a separate layer on top of the  $^{18}\text{O}$ -oxide, indicating that the major mass transport during oxidation is outward chromium diffusion. The mixed  $\text{Cr}^{16}\text{O}^{18}\text{O}^-$  provides information on the extent of any inward oxygen diffusion; the profile in Fig. 4.4(a) is asymmetric about the interface between the  $^{16}\text{O}$ - and  $^{18}\text{O}$ -oxide layers, indicating penetration into the inner oxide. Two independent oxygen diffusion processes are in effect. The first is isotropic oxygen self-diffusion occurring at the interface between the oxide layers. This isotropic diffusion has no net transport and would not contribute to film growth. The second process, association with the tailing of the  $\text{Cr}^{16}\text{O}^{18}\text{O}^-$  profile, is an anisotropic, localized inward oxygen diffusion assumed to be occurring down oxide grain boundaries. Oxygen diffusion coefficients can be calculated for the two processes from the areas of the  $\text{Cr}^{16}\text{O}^{18}\text{O}^-$  profile [10]. The diffusion coefficients for oxygen grain boundary diffusion are 2–3 orders of magnitude higher than for isotropic diffusion, but are still orders of magnitude too low to account for the observed oxidation rates. The major growth transport is by outward chromium diffusion; however,  $\sim 1\%$  of the oxide is created within the film as a result of inward oxygen diffusion. With time this inward diffusion could give rise to sufficient compressive stress to cause detachment of the scale and loss of oxidation protection.

There is also a small rise in the  $\text{Cr}^{16}\text{O}^{18}\text{O}^-$  and  $\text{Cr}^{16}\text{O}_2^-$  signals in the vicinity of the metal/oxide interface which corresponds to the zone where the original 2 nm thick,  $^{16}\text{O}$ -oxide film formed during surface pretreatment is situated. Expansion of the  $\text{Cr}^{16}\text{O}_2^-$  profile confirms a small but clearly distinct peak in this region (Fig. 4.4(b)) for polycrystalline chromium oxidized at  $825^\circ\text{C}$ . This result demonstrates that the  $^{18}\text{O}/\text{SIMS}$  technique is sufficiently



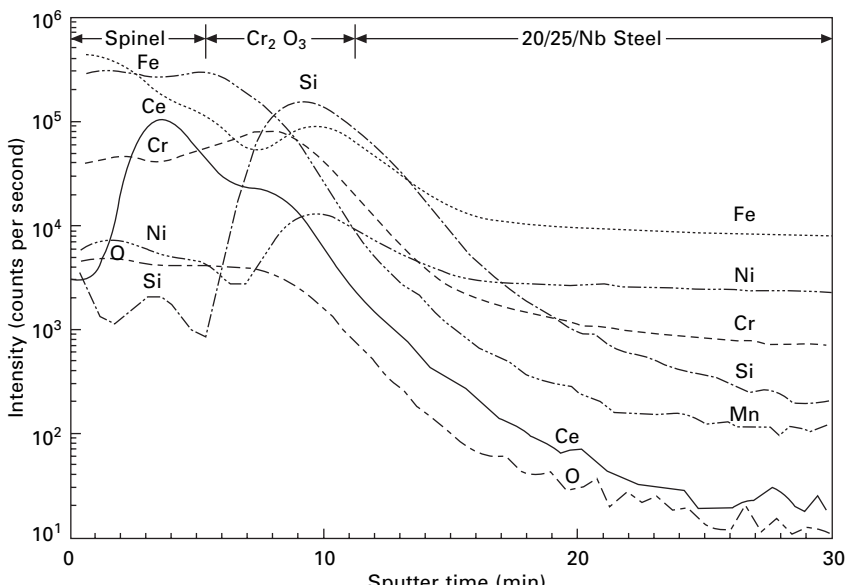
4.4 Negative polyatomic SIMS profiles: (a) for a  $1.4 \mu\text{m}$  thick chromium oxide ( $\text{Cr}_2\text{O}_3$ ) film formed on a (100) chromium single crystal at  $825^\circ\text{C}$  ( $1.1 \mu\text{m}$  of oxide produced in  $^{18}\text{O}_2$  followed by  $0.3 \mu\text{m}$  produced in  $^{16}\text{O}_2$ ); (b) expanded  $\text{Cr}^{16}\text{O}_2^-$  profile for a  $\text{Cr}_2\text{O}_3$  film formed on polycrystalline chromium at  $825^\circ\text{C}$  showing the location of the  $^{16}\text{O}$ -oxide at the metal/oxide interface as a result of the surface pretreatment. Sputtering was by 4 keV xenon. (From Hussey *et al.* [10].)

sensitive to allow a relatively thin layer of oxide to be detected underneath a very much thicker external layer. This thin prior oxide film, in fact, serves as an inert marker confirming oxide growth primarily by outward cation diffusion from the metal to the outer oxide surface, and formation of new oxide mainly on top of the existing scale.

#### 4.2.3 Chromia-forming alloys

The addition of small amounts of reactive elements such as cerium, yttrium, hafnium, thorium, lanthanum, or their oxide dispersions greatly increases the high-temperature oxidation resistance of Fe-Cr alloys under isothermal or cyclic conditions. [11]. Beneficial effects also result from ion implantation of the active element or from surface-applied coatings [11]. The ion implantation work of Bennett *et al.* [12] concerns the oxidation behavior of a 20Cr-25Ni-Nb stainless steel in CO<sub>2</sub> at temperatures in the range of 900 to 1050°C. SIMS can be used to locate the position of the reactive element after oxidation.

Figure 4.5 shows a SIMS profile through cerium implanted 20Cr-25Ni-Nb stainless steel oxidized at 900°C for 216 h. The profile indicates that the variation of the steel constituents is similar to that in the scale, which develops at this temperature on the unimplanted steel. The cerium concentration increases from the outer surface to a maximum within the spinel layer near the interface with the underlying Cr<sub>2</sub>O<sub>3</sub> layer. Silicon is enriched, presumably as silica, at the scale/steel interface. The broader peak does not necessarily indicate a thicker layer than the remainder of the scale, as it reflects the different sputtering rates of oxide and steel as the argon iron ion beam crosses that interface. The oxidation of the stainless steel changes between 900 and 1050°C from protective to nonprotective type behavior. Ion implantation of



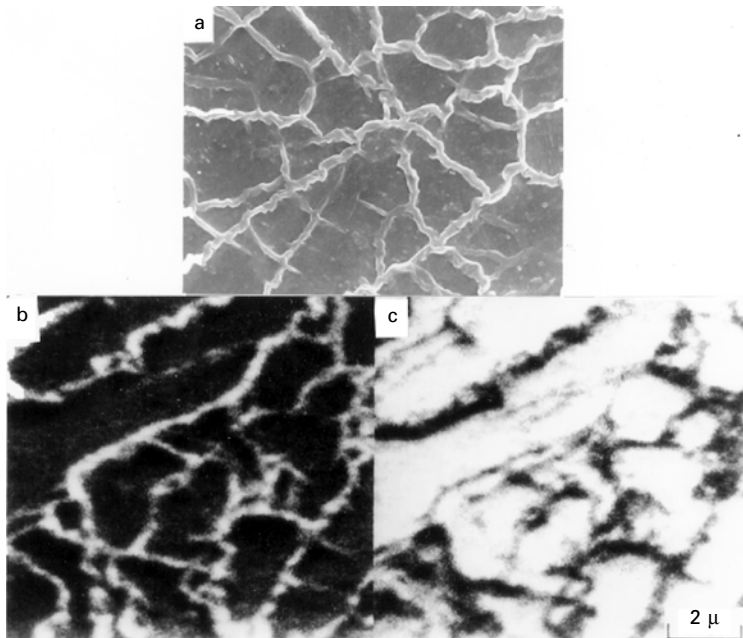
4.5 SIMS profile through the oxide scale formed on 20Cr-25Ni-Nb stainless steel implanted with  $10^{17}$  yttrium ions per cm<sup>2</sup> after 216 h of oxidation in carbon dioxide at 900°C. Sputtering was by 10.5 keV argon. (From Bennett *et al.* [12].)

cerium, yttrium and lanthanum provides continuing protection to the stainless steel to about 1000°C. Initial scale development is modified by the promotion of inward oxidant movement. The reactive element becomes incorporated as oxide grains and segregates along grain boundaries in the outer spinel layer of the scale adjacent to the inner Cr<sub>2</sub>O<sub>3</sub> layer. Cation transport through these boundaries will be energetically less favorable, so that continued scale growth will be inhibited.

#### 4.2.4 Alumina-forming alloys

##### *Nickel aluminide*

One of the main disadvantages of techniques like SIMS is the relatively poor spatial resolution compared with TEM. However, developments continue to improve the resolution of surface-analytical instruments. For example, with a liquid metal ion gun, it is now possible to obtain SIMS images with a spatial resolution better than 20 nm. This is particularly useful for examining oxide on NiAl where non-uniform Al<sub>2</sub>O<sub>3</sub> growth occurs at 1200°C [13–15]. A characteristic feature of the oxidation of NiAl, for example, is the growth of oxide ridges in the  $\alpha$ -Al<sub>2</sub>O<sub>3</sub> scale. The SEM micrograph in Fig. 4.6(a)



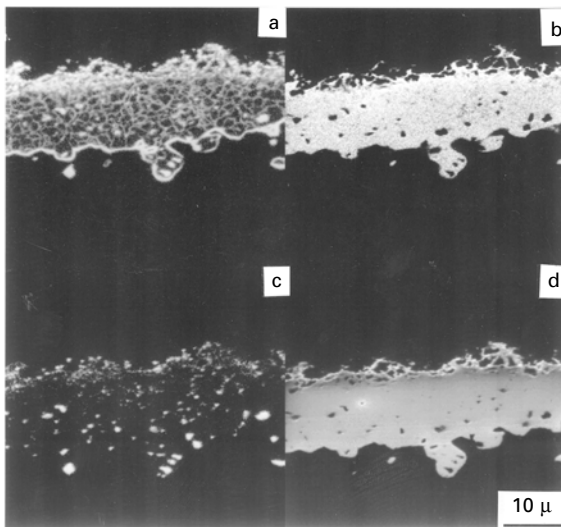
4.6 Oxide formed on  $\beta$ -NiAl at 1200°C after 4 h (2 h in  $^{16}\text{O}_2$  and 2 h in  $^{18}\text{O}_2$ ). (a) SEM micrograph, (b) planar  $^{18}\text{O}^-$  SIMS image, and (c) complementary  $^{16}\text{O}^-$  image. (From Prescott *et al.* [13].)

illustrates the ridge morphology observed at 1200°C. The oxide is much thinner between the ridges than in them. Figure 4.6(b) and (c) shows planar SIMS images of the ridged oxide. Figure 4.6(b) is an image in which the  $^{18}\text{O}^-$  species has been detected in the surface of the oxide. The white lines indicate regions of high  $^{18}\text{O}$  content, and they clearly correspond to the oxide ridges. The dark areas, between the white lines, indicate regions of scale with low  $^{18}\text{O}$  content. Figure 4.6(c) is the complementary  $^{16}\text{O}^-$  image for the same area of oxide. In this image, the areas between the ridges are brighter, which is indicative of higher  $^{16}\text{O}$  levels. From these planar images of the outer surface of the oxide, it is clear that, after the formation of an  $\alpha\text{-Al}_2\text{O}_3$  layer, the bulk of the new surface oxide growth is confined to the ridges.

In a series of planar images obtained from sputtering the oxide from the outer surface down to the substrate, it is possible to observe how the  $^{18}\text{O}$  distribution changes with depth [14]. The highest  $^{18}\text{O}$  levels are found to be associated with the outer region of the oxide ridges, which shows that the ridges continue to develop throughout the period of oxidation in  $^{18}\text{O}_2$ . Because  $^{18}\text{O}$  is detected on the outside of the  $\alpha\text{-Al}_2\text{O}_3$  ridges, it can be concluded that the growth is occurring by outward diffusion of aluminum.

As the time of oxidation at 1200°C increases, the ridged structure coarsens. The ridges become higher and wider, and the flat areas between the ridges gradually disappear. Yttrium and zirconium alloy additions slow the development of the ridges and reduce to some degree the extent of outward aluminum diffusion [13]. These thick scales formed by sequential oxidation in  $^{16}\text{O}_2$  and  $^{18}\text{O}_2$  can be examined by SIMS imaging of taper or cross-sections. For NiAl + 0.2% Zr after sequential oxidation for 400 h in  $^{16}\text{O}_2$  followed by 200 h in  $^{18}\text{O}_2$ , most of the  $^{18}\text{O}$  (Fig. 4.7(a)) is observed close to the scale/substrate interface or within channels or boundaries in the inner part of the oxide. The SIMS images clearly show that inward diffusion of oxygen along short-circuit paths is now beginning to play a significant role in the growth process. This change in growth mechanism appears to coincide with the coalescence or merging of the oxide ridges. The SIMS image in Fig. 4.7(c) indicates the distribution of the zirconium; it is dispersed through the scale as zirconium oxide ( $\text{ZrO}_2$ ) particles. The particles are finer in the outer portion of the scale and are coarser and more widely spaced close to the scale/substrate interface, probably reflecting the reduced rate of growth of the oxide as the film thickens.

It is not possible to determine by SIMS the precise location of zirconium (e.g., whether segregation has occurred to the oxide/alloy interface or to oxide grain boundaries). This is where higher-resolution electron microscopy with energy-dispersive X-ray analysis is important. STEM/X-ray data [16] on samples previously analyzed by SIMS show that for NiAl + Zr, no particles are present right at the oxide/substrate interface. Also, no interfacial voids

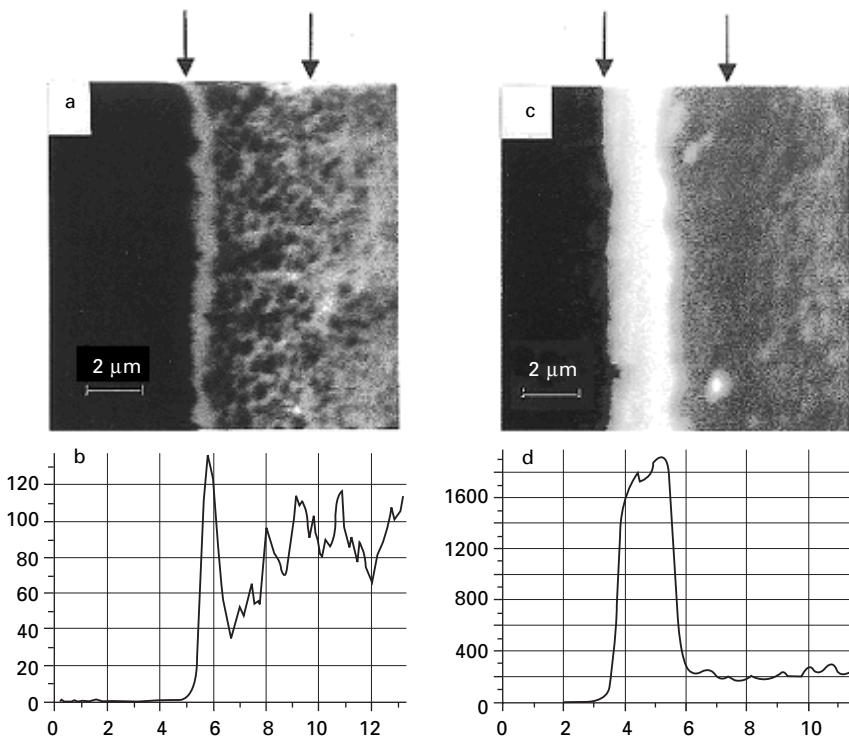


4.7 SIMS taper cross-section images of an oxide scale formed on  $\beta$ -NiAl at 1200°C for 600 h (400 h in  $^{16}\text{O}_2$  and 200 h in  $^{18}\text{O}_2$ ). (a)  $^{18}\text{O}$  image, (b)  $^{16}\text{O}$  image, (c)  $\text{Zr}^+$  image, and (d)  $\text{Al}^+$  image. Regions rich in a particular isotope or element appear white. (From Prescott *et al.* [15].)

are found and sulfur is not detected at the oxide/substrate interface. Zirconium does segregate to this interface and to all  $\alpha\text{-Al}_2\text{O}_3$  grain boundaries, an observation in agreement with the results of Pint, *et al.* [17]. This segregated zirconium may influence aluminum transport during oxide growth.

#### *FeCrAl alloys*

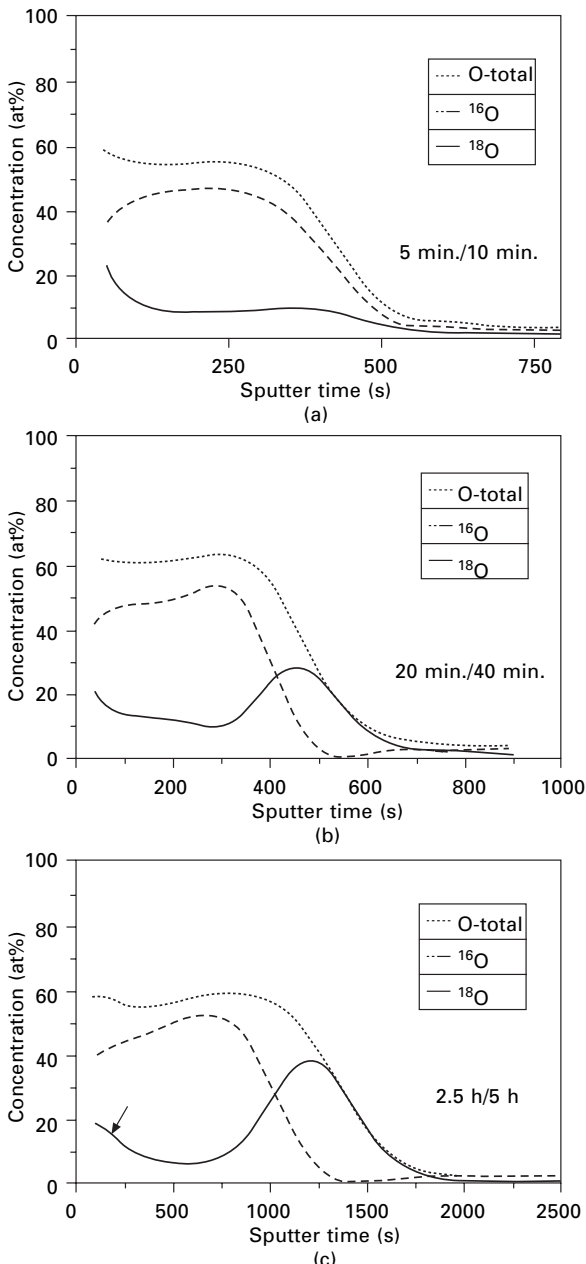
$\alpha\text{-Al}_2\text{O}_3$  scales on Fe–20Cr–5Al alloys, as seen in the  $^{18}\text{O}$  SIMS images in Fig. 4.8, grow by both outward aluminum diffusion and inward oxygen diffusion, similar to alumina growth on NiAl described above. In the image, regions rich in  $^{18}\text{O}$  appear white. It is evident from both the image (Fig. 4.8(a)) and the corresponding line profile (Fig. 4.8(b)) that the second oxidant,  $^{18}\text{O}$ , is present as a band at the metal/oxide interface (left-hand side of the image), within boundaries in the scale, and on the outside of the oxide. An  $^{18}\text{O}$  image of oxide on a Y-containing alloy (Fig. 4.8(c)) and profile (Fig. 4.8(d)) show that  $^{18}\text{O}$  is present in a wide band at the metal/oxide interface (left-hand side of the image). For the Y-containing alloy, the oxide grain structure changes from equiaxed to columnar, and STEM/X-ray data show that Y has segregated to the  $\alpha\text{-Al}_2\text{O}_3$  grain boundaries and to the alloy/oxide interface [18]. The segregation of Y in the case of FeCrAl alloys has actually suppressed outward cation diffusion rather than reducing it as in the case of



4.8 SIMS taper cross-section images of an oxide formed at 1200°C in 1.5 h in  $^{16}\text{O}_2$  followed by 3.5 h in  $^{18}\text{O}_2$  on FeCrAl: (a)  $^{18}\text{O}$  image, (b) profile. On FeCrAl + 0.1 wt% Y: (c)  $^{18}\text{O}$  image, and (d) profile. Arrows on the images indicate the position of the metal/oxide interface (left-hand side) and the oxide/gas interface (right-hand side). Regions rich in  $^{18}\text{O}$  appear white. (From Graham [4].)

$\alpha\text{-Al}_2\text{O}_3$  on NiAl (or indeed for  $\text{Cr}_2\text{O}_3$  on Cr or FeCr alloys). The notion that reactive elements reduce the extent of outward cation diffusion is now widely supported.

Quadakkers *et al.* [19–21] have used both SIMS and secondary neutral mass spectrometry (SNMS) to study the mechanism of alumina growth on Fe-20Cr-5Al and oxide-dispersion-strengthened (ODS) Incoloy alloy MA956 (Fe-20Cr-4.5Al-0.5 $\text{Y}_2\text{O}_3$ ). SNMS has some advantages over SIMS from the point of view of quantification. Yttrium oxide dispersion was found to suppress outward scale growth. As shown in Fig. 4.9, after a transient oxidation, the oxide on MA956 grows almost exclusively by oxygen grain boundary transport and so the thickening occurs by oxygen ( $^{18}\text{O}$ ) grain boundary transport at the scale/metal interface by alumina formation. A ‘shoulder’ in the  $^{18}\text{O}$  profile indicated by an arrow in Fig. 4.9(c) could represent a small amount of in-scale growth. The location of the shoulder could be correlated by SNMS



4.9 SNMS profiles: time dependence of oxygen isotope distribution (recalculated to 100% enrichment in  $^{18}\text{O}$ ) in oxide scales on MA956 after two-stage oxidation in air and then  $^{18}\text{O}$ -enriched air at 1000°C. Arrow indicates 'shoulder' in the  $^{18}\text{O}$  profile: (a) 5 min/10 min, (b) 20 min/40 min, and (c) 2.5 h/5 h. Sputtering was by 0.8 keV argon. (From Quadakkers *et al.* [20].)

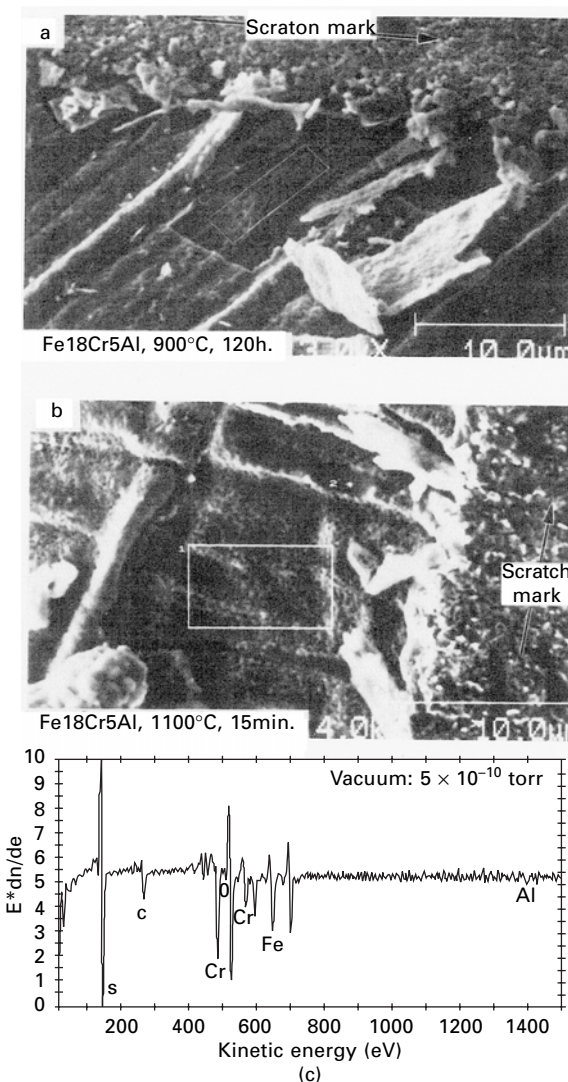
with the relative maximum of the in-scale chromium concentration. According to Quadakkers *et al.* [20], apart from in-scale growth, the shoulder in the  $^{18}\text{O}$ -concentration profile could be due to an enhanced isotope exchange between the oxygen, which is diffusing inward via grain boundaries with the oxygen in the grains. A possible reason for this effect would be a highly disturbed alumina lattice due to high amounts of dissolved chromium or the presence of a large number of interfaces due to coexistence of finely dispersed chromia particles with alumina grains. The shoulder in the  $^{18}\text{O}$  profile was detected in the scales on both MA956 and Fe-20Cr-5Al; they only differed in their location relative to the oxide surface, because of the different contributions of cation diffusion to the overall oxide growth process on the two alloys.

In-situ AES has been used to study segregation of, e.g., sulfur to the alloy/scale interface [22–24]. The studies by Hou and Stringer [23,24] on Fe-18Cr-5Al alloys indicated that regardless of oxidation temperature or interface morphology, i.e. oxide imprints versus voids, the sulfur content was always calculated to be ~19 at% (Fig. 4.10). Also, a similar level of carbon was detected. While the density of interfacial voids at the metal surface increased from 900 to 1100°C, the higher number did not affect scale failure. All failures took place at the scale/alloy interface, exposing large areas of metal surface which consisted of either voids or oxide-imprinted regions. Hou and Stringer's view [24] was that if sulfur and carbon were found everywhere on the metal side of interfaces, regardless of the interface morphology, then it seemed reasonable that the weakness of the interface was due mainly to the detrimental presence of these impurities. Recent AES work by Hou and co-workers [25,26] has determined the extent of sulfur segregation to  $\text{Al}_2\text{O}_3/\text{NiAl}$  interfaces.

## 4.3 Semiconductors

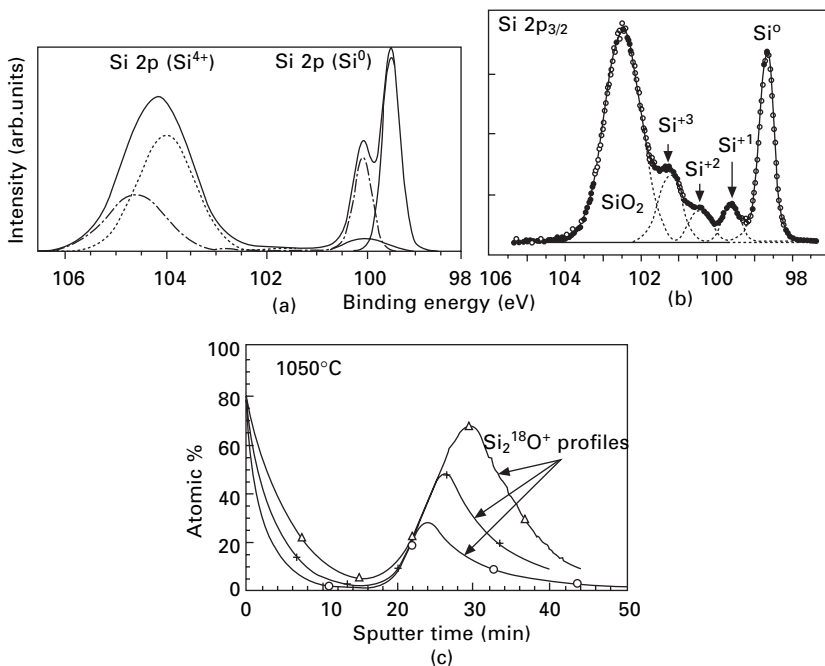
### 4.3.1 Silicon

The ability of silicon to form a high-quality thermal oxide with a low density of interfacial states has been a major factor in the successful development of metal–oxide–semiconductor (MOS) technology and the microelectronics industry. A typical XPS spectrum of a thin  $\text{SiO}_2$  film (thermal or anodic) is shown in Fig. 4.11(a). The peaks corresponding to the oxide ( $\text{Si } 2\text{p} (\text{Si}^{4+})$ ) and the substrate ( $\text{Si } 2\text{p} (\text{Si}^0)$ ) are indicated. Any silicon suboxide would be visible in the region 102.5–100.5 eV. Clearly, very little suboxide is present at the oxide/semiconductor interface. XPS and synchrotron radiation photo-emission spectroscopy (PES) have been used to determine the suboxide distribution of  $\text{SiO}_2/(100)\text{Si}$  interfaces for thermal oxides grown at 750°C in  $2 \times 10^{-5}$  torr oxygen [27]. As seen in Fig. 4.11(b), different suboxide peaks,



**4.10** SEM micrographs of scratch-induced scale fractures. The alumina scale was formed at (a) 900°C for 120 h and (b) 1100°C for 15 min. Scratches were made with a diamond stylus in ultrahigh vacuum. The marked areas on both micrographs indicate regions on which Auger analyses were made, and (c) is a typical Auger spectrum of the tested area. (From Hou and Stringer [24].)

$\text{Si}^{+1}$ ,  $\text{Si}^{+2}$  and  $\text{Si}^{+3}$ , are clearly observed by PES in this thin oxide, indicating different coordination of Si ions.  $^{18}\text{O/SIMS}$  data on (100)Si oxidized at higher pressure at, e.g., 1050°C (Fig. 4.11(c)) show that oxide growth occurs at both the gas/oxide and the  $\text{SiO}_2/\text{Si}$  interface with the latter predominating



4.11 (a) Typical XPS spectrum for a ~4 nm-thick  $\text{SiO}_2$  film (either thermal or anodic) on (100)Si. The peaks corresponding to the oxide ( $\text{Si} 2p (\text{Si}^{4+})$ ) and semiconductor ( $\text{Si} 2p (\text{Si}^0)$ ) have been deconvoluted into the  $2p_{3/2}$  and  $2p_{1/2}$  peaks. XPS spectra acquired in a PHI 5500 system using a monochromated  $\text{Al K}_\alpha$  source. (b)  $\text{Si} 2p_{3/2}$  synchrotron PES data taken with 130 eV photons from a ~0.4 nm-thick oxide formed on (100)Si at  $750^\circ\text{C}$  in  $2 \times 10^{-5}$  torr oxygen. The open circles are as-recorded data after standard Shirley background subtraction and subtraction of the  $\text{Si} 2p_{1/2}$  components. The dashed lines indicate the various suboxides.  $\text{Si}^{+x}$  and the substrate  $\text{Si}^0$  peak are labelled. The solid line is the sum of all the silicon peaks including their respective  $2p_{1/2}$  components. (c) SIMS profiles for  $\text{Si}_2^{18}\text{O}^+$  for oxide films formed on (100)Si at  $1050^\circ\text{C}$  in 10 torr oxygen after 2 h in  $^{16}\text{O}_2$  followed by 0.5 h (○), 1 h (+) and 2 h (△) in  $^{18}\text{O}_2$ . (From Graham [4].)

[28]. As seen in Fig. 4.11(c), the amount of oxide formation at the  $\text{SiO}_2/\text{Si}$  interface increases with oxidation time. The SIMS data suggest that the inward diffusion of oxygen probably occurs along short-circuit paths, such as micropores extending to the  $\text{SiO}_2/\text{Si}$  interface.

### 4.3.2 III-V semiconductors

Unlike silicon, III-V materials like GaAs and InP do not form high-quality native oxides, but Al-containing oxides on InAlP [29–31] have been found to

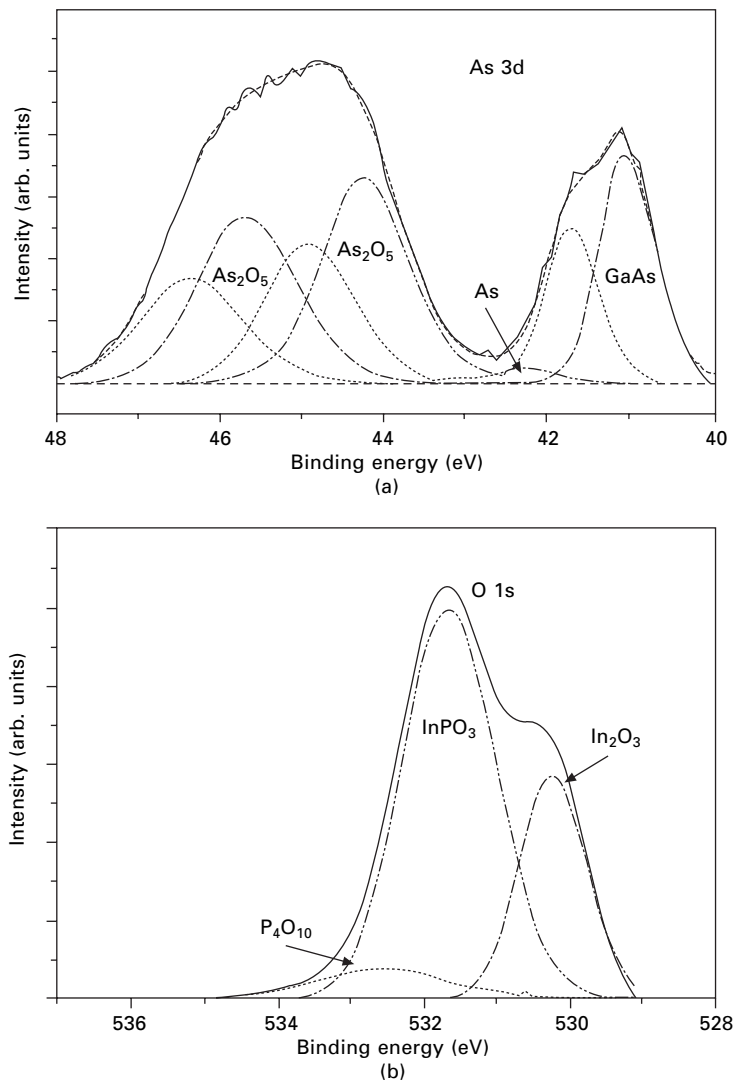
possess superior insulating properties which make them potentially useful for some device applications.

### *GaAs and InP*

Thermal oxides formed on GaAs(100) at 500°C in oxygen or moist air (air bubbled through H<sub>2</sub>O at 25 or 95°C) or moist nitrogen (N<sub>2</sub> bubbled through H<sub>2</sub>O at 95°C) comprise principally Ga<sub>2</sub>O<sub>3</sub> to a level of ~97% [32]. <sup>16</sup>O/<sup>18</sup>O SIMS depth profiling experiments show that oxide growth is principally by inward oxygen diffusion along oxide grain boundaries [32]. There are enrichments of arsenic at both the gas/oxide and the oxide/substrate interface. The latter amount of arsenic increases with oxidation time, and its accumulation likely leads to a high density of electronic traps and consequently to rather poor electrical properties for any MOSFETs (metal-oxide semiconductor field-effect transistors). A typical XPS As 3d spectrum of oxide formed at 500°C is shown in Fig. 4.12(a). The spectrum can be deconvoluted into four doublets corresponding to the 3d<sub>5/2</sub> and 3d<sub>3/2</sub> lines with a separation of 0.69 eV. These correspond, as indicated, to As<sub>2</sub>O<sub>5</sub>, As<sub>2</sub>O<sub>3</sub>, substrate GaAs and elemental arsenic. Figure 4.12(b) shows the deconvoluted O 1s spectrum for oxide formed on InP at 500°C; InPO<sub>3</sub>, In<sub>2</sub>O<sub>3</sub> and P<sub>4</sub>O<sub>10</sub> components are indicated. The amount of In<sub>2</sub>O<sub>3</sub> increases with oxidation time. XPS provides useful information on the chemical composition of thin oxides on III-V semiconductors.

### *InAlP*

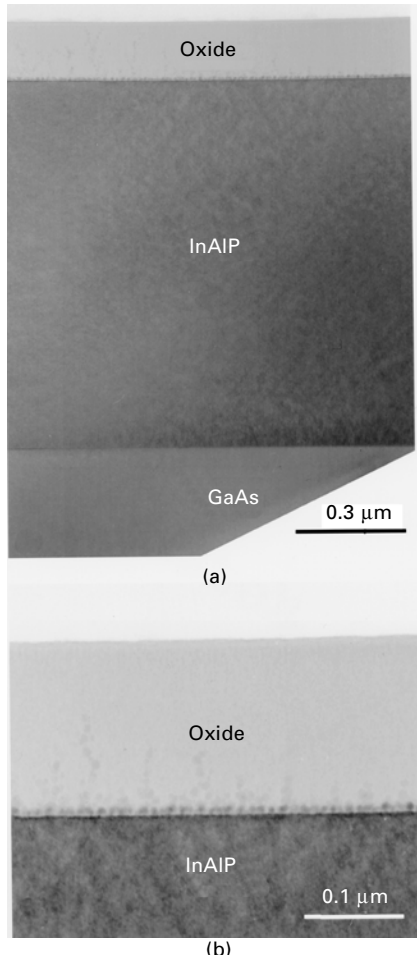
Oxidation of InAlP at 500°C in moist nitrogen produces uniformly thick amorphous layers [30]. TEM micrographs of the oxide formed after 1 h are shown in Fig. 4.13. The lower magnification image (Fig. 4.13 (a)) illustrates a uniformly thick oxide on the InAlP layer grown by molecular beam epitaxy (MBE) on GaAs. The higher magnification image (Fig. 4.13 (b)) shows the uniform oxide and the presence of particles near the oxide/InAlP interface which have been attributed to unoxidized indium [29,30]. An Auger profile of the oxide of Fig. 4.13 is shown in Fig. 4.14. The increase of indium at the substrate interface is clearly seen. Rutherford backscattering measurements indicate that the In:Al:P ratio in the oxide is the same as in the substrate, phosphorus being the major component in the oxide. These oxides are found to have good insulating properties, but the properties are improved if the residual indium particles present at the oxide/substrate interface are oxidized by a brief oxidation in oxygen at 500°C [33]. This reduces the current density by two orders of magnitude and the oxide breakdown field is significantly increased [33], making the oxide films potentially useful for some device applications.



4.12 (a) Deconvoluted XPS As 3d spectrum of ~6 nm-thick oxide formed on GaAs after 5 min in 10 torr oxygen at 500°C; (b) deconvoluted O 1s spectrum of ~8 nm-thick oxide formed on InP after 6 min in moist air. (From Graham [4].)

#### 4.4 Concluding remarks

This chapter has summarized some of the work using modern analytical techniques to characterize oxide films on metals and semiconductors. The detailed transport processes that occur during scale growth at high temperature can be identified from surface-analytical data. The information obtained by

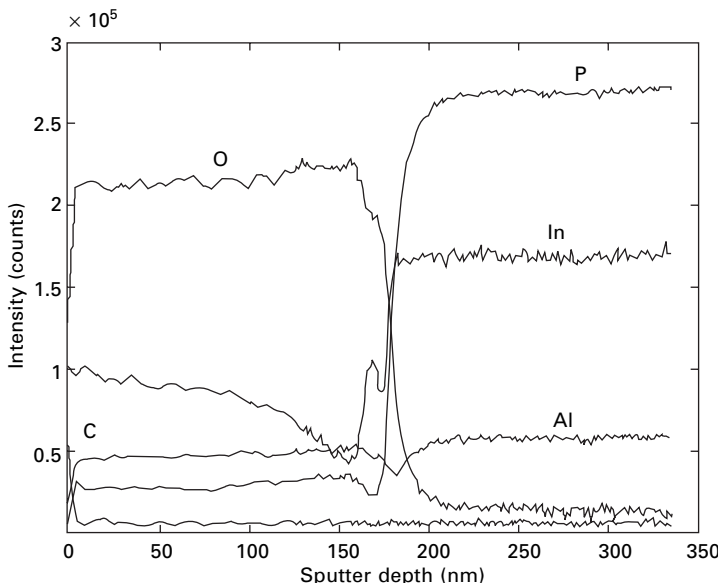


4.13 TEM micrographs of ~154 nm-thick oxide formed on InAlP after 1 h at 500°C in moist nitrogen. Cross-section prepared by ion milling. (From Graham *et al.* [30].)

the often complementary techniques leads to a better understanding of oxidation phenomena and mechanisms, and, in the case of semiconductors, could lead to improved device performance.

#### 4.5 Acknowledgements

The author acknowledges his former and present colleagues at NRC for their contribution to this research, particularly D.F. Mitchell, R.J. Hussey, R. Prescott, G.I. Sproule, J.R. Phillips, J.W. Fraser, S. Moisa, R. Driad, D. Landheer, X.



4.14 Auger electron spectroscopy (AES) profile of the oxide in Fig. 4.13, obtained by Physical Electronics, Inc. Sputtering was by 2 keV argon, with Zalar rotation.

Wu, A.J. Spring Thorpe and P.J. Barrios, and external collaborators C. Mennicke, E. Schumann and M. Rühle.

## 4.6 References

1. Marcus P and Mansfeld F, eds (2006), *Analytical Methods in Corrosion Science and Engineering*, CRC Press, Boca Raton, FL.
2. Graham M J and Hussey R J (1995), ‘Analytical techniques in high temperature corrosion’, *Oxid Met*, 44(1/2), 339–373.
3. Graham M J (1995), ‘The application of surface techniques in understanding corrosion phenomena and oxidation mechanisms’, *Corros Sci*, 37(9), 1377–1397.
4. Graham M J (2000), ‘Application of surface techniques to study oxide growth processes’, *Mater High Temp*, 17(1), 1–5.
5. Graham M J and Mitchell D F (1982), ‘A kinetic study of the initial oxidation of Ni(111) and (211) surfaces by RHEED and X-ray emission’, *Surf Sci*, 114, 546–562.
6. Mitchell D F and Graham M J (1981), ‘The initial stages of oxidation of Ni, Fe and Ta single crystals’, *Proc NACE Conf on High Temperature Corrosion*, Rapp R A (ed), NACE, Houston, TX, 18–22.
7. Graham M J, Hussey R J and Cohen M (1973), ‘Influence of oxide structure on the oxidation rate of nickel single crystals’, *J Electrochem Soc*, 120, 1523–1529.
8. Graham M J (1991), ‘The study of oxide scales using SIMS’, *Microscopy of Oxidation*, Bennett M J and Lorimer G W (eds), The Institute of Metals, London, 10–18.
9. Arlow J S, Mitchell D and Graham M J (1987), ‘The mechanism and kinetics of the oxidation of Cr(100) single crystal surfaces studied by reflection high energy electron

- diffraction, X-ray emission spectroscopy and secondary ion mass spectrometry/Auger sputter depth profiling', *J Vac Sci Technol*, A5, 572–576.
- 10. Hussey R J, Mitchell D and Graham M J (1987), 'The growth and structure of oxide films formed on single crystal (100) and polycrystalline chromium between 550 and 900°C', *Werkstoffe und Korrosion*, 38, 575–583.
  - 11. Stringer J and Hou P Y (1989), 'A comparison of the effects of reactive metal alloy additions, oxide dispersions, ion implantation and surface oxide coatings on high temperature oxidation', *Proc Symp on Corrosion and Particle Erosion at High Temperatures*, Srinivasan V and Vedula K (eds), TMS, 383–401.
  - 12. Bennett M J, Bishop H E, Chalker P R and Tuson A T (1987), 'The influence of cerium, yttrium and lanthanum ion implantation on the oxidation behaviour of a 20Cr-25Ni-Nb stainless steel in carbon dioxide at 900–1050°C', *Mater Sci Eng*, 90, 177–190.
  - 13. Prescott R, Mitchell D F and Graham M J (1993), 'A SIMS study of the effect of yttrium and zirconium on the growth of oxide on  $\beta$ -NiAl', *Proc 2nd Int Conf on Microscopy of Oxidation*, Newcomb S B and Bennett M J (eds), The Institute of Metals, London, 455–462.
  - 14. Prescott R, Mitchell D F and Graham M J (1994), 'A study of the growth of  $\alpha$ -Al<sub>2</sub>O<sub>3</sub> scales using high-resolution secondary ion mass spectrometry', *Corrosion*, 50, 62–71.
  - 15. Prescott R, Mitchell D F, Graham M J and Doychak J (1995), 'Oxidation mechanisms of  $\beta$ -NiAl + Zr determined by SIMS', *Corros Sci*, 37, 1341–1364.
  - 16. Schumann E, Yang J C, Rühle M and Graham M J (1996), 'High resolution SIMS and analytical TEM evaluation of alumina scales on NiAl containing Zr or Y', *Oxid Met*, 46(1/2), 37–49.
  - 17. Pint B A, Garatt-Reed A J and Hobbs L W (1993), 'The effect of a Zr alloy addition on the oxidation behaviour of  $\beta$ -NiAl: the transition from benefit to breakaway', *Proc 2nd Int Conf on Microscopy of Oxidation*, The Institute of Metals, London, 463–475.
  - 18. Mennicke C, Schumann E, Rühle M, Hussey R J, Sproule G I and Graham M J (1998), 'The effect of yttrium on the growth process and microstructures of  $\alpha$ -Al<sub>2</sub>O<sub>3</sub> on FeCrAl', *Oxid Met*, 49, 455–466.
  - 19. Quadakkers W J, Holzbrecher H, Briefs K G and Beske H (1989), 'Differences in growth mechanisms of oxide scales formed on ODS and conventional wrought alloys', *Oxid Met*, 32, 67–88.
  - 20. Quadakkers W J, Elshner A, Spier W and Nickel K (1990), 'Composition and growth mechanisms of alumina scales on FeCrAl-based alloys determined by SNMS', *Appl Surf Sci*, 52, 271–287.
  - 21. Quadakkers W J (1990), 'Growth mechanisms of oxide scales on ODS alloys in the temperature range 1000–1100°C', *Werkstoffe und Korrosion*, 41, 659–668.
  - 22. Grabke H-J, Wiemer D and Viehaus H (1991), 'Segregation of sulfur during growth of oxide scales', *Appl Surf Sci*, 47, 243–250.
  - 23. Hou P and Stringer J (1991), 'Observation of oxide/metal interface using scanning Auger microscopy with an *in-situ* scratch technique', *Microscopy of Oxidation*, Bennett M J and Lorimer G W (eds), The Institute of Metals, London, 362–368.
  - 24. Hou P Y and Stringer J (1992), 'Oxide scale adhesion and impurity segregation at the scale/metal interface', *Oxid Met*, 38, 323–345.
  - 25. Hou P Y and Priimak K (2005), 'Interfacial segregation, pore formation, and scale adhesion on NiAl alloys', *Oxid Met*, 63(1/2), 113–130.

26. Hou P and McCarty K F (2006), 'Surface and interface segregation in  $\beta$ -NiAl with and without Pt additions', *Scripta Mater*, 54, 937–941.
27. Lu Z H, Graham M J, Jiang D T and Tan K H (1993), 'SiO<sub>2</sub>/Si(100) interface studied by Al K<sub>α</sub> X-ray radiation and synchrotron photoelectron spectroscopy', *Appl Phys Lett*, 63(21), 2941–2943.
28. Hussey R J, Sproule G I, Mitchell D and Graham M J (1993), 'An <sup>18</sup>O/SIMS study of oxygen transport in thermal oxide films formed on silicon', *Proc 12th Int Corrosion Congr*, Houston, TX, Vol 5B, 3831–3841.
29. Barrios P J, Hall D C, Chowdhury U, Dupuis R D, Jasinski J B, Liliental-Weber Z, Kosel T H and Snider G L (2001), 'Properties of InAlP native oxides supporting MOS inversion-layer behaviour', *Abstract, 43rd Electronics Materials Conf*, Notre Dame, IN, 27–29 June.
30. Graham M J, Moisa S, Sproule G I, Wu X, Fraser J W, Barrios P J, Landheer D, Spring Thorpe A J and Extavour M (2003), 'Thermal oxidation of InAlP', *Mater High Temp*, 31–34.
31. Cao Y, Zhang J, Li X, Kosel T H, Fay P, Hall D C, Zhang X B, Dupuis R D, Jasinski J B and Liliental-Weber Z (2005), 'Electrical properties of InAlP native oxides for metal-oxide-semiconductor device applications', *Appl Phys Lett*, 86, 062105–3.
32. Hussey R J, Sproule G I and Graham M J (1997), 'The structure and composition of thermal oxides formed on GaAs at 500°C', *Proc 27th State-of-the-Art Program on Compound Semiconductors*, ECS Proc Vol 97–21, 305–316.
33. Graham M J (2007), 'Oxidation of III-V semiconductors', *Corros Sci*, 49, 31–41.

# 5

## Metal dusting corrosion of metals and alloys

---

T A R A M A N A R A Y A N A N, Princeton University, USA  
and C M CHUN, Exxon Mobil, USA

### 5.1 Introduction

Metal dusting is a corrosion phenomenon that metals and alloys undergo at temperatures in the range 450–850°C in gaseous environments that are supersaturated with respect to carbon. The corrosion process involves the break-up of the bulk metallic structure into powder or ‘dust’. When metal dusting occurs on pure metals, the degradation, for the most part, is uniform over the surface, with some degree of localized attack. On the other hand, when alloys undergo metal dusting corrosion, it is mostly localized on the surface. The present chapter is an attempt to combine the understanding of the metal dusting of selected pure metals and alloys to formulate some overall principles that govern the metal dusting of alloys. To that end the metal dusting corrosion of Fe, Co and Ni and selected Fe based, Fe-Ni based and Ni based alloys has been investigated. The majority of studies reported in this chapter have been carried out by the authors using a 50CO:50H<sub>2</sub> gas mixture as the corrosive environment.

Fe corrodes mainly by the initial formation of a metastable Fe<sub>3</sub>C layer on the surface. Subsequent deposition of graphitic carbon on this layer destabilizes the Fe<sub>3</sub>C whereupon it dissociates into iron atoms and carbon, the former migrating away from the interface via interplanar spaces in graphite while the latter either attaches itself to graphite or diffuses into the alloy interior. The iron atoms that migrate away generally coalesce into nano-sized metal particles that catalyze the formation of filamentous carbon on the exterior surface of graphite. Ni and Co, unlike Fe, do not form a metastable surface carbide. Corrosion, however, occurs by the direct intercalation of metal atoms from the bulk metal into graphite having planes aligned more or less perpendicular to the metal surface. Metal atom intercalation into graphite by carbide dissociation is expected to be kinetically faster than atom removal from the bulk metal and subsequent intercalation. Thus the metal dusting rates for Fe are much higher than those for Ni or Co. Ni and Co also undergo corrosive attack by internal precipitation of graphite that ultimately leads to

break-up of the bulk metal. The metal dusting of pure metals is covered in Section 5.4 of this chapter.

Three types of alloys, namely Ni based, Fe-Ni based and Fe based, are discussed in this chapter. The discussion is restricted to chromia forming alloys since it is felt that in the temperature range where metal dusting generally occurs, these alloys are the most suitable. In general, in such alloys, the local break-up of a surface chromia film or incomplete surface coverage by such a film leads to local carbon entry into the alloy. When this occurs, severe local carburization rapidly depletes the alloy subsurface region of Cr, thus disabling the capacity of the alloy to reform surface chromium oxide. Generally, the carbon flux that triggers metal dusting is less in the case of high chromium Ni-Cr alloys on account of the relatively low solubility and diffusivity of carbon in such alloys. In austenitic Fe-Ni based alloys, the higher carbon solubility leads to larger carbon flux and correspondingly faster alloy deterioration. The faster Cr diffusivity in ferritic Fe based high-Cr alloys favors rapid chromium oxide film formation on such alloys, providing better resistance to metal dusting. The three alloy classes are discussed in Section 5.5.

Control strategies for metal dusting are taken up next. Three approaches are considered: alloys with intrinsic metal dusting resistance, additives or metallic coatings that suppress carbon transfer to the surface, and finally metallic coatings that promote protective surface oxide formation. In alloy development, the main strategy considered is to include an additional alloying element to promote rapid surface coverage by an oxide, thus giving time for a slower growing protective Cr-rich oxide to develop beneath this outer oxide. The main additive that is discussed for the control of carbon transfer reaction is H<sub>2</sub>S. Metallic coatings include pure metals belonging to Groups IB, IVB, VB and VIB of the Periodic Table and selected alloy compositions. These different control strategies are covered in Section 5.6. Finally, Section 5.7 examines some of the future trends in metal dusting research.

## 5.2 Background

Metal dusting is a form of aggressive high temperature corrosion that many metals and alloys undergo in carbon-supersaturated environments.<sup>1–9</sup> Such environments are characteristic of many processes in the petrochemical industry, involving, for example, the conversion of hydrocarbons to high value chemicals and the production of syngas (CO + H<sub>2</sub>). The metal dusting reaction typically occurs over the temperature range 450–850°C. Metal dusting almost always occurs in concert with carbon deposition or coking, although coking can sometimes occur without metal dusting. The coke that forms consists of amorphous carbon, graphitic carbon and filamentous carbon (carbon nanotubes). The formation of filamentous carbon is catalyzed by metal particles

that form as a result of the metal dusting reaction. Coke formation and other deposit formation, generally termed fouling, interfere with many process operations. To the extent that coking is accompanied by the metal dusting reaction, the control of metal dusting can also control coking.

The metal dusting of pure metals, especially Fe, was studied extensively by Hochman.<sup>1</sup> The Hochman mechanism for the metal dusting of iron involves three steps. The first step is the formation of metastable iron carbide,  $\text{Fe}_3\text{C}$ , on the surface of iron. This reaction requires carbon activities higher than unity:



Following this reaction, carbon deposits on the metastable  $\text{Fe}_3\text{C}$  by any number of reactions, such as for example:



The immediate consequence of the carbon deposition reaction is that the thermodynamic activity of carbon at the interface between  $\text{Fe}_3\text{C}$  and deposited carbon is reduced to unity. Since iron carbide cannot exist thermodynamically at unit carbon activity, it starts to dissociate by the reaction



Reaction [5.4] generates iron powder or dust – thus the above scheme explains how bulk metal is converted to metallic powder. A pictorial representation of the Hochman mechanism has been given by Grabke.<sup>9</sup>

A key aspect of the metal dusting reaction that Hochman's researches did not quite resolve involves the fate of the metal particles generated by reaction [5.4], essentially how these are carried away from the reaction zone so that reaction [5.4] can continue in a kinetic sense. This question was addressed by Pippel *et al.*<sup>10</sup> and by Chun *et al.*<sup>11–13</sup> These investigators showed by high-resolution transmission electron microscopy that graphitic carbon with the (0001) planes in appropriate alignment to the  $\text{Fe}_3\text{C}$  can indeed provide sufficient interplanar spacing for the escape of metal atoms away from the reaction interface.

The design of high temperature alloys for corrosion resistance is based largely on the ability of the alloy to form a continuous and adherent surface oxide layer of  $\text{Cr}_2\text{O}_3$ ,  $\text{Al}_2\text{O}_3$  or  $\text{SiO}_2$  when exposed to the environment. In the metal dusting temperature range, both  $\text{SiO}_2$  and  $\text{Al}_2\text{O}_3$  would form very sluggishly so that the preferred alloys are chromia formers. While some alloys are more resistant than others, most alloys are susceptible to metal dusting to some degree as indicated in long-term (10,000 hr) investigations by Klower *et al.*<sup>14</sup> In general, when rupture of chromia film occurs, in many situations carbon can rush in to induce metal dusting as shown by Grabke.<sup>9</sup>

Chun *et al.* have conducted a series of investigations on pure metals,<sup>11–13</sup> Fe, Co and Ni; on ferritic steels over a range of Cr content;<sup>15</sup> on Ni based alloys<sup>16</sup> and on Fe-Ni based alloys.<sup>17,18</sup> These investigations have been carried out using CO-H<sub>2</sub> gas mixtures as the corrosive medium. The present chapter combines the results from these various studies to provide an overall understanding of the behavior of alloys in metal dusting environments and provides some general conclusions about the metal dusting of alloys. The study also provides some guidelines for the control of metal dusting.

### 5.3 Nature of the metal dusting environment

A CO-H<sub>2</sub> gas mixture, particularly 50CO:50H<sub>2</sub>, has been used over a broad temperature range from 450°C to 900°C at ambient pressure for up to 160 hours in investigations detailed in this chapter. Both the pseudo-equilibrium carbon activity (by not allowing carbon to precipitate) and the oxygen partial pressure of the gas mixture were estimated and are presented in Table 5.1. Carbon monoxide is the most potent metal dusting molecule and the presence of H<sub>2</sub> in CO tends to accelerate metal dusting corrosion. In fact reaction [5.2] has been shown to exhibit the fastest carbon transfer kinetics on metal surfaces.<sup>19,20</sup>

The metal dusting environment is characterized by carbon activities higher than unity and very low oxygen partial pressures. Generally the carbon activity decreases with increasing temperature while the oxygen partial pressure increases with temperature. There are differences in the metal dusting gas mixtures used by different investigators. Grabke<sup>9</sup> has used CO-H<sub>2</sub> mixtures in which the H<sub>2</sub> is presaturated with water vapor, the specific mixture having a composition 73.4% H<sub>2</sub>, 24.7% CO and 1.9% H<sub>2</sub>O. In most experiments in the present work a mixture of 50% CO with 50% H<sub>2</sub> has been used. With this mixture, a reaction between the two gases will lead to the generation of water vapor at the metal dusting temperature.

The reaction that transfers carbon to the metal surface to trigger metal dusting can be written as:



*Table 5.1* Pseudo activities of carbon and oxygen in the 50CO:50H<sub>2</sub> metal dusting environment as a function of temperature

Temperature (°C)	$a_c$	$P_{\text{O}_2}$ (atm)
450	5173	$4.3 \times 10^{-34}$
550	332	$8.9 \times 10^{-30}$
650	39	$2.2 \times 10^{-26}$
750	6.8	$1.2 \times 10^{-23}$

By considering the pseudo-equilibrium of reaction [5.2] where carbon is not allowed to precipitate out, one can calculate the activity of carbon from the equilibrium constant  $K_{5.2}$  of reaction [5.2] using a thermodynamic estimate of the amount of  $\text{H}_2\text{O}$  generated. Thus,

$$\log K_{5.2} = -7100/T + 7.496 \quad 5.5$$

and

$$a_c = K_{5.2} \cdot P_{\text{CO}} \cdot P_{\text{H}_2} / P_{\text{H}_2\text{O}} \quad 5.6$$

The oxygen partial pressure of the environment can be obtained by considering the equilibrium

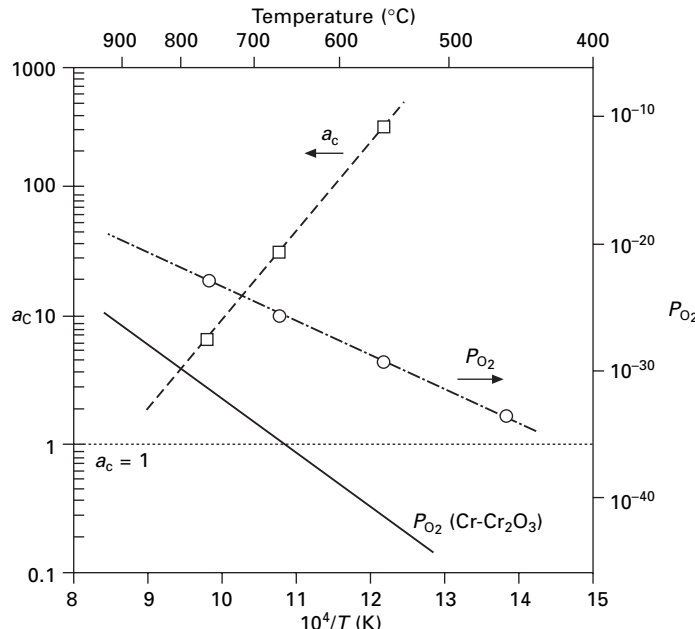


The equilibrium constant  $K_{5.7}$  and  $P_{\text{O}_2}$  are given by

$$\log K_{5.7} = (22,027/T) - 1.958 \log T \quad 5.8$$

$$P_{\text{O}_2} = (1/K_{5.7}) \cdot (P_{\text{H}_2\text{O}}/P_{\text{H}_2})^2 \quad 5.9$$

Carbon activity calculations and oxygen partial pressure calculations for the gas mixtures used in the experiments are presented in Table 5.1 and plotted in Fig. 5.1. Also shown is the coexistence  $\text{Cr}-\text{Cr}_2\text{O}_3$  oxygen pressure.



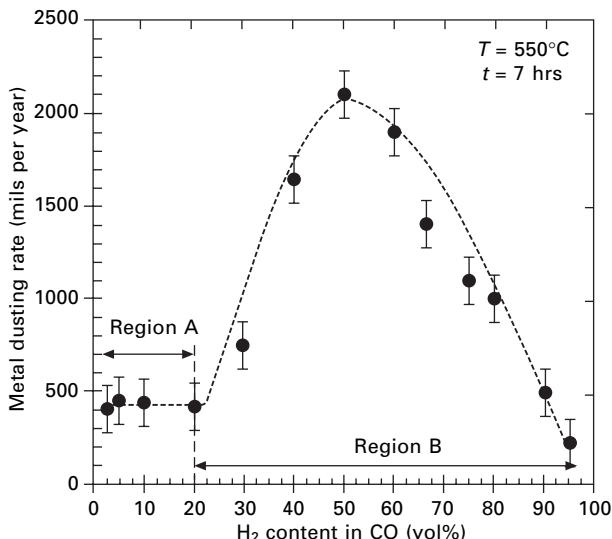
5.1 Pseudo carbon activity and oxygen activity as functions of temperature in the 50CO:50H<sub>2</sub> metal dusting environment.

Thus,  $\text{Cr}_2\text{O}_3$  is seen to be stable in the selected environments.  $\text{Al}_2\text{O}_3$  and  $\text{SiO}_2$  are even more stable and therefore can provide protection in metal dusting environments. Our experience shows that spinels such as  $\text{MnCr}_2\text{O}_4$ ,  $\text{FeCr}_2\text{O}_4$  and  $\text{NiCr}_2\text{O}_4$  are also stable and can provide protection from metal dusting under selected conditions.

## 5.4 Metal dusting of pure metals

### 5.4.1 Metal dusting of Fe

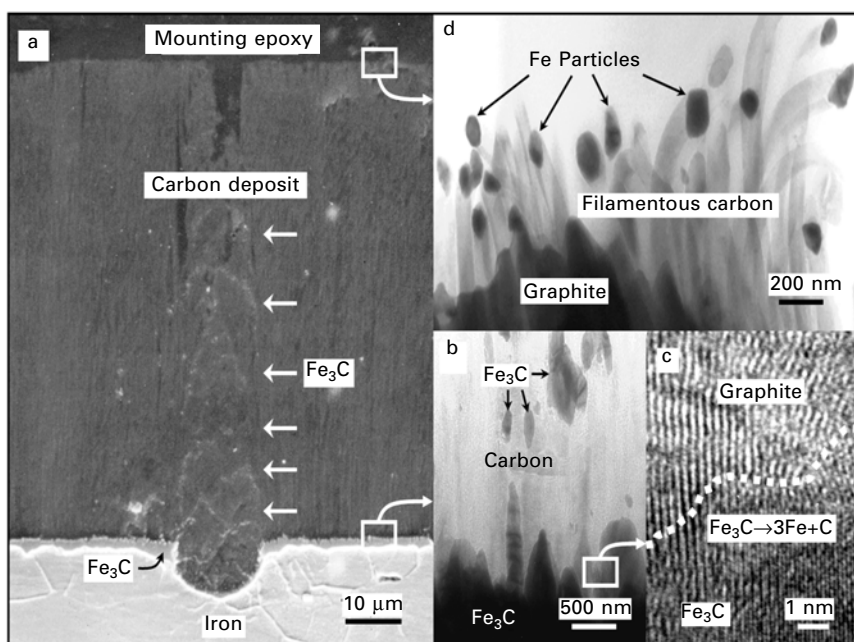
A detailed study of the metal dusting corrosion of Fe has been reported previously.<sup>11</sup> Some of the key findings are summarized here. Polycrystalline Fe foils of 100 to 250  $\mu\text{m}$  thickness were exposed to  $\text{CO}-\text{H}_2$  gas mixtures of varying  $\text{CO}/\text{H}_2$  ratios at temperatures ranging from 350 to 950°C for different time periods in a tubular reactor. The rates of corrosion were determined microscopically by measuring the recession of the metal surface with respect to an inert Au marker placed initially on the surface. For short durations of corrosion, up to about 7 hours, the rates depended on the  $\text{CO}/\text{H}_2$  ratio as indicated in Fig. 5.2 for reaction at 550°C. The general corrosion rate is seen to go through a maximum at equal concentrations of CO and H<sub>2</sub>. At low H<sub>2</sub> contents, the corrosion rate is more or less constant. While the reason for this constant region is unclear, the rate increase to reach a maximum and its subsequent decline are strong indications that reaction [5.2] is the rate-limiting carbon transfer reaction to the metal surface. According to reaction [5.2], the



5.2 Metal dusting rate of Fe as a function of H<sub>2</sub> content in CO determined after 7 hours of corrosion at 550°C.

forward rate of the carbon transfer reaction should be proportional to the product of the concentrations of CO and H<sub>2</sub>, thus exhibiting parabolic behavior. The corrosion rate maximum is expected to occur at the 50CO:50H<sub>2</sub> gas composition.

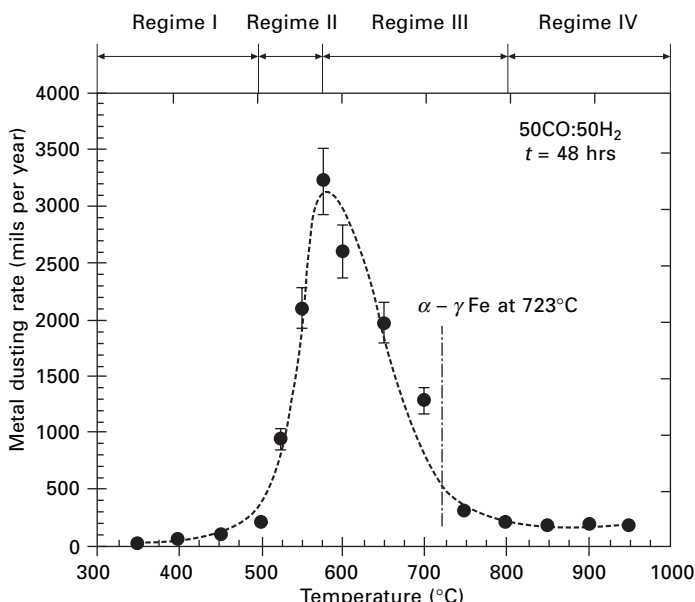
The morphology of corrosion for the 50CO:50H<sub>2</sub> mixture after 7 hours of corrosion is depicted in Fig. 5.3. Figure 5.3a shows that the metal surface is covered by a carbon deposit and further that both general and local corrosion events have occurred. In most regions, the corrosion morphology is characteristic of general corrosion; localized corrosion is observed only occasionally. Further, the corroded iron surface is covered by a surface layer of Fe<sub>3</sub>C. Pieces of Fe<sub>3</sub>C, dislodged from the surface layer, are seen embedded in the carbon deposit, Fig. 5.3b. The Fe<sub>3</sub>C/C interface is characterized by graphitic planes in more or less perpendicular alignment, Fig. 5.3c. Electron diffraction from this region reveals the presence of Fe particles in addition to graphite. The outer surface of the carbon deposit is profuse with filamentous carbon, Fig. 5.3d, with Fe particles at the tip of the filaments. Thus, the Hochman proposal<sup>1</sup> for metal dusting corrosion in accordance with reactions [5.1] and [5.4] seems to be operative.



5.3 Nature of Fe surface after corrosion in 50CO:50H<sub>2</sub> for 7 hours at 550°C showing (a) both localized and general corrosion, (b) surface Fe<sub>3</sub>C with fragments of Fe<sub>3</sub>C dislodged into the carbon deposit, (c) graphite planes containing Fe in perpendicular alignment with Fe<sub>3</sub>C, and (d) filamentous carbon at the outer surface.

The corrosion rate of Fe in CO–H<sub>2</sub> mixtures is observed to be strongly dependent on temperature; results for experiments with the 50CO:50H<sub>2</sub> mixture after 48 hours of corrosion are shown in Fig. 5.4. Four regimes can be identified: a low temperature region where the rate increases slowly with temperature, the next region where there is rapid rise in the corrosion rate leading to a maximum, then a region where the rate rapidly decreases with temperature, and finally a regime of more or less constant corrosion rate at the very high temperatures. It appears that the rapid rise in rate is characterized by more or less equal contributions to corrosion from iron carbide growth and iron carbide dissolution. The rapid decrease in rate in regime III can be explained by a situation where iron carbide growth rate is faster than its dissociation rate – much thicker iron carbide layers were observed in this region.<sup>11</sup> The degree of metastability of Fe<sub>3</sub>C (measured by its carbon activity) is what drives its dissociation. Since the carbon activity in Fe<sub>3</sub>C decreases with increase of temperature, it is reasonable to expect that its dissociation kinetics will slow down at the higher temperatures. In regime IV iron carbide is not present and a different metal dusting mechanism is operative.

Detailed cross-sectional transmission electron microscopy of the Fe<sub>3</sub>C/carbon deposit interface corresponding to regime II and regime III reveals that graphitic carbon with its (0001) planes perpendicular to the iron carbide surface is present in many regions of the interface (Fig. 5.3). A mechanism

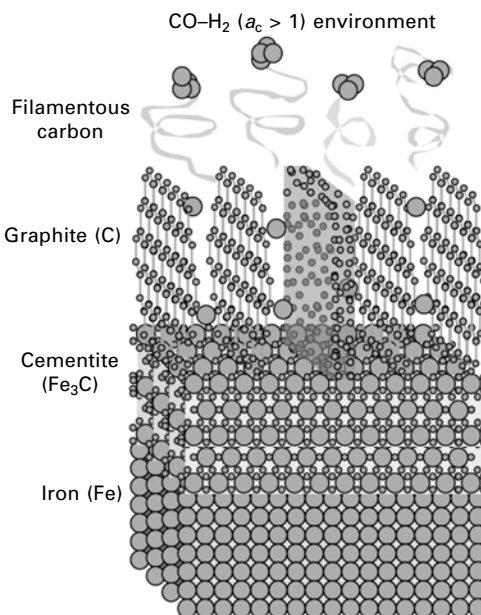


5.4 Corrosion rate of Fe in 50CO:50H<sub>2</sub> after 48 hours of exposure as a function of temperature (adapted from ref. 11).

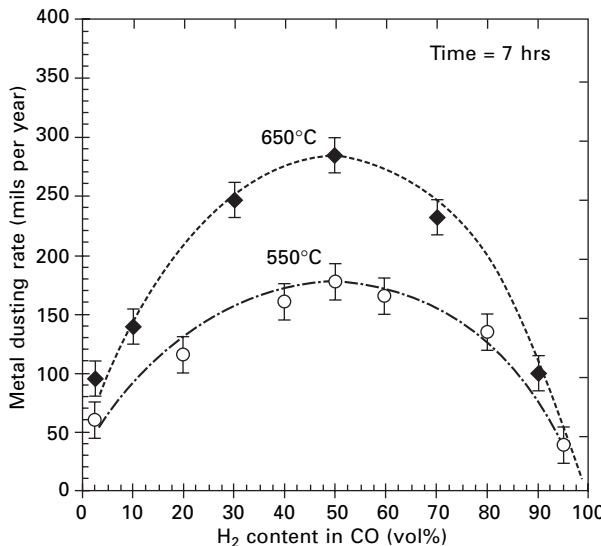
involving the outward transport of Fe atoms from dissociated  $\text{Fe}_3\text{C}$  through the spacing provided by perpendicularly oriented graphite planes is proposed (Fig. 5.5). At the outer surface of graphite, the iron atoms have been observed to coalesce into fine iron particles that catalyze the formation of filamentous carbon. Thus a pathway is created to move the iron atoms generated by iron carbide dissociation away from the corrosion interface. This is in agreement with studies reported previously by Pippel *et al.*<sup>10</sup> Perpendicularly aligned graphite has been observed next to the iron surface in regime IV where no iron carbide is present. A plausible explanation of the mechanism of metal dusting corrosion in this regime is the direct intercalation of Fe atoms from the bulk metal lattice into graphite, followed by their outward transport.

#### 5.4.2 Metal dusting of Ni and Co

The fundamental way in which Fe differs from Ni<sup>12</sup> and Co<sup>13</sup> from a metal dusting perspective is that the latter two metals do not form metastable carbides or carbides in general. Thus investigations of the metal dusting of Ni and Co reveal significant differences from Fe. Similar to Fe, for short exposure times (~7 hours or less), the metal dusting reaction is surface reaction controlled and shows a maximum rate at the 50CO:50H<sub>2</sub> composition (Fig. 5.6). At the interface between the metal and carbon deposit, no carbide



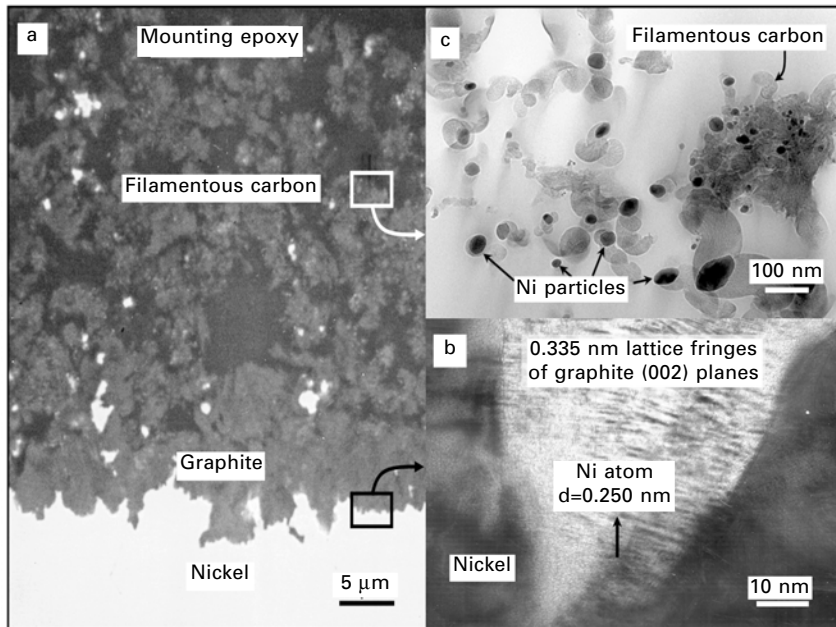
5.5 Schematic mechanism for Fe corrosion by  $\text{Fe}_3\text{C}$  dissociation and Fe transport through graphite (adapted from ref. 11).



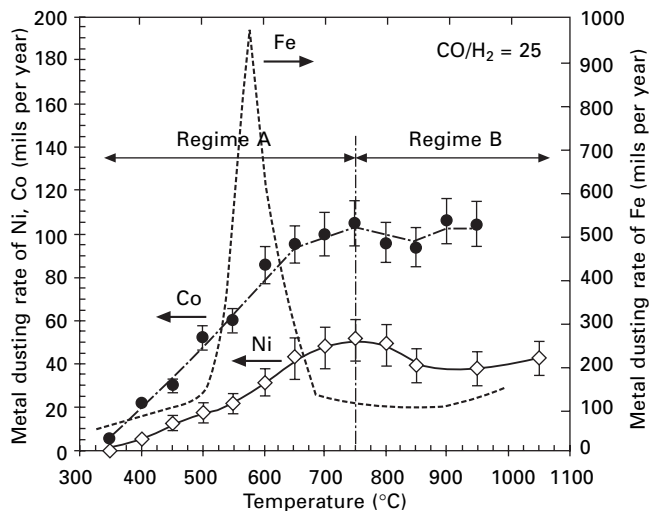
5.6 Metal dusting rate of Co after 7 hours of corrosion at 550°C and 650°C as a function of H<sub>2</sub> content in CO (adapted from ref. 13).

is observed, Fig. 5.7. Graphitic carbon is observed next to the metal surface as also is filamentous carbon at the outer surface of the carbon deposit. The situation, in some ways, is similar to regime IV described in the previous section for the metal dusting of Fe where Fe<sub>3</sub>C does not form. There is also evidence of graphite intrusion<sup>12,21,22</sup> into Ni. The metal dusting rate of Ni and Co in 50CO:50H<sub>2</sub> is shown in Fig. 5.8. Two regimes can be distinguished in the corrosion rate vs. temperature graph: from about 350 to 750°C, there is gradual increase in the metal dusting rate, and beyond this temperature the rate is more or less constant. Investigations of the carbon deposit using Raman spectroscopy<sup>13</sup> indicate that the nature of carbon changes gradually from amorphous to graphitic as the temperature increases, the carbon being almost completely graphitic above ~750°C. Electron diffraction from the carbon deposit next to the metal also confirms the predominance of graphitic carbon at the higher temperatures. Thus graphite of the right orientation seems to provide the pathway for direct metal intercalation and outward diffusion as discussed for Fe in regime IV. At the lower temperatures where the proportion of graphite is less, the metal dusting rate is also less.

Also superimposed in Fig. 5.8 is the metal dusting rate for Fe. It is seen that the maximum metal dusting rate of Fe is at least an order of magnitude larger than the maximum metal dusting rate for Ni or Co. Clearly the metastable carbide-induced metal dusting is a more intense phenomenon leading to higher corrosion rates. One possible explanation is that the dissociation of metastable Fe<sub>3</sub>C results in profuse amounts of iron of atomic dimensions



5.7 The corroding interface of Ni during metal dusting showing graphitic carbon next to the metal surface and filamentous carbon at the outer surface of graphite. Note the intrusion of carbon into Ni (adapted from ref. 12).



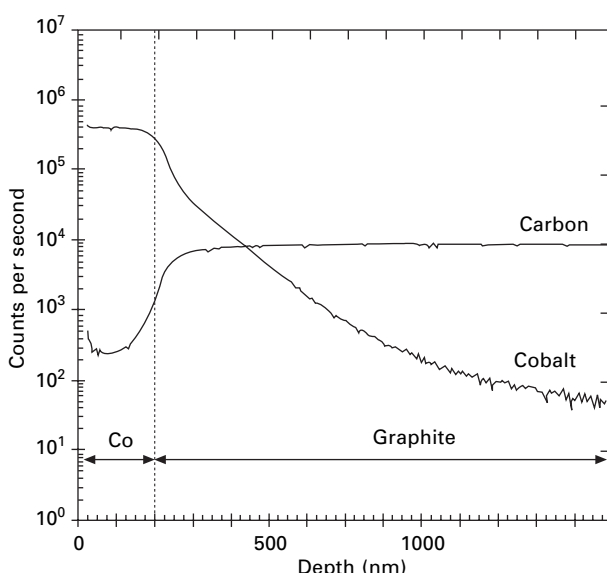
5.8 Metal dusting rate of Ni and Co as a function of temperature (adapted from ref. 13).

that are readily intercalated into the graphite lattice. The direct intercalation of metal atoms from bulk metal, as expected to occur for Ni and Co and for Fe in regime IV, is kinetically much slower.

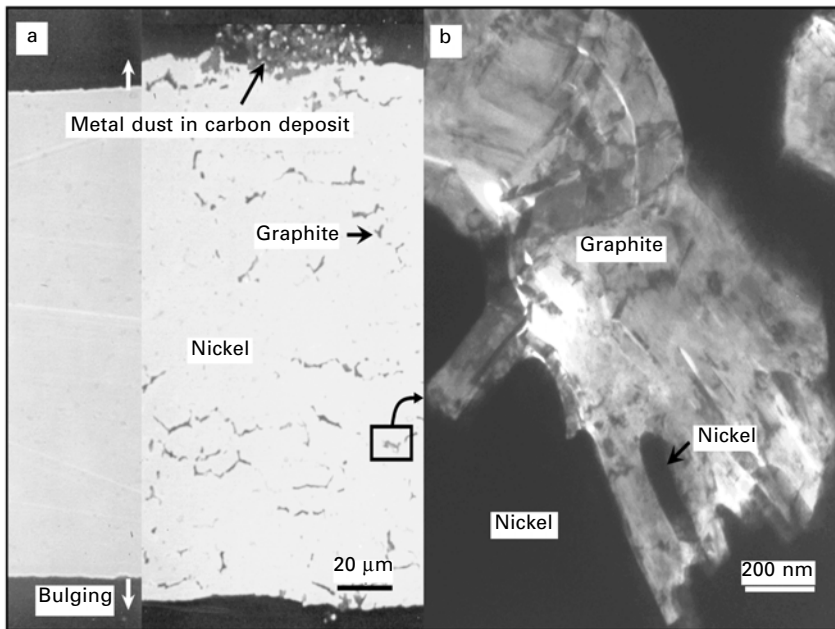
To confirm the intercalation of metal atoms from bulk metal into graphite, a thin film of Co having a thickness of 200 nm was sputter-coated on to the face of a single crystalline graphite rod with graphitic planes aligned perpendicular to the deposited Co.<sup>13</sup> After annealing for 550°C for 1 hour in an inert environment, a concentration depth profile for Co, obtained using a Cameca secondary ion mass spectrometer (Fig. 5.9), shows that indeed Co has diffused through basal planes in graphite.

Another mechanism that is operative for the metal dusting of Ni and Co is the diffusion of carbon into the metal followed by the precipitation of graphite in the interior. This can result in the dislodging of Ni particles of micron size into the carbon deposit. Such a reaction is not characteristic of Fe. An example of this form of bulk disintegration is shown in Fig. 5.10. The dimensional change in Ni by bulging resulting from internal graphite precipitation is evident from Fig. 5.10a.

The observation that Fe corrodes much faster than Ni in a metal dusting environment could be significant in the design of alloys for metal dusting resistance. Most alloys can be classified as Fe based, Ni based or Fe-Ni based. In what follows, the behavior of alloys in metal dusting environments is discussed, primarily based on experiments carried out by the authors.



5.9 Demonstration of the intercalation of Co into graphite using a Co-graphite diffusion couple at 550°C for 1 hour (adapted from ref. 13).



5.10 SEM and TEM images showing bulk disintegration of Ni by graphite precipitation upon exposure to 50CO:50H<sub>2</sub> at 550°C for 7 hours (adapted from ref. 12).

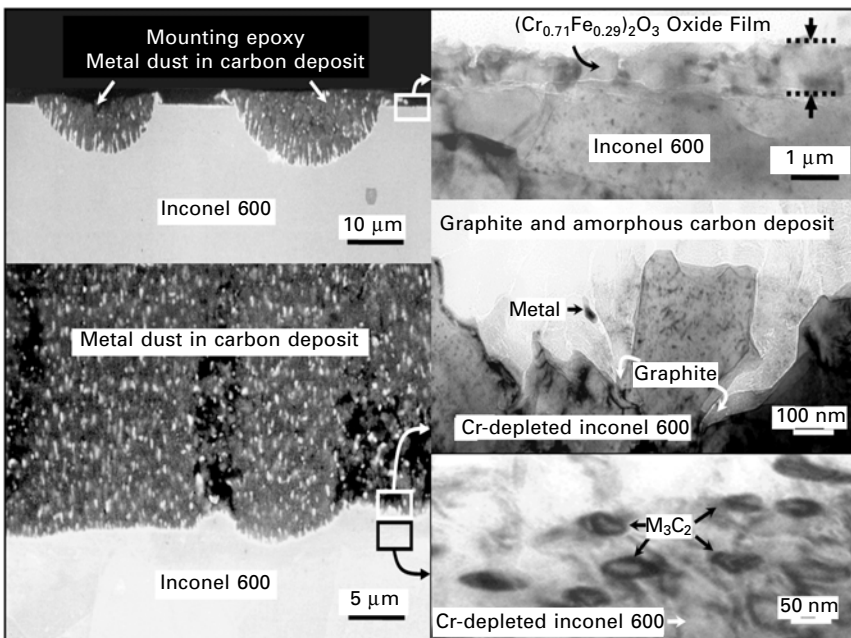
## 5.5 Metal dusting of alloys

### 5.5.1 Ni based alloys

A number of investigations have been reported in the literature on the metal dusting of Ni based alloys.<sup>14,16,23,24</sup> The present discussion focuses on studies conducted by the authors. Three different Ni based alloys, namely Inconel 600, Inconel 601 and Inconel 693, have been investigated at temperatures ranging from 450 to 750°C in a 50CO:50H<sub>2</sub> gas mixture. The sample surfaces were polished down to Linde B surface finish (0.05 μm alumina polish). Investigations have indicated that the susceptibility to metal dusting is higher for smoother surface finishes.<sup>16</sup> The compositions of the alloys studied are indicated in Table 5.2. The most notable aspect of the composition is the increase in Cr content from ~16% in Inconel 600 to ~30% in Inconel 693. The metal dusting resistance of these alloys also increases in the order of increasing Cr content. Since these alloys are designed to develop a protective Cr<sub>2</sub>O<sub>3</sub> film in the corrosive environment, metal dusting selectively occurs in regions where the oxide film has either failed to establish itself or been penetrated because of defects in the film. As a result, the observed corrosion is almost always localized as revealed by the cross-sectional scanning electron micrograph in Fig. 5.11. The SEM image shown in Fig. 5.11 corresponds to

Table 5.2 Chemical compositions of Ni based alloys studied

Alloy name	UNS designation	Composition (wt%)
Inconel 600	N06600	Bal.Ni:15.5Cr:8.0Fe:0.3Mn:0.3Si: 0.3Al:0.3Ti:0.08C
Inconel 601	N06601	Bal.Ni:23.0Cr:13.0Fe:0.2Mn:0.2Si: 1.4Al:0.4Ti:0.05C
Inconel 693	N06693	Bal.Ni:30.0Cr:4.0Fe:3.0Al:0.3Ti



5.11 Metal dusting corrosion of Inconel 600 at 750°C for 160 hours showing localized corrosive attack, regions protected by surface oxide, metal dust within carbon deposit, graphite intrusion into alloy, and M<sub>3</sub>C<sub>2</sub> carbide precipitates in the alloy subsurface region (adapted from ref. 16).

Inconel 600 after reaction in 50CO:50H<sub>2</sub> for 160hr at 750°C. The unattacked regions are characterized by a protective chromium-rich oxide film. In the regions of localized corrosion significant carbon deposition has occurred. Ni-rich metal particles (91Ni:8Fe:1Cr wt%) as large as ~1 μm in dimension are observable within the carbon deposit; much finer Ni-rich metal particles with dimensions of several nanometers have been observed by TEM. The alloy/carbon interface has a serrated appearance and shows several fragments of Ni-rich alloy on the verge being enveloped within the carbon deposit. In addition to Ni-rich particles, the carbon deposit and the alloy interior contain

$M_3C_2$  type carbide precipitates of varying sizes. The M in the carbide formula consists of about 48 wt% Cr, 45% Ni and 7% Fe. The alloy next to the carbide is severely depleted in Cr, with a composition of 84% Ni, 6% Cr and 10% Fe.

The above observations clearly indicate that metal dusting of Inconel 600 occurs by intrusion of carbon into the alloy in regions not protected by a surface oxide. In the high carbon activity provided by the intruding carbon, the precipitation of  $M_3C_2$  type carbide depletes the alloy significantly in Cr. Further, TEM studies (Fig. 5.11) have shown that graphitic carbon grows into the alloy, the dissolved carbon in the carbon-supersaturated alloy most likely attaching itself to the inward-growing carbon precipitate. Thus the presence of Ni-rich metal particles in the carbon deposit is a consequence of the breakdown of the alloy by a combination of  $M_3C_2$  precipitation and inward carbon growth.

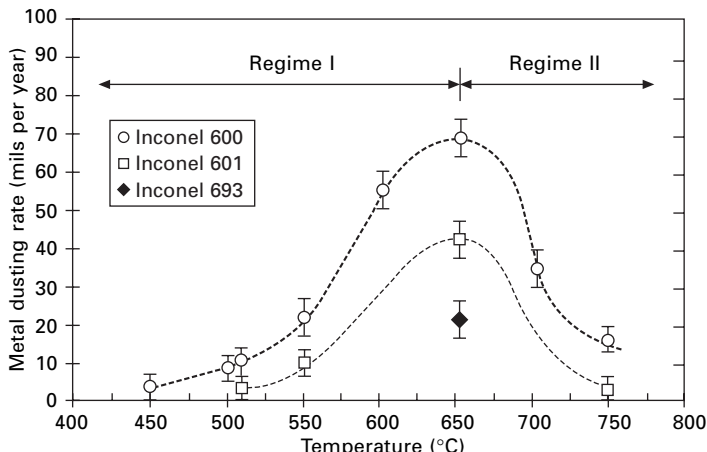
The general features described above for the metal dusting corrosion of Inconel 600 can also be extended to the other Ni based alloys except that the corrosion intensity decreases with increase of Cr content. The rate of corrosion is also a strong function of temperature. Shown in Table 5.3 are the density and maximum depth of corrosion pits on the different alloys as a function of temperature. The maximum local metal dusting rate is plotted as a function of temperature in Fig. 5.12. It is interesting to note that a maximum in the rate of metal dusting occurs around 650°C. Thus there are two corrosion regimes, regime I to the left of the maximum and regime II to the right of the maximum.

#### *Mechanism of metal dusting in regime I*

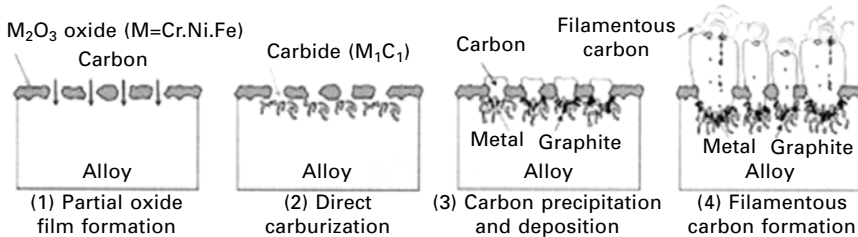
The increased rate of metal dusting with temperature in regime I can be generally attributed to faster kinetics of the different sequential steps in

*Table 5.3 Characteristics of pits after corrosion reaction of Ni based alloys at various temperatures for 160 hours in 50CO:50H<sub>2</sub>*

Alloy name	Temperature (°C)	Maximum pit depth (μm)	Pit diameter (μm)	Pit density (number of pits/cm <sup>2</sup> )
Inconel 600	450	~2	~20	~125,000
	550	~10	~45	~50,000
	650	~32	~95	~12,000
	750	~8	~20	~3000
Inconel 601	450	~1	~20	~10,500
	550	~4	~60	~6500
	650	~20	~130	~2300
	750	~1	~40	~120
Inconel 693	650	~8	~15	~80



5.12 Metal dusting rate of selected Ni based alloys as a function of temperature showing two regimes of corrosion (adapted from ref. 16).



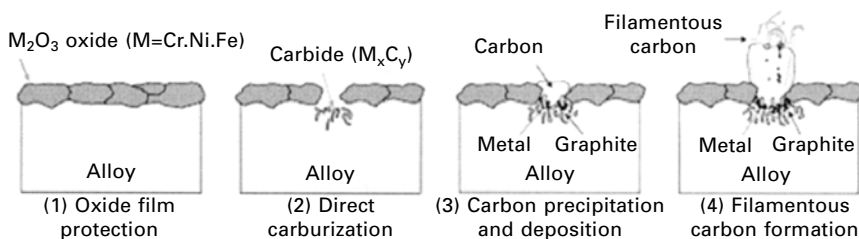
5.13 Schematic representation of the stages of corrosion progression for Ni based alloys in Regime I.

corrosion as the temperature increases. Four different steps have been proposed, namely *partial oxide film formation*, *direct carburization*, *carbon precipitation and deposition*, and *filamentous carbon formation*. These steps are schematically indicated in Fig. 5.13. In the temperature range 450–600°C, chromium oxide forms but sluggishly, thus a fully protective oxide film is not developed. The lower the temperature, the larger the number of discontinuities in the oxide film. This explains the larger density of pits at the lower temperatures. In locations where surface oxide is absent, carbon rushes in to precipitate the M<sub>3</sub>C<sub>2</sub> carbide in the second step. This is the stable carbide at the high carbon activities that prevail in the carbon-supersaturated alloy. Because of the high level of chromium depletion in the vicinity of the carbide precipitates, a Ni-rich alloy surrounds the precipitates; this alloy is incapable of forming a protective oxide film. As carburization proceeds, carbon also begins to deposit on the alloy surface (oxide-free regions). The deposited carbon consists of amorphous and graphitic forms, the graphitic

form predominating at the higher temperatures. Graphite also intrudes into the carburized alloy, the inward growth of graphite being assisted by the delivery of carbon from the carbon supersaturated alloy matrix. Thus, in step 3 in the reaction sequence, unreacted metal-rich particles become enveloped within the carbon deposit, forming regions of localized corrosion. A final step involves the intercalation of metal particles into graphite that is perpendicularly aligned to the corroding interface. The intercalated Ni atoms migrate to the outer environment, coalesce into Ni particles and catalyze the formation of filamentous carbon at the outer surface in the same manner as for the metal dusting of Ni. Since higher temperatures generally favor these steps in the corrosion sequence, the pit depth also reaches a maximum value around 650°C in regime I.

#### *Mechanism of metal dusting in regime II*

The stages of corrosion progression in regime II are shown in Fig. 5.14. These are very similar to regime I, the main difference being in the first two stages. At temperatures higher than 650°C, which typify regime II, two factors come into play. First, the temperatures are high enough to favor kinetically a complete layer of protective oxide. This tendency is greater the higher the temperature. Further, as shown in Fig. 5.1, the carbon activity of the environment decreases with temperature while the oxygen activity increases with temperature, providing a greater thermodynamic driving force for oxide formation. Thus, during the first stage the alloy is more or less protected from metal dusting corrosion. However, local defects in the oxide film can cause local rupture in the protective oxide. Also, in such regions, compositional fluctuations in the gas phase could occur; in particular hydrogen, being a smaller molecule, can more readily access the surface through defected regions of the oxide, thus creating even more reducing conditions than in the bulk gas mixture. As a consequence, re healing of the surface oxide is suppressed, allowing carbon to rush into the alloy, causing  $M_3C_2$  precipitation. The rest of the corrosion sequence is similar to regime I. This explains the lower rates of corrosion and lower density of pits observed at the higher temperatures.



5.14 Stages of corrosion progression for Ni based alloys in Regime II.

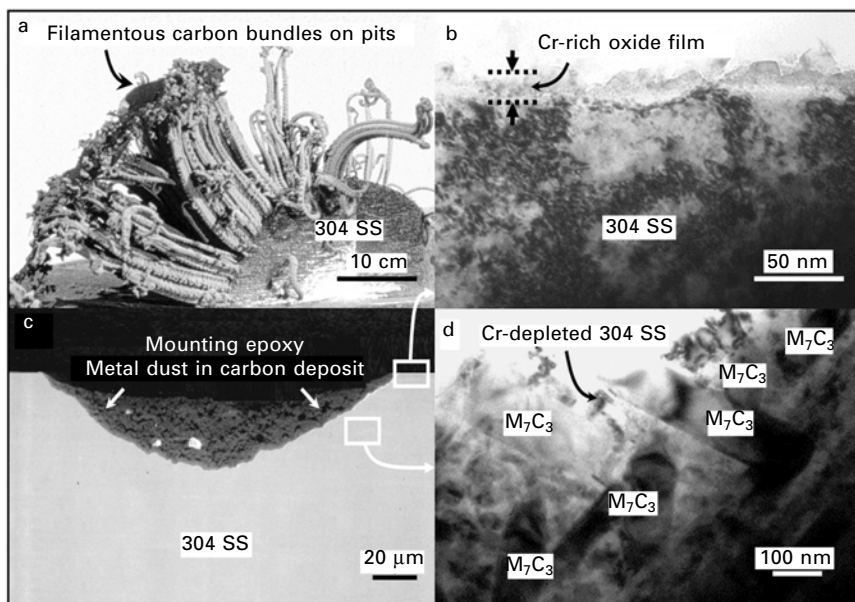
### 5.5.2 Fe-Ni based alloys

These alloys are characterized by an austenitic crystal structure. Examples of alloys belonging to this class are shown in Table 5.4 along with the corresponding compositions. Several studies of metal dusting of Fe-Ni based alloys are reported in the literature.<sup>17,18,25-28</sup> The alloys in this class are more susceptible to metal dusting than the Ni based alloys. Details are discussed here for two specific alloys, namely 304SS and the 35/45 alloy. As shown in Table 5.4, the former has about 19 wt% Cr while the latter has a substantially higher Cr level of ~32.0 wt%.

Just as in the case of Ni based alloys, the corrosive attack is localized, the unattacked regions being protected by a surface oxide which is rich in Cr. This is indicated by the scanning electron micrographs in Fig. 5.15. Figure

**Table 5.4** Chemical compositions of Fe-Ni based alloys studied

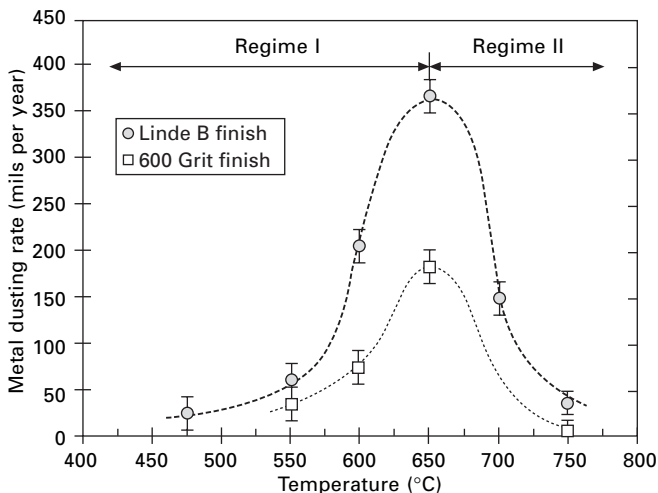
Alloy name	UNS designation	Composition (wt%)
304SS	S30400	Bal.Fe:18.7Cr:8.4Ni:1.88Mn:0.39Si:0.05C
35/45	N/A	Bal.Fe:32.1Cr:43.6Ni:0.9Nb:1.0Mn:1.7Si



**5.15** Metal dusting corrosion of 304 SS at 550°C for 160 hours showing filamentous carbon bundles on the surface, regions of localized corrosion filled with carbon deposit, regions protected by Cr-rich surface oxide, and M<sub>7</sub>C<sub>3</sub> carbides in the alloy subsurface (adapted from ref. 16).

**Table 5.5** Characteristics of pits after corrosion reaction of 304SS at various temperatures for 160 hours in 50CO:50H<sub>2</sub>

Temperature (°C)	Surface finish	Maximum pit depth (μm)	Pit diameter (μm)	Pit density (number of pits/cm <sup>2</sup> )
550	Linde B	~50	~310	~1650
	600 grit	~45	~320	~630
650	Linde B	~370	~680	~20
	600 grit	~180	~200	3
750	Linde B	~30	~150	2
	600 grit	No pits detected		



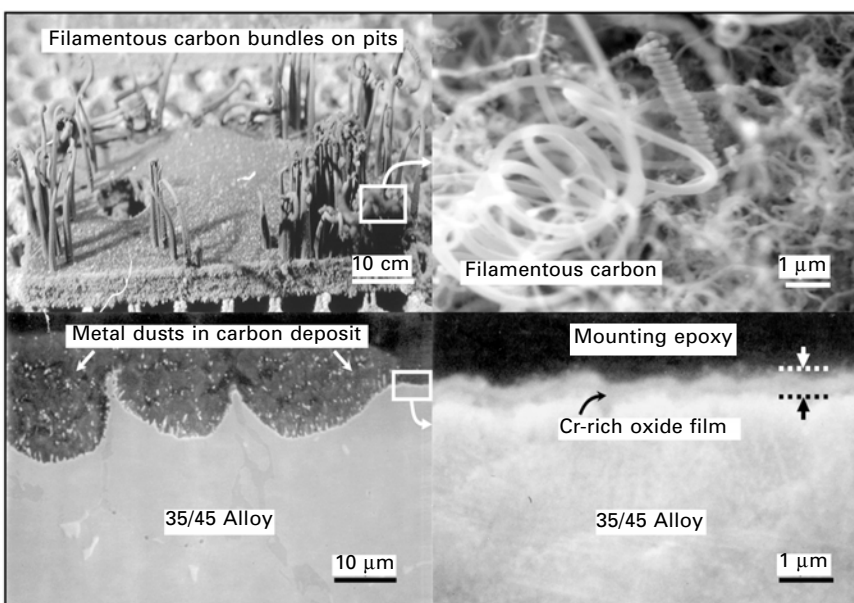
**5.16** Temperature dependence of the corrosion rate of 304 SS for Linde B Al<sub>2</sub>O<sub>3</sub> and 600 grit SiC surface finishes.

5.15a shows bundles of filamentous carbon growing out of regions of localized attack on 304 stainless steel (Linde B surface finish) at 550°C after 160 hours of corrosion in a 50CO:50H<sub>2</sub> gas mixture. Figure 5.15b indicates the pitted regions beneath the carbon bundles after these have been removed. Detailed TEM investigations of the corroded interface have revealed the presence of M<sub>7</sub>C<sub>3</sub> type carbides in the alloy subsurface, Fig. 5.15c. Away from the region of the pit, a Cr-rich oxide film provides protection from corrosion. The metal particles in the carbon deposit are enriched with respect to Ni, containing ~45 wt% Fe and ~55 wt% Ni. Table 5.5 shows the pit diameter, maximum pit depth and pit density for 304SS having Linde B surface finish as a function of temperature.

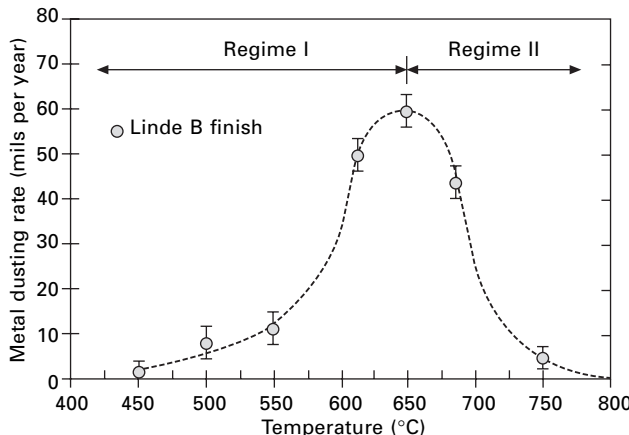
The rate of localized corrosion of 304SS as a function of temperature for two surface finishes, namely 600 grit SiC and Linde B alumina (0.05 μm finish), is shown in Fig. 5.16. It is interesting to note that there is again a

maximum in the rate of corrosion occurring around 650°C, just as in the case of the Ni based alloys. Thus two regimes of corrosion can be identified just as in the case of Ni based alloys. Also, the maximum corrosion rate for 304SS is seen to be about a factor of 8 larger than that for Inconel 600 (these two alloys have nearly similar Cr concentrations). This observation points up the greater susceptibility of Fe-Ni based alloys than Ni based alloys for metal dusting corrosion.

The high susceptibility of Fe-Ni based alloys for metal dusting is also evidenced by the optical and SEM images in Fig. 5.17 which corresponds to the 35/45 alloy after exposure to 50CO:50H<sub>2</sub> for 160 hours at 650°C. Just as for 304SS, bundles of carbon are evident on the corroded surface; these are made up of fine filamentous carbon. Beneath these bundles are revealed pitted regions of the alloy having carbon deposit containing metal particles. Regions away from the pitted areas are protected by a chromium-rich surface oxide. The Cr content of this alloy is close to that of the Ni based alloy, Inconel 693, but the pit density on this alloy is found to be substantially higher and the maximum localized corrosion rate is a factor of ~3 larger. The corrosion rate temperature curve for the 35/45 alloy with Linde B surface finish (Fig. 5.18) again goes through a maximum in the region of 650°C.



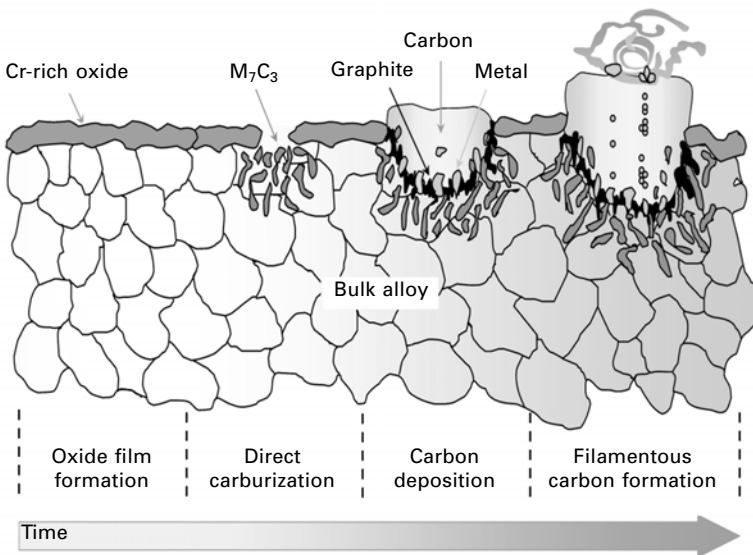
5.17 Optical and SEM images of the metal dusting of 35/45 alloy after 160 hours of corrosion at 650°C showing carbon bundles on the surface, localized corrosion regions filled with carbon deposit, alloy surface protected by Cr-rich oxide film, and filamentous carbon in the carbon bundles.



5.18 Localized corrosion rate of 35/45 alloy as a function of temperature for Linde B  $\text{Al}_2\text{O}_3$  surface finish.

The reason why one has a maximum in the corrosion rate–temperature curve is substantially the same as discussed earlier for the Ni based alloy systems. Thus, at lower temperatures to the left of the maximum, protective oxide formation is sluggish and as a result surface coverage by the oxide film is not complete. Thus carbon is able to enter the alloy causing carburization and precipitation of  $\text{M}_7\text{C}_3$  type carbide. Carbon precipitation and deposition occur at the surface of the carbide-saturated region. Again, the precipitation of profuse amounts of  $\text{M}_7\text{C}_3$  carbides in the alloy subsurface breaks the alloy into small regions of Fe-Ni enriched particles which become engulfed within the carbon deposit. In addition, through graphitic regions that are more or less perpendicularly aligned with the surface, metal atom intercalation and outward diffusion occur, leading to metal coalescence and catalytic formation of filamentous carbon at the outer surface. The inward growth of graphite into the alloy that was observed in Ni based alloys is not so evident in the case of Fe-Ni based alloys.

To the right of the maximum in the corrosion rate–temperature curve, oxide growth and complete surface coverage by protective oxide are facilitated by the enhanced kinetics at the higher temperatures and also by the higher oxygen partial pressures and slightly lower carbon activities. Thus, as shown in Fig. 5.19 and discussed earlier for Ni based alloys, there is a distinct stage in the progression of corrosion where oxide film protection is realized. If oxide film rupture occurs locally, there is a competition between oxide rehealing by oxidation and carbon entry into the alloy through cracks in the oxide. Depending on the nature of cracks (or defects) in the oxide and the Cr concentration in the alloy immediately beneath the surface oxide, conditions could become favorable for carbon intrusion into the alloy. This leads to the



5.19 Schematic representation of the progression of corrosion of Fe-Ni based alloys at the higher temperatures.

direct carburization stage. Unlike the Ni based alloy case where most of the carbides observed are the  $M_3C_2$  type, in the case of Fe-Ni based alloys the  $M_7C_3$  type carbide is seen to be predominant. Carbon deposition occurs from the gas phase on the surface of this heavily carburized region, leading to metal dusting as discussed previously.

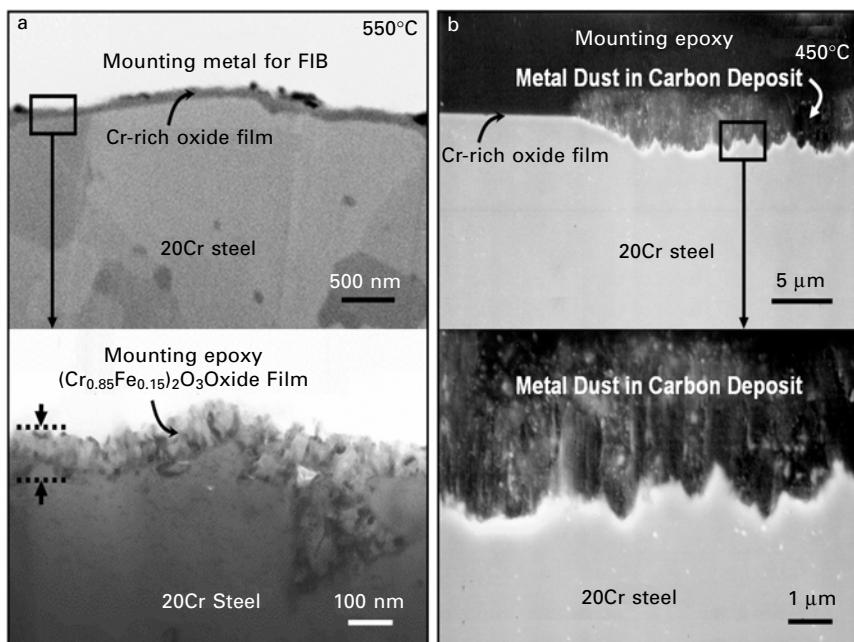
A significant question relates to why the metal dusting of austenitic Fe-Ni based alloys is more pronounced than that of Ni based alloys for similar Cr concentrations. This observation could be related to the fact that the solubility of carbon in austenitic Fe-Ni based alloys is significantly higher than that in Ni based alloys. Accordingly, the flux of carbon into the alloy in general is much higher, thus overriding the oxide rehealing process. Moreover, the kinetics of carburization are also faster because of the availability of more carbon in solid solution for reaction with the carbide-forming constituents in the alloy. For the Ni based alloys, under similar conditions, oxide rehealing is somewhat easier, since carbon dissolution and transport into the alloy is more sluggish on account of the much lower solubility and diffusivity.<sup>29</sup> On the other hand, the Cr diffusivity tends to be higher than that of austenitic Fe-Ni based alloys favoring protective oxide formation.<sup>9</sup> On this basis one can understand the greater susceptibility shown by austenitic Fe-Ni based alloys for metal dusting.

### 5.5.3 Fe based alloys

The metal dusting of Fe based alloys has been studied by some investigators.<sup>15,30-32</sup> The Fe based alloys considered here are those containing at least 20% Cr and having a ferritic crystal structure. Since the Linde B surface finish appeared to be generally more susceptible to attack, results are reported for this surface finish. The alloys investigated and their compositions are shown in Table 5.6. These include a model Fe-20Cr alloy and 446 steel. Investigations have been carried out by exposure to 50CO:50H<sub>2</sub> environments for ~160 hours in the temperature range 450–650°C. By and large these alloys showed excellent resistance to metal dusting corrosion except at the lower temperatures. Thus the Fe-20Cr experimental alloy (Linde B surface finish), upon exposure to the metal dusting gas at 550°C for 166 hours, showed no evidence of metal dusting, Fig. 5.20a. The alloy surface was

Table 5.6 Chemical compositions of Fe based alloys studied

Alloy name	UNS designation	Composition (wt%)
Fe-20Cr	N/A	Bal.Fe:20Cr
446	S44600	Bal.Fe:26Cr:0.8Mn:0.5Si:0.10C



5.20 Cross-sectional electron micrograph of Fe-20Cr alloy (Linde B Al<sub>2</sub>O<sub>3</sub> surface finish) showing protection by surface oxide at 550°C and regions of localized corrosion at 450°C.

uniformly covered with chromium-rich oxide ~100 nm thick containing some dissolved iron. The indicated composition of the oxide was obtained by EDX analysis from the thin oxide. However, upon decreasing the reaction temperature to 450°C, regions of metal dusting corrosion (corrosion rate ~6.5 mpy) could be identified as shown in Fig. 5.20b. At this low temperature and the prevailing Cr concentration in the alloy, incomplete surface coverage by the Cr-rich oxide provides a path for metal dusting to occur. The prelude to metal dusting in Fe based ferritic alloys could involve the successive precipitation of  $M_{23}C_6$  and  $M_7C_3$  carbides in the alloy subsurface. However, since rapid carburization occurs in a localized region, any  $M_{23}C_6$  that could have formed converts to  $M_7C_3$ , and only the latter carbide was identified by microanalysis. This observation is very similar to those for Fe-Ni based alloys.

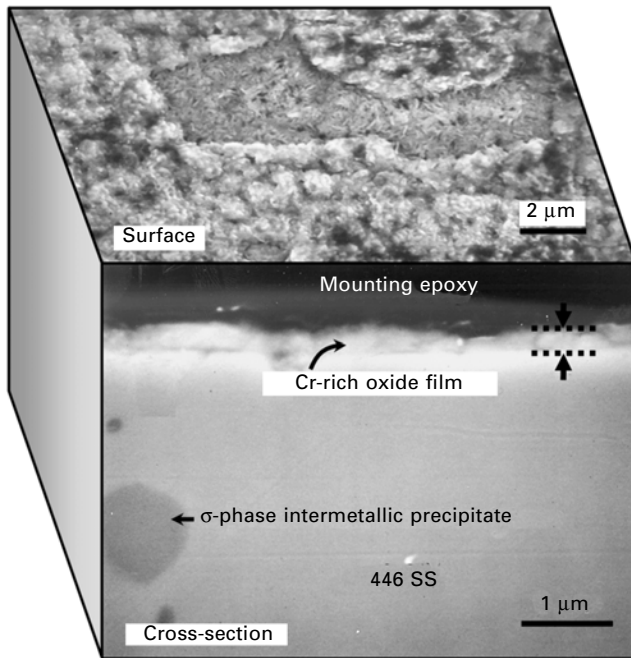
Chun and Ramanrayanan<sup>15</sup> have carried out a study of the metal dusting of low Cr steels having Cr contents of 1.25 Cr, 5 Cr, 9 Cr and 13 Cr in the temperature range 340–595°C. Both the 1.25 Cr steel and the 5 Cr steel behaved in a manner very similar to Fe. The formation of a layer of metastable  $M_3C$  carbide and its subsequent dissociation upon carbon deposition occurred on both these alloys. Corrosion became more and more localized as the Cr content increased. Significant metal dusting occurred on the 9 Cr and 13 Cr steels also, but no  $M_3C$  carbide could be detected. Severe local carburization in unprotected regions of the metal surface resulted in  $M_7C_3$  carbide formation, which subsequently became submerged in deposited carbon along with unreacted alloy particles.

The commercial ferritic steel 446, containing ~27% Cr, did not show any metal dusting corrosion in the 550–650°C temperature range. SEM images for the surface and cross-section are presented in Fig. 5.21. A continuous chromium-rich surface oxide is evident. No experiments were carried out at temperatures below 550°C. Chromium-rich intermetallic precipitates (sigma phase) can be seen in the alloy subsurface region (Fig. 5.21) – these brittle precipitates adversely affect the mechanical properties of the alloy.

The excellent metal dusting resistance of high-Cr ferritic alloys can be attributed to the relatively higher Cr diffusivity in the ferritic bcc lattice which facilitates a protective Cr-rich oxide film to develop at Cr concentrations equal to or higher than about 20%. This observation has also been made by Grabke.<sup>9</sup> However, for many structural applications, the mechanical properties of such steels may not be acceptable.

## 5.6 Control of metal dusting

Building on the understanding discussed in the previous sections, one can consider three approaches for controlling metal dusting corrosion. One approach is based on alloy compositions that have the intrinsic ability to form protective



5.21 SEM cross-section of 446 steel after metal dusting corrosion at 650°C showing protective surface oxide and intermetallic precipitates within the alloy.

oxide films in the metal dusting environment. A second approach targets the carbon transfer reaction occurring on the alloy surface and focuses on modifying the surface to suppress the carbon transfer reaction catalytically. There are essentially two ways to achieve this: one involves the incorporation of an additive in the environment which would preferentially interact with the alloy substrate to retard carbon transfer; the other is to use a metal coating that is catalytically inactive to the carbon transfer reaction. A third approach involves metal or alloy coatings that have the ability to form protective oxides readily under metal dusting conditions. These will be discussed in turn based on studies conducted by the authors.

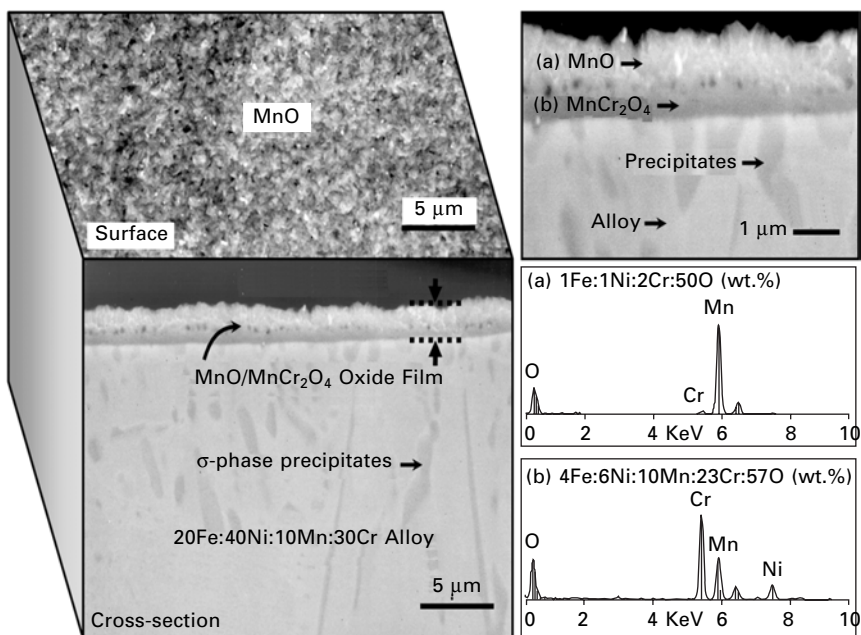
### 5.6.1 Alloys with intrinsic metal dusting resistance

As discussed in Section 5.5, chromia forming alloys that are widely considered for use in metal dusting environments suffer from the fact that in many cases a fully protective surface oxide is unable to form, or defected regions in the oxide are unable to reheat themselves for kinetic reasons. While high chromium ferritic alloys exhibit a better tendency for protective chromia film formation, the poor mechanical properties of such alloys render them unsuitable as bulk

materials in most applications. One way to facilitate protective film formation on Ni based or Fe-Ni based alloys is to introduce an alloying element that can form a very thermodynamically stable, yet rapidly growing surface oxide on the alloy initially in the metal dusting environment. The slower growing chromia film can then establish itself beneath the faster growing outer oxide. Manganese is a metal that can form a thermodynamically stable surface oxide in metal dusting environments and has a growth rate which is about two orders of magnitude higher than that of chromium oxide.<sup>33</sup> Thus, Fe-Ni-Cr-Mn alloys of appropriate compositions could, in principle, offer superior metal dusting resistance based on the above concept.

Different alloy compositions belonging to the Fe-Ni-Cr-Mn class were prepared by arc melting, followed by rolling to form sheets of 1/16 inch (1.6 mm) thickness and annealing overnight at 1100°C in argon followed by furnace cooling to room temperature. Rectangular samples of 0.5 inch × 0.25 inch (12.7 mm × 6.35 mm) were cut and polished down to 600 grit SiC followed by cleaning in acetone. The metal dusting corrosion resistance was investigated in the temperature range 650–850°C in 50CO:50H<sub>2</sub> for times extending up to 160 hours.

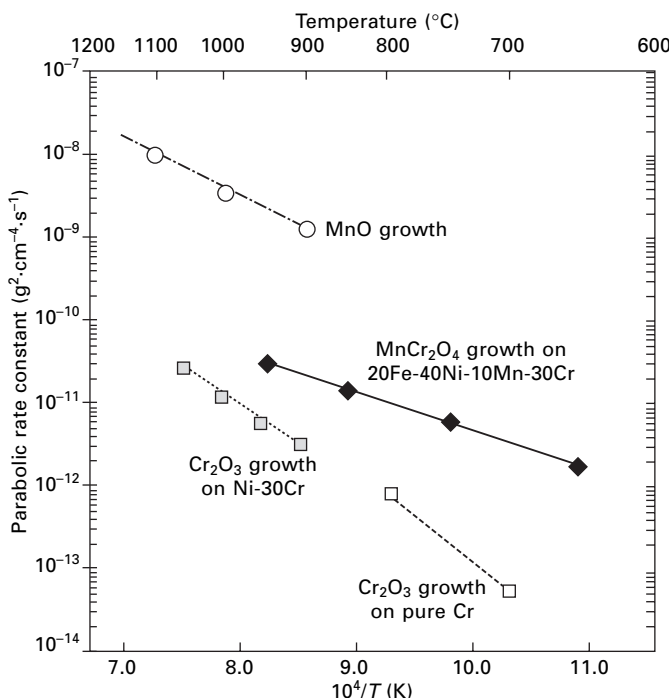
Shown in Fig. 5.22 is a cross-sectional scanning electron micrograph of a 20Fe-40Ni-10Mn-30Cr alloy after exposure at 850°C to a 50CO:50H<sub>2</sub>



5.22 Cross-sectional SEM and EDX spectra for 20Fe-40Ni-10Mn-30Cr alloy after exposure to 50CO:50H<sub>2</sub> at 850°C for 160 hours: shows outer MnO layer, inner MnCr<sub>2</sub>O<sub>4</sub> layer and intermetallic precipitates within the alloy.

environment for 160 hours. An outer surface of MnO, with a film of the MnCr<sub>2</sub>O<sub>4</sub> spinel beneath, is observed and provides full protection against metal dusting. No evidence of metal dusting is observed in the entire temperature range investigated. A time evolution study of surface film formation on this alloy indicates that immediately upon exposure, cubic MnO crystals nucleate on the surface and rapidly cover up the alloy, thus blocking carbon entry. Chromium oxide then nucleates and grows beneath the MnO. Simultaneously, a solid state reaction between MnO and Cr<sub>2</sub>O<sub>3</sub> occurs, leading to the formation of MnCr<sub>2</sub>O<sub>4</sub> beneath the outer MnO layer. While the fast-forming MnO surface layer provides initial protection from metal dusting, the underlying spinel layer provides long-term corrosion resistance.<sup>34,35</sup>

Cation diffusion through MnCr<sub>2</sub>O<sub>4</sub> is the rate-limiting step in the growth of the two-layered oxide discussed above. Thus the mass gain measured in the reaction of the alloy with the CO–H<sub>2</sub> mixture can be used to evaluate the parabolic growth constant<sup>34</sup> for MnCr<sub>2</sub>O<sub>4</sub>. The measured values are plotted as a function of temperature in Fig. 5.23. Also shown in Fig. 5.23 are the growth constants for MnO<sup>33</sup> and Cr<sub>2</sub>O<sub>3</sub>.<sup>36,37</sup> While the discovery of the above concept is exciting, further fine-tuning of the alloy chemistry is needed to



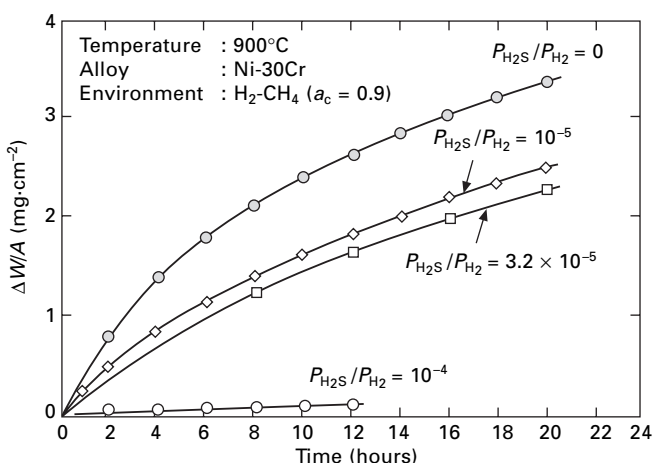
5.23 Parabolic rate constants for the growth of MnO, MnCr<sub>2</sub>O<sub>4</sub> and Cr<sub>2</sub>O<sub>3</sub> as a function of temperature.

prevent the formation of the brittle sigma phase in the alloy, evident in Fig. 5.22.

### 5.6.2 Suppressing the carbon transfer reaction

#### *Use of chemical additives*

Previous studies have shown that hydrogen sulfide at ppm levels has the ability to suppress carbon transfer onto metallic surfaces from carbonaceous molecules. Thus Grabke and co-workers<sup>38,39</sup> have investigated the dissociation of methane on Fe at high temperatures and found a significant H<sub>2</sub>S effect. At a temperature of 850°C, in methane–hydrogen environments having a carbon activity slightly less than unity, the amount of carbon uptake by iron is reduced by a factor of 10 when the H<sub>2</sub>S/H<sub>2</sub> ratio in the environment is 10<sup>-5</sup>. The fraction of the iron surface covered by sulfur is calculated to be about 0.9 at the above H<sub>2</sub>S level. Thus sulfur adsorbed on the Fe surface is responsible for retarding the carbon transfer reaction. Ramanarayanan and Srolovitz<sup>40</sup> have also found a significant influence of H<sub>2</sub>S on carbon transfer from methane to Fe-20Cr and Ni-30Cr alloy surfaces at high temperatures. Shown in Fig. 5.24 are thermogravimetric data for the uptake of carbon by Ni-30Cr in methane–hydrogen gas mixtures having a carbon activity of 0.9 at different concentrations of H<sub>2</sub>S in the carburizing gas mixture. The influence of H<sub>2</sub>S is seen to be significant. It was also shown in this study that the kinetics of carbon uptake by the alloy changed from a parabolic rate law in the absence of H<sub>2</sub>S to a linear rate law at H<sub>2</sub>S/H<sub>2</sub> ratios of about 10<sup>-4</sup> at 900°C, suggesting that it is indeed the surface transfer reaction that is being suppressed by H<sub>2</sub>S.



5.24 Suppression of carbon uptake by H<sub>2</sub>S from CH<sub>4</sub>–H<sub>2</sub> mixtures on Ni-30Cr alloy at 900°C (adapted from ref. 41).

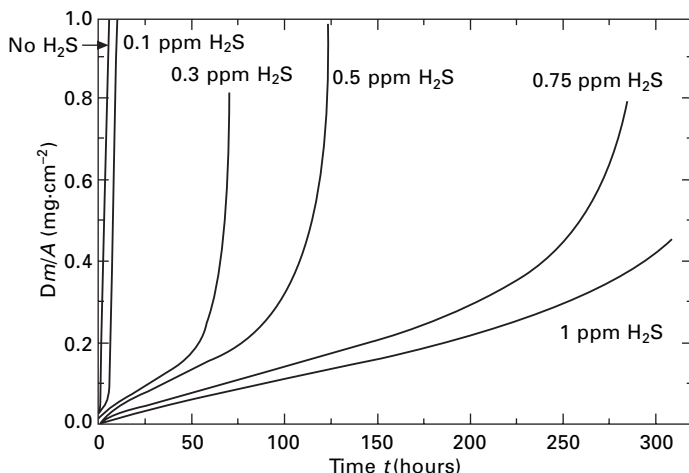
The maximum H<sub>2</sub>S effect was achieved at an H<sub>2</sub>S level just below that needed to precipitate the CrS phase on the alloy surface.<sup>40</sup>

Compared to carburizing environments, the metal dusting environment is characterized by much higher carbon activities. Even so, a significant retardation of metal dusting by H<sub>2</sub>S additions has been observed in studies by Schneider *et al.*<sup>41</sup> Using total carbon uptake measured thermogravimetrically as a measure of the metal dusting reaction, the effect of H<sub>2</sub>S is shown in Fig. 5.25 for Fe exposed to CO–H<sub>2</sub>–H<sub>2</sub>O–H<sub>2</sub>S at 500°C at a carbon activity of 1000. The data clearly indicate that even at high carbon activities, the influence of H<sub>2</sub>S on the carbon transfer reaction remains significant.

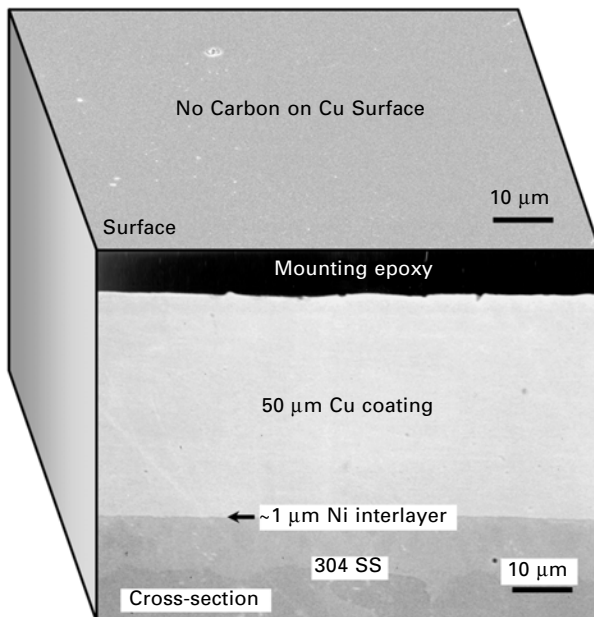
The use of H<sub>2</sub>S to control metal dusting has to be carefully evaluated for the specific application being considered. H<sub>2</sub>S is known to poison many catalyst surfaces and as such its use may not be attractive when metal dusting is occurring in a catalytic process.

### Metallic surface coatings

Metals belonging to Group IB of the Periodic Table, namely Cu, Ag and Au, are resistant to carbon transfer reactions from carbonaceous molecules. Thus in many metal dusting studies carried out by the authors<sup>11–13</sup> Au has been used as marker with respect to which metal or alloy recession has been measured microscopically during corrosion to determine both local and general rates of corrosion accurately. Of the three metals mentioned above, Cu is the least expensive and also the highest melting. Thus depending upon the temperature of application and the specific environmental conditions involved,



5.25 Effect of H<sub>2</sub>S on metal dusting of Fe at 500°C in CO–H<sub>2</sub>–H<sub>2</sub>O–H<sub>2</sub>S environments at  $a_c = 1000$  (adapted from ref. 41).



5.26 SEM cross-section of 50  $\mu\text{m}$  Cu coating on 304 SS with 1  $\mu\text{m}$  Ni interlayer after exposure to 50CO:50H<sub>2</sub> at 550°C for 44 hours.

Cu and Cu alloy coatings can be considered for providing effective resistance to carbon deposition.<sup>42–46</sup> They can also be used to control metal dusting.<sup>47–49</sup> The performance of Cu-coated 2  $\frac{1}{4}$ Cr– $\frac{1}{2}$ Mo steel, 304SS and Incoloy 803 has been investigated in 50CO–50H<sub>2</sub> at 550°C and 800°C. Shown in Fig. 5.26 is an SEM cross-section of a 50  $\mu\text{m}$  Cu coating on 304SS with a 1  $\mu\text{m}$  Ni interlayer after exposure to 50CO–50H<sub>2</sub> at 550°C for 44 hours. Hardly any carbon deposition was observed. However, interdiffusion across the interface must be taken into account. At a temperature of 800°C, interdiffusion is pronounced; however, no metal dusting is observed for the above system after 44 hours of corrosion. Investigations of a 30  $\mu\text{m}$  Cu coating with a 30  $\mu\text{m}$  interlayer on Incoloy 803 at 500°C show substantial resistance to interdiffusion effects. Thus Cu-coated alloy systems with appropriate Ni interlayers can be considered for providing metal dusting resistance, especially at the lower temperatures.

### 5.6.3 Coatings to promote protective surface oxide films

It was discussed in Section 5.5 that a primary reason why many chromia forming alloys, even with relatively high Cr concentrations, are susceptible to metal dusting is related to the paucity of achieving full surface coverage

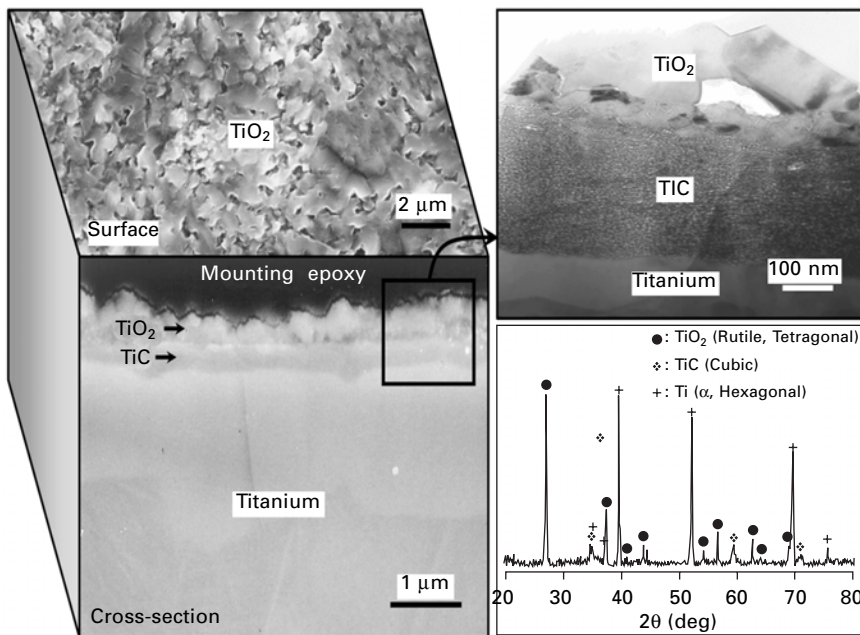
with a Cr-rich oxide film in the metal dusting temperature range. Thus metallic coatings designed to form a protective oxide barrier should have the capability to form the oxide film rapidly in the metal dusting environment. Two classes of coatings can be visualized: alloy coatings and pure metal coatings. These are discussed in turn.

In Section 5.1 the concept of a high-Cr alloy containing sufficient amounts of Mn to provide protection by a two-step protective oxide film formation sequence was discussed. Fe-Ni-Mn-Cr alloys of appropriate composition can function in this manner. It was also pointed out that certain alloy compositions in this system that are prone to brittle sigma phase formation cannot be considered for use as a bulk material. However, such compositions, especially if they exhibit excellent protective film forming tendencies, can be considered as coatings on both Ni based and Fe-Ni based alloy surfaces. The coating can be applied using techniques such as plasma spraying,<sup>50</sup> pack cementation,<sup>51</sup> chemical vapor deposition,<sup>52,53</sup> laser deposition,<sup>54,55</sup> etc.

Among pure metal coatings that can be considered to induce protective oxide formation in metal dusting environments, refractory metals belonging to Groups IVB, VB and VIB of the Periodic Table are of particular interest. Cr, of course, is known for its tendency for protective chromium oxide film formation. Thus chromizing<sup>51</sup> could be a suitable approach for corrosion control. In fact pure Cr, when exposed to a 50CO–50H<sub>2</sub> environment at 650°C for 24 hours, does not experience any corrosive damage. A chromium oxide surface film forms rapidly and prevents carbon deposition and metal dusting. As opposed to an alloy coating, a complete supply of Cr atoms on the surface ensures rapid coverage by chromia. Upon exposure of Ti to the 50CO–50H<sub>2</sub> environment at 650°C for 24 hours, neither metal dusting nor carbon deposition is observed. An SEM plan view and cross-sectional view revealing the Ti surface are shown in Fig. 5.27. A two-layered surface film is observed, the outer layer being TiO<sub>2</sub> while the inner layer is TiC as indicated by the X-ray diffraction spectrum, Fig. 5.27. A cross-sectional TEM image of the interface reveals the nanocrystalline nature of the inner TiC layer. This is further confirmed by the broadening of the X-ray peaks for TiC. Similar experiments with vanadium lead to a protective V<sub>2</sub>O<sub>3</sub> surface film about 0.5 μm thick. No underlying carbide layer is observed in this case. Situations that lead to an oxide/carbide layered surface film need further investigation.

## 5.7 Future trends

The discussion in this chapter has unveiled several important characteristics of metal dusting. First of all, it occurs in carbon supersaturated environments and in a temperature range of ~450–850°C. Secondly, the corrosion rate, in the case of most alloys, undergoes a maximum around 650°C, thus separating the corrosion process into a lower temperature regime where the rate increases



5.27 Electron micrographs and X-ray diffraction spectra of Ti after exposure to 50CO:50H<sub>2</sub> at 650°C for 24 hours showing outer TiO<sub>2</sub> and inner nanocrystalline TiC layers.

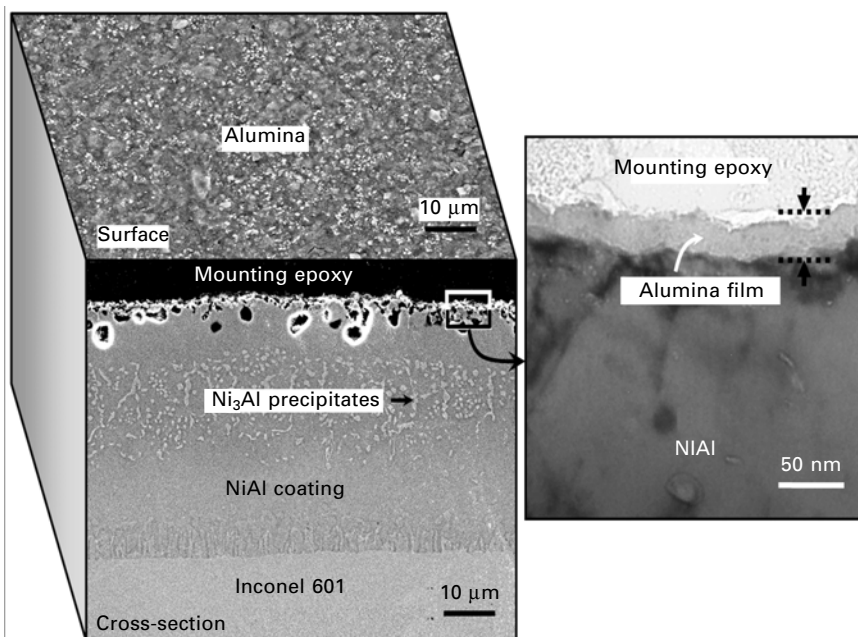
with temperature and a higher temperature regime where the rate decreases with temperature. The reasons for this, as detailed in this chapter, have to do with the paucity of protective chromium oxide formation at the lower temperatures and the different dependencies of the carbon activity and the oxygen activity of the environment on temperature. Fe based ferritic alloy systems behave rather differently because of the faster diffusivity of Cr in the bcc lattice of ferrite. Thirdly, the corrosion is almost always localized in nature, pointing up the inability of the protective oxide to reheat in such regions as a signifying force for corrosion.

Inasmuch as the overall temperature regime of metal dusting is below 850°C, chromia forming alloys will most likely be the most important class of alloys that will be considered for most applications. Ni based chromia forming alloys, in particular, have been found to provide significant corrosion resistance. Incoloy 693 is the most resistant Ni based chromia forming alloy made by the Special Metals Corporation. However, even at a high Cr content of ~30%, this alloy is still not immune to metal dusting. Thus, a most important aspect of future research in controlling metal dusting must involve the use of appropriate coating systems, although new alloy compositions and microstructures that can provide intrinsic resistance to metal dusting must

continue as an important avenue of research. Such research can also lead to advances in novel coating compositions.

Among chromia forming coatings, one can consider Cr-rich compositions such as Ni-50Cr or even a pure Cr coating. New concepts in coating compositions involve the use of alloy compositions that can provide corrosion resistance by an initial fast-forming surface oxide that blocks carbon entry, beneath which a protective chromium oxide film can establish itself. Manganese-containing chromia forming alloys discussed in this chapter form an important class of such materials. There is scope to explore other alloy compositions that can function in a similar manner. An important aspect of coating design also must take into account the use of appropriate interlayers, which can function both as a diffusion barrier to preserve the composition of the coating and to enhance the adherence of the coating to the alloy substrate. Determining the appropriate thickness for such interlayers is also an important consideration.

Beyond chromia forming coatings, research should also address coatings that can form alumina films, silica films and refractory metal oxide films (such as  $TiO_2$ ). Shown in Fig. 5.28 are some preliminary data on the metal dusting corrosion of NiAl coating on Incoloy 601. The coating was applied via a pack cementation approach involving a diffusion reaction around 800°C



5.28 SEM cross-section of  $\beta$ -NiAl coating on Inconel 601 after corrosion in  $50CO:50H_2$  at 650°C for 160 hours.

to form the  $\delta\text{-Ni}_2\text{Al}_3$  phase followed by heat treatment around 1080°C to convert the delta phase to  $\beta\text{-NiAl}$ . A protective alumina film is seen to suppress metal dusting corrosion. While protective  $\text{Al}_2\text{O}_3$  films can form at the higher temperatures, investigations over the entire metal dusting range are needed to understand the behavior of the coating at the lower temperatures.

## 5.8 Sources of further information and advice

Readers and researchers interested in a quick grasp of the subject are also referred to the following sources. These include the book<sup>56</sup> edited by H. Grabke and M. Schultz titled *Corrosion by Carbon and Nitrogen: Metal Dusting, Carburization and Nitridation* (EFC 41), published by Woodhead Publishing, Cambridge, England. Also of interest are articles from the EFC workshop on Carburization, Metal Dusting and Carbon Deposition, held at DECHEMA, Frankfurt, during 6–7 November 1997 and published in the journal *Materials and Corrosion*.<sup>57</sup> An additional source is the collection of articles from the EFC workshop on Coking and Decoking held at Porto, Portugal, during 6–7 May 1999 and also published in *Materials and Corrosion*.<sup>58</sup> Key research groups in the area include those of the authors (Dr T.A. Ramanarayanan, Frick Laboratory, Princeton University, Princeton, New Jersey, USA and C.M. Chun, ExxonMobil Research and Engineering, Annandale, New Jersey, USA), Dr H.J. Grabke (former Head of the Department of Physical Chemistry at the Max Planck Institut für Eisenforschung, Düsseldorf, Germany), Dr D.J. Young (School of Materials Science and Engineering, University of New South Wales, Sydney, Australia), Dr M. Schutze (DECHEMA, Frankfurt, Germany) and Dr K. Natesan (Argonne National Laboratory, Argonne, Illinois, USA). The Special Metals Corporation in Huntington, West Virginia, USA, has been active in alloy development for metal dusting corrosion resistance.

## 5.9 References

1. Hochman R F, 'Catastrophic deterioration of metals at high temperature in carbonaceous environments', in *Proc. Fourth Int. Congress on Metal Corrosion*, NACE 1972, 258–263
2. Koszman I, 'Factors affecting catastrophic carburization (metal dusting)', in Jansson S A and Foroulis Z A, *High Temperature Gas–Metal Reactions*, New York, AIME, 1973, 155–167
3. Perkins R A, Coons W C, Radd F J, 'Metal dusting corrosion in coal gasification environments', in *Properties of High Temperature Alloys*, The Electrochemical Society, 1976, 733–749
4. Hochman R F, in Foroulis ZA, Pettit F S, 'Catastrophic deterioration of high temperature alloys in carbonaceous atmospheres', in *Proc. Symp. Properties of High Temp. Alloys*, The Electrochemical Society, 1977, 715–732
5. Nava Paz J C, Grabke H J, 'Metal dusting', *Oxidation Metals*, 1993 **39** 437–456

6. Grabke H J, Krajak R, Nava Paz J C, 'On the mechanism of catastrophic carburization: metal dusting', *Corrosion Science*, 1993 **35** 1141–1145
7. Grabke H J, Krajak R, Muller-Lorenz E M, 'Metal dusting of high temperature alloys', *Materials and Corrosion*, 1993 **44** 89–97
8. Grabke H J, 'Metal dusting of low- and high-alloy steels', *Corrosion*, 1995 **51** 711–720
9. Grabke H J, 'Thermodynamics, mechanisms and kinetics of metal dusting', *Materials and Corrosion*, 1998 **49** 303–308
10. Pippel E, Woltersdorf J, Schneider R, 'Micromechanisms of metal dusting on Fe-base and Ni-base alloys', *Materials and Corrosion*, 1998 **49** 309–316
11. Chun C M, Mumford J D, Ramanarayanan T A, 'Mechanisms of metal dusting corrosion of iron', *J. Electrochem. Soc.*, 2002 **149** B348–355
12. Chun C M, Mumford J D, Ramanarayanan T A, 'Carbon-induced corrosion of nickel anode', *J. Electrochem. Soc.*, 2000 **147** 3680–3686
13. Chun C M, Mumford J D, Ramanarayanan T A, 'Metal dusting corrosion of cobalt', *J. Electrochem. Soc.*, 2003 **150** B76–B82
14. Klower J, Grabke H J, Muller-Lorenz E M, 'Metal dusting of Ni-based alloys', *Materials and Corrosion*, 1998 **49** 328–329
15. Chun C M, Ramanarayanan T A, 'Metal dusting corrosion of low-chromium steels', *Oxidation of Metals*, 2004 **62** 71–92
16. Chun C M, Bhargava G, Ramanarayanan T A, 'Metal dusting corrosion of nickel based alloys', *J. Electrochem. Soc.*, 2007 **154** C231–C240
17. Chun C M, Ramanarayanan T A, 'Metal dusting corrosion of austenitic 304 stainless steel', *J. Electrochem. Soc.*, 2005 **152** B169–B177
18. Chun C M, Ramanarayanan T A, 'Metal dusting corrosion of 35/45 alloy', unpublished research
19. Grabke H J, Tauber G, 'Kinetics of the decarburation of  $\alpha$  and  $\gamma$  iron in  $H_2O-H_2$  mixtures and of the carburization in  $CO-H_2$  mixtures', *Arch. Eisenhuttenwes.*, 1975 **46** 215–222
20. Shatynski S R, Grabke H J, 'The kinetics of carburization of  $\gamma$ -iron in  $CO-He$  and  $CO-H_2$  atmospheres at 920°C', *Arch. Eisenhuttenwes.*, 1978 **49** 129–133
21. Zeng Z, Natesan K, 'Relationship of carbon crystallization to the metal-dusting mechanism of nickel' *Chem. Mater.*, 2003 **15** 872–878
22. Zhang J, Young D J, 'Kinetics and mechanisms of nickel metal dusting. I. Kinetics and morphology', *Corrosion Science*, 2007 **49** 1496–1512
23. Strauss S, Krajak R, Grabke H J, 'Coking by metal dusting of Ni-base alloys', *Materials and Corrosion*, 1999 **50** 622–627
24. Nishiyama Y, Otsuka N, Kudo T, 'Metal dusting behavior of Cr-Ni steel and Ni-base alloys in a simulated syngas mixture', *Corrosion Science*, 2006 **48** 2064–2083
25. Strauss S, Grabke H J, 'Role of alloying elements in steel on metal dusting', *Materials and Corrosion*, 1998 **49** 321–327
26. Szakalos P, Petersson R, Hertzman S, 'An active corrosion mechanism for metal dusting on 304 stainless steel', *Corrosion Science*, 2002 **44** 2253–2270
27. Palasantzas G, Kooij H J, Dettosson J Th M, 'Carbon induced metal dusting of iron-nickel-chromium alloy surfaces: a scanning auger microscopy study', *Appl. Surf. Sci.*, 2004 **229** 190–196
28. Stevens K J, Levi T, Minchington I, Briggs N, Keast V, Bulcock S, 'Transmission electron microscopy of high pressure metal dusted 316 stainless steel', *Mater. Sci. Eng. A*, 2004 **385** 292–299

29. Bose S K, Grabke H J, 'Diffusion coefficient of carbon in Fe-Ni austenite in the temperature range 950–1100°C', *Z. Metallkunde*, 1978 **69** 8–15
30. Maier M, Norton J F, Frampton P D, 'Metal dusting of 9–20 Cr steels in increased pressure environments at 560°C', *Materials and Corrosion*, 1998 **49** 330–335
31. Muller-Lorenz E M, Grabke H J, 'Coking by metal dusting of steels', *Materials and Corrosion*, 1999 **50** 614–621
32. Chun C M, Ramanarayanan T A, 'The metal dusting corrosion of steels with varying concentrations of chromium', in Grabke H J and Schultze M, *Corrosion by Carbon and Nitrogen: Metal Dusting, Carburization and Nitridation*, Cambridge, Woodhead, 2007
33. Fueki K, Wagner J B, 'Oxidation of manganese in CO<sub>2</sub>–CO mixtures', *J. Electrochem. Soc.*, 1965 **112** 970–974
34. Chun C M, Ramanarayanan T A, 'Mechanism and control of carbon deposition on high temperature alloys', *J. Electrochem. Soc.*, 2007 **154** C465–C471
35. Chun C M, Ramanarayanan T A, 'Metal dusting resistant alloys', US Patent 6,692,838, 17, February 2004
36. Ramanarayanan T A, Mumford J D, Chun C M, Petkovic R A, 'Transport through chromia films', *Solid State Ionics*, 2000 **136–137** 83–90
37. Ramanarayanan T A, Petkovic-Luton R, 'Investigation on the growth mechanisms of α-Cr<sub>2</sub>O<sub>3</sub> on Ni base alloys with and without Y<sub>2</sub>O<sub>3</sub> dispersions', *Ber. Bunsen Ges. Physik. Chem.*, 1985 **89** 402–409
38. Oudar J, 'Sulphur–metal interactions', *Mater. Sci. Eng.*, 1980 **42** 101–109
39. Grabke H J, Petersen E M, Srinivasan S R, 'Influence of adsorbed sulfur on surface reaction kinetics and surface self-diffusion on iron', *Surface Science*, 1977 **67** 501–516
40. Ramanarayanan T A, Srolovitz H J, 'Carburization mechanisms of high chromium alloys', *J. Electrochem. Soc.*, 1985 **132** 2268–2274
41. Schneider A, Viefhaus H, Inden G, Grabke H J, Muller-Lorenz E M, 'Influence of H<sub>2</sub>S on metal dusting', *Materials and Corrosion*, 1998 **49** 336–339
42. Bernardo C A, Alstrup I, Rostrup-Nielsen J R, 'Carbon deposition and methane steam reforming on silica-supported Ni-Cu catalysts', *J. Catalysis*, 1985 **96** 517–534
43. Alstrup I, Tavares M T, Bernardo C A, Sørensen O, Rostrup-Nielsen J R, 'Carbon formation on nickel and nickel-copper alloy catalysts', *Materials and Corrosion*, 1998 **49** 367–372
44. Dalmon J A, Martin G A, 'Hydrogenolysis of C<sub>2</sub>H<sub>6</sub>, C<sub>3</sub>H<sub>8</sub> and n-C<sub>4</sub>H<sub>10</sub> over silica-supported nickel-copper catalysts', *J. Catalysis*, 1980 **66** 214–221
45. Tavares M T, Alstrup I, Bernard C A, 'Coking and decoking during methanation and methane decomposition on Ni-Cu supported catalysts', *Materials and Corrosion*, 1999 **50** 681–685
46. Kim H, Lu C, Worrell W L, Vohs J M, Gorte R J, 'Cu-Ni cermet anodes for direct oxidation of methane in solid oxide fuel cells', *J. Electrochem. Soc.*, 2002 **149** A247–A250
47. Ramanarayanan T A, Chun C, Mumford J D, 'Metal dusting resistant Cu-based alloy surfaces', US Patent 6,737,175, 18 May, 2004
48. Szakalos P, Lundberg M, Hernblom J, 'Cu base alloy', US Patent 7,041,252, 9 May 2006
49. Zhang J, Young D J, 'Metal dusting of Ni and its alloys', to appear in *Electrochemical Transactions Volume 3*, 2007

50. Pomeroy M J, 'Coatings for gas turbine materials and long term stability issues', *Materials and Design*, 2005 **26** 223–231
51. Pichoir R, Hauser JM, 'Current status of coatings for high temperature applications', in *Environmental Degradation of High Temperature Materials*, The Institution of Metallurgists, 1980 **1** 6/1–6/21
52. Warnes B M, Punola D C, 'Clean diffusion coatings by chemical vapor deposition', *Surf. Coat. Technol.*, 1997 **94–95** 1–6
53. Voudouris N, Christoglou C, Angelopoulos G N, 'Formation of aluminide coatings on nickel by a fluidized bed CVD process', *Surf. Coat. Technol.*, 2001 **141** 275–282
54. Chrisey D B, Hubler G K, *Pulsed Laser Deposition of Thin Films*, New York, John Wiley, 1994
55. Arnold C B, Aziz M J, 'Stoichiometry issues in pulsed laser deposition of alloys grown from multicomponent targets', *Appl. Phys. A*, 1999 **69** S23–S27
56. Grabke H J, Schultz M (editors), *Corrosion by Carbon and Nitrogen: Metal Dusting, Carburization and Nitridation* (EFC 41), Cambridge, Woodhead, 2007
57. Proc. EFC Workshop on 'Carburization, Metal Dusting, Carbon Deposition', DECHEMA, Frankfurt, 1997, *Materials and Corrosion*, 1998 **49** 303–396
58. Proc. EFC Workshop on 'Coking and Decoking', Porto, Portugal, 1999, *Materials and Corrosion*, 1999 **50** 613–672

# 6

## Tribological degradation at elevated temperature

---

M R O Y, Defence Metallurgical Research Laboratory, India

### 6.1 Introduction

Increased application of engineering components under aggressive environments, particularly at elevated temperature, has resulted in a greater number of elements subjected to frictional loading at high temperature. In order to study the materials for high temperature tribology, various methods for heating, loading and measurement at elevated temperature are employed. The most common tribological degradation processes are sliding wear, erosive wear and abrasive wear. The degradation processes due to the above mechanisms at elevated temperature have unique features.

Sliding wear is defined as material loss when two different surfaces are made to rub against each other. In many applications such as the nuclear, power generation, transport and materials processing industries, etc., sliding wear of materials at high temperature is a serious problem [1–4]. The situation during high temperature wear becomes worse because of increased oxidation rate, loss of strength of materials and the altered adhesion characteristics of the mating surfaces. To overcome these problems, materials and coatings having higher oxidation resistance and high temperature strength are developed. Attempts are also made to use preoxidized surfaces. An interesting approach is to condition the chemistry of the wearing surfaces so as to enhance the formation of wear protective glazed layers.

Solid particle erosion is defined as material loss due to impact of particles travelling with significant velocity. Solid particle erosion is mechanistically different from other forms of erosion such as liquid impact erosion, slurry erosion, cavitation erosion, etc. Several engineering components are degraded due to solid particle erosion at elevated temperature. A number of industrial systems that undergo erosion at elevated temperature are summarized in Table 6.1 [5–8]. Solid particle erosion of metals and alloys at elevated temperature is governed by the nature of the interaction between erosion and oxidation. This in turn is determined by the thickness, pliability, morphology, adhesion characteristics and toughness of the oxide scale.

*Table 6.1 Example of systems subjected to elevated temperature erosion*

System	Components	References
Combustion systems	Burner nozzles, reheater, super heater, economizer tube banks, boiler heat exchanger, in bed tubes, tube banks, etc.	5, 6
Coal gasification systems	Turbine, lock hopper valves	7
Coal liquefaction system	Valve to throttle the flow of product stream	7
Gas turbines	Blades	8

Abrasive wear is defined as material loss when a hard particle is made to slide against a soft material. Since abrasive wear is one of the common failure mechanisms of engineering components, it has become an important subject in tribology and materials science. Abrasive wear is classified as two-body abrasion or three-body abrasion. In two-body abrasion, abrasive particles move freely over a material face as in sand sliding down a chute. In three-body abrasion, abrasive particles act as interfacial elements between the solid body and the counter body. Abrasive wear can be classified as high stress abrasion or low stress abrasion depending on the applied stresses. Several components, such as the barrels and screws of injection moulding machines [9], mineral processing equipments, etc. [10], are subjected to abrasive wear at elevated temperature.

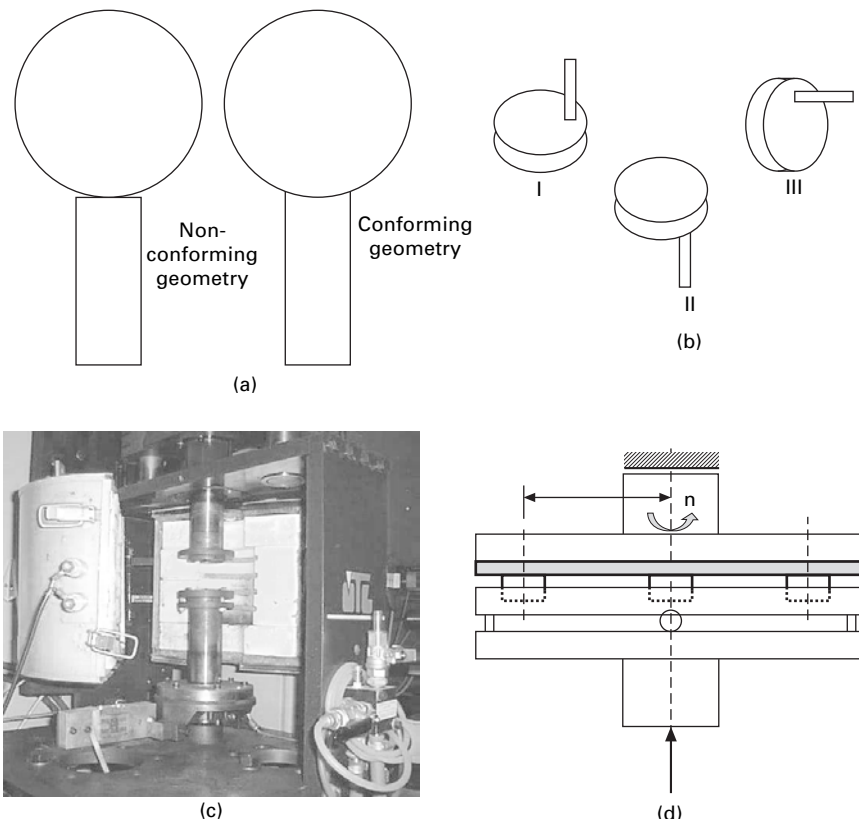
This chapter is divided into six sections. After introducing elevated temperature tribology in this first section, a compilation of elevated temperature tribological test facilities is made in Section 6.2. The important features of elevated temperature tribological degradation are discussed in Sections 6.3–6.5. Section 6.6 deals with the highlights of recent work. The direction of future research is the subject matter of Section 6.7. Finally, the chapter is concluded in Section 6.8. The description in this chapter will be limited to metallic materials for the sake of brevity. The tribological degradation processes are also confined to the most commonly occurring processes, namely sliding wear, erosive wear and abrasive wear.

## 6.2 High temperature wear test facilities

Various types of sliding wear, erosive wear and abrasive wear test rigs are discussed in this section. These test rigs are designed primarily for testing at elevated temperature.

### 6.2.1 Sliding wear test facilities

Although the problem of sliding wear has long been known, the importance of the various modes of material loss during sliding wear has been realized only in recent times. Depending on the geometry, the sliding wear test system can be broadly classified under two heads: (i) conforming geometry, and (ii) non-conforming geometry, as shown in Fig. 6.1a. Conforming geometry is more popular and permits exact calculation of wear rate and stress analysis. Non-conforming geometry is used not only to simulate wear conditions by journal bearing, roller, etc., but also to simulate specific environmental conditions. However, dealing with non-conforming geometry envisages change of the size and shape of wear scar with time. This makes stress analysis more



6.1 (a) Diagram showing difference between conforming and non-conforming geometry; (b) various types of pin on disc configuration; (c) high temperature sliding wear test rig; (d) schematic diagram of the pin on disc configuration of high temperature sliding wear test facilities.

difficult and delays or prevents the achievements of steady-state conditions. The most common conforming configuration for the sliding wear test is the pin on disc. This test method is standardized as per the G99-90 standard [11]. Several types of pin on disc configurations are shown in Fig. 6.1b. The advantages and disadvantages of various configurations are discussed in a separate publication [12].

For elevated temperature wear study, the pin on disc configuration as per the G99-90 standard [11] can be used. However, at elevated temperature, the material becomes soft and sliding a pin at a reasonably high load becomes difficult, hence the disc on disc configuration is preferred. In order to evaluate performances of various materials under elevated temperature sliding wear conditions, wear rigs capable of characterizing materials for such purposes are designed and fabricated. One such test rig is presented in Fig. 6.1c [13]. This is a disc on disc type configuration where the disc is attached to a holder mounted on a lever. It consists of a driving system whose speed is controlled by a frequency converter. The load is applied by a dead weight kinematics system. The test chamber is a furnace insulated with a special ceramic chamber and is powered by a variable transformer. Thermocouple devices control the temperature of the test chamber. The wear rate is measured by a low voltage displacement transducer (LVDT). The friction force and hence the friction coefficient are measured by an elastic bar with strain gauges. The outputs of the sensors are connected to a data recorder and a computer with data logging software (HBM Catman 3.0 Rel. 4).

The disc on disc test technique is very good and convenient so long as the applied load is very high. If the applied load is low and there is a shortage of material, the pin on disc configuration is used. The above test apparatus is modified to get a pin on disc configuration. The modified configuration is given in Fig. 6.1d.

### 6.2.2 Erosive wear test facilities

Erosive wear can be defined as degradation of material due to impact of particles travelling with significant velocity. A tribosystem suffering from erosive wear can be characterized as an open system. In such a system the counter body is continuously replaced. Another feature is that the wear of the counter body is unimportant.

Over the last few decades several test techniques or methodologies have been developed for studying the mechanism and assessing the extent of erosion. These tests can broadly be divided into two categories: (i) simulative tests that are designed to simulate a specific type of erosion, and (ii) tests that are intended to be used for fundamental studies. The main problem of simulative tests is that it is very expensive and difficult to conduct fundamental studies for material development or for understanding the mechanism of

erosion. Hence they are not popular for erosive wear studies at elevated temperature. For such studies, laboratory test techniques are preferred.

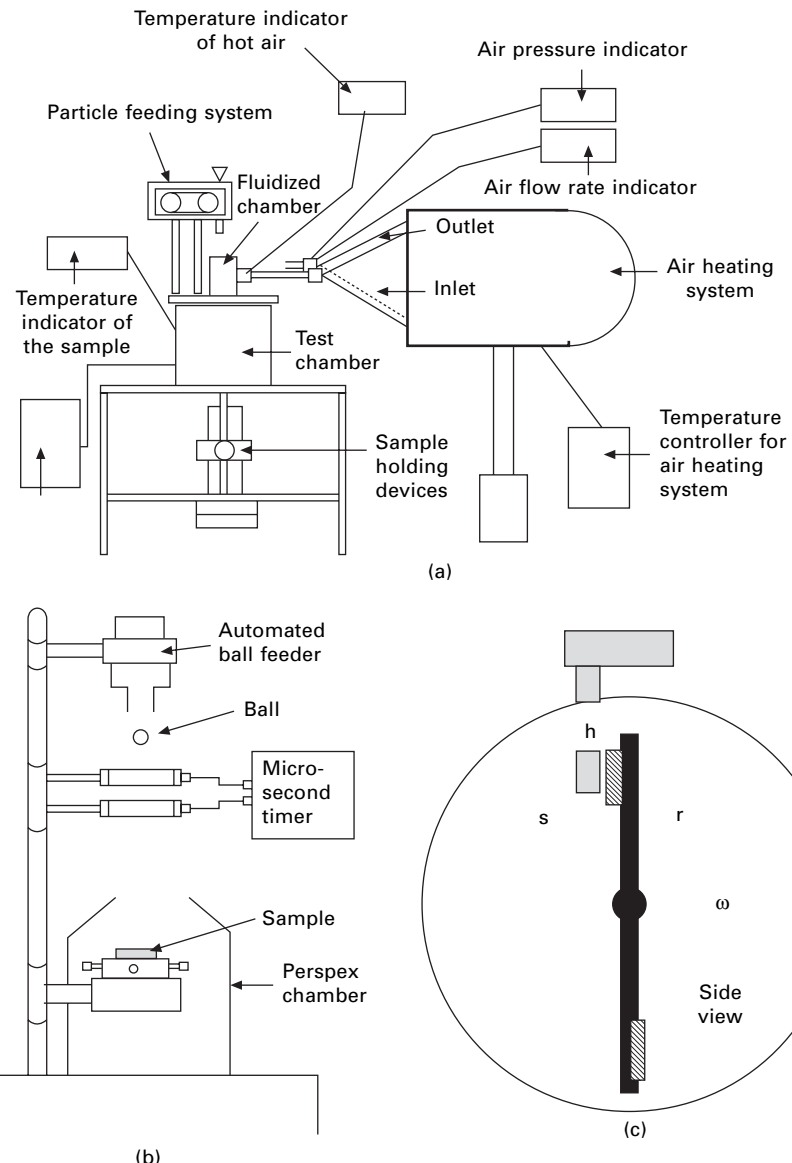
The most common laboratory test involves blasting a stream of airborne particles against the target, as standardized by G76-83 [11]. In this type of test, a known quantity of erodent is fed into an airstream, accelerated through a converging nozzle and directed towards the test specimen. A cleaned and weighed sample is exposed to a particle-laden airstream for a predetermined time and weighed after interrupting the test. The ratio of the weight loss suffered by the sample to the weight of erodent gives the dimensionless erosion rate.

The air jet type elevated temperature erosion rigs can be classified in two broad groups. The first group comprises erosion rigs, where both the fluid stream carrying the particles and the eroding target are heated to the same test temperature. These are called isothermal erosion rigs. In contrast, the second group of erosion rigs, called non-isothermal rigs, have the facility to heat the target material alone, while the fluid stream with the particles is not preheated before allowing it to enter the erosion chamber. In these types of rigs the colder fluid stream cools the target materials to some extent on impact. Nevertheless, the target material still attains a steady-state temperature.

The non-isothermal erosion rigs are easy to fabricate but they fail to simulate the erosion conditions. Hence, such rigs presently are not popular. In contrast, isothermal type erosion rigs can simulate erosion conditions but are difficult to fabricate. A schematic diagram of one such erosion rig fabricated by the author at DMRL is shown in Fig. 6.2a. The unique feature of this rig is its ability to alter the particle feed rate by over 100 times. Its particle feeding system is a miniaturized conveyer belt system and the particle feed rate is controlled by controlling the speed of the motor of the system. A further description of this rig is available elsewhere [14].

The test procedure involves heating the compressed air to the required temperature and then heating and soaking the test sample to that temperature. The heated samples are then exposed to compressed, heated, fluidized and accelerated airstreams carrying the particles. The elevated temperature erosion test is a multiple specimen test procedure. Cleaned, dried and weighed samples are exposed to erodents for various time intervals (say  $t_1, t_2, t_3, \dots$  where  $t_1 < t_2 < t_3$ ) corresponding to various masses of erodents  $m_1, m_2, \dots, m_n$ . A similar number of samples are again exposed to the airstream without carrying the particles. If  $M_1, M_2, \dots, M_n$  are the mass losses suffered by the specimen on exposure to the erodents for time intervals of  $t_1, t_2, \dots, t_n$  and if  $M'_1, M'_2, \dots, M'_n$  are the mass gains experienced by the samples when exposed to a plain airstream for time intervals,  $t_1, t_2, \dots, t_n$  then the incremental erosion rate can be computed as:

$$E_n = \frac{(M_n - M'_n) - (M_{n-1} - M'_{n-1})}{m_n - m_{n-1}} \quad 6.1$$



6.2 (a) Jet-type elevated temperature erosion test facilities;  
 (b) schematic representation of low velocity erosion test facility;  
 (c) schematic diagram of whirling arm erosion rig.

This procedure was repeated until  $E_{n-1}$  is equal to  $E_{n-2}$  and this  $E$  is considered to be the incremental erosion rate.

Determination of the impact velocity of the erodent is the main problem of the jet type of erosion rig. Three different techniques can be used for measuring impact velocity. In the photographic method, a high-speed camera

is used to photograph the successive positions of a single particle as a function of time and thus the impact velocity is computed. The second method, known as the rotating disc method, was developed by Ruff and Ives [15]. In this method the velocity is determined by estimating the time of flight of the particles between two discs fixed on a common shaft rotating at some specified velocity. A modified version of the rotating disc is the paddle wheel technique [16]. This method gives more reliable and statistically more accurate results for the velocity. The third method uses a laser doppler velocimeter (LDV). This is an accurate, non-interactive and on-line velocity measuring device. The LDV employs the well-known Doppler effect to measure the velocity of the particles. When light is scattered from a moving object, the stationary observer will see a change in frequency of the scattered light proportional to the velocity of the object. A laser light source is used because it is easily focused and is coherent.

In applications such as pipe bends in slurry transportation systems, impacts are primarily by big particles with very low impact velocity. To simulate such systems, heavy balls are dropped under gravity to impact the samples. A schematic presentation of such a system is given in Fig. 6.2b. Bitter [17] introduced such a system for the first time. The system contains a ball dispenser unit, the velocity measuring system, a ball counting unit and the sample holder. The ball dispenser and the sample holder can be taken up and down so as to alter the height over which the eroding particle falls. Before the steel ball impacts the sample it passes through a multiple photodiode unit, which measures the velocity of the passing ball and in addition keeps track of the total number of balls passing through. It should be mentioned here that this is a non-isothermal variety of test rig. In this system only the test specimen can be heated from the bottom. The impacting balls are not heated. Such an arrangement does not alter the temperature of the system, because the time of impact between the ball and the specimen is only momentary, leaving a very small time for the heat to transfer from the specimen to the impacting ball.

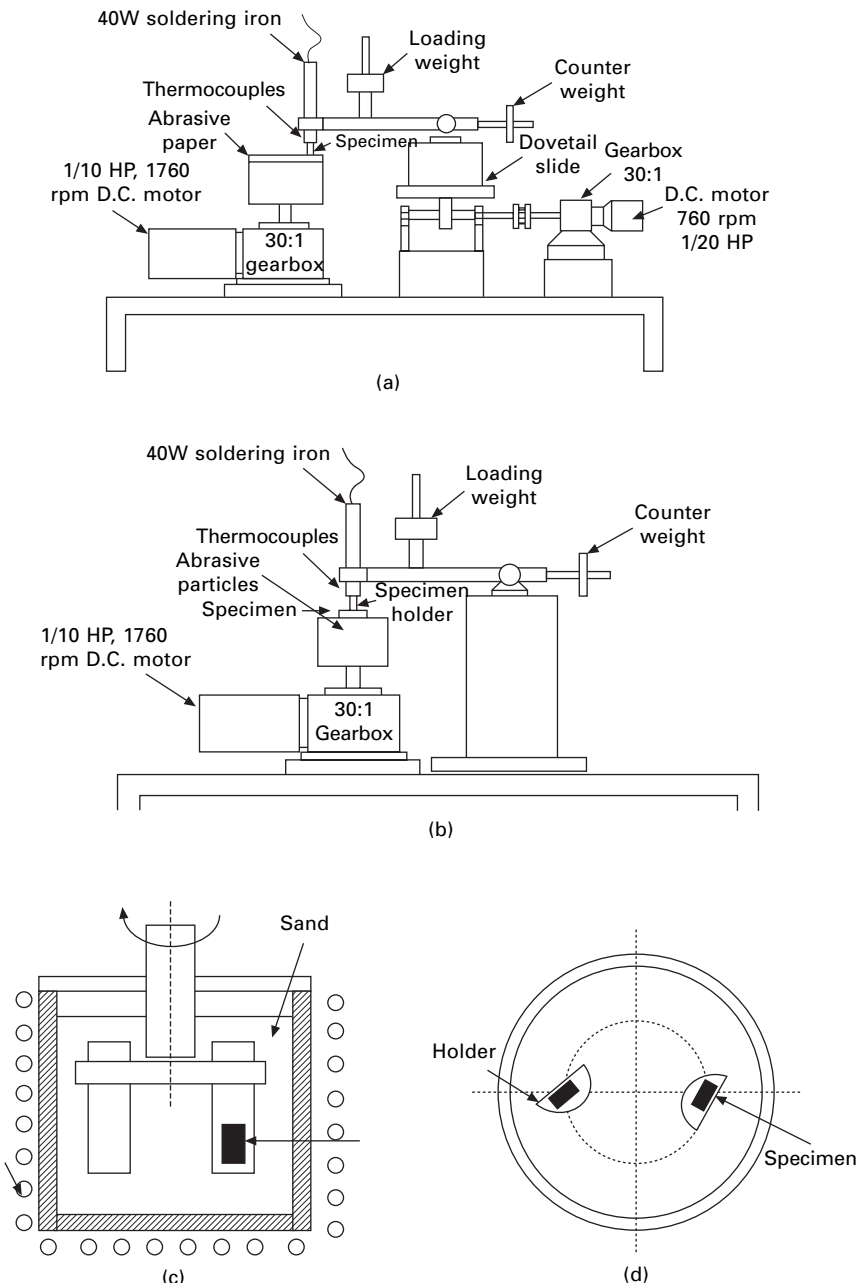
Whirling arm rigs have been developed to carry out tests at a precisely controlled velocity over a range of impact conditions. The target specimens are attached to the tips of the rotor arm and whirled through a certain or a narrow band of erosive particles. These rigs create a lot of noise and consume considerable power. A whirling arm erosion rig is schematically presented in Fig. 6.2c. These kinds of rigs simulate the degradation conditions prevalent in fluidized bed combustors. Tilly and Sage [18] developed the whirling arm erosion rig initially. One of the advantages of this type of rig is that the erodent velocity can be controlled precisely, since it is governed by the speed of rotation of the arms. The rig also permits testing to be carried out over a wide range of impact velocities. It uses erodent efficiently as all of the erodent is delivered to the target sample.

### 6.2.3 Abrasive wear testing

Abrasive wear is defined as the material loss when a hard particle is made to slide against a soft material. Abrasive wear is classified as two-body abrasion or three-body abrasion. In two-body abrasion, abrasive particles move freely over a material face as in sand sliding down a chute. In three-body abrasion, abrasive particles act as interfacial elements between the solid body and the counter body. It can be classified as high stress abrasion or low stress abrasion depending on the applied stresses.

In high stress abrasive wear testing, a pin or a disc is made to move at a velocity  $V$  under a load  $N$  against a flat surface of much larger counter surface. Two-body and three-body elevated temperature abrasive wear test equipments are shown in Fig. 6.3a and Fig. 6.3b [19], respectively. Figure 6.3a shows the equipment developed originally by Mishra. A 40W soldering iron controlled by a variable transformer is used to heat up the specimen and a thermocouple is mounted on the soldering iron for temperature indication. Adhesive-backed silicon carbide abrasive paper is used as the abrasive. The specimen being tested is loaded with a known weight and is moved in a spiral path so that the specimen always moves over fresh abrasive. As shown in Fig. 6.3b, in three-body abrasive wear testing the specimen in the form of a disc is abraded against loose silicon carbide abrasive particles. A 200W soldering iron controlled by a variable transformer is used to heat the specimen. Interrupting the test and measuring the weight of the specimen before and after each test to give the weight loss constitutes the wear testing methodology.

The configuration used for high stress abrasive wear is occasionally used for low stress abrasive wear at a low applied load, but for measurement of low stress abrasive wear normally a rubber wheel abrasive test rig is used. The main difference in the above two configurations is that in the first case the area exposed to wear remains constant with change of time, whereas in the rubber wheel abrasion test the wearing area changes continuously. In order to simulate the exact process, a laboratory simulative test technique has been developed. One example is the laboratory-scale jaw crusher test, which not only reproduces the gouging abrasion of large-scale mineral processing plants but also resembles three-body abrasion. It should be noted that in most abrasive testing, alumina or silicon carbide abrasives are used because they are readily available. These abrasives are much harder than naturally occurring abrasives. Hence, care must be taken in applying the results of the tests with such hard particles to service conditions involving much softer particles. The specifications of abrasive particles, such as hardness, shape, size, etc., will also influence the wear rate drastically. Compliance of the support also affects the test result. Abrasive wear rate can be expressed as mass loss or volume loss experienced by the abraded material per unit



6.3 (a) The two-body high temperature abrasive wear test rig; (b) the three-body high temperature abrasive wear test rig; (c), (d) A low stress elevated temperature abrasive wear rig [9].

mass of abrasive, i.e. gm/gm or cc/gm. The reciprocal of the abrasive wear rate is considered as the wear resistance (gm/cc).

Liu *et al.* [9] designed a low stress elevated temperature abrasion testing equipment. Their setup is shown in Figs 6.3c and 6.3d. It consists of a symmetric  $\pi$ -shaped specimen holder which is rotated in a stainless steel tank filled with abrasive sand. The setup is held inside an electric furnace to heat the sand and the sample to a maximum temperature of 923 K. The samples are rotated at a speed of 200 rpm corresponding to linear speed of 1.36 m/s. The abrasive wear rate is determined by interrupting the test after an interval of 20 h and measuring the volume loss as a function of time.

### 6.3 Important features of elevated temperature tribological degradation: sliding wear

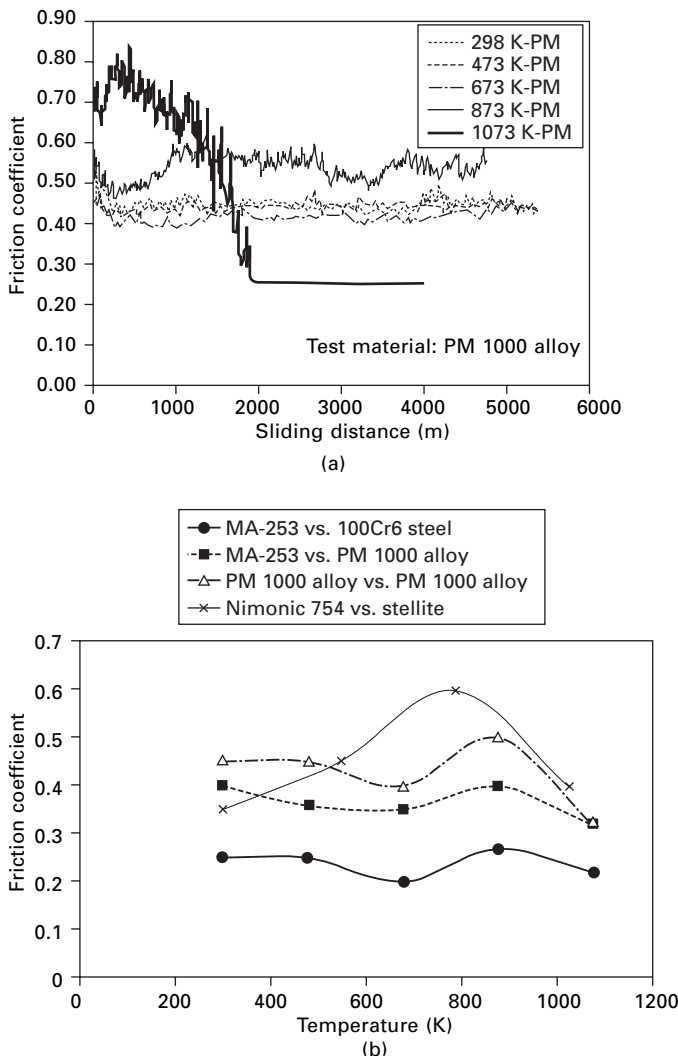
Interest in elevated temperature sliding wear has been generated in recent years. A compilation of the relevant literature is presented in ref. [20]. On the basis of the reported literature, the important features of elevated temperature sliding wear are described below.

#### 6.3.1 The effect of temperature on friction coefficient and wear rate

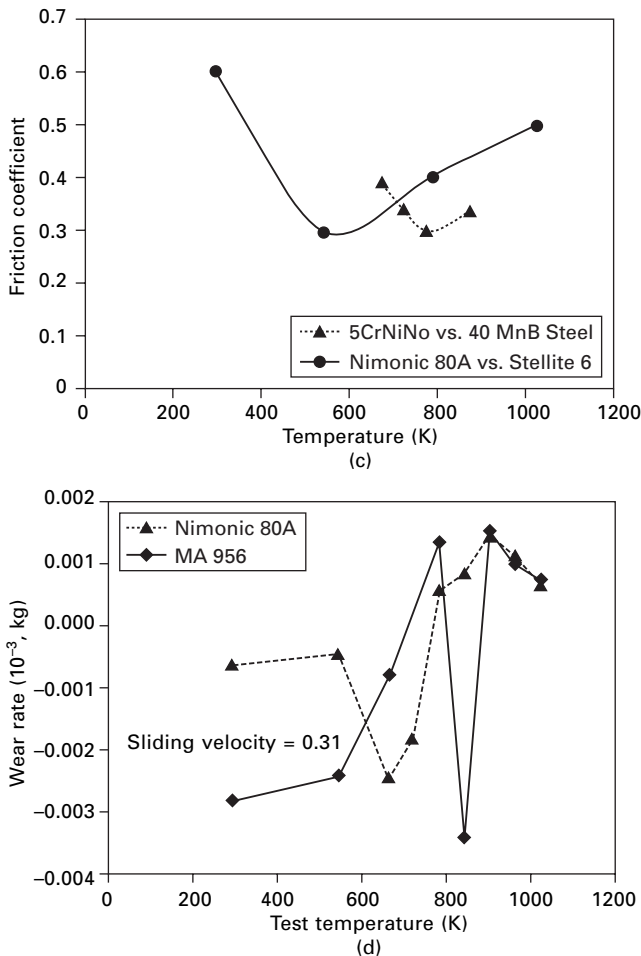
The variation of friction coefficient as a function of the sliding distance of a Ni based dispersion strengthened alloy PM 1000 against self-mating materials at different temperatures is shown in Fig. 6.4a [21]. It is clear that the friction coefficient changes over a narrow band. Further, the friction coefficient is a minimum at the maximum test temperature. At the highest temperature, the friction coefficient decreases from a very high value and attains a low steady state value. The friction coefficient is more or less constant at all other temperature levels. Figures 6.4b and 6.4c represent the influence of temperature on the friction coefficient for a variety of tribosystems [21–25]. It can be seen that friction coefficients of the test materials in some tribosystems attain the highest value at an intermediate temperature (Fig. 6.4b), whereas in some systems the lowest friction coefficient is noted at an intermediate temperature (Fig. 6.4c).

The influence of temperature on the wear rate of Nimonic 80A and MA 956 is shown in Fig. 6.4d [26,27]. The wear rate goes through a minimum at an intermediate temperature for both alloys. Similarly the variations of thickness loss with the sliding distance for 253 MA alloy against 100Cr6 steel and against PM 1000 alloy at different temperatures are presented in Figs 6.5a and 6.5b respectively [23,24]. While there is a thickness gain at 1073 K

against 100Cr6 steel, there is a thickness gain at ambient temperature against PM 1000 alloy. At all other temperatures, the materials initially lose thickness and then experience a thickness gain.



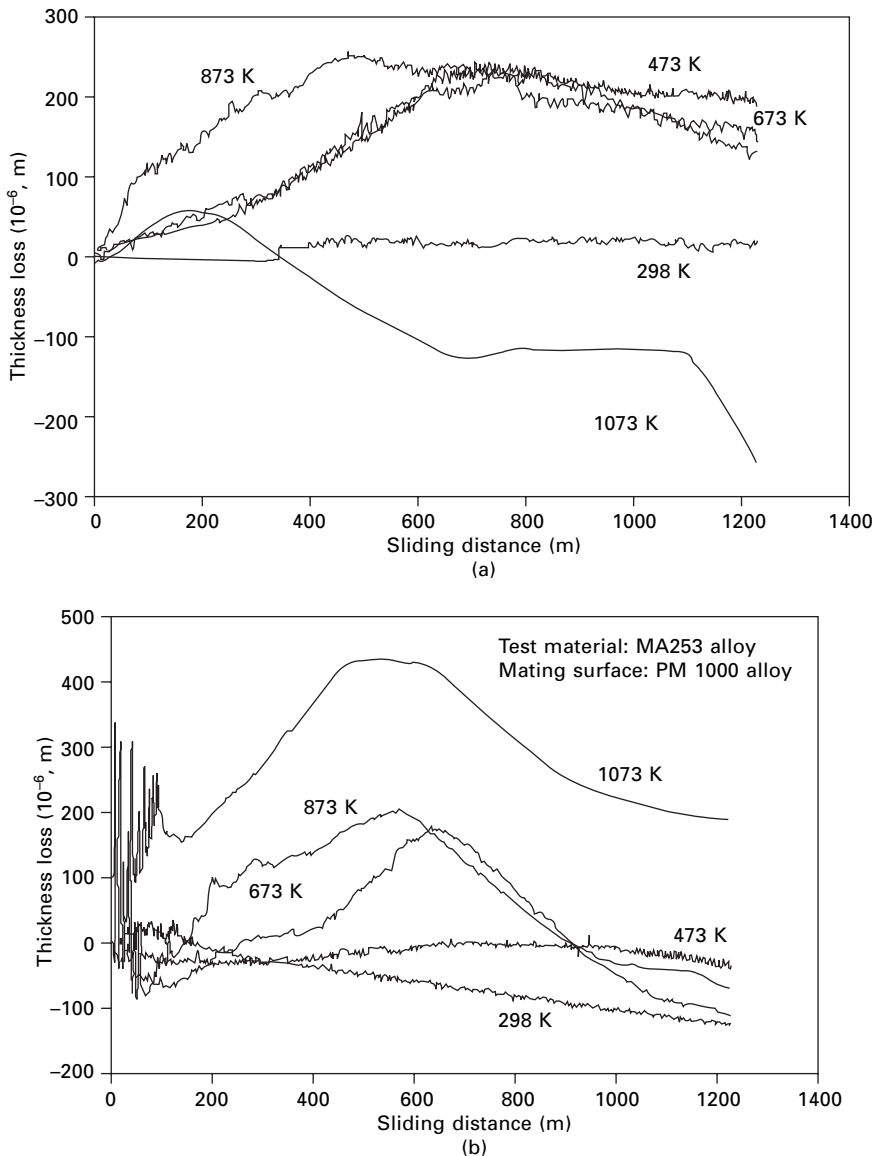
6.4 (a) Variation of friction coefficient as a function of sliding distance at various temperatures for PM 1000 alloy against self-mating surface [21]; (b) and (c) variation of friction coefficient as a function of temperature [21, 23–25]; (d) influence of test temperature on the wear rate of Nimonic 80A and MA 956.



6.4 (Continued)

### 6.3.2 The effect of sliding velocity on friction coefficient and wear rate

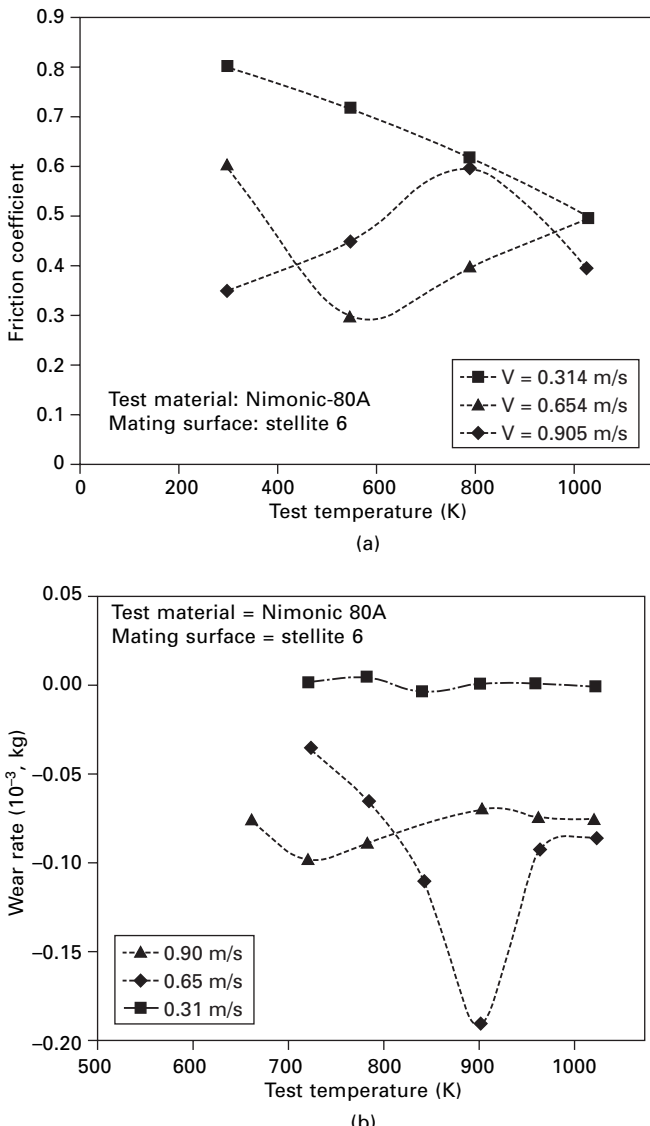
The influence of sliding velocity on the friction coefficient of Nimonic 80A against Stellite 6 is illustrated in Fig. 6.6a [22]. In this case, three different responses are noted. The friction coefficient decreases with increase in test temperature at low sliding velocity. At intermediate sliding velocity, it is minimum at an intermediate temperature. Finally, the friction coefficient goes through a maximum at around 800 K at high sliding velocity. Such variation of friction coefficient with sliding velocity is related to the formation of a glazed layer. There is further discussion on this topic in subsequent sections of this chapter.



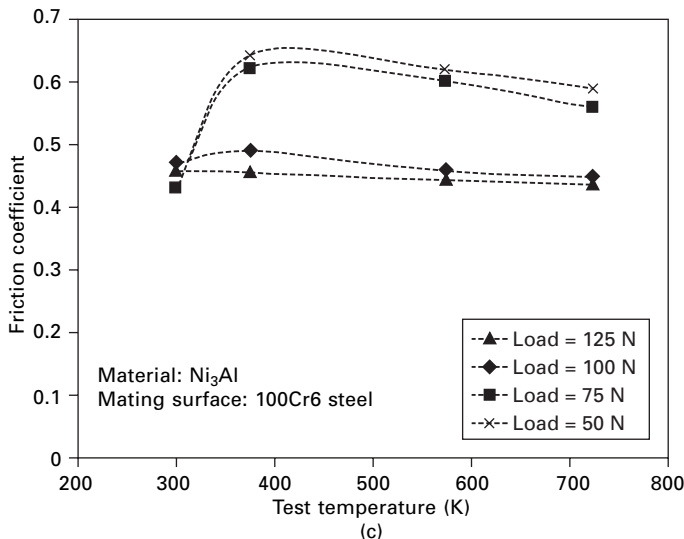
6.5 (a), (b) Variation of thickness loss as a function of sliding distance for MA 253 and PM 1000 alloys at different test temperatures [21,23].

The effect of sliding speed on the wear rate can be seen from Fig. 6.6b [22]. The variation of wear rate of Nimonic 80A against Stellite 6 as a function of temperature at three different sliding speeds is described in this figure. The wear rate is minimum at an intermediate temperature at all three

velocities. At low and near-ambient temperatures, the wear rate decreases with increase of sliding velocity. At elevated temperature the minimum wear rate is noted at an intermediate sliding velocity.



6.6 (a) Effect of sliding velocity on the friction coefficient of Nimonic 80A against Stellite 6 [22]; (b) effect of sliding velocity on the wear rate of Nimonic 80A at different temperatures; (c) effect of applied load on the friction coefficient of  $\text{Ni}_3\text{Al}$  at different temperatures.



6.6 (Continued)

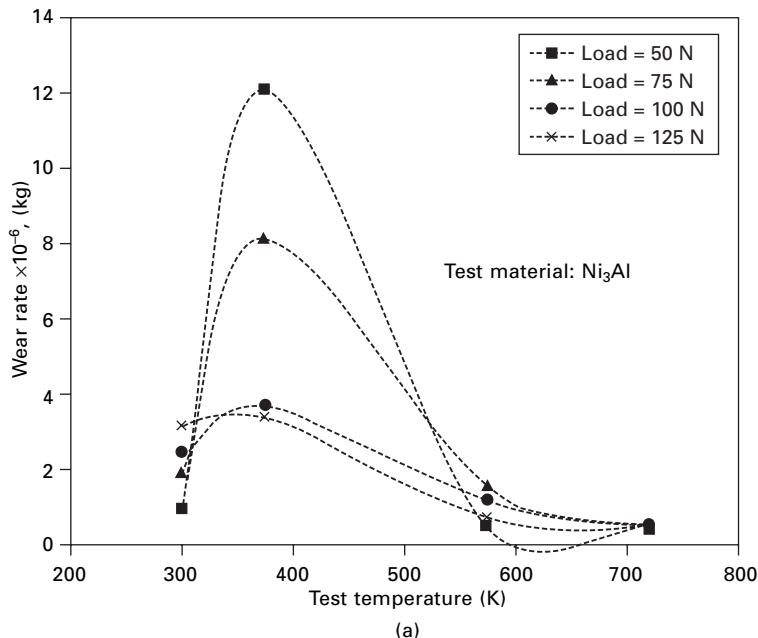
### 6.3.3 The effect of applied load on friction coefficient and wear rate

The influence of applied load on the friction coefficient is illustrated in Fig. 6.6c [28] wherein the friction coefficient is plotted as a function of test temperature at different loads. Except at 125 N, the friction coefficient goes through a maximum at 373 K for all loads. It decreases with further increase of temperature, and decreases with increase of applied load at a given temperature. It is maximum under ambient conditions at a load of 125 N, and minimum under ambient conditions at low loads and at 723 K with higher loads. The lowest and highest friction coefficients are recorded at room temperature and at 373 K for 75 N and 50 N loads respectively.

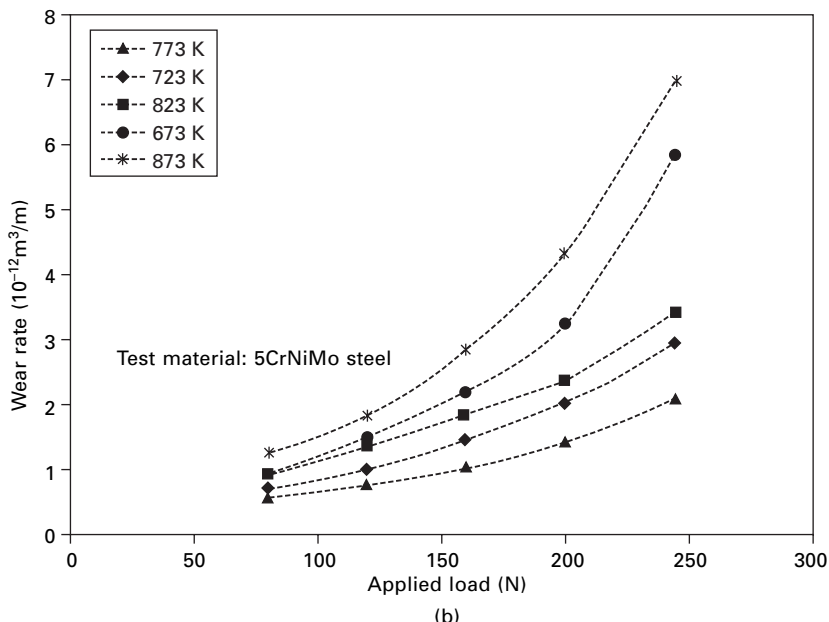
Figures 6.7a and 6.7b [25,28] give the effect of applied load on wear rate. According to Fig. 6.7a the wear rate of Ni<sub>3</sub>Al increases with increase of applied load at ambient temperature, whereas at higher temperature it decreases with increase of applied load. The wear rate is maximum at low load and at intermediate temperature. According to Tu *et al.* [25] the wear rate of 5CrNiMo steel increases with increase in applied load and is minimum at 773 K at all loads. This observation is shown in Fig. 6.7b.

### 6.3.4 The effect of the nature of mating surfaces on friction coefficient

Roy *et al.* [21] investigated the effect of Fe based and Ni based mating surfaces on the wear of 253 MA at elevated temperature. They used two



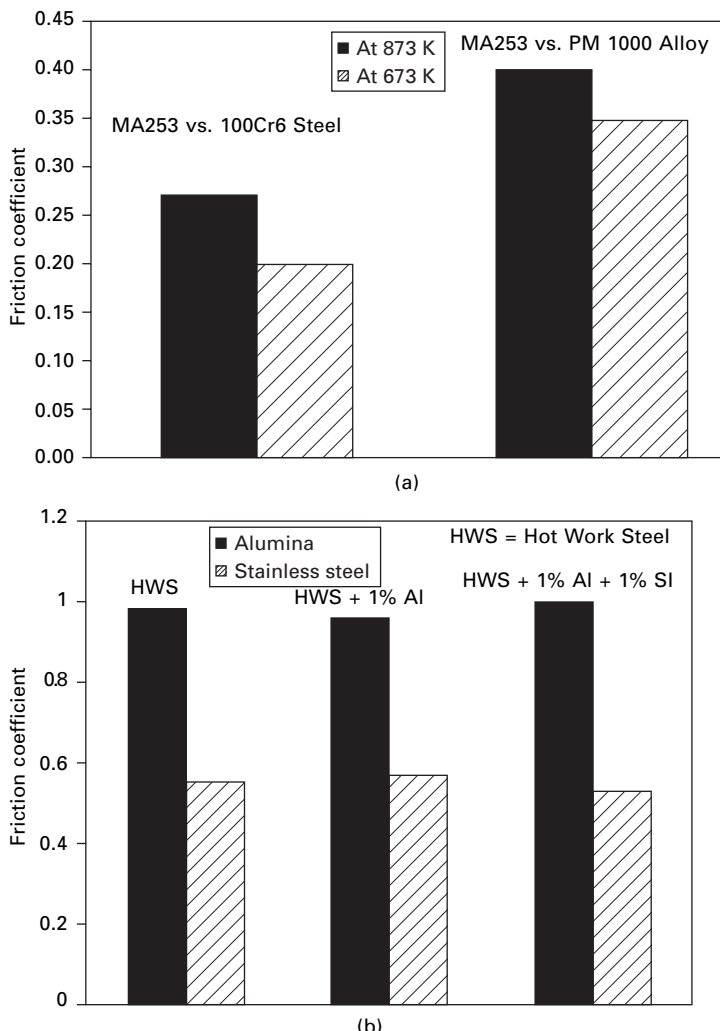
(a)



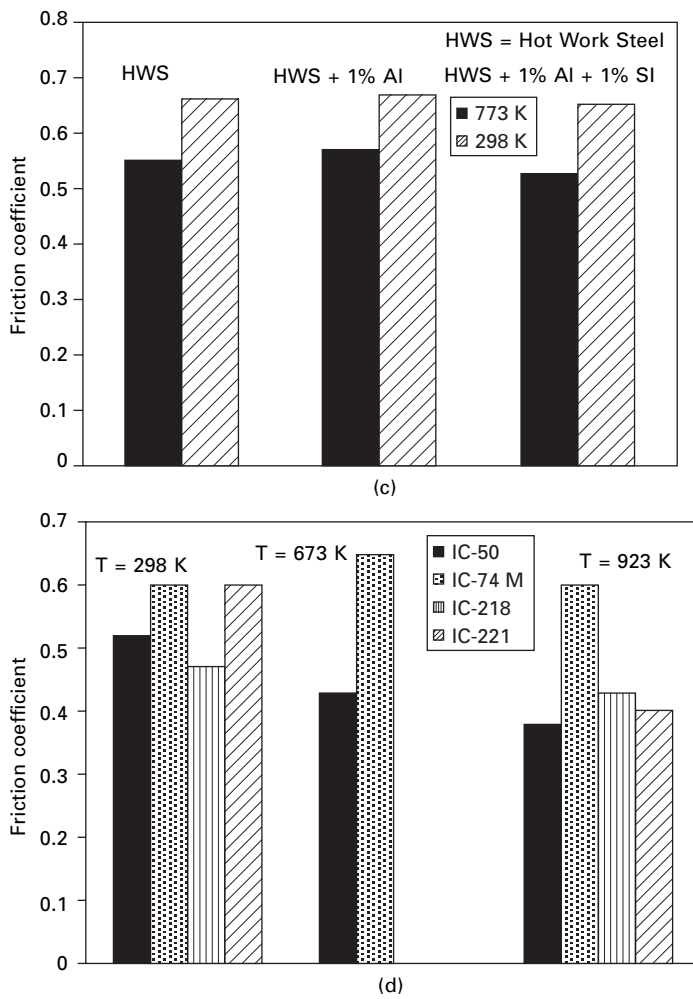
(b)

6.7 The influence of applied load on wear rate at different temperatures [25,28]: (a) Ni<sub>3</sub>Al; (b) Cr steel.

different mating surfaces, namely 100Cr6 steel which softens with increase of temperature and PM 1000 alloy which does not soften with increase of temperature. Their observation revealed that the friction coefficient at elevated temperature is low with the mating surface, which is softer as shown in Fig.



6.8 (a) Bar diagrams showing the influence of the mating surface on the friction coefficient of MA753 alloy at elevated temperature [21, 23,29]; (b) bar diagrams showing the effect of mating surfaces on the friction coefficient of various hot-working steels [21,26–28]; (c) bar diagrams showing the effect of alloying addition on the friction coefficient of various hot-working steels at various temperatures [21, 26–28]; (d) bar diagrams showing the effect of alloying addition on the friction coefficient of various Ni based alloys [21,26–28].



6.8 (Continued)

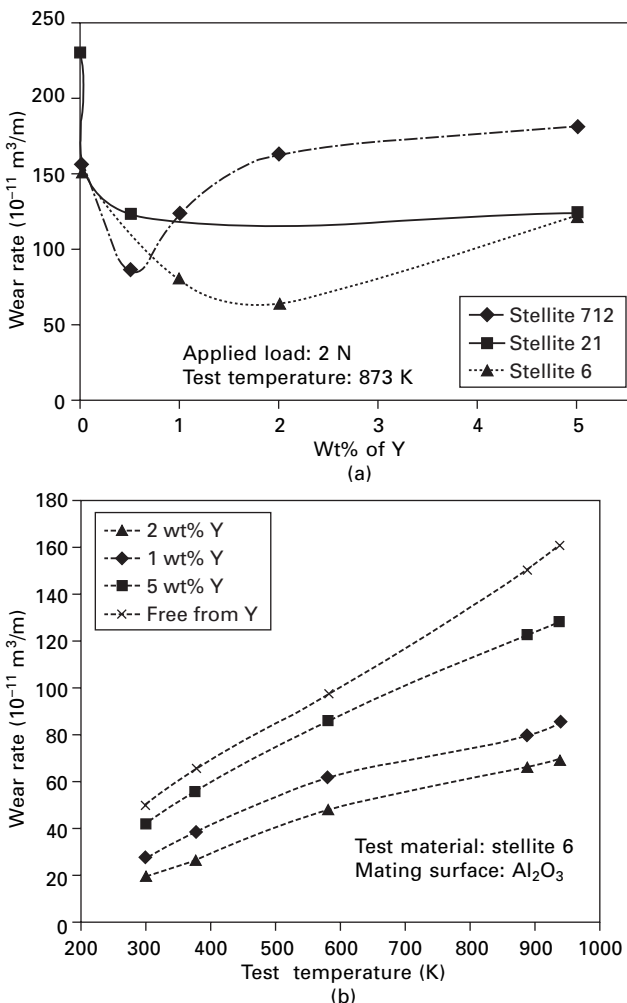
6.8a. Similarly, Fontalvo and Mitterer [29] also noted that the friction coefficient of hot-work steel is less with stainless steel counterface than with alumina as counterface at elevated temperature. Their observation is illustrated in Fig. 6.8b. It should be mentioned that stainless steel softens with increase of test temperature whereas alumina is able to retain its hardness with increase of test temperature.

### 6.3.5 The effect of alloying addition on friction coefficient and wear rate

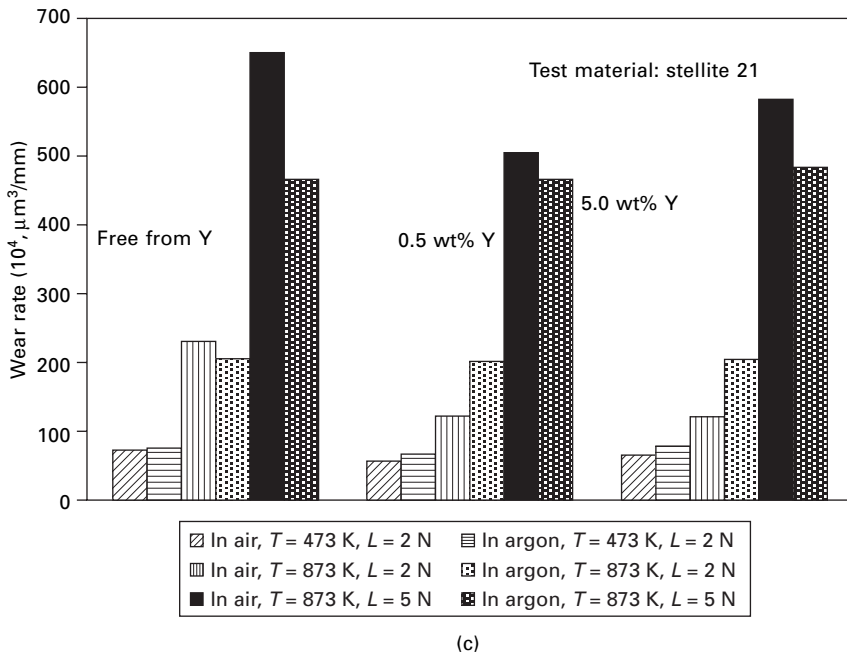
Fontalvo and Mitterer [29] studied the effect of alloying addition on friction coefficient. Their result is illustrated in Fig. 6.8c. In order to study the effect

of  $\text{Al}_2\text{O}_3$ -forming scale and  $\text{SiO}_2$ -forming scale, 1% Al and 1% Si were added to the hot-work steel. It is clear that alloying addition does not influence the friction behaviour either at ambient temperature or at elevated temperature. A series of experiments by Blau and Devore [30–32] found that the friction coefficient of a number of nickel aluminides was lower at elevated temperature than at ambient temperature. Their observations are summarized in Fig. 6.8d.

The importance of alloying addition on the wear rate is shown in Fig. 6.9 [33–35] wherein the variation of wear rate as a function of the Y content at



6.9 (a) Influence of Y addition on the wear rate of various alloys at elevated temperature [33,35]; (b) influence of Y addition on the wear rate of Stellite 6 at elevated temperature [33]; (c) bar diagram showing effect of environment on the wear rate of Stellite 21 at elevated temperature [35].



6.9 (Continued)

873 K (Fig. 6.9a) and at an applied load of 2 N for various Stellite alloys is depicted. It is clear from Fig. 6.9a that though the wear rate of Stellite 21 initially decreases and then remains constant with increase of Y content, the wear rate of Stellite 6 and Stellite 712 exhibits a minimum at Y content of 0.5% and 2% respectively. According to Fig. 6.9b, the wear rate of Stellite 6 increases with increase of test temperature at all Y contents even though a Y content of 2 wt% gives a minimum wear rate. It is to be noted that the presence of Y results in a lower wear rate than in alloy free from Y. The observations of Fontalvo and Mitterer [29] indicated that the wear rate decreased with increase in test temperature. Further addition of Al and Si resulted in a decrease in wear rate. Si addition caused minimum wear rate.

### 6.3.6 The effect of atmosphere on wear rate

Li and coworkers [19] investigated the effect of atmosphere on the wear rate. Their observations are presented in Fig. 6.9c. It is clear that at low load (2 N), the wear rate of Stellite 21 containing Y in air is lower than the wear rate of the same material in an argon environment. In contrast, the wear rate of Y containing Stellite 21 in an argon atmosphere is lower than the wear rate in air when the applied load is 5 N. It should be stated here that irrespective of the Y content of the wearing material Stellite 21, the mechanical

properties and the chemical compositions of the surface layers were found to be identical.

## 6.4 Important features of elevated temperature erosive wear

Over the last few decades or so, a substantial amount of work on elevated temperature erosion of metals and alloys has been carried out. This work is reviewed, providing details of materials subjected to elevated temperature erosion and the test conditions, in ref. [36]. The tests were conducted over a wide range of test conditions and test materials. Based on these investigations, the important factors that govern the solid particle erosive wear of metallic materials at elevated temperature are described below.

### 6.4.1 The effect of temperature on erosion rate

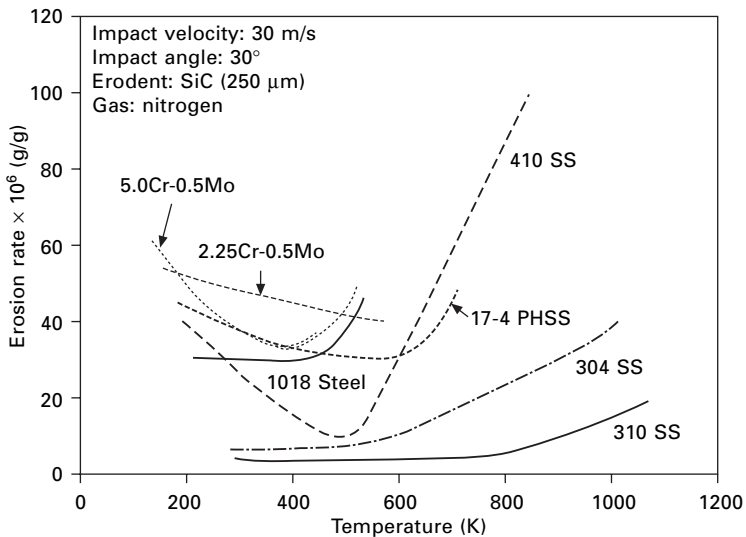
The variation of erosion rate with temperature for a number of metals and alloys is depicted in Fig. 6.10a [37, 38]. The erosion data of this figure are generated at high impact velocities and using mostly angular particles. The temperature dependence of the erosion rate shows three different trends. In one case, the erosion rate initially decreases with increase of temperature, reaches a minimum and then starts to increase with increasing temperature. Materials such as 5.0Cr-0.5Mo, 17-4 PHSS, 410 SS, Alloy 800, Ti-6Al-4V, tungsten, etc., belong to this group. The second type comprises metals exhibiting a temperature-independent erosion rate up to a critical temperature followed by an increase of erosion rate with increasing temperature. Metals like tantalum and lead (for oblique impact) and alloys like 310 SS (for oblique impact), 1018 steel and 1100 aluminium (for normal impact) belong to this group. Finally, the third group of materials show a monotonically increasing erosion rate with increasing temperature. Inco 600, carbon steel, 12Cr-1Mo-V steel, 2.25Cr-1.0Mo steel, lead and 20245 Al are some of the typical examples in this group.

### 6.4.2 The effect of impact velocity on erosion rate

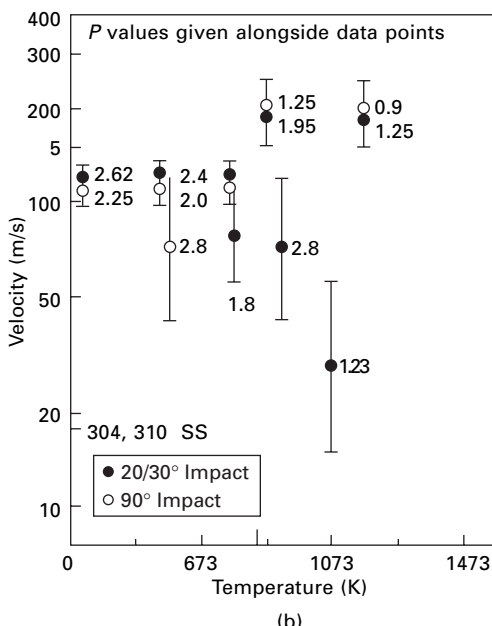
The velocity dependence of the erosion rate ( $E$ ) is characterized by the velocity exponent  $p$  given by

$$E = K_1 V^p \quad 6.2$$

where  $K_1$  is a constant and  $V$  is the impact velocity. The velocity exponents  $p$  reported by investigators are given in the velocity–temperature plot in Fig. 6.10b. The velocity exponent decreases with an increase in erosion test temperature for 304 SS to a value as low as 0.9 at low impact velocities. At



(a)



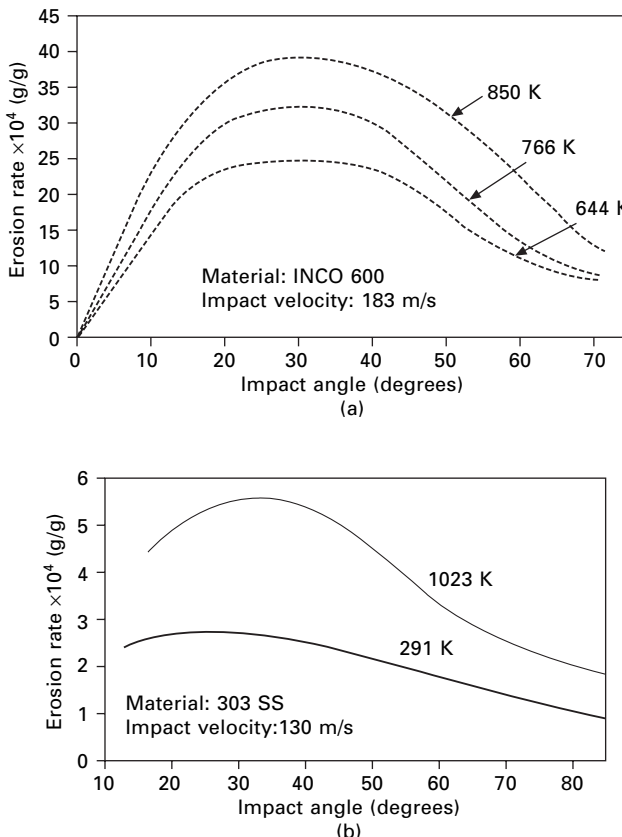
(b)

6.10 (a) Variation of erosion rate with temperature for a number of alloys [37,38]; (b) velocity exponent obtained by various investigators, plotted in velocity–temperature regime.

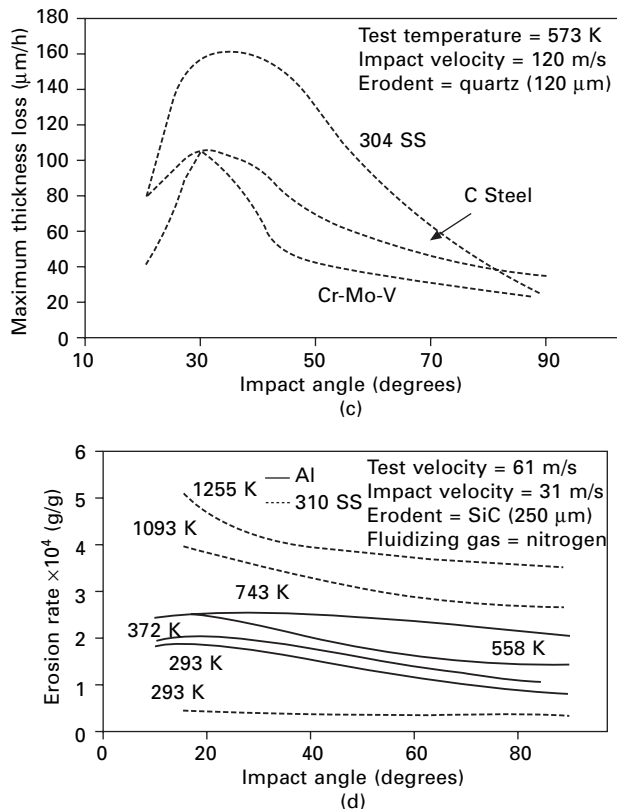
relatively higher impact velocities  $p$  appears to lie in the range of 2 to 3. Using angular SiC particles the influence of erodent size on the velocity exponent for erosion of 9Cr-1Mo steel at 923 K was reported by Levy and Man [39, 40].

#### 6.4.3 The effect of impact angle on erosion rate

The influence of impact angle on erosion rate at different temperatures for different test materials is presented in this section. However, most metallic materials, irrespective of temperature of erosion, exhibit a ductile behaviour, i.e. a maximum erosion rate at oblique impact angles (10° to 30°). The above observation is presented in Fig. 6.11, wherein the data from a large number of investigators have been compiled [41–46].



6.11 Variation of erosion rate with impact angle at various test temperatures: (a) INCO 600 [45], (b) 303 SS [42], (c) Cr-Mo-V, carbon and 304 SS [54], (d) aluminium and 310 SS [43].



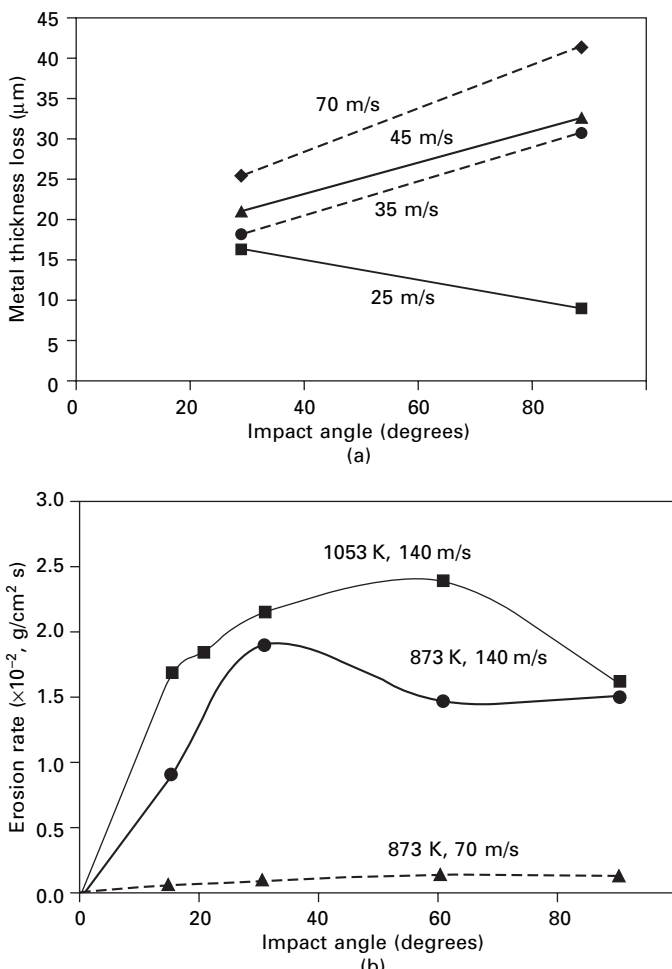
6.11 (Continued)

Levy [47] reported a higher erosion rate at normal impact than at oblique impact for 9Cr-1Mo steel at 1123 K using rounded  $\text{Al}_2\text{O}_3$  (130  $\mu\text{m}$ ) erodent for a range of impact velocities (30–70 m/s) as shown in Fig. 6.12a. However, when the impact velocity is reduced to 20 m/s, a maximum in the erosion rate occurred at an oblique impact angle. Observations by Chang *et al.* [43, 48] indicate that the peak erosion rate of Co at a test temperature of 1053 K occurred at an impact angle of 60° when impacted with 20  $\mu\text{m}$  angular alumina particles at impact velocities of 70–140 m/s. Their observations are shown in Fig. 6.12b. Interestingly, when the erosion test is carried out at 873 K and at an impact velocity of 140 m/s, the erosion rate peaks at an impact angle of 30° (Fig. 6.12b). Thus, the erosion rate–impact angle behaviour seems to be apparently conflicting.

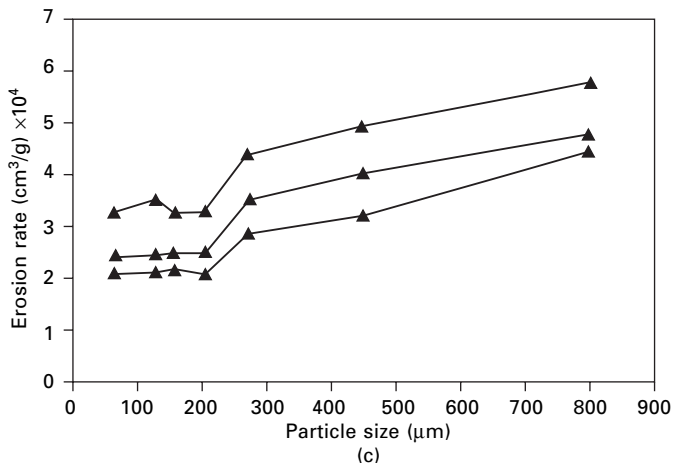
#### 6.4.4 The effect of particle size on erosion rate

Tabakoff and Vittal [44] conducted an erosion test on Inco 600 alloy with quartz particles in the size range between 70 and 800  $\mu\text{m}$ . According to their

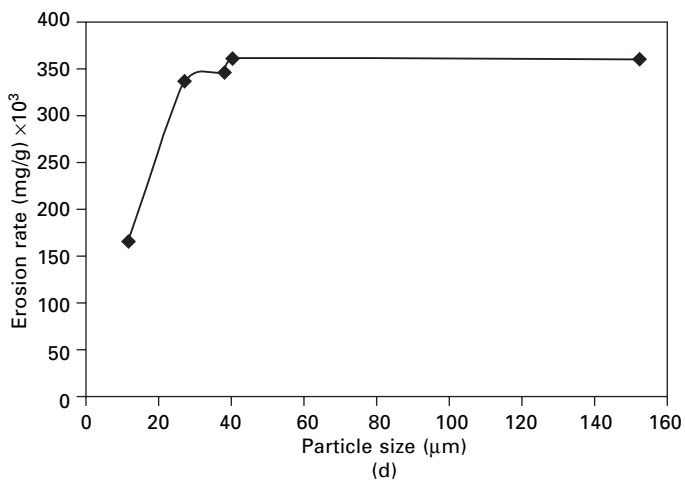
work, the erosion rate increases marginally with increase of particle size as shown in Fig. 6.12c. Zhou and Bahadur [45] investigated the effect of size of SiC on the erosion rate of 304 SS at 923 K for an impact angle of 30° and an impact velocity of 65 m/s. Their results indicate that the erosion rate increases with increase in particle size up to 40 µm and thereafter becomes independent of particle size (Fig. 6.12d). Levy *et al.* [39,40,47,49], however, reported only an increase of erosion rate with increase of particle size for 9Cr-1Mo steel eroded at a temperature of 923 K and for 1018 steel eroded at 723 K.



6.12 (a) Variation of metal thickness loss with impact angle for 9.0Cr-1.0Mo steel at 1123 K [48]; (b) variation of erosion rate of Co with impact angle at 1053 K [49]; (c) influence of particle size on the erosion rate of Inco 600 alloy [45]; (d) effect of particle size on the erosion rate of 304 SS at 923 K [46].



(c)



(d)

6.12 (Continued)

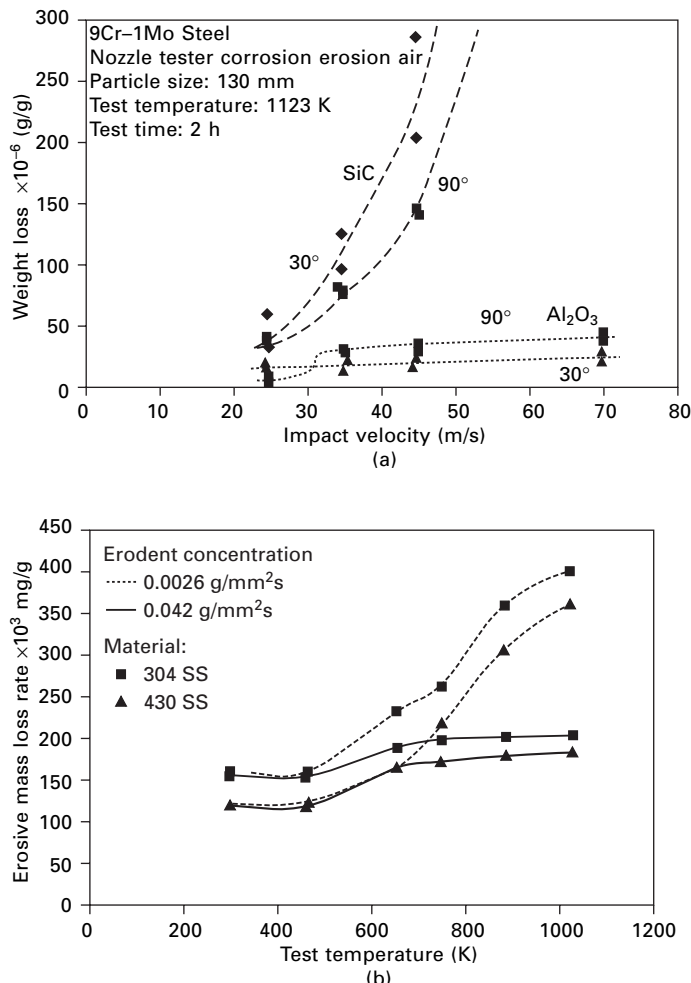
#### 6.4.5 The effect of particle shape on erosion rate

Levy *et al.* [39,40,47,49,50] investigated the erosion rate of a number of Cr-containing steels at 1123 K with angular SiC and spherical  $\text{Al}_2\text{O}_3$  as erodent particles. A typical result for 9Cr-1Mo steel is presented in Fig. 6.13a. The erosion rate is significantly higher when angular SiC erodent is used than when spherical  $\text{Al}_2\text{O}_3$  erodent is used.

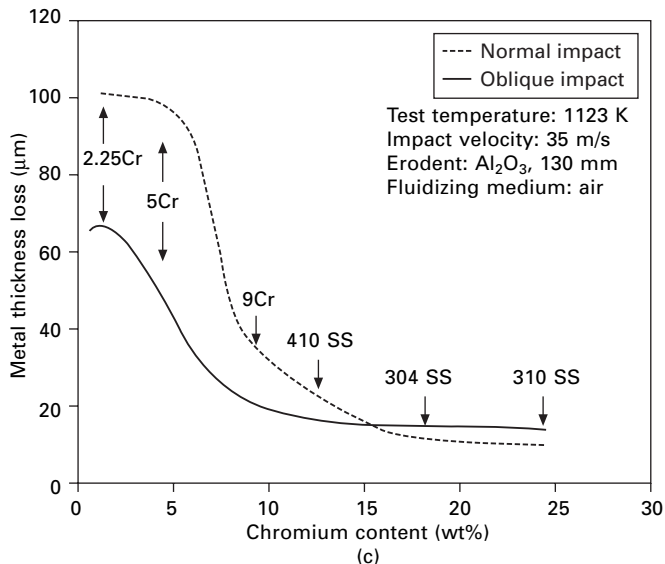
#### 6.4.6 The effect of particle feed rate on erosion rate

The influence of particle feed rate on the erosion rate of 304 and 430 SS over a large temperature range was investigated by Zhou and Bahadur [51]. The

reported results as illustrated in Fig. 6.13b suggest that increasing the feed rate by a factor of 16 has no influence on the erosion rate up to a temperature of about 773 K. However, beyond 773 K a lower feed rate results in a substantially higher erosion rate. Roy *et al.* [14] also noted a decrease of erosion rate with increase of particle feed rate, especially at low impact velocity.



6.13 (a) Variation of weight loss with impact velocity for 9.0Cr-1.0Mo steel at 1123 K showing the effect of particle shape on erosion behaviour [48]; (b) variation of erosion rate of 304 SS and 430 SS with test temperature showing the effect of feed rate on erosion rate [52]; (c) influence of Cr content on the erosion rate of steel [46].



6.13 (Continued)

#### 6.4.7 The effect of eroded material characteristics on erosion rate

The effect of eroded material characteristics on the erosion rate of the material is complicated by the fact that the behaviour of the oxide scale under erosion conditions needs to be considered in addition to the erosion behaviour of the metallic material *per se*. The oxidation characteristic of the eroded material plays a dominant role at elevated temperature when compared with the mechanical properties of the eroded materials.

Even at elevated temperature, if the erosion behaviour of the metallic material is considered at high impact velocities and at high particle feed rates, oxidation plays an insignificant role and the erosion behaviour is essentially that of the metal. The experimental data of Shida and Fujikawa [52] pertaining to 1.25Cr-1Mo-V, 2.25Cr-Mo, 12Cr-1Mo-V and plain carbon steel (up to 923 K), of Singh and Sundararajan [46,53] on 304, 316 and 410 stainless steel (up to 773 K), and of Levy *et al.* [54,55] on 2.25Cr-1.0Mo steel, 5Cr-0.5Mo steel, 1018 steel, 304 SS, 310 SS, 410 SS and 17-4 PHSS, can be considered as elevated temperature erosion of metals with minimum or negligible oxidation. Under such conditions the dependence of the strength of the material on temperature is a reasonable indicator of the temperature dependence of erosion resistance of the material. Erosion data further indicate that austenitic stainless steel has superior resistance to elevated temperature erosion than ferritic steel. The 410 stainless steel having a tempered martensitic

matrix exhibits an erosion resistance comparable to that of austenitic stainless steel.

The oxidation effect is reported to be important for elevated temperature erosion tests conducted at low impact velocities, at low particle feed rates and using rounded  $\text{Al}_2\text{O}_3$  erodent. The influence of Cr content on the erosion rate of steel is illustrated in Fig. 6.13c, which indicates that the erosion rate decreases to a very low value when the Cr content exceeds 10–12% [44]. In the case of steel having less than 10% Cr, a thick  $\text{Fe}_2\text{O}_3$  scale formed during erosion, leading to high erosion rates [56]. The experimental results of Chang *et al.* [57] also indicate the importance of the nature of the scale that forms during erosion at elevated temperature. It is also noted that materials with a high scaling rate such as nickel and cobalt exhibit the highest erosion rates, while the alumina-forming alloys such as CoCrAlY and NiCrAlY exhibit intermediate erosion rates. The superiority of  $\text{Al}_2\text{O}_3$ -forming alloy stems from the fact that the  $\text{Al}_2\text{O}_3$ -forming scale forms much more slowly than the  $\text{Cr}_2\text{O}_3$  scale.

The morphology of the oxide scale that forms during erosion plays an important role, as noted by the extensive work of Levy and co-workers [47, 49,53,58,59]. Segmented scales have better erosion resistance than thick, continuous and dense scale, since in the former case the spalled area is confined to crystalline oxide only. This observation is validated by adding Si to the steel. Addition of Si to low chromium steel results in the formation of a segmented scale even at high impact velocity and thereby reduces the erosion rate substantially as compared to the same steel without Si [59].

The above discussion clearly brings out certain features of the elevated temperature erosion of metallic materials. Almost all metallic materials exhibit ductile erosion response at room temperature, whereas at elevated temperature both brittle and ductile erosion responses are established [41,46,47]. The velocity exponents for metallic materials are around 2.5 during ambient temperature erosion. At elevated temperatures, the velocity exponents of metals and alloys vary over a wide range from 0.9 to more than 3.0 [41–43]. It is found that the erosion rate at room temperature increases with increase of particle size up to 50  $\mu\text{m}$ , beyond which the particle size has no effect on the erosion rate. The reported literature indicates that the erosion rate increases with increase of particle size at high temperatures [39,40,44,49]. At ambient temperature, changing the particle shape from angular to spherical alters the erosion response from brittle to ductile [60,61], while at elevated temperatures, brittle to ductile response is noted irrespective of the particle shape [39,40, 47]. The particle feed rate has a negligible effect on the room temperature erosion rate [62–64]. A remarkable effect of the particle feed rate has been noted at elevated temperatures [39]. The mechanical properties of the erodent have a nominal influence on room temperature erosion behaviour [65–73]. However, at elevated temperature this aspect has yet to be explored.

## 6.5 Important features of elevated temperature abrasive wear

As mentioned earlier, work on high temperature abrasive wear of metallic materials has been rather limited. Only a few studies in this area have been published [74–88]. Based on these studies, the following features can be outlined.

### 6.5.1 The effect of temperature on abrasive wear rate

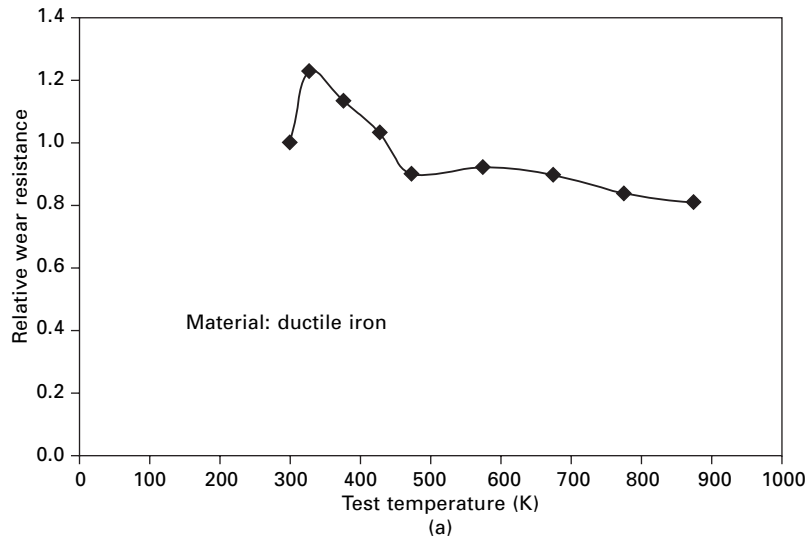
The variation of relative abrasive wear resistance (RAWR) as a function of temperature for ductile iron is presented in Fig. 6.14a [74]. It is clear that the abrasive wear resistance shows a maximum at around 323–373 K. The RAWR is 20% lower at higher temperature than at ambient temperature. The high value of the RAWR at around 323–373 K is attributed to dynamic strain ageing. In contrast, the decrease of RAWR with increase of temperature is related to loss of strength and ductility of the ductile iron at high temperature.

### 6.5.2 The effect of environment on abrasive wear rate

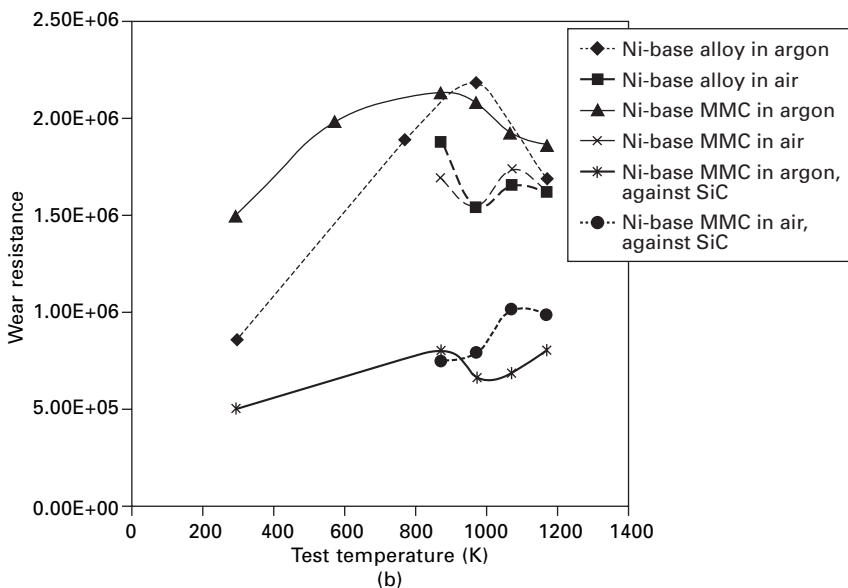
The abrasive wear resistance of Ni based alloy and of Ni based alloy reinforced with WC/W<sub>2</sub>C as a function of temperature is shown in Fig. 6.14b [75]. This figure compares wear resistance in argon and in air. In argon above 773 K the abrasive (flint) becomes soft and an increase in wear resistance is noted. However, when the abrasive remains hard as in the case of SiC, the wear resistance decreases with increase of temperature. In air, WC and W<sub>2</sub>C get oxidized and in the process become harder, thus wear resistance in air decreases with increase of temperature. This effect is not very significant in the argon atmosphere.

### 6.5.3 Two-body and three-body abrasion at elevated temperature

The work of Soemantri *et al.* [76] is presented in Fig. 6.15. Figure 6.15a shows the results of the two-body abrasion test, whereas Fig. 6.15b pertains to three-body abrasion. This work was carried out with commercially pure Al and Cu. As can be seen from Fig. 6.15, the wear rate of Cu is independent of temperature for two-body abrasion. Similarly, the two-body abrasive wear rate of Al is also nearly constant even though an increase in wear rate is noted at 323 K. In contrast, the wear rate of Cu increases with increase of temperature during three-body abrasion. However, for Al, the three-body



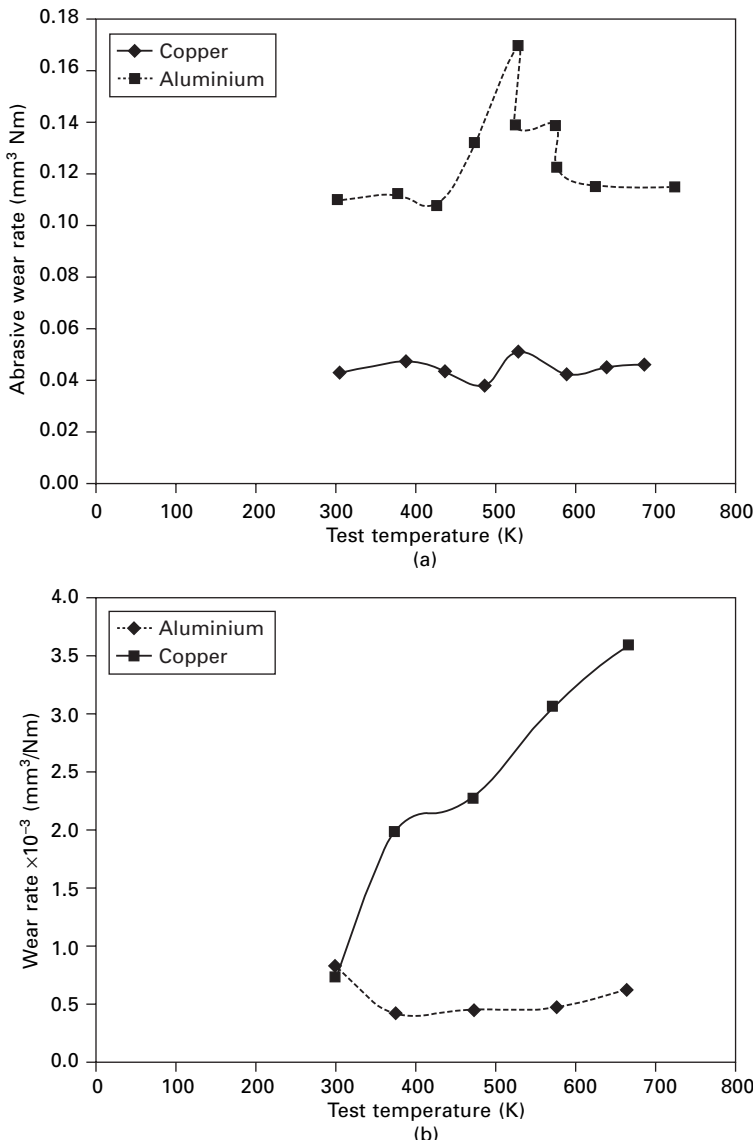
(a)



(b)

6.14 (a) Influence of test temperature on relative wear rate of ductile iron [74]; (b) effect of test temperature on wear resistance of Ni based alloy and Ni based composites [75].

abrasive wear rate is more or less independent of temperature. The study of oxidation of Cu shows considerable mass loss. If this mass loss due to oxidation is accounted for, then even Cu will show a temperature-insensitive wear rate. Mass loss due to oxidation becomes important during three-body



6.15 Effect of test temperature on abrasive wear rate: (a) two-body abrasion; (b) three-body abrasion [76].

abrasion, since the wear rate during three-body abrasion is considerably lower than that during two-body abrasion. Further, oxidation does not play an important role for Al during abrasion because Al quickly forms a tenacious oxide layer on exposure to high temperature.

## 6.6 Recent developments

Significant developments in high temperature tribology have been reported recently. However, most of these developments are confined to sliding wear and erosive wear only. As mentioned previously, the literature on elevated temperature abrasive wear is rather limited. Consequently, no effort is made here to highlight recent developments in high temperature abrasive wear.

### 6.6.1 Recent developments in elevated temperature sliding wear

It was demonstrated by Pauschitz *et al.* [21,23,24,79] that the nature of the glazed layers formed exhibits a variety of characteristics. Wearing conditions, wearing material and mating material govern formation of these layers. These layers determine the friction coefficient and the wear rate. They differ in physical appearance, mechanical properties, chemical compositions and failure mechanisms. Pauschitz *et al.* found that the following four different situations were possible:

- ‘No’ layer (NL) formation (wear is by pure delamination)
- Transfer layer (TL) formation
- Mechanically mixed layer (MML) formation
- Composite layer (CL) formation.

At room temperature, formation of no layer or formation of transfer layer can take place. When the hardness of the mating surface is significantly higher than the hardness of the wearing surface, no layer is formed. Under this condition, the composition of the near surface region and the composition of the debris are equal to the composition of the test specimen. In other words similar composition of the worn surface, wear debris and the bulk sample confirms pure delamination. The worn surface has a maximum average surface roughness  $R_a$  at ambient conditions. This maximum average surface roughness is accompanied by a maximum value of the average peak-to-valley height  $R_{z5}$  (between the five highest peaks and the five lowest valleys within the measuring length), the maximum value of the root-mean-square parameter r.m.s. ( $R_q$ ) corresponding to  $R_a$ , the maximum value of the vertical mean from the third highest peak to the third lowest valley  $R_{3z}$  within the measuring length (divided into five sections), and a very high maximum peak height of the profile above the mean line within the measuring length ( $R_p$ ). This behaviour alone is responsible for the high friction coefficient during delamination wear.

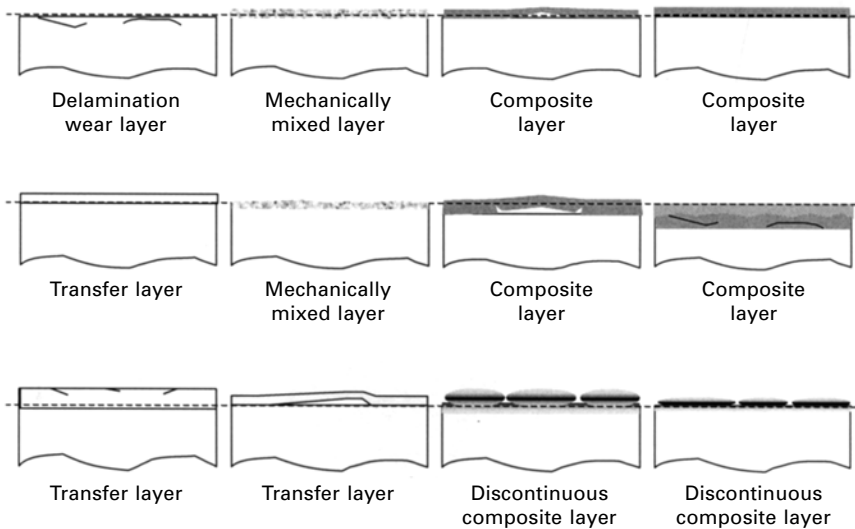
In contrast, if the mating surface is softer than the wearing material, a transfer layer (TL) is formed. TL formation takes place at near ambient temperature. As the transfer layer is primarily from the mating surface, the

chemical composition of that layer and the composition of the wear debris resemble closely that of the mating surface. Thus when the compositions of the worn surface and the debris are similar to the composition of the mating surface, the wear mechanism is governed by formation of TL. The surface roughness under such circumstances is low but increases with increase in temperature.

At relatively higher temperature, or under conditions of relatively soft but comparable hardness of the tribosystem, a mechanically mixed layer (MML) is formed. This layer is characterized by a low oxygen content and its composition is intermediate between that of the wearing sample and that of the mating material. Similar compositional features can be seen for wear debris as well. This hard but ductile layer formation is responsible for increase in surface roughness and other corresponding parameters. Interestingly, the friction coefficient exhibits a very low value under this condition. The roughness parameter during MML layer formation decreases with increase in temperature, in contrast to the case with TL where surface roughness increases with increase of temperature. When the MML layer is formed, a diffused adhesive interface between the MML and the substrate is also formed.

At high temperature, a composite layer (CL) is found. The composition of the worn surface with a composite layer and the composition of the wear debris are intermediate between that of the wearing sample and that of the mating surface. In addition, the CL contains a high amount of oxygen. This makes the layer hard and brittle and leads to a higher friction coefficient and a lower wear rate. The interface between the CL and the substrate is very weak, giving rise to detachment of the layer at the interface. The strength of this interface improves with increase in temperature. Further, the roughness of this layer is quite high, though it decreases with increase of temperature. Thus composite layer formation is characterized by a decrease of friction coefficient with increase of temperature.

The features of these layers were validated by Pauschitz *et al.* [79,21] using a series of systematic but comprehensive experiments. The formation of these layers and their failure mechanisms are presented in Fig. 6.16 schematically [79]. Their presence can explain all the observed behaviour of elevated temperature sliding wear of metallic materials [20]. Furthermore, by carrying out systematic chemical analysis of the worn surface and the wear debris it is possible to identify the various types of layers that form during elevated temperature wear. Further, systematic study by optical interferometer can also identify the types of layers that form and their failure mechanisms. By using both methods a complete failure analysis of the worn surface can be carried out without destroying the wearing sample.



6.16 Schematic representation of the various types of layers that formed during elevated temperature sliding wear and their failure mechanisms [24].

### 6.6.2 Recent developments in elevated temperature erosive wear

In recent years several interesting developments in the area of high temperature erosive wear have occurred. These developments have certainly enhanced our understanding of elevated temperature erosion of metals and alloys, and are highlighted below.

#### *Erosion oxidation interaction map*

It is noted that erosion conditions significantly influence oxidation. The factors that influence the operating mechanisms are impact velocity, impact angle, feed rate and temperature. Similarly, the particle size and particle shape also have a profound effect on this map. The combined influence of all these factors on the erosion rate remained known only qualitatively for a considerable time. Specific erosion mechanisms for various metallic materials have been described by Hogmark *et al.* [80], Wright *et al.* [81], Kang *et al.* [82] and Sundararajan [83]. Barkalow and Petit [84], for the first time, tried to organize such information in the form of an erosion oxidation map where the prevalence of various mechanisms is shown in the domain of particle kinetic energy and scale growth rate. Numerous experiments conducted by the author have led to the identification of the following four different mechanisms:

- Metal erosion
- Oxidation-affected erosion
- Oxidation-controlled erosion
- Oxide erosion.

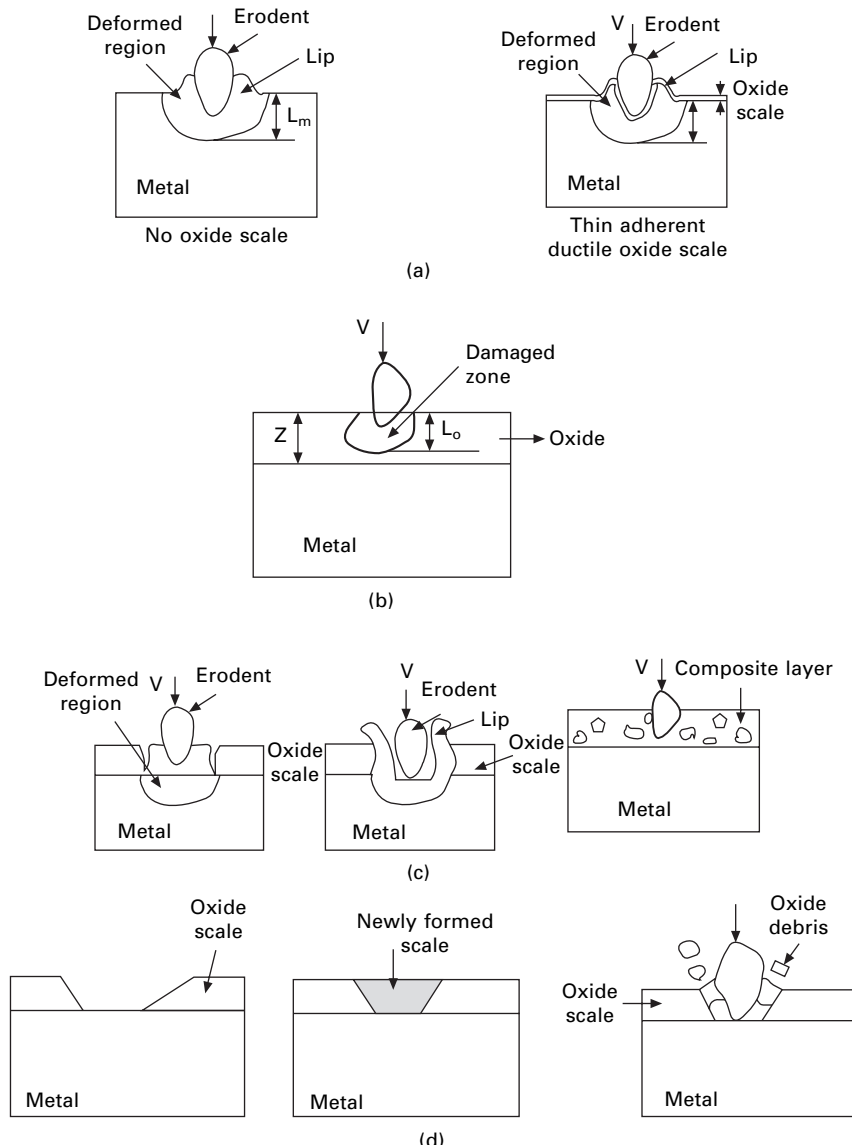
These mechanisms are presented schematically in Fig. 6.17. Because of the significance of various erosion conditions on erosion rate and erosion mechanisms, an erosion oxidation interaction map can be represented in a multidimensional configuration. A simplified representation of the erosion oxidation map can be made as a two-dimensional plot of impact velocity and temperature for a given impact angle and feed rate. Such an erosion-oxidation map at normal impact for commercially pure Ni is shown in Fig. 6.18a. In general, this map describes the transitional boundary between regimes of various operative mechanisms of erosion at elevated temperature. This map is able to clearly delineate the metal erosion, oxidation-affected erosion, oxidation-controlled erosion and oxide erosion regimes. The extent of each of these regimes depends on temperature, feed rate, impact angle and impact velocity. Examination of these maps infers the following:

- A low temperature imparts a metal erosion regime. With increase of temperature this metal erosion regime shifts to an oxide erosion regime via oxidation-affected erosion and oxidation-controlled erosion regimes.
- A higher feed rate extends the metal erosion regime and in turn alters the existence and extent of the other regimes.
- Oblique impact tends to reduce the extent of the metal erosion regime and promotes other regimes.

It is important to mention that the erosion-oxidation map has been constructed experimentally for the first time [20]. The influence of various erosion conditions on such a map can be explained on the basis of oxidation characteristics and mechanical properties of the eroding materials.

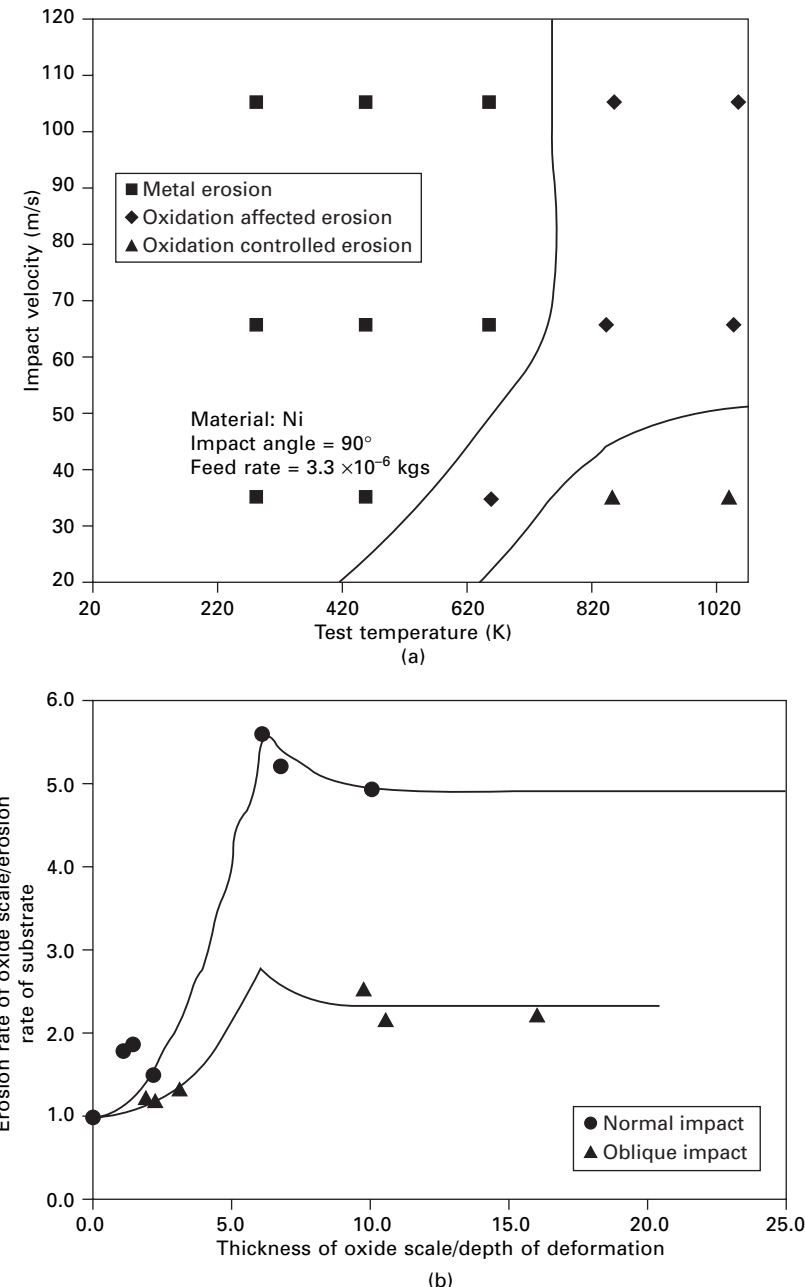
#### *Analysis of transition criteria for transition from metal erosion regime to oxide erosion regime*

Roy *et al.* [85], employing a new methodology, examined the transition criteria from the metal erosion regime to the oxide erosion regime. In their work, they eroded preoxidized Ni samples having various thicknesses of oxide scale, at ambient temperature. The ratio of the erosion rate of the oxide scale ( $E_o$ ) to the erosion rate of the substrate ( $E$ ) was plotted against the ratio of the initial thickness of the oxide scale ( $t$ ) to the depth of deformation ( $L$ ) due to impact. Their observations are portrayed in Fig. 6.18b. This figure reveals three distinct regimes. In regime one, the value of  $t/L$  is higher than 4.0. The erosion rate of the oxide scale assumes a relatively high but constant value. In regime two,  $t/L$  is higher than 0.5 but lower than 4.0. In this regime,



6.17 Schematic presentation of various erosion mechanisms at elevated temperature: (a) metal erosion; (b) oxide erosion; (c) oxidation-affected erosion; (d) oxidation-controlled erosion.

there is a smooth change of the relative erosion rate from a low value to a high value. Finally, in regime three,  $t/L$  is lower than 0.5. In this regime, the rate of change of the relative erosion rate is slow. In addition, there appears to be a peak in the relative erosion rate at approximately  $t/L = 6$ .



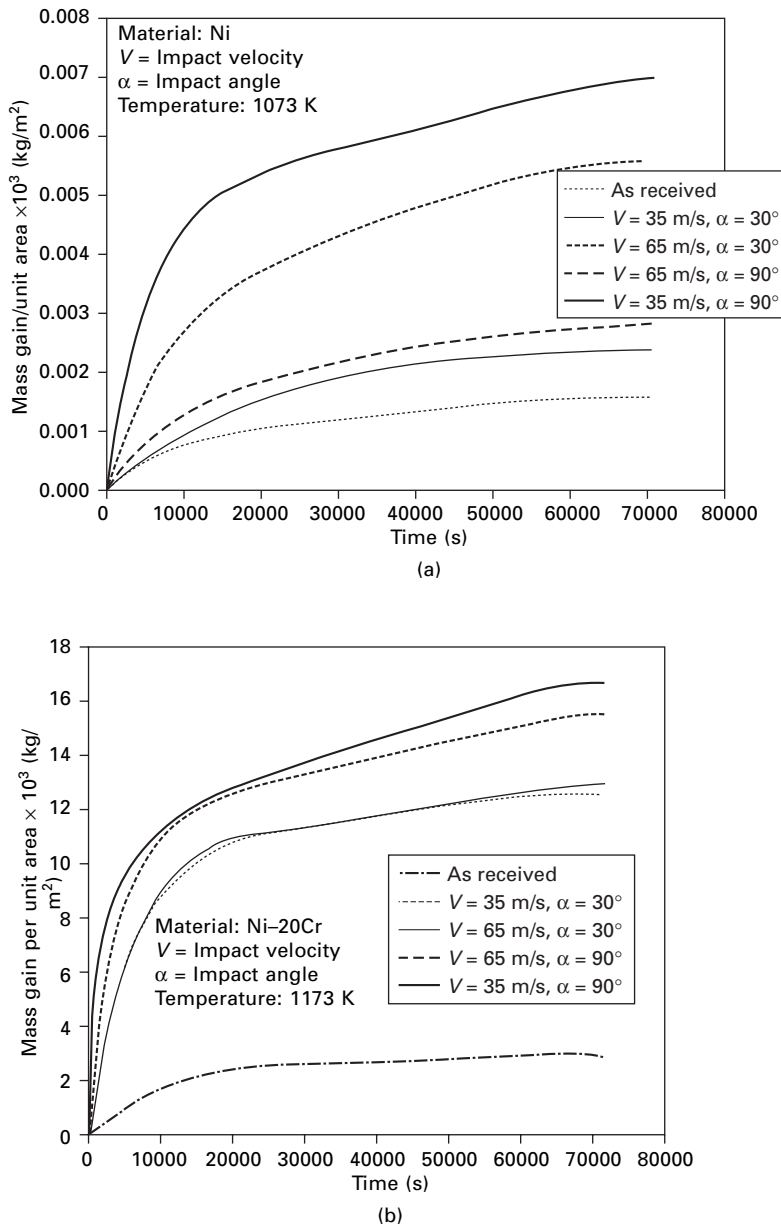
6.18 (a) Erosion oxidation interaction map for Ni; (b) variation of the ratio of the erosion rate of the oxide scale to the erosion rate of the substrate with the ratio of the thickness of the oxide scale to the depth of deformation [87].

Regime one can be deduced as an oxide erosion regime on the basis of erosion response, which is brittle, i.e. a higher erosion rate at normal impact, and on the basis of the velocity exponent, which is 3.0, of the erosion rate. Further, the material in this regime is removed by brittle chipping. In contrast, regime three is characterized by pure metallic erosion because the thickness of the oxide scale was negligibly low. In addition, the erosion response, the material removal mechanism and the velocity exponent of the erosion rate in this regime are consistent with that of erosion of metals and alloys at ambient temperature. Regime two represents the transition from the oxide erosion regime to the metal erosion regime and shows that this transition is not sharp but rather smooth. Thus as long as the depth of deformation is confined within the oxide scale, erosion takes place from the oxide scale only, and erosion behaviour similar to oxide erosion is prevalent. When there is no oxide scale, metal erosion is dominant. In the intermediate regime, erosion may take place from the oxide layer, but the deformation will extend to the substrate also.

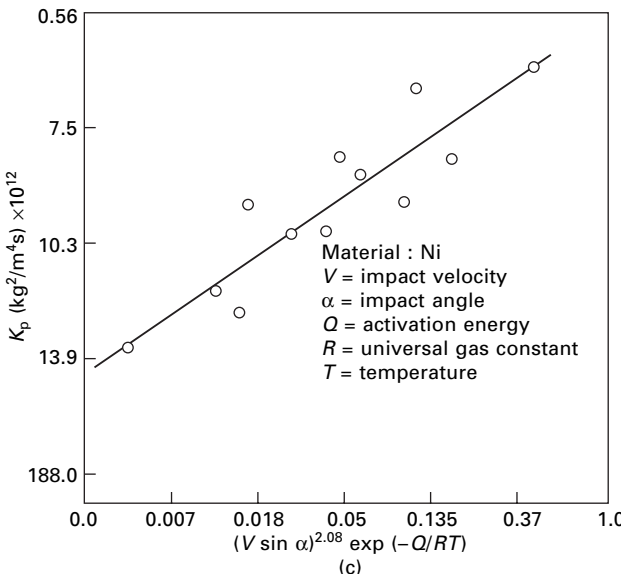
#### *Analysis of enhanced oxidation kinetics due to erosion induced roughness*

The oxidation kinetics of metals and alloys are found to alter during erosion or wear. The observation on enhanced oxidation kinetics is primarily centred on iron based alloys. The influence of sliding wear on oxidation was initially proposed by Quinn *et al.* [86]. According to these authors, the activation energy for the parabolic rate constant ( $K_p$ ) remains the same during static or wear-induced oxidation. However, the magnitude of  $K_p$  for wear-induced oxidation is higher than that for static oxidation. A similar contention is also made by Lim and Ashby [87] for wear-induced oxidation and by Levy and co-workers [39,88,89] for erosion-induced oxidation. Roy *et al.* [90] for the first time attempted to estimate the altered oxidation kinetics during erosion and subsequently tried to formulate a phenomenological model to explain such a result.

The observations of Roy *et al.* [90] are presented in Figs 6.19a and 6.19b. The variations of mass gain per unit area as a function of time at 1073 K for as-received and eroded Ni are given in Fig. 6.19a, whereas Fig. 6.19b depicts similar data at 1173 K for Ni-20Cr alloy. It is clear that the oxidation rate of Ni increases significantly for eroded samples as compared to as-received samples. The oxidation rate increases with increase of impact velocity. Increase of oxidation rate with increase of impact velocity is higher at normal impact than at oblique impact. With regard to the Ni-20Cr alloy it is noted that oxidation rate decreases with increase of impact velocity. Further, the influence of impact angle on oxidation kinetics is negligible.



6.19 (a) Variation of mass gain per unit area of Ni with time at 1073 K [92]; (b) variation of mass gain per unit area of Ni-20Cr alloy at 1173 K [92]; (c) variation of the parabolic rate constant with  $(V \sin \alpha)^{2.08} \exp(-Q/RT)$  [92].



## 6.19 (Continued)

The above observation for Ni is modelled by assuming that the parabolic rate constant is related to the surface roughness ( $R_a$ ) or impact velocity as

$$K = K_{O1}(R_a)^{x_1} \exp\left(\frac{-Q}{RT}\right) \quad 6.3$$

$$K = K_{O2}(V \sin \alpha)^{x_2} \exp\left(\frac{-Q}{RT}\right) \quad 6.4$$

where  $K_{O1}$  and  $K_{O2}$  are constant,  $V$  is the impact velocity and  $\alpha$  is the impact angle,  $Q$  is activation energy,  $R$  is the universal gas constant,  $T$  is the test temperature and  $x_1$  and  $x_2$  are the roughness exponent and velocity exponent, respectively. In order to establish the relation between the parabolic rate constant and the impacting condition, the average activation energy for the parabolic rate constant is determined by plotting  $\ln K$  (parabolic rate constant) against  $(1000/T)$  in  $\text{K}^{-1}$ . Using the average value of 22,400 for the activation energy, average parabolic rate constants at different eroding conditions are estimated. The natural logarithm of the average parabolic rate constant is then plotted against  $\ln R_a$  and  $\ln V \sin \alpha$ . The slopes of best-fit straight lines are then computed as constant  $K_{O1}$  and  $K_{O2}$  whereas the intercepts of the lines with the ordinate are calculated as exponents  $x_1$  and  $x_2$ . The expressions for rate constants are then obtained as

$$K = 4.67 \times 10^{-9} (V \sin \alpha)^{2.08} \exp\left(\frac{-22400}{RT}\right) \quad 6.5$$

$$K = 9.62 \times 10^{-7} (V \sin \alpha)^{4.26} \exp\left(\frac{-22400}{RT}\right) \quad 6.6$$

In order to assess the ability of the expression to predict the parabolic rate constant, the estimated rate constants are plotted against  $(V \sin \alpha^{2.08}) \exp(-22400/RT)$  in Fig. 6.19c. A straight line with good fit suggests the suitability of the expression.

A similar exercise cannot be carried out for Ni-20Cr alloy because of two factors. First, the nature of the oxide scale that forms on Ni-20Cr alloy can have dual grain size distribution [91]. Secondly, higher roughness in these alloys results in smaller globular oxide grains. Hence, even though the roughness is changing, the amount of grain boundary also gets altered and this in turn provides different extents of short circuit paths. Thus the pre-exponential factors in the Arrhenius-type equation should be a function of the roughness, grain size and the nature of the oxides that is present in the oxide scales of Ni-20Cr alloy. Hence similar modelling for Ni-20Cr alloy cannot be achieved.

## 6.7 Future trends

In spite of significant progress in elevated temperature wear of metals and alloys, certain areas still need to be addressed. The material flow behaviour under sliding wear is at high strain, at high strain rate, under isothermal deformation and under multi-axial compressive stress [92]. In contrast, the material flow behaviour under solid particle erosion is characterized by high strain, high strain rate, adiabatic deformation and multi-axial compressive stress [72]. Similarly during abrasive wear, material is deformed under high strain, high strain rate, and multi-axial compressive strain. The thermodynamic status of the deformation is neither adiabatic nor isothermal [92]. The material flow behaviour under such conditions, particularly at elevated temperature, is not well understood. Estimation of the mechanical properties of materials under such conditions is required for effective modelling of elevated temperature sliding wear behaviour of materials. Thus there is a clear need to develop a simplified test technique which will simulate the sliding wear conditions in a test sample and evaluate the mechanical behaviour under such conditions.

It is stated that formation of various types of layers such as transfer layer, mechanically mixed layers, composite layer, etc., having characteristic composition and surface roughness governs the elevated temperature wear behaviour of metallic materials. Similarly during elevated temperature erosion, metallic erosion, erosion from the composite layer and erosion on the oxide scale are reported. The reported literature on abrasive wear at high temperature is much sparser and hence such layers are not yet found in the literature. The

microstructural features and mechanical properties of these layers need to be characterized extensively and for a large variety of tribosystems.

The deformation and fracture behaviour of the oxide scale during tribological processes at elevated temperature is poorly understood. Further, the high strain rate flow behaviour of layered structures containing oxide scale and the substrate material or the layer and the substrate material also needs to be addressed. A serious deficiency of our understanding of elevated temperature wear is related to the lack of experimental data or theoretical analysis of the oxide scale behaviour under wear conditions. Such an understanding is required to model the spalling behaviour of the oxide scale once it reaches the critical thickness of spalling during tribological degradation.

The kinetics of oxidation during sliding wear, erosive wear and abrasive wear are an order of magnitude higher than that under static conditions. Efforts to estimate the increased oxidation rate quantitatively either through careful experiment or by rigorous theoretical analysis have hitherto been lacking for any of these tribological processes, even though such attempts have been made for elevated temperature erosion [90]. The reasons for such accelerated oxidation have not all been revealed. Thus, there is a clear need to carry out organized experiments to evaluate the oxidation behaviour of materials under various tribological conditions. Attempts should be made to separate out the influence of possible factors responsible for the enhanced oxidation kinetics of metallic materials during various tribological processes. For example, the influence of oxide thickness, test temperature, hardness of the substrate metal and applied load on the plasticity and ductility of various oxides is least understood.

Maps delineating the nature of the interaction between oxidation and tribological processes are to be constructed experimentally for a variety of materials through generation of a comprehensive database. Construction of such maps for several engineering materials subjected to the synergistic effect of oxidation and tribological processes is considered to be vital in future research in this area. One important drawback of tribology-oxidation maps is that to characterize a system one needs a large number of maps to cover the whole range of wear conditions. To date no effort has been made to develop parameters that take care of several tribo-oxidation conditions. Further, there is no unified system to extrapolate a tribo-oxidation map from one condition or process to another condition or process. This area needs to be addressed. One major challenge of future work is to develop these maps under sulphidising and chlorinating environments.

## 6.8 Concluding remarks

The present state of understanding and developments in the last few years in respect of various tribological degradation processes at elevated temperature

have been reviewed. Only three types of wear, namely dry sliding wear, abrasive wear and solid particle erosive wear, are covered in this work. It is to be understood that there exist several mechanisms of material loss that govern the rate of material loss in each and every wear process. The relative importance of these mechanisms is determined by the conditions of wear and hence extrapolation of any wear data is to be done with sufficient care.

Wear testing is carried out for several purposes. The selection of test equipments and test conditions is governed by the objective of the wear test. There exists significant scope for devising and developing new approaches to the wear testing of surface engineered materials and these can make a valuable contribution to our understanding and use of these economically important technologies.

The elevated temperature wear behaviour of metals and alloys has been reviewed in a systematic and brief manner. Wear of metallic materials at elevated temperature is receiving increased attention in recent times. Technological developments in all fields of science and engineering are resulting in development of materials capable of operating in demanding and harsh environments. Research and development into elevated temperature sliding wear of metals and alloys has been quite limited in this respect.

Almost all the investigators have identified the formation of a kind of glazed layer that controls the wear processes. Careful and systematic investigation has classified this glazed layer as a transfer layer, a mechanically mixed layer and composite layers. Formation of these layers depends on the wearing conditions. Each of these layers has characteristic composition and surface roughness. The mechanisms of failure of these layers have unique features.

Solid particle erosion is an area that has received increased scientific attention over the last few decades. Technological advancements in several high temperature applications such as gas turbine engines, power plants, etc., have led to increased interest in elevated temperature erosion. However, investigations into the elevated temperature erosion of metals and alloys have been very limited. One reason for the scarcity of published work in this discipline is the non-availability of suitable test facilities.

The presence of an oxide scale is responsible for the existence of a variety of material removal mechanisms during elevated temperature erosion of metallic materials. These mechanisms have been carefully verified by experimental work. Four distinct material removal mechanisms, namely metal erosion, oxidation-affected erosion, oxidation-controlled erosion and oxide erosion, have been experimentally established. These experimental observations have been substantiated by theoretical considerations. A suitable criterion for transition from one erosion regime to another regime is yet to evolve. Attempts have been made to analyse such transitions using preoxidized samples.

The prevalence of various mechanisms has been found to be dependent on

eroding conditions. The best way to demonstrate the influence of these conditions on the prevailing erosion mechanisms is to present erosion-oxidation interaction mechanism maps. Though attempts have been made earlier to construct such maps theoretically, experimental construction of such maps has been attempted only recently. The influence of various eroding conditions on such mechanisms has been studied quite extensively for Ni and Ni-20Cr alloy.

Study of the elevated temperature abrasive wear of metallic materials is far from satisfactory. Certainly this area needs sustained attention from investigators.

## 6.9 Acknowledgement

The author is grateful to the Defence Metallurgical Research Laboratory, Hyderabad, India, for their support in preparing the manuscript.

## 6.10 References

1. J. Mateos, J.M. Cuetos, R. Vijande and E. Fernández, *Tribol. Intl.*, 34 (2001) 345.
2. M. Roy, A. Pauschitz and F. Franek, *Wear*, 257 (2004) 799.
3. X. Jiang, W. Liu, S.Y. Dong and B.S. Xu, *Surf. Coat. Technol.*, 194 (2005) 10.
4. I.A. Inman, S. Datta, H.L. Du, J.S. Burnwell-Gray, S. Pierzgalski and Q. Luo, *Wear*, 254 (2003) 461.
5. I.G. Wright, *Mater. Sci. Eng.*, 88 (1987) 261.
6. W. Tabakoff and A. Hamed, *Proc. 6th Int. Conf. on Erosion by Liquid and Solid Impact*, paper no. 54 (Cambridge University, UK, 1984).
7. W. Sage and G.P. Tilly, *J. Aeronaut.*, 73 (1969) 429.
8. J.G.A. Bitter, *Wear* (1963) 164.
9. H.N. Liu, M. Sakamoto, M. Nomura and K. Ogi, *Wear*, 250 (2001) 71.
10. G. Sundararajan, M. Roy and D.K. Das, *Surface Engineering*, 13 (1997) 219.
11. *Annual Book of ASTM Standards, Metal Test Methods and Analytical Procedures*, Vol. OS. 02, *Wear and Erosion, Metal Corrosion*, 1990.
12. M. Roy, *Trans. Indian Inst. Metal*, 53 (2000), 623–638.
13. M. Roy, A. Pauschitz, J. Wernisch and F. Franek, *Wear*, 257 (2004) 799.
14. M. Roy, K.K. Ray and G. Sundararajan, *Mater. Metal Trans.*, 32A (2001) 1431.
15. A.W. Ruff and L.K. Ives, *Wear*, 35 (1975) 195.
16. S.K. Havis, K. Anand, H. Conrad and R.O. Scattergood, *Wear*, 107 (1985) 69.
17. J.G.A. Bitter, *Wear*, 6 (1963) 5.
18. G. P. Tilly and W. Sage, *Wear*, 16 (1968) 447.
19. A. Misra and I. Finnie, *Wear*, 60 (1980) 111.
20. A. Pauschitz, M. Roy and F. Franek, communicated to *Tribol. Intl.*
21. M. Roy, A. Pauschitz, J. Wernisch and F. Franek, *Mater. Corrosion*, 55 (2004) 259.
22. I.A. Inman, S.R. Rose and P.K. Dutta, *Wear*, 260 (2006) 919.
23. A. Pauschitz, M. Roy and F. Franek, *Tribologia*, 188 (2003) 127.
24. A. Pauschitz, M. Roy and F. Franek, *Tribologie und Schmierungstechnik*, 50 (2003) 40.

25. J.P. Tu, X.H. Jie, Z.Y. Mao and M. Matsumara, *Tribol. Intl.*, 31 (1998) 347.
26. I.A. Inman, S.R. Rose and P.K. Dutta, *Tribol. Intl.* (in press).
27. I.A. Inman, P.K. Dutta, H.L. Du, J.S. Burnell-Gray, S. Pierzgalsky and Q. Lou, *Tribol. Intl.*, 38 (2005) 812.
28. Y. Solmaz and M.H. Kelestemur, *Wear*, 257 (2004) 1015.
29. G.A. Fontalvo and C. Mitterer, *Wear*, 258 (2005) 1491.
30. P.J. Blau, *ASM Handbook*, ASM International, USA, Vol 18 (1992) 772.
31. P.J. Blau and C.E. Devore, *Wear of Materials*, ed. K.C. Ludema, ASTM, New York and Denver, CO, 9–13 April, 1989, 305.
32. P.J. Blau and C.E. Devore, *Tribol. Intl.*, Oct. (1990) 226.
33. L. Wang and D.Y. Li, *Wear* (2003) 535.
34. I. Radu and D.Y. Li, *Tribol. Intl.* (in press).
35. I. Radu and D.Y. Li, *Wear*, 259 (2005) 453.
36. M. Roy, *J. Appl. Phys. D*, 39 (2006) R101.
37. A.V. Levy, J. Yan and J. Patterson, *Proc. Int. Conf. on Wear of Material*, ed. K.C. Ludema, ASME, New York (1985) 708.
38. N. Gat and W. Tabakoff, *Wear*, 50 (1978) 85.
39. A.V. Levy and Y.F. Man, *Wear*, 111 (1986) 173.
40. A.V. Levy and Y.F. Man, *Wear*, 131 (1989) 53.
41. P.J. Shayler and K.H. Yee, *Wear*, 98 (1985) 127.
42. I. Finnie, A.V. Levy and D.H. McFadden, *ASTM STP 664*, ed. W.F. Adler, Philadelphia, PA (1976) 36.
43. C.T. Kang, S.L. Chang, F.S. Petit and N. Birks, *Proc. Third Berkeley Conf. on Corrosion-Erosion-Wear of Materials at Elevated Temperature*, ed. A.V. Levy, Berkeley, CA (1986).
44. W. Tabakoff and B.V.R. Vittal, *Wear*, 86 (1983) 89.
45. J. Zhou and S. Bahadur, *Corrosion and Particle Erosion at High Temperature*, ed. V. Srinivasan and K. Vedula, The Minerals, Metals and Materials Society, USA (1989) 315.
46. T. Singh, PhD Thesis, Banaras Hindu University, Varanasi, India, 1952.
47. A.V. Levy, *Corrosion and Particle Erosion at High Temperature*, ed. V. Srinivasan and K. Vedula, The Minerals, Metals and Materials Society, USA (1989) 207.
48. S.L. Chang, F.S. Petit and N. Birks, *Oxid. Metals*, 34(1/2) (1990) 47.
49. A.V. Levy, B.W. Wang, Y.F. Man and N. Zee, *Wear*, 131 (1989) 85.
50. A.V. Levy and B.Q. Wang, *Wear*, 131 (1989) 71.
51. J. Zhou and S. Bahadur, *Proc. Corrosion-Erosion Wear of Materials at Elevated Temperature*, ed. A.V. Levy, Berkeley, CA (1991) 13–1.
52. Y. Shida and H. Fujikawa, *Wear*, 103 (1985) 281.
53. T. Singh and G. Sundararajan, *Met. Trans.*, 21A (1990) 3187.
54. B.Q. Wang, G.Q. Geng and A.V. Levy, *Wear*, 159 (1992) 233.
55. A.V. Levy, E. Slamovich and N. Zee, *Wear*, 110 (1996) 117.
56. A.V. Levy and Y.F. Man, *Wear*, 131 (1989) 39.
57. S.L. Chang, F.S. Petit and N. Birks, *Oxid. Metals*, 34(1/2) (1990) 71.
58. A.V. Levy and B. Wang, *Surf. Coat. Technol.*, 33 (1987) 285.
59. Q. Geng, B. Wang, P. Hou and A.V. Levy, *Wear*, 150 (1991) 89.
60. A.K. Cursons, and I.M. Hutchings, *Proc. 6th Int. Conf. on Erosion by Solid and Liquid Impact*, ed. J.E. Field and N.S. Corney, Cavendish Laboratory, Cambridge University, Cambridge, UK, September 1983.
61. A.V. Reddy and G. Sundararajan, *Wear*, 111 (1986) 313.

62. D. Mills and J.S. Mason, *Proc. 6th Int. Conf. on Erosion by Solid and Liquid Impact*, ed. J.E. Field and N.S. Corney, Cavendish Laboratory, Cambridge University, Cambridge, UK, September 1983.
63. J.P. Young and A.W. Ruff, *J. Eng. Mater. Tech. Trans. ASME*, 99 (1977) 121.
64. K. Anand, S.K. Hovis, H. Conrad and R.O. Scattergood, *Wear*, 118 (1987) 243.
65. S. Chinnadurai and S. Bahadur, *Wear*, 186–187 (1995) 299.
66. M. Sahoo, A. Lui, G. Morin and V.K. Sikka, *Mechanical Properties and Erosion Behaviour of Nickel Aluminide*, Report MTL 89–68 (J), Canada Centre for Mineral and Energy Technology. CANMET, 1981.
67. I. Kleis, *Z. Werkstofftech.*, 15 (1984) 69.
68. S. Soderberg, H. Hogmark, U. Engman and H. Swahn, *Tribol. Intl.*, 14 (1981) 333.
69. K.C. Goretta, R.C Arroyo, C.T. Wu and J.L. Routbort, *Wear*, 147 (1991) 145.
70. T. Foley and A.V. Levy, *Wear*, 91 (1983) 45.
71. A. Behrendt, *Proc. 3rd Int. Conf. on Erosion and Allied Phenomenon*, ed. A.A. Fyall and R.B. King, Royal Aircraft Establishment, UK, 1970.
72. M. Roy, Y. Tirupataiah and G. Sundararajan, *Mater. Sci. Eng.*, A165 (1993) 51.
73. M. Roy, Y. Tirupataiah and G. Sundararajan, *Mater. Sci. Technol.*, 11 (1995) 791.
74. O. Celik, H. Ahlatci, E.S. Kayali and H. Cimenoglu, *Wear*, 258 (2005) 189.
75. H. Berns and S. Koch, *Wear*, 225–229 (1999) 154.
76. S. Soemantri, A.C. McGee and I. Finnie, *Wear*, 104 (1985) 77.
77. H.N. Liu, M. Sakamoto, M. Nomura and K. Ogi, *Wear*, 250 (2001) 71.
78. H. Berns and S.D. Franko, *Wear*, 203–204 (1997) 608.
79. A. Pauschitz, M. Roy and F. Franek, *Transient Phenomena in Tribological Processes*, ed. D. Dowson, Elsevier Science BV, Amsterdam (2004), p. 721.
80. S. Hogmark, A. Hammarsten and S. Soderberg, *Proc. 6th Int. Conf. on Erosion by Liquid and Solid Impact*, ed. J.E. Field and N.S. Corney, Cavendish Laboratory, Cambridge University, Cambridge, UK, September 1979.
81. I.G. Wright, V. Nagarajan and J. Stringer, *Oxid. Metals*, 25 (1986) 175.
82. C.T. Kang, F.S. Petit and N. Birks, *Metal. Trans. A*, 18A (1987) 1785.
83. G. Sundararajan, *Wear*, 145 (1991) 251.
84. R.H. Barkalow and F.S. Petit, in *Corrosion/Erosion of Coal Conversion System Materials*, Berkeley, CA, 1979.
85. M. Roy, K.K. Ray and G. Sundararajan, *Wear*, 217 (1998) 312.
86. T.F.J. Quinn, J.L. Sullivan and D.M. Rowson, *Wear*, 94 (1984) 175.
87. S.C. Lim and M.F. Ashby, *Acta. Metal.*, 35 (1987) 1.
88. A.V. Levy, E. Slavovich and N. Zee, *Wear*, 110 (1996) 117.
89. A. Drotlew, P. Christodonlou and V. Gutowsky, *Wear*, 211 (1997) 120.
90. M. Roy, K.K. Ray and G. Sundararajan, *Oxid. Metals*, 51 (1999) 257–272.
91. D. Caplan and G.I. Sproule, *Oxid. Metals*, 9 (1975) 459.
92. M. Roy, *Proc. Int. Conf. on Advances in Materials and Materials Processing*, Kharagpur, India, 3–5 February, 2006, 202–209.

## Hot corrosion of alloys and coatings

S P R A K A S H, Indian Institute of Technology Roorkee, India

### 7.1 What is hot corrosion?

Hot corrosion is a complex phenomenon involving sulphidation, oxidation or both. Hot corrosion is a form of accelerated oxidation which affects the surfaces exposed to high-temperature gases contaminated with sulphur and alkali metal salts. These contaminants combine in the gas phase to form alkali metal sulphates. If the temperature of the alloy or coating surface is below the dew point of the alkali sulphate vapours and above the sulphate melting points, molten sulphate deposits are formed. Molten sodium sulphate is the principal agent in causing hot corrosion.

Metallic corrosion is the surface wastage that occurs when metals are exposed to a reactive environment. The chemical compounds that constitute the products of such wastage are close cousins of the metalliferous mineral rocks that we find in the Earth's crust. In other words, corrosion reactions cause metals to revert to their original ores. At temperatures above 200°C there is usually significant reaction of most metals in dry air, and the rate and extent of reaction progressively increase either as the temperature is raised or the air is contaminated by other gases. In general, it may be said that the degree of wastage is largely governed by the ionic conducting properties of the corrosion product when it is present as a solid scale by its mechanical strength and adherence to the underlying metal. The study of high temperature corrosion products is therefore a study of semiconducting oxides, sulphides and so on and the influences of temperature, pressure and ionic contaminants on their mechanical coherence, stability and permeability (West, 1986).

According to Hancock (1987), hot corrosion is an accelerated form of oxidation which occurs when metals are heated in the temperature range 700–900°C in the presence of sulphate deposits formed as a result of the reaction between sodium chloride and sulphur compounds in the gas phase around the metals.

If the concentration of the sulphate exceeds the saturation vapour pressure at the operating metal temperature for turbine blades and vanes (700–1100°C),

then deposition of the  $\text{Na}_2\text{SO}_4$  will occur on the surface of these components. At higher temperatures the deposits of  $\text{Na}_2\text{SO}_4$  are molten (m.p. = 884°C) and can cause accelerated attack of the Ni- and Co-base superalloys. This type of attack is commonly called 'hot corrosion'. The accelerated corrosion can also be caused by the other salts, viz. vanadates or sulphate-vanadate mixtures, and in the presence of solid or gaseous salts such as chlorides.

## 7.2 Types of hot corrosion

Hot corrosion can occur at high temperatures where the deposit is in the liquid state right from the beginning or the solid deposit turns into liquid during the exposure as a result of reaction with the environment. These two types of hot corrosion processes are termed High Temperature Hot Corrosion (HTHC) or Type I, and Low Temperature Hot Corrosion (LTHC) or Type II, respectively (Khanna and Jha, 1998).

### 7.2.1 Type I hot corrosion

High temperature (Type I) hot corrosion (HTHC) is normally observed in the temperature range of about 825–950°C when the condensed phase is clearly liquid. The typical microstructure for HTHC shows the formation of sulphides and a corresponding depletion of the reactive components in the alloy substrate. The external corrosion products consist of oxide precipitates dispersed in the salt film. The presence of the pore, crevice or crack across a protective film can lead to the sulphidation of the alloy substrate. This results in a significant shift in the basicity of the salt film. Once the fused salt contacts the alloy substrate, the rate and duration of the rapid corrosion kinetics are decided by the magnitude and gradient of salt basicity relative to the local solubilities for the oxide scale phases (Rapp and Zhang, 1994).

### 7.2.2 Type II hot corrosion

Low temperature (Type II) hot corrosion (LTHC) occurs well below the melting point of  $\text{Na}_2\text{SO}_4$  (884°C). The reaction product morphology is characterized by a non-uniform attack in the form of pits, with only little sulphide formation close to the alloy/scale interface and little depletion of Cr or Al in the alloy substrate (Rapp and Zhang, 1994).

Luthra (1985) reported LTHC behaviour for a number of Co-Cr, Co-Al and Co-Cr-Al alloys. After a low melting  $\text{CoSO}_4\text{-Na}_2\text{SO}_4$  liquid phase was formed, the acidic dissolution of CoO at the oxide/salt interface supported the precipitation of either  $\text{Co}_3\text{O}_4$  or  $\text{CoSO}_4$  near the salt/gas interface. The negative solubility gradient was maintained by gradients in the basicity and oxygen activity in the salt film. For sufficient acidic cobalt-solute ions in the

salt film, counter-transportation of  $\text{Co}^{2+}/\text{Co}^{3+}$  ions carried the reduction reaction to the salt/gas interface. In this case the dissolution/precipitation of cobalt compounds prevents the formation of a protective scale of  $\text{Cr}_2\text{O}_3$  or  $\text{Al}_2\text{O}_3$ .

## 7.3 Chemistry of hot corrosion

### 7.3.1 Hot corrosion degradation sequence

When superalloys undergo hot corrosion degradation, this process almost always consists of two stages (Pettit and Giggins, 1987; Pettit and Meier, 1984). It is a fact that all corrosion resistant alloys degrade via such a sequence and it is the result of using selective oxidation to develop oxidation or corrosion resistance. It is convenient to place emphasis on the two stages, namely, an initiation stage during which the alloys behave as they would have behaved in the absence of the deposit, and a propagation stage where the deposit has caused the protective properties of the oxide scales to become significantly different from what they would have been, had no deposit been present. Such conditions are depicted schematically in Fig. 7.1.

#### *The initiation stage*

During the initiation stage of hot corrosion, elements in the alloy are oxidized and transferred from metallic atoms to the reducible substances in the deposit. To develop resistance to hot corrosion one should strive to have the superalloys which can remain in the initiation stage as long as possible.

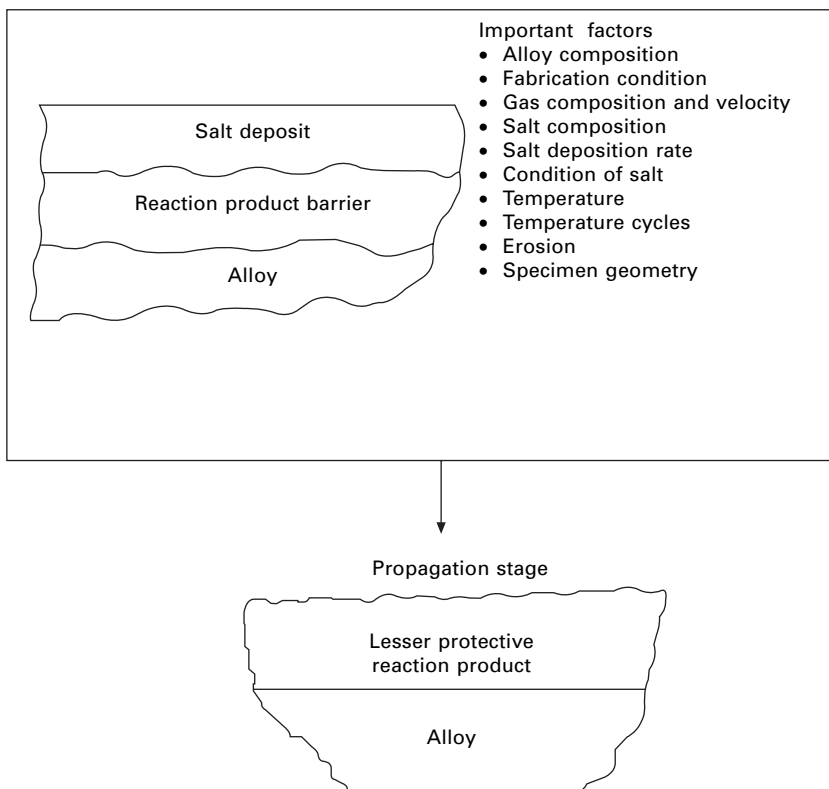
In some cases of hot corrosion an increasing amount of sulphide particles becomes evident in the alloy beneath the protective reaction product barrier. In other cases, small holes become evident in the protective reaction product barrier where the molten deposit begins to penetrate it. Eventually the protective barrier formed via selective oxidation is rendered ineffective and the hot corrosion process enters the propagation stage (Pettit and Giggins, 1987).

#### *The propagation stage*

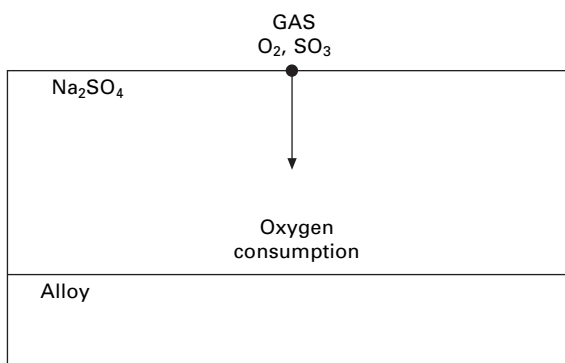
The propagation stage of the hot corrosion sequence is the stage at which the superalloy must be removed from service since, this stage always has much larger corrosion rates than for the same superalloy in the initiation stage. Before—describing the types of propagation modes by which superalloys undergo hot corrosion attack, it is of value to examine how deposits upon the surfaces of superalloys may affect their corrosion behaviour. In Fig. 7.2 a deposit of  $\text{Na}_2\text{SO}_4$  is depicted schematically upon the surface of a superalloy. As indicated in the figure, superalloy will react with elements in the deposit provided that the deposit prevents free access of the gas. Since superalloys

### HOT CORROSION CHRONOLOGY

Initiation stage



7.1 Schematic diagram illustrating the conditions that develop during the initiation and propagation of hot corrosion attack and identifying the factors that determine the time of transition from the initiation to the propagation stage (Pettit and Meier, 1984).



7.2 Schematic diagram showing a  $Na_2SO_4$  deposit upon an alloy separating the alloy from the gas phase (Pettit and Meier, 1984).

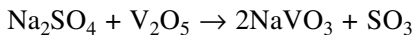
always contain elements that have high affinities for oxygen, an oxygen gradient is established across the deposit. Hence, an important effect of the deposit is to separate the superalloy from the gas environment. This situation usually results in a lower oxygen activity over the surface of the alloy than what would have been established in the absence of a deposit (Pettit and Meier, 1984; Pettit and Giggins, 1987).

## 7.4 Salt fluxing

The salt fluxing reactions for superalloys may be either acidic or basic in nature. The deficiency of oxide ions in the processes by which the reaction product barrier becomes non-protective due to the formation of species that are soluble in the liquid deposit gives rise to what is called the ‘fluxing’ reaction. In a molten sulphate deposit the following equilibrium can be used to define the acidity or basicity:



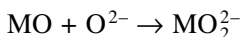
where the equilibrium constant  $K = P_{\text{SO}_3} \cdot a_{\text{O}^{2-}}$  where  $P_{\text{SO}_3}$  is the pressure of  $\text{SO}_3$  and  $a_{\text{O}^{2-}}$  is the activity of the oxide ions in the melt. In sulphate melts, the acidity is determined by the  $\text{SO}_3$  pressure and increases as the  $\text{SO}_3$  pressure is increased. The acidity need not be controlled only by the  $\text{SO}_3$  pressure in the gas since there are other ingredients in some systems that may affect acidity. For example  $\text{V}_2\text{O}_5$  can react with  $\text{Na}_2\text{SO}_4$  to increase the acidity of the melt via the following reaction:



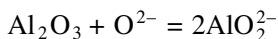
Molybdenum and tungsten in the alloy can create similar effects when their oxides are formed as corrosion products (Pettit and Giggins, 1987).

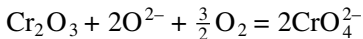
The initial concept of basic fluxing was first proposed by Bornstein and Decrescente (1970) and then described in thermodynamic terms for the hot corrosion of nickel by Goebel and Pettit (1970).

Pettit and Giggins (1987) have suggested that an essential feature of this process is that oxide ions are produced in the  $\text{Na}_2\text{SO}_4$  deposit due to removal of oxygen and sulphur from the deposit via reaction with the alloy and metal. Furthermore, oxide scales ( $\text{MO}$ ) that normally would form as a protective barrier on the surface of these alloys can react with oxide ions via reactions such as:



The protective oxide scales, e.g.  $\text{Al}_2\text{O}_3$  or  $\text{Cr}_2\text{O}_3$ , can react with  $\text{O}^{2-}$  ions to form soluble aluminates or chromate ions, respectively:





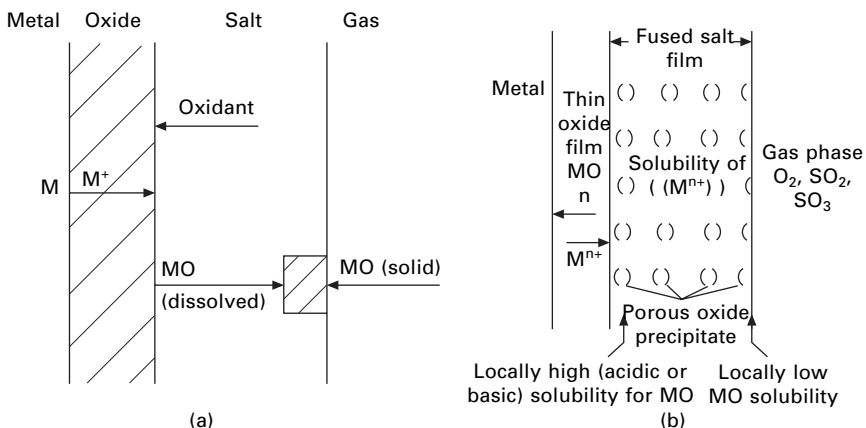
and their protective properties are destroyed. Such basic fluxing has a number of distinct features. Sulphides are usually found in the alloy substrate as a result of S removal from  $\text{Na}_2\text{SO}_4$  to produce oxide ions. The amount of attack depends upon the production of oxide ions by the melt. Hence a supply of  $\text{Na}_2\text{SO}_4$  is necessary for the attack to continue and the type of fluxing is often not self-sustaining. This form of attack is usually restricted to high temperatures (900°C) since the  $\text{O}^{2-}$  ion production is slow at lower temperatures and is more likely to be important in gases without an acidic component (e.g.  $\text{SO}_3$ ). However, according to Rapp and Goto (1981) basic fluxing can also occur in gases with acidic components. These authors have proposed that protective scales on alloy could be made non-protective when the solubility gradients of the protective oxides in the molten deposit were negative, since continuous dissolution and reprecipitation of oxide are then possible. Their mechanism permits fluxing to be either basic or acidic, within the need for a source or sink for  $\text{O}^{2-}$  ions, which means that attack may continue without the additional supply of the deposit. But Shores (1983) has examined the Rapp–Goto precipitation criteria for a variety of conditions and remarked that basic fluxing reactions are not always self-sustaining.

Rapp and Goto (1981) proposed that, if the gradient in solubility of the protective oxide with distance into the salt layer was negative at the oxide/salt interface, accelerated attack could be sustained. This provides a quantitative expression for the earlier concepts of solubility gradients and oxide precipitation, that is, when

$$\left( \frac{d(\text{solubility of oxide})}{dx} \right)_{x=0} < 0$$

Oxide can dissolve at the oxide/salt interface, migrate down a concentration gradient away from that side to a region of low solubility, and precipitate. At steady state, oxide dissolves and is transferred away from the oxide/salt interface, just as fast as the oxide layer grows (Fig. 7.3).

Rapp and Goto recognized that such a gradient can be established across a thin salt film and that it need not be a consequence of the removal of sulphur from  $\text{Na}_2\text{SO}_4$  or the introduction of acidic ions from the corrosion products as required by the Goebel and Pettit (1970) model. When the Rapp–Goto (1981) criterion for the oxide solubility is satisfied, fluxing is expected. The solubility of an oxide depends on the acidity or basicity of the melt and in some cases on  $p_{\text{SO}_3}$  as well. In basic fluxing the solubility decreases with increasing  $p_{\text{SO}_3}$  (decreasing activity of  $\text{O}^{2-}$ ). In acidic fluxing the solubility increases with increasing  $p_{\text{SO}_3}$  (decreasing activity of  $\text{O}^{2-}$ ). Rapp and Goto (1981) suggested that the electrochemical reduction reaction should generally



7.3 (a) Schematic diagram for fluxing showing dissolution of metal oxide at the oxide/salt interface (Shores, 1983); (b) precipitation of a porous MO oxide supported by the solubility gradient in a fused salt film (Rapp and Zhang, 1994).

be expected to create a condition of local high basicity, because reduction reactions may generate oxide ions as reaction products.

#### 7.4.1 The basic fluxing mode

Basic fluxing reactions occur because sulphur is removed from the  $Na_2SO_4$  and consequently oxide scale. It is important to notice that the concentration of oxide ions available for basic fluxing is limited by the amount of the deposit present upon the surface of the superalloy. Hence, basic fluxing reactions are not self-sustaining but require a continuous source of  $Na_2SO_4$  in order for this type of degradation to proceed indefinitely (Pettit and Meier, 1984).

#### 7.4.2 The acidic fluxing mode

The acidic fluxing reactions involve the development of non-protective reaction products on superalloys as a result of a liquid deposit on the surface of the superalloy which has a deficiency of oxide ions. The deficiency of oxide ions in the  $Na_2SO_4$  can arise due to an acidic component present in the gas or an acidic phase formed as an oxidation product upon the superalloy. When the acidic component is present in the gas the non-protective oxide scale ensues due to rapid transport of certain ionic species in the acidic melt. If the melt becomes acidic due to formation of an oxide from an element in the superalloy, the attack becomes self-sustaining even with a small amount of  $Na_2SO_4$ . The refractory elements Mo, W and V form oxides that cause  $Na_2SO_4$

to become acidic, and hence these elements when oxidized in the presence of  $\text{Na}_2\text{SO}_4$  deposit on superalloys usually cause catastrophic self-sustaining hot corrosion via acidic fluxing (Pettit and Meier, 1984).

## 7.5 Salt chemistry

### 7.5.1 Sulphate solution chemistry

As described by Rapp (1986, 2002) oxyanion melts of alkali nitrates, carbonates, hydroxides and sulphates exhibit an acid–base character, whereby the acid components may be considered as  $\text{NO}_2(\text{g})$ ,  $\text{CO}_2(\text{g})$ ,  $\text{H}_2\text{O}(\text{g})$  or  $\text{SO}_3(\text{g})$  respectively. Although the use of the Lux–Flud selection of  $\text{NO}_3^-$ ,  $\text{CO}_3^{2-}$ ,  $\text{OH}^-$  and  $\text{SO}_4^{2-}$  as the basic components is common for such fused salts, alternatively the oxide ion can be changed as the Lewis base is common for all of these salts. For a melt of pure  $\text{Na}_2\text{SO}_4$ , the equilibrium is given by the reaction



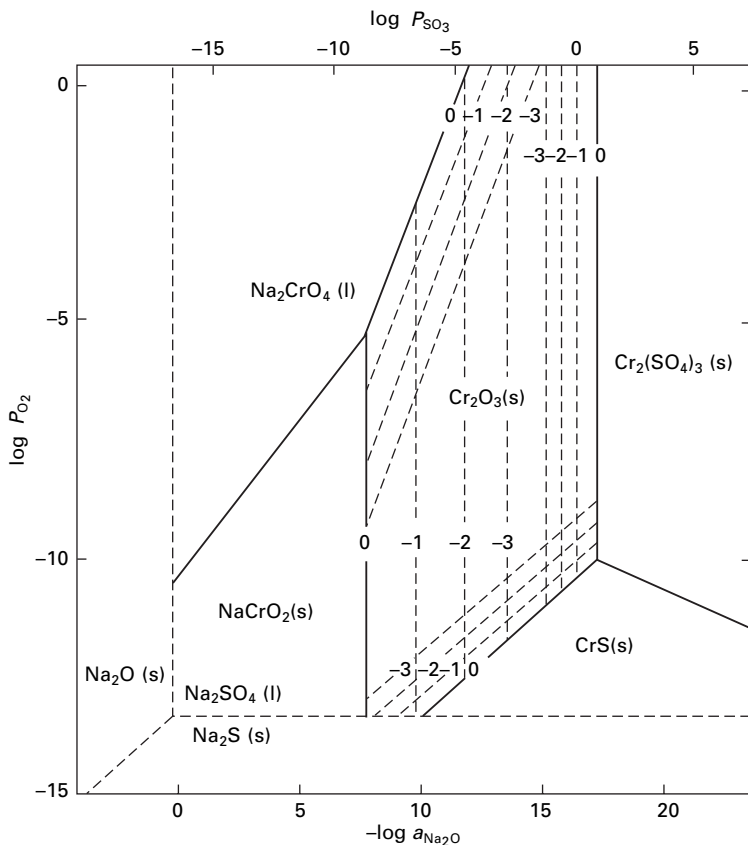
Rapp explained the expected stability of the protective oxide  $\text{Cr}_2\text{O}_3$  with respect to dissolution either as acidic solutes such as  $\text{Cr}_2(\text{SO}_4)_3$  or as basic solutes such as  $\text{Na}_2\text{CrO}_4$  or  $\text{NaCrO}_2$ . The phase stability diagram for the Cr–S–O system can be superimposed on that for Na–S–O, as shown in Fig. 7.4. The two abscissa scales at the bottom and top of the figure provide alternative parameters for melt basicity (or acidity). Under no conditions does the metal chromium remain stable in contact with  $\text{Na}_2\text{SO}_4$  at 1200 K (927°C).

### 7.5.2 Vanadate solution chemistry

Figure 7.5 is the phase stability diagram for the Na–V–S–O system at 900°C. The dashed lines are isoactivity lines for the vanadate species in the salt solution. The dependence of the equilibrium concentrations of various vanadate solutes in sodium sulphate–vanadate solutions on the melt basicity, defined as  $-\log a_{\text{Na}_2\text{O}}$ , is determined by considering the equilibrium reactions:



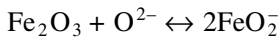
The equilibrium concentration of each vanadium compound varies continuously with melt basicity.  $\text{Na}_3\text{VO}_4$  is the dominant component in the melt at basicity less than 8.2 and  $\text{V}_2\text{O}_5$  is dominant at basicity greater than 16.3. For basicities between 8.2 and 16.3,  $\text{NaVO}_3$  is the most important vanadium solute (Hwang and Rapp, 1989).



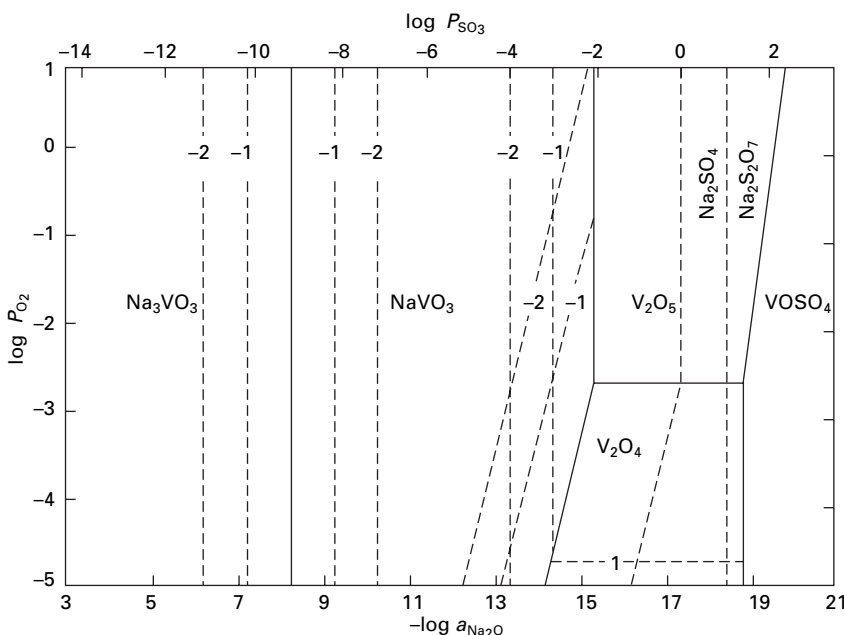
7.4 Na-Cr-S-O phase stability diagram for 1200 K (Rapp, 1986).

## 7.6 Hot corrosion of Fe, Ni and Co based alloys

To understand the accelerated oxidation of metals and alloys under sulphate salt coating, wide ranges of corrosion kinetics and morphologies have been observed by Shi (1993) under controlled laboratory conditions, and he has proposed several kinds of mechanisms. The  $Na_2SO_4-Na_2O$  eutectic melt was reported to be responsible for the formation of the abundant sulphide in the scale and was believed to play an important role in the present form of accelerated corrosion. Moreover  $Fe_2O_3$  can dissolve into the eutectic melt according to the reaction:



According to Shi, a reduction of sulphate ions occurs at the scale/melt interface; a negative gradient of concentration of  $O^{2-}$  and thereby of  $2FeO_2^-$  could be established across the melt. He also proposed further fluxing of  $Fe_2O_3$  with



7.5 Phase stability diagram for Na-V-S-O system at 900°C (Hwang and Rapp, 1989).

dissolution of  $Fe_2O_3$  at the scale/melt interface and reprecipitation at the melt/gas interface.

The mechanism of  $Na_2SO_4$ -induced hot corrosion for nickel-base superalloys has been reported by Goebel *et al.* (1973) in the temperature range 650–1000°C and by Misra (1986) in the temperature range 750–950°C. According to them the alloys underwent catastrophic corrosion. The accelerated oxidation has been ascribed to the formation of the liquid flux based on  $Na_2SO_4$  which normally dissolves the protective oxide scales. They proposed the occurrence of catastrophic or self-sustaining rapid oxidation in alloys which contain Mo, W or V because solution of oxides of these elements with  $Na_2SO_4$  decreases the oxide ion activity of the molten salts, which further produces the melts which are acidic fluxes for oxide scales.

The effect of Mo on the hot corrosion of superalloys has been further reported by Peters *et al.* (1976), Pettit and Meier (1984) and Fryburg *et al.* (1984). They observed that alloy containing Mo suffers catastrophic oxidation. It has been reported that  $MoO_2$  reacts with  $Na_2SO_4$  to produce an acid ( $SO_2$ -rich) salt, leading to acidic fluxing. The  $MoO_3$  gets incorporated into the  $Na_2SO_4$  via the formation of compounds such as  $Na_2MoO_4$ ,  $Na_2MoO_4 \cdot MoO_3$  and  $Na_2MoO_4 \cdot 2MoO_4$ . All these phases are liquid and are reported to have high solubility for  $Al_2O_3$  and  $Cr_2O_3$ .

The high temperature oxidation behaviour of Nimonic alloys (75, 80A, 90 and 105) has been investigated in the presence of varying amounts of  $\text{Na}_2\text{SO}_4$  in an air environment by Malik and Ahmad (1983). The effect of  $\text{Cr}_2(\text{SO}_4)_3$ ,  $\text{NiSO}_4$  or  $\text{CoSO}_4$  additions in the presence or absence of  $\text{Na}_2\text{SO}_4$  has also been investigated. Up to 800°C, the lower oxidation rates for  $\text{Na}_2\text{SO}_4$ -coated alloys have been attributed to a scale morphology consisting of inner scales of  $\text{Cr}_2\text{O}_3$  acting as a protective oxide film and external scales of  $\text{NiO}$ .

The kinetics of corrosion and the morphology of the scales formed on pure iron, manganese and chromium with  $\text{Na}_2\text{SO}_4$  deposits have been studied in the temperature range 600–800°C under 1 atmosphere of a gas mixture containing  $\text{O}_2$  (3.6%),  $\text{SO}_2$  (0.25%) and  $\text{N}_2$  (balance) by Nanni *et al.* (1987). At all the temperatures, salt-coated iron has been observed to exhibit accelerated attack whereas the corrosion rate of chromium was not appreciably affected by the deposited salt. Nanni *et al.* have further suggested that the enhanced corrosion phenomena are due to low melting liquid sulphate formation.

The interactions of some metal oxides such as  $\text{Co}_3\text{O}_4$ ,  $\text{NiO}$ ,  $\text{Al}_2\text{O}_3$ ,  $\text{Cr}_2\text{O}_3$ ,  $\text{Fe}_2\text{O}_3$ ,  $\text{SiO}_2$ , etc. with  $\text{Na}_2\text{SO}_4$  have been studied by Malik and Mobin (1987) in the temperature range 900–1200 K (627–927°C) and by Mobin *et al.* (1996) at temperatures of 1100 and 1200 K (827 and 927°C). According to them the high temperature reaction products usually contain a three-phase structure, namely  $\text{Na}_2\text{O}-\text{MO}-\text{M}_2\text{O}_3$  and metal sulphide and or metal sulphate. The formation of  $\text{Na}_2\text{O}-\text{M}_2\text{O}$  was further reported to be dependent upon the solid state solubility of metal oxide in the molten salt at high temperature, and under limited solubility conditions  $\text{Na}_2\text{O}-\text{M}_2\text{O}$  was invariably formed, but as soon as conditions were relaxed the oxide  $\text{M}_2\text{O}_3$  precipitated and was observed to form a separate phase.

The phenomena and mechanism of sub-melting point hot corrosion (Type II hot corrosion) of nickel and cobalt base alloys, including M-Cr-Al-Y coatings, caused by  $\text{Na}_2\text{SO}_4$  deposit has been reviewed by Shih *et al.* (1989). The mechanism of low temperature hot corrosion of iron, AISI 304 stainless steel and Fe-Cr alloys under  $\text{K}_2\text{SO}_4-\text{Na}_2\text{SO}_4$  deposit has been described as the dissolution of iron at the oxide–melt interface and reprecipitation of  $\text{Fe}_2\text{O}_3$  as porous particles at the melt–gas interface. Further, Shih *et al.* described the catastrophic hot corrosion of B-1900 alloy under  $\text{Na}_2\text{SO}_4$  deposit at 750°C and 827°C, in which it has been proposed that  $\text{MoO}_3$  plays a role in the reduction reaction, probably as  $\text{Mo}_2\text{O}_7^{2-}$ .

The high temperature corrosion behaviour of alloy 800H has been studied by Xu *et al.* (1994) in an oxidizing and a reducing sulphidizing environment at 750°C and 850°C respectively. When corroded in  $\text{SO}_2-\text{O}_2$ , the protective chromia scale which developed on the alloy in the early stages was found to crack and spall in quite a short time. According to the authors, this further led to the growth of iron and nickel sulphides beneath the chromia layer, thereby causing more chromia spallation.

Shi (1995) studied the possibility of  $\text{Na}_2\text{SO}_4\text{-Na}_2\text{O}$  eutectic melt being formed on metals deposited with  $\text{Na}_2\text{SO}_4$  in oxygen and air at a temperature of 750°C. In the case of Ni, Co, Al, Cr and their alloys, he could not detect formation of  $\text{Na}_2\text{SO}_4\text{-Na}_2\text{O}$ . In the case of iron-base alloy with high Cr or Al content, where  $\text{Cr}_2\text{O}_3$  or  $\text{Al}_2\text{O}_3$  was observed, again no  $\text{Na}_2\text{SO}_4\text{-Na}_2\text{O}$  eutectic was observed, but at lower Cr or Al content this eutectic melt was found and might have resulted from an accelerated rate of corrosion.

High temperature corrosion of Inconel-600 tube used as a furnace accessory has been reported by Krishna and Sidhu (2001). The corrosion of the tube was found to be due to severe oxidizing and sulphidizing atmospheres generated by interdiffusion of base metal constituents and sulphur through the microchannels.

Pantony and Vasu (1968) reported that under sufficient quantities of molten vanadium to cover the specimens, metals such as iron, cobalt, titanium, molybdenum, tungsten and vanadium show a corrosion rate which is linear with respect to time. Nickel, which was considered to be more resistant, was observed to obey an approximately logarithmic rate law, while chromium was found to be the most resistant to corrosion. In these two cases Pantony and Vasu observed a coherent corrosion layer, which was a protective barrier. In all cases corrosion rates vary inversely with the depth of melt. The inward diffusion of oxygen and the outward diffusion of corrosion products has also been observed. According to Pantony and Vasu, attempts to prevent vanadic corrosion of the pure metals either electrochemically or by means of additives are largely unsuccessful owing to the transition semiconductance of molten vanadium pentoxide.

Suito and Gaskell (1971) studied the thermodynamics of melts in the system  $\text{VO}_2\text{-V}_2\text{O}_5$  and suggested that the non-stoichiometric liquid oxide may act as a corrosive medium. Corrosion resistance of various metals and alloys has also been analysed by Kerby and Wilson (1973) in the liquid vanadates. They found that the stainless steels and particularly 440 stainless steel (25 wt% Cr) shows the best corrosion resistance to liquid  $\text{V}_2\text{O}_5$ . The rate of corrosion of Armco iron by liquid  $\text{V}_2\text{O}_5$  has been reported to be controlled initially by the diffusion of oxygen across the metal oxide–liquid vanadate interface. As the available oxygen ions get depleted from the melt, the rate-controlling mechanism is observed to be changed to the sorption of oxygen at the liquid vanadate gas phase interface.

A 50Cr-50Ni alloy has been corroded in pure  $\text{V}_2\text{O}_5$  and sodium vanadates in the temperature range 750–950°C in a rotating disc apparatus by Dooley and Wilson (1975). In pure  $\text{V}_2\text{O}_5$  at 810°C, a  $\text{Cr}_2\text{O}_3$  scale was observed on the alloy which subsequently got dissolved slowly into the liquid melt and was thus proposed as a barrier layer by them. In case of  $\text{NV}_6$  this barrier layer was not observed. The increased basic character of the melt and its consequently greater fluxing ability towards acidic oxides was thought to be

a more important process than the increased ionic conductivity of NV<sub>6</sub> over V<sub>2</sub>O<sub>5</sub> at this temperature. At 950°C the corrosion in terms of both dissolution rate and corrosion rate was reportedly greater in V<sub>2</sub>O<sub>5</sub> than in NV<sub>6</sub>.

The association of the high temperature corrosion of superalloys with contaminants has been reported by Hancock (1987). He proposed that to compare contaminant conditions the contaminant flux rate (CFR) rather than the contaminant level in the fuel or environment should be considered. He further suggested that at temperatures above 700°C where vanadates cause fluxing of the protective oxide scales, corrosion could be determined by the CFR and temperature rather than by material selection.

Iyer *et al.* (1987) carried out investigations on the high temperature corrosion of a nickel base superalloy by vanadium at 700°C. They reported that vanadium, present as vanadium pentoxide, attacked the alloy severely at this temperature of investigation. Their study of a ternary oxide system and spot tests showed that two low-melting eutectics, namely NiO-V<sub>2</sub>O<sub>5</sub>-Cr<sub>2</sub>O<sub>3</sub> melting at 550°C and V<sub>2</sub>O<sub>5</sub>-Cr<sub>2</sub>O<sub>3</sub>-Fe<sub>2</sub>O<sub>3</sub> melting at 480°C, were formed. The formation of these liquid eutectics and the presence of corrosive V<sub>2</sub>O<sub>5</sub> were reported to have caused severe damage to the superalloy.

Swaminathan *et al.* (1993) studied the hot corrosion attack of different amounts of V<sub>2</sub>O<sub>5</sub> on nickel based superalloys, namely Nimonic 80A, Hastealloy C-276 and Superni 600, for a period of 100 hours at 923, 973 and 1023 K (650, 700 and 750°C) in air. A parabolic rate law was applicable for two different ranges of temperatures at 973 and 1023 K (700 and 750°C) and the protection was ascribed to the formation of a solid Ni<sub>3</sub>V<sub>2</sub>O<sub>8</sub> layer.

Vanadium and sodium are common impurities in low-grade petroleum fuels. Molten sulphate-vanadate deposits resulting from the condensation of combustion products of such fuels are extremely corrosive to high temperature materials in the combustion systems. Thermodynamic calculations for the equilibrium concentrations of Na<sub>3</sub>VO<sub>4</sub>, NaVO<sub>3</sub> and V<sub>2</sub>O<sub>5</sub> in a mixed sodium sulphate-vanadate solution containing 30 mol% vanadate as a function of melt basicity have been reported by Hwang and Rapp (1989). They suggested that vanadate ions greatly increase the acidic solubility of all metal oxides compared to that in pure Na<sub>2</sub>SO<sub>4</sub>.

The kinetics of the reactions between Na<sub>2</sub>SO<sub>4</sub> (X) and V<sub>2</sub>O<sub>5</sub> (Y) have been studied by Kolta *et al.* (1972). They concluded that the rate of the reaction depends both on the temperature (600–1300°C) and on the molar ratios of X to Y. They further found that with increase in the reaction period (>30 min) there was a decrease in the reaction rate which finally reached zero order. This decrease in the reaction rate has been attributed to the formation of vanadosulphate complexes such as (NaV<sub>3</sub>O<sub>8</sub>)<sub>2</sub>.Na<sub>2</sub>SO<sub>4</sub> and (NaVO<sub>3</sub>)<sub>2</sub>.Na<sub>2</sub>SO<sub>4</sub> which get decomposed at higher temperatures, giving the meta- and pyro-vanadates respectively.

The effect of vanadium and sodium on the accelerated oxidation of nickel-

based alloys has been reported by Bornstein *et al.* (1975). They observed the initial rapid rate of oxidation between  $V_2O_5$  and the metal substrate which is attributed to the reduction of  $V_2O_5$  by the substrate. Intermetallic systems  $Ni_3Al$  and  $NiAl$  were found to be particularly susceptible to  $V_2O_5$  corrosion. According to the authors, the sulphidation attack alters the composition of the melt to produce more oxide ions, i.e.

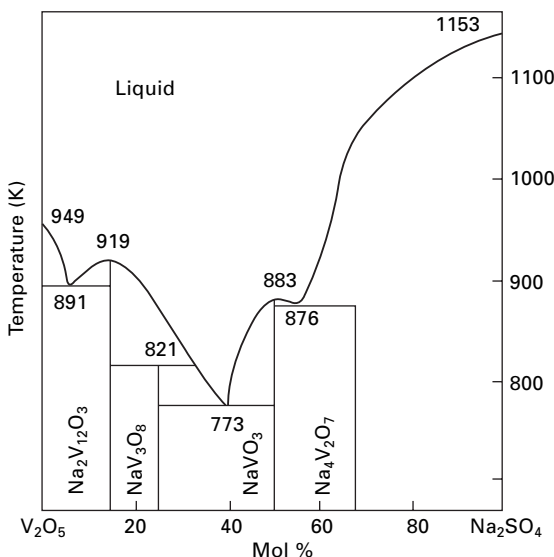


Severity of attack was found to decrease with increase in the initial oxide ion content of the melt. Oxides such as  $Cr_2O_3$  have been suggested to react preferentially with oxide ions.

Thermogravimetric studies which delineate the conditions for simultaneous sulphate and vanadate induced corrosion at 650–800°C have been carried out by Seiersten and Kofstad (1987). They found that the corrosion caused by sodium sulphate/sodium vanadate mixtures has a complex mechanism. Samples coated with sodium vanadate were exposed to  $O_2 + 4\% SO_2$  and the initial reaction was observed to be the same as that observed in pure oxygen. After an incubation period the duration was found to decrease with increasing temperature and when sufficient  $SO_3$  had been dissolved in the molten vanadate, which resulted in the formation of a mixture of  $NiSO_4$  and  $Na_2SO_4$  near the metal. When a molten  $NiSO_4-Na_2SO_4$  solution containing small amounts of vanadate was formed as an intermediate layer, the reaction reportedly proceeded as sulphate-induced hot corrosion. The corrosion mechanism was observed to change from initial vanadate-induced to essentially sulphate-induced hot corrosion when the sulphur trioxide pressure was high enough to form sodium sulphate.

According to Otero *et al.* (1987)  $Na_2SO_4-60\%V_2O_5$  deposit was detected on a number of components in actual service that were operated at high temperature and were in contact with high-temperature gases from combustion of dirty fuels containing certain amounts of impurities, i.e. Na, V, S, etc. The presence of sulphur and its oxidized compounds was reported to favour the formation of isolated lobes with radial morphology having great permeability to facilitate the access of oxygen, which led to further reduction in the protective character of the scale. The presence of vanadium and its oxidized products was observed to generate compounds with aciculate morphology, identified to look like alkaline vanadate complexes. These aciculated shapes further contribute to reducing the protective character of the scale. The equilibrium diagram for varying composition of  $Na_2SO_4$  is shown in Fig. 7.6 and the mixture of  $Na_2SO_4-60\%V_2O_5$  is seen to be the lowest eutectic temperature. From the phase diagram of  $Na_2SO_4-V_2O_5$  system, the melting point of  $Na_2SO_4-60\% V_2O_5$  is 773K which is the lowest temperature in this system.

In this aggressive environment ( $Na_2SO_4-60\%V_2O_5$ ) the hot corrosion



7.6 Phase diagram for  $\text{Na}_2\text{SO}_4$ - $\text{V}_2\text{O}_5$  system (Otero *et al.*, 1987).

behaviour of Superalloy IN-657 at 1000 K (727°C) was investigated by Otero *et al.* (1990, 1992). They reported that the corrosion rate of the alloy in contact with molten salt mixtures was reduced by approximately one order of magnitude over exposure times of 210 h when the amount of molten salt was kept constant. During the initial stages of exposure the corrosion rate was found to increase with increasing temperature up to 1000 K (727°C) and then to decrease at higher temperature. After 100 hours of exposure the influence of temperature was insignificant.

Tiwari and Prakash (1996, 1997) and Tiwari (1997) have also reported studies on superalloys in the temperature range 700–900°C in pure  $\text{Na}_2\text{SO}_4$ ,  $\text{Na}_2\text{SO}_4$ -15%  $\text{V}_2\text{O}_5$  and  $\text{Na}_2\text{SO}_4$ -60%  $\text{V}_2\text{O}_5$ . They observed accelerated corrosion rates for  $\text{Na}_2\text{SO}_4$ -60%  $\text{V}_2\text{O}_5$  composition, i.e. eutectic with melting point of 500°C.

Oxidation and hot corrosion in sulphate, chloride and vanadate environments of a cast nickel-based superalloy have been reported by Deb *et al.* (1996). Weight gain studies were carried out in air for uncoated samples and for samples coated with 100%  $\text{Na}_2\text{SO}_4$ , 75%  $\text{Na}_2\text{SO}_4$  + 25%  $\text{NaCl}$ , and 60%  $\text{Na}_2\text{SO}_4$  + 30%  $\text{NaVO}_3$  + 10%  $\text{NaCl}$ . The presence of sulphur in the form of sulphates was reported to cause internal sulphidation of the alloy beneath the external oxide layer. Deb *et al.* observed the formation of volatile species by chlorides, which further led to formation of voids and pits at grain boundaries that reportedly provide an easy path for flow of corrodents. The presence of vanadate in conjunction with sulphate and chloride is proposed to provide

additional fluxing action. According to Deb *et al.* this destroys the integrity of the alloy and weakens its mechanical properties.

Almeraya *et al.* (1998) carried out electrochemical studies of hot corrosion of AISI-SA-213-TP-347H steel in 80 wt% V<sub>2</sub>O<sub>5</sub> + 20 wt% Na<sub>2</sub>SO<sub>4</sub> at 540–680°C and reported corrosion rate values of around 0.58–7.14 mm/year. They further observed an increase in corrosion rate with time. However, they also observed that corrosion potential decreases with increase in temperature from 540 to 680°C.

Lee and Lin (1999) studied the oxidation, mixed oxidation–sulphidation and hot corrosion of ductile iron aluminide Fe<sub>3</sub>Al with Cr addition at temperatures of 605–800°C. They observed that hot corrosion of iron aluminide was significantly more severe than oxidation and mixed oxidation–sulphidation. According to Lee and Lin, this can be attributed to the formation of aluminium sulphide at the metal–salt interface as a result of high sulphur potential in the molten salt at the oxide–metal interface.

## 7.7 How to avoid hot corrosion

In general hot corrosion can be avoided by:

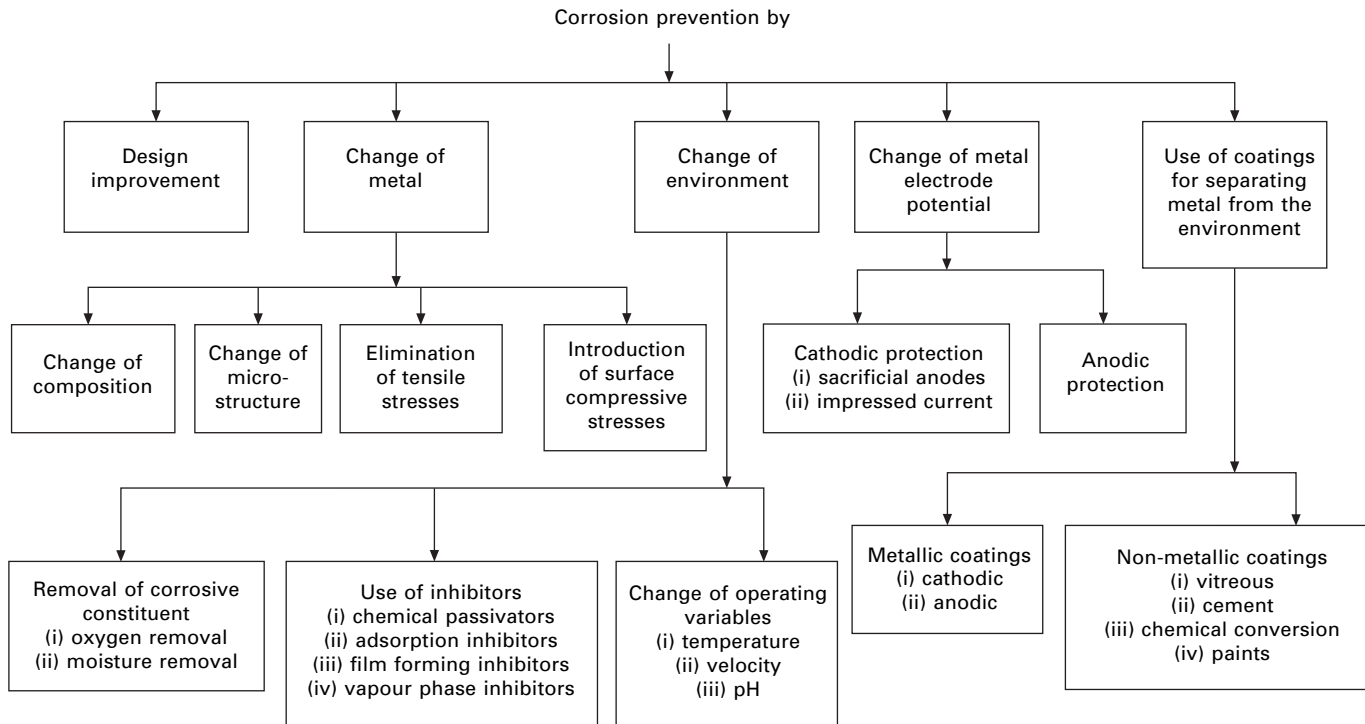
- Proper design
- Proper material selection
- Changing the environment
- Use of coatings.

Although corrosion problems cannot be completely remedied, it is estimated that corrosion-related costs can be reduced by more than 30% with development and use of better corrosion control technologies. Corrosion control measures include corrosion inhibitors, cathodic protection, and coatings (Priyantha *et al.*, 2003). Corrosion of metals occurs when they come in electrical contact with a corrosive environment. Therefore metallic corrosion can be prevented by either changing the metal or altering the environment or by separating the metal from the environment as shown in Fig. 7.7 (Narayan, 1983).

Depletion of high grade fuels and for economic reasons uses of residual fuel oil in energy generation systems are well known. Fuels with sulphur and other impurities bring about hot corrosion which significantly reduces the life of components (Sharma, 1996). The option to use low grade fuel limits improvement in hot corrosion environments. In that case hot corrosion preventive methods to the existing environment are (a) change of metal, i.e. use of superalloy, (b) use of inhibitors and (c) use of coatings.

### 7.7.1 Use of superalloys

The deposition of molten salt on the surface of alloys results in accelerated corrosion for components used in boilers and gas turbines. In general, alloying



7.7 Classification of corrosion prevention methods (Narayan, 1983).

elements that can improve the hot corrosion resistance of materials such as Cr, Al, etc., often have a negative effect on mechanical properties in high temperature environments and are expensive (Wu and Okuyama, 1996).

Choice of substrate metal is usually governed by cost, weight and general physical, mechanical or fabrication properties and these factors will normally dictate a very limited number of possible materials, none of which may be ideal in resisting the corrosive environment that will be encountered in service. Ideally a protective metal coating should exclude completely the corrosive environment from the substrate metal and, if this can be achieved, only the resistance of the coating metal itself to that corrosive environment needs to be considered (Shreir, 1976).

### 7.7.2 Use of inhibitors

Inhibitors and fuel additives have been used with varying success to prevent oil ash corrosion. There are a number of inhibitors commercially available that are intended to reduce the severity of oil ash corrosion. Because of its effectiveness and relatively low cost the most common fuel additives are based upon MgO (Paul and Seeley, 1991). The inhibition of hot corrosion by MgSO<sub>4</sub> has also been reported by Barbooti *et al.* (1988) for stainless steel 304. Further the MgO, CaO, ZnSO<sub>4</sub>, PbO and SnO<sub>2</sub> based inhibitors are reported to be effective to decrease the extent of hot corrosion pertaining to molten salt environment (Na<sub>2</sub>SO<sub>4</sub>–60%V<sub>2</sub>O<sub>5</sub>) for iron-, nickel- and cobalt-based superalloys by Gitanjaly and Prakash (1999), Gitanjaly *et al.* (2002) and Gitanjaly (2003).

For adequate corrosion protection of a metal in an aggressive environment, it is important to select materials and techniques that are compatible. For example, addition of an organic inhibitor (e.g. pyridines, pyrimidines, quinolines) is sufficient to mitigate corrosion of metals in many corrosive media. However, these inhibitors have shown only limited success due to solubility and/or thermal stability problems in high-temperature, concentrated salt solutions such as in chemical heat pumps (Priyantha *et al.*, 2003).

### 7.7.3 Use of coatings

The first and foremost question which comes into our mind is why coatings? Simply, it can be answered that coatings can achieve the following:

- improve performance
- extend lifetime
- enhance appearance.

The following are the major coating methods:

- Thermal spraying

- Electro/electroless spraying
- Chemical vapour deposition
- Physical vapour deposition.

General characteristics of major coating methods are presented in Table 7.1.

Increasing demands imposed on materials make it more difficult or, at the current stage of development, even impossible to combine the different properties required in one single material. Therefore, a composite system of a base material providing the necessary mechanical strength with a protective surface layer different in structure and/or chemical composition and supplied by a surface treatment can be an optimum choice in combining material properties. Although protective surface treatments are widely used at low temperature, their use at elevated temperature is more recent. Current high-temperature applications are limited largely to the aerospace industry. An enormous challenge exists now to develop and apply these techniques to other high-temperature applications (Stroosnijder *et al.*, 1994; Li *et al.*, 2003).

Wang and Luer (1994) have reported the recent use of coatings to protect the heat exchanger tubes of fluidized bed combustors from erosion-corrosion problems, and Hocking (1993) has also suggested the use of corrosion resistant alloys as coatings to protect substrate alloys having good mechanical properties. Hidalgo *et al.* (1997, 1998, 1999, 2000) have further discussed the use of plasma sprayed thin anti-wear and anti-oxidation coatings to take care of the high temperature erosion and corrosion problems in energy generation systems.

## 7.8 High temperature coatings

There are three main kinds or compositions of barriers: inert or essentially inert, inhibitive and sacrificial. Various combinations of these types are found in coating systems designed to use some or all of the several protective advantages provided. It must be remembered that there is no such thing as a 'perfect' coating in a practical sense, so none of these types or any combination can be expected to give perfect protection (Hamner, 1977). The coating can be defined as a layer of material, formed naturally or synthetically or deposited artificially on the surface of an object made of another material, with the aim of obtaining required technical or decorative properties (Burakowski and Wierzchon, 1999).

The demand for higher performance and increased efficiency has resulted in the progressive increase in the temperatures of operation of turbines. This has been accompanied by the development of single crystal blade technology, more advanced corrosion-resistant coatings and complex cooling techniques (Stott *et al.*, 1994; Conner and Connor, 1994). The development of modern coal-fired power generation systems with higher thermal efficiency requires the use of construction materials of higher strength and with improved resistance

**Table 7.1** General characteristics of major coating methods

Characteristic	Electro/electroless plating	Thermal spray	Chemical vapour deposition	Physical vapour deposition
Equipment cost	Low	Low to moderate	Moderate	Moderate to high
Operating cost	Low	Low to moderate	Low to moderate	Moderate to high
Substrate temperature	Low	Low to moderate	Moderate to high	Low
Coating thickness	Moderate to thick (10 µm to mm)	Thick (50 µm to cm), high coating rates	Thin to thick (0.1 µm to mm)	Very thin to moderate
Adherence	Moderate mechanical bond, very good chemical bond	Good mechanical bond	Very good chemical bond	Moderate mechanical bond, very good chemical bond
Process environment	Aqueous solution	Atmospheric to soft vacuum	Atmospheric to medium vacuum	Hard vacuum
Coating materials	Metals	Powder/wire, polymers, metals, ceramics	Metals/ceramics/polymers	Metals/ceramics/polymers

to the aggressive service atmospheres. These requirements can be fulfilled by protective coatings (Nickel *et al.*, 2002).

Coatings have been used with some success in field applications. Most of the high-chromium coatings offer some resistance to oil ash corrosion. Other coating systems such as silicon may also be helpful. However, in many instances, porosity and defects in the coating allow the substrate to be attacked. Also the coating may spall off in some cases. Studies in Japan and the former Soviet Union, with exposure periods up to 6500 h, have demonstrated the resistance of chromium diffusion coatings in field applications. Spray coatings of 50% Cr and 50% Ni have also been applied with success to local areas of superheater tubes and have survived for 20,000 h with only minimal attack. Therefore, coatings can be effective in controlling oil ash corrosion (Paul and Seeley, 1991).

### 7.8.1 Coating-substrate system requirements

In oxidizing environments at high temperature, a coating in general owes its oxidation resistance to the formation of a protective oxide layer. Therefore, in selecting coating materials, it is important that the coating–substrate system meets the following requirements (Chatterjee *et al.*, 2001; Kofstad, 1966):

- The coating should be chemically and thermally stable (forming an integral coating–metal/alloy system) during the service life of the component.
- It should have properties compatible with those of the metallic substrate.
- The rate of interdiffusion of the elements in the integral system (i.e., between coating and substrate alloy) must be slow during the desired service life.
- The protective layer and the metallic substrate should have matching thermal expansion coefficients to avoid cracking and exfoliation of the coating during thermal cycling.
- A protective coating should exhibit some mechanical ‘elasticity’ under operating conditions to accommodate creep and plastic deformation.
- A coating material should resist damage from impact, erosion and abrasion depending on the specific applications of the metallic components.
- It should exhibit a spontaneous ‘self-healing’ property for self-repair in case failure occurs due to cracking or spallation of the layer. So the coating should act as a reservoir for the highly oxidizable metallic constituent(s) for early development of a protective scale.
- It should be relatively easy to apply the coating on substrates, and the defects that may occur during handling of the component should be repairable without accompanying adverse effects on the sound neighbouring areas.

Consequently, the development of a truly satisfactory coating that meets all of the above requirements is a difficult task. Accordingly, compromises are often made, depending on the specific application of the coated material in a particular environment. Moreover, because of coating–environment and coating–substrate reactions, the structures of the actual protective coating systems are complex.

The oxidation behaviour of NiCrAlY, Ni-20Cr, Stellite-6 and Ni<sub>3</sub>Al coatings formulated by the argon-shrouded plasma spray process on five types of superalloys, namely Superni 75, Superni 600, Superni 601, Superni 718 and Superfer 800H, has been investigated. The oxidation studies were conducted in air as well as molten salt (Na<sub>2</sub>SO<sub>4</sub>-60%V<sub>2</sub>O<sub>5</sub>) environments under cyclic conditions in a laboratory furnace at an elevated temperature of 900°C for an oxidation run of 50 cycles in all the cases. NiCrAlY was first deposited as a bond coat in all the coatings. All the coating powders were commercially available except Ni<sub>3</sub>Al, which was prepared from a stoichiometric mixture of nickel–aluminium. All the coatings were found to be beneficial in increasing the resistance to oxidation and hot corrosion in air, molten salt and coal-fired boiler environments. Salient conclusions from the study are enumerated below:

- (1) Ni<sub>3</sub>Al, NiCrAlY, Ni-20Cr and Stellite-6 coatings were successfully obtained on the given Ni- and Fe-based superalloys by the shrouded plasma spray process on the superalloys. All the coatings showed porosity in the range 2–4%. It was possible to obtain a thickness in the range 200–250 µm for the NiCrAlY, Ni-20Cr and Ni<sub>3</sub>Al coatings, whereas somewhat thicker coatings around 350–450 µm could be deposited in case of the Stellite-6.
- (2) The interdiffusion of various elements among the substrate and plasma sprayed coatings was observed to be marginal as has been indicated by EPMA. The diffusion between the bond coat and the top coat was relatively high. Aluminium was found to be the most vulnerable element to the diffusion phenomenon.
- (3) Superni 600 showed a maximum resistance to cyclic oxidation in air at 900°C among the given superalloys, which might be attributed to the presence of a continuous band of Cr just at the scale/substrate interface in the oxidized superalloy, as was revealed by EPMA. Superni 75 indicated the lowest resistance to air oxidation under cyclic conditions at 900°C in comparison to all the investigated superalloys, where the chromia layer present in the scale was found to be relatively discontinuous (EPMA).
- (4) The oxidation rates for the investigated superalloys based on the overall weight gains after 50 cycles of oxidation in the Na<sub>2</sub>SO<sub>4</sub>-60%V<sub>2</sub>O<sub>5</sub> environment could be arranged in the following order:

Superfer 800H > Superni 601 > Superni 600 > Superni 75

- (5) The rate of oxidation was observed to be high in the early cycles of the study in both the given environments for all types of coatings, which may be attributed to the fact that during the transient period of oxidation, the oxidizing species might have penetrated in the coating along the interconnected network of pores and splat boundaries to cause rapid oxidation. However, once all these possible diffusion paths are blocked by the formation of the oxides, the oxidation then becomes limited mainly to the surface of the coatings, thereby entering into a steady state.
- (6) In the case of the Stellite-6 coating, chromium and oxygen were found to coexist along the splat boundaries in both environments studied, whereas cobalt-rich splats remained unoxidized.
- (7) During oxidation studies in air, all the coatings have shown overall weight gains higher than their uncoated counterpart superalloys. However, in all the coated cases, the oxidation behaviour was found to be governed by a parabolic rate law. Moreover, internal oxidation of the substrate superalloys has not been observed in general.
- (8)  $\text{Ni}_3\text{Al}$  appeared to be a better coating against air oxidation in comparison to Ni-20Cr and Stellite-6 coatings. This resistance might partly be imparted by the presence of thin continuous streaks of Cr at the bond coat/base alloy interface, especially in case of  $\text{Ni}_3\text{Al}$  coated Superni 75 and 601 (EPMA). On the contrary the relatively low oxidation resistance shown by Ni-20Cr coatings may partially be attributed to the absence of such continuous chromia layers.
- (9) In the case of Stellite-6 coated Superfer 800H, EPMA indicated a thin and continuous layer of chromium oxide at the bond coat/base alloy interface during air oxidation, which may also serve to protect the substrate alloy during long-term use. However, in other Stellite-6 coated superalloys, no such continuous layer of chromia was seen during air oxidation.
- (10) In the molten salt environment, the coatings were found to be successful in reducing the overall weight gains in most of the cases, hence the corrosion rates. The coatings could be arranged as follows on the basis of their performance in developing hot corrosion resistance:

$\text{NiCrAlY} > \text{Ni-20Cr} > \text{Ni}_3\text{Al} > \text{Stellite-6}$

- (11) The  $\text{NiCrAlY}$  coated Superfer 800H superalloy showed the highest oxidation resistance to both air and molten salt environments. The best protection indicated by the  $\text{NiCrAlY}$  coating, in general, might also be attributed to the simultaneous formation of an additional protective oxide  $\alpha\text{-Al}_2\text{O}_3$  along with  $\text{Cr}_2\text{O}_3$  and  $\text{NiCr}_2\text{O}_4$ , which grows very slowly and is thermodynamically stable. Moreover, the presence of yttrium in

the coating might also have reduced the scale growth rates and hence the overall weight gains.

- (12) In most cases, the effect of the base superalloys on the oxidation behaviour in air and molten salt was considerable, except in the case of air oxidation of the Ni<sub>3</sub>Al coated Ni-base superalloys, and NiCrAlY coated superalloys, where the oxidation rates were not significantly different.
- (13) The EPMA analysis has indicated diffusion of some of the other basic elements of the superalloy substrates such as Mn, Mo, Ta and Si into the scales in many cases, while diffusion of Cr from the bond coat to the Ni<sub>3</sub>Al coating was also noted. However, the diffusion stability can be considered a life-limiting factor if coatings are operated at temperatures greater than 1000°C for prolonged periods of time.
- (14) Only minor spalling of the scales was observed in powder form during the molten salt corrosion for most of the coated cases. The scales in general showed no tendency towards spalling or cracking and were found to be intact.
- (15) The temperature at which the coatings have been found useful for the given superalloys in reducing corrosion can enhance efficiency by a significant fraction, particularly in the case of boilers.
- (16) The NiCrAlY coating may be recommended as the best coating for the superalloys under investigation to be used for boilers and gas turbines (as well as other similar high temperature applications) so far as hot corrosion and oxidation resistance are concerned, based upon the findings of the current study. Also this coating has been found to be successful in maintaining its integrity with its respective substrates throughout the exposure to both environments of the study, without any significant spalling of its oxide scales.

## 7.9 References and further reading

- Agarwal, A., Katipelli, L. R. and Dahotre, N. B. (2000), 'Elevated Temperature Oxidation of Laser Surface Engineered Composite Boride Coating on Steel', *Metall. Mater. Trans. A*, Vol. 31A, No. 2, pp. 461–73.
- Almeraya, C. F., Martinez, V. A. and Gonzalez, R. J. G. (1998), 'Electrochemical Studies of Hot Corrosion of Type 347H Stainless Steel', *British Corros. J.*, Vol. 33, No. 4, pp. 288–91.
- Barbooti, M. M., Al-Madfaei, S. H. and Nassouri, H. J., (1988), 'Thermochemical Studies on Hot Ash Corrosion of Stainless Steel 304 and Inhibition by Magnesium Sulphate', *Thermochimica Acta*, Vol. 126, pp. 43–49.
- Bornstein, N. S. and Decrescente, M. A. (1970), 'The Role of Sodium and Sulfur in the Accelerated Oxidation Phenomena – Sulfidation', *Corrosion*, Vol. 26, No. 7, pp. 209–14.
- Bornstein, N. S., Decrescente, M. A. and Roth, H. A. (1975), 'Effect of Vanadium and Sodium Compounds on the Accelerated Oxidation of Nickel Base Alloys', *Proc. Conf. on Gas Turbine Materials in the Marine Environment*, MMIC-75-27, Columbus, OH, pp. 115–60.

- Burakowski, T. and Wierzchon, T. (1999), *Surface Engineering of Metals: Principles, Equipment, Technology*, CRC Press, Boca Raton, FL.
- Chatterjee, U. K., Bose, S. K. and Roy, S. K. (2001), *Environmental Degradation of Metals*, Marcel Dekker, New York.
- Conner, J. A. and Connor W. B. (1994), 'Ranking Protective Coatings: Laboratory vs. Field Experience', *JOM*, December, pp. 35–8.
- Deb, D., Iyer, S. R. and Radhakrishnan, V. M. (1996), 'A Comparative Study of Oxidation and Hot Corrosion of a Cast Nickel Base Superalloy in Different Corrosive Environments', *Mater. Letters*, Vol. 29, pp. 19–23.
- Dooley, R. B. and Wilson, J. R. (1975), 'The Corrosion of 50Cr-50Ni Alloy in Liquid Vanadate Systems in the Temperature Range 750–950°C', *Trans. ASME*, July, pp. 422–28.
- Fryburg, G. C., Kohl, F. J. and Stearns, C. A. (1984), 'Chemical Reactions Involved in the Initiation of Hot Corrosion of IN-738', *J. Electrochem. Soc.*, Vol. 131, No. 12, pp. 2985–96.
- Gitanjaly (2003), 'Role of Inhibitors on Hot Corrosion of Superalloys in  $\text{Na}_2\text{SO}_4\text{-V}_2\text{O}_5$  Environment', PhD Thesis, Met. and Mat. Eng. Dept, IIT, Roorkee, India.
- Gitanjaly and Prakash, S. (1999), 'Review on Effect of Additives on the Hot Corrosion,' *5th NACE Proc.*, New Delhi, India, 22–24 November, pp. 174–82.
- Gitanjaly, Prakash, S. and Singh, S. (2002), 'Effects of MgO and CaO on Hot Corrosion of Fe Base Superalloy Superfer 800H in  $\text{Na}_2\text{SO}_4\text{-}60\%\text{V}_2\text{O}_5$  Environment', *British Corros. J.*, Vol. 37, No. 1, pp. 56–62.
- Goebel, J. A. and Pettit, F. S. (1970), 'Na<sub>2</sub>SO<sub>4</sub>-Induced Accelerated Oxidation (Hot Corrosion) of Nickel', *Met. Trans.*, Vol. 1, pp. 1943–54.
- Goebel, J. A., Pettit, F. S. and Goward, G. W. (1973), 'Mechanisms for the Hot Corrosion of Nickel-Based Alloys', *Metall. Trans.*, Vol. 4, pp. 261–75.
- Hamner, N. E. (1977), 'Coatings for Corrosion Protection', Ch. 14 in *NACE Basic Corrosion Course*, Houston, TX.
- Hancock, P. (1987), 'Vanadic and Chloride Attack of Superalloys', *Mater. Sci. Technol.*, Vol. 3, pp. 536–44.
- Haugsrud, R. (2003), 'On the High-Temperature Oxidation of Nickel', *Corros. Sci.*, Vol. 45, No. 1, pp. 211–35.
- Hidalgo, V. H., Varela, F. J. B. and Rico, E. F. (1997), 'Erosion Wear and Mechanical Properties of Plasma-Sprayed Nickel- and Iron-Based Coatings Subjected to Service Conditions in Boilers', *Trib. Int.*, Vol. 30, No. 9, pp. 641–49.
- Hidalgo, V. H., Varela, F. J. B. and Menendez, A. C. (1998), 'Characterization and High Temperature Behaviour of Thermal Sprayed Coatings Used in Boilers', *Proc. 15th Int. Thermal Spray Conf.*, 25–29 May, Nice, France, pp. 617–21.
- Hidalgo, V. H., Varela, F. J. B., Martinez, S.P. and Espana, S. G. (1999), 'Characterization and High Temperature Behaviour of Cr<sub>3</sub>C<sub>2</sub>-NiCr Plasma Sprayed Coatings', *Proc. United Thermal Spray Conf.*, Germany, pp. 683–86.
- Hidalgo, V. H., Varela, J. B., de la Calle, J. M. and Menendez, A. C., (2000), 'Characterisation of NiCr Flame and Plasma Sprayed Coatings for Use in High Temperature Regions of Boilers', *Surface Eng.*, Vol. 16, No. 2, pp. 137–42.
- Hiramatsu, N. and Stott, F. H. (2000), 'The Effects of Molybdenum on the High-Temperature Oxidation Resistance of Thin Foils of Fe-20Cr-5Al at Very High Temperatures', *Oxid. Met.*, Vol. 53, No. 5–6, pp. 561–75.
- Hocking, M. G. (1993), 'Coatings Resistant to Erosive/Corrosive and Severe Environments', *Surf. Coat. Technol.*, Vol. 62, pp. 460–66.

- Hwang, Y. S. and Rapp., R. A. (1989), 'Thermochemistry and Solubilities of Oxides in Sodium Sulfate-Vanadate Solutions', Corrosion, Vol. 45, No. 11, pp. 933–37.
- Iyer, S. R., Iyer, K. J. L. and Radhakrishnan, V. M. (1987), 'High Temperature Corrosion of a Ni-Base Superalloy by Vanadium', *Proc. 10th ICMC*, Madras, India, Vol. IV, pp. 3665–70.
- Kerby, R. C. and Wilson J. R. (1973), 'Corrosion of Metals by Liquid Vanadium Pentoxide and the Sodium Vanadates', Trans. ASME, January, pp. 36–44.
- Khanna, A. S. and Jha, S. K. (1998), 'Degradation of Materials under Hot Corrosion Conditions', Trans. Indian Inst. Met., Vol. 51, No. 5, pp. 279–90.
- Kofstad, P. (1966), *High Temperature Oxidation of Metals*, John Wiley and Sons, New York.
- Kolta, G. A., Hewaidy, L. F. and Felix, N. S. (1972), 'Reactions between Sodium Sulphate and Vanadium Pentoxide', *Thermochim. Acta*, Vol. 4, pp. 151–64.
- Krishna, B. V. and Sidhu, R. K. (2001), 'High Temperature Corrosion of INCONEL 600 Tube – a Case Study', *Met. Mater. Procs*, Vol. 14, No. 1, pp. 21–26.
- Kuiry, C., Seal, S., Bose, S. K. and Roy, S. K. (1994), 'Effect of Surface Preparation on the High-Temperature Oxidation Behaviour of AISI 316 Stainless Steel', *ISIJ Int.*, Vol. 34, No. 7, pp. 599–606.
- Lee, W. H. and Lin, R. Y. (1999), 'Oxidation, Sulphidation and Hot Corrosion of Intermetallic Compound Fe<sub>3</sub>Al at 605°C to 800°C', *Mater. Chem. Phys.*, Vol. 58, No. 3, pp. 231–42.
- Levy, M., Huie, R. and Pettit, F. (1989), 'Oxidation and Hot Corrosion of Some Advanced Superalloys at 1300 to 2000°F (704 to 1093°C)', Corrosion, Vol. 45, No. 8, pp. 661–74.
- Li, M. H., Zhang, Z. Y., Sun, X. F., Li, J. G., Yin, F. S., Hu, W. Y., Guan, H. R. and Hu, Z. Q. (2003), 'Oxidation Behaviour of Sputter-Deposited NiCrAlY coating', *Surf. Coat. Technol.*, Vol. 165, No. 3, pp. 241–47.
- Liu, P. S., Liang, K. M., Zhou, H. Y., Gu, S. R., Sun, X. F., Guan, H. R., Jin, T. and Yang, K. N. (2001), 'Cyclic Oxidation Behavior of Aluminide Coatings on the Co-Base Superalloy DZ40M', *Surf. Coat. Technol.*, Vol. 145, pp. 75–79.
- Luthra, K. L. (1985), 'Kinetics of the Low Temperature Hot Corrosion of Co-Cr-Al Alloys', *J. Electrochem. Soc.*, Vol. 132, No. 6, pp. 1293–98.
- Malik, A. U. and Ahmad, S. (1983), 'Na<sub>2</sub>SO<sub>4</sub>-Induced Corrosion of Some Nimonic Alloys at 650 to 1000°C', *Metallkunde*, Vol. 74, No. 12, pp. 819–24.
- Malik, A. U. and Mobin, M. (1987), 'Studies on Some Solid State Reactions Relevant to Hot Corrosion', *Proc. 10th ICMC*, Madras, India, Vol. IV, pp. 3345–65.
- Misra, A. K. (1986), 'Mechanism of Na<sub>2</sub>SO<sub>4</sub>-Induced Corrosion of Molybdenum Containing Nickel-Base Superalloys at High Temperatures', *J. Electrochem. Soc.*, Vol. 133, No. 5, pp. 1029–37.
- Mobin, M., Malik, A. U., Ahmad, S., Hasan, S. K. and Ajmal, M., (1996), 'Studies on the Interactions of Metal Oxides and Na<sub>2</sub>SO<sub>4</sub> at 1100 and 1200 K in Oxygen', *Bull. Mater. Sci.*, Vol. 19, No. 5, pp. 807–21.
- Nanni, P., Buscaglia, V., Asmundis, C. D. and Roy, S. K. (1987), 'Sodium Sulphate Induced Hot Corrosion of Pure Fe, Mn and Cr in Combustion Gas', *Proc. 10th ICMC*, Madras, India, Vol. IV, pp. 3413–22.
- Narayan, R. (1983), *An Introduction to Metallic Corrosion and its Prevention*, Oxford and IBH Publishing, New Delhi, India.
- Nickel, H., Quadakkers, W. J. and Singheiser, L. (2002), 'Analysis of Corrosion Layers on Protective Coatings and High Temperature Materials in Simulated Service

- Environments of Modern Power Plants Using SNMS, SIMS, SEM, TEM, RBS and X-ray Diffraction Studies', *Anal. Bioanal. Chem.*, Vol. 374, pp. 581–87.
- Otero, E., Merino, M. C., Pardo, A., Biezma, M. V. and Buitrago, G., (1987), 'Study on Corrosion Products of IN657 Alloy in Molten Salts', *Proc. of 10th ICMC*, Madras, India, Vol. IV, pp. 3583–91.
- Otero, E., Pardo, A., Hernaez, J. and Perez, F. J. (1990), 'The Hot Corrosion of IN-657 Superalloy in  $\text{Na}_2\text{SO}_4\text{-V}_2\text{O}_5$  Melt Eutectic', *Corros. Sci.*, Vol. 30, pp. 677–83.
- Otero, E., Pardo, A., Hernaez, J. and Perez, F. J., (1992), 'The Corrosion of Some Superalloys (At 1000 K) in Molten Eutectic Mixture 60%  $\text{V}_2\text{O}_5$ -40%  $\text{Na}_2\text{SO}_4$ . The Influence of the Oxygen and Carbon Residues', *Corrosion. Science*, Vol. 34, pp. 1747–57.
- Pantony, D. A. and Vasu, K. L. (1968), 'Studies in the Corrosion of Metals Under Melts – 1. Theoretical Survey of Fire-Side Corrosion of Boilers and Gas-Turbines in the Presence of Vanadium Pentoxide', *J. Inorg. Nucl. Chem.*, Vol. 30, pp. 423–32.
- Paul, L. D. and Seeley, R. R. (1991), 'Oil Ash Corrosion – a Review of Utility Boiler Experience', *Corrosion*, Vol. 47, No. 2, pp. 152–59.
- Peters, K. R., Whittle, D. P. and Stringer, J. (1976), 'Oxidation and Hot Corrosion of Nickel-Based Alloys Containing Molybdenum', *Corros. Sci.*, Vol. 16, pp. 791–804.
- Pettit, F. S. and Giggins, C. S. (1987), 'Hot Corrosion', Ch. 12, in *Superalloys II*, C. T., Sims, N. S. Stollof, and W. C. Hagel, (eds), John Wiley and Sons, New York.
- Pettit, F. S. and Meier, G. H. (1984), 'Oxidation and Hot Corrosion of Superalloys', in *Superalloys*, M. Gell, C. S. Kartovich, R. H. Bricknel, W. B. Kent and J. F. Radovich (eds), Met. Soc. AIME, Warrendale, PA, pp. 651–687.
- Priyantha, N., Jayaweera, P., Sanjurjo, A., Lau, K., Lu, F. and Krist, K. (2003), 'Corrosion-Resistant Metallic Coatings for Applications in Highly Aggressive Environments', *Surf. Coat. Technol.*, Vol. 163–164, pp. 31–36.
- Rapp, R. A. (1986), 'Chemistry and Electrochemistry of the Hot Corrosion of Metals', *Corrosion*, Vol. 42, No. 10, pp. 568–77.
- Rapp, R. A. (2002), 'Hot Corrosion of Materials: A Fluxing Mechanism', *Corros. Sci.*, Vol. 44, No. 2, pp. 209–21.
- Rapp, R. A. and Goto, K. S. (1981), 'The Hot Corrosion of Metals by Molten Salts', *Symposium on Fused Salts*, J. Braunstein and J. R. Selman (eds), The Electrochemical Society, Pennington, NJ, p. 159.
- Rapp, R. A. and Zhang, Y. S. (1994), 'Hot Corrosion of Materials: Fundamental Studies', *JOM*, Vol. 46, No. 12, pp. 47–55.
- Roy, K., Bottino, C., Rakesh, V. R., Kuiry, S. C. and Bose, S. K. (1995), 'Improved High Temperature Oxidation Behaviour of AISI 347 Grade Stainless Steel by Superficial Coating of  $\text{CeO}_2$ ', *ISIJ Int.*, Vol. 35, No. 4, pp. 433–42.
- Sadique, S. E., Mollah, A. H., Islam, M. S., Ali, M. M., Megat, M. H. H. and Basri, S. (2000), 'High-Temperature Oxidation Behavior of Iron-Chromium-Aluminum Alloys', *Oxid. Met.*, Vol. 54, No. 5–6, pp. 385–400.
- Seal, S., Bose, S. K. and Roy, S. K. (1994), 'Improvement in the Oxidation Behaviour of Austenitic Stainless Steels by Superficially Applied, Cerium Oxide Coatings', *Oxid. Met.*, Vol. 41, No. 1–2, pp. 139–78.
- Seiersten, M. and Kofstad, P. (1987), 'The Effect of  $\text{SO}_3$  on Vanadate-Induced Hot Corrosion', *High Temp. Technol.*, Vol. 5, No. 3, pp. 115–22.
- Sharma, R. N. (1996), 'Hot Corrosion Behaviour of Iron- and Nickel-Base Superalloys in Salt Environments at Elevated Temperatures', PhD Thesis, Met. and Mat. Eng. Dept., UOR, Roorkee, India.
- Shi, L. (1993), 'Accelerated Oxidation of Iron Induced by  $\text{Na}_2\text{SO}_4$  Deposits in Oxygen at

- 750°C – a New Type Low-Temperature Hot Corrosion’, *Oxid. Met.*, Vol. 40, No. 1–2, pp. 197–211.
- Shi, L. (1995), ‘On the Possibility of a  $\text{Na}_2\text{SO}_4$ - $\text{Na}_2\text{O}$  Eutectic Melt Developing on Metals Coated with  $\text{Na}_2\text{SO}_4$  Deposit in Oxygen/Air at Intermediate Temperatures’, *Corros. Sci.*, Vol. 37, No. 8, pp. 1281–87.
- Shih, S., Zhang, Y. and Li, X. (1989), ‘Sub-Melting Point Hot Corrosion of Alloys and Coatings’, *Mater. Sci. Eng. A*, Vol. A120, pp. 277–82.
- Shores, D. A. (1983), ‘New Perspectives on Hot Corrosion Mechanisms’, in *High Temperature Corrosion*, R. A. Rapp (ed.), NACE, Houston, TX.
- Shreir, L. L. (1976), *Corrosion Control*, Vol. 2 of *Corrosion*, Newnes-Butterworths, London.
- Stott, F. H. (1998), ‘The Role of Oxidation in the Wear of Alloys’, *Trib. Int.*, Vol. 31, No. 1–3, pp. 61–71.
- Stott, F. H., De Wet, D. J. and Taylor, R. (1994), ‘The Degradation Resistance of Thermal Barrier Coatings to Molten Deposits at Very High Temperatures’, *Trans. Mater. Res. Soc. Jpn.*, Vol. 14A, pp. 135–40.
- Stroosnijder, M. F., Mevrel, R. and Bennet, M. J. (1994), ‘The Interaction of Surface Engineering and High Temperature Corrosion Protection’, *Mater. High Temp.*, Vol. 12, No. 1, pp. 53–66.
- Suito, H. and Gaskell, D. R. (1971), ‘The Thermodynamics of Melts in the System  $\text{VO}_2$ - $\text{V}_2\text{O}_5$ ’, *Metall. Trans.*, Vol. 2, pp. 3299–303.
- Swaminathan, J., Raghavan, S. and Iyer, S. R. (1993), ‘Studies on the Hot Corrosion of Some Nickel-Base Superalloys by Vanadium Pentoxide’, *Trans. IIM*, Vol. 46, No. 3, pp. 175–81.
- Tiwari, S. N. (1997), ‘Investigations on Hot Corrosion of Some Fe-, Ni- and Co-Base Superalloy in  $\text{Na}_2\text{SO}_4$ - $\text{V}_2\text{O}_5$  Environment under Cyclic Conditions,’ PhD Thesis, Met. and Mat. Eng. Dept, UOR, Roorkee, India.
- Tiwari, S. N. and Prakash, S. (1996), ‘Hot Corrosion Behaviour of an Iron-Base Superalloy in Salt Environment at Elevated Temperatures’, *Proc. Symp. on Metals and Materials Research*, IIT, Madras, India, 4–5 July, pp. 107–17.
- Tiwari, S. N. and Prakash, S. (1997), ‘Studies on the Hot Corrosion Behaviour of Some Superalloys in  $\text{Na}_2\text{SO}_4$ - $\text{V}_2\text{O}_5$ ’, *Proc. SOLCEC*, Kalpakkam, India, 22–24 January, Paper C33.
- Wang, B. Q. and Luer, K. (1994), ‘The Relative Erosion–Corrosion Resistance of Commercial Thermal Sprayed Coatings in a Simulated Circulating Fluidized Bed Combustor Environment’, *Proc. 7th National Spray Conf.*, 20–24 June, Boston, MA, pp. 115–20.
- West, J. M. (1986), *Basic Corrosion and Oxidation*, Ellis Horwood, Chichester, UK.
- Wu, C. and Okuyama, M. (1996), ‘Evaluation of High Temperature Corrosion Resistance of Al Plasma Spray Coatings in Molten Sulfates at 1073 K by Electrochemical Measurements’, *Mater. Trans., JIM*, Vol. 37, No. 5, pp. 991–97.
- Wu, Y. and Hwang, S. K. (2002), ‘Microstructural Refinement and Improvement of Mechanical Properties and Oxidation Resistance in EPM TiAl-Based Intermetallics with Yttrium Addition’, *Acta Materialia*, Vol. 50, pp. 1479–93.
- Xu, H., Hocking, M. G. and Sidky, P. S. (1994), ‘Sulfidation-Oxidation Behavior of Alloy 800H in  $\text{SO}_2$ - $\text{O}_2$  and  $\text{H}_2$ - $\text{H}_2\text{S}$ - $\text{CO}$ - $\text{CO}_2$  Atmospheres’, *Oxid. Met.*, Vol. 41, No. 1–2, pp. 81–101.

## Oxide scales on hot-rolled steel strips

R Y CHEN and W Y D YUEN,  
BlueScope Steel, Australia

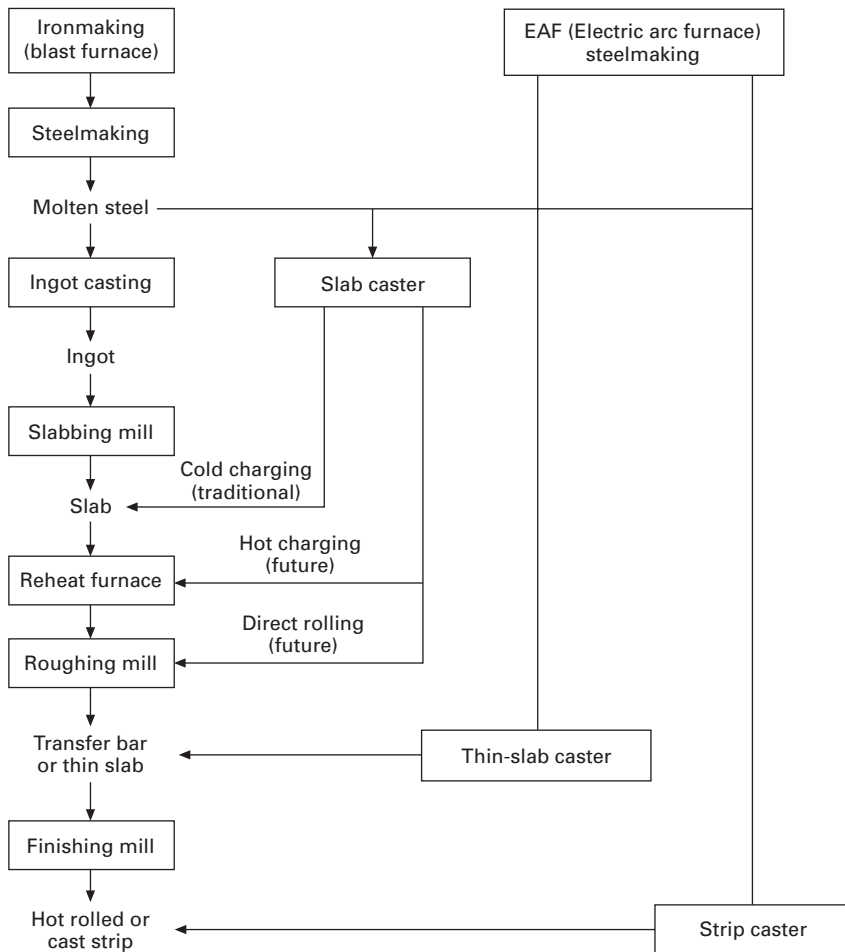
### 8.1 Introduction

With the continuing growth of the world economy, steel consumption has been rapidly increasing since 2000 [1–3]. Total world steel consumption in 2006 reached about 1100 million metric tons (mmt), an increase of 40% over the consumption in 2000 (777 mmt). The consumption forecast for 2007 is 1180 mmt, 1225 mmt by 2010 and 1408 mmt for 2015, respectively. Amongst the total volume of steel consumed, nearly 50% are flat-rolled steel sheets and plates [1], with hot rolling as an essential process to make these products.

In the past 150 years since the invention of the Bessemer process in 1856, the methods of sheet and strip steel production have undergone several major transformations [4]. The conventional and new hot strip processing routes are summed up in Fig. 8.1, modified from that presented by Guthrie [4] to incorporate the rapidly developing electric arc furnace (EAF) technology in the past 20 years.

The conventional strip hot rolling process comprises reheating of thick slabs (220–250 mm thick) to 1200–1300°C in a reheat furnace, normally using natural gas combustion for heating, roughing rolling the thick slabs to transfer bars with a thickness of about 30 mm, and finishing rolling the transfer bars to final hot rolled strips with thicknesses in the range of 1.5–6 mm. The layout of a conventional hot strip mill can be quite different, but the stages where oxide scales form are very similar.

Severe steel oxidation occurs during slab reheating. Usually, more than a sufficient amount of air is used for the combustion and therefore the furnace atmosphere contains free oxygen as well as water vapour and carbon dioxide. Oxide scales formed in the reheat furnace (called the primary scale) represent a yield loss of 1–2% of the total steel volume processed. The thick scale formed is then removed by hydraulic descaling prior to roughing rolling. During roughing rolling, the hot steel surface is exposed to ambient air and very often the top surface of the strip is covered with a blanket of water. Presumably, supporting the water blanket is a layer of water vapour underneath,



8.1 Conventional and newly developed hot strip processing routes, modified from the schematic illustration by Guthrie [4].

which is oxidizing to the hot steel surface. As a substantial amount of water is used during hot rolling for descaling and cooling, the ambient air contains a significant amount of moisture. The newly formed scale (called the secondary scale) is removed using high pressure water jets at each pass or selected passes during roughing rolling. The scale regrown on the transfer bar after roughing rolling is removed using a second hydraulic descaler before it is fed to the finishing mill. During finishing rolling and cooling on the run-out table, the oxide scale (called the tertiary scale) continues to grow, but deforms with the steel substrate at each rolling stand. At the time of coiling, the scale is usually 5–15 µm thick; it is then retained on the strip surface and will undergo a series of reactions and phase transformations in the coil during

coil cooling [5,6]. The conditions of scale formation in a conventional hot strip processing route are summarized in Table 8.1.

In the past 20 years, the conventional steel processing route has faced a fierce challenge from the newly developed thin slab casting and direct hot rolling process, which was assisted by the increasing acceptance of the minimill technology.

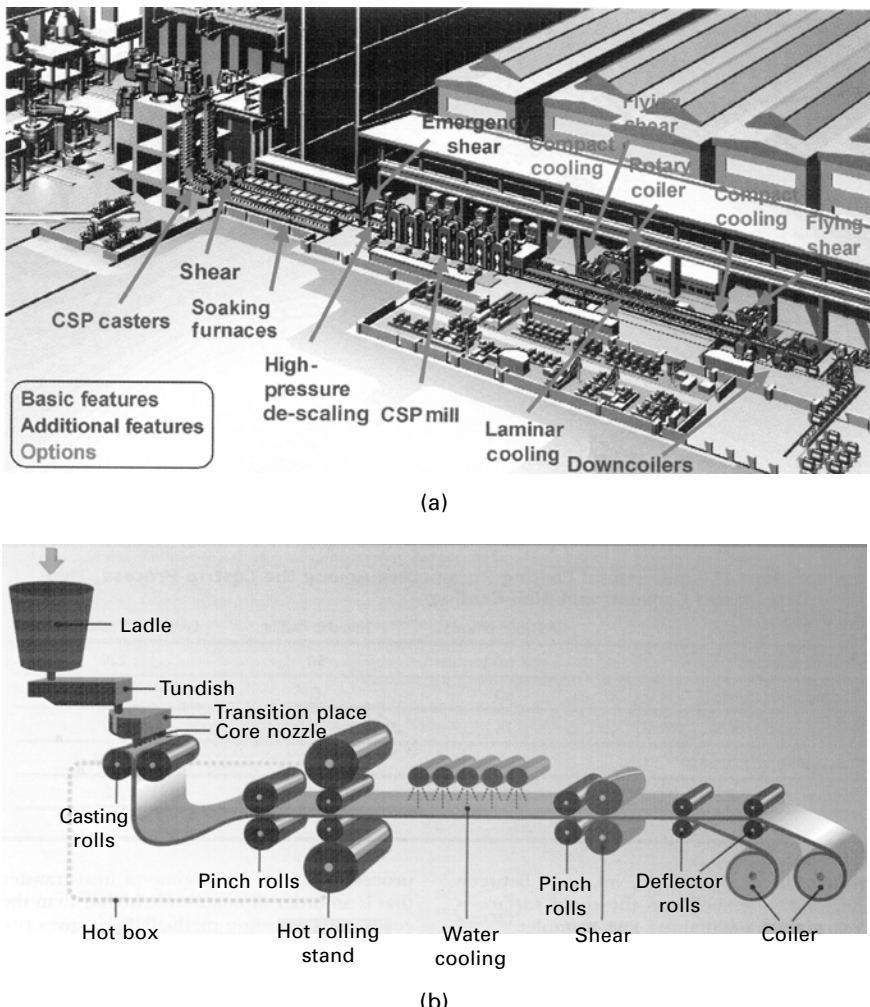
After the first minimill [7] was built by LASCO (Lake Ontario Steel Co.) in 1964, the technology and market share of steel products manufactured by the electric arc furnace (EAF) technologies gained continuous growth in the following 25 years. In 1989, the first commercial-scale thin-slab caster was built by Nucor at Crawfordsville in Indiana, USA. The commissioning of this compact strip process (CSP) was regarded as another turning point in steelmaking history, ranking equally with the Bessemer process in 1856 and the John Tyrus continuous rolling mill at Ashland in 1924. By May 2006, 26 CSP plants with a total annual capacity of more than 43 million tons had been put into operation worldwide or were being commissioned [8]. One example of a modern plant using the CSP process is the ‘next generation’ minimill being built by SeverCorr near Columbus in northeast Mississippi, USA [9].

With the rapid development of the thin slab casting and direct hot rolling process, it is now possible to produce liquid steel, to cast solid steel slabs, and to roll the slabs in-line to hot rolled strips and put hot coils or plates on a truck in a few hours. As compared to the conventional process, the capital outlay for such a process is significantly reduced. Energy requirement and greenhouse gas emissions per ton are the lowest, while manpower required is also substantially reduced. Technically, it eliminates the primary roughing rolling process and avoids cooling the slabs after casting and then reheating them to excessively high temperatures (1200–1300°C) for roughing rolling.

In a typical CSP process, as schematically shown in Fig. 8.2(a), liquid steel produced by an EAF process is cast to 50–90 mm thick slabs (one-third to one-fifth the thickness of slabs produced by conventional casting) [8]. The thin slab is then transferred through a tunnel furnace where the temperatures throughout the slab body are equalized. The tunnel furnace is normally kept

*Table 8.1 Scale formation in a conventional hot strip processing route*

Type of scale	Thickness	Temperatures	Atmosphere	Duration
Primary scale	1–5 mm	1200–1300°C	Furnace gas	Hours
Secondary scale	100–300 µm	1100–1200°C	Air/steam	Minutes
Tertiary scale	10–30 µm	850–1100°C	Air/steam	Seconds
Scale retained on strip	5–15 µm	500–880°C	Air/steam	Days



8.2 Schematic illustrations of two new hot strip processing routes: (a) overall concept of Compact Strip Production [8]; (b) Castrip® process [15].

at 1100–1150°C, heated by natural gas combustion. Because of the high charging temperatures of the slabs, much-reduced heating capacity is required in the tunnel furnace. The equalization time is around 15–20 minutes. Thereafter, the slab is descaled and rolled through a finishing mill to the final strip thickness. As compared to the conventional route, the much lower reheat temperatures and shorter residence time in the tunnel furnace have resulted in much-reduced steel yield loss, although this is offset by the increased steel loss due to the increased surface area of thinner slabs. Steel oxidation during

finishing rolling is similar to that in a conventional process. The CSP process is now used not only to produce mild steel but also increasingly to produce higher strength grade steel products [10].

There are some variations to the typical CSP process. One of them was to include an additional tunnel furnace and an in-line roughing process immediately after the caster. Another variation is the ISP (in-line strip process) [11] in which, instead of charging the thin slab directly into the tunnel furnace, a three-stand reduction mill is positioned at the exit of the thin slab caster. The strip after this rolling step is then reheated in an induction furnace to the required finish-rolling temperature. In another process, a walking beam furnace is used for slab temperature equalization. Despite the differences in the actual layout of these processes, the general principles of making the final hot bands directly from molten steel in a continuous process were not changed.

A more recent breakthrough development is the realization of Sir Henry Bessemer's dream – producing sheet steel directly from molten steel using a twin-roll caster. Following extensive research and development in a joint venture between BlueScope Steel (then BHP Steel) and Ishikawajima-Harima Heavy Industries (IHI) [12], the first commercial strip casting facility for manufacturing plain-carbon steel strip was constructed in 2002 at Nucor's Crawfordsville site, the place where the first thin slab caster was installed, as a joint venture between Nucor, BlueScope Steel and IHI. The yearly capacity of this facility is 540,000 tons. The process is now called the Castrip® Process [13]. By early 2007, 450,000 tons of 0.76–1.8 mm thick cast strips had been produced and used for various applications [14] and a new standard ASTM A1039 [15] had been developed for Castrip® products. Currently, a second commercial Castrip® facility with improved features and a higher yearly capacity (674,000 tons) is being installed at Nucor-Yamato Steel in Blytheville, Arkansas, USA [14].

Figure 8.2(b) is a schematic of the Castrip® process. In this process, molten steel is poured into a twin-roll caster and directly cast into 1–3 mm thick solid strip. As the solid strip surface is as hot as over 1400°C when it comes out of the twin rolls, an enclosed chamber under the twin-roll caster is required to provide a protective atmosphere to prevent the strip surface from excessive oxidation. The hot strip is then given a reduction of about 30% at 1000–1100°C by a single or twin hot rolling stands and then cooled on a short run-out table before it is coiled. The entire length of the line is under 60 metres for the first commercial line and will be under 50 metres for the second line [14]. It can be seen that in this process, there is neither strip reheating nor descaling in the process. The strip is oxidized only between the hot box and the finishing mill and on the run-out table where water cooling is applied. The duration of strip oxidation depends on the strip casting speed, which is currently in the range of 80–120 metres per minute.

The consequences of strip oxidation are multi-fold. First, it results in a significant loss of steel materials. As mentioned earlier, in the conventional hot rolling processes, 1–2% of steel is lost during reheating due to scale formation, which amounts to \$5 to \$10 per ton of steel manufactured based on the current slab price [16]. More loss due to steel oxidation was also incurred in the subsequent roughing rolling, transferring and finishing rolling processes. The yield loss associated with the thin-slab casting and direct rolling process would be much reduced as the reheat temperatures were lower, the reheat duration was shorter and the roughing rolling step was also shorter or not required at all. The yield loss associated with reheating and roughing rolling is completely removed in the Castrip® processes as they are not required.

The second consequence is the potential deterioration of strip surface quality caused by scale [17]. Incorrect thickness and type of scale on the strip surface during hot rolling can reduce the service life of work rolls, which in turn can cause strip defects. If the scale is too thick, it increases the cost of acid pickling and affects pickling speed, particularly when the scale develops a thick hematite layer on the surface [18–20].

Based on their chemical compositions, steel products are generally classified into different groups [21] with carbon steel representing the largest group of engineering steel products. Carbon steels are further divided into several groups, such as very low carbon steels (<0.10% C) and low carbon steels (0.1–0.25% C). In the past decade, a group of steels containing virtually no carbon, called interstitial-free steel (IF-steel), has emerged as an important steel group to supply the automotive steel and durable household goods markets. Normally, small amounts of titanium and/or niobium at levels up to 0.08% are added to react with carbon and nitrogen, which normally reside in the interstitial sites of the steel, so that dislocations can move more freely upon extensive deformation, such as deep drawing.

Another important steel group is alloy steels containing a combination of various alloying elements such as silicon, chromium, titanium, columbium, vanadium, molybdenum, etc., to meet their special requirements. One important alloy steel group is the ‘high-strength low-alloy’ or HSLA steel group. Silicon at levels of 0.1–0.9% is the most common alloying elements in this group. Other steel groups are tool steels usually containing higher levels of carbon and other alloying elements, electric steels normally containing higher levels of silicon and aluminium (up to 3.3%), steels used in power plant applications normally containing a combination of chromium and molybdenum, stainless steels containing very high levels of chromium or chromium and nickel, and heat-resistant iron-based alloys. This chapter will be limited to discussions of the oxidation behaviour of carbon steels and low alloy steels. For comparison purposes, some important results of iron oxidation will be included.

Steel composition is also affected by the deoxidation practice in steelmaking.

The most common deoxidizers are aluminium and silicon [22–24]. When aluminium is used as the sole deoxidiser, the steel is called Al-killed. Usually, Al-killed steels contain a very low level of silicon if silicon is not purposely added as an alloying element. However, if silicon is used as a deoxidizer, the steel will inevitably contain a small amount of silicon at about 0.1–0.3%, depending on the degree of deoxidation required [23–25].

## 8.2 Long-term oxidation of iron and steel

### 8.2.1 Pure iron oxidation in air or oxygen

The high temperature oxidation behaviour of pure iron has been thoroughly studied in several early investigations [26–31] and was reviewed recently [6]. It was generally accepted that in the temperature range of 700–1250°C, the oxidation kinetics of pure iron in air and oxygen are very similar and follow the parabolic law. The scale structure developed comprises three oxide layers, with wustite being the innermost layer followed by an intermediate magnetite layer and an outermost layer of hematite. The thickness ratios of these three oxide layers are nearly constant at 95:4:1.

If the oxidation kinetics are expressed using the Pilling–Bedworth-type equation [26], then

$$\frac{dW}{dt} = k'_p / W \quad \text{or} \quad W^2 = k_p t + W_0^2 \quad 8.1$$

where  $W$  denotes the weight gain per unit area,  $t$  the oxidation time, and  $W_0$  the initial scale weight at the start ( $t = 0$ ) of the parabolic oxidation stage. The parabolic rate constant  $k_p$  ( $= 2 k'_p$ ), usually measured in  $\text{g}^2\text{cm}^{-4}\text{s}^{-1}$ , is expressed as [6]

$$k_p (\text{g}^2\text{cm}^{-4}\text{s}^{-1}) = k_p^0 \exp(-Q/RT) = 3.047 \exp(-157539/RT) \quad 8.2$$

where  $Q$  is the activation energy of iron oxidation in  $\text{J} \cdot \text{mol}^{-1}$ ,  $T$  the absolute temperature in K, and  $R$  the gas constant in  $\text{J} \cdot \text{K}^{-1} \text{mol}^{-1}$ . If the oxidation kinetics are expressed using the Tammann-type equation [32], then

$$\frac{dx}{dt} = k'_x / x \quad \text{or} \quad x^2 = k_x t + x_0^2 \quad 8.3$$

where  $x$  denotes the total scale thickness,  $t$  the oxidation time, and  $x_0$  the initial scale thickness at the start ( $t = 0$ ) of the parabolic oxidation stage. The parabolic rate constant  $k_x$  ( $= 2 k'_x$ ), usually measured in  $\text{cm}^2\text{s}^{-1}$ , can be calculated from the measured  $k_p$  values using the following equation,

$$k_p (\text{g}^2\text{cm}^{-4}\text{s}^{-1}) = \alpha k_x (\text{cm}^2\text{s}^{-1}) \quad 8.4$$

where  $\alpha$  is a conversion factor which varies with the Fe:O ratio and wustite density at different temperatures and can be estimated using the following equation [6]:

$$\alpha = 1.7017 + 0.0000844T \quad 8.5$$

It should be mentioned that the scale thickness measured at room temperature would be different from that calculated using Equation (8.3) as the scale density at room temperature differs from that at the oxidation temperature.

The conditions of using Equations (8.1)–(8.5) to calculate the parabolic rate constants for pure iron are that (a) the oxidation takes place under isothermal conditions, (b) the scale structure developed is compact and adherent to the substrate, and (c) the thickness ratios of the three oxides are maintained nearly constant at 95:4:1. These equations cannot be used if the actual oxidation conditions deviate from the above conditions. Such situations include the initial stage of oxidation, separation of scale–substrate interface and formation of blisters in the scale.

At 580–700°C, although the scale formed is still three-layered, the thickness ratios deviate from the 95:4:1 ratios significantly, and therefore Equations (8.1)–(8.5) cannot be used for calculating scale growth for this temperature range [6].

### 8.2.2 Oxidation of low carbon, low silicon steel in air or oxygen

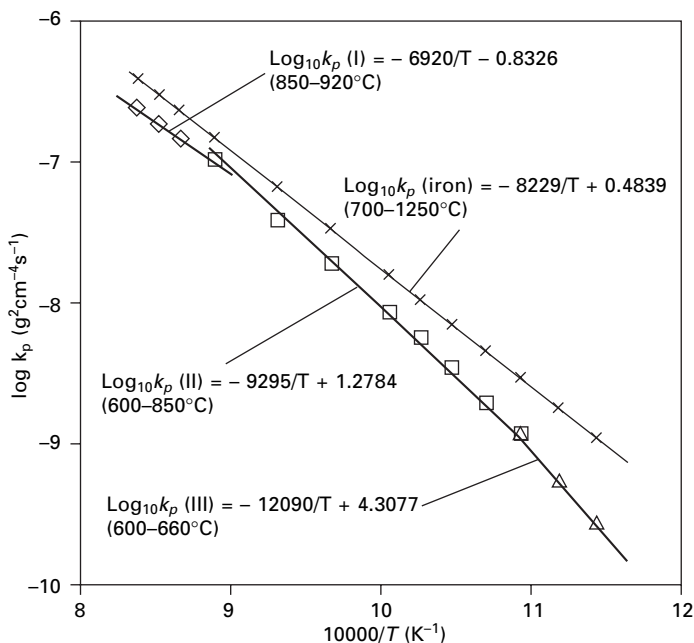
Using the oxidation data obtained by Sachs and Tuck [33] for a mild steel equivalent to SAE-AISI 1006, by Raman *et al.* [34] for a steel having similar composition, and those by Abuluwefa *et al.* for a similar steel (Fe-0.04C-0.2Mn-0.02Si) in 1–15% O<sub>2</sub>–N<sub>2</sub>[35], an equation was recently derived [6] to calculate the parabolic rate constant of SAE-AISI 1006 steel (or steels having similar compositions) oxidation in air in the range of 700–1250°C:

$$k_x (\text{cm}^2\text{s}^{-1}) = 0.084\exp(-143264/RT) \quad 8.6$$

More recently, the oxidation of a steel containing 0.055C-0.23Mn-<0.005Si in flowing air at 600–920°C was evaluated [36]. It was found that the oxidation kinetics for the temperature and duration examined followed the parabolic law, except for oxidation at 600°C for longer than 100 min. At higher temperature (>930°C), blisters started to form in the scale after a short duration (<5 min). Once blisters formed, the oxidation kinetics deviated from the parabolic law.

Arrhenius plots of the kinetics data for the temperature range 600–920°C, Fig. 8.3, show that the rate constant parameters are different in different temperature ranges, as listed in Table 8.2.

The scale structure developed at 900°C is shown in Fig. 8.4 and the percentages of the wustite layer thickness prior to and after isothermal holding at the target temperatures are compared in Fig. 8.5. It is seen that the wustite layer had not formed at the start of the isothermal holding at temperatures



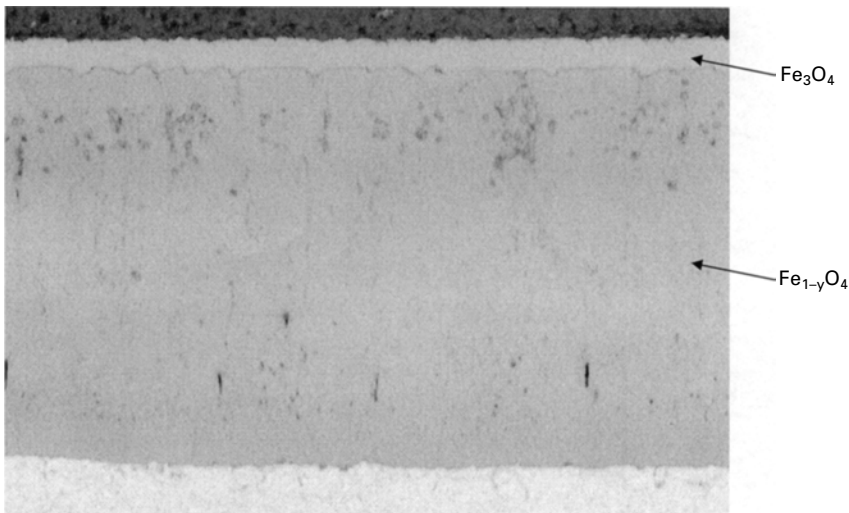
8.3 Arrhenius plots of parabolic rate constants for oxidation of 0.06C-0.23Mn steel, as compared to iron oxidation ( $\times$ ) in the same temperature range [36].

Table 8.2 Rate constant parameters for oxidation of 0.06C-0.23Mn steel [36]

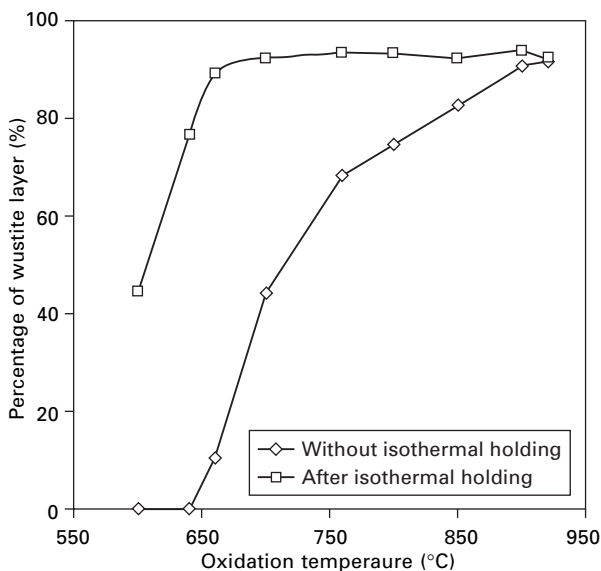
Temperature range	$k_p^0 (\text{g}^2 \text{cm}^{-4} \text{s}^{-1})$	$Q (\text{kJ mol}^{-1})$
600–660°C	20,300	-226.4
660–850°C	19.0	-178.0
850–920°C	0.147	-130.0

below 650°C. At 650–850°C, the initial wustite layer thickness was significantly smaller than that developed after isothermal holding and the difference became very smaller at temperatures above 850°C.

As the samples were heated in air, a thin magnetite layer would have formed first when the sample was heated from room temperature to 570°C. Once the temperature was raised to above 570°C, wustite would start to nucleate at the magnetite–steel interface. However, a stable wustite phase could not form during heating before the sample temperature reached a temperature above 650°C. After the formation of stable wustite nuclei, they would grow into a continuous layer, and after a sufficiently long period of time, become the predominate layer in the scale. The initial scale structure



8.4 Oxide scale formed on 0.06C-0.23Mn steel after isothermal holding at 900°C for 10 minutes (500×).



8.5 Percentages of wustite layer thicknesses in the scales formed on 0.06C-0.23Mn steel at different temperatures with and without isothermal holding.

would be different if the samples were heated in a protective atmosphere before air was introduced into the furnace.

Laboratory experiments were usually conducted in two different ways. In some studies, the steel samples were heated unprotected (e.g. in air) to the

target temperatures and then held at the target temperatures isothermally. The advantage of this is that because some oxide scale has formed during heating, there is no or very little overheating caused by the sudden release of reaction heat (called overtemperature in one previous study [37]) when the isothermal holding starts. The disadvantage of this is that the oxide scale structure formed during heating would be different from the typical scale structure developed after isothermal holding and would possibly affect the final scale structure developed when the target temperatures are relatively low and the isothermal holding duration is short. If the temperatures are high ( $>800^{\circ}\text{C}$ ), the wustite layer would grow quickly and take control of the oxidation rate after a relatively short time. However, if the oxidation temperatures are relatively low ( $700\text{--}800^{\circ}\text{C}$ ), it would take longer time for the typical scale structure to develop.

In other studies, steel samples are heated in a protective atmosphere to the target temperature and held at that temperature for a short period of time before reaction gas is introduced to oxidize the steel. The issues associated with this approach are (a) the initial supply rate of oxidizing gas is lower than the intended gas supply rate, since the reaction gas has to mix with the protective gas first before the reactor chamber is completely occupied by the reaction gas, and (b) the sample temperature is usually raised to a level significantly higher than the intended temperature because of the overtemperature effect and then returned slowly towards the target temperature. Therefore, the observed oxidation rates at the initial stage are actually those obtained over a higher temperature range, rather than those exhibited at the target temperature.

Päädassi [30] and Sheasby *et al.* [56] conducted parallel experiments to compare the oxidation kinetics and the scale structures developed under these two types of conditions and found that the long-term oxidation kinetics and the scale structures developed were not affected.

### 8.2.3 Effects of water vapour addition on iron and steel oxidation in air or oxygen

In an early study, Rahmel and Tobolski [38] examined the effect of water vapour addition in oxygen on the long-term oxidation behaviour of pure iron. It was found that, at  $750^{\circ}\text{C}$ , the oxidation rates in  $69\%\text{O}_2 + 31\%\text{H}_2\text{O}$  and  $31\%\text{O}_2 + 69\%\text{H}_2\text{O}$  were slightly slower than that in pure oxygen. At  $850^{\circ}\text{C}$ , the presence of 2% of  $\text{H}_2\text{O}$  in oxygen decreased the oxidation rate, but when the  $\text{H}_2\text{O}$  level increased to 12–69%, the oxidation rate increased. At  $950^{\circ}\text{C}$ , the oxidation rate increased with the level of  $\text{H}_2\text{O}$  up to 12%, beyond which not much further increase was observed. The effect of carbon dioxide in oxygen was also examined at  $950^{\circ}\text{C}$ ; it was similar to that of water vapour, but the increase in oxidation rate was smaller.

Based on the observation of numerous porosities in the scales, the authors developed the famous void migration theory to explain the increased oxidation rates in the presence of water vapour and carbon dioxide at 850°C and 950°C. While the void migration theory was readily accepted in the high temperature corrosion community [39], most of the porosities presented in the Rahmel and Tobolski study were more likely caused by poor metallographic preparation. Porosities in scale will be further discussed in this chapter.

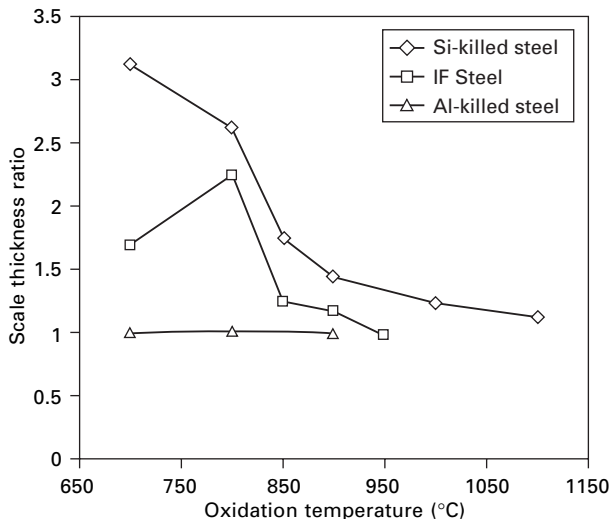
Later studies by others [40–44] indicated that the presence of water vapour in air or oxygen had an even more profound effect on the oxidation of steel and Fe-C alloys. It was generally accepted that the presence of water vapour improved the scale adherence and hence increased the oxidation rate or prolonged the period when the parabolic oxidation kinetics were held.

The moisture contents examined in most of these later studies were very high, which were more relevant to steel oxidation during reheating in a reheat furnace where the moisture content was in the range of 10–20%. Outside the reheating furnace, the hot steel surface is exposed to either steam or ambient air. The moisture content in the ambient air was only up to several percent, depending on the ambient temperature and the ventilation condition of the plant. Very few early studies had examined the effect of small amounts of moisture in air or oxygen on the oxidation behaviour of iron and steel [38,44].

In a recent study, the oxidation behaviours of several low and ultra-low carbon steels in nearly dry air (containing less than 0.1% H<sub>2</sub>O) were first examined [45]. The steels examined were two Al-killed low carbon steels (0.06C-0.23Mn), one Ti-containing interstitial-free steel, and one Si-killed low carbon steel (0.05C-0.57Mn-0.28Si). The oxidation rates of the IF and Si-killed steels were significantly lower than those of the Al-killed steels but the difference became smaller at 900–950°C for the IF steel. Poor scale adhesion was observed in the scales formed on the Si-killed and IF steels. For the IF steel, wrinkle-like blisters were observed in the scales formed in the lower temperature range (700–800°C), whereas many fine round bubbles were found in the scales formed at 850–950°C, as will be seen later in Fig. 8.9.

The effects of a small amount of moisture addition (2.8%) on the oxidation behaviours of the above steels were then investigated in a subsequent study [46]. Very different effects on the oxidation kinetics were observed, as shown in Fig. 8.6. The experimental conditions for the data points used in Fig. 8.6 are listed in Table 8.3.

For the Al-killed steels (0.06C-0.23Mn), the effect on the oxidation kinetics was negligible, but for the Si-killed and IF steels, the effects were significant, particularly at the low temperature range. At 700–800°C, the scale thickness formed on the Si-killed steel in moist air was 2.5–3 times that formed in the



**8.6** The effect of water vapour presence in air on the scaling rates of three commercial low and ultra-low carbon steels [46]. Scale thickness ratio = scale thickness formed in moist air (2.8% H<sub>2</sub>O)/scale thickness formed in nearly dry air (0.1% H<sub>2</sub>O). (a) Substoichiometric combustion; (b) excess air combustion.

**Table 8.3** Oxidation conditions used to obtain the data shown in Fig. 8.6

Temperature	Al-killed steel	Si-killed steel	Ti-IF steel
700°C	30 min	120 min	10 min
800°C	30 min	30 min	10 min
850°C	N/A	60 min	30 min
900°C	15 min	60 min	30 min
950°C	N/A	N/A	30 min
1000°C	N/A	10 min	N/A
1100°C	N/A	5 min	N/A

nearly dry air. The scale thickness differences for the IF steel were smaller but still significant at temperatures below 850°C.

It should be noted that in these studies [45,46], the oxidation experiments were conducted by heating the steel samples in the reaction gases, and therefore a certain scale thickness and structure were already developed when the isothermal holding period started. The effects of moisture presence on the oxidation behaviour of the steel examined could be different if the samples were heated in a protective atmosphere without pre-oxidation.

The void migration theory proposed by Rahmel and Tobolski [38] can be used to explain the improved scale adhesion and hence increased oxidation rate of steel as a result of H<sub>2</sub>O presence in air or oxygen when genuine

porosities are present in the scale. However, as will be discussed later, not all scales developed voids or porosities in them, and when this happens the void migration theory became invalid [41].

To explain the improved scale–steel adhesion in this latter situation, a theory was proposed by Tuck *et al.* [41] that the presence of hydrogen in certain forms would increase the mobility of dislocations in the wustite phase and hence improve its plasticity, which in turn would be more effective in the annihilation of vacancies left behind as a result of outward diffusion of iron ions.

To investigate the effect of water presence in air or oxygen on the scale adherence, it is essential to consider the permeability of hydrogen or hydrogen-containing species through the oxide layer. In the study carried out by Tuck *et al.* [41], various possible forms of hydrogen or hydrogen-containing species were considered. These included hydrogen molecules ( $H_2$ ), neutral hydrogen atoms ( $H$ ), hydrons ( $H^+$ ), and hydroxyl anions  $OH^-$ . For compact scales, the most likely form of hydrogen or hydrogen-containing species to transport through the scale layer was concluded to be neutral hydrogen atoms travelling through the interstitial sites or  $OH^-$  via the oxygen sites.

In more recent studies, in order to interpret the observed accelerated steel oxidation in steam in the range of 400–900°C for power plant applications, various possibilities of ‘water’, oxygen and hydrogen transports through the oxide scales were again considered [47], but no conclusion was made as to which species was the predominant one and responsible for the observed oxidation rates and scale structures developed.

Amongst these more recent studies, perhaps the most interesting results were those obtained in the studies carried out by Nakagawa *et al.* [48]. In these studies, oxidation experiments were conducted for three ferritic steels containing about 0.1% carbon and 2–12% chromium at 600°C. Tube samples were used in the oxidation experiment. During each oxidation experiment, 50%  $H_2O$ –Ar was flowing inside the tube sample, whereas the outside of the tube was exposed to air. Despite the different atmospheres, similar scale thickness and structures were observed on both sides of the test tube, comprising primarily an outer layer of magnetite and an inner layer of spinel oxide of iron and chromium, although a thin layer of hematite was also observed outside the tube. Based on this observation, it was believed that hydrogen had diffused through the wall of the steel tube, including the oxide layers, and promoted oxidation of the outer tube surface. Without the assistance of water vapour present inside the tube, the oxidation rates of these steels in dry air were much slower [47].

Hydrogen permeability experiments were then conducted to relate the amount of hydrogen diffusing through the oxidized samples to steel composition and scale thickness. Disc-shape samples were used in the hydrogen permeability tests, with one side of the disc exposed to flowing 50%  $H_2O$ –Ar gas and the

other side to flowing Ar gas as a hydrogen carrier. The results of these tests clearly indicated that hydrogen had diffused through the disc samples and the amounts of permeated hydrogen from the 50% $H_2O$ -Ar side decreased parabolically with time, indicating that hydrogen permeation through the scale layer was controlled by solid phase diffusion.

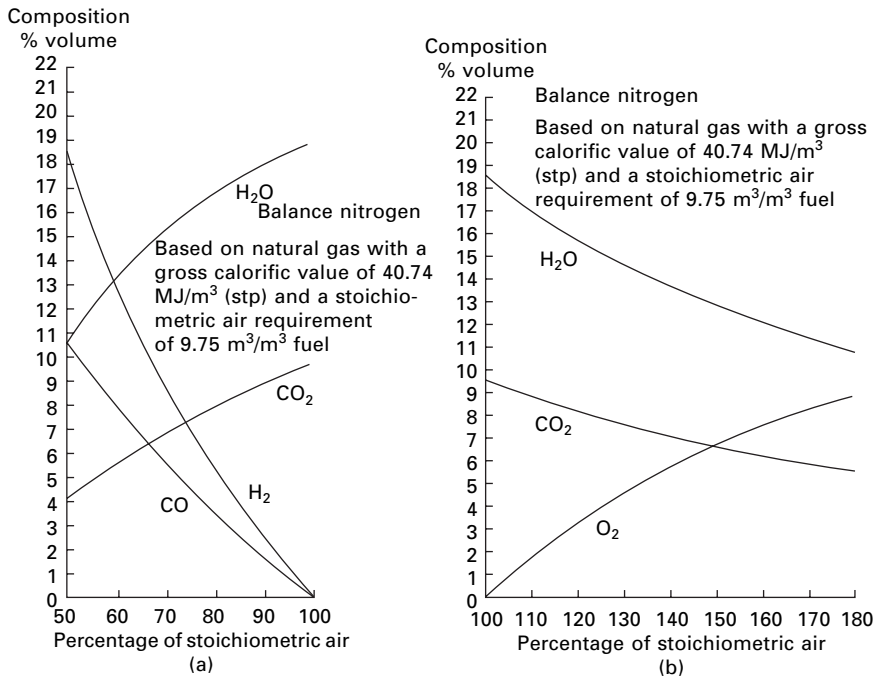
The study of Nakagawa *et al.* clearly demonstrated that (a) hydrogen is generated during steel oxidation in steam, (b) the steels examined and the oxide layers growing on them were permeable to hydrogen, and (c) the permeability through the oxide layers (magnetite and iron–chromium spinel) formed was lower than that through the steel substrates. A further study by Ueda *et al.* [49] found that wustite was also permeable to hydrogen at 800°C, but the permeability of hydrogen through wustite and magnetite was one to two orders of magnitude lower than that through iron.

An alternative theory to explain the improved scale adhesion as a result of water presence in the oxidizing atmosphere is the balanced transport theory developed by Hultquist *et al.* [50,51]. In this theory, it was proposed that the presence of hydrogen in some oxide scales would modify their transport mechanisms to improve the balance between oxygen-ion and metal-ion transports so that the tendency for scale spallation or scale cracking can be lowered.

In summary, it has been observed that the presence of water vapour in air or oxygen improves the scale adhesion formed at high temperatures. When voids or pores are generated in the scale, the void migration theory proposed by Rahmel and Tobolski [38] can be used to explain the improved scale adhesion. However, when voids or pores are not present in the scale, the void migration mechanism is invalid. Two other promising theories have been proposed to explain the improved scale–steel adhesion in this latter case. One is the traditional theory of improved plasticity as a result of improved dislocation mobility in the wustite scale due to the presence of hydrogen in certain forms in the scale. The other is the balanced transport theory recently developed by Hultquist *et al.* However, the actual mechanisms by which these proposed theories work are still not clear.

#### 8.2.4 Oxidation in reheat furnace atmospheres

As discussed earlier, slab reheating in the conventional strip process route is achieved by burning natural gas or other fuels in a reheat furnace. In the thin slab casting route, equalization of slab temperature is usually achieved in a natural-gas-combusted tunnel furnace. The common feature in these processes is that the slab is oxidizing in an atmosphere containing a mixture of several gas species. Normally, the furnaces are operated under air-rich combustion conditions, i.e. more than sufficient amounts of air are used to react with the fuels introduced to the furnaces, and therefore, when in equilibrium, the



8.7 Compositions of furnace atmosphere under different combustion conditions [52]: (a) Substoichiometric combustion; (b) excess air combustion.

furnace atmospheres contain  $\text{H}_2\text{O}$  and  $\text{CO}_2$  as the main combustion products and small amounts of unreacted oxygen with the balance being nitrogen. When insufficient amounts of air are used, the combustion is called substoichiometric combustion [52]. In this case, all oxygen is consumed and the atmospheres contain some unreacted hydrogen and carbon monoxide. Fig. 8.7 shows how the gas composition in a typical gas-fired reheat furnace varies with the percentage of stoichiometric air used [52,53]. The gas compositions would be different when other fuels are used.

From Fig. 8.7, it can be seen that, regardless of the stoichiometric air percentage used, the furnace atmospheres always contain significant amounts of water vapour and carbon dioxide. At air percentages in the range of 80–120%, their levels are in the ranges of 16–18.5% and 8–9.5%, respectively. It is therefore essential to understand the contributions of these gases to the overall oxidation behaviour of iron and steel in the reheat furnace atmospheres in the presence or absence of free oxygen.

Oxidation of iron and some commercial steels in reheat furnace atmospheres was extensively studied by the GKN group from the late 1950s to the early 1970s [33,54] and was reviewed by Sachs and Tuck [25] and by Ajersch

[55]. Some of the aspects needing further clarification were studied by Sheasby *et al.* [56] in the 1980s, by Abuluwefa *et al.* [57,58] in the 1990s, and more recently by Lee and Choi [59] and Lee *et al.* [60]. Some of these previous studies will be discussed in more detail.

#### *Early studies carried out by the GKN group*

In the studies carried out by the GKN group [33,61–63], the oxidation behaviour of pure iron, a low-carbon low-silicon steel (0.065C-0.29Mn) and two medium-carbon steels which contained small amounts of other alloying elements (0.425C-0.21Si-0.77Mn-0.28Ni-0.20Cr and 0.4C-0.24Si-0.95Mn-0.14Ni-0.13Co-0.28Mo) in several simulated reheat furnace atmospheres at 700–1200°C was examined. The main purpose was to evaluate the effect of free-oxygen content in the range of 0.9–5.4% and the water vapour content in the range of 7.2–20% on the oxidation kinetics of iron and various steels.

Under isothermal oxidation conditions, the effects of gas composition on the oxidation rates for both iron and the 0.065C-0.29Mn steel were found to be more significant at higher temperatures, with very small differences observed at 700–800°C.

For pure iron, the oxidation rates in the low oxygen (0.9%) atmospheres followed a coupled linear-parabolic kinetics, exhibiting a slow transition from linear kinetics controlled by surface reactions to parabolic kinetics controlled by solid phase diffusion. Increasing H<sub>2</sub>O content from 10% to 20% increased the iron oxidation rate when the oxygen content was low, especially at temperatures above 1000°C. In the atmospheres containing higher levels of oxygen (3.6–5.4%), the oxidation of pure iron followed the parabolic law and the effect of steam content became very small.

For the 0.065C-0.29Mn steel examined, the oxidation behaviour was significantly different. First, under the same isothermal oxidation conditions, the oxidation rates were invariably lower than those of pure iron in all atmospheres. Second, the oxidation rate increased not only with oxygen content but also with H<sub>2</sub>O content. The observed increase of oxidation rates in the high H<sub>2</sub>O atmospheres was attributed to the improved adherence of the scale–steel interface.

Oxide scale structures observed were found to be different on the two sides of the samples used (steel samples: 25 × 9 × 8 mm; iron samples: 25 × 9 × 2 mm) when the reaction gas was supplied at a rate of 1 litre/min. In all cases, it was found that the typical three-layered (hematite/magnetite/wustite) oxide scale structures with a smooth scale surface were observed on the sample surfaces facing the gas flow, whereas hematite and magnetite were absent at the ‘back’ surfaces and the scale had the idiomorphic [56,64], multi-faceted appearance associated with scaling in pure carbon dioxide and steam, as will be further discussed later. The relatively slow gas flow rate

could be responsible for the different scale morphologies observed on the two sides of the samples.

The oxidation rates of two medium-carbon steels under the same isothermal oxidation conditions were found to be consistently 40% lower than those of the low-carbon low-silicon steel and 70% lower than those of pure iron. What alloying element or elements contributed more to the slower oxidation rates was not discussed.

Using the isothermal oxidation data derived, the authors attempted to predict iron and steel oxidation in different reheat furnace atmospheres examined at two different heating rates, 13°C/min and 6.5°C/min, and the predicted results were compared with their experimental results. Fairly good agreement was obtained in most cases between the predicted results and the experimental results, except for steel oxidation in high oxygen atmospheres, where the scales tended to separate from the substrate during oxidation in the range of 900–1000°C.

#### *Sheasby et al.'s study*

In a study to investigate the contributions of free oxygen and water vapour in reheat furnace atmospheres to the overall steel oxidation, Sheasby *et al.* [56] examined the oxidation behaviours of two pure iron samples (with impurity carbon contents of 3 and 21 ppm) and several commercial mild steels (containing 0.17–0.27C, 0.013–0.58Mn and 0.005–0.1Si) in three gas mixtures: 4O<sub>2</sub>-N<sub>2</sub>, 20H<sub>2</sub>O-N<sub>2</sub> and 4O<sub>2</sub>-20H<sub>2</sub>O-N<sub>2</sub>. Most of the experiments were conducted at 1200°C, with some additional ones at 700°C and 900°C, for up to 3 hours. The gas flow rate was 6 litres/min, corresponding to a linear velocity of 10.4 cm/s. This gas flow rate was greater than the critical gas velocity identified by Abuluwefa *et al.* [57], as will be discussed later, and therefore the oxidation rate would not be limited by the supply rate of oxidizing gases.

In these experiments, most samples were heated to the target oxidation temperature in a protective atmosphere before the reaction gas mixture was introduced. Consistent with the observations made by others, a temperature spike, or overtemperature [37], of up to about 20°C was invariably observed at the early stage of oxidation, particularly when the oxidation experiments were conducted in free-oxygen containing atmospheres.

Interesting oxidation behaviour was observed for pure iron in 4O<sub>2</sub>-N<sub>2</sub> and 4O<sub>2</sub>-20H<sub>2</sub>O-N<sub>2</sub> gas at 1200°C. Despite the presence of a significant amount of oxygen in the atmosphere, wustite was the only product observed after oxidation for as long as 225 seconds. Initially, when observed after oxidation for 30 seconds, the scale was a smooth, fine-grained and continuous layer of wustite. However, when observed after oxidation for 225 seconds of oxidation, an uneven surface structure (originally named idiomorphic structure by Pfeil

[64]) was observed, with some grains growing much faster than others and then the protruding fronts bridging each other, leaving small pores trapped at the roots of those preferentially grown wustite grains. This pore formation mechanism was first proposed in an earlier study of Sachs and Tuck [25] and was now clearly revealed by Sheasby *et al.* Observed after oxidation for 300 seconds, the scale retained an uneven surface morphology but higher oxides, namely hematite and magnetite, were observed to cap the protruding oxide grains. After further oxidation to 600 seconds, the scale surface was flattened and uniform scale thickness and structures were developed, but the pores trapped in the early stage of oxidation remained at the inner part of the scale. The scale structure remained the same for the rest of the oxidation duration with the layer ratios of the hematite, magnetite and wustite layer approaching those identified by previous studies for iron oxidation in air and oxygen [29,30].

When pure iron was oxidized in the oxygen-free  $20\text{H}_2\text{O-N}_2$  atmosphere, a smooth, pore-free and continuous wustite layer was formed for the entire duration of the experiment at  $1200^\circ\text{C}$ . Pore-free scale structures were also observed in the scales formed at  $700^\circ\text{C}$  and  $950^\circ\text{C}$  in  $4\text{O}_2\text{-N}_2$ ,  $4\text{O}_2\text{-}20\text{H}_2\text{O-N}_2$  and  $80\text{O}_2\text{-}20\text{H}_2\text{O}$ .

Based on the above observations, it was concluded that the development of the idiomorphic structure to trap pores inside the scale layer at the early stage was the only mechanism responsible for the observation of pores in the scale formed on pure iron with very low levels of carbon content. The temperature range to form such porosities should be above  $1000^\circ\text{C}$ .

In order to reconcile the above observation of pore formation with the observation of porosities made by Rahmel and Tobolski [38] in the scale formed at  $950^\circ\text{C}$  on pure iron in  $\text{H}_2\text{O}(10\text{--}70\%)\text{-N}_2$  gases, Sheasby *et al.* conducted additional experiments using pure iron samples containing 30–100 ppm carbon, and stated that when carbon contents were more than 50 ppm, pores formed in the scales at  $950^\circ\text{C}$ . However, no micrographs were presented in the paper to support the statement. Based on the additional results obtained, the authors concluded that the pores observed by Rahmel and Tobolski [38] were likely caused by the 60 ppm carbon impurity contained in the pure iron sample they used. Although this explanation was plausible and supported by the claimed experimental evidence, the micrographs shown by Rahmel and Tobolski [38] revealed severe sample preparation damages to the scale, which had hindered the clear revelation of the true scale structures, including the claimed porosities.

For the Fe-C steels examined, pores formed after oxidation at  $1200^\circ\text{C}$  in both  $4\text{O}_2\text{-N}_2$  and  $4\text{O}_2\text{-}20\text{H}_2\text{O-N}_2$ , but the scale morphologies were different. After oxidation in  $4\text{O}_2\text{-}20\text{H}_2\text{O-N}_2$ , the scale was adherent, with pores migrating outwards and growing in size while migrating. The migrating pores also had a cap or triangle shape with the convex surface pointing

outwards, but no pores were observed at the outer region of the wustite layer. This morphology was similar to those found in the scales formed on commercial steels in the reheat furnace [25]. The pores formed in the scales developed in  $4\text{O}_2\text{-N}_2$  were very different in shape and were not migrating. Scale detachment occurred after longer than 15 minutes of exposure in  $4\text{O}_2\text{-N}_2$ . When adherent scale developed, the authors found that the kinetics of scale formation were not influenced to a great extent either by the amounts of carbon (up to 0.27%), manganese (up to 0.6%) and silicon (up to 0.1%), or by the presence of interconnected pores or isolated pores present in the scales.

#### *Abuluwefa et al.'s studies*

More recently, Abuluwefa *et al.* [35] first examined the oxidation kinetics of a low-carbon, low-silicon (0.02Si) steel (0.04C-0.2Mn) in atmospheres containing 1–15% oxygen in nitrogen at 1000–1250°C. It was found that the initial oxidation kinetics in dilute oxygen atmospheres at the temperature range examined followed the linear law and the linear rate constant was more sensitive to the gas composition, increasing with increasing oxygen partial pressure, than to the oxidation temperature. Subsequent oxidation kinetics after the formation of relatively thick scale followed the parabolic law and the parabolic rate constants were independent of the actual oxygen partial pressure, which was also the same as those obtained in air. The results indicated that once a relatively thick scale developed, solid phase iron diffusion through the wustite layer became the controlling step of steel oxidation. A critical gas velocity, beyond which the oxidation rate did not increase with the gas supply rate, was also identified through experiments. This critical velocity was found to be 4.2 cm/s at 1150°C.

Further studies were then conducted to examine the contributions of  $\text{H}_2\text{O}$  and  $\text{CO}_2$  in the oxidation of the same steel in simulated reheat furnace atmospheres in the presence or absence of free oxygen [57]. Laboratory experiments were conducted at 800–1150°C in binary  $\text{CO}_2$ (7–15%)- $\text{N}_2$  and  $\text{H}_2\text{O}$ (3–10%)- $\text{N}_2$  gases, ternary  $\text{O}_2$ (6%)- $\text{CO}_2$ (6–10%)- $\text{N}_2$  and  $\text{O}_2$ (6%)- $\text{H}_2\text{O}$ (3–6%)- $\text{N}_2$  gases, and quaternary  $\text{O}_2$ (1–6%)- $\text{CO}_2$ (10%)- $\text{H}_2\text{O}$ (3%)- $\text{N}_2$  gases at 900–1150°C.

Linear oxidation kinetics were observed for oxidation of the steel examined in the binary  $\text{CO}_2$ (7–15%)- $\text{N}_2$  and  $\text{H}_2\text{O}$ (3–10%)- $\text{N}_2$  gases and the rate constant was linearly related to the partial pressure of  $\text{CO}_2$  and  $\text{H}_2\text{O}$ , respectively. After analyses of their respective activation energy, it was concluded that the rate of oxidation in these two gases was controlled by the rate of dissociation of  $\text{CO}_2$  and  $\text{H}_2\text{O}$ , respectively, on the wustite surface.

In the atmospheres containing free oxygen, even as low as 1%, the initial rate of oxidation was primarily determined by the oxygen potential. The contributions from the  $\text{H}_2\text{O}$  and  $\text{CO}_2$  components to the initial oxidation rate

were very small and additive to that of oxygen. In other words, if the initial overall oxidation rate was expressed as

$$x = k_{l,t} t \quad 8.7$$

where  $x$  and  $t$  were total scale thickness and time, as defined previously, the total initial linear oxidation rate,  $k_{l,p}$ , in a gas mixture comprising free oxygen and either  $\text{H}_2\text{O}$  or  $\text{CO}_2$  or both could be calculated using the following equation:

$$k_{l,\text{O}_2} + k_{l,\text{H}_2\text{O}} + k_{l,\text{CO}_2} \quad 8.8$$

Assuming that the contribution made by the free oxygen was controlled by boundary layer diffusion [35] whereas those made by carbon dioxide and water vapour were controlled by the rates of surface reactions [57], the authors derived separate equations to calculate the components on the right-hand side of Equation (8.8). Based on laboratory examination results, the authors believed that when the steel was oxidized in dilute  $\text{O}_2\text{-N}_2$  atmospheres, the oxidation rate followed a linear kinetics law until the scale thickness was 400–500 microns. Thereafter, the oxidation kinetics gradually changed from linear to parabolic.

Examination of the scale structures indicated that when the experiments were conducted in binary  $\text{H}_2\text{O-N}_2$  and  $\text{CO}_2\text{-N}_2$  gases, the oxide scales contained wustite only, but when free oxygen was present, higher oxides were also observed. Unfortunately, due to the very poor metallographic sample preparation, the true scale structures could not be revealed.

The same researchers [58] then proceeded to conduct plant trials to examine the oxidation behaviour of the same steel in an industrial walking-beam reheat furnace using low (~5%) and high (18%) air/gas ratios. The measured free oxygen contents in the two atmospheres generated were 1.5% and 3% of free oxygen. In conducting the plant trials, steel coupons ( $12 \times 12 \times 3$  cm) were placed on top of a slab and carried by the slab through the furnace. To examine oxide scale thicknesses and structures at different stages of reheating, a series of samples were retrieved from the side ports of the furnace for weighing and metallographic examination.

The results of the plant trials indicated that by changing from high air/gas ratio to low air/gas ratio to reduce the free oxygen level from 3% to 1.5%, the total scale thickness generated was reduced by 35%. By comparing the trial results and the results of theoretical prediction, it was concluded that the scale growth on steel slabs during reheating in an industrial furnace was controlled by a mixed linear–parabolic mechanism. At low air/gas ratios, the linear mechanism was predominant, whereas at high air/gas ratios, the parabolic mechanism became important, particularly when thick scales developed. Therefore, when reheating at low air/gas ratios, Equation (8.8) can be used to calculate the overall oxidation rate at different temperatures when the

actual gas compositions are known. Unfortunately, poor metallographic preparation of the scale samples prevented the authors from correctly relating their kinetics data and theoretical predictions to the scale structures generated in the laboratory experiments and industrial trials.

#### *Lee and Choi's study*

Lee and Choi [59] studied the isothermal oxidation kinetics of several commercial low and ultra-low carbon steels at 1100–1250°C in air and in a gas mixture containing 85%N<sub>2</sub>-10%CO<sub>2</sub>-5%O<sub>2</sub>. The main compositions of the steels examined were 0.004C-0.6Mn-0.06Ti-<0.03Si (high strength steel), 0.003C-0.5Mn-<0.03Si (baked hardened steel) and 0.04C-0.3Mn-<0.003Si (Al-killed low carbon steel). Similar oxidation kinetics were observed for these three steels in both atmospheres. Consistent with the results of Abuluwafa *et al.* [35,57,58], the oxidation kinetics followed the linear law for a brief period and then changed to parabolic at the later stage. It was also observed from the kinetics curves presented that the initial linear kinetics periods were longer with lower oxidation rates when the samples were oxidized in the N<sub>2</sub>-10%CO<sub>2</sub>-5%O<sub>2</sub> gas as compared to oxidation in air. However, the oxidation behaviours in the very early stages were not studied in detail.

It is not clear why the author used 10% CO<sub>2</sub>, instead of water vapour, in the reaction gas to simulate steel reheating. The scales presented were all detached from the steel substrates with some minor preparation damage inside the scale layers, but the typical porous scale structures normally observed in mill scales were not generated in their simulations. This formed a clear contrast to the situation presented by Sheasby *et al.* [56] who demonstrated that the typical porous scale structure could be reproduced in an atmosphere containing N<sub>2</sub>-20H<sub>2</sub>O-4O<sub>2</sub>. This poses a question whether porosities can actually form without the presence of water vapour in the atmosphere. Further studies will be required to clarify this.

#### *Oxidation in CO<sub>2</sub>, CO<sub>2</sub>/CO, H<sub>2</sub>O and H<sub>2</sub>O/H<sub>2</sub>*

The contributions of H<sub>2</sub>O and CO<sub>2</sub> components to the overall oxidation kinetics revealed were also supported by previous studies on iron and steel oxidation in pure CO<sub>2</sub> [33,65–69], pure H<sub>2</sub>O [33,69], CO<sub>2</sub>-CO mixtures [65, 67–68, 70–73] and H<sub>2</sub>O-H<sub>2</sub> [74] mixtures. It had been observed that iron and steel oxidation in pure CO<sub>2</sub> and CO<sub>2</sub>/CO initially followed the linear kinetics law as the oxidation kinetics were controlled by surface reaction or the rate of gas phase dissociation. At the later stage, the reaction followed the parabolic law as diffusion of iron through the wustite layer became the controlling step. Similar patterns of oxidation kinetics were also observed for oxidation in H<sub>2</sub>O [33] and H<sub>2</sub>O-H<sub>2</sub> gas mixtures [74] but the rates were generally

greater. In both cases, the scale generated was a single layer of wustite in the initial stage, even in the situation where magnetite and hematite were thermodynamically stable.

Although the oxidation rates of iron and steel in H<sub>2</sub>O and CO<sub>2</sub> were much lower than those in oxygen and air in the initial stage, the scale thicknesses developed in all gases after several hours of oxidation at high temperatures became comparable [40,69]. It was believed that the poorer scale–steel interface adhesion after a longer time of oxidation had slowed down the oxidation rates of iron and steel in oxygen or air, allowing those in H<sub>2</sub>O and CO<sub>2</sub> to catch up [33,69].

#### *Oxidation in substoichiometric combustion gases*

The discussions above have been limited to iron and steel oxidation in the atmospheres produced by excessive air combustion, i.e. more than 100% of combustion air was used, and therefore the atmosphere contained a certain amount of free oxygen. More recently, Lee *et al.* [60] extended the gas composition range to the substoichiometric regime.

Scale-free reheating using extremely substoichiometric combustion was closely examined in the late 1960s to early 1970s [53,75]. In theory, to achieve scale-free reheating, the percentage of combustion air should be reduced to about 50%. In practice, varied air/gas percentages were proposed to achieve minimized-scale reheating by heating at 100% air at temperatures below 760°C, at 100%–50% combustion air in the range of 760–1040°C and at 50% combustion air at temperatures above 1040°C. Despite the apparent advantage in reducing steel yield loss during reheating, the concept and technology have not been adopted by the steel industry and no further development was undertaken until very recently [16]. The actual reasons for this were unclear, but the main issues could be the high cost of implementation, less reliable operation because of the low air–fuel ratios to be used, and safety concerns as a result of potential release of carbon monoxide to the surroundings of the furnace. In addition, a certain amount of scaling is usually required for slab reheating to remove surface defects and mould powder on the slab surface.

In a project conducted from September 2005 to August 2006 sponsored by the US Department of Energy in partnerships with many US steel companies, the scale-free reheating concept was assessed again [16]. At the completion of the project, it was concluded that 64% of the reheat furnaces in the US steel industry could be converted to scale-free reheat furnaces. The potential benefits of adopting scale free reheating included increased yield by 1% to 2%, reduced total energy consumption and cost of steel production and improved product quality. Recommendations were made to move the project into its second phase to conduct plant testing to identify various issues that

need to be resolved with an aim to identify potential pilot unit installation at the end of Phase II.

Instead of examining the extreme case, Lee *et al.* [60] examined the oxidation behaviour of a low carbon and low silicon steel in the atmospheres generated by 95% and 99% stoichiometric combustion airs as compared to that exhibited at 101%, 108% and 112% excess combustion airs. The compositions of these gas mixtures are shown in Table 8.4. It was found that parabolic kinetics were followed for oxidation in the atmosphere generated by 112% excess air, which contained free oxygen of 2.1%. When oxidized in the atmosphere produced by 108% excess air (containing 1.4% free oxygen), initial linear followed by parabolic kinetics were observed, and the linear kinetics were observed for oxidation in the atmosphere generated by 95, 99 and 101% air combustion. Interestingly,  $\text{Fe}_3\text{O}_4$  was thermodynamically stable in the gas mixtures generated by 95, 99 and 101% air, but only wustite was observed in all scales formed in these atmospheres.

Using gas diffusion theory, the fluxes of various oxidizing agents, namely free oxygen, water vapour and carbon dioxide, were calculated and compared with the actual oxygen intake by the scale. The results indicated that in any of the gas mixtures used, the free oxygen fluxes were far from sufficient to sustain the observed oxidation rates, but those of  $\text{CO}_2$  and  $\text{H}_2\text{O}$  were sufficient. Accordingly, it was concluded that the principal reactant for steel oxidation was not free oxygen; instead,  $\text{CO}_2$  and  $\text{H}_2\text{O}$  were the dominating reaction species, in all cases, even in the gases containing free oxygen.

Clearly, the conclusions made by Lee *et al.* [60] were in disagreement with those obtained by Abuluwefa *et al.* [57,58] for oxidation in the gas mixtures containing free oxygen. As discussed earlier, Abuluwefa *et al.* [57,58] concluded that in the presence of free oxygen, the main oxidizing species was oxygen although  $\text{H}_2\text{O}$  and  $\text{CO}_2$  also contributed to the oxidation process, with the overall oxidation rate being the sum of the contributions made by the three gas species. The apparent inconsistency can be resolved by comparing the gas flows used in these studies.

By examining the experimental details of Lee *et al.*'s study, it was noticed that the gas flow rate used was very low at 0.24 cm/s as reported in the open

Table 8.4 Gas compositions (%) used in Lee *et al.*'s study [60]

Air (%)	$\text{CO}_2$	CO	$\text{N}_2$	$\text{O}_2$	$\text{H}_2\text{O}$	$\text{H}_2$
112	8.6	$4 \times 10^{-5}$	72	2.1	17	$4 \times 10^{-5}$
108	8.9	$4 \times 10^{-5}$	72	1.4	18	$4 \times 10^{-5}$
101	9.4	$1 \times 10^{-4}$	72	0.19	19	$1 \times 10^{-4}$
99	9.4	0.19	71	$8 \times 10^{-8}$	19	0.19
95	8.9	0.96	70	$3 \times 10^{-9}$	19	1.0

publication [60] or 0.31 cm/s ( $300 \text{ cm}^3/\text{min}$ ) through a tube furnace with a 35 mm inner diameter) as reported in the original PhD thesis [76]. This was only 5% of the critical gas velocity (4.2 cm/s) identified by Abuluwefa *et al.*, [57], beyond which the steel oxidation rate does not increase with increased gas flow rate, and only 2% of the actual gas flow rate used by Abuluwefa *et al.* It was mostly likely that the gas flow rate used in Lee *et al.*'s study was too small to sustain reactions involving free oxygen. As a result, the free oxygen in the gas stream would be quickly consumed by the oxidation reaction as soon as the gas mixture entered the reaction chamber. Once free oxygen was consumed, the subsequent oxidation process was sustained by the remaining reactions between the steel and  $\text{H}_2\text{O}$  and/or  $\text{CO}_2$ , as concluded in their study.

### *Summary*

Summarizing the above studies on iron and steel oxidation in reheat furnace atmospheres, it can be concluded that:

- Oxidation of iron and steel in reheat furnace atmospheres initially follows the linear rate law. The initial period can be very long when the free oxygen concentration is low or absent.
- The initial linear oxidation rate is more sensitive to oxygen content than to temperature.
- During the linear oxidation period, the contributions from various oxidation species were additive, i.e. the total oxidation rate is the sum of the oxidation rates contributed by all participating gases, with free oxygen being the predominant one.
- The initial period is significantly shortened when the free oxygen concentration is relatively high.
- In the initial oxidation period, only wustite forms as oxidation product. Initially, wustite forms as a smooth layer with uniform thickness, then as a result of preferential growth of selective grains, an irregular or idiomorphic structure develops.
- After the initial linear period, the oxidation kinetics became parabolic if the scale remains adherent. The oxidation rate became independent of the oxygen concentration and concentrations of other gas species at the parabolic oxidation stage.
- When the kinetics become parabolic, higher oxides (magnetite or magnetite and hematite) form as the outer layers of the scale.
- In principle, there is a critical scale thickness at which the oxidation kinetics change from linear to parabolic. Such a critical scale thickness has not been determined.

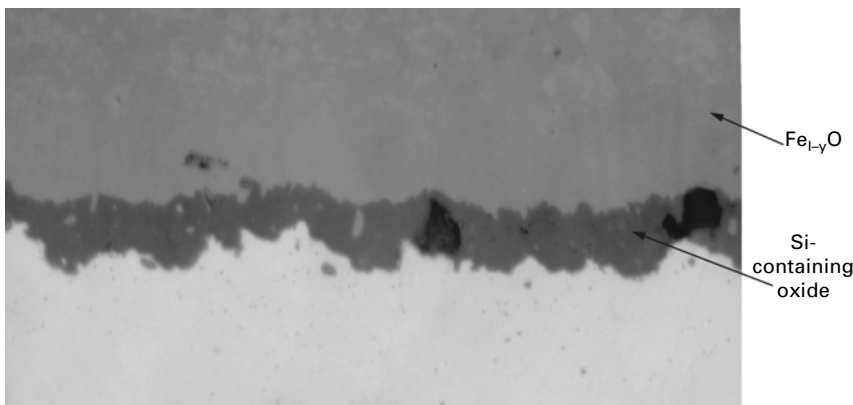
### 8.2.5 Effects of alloying elements

The oxidation behaviours of many commercial steels have been examined in various previous studies [33,35,45,56–60,77]. However, none of these studies was designed to systematically examine the effects of various alloying elements. As mentioned earlier, it was generally accepted that the oxidation rate of steel was slower than that of pure iron under the same oxidation conditions. Among all the alloy elements present in low carbon steels, silicon was the most important one.

The effects of silicon on steel oxidation are multi-fold. First, the presence of a small amount of silicon results in the formation of a uniform fayalite ( $\text{Fe}_2\text{SiO}_4$ ) layer at the scale–steel interface at temperatures below 1150°C. A typical fayalite layer formed on a steel containing 0.05C-0.7Mn-0.3Si at 1150°C for 5 minutes in moist air (containing 2.8%  $\text{H}_2\text{O}$ ) is shown in Fig. 8.8. Formation of this layer generally provided good protection to the steel [46]. It also strengthens the bond between the wustite layer and the steel substrate and can cause incomplete descaling [78,79]. One typical consequence of incomplete descaling prior to finishing rolling is the generation of red scale on hot rolled strip [80,81]. In addition, when the reheat temperatures are too high, the presence of silicon in steel can cause the following eutectic reaction to take place at the scale–steel interface at temperatures above 1178°C [82]:



where  $\text{L}_{01}$  is a molten phase. The formation of this molten phase can drastically increase steel oxidation rate and cause localized surface defects [83,84].



8.8 A silicon-containing oxide layer (presumably fayalite) formed on a low carbon steel containing 0.05C-0.28Si-0.57Mn at 1100°C for 5 min in moist air (2.8%  $\text{H}_2\text{O}$ ). The total scale thickness is 0.5 mm with a typical three-layered hematite/magnetite/wustite structure (not shown) [46].

This molten phase can even form in steels containing very low levels of silicon and promote intergranular oxidation [85]. As a result of the much greater affinity between silicon and oxygen (than iron and oxygen), even with very low silicon contents in the steel, fine internal silicon-containing oxide particles are often found to disperse at the surface layer of the steel substrate [85,86], which can be detrimental to the steel surface properties and downstream steel processing, such as metallic coating. To minimize this detrimental effect, a fine balance between external oxidation and internal oxidation should be maintained [86,87]. Kinetics inversion [88] with greater oxidation rates at lower temperatures was also observed in the oxidation of Si-containing steel in an N<sub>2</sub>-27%H<sub>2</sub>O environment [89]. The greater silicon diffusivity at higher temperatures was believed to have promoted the formation of a more protective Si-containing oxide layer next to the steel substrate. The above effects will require a separate review and will not be discussed further in this chapter.

Residual elements, such as nickel, copper and tin, are normally found in the steels made from or substantially from scrap steels. The presence of these elements in the steels had some effects on their oxidation kinetics but these were not significant [97,98]. The main concern with the presence of copper and tin is surface hot shortness, which is caused by the presence of a molten copper-rich phase on the steel surface as a result of steel oxidation. This molten copper-rich phase can penetrate austenite grain boundaries and cause surface cracking during subsequent hot rolling. Nickel is beneficial in alleviating surface hot shortness but it can cause sticky scale as a result of network-like internal iron oxide formation. Further discussion of surface hot shortness behaviour is beyond the scope of the current review.

In the study carried out by Lee and Choi [59], internal oxides were invariably observed in several commercial low and ultra-low carbon steels containing very low levels of silicon (<0.03%) and relatively high levels of manganese (0.3–0.6%). The main species of the internal oxides was identified to be manganese oxide. The presence of internal manganese oxide has not been reported in other studies. Other elements, such as Si, Ti, S and P, were also found in some of the internal oxides.

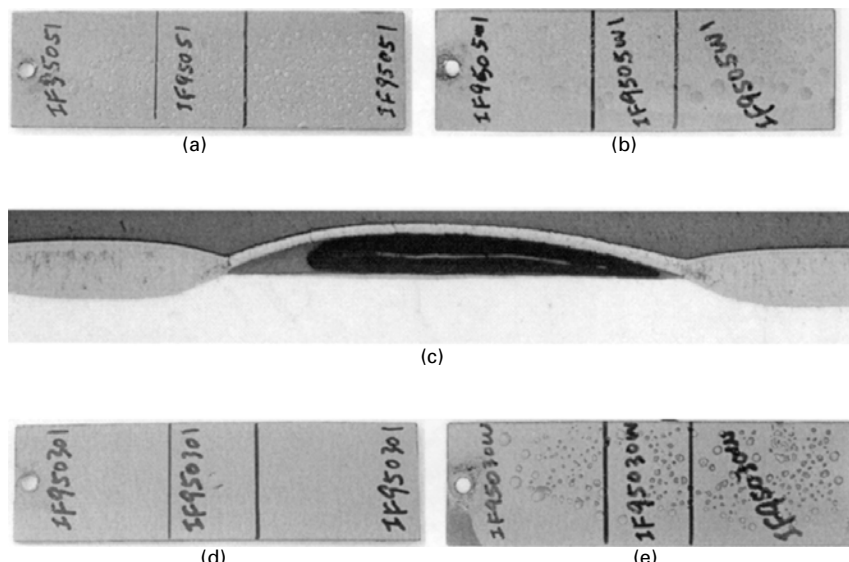
In other recent studies of Chen and Yuen [45,46], the oxidation behaviour of a Ti-IF steel (Al-killed) was found to be completely different from those of iron and Al-killed low carbon steel. Because of its very low carbon content and low levels of other alloying elements, this steel was expected to behave similarly to pure iron. However, much slower oxidation rates were observed at temperatures below 850°C. The scale structures developed were also different. At 700–800°C, the steel was very resistant to oxidation with very thin scale formed even after several hours of exposure to dry air (<0.1% H<sub>2</sub>O) and moist air (2.8% H<sub>2</sub>O), although the rates were higher in the latter case. The oxidation resistance was reduced partially at 850°C and lost nearly

completely at temperatures above 900°C. Bubble-like blisters were observed at 850–950°C and more were observed after oxidation at 950°C for a short time (Figs 8.9(a) and (b)). By examining the cross-sections of the scales, e.g. Figure 8.9(c), it appeared that the blisters were more likely formed at the very early stage of isothermal holding, rather than during subsequent cooling as originally thought [45]. More interestingly, the blisters were buried in the scale after oxidation at 950°C for 30 minutes in ambient air, Fig. 8.9(d). An addition of 2.8% of water vapour in the airstream appeared to have prolonged the time to bury the blisters formed at the early stage, Fig. 8.9(e).

The mechanisms responsible for the observed peculiar oxidation behaviours were still not clear. It was likely that the presence of a relatively high level of titanium and perhaps aluminium could have played a role but further studies will be required to clarify this. Similar peculiar oxidation behaviours were not reported in other studies of IF steel oxidation.

### 8.2.6 Porosity in scale

Porosity in scale had been reported in many previous studies. Generally, three types of porosities are reported; genuine porosity formed inside the scale during steel oxidation, porosity generated during cooling due to mismatch of thermal expansion coefficients between the steel substrate and different



8.9 Oxide scales formed on a Ti-IF steel after oxidation at 950°C in nearly dry air (<0.1% H<sub>2</sub>O) and moist air (2.8% H<sub>2</sub>O): (a) 5 min in dry air; (b) 5 min in moist air; (c) cross-sectional observation of a bubble-like blister shown in (a); (d) 30 min in dry air; (e) 30 min in moist air.

scale layers, and artefact porosity caused by damages incurred during metallographic sample preparation. Unfortunately, many studies had wrongly treated the latter two types as genuine porosity, and even sometimes developed in-depth fundamental theories to interpret the artefacts generated. One possible reason for this was the lack of understanding of how to prove whether genuine porosities are present in the scale or otherwise.

Based on the experiences of the present authors and those of others, several methods can be used to prove the existence of genuine porosity in the scale. One of the most commonly used methods was to use scanning electron microscopy (SEM) to examine the fractured cross-sections of the oxide scale [90–94]. This method is called the fractographic method. To prepare a sample for fractographic analyses when the scale is attached to the steel substrate, it may be necessary to immerse the sample in liquid nitrogen for a few minutes to embrittle the steel substrate. To examine porosity at the scale–steel interface, the scale layer can be removed by stripping using a strong adhesive. When the scale–steel interface adhesion is too strong, some forms of other mechanical aids should be used [95].

In order to observe the genuine porosities, their distributions in the scale and their interrelation with the scale microstructure, careful preparation of the metallographic sample is unavoidable. Superb metallographs have been presented in the studies of Païdassi [30] and Sheasby *et al.* [56]. The details of a method used in the present authors' laboratories to reveal the scale structures formed on steel strips [5,36,46,96–98] were described in a recent paper [83]. The method allowed the authors to examine oxide scales on various hot rolled strips to thicknesses as thin as one micron. It was later found that, using the principles described, a very efficient way was to combine automatic grinding and coarse polishing using an automatic polisher with manual polishing for the last polishing steps.

In a recent study conducted by Jonsson *et al.* [99], a focus ion beam milling method was used to generate a smooth cross-section of the oxide scale for analyses. The study produced some very high quality images, although some artefact porosities were still visible in several of the images shown.

There were several types of genuine porosities observed by various researchers. The first type was a void observed in the magnetite layers formed on iron and steel at temperatures below 570°C [91,93], where the gas used could be moist air, dry air or CO<sub>2</sub>. The voids were very fine in size and were observed at grain boundaries as well as inside magnetite grains. This type of porosity is also known as Kirkendall voids [100]. The formation of voids appeared to be associated with the formation of a duplex scale structure [101]. Recently, some theoretical treatments using conventional diffusion theories were made by Maruyama *et al.* [102] and Ueda *et al.* [92] to provide a semi-quantitative and quantitative explanation of their formation mechanism and their location in the scale.

The second type of genuine porosity was that produced using carefully planned experiments by Sheasby *et al.* [56]. This type of porosity was only observed in the wustite layer and only formed at the very early stage of oxidation. As discussed earlier, they were formed as a result of preferred growth of some wustite grains into a so-called idiomorphic surface structure, which was followed by bridging of the protruding fronts, thus trapping pores or voids at the roots of those fast-growing grains. These voids or pores would remain at the region near the scale–steel interface if the steel was exposed to dry oxygen or air. However, they were able to migrate outwards if water vapour was present in the gas phase. The conditions of formation of this type of pore were identified as (1) the oxidation temperature must be sufficiently high (e.g. above 1000°C) and (2) there must be free oxygen present in the gas phase.

The third type of porosity was that normally observed in mill scales. Generally, oxide scales generated in the reheat furnace comprised a dense population of porosities at the inner region of the wustite layer. The porosity population decreased but the size increased towards the mid-section of the wustite layer. No porosities were observed at the outer region of the wustite layer or inside the magnetite or hematite layers. Similar porosity morphology was also observed in Sheasby *et al.*'s study [56] in the scales formed on pure iron containing more than 50 ppm of carbon and on carbon steels under laboratory simulation conditions (5O<sub>2</sub>-20H<sub>2</sub>O). However, when the oxide comprised a single wustite layer, pores were not observed. It was likely that when the scale comprised a wustite phase only, the scale was plastic and as a result it was able to annihilate any vacancies generated so that void formation at the scale–steel interface was avoided. However, once higher oxides, i.e. magnetite and hematite, formed, the wustite layer could not deform freely to maintain the scale–steel contact. In this case, with the outward diffusion of iron ions, vacancies would accumulate to form voids at the scale–steel interface, which would then migrate away into the scale via the void migration mechanisms proposed by Rahmel and Tobolski [38].

The porosities discussed above are those normally observable under a microscope or SEM. They probably belong to a different regime from those of very fine pores (<50 nm) discussed by Anghel *et al.* [103]. Unfortunately, even in a study dedicated to the discussion of various fine ‘pores’, the only optical image shown in Anghel *et al.*'s study revealed numerous artefact porosities generated by poor sample preparation.

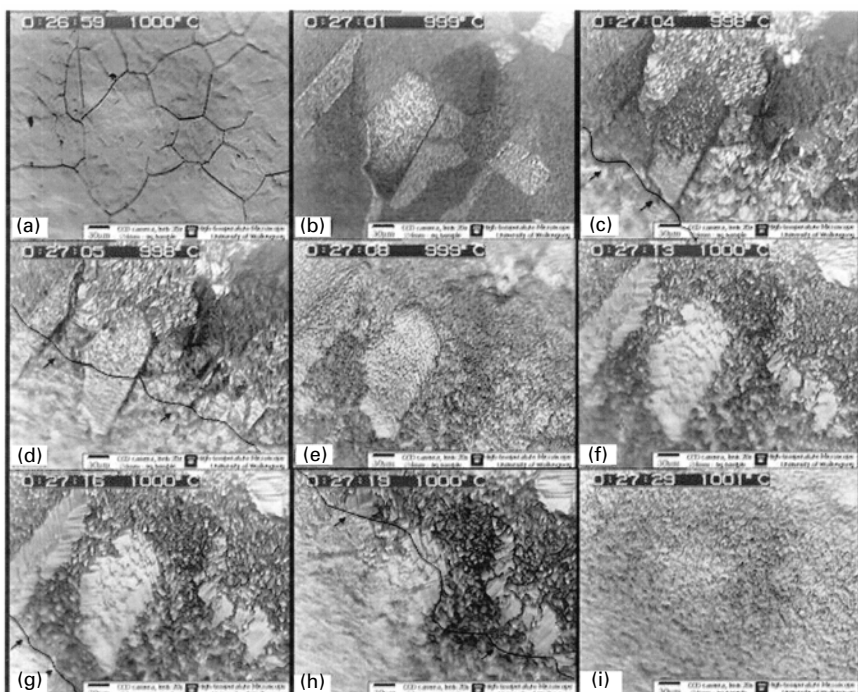
### **8.3 Short-time oxidation of iron and steel**

In very early stages of iron oxidation, the oxidation kinetics usually show a different pattern, as the scale structure may be different from those developed in the later stages. One contributing factor was the ‘overtemperature’ [37] or

temperature ‘spike’ phenomenon [56] as mentioned earlier. Other factors include inconsistent gas composition and scale structures as also discussed earlier. This early kinetics pattern was thought to have no effect on the oxidation kinetics at the later stages [56].

A number of recent studies have focused on steel oxidation within a short time at high temperatures [104–109]. Understanding short-time oxidation is important in strip hot rolling because ‘old’ and thick scales formed on the strip surface should be removed prior to hot rolling. This is achieved by hydraulic descaling. After descaling, a new oxide layer forms before the strip enters the rolling mill. The times allowed for the growth of the new scale vary but they are generally very short. Therefore it is important to understand the oxide thickness and structure formed within the very short time prior to hot rolling and the behaviour of the scale formed during hot rolling.

Using a high temperature microscope equipped with a CCD camera capable of taking 24 frames of photos per second, Melfo and Dippenaar examined steel oxidation within 30 seconds upon exposure to oxygen at 880–1050°C [104,105] and made some interesting observations. The images shown in Fig. 8.10 revealed how the surface morphology changed with time when a steel sample was oxidized in air at 1000°C.



8.10 Oxide scale surface morphology evolution at the very early stage of oxidation in flowing air (flow rate 50 cm<sup>3</sup>/s) at 1000°C [104].

At the beginning of oxidation, sharp austenite grain boundaries were visible on the sample surface (Fig. 8.10(a)). Within the first 4 seconds of exposure to air, oxide nuclei randomly formed and grew on the steel surface with sharp austenite grain boundaries still visible (Fig. 8.10(b)). The oxide formed was believed to be wustite. At the fifth second, a new, finer oxide region seemed to form at the left-bottom corner (Fig. 8.10(c)), which then rapidly swept through the entire surface within several seconds (Figs 8.10(d), (e)). After this sweeping action, the finer oxide grew to an appearance similar to that of the original oxide at the time the sweeping action started. At this stage, the original austenite grain boundaries were still vaguely visible (Fig. 8.10(f)). At about the fifteenth second, another sweeping action was observed with a fine oxide region forming at the same corner and then sweeping through the entire surface again within several seconds (Figs 8.10(g), (h)). After this second sweeping action, the original austenite grain boundaries were wiped off and the sample surface appeared uniform and featureless (Fig. 8.10(i)).

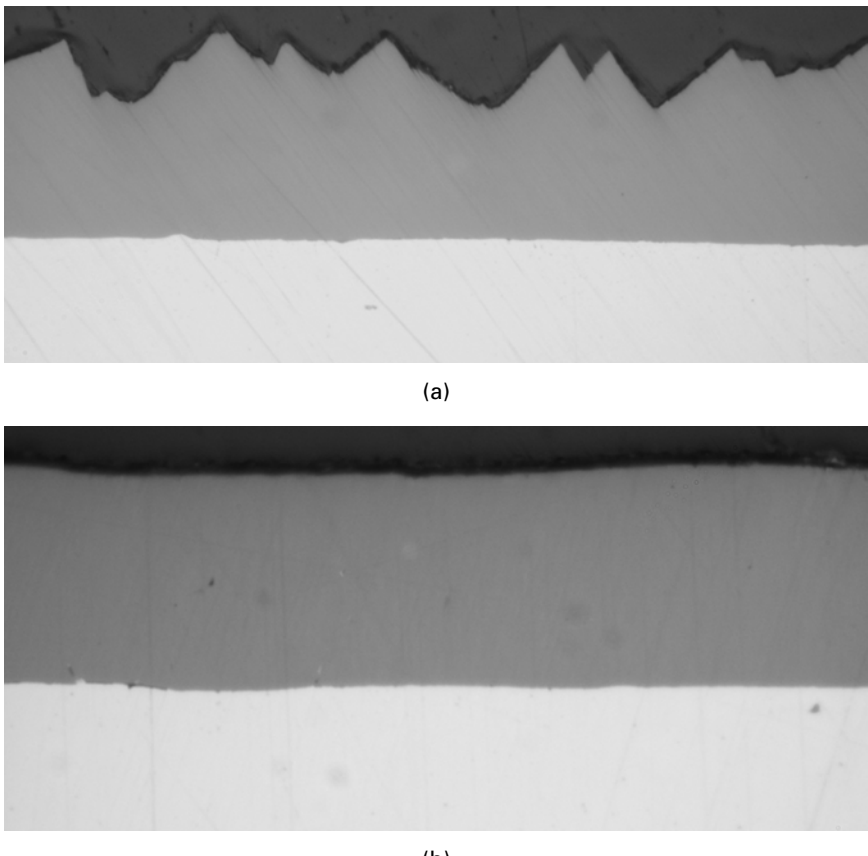
For the sample oxidized at 1050°C, two sweeping actions were observed within 30 seconds, but the oxide grains were much larger. The austenite grain boundaries were wiped off at the first sweeping action at about the tenth second and the sweeping action was completed within only one second.

Without further analyses to provide more evidence, the products of the two sweeping actions were thought to be phase transformation processes, with the first transforming wustite to magnetite and the second transforming magnetite to hematite, or pseudo-magnetite for the first sweeping action which was reduced back to wustite subsequently during further growth and a final stable magnetite phase formed in the second sweeping action.

To examine the correctness of the mechanisms proposed by Melfo and Dippenaar, some laboratory experiments were conducted using similar oxidation procedures [106]. A series of samples were exposed to flowing air for 6, 12, 18, 24 and 30 seconds, after they were heated to a target temperature of 1000°C and equalized at this temperature for several minutes in high purity argon. After each exposure, air flow was replaced immediately with high purity argon flow and the sample was cooled rapidly in argon to room temperature. The sample surface and cross-sections were then examined using optical microscopy and SEM, and the scale structures were analysed using XRD. It was found that, although there were differences in the surface topography, the entire scale layers on all samples were all occupied by a single wustite layer, as typically shown in Fig. 8.11(a) and (b).

In the study carried out by Sheasby *et al.* [56] it was found that a single layer of wustite formed at 1200°C for a short time in 4O<sub>2</sub>-N<sub>2</sub>, which was smooth initially after 30 seconds of exposure, similar to that shown in Fig. 8.11, but became irregular after 210 seconds of exposure.

In some more recent studies carried out by Suárez *et al.* [107–109], the



8.11 (a) and (b) Single layer wustite observed on 0.05C-0.21Mn steel after oxidation at 1000°C for 24 seconds in flowing air (500 $\times$ ) [106].

oxide scale structures developed on an ultra-low carbon steel containing 0.005C-0.078Si-0.55Mn-0.063Ti in dry air for 1 to 480 seconds at 1050°C [107] and for 1 to 240 seconds at 950°C, 1050°C and 1150°C were examined. Excellent metallographs were produced in these studies. Based on their observations, it was concluded that within the oxidation durations examined, a single layer of wustite was invariably developed on the steel.

The above observations of a single layer of wustite on low carbon, low silicon steel at the very early stage of oxidation at high temperatures were also supported by a recent study of Henk Bolt [110] who used high temperature X-ray diffraction to monitor the oxide scale structure evolution at different stages in a laboratory simulation of finishing rolling, cooling and coiling of steel. It was found that when tertiary scale started to grow after descaling, wustite formed first and it took some time for magnetite to grow.

One common condition used in the experiments described above to examine the short-term oxidation of steel was to heat the steel sample in a protective atmosphere and hold it at the target temperature for a short time before the commencement of each oxidation experiment. In this way, steel oxidation during heating was suppressed. Such a simulation process would be much closer to the oxidation of a steel surface after hydraulic descaling.

Based on the discussion above, it can be concluded that oxide scale formed in air within a very short time at the rolling temperatures is a thin, single layer of wustite. However, more studies will be required to explain the sweeping actions observed by Melfo and Dippenaar.

The finding of a single wustite layer development within a very short time at the rolling temperatures (950–1150°C) is very important in steel processing. It has been thought by many that the scale would be multi-layered when it enters the roll-bite of the first stand of the finishing mill. Based on the discussion above, the scale structure entering the roll-bite is actually a very deformable single-layered wustite, which would deform with the steel substrate readily if its temperature is sufficiently high.

With the improved understanding of the oxide scale structure entering the finishing mill, some related questions can be raised:

1. What would be the scale structure developed after each rolling reduction and regrow between two rolling stands?
2. What would be the scale structure immediately after finishing rolling?
3. How does the scale grow on the run-out table?
4. Finally, what would be the final scale structure at the time of coiling?

As the scale is very thin (less than 30 microns) during finishing rolling and the finishing rolling temperatures are high (normally in the range of 1050–850°C), based on the results and discussion presented earlier, it would be expected that the oxide scale would retain a wustite structure throughout the finishing rolling process. Then, upon water cooling, which has a quenching effect, this wustite structure, at least the main part of it, would be retained throughout the run-out table [96]. At the time of coiling, in theory, wustite would be expected to be the main or the sole component of the scale. However, formation of higher oxides (magnetite and hematite) cannot be excluded. Henk Bolt [110] had suggested that once the magnetite layer formed, it would grow quickly. In our previous study on the oxide scale structures formed on hot rolled strip [5], three-layered scale structures were observed on the samples taken from the outer wrap of the coil immediately after coiling. However, the samples taken were allowed to cool in ambient air. Higher oxides (magnetite and hematite) would have developed on the wustite layer during cooling in air. Further studies are clearly required to clarify this.

After coiling, this wustite layer will grow at the expense of higher oxides (if they formed), be enriched with iron, and eventually undergo the decomposition process at the centre region of the coil, where oxygen is depleted, but be oxidized to form higher oxides at the edge regions, developing into the room temperature structures presented previously [5].

## 8.4 Deformation and failure of oxide scale during hot rolling

Hot rolling is an essential step in the manufacture of hot rolled strip, even in the Castrip® process (Fig. 8.2(b)). Table 8.5 lists the hot rolling conditions in different strip processing processes. Although hydraulic descaling is applied prior to either roughing rolling or finishing rolling, a fresh oxide scale layer always forms on the newly exposed steel surface before the steel enters the roll-bite of either mill. The scale thickness and structure at the time of rolling would depend on the temperatures and time allowed for the scale to grow after each descaling step.

In the case of finishing rolling, it has been demonstrated that in most cases, the scale thickness was less than 30 microns when the transfer bar enters the finishing mill. At such a thickness, the scale would comprise a single layer of wustite only, as discussed above. The scale thickness entering the roughing mill would be relatively thick at some passes when descaling is not applied at all passes. Even in this case, based on the discussion above, it could still comprise a single layer of wustite or at least contain a wustite layer as its main component. Therefore, the mechanical properties of the wustite layer at the respective rolling temperature ranges for roughing rolling and finishing rolling would determine the deformation behaviour and perhaps

*Table 8.5 Hot rolling conditions for various processing routes*

Rolling step	Conventional	Thin slab casting – direct rolling	Castrip® process
Roughing rolling	<ul style="list-style-type: none"> <li>▪ Multi-stands or multi-passes</li> <li>▪ Up to 40% reduction at one pass [127]</li> </ul>	<ul style="list-style-type: none"> <li>▪ 0–2 stands</li> <li>▪ 1100–1150°C</li> </ul>	No
Finishing rolling	<ul style="list-style-type: none"> <li>▪ Multi-stands</li> <li>▪ Up to 50% reduction at one stand</li> <li>▪ Rolling temperatures: 850–1100°C</li> </ul>	<ul style="list-style-type: none"> <li>▪ Multi-stands</li> <li>▪ Up to 50% reduction at one stand</li> <li>▪ Rolling temperatures: 850–1100°C</li> </ul>	<ul style="list-style-type: none"> <li>▪ One or two stands</li> <li>▪ Up to 30% reduction at one stand</li> <li>▪ Rolling temperature: 1000–1100°C</li> </ul>

failure mode of the scale in these processes. For rolling strips with thicker scales on them, a good understanding of the mechanical properties of hematite and magnetite at the rolling temperatures would be also important.

#### 8.4.1 Mechanical properties of oxide scales

The mechanical properties were investigated in some early studies. In these studies, the creep properties [111], tensile strengths [112], flow stress [113] and high temperature hardness [113,114] of various oxides were measured. The mechanical properties of wustite were also related to scale–steel interface adhesion [115] and marker movement [116] in the wustite scale layer. Based on these early studies, it was concluded that at temperatures above 800°C, wustite was deformable, and even in the range of 650–800°C, wustite still possessed certain plasticity [117], while magnetite and hematite were not deformable even at 1000°C.

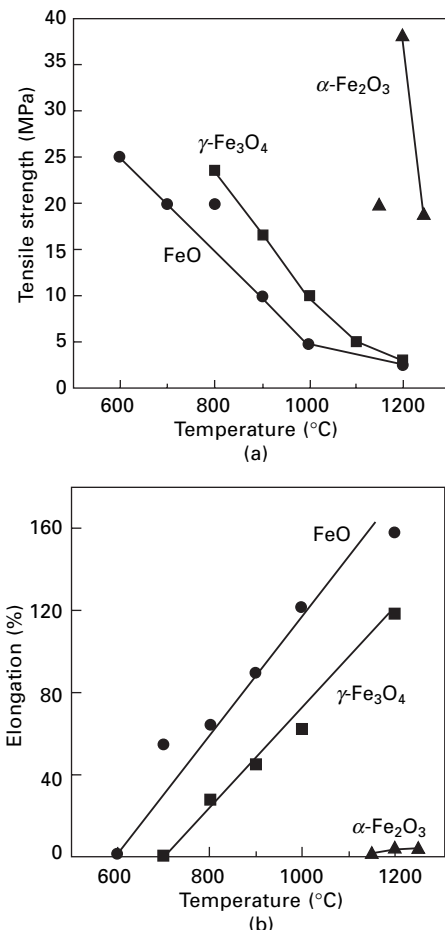
Some more recent attempts were made to construct deformation mechanism maps for the three oxides, namely wustite, magnetite and hematite [118–120]. Deformation mechanism maps were introduced by Ashby and Frost [121] as a tool to identify the predominant deformation mechanisms and the rates of deformation (strain rates) under certain stress and temperature conditions for solid metals and ceramics. However, the maps constructed for iron oxides were primarily based on theoretical calculation because experimental data available were very limited and estimation was based on data from other oxide systems.

Recently, Echsler *et al.* [122,123] studied the deformation behaviours of thick iron oxide scale (>100 µm) growing on a mild steel containing 0.04C-0.15Si-0.2Mn using a four-point-bend method at 800, 900 and 1000°C in dry air, humid air (7–19.5%) and laboratory air at strain rates of  $3.7\text{--}4.7 \times 10^{-5}\text{ s}^{-1}$  and  $3.6\text{--}4.6 \times 10^{-4}\text{ s}^{-1}$ . Their experimental results confirmed that the theoretical calculation results of Frost and Ashby [118] were reasonably accurate. Their results also indicated that the moisture content in air had very little effect on the plasticity of the scale within the temperatures examined. The four-point-bend method (called differently the four-point hot-bending method or 4PHBT) was also used by Picqué *et al.* [124] to study the mechanical properties of 70–100 µm thick oxide scales formed on an extra low carbon steel. The strain rates used for the experimental studies were in the range of  $7 \times 10^{-5}$  to  $1.4 \times 10^{-2}\text{ s}^{-1}$ . It was found that the scale plasticity increased with temperature, with a transition temperature around 700°C at the lowest strain rates and higher at higher strain rates.

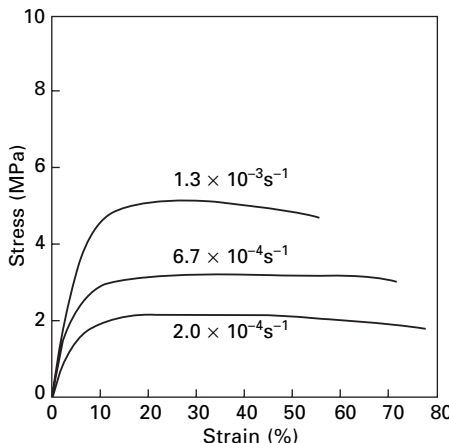
In another recent study carried out by Hidaka *et al.* [125,126], the deformation and fracture behaviour of pure FeO, Fe<sub>3</sub>O<sub>4</sub> and Fe<sub>2</sub>O<sub>3</sub> were investigated using tensile testing methods at 600–1250°C at strain rates of  $2.0 \times 10^{-3}$  to  $6.7 \times 10^{-5}\text{ s}^{-1}$ . This study clearly demonstrated that in the range

of strain rates examined, wustite possessed good plasticity at temperatures above 700°C, whereas the temperature range at which magnetite started to show good plasticity was above 800°C. In contrast, hematite did not show any plasticity even at 1250°C. The apparent tensile strengths and fracture elongations for these three oxides measured at a strain rate of  $2.0 \times 10^{-4} \text{ s}^{-1}$  are shown in Fig. 8.12 [125]. The deformation behaviour of wustite and magnetite were also affected by strain rate, as seen in Fig. 8.13 for wustite at 1150°C [126]. It is seen that the tensile strength increases and the fracture elongation decreases significantly with strain rate increasing from  $2.0 \times 10^{-4} \text{ s}^{-1}$  to  $1.3 \times 10^{-3} \text{ s}^{-1}$ .

The above studies were all conducted under very slow strain rates and



8.12 (a) Apparent tensile strength and (b) fracture elongation of FeO,  $\gamma\text{-Fe}_3\text{O}_4$  and  $\alpha\text{-Fe}_2\text{O}_3$  measured at a strain rate of  $2.0 \times 10^{-4} \text{ s}^{-1}$  [124].



8.13 Stress-strain relationships of FeO at various strain rates at 1150°C [125].

Table 8.6 Strain rates at various stands of a five-stand finishing mill [127]

Stand	Reduction (%)	Average contact time (s)	Average strain rate ( $\text{s}^{-1}$ )
F1	52.5	0.041	13
F2	47.5	0.015	32
F3	32.5	0.0059	54
F4	27.5	0.0030	92
F5	12.5	0.0017	74

provide some insights into the plasticity of different oxides under those conditions. However, the following are known:

- The strain rates during hot rolling of strips are much higher at  $1\text{--}10^4 \text{ s}^{-1}$ . Table 8.6 lists the average strain rates measured at all stands in a five-stand finishing mill for rolling a 30 mm transfer bar into a 2.6 mm thick hot strip [127].
- The strain rate on the surface layer is greater than the average strain rate during hot rolling if the steel strength across its thickness is uniform.
- The strain amounts (reduction in thickness) during hot rolling of steel strip are much greater (10–50%) than those introduced in previous laboratory studies.
- The true strength increases with both strain rate and strain amount [128].

In other words, although the scale shows good plasticity at low strain rates and smaller strains, the plasticity may be lost or partly lost when the strain rates and/or the strain amounts are high.

On the other hand, the scale plasticity and strength may be quite different when the scale adheres well to the steel substrate and the thickness is small, as pointed out by Douglass [117]. Although Echsler *et al.* [122,123] and Picqué *et al.* [124] had attempted to study the behaviour of scales growing on a steel substrate, the scale thickness investigated by these researchers was much greater than that normally entering the roll-bites during finishing hot rolling of steel, and more importantly, the strain rates investigated were many orders of magnitude smaller than those observed in hot rolling of steel strips.

In addition, during hot rolling of steel, the surface scale is in physical contact with the roll surface. As a result, the scale temperature would be lower than that of the steel substrate, which would affect its deformability. The magnitude of temperature reduction as a result of physical contact between the strip and the rolling rolls would be affected by many factors with the total contact time being the predominant factor.

#### 8.4.2 Failure modes of oxide scale under simulated hot rolling conditions

In a recent study carried out by Krzyzanowski and Beynon [129,130], the deformation and failure mechanisms of oxide scales with thickness in the range of 10–300 µm formed on a mild steel containing 0.17C-0.13Si-0.72Mn were investigated using a high temperature tensile test technique over the range of 830–1150°C. The strains applied were in the range of 1.5–20% and strain rates were 0.02–4.0s<sup>-1</sup>. As compared to the studies conducted previously [111–121], these conditions were much closer to those normally applied in strip hot rolling (Table 8.6). Scale failure was not observed when the scales were very thin and the deformation temperatures were in the range of 900–1130°C. However, instead of closely examining the deformation behaviour of thin scale (<30 microns), these studies put great effort into examining the failure mechanisms of relatively thick scales (>>30 µm) observed under different conditions. The approach was later extended to examine the effect of steel composition [131,132].

Two failure modes leading to oxide spallation were observed in these studies, depending on the temperature, strain and strain rate applied. The first mode was initial through-scale crack formation followed by crack initiation and propagation along the scale–steel interface between adjacent through-thickness cracks. This mode was mostly observed at lower temperatures. At higher temperatures, the second mode prevailed, which was slipping of oxide scale relative to the steel surface prior to spallation without generating through-thickness cracks. Table 8.7 summarizes the results observed in these studies [129].

Table 8.7 States of oxide scale after hot tensile tests under different conditions [129]

Temp. (°C)	Strain (%)	Strain rate(s <sup>-1</sup> )	Oxidation time (s)	Crack type
830	1.0	0.2	1500	Irregular small cracks
	1.5			Through-thickness cracks
	2.0	0.1		Through-thickness cracks, spallation
		0.2		
		2.0		Through-thickness cracks, whole spallation
		4.0		
900	1.5	0.2	300	No through-thickness cracks
	2.0			
	10.0			Slipping during tension, no spallation
	20.0	1.0		
	10.0	2.0		
		3.0		
975	5.0	0.2	100	No cracks
		2.0		Through-thickness cracks in the middle part
		4.0	800	Slipping during tension, no cracks
		0.2		
		4.0		
1150	2.0	0.2	100	No through-thickness cracks
	5.0			Slipping during tension, no spallation, delamination
	5.0	4.0	800	Slipping during tension, no spallation
	10.0	0.2		
	5.0	0.2		Slipping during tension, no spallation
		4.0		Slipping during tension, no spallation, delamination

### 8.4.3 Laboratory hot rolling simulation

Many studies have been conducted to examine the scale deformation and failure during laboratory hot rolling or other hot working conditions. These are summarized here.

### *Okada et al.'s study*

In an earlier study, Okada *et al.* [133] conducted laboratory experiments to examine the deformation behaviour of very thin scales during hot rolling at 790–1059°C. A two-stand laboratory rolling simulator was used for the experiments, with the first stand for delivering the heated sample and the second stand for rolling. Both stands had a diameter of 20 cm. The steel examined was a low carbon steel containing 0.05% C and the sample dimensions were  $0.8 \times 7 \times 30$  cm. In a typical rolling experiment, the sample was first wrapped in a stainless envelope, heated in argon to a temperature between 900°C and 1200°C and kept at the target temperature for 30 minutes. The heated sample was then transferred to the first rolling stand and the stand was allowed to remove the sample from its stainless wrap and deliver it to the second stand. The travelling time between the first stand and the second stand was varied between 0.5 and 2.5 seconds, which were the times allowed for steel oxidation. As the oxidation times were very short, the scales formed were all very thin (<10 µm). The rolling temperature was monitored using a pyrometer installed immediately below the second stand. The range of reduction ratios examined was 5% to 50%. Rolling speed was not specified in the study. After rolling, the steel samples were water-cooled in an enclosed chamber where flow argon was used as a protective atmosphere.

As the scales generated were very thin, no cracks were observed in all the rolled samples even at 50% reduction at the lowest rolling temperature of 790°C. In addition, it was found that the scale thickness was reduced at the same rate as the overall reduction ratio applied to the steel sample.

### *Krzyzanowski et al.'s study*

To obtain experimental data to support their numerical modelling, stalled rolling experiments were conducted to examine the cracking behaviour of oxide scale at different points in the roll-gap during hot rolling [134]. Oxide scales with thickness ranging from 30 to 300 microns were generated and rolled at 700–1000°C. The rolling experiments were conducted using a laboratory rolling mill with a roll diameter of 13.4 cm rotating at 10 revolutions per minute (rpm). The dimensions of the test pieces were  $14 \times 1.2 \times 0.55$  cm. The reduction ratio applied was 20%. These conditions corresponded to a strain rate of  $1.4 \text{ s}^{-1}$ , total strain of 20%, and contact time of 0.143 seconds.

It was concluded that there was a lower limit of the scale thickness for a particular steel grade and rolling temperature below which the scales entered the roll gaps without through-thickness cracks. For the steel examined, which contains 0.19C-0.18Si-0.79Mn, no through-thickness cracks were observed for the 30 µm thick scale even at a rolling temperature as low as 700°C. These results were consistent with those of Okada *et al.* [133]. However,

when the scale thickness exceeded the lower limit and the rolling temperatures were not high enough, the longitudinal tensile stress at entry into the roll gap favoured through-thickness crack formation.

Unfortunately, as mentioned earlier, the authors did not pay too much attention in defining the lower scale thickness limits and rolling temperatures for different steels, but rather, more efforts were devoted to studying the cracking behaviours of thicker scales, which were not very often encountered in finishing hot rolling.

#### *Li and Sellars' study*

Li and Sellars [135] conducted laboratory rolling tests to examine the deformation and cracking behaviour of oxide scales formed on a low carbon steel containing 0.17C-0.18Si-0.73Mn-0.1Ni-0.38Cu-0.1Cr. The test pieces had a thickness of 2.5 cm. The target rolling temperature was 1000°C, measured using a thermocouple inserted 2 mm below the top surface of the test piece. During a typical rolling test, the test piece was heated in a controlled atmosphere for a predetermined duration to obtain the desired scale thickness. Retrieved from the furnace, the test piece was cooled in air to the prescribed rolling temperature and rolled at a speed of 0.23 m/s. The actual surface temperature of the test piece during hot rolling was not measured but it would be lower than the rolling temperature indicated by the thermocouple. In one of the tests shown when a reduction of 39% was applied, the subsurface temperature was lowered to as low as 880°C, indicating an even lower surface temperature as a result of physical contact between the test piece and the cold roll surfaces. The rolling reductions tested were 10, 20, 30 and 50%, corresponding to strain rates of about  $5\text{ s}^{-1}$ .

Two types of scales were generated for the rolling tests. The thick scales had thicknesses in the range of 200–670 µm with a three-layered scale structure, generated by heating in air at 1050–1080°C for 15–70 minutes. The thin scales were in the range of 22–40 µm in thickness and possessed a single layer of wustite, generated by oxidation in cracked natural gas.

It was found that when rolling thin scales, no cracks were generated at 10% reduction, but fine and short cracks were observed after 29–39% reductions of the 30 µm scale, and after 48% reduction of the 34 µm scale. It was also claimed that full extrusion of fresh steel was found through most of the cracks in the thin scales after more than 20% reduction of the test pieces, but no micrographs were shown to support this claim.

When rolling thick scales, cracks were observed on all rolled samples, even at 10% reduction. Much denser cracks were observed at higher reductions (17% and 39%). Full extrusion of fresh steel into the cracks in the scale was only found in some wide cracks when the reductions were high (e.g. ~40%).

### *Yu and Lenard's study*

Yu and Lenard [136] conducted rolling experiments using a laboratory rolling mill to examine oxide scale thickness reductions under various rolling conditions. The observed results were then used to derive an equation to relate the strength of the scale, or resistance to scale deformation, to contact time between the test piece and rolling temperature. The steel used for the experiments was a silicon-killed low carbon steel containing 0.14C-0.24Si-0.76Mn and the sample size was  $304 \times 38 \times 4.69$  mm. The scales were generated through oxidation of the steel pieces in flowing nitrogen at 950–1000°C for 20–30 minutes. Four scale thicknesses were generated, which were 17.78, 45.15, 45.57 and 52.2  $\mu\text{m}$ .

In a typical rolling test, the test piece was heated to 50°C above the target rolling temperature, removed from the furnace until the desired temperature for rolling was reached as indicated by an entry pyrometer, and then rolled. After rolling the test piece was cooled in nitrogen to room temperature. As the rolling temperature was measured by a pyrometer, the body temperature would be higher than that of the scale at the time of rolling. The recorded rolling temperatures were in the range of 800–1000°C. It was found that in all cases, the scale experienced more strains than did the overall strains applied. Based on the measured scale thickness reductions, an empirical equation was derived to relate  $\sigma$ , the scale strength in MPa, to the contact time between the roll surface and the scale,  $\Delta t$ , and rolling temperature:

$$\sigma = 6732.101\Delta t^{1.102}\exp(1075.486/T) \quad 8.10$$

where the ranges of applicability were within  $T = 800$ –1000°C and  $\Delta t = 10$ –25 ms. From Equation (8.10), it can be seen that the scale strength, or resistance to deformation, increases with increased contact time and decreased rolling temperature.

Apart from deformation, cracks were also observed in the deformed scales, but the relationship between cracking and rolling conditions was not established in this study. The study also measured many other rolling parameters under different rolling conditions for various scale thicknesses. One of the important parameters measured was friction. Consistent with others [137–139], Yu and Lenard found that lower friction was obtained for thicker scale.

### *Hot 'sandwich' rolling studies*

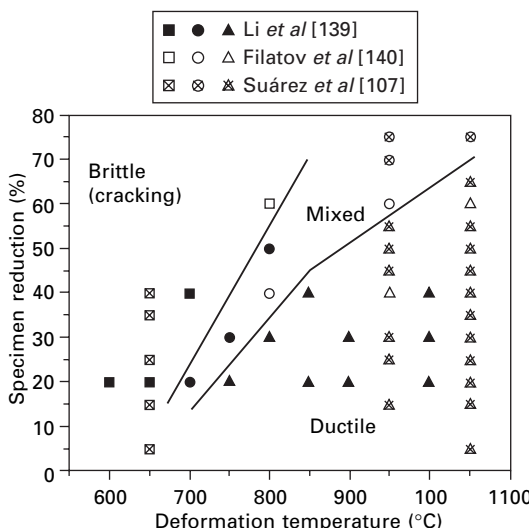
In the rolling experiments discussed above, the scale was always in contact with the roll surface, which has a chilling effect on the scale. The chilling effect was more profound when the contact time was longer, as also reflected in Equation (8.10). To eliminate this effect, Li *et al.* [140] and Filatov *et al.* [141] used a ‘sandwich’ rolling method to examine the deformation and

cracking behaviour of oxide scales at different rolling temperatures and reductions. In Li *et al.*'s study, two steel pieces were oxidized first to grow about 100 µm thick scale on each and then the two oxidized surfaces were pressed together to form a 'sandwiched' sample with two layers of oxides trapped between two steel plates. The 'sandwiched' samples were then heated to various rolling temperatures and rolled with different reductions. The rolling speed was 14 cm/s. After rolling, the oxide surfaces were examined to determine whether they were cracking during rolling.

Using the same principle, Filatov *et al.* [141] made two different types of 'sandwiched' samples for rolling tests. One was three-layered with the oxide being the middle layer, and the other was five-layered where the top, middle and bottom layers were steel plates. The rolling temperatures were in the range of 800–1050°C and rolling reductions were 40–60%. Figure 8.14 shows the results of these studies. In Fig. 8.14, ductile scales refer to those deformed without cracking and brittle scales to those with cracks. It is seen that there is a transition temperature above which the scale is deformed without generating any cracks in it at a certain rolling reduction. This brittle–ductile transition temperature is a function of strain (rolling reduction), with lower transition temperatures at greater rolling reductions.

#### *Hot-forging study by Suárez *et al.**

Suárez *et al.* [107,109] used a hot-forging simulator to conduct plane strain compression experiments to investigate the deformation behaviour of thin



8.14 Brittle–ductile transition temperatures of thin oxide scales at different reduction rates (strain amounts) [107,139–140].

oxide scales in the range of 10–20 µm formed at 1050°C in air on an ultra-low carbon steel. The compression experiments were conducted at 650, 950 and 1050°C at a strain rate of 10 s<sup>-1</sup> with reductions of 5–70%.

It was found that at 950°C and 1050°C, the scale deformed without cracking at reductions below 55% and 65%, respectively, whereas at 650°C cracks were produced. The observed results were consistent with those obtained by Filatov *et al.* [141] and Li *et al.* [140], as shown in Fig. 8.14. It was also found that the thin wustite layer formed at 1050°C had a columnar structure with a strong {100}<001> texture and, although the wustite deformed with the substrate, its texture structure remained unchanged.

In summary, based on the rolling experiments undertaken by various researchers, the scale deformability exhibited in hot rolling is a function of scale thickness, scale temperature, strain rate and total rolling reduction (strain amount). The scale is more deformable when it is thinner, rolled at a higher temperature, has a shorter contact time with the rolling rolls, and is subject to smaller reduction at slower strain rate. It is clear that there is a scale thickness limit below which no cracks would form during hot rolling under certain rolling conditions. This critical thickness is a function of rolling temperature, rolling speed (determining strain rate and contact time) and rolling reduction, and needs to be quantified.

#### 8.4.4 Numerical simulation of scale deformation and failure during hot rolling

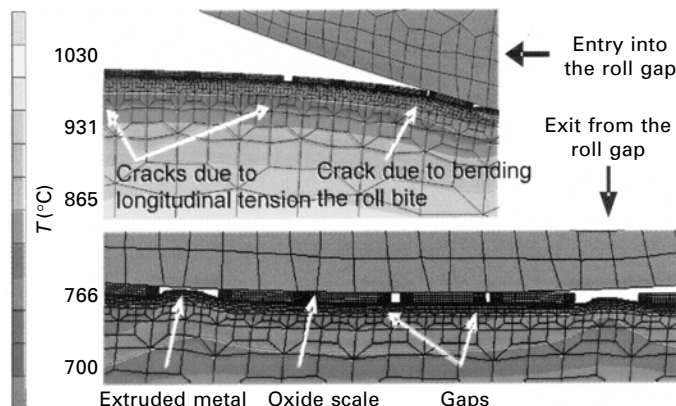
Apart from the extensive experimental studies carried out to understand the deformation and cracking behaviour of the oxide scale, as discussed above, recent attempts have been made to quantify the effects of different hot rolling conditions on the deformation and cracking behaviour of tertiary oxide scale during finishing hot rolling through numerical simulation. In a series of studies, Beynon and co-workers, supported by their own laboratory experimental results and those of others, conducted finite element (FE) analyses of the complex oxide deformation and fracture phenomena in the roll-bite [142,143]. In particular, the nature of the failure of the oxide scale in the vicinity of the roll-bite entry was studied in detail.

The FE model proposed by Beynon *et al.* [144] comprised a macro model, which described the overall strip/roll deformation and computed the stresses and strains in the scale and the strip substrate during hot rolling, and a micro model which described details of the oxide scale fracture. The boundary conditions for the micro model were taken from the results of the macro model. The oxide scale was represented by a batch of scale fragments joining together to form a total thickness of 10–100 µm and length of about 20 mm in the micro model. Based on observations from their laboratory hot rolling experiments, the size of the oxide fragments was appropriately selected to

enable the spacing and distribution of the cracks along the length of the oxide scale to be predicted.

From their FE modelling results, Beynon *et al.* observed that prior to the contact at the roll-bite entry, longitudinal tension in the scale was generated due to the backward slip (the work roll moving faster than the strip). At the initiation of contact, the indentation of the work roll on the strip further generated a bending stress on the oxide scale. The scale behaviour under these combined stresses depended on the hot rolling conditions [145]. At higher temperatures, the oxide scale was more ductile and would slide over the strip rather than fracture, giving rise to delaminated scale. At low temperatures (typically less than 800°C), however, the scale was more brittle and would fracture readily. The transition between these two failure modes was found to be sharp and sensitive to the steel grade. In their model, the critical strain for failure was used as a criterion for the brittle failure, while the strain energy release, based on the *J*-integral, was used to predict ductile failure.

Beynon *et al.* noticed from their modelling work that if the oxide scale did fracture, big gaps (formed from through-thickness cracks) were generated by the tensile stresses prior to the roll-bite contact, while small gaps were induced by the bending stresses at the start of roll-bite contact. The smaller gaps could be somewhat ‘healed’ as they passed through the roll-bite, while for larger gaps, the metal underneath the scale could be extruded into these gaps under the work roll pressure, giving rise to surface defects. This is illustrated in Fig. 8.15 [146]. Moreover they demonstrated that cracks in the oxide scale could form in the roll-bite under the roll pressure [147]. In this case, cracking in the oxide scale started at the scale–work roll interface (where the temperature was relatively low due to the chilling effect of the work roll) and propagated towards the strip. This crack propagation could



8.15 FE results illustrating scale cracking in front of the roll-bite entry and metal extrusion inside the roll-bite [145].

stop in the oxide sub-layer closer to the strip due to the increased temperature (hence increased ductility) of the oxide scale.

The recent study by Picqué *et al.* [124] agreed with the modelling results of Beynon *et al.* In particular, the experimental results obtained by Picqué *et al.* were consistent with those presented in Fig. 8.14, indicating that there was a critical temperature (typically around 700°C, but strain-rate dependent) under which the scale exhibited brittle failure. Based on these experimental data to provide the constitutive relations for the oxide scale, they performed FE analyses using the commercial software Forge2® to compute the oxide scale deformation behaviour at the roll-bite entry for a typical Stand 2 of a hot strip mill. They found that the oxide scale could indeed crack just prior to the roll-bite due to the tensile and bending stresses induced in the scale. These cracks were observed to widen in the roll-bite, with fresh metal extruded into the gaps. However, Picqué *et al.* did not observe fragmentation of the intact scale in the roll-bite under the roll pressure. They suggested that the mechanism of crack formation in the roll-bite was probably caused by a combination of tensile stress and local indentation by the work roll roughness peaks, which was more predominant for worn rolls.

The suggestion made by Picqué *et al.* agreed with the results of earlier work of Okada *et al.* [133], who observed that the oxide scale was reduced uniformly in accordance with the reduction ratio of the strip in their experimental rolling mill for the temperature range 790–1059°C, with reduction as high as 50%. No cracks were found in the strip from their experiments unless the scale was thick. One other explanation was that the oxide scale was possibly rather resistant to fracture if smoothly ground rolls were used (which was presumably the case for the laboratory rolling mill rolls used by Okada *et al.*). When a worn roll is used, particularly when it is subject to banding (shedding of the oxide on the work roll surface), the work roll becomes very rough and the asperities on the roll surface could generate stress concentration on the scale, giving rise to cracking. In practice, the work roll wear has been observed to have a significant impact on the rolled-in scale defect.

While the FE studies have significantly advanced the understanding of the fracture behaviour of the oxide scale under hot rolling conditions, further development is needed to explain fully the observations at the hot strip mill, taking into account the scale thickness and temperature evolution as the strip is deformed in the finishing stands. The oxide scale is thicker and hotter in the early stands and thinner and colder in the later stands (see, for example, Okada *et al.* [133] and Yuen *et al.* [148]). Accordingly, the oxide scale can be more ductile in the early stands if its temperature is the dominant factor. However, it can be more brittle if thickness becomes predominant. Practical experience indicates that roll-in scale defects largely originate in the early stands with high finishing entry temperatures. This suggests that when the

finishing entry temperatures are too high, the scale may grow too much to a thickness exceeding its ductile limit. FE models should be refined further to quantify the conditions under which strip defects caused by cracked scale would not be generated. In addition, the work roll surface texture is possibly one of the key parameters which also needs to be considered.

Moreover, since the scale deformation behaviour depends highly on the oxide scale thickness, appropriate scale thickness as observed in hot strip rolling should be used. In the studies carried out by Beynon *et al.*, the scale thickness range receiving more attention was 30–300 µm, which was rather thick and could have exceeded the ductile thickness limits under the conditions examined. The conclusions reached in their work then might not necessarily apply to that normally observed in finishing hot rolling where the oxide scale thickness is only in the range of 5–30 µm, although they might be useful for studying oxide deformation and fracture behaviour during roughing rolling where the scale thickness would be greater. Previous examination [5] of normal hot rolled steel strips had indicated that neither cracks nor metal extrusion was present in the oxide scale layers when the samples were taken immediately after coiling. Although fine crack lines were usually present in the strip samples after the strip coils were cooled to room temperature [19,149], these cracks were all closed cracks and were believed to be generated during subsequent sample handling, such as bending or straightening during uncoiling.

In summary, there have been some numerical simulation studies, notably those carried out by Beynon and co-workers, conducted to quantify the fracture behaviour of thick oxide scales during finishing hot rolling. However, not much effort had been made to study the deformation behaviours of thinner scales normally present on hot rolled steel strips. Future simulation work should put more focus on the deformation behaviour and the tendency to fracture of thinner oxide scales in relation to various hot rolling parameters, i.e. rolling temperature, rolling speed (hence roll-steel contact time and strain rate) and rolling reduction, and should define safe operation regimes for the hot rolling process. The effects of roll surface conditions and temperature gradient across the scale thickness should also be considered in the modelling.

## 8.5 Electron backscatter diffraction (EBSD) analyses of oxide scale structure

Since its development in the 1970s and 1980s, the electron backscatter diffraction (EBSD) technique has become the most widely used method for micro-texture investigations in recent years [150,151]. The EBSD system is usually attached to a Scanning Electron Microscope. By arranging the specimen at an appropriate angle, an electron diffraction pattern can be generated and captured on film, a camera or a screen. The diffraction pattern is called a Kikuchi diffraction pattern, which consists of pairs of parallel lines, each of

which represents a set of atomic planes. If the phase being analysed is known, then the pattern can be used to determine the orientation of the area being analysed. If the phase is not known, the pattern can be used to assist in determining its phase structure. As an EBSD pattern is generated from a fine electron beam (typically  $<0.5\text{ }\mu\text{m}$  in diameter), the EBSD technique can be used to determine the phase structure or the orientation of a very small phase or area. Combined with the SEM image taken and composition analyses using wavelength dispersive X-ray spectroscopy (WDS) and/or energy dispersive X-ray spectroscopy (EDS), a comprehensive understanding of the phase structure, crystallographic orientation and chemistry of a small phase or area can be achieved. The EBSD technique can also be used for grain boundary characterizations [151,152].

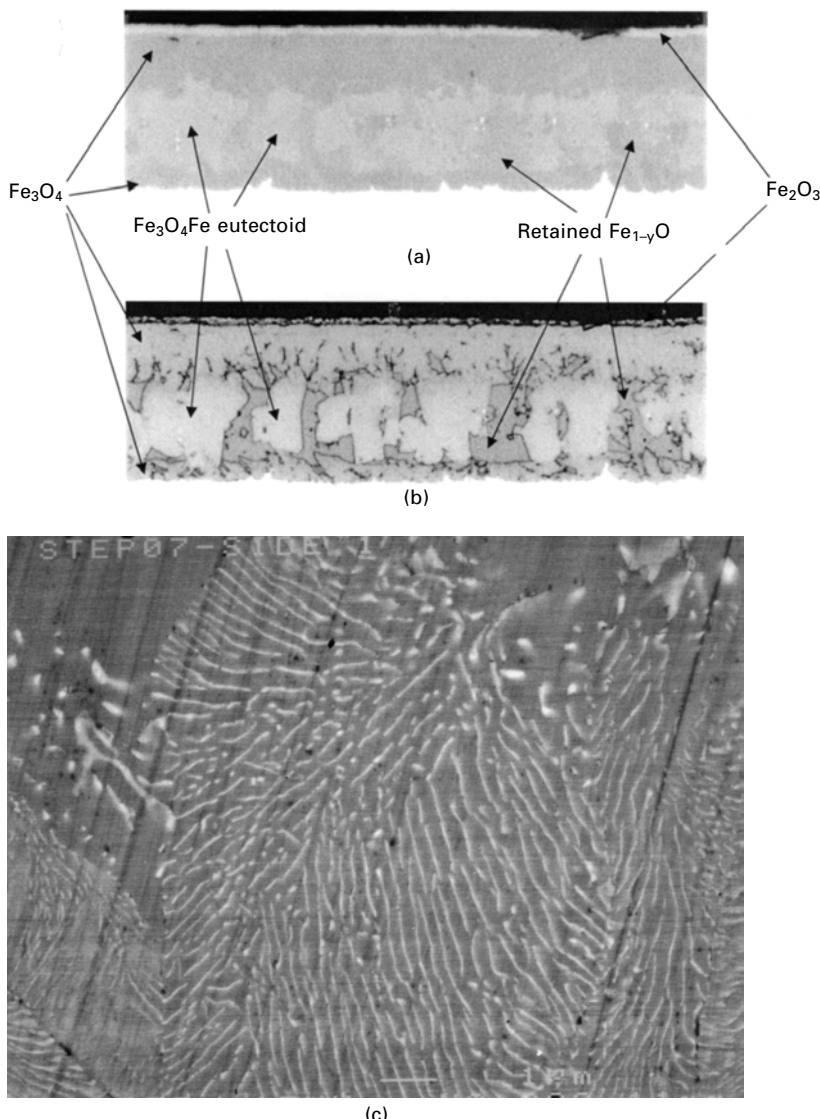
As one of the early applications of the EBSD technique to the study of steel products, Randle found that the technique could be used to differentiate hematite, magnetite and wustite based on their respective pattern symmetry, Kikuchi band widths and pattern intensities, although no details of the phase recognition and analysis were provided [151]. In more recent years, Higginson and co-workers further explored the capability of EBSD in the analyses of iron oxide scale layers growing on low and ultra-low carbon steels, leading to a continuous stream of publications of their research results [153–162]. The technique was also used in the studies of other research groups [99,109,163–166].

The work carried out by Higginson and co-workers was centred on identification or differentiation of various oxide phases. Differentiation between the hematite and other phases was not difficult. However, differentiations between wustite, magnetite and the iron substrate were found to be particularly challenging as these three phases all possess cubic symmetry and their Kikuchi patterns show great similarities. In order to differentiate wustite and magnetite, their indexing parameters needed to be optimized and the confidence index (CI) for each phase developed [154,155]. As with the iron phase substrate, a second stage differentiation was required and this was achieved simply by using the large differences in Fe and O contents between the oxide and the steel substrate to filter the possible phases [154]. Apart from differentiating discrete scale layers, magnetite precipitates in the wustite layer were also successfully differentiated. However, results of identification of eutectoid iron as a decomposition product of wustite formed during slow cooling have not been presented in Higginson and co-workers' studies.

After various phases are differentiated using their respective optimized indexing parameters, automated EBSD maps can then be generated to reveal various phase layers, which can even be presented in colour [154].

It has been clearly demonstrated by Chen and Yuen that wustite, magnetite, hematite,  $\text{Fe}_3\text{O}_4/\text{Fe}$  eutectoid, and the steel substrate can be unambiguously differentiated with high metallographic contrasts using optical microscopy

with the occasional assistance of SEM and XRD [5,6,84,96], as shown in Fig. 8.16. Although the EBSD method can be used to differentiate these phases, it would be inconvenient and expensive to use it as a routine method.

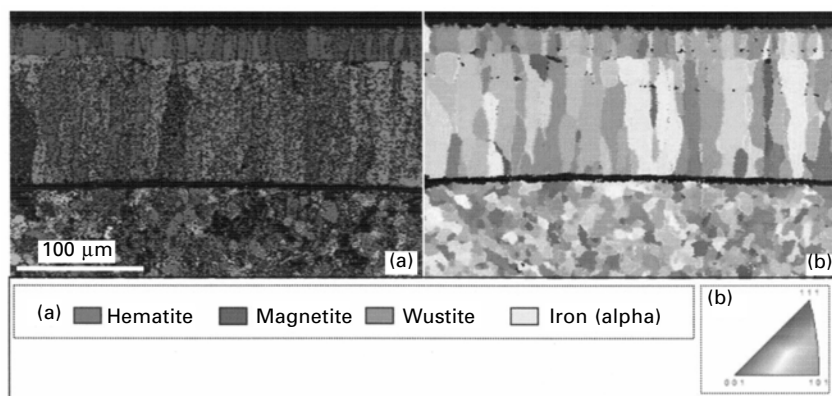


8.16 Oxide scale structures on steel identified using (a)–(b) optical microscopy, and (c) scanning electron microscopy: (a) unetched ( $1000\times$ ); (b) etched using 1% HCl in ethanol for 10 seconds ( $1000\times$ ); (c) SEM image of the eutectoid region (original magnification  $8000\times$ ).

The most successful application of the EBSD technique in the study of the oxide scale structures by Higginson and his co-workers is perhaps in the identification of grain boundaries in the oxide layer using the image quality (i.e. diffraction pattern quality) mapping method. An example of this is shown in Fig. 8.17 [154]. Conventional methods have failed to clearly reveal grain boundaries in the oxide layers. With the application of image quality maps, grain boundaries can be revealed because low quality diffraction patterns (Kikuchi patterns) are usually obtained from grain boundary locations [152,156]. In addition, the levels of grain boundaries, whether they are high ( $>15^\circ$ ) or low ( $2-15^\circ$ ) misorientation grain boundaries, can be calculated and mapped [156]. Using this technique, the thick wustite layer in the oxide scale formed on a steel containing 0.10C-0.05Ni-0.34Mn-0.1Si at 800–1100°C for 30–180 min was found to possess a columnar structure in the outer region and a finer grain layer at the base [153] near the steel substrate. A similar two-layered structure in the wustite layer was also observed in the study carried out by Szpunar and Kim [163].

Using the focused ion beam method for grain size analyses and EBSD for phase identification, Jonsson *et al.* [99] also confirmed that the magnetite layer formed on pure iron at 500°C in oxygen possessed the duplex structure with two distinct layers – a columnar outer layer and a fine-grained inner layer. The grain orientation contrast revealed by the focused ion beam method is similar to that revealed using the EBSD technique.

The third application was to define the orientation relationships between various phases, i.e. relationships between the wustite phase and the steel substrate, precipitated magnetite and parent wustite phase, magnetite layer and wustite layer, and magnetite layer and hematite layer. It was found that pro-eutectoid magnetite, formed either at the base of the wustite phase or inside the wustite layer, had the same orientation as its parent wustite phase.



8.17 EBSD analyses of the oxide scale formed on a low carbon steel containing 0.10C-0.10Si-0.34Mn at 900°C for 45 min in air [154].

In some studies, it was observed that the preferred growth direction for hematite was 0001, and those for wustite and magnetite were 001 [157,160]. In others, the textures were found to be not very strong [159,160].

As discussed early, Suárez *et al.* [109] used the EBSD method to reveal the grain structure of the wustite layer and its texture and found that when the wustite layer was thin (grown at 1050°C in air), it was only single-layered with a columnar structure, which possessed a strong {100}<001> texture, even after deformation under plain strain compression conditions.

Further studies conducted by Basabe and Szpunar [164] indicated that the wustite layers formed on a steel containing 0.06C-0.32Mn at 850°C, 900°C and 950°C for 10 seconds had different orientation characteristics. Although they all had columnar structures, the wustite layer formed at 850°C had a weak texture, whereas those formed at 900–950°C possessed stronger {001}<100> textures. Kim and Szpunar [165] also found that the magnetite layer had a columnar structure and possessed a <001>///GD (GD = growth direction) texture, and after examining oxide scales growing on many pure iron and steel samples, it was concluded that there was no clear relationship between the textures developed in the scale and those in the steel substrates.

In summary, the EBSD technique has been used for phase recognition, grain size analyses and texture determination for oxide scales growing on various commercial steel products. Although there was some success in the differentiation of various iron oxides, the method did not show advantages over the conventional metallographic method. This method, however, revealed clearly the grain sizes and shapes in various oxide layers. In this respect, it is advantageous. An alternative method to reveal oxide grain size and shape is the FIB method. Determined using the EBSD technique, it appeared that there was a tendency to form stronger textures in the wustite and magnetite layers at temperatures above 900°C, with their <001> directions parallel to the oxide growing direction.

## 8.6 Conclusions

This chapter reviews recent studies on steel strip oxidation and the behaviour of oxide scale during hot rolling. The following conclusions can be made from the review.

1. Long-term oxidation of steel in air and oxygen follows the parabolic law when the scale remains adherent to the steel, but the oxidation rate of steel is slower than that of pure iron. Generally for steel oxidation, the scale–steel interface adhesion is lost over longer oxidation times and at temperatures above 950°C.
2. Oxidation in reheat furnace atmospheres follows the linear law initially and may become parabolic at the later stage if the furnace atmosphere contains a sufficient amount of free oxygen.

3. In the presence of free oxygen, the dominant oxidizing species in the reheat furnace atmosphere is oxygen.
4. The contributions made to the overall oxidation rate in the reheat furnace by water vapour and carbon dioxide are additive to that of free oxygen, but they only become important when the free oxygen levels are low or absent.
5. Oxide scale formed in air or oxygen-containing atmosphere within a very short time (e.g. less than 100 seconds) comprises a single-layered wustite only, although thermodynamically it is possible for other oxides to form.
6. Therefore, the oxide scale entering the roll-bite of a finishing mill is likely to be a single-layer, more deformable wustite.
7. Wustite is plastic or ductile at temperatures above 700°C when deformed slowly, but its plasticity is partially lost if the strain rates and/or the strain amounts are too high.
8. The deformation resistance of wustite increases with lengthened contact time between the scale and the roll surface and at lower temperatures.
9. In general, the scale is more ductile when it is thinner and rolled at higher temperatures with lower strains and lower strain rates.
10. At the normal thickness (<30 µm) and normal hot rolling temperatures, reductions and reduction rates used in a typical finishing rolling mill, the oxide scale formed on the hot band is believed to be deformable or ductile.
11. However, if the rolling speed is reduced, the hot band temperature is too low, the secondary oxide scale is not removed properly, or the roll surfaces have deteriorated, the scale may crack during rolling.
12. Future laboratory and numerical simulation work should focus more on the deformation behaviour and tendency to cracking for thinner scales under the conditions relevant to finishing hot rolling, so that safe operation windows for hot rolling without causing scale cracking and damage to the roll and strip surfaces can be more accurately determined.
13. Electron backscatter diffraction (EBSD) has been successfully applied to reveal grain boundaries in oxide scales and analyse their texture structures by some previous studies. It has also been used for phase identification, which is inconvenient and expensive and appears to have no advantages over the conventional metallographic method.

## 8.7 References

1. P. F. Marcus, K. M. Kirsis and D. F. Barnett, 'Steel Strategist #32: The Age of Profits', World Steel Dynamics, August 2006, 240–256.
2. International Iron and Steel Institute, 'World Steel in Figures', 2006, [www.worldsteel.org](http://www.worldsteel.org).

3. International Iron and Steel Institute, ‘International Iron and Steel Institute (IISI) Short range outlook and medium term forecast’, MPT Int. **29**, No. 6, 18 (Nov. 2006).
4. R. I. L. Guthrie, ‘Steel strips – the long and winding road’, Iron Steel Techno. **3**, No. 9, 104–114 (Sept. 2006).
5. R. Y. Chen and W. Y. D. Yuen, ‘Oxide-scale structures formed on commercial hot-rolled steel strip and their formation mechanisms’, Oxid. Met. **56**, 89–118 (2001).
6. R. Y. Chen and W. Y. D. Yuen, ‘Review of the high-temperature oxidation of iron and carbon steels in air or oxygen’, Oxid. Met. **59**, 433–468 (2003).
7. J. Stubbles, ‘The minimill story’, Iron Steel Techno. **3**, No. 10, 25–34 (Oct. 2006).
8. C.-P. Reip, W. Henning, J. Kempken and S. Krämer, ‘Challenges and solutions of compact strip production’, MPT Int. **29**, No. 3, 66–70 (May 2006).
9. SMS Demag AG and SeverCorr LLC, ‘SeverCorr to build “next generation” minimill’, MPT Int. **29**, No. 4, 54–58 (Sept. 2006).
10. J. M. Rodriguez-lbabe, ‘Thin slab direct rolling of microalloyed steels’, Mater. Sci. Forum **500–501**, 49–63 (2005).
11. www.arvedi.it, ‘Arvedi to realize thin-slab casting in endless mode on a new mini-mill’, MPT Int. **29**, No. 5, 56–59 (Oct. 2006).
12. W. Blejde and R. Mahapatra, ‘Development of low carbon thin strip production capability at Project M’, Iron & Steelmaker **27**, No. 4, 29–33 (April 2000).
13. P. Campbell, W. Blejde, R. Mahapatra, R. Wechsler and G. Gillen, ‘The Castrip® process – direct casting of steel sheet at Nucor Crawfordsville’, Iron Steel Technol. **2**, No. 7, 56–62 (July 2005).
14. M. Schueren, P. Campbell, W. Blejde, and R. Rahapatra, ‘The Castrip® process – an update on process development at Nucor Steel’s first commercial strip casting facility’, AISITech 2007, Indianapolis, Indiana, USA, 10 May, 2007.
15. ASTM A1039/A 1039M – 04, Standard Specification for Steel, Sheet, Hot Rolled, Carbon, Commercial and Structural, Produced by the Twin-Roll Casting Process, 2004.
16. A. G. Thekdi, Development of next generation heating system for scale free steel reheating, Department of Energy Award Number DE-FG36-05GO15184, US Department of Energy, August 2006, www.osti.gov/bridge.
17. V. B. Ginzburg, ‘Scaling of steel in hot strip mill’, pp. 483–508, *Steel-Rolling Technology: Theory and Practice*, Marcel Dekker, New York, 1989.
18. R. Y. Chen and W. Y. D. Yuen, ‘Effects of finishing and cooling temperatures on the scale structure and picklability of hot rolled strip’, Iron & Steelmaker **27**, No. 4, 47–53 (April 2000).
19. R. Y. Chen, W. Y. D. Yuen and R. Hull, ‘Effects of hot rolling conditions and scale breaking on the pickling performance of hot-rolled steel strip’, SEAISI Quarterly, July 2000, 68–82.
20. R. Y. Chen, W. Y. D. Yuen and T. Mak, ‘Oxide scale growth and its pickling characteristics of hot-rolled steel strip’, 43rd MWSP Conf. Proc., ISS, **39**, 287–299 (2001).
21. V. B. Ginzburg, ‘Classification of steels and alloys’, *Steel-Rolling Technology: Theory and Practice*, Marcel Dekker, New York, 1989, pp. 43–69.
22. V. B. Ginzburg, ‘Deoxidation of steel’, *Steel-Rolling Technology: Theory and Practice*, Marcel Dekker, New York, 1989, 147.
23. E. T. Turkdogan, *Fundamentals of Steelmaking*, The Institute of Materials, London, 1996, pp. 193–199, 262–269.

24. B. Deo and R. Boom, *Fundamentals of Steelmaking Metallurgy*, Prentice Hall International, New York, 1993, pp. 84–99.
25. K. Sachs and C. W. Tuck, ‘Surface oxidation of steel in industrial furnaces’, *Reheating for Hot Working*, The Iron and Steel Institute, London, 1968, pp. 10–17.
26. N. B. Pilling and R. E. Bedworth, ‘The oxidation of metals at high temperatures’, *J. Inst. Metals* **29**, 529–591 (1923).
27. K. Heindlhofer and B. M. Larsen, ‘Rates of scale formation on iron and a few of its alloys’, *Trans. Amer. Soc. Steel Treaters* **21**, 865–895 (1933).
28. J. K. Stanley, J. von Joene and R. T. Huntoon, ‘The oxidation of pure iron’, *Trans. Amer. Soc. Metals* **43**, 426–453 (1951).
29. M. H. Davies, M. T. Simnad and C. E. Birchenall, ‘On the mechanism and kinetics of the scaling of iron’, *Trans. AIME* **191**, 889–896 (1951); ‘A corrected interpretation of the mechanism of growth of magnetite during oxidation’, *Trans. AIME* **193**, 1250 (1953).
30. J. Païdassi, ‘The kinetics of the air oxidation of iron in the range of 700–1250°C’, *Acta Metall.* **6**, 184–194 (1958); ‘Contribution to the study of oxidation of iron in the air in the range of 700–1250°C’, *Rev. Métall.* **8**, 569–585 (1957).
31. N. G. Schmahl, H. Baumann and H. Schenck, ‘Temperature dependence of scaling of pure iron in oxygen’, *Archiv für Eisenhüttenwesen* **29**, 83–88 (1958).
32. G. Tammann, ‘Oxidation of metals’, *Z. Anorg. Allgem. Chem.* **111**, 78–89 (1920).
33. K. Sachs and C. W. Tuck, ‘Scale growth during re-heating cycles’, *Werkst. Korros.* **11**, 945–954 (1970).
34. R. K. Singh Raman, B. Gleeson and D. J. Young, ‘Theoretical prediction and experimental measurements of anisothermal oxidation kinetics’, Proc. 13th Int. Corros. Conf., Australia, 1996, Paper 297.
35. H. Abuluwefaa, R. L. L. Guthrie and F. Ajersch, ‘The effect of oxygen concentration on the oxidation of low-carbon steel in the temperature range 1000 to 1250°C’, *Oxid. Met.* **46**, 423–440 (1996).
36. R. Y. Chen and W. Y. D. Yuen, ‘Oxidation of a low carbon, low silicon steel in air at 600–920°C’, *Mater. Sci. Forum* **522–523**, 77–85 (2006).
37. D. Caplan, ‘Overtemperature in metal scaling’, *J. Electrochem. Soc.* **107**, 359–360 (1960).
38. A. Rahmel and J. Tobolski, ‘The effects of water vapour and carbon dioxide on the oxidation of iron in oxygen at high temperatures’, *Corros. Sci.* **5**, 333–346 (1965).
39. N. Birks, G. H. Meier and F. S. Pettit, *Introduction to the High-Temperature Oxidation of Metals*, Second Edition, 2006, Cambridge University Press, Cambridge, UK, 176–183.
40. C. W. Tuck, M. Odgers and K. Sachs, ‘The oxidation behaviour of pure iron and mild steel in oxygen, water vapour and carbon dioxide at temperatures between 850 and 1000°C’, *Werkst. Korros.* **17**, 34–42 (1966).
41. C. W. Tuck, M. Odgers and K. Sachs, ‘The oxidation of iron at 950°C in oxygen/water vapour mixtures’, *Corros. Sci.* **9**, 271–285 (1969).
42. C. W. Tuck and M. Odgers, ‘The influence of steam on the oxidation of pure iron and mild steel in oxygen at high temperatures’, Internal Report 864, 1966, GKN Group Research Centre, UK.
43. C. W. Tuck, ‘Possible mechanisms of oxidation in steam-bearing atmospheres’, Internal Report 933, 1967, GKN Group Research Centre, UK.
44. J. Baud, A. Ferrier, J. Manenc and J. Bénard, ‘The oxidation and decarburising of Fe-C alloys in air and the influence of relative humidity’, *Oxid. Met.* **9**, 69–97 (1975).

45. R. Y. Chen and W. Y. D. Yuen, 'The effects of steel composition on the oxidation kinetics, scale structure, and scale–steel interface adherence of low and ultra-low carbon steels', Mater. Sci. Forum, **522–523**, 451–459 (2006).
46. R. Y. Chen and W. Y. D. Yuen, 'Effects of a small amount of moisture addition on the oxidation behaviour of low and ultra-low carbon steels in air at high temperatures', unpublished results, 2007.
47. S. R. J. Saunders and L. N. McCartney, 'Current understanding of steam oxidation – power plant and laboratory experience', Mater. Sci. Forum **522–523**, 119–128 (2006).
48. K. Nakagawa, Y. Matsunaga, and T. Yanagisawa, 'Corrosion behaviour of ferritic steels on the air sides of boiler tubes in a steam/air dual environment', Mater. High Temp. **20**, 67–73 (2003), Mater. High Temp. **18**, 51–56 (2001).
49. M. Ueda, H. Kurokawa, K. Kawamura and T. Maruyama 'Hydrogen permeation measurement of iron and its oxide membranes by using a dew point hydrometer', 2004 Joint International Meeting (206th Meeting of The Electrochemical Society and 2004 Fall Meeting of the Electrochemical Society of Japan), Honolulu, Hawaii, 3–8 October 2004, Paper 1767; <http://www.electrochem.org/dl/ma/206/pdfs/1767.pdf>.
50. G. Hultquist, E. Hörlund, C. Anghel and Q. Dong, 'Balanced transport in the growth of protective oxide scales', CAMP-ISIJ **16**, 1337–1338 (2003).
51. G. Hultquist, C. Anghel and P. Szakalos, 'Effects of hydrogen on the corrosion resistance of metallic materials and semiconductors', Mater. Sci. Forum **522–523**, 139–146 (2006).
52. The Energy Technology Support Unit (ETSU) and British Steel, *Good Practice Guide 76: Continuous Steel Reheating Furnaces: Specification, Design and Equipment*, Energy Efficiency Office, Department of the Environment, UK, 1993.
53. E. A. Cook, 'Scale-free heating of slabs and billets', Iron Steel Engineer Year Book, 1970, 175–181; or Iron Steel Engineer, March 1970, 63–69.
54. C. W. Tuck, 'Oxidation and scale removal: a review of work carried out at the GKN Group Research Centre', Internal Report of GKN Group Research Centre, 1968.
55. F. Ajersch, 'Scale formation in steel processing operation', 34th MWSP Conf. Proc., ISS-AIME, **30**, 419–437 (1993).
56. J.S. Sheasby, W. E. Boggs and E. T. Turkdogan, 'Scale growth on steels at 1200°C: rationale of rate and morphology', Met. Sci. **18**, 127–136 (1984).
57. H. T. Abuluwefa, R. I. L. Guthrie and F. Ajersch, 'Oxidation of low carbon steel in multicomponent gases: Part I. Reaction mechanisms during isothermal oxidation', Metall. Mater. Trans. A, **28A**, 1633–1641 (1997).
58. H. T. Abuluwefa, R. I. L. Guthrie and F. Ajersch, 'Oxidation of low carbon steel in multicomponent gases: Part II. Reaction mechanisms during reheating', Metall. Mater. Trans. A, **28A**, 1643–1651 (1997).
59. D. B. Lee and J. W. Choi, 'High temperature oxidation of steels in air and CO<sub>2</sub>–O<sub>2</sub> atmosphere', Oxid. Met. **64**, 319–329 (2005).
60. V. H. J. Lee, B. Gleeson and D. J. Young, 'Scaling of carbon steel in simulated reheat furnace', Oxid. Met. **63**, 15–31 (2005).
61. M. Odgers and C. W. Tuck, 'Scaling of mild steel and pure iron in simulated re-heating furnace atmospheres', Internal Report No. 947, GKN Group Research Centre, August 1967.
62. C. W. Tuck and M. Odgers, 'The scaling of two C/Mn steels in the range of 700–1200°C', Internal Report No. 1031, GKN Group Research Centre, April 1968.

63. C. W. Tuck, 'Prediction of quantitative scaling in mixed atmospheres: pure iron and mild steel', Internal Report No. 978, GKN Group Research Centre, January 1968.
64. L. B. Pfeil, 'The oxidation of iron and steel at high temperatures', J. Iron Steel Inst. **119**, 501–560 (1929).
65. R. Bredesen and P. Kofstad, 'On the oxidation of iron in CO<sub>2</sub>+CO mixtures. III: Coupled linear parabolic kinetics', Oxid. Met. **36**, 27–56 (1991).
66. W. W. Smeltzer, 'The kinetics of wustite scale formation on iron', Acta Metall. **8**, 377–383 (1960).
67. R. Bredesen and P. Kofstad, 'On the oxidation of iron in CO<sub>2</sub>+CO mixtures. I: Scale morphology and reaction kinetics', Oxid. Met. **34**, 361–379 (1990).
68. R. Bredesen and P. Kofstad, 'On the oxidation of iron in CO<sub>2</sub>+CO mixtures. II: Reaction mechanisms during initial oxidation', Oxid. Met. **35**, 107–137 (1991).
69. M. Odgers and C. W. Tuck, 'The effect of atmosphere on the oxidation mechanism of iron and mild steel', GKN Group Research Laboratory, Internal Report No. 822, June 1967.
70. W.W. Smeltzer, 'The oxidation of iron in carbon dioxide–carbon monoxide atmospheres', Trans. TMS-AIME **218**, 674–681 (1960).
71. C. Yan and F. Oeters, 'Kinetics of iron oxidation with CO<sub>2</sub> between 1300 and 1450°C', Steel Research **65**, 355–361 (1994).
72. F. S. Pettit and J. B. Wagner, Jr, 'Transition from the linear to the parabolic rate law during the oxidation of iron to wustite in CO-CO<sub>2</sub> mixtures', Acta Metall. **12**, 35–40 (1964).
73. F. Pettit, R. Yinger and J. B. Wagner, Jr, 'The mechanism of oxidation of iron in carbon monoxide–carbon dioxide mixtures', Acta Metall. **8**, 617–623 (1960).
74. E. T. Turkdogan, W. M. McKewan and L. Zwell, 'Rate of oxidation of iron to wustite in water–hydrogen gas mixtures', J. Phys. Chem. **69**, 327–334 (1965).
75. J. P. Yost, 'Scale-free heating in the steel industry', Iron Steel Engineer **43**, No. 7, 148–150 (July 1966).
76. V. H. J. Lee, 'Scaling behaviour of steels in simulated reheat furnace conditions', PhD Thesis, The University of New South Wales, Australia, May 1997.
77. D. Poirier, E. W. Grandmaison, M. D. Matovic, K. R. Barnes and B. D. Belson, 'High temperature oxidation of steel in an oxygen-enriched low NO<sub>x</sub> furnace environment', IFRF Combustion Journal, Article Number 200602, September 2006 (this article was downloaded directly from the Internet).
78. S. Taniguchi, Y. Hanamoto and J. Nakata, 'Influence of cooling rate and steel composition on the scale failure characteristics during cooling of Si-containing low carbon steels', Mater. Sci. Forum **522–523**, 505–512 (2006).
79. M. Takeda and T. Onishi, 'Oxidation behaviour and scale properties on the Si containing steels', Mater. Sci. Forum **522–523**, 477–488 (2006).
80. H. Okada, T. Fukagawa, H. Ishihara, A. Okamoto, M. Azuma and Y. Matsuda, 'Prevention of red scale formation during hot rolling of steels', ISIJ Int. **35**, 886–891 (1995).
81. H. Okada, T. Fukagawa, H. Ishihara, A. Okamoto, M. Azuma and Y. Matsuda, 'Effects of hot rolling and descaling condition on red scale defects formation', Tetsu-to-Hagané **80**, 849–854 (1994).
82. V. Raghavan, *Phase Diagrams of Ternary Iron Alloys, Part 5: Ternary Systems Containing Iron and Oxygen*, The Indian Institute of Metals, Calcutta, 260–277 (1989).

83. T. Fukagawa, H. Okada and Y. Maehara, ‘Mechanism of red scale defect formation in Si-added hot-rolled steel sheets’, *ISIJ Int.* **34**, 906–911 (1994).
84. R. Y. Chen and W. Y. D. Yuen, ‘Examination of oxide scales of hot rolled steel products’, *ISIJ Int.* **45**, 52–59 (2005).
85. T. Kizu, Y. Nagataki, T. Inazumi and Y. Hosoya, ‘Intergranular and internal oxidation during hot-rolling process in ultra-low carbon steel’, *ISIJ Int.* **42**, 206–214 (2002).
86. A. Atkinson, ‘A theoretical analysis of the oxidation of Fe-Si alloys’, *Corros. Sci.* **22**, 87–102 (1982).
87. A. E. Hughes, ‘A simplified treatment of the limiting conditions for selective oxidation of binary alloys’, *Corros. Sci.* **22**, 103–110 (1982).
88. A. S. Khanna, P. Rodriguez and J. B. Gnanamoorthy, ‘Oxidation kinetics, breakaway oxidation, and inversion phenomenon in 9Cr-1Mo steels’, *Oxid. Met.* **26**, 171–200 (1986).
89. B. Gleeson, R. K. Singh Raman and D. J. Young, ‘Effects of silicon and steam on the short-term oxidation behaviour of carbon steels’, *CAMP-ISIJ* **16**, 1345–1348 (2003).
90. P. Kofstad, ‘On the formation of porosity and microchannels in growing scales’, *Oxid. Met.* **24**, 265–276 (1985).
91. R. J. Hussey and M. J. Graham, ‘Some observations on void formation in  $\text{Fe}_3\text{O}_4$  layers on Fe’, *Corros. Sci.* **21**, 255–258 (1981).
92. M. Ueda, K. Kawamura and T. Maruyama, ‘Void formation in magnetite scale formed on iron at 823 K – elucidation by chemical potential distribution’, *Mater. Sci. Forum* **522–523**, 37–44 (2006).
93. N. Bertrand, C. Desgranges, D. Gauvain, D. Monceau and D. Poquillon, ‘Low temperature oxidation of pure iron: growth kinetics and scale morphologies’, *Mater. Sci. Forum* **461–464**, 591–598 (2004).
94. Y. Chen, ‘Observation of voids in the Mn(Fe)S layers of Fe-Mn and Fe-Mn-Mo alloys’, *J. Mater. Sci. Lett.* **14**, 1243–1245 (1995).
95. P. Y. Hou, Y. Niu and C. Van Lienden, ‘Analysis of pore formation at oxide–alloy interfaces – I: Experimental results on FeAl’, *Oxid. Met.* **59**, 41–61 (2003).
96. R. Y. Chen and W. Y. D. Yuen, ‘A study of the scale structure of hot-rolled steel strip by simulated coiling and cooling’, *Oxid. Met.* **53**, 539–560 (2000).
97. R. Y. Chen and W. Y. D. Yuen, ‘Copper enrichment behaviours of copper-containing steels in simulated thin-slab casting processes’, *ISIJ Int.* **45**, 807–816 (2005).
98. R. Y. Chen and W. Y. D. Yuen, ‘Isothermal and step-isothermal oxidation of copper-containing steels in air at 980–1220°C’, *Oxid. Met.* **63**, 145–168 (2005).
99. T. Jonsson, A. Järdnäs, J.-E. Svensson, L.-G. Johansson and M. Halvarsson, ‘The effect of traces of  $\text{SO}_2$  on iron oxidation: a microstructural study’, *Oxid. Met.* **67**, 193–213 (2007).
100. D. Caplan and M. Cohen, ‘Scaling of iron at 500°C’, *Corros. Sci.* **3**, 139–143 (1963).
101. A. Atkinson, ‘Transport processes during the growth of oxide films at elevated temperature’, *Rev. Modern Phys.* **57**, 437–470 (1985).
102. T. Maruyama, N. Fukagai, M. Ueda and K. Kawamura, ‘Chemical potential distribution and void formation in magnetite scale formed in oxidation of iron at 823 K’, *Mater. Sci. Forum* **461–464**, 807–814 (2004).
103. C. Anghel, G. Hultquist, Q. Dong, J. Rundgren, I. Saeki and M. Limbäck, ‘Gas-tight oxides – reality or just a hope’, *Mater. Sci. Forum* **522–523**, 93–101 (2006).

104. W. M. Melfo and R. J. Dippenaar, 'In situ observations of early oxidation formation in steel under hot-rolling conditions', *J. Microscopy* **225**, 147–155, (2007).
105. W. M. Melfo and R. J. Dippenaar, 'In-situ study of scale formation under finishing-mill operating conditions', Proc. AISTech'06, Cleveland, Ohio, USA, May 2006.
106. R. Y. Chen and W. Y. D. Yuen, 'Oxide scales developed on a low carbon low silicon steel within 30 seconds in flowing air at 1000°C', unpublished results, 2007.
107. L. Suárez, G. Bourdon, X. Vanden Eynde, M. Lamberigts and Y. Houbaert, 'Ternary scale behaviour during finishing hot rolling of steel flat products', *Adv. Mater. Res.* **15–17**, 732–737 (2007).
108. L. Suárez, R. Coto, X. Vanden Eynde, M. Lamberigts and Y. Houbaert, 'High temperature oxidation of ultra-low-carbon steel', *Def. Diff. Forum* **258–260**, 158–163 (2006).
109. L. Suárez, R. Petrov, L. Kestens, M. Lamberigts and Y. Houbaert, 'Texture evolution of tertiary oxide scale during steel plate finishing hot rolling simulation tests', *Mater. Sci. Forum* **550**, 557–562 (2007).
110. P. Henk Bolt, 'Understanding the properties of oxide scales on hot rolled steel strip', *Steel Research Int.* **75**, 399–404 (2004).
111. J. D. Mackenzie and C. E. Birchenall, 'Plastic flow of iron oxides and the oxidation of iron', *Corrosion – NACE* **13**, 783t–785t (1957).
112. R. F. Tylecote, 'Factors influencing the adherence of oxides on metals', *J. Iron Steel Inst.* **196**, 135–141 (1960).
113. F. Matsuno and S.-I. Nishikida, 'Mechanical properties of FeO–MnO s.s. and FeO–MgO s.s.', *Trans. ISIJ* **26**, B-251 (1986).
114. J. H. Westbrook, 'The temperature dependence of hardness of some common oxides', *Rev. Hautes Tempér. et Réfract.* **3**, 47–57 (1966).
115. H. Angell and F. Wever, 'Some basic problems of the formation and adherence of scale on iron', *Acta Metall.* **5**, 695–708 (1957).
116. R. F. Tylecote and T. E. Mitchell, 'Marker movements in the oxidation of iron and some other metals', *J. Iron Steel Inst.* **196**, 445–453 (1960).
117. D. L. Douglass, 'The role of oxide plasticity on the oxidation behaviour of metals: a review', *Oxid. Met.* **1**, 127–142 (1969).
118. H. J. Frost and M. F. Ashby, *Deformation-Mechanism Maps – The Plasticity and Creep of Metals and Ceramics*, Pergamon Press, Oxford, UK, 1982.
119. M. Schütze, *Protective Oxide Scales and Their Breakdown*, John Wiley & Sons, Chichester, UK, 1997.
120. M. Schütze, 'Plasticity of protective oxide scales', *Mater. Sci. Techno.* **6**, 32–38 (1990).
121. M. F. Ashby, 'A first report on deformation-mechanism maps', *Acta Metall.* **20**, 887–897 (1972).
122. H. Echsler, S. Ito and M. Schütze, 'Mechanical properties of oxide scales on mild steel at 800–1000°C', *Oxid. Met.* **60**, 241–269 (2003).
123. H. Echsler and M. Schütze, 'Deformation and fracture properties of oxide scales on mild steel at elevated temperatures', *Camp-ISIJ* **16**, 1329–1332 (2003).
124. B. Picqué, P.-O. Bouchard, P. Montmitonnet and M. Picard, 'Mechanical behaviour of iron oxide scale: experimental and numerical study', *Wear* **260**, 231–242 (2006).
125. Y. Hidaka, T. Anraku and N. Otsuka, 'Deformation of iron oxides upon tensile tests at 600–1250°C', *Oxid. Met.* **59**, 97–113 (2003).
126. Y. Hidaka, T. Anraku and N. Otsuka, 'Deformation of FeO oxide scales upon tensile tests at 600–1200°C', *Mater. Sci. Forum* **369–372**, 555–562 (2001).

127. V. Panjkovic, BlueScope Steel Research, private communication, 2007.
128. V. B. Ginzburg, 'Strain rate', *Steel-Rolling Technology: Theory and Practice*, Marcel Dekker, New York, 1989, pp. 21–22.
129. M. Krzyzanowski and J. H. Beynon, 'The tensile failure of mild steel oxides under hot rolling conditions', *Steel Research* **70**, 22–27 (1999).
130. M. Krzyzanowski and J. H. Beynon, 'Measurement of oxide properties for numerical evaluation of their failure under hot rolling conditions', *J. Mater. Processing Techno.* **125–126**, 398–404 (2002).
131. M. Krzyzanowski and J. H. Beynon, 'Compositional effect on oxide scale failure during hot rolling of steel', *Metal Forming 2000*, M. Pietrzyk *et al.* (eds), 2000, Balkema, Rotterdam, 331–334.
132. K. S. Tan, M. Krzyzanowski and J. H. Beynon, 'Effect of steel composition on failure of oxide scales in tension under hot rolling conditions', *Steel Research* **72**, 250–258 (2001).
133. H. Okada, Y. Matsuda and K. Sakamoto, 'Study of deformation of scale in hot strip rolling for future reduction of scale related surface defects', *Advanced Technology of Plasticity 1993 – Proc. 4th Int. Conf. on Technology of Plasticity*, Beijing, 1993, 711–716.
134. M. Krzyzanowski, J. H. Beynon and C. M. Sellars, 'Analysis of secondary oxide-scale failure at entry into the roll gap', *Metall. Mater. Trans. B*, **31B**, 1483–1490 (2000).
135. Y. H. Li and C. M. Sellars, 'Cracking and deformation of surface scale during hot rolling of steel', *Mater. Sci. Techno.* **18**, 304–311 (2002).
136. Y. Yu and J. G. Lenard, 'Estimating the resistance to deformation of the layer of scale during hot rolling of carbon steel strips', *J. Mater. Processing Techno.* **121**, 60–68 (2002).
137. J. G. Lenard, 'The coefficient of friction during hot rolling of low carbon steel strips', *J. Tribology (Trans. ASME)* **124**, 840–845 (2002).
138. A. Shirizly and J. G. Lenard, 'The effect of scaling and emulsion delivery on heat transfer during the hot rolling of steel strips', *J. Mater. Processing Techno.* **101**, 250–259 (2000).
139. P. A. Munther and J. G. Lenard, 'The effect of scaling on interfacial friction in hot rolling of steels', *J. Mater. Processing Techno.* **88**, 105–113 (1999).
140. Y. H. Li, M. Krzyzanowski, J. H. Beynon and C. M. Sellars, 'Physical simulation of interfacial conditions in hot forming of steels', *Acta Metall. SINICA (English Letters)* **13**, 359–368 (2000).
141. D. Filatov, O. Pawelski and W. Rasp, 'Hot-rolling experiments on deformation behaviour of oxide scale', *Steel Research Int.* **75**, No. 1, 20–25 (2004).
142. J. H. Beynon, M. Krzyzanowski and N. Taranets, 'Surface scale evolution in the hot rolling of steel', *Iron and Steel 40*, Supplement, November 2005, pp. 83–90.
143. J. H. Beynon and M. Krzyzanowski, 'Oxide scale behaviour during thermomechanical processing', *Proc. 3rd Int. Conf. Adv. Mater. Processing*, J. F. Nie and M. Barnett (eds), Institute of Materials Engineering Australasia, 2004, 39–46.
144. J. H. Beynon and M. Krzyzanowski, *Int. Conf. Modelling of Metal Rolling Processes* 3, London, December 1999, 360–369.
145. M. Krzyzanowski, J. H. Beynon, M. F. Frolich and S. Clowe, 'Modelling of oxide scale evolution in hot rolling and descaling', *Mater. Sci. Forum* **539–543**, 2461–2466 (2007).
146. M. Krzyzanowski, P. Suwanpinij and J. H. Beynon, *Materials Processing and*

- Design: Modelling, Simulation and Applications, NUMIFORM 2004, **712**, 1961–1966 (2004).
- 147. M. Krzyzanowski, M. Trull and J.H. Beynon, Euromech 435 Colloquium FWMF, Valenciennes, France, June 2002, 95–102.
  - 148. W. Y. D. Yuen, A. Dixon and R. Y. Chen, ‘Modelling the oxide growth and its applications to hot rolling’, Proc. SEAISI 2005 Conference, Hanoi, Vietnam, May 2005, Session 9, Paper 4.
  - 149. R. M. Hudson, ‘Pickling of hot rolled strip: an overview’, Iron & Steelmaker **18**, No. 9, 31–39 (Sept. 1991).
  - 150. D. J. Dingley and V. Randle, ‘Review: Microstructure determination by electron back-scatter diffraction’, J. Mater. Sci. **27**, 4545–4566 (1992).
  - 151. V. Randle, ‘Application of electron backscatter diffraction to steel products’, Ironmaking and Steelmaking **21**, 209–214 (1994).
  - 152. V. Randle, ‘Application of electron backscatter diffraction to grain boundary characterisation’, Int. Mater. Reviews **49**, 1–11 (2004).
  - 153. R. L. Higginson, G. D. West and M. A. E. Jepson, ‘The characterisation of oxide scales grown on nickel containing steel substrates using electron backscatter diffraction’, Mater. Sci. Forum **539–543**, 4482–4487 (2007).
  - 154. R. L. Higginson, M. A. E. Jepson and G. D. West, ‘Use of EBSD to characterise high temperature oxides formed on low alloy and stainless steels’, Mater. Sci. Techno. **22**, 1325–1332 (2006).
  - 155. G. D. West, S. Biroscia and R. L. Higginson, ‘Phase determination and microstructure of oxide scales formed on steel at high temperature’, J. Microscopy **217**, 122–129 (2005).
  - 156. S. Biroscia and R. L. Higginson, ‘Phase identification of oxide scale on low carbon steel’, Mater. High Temp. **22**, 179–184 (2005).
  - 157. G. D. West and R. L. Higginson, ‘Characterization of high temperature oxidation using electron backscatter diffraction’, Mater. High Temp. **22**, 201–205 (2005).
  - 158. R. L. Higginson and G. D. West, ‘The study of texture development of high temperature oxide scales on steel substrates using electron backscatter diffraction’, Mater. Sci. Forum, **495–497**, 399–404 (2005).
  - 159. S. Biroscia, D. Dingley and R. L. Higginson, ‘Microstructural and microtextural characterization of oxide scale on steel using electron backscatter diffraction’, J. Microscopy, **213**, 235–240 (2004).
  - 160. R. L. Higginson, B. Roebuck and E. J. Palmiere, ‘Texture development in oxide scales on steel substrates’, Scripta Mater. **47**, 337–342 (2002).
  - 161. S. Biroscia and R. L. Higginson, ‘Study of scale growth on steel substrates using electron back scatter diffraction’, Mater. Sci. Forum **426–432**, 3611–3616 (2003).
  - 162. D. P. Burke and R. L. Higginson, ‘Characterization of multicomponent scales by electron back scattered diffraction (EBSD)’, Scripta Mater. **42**, 277–281 (2000).
  - 163. J. A. Szpunar and B.-K. Kim, ‘High temperature oxidation of steel: new description of structure and properties of oxide’, Mater. Sci. Forum **539–543**, 223–227 (2007).
  - 164. V. V. Basabe and J. A. Szpunar, ‘Texture of oxide scales during hot rolling of low carbon steel’, Mater. Sci. Forum **495–497**, 339–343 (2005).
  - 165. B.-K. Kim and J. A. Szpunar, ‘Anisotropic microstructure of iron oxides formed during high temperature oxidation of steel’, Mater. Sci. Forum **408–412**, 1711–1716 (2002).
  - 166. V. V. Basabe and J. A. Szpunar, ‘Growth rate and phase composition of oxide scales during hot rolling of low carbon steel’, ISIJ Int. **44**, 1554–1559 (2004).

## **Part II**

Developments in protective oxide  
scales and coatings

---



# High-temperature corrosion mechanism of layered ternary ceramics

Z J LIN, M S LI and Y C ZHOU  
Chinese Academy of Sciences, China

## 9.1 Introduction

Layered ternary ceramics (LTCs), an extension of the *MAX* phase [1], have recently been described [2]. LTCs such as  $M_{n+1}AX_n$  phases (where  $M$  is an early transition metal,  $A$  is an A-group (mostly IIIA or IVA) element, and  $X$  is either C or N) possess salient properties, including high strength and elastic modulus, damage tolerance at room temperature, excellent electrical and thermal conductivities, and good thermal shock resistance. An important property of *MAX* phases is their easy machinability. Unlike traditional ceramics, *MAX*-phase compounds can be readily machined by using an electrical discharge method or by conventional cutting tools. A photograph of several *MAX*-phase parts machined by an electrical discharge method and conventional cutting tools is displayed in Fig. 9.1. Due to the similarity in crystal structures, ternary carbides in the  $T$  ( $T = \text{Sc, Zr, Hf, U}$ )–Al–C [3–12] and  $A$  ( $A = \text{Al, Sc, Lu, Gd}$ )–B–C [13–19] systems are included among the LTCs. Crystal structures of several representative LTCs including  $\text{Cr}_2\text{AlC}$  [20–22],  $\text{Ti}_3\text{SiC}_2$  [23,24],  $\text{Ti}_4\text{AlN}_3$  [25],  $\text{Ta}_4\text{AlC}_3$  [26,27],  $\text{ScAl}_3\text{C}_3$ ,  $\text{Zr}_2\text{Al}_3\text{C}_4$ ,  $\text{Zr}_3\text{Al}_3\text{C}_5$  [7],  $\text{Al}_3\text{BC}$  [19] and  $\text{Al}_3\text{BC}_3$  [19] are displayed in Fig. 9.2, with the corresponding structural parameters listed in Table 9.1 [7,19,21–27]. In addition, typical properties of three LTCs, i.e.,  $\text{Ti}_3\text{SiC}_2$  [1,28,29],  $\text{Ti}_3\text{AlC}_2$  [30,31] and  $\text{Zr}_3\text{Al}_3\text{C}_5$  [11], are summarized in Table 9.2. The unique crystal structures and bonding characteristics in  $T$ –Al–C and  $A$ –B–C systems endow these carbides with enhanced stiffness at elevated temperatures. For example, the high-temperature Young's modulus of  $\text{Zr}_3\text{Al}_3\text{C}_5$  remained 291 GPa at 1600°C, which is superior to those for most refractory materials [11].  $T$ –A–C and A–B–C significantly extend the applications of *MAX* phases at elevated temperatures. Thus, LTCs are promising candidates for applications in a wide temperature range.

Here we review progress on the high-temperature corrosion behavior of LTCs. LTCs are a large family of solids. To conserve space, only the corrosion mechanisms of several representative LTCs are presented. This chapter is structured as follows. In the next section, synthesis and microstructure of



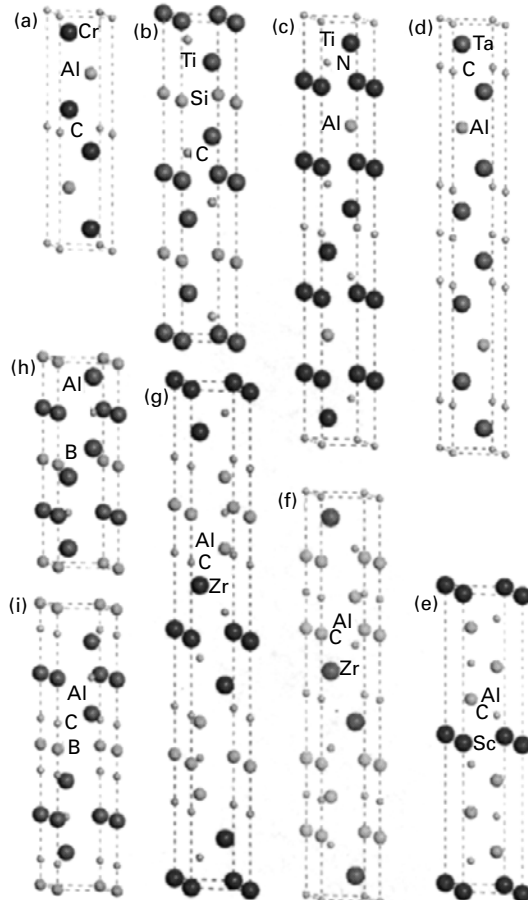
9.1 Photograph of several *MAX*-phase parts machined by the electrical discharge method and conventional high-speed steel cutting tools.

LTCs are briefly introduced. The third section deals with high-temperature oxidation and hot corrosion mechanism of representative LTCs such as  $Ti_3SiC_2$ ,  $Ti_3AlC_2$ ,  $Ti_2AlC$  and  $Zr_3Al_3C_5$ . Moreover, improvements on the high-temperature oxidation resistance of LTCs by surface modification, composite preparation and solid solution treatment are discussed. High-temperature hot corrosion mechanism of LTCs in molten salts including  $Na_2SO_4$ ,  $NaCl$  and  $K_2CO_3$  will be presented in the fourth section. Finally, conclusions are drawn and future trends are highlighted.

## 9.2 Microstructure and synthesis of layered ternary ceramics (LTCs)

### 9.2.1 Microstructure

The crystal structures of  $M_{n+1}AX_n$  phases consist of two basic units, i.e., the nonstoichiometric  $MX_x$  unit and the A atomic plane [1,2]. The most common atomic ratios for  $M:A:X$  are 2:1:1, 3:1:2 and 4:1:3. Thus, they are usually called 211, 312 and 413 phases for brevity.  $Cr_2AlC$ ,  $Ti_3SiC_2$  and  $Ti_4AlN_3$  are three representative compounds of 211, 312 and 413 phases, respectively (Figs 9.2(a)–(c)). The most pronounced difference between the crystal structures



9.2 Crystal structures of several representative layered ternary ceramics: (a)  $\text{Cr}_2\text{AlC}$ , (b)  $\text{Ti}_3\text{SiC}_2$ , (c)  $\text{Ti}_4\text{AlN}_3$ , (d)  $\text{Ta}_4\text{AlC}_3$ , (e)  $\text{ScAl}_3\text{C}_3$ , (f)  $\text{Zr}_2\text{Al}_3\text{C}_4$ , (g)  $\text{Zr}_3\text{Al}_3\text{C}_5$ , (h)  $\text{Al}_3\text{BC}$ , (i)  $\text{Al}_3\text{BC}_3$ .

shown in Figs 9.2(a)–(c) is the number of  $M$ -layers within every two  $A$ -layers, i.e., there are two, three and four  $M$ -layers within every two  $A$ -layers in  $M_2AX$ ,  $M_3AX_2$  and  $M_4AX_3$ , respectively.  $\text{Ta}_4\text{AlC}_3$  is an exception; this compound was recently identified [27] and its crystal structure (Fig. 9.2(d)) was determined [26].

Ternary  $T$ –Al–C compounds (Figs 9.2(e)–(g)) can be viewed as the intergrown structures consisting of two kinds of layers. One is the  $(T\text{-C})_m$  ( $m = 1, 2$  or  $3$ ) slab in the NaCl-type structure and the other consists of an Al–C unit in an arrangement similar to that of the binary aluminum carbide  $\text{Al}_4\text{C}_3$ . Wang *et al.* [12] identified the close relationships between the atomic radii of transition metal elements and lattice mismatch, as well as the strain

**Table 9.1** Summary of crystal structural parameters of several representative layered ternary ceramics

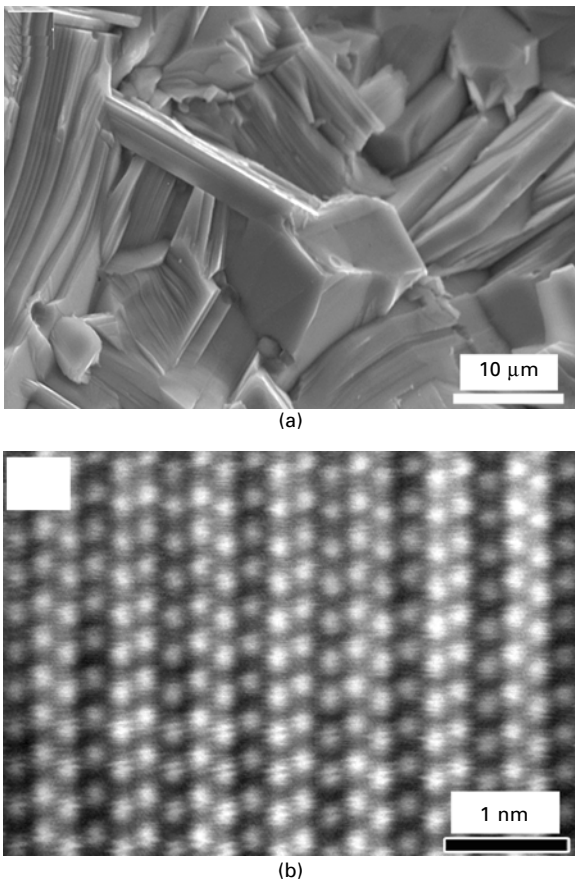
	Compound	Structural parameter	References
<i>MAX-phases</i>	$\text{Cr}_2\text{AlC}$	S.G.: $P6_3/\text{mmc}$ , $a = 0.2858$ nm, $c = 1.2818$ nm, Cr (1/3, 2/3, 0.086), Al (2/3, 1/3, 1/4), C (0, 0, 0)	21, 22
	$\text{Ti}_3\text{SiC}_2$	S.G.: $P6_3/\text{mmc}$ , $a = 0.3068$ nm, $c = 1.7670$ nm, Ti1 (0, 0, 0), Ti2 (1/3, 2/3, 0.1350), Si (0, 0, 1/4), C (1/3, 2/3, 0.05741)	23, 24
	$\text{Ti}_4\text{AlN}_3$	S.G.: $P6_3/\text{mmc}$ , $a = 0.2988$ , $c = 2.3372$ , Ti1 (1/3, 2/3, 0.0542), Ti2 (0, 0, 0.1547), Al (1/3, 2/3, 1/4), N1 (0, 0, 0), N2 (2/3, 1/3, 0.1050)	25
	$\text{Ta}_4\text{AlC}_3$	S.G.: $P6_3/\text{mmc}$ , $a = 0.3091$ nm, $c = 2.3708$ nm, Ta1 (1/3, 2/3, 0.0552), Ta2 (2/3, 1/3, 0.1602), Al (1/3, 2/3, 1/4), C1 (0, 0, 0), C2 (0, 0, 0.1113)	2, 26
	$\text{ScAl}_3\text{C}_3$	S.G.: $P6_3/\text{mmc}$ , $a = 0.3301$ nm, $c = 1.6512$ nm, Sc (0, 0, 0), Al1 (1/3, 2/3, 0.1299), Al2 (2/3, 1/3, 1/4), C1 (2/3, 1/3, 0.0883), C2 (1/3, 2/3, 1/4)	
<i>T-Al-C</i>	$\text{Zr}_2\text{Al}_3\text{C}_4$	S.G.: $P6_3/\text{mmc}$ , $a = 0.3300$ nm, $c = 2.2400$ nm, Zr (1/3, 2/3, 0.0592), Al1 (0, 0, 0.1604), Al2 (2/3, 1/3, 1/4), C1 (0, 0, 0), C2 (2/3, 1/3, 0.1302), C3 (0, 0, 1/4)	8
	$\text{Zr}_3\text{Al}_3\text{C}_5$	S.G.: $P6_3/\text{mmc}$ , $a = 0.3300$ nm, $c = 2.7600$ nm, Zr1 (0, 0, 0), Zr2 (2/3, 1/3, 0.0962), Al1 (2/3, 1/3, 0.1780), Al2 (0, 0, 1/4), C1 (1/3, 2/3, 0.0504), C2 (0, 0, 0.1537), C3 (1/3, 2/3, 1/4)	7, 8
<i>A-B-C</i>	$\text{Al}_3\text{BC}$	S.G.: $P6_3/\text{mmc}$ , $a = 0.3436$ nm, $c = 1.1326$ nm, Al1 (1/3, 2/3, 0.0758), Al2 (0, 0, 1/4), B (0, 0, 0), C (1/3, 2/3, 1/4)	19
	$\text{Al}_3\text{BC}_3$	S.G.: $P6_3/\text{mmc}$ , $a = 0.3363$ nm, $c = 1.5582$ nm, Al1 (1/3, 2/3, 0.1224), Al2 (0, 0, 1/4), B (0, 0, 0), C1 (0, 0, 0.0914), C2 (1/3, 2/3, 1/4)	19

Table 9.2 Summary of typical properties of  $Ti_3SiC_2$  [1,28,29],  $Ti_3AlC_2$  [1,30,31] and  $Zr_3Al_3C_5$  [11]

Properties	$Ti_3SiC_2$	$Ti_3AlC_2$	$Zr_3Al_3C_5$
Theoretical density ( $g\ cm^{-3}$ )	4.50	4.24	5.28
Electrical resistivity ( $\mu\Omega\cdot m$ )	0.22	0.29	1.45
Thermal conductivity ( $W \cdot m^{-1} K^{-1}$ )	37	–	14.3
Heat capacity ( $J \cdot mol^{-1} K^{-1}$ )	110	–	193
Coefficient of thermal expansion ( $\times 10^{-6}\ K^{-1}$ )	9.1	9.0	7.7
Young's modulus (GPa)	322–333	297	374
Shear modulus (GPa)	134–139	124	157
Bulk modulus (GPa)	185–206	165	202
Hardness (GPa)	4.0	2.7–3.5	12.5
Fracture toughness ( $MPa \cdot m^{1/2}$ )	7.0	7.2	4.68
Bending strength (MPa)	450	375	488
Compressive strength (MPa)	900	570–764	2330

energy. The proposed method is not only helpful in explaining the trend in crystal structure of  $T$ -Al-C based ceramics, but may also be used to predict the crystal structure of layered compounds constructed by alternately stacked structural units. The lattice misfits between the binary  $T$ -C slab and the Al-C unit (or Al) are important for forming  $T$ -Al-C type crystal structures instead of MAX-phase type ones. A-B-C compounds generally possess a linear C-B-C unit, which plays an important role in determining their mechanical performance.

The unique properties of LTCs are strongly related to their crystal structures and microstructures. The combination of X-ray diffraction (XRD) or Neutron diffraction, scanning electron microscopy (SEM) and transmission electron microscopy (TEM) techniques such as selected area electron diffraction (SAED), convergent beam electron diffraction, high-resolution TEM (HRTEM), and Z-contrast scanning transmission electron microscopy (STEM), represent powerful methods to link microstructures of materials to macroscopic properties, allowing LTCs to be investigated in unprecedented detail. With these techniques, LTCs can be characterized from millimeter or micrometer scale down to atomic scale. Figures 9.3(a) and (b) are a SEM image of fracture surfaces of  $Ta_4AlC_3$  and a high-resolution Z-contrast STEM image of  $Cr_2AlC$  [22], respectively. Obviously, layered structural features of LTCs can be clearly characterized from micrometer down to atomic scale. Microstructural information obtained using these techniques is useful in optimizing both the processing and properties of LTCs down to the atomic-scale level, and thus provides insights into understanding the ‘processing–structure–property’ relationships of LTCs. Details on the microstructural characterizations of LTCs using TEM were recently reviewed in Reference 2.



9.3 (a) SEM image of fracture surfaces of  $\text{Ta}_4\text{AlC}_3$ ; (b) high-resolution Z-contrast STEM image of  $\text{Cr}_2\text{AlC}$ .

### 9.2.2 Synthesis

Synthesizing single-phase materials is the first step in investigating the intrinsic properties of LTCs. Attempts have been made to develop various processing methods. Preparing single-phase LTCs is tedious work since the formation region, as shown in the phase diagram, is narrow. Moreover, experimental parameters such as raw materials, temperature, pressure, etc., may influence the purity and microstructure of final products. However, by good control of the experimental parameters, a series of LTCs have been fabricated in powders, bulk materials and thin films. Most early work on LTCs concentrated on processing methods, and simply listing them is cumbersome. For brevity, only synthesizing methods of several representative compounds are introduced here. Table 9.3 summarizes typical processing methods for  $\text{Ti}_3\text{SiC}_2$

Table 9.3 Summary of typical methods for synthesizing three representative layered ternary ceramics. 'C' and 'R' denote compound and reference, respectively

C	Method	Processing parameters	Contributions	R
$\text{Ti}_3\text{SiC}_2$	CVD	(1) $\text{TiCl}_4$ , $\text{SiCl}_4$ , $\text{CCl}_4$ and $\text{H}_2$ , graphite and Ta substrates; (2) 1000–1300°C, pressure $10^5\text{ Pa}$	(1) $\text{Ti}_3\text{SiC}_2$ film with minor amount of $\text{TiSi}_2$ was deposited; (2) The anisotropic nature and abnormal plasticity of $\text{Ti}_3\text{SiC}_2$ were discovered	32
	Solid state reaction	(1) $\text{Ti:Si:C} = 0.42:0.29:0.29$ ; (2) 1100°C, 10 h; (3) Removal of $\text{TiSi}_2$ and $\text{TiO}_2$	(1) $\text{Ti}_3\text{SiC}_2$ powders (95 wt%) were prepared; (3) Oxidation tests at 400–1250°C demonstrated that $\text{Ti}_3\text{SiC}_2$ has better oxidation resistance than $\text{TiC}$	34
	HIP-SHS	(1) Ti, Si and graphite; (2) Synthesis of $\text{Ti}_3\text{SiC}_2$ powders by SHS; (3) HIP at 1400°C	(1) Bulk $\text{Ti}_3\text{SiC}_2$ (82 vol%, with $\text{TiC}$ impurity) was prepared; (2) The decomposition temperature of $\text{Ti}_3\text{SiC}_2$ in Ar was determined to be 1500°C	35
	Arc-melting	(1) Ti, Si and C, arc-melting; (2) Annealing at 1200°C, 100 h	(1) Bulk $\text{Ti}_3\text{SiC}_2$ (2 vol% $\text{TiC}$ ) was fabricated; (2) The Ti-Si-C phase diagram at 1200°C was constructed	36
	HIP	(1) $\text{Ti:C:SiC} = 3:2:2$ ; (2) HIP at 1600°C and under 40 MPa for 4 h	(1) Bulk $\text{Ti}_3\text{SiC}_2$ (2 vol% impurity) was synthesized; (2) Thermal and mechanical properties were tested	28
	HP/solid-liquid reaction	(1) $\text{Ti:Si:C} = 0.42:0.23:0.35$ ; (2) HP at 1450–1600°C, 38 MPa, 1 h	(1) Bulk $\text{Ti}_3\text{SiC}_2$ (93 wt%) was prepared; (2) Effect of processing parameters on the purity, density and mechanical properties of $\text{Ti}_3\text{SiC}_2$ was studied	37
	PDS	(1) $\text{Ti:SiC:TiC} = 4:2:1$ ; (2) Sintering at 1250–1450°C under 50 MPa	(1) $\text{Ti}_3\text{SiC}_2$ (92 vol%) was prepared; (2) Experimental parameters using Ti, SiC and $\text{TiC}$ were investigated	39
	PS	(1) Mechanically alloyed $\text{Ti:Si:C} = 3:1:2$ ; (2) Cold isostatic pressing, 200 MPa, 1100–1500°C, 1 h	(1) 99% dense $\text{Ti}_3\text{SiC}_2$ (80 wt%) was obtained; (2) Effect of mechanical alloying time and sintering temperature was investigated	40
	MS	(1) $\text{Ti}_3\text{SiC}_2$ or Ti, Si and $\text{C}_{60}$ targets; (2) MgO substrate, 600–900°C	(000 $\bar{l}$ )-oriented epitaxial $\text{Ti}_3\text{SiC}_2$ films were deposited by using two deposition methods	42

Table 9.3 (Continued)

C	Method	Processing parameters	Contributions	R
Ti <sub>3</sub> SiC <sub>2</sub>	HP	(1) Ti, Si, C and Al; (2) HP, 1550°C, 5 min, 1400°C, 1 h, 40 MPa	TiC-free bulk Ti <sub>3</sub> SiC <sub>2</sub> ceramic with excellent oxidation was achieved by Al addition	41
Zr <sub>3</sub> Al <sub>3</sub> C <sub>5</sub>	Solid-liquid reaction	(1) Zr-Al intermetallics, C, Zr:Al:C = 3:3:5; (2) HP, 1500°C, 1 h	(1) Zr <sub>3</sub> Al <sub>3</sub> C <sub>5</sub> powders (99.2 wt%) were synthesized; (2) The oxidation behavior of Zr <sub>3</sub> Al <sub>3</sub> C <sub>5</sub> was tested	10
	HP/solid-liquid reaction	(1) Zr, Al, graphite using Si and Y <sub>2</sub> O <sub>3</sub> as additives; (2) HP, 1750°C, 40 MPa, 2 h	(1) Bulk Zr <sub>3</sub> Al <sub>3</sub> C <sub>5</sub> (95 wt%) was synthesized in situ; (2) Mechanical and physical properties of Zr <sub>3</sub> Al <sub>3</sub> C <sub>5</sub> at ambient and elevated temperatures were investigated	11
	Solid state reaction	(1) Al, ZrC, graphite, amorphous carbon; (2) 1600°C, 1 h	High-purity Zr <sub>3</sub> Al <sub>3</sub> C <sub>5</sub> powders were synthesized at 1600°C in vacuum	9
	PECS	(1) Zr <sub>3</sub> Al <sub>3</sub> C <sub>5</sub> powders; (2) PECS, 2000°C, vacuum, 5 min	(1) Bulk Zr <sub>3</sub> Al <sub>3</sub> C <sub>5</sub> was fabricated; (2) Flexural strength and hardness were primarily evaluated	6
Al <sub>3</sub> BC <sub>3</sub>	PS	(1) Al <sub>3</sub> C <sub>4</sub> , B <sub>4</sub> C (8Al/4B/7C); (2) 1800°C, several minutes (1) Al, B, C; (2) 1400°C, 15 min, heat to 2000°C	(1) Al <sub>3</sub> BC <sub>3</sub> powders were synthesized; (2) Crystallographic data of Al <sub>3</sub> BC <sub>3</sub> were determined High-purity single crystalline Al <sub>3</sub> BC <sub>3</sub> was prepared	14
	Chemical reaction synthesis	(1) Al:B:C = 40:2:3; (2) 1927°C, 1 h; (3) Removal of residual Al and Al <sub>4</sub> C <sub>3</sub> byproducts	(1) Single crystalline Al <sub>3</sub> BC <sub>3</sub> was fabricated; (2) Bulk modulus of Al <sub>3</sub> BC <sub>3</sub> was presented; (3) No phase transition was found	15
	SPS	(1) Al <sub>3</sub> C <sub>4</sub> , B <sub>4</sub> C (Al:B:C = 8:4:7); (2) PS, 1800°C, 2 h; (3) SPS, 1650°C, 35 MPa, 10 min, vacuum	(1) Pure Al <sub>3</sub> BC <sub>3</sub> powders as well as bulk material were prepared; (2) Thermal and mechanical properties of bulk Al <sub>3</sub> BC <sub>3</sub> were examined	16

[28,32–42],  $Zr_3Al_3C_5$  [5,6,9–11] and  $Al_3BC_3$  [14–16]. The main contributions of the corresponding work are also highlighted.

During the synthesis of  $Ti_3SiC_2$ , impurities such as  $TiC$ ,  $SiC$ ,  $TiSi_2$  and  $Ti_5Si_3$  were observed in the final products. In order to obtain single-phase  $Ti_3SiC_2$ , a number of synthesis methods with various initial materials have been tested. Raw materials that were used to prepare bulk  $Ti_3SiC_2$  can be summarized as  $Ti/Si/C$  [34–37,41],  $Ti/SiC/C$  [28],  $Ti/Si/TiC$  [38],  $Ti/SiC/TiC$  [39] and  $Ti/Si/C/SiC$  [33]. The processing methods include chemical vapor deposition (CVD) [32], solid state reaction [34], hot isostatic pressing–self propagation high-temperature synthesis (HIP–SHS) [35], arc melting–annealing [36], solid–liquid reaction synthesis [37], hot isostatic pressing (HIP) [28], hot pressing (HP) [41], spark plasma sintering–pulse discharge sintering (SPS–PDS) [39], pressureless sintering (PS) [40] and magnetron sputtering (MS) [42]. Currently, high-purity  $Ti_3SiC_2$  can be readily synthesized with a minor amount of Al addition. However, research on synthesis of *T*-Al-C and A-B-C compounds is less reported because many of their physical and mechanical properties are unknown.

Raw materials for synthesis of LTCs can be either corresponding elemental powders or binary compounds. As demonstrated in Table 9.3,  $Ti_3SiC_2$  can be synthesized using a wide range of raw materials. In certain cases, however, the selection of raw materials is important for both processing parameters and purity of the final products. For example, the use of  $Ti/TiN/Al$  as starting materials significantly improved the purity of the final product and simplified the processing conditions during the synthesis of bulk  $Ti_2AlN$  ceramic [43].

### **9.3 High-temperature oxidation mechanism of layered ternary ceramics**

#### **9.3.1 High-temperature oxidation mechanism of $Ti_3SiC_2$**

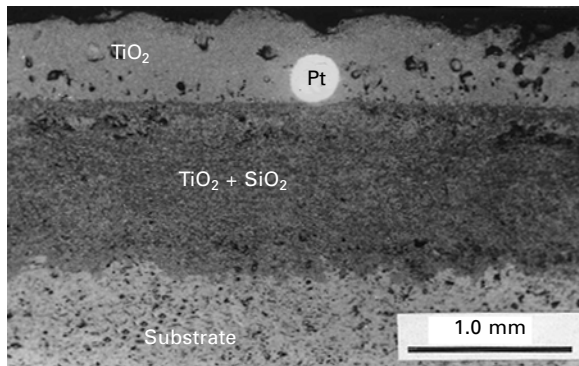
$Ti_3SiC_2$  is a promising candidate for high-temperature structural applications. Oxidation resistance is one of the most important factors for materials used in high-temperature environments. The oxidation behavior has been extensively investigated. Racault *et al.* [34] studied the oxidation resistance of  $Ti_3SiC_2$  powders at 400–1250°C in dry air. The starting oxidation temperature of  $Ti_3SiC_2$  was determined to be 400°C. The oxidation of  $Ti_3SiC_2$  displayed a two-step characteristic over the whole temperature range. At the first stage ( $t < 20$ –30 min), the oxidation rate was relatively fast, and the mass changes varied from 5% to 45% of the total mass. The second stage was a relatively slow oxidation process with mass gains being less than 10% after oxidation for 10 h. Barsoum *et al.* [44] showed that the oxidation of  $Ti_3SiC_2$  followed a parabolic rate law. The parabolic rate constant increased from  $1 \times 10^{-9} \text{ kg}^2\text{m}^{-4}\text{s}^{-1}$  at 900°C to  $1 \times 10^{-4} \text{ kg}^2\text{m}^{-4}\text{s}^{-1}$  at 1400°C with an activation

energy of  $370 \pm 20 \text{ kJ mol}^{-1}$ . They claimed that the good oxidation resistance of  $\text{Ti}_3\text{SiC}_2$  originated from the contribution of Si.  $\text{TiO}_2$  and  $\text{SiO}_2$  formed during the oxidation process. The formation of  $\text{SiO}_2$  hindered the inward diffusion of oxygen and resulted in a good high-temperature oxidation resistance. In addition, Barsoum *et al.* [44] proposed that the oxidation of  $\text{Ti}_3\text{SiC}_2$  proceeded by inward diffusion of oxygen and simultaneously outward diffusion of Ti and carbon while Si was immobile. Radhakrishnan *et al.* [45] studied the oxidation behavior of  $\text{Ti}_3\text{SiC}_2$  (2 vol%  $\text{TiSi}_2$ ) at  $1000^\circ\text{C}$  for 50 h. The oxidation kinetics followed a parabolic-linear rate law. The oxidation at the initial stage followed a parabolic rate law, and then it became linear. Sun *et al.* [46,47] systematically investigated the oxidation mechanism of  $\text{Ti}_3\text{SiC}_2$ . The mass gain at  $900\text{--}1100^\circ\text{C}$  was relatively low and the oxidation kinetics followed the parabolic rate law. The oxidation kinetics were complicated at  $1200\text{--}1300^\circ\text{C}$ , which can be regarded as a two-step parabolic rate law. The parabolic rate constants of  $\text{Ti}_3\text{SiC}_2$  oxidation in air are summarized in Table 9.4. For comparison, the corresponding reported values for  $\text{Ti}_3\text{Si}_{0.9}\text{Al}_{0.1}\text{C}_2$  and  $\text{Ti}_3\text{AlC}_2$  are also included.

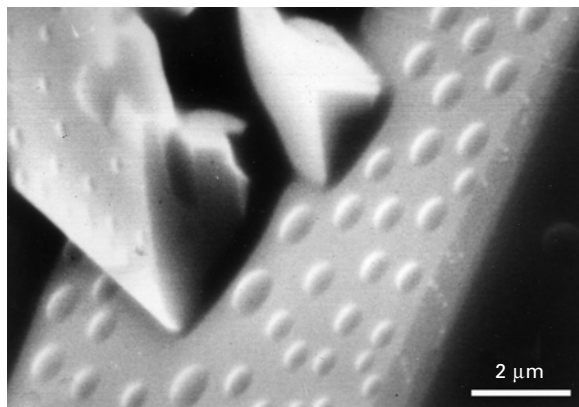
A Pt-marker experiment was conducted to investigate the oxidation mechanism of  $\text{Ti}_3\text{SiC}_2$  [47]. The experimental details are as follows. A platinum wire 0.3 mm in diameter was welded on a  $\text{Ti}_3\text{SiC}_2$  specimen. Afterwards, the sample was oxidized in a furnace at  $1200^\circ\text{C}$  for 100 h. The corresponding cross-sectional micrograph is displayed in Fig. 9.4 [47]. The bright spot corresponds to the Pt mark. The Pt wire locates beneath the outmost  $\text{TiO}_2$  layer. Based on a series of microstructural analyses, the oxidation mechanism of  $\text{Ti}_3\text{SiC}_2$  can be understood as follows: the oxidation kinetics of  $\text{Ti}_3\text{SiC}_2$  were determined by the outward diffusion of Ti as well as the inward diffusion of oxygen. The outward diffused Ti produced the coarse outermost  $\text{TiO}_2$  layer, while the inward diffused oxygen reacted with the  $\text{Ti}_3\text{SiC}_2$  substrate and formed a mixed  $\text{TiO}_2$  and  $\text{SiO}_2$  layer. Interestingly, bubbles were observed at the surfaces of the outermost oxides, as shown in Fig. 9.5. Energy dispersive spectroscopy (EDS) analyses revealed that the bubbles are rich in silicon, while Si was difficult to detect at the regions surrounding the bubbles. Therefore, Sun *et al.* [46] proposed that the oxide scale formed during the initial oxidation

*Table 9.4* Parabolic rate constants for  $\text{Ti}_3\text{SiC}_2$  [46,47],  $\text{Ti}_3\text{AlC}_2$  [61] and  $\text{Ti}_3\text{Si}_{0.9}\text{Al}_{0.1}\text{C}_2$  [59] during oxidation at  $1000\text{--}1300^\circ\text{C}$  in air

Temperature	Parabolic rate constant ( $\text{kg}^2\text{m}^{-4}\text{s}^{-1}$ )		
	$\text{Ti}_3\text{SiC}_2$	$\text{Ti}_3\text{AlC}_2$	$\text{Ti}_3\text{Si}_{0.9}\text{Al}_{0.1}\text{C}_2$
$1000^\circ\text{C}$	$2.4 \times 10^{-9}$	$3.2 \times 10^{-11}$	$4.1 \times 10^{-11}$
$1100^\circ\text{C}$	$4.0 \times 10^{-7}$	$1.2 \times 10^{-10}$	$2.7 \times 10^{-10}$
$1200^\circ\text{C}$	$2.2 \times 10^{-6}$	$4.0 \times 10^{-10}$	$4.2 \times 10^{-10}$
$1300^\circ\text{C}$	$9.6 \times 10^{-6}$	$2.4 \times 10^{-9}$	$1.1 \times 10^{-9}$



9.4 Cross-sectional SEM image of Ti<sub>3</sub>SiC<sub>2</sub> sample oxidized at 1200°C for 100 h. The white spot corresponds to the position of a Pt wire.



9.5 Bubbles in the oxide surfaces of a Ti<sub>3</sub>SiC<sub>2</sub> specimen oxidized at 1100°C in air.

stage reduced the oxygen partial pressure between the oxide scale and the substrate. As a consequence, Si tended to be oxidized by forming SiO. The outward diffused SiO was then further oxidized into SiO<sub>2</sub>, where the oxygen pressure is high enough. Thus, the overall oxidation process can be described using the following equation:



When the oxygen partial pressure is relatively low, the following equation is preferred:

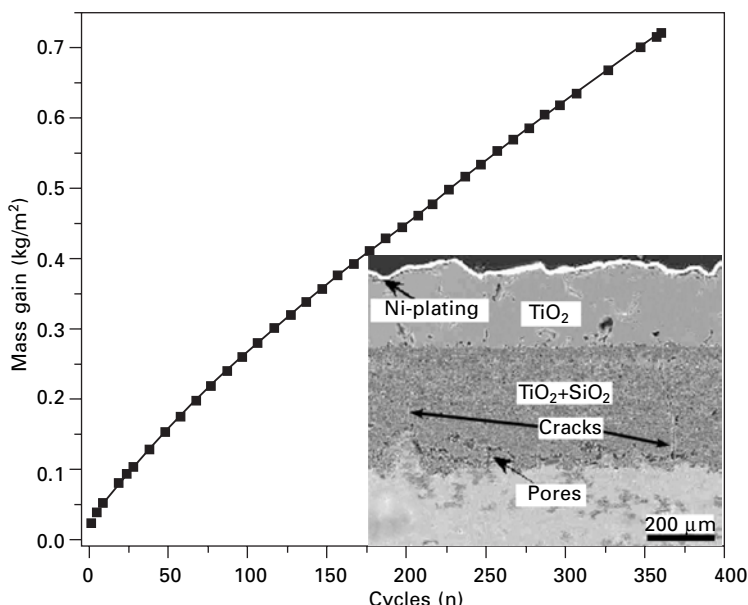


Further oxidation of SiO at a higher oxygen pressure follows:



In addition, Sun *et al.* [47] investigated the influence of TiC impurity on the oxidation resistance of  $\text{Ti}_3\text{SiC}_2$ . The activation energies for TSC<sup>ZS610</sup> (88 wt%  $\text{Ti}_3\text{SiC}_2$ ) and TSC<sup>ZS510</sup> (93 wt%  $\text{Ti}_3\text{SiC}_2$ ) were determined to be 253 and 343  $\text{kJ}\cdot\text{mol}^{-1}$ , respectively. In other words, the TiC impurity is deleterious to the high-temperature oxidation resistance of  $\text{Ti}_3\text{SiC}_2$ . This result is also useful in understanding the reason why the oxidation behaviors reported by different researchers are scattered. Yang [48] and his coworkers also studied the oxidation behavior of  $\text{Ti}_3\text{SiC}_2$  at 1000°C, reporting that a relatively loose  $\text{SiO}_2$  oxide layer forms at the initial oxidation stage.  $\text{TiO}_2$  has a faster growth rate. Therefore, the  $\text{TiO}_2$  layer covers the outer oxide layer. As a result, the oxide scales formed on the  $\text{Ti}_3\text{SiC}_2$  substrate are inner  $\text{TiO}_2$  and  $\text{SiO}_2$  layer and outer  $\text{TiO}_2$  scale.

The cyclic oxidation behavior of  $\text{Ti}_3\text{SiC}_2$ -base materials was investigated at 1100°C in air [49]. Scale spallation and mass loss were not observed. It was proposed that the outer  $\text{TiO}_2$  layer was under a low compressive stress, while the inner  $\text{TiO}_2 + \text{SiO}_2$  scale was under tensile stress during the cooling stage. Thus, the oxide scale is adherent and resistant to cyclic oxidation. Cyclic oxidation and acoustic emission (AE) tests were carried out to investigate the cracking behavior of oxide scales formed on  $\text{Ti}_3\text{SiC}_2$ -based ceramics at 1100°C [50]. As can be seen in Fig. 9.6, the oxide scale did not spall from the

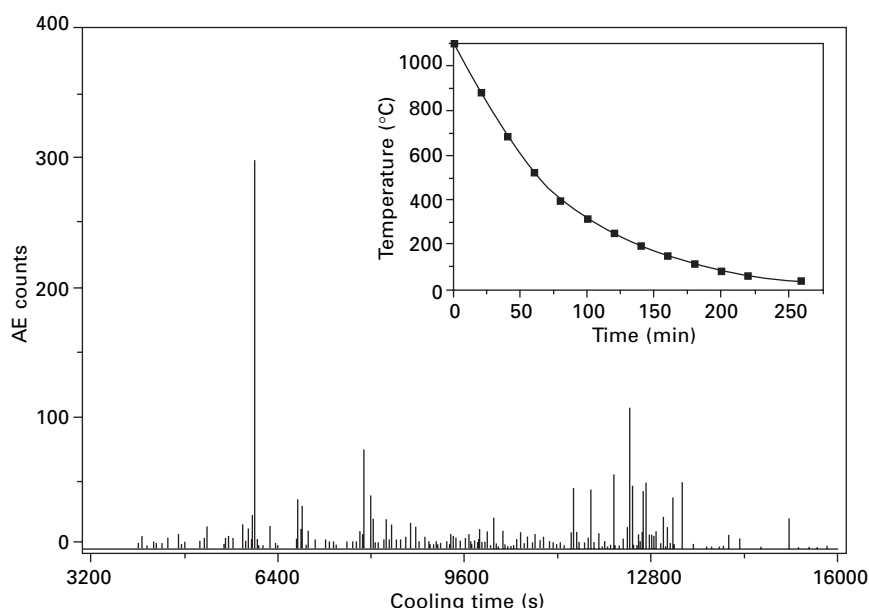


9.6 Cyclic oxidation kinetics of  $\text{Ti}_3\text{SiC}_2$  oxidized at 1100°C in air. The inset shows a cross-sectional micrograph of a sample after 360 cycles.

substrate during the cyclic oxidation at 1100°C for 360 cycles. However, a great number of microcracks penetrating the whole inner oxide layer were observed (Fig. 9.6). The AE test showed that the oxide scale did not crack during the isothermal oxidation at 1100°C for 1 hour (Fig. 9.7) [49], but the scale cracked during the cooling stage. Cracks in the inner oxide layer served as paths for the outward diffusion of Ti and inward diffusion of oxygen, increasing the growth rate of the outer oxide layer. A small mismatch in coefficients of thermal expansion (CTE) between the oxides and the substrate ensured a low thermal stress between the oxide scales and the  $\text{Ti}_3\text{SiC}_2$  substrate. Consequently,  $\text{Ti}_3\text{SiC}_2$  exhibited excellent long-term cyclic oxidation resistance.

### 9.3.2 Improvements to the high-temperature oxidation behavior of $\text{Ti}_3\text{SiC}_2$

As discussed above, the high-temperature oxidation resistance of  $\text{Ti}_3\text{SiC}_2$  above 1100°C is unsatisfactory. Therefore, attempts have been made to improve the high-temperature oxidation behavior of  $\text{Ti}_3\text{SiC}_2$ . This work can be classified into three categories: surface modification, composite preparation, and solid solution treatment.

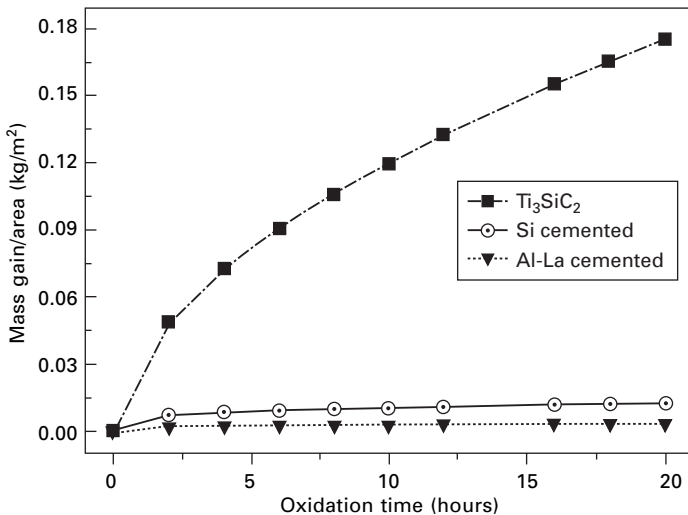


9.7 Acoustic emission count versus cooling time collected during cooling for  $\text{Ti}_3\text{SiC}_2$  oxidized at 1100°C for 1 hour.

### Surface modification

El-Raghy and Barsoum [51] prepared a surface  $\text{TiSi}_2 + \text{SiC}$  layer by reaction between an Si wafer and  $\text{Ti}_3\text{SiC}_2$  at 1200–1350°C. The high-temperature oxidation resistance of the treated samples was increased by three orders of magnitude compared with that of untreated  $\text{Ti}_3\text{SiC}_2$ . A silicide coating consisting mainly of  $\text{TiSi}_2$  and  $\text{SiC}$  was also prepared on  $\text{Ti}_3\text{SiC}_2$ -based ceramic by the pack cementation method [52]. A single layer of mixed  $\text{SiO}_2$  and  $\text{TiO}_2$  oxide scale formed on the surface of the coated sample during isothermal oxidation at 1100°C and 1200°C for 20 h. The parabolic rate constant was decreased by 2–3 orders of magnitude compared with those of the untreated specimens (Fig. 9.8). In addition, the coated samples displayed much better cyclic oxidation resistance. However, during the preparation of the coating, a number of fine cracks formed in the outer layer of the coating. The oxidation rate was accelerated when these cracks penetrated through the entire coating. So, further attempts on improving the oxidation resistance of  $\text{Ti}_3\text{SiC}_2$  were made.

Li *et al.* [53] conducted Al-La thermal diffusion on  $\text{Ti}_3\text{SiC}_2$ -based ceramics by the pack cementation method. The complete aluminide coatings have not been obtained. Interestingly, Al and La penetrated into the  $\text{Ti}_3\text{SiC}_2$  substrate quickly. Al was found to distribute into the whole interior of the specimen after cementation at 1100°C for 4 h. Al existed as either a solid solution or dispersed  $\text{AlLa}_3$  particles. A continuous  $\text{Al}_2\text{O}_3$  scale with a small amount of  $\text{TiO}_2$  on the outer layer formed during the oxidation of cemented  $\text{Ti}_3\text{SiC}_2$  at



9.8 Mass gain per unit area as a function of oxidation time for Si-cemented and Al-La co-cemented  $\text{Ti}_3\text{SiC}_2$  samples oxidized at 1100°C, together with that of an untreated sample for comparison.

1100°C in air for 20 h. The parabolic rate constant of the treated  $\text{Ti}_3\text{SiC}_2$  was decreased by two orders of magnitude, suggesting that the cementation remarkably improved the oxidation resistance of  $\text{Ti}_3\text{SiC}_2$ . It was proposed that Al distributed in  $\text{Ti}_3\text{SiC}_2$  acted as a ‘reservoir’ to supply enough Al for the formation of a continuous  $\text{Al}_2\text{O}_3$  layer during the oxidation process.

### *Composite preparation*

Tong *et al.* [54] fabricated  $\text{Ti}_3\text{SiC}_2/\text{SiC}$  composites. Oxidation tests at 1000°C demonstrated that  $\text{Ti}_3\text{SiC}_2/\text{SiC}$  composites displayed enhanced oxidation resistance compared to  $\text{Ti}_3\text{SiC}_2$ . Zhou *et al.* [55] investigated the high-temperature oxidation resistance of  $\text{Ti}_3\text{Si}_{1-x}\text{Al}_x\text{C}_2/\text{SiC}$  composites. SiC could improve both the high-temperature mechanical strength and the high-temperature oxidation resistance of the  $\text{Ti}_3\text{Si}_{1-x}\text{Al}_x\text{C}_2$  substrate. The incorporation of oxidation-resistant reinforced phases such as SiC and  $\text{Al}_2\text{O}_3$  can reduce the surface area of  $\text{Ti}_3\text{SiC}_2$  substrate that is directly exposed to air and consequently improve the oxidation resistance. However, the overall oxidation resistance is determined by the matrix materials. This method failed to improve the intrinsic oxidation resistance of  $\text{Ti}_3\text{SiC}_2$ .

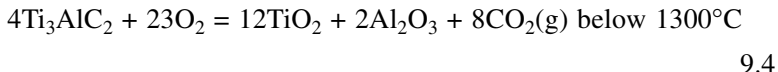
### *Solid solution treatment*

As far as improvement in high-temperature oxidation resistance of  $\text{Ti}_3\text{SiC}_2$  is concerned, solid solution is the most successful method. By combining TEM and first principles calculations, Yu *et al.* [56,57] proposed that both Si and Al could reduce the twin boundary energy and finally lead to the formation of layered ternary  $\text{Ti}_3\text{SiC}_2$  or  $\text{Ti}_3\text{AlC}_2$ . Moreover, Al is more efficient than Si in reducing the twin boundary energy of TiC. In addition, as discussed above, Li *et al.* [53] found that the distribution of Al in  $\text{Ti}_3\text{SiC}_2$  could act as an effective reservoir of Al. Theoretically, Wang and Zhou [58] predicted the possibility of forming  $\text{Ti}_3\text{Si}_{1-x}\text{Al}_x\text{C}_2$  solid solutions with enhanced oxidation resistance.

Intrigued by these facts, Zhou *et al.* [41] synthesized  $\text{Ti}_3\text{Si}_{1-x}\text{Al}_x\text{C}_2$  solid solutions. The oxidation behavior of  $\text{Ti}_3\text{Si}_{0.9}\text{Al}_{0.1}\text{C}_2$  solid solution in air was investigated at 1000–1350°C [59]. The parabolic rate constants were decreased by 2–4 orders of magnitude compared with those of the untreated  $\text{Ti}_3\text{SiC}_2$ . The high activity and diffusion of Al and the low solubility of oxygen in the solid solution are key factors for the formation of a continuous  $\text{Al}_2\text{O}_3$  scale. The oxidation resistance of  $\text{Ti}_3\text{Si}_{0.9}\text{Al}_{0.1}\text{C}_2$  deteriorated at 1350°C because of the depletion of  $\alpha\text{-Al}_2\text{O}_3$ . The extensive reaction between  $\text{TiO}_2$  and  $\text{Al}_2\text{O}_3$  consumed a significant amount of  $\text{Al}_2\text{O}_3$  by forming  $\text{Al}_2\text{TiO}_5$ .

### 9.3.3 High-temperature oxidation mechanism of $Ti_3AlC_2$ and $Ti_2AlC$

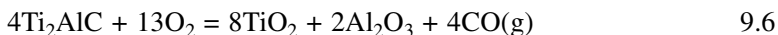
Barsoum *et al.* [60] reported that the high-temperature oxidation resistance of  $Ti_3AlC_2$  and  $Ti_2AlC$  was unsatisfactory because a mixed and non-protective oxide scale formed during the oxidation in air. In contrast, Wang and Zhou [61,62] showed that  $Ti_3AlC_2$  and  $Ti_2AlC$  exhibited excellent high-temperature oxidation resistance. Later, Sundberg *et al.* [63] confirmed that the oxidation resistance of  $Ti_2AlC$  was excellent and claimed that the results were consistent with those reported by Wang and Zhou [62]. We find that impurities such as TiC and TiAl seriously deteriorate the oxidation resistance of layered ternary Ti-Al-C ceramics. XRD characterization is not enough because the reflections of impurities such as TiAl may strongly overlap those of  $Ti_2AlC$  [64]. Therefore, microstructures of the samples should be carefully examined prior to oxidation tests. Wang and Zhou [61] concluded that the oxidation of  $Ti_3AlC_2$  took place according to the following reactions:



Above  $1300^\circ C$ , complex oxide  $Al_2TiO_5$  formed:

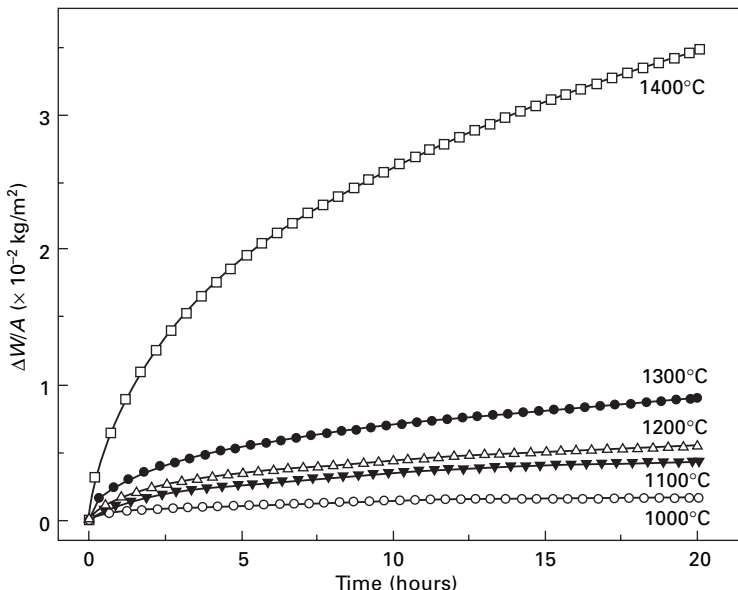


The overall oxidation of  $Ti_2AlC$  can be depicted using the following equation [62]:



The isothermal oxidation behavior of bulk  $Ti_3AlC_2$  [61] and  $Ti_2AlC$  [62] was investigated in air for 20 h. Figure 9.9 displays the weight gain per unit area versus oxidation time for  $Ti_3AlC_2$  samples oxidized at  $1000\text{--}1400^\circ C$  in air. The oxidation of  $Ti_3AlC_2$  at  $1000\text{--}1400^\circ C$  generally followed a parabolic rate law with parabolic rate constants  $k_p$  being  $4.1 \times 10^{-11}$  and  $1.7 \times 10^{-8} \text{ kg}^2\text{m}^{-4}\text{s}^{-1}$  at  $1000$  and  $1400^\circ C$ , respectively. Moreover, the oxidation of  $Ti_2AlC$  obeyed a cubic rate law with cubic rate constants  $k_c$  increasing from  $2.38 \times 10^{-12}$  to  $2.13 \times 10^{-10} \text{ kg}^3\text{m}^{-6}\text{s}^{-1}$  as the temperature increased from  $1000$  to  $1300^\circ C$ . In addition, no mass loss was observed during the cyclic oxidation tests for  $Ti_3AlC_2$  and  $Ti_2AlC$  at  $1300^\circ C$  for 100 cycles (1 hour for each cycle). Sundberg *et al.* [63] also reported that  $Ti_2AlC$  displayed excellent thermal cyclic stability at  $1350^\circ C$  for up to 8000 on/off cycles.

In order to understand the excellent high-temperature oxidation resistance of  $Ti_3AlC_2$  and  $Ti_2AlC$ , detailed microstructural analyses were conducted on the oxide scale formed on these two compounds [61–63,65,66]. XRD and SEM analyses showed that the scales formed at temperatures below  $1300^\circ C$  were dense, layered, adherent, and resistant to cyclic oxidation. The inner

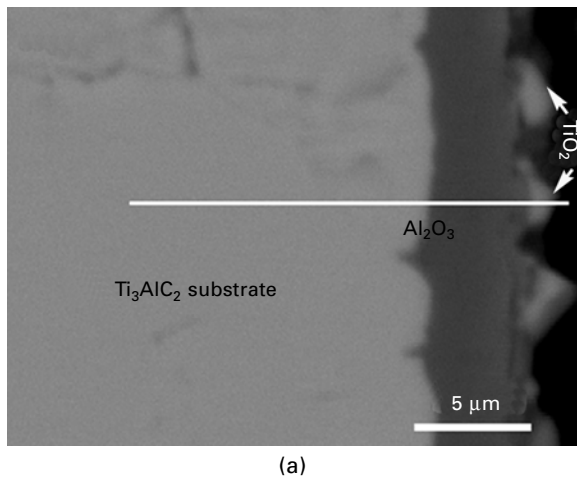


9.9 Mass gain per unit area versus oxidation time for  $\text{Ti}_3\text{AlC}_2$  samples oxidized at 1000–1400°C in air.

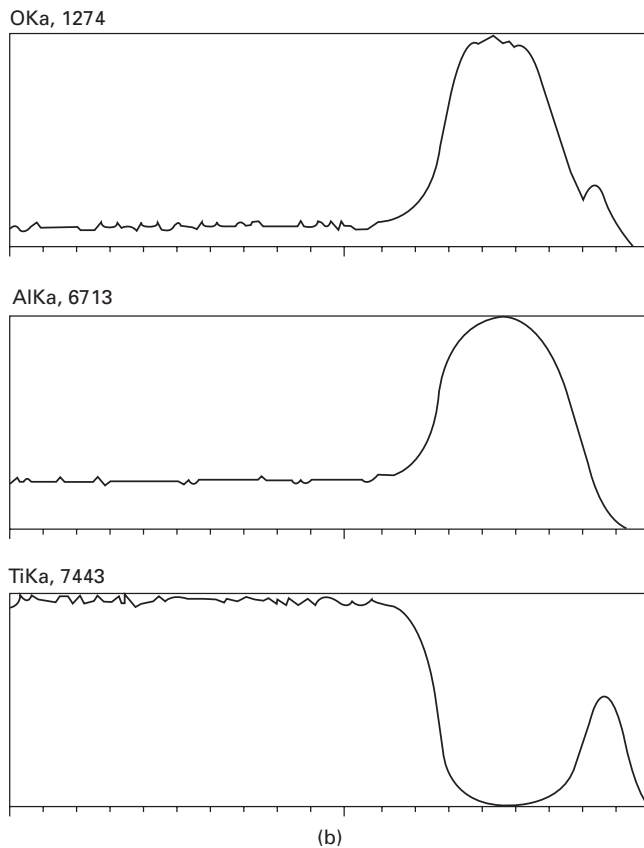
scale formed at temperatures below 1300°C was a continuous  $\alpha\text{-Al}_2\text{O}_3$  layer. At 1300°C,  $\text{TiO}_2$  reacted with  $\text{Al}_2\text{O}_3$  to form  $\text{Al}_2\text{TiO}_5$ . Thus, the outer layer changed from a rutile structure  $\text{TiO}_2$  (below 1200°C) to a mixture of  $\text{TiO}_2$  and  $\text{Al}_2\text{TiO}_5$ . For specimens oxidized at 1400°C, the scale consisted of a mixture of  $\text{Al}_2\text{TiO}_5$  and predominantly  $\alpha\text{-Al}_2\text{O}_3$ . The formation of a continuous  $\text{Al}_2\text{O}_3$  layer on the surface of  $\text{Ti}_3\text{AlC}_2$  and the strong adhesion of this layer to the substrate contribute to the excellent oxidation resistance of  $\text{Ti}_3\text{AlC}_2$ .

Figure 9.10 shows a typical SEM micrograph of  $\text{Ti}_3\text{AlC}_2$  oxidized at 1200°C for 20 h. Microstructures of the  $\text{Ti}_3\text{AlC}_2/\text{Al}_2\text{O}_3$  interface were further investigated by TEM [65,66]. Figure 9.11(a) shows a bright field TEM image of the oxide scale and the  $\text{Ti}_3\text{AlC}_2$  substrate. The scale was approximately 3  $\mu\text{m}$  thick. SAED analyses revealed that the outermost oxide was a discontinuous  $\text{TiO}_2$  layer while the inner oxide was an intact  $\text{Al}_2\text{O}_3$  layer. Further microstructural characterizations at the interface were conducted. Two typical SAED patterns taken across the  $\text{Ti}_3\text{AlC}_2/\text{Al}_2\text{O}_3$  interface are displayed in Figs 9.11(b) and (c) in which  $\alpha$  and  $H$  denote  $\alpha\text{-Al}_2\text{O}_3$  and hexagonal  $\text{Ti}_3\text{AlC}_2$ , respectively [65]. The sharp electron diffraction spots with no satellites or broadening indicate that the  $\text{Al}_2\text{O}_3$  scale has excellent crystallinity. The two sets of crystallographic orientation relationships (OR) between  $\text{Ti}_3\text{AlC}_2$  and  $\text{Al}_2\text{O}_3$  determined from these patterns can be expressed as:

$$(0001)\text{Ti}_3\text{AlC}_2//(0001)\text{Al}_2\text{O}_3 \text{ and } [11\bar{2}0]\text{Ti}_3\text{AlC}_2//[\bar{1}2\bar{1}0]\text{Al}_2\text{O}_3 \quad (OR-1) \quad 9.7$$

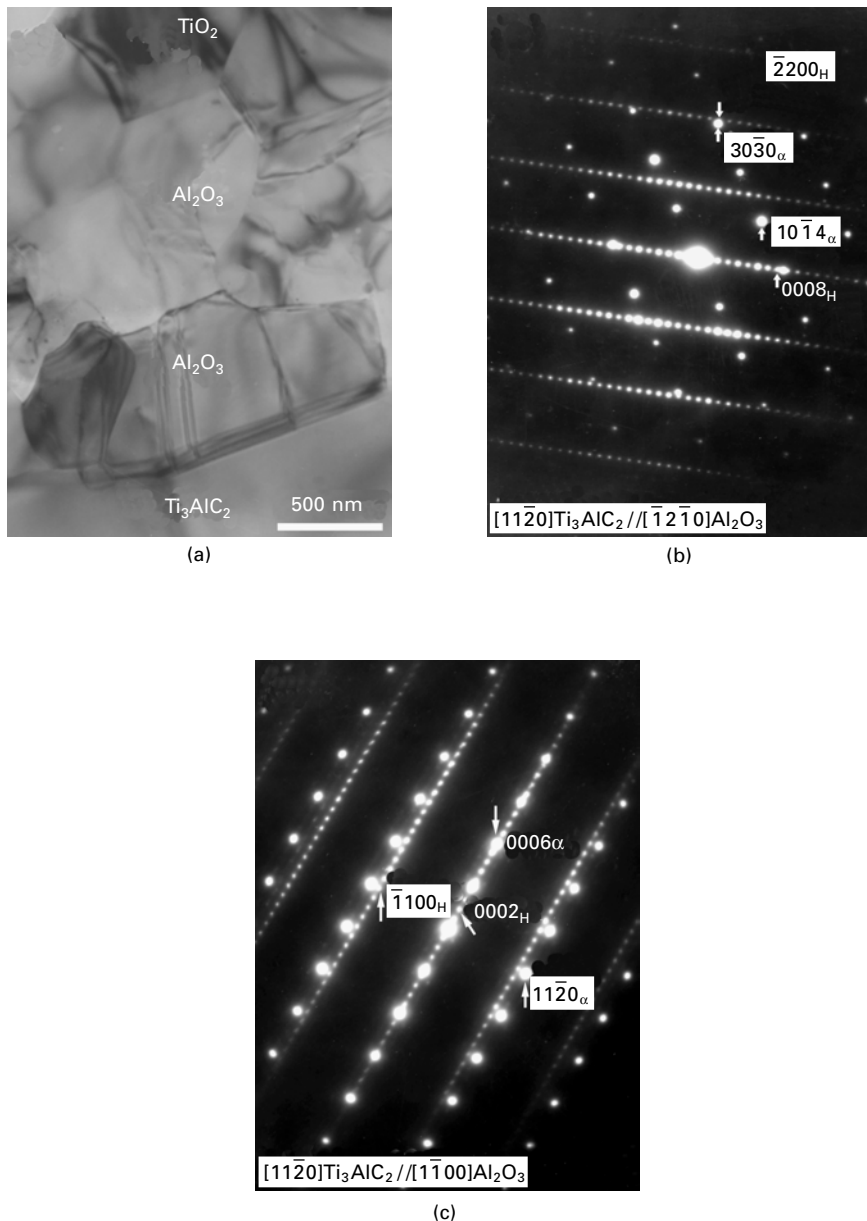


(a)

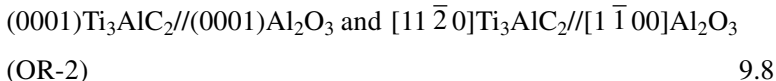


(b)

9.10 (a) Cross-sectional SEM image of  $\text{Ti}_3\text{AlC}_2$  after oxidation at 1200°C for 20 h; (b) corresponding line-scanning profiles for Ti, Al and O along the line shown in (a).



9.11 (a) Bright field TEM image of the oxide scale and the  $\text{Ti}_3\text{AlC}_2$  substrate; (b) and (c) two typical composite SAED patterns taken across the  $\text{Ti}_3\text{AlC}_2/\text{Al}_2\text{O}_3$  interface.

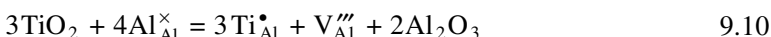


Interfacial misfits along different directions for OR-1 and OR-2 were calculated and two candidate interfacial structure models were proposed. High-resolution TEM imaging revealed that the  $\text{Ti}_3\text{AlC}_2/\text{Al}_2\text{O}_3$  interface was free of amorphous phase. Such an adherent  $\text{Al}_2\text{O}_3$  scale with high integrity would efficiently protect the  $\text{Ti}_3\text{AlC}_2$  substrate, leading to excellent high-temperature oxidation resistance.

Extensive investigations on the oxidation of TiAl and  $\text{Ti}_3\text{Al}$  intermetallics at elevated temperatures indicated that these compounds fail to form a protective  $\text{Al}_2\text{O}_3$  scale [67–69]. Thermodynamic calculations by Luthra [70] revealed that protective  $\text{Al}_2\text{O}_3$  scale could form only on Al-rich Ti-Al alloys between 1100 and 1300°C. It is surprising and interesting that, although the aluminum contents in  $\text{Ti}_3\text{AlC}_2$  and  $\text{Ti}_2\text{AlC}$  are only 16.7 at% and 25 at% respectively, a protective  $\text{Al}_2\text{O}_3$  scale forms during high-temperature oxidation in air. This continuous  $\text{Al}_2\text{O}_3$  scale effectively protected the  $\text{Ti}_3\text{AlC}_2$  and  $\text{Ti}_2\text{AlC}$  substrates [61,62,65,66]. It is known that  $\text{Al}_2\text{O}_3$  grains consolidate by diffusion of oxygen through oxygen vacancy within  $\text{Al}_2\text{O}_3$ . A reduction atmosphere ( $\text{H}_2$  or CO) will promote the sintering of  $\text{Al}_2\text{O}_3$  by increasing the oxygen vacancy concentration, which is the main reason why transparent  $\text{Al}_2\text{O}_3$  ceramic needs to be sintered in a reduction atmosphere. Wang and Zhou [61] attributed the formation of continuous  $\text{Al}_2\text{O}_3$  layers to a significant amount of carbon in  $\text{Ti}_3\text{AlC}_2$ . The defect chemistry reaction for the formation of oxygen vacancy ( $\text{V}_\text{O}^{\bullet\bullet}$ ) can be expressed as:



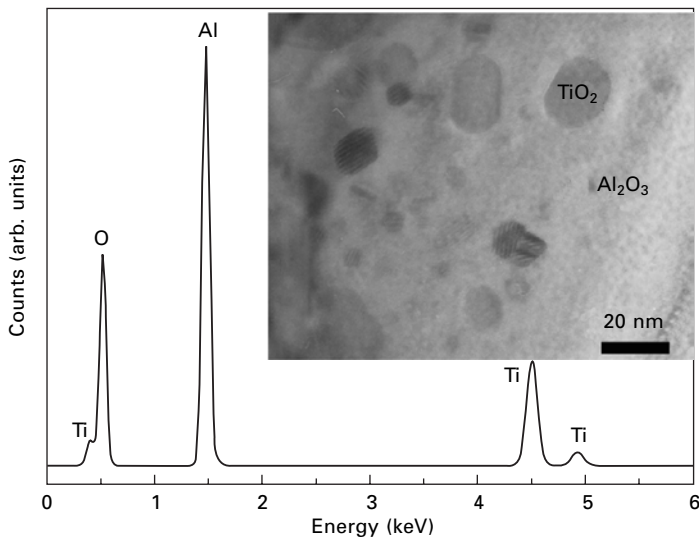
The formation of CO under a low oxygen partial pressure would promote the formation of  $\text{V}_\text{O}^{\bullet\bullet}$  by consuming  $\text{O}_2$ . Consequently, the formation of  $\text{V}_\text{O}^{\bullet\bullet}$  enhanced the consolidation of as-formed  $\text{Al}_2\text{O}_3$  through the diffusion of oxygen to form a continuous  $\text{Al}_2\text{O}_3$  layer. In addition, Ti was detected within the  $\text{Al}_2\text{O}_3$  scale [66]. As shown in Fig. 9.12, HRTEM imaging and EDS analyses demonstrated that titanium was detected in the  $\text{Al}_2\text{O}_3$  scale and  $\text{TiO}_2$  precipitates were observed. In other words, Ti solution in  $\text{Al}_2\text{O}_3$  scale occurred during the outward diffusion of Ti, and the energy favor defect chemistry equation is [71]:



which follows the following equilibrium:

$$K_1 = [\text{Ti}_{\text{Al}}^\bullet]^3 \cdot [\text{V}_{\text{Al}}'''] \cdot [\text{Al}_{\text{Al}}^\times]^{-4} \quad 9.11$$

On the other hand, the Schottky reaction of  $\text{Al}_2\text{O}_3$  (equation 9.12) has a relatively low formation energy:



9.12 EDS profile acquired from the precipitates within the  $\text{Al}_2\text{O}_3$  scale. The inset shows a corresponding HRTEM image of the oxide scale containing  $\text{TiO}_2$  precipitates.

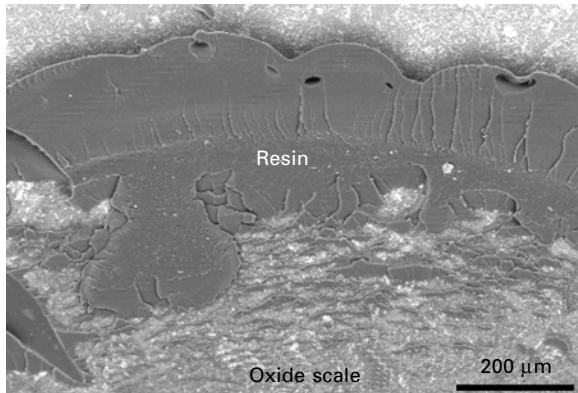


The corresponding equilibrium is:

$$K_2 = [\text{V}_{\text{Al}}^{\prime\prime\prime}]^2 \cdot [\text{V}_{\text{O}}^{\bullet\bullet}]^3 \cdot [\text{Al}_{\text{Al}}^{\times}]^{-2} \cdot [\text{O}_{\text{O}}^{\times}]^{-3} \quad 9.13$$

The solution of Ti in the  $\text{Al}_2\text{O}_3$  scale increased  $[\text{Ti}_{\text{Al}}^{\bullet}]$  and  $[\text{V}_{\text{Al}}^{\prime\prime\prime}]$ . The increment of  $[\text{V}_{\text{Al}}^{\prime\prime\prime}]$  in turn reduced  $[\text{V}_{\text{O}}^{\bullet\bullet}]$  since  $K_2$  is a constant at certain temperatures. As a consequence, the Ti solution reaction in  $\text{Al}_2\text{O}_3$  reduces  $[\text{V}_{\text{O}}^{\bullet\bullet}]$  and ensures a low growth rate of the oxide scales on  $\text{Ti}_3\text{AlC}_2$  and  $\text{Ti}_2\text{AlC}$  substrates.

The CTE values for  $\text{Ti}_3\text{AlC}_2$ ,  $\text{Ti}_2\text{AlC}$  and  $\text{Al}_2\text{O}_3$  are in the range of 8–9.0  $\times 10^{-6} \text{ K}^{-1}$  [61,62]. The small difference in CTE between  $\text{Ti}_3\text{AlC}_2$ ,  $\text{Ti}_2\text{AlC}$  and  $\text{Al}_2\text{O}_3$  results in a low thermal stress generated during thermal cyclic tests. In addition, tensile pull tests were conducted to evaluate the adhesion between the oxide scales and  $\text{Ti}_3\text{AlC}_2$  and  $\text{Ti}_2\text{AlC}$  substrates. Figure 9.13 shows a SEM image of surface morphology of  $\text{Ti}_2\text{AlC}$  after pull-off tests. Some epoxy films remained on the sample surface, and the oxide scale was conserved after the pull-off test. The samples for the adhesion test did not fail at the oxide scale/substrate interface but at the oxide scale/adhesive interface. The average of critical loads of the test samples was about 490 N, which corresponded to an adhesive strength of about 85 MPa. It should be noted that the oxide scale was not detached, indicating that the measured adhesion reflected the strength of the oxide scale/adhesive interface rather



9.13 SEM image of surface morphologies of  $\text{Ti}_2\text{AlC}$  after pull-off tests.

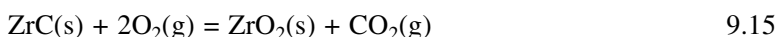
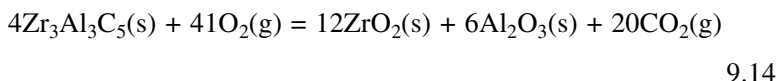
than that of the oxide scale/ $\text{Ti}_3\text{AlC}_2$  (or  $\text{Ti}_2\text{AlC}$ ) interface. In other words, the adhesion of the oxide scale/ $\text{Ti}_3\text{AlC}_2$  and  $\text{Ti}_2\text{AlC}$  substrates exceeds the measured value (85 MPa). The adhesive strength of the oxide scale/ $\text{Ti}_3\text{AlC}_2$  and  $\text{Ti}_2\text{AlC}$  substrates is higher than that of the  $\text{Al}_2\text{O}_3$  scale on other substrates. Strong adhesive strength also contributes to the thermal-cyclic resistance of the protective  $\text{Al}_2\text{O}_3$  scale on the carbide substrates.

Alloys that operate at elevated temperatures rely on the formation of a surface oxide layer to protect them against aggressive oxidation. For  $\text{Ti}_3\text{AlC}_2$  and  $\text{Ti}_2\text{AlC}$ , the unique crystal structures, bonding properties and defect reactions, as well as excellent compatibility between  $\text{Al}_2\text{O}_3$  and these two ternary compounds, lead to the formation of a slow growing and protective oxide scale on  $\text{Ti}_3\text{AlC}_2$  and  $\text{Ti}_2\text{AlC}$  during the high-temperature oxidation process.

### 9.3.4 High-temperature oxidation mechanism of $\text{Zr}_3\text{Al}_3\text{C}_5$

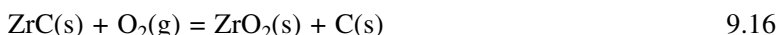
$\text{Zr}_3\text{Al}_3\text{C}_5$  is the most extensively investigated  $T$ -Al-C compound to date. It maintains a high elastic stiffness at temperatures up to  $1600^\circ\text{C}$  [11], which is higher than that tolerated by most refractory materials. These unique properties render  $\text{Zr}_3\text{Al}_3\text{C}_5$  a strong contender for ultra-high temperature applications. Hashimoto *et al.* [5] fabricated  $\text{Zr}_3\text{Al}_3\text{C}_5$  composites and reported that they displayed good oxidation resistance up to  $1000^\circ\text{C}$ . Recently, oxidation of  $\text{Zr}_3\text{Al}_3\text{C}_5$  powders was systematically investigated by simultaneous thermogravimetry-differential scanning calorimetry (TG-DSC) methods [10]. For comparison, the oxidation of binary ZrC powders was also performed under the same experimental conditions. Figures 9.14(a) and (b) show the simultaneous TG-DSC curves for  $\text{Zr}_3\text{Al}_3\text{C}_5$  and ZrC powders, respectively

[10]. The degree of oxidation  $\alpha$  (%), defined as the ratio of the measured mass gain to a theoretical mass gain, was used to characterize the oxidation of these two compounds [72]. Theoretical mass gains of  $Zr_3Al_3C_5$  and ZrC were calculated by assuming complete oxidation according to equations 9.14 and 9.15, respectively:

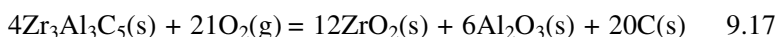


For  $Zr_3Al_3C_5$ , oxidation started at 400°C and greatly accelerated at 600°C. The degree of oxidation exceeded 100% at about 750°C, and rose to a maximum value of 148% at about 870°C (position A in Fig. 9.14(a)), and then gradually returned to 100%. At the same time, an exothermic oxidation determined by DSC began at 400°C and terminated at 1200°C (position C in Fig. 9.14(a)), corresponding to the observed rapid mass gain. These two temperatures reflected the starting and complete oxidation temperatures of  $Zr_3Al_3C_5$  powders. For ZrC, the starting and complete oxidation temperatures of ZrC were approximately 300°C and 780°C, respectively. These two temperatures are about 100°C and 400°C lower than the corresponding temperatures of  $Zr_3Al_3C_5$ . It is known that the oxidation behavior of powder samples is sensitive to powder sizes, i.e., fine powers are more easily oxidized than coarser ones. BET specific surface area measurement demonstrated that the specific surface areas of  $Zr_3Al_3C_5$  and ZrC powders were  $2.54\text{ m}^2\text{g}^{-1}$  and  $1.85\text{ m}^2\text{g}^{-1}$ , respectively. In other words,  $Zr_3Al_3C_5$  powders had a larger specific surface area than ZrC powders. Therefore, it was concluded that  $Zr_3Al_3C_5$  had better oxidation resistance than ZrC.

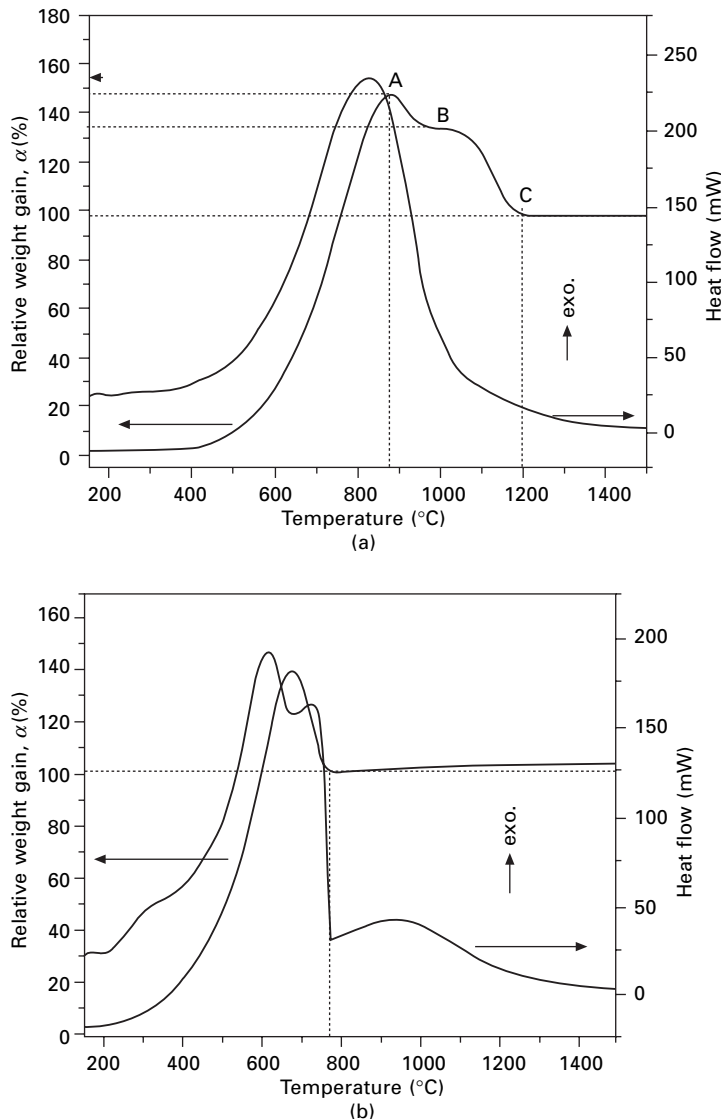
The oxidation degree of ZrC and  $Zr_3Al_3C_5$  both overshot 100% based on the TG results. Shimada [72] ascribed the overshooting of ZrC oxidation to the formation of free carbon in the products according to the following reaction:



Furthermore, thermodynamic calculations revealed that the oxidation of ZrC under low oxygen partial pressure could occur by forming equivalent amounts of  $ZrO_2$  and carbon. Similarly, He *et al.* [10] proposed that carbon formed during the oxidation of  $Zr_3Al_3C_5$  based on the following reaction:



According to reaction 9.17, if the carbon in  $Zr_3Al_3C_5$  is unoxidized, the observed mass gain would reach 156% (Fig. 9.14(a)) of the theoretical one. This calculated value is in good agreement with the measured experimental maximum value (148%), suggesting that most carbon in  $Zr_3Al_3C_5$  was



9.14 Simultaneous TG-DSC curves for (a)  $\text{Zr}_3\text{Al}_3\text{C}_5$  and (b)  $\text{ZrC}$  powders.

unoxidized and retained in products at around  $870^\circ\text{C}$ . The decrease of  $\alpha$  value at  $870\text{--}1200^\circ\text{C}$  in Fig. 9.14(a) could be divided into two steps (AB and BC), which corresponded to the loss of retained carbon on and beneath the oxide scales.

## 9.4 Hot corrosion mechanism of layered ternary ceramics

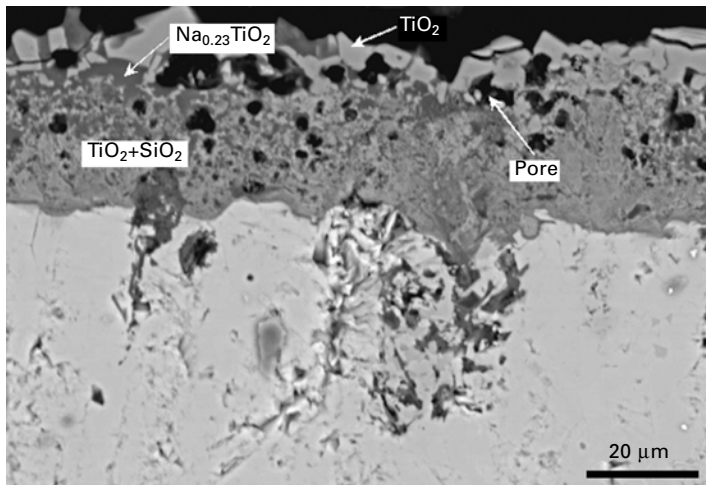
### 9.4.1 Hot corrosion mechanism of $\text{Ti}_3\text{SiC}_2$ against various molten salts

Sun and Zhou [73] investigated the hot corrosion behavior of  $\text{Ti}_3\text{SiC}_2$  with the following experimental procedures: hot corrosion test of salt-coated sample → rinse using hot water → weighing → re-coated with salt film. When the samples were coated with  $\text{Na}_2\text{SO}_4$  salt,  $\text{Ti}_3\text{SiC}_2$  displayed good hot corrosion resistance, and the corrosion kinetics followed the parabolic rate law at 850–950°C. However, the hot corrosion became severer at 950°C. The corrosion scales formed at 850°C and 900°C were compacted and mixed  $\text{TiO}_2$  and  $\text{SiO}_2$  layers. It was reported that the coated  $\text{Na}_2\text{SO}_4$  did not accelerate the corrosion of  $\text{Ti}_3\text{SiC}_2$ . The corrosion kinetics were lower than those in isothermal oxidation in air, which was interpreted by the fact that the  $\text{Na}_2\text{SO}_4$  film reduced the oxygen partial pressure at the interface between the oxide scale and the substrate. However, the chemical reactions between  $\text{TiO}_2$  and  $\text{SiO}_2$  with  $\text{Na}_2\text{SO}_4$  became intense at 950°C. As a consequence, corrosion products such as  $\text{Na}_{0.23}\text{TiO}_2$  and  $\text{Na}_2\text{SiO}_3$  were detected.

When coated with 75 wt%  $\text{Na}_2\text{SO}_4$  + 25 wt%  $\text{NaCl}$  mixed salts, the hot corrosion kinetics of  $\text{Ti}_3\text{SiC}_2$  still obeyed the parabolic rate law, which is the same as those coated with monoclinic  $\text{Na}_2\text{SO}_4$ . However, the mass gains were much larger than those in  $\text{Na}_2\text{SO}_4$  salt. Therefore, it was concluded that the presence of  $\text{NaCl}$ , or more precisely  $\text{Cl}^-$ , would accelerate the hot corrosion of  $\text{Ti}_3\text{SiC}_2$ . Typical hot corrosion products were needle-like, consisting of  $\text{Na}_{0.23}\text{TiO}_2$ ,  $\text{Na}_2\text{SiO}_3$  and a small amount of  $\text{TiO}_2$ . Large pores were observed in the corrosion scales, resulting in poor protectivity of the substrate. In this method, the kinetics reflected an overall mass change between mass gain by corrosion and mass loss due to the dissolution of soluble salts and corrosion products.

In order to overcome this problem, Liu *et al.* [74,75] investigated the hot corrosion behavior of  $\text{Na}_2\text{SO}_4$ -coated  $\text{Ti}_3\text{SiC}_2$  at 900–1000°C using TG analysis, which can continuously record the mass change through the entire experimental process.  $\text{Ti}_3\text{SiC}_2$  suffered from severe hot corrosion attacks in molten  $\text{Na}_2\text{SO}_4$  salt. The corrosion kinetics approximately followed the parabolic rate law at 900°C. However, an initially high-rate corrosion stage was observed at 1000°C. After this stage, the corrosion kinetics decreased and followed the parabolic rate law. The corrosion scales were composed of  $\text{TiO}_2$  and  $\text{SiO}_2$ . Typically, the outer scale had large grain size and was porous while the inner layer was dense with fine grain sizes (Fig. 9.15). It is seen that the experimental conditions have a strong influence on the results.

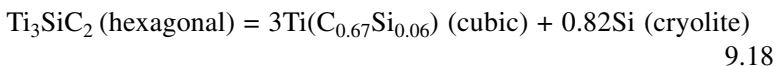
Liu *et al.* [76] also investigated the hot corrosion behavior of  $\text{Ti}_3\text{SiC}_2$  in mixed salt of 68 at%  $\text{K}_2\text{CO}_3$  and 32 at%  $\text{Li}_2\text{CO}_3$  at 650–850°C. At 700–



9.15 Cross-sectional SEM micrograph of Ti<sub>3</sub>SiC<sub>2</sub> after hot corrosion test for 20 h.

850°C, Ti<sub>3</sub>SiC<sub>2</sub> suffered from serious corrosion attacks by the mixed salts. Ti<sub>3</sub>SiC<sub>2</sub> displayed better corrosion resistance at 650°C. The surface chemical reaction-controlled shrinking core model was applied to describe the relationship between the degree of the corrosion and reaction time of the corrosion of Ti<sub>3</sub>SiC<sub>2</sub> in the temperature range of 700–850°C. The apparent activation energy was determined to be 206 kJ·mol<sup>-1</sup>. The degradation of the fractural strength, for corroded specimens with mass loss up to 10%, was about 25% compared with that of the original samples.

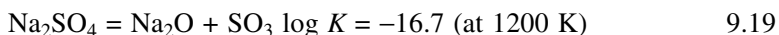
Barsoum *et al.* [77] investigated the stability of Ti<sub>3</sub>SiC<sub>2</sub> in molten cryolite (47% NaF + 43% AlF<sub>3</sub> + 5% CaF<sub>2</sub> + 5% Al<sub>2</sub>O<sub>3</sub>), and found the topotactic transformation of Ti<sub>3</sub>SiC<sub>2</sub> into a partially ordered cubic Ti(C<sub>0.67</sub>Si<sub>0.06</sub>) phase by the diffusion of Si into molten cryolite. Immersion of Ti<sub>3</sub>SiC<sub>2</sub> in molten cryolite at 960°C led to the preferential diffusion of Si atoms out of their basal planes. Si was proposed to diffuse along the basal planes within a grain, and then along the grain boundaries to the surface. When the concentration of Si was below a certain critical value, the constraints on the Ti-C layers on either side of the Si atomic planes were relaxed and the energetic favored cubic configuration formed. This transformation can be described using the following reaction:



#### 9.4.2 Hot corrosion mechanism of $\text{Ti}_3\text{AlC}_2$ and $\text{Ti}_2\text{AlC}$ against $\text{Na}_2\text{SO}_4$

Hot corrosion behavior of  $\text{Na}_2\text{SO}_4$ -coated  $\text{Ti}_3\text{AlC}_2$  and  $\text{Ti}_2\text{AlC}$  ceramics in air was investigated [78,79]. It was demonstrated that the hot corrosion of  $\text{Ti}_3\text{AlC}_2$  was slow at low temperatures of 700°C and 800°C, while it was severely attacked by fused sodium sulfate at 900°C and 1000°C. No protective scale was observed on  $\text{Ti}_3\text{AlC}_2$ , and sulfur-rich layers were present at the substrate/scale interface. Wang and Zhou [78] claimed that electrochemical reactions of  $\text{Ti}_3\text{AlC}_2$  with sodium sulfate at the substrate/scale interface dominated at 800°C and 900°C because of the linear hot corrosion kinetics; while the parabolic kinetics at 1000°C implied that the rate-limiting step was the diffusion of hot corrosion medium. A mechanism coupled with electrochemistry and dissolution–precipitation was proposed to interpret the hot corrosion behaviors of  $\text{Ti}_3\text{AlC}_2$  [78].

Several hot corrosion mechanisms including sulfidation, acid–basic dissolution and electrochemistry have been proposed. No matter what the mechanisms are, it is important to understand the character of  $\text{Na}_2\text{SO}_4$  first.  $\text{Na}_2\text{SO}_4$  is an electrolyte, which follows the following equilibrium:



So, any reaction that favors the consumption of  $\text{Na}_2\text{O}$  or  $\text{SO}_3$  will lead to the dissociation of  $\text{Na}_2\text{SO}_4$  and vice versa. Molten  $\text{Na}_2\text{SO}_4$  is an ionic conductor; the hot corrosion mechanism should generally be electrochemistry [78]. In other words, hot corrosion itself is an electrochemical process that includes anodic oxidation, cathodic reduction and ion diffusion. As for the hot corrosion of  $\text{Ti}_3\text{AlC}_2$ , the anodic oxidation process mainly consists of the anodic dissolution of Ti and Al:



At the same time when anodic dissolution occurs, strong reductivity yields, which results in the reduction of  $\text{SO}_4^{2-}$  through the following reaction:



Some  $\text{O}^{2-}$  anion combined with  $\text{Ti}^{4+}$  and  $\text{Al}^{3+}$  and formed  $\text{TiO}_2$  and  $\text{Al}_2\text{O}_3$ ; others increased the basicity of the molten salt.  $\text{SO}_4^{2-}$  anion and its reduction product  $\text{SO}_2$  can migrate inward through the non-protective scale, and in places like the scale/ $\text{Ti}_3\text{AlC}_2$  interface where the reductivity is high enough for the formation of sulfides. Sulfur-rich bands were observed in the corrosion scale/ $\text{Ti}_3\text{AlC}_2$  interface, suggesting a higher reductivity there. The cathodic reaction process consists of the reduction of  $\text{SO}_4^{2-}$  anion and oxygen. The

mass gain during the hot corrosion process comes from the uptake of oxygen in air. In molten sulfate there is equilibrium:



Oxygen in the atmosphere can be dissolved in the melt according to the following equation:

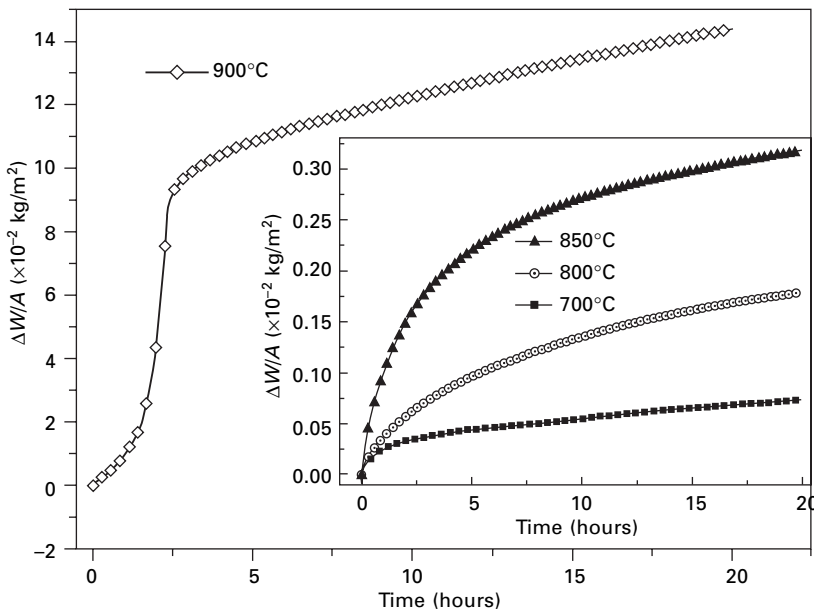


Besides molecular form in the melt, oxygen mainly exists as  $\text{O}_2^{2-}$ . Because of the slow solubility of oxygen and its low diffusion rate in molten salt [78], diffusion of molecular oxygen to the alloy surface in fused salt cannot account for such high mass gains at 900°C and 1000°C. The  $\text{O}^{2-}$ -concentration according to reaction 9.23 increased with increasing temperature; at the same time, the concentration of  $\text{O}_2^{2-}$  increased, which consequently accelerated the corrosion of  $\text{Ti}_3\text{AlC}_2$ .  $\text{O}_2^{2-}$  migrated to the surface of the corrosion scale, and was reduced ( $\text{O}_2^{2-} + 2\text{e}^- = 2\text{O}^{2-}$ ), contributing to the formation of new oxides. Because fused  $\text{Na}_2\text{SO}_4$  is a strong electrolyte, the diffusion of  $\text{O}_2^{2-}$  ion to the surface of the scale could support such high corrosion mass gains. The reduction of  $\text{SO}_4^{2-}$  anions would result in the increase of basicity in molten salt, promoting the basic dissolution of oxides, especially  $\text{Al}_2\text{O}_3$  [78].



The influence of Al content on the hot corrosion behavior of layered ternary titanium aluminum carbides was investigated by exploring the hot corrosion behavior of  $\text{Ti}_2\text{AlC}$ . Figure 9.16 displays the reaction kinetics of  $\text{Na}_2\text{SO}_4$ -coated  $\text{Ti}_2\text{AlC}$  at 700–900°C [79]. It followed the parabolic rate law and protective  $\text{Al}_2\text{O}_3$  scale retarded the further corrosion of the  $\text{Ti}_2\text{AlC}$  substrate below the melting point of  $\text{Na}_2\text{SO}_4$  [79]. However,  $\text{Ti}_2\text{AlC}$  also suffered severe hot corrosion attacks at 900°C and 1000°C because porous and non-protective scales failed to protect the  $\text{Ti}_2\text{AlC}$  substrate. Chemical reactions between  $\text{Ti}_2\text{AlC}$  and the  $\text{Na}_2\text{SO}_4$  salt dominated the corrosion process, and sulfur segregated at the scale/substrate interfaces.

As discussed above, a continuous and protective  $\text{Al}_2\text{O}_3$  scale formed on  $\text{Ti}_3\text{AlC}_2$  and  $\text{Ti}_2\text{AlC}$  substrates during the high-temperature corrosion process. However,  $\text{Ti}_3\text{AlC}_2$  and  $\text{Ti}_2\text{AlC}$  suffered from serious hot corrosion attacks in molten  $\text{Na}_2\text{SO}_4$  salt [78,79]. It was reported that the hot corrosion resistance of  $\text{Al}_2\text{O}_3$  was good at about 1000°C [80]. Thus, a simple pre-oxidation treatment was proposed, which significantly improved the  $\text{Na}_2\text{SO}_4$ -induced hot corrosion resistance of  $\text{Ti}_3\text{AlC}_2$  and  $\text{Ti}_2\text{AlC}$  [79,81]. A convenient and efficient pre-oxidation treatment could form a continuously protective  $\text{Al}_2\text{O}_3$  scale, and consequently improve the hot corrosion resistance of  $\text{Ti}_3\text{AlC}_2$  and  $\text{Ti}_2\text{AlC}$  by preventing the infiltration of  $\text{Na}_2\text{SO}_4$  to the substrates. The simple



9.16 Hot corrosion kinetics of  $\text{Na}_2\text{SO}_4$ -coated  $\text{Ti}_2\text{AlC}$  at 700–900°C.

treatments decreased the hot corrosion rates of  $\text{Ti}_3\text{AlC}_2$  and  $\text{Ti}_2\text{AlC}$  by 2–4 orders of magnitude.

Pre-oxidation treatment was also applied to improve the hot corrosion resistance of  $\text{Ti}_3\text{SiC}_2$  [82]. A duplex oxide scale with an outer  $\text{TiO}_2$  layer and inner mixed  $\text{TiO}_2 + \text{SiO}_2$  scale formed during the pre-oxidation process. The pre-oxidation treated specimens exhibited good hot corrosion resistance against 75 wt%  $\text{Na}_2\text{SO}_4$  + 25 wt%  $\text{NaCl}$  melts at 850°C for 50 h. However, the outer  $\text{TiO}_2$  layer degraded at a faster rate than its consumption by the mixed salts. Once the outer layer is damaged, the hot corrosion rate increases sharply.

## 9.5 Summary and future trends

We have introduced the unique crystal structure, multi-scale microstructure, and synthesis method for highly promising layered ternary ceramics. LTCs are a new family of solids that exhibit superior properties such as high elastic modulus, good electrical and thermal conductivities and high damage tolerance. The high-temperature isothermal and cyclic oxidation, as well as the hot corrosion mechanism under various corrosion media, was illustrated. In addition, several future trends on high-temperature corrosion of highly promising LTCs are highlighted as follows.

### 9.5.1 Developing new corrosion-resistant LTCs in the form of bulk materials and coatings

Previous work on the hot corrosion of  $Ti_3SiC_2$  and  $Ti_3AlC_2$  against molten salts is unsatisfactory. Moreover, it has been demonstrated that  $Cr_2AlC$  displayed excellent high-temperature oxidation resistance [22]. Therefore, developing new LTCs is needed. In addition, Cr is generally believed to be the best element to protect against hot corrosion. Our latest results demonstrate that both  $Cr_2AlC$  and Cr-Al-C composites exhibit excellent high-temperature oxidation and hot corrosion resistance [83, 84]. Thus, more attention should be paid to the Cr-Al-C system. Their excellent high-temperature isothermal and cyclic oxidation resistance makes LTCs such as  $Ti_3AlC_2$ ,  $Ti_2AlC$  and  $Cr_2AlC$  promising candidates as corrosion-resistant material and also coatings. Because of the excellent compatibility between oxides and LTCs (e.g.,  $Ti_3AlC_2$ ,  $Ti_2AlC$ ,  $Cr_2AlC$ ), LTCs may be used as a bond coat layer for thermal barrier coatings. In addition,  $T$ -Al-C and A-B-C compounds enhance the application temperature. The possibility of these systems for ultra-high temperature corrosion-resistant materials should be investigated.

### 9.5.2 Mechanism of selective oxidation of LTCs

Despite the similarities in crystal structures of LTCs, selective oxidation takes place during the oxidation of  $Ti_2AlC$ ,  $Ti_3AlC_2$ ,  $Cr_2AlC$ , etc. On the other hand, mixed  $SiO_2$  and  $TiO_2$  scales form during the oxidation of  $Ti_3SiC_2$ . Thus, further investigations on the mechanism of selective oxidation of LTCs are of great scientific and technological importance. The activity of protective scale-forming elements (such as aluminum or silicon) and the coefficient of diffusion are the two most important factors that determine the ability of a material to form protective scales. Therefore, quantitative analyses are necessary.

### 9.5.3 Mechanism of interaction between LTCs and various environmental media

Most previous works on the corrosion behavior of LTCs have been at a qualitative or semi-quantitative level, which has produced a scatter of the reported results. Recently, we found that factors in the corrosion environment such as humidity also have a strong influence on the corrosion behavior of LTCs such as Ti-Al-C compounds [85]. Thus, systematic and quantitative investigations on the corrosion mechanism of LTCs will be very useful.

## 9.6 Acknowledgements

The authors would like to acknowledge all published sources (Elsevier Ltd. and Carl Hanser Verlag GmbH & Co. KG) that we have made use of, and the financial support by the National Outstanding Young Scientist Foundation for Y. C. Zhou under Grant no. 59925208, and by the Natural Sciences Foundation of China under Grant nos. 50232040, 50302011 and 90403027.

## 9.7 References

1. Barsoum M W, 'The  $M_{N+1}AX_N$  phases: a new class of solids; thermodynamically stable nanolaminates', *Prog Solid State Chem*, 2000 **28** 201–281.
2. Lin Z J, Li M S, Zhou Y C, 'TEM investigations on layered ternary ceramics', *J Mater Sci Technol*, 2007 **23**(2) 145–165.
3. Schuster J C, Nowotny H, 'Investigations of the ternary systems (Zr, H, Nb, Ta)-Al-C and studies on complex carbides', *Z Metallkd*, 1980 **71** 341–346.
4. Gesing T M, Jeitschko W, 'The crystal structures of  $Zr_3Al_3C_5$ ,  $ScAl_3C_3$ , and  $UAl_3C_3$  and their relation to the structures of  $U_2Al_3C_4$  and  $Al_4C_3$ ', *J Solid State Chem*, 1998 **140** 396–401.
5. Hashimoto S, Yamaguchi A, Yasuda M, 'Fabrication and properties of novel composites in the system Al-Zr-C', *J Mater Sci*, 1998 **33** 4835–4842.
6. Leela-adisorn U, Choi S M, Tera N, Takeuchi T, Hashimoto S, Honda S, Awaji H, Hayakawa K, Yamaguchi A, 'Sintering and mechanical properties of  $AlZrC_2$ ', *J Ceram Soc Jap*, 2005 **113**(2) 188–190.
7. Wang J Y, Zhou Y C, Lin Z J, Liao T, He L F, 'First-principles prediction on mechanical properties and electronic structure of ternary aluminum carbide  $Zr_3Al_3C_5$ ', *Phys Rev B*, 2006 **73** 134107.
8. Lin Z J, Zhuo M J, He L F, Zhou Y C, Li M S, Wang J Y, 'Atomic scale microstructure of  $Zr_2Al_3C_4$  and  $Zr_3Al_3C_5$  ceramics', *Acta Mater*, 2006 **54** 3843–3851.
9. Leela-adisorn U, Choi S M, Matsunaga T, Hashimoto S, Honda S, Hayakawa K, Awaji H, Yamaguchi A, 'Al $ZrC_2$  synthesis', *Ceram Inter*, 2006 **32** 431–439.
10. He L F, Zhou Y C, Bao Y W, Wang J Y, Li M S, 'Synthesis and oxidation of  $Zr_3Al_3C_5$  powders', *Inter J Mater Res (formerly Z Metallkd)*, 2007 **98**(1) 3–9.
11. He L F, Zhou Y C, Bao Y W, Lin Z J, Wang J Y, Li M S, 'Synthesis, physical and mechanical properties of bulk  $Zr_3Al_3C_5$  ceramic', *J Am Ceram Soc*, 2007 **90**(4) 1164–1170.
12. Wang J Y, Zhou Y C, Liao T, Lin Z J, 'Trend in crystal structure of layered ternary T-Al-C carbides ( $T = Sc, Ti, V, Cr, Zr, Nb, Mo, Hf, W$ , and  $Ta$ )', *J Mater Res*, 2007 **22**(10) 2685–2690.
13. Hillebrecht H, Meyer F D, 'Synthesis, structure, and vibrational spectra of  $Al_3BC_3$ , a carbidecarborinate of aluminum with linear  $(C=B=C)^{5-}$  anions', *Angew Chem Int Ed Engl*, 1996 **35** 2499–2500.
14. Inoue Z, Tanaka H, Inomata Y, 'Synthesis and X-ray crystallography of aluminium boron carbide,  $Al_8B_4C_7$ ', *J Mater Sci*, 1980 **15** 3036–3040.
15. Solozhenko V L, Meyer F D, Hillebrecht H, '300-K equation of state and high-pressure phase stability of  $Al_3BC_3$ ', *J Solid State Chem*, 2000 **154** 254–256.
16. Wang T, Yamaguchi A, 'Some properties of sintered  $Al_8B_4C_7$ ', *J Mater Sci Lett*, 2000 **19** 1045–1046.

17. Bauer J, Boucekkine G, Frapper G, Halet J F, Saillard J Y, Zouchoune B, 'Small boron carbon chains stabilized in rare earth metallic frameworks: a bonding analysis', *J Solid State Chem*, 1997 **133** 190–194.
18. Wang J Y, Zhou Y C, Lin Z J, Liao T, 'Pressure-induced polymorphism in Al<sub>3</sub>BC<sub>3</sub>: a first-principles study', *J Solid State Chem*, 2006 **179** 2703–2707.
19. Wang J Y, Zhou Y C, Liao T, Lin Z J, 'First-principles prediction on low shear-strain resistance of Al<sub>3</sub>BC<sub>3</sub>: a metal borocarbide containing short linear BC<sub>2</sub> unit', *Appl Phys Lett*, 2006 **89** 021917.
20. Lin Z J, Zhuo M J, Zhou Y C, Li M S, Wang J Y, 'Atomic scale characterization of Cr<sub>2</sub>AlC ceramic', *J Appl Phys*, 2006 **99** 076109.
21. Jeitschko W, Nowotny H, Benesovsky F, 'Carbides of formula T<sub>2</sub>MC', *J Less-common Met*, 1964 **7** 133–138.
22. Lin Z J, Zhou Y C, Li M S, Wang J Y, 'In-situ hot pressing/solid–liquid reaction synthesis of bulk Cr<sub>2</sub>AlC', *Z Metallkd*, 2005 **96** 291–296.
23. Jeitschko W, Nowotny H, 'Die Kristallstruktur von Ti<sub>3</sub>SiC<sub>2</sub> – ein neuer Komplexcarbidtyp', *Montash Chem*, 1967 **98** 329–337.
24. Sun Z M, Zhou Y C, 'Ab initio calculation of titanium silicon carbide (Ti<sub>3</sub>SiC<sub>2</sub>)', *Phys Rev B*, 1999 **60** 1441–1443.
25. Rawn C J, Barsoum M W, El-Raghy T, Procipio A, Hoffmann C M, Hubbard C R, 'Structure of Ti<sub>4</sub>AlN<sub>3</sub> – a layered M<sub>n+1</sub>AX<sub>n</sub> nitride', *Mater Res Bull*, 2000 **35** 1785–1796.
26. Lin Z J, Zhuo M J, He L F, Zhou Y C, Li M S, Wang J Y, 'Structural characterization of a new layered-ternary Ta<sub>4</sub>AlC<sub>3</sub> ceramic', *J Mater Res*, 2006 **21** 2587–2592.
27. Manoun B, Saxena S K, El-Raghy T, Barsoum M W, 'High-pressure X-ray diffraction study of Ta<sub>4</sub>AlC<sub>3</sub>', *Appl Phys Lett*, 2006 **88** 201902.
28. Barsoum M W, El-Raghy T, 'Synthesis and characterization of a remarkable ceramic: Ti<sub>3</sub>SiC<sub>2</sub>', *J Am Ceram Soc*, 1996 **79**(7) 1953–1956.
29. Barsoum M W, El-Raghy T, Rawn C J, Porter W D, Wang H, Payzant E A, Hubbard C R, 'Thermal properties of Ti<sub>3</sub>SiC<sub>2</sub>', *J Phys Chem Solid*, 1999 **60** 429–439.
30. Tzenov N V, Barsoum M W, 'Synthesis and characterization of Ti<sub>3</sub>AlC<sub>2</sub>', *J Am Ceram Soc*, 2000 **83** 825–832.
31. Wang X H, Zhou Y C, 'Microstructure and properties of Ti<sub>3</sub>AlC<sub>2</sub> prepared by solid–liquid reaction synthesis and simultaneous in-situ hot pressing process', *Acta Mater*, 2002 **50** 3141–3149.
32. Nickl J J, Schweitzer K K, Luxenberg P, 'Gasphasenabscheidung im Systeme Ti-C-Si', *J Less Common Met*, 1972 **26** 283–287.
33. Klemm H, Tanihata K, Miyamoto Y, 'Gas pressure combustion sintering and hot isostatic pressing in the Ti-Si-C system', *J Mater Sci*, 1993 **28** 1557–1562.
34. Racault C, Langlais F, Naslain R, 'Solid-state synthesis and characterization of the ternary phase Ti<sub>3</sub>SiC<sub>2</sub>', *J Mater Sci*, 1994 **29** 3384–3392.
35. Lis J, Miyamoto Y, Pampuch R, Tanihata K, 'Ti<sub>3</sub>SiC<sub>2</sub>-based materials prepared by HIP-SHS techniques', *Mater Lett*, 1995 **22** 163–168.
36. Arunajatesan S, Carim A H, 'Synthesis of titanium–silicon carbide', *J Am Ceram Soc*, 1995 **78**(3) 667–672.
37. Zhou Y C, Sun Z M, Chen S Q, Zhang Y, 'In-situ hot pressing/solid–liquid reaction synthesis of dense titanium silicon carbide bulk ceramics', *Mater Res Innovat*, 1998 **2** 142–146.
38. Li J T, Miyamoto Y, 'Fabrication of monolithic Ti<sub>3</sub>SiC<sub>2</sub> ceramic through reactive sintering of Ti/Si/2TiC', *J Mater Synth Proc*, 1999 **7** 91–96.

39. Zhang Z F, Sun Z M, Hashimoto H, 'Rapid synthesis of ternary carbide through pulse-discharge sintering from Ti/Si/TiC powder', *Scripta Mater*, 2001 **45** 1461–1467.
40. Li J F, Matsuki T, Watanabe R, 'Fabrication of highly dense  $Ti_3SiC_2$  ceramic by pressureless sintering of mechanically alloyed elemental powders', *J Mater Sci*, 2003 **38** 2661–2666.
41. Zhou Y C, Zhang H B, Liu M Y, Wang J Y, Bao Y W, 'Preparation of TiC free  $Ti_3SiC_2$  with improved oxidation resistance by substitution of Si with Al', *Mater Res Innovat*, 2004 **8**(2) 97–102.
42. Palmquist J P, Jansson U, Seppänen T, Persson P O Å, Birch J, Hultman L, Isberg P, 'Magnetron sputtered epitaxial single-phase  $Ti_3SiC_2$  thin films', *Appl Phys Lett*, 2002 **81** 835–837.
43. Lin Z J, Zhuo M J, Li M S, Wang J Y, Zhou Y C, 'Synthesis and microstructure of layered-ternary  $Ti_2AlN$  ceramic', *Scripta Mater*, 2007 **56** 1115–1118.
44. Barsoum M W, El-Raghy T, Ogbuji L, 'Oxidation of  $Ti_3SiC_2$  in air', *J Electrochem Soc*, 1997 **144** 2508–2516.
45. Radhakrishnan R, Williams J J, Akinc M, 'Synthesis and high-temperature stability of  $Ti_3SiC_2$ ', *J Alloy Compd*, 1999 **285** 85–88.
46. Sun Z M, Zhou Y C, Li M S, 'Oxidation behavior of  $Ti_3SiC_2$ -based ceramic at 900–1300°C in air', *Corros Sci*, 2001 **43**(6) 1095–1106.
47. Sun Z M, Zhou Y C, Li M S, 'High temperature oxidation behavior of  $Ti_3SiC_2$ -based materials in air', *Acta Mater*, 2001 **49** 4347–4353.
48. Yang S L, Sun Z M, Hashimoto H, Park Y H, Abe T, 'Oxidation of  $Ti_3SiC_2$  at 1000°C in air', *Oxid Met*, 2003 **59** 155–165.
49. Sun Z, Zhou Y, Li M, 'Cyclic oxidation behavior of  $Ti_3SiC_2$ -based material at 1100°C', *Oxid Met*, 2002 **57**(5/6) 379–394.
50. Liu G M, Li M S, Zhang Y M, Zhou Y C, 'Cracking behavior of oxide scales formed on  $Ti_3SiC_2$ -based ceramic', *Mater Sci Eng A*, 2003 **360**(1/2) 408–414.
51. El-Raghy T, Barsoum M W, 'Diffusion kinetics of the carburization and silicidation of  $Ti_3SiC_2$ ', *J Appl Phys*, 1998 **83** 112–119.
52. Liu G M, Li M S, Zhang Y M, Zhou Y C, 'Oxidation behaviors of silicide coatings on  $Ti_3SiC_2$ -based ceramic', *Mater Res Innov*, 2002 **6** 226–231.
53. Li M S, Liu G M, Zhang Y M, Zhou Y C, 'Influence of Al-La co-cementation on the oxidation of  $Ti_3SiC_2$ -based ceramic', *Oxid Met*, 2003 **60**(1/2) 179–193.
54. Tong X H, Okano T, Iseki T, Yano T, 'Synthesis and high temperature mechanical properties of  $Ti_3SiC_2/SiC$  composites', *J Mater Sci*, 1995 **30** 3087–3090.
55. Zhou Y C, Wan D T, Bao Y W, Wang J Y, 'In-situ processing and high-temperature properties of  $Ti_3Si(Al)C_2/SiC$  composites', *Int J Appl Ceram Technol*, 2006 **3**(1) 47–54.
56. Yu R, Zhan Q, He L L, Zhou Y C, Ye H Q, 'Si-induced twinning of TiC and formation of  $Ti_3SiC$  platelets', *Acta Mater*, 2002 **50** 4127–4135.
57. Yu R, He L L, Ye H Q, 'Effects of Si and Al on twin boundary energy of TiC', *Acta Mater*, 2003 **51** 2477–2484.
58. Wang J Y, Zhou Y C, 'First-principles study of equilibrium properties and electronic structure of  $Ti_3Si_{0.75}Al_{0.25}C_2$  solid solution', *J Phys Condens Matter*, 2003 **15** 5959–5968.
59. Zhang H B, Zhou Y C, Bao Y W, Li M S, 'Improvement in the oxidation resistance of  $Ti_3SiC_2$  by forming a  $Ti_3Si_{0.9}Al_{0.1}C_2$  solid solution', *Acta Mater*, 2004 **52** 3631–3637.

60. Barsoum M W, Tzenov N, Procopio A, El-Raghy T, Ali M, 'Oxidation of  $Ti_{n+1}AlX_n$  ( $n = 1-3$  and  $X = C, N$ ) II. Experimental results', *J Electrochem Soc*, 2001 **148**(8) C551–562.
61. Wang X H, Zhou Y C, 'Oxidation behavior of  $Ti_3AlC_2$  at 1000–1400°C in air', *Corros Sci*, 2003 **45**(5) 891–907.
62. Wang X H, Zhou Y C, 'High temperature oxidation behavior of  $Ti_2AlC$  in air', *Oxid Met*, 2003 **59**(3/4) 303–320.
63. Sundberg M, Malmqvist G, Magnusson A, El-Raghy T, 'Alumina forming high temperature silicides and carbides', *Ceram Intern*, 2004 **30** 1899–1905.
64. Lin Z J, Zhuo M J, Zhou Y C, Li M S, Wang J Y, 'Microstructural characterization of layered-ternary  $Ti_2AlC$ ', *Acta Mater*, 2006 **54** 1009–1015.
65. Lin Z J, Zhuo M J, Zhou Y C, Li M S, Wang J Y, 'Interfacial microstructure of  $Ti_3AlC_2$  and  $Al_2O_3$  oxide scale', *Scripta Mater*, 2006 **54** 1815–1820.
66. Lin Z J, Zhuo M J, Zhou Y C, Li M S, Wang J Y, 'Microstructures and adhesion of the oxide scales formed on titanium aluminum carbide substrates', *J Am Ceram Soc*, 2006 **89** 2964–2966.
67. Becker S, Rahmel A, Schorr M, Schütze M, 'Mechanism of isothermal oxidation of intermetallic TiAl and of TiAl alloys', *Oxid Met*, 1992 **38** 425–464.
68. Reddy R G, Wen X, Divakar M, 'Isothermal oxidation of TiAl alloy', *Metall Mater Trans A*, 2001 **32** 2357–2361.
69. Chu M S, Wu S K, 'The improvement of high temperature oxidation of Ti–50Al by sputtering Al film and subsequent interdiffusion treatment', *Acta Mater*, 2003 **51** 3109–3120.
70. Luthra K L, 'Stability of protective oxide-films on Ti-base alloys', *Oxid Met*, 1991 **36** 475–490.
71. Atkinson K J W, Grimes R W, Levy M R, Coull Z L, English T, 'Accommodation of impurities in  $\alpha$ - $Al_2O_3$ ,  $\alpha$ - $Cr_2O_3$  and  $\alpha$ - $Fe_2O_3$ ', *J Europ Ceram Soc*, 2003 **23** 3059–3070.
72. Shimada S, 'A thermoanalytical study on the oxidation of ZrC and HfC powders with formation of carbon', *Solid State Ionics*, 2002 **149** 319–326.
73. Sun Z M, Zhou Y C, 'High temperature oxidation and hot corrosion behavior of  $Ti_3SiC_2$ -based materials', *Key Eng Mater*, 2002 **224**(2) 791–796.
74. Liu G M, Li M S, Zhang Y M, Zhou Y C, 'Hot corrosion of  $Ti_3SiC_2$ -based ceramics coated with  $Na_2SO_4$  at 900 and 1000°C in air', *Corros Sci*, 2003 **45** 1217–1226.
75. Liu G M, Li M S, Zhou Y C, Zhang Y M, 'Hot corrosion behavior of  $Ti_3SiC_2$  in the mixture of  $Na_2SO_4$ - $NaCl$  melts', *J Europ Ceram Soc*, 2004 **25** 1033–1039.
76. Liu G M, Li M S, Zhang Y M, Zhou Y C, 'Corrosion behavior and strength degradation of  $Ti_3SiC_2$  in the eutectic  $K_2CO_3$  and  $Li_2CO_3$  mixture', *J Europ Ceram Soc*, 2003 **23**(11) 1957–1962.
77. Barsoum M W, El-Raghy T, Farber L, Amer M, Christini R, Adams A, 'The topotactic transformation of  $Ti_3SiC_2$  into a partially ordered cubic  $Ti(C_{0.67}Si_{0.06})$  phase by the diffusion of Si into molten cryolite', *J Electrochem Soc*, 1999 **146**(10) 3919–3923.
78. Wang X H, Zhou Y C, 'Hot corrosion of  $Na_2SO_4$ -coated  $Ti_3AlC_2$  in air at 700–1000°C', *J Electrochem Soc*, 2004 **151**(9) B505–511.
79. Lin Z J, Zhou Y C, Li M S, Wang J Y, 'Hot corrosion and protection of  $Ti_2AlC$  against  $Na_2SO_4$  salt in air', *J Europ Ceram Soc*, 2006 **26** 3871–3879.
80. Lawson M G, Pettit F S, Blachere J R, 'Hot corrosion of alumina', *J Mater Res*, 1993, **8** 1964–1971.

81. Lin Z J, Zhou Y C, Li M S, Wang J Y, 'Improving the Na<sub>2</sub>SO<sub>4</sub>-induced corrosion resistance of Ti<sub>3</sub>AlC<sub>2</sub> by pre-oxidation in air', *Corros Sci*, 2006 **48** 3271–3280.
82. Liu G M, Li M S, Zhou Y C, 'Influence of pre-oxidation on the hot corrosion of Ti<sub>3</sub>SiC<sub>2</sub> in the mixture of Na<sub>2</sub>SO<sub>4</sub>-NaCl melts', *Corros Sci*, 2006 **48** 650–661.
83. Lin Z J, Li M S, Wang J Y, Zhou Y C 'High temperature oxidation and hot corrosion of Cr<sub>2</sub>AlC', *Acta Mater*, 2007 **55**(18) 6182–6191.
84. Lin Z J, Li M S, Wang J Y, Zhou Y C, 'High temperature oxidation and hot corrosion behavior of a Cr-Al-C composite', *J Am Ceram Soc*, 2007 **90**(12) 3930–3937.
85. Lin Z J, Li M S, Wang J Y, Zhou Y C 'Influence of water vapor on the oxidation behavior of Ti<sub>3</sub>AlC<sub>2</sub> and Ti<sub>2</sub>AlC', *Scripta Mater*, 2008 **58**(1) 29–32.

# 10

## Formation and growth of protective alumina scales

---

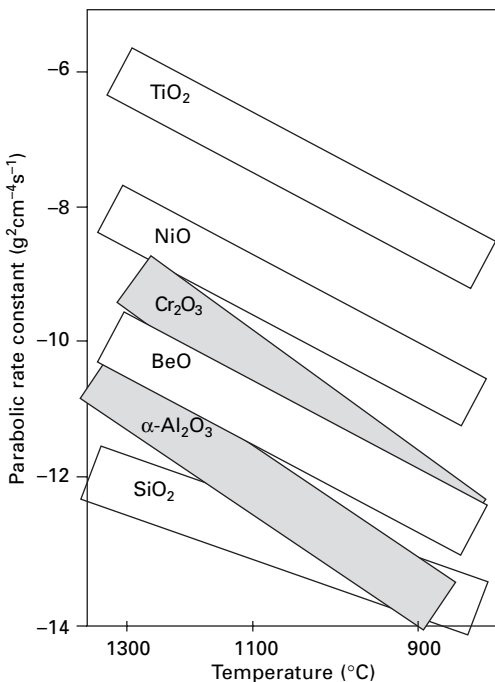
S CHEVALIER, University of Bourgogne, France

### 10.1 Introduction

The best protection of metallic materials against high temperature oxidation is based on the formation of a protective oxide scale which acts as a diffusion barrier, isolating the base materials from the aggressive atmospheres [1–6]. Although the principle is quite simple, its application is complex, since to act as a real barrier the oxide scale has to be dense and homogeneous, and has to cover the entire alloy surface, to possess mechanical properties as close as possible to the base materials, to consume the least metal possible [7], to keep stable (oxide transformations are to be proscribed most of the time), to be able to resist any change of atmosphere (presence of water vapour, for example [8–10]) and above all to keep adherent to the substrate, even after thermal shocks. Even if some of these parameters are easily counterbalanced by the use of commercial alloys, most of them are difficult to control due to the lack of knowledge about the high temperature oxidation mechanisms.

The most protective oxide layers are generally composed of chromia,  $\text{Cr}_2\text{O}_3$ , alumina,  $\text{Al}_2\text{O}_3$ , or silica,  $\text{SiO}_2$ . These refractory oxides grown on Fe, Co or Ni based alloys possess high melting points. 12 wt% of Cr and/or 5 wt% of Al are necessary to form chromia on the chromia-forming alloys and/or to form alumina on the alumina-forming alloys, respectively. The formation of silica is obtained on silicides,  $\text{MoSi}_2$  or  $\text{FeSi}_2$  for example, whose properties are quite different from those of chromia- or alumina-forming alloys.

According to the literature, the parabolic rate constants determined during the growth of alumina scales are lower than the parabolic rate constant of chromia scales (Fig. 10.1) [11]. To guarantee the pre-cited protective properties, chromia and alumina scales have to be employed in an adequate temperature range,  $T \leq 900^\circ\text{C}$  for  $\text{Cr}_2\text{O}_3$  and  $T \leq 1300^\circ\text{C}$  for  $\text{Al}_2\text{O}_3$ . Although such temperatures may be maintained during isothermal exposures, the situation can be different during exposure under thermal cycling, i.e. successive exposure at oxidising temperature followed by rapid cooling. If the temperature drop



10.1 Parabolic rate constants in alumina and chromia scales (adapted from [11]).

reaches a critical value ( $\Delta T > \Delta T_{\text{critical}}$ ), the oxide scale tends to spall, losing any protective effect. The reasons why oxide scales spall from the metallic substrate are numerous. But the differences in thermal expansion coefficients (TEC) between the oxide layers and the underlying metals or alloys also have a major influence. The main reasons are the thermal stresses generated during cooling owing to differences between the base metal TEC and that of the oxide scale. The thermal and/or residual stresses are known to play a major role during the oxidation of metallic alloys [1,12–18].

## 10.2 Alumina scales: growth and properties

### 10.2.1 Kinetics consideration

The formation of an alumina scale generally needs at least 5 wt% in alloys such as Fe-Cr or Ni-Cr. Over this aluminium content, the mechanical properties, mainly the alloy ductility, are poor, leading to machinability problems. Below this aluminium content, it is not possible to form a covering alumina scale, despite a favourable value for the free enthalpy of formation ( $-1238 \text{ kJ.mol}^{-1}$  at  $1100^\circ\text{C}$  [19]). These alloys generally contain enough chromium (typically around 20 wt%) to allow the growth of chromia layers. But, as the

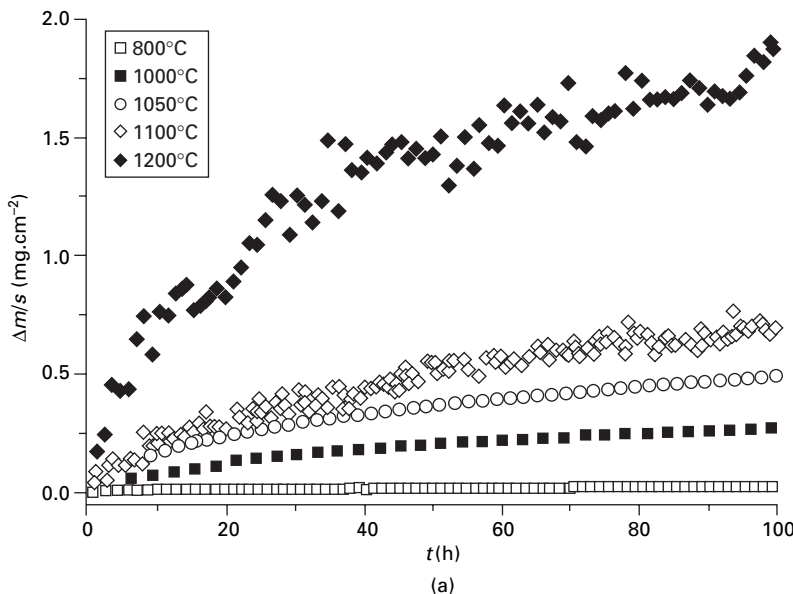
Fe-Cr-Al and Ni-Cr-Al alloys are mainly used at temperatures over 1000°C, the chromia scale is no longer able to give any beneficial effect, due to volatilisation problems [20]. Reports have indicated, however, that nanocrystal structure can promote the diffusion of Al in Ni-Cr-Al alloy coatings. The minimum aluminium content for formation of  $\alpha$ -Al<sub>2</sub>O<sub>3</sub> on a Ni-20Cr-Al alloy coating can be reduced to ~2 wt% when the grain size is of the order of 60 nm [21].

Alumina scale growth and above all the understanding of the scale growth mechanisms are much more complicated than for chromia scales. The main reason is the possible formation of transient alumina phases, which depends on the oxidation temperature, the partial pressure of oxygen, and the presence of dopant or impurities in the oxide layer. The most stable and protective alumina scale is the  $\alpha$ -alumina (corundum structure), but its formation and growth are not possible in all conditions. It is then fundamental to study how the transient alumina nucleates, but also the criteria or driving force that do or do not transform them into  $\alpha$ -alumina, to completely understand the high temperature reactivity of alumina-forming alloys.

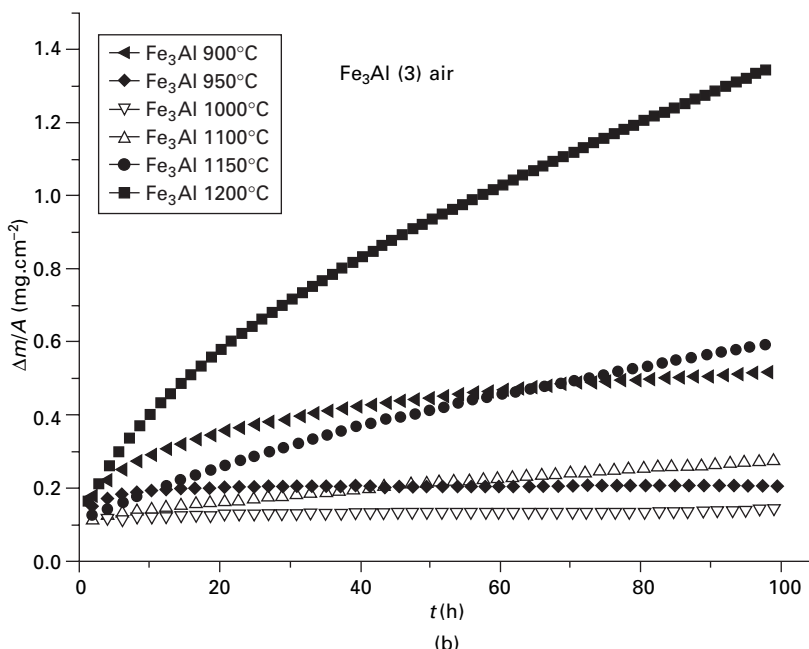
As a consequence, the kinetic data are somewhat complicated to interpret compared to the case of chromia layers (Figs 10.2a and 10.2b). The first remark is that, for most of the commercial alloys, the oxidation rates are lower at 1000°C than at 900–950°C [22,23]. For the case presented in Fig. 10.2a, weight gains increase typically with temperature. This is not true for Fig. 10.2b, for which weight gains at 1000°C appear lower than those at 900°C and 950°C. Numerous works have exposed deviation from the parabolic rate law in alumina scale kinetic data [24] or the necessity to apply a complete rate law [25]. The complete rate law takes into consideration the superimposition of two limited steps during the oxide scale growth: one (or several) interfacial chemical reactions and diffusion of species across the alumina scale [5]. However, many discrepancies appear in the data collected in the literature; for example, differences spanning several orders of magnitude can be found in values of parabolic rate constants ( $k_p$ ) [26–32] and activation energies ( $E_a$ ) [33–36] (Fig. 10.3 and Table 10.1).

### 10.2.2 Alumina scale growth mechanism

Study of alumina scale growth mechanisms also shows numerous contradictory results. The formation of the alumina layers has been attributed to oxygen or aluminium or a mixed diffusion process. The experiments shown in Fig. 10.4 were performed on a model Fe-20Cr-5Al alloy in the temperature range 1000–1200°C; they clearly evidence that the alumina scale grew, in these conditions, via oxygen and aluminium grain boundary diffusion [32]. Table 10.2 represents a synthesis of the different growth mechanisms proposed in the literature [27,37–49].

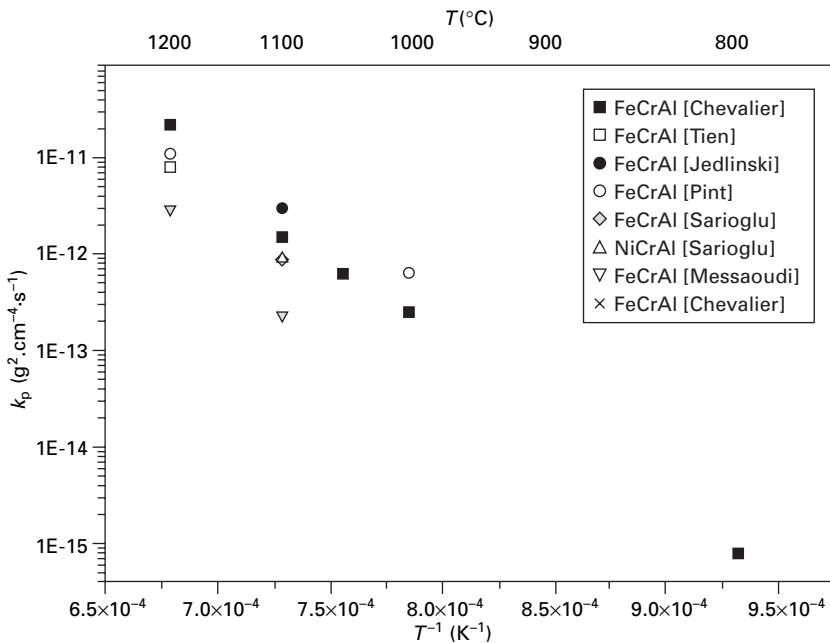


(a)



(b)

10.2 Isothermal oxidation kinetic curves for alumina-forming alloys:  
 (a) case of a model Fe-20Cr-5Al; (b) case of an iron aluminide  $\text{Fe}_3\text{Al}$  oxidised in air under atmospheric pressure.



10.3 Comparison of  $k_p$  values established during alumina scale growth.

Table 10.1 Activation energies determined during alumina scale growth

Material (wt%)	$T$ (°C)	$E_a$ (kJ.mol <sup>-1</sup> )
Fe-25Cr-4Al	1000–1200	388
Al deposited on foils	1050–1150	362
Fe-20Cr-5Al	800–1350	230
Fe-20Cr-5Al	800–1200	323

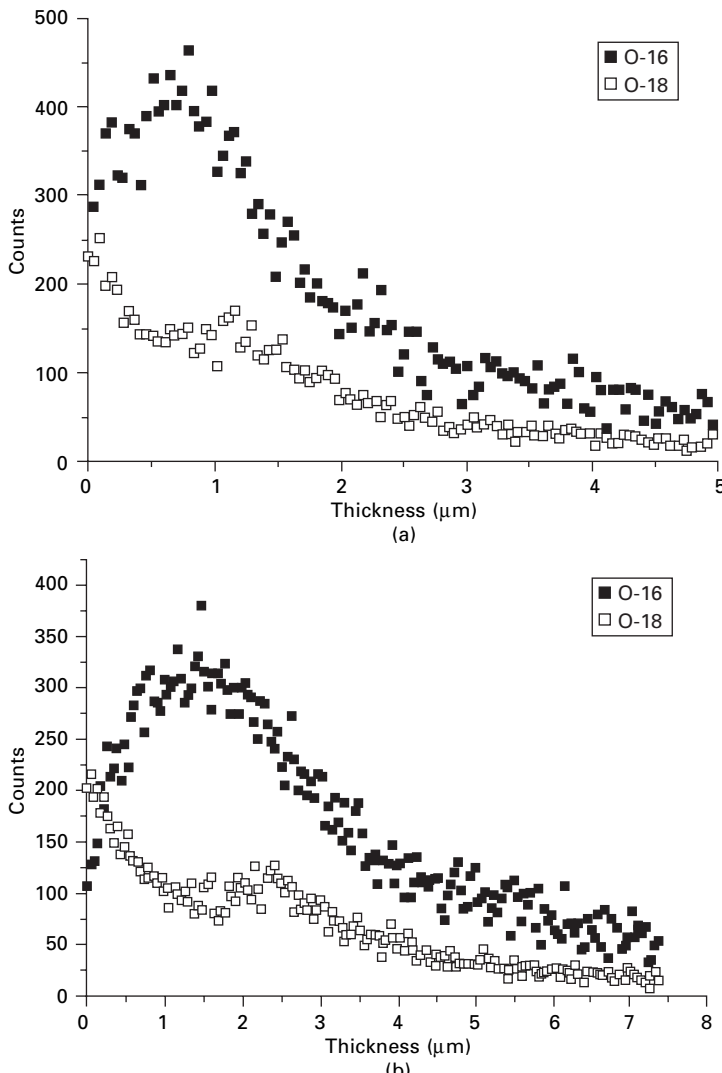
Although the situation is not always clear at high temperature, it was evidenced that at low temperature, aluminium cations migrate externally to form the alumina scale [50]. This suggests that the transient alumina, which nucleates at low temperature, does not grow in the same way as the  $\alpha$ -alumina that is able to develop at higher temperatures.

The growth mechanism has a major influence on the oxide grain morphology, since this appears coarse and not well defined when mixed aluminium and oxygen transport has been established [32,51] (Fig. 10.5). In some cases, the alumina scale looks highly convoluted [52] (Fig. 10.6); this convoluted aspect of the scale could be due to oxygen diffusion via oxide grain boundaries and aluminium diffusion via the bulk of the grain, allowing the nucleation and growth of new oxide grains within the existing oxide layer. This model, proposed by Wood and Stott [53], suggests that the consequently lateral

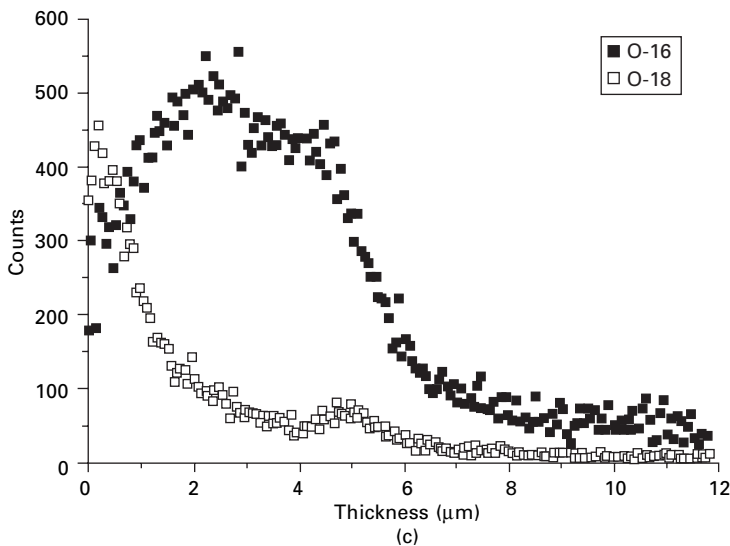
growth of oxide grain is able to provoke the local detachment of the alumina scale from the underlying substrate.

### 10.2.3 Transient alumina formation and transformation

The exact role played by the transient alumina and its transformation is not clearly established. Numerous works have evidenced the nucleation and



10.4 SNMS profiles of oxygen isotopes after successive oxidation of an FeCrAl alloy under  $^{16}\text{O}_2/^{18}\text{O}_2$ : (a) at 1050°C; (b) at 1100°C; (c) at 1200°C.

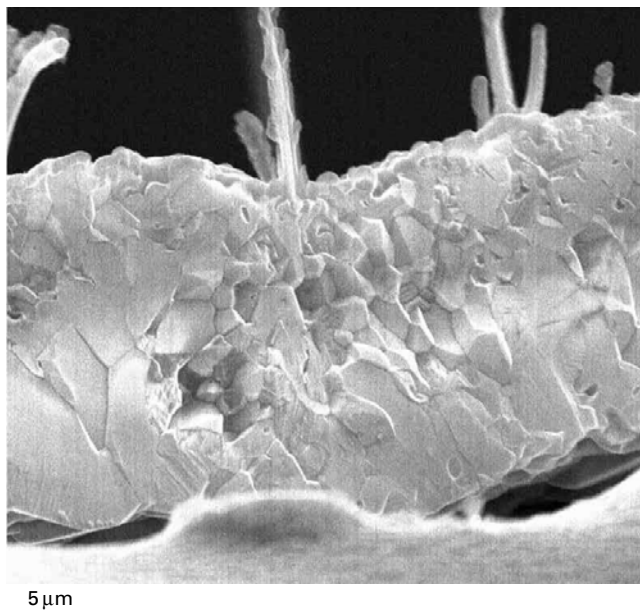


## 10.4 (Continued)

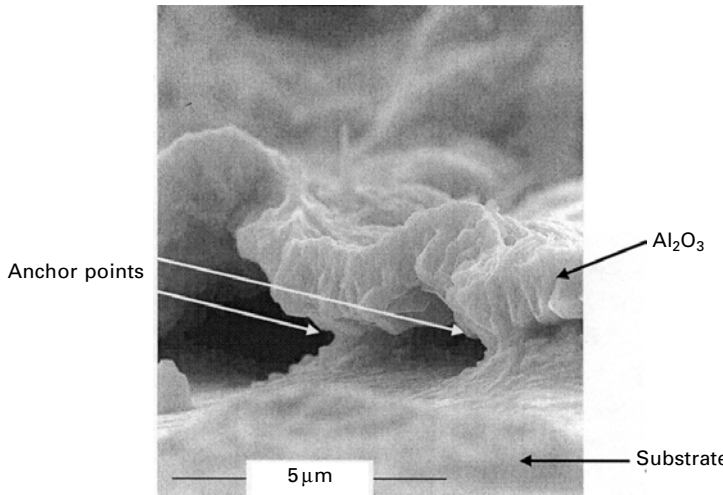
Table 10.2 Transport mechanisms established from isotopic marker experiments during high temperature oxidation of alumina-forming alloys

Material (wt%)	T (°C)	Transport mechanisms
Ni-Al	1000	Al diffusion
Fe-23Cr-5Al	1082	Al diffusion
Fe-20Cr-5Al	900–1100	Mixed
β-NiAl	1000–1200	Mixed and gb (grain boundaries)
β-NiAl	1200	Mixed and gb (grain boundaries)
Ni-Al	1200	Mixed
Fe-20Cr-5Al	1200	Mixed
Ni-Al	1500	Mixed
Fe-20Cr-5Al	1200	External diffusion of aluminium
β-NiAl	1200	Oxide formation at interfaces
Fe-23Cr-5Al	1000	External diffusion of aluminium (very small oxygen transport during the first steps of oxidation)
Fe-20Cr-5Al	1200	Aluminium and oxygen diffusion
Fe-20Cr-5Al	1100	Aluminium and oxygen diffusion

growth of transient alumina ( $\gamma\text{-Al}_2\text{O}_3$ ,  $\delta\text{-Al}_2\text{O}_3$ ,  $\theta\text{-Al}_2\text{O}_3$ ) followed by its transformation in stable  $\alpha\text{-Al}_2\text{O}_3$  [54–60]; the transformation from  $\theta$  to  $\alpha$  generally leads to a volume contraction of around 14% [61], due to different oxide density. Grabke *et al.* proposed a scheme showing the temperature dependence of the transformation from one transient alumina to another in the case of NiAl [62]. It claimed that for  $T < 850^\circ\text{C}$ , the  $\gamma\text{-Al}_2\text{O}_3$  phase is

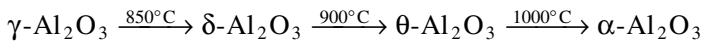


10.5 Fracture cross-section of an alumina scale formed on an Fe-20Cr-5Al alloy after 100 h at 1100°C.



10.6 Fracture cross-section showing the convoluted shape of the alumina scale grown during the oxidation of an Fe-20Cr-5Al model alloy.

stable for  $850^{\circ}\text{C} < T < 1000^{\circ}\text{C}$  the  $\theta\text{-Al}_2\text{O}_3$  phase is stable, and  $\alpha\text{-Al}_2\text{O}_3$  is stable at  $T > 1000^{\circ}\text{C}$ . The temperature stability of these alumina phases can be described as follows [63]:



$\gamma\text{-Al}_2\text{O}_3$ ,  $\delta\text{-Al}_2\text{O}_3$  and  $\theta\text{-Al}_2\text{O}_3$  have been reported as the main transient alumina. These phases, which transform into  $\alpha\text{-Al}_2\text{O}_3$ , have different crystallographic structures.  $\gamma\text{-Al}_2\text{O}_3$  has a cubic spinel type structure (space group Fd3m) [64]. The lattice parameter of  $\gamma\text{-Al}_2\text{O}_3$  varies from 0.797 nm to 0.800 nm. The structure of  $\delta\text{-Al}_2\text{O}_3$  is controversial: one commonly reported structure is an ordered form of  $\gamma\text{-Al}_2\text{O}_3$ , where the crystal structure can be described as tetragonal and the unit cell parameters are  $a_{\delta} = a_{\gamma}$ ,  $b_{\delta} = a_{\gamma}$ ,  $c_{\delta} = 3a_{\gamma}$ ; another is orthorhombic, where  $a_{\delta} = a_{\gamma}$ ,  $b_{\delta} = 2a_{\gamma}$ ,  $c_{\delta} = 1.5a_{\gamma}$  [65]. The crystal structure of  $\delta\text{-Al}_2\text{O}_3$  remains unknown.  $\theta\text{-Al}_2\text{O}_3$  has monoclinic symmetry (space group C2/m) with lattice parameters  $a = 1.1813$  nm,  $b = 0.2906$  nm,  $c = 0.5655$  nm and  $\beta = 10.41^{\circ}$ . The stable  $\alpha\text{-Al}_2\text{O}_3$  structure has trigonal symmetry with rhombohedral centring (space group  $R\bar{3}c$ ). The O anions occupy approximately h.c.p. (hexagonal close packed) positions and the Al cations are located in octahedral coordinated interstitial sites in the anion sublattice [64].

In a study related to the oxidation of  $\beta\text{-NiAl}$  from  $800^{\circ}\text{C}$  to  $1000^{\circ}\text{C}$ , Doychak *et al.* [66], using transmission electronic microscopy and electronic diffraction, showed that the transient oxides have high epitaxial relationship with metal. They also noted that the transformation of  $\gamma\text{-Al}_2\text{O}_3$  into  $\alpha\text{-Al}_2\text{O}_3$  implies an intermediate phase,  $\delta\text{-Al}_2\text{O}_3$ . Ramanarayanan *et al.* [67] described the existence of  $\delta\text{-Al}_2\text{O}_3$  mixed with  $\alpha\text{-Al}_2\text{O}_3$  on an iron-containing alloy at  $900^{\circ}\text{C}$ . This type of alumina was also noted in the oxidation of Pt-Al alloys at  $1200^{\circ}\text{C}$  [68]. In this case, it was observed on the top of the  $\text{Pt}_5\text{Al}_3$  phase, whereas  $\alpha\text{-Al}_2\text{O}_3$  was formed on the top of the  $\text{PtAl}_2$  phase. There are, however, doubts about the existence of the  $\delta\text{-Al}_2\text{O}_3$  phase and confusion is possible when it comes to distinguish it from  $\theta\text{-Al}_2\text{O}_3$  [69]. It is generally established that transient alumina have needle-like or platelet-like morphology, but most of the time it appears to be very difficult to distinguish precisely transient alumina from  $\alpha$ -alumina other than by considering the surface morphology of the scale [70].

#### 10.2.4 Oxygen and cation diffusion coefficients in alumina scales

The short-circuits considered for diffusion within oxides in the temperature range  $800\text{--}1000^{\circ}\text{C}$  are oxide grain boundaries. According to Harrison [71], three diffusion regimes could be identified. The A regime is defined by  $\sqrt{Dt} \gg d$ ,  $d$  being the grain size; in that case, the volume penetration is

superior to the short-circuit size, especially the grain boundaries. The C regime claims that the penetration is continuous at the grain boundaries ( $\sqrt{Dt} \ll \delta$ ,  $\delta$  being the grain boundary width). Finally, the B regime is an intermediate regime where three processes participate in diffusion: volume, grain boundary and lateral diffusion  $\left(\delta \ll \sqrt{Dt} \ll \frac{d}{2}\right)$ .

Marker experiments made with  $^{18}\text{O}$  lead to the determination of oxygen diffusion coefficients via alumina grain boundaries and via the oxide bulk. Taking into consideration the plots of  $\ln [^{18}\text{O}] = f(x)$ , the first part of the curve corresponds to the apparent diffusion of oxygen. From the three diffusion regimes, the B regime is usually chosen for the study of intergranular diffusion [72,73]. In this regime,  $\delta \ll \sqrt{Dt} \ll \frac{d}{2}$  with  $\delta$  the grain boundary width and  $d$  the oxide grain size.

The apparent diffusion of oxygen corresponds to the diffusion in the bulk and the oxide grain boundaries. It is expressed in the case of dislocation and bulk diffusion [74] but can be used in the case of grain boundary and bulk diffusion [75,76], if we assume that the beginning of the oxygen distribution profile corresponds to  $D_{\text{app}}$  (A regime) [72]:

$$D_{\text{app}} = (1 - f)D_b + fD_{\text{gb}} \quad 10.1$$

where  $f$  is the fraction of sites associated with the grain boundaries;  $f$  can be expressed as

$$f = \frac{3\delta}{\phi} \quad 10.2$$

$\delta$  being the grain boundary width (generally assumed to be 1 nm) and  $\phi$  the average oxide crystallite size.  $D_{\text{app}}$  is determined from the second Fick's law solution:

$$\frac{C(x, t) - C_s}{C_o - C_s} = \operatorname{erf}\left(\frac{x}{2\sqrt{D_{\text{app}}t}}\right) \quad 10.3$$

where  $C_s$  is the oxygen-18 concentration at the oxide scale surface,  $C_o$  is the natural concentration in oxygen-18 within the oxide layer (0.2 at% [77]) and  $t$  is the diffusion time.

This model which associates the beginning of the distribution profile with an apparent diffusion coefficient has been recently discussed by Fielitz *et al.* [78] who proposed that the first part of the oxygen diffusion profile in polycrystalline mullite corresponded to the bulk diffusion coefficient in the B regime and not to the apparent diffusion coefficient.

The second part of the diffusion curve,  $\ln [^{18}\text{O}] = f(x)$ , allows the determination of the oxygen grain boundary diffusion coefficient. By applying the Whipple-LeClaire model [79–81],  $D_{\text{gb}}$  is expressed by:

$$D_{gb}\delta = 0.661 \sqrt{\frac{4D_b}{t}} \left( -\frac{\partial \ln C}{\partial x^{6/5}} \right)^{-5/3} - D_{app} \quad 10.4$$

where  $\left( \frac{\partial \ln C}{\partial x^{6/5}} \right)$  is the slope of the curve  $\ln[^{18}\text{O}] = f(x^{6/5})$ . By combining equations (10.1) and (10.4), the following relation can be obtained:

$$(1-f)D_b + \frac{0.661f}{\delta} \sqrt{\frac{4D_b}{t}} \left( -\frac{\partial \ln C}{\partial x^{6/5}} \right)^{-5/3} - D_{app} = 0 \quad 10.5$$

This relation allows the determination of the oxygen bulk diffusion coefficient,  $D_b$ . Using  $D_{app}$  and  $D_b$ , relation (10.1) allows the calculation of  $D_{gb}$ .

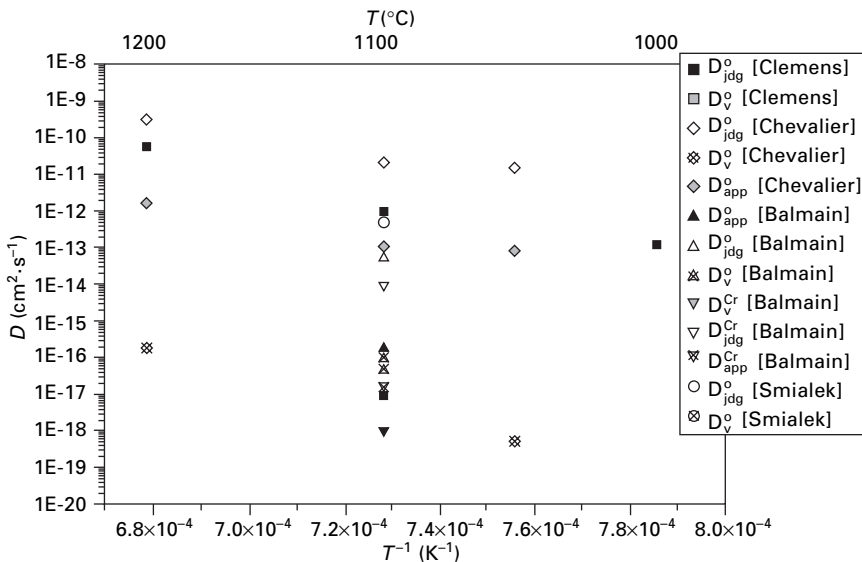
Oxygen-18 diffusion experiments led to the determination of oxygen diffusion coefficients. In the temperature range from 1050 to 1200°C, the results are shown in Table 10.3 [82]. Comparison with the literature is difficult, since very few experiments have been performed on thermally grown alumina scale [82–86] (Fig. 10.7), whereas numerous works have concerned the determination of diffusion coefficients in synthetic alumina [87–98].

The diffusion experiments performed on both synthetic and thermally grown alumina have shown that aluminium diffusion predominates over oxygen diffusion in the alumina grain boundaries, but the values calculated in the case of synthetic alumina are largely different from the values determined in thermally grown scales. The chemistry (especially the impurity level or dopant concentration evolution) and/or microstructure (grain size, transient alumina formation, etc.) of the two types of alumina could explain these differences [99,100], thus it appears very difficult to compare diffusion experiments on synthetic and thermally grown alumina.

Chromium is used as an isotopic marker for aluminium. Taking into account that both chromium and aluminium cations diffuse in the same way, the results obtained on chromium diffusion coefficients in alumina scales can be applied to aluminium cation diffusion coefficients in the same scale. Indeed, it is easier to use a chromium isotope as a diffusive species than to use aluminium, which has no natural isotope; one can only use an artificial aluminium isotope,  $^{26}\text{Al}$ , which is radioactive and very expensive. Very few works have used this radioactive tracer [90,101].

*Table 10.3* Oxygen diffusion coefficients determined in  $\alpha\text{-Al}_2\text{O}_3$  grown on an Fe-25Cr-5Al alloy at 1050, 1100 and 1200°C.

	1050°C	1100°C	1200°C
$D_{app}^0$ ( $\text{cm}^2 \cdot \text{s}^{-1}$ )	$8.0 \times 10^{-14}$	$1.1 \times 10^{-13}$	$1.6 \times 10^{-12}$
$D_b^0$ ( $\text{cm}^2 \cdot \text{s}^{-1}$ )	$5.7 \times 10^{-19}$	$8.3 \times 10^{-17}$	$1.9 \times 10^{-16}$
$D_{gb}^0$ ( $\text{cm}^2 \cdot \text{s}^{-1}$ )	$1.6 \times 10^{-11}$	$2.2 \times 10^{-11}$	$3.2 \times 10^{-10}$



10.7 Comparison of oxygen or chromium diffusion coefficients in thermally grown alumina.

### 10.3 Influence of minor element addition

All commercial steels contain minor element additions. Added at a low level, they play a huge role in the alloy properties, mechanical and/or anti-corrosion. Their presence in the metallic materials drastically influences the oxidation rate, the scale morphology and the oxide layer growth mechanisms. These minor elements are usually Mn, Ti, Si, etc. Even if they are added at very low levels, they are able to form mixed oxide phases, or they can segregate at oxide grain boundaries, then influencing the oxidation behaviour of the alloys. Owing to the presence of minor elements, multi-component oxides can grow within the alumina scales, such as spinel oxide ( $\text{Ni}(\text{Cr},\text{Al})_2\text{O}_4$ ) or perovskite-type oxide ( $\text{LaAlO}_3$ ).

#### 10.3.1 Reactive element addition

The most spectacular effect on the high temperature oxidation behaviour of metallic materials is observed when reactive elements (RE) are added in small quantities. They decrease the oxidation rate and drastically increase the oxide adherence to the doped metallic substrates. The protective barrier keeps its effectiveness even when submitted to thermal shocks; it then guarantees an excellent lifetime of the materials under service conditions. The beneficial effect of reactive elements on the high temperature resistance of alloys has been known for more than 50 years [102,103]. The reasons why

they are so efficient are still unclear. Numerous hypotheses have been proposed in order to explain the beneficial effect of reactive elements. As no clearly defined model has been proposed to explain it completely, and considering the large number of published papers on this problem, one can suppose that no single theory has been envisaged to explain their role, taking into account the reactive elements, the tested materials, the native oxide scale and the nature of the oxidising atmosphere [1]. As an example, some RE additions give the well-known beneficial effect, whereas others can have a disastrous influence on the oxidation properties of alloys.

According to the literature [105], the decrease of the oxidation rate and the improvement of the oxide layer adherence are not the only beneficial effects resulting from the addition of reactive elements; they can also:

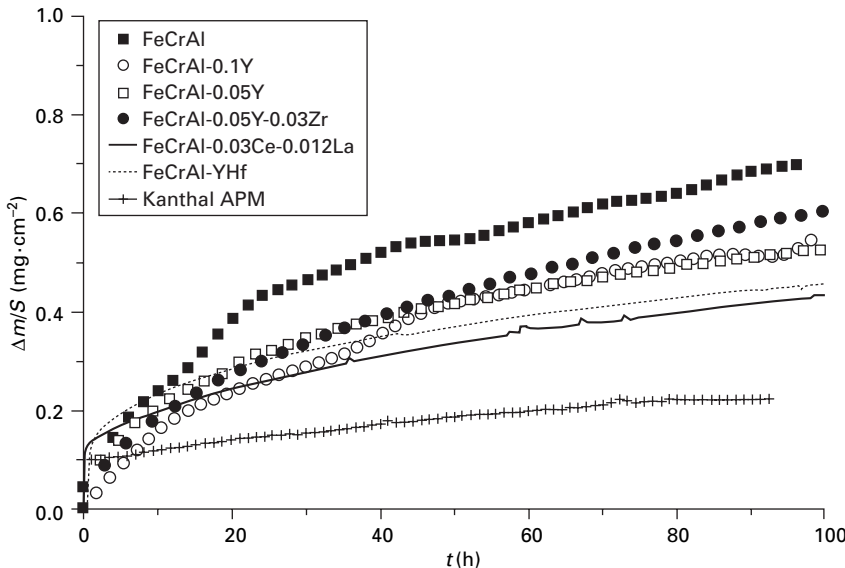
- favour the nucleation and growth of the protective oxide scale [106–109];
- decrease the oxide grain size [33] and consequently improve the oxide scale mechanical properties (especially its plasticity [110,111] which can modify the growth and/or thermal stresses generated within the scale during its growth or its cooling to room temperature [112–114], and its creep property [115,116]);
- avoid the detrimental sulphur effect [117–119];
- influence the transformation of transient phases (in the case of alumina scales) [120,121];
- suppress the dislocation climb in the metal and then limit the cation transport (poisoned interface model) [122,123].

A tentative list of the beneficial effects ascribed to the introduction of RE in model or commercial alloys will be made in this chapter.

### 10.3.2 Influence on kinetics

In comparison to its effect in chromia scales, in which the oxidation rate can be decreased by a factor of 100 in the presence of RE, the introduction of RE has a slight influence on the oxidation rate of alumina-forming alloys (Fig. 10.8 and Table 10.4) [33,34,124–127]. The addition of Zr or  $\text{Y}_2\text{O}_3$  decreases the oxidation rate of FeCrAl steels by a factor of only 3 [128]. This is confirmed by the results summarised in Figs 10.3 and 10.9 [29–31,34,56,129–133].

The quantity of RE introduced in the alloys plays a considerable role on the oxidation rates. When added over a critical content, the RE leads to negative effects, typically a large increase in the oxidation rate [134,135]. This ‘overdoping’ effect is probably due to an increase of oxygen diffusion due to the presence of oxygen vacancies in the RE oxides (REO).



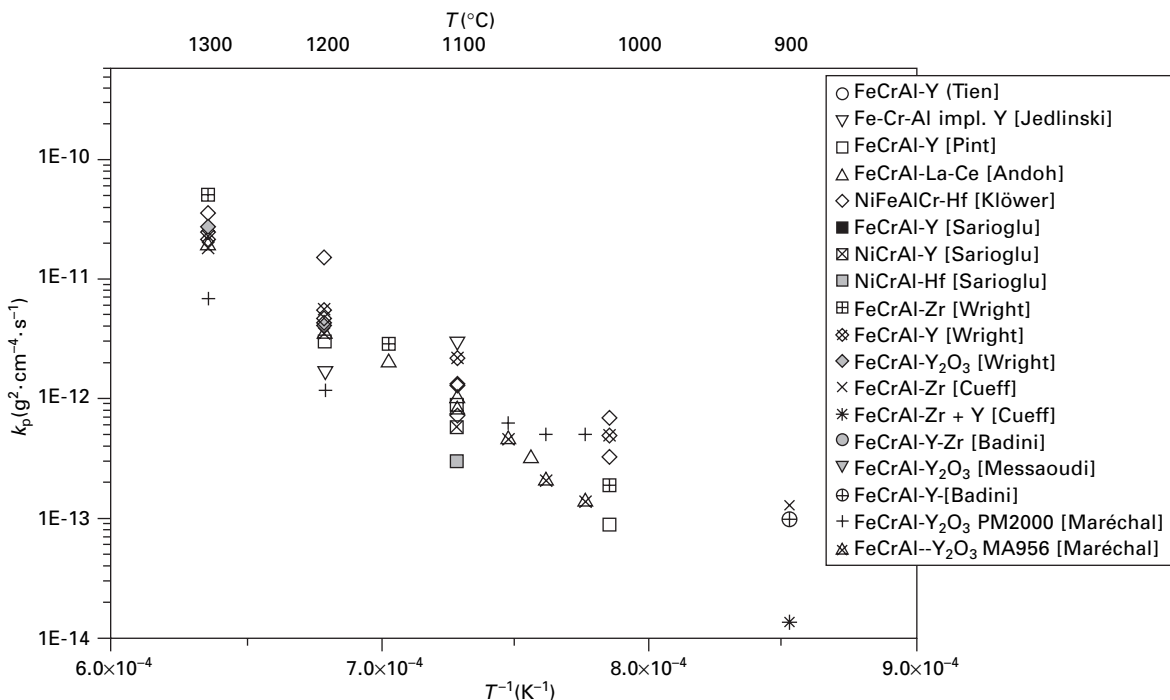
10.8 Kinetic curves showing the influence of RE addition on the oxidation behaviour of an FeCrAl alloy at 1100°C.

Table 10.4 Activation energy values of the oxidation reaction of several alumina-forming alloys doped with RE

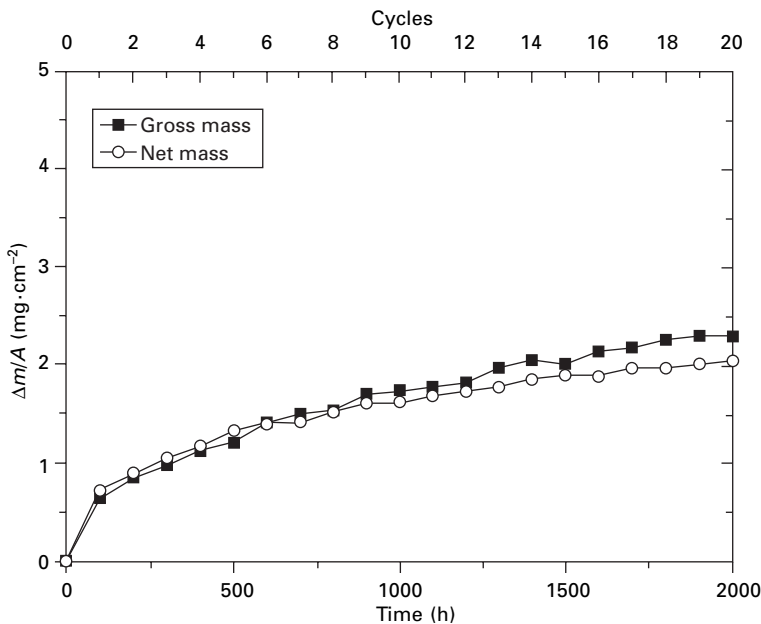
Material (wt%)	T (°C)	$E_a$ (kJ.mol⁻¹)
Fe-20Cr-4.5Al-0.5Ti-0.5Y <sub>2</sub> O <sub>3</sub>	1000-1200	388
Fe-25Cr-4Al-0.5Y		388
Ni-16Cr-4.5Al-0.01Y	950-1150	400
Fe-20Cr-5Al-0.02La-0.04Ce (foils)	1050-1150	289
NiAl-Y <sub>2</sub> O <sub>3</sub>	900-1200	200
Fe <sub>3</sub> Al-ODS	1000-1300	251
Fe-20Cr-5Al-Zr (APM)	1000-1300	274
Fe-20Cr-5Al-Y <sub>2</sub> O <sub>3</sub> (MA956)	1000-1300	178
Fe-20Cr-5Al-Y <sub>2</sub> O <sub>3</sub> (PM2000)	1000-1300	143
Fe-20Cr-5Al-0.09Y	800-1350	495
Fe-20Cr-5Al-Y-Zr-Ti	800-1350	280
Fe-20Cr-5Al-0.4Ti	800-1350	316
Fe-20Cr-5Al-0.1Zr	800-1350	380

### 10.3.3 Effect on alumina scale adherence

The most spectacular effect of RE introduction on the chromia and alumina scales is their drastic adherence to the underlying substrates. Cyclic oxidation tests clearly evidence their resistance to spallation, since the oxide layers keep adherent to the alloys, even after a lot of cycles (Fig. 10.10). The



10.9 Parabolic rate constants determined during the oxidation of some RE-doped alumina-forming alloys.



10.10 Net and gross weight during cyclic oxidation tests of an Fe-Cr-Al-Y steel at 1100°C.

superimposition of the gross (sample and eventual spalled oxides) and net (sample only) mass is a significant indication of the good adherence of the corrosion products at the substrate surface [136].

#### 10.3.4 Location of reactive elements (RE) in alumina scales

The REs in the oxide scales are most of the time very difficult to detect. Their presence at the surface of oxide layers as perovskite phases or  $MA\text{O}_3$  [28], as garnets ( $\text{Y}_3\text{Al}_5\text{O}_{12}$ ) [133,137–139], or as not well-defined phases ( $\text{YAl}_x\text{O}_y$ ) [140,141] is often observed after long exposures in oxidising atmospheres at high temperature. Their precise location within the oxide scale needs to be established by TEM cross-section. Table 10.5 summarises the results obtained by TEM observations of thermally grown or synthetic alumina doped with RE [33,45,124,140,142–160]. Most of the TEM analyses locate the RE at the oxide grain boundaries, within the thermally grown as well as the synthetic oxides. The RE solubility in  $\text{Cr}_2\text{O}_3$  and in  $\text{Al}_2\text{O}_3$  is very low (around 10 wt ppm for Y in  $\text{Al}_2\text{O}_3$  [161]). Figure 10.11 illustrates the segregation of RE at the grain boundaries of thermally grown alumina.

Ceramists use a classical method, such as uniaxial or isostatic pressing followed by sintering, to prepare REO doped alumina. After exposure at

Table 10.5 TEM analyses in thermally grown and synthetic alumina doped by RE

Material (wt%)	T (°C)	RE location (gb = grain boundaries)
Fe20Cr5Al-0.5Y <sub>2</sub> O <sub>3</sub>	1000	Y and Ti at Al <sub>2</sub> O <sub>3</sub> gb
Fe20Cr5Al-0.5Y <sub>2</sub> O <sub>3</sub>	1100	Y at Al <sub>2</sub> O <sub>3</sub> gb (garnet, <sub>3</sub> Al <sub>5</sub> O <sub>12</sub> , precipitates close to the Al <sub>2</sub> O <sub>3</sub> gb)
Ni16Cr5Al-0.01Y	1150	Y tends to segregate at Al <sub>2</sub> O <sub>3</sub> gb
β-NiAl-0.2Zr	1000–1400	Zr at Al <sub>2</sub> O <sub>3</sub> gb
NiAl-0.2Zr	1200	Zr at Al <sub>2</sub> O <sub>3</sub> gb and at metal/oxide interface
NiAl-0.1Y	1200	Y at Al <sub>2</sub> O <sub>3</sub> gb and at metal/oxide interface (High Resolution Electron Microscopy: no phase detected at gb)
Fe20Cr5Al-0.5Y <sub>2</sub> O <sub>3</sub>	1200	Y and Ti segregation at Al <sub>2</sub> O <sub>3</sub> gb
Fe20Cr5Al-0.1ZrO <sub>2</sub>	1200	Zr segregation at Al <sub>2</sub> O <sub>3</sub> gb
Fe20Cr5Al doped with different cations	1200	Y, Zr, La, Hf, Ti, Yb, Ce, etc., at Al <sub>2</sub> O <sub>3</sub> gb
Fe20Cr5Al-0.1Y	1200	Y at Al <sub>2</sub> O <sub>3</sub> gb and at metal/oxide interface (segregation <1 monolayer)
Fe20Cr5Al-0.17Y <sub>2</sub> O <sub>3</sub> , Fe20Cr5Al-0.7Y <sub>2</sub> O <sub>3</sub>	1200	Y at Al <sub>2</sub> O <sub>3</sub> gb
Fe20Cr5Al-0.1La	1200	La at Al <sub>2</sub> O <sub>3</sub> gb (segregation more intense at columnar gb than at equiax gb, no secondary phase detected at gb by High Resolution Electron Microscopy)
Fe20Cr5Al-0.1La–0.03Zr	1200	La and Zr at Al <sub>2</sub> O <sub>3</sub> gb
Fe20Cr5Al-mischmetal (La + Ce)	1100	La and Ce columnar gb of Al <sub>2</sub> O <sub>3</sub> and at metal/oxide interface
Fe20Cr5Al-0.1Y	1200	Y at Al <sub>2</sub> O <sub>3</sub> gb (no secondary phase detected at gb)
Fe20Cr5Al-0.1La	1200	La at Al <sub>2</sub> O <sub>3</sub> gb (no secondary phase detected at gb)
Fe20Cr5Al-0.03Ce	1200	Ce at Al <sub>2</sub> O <sub>3</sub> gb (no secondary phase detected at gb)
Fe20Cr5Al-0.09Sm	1200	Y at Al <sub>2</sub> O <sub>3</sub> gb (no secondary phase detected at gb)
Al <sub>2</sub> O <sub>3</sub> sintered with 0.045 mol% Y <sub>2</sub> O <sub>3</sub>	1400	Y at Al <sub>2</sub> O <sub>3</sub> gb (no secondary phase detected at gb)
Al <sub>2</sub> O <sub>3</sub> sintered with 0.045 mol% La <sub>2</sub> O <sub>3</sub>	1400	La at Al <sub>2</sub> O <sub>3</sub> gb (no secondary phase detected at gb)
Al <sub>2</sub> O <sub>3</sub> sintered with 0.045 mol% Lu <sub>2</sub> O <sub>3</sub>	1400	Lu at Al <sub>2</sub> O <sub>3</sub> gb (no secondary phase detected at gb)
PtAl-Zr	1200	Zr at Al <sub>2</sub> O <sub>3</sub> gb and at metal/oxide interface (no secondary phase detected at gb by High Resolution Electron Microscopy)

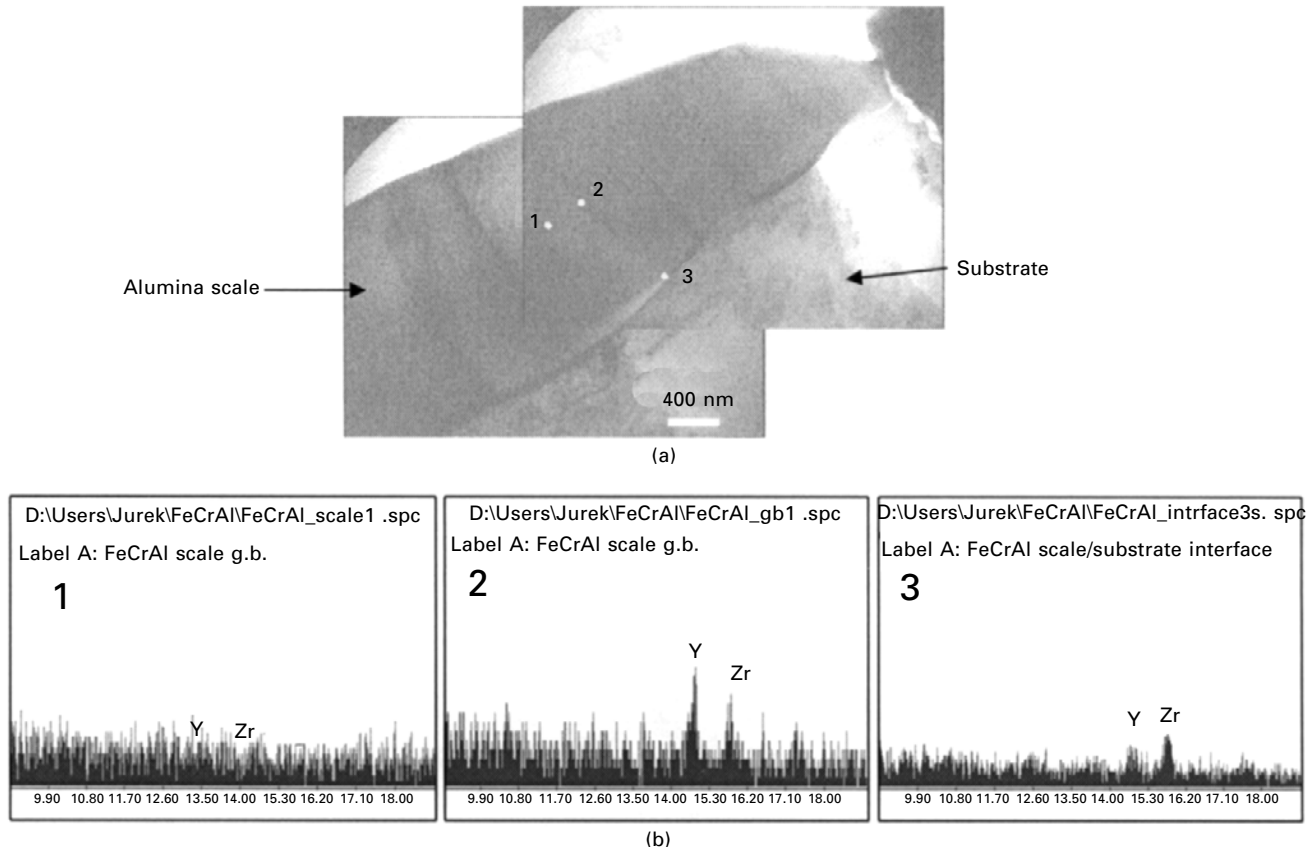
Table 10.5 (Continued)

Material (wt%)	T (°C)	RE location (gb = grain boundaries)
Al <sub>2</sub> O <sub>3</sub> hot pressed and doped with 1000 at. ppm Y	1475	Y at Al <sub>2</sub> O <sub>3</sub> gb (~9 at% in 1 nm at gb: corresponds to the formation of a monolayer of secondary phase)
Al <sub>2</sub> O <sub>3</sub> hot pressed and doped with 500 at. ppm La	1475	La at Al <sub>2</sub> O <sub>3</sub> gb (~9 at% in 1 nm at gb: corresponds to the formation of a monolayer of secondary phase)
Fe20Cr5Al-0.1La (foil)	1150	La at Al <sub>2</sub> O <sub>3</sub> gb
Al <sub>2</sub> O <sub>3</sub> hot pressed and doped with 100 at. ppm Nd or Zr and co-doped with Nd/Zr and Sc/Zr	1475	All dopants segregate at Al <sub>2</sub> O <sub>3</sub> gb (Sc <sup>3+</sup> and Zr <sup>4+</sup> segregation is less intense)
Al <sub>2</sub> O <sub>3</sub> hot pressed and doped with 1000 at. ppm Y	1475	Average concentration of Y at gb and triple points ~3.3 ± 0.9 atoms/nm <sup>2</sup>
Al <sub>2</sub> O <sub>3</sub> hot pressed and doped with 100 and 1000 at. ppm Y	1450	Y concentration at gb proportional to its initial concentration

high temperature, they observe the same phase formation and the same segregation phenomena. As an example, garnet phases, Y<sub>3</sub>Al<sub>5</sub>O<sub>12</sub>, were identified at the triple point in sintered alumina [162–164]. Creep properties (increase of creep resistance), sintering properties (decrease of sintering rate) and also the alumina grain size (alumina grain growth is limited during sintering) are drastically modified by the presence of REO [165–170]. Yttrium or lanthanum segregation at synthetic alumina grain boundaries decreases the diffusion process at the grain boundaries and then changes the sintered alumina properties. Garnet formation corresponds then to the saturation of grain boundaries in yttrium [160]. A recent work showed that the creep resistance of doped sintered alumina was directly controlled by the ionic bond strength at Al<sub>2</sub>O<sub>3</sub> grain boundaries in the presence of a low quantity of dopants [171]. Other works have proposed that sliding mechanisms at alumina grain boundaries could explain the improved creep properties [172].

In the case of alumina scales formed on alumina-forming materials, the presence of the garnet phases is explained by the diffusion of RE from the underlying metal to the oxide surface via the oxide grain boundaries. This theory, called ‘dynamic segregation’, has been proposed by Pint and is based on the oxygen potential gradient across the oxide scale [128]. The consequences of the diffusion of the RE towards the gas–oxide interface are, on the one hand, to suppress the diffusion of metal ions, and on the other hand, to form a mixed Al–RE oxide at the oxide surface.

The previous results have shown that the efficient dopants in thermally grown alumina (those for which the oxidation rate is decreased, the oxide



10.11 Illustration of the segregation of yttrium and zirconium at the alumina grain boundaries and at the metal–oxide interface in the case of an FeCrAl–Y–Zr alloy oxidised for 50 h at 1100°C: (a) bright field image; (b) EDX analyses of the indicated zones (1: interior of the grain, 2: grain boundary, 3: triple point at the metal–oxide interface).

scale adherence is improved and the oxide grain morphology is changed usually segregate to the alumina grain boundaries (see Table 10.5). Nevertheless, other dopants, such as Ti, Nb, Ta, Ca, etc. are found to segregate at the oxide grain boundaries but without giving any beneficial improvement in oxide layer performance at high temperature [147,148]. The dopant size could play a role in its efficiency in increasing the oxidation resistance, but the results are mainly contradictory. Recent studies performed on steels containing several RE (Y and Zr, for example) evidenced that both dopants segregated at the oxide grain boundaries as well as at the metal–oxide interface. Mixed phases,  $(\text{Zr}, \text{Y})\text{O}_{2-x}$ , were identified in the oxide layers [173]. EDX analyses performed using a TEM confirmed the association of Y and Zr, but did not allow the characterisation of a mixed oxide phase composed of Y and Zr. These EDX analyses revealed a higher Y concentration at the alumina grain boundaries, whereas the Zr level was higher at the metal–oxide interface [48,174]. No explanation could be given for such differences in the dopant concentration dependence on the segregation zone. The same phenomena were observed when La and Zr were the dopants [175]. Even if there is no doubt about the presence of RE at the oxide grain boundaries, recent HREM studies did not allow the detection of any phase at the grain boundaries [144,154,159].

### 10.3.5 Influence of reactive elements in alumina scale growth mechanism

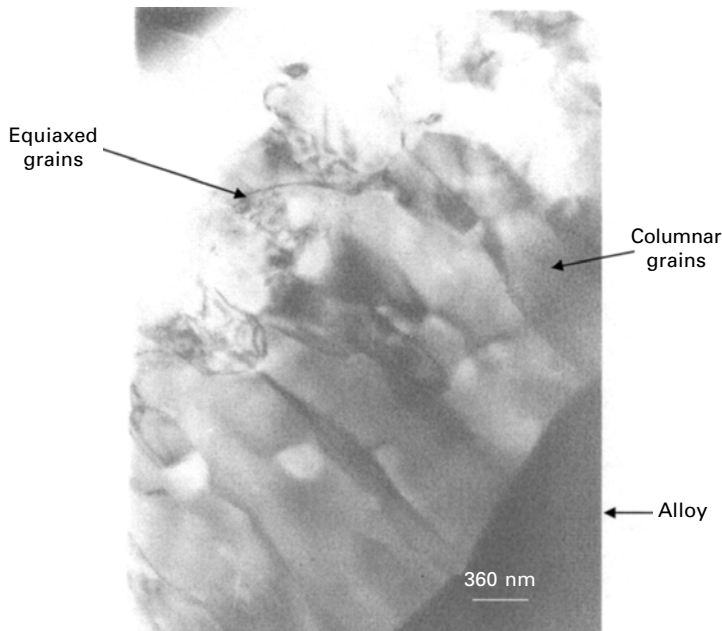
The main consequence of the RE segregation at the oxide grain boundaries is the change in the oxide scale growth mechanism. Table 10.6 shows that the transport of oxygen becomes predominant in RE doped alumina layers [26,27,37,38,40–48,174,176–180].

As a consequence, the morphology and the size of the oxide grains result in the scale change. Indeed, the annihilation of cation diffusion leads to the formation of thin columnar alumina grains [181,182]. For alumina scales, a thin oxide layer composed of small equiaxed grains is observed most of the time in the external part of the scale, close to the oxide–gas interface [51,183,184]. This thin layer is formed on the top of a layer made of more or less thin columnar alumina grains (Fig. 10.12). It has been evidenced that the equiaxed layer thickness stays constant as the oxidation progresses, whereas the columnar scale thickens. This suggests that the external layer made of equiaxed grains probably grows at the beginning of the oxidation process, and the oxidation process is different in the two layers. As evidence, TEM analyses revealed that La segregated at the columnar grain boundaries, but never at the equiaxed grain boundaries [180,182,185].

The segregation of RE at alumina grain boundaries leads to the decrease of the oxygen diffusion coefficient, as indicated in Fig. 10.13, even if the results appear sometimes contradictory. Once more, the comparison of oxygen

*Table 10.6 Transport mechanisms established from isotopic marker experiments during high temperature oxidation of doped alumina-forming alloys*

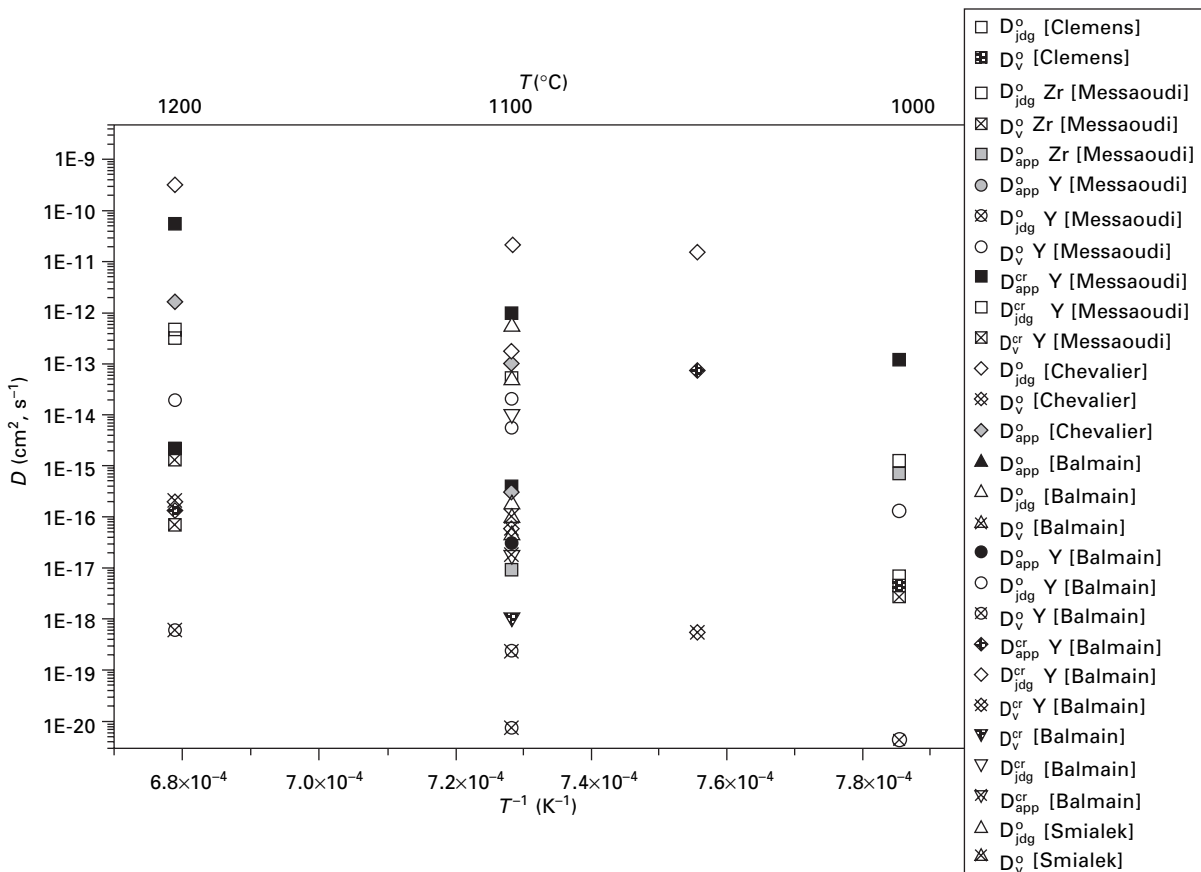
Material (wt%)	T (°C)	Transport mechanisms
NiAl-0.5Y	1000	Mixed
Fe23Cr5Al-Y	1080	Anion diffusion appears more important
Fe20Cr5Al-0.35Y	900– 1100	Oxygen transport at grain boundaries (slight cation contribution)
Fe23Cr5Al-0.2Zr	1200	Cation and anion transport via different ways
Fe23Cr5Al-0.2Zr-0.035 mischmetal (La + Ce)	1200	Cation and anion transport via different ways
Fe23Cr5Al-0.2Zr-0.035 mischmetal (La + Ce)	1200	Cation and anion transport via different ways
Fe23Cr5Al-0.2Zr-0.035 mischmetal-0.1Hf-0.04Y	1200	Cation and anion transport via different ways
Fe23Cr5Al-0.2Zr + Y implantation	1200	Cation and anion transport via different ways
β-NiAl-0.1Y	1200	Anion diffusion (Al external diffusion not completely stopped)
β-NiAl-0.2Zr	1200	Anion diffusion (Al external diffusion not completely stopped)
NiAl + Y implantation	1200	Mixed
NiAl-0.2Zr	1200	Mainly oxygen diffusion (slight oxygen enrichment at the gas/oxide interface)
Fe20Cr5Al-Y <sub>2</sub> O <sub>3</sub> -Al <sub>2</sub> O <sub>3</sub>	1200	Predominant anion diffusion (slight enrichment at the gas/oxide interface, meaning oxygen bulk diffusion)
NiAl + Y implantation	1500	Predominantly anion diffusion
NiAl-0.2Zr	1500	Mainly oxygen diffusion (slight oxygen enrichment at the gas/oxide interface)
Fe20Cr5Al-0.09Y	1200	Simultaneous diffusion of aluminium and oxygen
β-NiAl + Y implantation	1200	Predominantly cation diffusion (slight anion contribution)
Fe20Cr5Al-0.5Y <sub>2</sub> O <sub>3</sub>	800	Predominantly cation diffusion at beginning of oxidation
Fe23Cr5Al + Y implantation	1000	Predominantly cation diffusion at beginning of oxidation (slight anion contribution)
Fe20Cr5Al-0.17Y <sub>2</sub> O <sub>3</sub>	1100	Oxygen diffusion at grain boundaries
Fe20Cr5Al-0.7Y <sub>2</sub> O <sub>3</sub>	1100	Oxygen diffusion at grain boundaries
Fe20Cr5Al-0.09Y	1200	Oxygen diffusion
Fe20Cr5Al-0.05Y, Fe20Cr5Al-0.09Y, Fe20Cr5Al-0.05Y-0.03Zr	1100	Oxygen diffusion
Fe20Cr5Al-0.05Y-0.04Zr- 0.05Hf, Fe20Cr5Al-0.03Ce- 0.012La	1100	Simultaneous diffusion of aluminium and oxygen after 6 h of oxidation; oxygen diffusion after 96 h



10.12 TEM cross-section morphology of  $\alpha$ -Al<sub>2</sub>O<sub>3</sub> scales formed on Fe-Cr-Al-RE alloys after 100 h in air at 1100°C.

diffusion coefficients determined in thermally grown and in synthetic oxides appears very delicate.

Numerous studies [186] claim that the presence of RE influences the transformation of transient alumina ( $\gamma$ -Al<sub>2</sub>O<sub>3</sub>, for example [187]). The results of these studies are contradictory, since some authors attribute no RE influence on the transient alumina transformation [188], others propose that their presence accelerates the transformation into stable alumina [50,120,189–192], whereas still others indicate that the presence of RE induces a decrease of the allotropic transformation [56,124,133,193–195]. These contradictory results mostly come from difficult identification of alumina phases across the entire thermally grown scale. The use of coupled analytical tools (SEM, XRD at different glancing angles, XPS, TEM, etc.) is necessary to identify precisely the phases formed in alumina scales [70,196]. In addition to the RE influence, Cr presence is known to accelerate the transition from  $\theta$ -Al<sub>2</sub>O<sub>3</sub> to  $\alpha$ -Al<sub>2</sub>O<sub>3</sub> [197]. The presence of transient alumina is sometimes wanted in order to get specific properties. As an example, ceramists are interested in stabilising  $\gamma$ -Al<sub>2</sub>O<sub>3</sub> because it possesses a considerable specific area compared to that of  $\alpha$ -Al<sub>2</sub>O<sub>3</sub> ( $\sim 100$  and  $10\text{ m}^2\text{g}^{-1}$ , respectively) [193,198]; such alumina are used as catalyst support or as a filter layer in ceramic membrane [195]. However, to obtain resistance against corrosion and more especially against oxidation at high temperature, transient alumina are usually not desirable for two



10.13 Comparison of oxygen and chromium diffusion coefficients in thermally grown alumina scales doped with RE.

reasons: firstly, their growth rates are higher than that of  $\alpha$ -alumina, which leads to more Al consumption and catastrophic oxidation behaviour, especially in foils; and secondly their transformation produces a large volume contraction that is able to generate stresses in the oxide scale and then to provoke its spallation or crack formation [199].

### 10.3.6 Role of reactive elements on the sulphur effect

The presence of sulphur plays an important role on the formation and adherence of the alumina scales due to its segregation between the thermally grown oxide layer and the underlying metallic substrate. This element is present in all commercial alloys. Numerous studies showed that its presence as an alloying element was responsible for bad oxidation resistance of metallic materials [200–204]. Even if its level can be significantly reduced, it is quite impossible to suppress it from commercial alloy composition, due to the long and costly reducing treatments. A recent study showed that even if two nickel aluminides (NiAl and Ni40Al) contained the same level of sulphur (3.2–3.7 ppm), sulphur was detected by AES (Auger Electron Scanning Microscopy) at the  $\alpha\text{-Al}_2\text{O}_3$ –Ni40Al interface, whereas it was never detected at the  $\alpha\text{-Al}_2\text{O}_3$ –NiAl interface [205]. Interactions between S and chemical elements such as C, N, P or Cl present in metallic materials also have to be taken into consideration [206,207].

Once more, the presence of reactive elements allows protective oxide scales to form, even in the presence of sulphur. It is generally proposed that the reactive elements react with S and form sulphides, then stopping their detrimental effect on the oxide scale adherence [208,209]. However, very few studies were able to identify such compounds [210,211], even if S was detected [212]. The role played by the RE then is preventing sulphur segregation at the oxide scale–metal interface [213].

## 10.4 Recent developments in alumina-forming materials: intermetallics

Intermetallics have been developed recently, owing to their specific properties [214]. Aluminides are of particular interest because they have high melting points, low densities and considerable resistance to high temperature corrosive atmospheres [215]. Their interesting properties made them excellent candidates for aeronautical applications [216–218].

Most alloys and superalloys have to be used at temperatures lower than  $0.4T_m$  ( $T_m$  being their melting point in K) because of their creep capacity, whereas ceramics and intermetallics are able to work at higher temperatures, although their cost and difficulties due to their elaboration can limit their use. The development of aluminides is based on the huge aluminium ‘reservoir’,

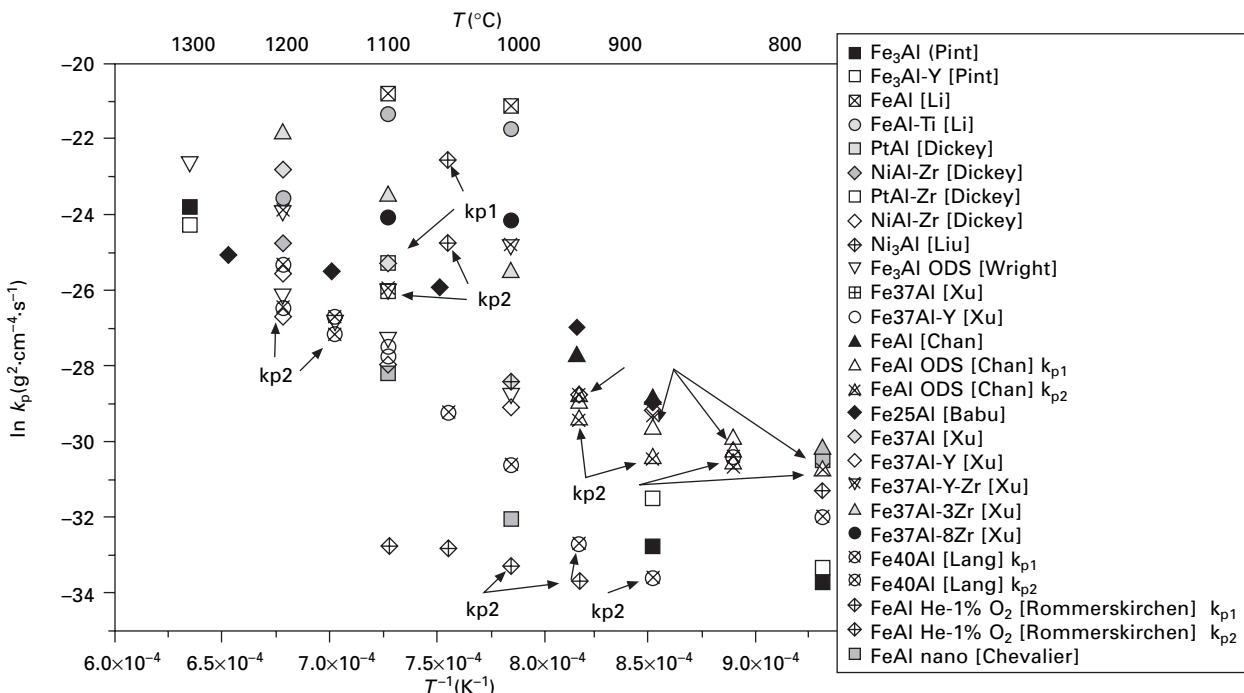
compared to classical alumina-forming materials (typically Fe-20Cr-5Al). Indeed, when they are exposed to long-term oxidation at high temperature, the Al consumption leads to Al depletion in the underlying substrate [219,220]. As a consequence, when Al reaches a critical level, around 1.7 wt% in FeCrAl alloys [221–223], no more protective alumina can grow. Chromium and/or iron oxide formation then becomes predominant and promotes a huge degradation of the materials. Increasing the Al content gives spectacular effects on the long-term high temperature performance of materials [26,126,155,197,224–232] (Fig. 10.14).

The main reason why metal aluminides (such as FeAl, NiAl, TiAl, NbAl<sub>3</sub>, etc.) have been developed is their potential aluminium ‘reservoir’ which guarantees the constitution of protective alumina scales, even after long exposures at high temperature or repeated thermal cycling. However, adding more than 5% of aluminium in metals decreases considerably their mechanical properties, especially at ambient temperature. Most aluminides are then brittle, which constitutes a difficulty during machinability and shaping. This difficulty is diminished by additions of minor elements (such as B, Zr, Y<sub>2</sub>O<sub>3</sub>, Cr, Ce, Nb, etc.), which improve the room temperature mechanical properties [232–240].

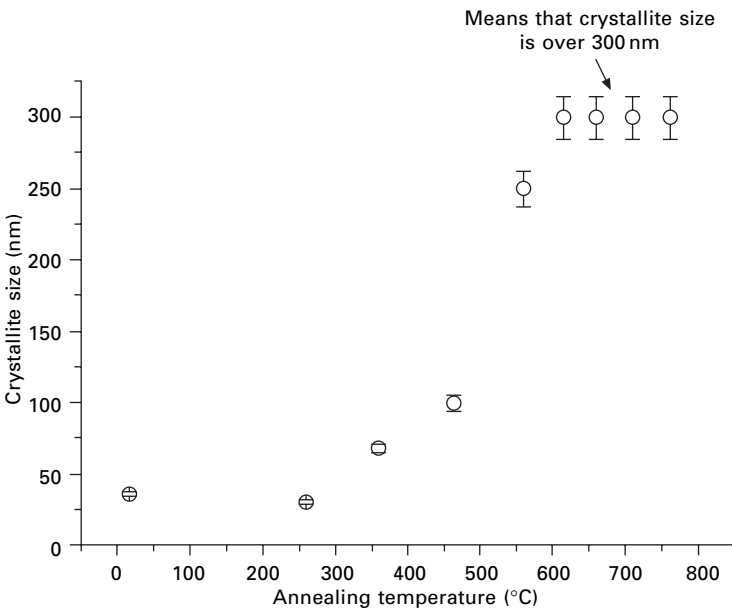
Two other solutions can be considered in order to improve the aluminide mechanical properties: by modifying their microstructure using an innovative elaboration process [241–243], or by applying the intermetallic compounds directly on a metal or alloy surface [33,244–251].

#### 10.4.1 Effect of microstructure on the high temperature oxidation behaviour of FeAl

The comparison of the high temperature oxidation behaviour of classically elaborated intermetallics with that of newly made FeAl, using the SPS (spark plasma sintering) process, shows that the elaboration process has an influence on their high temperature performance (Fig. 10.14) [252]. The  $k_p$  values obtained on nanostructured FeAl appear small compared to those of other FeAl compounds. The oxide scale adherence was also found to be increased [26,252]. The SPS process leads to a nanostructured material composed of crystallite of less than 50 nm size. Figure 10.15 gives the evolution of the crystallite size with the temperature, using X-ray diffraction peak analyses. It shows that the crystallite size is modified when the temperature reaches 600°C; this means that the nanostructure probably influences the first steps of the oxidation process (nucleation and growth of alumina). Pint *et al.* [253] found that the decrease of intermetallic compound grain size requires less Al to allow the growth of an alumina scale, compared to FeAl composed of large grains. Small crystallite size seems to allow the growth of small alumina grains (at least during the beginning of the oxidation process) and then gives



10.14 Arrhenius plot of  $k_p$  values of some aluminides oxidised at high temperature;  $k_{p1}$  and  $k_{p2}$  mean that two parabolic rate constants were determined, in the first and second parts of the kinetic curve respectively.



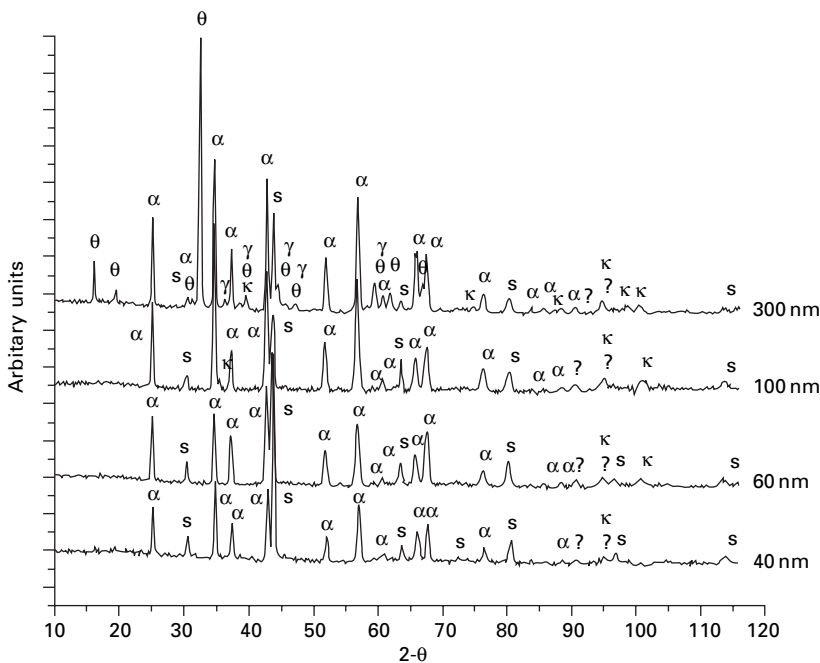
10.15 FeAl crystallite size evolution after 30 min annealing under inert atmosphere (after Chevalier [6]).

different mechanical properties of the oxide scale; smaller oxide grains enable the release of thermal and/or growth stress in the scale by plastic deformation [254].

The second influence of the intermetallic grain size concerns the nature of the phases grown during the oxidation tests. Figure 10.16 represents the X-ray diffraction analyses of the corrosion products formed on FeAl having different starting crystallite size (from 40 to 300 nm). The experiments were performed using a  $1^\circ$  glancing angle in order to obtain superficial information. The results clearly indicate that  $\alpha\text{-Al}_2\text{O}_3$  is the main phase formed on samples having 40, 60 and 100 nm crystallite size. Transient alumina ( $\theta\text{-Al}_2\text{O}_3$  and  $\gamma\text{-Al}_2\text{O}_3$ ) are identified on samples with crystallite size over 300 nm [6]. The microstructure of the starting FeAl compounds thus plays a huge role on the nature of the alumina phase and on the high temperature oxidation behaviour, as was shown previously in this chapter.

#### 10.4.2 Aluminide diffusion coating performance in oxidising atmospheres

Aluminide diffusion coating is applied by the classical pack cementation process. This technique has been used since the last century [255–258], even though its industrial and technical applications are more recent [259,260]. It

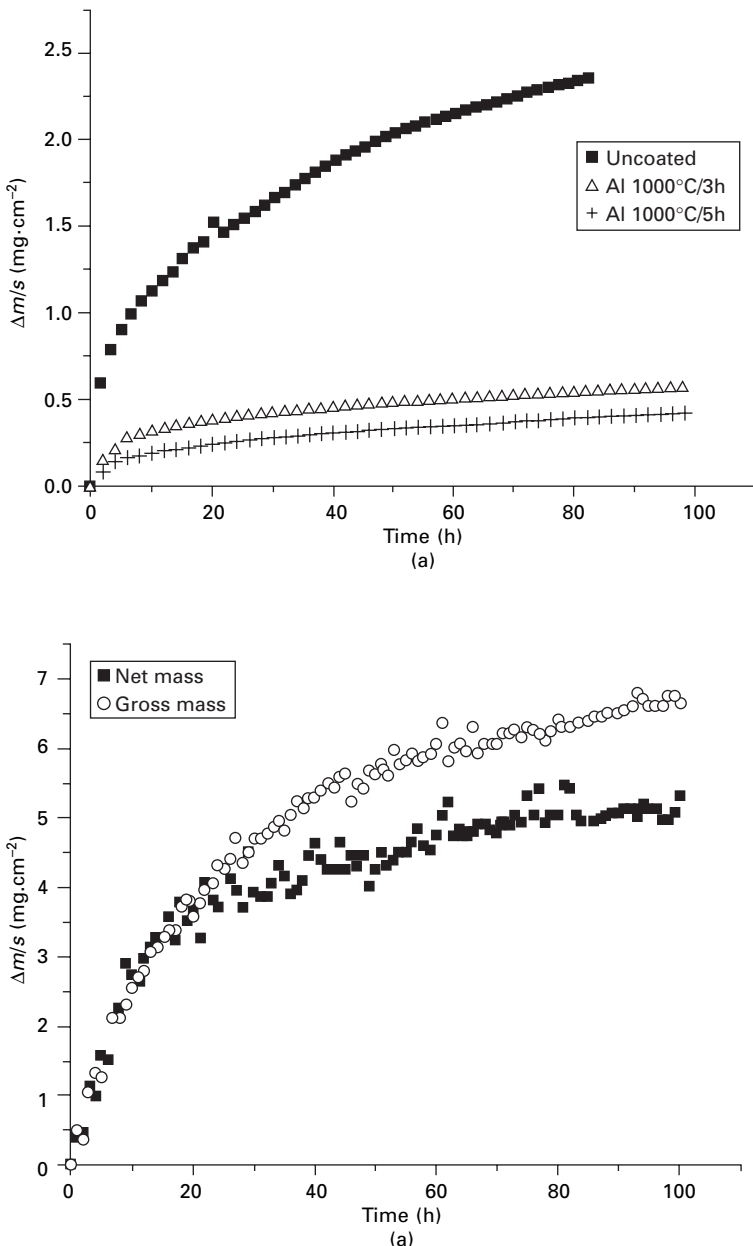


10.16 XRD patterns showing alumina phases formed after 100 h oxidation at 1000°C on FeAl compounds with different crystallite size 40 nm, 60 nm, 100 nm and 300 nm (after Chevalier [6]).

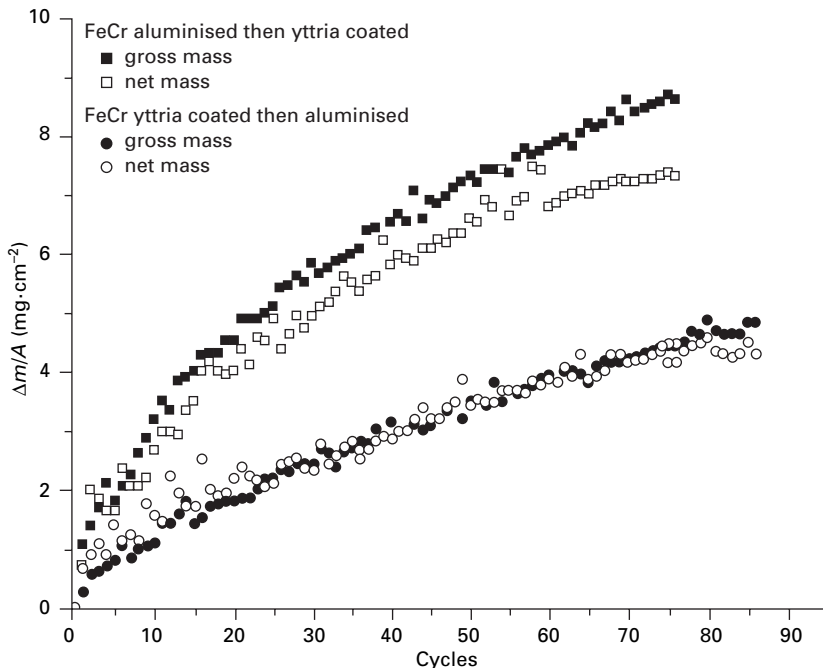
has been used, for example, to increase the Al content on the surface of Fe-20Cr-5Al foils, in order to increase their lifetime in oxidising atmospheres, even after thousands of hours in use [261].

Aluminide diffusion coatings are classically deposited from a powder (cement) composed of an activator ( $\text{NH}_4\text{Cl}$ ), a metallic donor (Al) and an inert filler ( $\text{Al}_2\text{O}_3$ ) [262–268]. The aluminisation process is performed on steels [244,246,247,269–273], superalloys [274–281], non-ferrous metals [282–284], etc.

Figure 10.17 illustrates the high temperature oxidation behaviour of an aluminide diffusion coating made of an  $(\text{Fe,Cr})_3\text{Al}$  and  $(\text{Fe,Cr})\text{Al}$  mixture and performed on an Fe-30Cr model alloy [285]. The isothermal tests show the beneficial effect of the coating, but the cyclic experiment evidences spallation of the alumina scale after around 25 cycles (as shown by the deviation between the gross and the weight gain curves). Even if the Al reservoir is large enough to allow the rebuilding of the scale after alumina layer spallation, its weak adherence leads to high Al consumption. By associating a thin reactive element oxide film (an  $\text{Y}_2\text{O}_3$  layer of around 200 nm thick realised by Metal-Organic Chemical Vapour Deposition, MOCVD) and a pack cementation process, the resistance to spallation can



10.17 Oxidation kinetics of an aluminide diffusion coating formed on an Fe-30Cr steel (aluminisation at 1000°C for 3 h and/or 5 h):  
 (a) isothermal oxidation tests at 1000°C; (b) cyclic oxidation tests,  
 one cycle being composed of 24 h at 1000°C followed by air cooling  
 (after Hougninou [285]).



10.18 Cyclic oxidation tests (one cycle being composed of 24 h at 1000°C followed by air cooling) of iron aluminide diffusion coatings doped by  $\text{Y}_2\text{O}_3$ ; influence of yttria coating localisation on the resistance against spallation (after Hougninou *et al.* [286]).

be drastically improved, as proved in Fig. 10.18 [286]. It is important to note that the means of introduction of the reactive element oxide has a huge importance on the aluminide diffusion coating resistance against thermal shocks; when it is applied prior to the aluminisation process, no alumina scale spallation occurs (even after 90 cycles or 2160 h exposure), whereas if the yttria coating is applied after the aluminisation, the oxide scale is not adherent and grows even faster than that of the simply aluminised sample. This phenomenon was already observed on FeCrAl materials [136,287,288].

## 10.5 References

1. J. Bénard, *L'oxydation des Métaux*, Gauthier-Villars et Cie, Paris (1962).
2. G. Béranger, J.C. Colson, F. Dabosi, *Corrosion des Matériaux à Haute Température*, Les Editions de Physique, Ecole d'Hiver du CNRS (Piau-Engaly 1985).
3. M. Caillet, A. Galerie, S. Audisio, H. Mazille, *La Protection contre la Corrosion*, Les Editions de Physique, Paris (1987).
4. P. Kofstad, *High Temperature Corrosion*, Elsevier Applied Science (1988).
5. P. Sarrazin, A. Galerie, J. Fouletier, *Les Mécanismes de la Corrosion Sèche. Une approche cinétique*, EDP Sciences (2000).

6. S. Chevalier, *Traitements de Surface et Nouveaux Matériaux: Quelles solutions pour lutter contre la dégradation des matériaux à haute température?*, Les Editions Universitaires de Dijon, Dijon (2007).
7. A. Green, B. Bastow, Proc. 2nd Int. Conf. on the Microscopy of Oxidation, S.B. Newcomb and M.J. Bennett, eds (March 1993) 137–149.
8. S. Jianian, Z. Longjiang, L. Tiefan, *Oxid. Met.*, **48** (1997) 347.
9. Z. Yurek, *Solid State Phenomena*, **41** (1995) 185.
10. S. Henry, Thèse de Doctorat, INPG, Grenoble (2000).
11. H. Hindam, D.P. Whittle, *Oxid. Met.*, **18** (1982) 245.
12. J.K. Tien, J.M. Davidson, *Stress Effects and the Oxidation of Metals*, J.V. Cathart, ed., New York, AIME (1975) p. 200.
13. D. Delaunay, A.M. Huntz, P. Lacombe, *Corros. Sci.*, **20** (1980) 1109.
14. A.M. Huntz, *Mater. Sci. Tech.*, **4** (1988) 1079.
15. A.M. Huntz, M. Schuetze, *Mater. High Temp.*, **12** (1994) 151.
16. H.E. Evans, *Mater. High Temp.*, **12** (1994) 219.
17. H.E. Evans, *Int. Mater. Rev.*, **40** (1995) 1.
18. M. Schuetze, *J. Corros. Sci. Eng.* 6 (2003), <http://www.umist.ac.uk/corrosion/JCSE/>.
19. K. Ishii, S. Taniguchi, *Oxid. Met.*, **54** (2000) 491.
20. G. Strehl, D. Naumenko, H. Al-Badairy, L.M. Rodriguez Lobo, G. Borchardt, G. Tatlock, W.J. Quadakkers, *Mater. High Temp.*, **17** (2000) 87.
21. Z. Liu, W. Gao, K. Dahm, F. Wang, *Acta Metall. Mater.*, **46** (1998) 1691.
22. H. El Kadiri, R. Molins, Y. Bienvenu, *Mater. Sci. Forum*, **461–464** (2004) 1107.
23. P. Juzon, PhD Thesis, University of Burgundy, Dijon (2006).
24. G. Borchardt, G. Strehl, *Materials Aspects in Automotive Catalytic Converters*, H. Bode, ed. (2002) p. 1.
25. N. Babu, R. Balasubramaniam, A. Ghosh, *Corros. Sci.*, **3** (2001) 2239.
26. S. Chevalier, C. Hougninou, S. Paris, F. Bernard, E. Gaffet, Z.A. Munir, J.P. Larpin, *J. Corros. Sci. Eng.*, 6 (2003), <http://www.umist.ac.uk/corrosion/JCSE/>.
27. B.A. Pint, J.R. Martin, L.W. Hobbs, *Oxid. Met.*, **39** (1993) 167.
28. J.K. Tien, F.S. Pettit, *Metall. Trans.*, **3** (1972) 1587.
29. J. Jedlinski, M. Krasovec, G. Borchardt, J.W. Quadakkers, *J. Phys. IV*, **3** (1993) 591.
30. C. Sarioglu, M.J. Stiger, J.R. Blachere, R. Janakiraman, E. Schumann, A. Ashary, F.S. Pettit, G.H. Meier, *Mater. Corros.*, **51** (2000) 358.
31. K. Messaoudi, PhD Thesis, University Paris XI, Orsay (1997).
32. S. Chevalier, C. Nivot, J.P. Larpin, *Oxid. Met.*, **61** (2004) 195.
33. T.A. Ramanarayanan, R. Ayer, R. Petkovic-Luton, D.P. Leta, *Oxid. Met.*, **29** (1988) 445.
34. A. Andoh, S. Taniguchi, T. Shibata, *Oxid. Met.*, **46** (1996) 481.
35. M. Göbel, J. Schimmelpfennig, A. Glazkov, G. Borchardt, C. Messaoudi, B. Lesage, C. Mennicke, E. Schumann, M.J. Bennett, J. Le Coze, *Metal-supported Automotive Catalytic Converters*, H. Bode, Ed., Wuppertal, Germany (October 1997), p. 191.
36. S. Chevalier, B. Lesage, C. Legros, G. Borchardt, G. Strehl, M. Kilo, *Def. Diff. Forum*, **237–240** (2005) 899.
37. E.W.A. Young, J.H.W. de Witt, *Oxid. Met.*, **26** (1986) 351.
38. A.M. Huntz, *Mater. Sci. Eng. A*, **87** (1987) 251.
39. W.J. Quadakkers, W. Speier, H. Holzbrecher, H. Nickel, Proc. Conf. Microscopy of Oxidation, M.J. Bennett and G.W. Lorimer, eds (1990) 149.

40. W.J. Quadakkers, A. Elschner, W. Speier, H. Nickel, *Appl. Surf. Sci.*, **52** (1991) 271.
41. R. Prescott, D.F. Mitchell, M.J. Graham, Proc. 2nd Int. Conf. on the Microscopy of Oxidation, S.B. Newcomb and M.J. Bennett, eds (March 1993) 455.
42. A. Glazkov, M. Göbel, J. Jedlinski, J. Schimmelpfennig, G. Borchardt, S. Weber, S. Scherrer, J. Le Coze, *J. Phys. IV*, **5** (1995) 379.
43. J. Jedlinski, M.J. Graham, G.I. Sproule, D.F. Mitchell, G. Borchardt, A. Bernasik, *Mater. Corros.*, **46** (1995) 297.
44. J. Jedlinski, M.J. Graham, G.I. Sproule, D.F. Mitchell, A. Bernasik, G. Borchardt, Proc. 3rd Int. Conf. on the Microscopy of Oxidation, S.B. Newcomb and J.A. Little, eds (September 1996) 74.
45. C. Mennicke, E. Schumann, M. Rühle, R.J. Hussey, G.I. Sproule, M.J. Graham, *Oxid. Met.*, **49** (1998) 455.
46. M.J. Graham, *Mater. High Temp.*, **17** (1999) 1.
47. M.J. Graham, R.J. Hussey, *Corros. Sci.*, **44** (2002) 319.
48. S. Chevalier, G. Strehl, J. Favergon, F. Desserrey, S. Weber, O. Heintz, G. Borchardt, J.P. Larpin, *Mater. High Temp.*, **20** (2003) 253.
49. S. Chevalier, J.P. Larpin, P. Dufour, G. Strehl, G. Borchardt, K. Przybylski, S. Weber, H. Scherrer, *Mater. High Temp.*, **20** (2003) 365.
50. K.M.N. Prasanna, A.S. Khanna, R. Chandra, W.J. Quadakkers, *Oxid. Met.*, **46** (1996) 465.
51. V.K. Tolpygo, *Oxid. Met.*, **51** (1999) 449.
52. C. Nivot, Master of Science, Université de Bourgogne, Dijon (2001).
53. G.C. Wood, F.H. Stott, *High Temperature Corrosion*, NACE-6, R.A. Rapp, ed., San Diego, CA (March 1981) p. 227.
54. Y.S. Lin, *J. Mater. Sci.*, **26** (1991) 715.
55. M. Boualam, G. Beranger, M. Lambertin, Proc. 2nd Int. Conf. on the Microscopy of Oxidation, S.B. Newcomb and M.J. Bennett, eds (March 1993) 243.
56. B.A. Pint, J.R. Martin, L.W. Hobbs, *Solid State Ionics*, **78** (1995) 99.
57. J.C. Yang, E. Schumann, I. Levin, M. Rühle, Proc. 3rd Int. Conf. on the Microscopy of Oxidation, S.B. Newcomb and J.A. Little, eds (September 1996) 256.
58. V.K. Tolpygo, D.R. Clarke, *Mater. High Temp.*, **17** (2000) 59.
59. D.F. Susan, A.R. Marder, *Oxid. Met.*, **57** (2002) 131.
60. D.F. Susan, A.R. Marder, *Oxid. Met.*, **57** (2002) 159.
61. R. Prescott, M.J. Graham, *Oxid. Met.*, **38** (1992) 233.
62. H.J. Grabke, M.W. Brumm, B. Wagemann, *Mater. Corros.*, **47** (1996) 675.
63. K. Natesan, *Mater. Sci. Eng.*, **A258** (1998) 126.
64. K. Wefers, C. Mistra, Alcoa Technical Paper, **19** (1987).
65. V. Jayaram, C.G. Levi, *Acta Metall.*, **37** (1989) 569.
66. J.K. Doychak, J.L. Smialek, T.E. Mitchell, Proc. Int. Cong. Metall. Corros., **1** (1984) 35.
67. T.A. Ramanarayanan, M. Raghavan, R. Petkovic-Luton, *High Temp. Corros.*, (Suppl.) (1983) 199.
68. E.J. Felton, F.S. Pettit, *Oxid. Met.*, **10**(3) (1976) 184.
69. G.C. Rybicki, J.L. Smialek, *Oxid. Met.*, **31** (1989) 275.
70. S. Chevalier, R. Molins, O. Heintz, J.P. Larpin, Proc. 6th Int. Conf. on the Microscopy of Oxidation, G.J. Tatlock and H.E. Evans, eds, Birmingham, UK, (2005) 365.
71. L.G. Harrison, *Trans. Faraday Soc.*, **57** (1961) 1191.

72. J. Philibert, *Diffusion et Transport de Matière dans les Solides*, Les Editions de Physique (1990), p. 227.
73. J. Philibert, A. Vignes, Y. Bréchet, P. Combrade, *Métallurgie: Du Minerai au Matériau*, Masson (1998) p. 389.
74. E.W. Hart, *Acta. Metall.*, **5** (1957) 597.
75. W.W. Smeltzer, R.R. Haering, J.S. Kirkaldy, *Acta Metall.*, **9** (1961) 880.
76. A. Atkinson, R.I. Taylor, A. Hughes, *Phil. Mag. A*, **45** (1982) 823.
77. C.M. Lederer, J.M. Hollander, I. Perlman, *Table of Isotopes*, 6th edn, John Wiley & Sons, New York (1967).
78. P. Fielitz, G. Borchardt, M. Schmücker, H. Schneider, *Solid State Ionics*, **160** (2003) 75.
79. A.S. Nowick, J.J. Burton, eds, *Diffusion in Solids*, Academic Press (1975).
80. R.T.P. Whipple, *Phil. Mag.*, **45** (1954) 1225.
81. A.D. Le Claire, *Phil. Mag.*, **7** (1962) 141.
82. S. Chevalier, B. Lesage, C. Legros, G. Borchardt, G. Strehl, M. Kilo, *Def. Diff. Forum*, **237–240** (2005) 899.
83. D. Clemens, K. Bongartz, W.J. Quadakkers, H. Nickel, H. Holzbrecher, J.S. Becker, *Fresenius J. Anal. Chem.*, **353** (1995) 267.
84. J. Balmain, A.M. Huntz, J. Philibert, *Def. Diff. Forum*, **143–147** (1997) 1189.
85. K. Messaoudi, A.M. Huntz, B. Lesage, *Mater. Sci. Eng. A*, **247** (1998) 248.
86. J.L. Smialek, R. Gibala, *High Temperature Corrosion*, NACE-6, R.A. Rapp, ed., San Diego, CA (March 1981) p. 274.
87. L. Badrour, E.G. Moya, J. Bernardini, F. Moya, *J. Phys. Chem. Solids*, **50** (1989) 551.
88. J.D. Cawley, J.W. Halloran, A.R. Cooper, *J. Am. Ceram. Soc.*, **74** (1991) 2086.
89. D. Prot, M. Miloche, C. Monty, *Mater. Sci. Forum*, **126–128** (1993) 403.
90. M. Le Gall, B. Lesage, J. Bernardini, *Phil. Mag. A*, **70** (1994) 761.
91. I. Sakaguchi, V. Srikanth, T. Ikegami, H. Haneda, *J. Am. Ceram. Soc.*, **78** (1995) 2557.
92. M. Le Gall, A.M. Huntz, B. Lesage, C. Monty, *J. Mater. Sci.*, **30** (1995) 201.
93. M. Backhaus-Ricoult, A. Peyrot-Chabrol, *Phil. Mag. A*, **73** (1996) 973.
94. C. Monty, *Mater. Sci. Forum*, **207–209** (1996) 633.
95. D. Prot, M. Le Gall, B. Lesage, A.M. Hunts, C. Monty, *Phil. Mag. A*, **73** (1996) 935.
96. D. Prot, C. Monty, *Phil. Mag. A*, **73** (1996) 899.
97. I. Sakaguchi, H. Haneda, V. Srikanth, T. Ikegami, *Mater. Res. Bull.*, **31** (1996) 837.
98. W. Hu, P. Karduck, G. Goostein, *Acta Mater.*, **45** (1997) 4535.
99. G. Petot-Ervas, D. Deweerder, M. Loudjani, B. Lesage, A.M. Huntz, *Advanced Ceramics*, **23**, *Nonstoichiometric Compounds*, Am. Ceram. Soc. (1987) p. 125.
100. J. Philibert and A.M. Huntz, *Proc. 2nd Int. Conf. on the Microscopy of Oxidation*, S.B. Newcomb and M.J. Bennett, eds., (1993) 253.
101. P. Fielitz, G. Borchardt, M. Schücker, H. Schneider, *Solid State Ionics*, **177** (2006) 493.
102. L.B. Pfeil, UK Patent no. 459848 (1937).
103. L.B. Pfeil, UK Patent no. 574088 (1945).
104. J. Quadakkers, L. Singheiser, *Mater. Sci. Forum*, **369–372** (2001) 77.
105. E. Lang, ed., *Role of Active Elements in the Oxidation Behaviour of High Temperature Metals and Alloys*, Elsevier, Amsterdam (1989).
106. J. Stringer, I.G. Wright, *Oxid. Met.*, **5** (1972) 59.

107. J. Stringer, B.A. Wilcox, R.I. Jaffee, *Oxid. Met.*, **5** (1972) 11.
108. D.P. Whittle, J. Stringer, *Phil. Trans. R. Soc. Lond. A*, **295** (1980) 309.
109. H. Yedong, F.H. Stott, *Corros. Sci.*, **36** (1994) 1869.
110. Y. Zhang, W.W. Gerberich, D.A. Shores, *J. Mater. Res.*, **12** (1997) 697.
111. D. Zhu, J.H. Stout, J.C. Nelson, D.A. Shores, *Mater. Sci. Forum*, **251–254** (1997) 437.
112. A.M. Huntz, *Mater. Sci. Eng. A*, **87** (1987) 251.
113. C. Forest, J.H. Davidson, *Oxid. Met.*, **43** (1995) 479.
114. C. Sarioglu, M.J. Stiger, J.R. Blachere, R. Janakiraman, E. Schumann, A. Ashary, F.S. Pettit, G.H. Meier, *Mater. Corros.*, **51** (2000) 358.
115. V.K. Tolpygo, J.R. Dryden, D.R. Clarke, *Acta. Mater.*, **46** (1998) 927.
116. V.K. Tolpygo, D.R. Clarke, *Oxid. Met.*, **49** (1998) 187.
117. A.W. Funkenbusch, J.G. Smeggil, N.S. Bornstein, *Metal. Trans.*, **16A** (1985) 1164.
118. D.G. Lees, *Oxid. Met.*, **27** (1987) 75.
119. J.L. Smialek, Proc. Int. Conf. on the Microscopy of Oxidation, M.J. Bennett and G.W. Lorimer' eds (1990) 258.
120. I. Rommerskirchen, V. Kolarik, *Mater. Corros.*, **47** (1996) 625.
121. M.A. Montalegre, J.L. Gonzalez-Carrasco, *Intermetallics*, **11** (2003) 169.
122. B. Pieraggi, R.A. Rapp, *J. Electrochem. Soc.*, **140** (1993) 2844.
123. B. Pieraggi, R.A. Rapp, J.P. Hirth, *Oxid. Met.*, **44** (1995) 63.
124. H.M. Tawancy, N. Sridhar, *Oxid. Met.*, **37** (1992) 143.
125. J.L. Gonzalez-Carrasco, P. Perez, P. Adeva, J. Chao, *Intermetallics*, **7** (1999) 69.
126. I.G. Wright, B.A. Pint, P.F. Tortorelli, *Oxid. Met.*, **55** (2001) 333.
127. M. Göbel, J. Schimmelpfennig, A. Glazkov, G. Borchardt, C. Messaoudi, B. Lesage, C. Mennicke, E. Schumann, M.J. Bennett, J. Le Coze, *Metal-supported Automotive Catalytic Converters*, H. Bode, Ed., Wuppertal, Germany (October 1997), p. 191.
128. B.A. Pint, *Oxid. Met.*, **45** (1996) 1.
129. J.K. Tien, F.S. Pettit, *Metall. Trans.*, **3** (1972) 1587.
130. L. Maréchal, B. Lesage, A.M. Huntz, R. Molins, *Oxid. Met.*, **60** (2003) 1.
131. C. Badini, F. Laurella, *Surf. Coat. Tech.*, **135** (2001) 291.
132. J. Klöwer, J.G. Li, *Mater. Corros.*, **47** (1996) 545.
133. R. Cueff, H. Buscail, E. Caudron, F. Riffard, *Mater. Sci. Forum*, **369–372** (2001) 311.
134. J. Klöwer, J.G. Li, *Mater. Corros.*, **47** (1996) 545.
135. J. Klöwer, *Mater. Corros.*, **51** (2000) 373.
136. S. Chevalier, A.P. Dawah Tankeu, H. Buscail, C. Issartel, G. Borchardt, J.P. Larpin, *Mater. Corros.*, **55** (2004) 610.
137. K.Y. Kim, S.H. Kim, K.W. Kwon, I.H. Kim, *Oxid. Met.*, **41** (1994) 179.
138. B.A. Pint, L.W. Hobbs, *J. Electrochem. Soc.*, **141** (1994) 2443.
139. B.A. Pint, *Mater. Sci. Forum*, **251–254** (1997) 397.
140. B.A. Pint, A. J. Garratt-Reed, L.W. Hobbs, *J. Am. Ceram. Soc.*, **81** (1998) 305.
141. Y. Wu, K. Hagihara, Y. Umakoshi, *Intermetallics*, **12** (2004) 519.
142. K. Przybylski, A.J. Garratt-Reed, B.A. Pint, E.P. Katz, G.J. Yurek, *J. Electrochem. Soc.*, **134** (1987) 3207.
143. B.A. Pint, A.J. Garratt-Reed, L.W. Hobbs, Proc. 2nd Int. Conf. on the Microscopy of Oxidation, S.B. Newcomb and M.J. Bennett, eds (March 1993) 463.
144. E. Schumann, J.C. Yang, M.J. Graham, M. Rühle, *Mater. Corros.*, **46** (1995) 218.
145. E. Schumann, J.C. Yang, M.J. Graham, M. Rühle, *Mater. Corros.*, **47** (1996) 631.
146. B.A. Pint, A.J. Garratt-Reed, L.W. Hobbs, *J. Phys. IV*, **3** (1993) 247.

147. B.A. Pint, K.B. Alexander, Proc. 3rd Int. Conf. on the Microscopy of Oxidation, S.B. Newcomb and J.A. Little, eds (September 1996) 153.
148. B.A. Pint, K.B. Alexander, *J. Electrochem. Soc.*, **145** (1998) 1819.
149. C. Mennicke, E. Schumann, J. Le Coze, J.L. Smialek, G.H. Meier, M. Rühle, Proc. 3rd Int. Conf. on the Microscopy of Oxidation, S.B. Newcomb and J.A. Little, eds (September 1996) 95.
150. S.B. Newcomb, R.E. Dunin-Borkowski, C.B. Boothroyd, A. Czyska-Filemonowicz, D. Clemens, W.J. Quadakkers, Proc. 3rd Int. Conf. on the Microscopy of Oxidation, S.B. Newcomb and J.A. Little, eds (September 1996) 166.
151. M. Kohno, S. Ishikawa, K. Ishii, Satoh, Proc. 3rd Int. Conf. on the Microscopy of Oxidation, S.B. Newcomb and J.A. Little, eds (September 1996) 55.
152. R. Molins, A. Germidis, E. Andrieu, Proc. 3rd Int. Conf. on the Microscopy of Oxidation, S.B. Newcomb and J.A. Little, eds (September 1996) 3.
153. K. Ishii, M. Kohno, S. Ishikawa, S. Satoh, Mater. Trans., **38** (1997) 787.
154. H. Yoshida, Y. Ikuhara, T. Skuma, J. Mater. Res., **13** (1998) 2597.
155. E.C. Dickey, B.A. Pint, K.B. Alexander, I.G. Wright, J. Mater. Res., **14** (1999) 4531.
156. J. Bruley, J. Cho, H.M. Chan, M.P. Harmer, J.M. Rickman, J. Am. Ceram. Soc., **82** (1999) 2865.
157. N. Hiramatsu, F.H. Stott, *Oxid. Met.*, **51** (1999) 479.
158. Y.Z. Li, C. Wang, H.M. Chan, J.M. Rickman, M.P. Harmer, J.M. Chabala, K.L. Gavrilov, R. Levi-Setti, J. Am. Ceram. Soc., **82** (1999) 1497.
159. M.A. Gülgün, V. Putlayev, M. Rühle, J. Am. Ceram. Soc., **82** (1999) 1849.
160. C.M. Wang, G.S. Cargill III, H.M. Chan, M.P. Harmer, *Acta Mater.*, **48** (2000) 2579.
161. E. Sato, C. Carry, J. Am. Ceram. Soc., **79** (1996) 2156.
162. M.A. Gülgün, W.Y. Ching, M. Rühle, Mater. Sci. Forum, **294–296** (1999) 289.
163. M.K. Loudjani, J. Roy, A.M. Huntz, J. Am. Ceram. Soc., **68** (1985) 559.
164. C.M. Wang, G. Slade Cargill III, H.M. Chan, M.P. Harmer, J. Am. Ceram. Soc., **85** (2002) 2492.
165. S. Lartigue, C. Carry, L. Priester, J. Phys. Colloq., C1, **51** (1990) 985.
166. J.D. French, J. Zhao, M.P. Harmer, H.M. Chan, G.A. Miller, J. Am. Ceram. Soc., **77** (1994) 2857.
167. J. Fang, A.M. Thompson, M.P. Harmer, H.M. Chan, J. Am. Ceram. Soc., **80** (1997) 2005.
168. J. Cho, C.M. Wang, H.M. Chan, J.M. Rickman, M.P. Harmer, *Acta Mater.*, **47** (1999) 4197.
169. Y.Z. Li, C. Wang, H.M. Chan, J.M. Rickman, M.P. Harmer, J.M. Chabala, K.L. Gavrilov, R. Levi-Setti, J. Am. Ceram. Soc., **82** (1999) 1497.
170. R. Voytovych, I. MacLaren, M.A. Gülgün, R.M. Cannon, M. Rühle, *Acta Mater.*, **50** (2002) 3453.
171. H. Yoshida, Y. Ikuhara, T. Sakuma, *Acta Mater.*, **50** (2002) 2955.
172. O.A. Ruano, J. Wadsworth, O.D. Sherby, *Acta Mater.*, **51** (2003) 3617.
173. D. Munhoven, D. Lemarchand, P. Auger, V. Prunier, Proc. 3rd Int. Conf. on the Microscopy of Oxidation, S.B. Newcomb and J.A. Little, eds (September 1996) 62.
174. S. Chevalier, J.P. Larpin, G. Strehl, G. Borchardt, K. Przybylski, Ann. Chim. Sci. Matér., **28** (2003) 197.

175. M. Kohno, S. Ishikawa, K. Ishii, S. Satoh, Proc. 3rd Int. Conf. on the Microscopy of Oxidation, S.B. Newcomb and J.A. Little, eds (September 1996) 55.
176. W.J. Quadakkers, W. Speier, H. Holzbrecher, H. Nickel, Proc. Int. Conf. on the Microscopy of Oxidation, M.J. Bennett and G.W. Lorimer, eds (1990) 149.
177. J. Jedlinski, G. Borchardt, *Oxid. Met.*, **36** (1991) 317.
178. A. Czyszka-Filemonowicz, K. Szot, A. Wasilkowska, P.J. Ennis, U. Breuer, A. Gil, W.J. Quadakkers, Proc. 3rd Int. Conf. on the Microscopy of Oxidation, S.B. Newcomb and J.A. Little, eds (September 1996) 185.
179. W.J. Quadakkers, D. Clemens and M.J. Bennett, Proc. 3rd Int. Conf. on the Microscopy of Oxidation, S.B. Newcomb and J.A. Little, eds (September 1996) 195.
180. S. Chevalier, K. Przybylski, G. Borchardt, J.P. Larpin, *Mater. Sci. Forum*, **461–464** (2004) 53.
181. M. Turker, T.A. Hugues, *Oxid. Met.*, **44** (1995) 505.
182. S. Chevalier, K. Przybylski, unpublished results.
183. B.A. Pint, A.J. Garratt-Reed, L.W. Hobbs, *Oxid. Met.*, **56** (2001) 119.
184. F.H. Stott, N. Hiramatsu, *Mater. High Temp.*, **17** (2000) 93.
185. K. Ishii, S. Satoh, M. Kobayashi, T. Kawasaki, *Metal-supported Automotive Catalytic Converters*, H. Bode, ed., Wuppertal, Germany (October 1997) p. 55.
186. F.H. Stott, *Mater. Sci. Forum*, **251–254** (1997) 19.
187. R. Molins, A. Germidis, E. Andrieu, Proc. 3rd Int. Conf. on the Microscopy of Oxidation, S.B. Newcomb and J.A. Little, eds (September 1996) 3.
188. A. Epishin, A. Glazkov, J. Jedlinski, B. Golovko, G. Borchardt, M. Bronfin, M. Konopka, Proc. 3rd Int. Conf. on the Microscopy of Oxidation, S.B. Newcomb and J.A. Little, eds (September 1996) 85.
189. I. Rommerskirchen, V. Kolarik, *Oxidation of Intermetallics*, H.J. Grabke and M. Schütze, eds, Wiley VCH (1998) 109.
190. R. Cueff, H. Buscail, E. Caudron, C. Issartel, F. Riffard, *Oxid. Met.*, **58** (2002) 439.
191. R. Cueff, H. Buscail, E. Caudron, C. Issartel, F. Riffard, *Corros. Sci.*, **45** (2003) 1815.
192. C. Dang Ngoc Chan, C. Huvier, J.F. Dinhut, *Intermetallics*, **9** (2001) 817.
193. S. Braun, L.G. Appel, L.B. Zinner, M. Schmal, *British Ceram. Trans.*, **98** (1999) 77.
194. X. Peng, T. Li, W.P. Pan, *Scripta Mater.*, **44** (2001) 1033.
195. B. Ersoy, V. Gunay, *Ceram. Int.*, **30** (2004) 163.
196. S. Chevalier, A. Galerie, O. Heintz, R. Chassagnon, A. Crisci, unpublished results.
197. Z. Liu, W. Gao, *Oxid. Met.*, **54** (2000) 189.
198. S. Zhao, J. Zhang, D. Weng, X. Wu, *Surf. Coat. Tech.*, **167** (2003) 97.
199. V. Kolarik, A. Kolb-Telieps, H. Hattendorf, M. del Mar Juez-Lorenzo, H. Fietzek, R. Hojda, *Materials Aspects in Automotive Catalytic Converters*, H. Bode, ed. (2002) p. 117.
200. J.L. Smialek, *Metall. Trans. A*, **22** (1991) 739.
201. P.Y. Hou, J. Stringer, *Oxid. Met.*, **38** (1992) 323.
202. P.Y. Hou, *Mater. Corros.*, **51** (2000) 329.
203. T. Amano, T. Watanabe, K. Michiyama, *Oxid. Met.*, **53** (2000) 451.
204. P. Hou, *Oxid. Met.*, **52** (1999) 337.
205. P.Y. Hou, *J. Corros. Sci. Eng.*, to appear.
206. H.J. Grabke, R. Dennert, B. Wagemann, *Oxid. Met.*, **47** (1997) 496.

- 207 W. Dong, H.E. Bishop, D. Johnson, D.G. Lees, G.W. Lorimer, *Oxid. Met.*, **54** (2000) 509.
- 208 J.L. Smialek, *Metall. Trans. A*, **18** (1987) 164.
- 209 D.R. Sigler, *Oxid. Met.*, **40** (1993) 295.
- 210 S.B. Shendye, D.A. Downham, *Oxid. Met.*, **43** (1995) 435.
- 211 A. Ul-Hamid, *Oxid. Met.*, **58** (2002) 23.
- 212 M.J. Graham, R.K. Wild, H.J. Grabke, *Mater. High Temp.*, **12** (1994) 135.
- 213 H. Al-Badairi, G.J. Tatlock and J. Le Coze, Proc. 3rd Int. Conf. on the Microscopy of Oxidation, S.B. Newcomb and J.A. Little, eds (September 1996) 105.
- 214 M.P. Brady, P.F. Tortorelli, *Intermetallics*, **12** (2004) 779.
- 215 G.H. Meier, *Oxidation of Intermetallics*, H.J. Grabke and M. Schütze, eds, Wiley VCH (1998) 15.
- 216 J.C. Zaho, J.H. Westbroek, *MRS Bulletin*, **28** (2003) 622.
- 217 D. M. Dimiduk, J.H. Perepezko, *MRS Bulletin*, **28** (2003) 639.
- 218 A. Lasalmonie, *Intermetallics*, **14** (2006) 1123.
- 219 B. Lesage, L. Maréchal, A.M. Huntz, R. Molins, *Def. Diff. Forum*, **194–199** (2001) 1707.
- 220 L. Maréchal, Thèse de Doctorat, Université de Paris-Sud, Orsay (2002).
- 221 G. Merceron, Thèse de Doctorat, Ecole des Mines de Paris (2000).
- 222 G. Merceron, R. Molins, J.L. Strudel, *Mater. High Temp.*, **17** (2000) 149.
- 223 I. Gurrapa, S. Weinbrusch, D. Naumenko, W.J. Quadakkers, *Mater. Corros.*, **51** (2000) 224.
- 224 B.A. Pint, K.B. Alexander, P.F. Tortorelli, *Mat. Res. Symp. Proc.*, **364** (1995) 1315.
- 225 I. Rommerskirchen, B. Eltester, H.J. Grabke, *Oxidation of Intermetallics*, H.J. Grabke and M. Schütze, eds, Wiley VCH (1998), 175.
- 226 C.H. Xu, W. Gao, H. Gong, *Intermetallics*, **8** (2000) 769.
- 227 D. Li, Y. Xu, D. Lin, *J. Mater. Sci.*, **36** (2001) 979.
- 228 C. Dang Ngoc Chan, C. Huvier, J.F. Dinhut, *Intermetallics*, **9** (2001) 817.
- 229 N. Babu, R. Balasubramaniam, A. Ghosh, *Corros. Sci.*, **43** (2001) 2239.
- 230 F. Lang, Z. Yu, S. Gedevanishvili, S. C. Deevi, T. Narita, *Intermetallics*, **11** (2003) 697.
- 231 C.H. Xu, W. Gao, S. Li, *Corros. Sci.*, **43** (2001) 671.
- 232 J.L. Smialek, J. Doychak, D.J. Gaydosh, *Oxid. Met.*, **34** (1990) 259.
- 233 J.R. Knibloe, R.N. Wright, C.L. Trybus, V.K. Sikka, *J. Mater. Sci.*, **28** (1993) 2040.
- 234 R. Balasubramaniam, *Scripta Mater.*, **34** (1996) 127.
- 235 M. Cieslar, M. Karlik, M. Benko, T. Cernoch, *Mater. Sci. Eng. A*, **324** (2002) 23.
- 236 K. Ito, T. Hayashi, M. Yokobayashi, H. Numakura, *Intermetallics*, **12** (2004) 407.
- 237 H. Skoglund, M. Knutson Wedel, B. Karlsson, *Intermetallics*, **12** (2004) 977.
- 238 D.G. Morris, M.A. Munoz-Morris, C. Baudin, *Acta Mater.*, **52** (2004) 2827.
- 239 Z.G. Yang, P.Y. Hou, *Mater. Sci. Eng. A*, **391** (2005) 1.
- 240 R. Sakidja, J.S. Park, J. Hamann, J.H. Perepezko, *Scripta Mater.*, **53** (2005) 723.
- 241 F. Bernard, E. Gaffet, *Int. J. SHS*, **10** (2001) 109.
- 242 P. Mossino, *Ceram. Int.*, **30** (2004) 311.
- 243 E. Gaffet, G. Le Caër, Mechanical processing for nanomaterials, *Encyclopedia of Nanoscience and Nanotechnology*, H.S. Nalwa, ed., **5** (2004) 91.
- 244 G.W. Goward, *Surf. Coat. Tech.*, **108–109** (1998) 73.
- 245 R. Mevrel, P. Pichoir, *Mater. Sci. Eng.*, **88** (1987) 1.
- 246 L. Levin, A. Ginzburg, L. Klinger, T. Werber, A. Katsman, P. Schaaf, *Surf. Coat. Tech.*, **106** (1998) 209.

247. C. Christoglou, N. Voudouris, G.N. Angelopoulos, Surf. Coat. Tech., **155** (2002) 51.
248. S. Naveos, G. Oberlaender, Y. Cadoret, P. Josso, M. Bacos, Mater. Sci. Forum, **461-464** (2004) 375.
249. C. Hougninou, S. Chevalier, J.P. Larpin, Appl. Surf. Sci., **236** (2004) 256.
250. N. Vialas, D. Monceau, Surf. Coat. Tech., **201** (2006) 3846.
251. P. Juzon, M. Ziemnicka, S. Chevalier, K. Przybylski, J.P. Larpin, Appl. Surf. Sci., **253** (2007) 4928.
252. S. Paris, PhD thesis, University of Burgundy, Dijon (2004).
253. B.A. Pint, J. Leibowitz, J.H. de Van, Oxid. Met., **51** (1999) 181.
254. S. Yang, F. Wang, W. Wu, Intermetallics, **9** (2001) 741.
255. T.V. Aller, US Patent no. 1155974 (1914).
256. H.B.C. Allison, L.A. Hawkins, General Electric Rev., **17** (1914) 947.
257. E.G. Gilson, US Patent no. 1091057 (1914).
258. E. Ruder, Trans. Am. Electrochem. Soc., **21** (1915) 253.
259. E.S. Nichols, J.A. Burger, D.K. Hanink, Mech. Eng. (1965) 52.
260. A.D. Joseph, US Patent no. 3102044 (1960).
261. M.J. Bennett, J.R. Nicholls, N.J. Simms, D. Naumenko, W.J. Quadakkers, V. Kochubey, R. Fordham, R. Bachorczyk, D. Goossens, H. Hattendorf, A.B. Smith, D. Britton, Mater. Corros., **56** (2005) 854.
262. G.W. Goward, D.H. Boone, Oxid. Met., **3** (1969) 475.
263. S.R. Levin, R.M. Caves, J. Electrochem. Soc., **121** (1974) 1051.
264. D.H. Boone, D.A. Crane, D.P. Whittle, Thin Solid Films, **84** (1981) 39.
265. Z.E. Majid, PhD thesis, University of Burgundy, Dijon (1983).
266. R. Mévrel, C. Duret, R. Pichoir, Mater. Sci. Tech., **2** (1986) 201.
267. R. Mévrel, R. Pichoir, Mater. Sci. Eng., **88** (1987) 1.
268. P.F. Tortorelli, K. Natesan, Mater. Sci. Eng., **A258** (1998) 115.
269. K. Stein-Fechner, J. Konys, O. Wedemeyer, J. Nucl. Mater., **249** (1997) 33.
270. W.T. Tsai, K.E. Huang, Thin Solid Films, **366** (2000) 164.
271. M.T. Kim, J.S. Jung, Surf. Coat. Tech., **161** (2002) 218.
272. N.E. Maragoudakis, G. Stergioudis, H. Omar, H. Paulidou, D.N. Tsipas, Mater. Lett., **53** (2002) 406.
273. Y. Zhang, B.A. Pint, K.M. Cooley, J.A. Haynes, Surf. Coat. Tech., **200** (2005) 1231.
274. R. Bianco, R.A. Rapp, J. Electrochem. Soc., **140** (1993) 1181.
275. R. Bianco, R.A. Rapp, J.L. Smialek, J. Electrochem. Soc., **140** (1993) 1191.
276. E. Basuki, A. Crosky, B. Gleeson, Mater. Sci. Eng. A, **224** (1997) 27.
277. J.A. Hearley, J.A. Little, A.J. Sturgeon, Surf. Coat. Tech., **123** (2000) 210.
278. Z.D. Xiang, J.S. Burnell-Gray, P.K. Datta, J. Mater. Sci., **36** (2001) 5673.
279. C. Christoglou, N. Voudouris, G.N. Angelopoulos, Surf. Coat. Tech., **141** (2001) 275.
280. S. Wöllmer, S. Zaferer, M. Göken, T. Mack, U. Glatzel, Surf. Coat. Tech., **167** (2003) 83.
281. J.W. Lee, Y.C. Kuo, Surf. Coat. Tech., **200** (2005) 1225.
282. R. Streiff, S. Poize, *High Temperature Corrosion*, NACE-6, R.A. Rapp, ed., San Diego, CA (March 1981), p. 591.
283. D. Yoshida, Y. Shibata, S. Hayashi, T. Narita, Oxid. Met., **64** (2005) 119.
284. W. Deqing, S. Ziyuan, T. Yingli, Appl. Surf. Sci., **250** (2005) 238.
285. C. Hougninou, PhD thesis, University of Burgundy, Dijon (2004).

286. C. Hougninou, S. Chevalier, J.P. Larpin, *Oxid. Met.*, **65** (2006) 409.
287. S. Chevalier, G. Strehl, H. Buscail, G. Borchardt, J.P. Larpin, *Mater. Corros.*, **55** (2004) 352.
288. S. Chevalier, G. Strehl, H. Buscail, C. Issartel, G. Borchardt, J.P. Larpin, *Mater. Corros.*, **57** (2006) 476.

## Oxidation of Ti-Al intermetallic compounds

S T A N I G U C H I, Formerly Osaka University, Japan

### 11.1 Introduction

#### 11.1.1 Advantages and potential applications of TiAl-base alloys

There are a few intermetallic compounds in the binary Ti-Al system. TiAl and its alloys have been studied much more than the others. Therefore, the main part of this chapter is devoted to TiAl, and issues regarding  $Ti_3Al$  and  $TiAl_3$  will be dealt with to a lesser degree.

Materials based on  $\gamma$ -TiAl are currently receiving much attention because of their attractive properties (Kim and Froes, 1990; Froes *et al.*, 1992), i.e. high mechanical strength at elevated temperatures and low density. Their specific strengths are comparable with those of Ni-base superalloys. These are a strong driving force for extensive research activities, some of which have been directed to replace engine components made of conventional high-temperature alloys including Ni-base superalloys with TiAl alloys. Their maximum application temperature is expected to be less than 1150 K. As a result of comprehensive research (Kim, 1995a, 1999, 2003), a few TiAl alloys are in practical use as automotive engine components. Worldwide effort, targeting aerospace engines and frames and gas turbine applications, has been reported (Bartolotta and Krause, 1999; Das *et al.*, 2003).

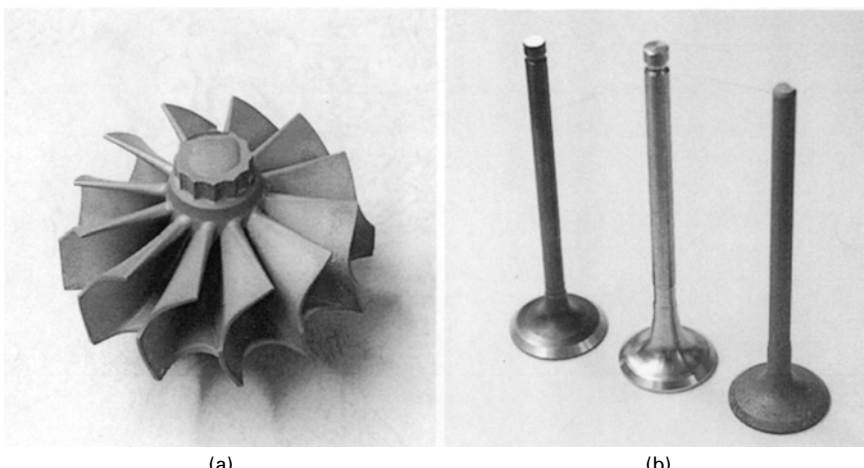
Production techniques such as precision casting, centrifugal casting, forging, rolling, extrusion, hot isostatic pressing (HIP) and welding are well developed. These have led to production of turbocharger wheels (Noda, 1998; Baur *et al.*, 2003), engine valves (Noda, 1998; Baur *et al.*, 2003; Sommer and Keijzers, 2003; Blum *et al.*, 2003), turbine blades (Bartolotta and Krause, 1999; Austin and Kelly, 1995), corrugated plates (Das *et al.*, 2003), honeycomb structures (Froes *et al.*, 1992; Bartolotta and Krause, 1999), etc. Further, methods of producing large ingots and near-net-shape casting are now available. Powder metallurgy and joining techniques have also been improved. It is noteworthy that many of the production techniques developed for processing

Ti alloys and Ni-base superalloys are applicable to TiAl alloys. This will bring about great economic merit at practical production stages.

Examples of products of TiAl alloys are shown in Fig. 11.1; (a) is a turbocharger wheel of a passenger car, and the centre photo of (b) is an engine valve made of a TiAl–Mn alloy by HIP. The right-hand photo of (b) is a similar valve after oxidation at high temperature for a long time. It shows only surface tarnishing and its mechanical strength was not degraded by the exposure. The left-hand photo shows a conventional steel valve.

A short history of the development of TiAl-base materials can be seen in a series of proceedings (Kim, 1995a, 1999, 2003) of symposia ‘Gamma Titanium Aluminides’ that cover a wide range of the topics. In addition, a considerable number of studies on TiAl alloys have been reported at other international meetings (e.g. Whang, 1990; Izumi, 1991). It should be emphasised that meetings specified on high-temperature oxidation and corrosion of intermetallics (Grobstein and Doychak, 1989; Grabke and Schütze, 1996) have also been held. Monographs (Aitken, 1967; Welsch and Desai, 1996) have been available on oxidation and corrosion of intermetallic compounds.

However, the main drawbacks of TiAl alloys are insufficient room-temperature ductility and poor oxidation resistance above about 1000 K. When these drawbacks are overcome, TiAl alloys will find much wider areas of application. This chapter mainly deals with the oxidation behaviour of TiAl alloys and measures for improving their oxidation resistance. Details of other properties are excluded, because they are beyond the scope of this chapter.



11.1 (a) A turbocharger wheel made of a TiAl alloy for a passenger car; (b) centre: an engine valve made of a TiAl–Mn alloy by HIP; right: after a long time of oxidation; left: a conventional steel valve.

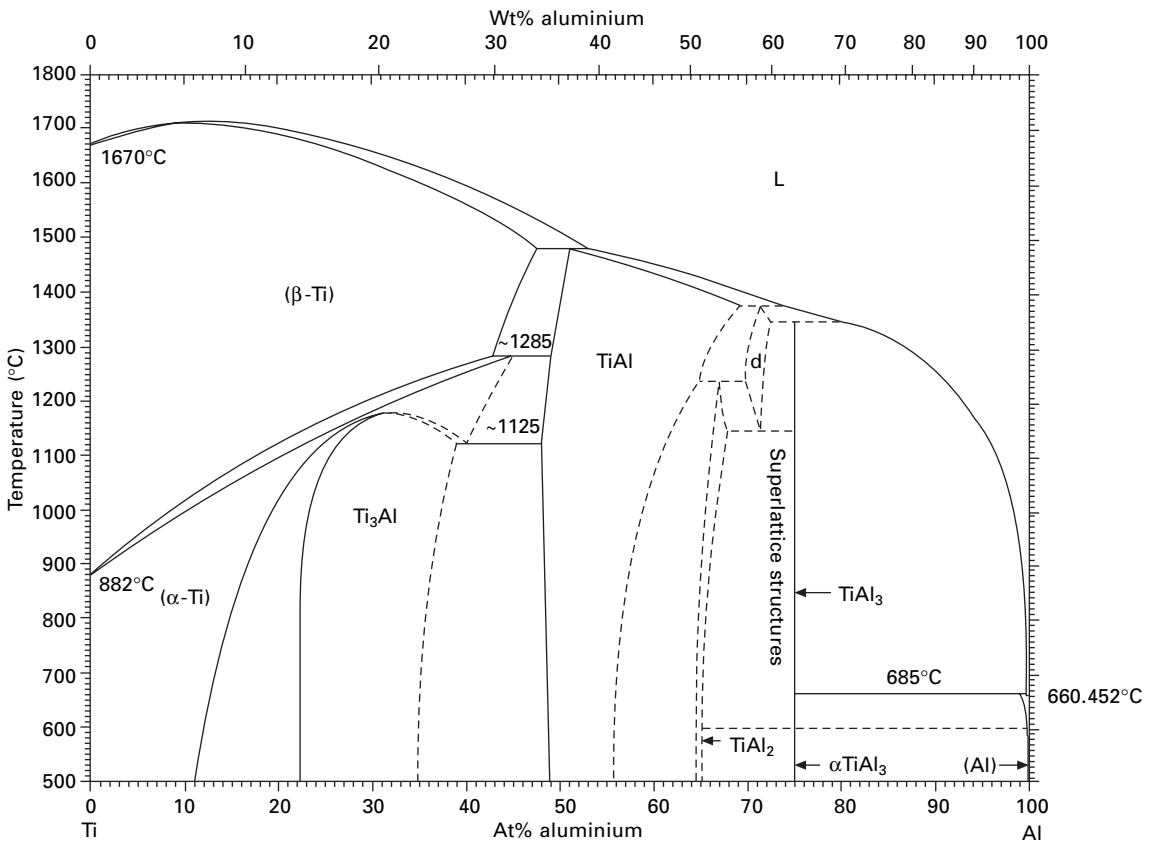
### 11.1.2 Some properties of Ti-Al intermetallic materials

Before deepening the discussion on oxidation it seems appropriate to start by reviewing some fundamental knowledge regarding  $\text{TiAl}$ ,  $\text{Ti}_3\text{Al}$  and  $\text{TiAl}_3$  for better understanding the following sections. According to an equilibrium phase diagram of the Ti-Al system shown in Fig. 11.2 (ASM, 1990), this system has the following intermetallic compounds:  $\text{Ti}_3\text{Al}$  ( $\alpha_2$  phase),  $\text{TiAl}$  ( $\gamma$  phase),  $\text{TiAl}_2$ ,  $\text{TiAl}_3$  and a high-temperature phase of  $\delta$ . Among these, materials based on  $\text{Ti}_3\text{Al}$ ,  $\text{TiAl}$  and  $\text{TiAl}_3$  are expected to be lightweight heat-resisting structural materials.

$\text{Ti}_3\text{Al}$  has an ordered hexagonal lattice of  $\text{D}0_{19}$  structure with a wide composition range from 22 to 39 at% Al. It decomposes congruently at 1457 K at a composition of 32 at% Al.  $\text{Ti}_3\text{Al}$  with stoichiometric composition is very brittle at room temperature. To improve its ductility,  $\alpha_2 + \beta$  two-phase structure is attained by small additions of  $\beta$ -phase stabilisers such as V, Nb, Mo or Ta. As a result, its room-temperature ductility and high-temperature workability have been improved (Larsen *et al.*, 1990; Froes *et al.*, 1992). In particular, the effect of Nb addition is significant in this respect. For example, Ti-14Al-21Nb (mass%) has good workability, room-temperature ductility, high specific strength and high creep strength. Candidates of this group are Ti-(23–25)Al-(10–30)Nb, Ti-24Al-11Nb, Ti-25Al-17Nb-1Mo, Ti-23.5Al-24Nb and Ti-25Al-10Nb-3V-1Mo (all in at%) (Froes *et al.*, 1992). The last one, called super- $\alpha_2$ , is envisaged as material for aircraft. These alloys are also expected to replace conventional Ti alloys. In addition, composite materials based on  $\text{Ti}_3\text{Al}$  reinforced by SiC fibre have been developed (Larsen *et al.*, 1990). They have higher values of specific strength, rigidity, wear strength and fracture toughness compared with  $\text{Ti}_3\text{Al}$  without the reinforcement.  $\text{Ti}_3\text{Al}$  alloys thus developed have mechanical properties superior to those of conventional Ti alloys. However, the oxidation behaviour of  $\text{Ti}_3\text{Al}$  alloys at high temperature has been studied much less in comparison with that of  $\text{TiAl}$  alloys.

$\text{TiAl}$  has a specific mass of  $3.8 \text{ g}\cdot\text{cm}^{-3}$  and a face centred tetragonal structure of  $\text{L}1_0$  with the lattice parameter ratio,  $c/a$ , of about 1.02. Its homogeneity ranges from 49 to 69 at% Al and its maximum melting temperature is 1760 K. Its toughness between room temperature and 1100 K is more than 400 MPa and oxidation resistance is relatively good. The single phase of  $\gamma$  is very brittle, and Ti-48at%Al consists of  $\gamma$  and  $\alpha_2$  phases. The microstructure of the two-phase alloys can be considerably changed by combination of heat treatments (Kim, 1995b). This in turn allows widely variable mechanical properties.

On the other hand,  $\text{TiAl}_3$  has a  $\text{D}0_{22}$  structure and its composition range is almost zero. Since it is the lightest among the Ti-Al intermetallics, it is a



11.2 Equilibrium phase diagram of the Ti-Al system (from ASM International., 1990, reproduced with permission).

candidate for aircraft components. Furthermore, it shows excellent oxidation resistance by forming protective  $\text{Al}_2\text{O}_3$  scales (Umakoshi *et al.*, 1989; Mabuchi and Nakayama, 1991) because of its very high Al content. However, its application as a structural material is quite difficult at this moment because of its very low ductility. In spite of research effort (Mabuchi and Nakayama, 1991; Nakayama and Mabuchi, 1993) its ductility has not been improved to a level of practical application. In addition, the phase diagram shows that if the Al content is increased for some reason during service at elevated temperatures, a liquid phase appears (see Fig. 11.2). This reduces the reliability of such materials as high-temperature structural materials.  $\text{TiAl}_3$  layers formed by aluminising  $\text{TiAl}$  (Yoshihara *et al.*, 1991) are considered to be a protective coating.

A range of mechanical properties and some fundamental properties of  $\text{Ti}_3\text{Al}$  and  $\text{TiAl}$  are summarised in Table 11.1 (Kim and Froes, 1990) for better understanding, together with those of Ti alloys and Ni-base superalloys for comparison. Ti-Al intermetallics and Ti alloys have very low densities: about half of those of Ni-base superalloys. This is a great advantage of Ti-Al intermetallic alloys as moving parts or as bodies of vehicles, etc. There is no large difference in mechanical properties between  $\text{TiAl}$  alloys and Ni-base superalloys except creep strength. Further, Ti alloys are prone to ignition, but Ti-Al intermetallics are not. This is very important for the safety of high-temperature facilities. Creep curves indicated that  $\text{TiAl}$  has the highest strength, next is  $\text{Ti}_3\text{Al}$  and then a group of modern Ti alloys follow among Ti alloys and Ti-Al intermetallics (Froes *et al.*, 1992). From the viewpoint of oxidation, however,  $\text{Ti}_3\text{Al}$  and  $\text{TiAl}$  do not form protective  $\text{Al}_2\text{O}_3$  scales under ordinary oxidation conditions, in spite of their high Al contents. This is a significant problem.

Usually, engineering  $\text{TiAl}$  alloys contain several alloying elements for controlling their microstructure and thus improving their mechanical properties.

**Table 11.1** Properties of titanium aluminides, titanium-base conventional alloys and superalloys (from Kim and Froes, 1990, reproduced with permission)

Property	Ti-base	$\text{Ti}_3\text{Al}$ -base	$\text{TiAl}$ -base	superalloys
Structure	hcp/bcc	D0 <sub>19</sub>	L1 <sub>0</sub>	fcc/L1 <sub>2</sub>
Density, g/cm <sup>3</sup>	4.5	4.1–4.7	3.7–3.9	8.3
Modulus, GPa	95–115	110–145	160–180	206
Yield strength, MPa	380–1150	700–990	400–650	–
Tensile strength, MPa	480–1200	800–1140	450–800	–
Ductility, % at RT	10–25	2–10	1–4	3–5
Ductility, % at HT	12–50	10–20	10–60	10–20
Fracture toughness, MPa $\sqrt{\text{m}}$	High	13–30	10–20	25
Creep limit, °C	600	760	1000	1090
Oxidation, °C	600	650	900	1090

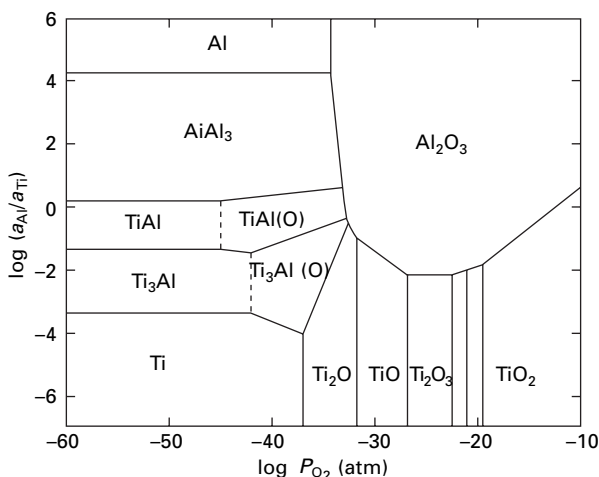
However, the compatibility between the mechanical property and oxidation resistance has not been well established. For instance (Kim and Froes, 1990), additions of a few mass% of V, Cr or Mn improve ductility of two-phase TiAl alloys and also enhance their oxidation. Contrary to this, Nb, Ta or W improves the oxidation resistance but reduces the ductility. Surface treatment is a possible way to obtain sufficient resistance against environmental attack including high-temperature oxidation, when sufficient resistance cannot be attained by alloying addition and/or controlling microstructure. Influence of alloying addition and surface treatment will be dealt with later.

## 11.2 Oxidation characteristics of TiAl-base alloys

### 11.2.1 Phase relations

The main oxides formed during the oxidation of Ti-Al intermetallic alloys are  $\text{TiO}_2$  (rutile) and  $\text{Al}_2\text{O}_3$  ( $\alpha$ - $\text{Al}_2\text{O}_3$ ); the diffusion of cations and anions through the former is much faster than through the latter. Therefore, the formation of an  $\text{Al}_2\text{O}_3$  scale or at least a dense and continuous  $\text{Al}_2\text{O}_3$  layer in the scale is a prerequisite for obtaining sufficient oxidation resistance under application conditions. The stability of the phases concerned and phase relations should well be understood in the discussion on the oxidation characteristics.

According to the chemical potential diagram of the Ti-Al-O system shown in Fig. 11.3 (Inaba and Murata, 1997), where the ratio of Al activity to Ti activity is plotted against oxygen partial pressure,  $\text{Ti}_3\text{Al}$  and  $\text{TiAl}$  coexist with  $\text{Al}_2\text{O}_3$  through these containing oxygen in solution. However, in practice

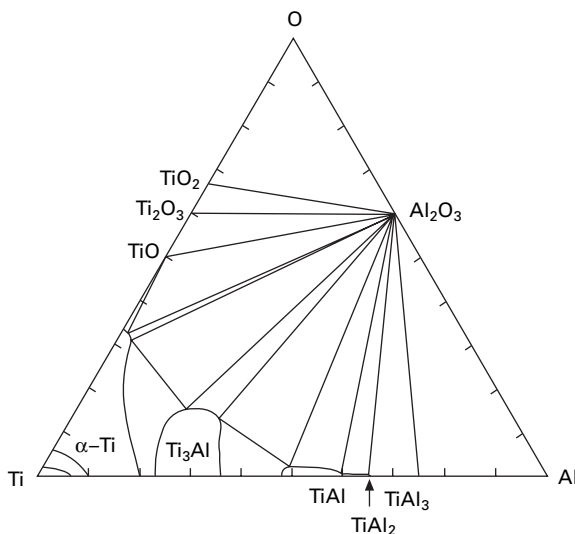


11.3 Chemical potential diagram of the Ti-Al-O system at 1273 K (from Inaba and Murata, 1997, reproduced with permission).

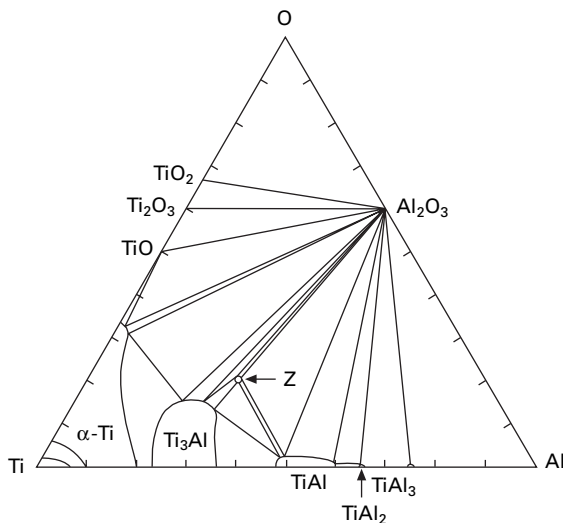
it is quite difficult to selectively oxidise Al without forming titanium oxides. The main possible reasons are that both Ti and Al have similar affinities to oxygen, and that  $\text{TiO}_2$  grows much faster than  $\text{Al}_2\text{O}_3$ . Though an  $\text{Al}_2\text{O}_3$  scale is formed in a very limited case, it is not maintained for a long time and is overgrown by  $\text{TiO}_2$ . Figure 11.3 indicates that  $\text{Al}_2\text{O}_3$  remains stable on  $\text{TiAl}_3$  and this has been experimentally confirmed.

A possible equilibrium phase diagram of the Ti-Al-O system can be drawn as Fig. 11.4 on the basis of relevant literature (Li *et al.*, 1992; Zhang *et al.*, 1992; Copland *et al.*, 1999). Here, a few kinds of titanium oxides are omitted for simplicity. It should be noted that the oxygen solubility in  $\text{Ti}_3\text{Al}$  is about 15.4 at% and in  $\text{TiAl}$  is about 2.5 at% at 1273 K. According to this diagram an  $\text{Al}_2\text{O}_3$  scale would be formed directly on  $\text{Ti}_3\text{Al}$  and  $\text{TiAl}$ . However, in reality a Ti-Al-O compound is formed between the scale and substrate, when the scale is  $\text{Al}_2\text{O}_3$  or very protective and thus remains stable. The presence of such a compound coincides with Fig. 11.3.

This compound was found to have a composition of  $\text{Ti}_5\text{Al}_3\text{O}_2$  and a cubic structure with a lattice constant of 0.69 nm. This has been tentatively called the Z phase (Zheng *et al.*, 1995) or the X phase (Dettenwanger *et al.*, 1996). These two are effectively the same. The Z phase is thermodynamically unstable (Copland *et al.*, 1999) but remains for a very long time. Therefore, it is better to use a phase diagram containing the Z phase as shown in Fig. 11.5, which was composed on the basis of the literature (Zheng *et al.*, 1995; Kussmaul *et al.*, 1998; Copland *et al.*, 1999), to understand the processes of formation



11.4 Possible equilibrium phase diagram of the Ti-Al-O system at 1273 K (from Copland *et al.*, 1999, reproduced with permission).

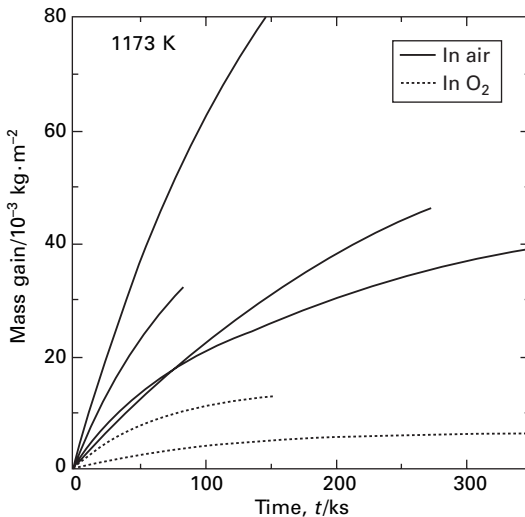


11.5 Practical phase relations of the Ti-Al-O system at 1273 K (from Copland *et al.*, 1999, reproduced with permission).

of scale structure (or so-called diffusion path) and subsurface structure. On the other hand, data on diffusivity of the relevant elements are very few for  $Ti_3Al$  and  $TiAl$ , and data on the influence of additional elements on activities of Al and Ti are lacking. This hinders the progress of theoretical treatment of the phenomena.

### 11.2.2 Oxidation curves

Examples of oxidation kinetic curves (mass gain due to oxidation per surface area vs. time) of binary  $TiAl$  alloys in air and in oxygen are shown in Fig. 11.6. Each curve was obtained at different institutions. It is noteworthy that the oxidation is faster in air than in oxygen. This difference is attributable to  $N_2$  (Rakowski *et al.*, 1995; Quadakkers *et al.*, 1997) and water vapour ( $H_2O$ ) (Kremer and Auer, 1997) in air. Generally, they enhance the oxidation. Next, the scattering data in air are wider than those in oxygen. This is also attributable to the influence of  $H_2O$  in air, the content of which varies with location and climate. The presence of the  $\alpha_2$  phase, microstructure and surface conditions have been pointed out as the reasons for the difference among specimens. Even if a specimen has a composition corresponding to the single  $\gamma$  phase, it usually contains a certain amount of the  $\alpha_2$  phase. The amount and microstructure vary widely with the heat treatment and the history of the specimen preparation, so the oxidation behaviour varies widely. For example, if the specimen was covered with a thin  $Al_2O_3$  scale in the initial stages of oxidation,  $Al_2O_3$  is not maintained if the  $\alpha_2$  phase is present beneath the



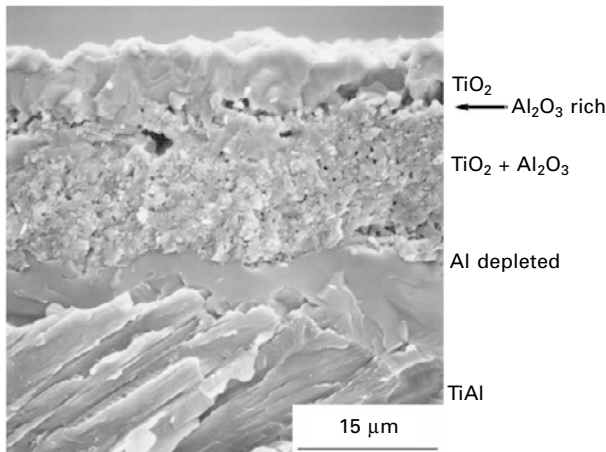
11.6 Oxidation curves of binary TiAl alloys in air and in oxygen at atmospheric pressure at 1173 K, based on the literature (Umakoshi *et al.*, 1989; Kasahara *et al.*, 1989; Maki *et al.*, 1992; Becker *et al.*, 1992; Meier *et al.*, 1993).

scale, because of insufficient supply of Al. In addition, the  $\alpha_2$  phase has large oxygen solubility, and this makes the  $\text{Al}_2\text{O}_3$  on it unstable (Brady *et al.*, 1997). Surface treatments such as polishing, abrasion, etc. also influence the oxidation behaviour, though such influence becomes less above about 1050 K.

### 11.2.3 Structure of oxide scale

In general, the high-temperature oxidation of TiAl results in a scale consisting of an outer  $\text{TiO}_2$  layer and an inner porous layer which is a mixture of  $\text{Al}_2\text{O}_3$  and  $\text{TiO}_2$  (Taniguchi *et al.*, 1991a) as shown in Fig. 11.7. The  $\text{TiO}_2$  grains of the outer  $\text{TiO}_2$  layer are large, indicating the sintering between the  $\text{TiO}_2$  grains during the oxidation. There is a thin intermediate layer very rich in  $\text{Al}_2\text{O}_3$  between the two layers. The thickness and compactness of this  $\text{Al}_2\text{O}_3$ -rich layer decide the protectiveness of the scale to a large degree. In later stages of oxidation  $\text{Al}_2\text{O}_3$  is enriched in the bottom area of the scale. This also provides additional protection. The lamellar feature of the substrate reflects the original grains consisting of  $\gamma$  and  $\alpha_2$  phases.

In addition, there is an Al-depleted or Z-phase layer beneath the scale. This layer is much harder than the  $\alpha_2$  phase or the  $\gamma$  phase, and thus embrittles the material exposed to an oxidising atmosphere. During this oxidation stage (called Stage II in the next section) the scale grows mainly by inward diffusion of oxygen, while outward diffusion of titanium contributes to some degree.



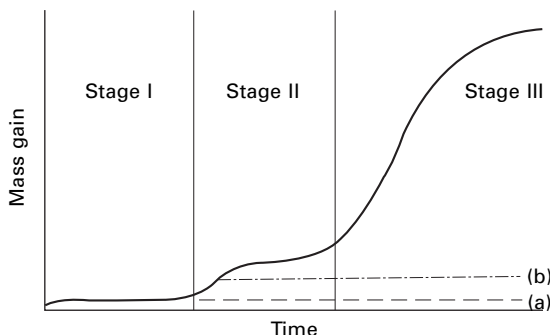
11.7 SEM micrograph of a fractured cross-section of a TiAl specimen oxidised at 1200 K for 100 ks in oxygen at atmospheric pressure, showing a layered scale structure and an Al-depleted layer.

Because of such a scale structure, its oxidation resistance is insufficient at high temperatures. The formation of a definite and continuous Al<sub>2</sub>O<sub>3</sub> layer is a prerequisite for obtaining the sufficient oxidation resistance.

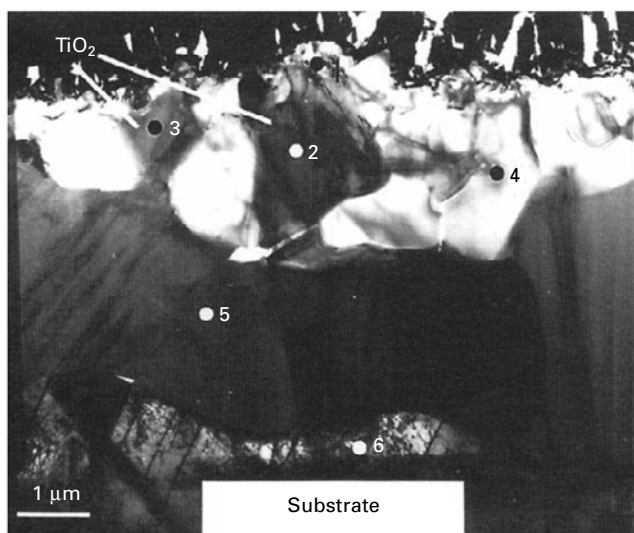
#### 11.2.4 Oxidation sequences

The oxidation sequence follows three stages (Becker *et al.*, 1992) as shown in Fig. 11.8. The development of scale structure is as follows. At low temperatures or in the initial periods of oxidation, TiAl stays at Stage I with a scale consisting mainly of Al<sub>2</sub>O<sub>3</sub> with a small amount of TiO<sub>2</sub> grains on its top (Taniguchi *et al.*, 2000), or an Al-rich scale. Therefore, the oxidation is slow. An Al-depleted layer is developed beneath the scale because of the growth of Al<sub>2</sub>O<sub>3</sub>. When the Al activity beneath the scale falls to a certain value or mechanical failure of the scale takes place owing to oxide growth stress, TiO<sub>2</sub> starts to grow, accompanied by a large volume increase. The growth of TiO<sub>2</sub> grains into an Al<sub>2</sub>O<sub>3</sub> scale from an Al-depleted layer is shown in Fig. 11.9 (Taniguchi *et al.*, 2000). This damages the Al<sub>2</sub>O<sub>3</sub> scale and leads to loss of protectiveness. This is the transition from Stage I to Stage II.

The transition to Stage II takes place sooner as the oxidation temperature rises. This transition can be understood as in Fig. 11.10 (Taniguchi *et al.*, 1996): (a) shows an outer surface with oxide nodules on the flat area, and (b) and (c) are cross-sections of the flat part and the nodule, respectively. The flat part (b) is covered with an Al<sub>2</sub>O<sub>3</sub> scale with a thickness of about 0.5 μm with a few TiO<sub>2</sub> crystals on it. An Al-depleted layer of almost uniform



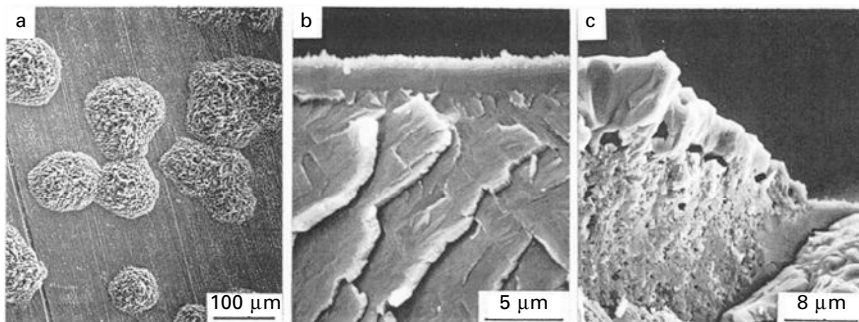
11.8 Oxidation sequences of TiAl alloys consisting of three stages.



11.9 TEM micrograph of a TiAl specimen oxidised in 0.013 Pa oxygen at 1273 K for 21.6 ks, showing the growth of  $\text{TiO}_2$  grains into the  $\text{Al}_2\text{O}_3$  scale. 1 and 4:  $\text{Al}_2\text{O}_3$ ; 2 and 3:  $\text{TiO}_2$ ; 5: Z phase; 6: TiAl substrate (Taniguchi *et al.*, 2000).

thickness of about  $1.5 \mu\text{m}$  was formed. This was found to be the Z phase. The oxide nodule (c) has a structure similar to that in Stage II: see Fig. 11.7. These nodules grow horizontally and also vertically to cover the whole specimen surface.

The majority of research on TiAl alloys has been performed in a temperature range of 1000–1300 K and for periods of up to about 400 ks, so such researches have been dealing with Stage II. During this period the oxidation rate decreases with time until the transition to Stage III, and the oxidation follows a nearly parabolic manner, or more precisely the rate follows the slightly lower side



11.10 SEM micrographs of (a) surface, and (b) and (c) fractured cross-sections of a TiAl specimen oxidised at 1200 K for 100 ks in oxygen at atmospheric pressure, showing (a) oxide nodules on flat area, (b)  $\text{Al}_2\text{O}_3$  scale and Al-depleted layer of both uniform thickness, and (c) oxide nodule (Taniguchi *et al.*, 1996).

of a parabolic line, because of enrichment of  $\text{Al}_2\text{O}_3$  near the scale/substrate interface.

During further oxidation, the scale thickens to such an extent that the supply of Al to the  $\text{Al}_2\text{O}_3$ -rich layer becomes slow. This lowers the stability of  $\text{Al}_2\text{O}_3$  of this layer and Al dissolves into  $\text{TiO}_2$  grains. Such Al diffuses outwards. When Al reaches the outer part of the  $\text{TiO}_2$  layer where the oxygen potential is high enough, Al is oxidised to  $\text{Al}_2\text{O}_3$  which precipitates as isolated particles. Therefore, such  $\text{Al}_2\text{O}_3$  particles have little protectiveness against oxidation. This is the transition to Stage III. The preferable oxidation behaviour is, of course, that shown by line (a) in Fig. 11.8, where the rate of oxidation stays very low.

### 11.2.5 The Z phase

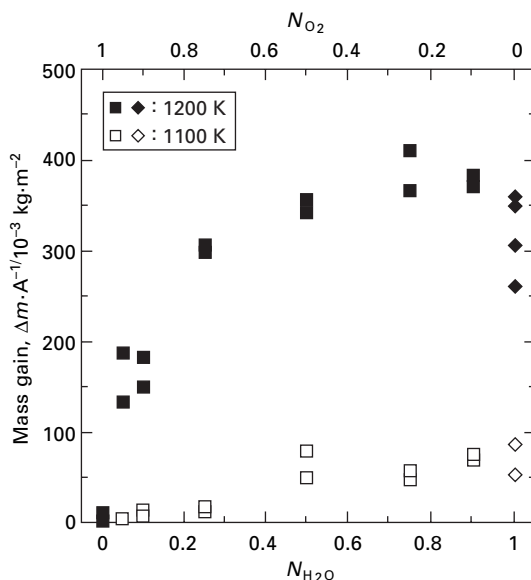
Whenever protective scales are maintained, there is a definite thin layer consisting of the Z phase beneath them. Such a case occurs, for instance, by a minor addition of Zr (Taniguchi *et al.*, 1996), implantation of Nb ions (Taniguchi *et al.*, 1998a), surface roughening of Ti-50at%Al by polishing with coarse grit paper (Copland *et al.*, 1999), etc. The layer of the Z phase is formed even on two-phase TiAl alloys containing lamellar grains consisting of  $\gamma$  and  $\alpha_2$  phases. This implies that the fast diffusion of Al along the boundaries of lamellae contributes to the formation of an initial  $\text{Al}_2\text{O}_3$  scale. Figure 11.10(b) shows that the shape of the Z-phase layer is not modified by the lamellar structure of the substrate, supporting the above view. At a certain time during Stage II,  $\text{Ti}_3\text{Al}$  nucleates at the interface between the Z-phase layer and the substrate, and grows towards the scale (Dettenwanger *et al.*, 1996). This is expressed by the following reaction:



Therefore, the originally single phase Al-depleted layer becomes a mixture of the Z phase,  $\text{Ti}_3\text{Al}$  and  $\text{Al}_2\text{O}_3$ . However, such  $\text{Al}_2\text{O}_3$  grows as thin discrete platelets whose direction is almost normal to the substrate surface (Taniguchi *et al.*, 1991a; Meier *et al.*, 1993; Copland *et al.*, 1999), therefore they cannot provide any protection.  $\text{Ti}_3\text{Al}$  formed by reaction [11.1] is prone to oxidise to form mixed  $\text{TiO}_2$  and  $\text{Al}_2\text{O}_3$  grains, hence the prevention of this reaction seems worthwhile for maintaining good oxidation resistance.

### 11.2.6 Influence of gas species

In the application of TiAl alloys to engine parts, it is necessary to understand the influence of gas species contained in combustion gas such as water vapour ( $\text{H}_2\text{O}$ ),  $\text{CO}_2$  and  $\text{N}_2$ , and to take suitable countermeasures. All these gases enhance the oxidation, with  $\text{H}_2\text{O}$  having the largest influence and  $\text{N}_2$  the smallest (Taniguchi *et al.*, 1999b, 2001a). Figure 11.11 (Taniguchi *et al.*, 1999b) shows that addition of 10 vol%  $\text{H}_2\text{O}$  to  $\text{O}_2$  significantly enhances the mass gain due to oxidation, and further additions have more influence. This influence is larger at a higher temperature. The influences of  $\text{CO}_2$  and  $\text{N}_2$  have been similarly reported (Taniguchi *et al.*, 1999b).



11.11 Influence of water vapour on the mass gain due to oxidation of TiAl specimens at 1100 and 1200 K for 100 ks in  $\text{O}_2\text{-H}_2\text{O}$  mixtures at atmospheric pressure (Taniguchi *et al.*, 1999b).

The addition of H<sub>2</sub>O to O<sub>2</sub> resulted in nearly linear kinetics with scales which did not contain an Al<sub>2</sub>O<sub>3</sub>-rich layer. Al<sub>2</sub>O<sub>3</sub> grains were dispersed in the scale. The influence of H<sub>2</sub>O was attributed to the enhanced diffusion in TiO<sub>2</sub> (Kremer and Auer, 1997). The presence of H<sub>2</sub>O results in the formation of OH<sup>-</sup>, which replaces O<sup>2-</sup> of the lattice site of TiO<sub>2</sub> (Sarrazin *et al.*, 1978). This decreases the oxygen ion vacancy of TiO<sub>2</sub> according to the valence control rule, and seems to slow the oxidation by slowing the transport of oxygen through TiO<sub>2</sub> grains. However, OH<sup>-</sup> is thought to diffuse much faster than O<sup>2-</sup>, because the resistance by the surrounding cations is small owing to its charge being smaller than that of O<sup>2-</sup>. Since H<sub>2</sub>O mainly influences the growth of TiO<sub>2</sub>, the alloys which form scales containing TiO<sub>2</sub> oxidise much faster, even though they show good oxidation resistance in a dry atmosphere (Yoshihara *et al.*, 2007). The influence of TiH<sub>2</sub> detected (Kremer and Auer, 1997) in the internal oxidation zone of the substrate on the oxidation behaviour is unknown. The influence of H<sub>2</sub>O or OH<sup>-</sup> on the diffusion through Al<sub>2</sub>O<sub>3</sub> grains is unclear for the application conditions, though it seems much smaller than that on TiO<sub>2</sub>.

CO<sub>2</sub> forms TiC in the scale at and around the scale/substrate interface during the oxidation (Taniguchi *et al.*, 1999b) and TiC thus formed may disturb the sintering between the oxide grains, keeping the scale more porous. TiC is oxidised with the progress of oxidation, and carbon released by the oxidation reacts again with Ti to form TiC. The boundary between the TiC-rich area and the TiO<sub>2</sub>-rich area is discerned by the change of structural feature.

The outer layer of the scale is occupied by relatively large TiO<sub>2</sub> grains with a feature implying the sintering effect between them. However, these TiO<sub>2</sub> grains show particular shapes such as protrusions and faceted prisms in H<sub>2</sub>O- and CO<sub>2</sub>-containing atmospheres respectively, indicating preferential growth along a certain direction. This agrees with a large crystalline anisotropy of TiO<sub>2</sub>.

In the presence of N<sub>2</sub> the initially formed scale is associated with nitrides, unlike the scale formed in oxygen. The initial scale is a mixture of Al<sub>2</sub>O<sub>3</sub> and TiN (also Ti<sub>2</sub>AlN in some cases). The nitride disturbs the formation of a dense and continuous Al<sub>2</sub>O<sub>3</sub> scale. A thermodynamic consideration based on a P<sub>O<sub>2</sub></sub> – P<sub>N<sub>2</sub></sub> diagram (Rakowski *et al.*, 1995; Akai *et al.*, 1996) showed that there is a situation where Al is oxidised and Ti is nitrided. These nitrides are oxidised as the oxidation proceeds. Nitrogen freed by this reacts with the substrate to form nitrides again. This process is repeated, hence a certain amount of nitrides is always present near the scale/substrate interface.

The nitride formation is enhanced by the presence of Nb as alloying element (Figge *et al.*, 1993; Sunderkötter *et al.*, 1999). When a nitride layer covers the substrate surface completely, the oxidation resistance is significantly improved owing to the layer that works as an effective diffusion barrier.

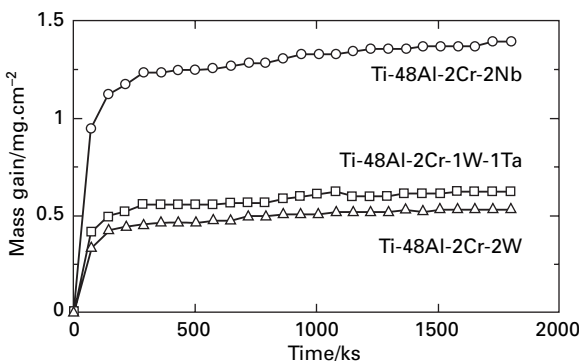
Even though these gas species enhance the oxidation of binary TiAl alloys, suitable alloy composition gives superior oxidation resistance as shown in Fig. 11.12 (Li and Taniguchi, 2004), showing the cyclic oxidation curves of a range of alloys in a simulated combustion gas ( $N_2$ -15 $O_2$ -7 $CO_2$ -6 $H_2O$  in vol%) at 1173 K. The scales formed here were very rich in  $Al_2O_3$ . These curves correspond to line (b) in Fig. 11.8, showing the large effect of W addition, and that the interaction between gas species and alloying additions is complex.

### 11.2.7 Influence of additional elements

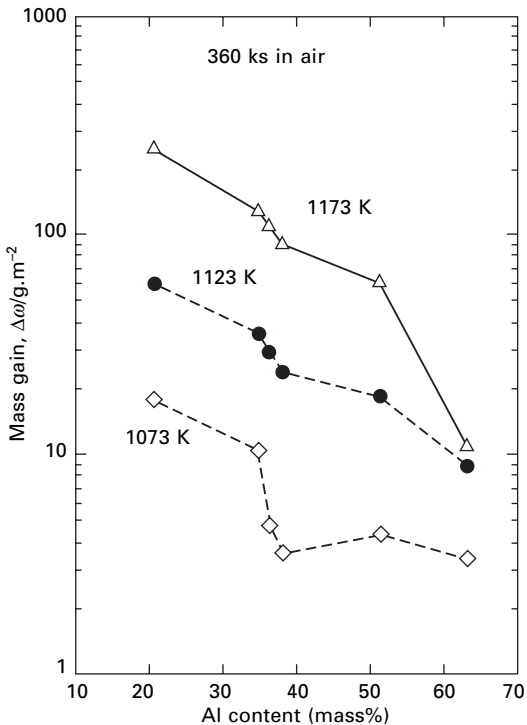
Figure 11.13 (Shida and Anada, 1993a) indicates that the mass gain due to oxidation decreases with increasing Al content in binary TiAl alloys. In other words, the oxidation resistance increases with an increase in the Al content. However, alloys with single  $\gamma$  phase should be avoided because of their very low ductility. Therefore, alloying addition is necessary to improve the oxidation resistance and accordingly there are many such studies (Hanamura *et al.*, 1991; McKee and Huang, 1992; Shida and Anada, 1993b; Kumagai *et al.*, 1993; Taniguchi *et al.*, 1998b; Shemet *et al.*, 2000).

The influence of third elements can be summarised as in Fig. 11.14. Many other reports have been examined, but a similar tendency has been obtained. The vertical coordinate shows the ratio of mass gain of the doped specimen to that of the binary TiAl under the same oxidation conditions. The number attached to the element means mass%, except for those marked. Additions of the elements below the broken line reduce the oxidation rate and vice versa. A ratio below 0.03 means the formation of protective  $Al_2O_3$  scales.

Vanadium, chromium and manganese, which improve the ductility of TiAl alloys, also enhance oxidation. On the other hand, Nb, Mo and W

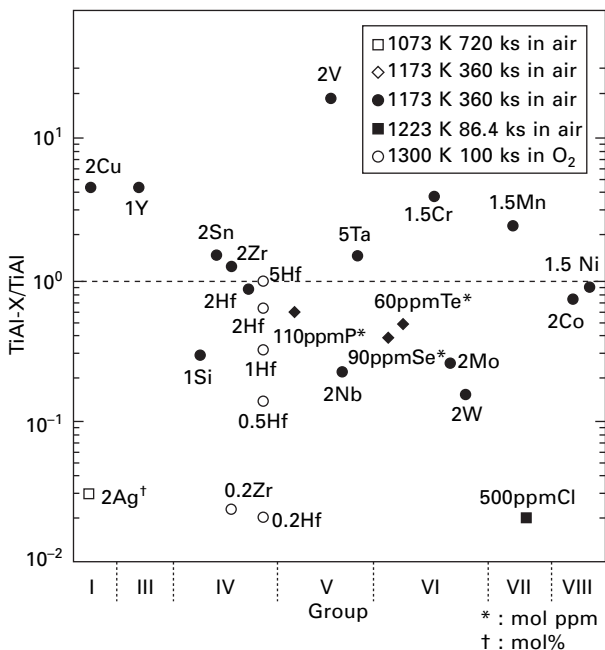


11.12 Cyclic oxidation curves of Ti-48Al-2Cr-2Nb, Ti-48Al-2Cr-2W and Ti-48Al-2Cr-1W-1Ta (at%) in a simulated combustion gas at 1173 K (Li and Taniguchi, 2004).

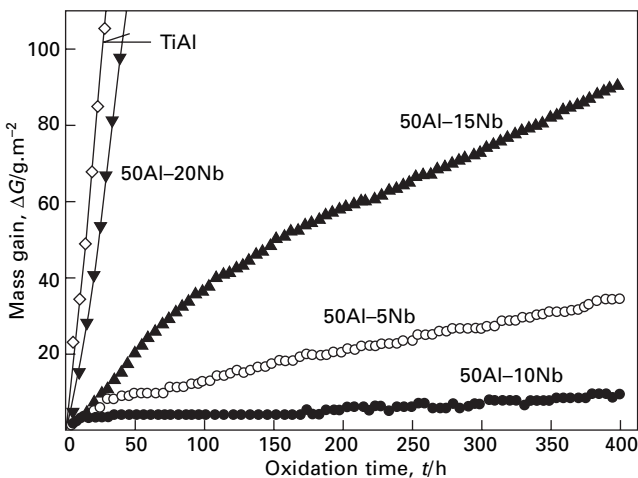


11.13 Influence of the Al content on the mass gain due to oxidation of binary TiAl alloys in air for 360 ks (from Shida and Anada, 1993a, reproduced with permission).

improve oxidation resistance. Reports on the influence of Ta (McKee and Huang, 1992; Shida and Anada, 1993b; Welsch *et al.*, 1996) have been controversial, so a further study is needed. Figure 11.14 includes alloying element additions of up to a few percent. Large additions show a different tendency. This can be seen, for example, in Hf addition: minor addition of Hf improves oxidation resistance significantly by forming an  $\text{Al}_2\text{O}_3$  scale, but the mass gain increases with an increase in the Hf content. Excess Hf may form  $\text{HfO}_2$  particles, the diffusion of oxygen through which is much faster than through  $\text{Al}_2\text{O}_3$ . Another example can be seen in Nb addition as shown in Fig. 11.15 (Yoshihara *et al.*, 1993). Here, the Al content is kept at 50 at% and a part of Ti is replaced with Nb. The mass gain due to 5 h cyclic oxidation at 1223 K in air decreases with an increase in the Nb content up to 10 at%. Virtually pure  $\text{Al}_2\text{O}_3$  scales were formed. Similar results were obtained when the temperature was lowered to 1173 K. However, an excess amount of Nb deteriorated the oxidation behaviour. The excess Nb would form  $\text{Nb}_2\text{O}_5$ , which grows much faster than  $\text{Al}_2\text{O}_3$ . Though studies on combined addition are relatively few, it can be said that Nb, Ta or W seems indispensable for



11.14 Summary of the ratio of the mass gain of doped TiAl to that of binary TiAl oxidised under the same conditions, based on the literature (Hanamura *et al.*, 1991; Shida and Anada, 1993b; Kumagai *et al.*, 1993; Taniguchi *et al.*, 1996, 1998b; Shemet *et al.*, 2000).



11.15 Influence of Nb addition on cyclic oxidation behaviour of TiAl-Nb alloys at 1223 K in air (from Yoshihara *et al.*, 1993, reproduced with permission).

obtaining sufficient oxidation resistance with good balance of mechanical properties.

A literature survey revealed the following guidelines for improving the oxidation resistance.

### *Slowing $TiO_2$ growth*

As shown in Fig. 11.7,  $TiO_2$  grains are included in the scale even in the  $Al_2O_3$ -rich layer. If the growth of  $TiO_2$  grains is slowed,  $Al_2O_3$  would be enriched in the scale, improving oxidation resistance. As  $TiO_2$  crystals contain oxygen ion vacancies and interstitial titanium ions as the lattice defects, the former increase and the latter decrease as the oxygen partial pressure decreases (Kofstad, 1983). Oxygen diffuses inwards as anions preferentially via oxygen ion vacancy sites in  $TiO_2$  crystals, and titanium diffuses as cations outwards via interstitial titanium ion sites. A small amount of Al dissolves into  $TiO_2$ , and also diffuses. However, the diffusion of oxygen contributes largely to the scale growth. If a protective  $Al_2O_3$  scale is maintained for a long time, the oxidation curve would be like line (a) in Fig. 11.8; and when the growth of  $TiO_2$  is significantly slow, the oxidation curve would be like line (b).

According to the valence-control rule, dissolution of ions whose valences are higher than those of titanium ions can reduce the oxygen ion vacancy. Hence, the oxidation resistance can be improved. In this respect, additions of Nb, Ta, Mo, W, P, Se or Te would be beneficial. Figure 11.14 shows this tendency, so possibly this mechanism is operating. Dissolution of Nb in  $TiO_2$  grains, for instance, was confirmed (Figge *et al.*, 1993). However, the scale still contains  $TiO_2$  grains. In contrary, dissolution of V, Cr or Mn into  $TiO_2$  grains enhances oxidation. This can be explained on the same ground. Here, V seems to have a valence less than 4.

### *Stabilisation of the Z phase*

This idea seems equivalent to prevention of reaction [11.1]. During the growth of protective  $Al_2O_3$  scales (line (a) in Fig. 11.8) and relatively protective scales at Stage II (line (b)), a definite layer of the Z phase is formed beneath the scale. The  $\alpha_2$  phase formed by reaction [11.1] has a large oxygen solubility, and a part of  $Al_2O_3$  on it will be decomposed, losing the protectiveness.

According to Wagner's scaling model (Wagner, 1959), to prevent internal oxidation of Al, addition of elements which decrease the solubility and diffusivity of oxygen in the substrate, and increase the diffusivity of Al, is effective. However, considerations based on this viewpoint have been very few and necessary data are scarce. At a certain stage of oxidation, Mo or W is enriched in the subsurface zone, and would reduce the oxygen solubility (Shida and Anada, 1994). However, further research is needed to confirm

this point. Data regarding the influence of additional elements on the Al activity are few, in particular at practical oxidation temperatures.

Small additions of Ag, Ti-48Al-2Ag and Ti-50Al-2Ag (both), formed continuous external  $\text{Al}_2\text{O}_3$  scales, which were protective for a very long exposure of 6000 h at 800°C in air (Shemet *et al.*, 2000). This was accounted for by the stabilisation of the Z phase, though the mechanism for this has not been clear. The excess Ag spoiled the oxidation resistance by dissolving Al in Ag, decreasing the Al activity of the alloy.

#### *Barrier of oxide of additional element*

The addition of 1 mass% Si (Maki *et al.*, 1992) and 3 or 5 mass%  $\text{Si}_3\text{N}_4$  (Lee, 2000) to TiAl led to the formation of scales containing  $\text{SiO}_2$  grains, which were enriched at a certain depth in the scales. Because of this the diffusion of both oxygen and metal was hindered to some degree, and hence the oxidation resistance was improved. Combined addition of Si and Nb was further effective (Maki *et al.*, 1992). In this way the enrichment of oxides of additional elements can reduce the oxidation rate, providing that the diffusion through such oxides is slower than through  $\text{TiO}_2$ . However, before this enrichment becomes effective, considerable oxidation takes place.

#### *Maintaining the initially formed $\text{Al}_2\text{O}_3$ scale*

The influence of additional elements so far discussed appears in Stage II of the oxidation: see Fig. 11.8. However, maintaining the initially formed  $\text{Al}_2\text{O}_3$  scale, or keeping Stage I, is more effective. The addition of 0.2 mass% Zr or Hf seems to fall in this category. Modification of the  $\text{Al}_2\text{O}_3$  scale by minor addition of Zr or Hf has often been discussed for the oxidation of Fe-20Cr-5Al (mass%) alloys containing these minor elements. They form very protective  $\text{Al}_2\text{O}_3$  scales. The fundamental points are as follows. The additives (i) enhance the nucleation of  $\text{Al}_2\text{O}_3$  grains at the beginning of oxidation, increasing the purity of the  $\text{Al}_2\text{O}_3$  scale, (ii) reduce the scale growth stress, and (iii) slow the diffusion of oxygen along grain boundaries of the scale. These seem applicable to the oxidation of TiAl; (i) results in the scale without  $\text{TiO}_2$  grains, (ii) prevents mechanical failure of the scale, which seems a reason for the transition to Stage II, and (iii) stabilises the Z phase by preventing its supersaturation with oxygen.

#### *Formation of the Laves phase*

A small addition of Cr enhances the oxidation; however, the addition of a large amount of Cr, e.g. 15 at%, to TiAl with nearly stoichiometric compositions resulted in protective  $\text{Al}_2\text{O}_3$  scales. Such alloys consisted of the Laves phase,

$\text{Ti(Al,Cr)}_2$ , and the  $\gamma$  phase (Brady *et al.*, 1997). The presence of the Laves phase stabilised the protective  $\text{Al}_2\text{O}_3$  scale. However, the Laves phase is brittle, so its influence on the mechanical properties should be carefully examined. If this phase degrades the mechanical properties, it can only be used as a coating.

### *Halogen effect*

Since halogen and halogen compounds, in general, enhance corrosion of metallic materials at room temperature and also at elevated temperatures, they should be avoided in the service environment. However, Fig. 11.14 indicates that a minor addition of Cl improves the oxidation resistance remarkably, by forming protective  $\text{Al}_2\text{O}_3$  scales (Kumagai *et al.*, 1993). This specimen was made by HIP of Ti and Al powders. The Ti powders were produced by a Hunter method, so Cl was included as fine NaCl particles in micropores. Halogen or halogen compounds cannot be included during ordinary ingot-metallurgy processes. Since this finding, details of this effect have been extensively studied by using an ion implantation technique (Schütze and Hald, 1997; Taniguchi *et al.*, 2001b) which allowed introduction of halogen elements into the surface layer of TiAl with controlled distributions. The halogen effect was also confirmed by pre-treatment of a TiAl specimen in NaCl vapour-containing atmosphere (Hara and Kitagawa, 1998) or in a dilute HF solution (Zschau *et al.*, 2003). Regarding the effect of implantation of Cl ions, the specimen formed a protective  $\text{Al}_2\text{O}_3$  scale which stood at least for 20 cycles (400 h) at 1200 K in oxygen (Taniguchi *et al.*, 2001b).

As a mechanism for improvement, for instance, preferential chlorination of Al over Ti was proposed on the basis of thermodynamic considerations (Schütze and Hald, 1997; Schütze *et al.*, 2002). There is a situation where Al is preferentially chloridised in the subsurface zone of the specimen, and Al-chloride vapour is converted to  $\text{Al}_2\text{O}_3$  when it enters the oxide scale where the oxygen potential is high enough to form the oxide. This view is also applicable to F, Br and I.

### *Formation of the $\beta$ phase*

To make TiAl alloys consisting of the  $\gamma$  and  $\beta$  phases seems better, because the diffusion of Al in the  $\beta$  phase, which is a bcc solid solution, seems much faster than in the  $\gamma$  phase of ordered structure. Therefore, large amounts of  $\beta$  former elements may improve the oxidation resistance. This view was confirmed experimentally (Perkins *et al.*, 1987) and addition of 15 mass% Cr or 30 mass% V, or combined addition of these elements, led to excellent oxidation resistance at 1673 K, though this did not work at 1373 K, which is far higher than the application temperature. However, a thin surface layer of

the  $\beta$  phase was formed by ion implantation, and this will be discussed in the next section.

### 11.2.8 Surface treatments

Surface treatment is a possible way to obtain sufficient resistance against environmental attack, including oxidation, without spoiling the required mechanical properties of the substrate. Though surface treatment incurs additional cost, it should be used where the required performance cannot be obtained by other methods such as controlling microstructure and/or alloying additions under severe service conditions. Therefore, it seems better to review a range of surface treatments for a wide choice.

#### *Diffusion coating*

A traditional surface treatment for improving oxidation resistance is pack cementation or diffusion coating such as aluminising, chromising and siliconising. Protective  $\text{Al}_2\text{O}_3$  scales grew on  $\text{TiAl}_3$  layers which had been formed on TiAl by aluminising (Yoshihara *et al.*, 1991; Jung and Kim, 2002; Gauthier *et al.*, 2003). Though the resistance to cycle oxidation of such a coated specimen is excellent, it degrades after a certain period of oxidation due to diffusion of Al into the substrate, e.g. a breakaway kinetics sets in after about 450 ks in 18 ks-cycle oxidation at 1173 K in air (Yoshihara *et al.*, 1991). On the other hand, cracking took place in the coating on specimen corners (Yoshihara *et al.*, 1991) or flat areas (Jung and Kim, 2002), depending on the aluminising conditions. This was attributed to the brittle nature of  $\text{TiAl}_3$ . To overcome this difficulty, small amounts of V, Cr, Fe or Nb were added to TiAl substrates (Jung and Kim, 2002) with a view that these elements will enter the  $\text{TiAl}_3$  coating and modify its structure from brittle  $\text{DO}_{22}$  to more ductile  $\text{L1}_2$ , but this trial failed.

Aluminising by other methods was also tried. Electrodeposition of Al onto TiAl in molten salt resulted in the formation of a  $\text{TiAl}_3$  layer free of cracking (Fukumoto *et al.*, 2004). This coating showed excellent oxidation resistance in cyclic oxidation at 1273 K in air. On the other hand, combination of sputter deposition of Al and subsequent annealing to form a  $\text{TiAl}_3$  layer failed in an oxidation test (Chu and Wu, 2005). Researches on chromising and siliconising have been very few and no improvement in the oxidation resistance was reported.

#### *Pre-oxidation*

Preferential oxidation of Al would occur in a low  $P_{\text{O}_2}$  atmosphere despite the small difference in Gibbs energy of formation between  $\text{TiO}_2$  and  $\text{Al}_2\text{O}_3$ .

Pre-oxidation under low  $P_{O_2}$  attained by a vacuum pump resulted in the formation of  $Al_2O_3$  scales (Kobayashi *et al.*, 1990; Yoshihara *et al.*, 1991). During the subsequent oxidation in air they were protective for certain periods of time, followed by breakaway oxidation. The pre-oxidation in atmosphere of much lower  $P_{O_2}$ , led to the formation of much more protective  $Al_2O_3$  scales. This was attained by the oxidation of specimens which were encapsulated in a silica tube with powders of  $Cr_2O_3 + Cr$  (Taniguchi *et al.*, 1992),  $Cr_2O_3$  (Taniguchi *et al.*, 1994c),  $SiO_2$  (Taniguchi *et al.*, 1994a) or  $TiO_2$  (Taniguchi *et al.*, 1994b), and heated at 1200 K for 100 ks. Such specimens stood for a long time during cyclic oxidation at 1300 K in oxygen. A combination of addition of 0.2 mass% Hf and pre-oxidation of this kind gave excellent oxidation resistance (Taniguchi *et al.*, 1995).

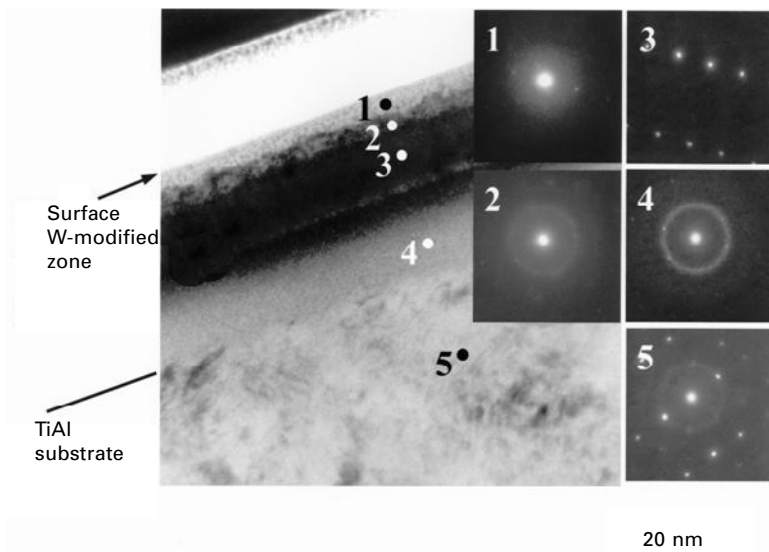
Treatment in a fluidised bed of  $Al_2O_3$  powders with  $Cr_2O_3$ ,  $Nb_2O_5$  or  $WO_3$  powders as additives at 973–1323 K for 7.2 ks improved the oxidation resistance; excellent resistance was obtained with  $WO_3$  powders (Kawaura *et al.*, 1999). For this case a combination of surface alloying, mechanical working by tumbling powders and pre-oxidation in a low  $P_{O_2}$  atmosphere seems to have given a good synergy.

### *Ion implantation*

Ion implantation enables considerable enrichment of an additional element in a thin surface layer of a depth of up to a few hundred nanometres without changing bulk properties. Almost all the elements can be implanted. The depth of implanted element depends on its mass, acceleration voltage and dose. For example, Nb enters to a depth of 100 nm, with a maximum concentration of 42 at% at a depth of 70 nm, with a near-Gaussian distribution by implantation of Nb ions of a dose of  $10^{21}$  ions · m<sup>-2</sup> at 50 keV (Taniguchi *et al.*, 1998a). It is noteworthy that the depth is small but the concentration is very high. The modified surface layer is very thin, but the scale formed by this method is protective for a very long time.

The implanted depth seems more important than the concentration when it exceeds a certain value. The ion dose and the implantation depth of the element can be well controlled by adjusting the implantation conditions. In this respect, ion implantation is an excellent research tool.

Extensive research (Schütze and Hald, 1997; Schütze *et al.*, 2002; Taniguchi *et al.*, 1999a, 2001b, 2004; Schumacher *et al.*, 1999; Haanappel and Stroosnijder, 1999; Lei *et al.*, 2002; Yoshihara and Taniguchi, 2005) was carried out for more than 25 elements and the results allow the following grouping according to the influence on oxidation resistance.  $\beta$ -phase stabilisers such as Nb, Mo, Ta and W have an excellent effect by forming a thin  $\beta$ -phase layer on TiAl as shown in Fig. 11.16 (Taniguchi *et al.*, 2004). Diffusion of Al in this phase seems much faster than in TiAl. Such specimens form very



11.16 TEM bright field image and electron diffraction patterns of a W-implanted (100 keV,  $10^{21}$  ions · m $^{-2}$ ) TiAl specimen. 1: amorphous; 2: amorphous +  $\beta$ -Ti; 3:  $\beta$ -Ti; 4:  $\beta$ -Ti; 5: TiAl (Taniguchi *et al.*, 2004).

protective Al<sub>2</sub>O<sub>3</sub> scales during initial periods of oxidation and maintain excellent oxidation resistance even in cyclic oxidation at 1200 K for a long time. Halogens such as F, Cl, Br and I result in protective Al<sub>2</sub>O<sub>3</sub> scales as already shown under the heading ‘Halogen effect’ in Section 11.2.7. Al, Si, P, Cu, Zn, Y and Er show little or no improvement, and B, C, N, Mg, Ar, Ti, V, Cr, Fe, Se, Zr and Ag degrade the oxidation resistance. There are slight disagreements among the literature depending on oxidation conditions.

The above results were obtained for binary TiAl alloys. There might be some difference when the specimen contains alloying additions. However, combined implantation gave more influence. For instance, single implantation of C is ineffective, but combined implantation of C + Nb (Li *et al.*, 2001a) is very effective. High temperature implantation of Nb (Li *et al.*, 2001b) and high-temperature combined implantation of Al + Nb (Li *et al.*, 2002) improved the oxidation resistance to some degree.

The disadvantage of ion implantation is that the ion beam runs straight in ordinary processing, so it is inefficient to apply to objects with curved surfaces or complex shapes, even by combining rotation or use of multi-ion sources. However, it is noteworthy that plasma-based ion implantation (Zhu *et al.*, 2002) was tried and F ions were implanted to a model turbocharger wheel. The oxidation resistance obtained was the same as that for the flat plate of the same material. Research is being carried out to apply this method to metal ions.

### *Overlay coating*

A few kinds of MCrAl(Y) type coatings with thickness of around a few tens of microns have been tested including CoCrAl (Taniguchi *et al.*, 1993a), FeCrAlY (Bennett and Bull, 1997) and Ti-50Al-15Cr (Zhou *et al.*, 2001) by magnetron sputtering. The coatings improved the oxidation resistance to some degree and the effect became small as the oxidation temperature was increased to 1273 K. These coatings form Al<sub>2</sub>O<sub>3</sub> scales on exposure and the breakaway takes place when the Al content decreases to a critical value or the supply of Al from the substrate becomes insufficient. The fundamental idea of MCrAl(Y) type coating is to form Al<sub>2</sub>O<sub>3</sub> scales by the oxidation of Al in the coating; therefore the diffusion of Al to the substrate should be prevented if long-term protection is needed, and also to prevent the diffusion of substrate elements to the coating for stabilisation of the microstructure. A barrier layer, e.g. CrN (Du *et al.*, 2003), was formed between the coating and the substrate to prevent diffusion of Al to the substrate.

In addition, a large difference in chemical potential of the relevant elements between the coating and the substrate should be avoided, to reduce the driving force of their diffusion. TiAlCrYN coating on a TiAl alloy (Leyens *et al.*, 2003) seems reasonable in this respect. Some MCrAl(Y) coatings are not dense and thus micropores are developed at boundaries of columnar grains or at the Al<sub>2</sub>O<sub>3</sub>/coating interface. This degrades the protectiveness of the coating.

Several types of ceramic coatings were examined including Si<sub>3</sub>N<sub>4</sub> coating by ion beam enhanced deposition (Taniguchi *et al.*, 1993c), SiO<sub>2</sub> coating by a sol-gel method (Taniguchi *et al.*, 1993b) and Al<sub>2</sub>O<sub>3</sub> coating by thermal chemical vapour deposition (CVD) (Taniguchi *et al.*, 1991b). All the coatings except for the CVD-Al<sub>2</sub>O<sub>3</sub> coating were cracked during the initial oxidation stages. However, the coated specimens showed good oxidation resistance, because the protective Al<sub>2</sub>O<sub>3</sub> scales were formed beneath the coatings, before the damage became significant. The CVD-Al<sub>2</sub>O<sub>3</sub> coating was very dense and very adherent to the substrate, and hence kept excellent oxidation resistance.

Thin coatings of BaTiO<sub>3</sub>, SrTiO<sub>3</sub> or CaTiO<sub>3</sub> were formed by hydrothermal treatment of TiAl in aqueous solutions of Ba(OH)<sub>2</sub>, Sr(OH)<sub>2</sub> or Ca(OH)<sub>2</sub> + NaOH respectively at 473 K (Yoshimura *et al.*, 1993, 1995). As the oxidation resistance was poor in the as-coated state, they were annealed in a vacuum at 1173–1473 K, then an Al<sub>2</sub>O<sub>3</sub> layer of a few microns thickness was formed beneath the coating. These specimens endured cyclic oxidation at 1173 K.

### *Sulphidation treatment*

The sulphidation of TiAl in a gas mixture of H<sub>2</sub> and H<sub>2</sub>S formed titanium sulphides on its surface. As a result of this, Al was enriched beneath the

sulphide layer. The oxidation of the specimen after removal of these sulphides led to the formation of a protective  $\text{Al}_2\text{O}_3$  scale (Narita and Yoshioka, 1994). Even Al can be enriched by aluminising; this method forces Al to enter the substrate, generating internal stresses. Consequently,  $\text{TiAl}_3$  thus formed is prone to cracking. In contrast, in the sulphidation Ti was removed from the surface layer and  $\text{TiAl}_3$  was formed as a consequence of the sulphidation without causing high stress, therefore  $\text{TiAl}_3$  remained sound.

### 11.2.9 Control of microstructure and surface roughening

Grain refining of the substrate and surface working by polishing, sand blasting or shot peening are effective for Cr- or Al-containing steels to form protective scales rich in  $\text{Cr}_2\text{O}_3$  or  $\text{Al}_2\text{O}_3$ , respectively. The influence of microstructure has also been studied for binary TiAl alloys (Umehara and Togawa, 1992; Umehara and Koshizaki, 1997; Kasahara and Takei, 1993; Gil *et al.*, 1993). Their oxidation resistance increases with increasing Al content. However, the results are not clear-cut. For instance, a cast alloy has better oxidation resistance than a forged alloy of the same lot (Gil *et al.*, 1993). This was explained in terms of the Al content in the  $\alpha_2$  phase, which was larger for the cast alloy and became small by heat treatment.

The grain size also influences the oxidation behaviour depending on the microstructure. Cast materials sometimes have large  $\gamma$  grains and lamellar grains. Because of the large difference in the Al content between  $\gamma$  and  $\alpha_2$  grains,  $\text{Al}_2\text{O}_3$  forms on  $\gamma$  grains and  $\text{TiO}_2$  grows on  $\alpha_2$  grains. However, a continuous  $\text{Al}_2\text{O}_3$  scale is formed on lamellar grains when the widths of lamellae are decreased by heat treatment, probably owing to the enhanced Al diffusion along the  $\gamma/\alpha_2$  interface which is increased by the treatment.

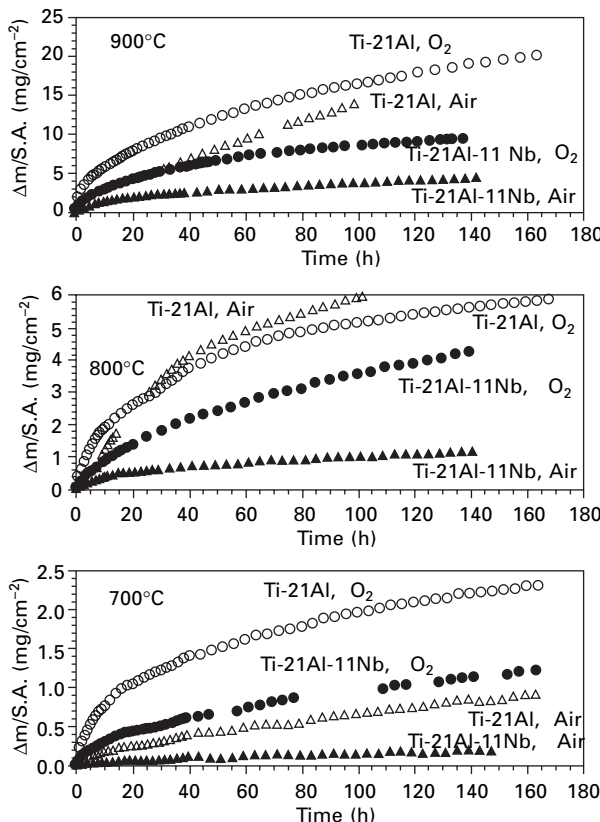
Surface polishing or roughening is effective in some cases, e.g. a combination of high Al content (Ti-50Al) and surface polishing (Copland *et al.*, 1999). Enhanced diffusion of Al by lattice defects and dislocations, increased by the treatment, seems to be the reason. Therefore, the influence of microstructure and surface roughening becomes small as the oxidation temperature rises. At higher temperatures the lattice defects and dislocations are minimised, and fine grains grow to large ones.

## 11.3 Oxidation characteristics of $\text{Ti}_3\text{Al}$ and $\text{Ti}_3\text{Al-Nb}$ alloys

$\text{Ti}_3\text{Al}$  alloys have lower oxidation resistance than TiAl alloys owing to the lower Al content, and the former have lower mechanical strengths than the latter. Therefore, their potential application temperature seems lower than that for TiAl alloys, i.e. up to around 1000 K, or they would be substitutes of current high-temperature Ti alloys. Since stoichiometric  $\text{Ti}_3\text{Al}$  is very

brittle at room temperature,  $\beta$ -stabilising elements such as V, Nb, Mo, Ta or W should be added to it. As Nb has the largest effect in this respect, almost all candidate Ti<sub>3</sub>Al alloys contain Nb.

The following conclusions can be drawn from a survey of the literature regarding oxidation behaviour (Wallace *et al.*, 1992; Rakowski *et al.*, 1993; Gauer *et al.*, 1994; Koo *et al.*, 1994; Dettenwanger and Schütze, 2000). In general, Ti<sub>3</sub>Al oxidises much faster than Ti<sub>3</sub>Al-Nb alloys in air and in oxygen under atmospheric pressure under the same conditions. Both kinds of alloys oxidise faster in oxygen than in air. These tendencies can be seen in Fig. 11.17 (Rakowski *et al.*, 1993), showing an example of oxidation curves. The influence of Nb on the oxidation characteristics is similar for Ti<sub>3</sub>Al and for TiAl; (a) Nb is dissolved in TiO<sub>2</sub>, reducing its growth rate according to the valence control rule, (b) Nb enhances the formation of a nitride layer on the substrate surface, and (c) Nb is enriched in the subsurface zone as the oxidation



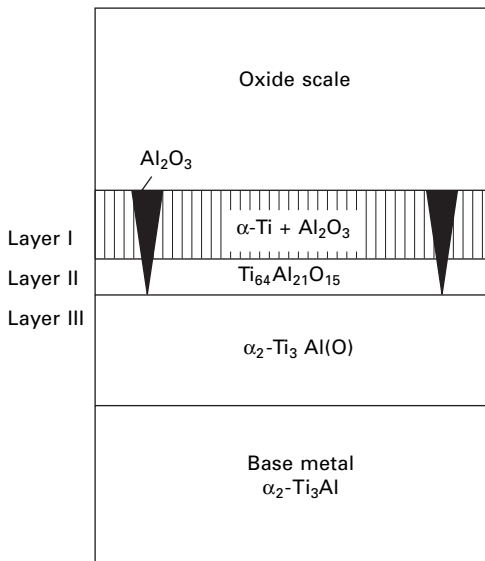
11.17 Oxidation curves of Ti-21Al and Ti-21Al-11Nb (at%) in air and in oxygen (from Rakowski *et al.*, 1993, reproduced with permission).

progresses. The overall oxidation rate is therefore reduced by the Nb addition. For the difference in the oxidation behaviour between oxidation in air and in oxygen, the influence of nitrogen has been pointed out, as in the case of TiAl. Actually, thin continuous TiN layers were found covering the substrate surfaces in air oxidation. These nitride layers can slow down the diffusion of oxygen and metal, resulting in better oxidation resistance. Nb is enriched at the scale/substrate interface by the oxidation of Ti and Al, which enhances the nitride formation. The formation of nitride in air implies that the scale is not completely dense. The thickness of the nitride layer remains almost constant during the oxidation, suggesting steady formation of nitride and its oxidation.

The oxidation curves are nearly parabolic, in general, with occasional turbulences in some cases due to local and partial mechanical failure of the scale. The failure often observed is partial scale spallation. When this failure is repeated, the scale shows a layered structure. Nb-containing alloys are more resistant to partial spallation. The rate constants obtained on the assumption of parabolic oxidation are situated near the midpoints between  $\text{TiO}_2$ -forming kinetics and  $\text{Al}_2\text{O}_3$ -forming kinetics in Arrhenius plots (Rowe, 1990; Wallace *et al.*, 1992; Koo *et al.*, 1994), giving activation energies ranging from 210 to 310  $\text{kJ}\cdot\text{mol}^{-1}$ , depending on the additives.

The structure of the scale on  $\text{Ti}_3\text{Al}$  is similar to that on TiAl (see Fig. 11.7), except that the scale on  $\text{Ti}_3\text{Al}$  is much thicker and no definite  $\text{Al}_2\text{O}_3$ -rich layer is formed. However, the scale on  $\text{Ti}_3\text{Al}$ -Nb alloys is somewhat different. There is some enrichment of  $\text{Al}_2\text{O}_3$  in an outer thin layer of the scale, and the other part of the scale consists primarily of  $\text{TiO}_2$ , though this enrichment does not provide protectiveness.

The oxidation of  $\text{Ti}_3\text{Al}$  and its alloys is accompanied by the dissolution of oxygen and nitrogen in the subsurface zone, resulting in the embrittlement of the materials. For instance the hardness of this zone is more than 400 in the Knoop scale after oxidation at 1193 K, in contrast to the value of 150 for the intact substrate. This embrittlement is alleviated to some degree by addition of Nb. In addition to this embrittlement, the formation of internal oxides occurs as shown in Fig. 11.18 (Dettenwanger, 2000), which indicates the details of the microstructure around the scale/substrate interface confirmed by TEM observations. Here, Layer I beneath the scale consists of  $\alpha$ -Ti with dissolved oxygen and  $\text{Al}_2\text{O}_3$  as internal oxides.  $\text{Al}_2\text{O}_3$  is discontinuous and in the form of platelets orientating almost normal to the substrate, so these  $\text{Al}_2\text{O}_3$  platelets cannot provide protectiveness. Some of them are like large pegs reaching to the next layer. There is Layer II, which seems to consist of the Z phase. The formation of these  $\text{Al}_2\text{O}_3$  pegs and the compound with dissolved oxygen are the causes of the embrittlement by the oxidation. The structure of scales formed in air is similar to that formed in oxygen, except for a thin and continuous adherent nitride layer.



11.18 Structure of subsurface zone of  $\text{Ti}_3\text{Al}$  after oxidation (from Dettenwanger and Schütze, 2000, reproduced with permission).

Researches on the influence of alloying additions have been rather few for  $\text{Ti}_3\text{Al}$  alloys. A possible reason is that most candidate alloys contain Nb which improves the oxidation resistance to some degree, and thus there is little room for further improvement by a further addition. Additions to Ti-25Al-10Nb (at%) were tried (Koo *et al.*, 1994) with results that 0.5 at% Si or 0.3 at% Cr improves the oxidation resistance slightly at 973 and 1073 K, but 0.5 at% Y is effective only at 1173 K.

Important conclusions that  $\text{Al}_2\text{O}_3$  scales cannot be formed on  $\text{Ti}_3\text{Al}$  alloys by alloying addition only and that dissolution of oxygen in the subsurface zone should be avoided necessitate protective coatings for use at relatively high service temperatures and for long periods. In order to circumvent these disadvantages, coatings have been tested. For example, oxidation curves of Ti-24Al-12.5Nb-1.5Mo (at%) coated with Fe-24Cr-8Al-0.5Y or Co-30Cr films with a thickness of 80  $\mu\text{m}$  by plasma spraying showed good oxidation resistance at 1088 K in air, and embrittlement was significantly reduced (McKee, 1993). In these coatings, a W film with a thickness of 1–2  $\mu\text{m}$  was inserted for preventing interdiffusion between the coating and the substrate. The oxidation rate was significantly reduced by the coating. The oxidation resistance was also increased by coating of Fe-15Cr-5Al-0.3Y made by sputter ion plating (Bennett and Bull, 1997). Densification of the film by shot peening gave better oxidation resistance.

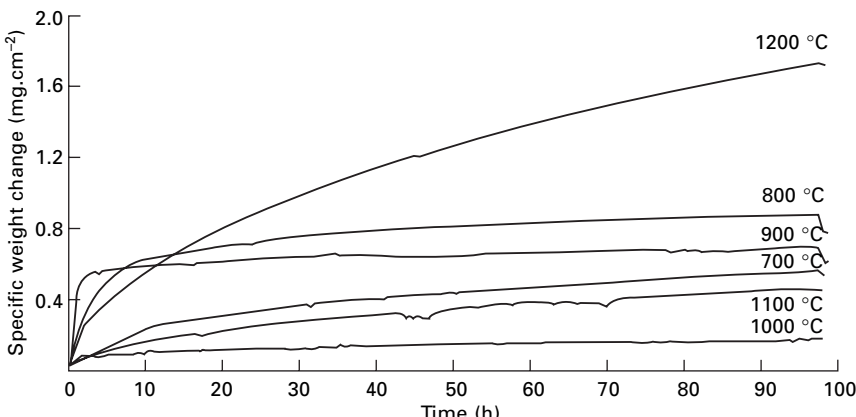
Diffusion coating has also been studied. Aluminising of Ti-14Al-24Nb (mass%) (Subrahmanyam, 1988) improved the resistance of cyclic oxidation.

Similarly the application of  $\text{TiSi}_2$  by siliconising (Cockeram and Rapp, 1996) improved the oxidation resistance, and addition of B or Ge to the film further improves it. Silica formed during oxidation, giving some protectiveness, and kinetics were a little slower than in the oxidation of  $\text{Ti}_5\text{Si}_3$  and a little faster than  $\text{SiO}_2$ -forming kinetics.

### 11.4 Oxidation characteristics of $\text{TiAl}_3$ -base alloys

Studies on oxidation of  $\text{TiAl}_3$  and its alloys have been performed using bulk specimens and those formed by aluminising. Figure 11.19 (Smialek and Humphrey, 1992) shows isothermal oxidation curves of  $\text{TiAl}_3$ , made by arc melting and drop casting, in  $\text{O}_2$  of atmospheric pressure. Each curve follows a nearly parabolic manner except for the initial periods where the oxidation is relatively fast and with some slight turbulence in the curve. However, its temperature dependence is quite complex. The initial rapid mass gains below 1273 K were explained in terms of the presence of unreacted Al as a second phase in the original specimen. The second phase was in a liquid state at the oxidation temperatures. The type of  $\text{Al}_2\text{O}_3$  detected was  $\alpha\text{-Al}_2\text{O}_3$ , and no transient aluminas such as  $\gamma$ -,  $\delta$ - and  $\theta\text{-Al}_2\text{O}_3$ , often observed in the oxidation of high-Al materials such as NiAl, were detected. Alumina scales grow from the beginning of oxidation at 1273–1473 K with parabolic rate constants which are the same as those of typical alumina forming alloys.

$\text{TiAl}_3$  is very brittle because of its crystal structure. Research has been carried out into improving its ductility by changing the crystal structure from  $\text{DO}_{22}$  to  $\text{L1}_2$  by alloying addition (Parfitt *et al.*, 1991). At the same time the



11.19 Oxidation curves of  $\text{TiAl}_3$  in oxygen under atmospheric pressure (from Smialek and Humphrey, 1992, reproduced with permission).

influence of the crystal structure of  $TiAl_3$  on the oxidation properties is also important. Elements such as Cr, Mn, Fe, Ni and Cu are known to improve the ductility. Addition of 8 at% Cr improves the oxidation resistance to the level of that of  $NiAl$ . On the contrary, small additions of Mn or Mn + V accelerate the oxidation remarkably. This again shows a difficulty in compatibility of alloying elements between mechanical property and oxidation resistance.

## 11.5 Future trends

As a result of extensive research activity on Ti-Al alloys, we now have a high level of freedom in controlling the microstructure, adjusting alloying additions and choosing suitable surface treatment. This allows us to manufacture parts with desired mechanical properties and sufficient resistance to environmental attack at the laboratory level. Nevertheless, without carrying out tests under practical conditions, we cannot go forward with candidate alloys. Tests under exact and specified application conditions for individual parts are necessary, where the parts are under mechanical stress and exposed to severe conditions of varying temperature and gas composition. These conditions would be very different from those of laboratory tests where gas composition is usually constant, there is no mechanical loading, and the temperature change is regular even in cyclic oxidation. The oxidation temperatures have been a little higher than those practical in many researches, even though data over a wide range of temperatures are needed for accessing activation energy or mechanistic study. In other words, we need more practical experience and, by collecting, examining and/or dissecting the problems arising from the practical usage, more efficient development of individual components or parts is possible.

On the other hand, it can be said from a scientific viewpoint that data for fundamental parameters are lacking. For instance, the influence of additional elements on diffusivity and activity of relevant elements is poorly known. Phase equilibrium diagrams of tertiary and quaternary systems are very few. These are indispensable for theoretical understanding of the phase relations. The mechanism of the influence of combined addition of alloying elements is unclear, although the most suitable combination would be made from the viewpoints of production cost, environmental protection and high performance.

## 11.6 Acknowledgements

The author sincerely thanks the following institutions and publishers for granting reproduction of the table and figures cited in this chapter: The Minerals, Metals and Materials Society for Table 11.1, *ASM International* for Fig. 11.2, The Ceramic Society of Japan for Fig. 11.3, Elsevier Limited for Figs 11.4, 11.5 and 11.19, The Japan Institute of Metals for Figs 11.13

and 11.15, The Institute of Materials for Fig. 11.17, and *Oxidation of Metals* for Fig. 11.18.

## 11.7 References

- Aitken E A (1967), ‘Corrosion behavior’ in Westbrook J H, *Intermetallic Compounds*, New York, John Wiley & Sons, 491–516.
- Akai M, Taniguchi S and Shibata T (1996), ‘Oxidation characteristics of Ti-14Al-21Nb (mass%) alloy in N<sub>2</sub>-O<sub>2</sub> at high temperatures’, *Zairyo-to-Kankyo*, **45** (11), 646–653.
- ASM (1990), *Binary Alloy Phase Diagrams*, Second Edition, plus updates, on CD-ROM, The Materials Information Center, ASM International.
- Austin C M and Kelly T J (1995), ‘Progress in implementation of cast gamma titanium aluminide’, *Gamma Titanium Aluminides*, Las Vegas, TMS.
- Bartolotta P A and Krause D L (1999), ‘Titanium aluminide applications in the high speed civil transport’, *Gamma Titanium Aluminides 1999*, San Diego, TMS.
- Baur H, Wortberg D B and Clemens H (2003), ‘Titanium aluminides for automotive applications’, *Gamma Titanium Aluminides 2003*, San Diego, TMS.
- Becker S, Rahmel A, Schörr M and Schütze M (1992), ‘Mechanism of isothermal oxidation of the intermetallic TiAl and of TiAl alloys’, *Oxid Met*, **38** (5/6), 425–464.
- Bennett M J and Bull S J (1997), ‘Protection of titanium aluminides by FeCrAlY coatings’, *Mater Corros*, **48** (1), 48–55.
- Blum M, Busse P, Jarczyk G, Franz H, Laudenberg H J, Segtrop K and Seserko P (2003), ‘First production results from a prototype plant for mass production of γ-TiAl valves’, *Gamma Titanium Aluminides 2003*, San Diego, TMS.
- Brady M P, Smialek J L, Smith J and Humphrey D L (1997), ‘The role of Cr in promoting protective alumina scale formation by γ-based Ti-Al-Cr alloys – I. Compatibility with alumina and oxidation behavior in oxygen’, *Acta Mater*, **45** (6), 2357–2369.
- Chu M S and Wu S K (2005), ‘Oxidation behavior of Ti-50Al intermetallics with thin TiAl<sub>3</sub> film at 1000°C’, *Oxid Met*, **63** (1/2), 1–13.
- Cockeram B and Rapp R A (1996), ‘Isothermal and cyclic oxidation resistance of boron-modified and germanium-doped silicide coatings for titanium alloys’, *Oxid Met*, **45** (5/6), 427–468.
- Copland E H, Gleeson B and Young D J (1999), ‘Formation of Z-Ti<sub>50</sub>-Al<sub>30</sub>-O<sub>20</sub> in the sub-oxide zones of γ-TiAl based alloys during oxidation at 1000°C’, *Acta Mater*, **47** (10), 2937–2949.
- Das G, Bartolotta P A, Kestler H and Clemens H (2003), ‘The development of sheet gamma TiAl technology under the enabling propulsion materials/high speed civil transport (EPM/HSCT) program’, *Gamma Titanium Aluminides 2003*, San Diego, TMS.
- Dettenwanger F, Schumann E, Rakowski J, Meier G H and Rühle M (1996), ‘Development and microstructure of the Al-depleted layer of oxidized TiAl’, *Mater Corros*, **48** (1), 23–27.
- Dettenwanger F and Schütze M (2000), ‘Isothermal oxidation of α<sub>2</sub>-Ti<sub>3</sub>Al’, *Oxid Met*, **54** (1/2), 121–138.
- Du H L, Datta P K, Griffin D, Aljarany A and Burnell-Gray J S (2003), ‘Oxidation and sulfidation behavior of AlTiN-coated Ti-46.7Al-1.9W-0.5Si intermetallic with CrN and NbN diffusion barriers at 850°C’, *Oxid Met*, **60** (1/2), 29–46.
- Figge U, Elschner A, Zheng N, Schuster H and Quadakkers W J (1993), ‘Surface analytical

- investigations on the oxidation behaviour of TiAl-base intermetallics', *Fresenius J Anal Chem*, **346** (1–3), 75–78.
- Froes F H, Suryanarayana C and Eliezer D (1992), 'Synthesis, properties and applications of titanium aluminides', *J Mater Sci*, **27** (19), 5113–5140.
- Fukumoto M, Hara M and Nagataki T (2004), 'Effect of Al electrodeposition treatment using molten salt on the high-temperature oxidation of TiAl', *Oxid Met*, **61** (1/2), 1–16.
- Gauer L, Alperine S, Steinmetz P and Vassel A (1994), 'Influence of niobium additions on high-temperature oxidation behavior of Ti<sub>3</sub>Al alloys and coatings', *Oxid Met*, **42** (1/2), 49–74.
- Gauthier V, Dettenwanger F, Schütze M, Shemet V and Quadakkers W J (2003), 'Oxidation-resistant aluminide coatings on  $\gamma$ -TiAl', *Oxid Met*, **59** (3/4), 233–255.
- Gil A, Wallura E, Grubmeier H and Quadakkers W J (1993), 'The influence of cooling rate during alloy casting on the oxidation behaviour of TiAl-based intermetallics', *J Mater Sci*, **28** (21), 5869–5874.
- Grabke H J and Schütze M (1996), *Oxidation of Intermetallic Compounds*, Weinheim, Wiley-VCH.
- Grobstein T and Doychak J (1989), *Oxidation of High-Temperature Intermetallics*, Warrendale, PA, TMS.
- Haanappel V A C and Stroosnijder M F (1999), 'Ion implantation technique as research tool for improving oxidation behavior of TiAl based intermetallic alloys', *Surface Engineering*, **15** (2), 119–125.
- Hanamura T, Ikematsu Y, Morikawa H and Takamura J (1991), 'Improvement of oxidation resistance and ductility in titanium aluminides by small addition of Vb or VIb elements', *Intermetallic Compounds* (JIMIS-6), Sendai, *Japan Inst Met*.
- Hara M and Kitagawa Y (1998), 'Effect of pre-oxidation in O<sub>2</sub> containing trace NaCl vapor on high temperature oxidation of TiAl' *Hyomengijutsu*, **49** (9), 101–102.
- Inaba H and Murata Y (1997), 'Analysis of interface reactions of TiAl/Al<sub>2</sub>O<sub>3</sub> and TiAl/TiO<sub>2</sub> by the use of chemical potential diagram', *J Ceramic Soc Japan*, **105** (9), 740–745.
- Izumi O (1991), *Intermetallic Compounds* (JIMIS-6), Sendai, *Japan Inst Met*.
- Jung H G and Kim K Y (2002), 'Effect of ternary elements on the oxidation behavior of aluminized TiAl alloys', *Oxid Met*, **58** (1/2), 197–216.
- Kasahara K, Hashimoto K, Doi H and Tsujimoto T (1989), 'Oxidation behavior of intermetallic compounds TiAl at high temperatures', *J Japan Inst Met*, **53** (1), 58–62.
- Kasahara K and Takei A (1993), 'Effect of microstructure on oxidation of TiAl intermetallic compound', *J Japan Inst Met*, **57** (5), 544–548.
- Kawaura H, Nishino K and Saito T (1999), 'New surface treatment using a fluidized bed for improving oxidation resistance of TiAl-base alloys', *J Japan Inst Met*, **63** (12), 1584–1590.
- Kim Y W (1995a), *Gamma Titanium Aluminides*, Las Vegas, TMS.
- Kim Y W (1995b), 'Trends in development of gamma TiAl alloys', *Gamma Titanium Aluminides*, Las Vegas, TMS.
- Kim Y W (1999), *Gamma Titanium Aluminides 1999*, San Diego, TMS.
- Kim Y W (2003), *Gamma Titanium Aluminides 2003*, San Diego, TMS.
- Kim Y W and Froes F H (1990), 'Physical metallurgy of titanium aluminides', *High Temperature Aluminides and Intermetallics*, Indianapolis, TMS.
- Kobayashi E, Yoshihara M and Tanaka R (1990), 'Improvement in oxidation resistance

- of the intermetallic compound titanium aluminide by heat treatment under a low partial pressure oxygen atmosphere', *High Temp Tech*, **8** (3), 179–184.
- Kofstad P (1983), *Nonstoichiometry, Diffusion, and Electrical Conductivity in Binary Metal Oxides*, Malabar, FL, Robert E. Krieger.
- Koo C H, Evans J W, Song K Y and Yu T H (1994), 'High-temperature oxidation of  $Ti_3Al-Nb$  alloys', *Oxid Met*, **42** (5/6), 529–544.
- Kremer R and Auer W (1997), 'Influence of moisture on the oxidation of  $\gamma$ -TiAl', *Mater Corros*, **48** (1), 35–39.
- Kumagai M, Shibue K and Kim M S (1993), 'Influence of minor elements on oxidation behavior of TiAl intermetallic compound', *J Japan Inst Met*, **57** (6), 721–725.
- Kussmaul A, Seifert H J, Golczewski J A, Lukas H L and Aldinger F (1998), 'Thermodynamic calculation of diffusion paths applied to the oxidation of  $\gamma$ -TiAl', *Z Metallkd*, **89** (10), 683–686.
- Larsen J M, Williams K A, Balsone S J and Stucke M A (1990), 'Titanium aluminides for aerospace applications', *High Temperature Aluminides and Intermetallics*, Indianapolis, TMS.
- Lee D B, Lee Y C, Kim Y J and Park S W (2000), 'The effect of  $Si_3N_4$  additions on the oxidation resistance of TiAl alloys', *Oxid Met*, **54** (5/6), 575–589.
- Lei M K, Zhu X P and Wang X J (2002), 'Oxidation resistance of ion-implanted  $\gamma$ -TiAl-base intermetallics', *Oxid Met*, **58** (3/4), 361–374.
- Leyens C, Braun R, Hovsepian P Eh and Müns W-D (2003), 'Environmental protection of gamma titanium aluminides', *Gamma Titanium Aluminides 2003*, San Diego, TMS.
- Li X L, Hillel R, Teyssandier F, Choi S K and Van Loo F J J (1992), 'Reactions and phase relations in the Ti-Al-O system', *Acta Metall Mater*, **40** (11), 3149–3157.
- Li X Y, Taniguchi S, Zhu Y C, Fujita K, Iwamoto N, Matsunaga Y and Nakagawa K (2001a), 'Effects of C, Nb and C + Nb combined ion implantation on the oxidation resistance of  $\gamma$ -TiAl based alloy', *Mater Sci Eng*, **A316**, 224–230.
- Li X Y, Zhu Y C, Fujita K, Matsunaga Y, Nakagawa K and Taniguchi S (2001b), 'Improvement of oxidation resistance of  $\gamma$ -TiAl based alloy by high temperature Nb implantation', *Mater High Temp*, **18** (S), 379–384.
- Li X Y, Taniguchi S, Zhu Y C, Fujita K, Iwamoto N, Matsunaga Y and Nakagawa K (2002), 'Oxidation behavior of TiAl protected by Al and Nb combined ion implantation at high temperature', *Nuclear Instr Methods Phys Res*, **B 187**, 207–214.
- Li X Y and Taniguchi S (2004), 'Oxidation behavior of TiAl based alloys in a simulated combustion atmosphere', *Intermetallics*, **12** (1), 11–21.
- Mabuchi H and Nakayama Y (1991), 'Development of Al-Ti-X ternary  $L1_2$  intermetallic compounds', *Bull Japan Inst Met*, **30** (1), 24–30.
- Maki K, Shioda M, Sayashi M, Shimizu T and Isobe S (1992), 'Effect of silicon and niobium on oxidation resistance of TiAl intermetallics', *Mater Sci Eng*, **A153** (1–2), 591–596.
- McKee D W (1993), 'Oxidation and protection of  $Ti_3Al$ -based intermetallic alloys', *Mat. Res. Soc., Symp. MRS*, **288**, 953–958.
- McKee D W and Huang S C (1992), 'The oxidation behavior of gamma-titanium aluminide alloys under thermal cycling conditions', *Corros Sci*, **33** (12), 1899–1914.
- Meier G H, Pettit F S and Hu S (1993), 'Oxidation behavior of titanium aluminides', *J Phys IV Colloque C9, supplément au Journal de Physique III*, **3** (Dec.), 395–402.
- Nakayama Y and Mabuchi H (1993), 'Formation of ternary  $L1_2$  compounds in  $Al_3Ti$ -base alloys' *Intermetallics*, **1** (1), 41–48.

- Narita T and Yoshioka T (1994), 'Sulfidation properties of Ti-Al intermetallic compounds in H<sub>2</sub>S-H<sub>2</sub> atmospheres', *Trans Mat Res Soc Japan*, **14**, 233–238.
- Noda T (1998), 'Application of cast gamma TiAl for automobiles', *Intermetallics*, **6** (7–8), 709–713.
- Parfitt L J, Smialek J L, Nic J P and Mikkola D E (1991), 'Oxidation behavior of cubic phases formed by alloying Al<sub>3</sub>Ti with Cr and Mn', *Scripta Metall Mater*, **25** (3), 727–731.
- Perkins R A, Chiang K T and Meier G H (1987), 'Formation of alumina on Ti-Al alloys', *Scripta Metall*, **21** (11), 1505–1510.
- Quadakkers W J, Schaaf P, Zheng N, Gil A and Wallura E (1997), 'Beneficial and detrimental effects of nitrogen on the oxidation behaviour of TiAl-based intermetallics' *Mater Corros*, **48** (1), 28–34.
- Rakowski J, Monceau D, Pettit F S, Meier G H and Perkins R A (1993), 'The oxidation and embrittlement of  $\alpha_2$  (Ti<sub>3</sub>Al) titanium aluminides', *Microscopy of Oxidation 2*, Cambridge, The Institute of Materials.
- Rakowski J, Pettit F S, Meier G H, Dettenwanger F, Schumann E and Rühle M, (1995) 'The effect of nitrogen on the oxidation of  $\gamma$ -TiAl', *Scripta Metall Mater*, **33** (6), 997–1003.
- Rowe R G (1990), 'Recent developments in Ti-Al-Nb titanium aluminide alloys', *High-Temperature Aluminides and Intermetallics*, Indianapolis, TMS.
- Sarrazin P, Motte F, Besson J and Coddet C (1978), 'Mécanisme d'oxydation du titane et de l'alliage TA6V4 par la vapeur d'eau', *J Less-Common Met*, **59** (2), 111–117.
- Schumacher G, Dettenwanger F, Schütze M, Hornauer U, Richter E, Wieser E and Möller W (1999), 'Microalloying effect in the oxidation of TiAl materials', *Intermetallics*, **7** (10), 1113–1120.
- Schütze M and Hald M (1997), 'Improvement of the oxidation resistance of TiAl alloys by using the chlorine effect', *Mater Sci Eng*, **A239–240**, 847–858.
- Schütze M, Schumacher G, Dettenwanger F, Hornauer U, Richter E, Wieser E and Möller W (2002), 'The halogen effect in the oxidation of intermetallic titanium aluminides', *Corros Sci*, **44** (2), 303–318.
- Shemet V, Tyagi A K, Becker J S, Lersch P, Singheiser L and Quadakkers W J (2000), 'The formation of protective alumina-based scales during high-temperature air oxidation of  $\gamma$ -TiAl alloys', *Oxid Met*, **54** (3/4), 211–235.
- Shida Y and Anada H (1993a), 'Oxidation behavior of binary Ti-Al alloys in high temperature air environment', *Mater Trans JIM*, **34** (3), 236–242.
- Shida Y and Anada H (1993b), 'The influence of ternary element addition on the oxidation behaviour of TiAl intermetallic compound in high temperature air', *Corros Sci*, **35** (5–8), 945–953.
- Shida Y and Anada H (1994), 'Role of W, Mo, Nb and Si on oxidation of TiAl in air at high temperatures', *Mater Trans JIM*, **35** (9), 623–631.
- Smialek J L and Humphrey D L (1992), 'Oxidation kinetics of cast TiAl<sub>3</sub>', *Scripta Metall Mater*, **26** (11), 1763–1768.
- Sommer A W and Keijzers G C (2003), 'Gamma TiAl and the engine exhaust valve', *Gamma Titanium Aluminides 2003*, San Diego, TMS.
- Subrahmanyam J (1988), 'Cyclic oxidation of aluminized Ti-14Al-24Nb alloy', *J Mater Sci*, **23** (6), 1906–1910.
- Sunderkötter J D, Gobel M, Haanappel V A C, Perez P and Stroosnijder M F (1999), 'The niobium effect on the oxidation behaviour of TiAl-based alloys: An approach to decouple relevant parameters', *Gamma Titanium Aluminides 1999*, San Diego, TMS.

- Taniguchi S, Shibata T and Itoh S (1991a), 'Oxidation behaviour of TiAl at high temperatures in purified oxygen', *Mater Trans JIM*, **32** (2), 151–156.
- Taniguchi S, Shibata T and Takeuchi K (1991b), 'Protectiveness of a CVD-Al<sub>2</sub>O<sub>3</sub> film on TiAl intermetallic compound against high-temperature oxidation' *Mater Trans JIM*, **32** (3), 299–301.
- Taniguchi S, Shibata T and Sakon S (1992), 'Improvement in oxidation resistance of TiAl by preoxidation at 1200 K in a pack mixture of Cr<sub>2</sub>O<sub>3</sub> and Cr powders', *Zairyo-to-Kankyo*, **41** (7), 453–460.
- Taniguchi S, Shibata T, Asanuma N, Lou H, Wang F and Wu W (1993a), 'Oxidation behavior of TiAl coated with a fine-grain Co-30Cr-4Al film', *Oxid Met*, **39** (5/6), 457–473.
- Taniguchi S, Shibata T and Katoh N (1993b), 'Improvement in the high-temperature oxidation resistance of TiAl by sol-derived SiO<sub>2</sub> coating', *J Japan Inst Met*, **57** (6), 666–673.
- Taniguchi S, Shibata T, Yamada T, Liu X H and Zou S C (1993c), 'High-temperature oxidation resistance of TiAl improved by IBED Si<sub>3</sub>N<sub>4</sub> coating', *ISIJ Intern*, **33** (8), 869–876.
- Taniguchi S, Shibata T and Murakami A (1994a), 'Improvement in the oxidation resistance of TiAl by preoxidation in a SiO<sub>2</sub>-powder pack', *Oxid Met*, **41** (1/2), 103–113.
- Taniguchi S, Shibata T, Murakami A and Chihara K (1994b), 'Improvement in the oxidation resistance of TiAl by preoxidation in a TiO<sub>2</sub>-powder pack', *Oxid Met*, **42** (1/2), 17–29.
- Taniguchi S, Shibata T, Murakami A and Chihara K (1994c), 'Improvement in the oxidation resistance of TiAl by preoxidation in a Cr<sub>2</sub>O<sub>3</sub> powder pack', *Mater Trans JIM*, **35** (9), 616–622.
- Taniguchi S, Shibata T and Sakon S (1995), 'Oxidation resistance of TiAl significantly improved by combination of preoxidation and Hf addition', *Mater Sci Eng*, **A198** (1–2), 85–90.
- Taniguchi S, Juso H and Shibata T (1996), 'Improvement in high-temperature oxidation resistance of TiAl by addition of 0.2 mass% Zr', *Mater Trans JIM*, **37** (3), 245–251.
- Taniguchi S, Uesaki K, Zhu Y C, Zhang H X and Shibata T (1998a), 'Influence of niobium ion implantation on the oxidation behaviour of TiAl under thermal cycle conditions', *Mater Sci Eng*, **A249** (1–2), 223–232.
- Taniguchi S, Juso H and Shibata T (1998b), 'Effect of Hf additions on the isothermal oxidation behavior of TiAl at high temperatures', *Oxid Met*, **49** (3/4), 325–348.
- Taniguchi S, Uesaki K, Zhu Y C, Matsumoto Y and Shibata T (1999a), 'Influence of implantation of Al, Si, Cr or Mo ions on the oxidation behaviour of TiAl under thermal cycle conditions', *Mater Sci Eng*, **A266**, 267–275.
- Taniguchi S, Hongawara N and Shiba T (1999b), 'Influence of gaseous species on the oxidation behaviour of TiAl at high temperatures', *Gamma Titanium Aluminides 1999*, San Diego, TMS.
- Taniguchi S, Fujimoto S, Katoh T and Shibata T (2000), 'TEM observation of the initial oxidation stages of TiAl and TiAl-0.2Zr', *Mater High Temp*, **17** (1), 35–40.
- Taniguchi S, Hongawara N and Shibata T (2001a), 'Influence of water vapour on the isothermal oxidation behaviour of TiAl at high temperatures', *Mater Sci Eng*, **A307** (1–2), 107–112.
- Taniguchi S, Fujioka T, Nakajima M, Shibata T, Yoshihara M and Zhu Y C (2001b), 'Improvement in the oxidation resistance of TiAl by ion implantation of a range of elements', *Mater High Temp*, **18** (S), 329–335.

- Taniguchi S, Yoshihara M and Fujita K (2004), 'Oxidation resistance of TiAl improved by ion implantation of beta-former elements', *Mater Trans*, **45** (5), 1693–1699.
- Umakoshi Y, Yamaguchi M, Sakagami T and Yamane T (1989), 'Oxidation resistance of intermetallic compounds  $\text{Al}_3\text{Ti}$  and TiAl', *J Mater Sci*, **24** (5), 1599–1603.
- Umeshara H and Koshizaki N (1997), 'Oxidation behavior of TiAl at high temperature in Ar-20%O<sub>2</sub> and N<sub>2</sub>-20%O<sub>2</sub>', *Zairyo-to-Kankyo*, **46** (7), 449–455.
- Umeshara H and Togawa Y (1992), 'High-temperature oxidation of intermetallic compounds of Ti-Al system' *Zairyo-to-Kankyo*, **41** (10), 684–689.
- Wagner C (1959), 'Reaktionstypen bei der Oxydation von Legierungen', *Zeitschrift für Elektrochemie*, **63** (7), 772–782.
- Wallace T A, Clark R K, Wiedemann K E and Sankaran S N (1992), 'Oxidation characteristics of Ti-25Al-10Nb-3V-1Mo', *Oxid Met*, **37** (3/4), 111–124.
- Welsch G and Desai P D (1996), *Oxidation and Corrosion of Intermetallic Alloys*, West Lafayette, Indiana, Metals Information Analysis Center, CINDAS, Purdue University.
- Welsch G, Smialek J. L, Doychak J, Waldman J and Jacobson NS (1996), 'High temperature oxidation and properties', in Welsch G and Desai P D, *Oxidation and Corrosion of Intermetallic Alloys*, West Lafayette, Indiana, Metals Information Analysis Center, CINDAS, Purdue University, 121–266.
- Whang S H (1990), *High-temperature Aluminides and Intermetallics*, Indianapolis, TMS.
- Yoshihara M, Suzuki T and Tanaka R (1991), 'Improvement of oxidation resistance for TiAl by surface treatment under a low partial pressure oxygen atmosphere and aluminum diffusion coating', *ISIJ Inter*, **31** (10), 1201–1206.
- Yoshihara M, Imamura N, Kobayashi E, Miura K, Mishima Y, Suzuki T and Tanaka R (1993), 'Oxidation resistance and effects of the heat treatment under low partial pressure oxygen atmosphere in intermetallic compound TiAl containing Nb', *J Japan Inst Met*, **57** (5), 574–581.
- Yoshihara M and Taniguchi S (2005), 'Effect of ion-implantation on high temperature oxidation behaviour of TiAl', *Zairyo-to-Kankyo*, **54** (9), 440–449.
- Yoshihara M, Taniguchi S and Kubota T (2007), 'Influence of H<sub>2</sub>O, CO<sub>2</sub> and N<sub>2</sub> on the oxidation behavior of TiAl-based alloys', *J Japan Inst Met*, **71** (1), 16–24.
- Yoshimura M, Urushihara W, Yashima M and Kakihana M (1993), 'Titanate film coating on TiAl by solvothermal processing', *3rd Japan Inter. SAMPE Symp*, Chiba, Japan, SAMPE.
- Yoshimura M, Urushihara W, Yashima M and Kakihana M (1995), 'CaTiO<sub>3</sub> coating on TiAl by hydrothermal-electrochemical technique', *Intermetallics*, **3** (2), 125–128.
- Zhang M X, Hsieh K C, DeKock J and Chang Y A (1992), 'Phase diagram of Ti-Al-O at 1100°C', *Scripta Metall Mater*, **27** (10), 1361–1366.
- Zheng N, Fischer W, Grubmeier H, Shemet V and Quadakkers W J (1995), 'The significance of sub-surface depletion layer composition for the oxidation behavior of  $\gamma$ -titanium aluminides', *Scripta Metall Mater*, **33** (1), 47–53.
- Zhou C, Yang Y, Gong S and Xu H (2001), 'Effect of Ti-Al-Cr coatings on the high temperature oxidation behavior of TiAl', *Mater Sci Eng*, **A307**(1–2), 182–187.
- Zhu Y C, Li X Y, Fujita K, Iwamoto N, Matsunaga Y, Nakagawa K and Taniguchi S (2002), 'The improvement of the oxidation resistance of TiAl alloys by fluorine plasma-based ion implantation', *Surf Coat Technol*, **158–159**, 503–507.
- Zschau H E, Gauthier V, Schumacher G, Dettenwanger F, Schütze M, Baumann H, Bethge K and Graham M (2003), 'Investigation of the fluorine microalloying effect in the oxidation of TiAl at 900°C in air', *Oxid Met*, **59** (1/2), 183–200.

# 12

## Oxidation of metal matrix composites

---

Z LI and W GAO, The University of Auckland,  
New Zealand

### 12.1 Introduction

The demands being made on materials for modern industrial applications are becoming more and more severe. Particularly, fast development of automotive, aerospace and aviation engineering is the most powerful impetus for exploration of lighter and stronger materials which can work in the ultimate conditions, including high temperature, high pressure, high load, fatigue, corrosion and oxidation. It is quite difficult for current material systems to meet all these requirements. Composites, integrated with several components having different properties, have been proven to possess much improved mechanical properties and are receiving more and more attention during the past decades.

Involvement of reinforcing phases into the matrix changes the structures, defects and therefore diffusion processes within the bulk material, thus affecting the environmental performance (corrosion and oxidation) which is very sensitive to these changes. Unveiling the mechanisms involved in the environmental degradation processes of composites will provide fundamental knowledge, and be essential to the successful design and development of advanced engineering materials applicable to severe environments. In this chapter, a brief summary of the high temperature oxidation behaviours of various metal matrix composites, especially titanium matrix composites, iron and nickel aluminide based intermetallic matrix composites, will be given based on experimental observations reported in the open literature.

### 12.2 Classification of metal matrix composites

Metal matrix composites (MMCs) are a group of materials (such as metals, alloys or intermetallic compounds) incorporated with various reinforcing phases, such as particulates, whiskers or continuous fibres. Based on the mechanical properties of the reinforcing phases, the composite materials could be simply divided into two categories [1]. In the first category, the matrix is reinforced with a ductile component, typically a refractory, such as

Mo, Nb, W and/or steel in the morphology of wire or particle [2,3]. The composite toughened could show improved high temperature stability and fatigue performance. In the second category, the matrix is reinforced with fibres, whiskers or particulates that have high strengths [4–8]. The main purpose is to improve the high temperature creep strength, to modify the fracture behaviour to provide improvements in ambient temperature toughness.

Another classification of composite materials is based on the morphology of the reinforcement introduced into the matrix. The composites therefore could be categorised into two main groups: continuous reinforced system and discontinuous reinforced system. In the former, the matrix contains continuous fibres or filaments, which typically distribute in a uniaxial direction and enhance the strength and creep resistance of the matrix. In the latter, the matrix contains particulates, whiskers or chopped fibres, which distribute in the matrix uniformly in random orientations. Moderate toughening and reasonable levels of strengthening can be achieved.

## 12.3 Reinforcing phase

### 12.3.1 Fibre

There are three main types of continuous fibres being used as the reinforcing phases in MMCs. Boron (B) fibres/filaments were developed in the early 1960s, and were the first high strength and high modulus ceramic fibres produced by the chemical vapour deposition (CVD) technique [9–14]. However, tests indicated that B fibres display only short-term strength at high temperatures, since environmental attack on their reactive surface leads to the formation of defects that quickly degrade the tensile strength.

The need for higher utilisation temperature is one of the driving forces for the development of fibres/filaments with better environmental stabilities. Silicon carbide (SiC) fibres were then pursued by several companies, such as Textron Specialty Materials (SCS-type fibres), Lowell, British Petroleum (Sigma fibres) and Atlantic Research Corporation/3M (Trimarc I and II fibres) [15–22]. The CVD SiC fibres have been proven to be of consistent quality. With proper surface modifications, they will be much more inert in elevated temperature matrices than the B fibres. Studies on the influences of long-term thermal exposure in air and argon of SCS-6 SiC fibres had been conducted. After isothermal treatments at 800 and 1000°C in argon up to 700 h, no degradation in tensile strength was observed. Similar exposure in air at 1000°C, however, decreased the mean strength to about half of the original value and severe oxidation of the surface layer forming silica was observed, indicating that the environment may play an important role in the premature decrease in strength for fibres tested in atmospheres with reactive gas species.

Ceramics based on oxides inherently have great stability at elevated temperatures in oxidising atmospheres due to their high melting points, high thermal stability and high oxidation resistance [23–29]. Small diameter alumina fibres were then produced in the 1970s. Commercially available alumina fibres are often associated with silica, as its presence allows the rapid growth of  $\alpha\text{-Al}_2\text{O}_3$  grains to be controlled. However,  $\text{SiO}_2$  reduces the Young's modulus and creep strength of the fibres. These fibres can be used up to 1000°C, above which they will show much greater susceptibility to creep deformation. However, it has been reported that single crystalline oxide fibres produced by the internal crystallisation method may retain their high creep resistance up to about 1600°C [30].

### 12.3.2 Whisker and particulate

Discontinuous reinforcing phases are often not as effective as continuous fibre reinforcements in promoting mechanical properties such as stiffness, strength or creep resistance. Their low cost and ease of manufacture, however, make them very attractive as reinforcing agents for certain applications [31].

Whisker-type reinforcing phases are acicular single crystals with a diameter in the range of 0.01–10 µm and an aspect ratio of usually over 10. The technological importance of whiskers as a form of material with properties distinct from those of the bulk material is that whiskers can have strength as high as those of dislocation-free crystals. Whiskers are incorporated into the matrices primarily for stiffness, creep and wear resistance. The typical materials used as whiskers are SiC,  $\text{Si}_3\text{N}_4$ ,  $\text{SiO}_2$ , NbC, TiC, TiN and TaC.

The dimensions of particulate reinforcements are approximately equal in all directions. The shape of the particles might be spherical, cubic, platelike, or any regular or irregular geometry. The efficiency of particulate reinforcement depends on several factors, such as size, geometry, distribution and volume fraction. For structural applications, a reinforcement volume fraction of 5–30% is adequate, while for electronic applications, a high volume fraction of up to 75% might be necessary. Typical particulate reinforcing phases are  $\text{Al}_2\text{O}_3$ , AlN,  $\text{B}_4\text{C}$ , BN, SiC,  $\text{Si}_3\text{N}_4$ ,  $\text{TiB}_2$ , TiC, TiN and WC.

## 12.4 Matrix

The candidates for the matrix are most of the industrial applicable metals, alloys and intermetallic compounds:

- Light metals: Al and its alloys [32–35], Mg and its alloys [36–38], Ti and its alloys [39–42]
- Copper, beryllium and silver: used mainly for thermal management and electrical contacts [43–50]

- Steels: white iron, low alloy steels and stainless steels [51–54]
- Intermetallic compounds: titanium aluminides [55–60], nickel aluminides [61–64], iron aluminides [65–68] and molybdenum silicides [69,70].

For intermetallic matrix composites, titanium aluminides are much favoured. Titanium aluminides, including  $Ti_3Al$ ,  $TiAl$  and  $TiAl_3$ , offer potential for increased temperature range operation and enhanced high temperature strength, stiffness and oxidation resistance compared with conventional titanium alloys. Their composites promise a balance of comprehensive properties applicable to various fields, especially aerospace, in which lighter and stronger materials are always preferred.

## 12.5 Fabrication

Processing is critical to the effective control of composition, microstructure and performance of MMCs. A number of techniques have been successfully developed and utilised for fabrication of various composites. The main processing methods are: XD<sup>TM</sup> processing [71], self-propagating high-temperature synthesis [72], liquid metal infiltration [73], rheocasting [74], mechanical alloying [75], powder cloth [76], fibre coating [77], spray deposition [78] and foil–fibre–foil process [79,80], etc. A good number of excellent reviews provide detailed information on the development and viability of various processing routes for MMC processing [81–83].

## 12.6 Mechanical properties

In general, continuous fibre reinforced composite systems exhibit superior longitudinal properties, such as longitudinal strength, creep and fatigue crack growth resistance, compared with the matrix alloys. However, their transverse strength is considerably lower than their longitudinal strength and is also lower than that of the matrix alloys [84–98]. The strong anisotropy in mechanical properties imposes a constraint on the use of these materials. The tensile properties, compressive yield strength, fatigue strength and high temperature creep resistance of particulate or whisker reinforced composites are normally higher than those of matrices, whereas the elongation/ductility shows a marked decrease. With the incorporation of hard particles such as  $Al_2O_3$ ,  $SiC$ ,  $Si_3N_4$ ,  $TiB$  or  $TiC$ , the hardness and wear resistance of the materials could be significantly improved. The properties of the composites reinforced with particulates or whiskers are commonly inferior to those obtained with continuous reinforcements. The volume fraction, the state of the interface between particle and matrix, the distribution and the size/shape of the particulates significantly affect the mechanical properties [99–109].

## 12.7 Corrosion of metal matrix composites

Fibres, whiskers or particulates have been incorporated into various metal, alloy or intermetallic matrices to obtain composite materials with significantly improved mechanical properties. This purpose is partially achieved since higher tensile strength, fatigue resistance, creep resistance and/or wear resistance has been observed. In their services, however, composite materials will be exposed to various environments with high temperatures, high pressures or corrosive media. The reinforcing phases and matrices may have quite different responses to these environmental attacks. Furthermore, additional phase boundaries are introduced into the matrices, resulting in a significantly increased number of weak points. Corrosion or oxidation of composites might show some features that are quite different from those of the unreinforced matrices. It will then be of great importance to investigate the environmental resistance of composite materials. The knowledge obtained will be essential to the design and development of novel composite materials with balanced properties. In comparison with the works on characterisation of mechanical properties of MMCs, systematic studies on their environmental resistance are relatively limited. Aqueous corrosion properties of some MMCs can be found in Refs 110–125. The presence of reinforcement could affect the corrosion behaviour of the matrix such as in the phenomena of galvanic coupling between particles and matrix, and localised corrosion at the interface. Moreover, defects in the matrix produced during manufacture could have an adverse effect on corrosion resistance. In this and the following sections, the high temperature oxidation of some MMCs will be briefly reviewed based on the experimental observations reported in the open literature.

## 12.8 Titanium alloys, titanium aluminides and composites

Titanium has been reputed to be the ‘Third Element’ with importance and applications only after iron and aluminium. Al, Sn, Zr, Mo, Nb, Si and O are normally added into Ti to form various alloys for enhanced chemical, mechanical and physical properties. Based on the phase structure, Ti alloys can be classified as either  $\alpha$ , near- $\alpha$ ,  $\alpha$ - $\beta$  or  $\beta$  alloys [126–128]. As structural materials used at elevated temperatures, however, the commercial Ti alloys have useful strength and resistance to oxidation at temperatures up to only 600°C, far below 1100°C, the temperature in service for Ni-based superalloys [129]. However, their high specific strength makes them an attractive alternative to superalloys for certain gas turbine components. In fact, Ti alloys possess a weight reduction advantage of approximately 40% over their Ni-based counterparts.

At the beginning of the 1970s, Ti-Al intermetallic compounds were

developed as the first intensive and successful structural materials with fundamental deformation studies. Titanium aluminides have become attractive structural materials for application to the aviation industry because of their low density, high melting point, high specific strength and relatively good ductility [130–136]. The development of  $Ti_3Al$  and its alloys (mainly further alloyed with Nb to form the ‘orthorhombic’ or O-phase) has been driven by the need to bridge the gap in temperature capability between conventional near- $\alpha$  Ti alloys and Ni-based superalloys such as INCO 718 or INCO 713 [137].  $Ti_3Al$  has a specific modulus and stress rupture resistance comparable to that of the superalloys. Addition of alloying elements and heat treatment can significantly improve its room temperature mechanical properties, and become the key point for the current development of  $Ti_3Al$ -based alloys.

$\gamma$ -TiAl and its alloys are pursued mainly because of the desire to raise the thrust-to-weight ratio of high performance aircraft engines [138–140].  $\gamma$ -TiAl remains ordered to its melting point at about 1440°C, which helps to retain strength and resist creep to high temperatures, and also results in high stiffness over a wide temperature range. Although the difficulty with plastic deformation hinders its development,  $\gamma$ -TiAl and its alloys are still the most attractive candidate materials for components in aeroengines.  $TiAl_3$ , having a tetragonal structure, is of interest in the development of a new class of structural materials, and is also a good coating material for Ti-Al-based alloys used at elevated temperatures [141].

The oxidation resistance of titanium aluminides, especially  $Ti_3Al$  and  $TiAl$ , is not sufficient at elevated temperatures. Thus, a key factor in increasing their maximum operating temperature in service is enhancing their oxidation resistance while maintaining their excellent mechanical properties. Increase of Al content in the alloy could lead to the formation and maintenance of the protective alumina scale; however, a serious problem associated with this is the deterioration of mechanical properties. The alloys become more and more brittle, and their workability also becomes worse. They are also extremely hard to cut, machine, drill and join the materials and the parts. For example, the Young’s modulus of polycrystalline  $TiAl_3$  at room temperature reaches 216 GPa, much higher than that of other Ti aluminides, and it is of the same order for the Ni-based superalloys. However, this compound exhibits extreme brittleness at temperatures below 600°C due to the low symmetry  $DO_{22}$  structure with few slip systems [142].

The main purpose of fabricating titanium matrix composites (TMCs) is to get more balanced chemical and physical properties from these systems. For example,  $Al_2O_3$  or  $SiC$  with long and continuous fibre-reinforced TMCs have been of particular interest due to their merits of retention of a high level of specific strength and stiffness at high service temperatures, which are the fundamental requirements for aerospace applications. Incorporation of discontinuous reinforcements, including  $TiB$ ,  $TiC$ ,  $TiN$ ,  $SiC$ ,  $Si_3N_4$ ,  $TiB_2$ ,

$\text{B}_4\text{C}$ ,  $\text{ZrB}_2$  and  $\text{Al}_2\text{O}_3$ , into Ti-based matrices could provide increased stiffness and good creep, fatigue and wear resistance. Actually, the successful development of manufacturing processes, to a large extent, results in the large family of low-cost discontinuously reinforced TMCs with reproducible structural and functional properties.

## 12.9 Oxidation of titanium matrix composites

The high temperature oxidation resistance of an engineering alloy largely relies on the formation of an external protective oxide scale on its surface, which should be slow growing, chemically and mechanically stable, adherent and non-permeable to corrosive gas species [143]. Therefore, for conventional engineering alloys or coating systems, if the content of certain elements, such as Al, Cr and/or Si, in the bulk or in the near surface region is high enough to guarantee the formation and/or healing of a protective oxide scale, such as  $\text{Al}_2\text{O}_3$ ,  $\text{Cr}_2\text{O}_3$  and/or  $\text{SiO}_2$ , on the top surface, the system will confer adequate high temperature oxidation resistance.

For composite materials, however, the case is different, since this basic requirement must be met by both the matrix and the reinforcement at the same time. Otherwise, damage induced by environmental attack in any one of these two phases will result in severe degradation of the whole system. Unfortunately, in most real cases, addition of reinforcing phases into the matrix is not intended to increase the high temperature oxidation resistance of the composites fabricated, i.e., the choice of reinforcement is decided by the mechanical properties desired. Therefore, the addition often does not provide better oxidation resistance to the whole composite material system, while in some cases the situation might become worse, since the incorporation of reinforcing phases might damage the integrity of the material system and therefore lead to the presence of weak points along the interfaces or on the surfaces, where oxidation process might be accelerated through enhanced diffusion.

### 12.9.1 Oxidation of fibre-reinforced titanium matrix composites

A survey of the open literature indicated that the information available on the oxidation behaviour of continuous fibre-reinforced TMCs is extremely limited, although much work has been carried out to characterise the performance of these composite systems under severe mechanical loadings and temperature variations. Studies on the mechanical behaviours of fibre-reinforced TMCs clearly demonstrated that temperature and atmosphere had quite strong influences on the mechanical response of the material systems. Tests at elevated temperatures and in oxygen-containing atmospheres normally

resulted in a significant loss of mechanical strength. These results indicated that the environment plays an important role in the damage process of the composites and severely degrades the composites, due to the formation and growth of brittle oxide layers on matrix surfaces and/or along the fibre/matrix interfaces.

SiC exhibits excellent oxidation resistance at moderately high temperatures due to the formation of a coherent layer of  $\text{SiO}_2$  on the surface, which suppresses further oxidation [144,145]. However, the non-stoichiometric nature of commercially available SiC fibres modifies the rate of oxygen diffusion through the scale, resulting in active oxidation. Oxidation exposure at temperatures higher than 600°C in air therefore will lead to a severe reduction of the fibre strength [146,147]. Hot corrosion tests under load were performed by Song *et al.* [148]. Their results showed that after exposure at 950°C for 3 h in air under an applied load of 20 g, the fibre surfaces corroded by  $\text{Na}_2\text{SO}_4$  were extremely rough and revealed severe exfoliation and cracking, probably caused by the dissolution of fibre involving gas evolution in molten salt. Pitting was also observed locally on the exfoliated fibre surfaces. Song *et al.* believed that this is related to the rapid oxidation–dissolution of the fibres due to the formation of the liquid  $\text{Na}_2\text{SiO}_3$ . These results clearly showed that the environmental stability of the reinforcing components should be carefully considered prior to the design of a composite system that will be exposed to corrosive atmospheres.

On the other hand, if all fibres are covered completely with matrix, oxidation of the composite system will be limited to the surface (as long as there are no cracks), and the process is diffusion controlled. In this way, the oxidation performance of the composite will mainly rely on the oxidation resistance of the matrix alloy. However, in most real applications, this is not the case. The interface between the fibre and the matrix always has a large number of physical defects, which provide additional transportation routes for attacking gas species.

Wei investigated the effect of long-term high-temperature exposure on the interfacial properties of a SiC continuous fibre-reinforced Ti alloy. It was shown that the presence of the fibre/matrix interface allows for rapid inward diffusion of oxygen and leads to the oxidation transformation of the interfacial zone, resulting in embrittlement of the fibre/matrix interface through combined oxidation and attack of the Ti matrix on the fibres and fibre coating [149]. Wittig and Allen performed a micromechanical analysis on single-ply continuous fibre SiC/Ti-15V-3Al-3Sn-3Cr composite to study the complex interactions between the composite microstructural components and the surrounding environment at temperatures ranging from 500 to 700°C [150]. Their results indicated that the oxidised surface layer is prone to cracking upon subsequent mechanical loading, and this effect is strongly temperature dependent. However, in this study, the direct interaction of SiC fibre with the

environment, and the potential effects of this interaction to the oxidation resistance of the composite system, were not considered.

By noticing the preferential attack of SiC fibres along the interface through easy access of oxygen and consequent loss of mechanical strength, researchers accepted that development of an interfacial coating to protect SiC fibres is critical for the safe utilisation of composites. This presents a major technical challenge since the interlayer must be thermodynamically compatible with both the fibre and the matrix. Carbon, highly oriented graphite, hexagonal BN, TaC, ZrC and/or mullite ( $3\text{Al}_2\text{O}_3\cdot2\text{SiO}_2$ ) are being modified to develop an oxidation resistant interfacial barrier coating for SiC fibres [151–157].

$\text{Al}_2\text{O}_3$  has a high resistance to attacks by molten metals and chemical inertness in both oxidising and reducing atmospheres up to 1000°C.  $\text{Al}_2\text{O}_3$  fibres are finding wide applications in metal and ceramic matrix composites [158–160]. However, incorporation of alumina fibres with higher oxidation resistance does not always improve the overall performance of composites in aggressive environments.

Fish and Duquette studied the isothermal and cyclic oxidation behaviours of chopped alumina fibre (DuPont PRD166  $\text{Al}_2\text{O}_3$  fibre containing 15% stabilised  $\text{ZrO}_2$ ) reinforced Ti-54Al (at%) composites at 950 and 1070°C in air [161]. During isothermal oxidation tests, the composites exhibited larger mass gains than monolithic TiAl and increased proportionally with the volume fraction of reinforcing fibres. The alumina layer was formed mainly along the fibres, and its thickness was greatest near the surface of the composites and diminished towards the centre. Oxygen diffusion along the fibres and subsequent oxidation of the matrix along the perimeter of the fibres are responsible for the increased mass gain of the composites. In cyclic oxidation performed at 1070°C, the oxide adherence on the monolithic TiAl alloy is poor, whereas none of the composites exhibited any scale failure. The authors proposed that the alumina fibres might inhibit outward diffusion of Ti by promoting a continuous scale of  $\text{Al}_2\text{O}_3$  based on Wagner's internal oxidation theory, and thereby improve the cyclic oxidation resistance of the composites. The studies performed by Nourbakhsh *et al.* showed that Ti-50Al alloy reinforced with PRD-166 alumina fibres did not show good resistance to oxidation. A thick oxide scale composed of several non-protective layers was developed during air annealing for 40 days at 950°C. More importantly, the alumina fibres were not chemically compatible with the matrix. Part of the alumina fibres were dissolved into the matrix, leading to the formation of a  $\gamma$  layer around the fibre [162].

### 12.9.2 Oxidation of particulate or whisker reinforced titanium matrix composites

Due to their easy fabrication, studies on the mechanical properties and oxidation performance of particulate or whisker reinforced TMCs are more active in

comparison with those on continuous fibre-reinforced composites. For example, oxidation behaviours of TiC and/or TiB particle-reinforced Ti alloy composites and SiC,  $\text{Si}_3\text{N}_4$  and/or  $\text{TiB}_2$  particle-reinforced TiAl alloy composites have been studied and reported.

Lee *et al.* studied the high temperature oxidation properties of SiC particle-reinforced  $\text{Ti}_3\text{Al}$  and TiAl alloys, and  $\text{Si}_3\text{N}_4$ -dispersed TiAl alloys [163–165]. Their results showed that addition of these dispersions could improve the oxidation and scale spallation resistances, though the microstructure of the oxide scale was not significantly changed. The mechanisms proposed by these authors were as follows:

1. Incorporation of secondary dispersions into the matrix could reduce the grain size and provide a large number of heterogeneous nucleation sites for the formation of oxide, therefore an oxide scale with a fine grain size could be formed, and this structural feature is beneficial to scale adherence.
2. Due to the refinement of grain size in the matrix, fast outward diffusion of Al along grain boundaries could be enhanced, which would increase the alumina-forming ability.
3. Oxidation of SiC or  $\text{Si}_3\text{N}_4$  particles leads to the formation of  $\text{SiO}_2$  within the oxide scale. Obviously, a sublayer enriched with  $\text{Al}_2\text{O}_3$  and/or  $\text{SiO}_2$  would act as the barrier for the inward and/or outward diffusion of reactants [166].

It is reasonable to see that incorporation of SiC or  $\text{Si}_3\text{N}_4$  particles into Ti-based matrices could improve the overall oxidation resistance of the composite systems, since oxidation of uniformly distributed Si-containing dispersoids could result in the formation of oxide layer(s) enriched with  $\text{SiO}_2$ , which is slow growing and oxidation protective. On the other hand, studies on the oxidation of Ti-based alloys reinforced with TiC, TiB and/or  $\text{TiB}_2$  particles indicated that the composite systems with less oxidation-resistant reinforcements might have a better oxidation resistance than the unreinforced alloys [167,168]. These results were quite interesting and suggested that improvement of oxidation resistance might not always depend on the formation of slow-growing oxides, due to the addition of highly oxidation-resistant particles; modifications on the structures of the composite materials and then on the structural characteristics of the thermally grown oxide scales could also contribute to the enhancement of high temperature oxidation resistance.

Gao *et al.* studied the oxidation behaviours of  $\text{Ti}_3\text{Al}-\text{TiC}$  composites prepared by mechanical milling and hot isostatic pressing at 700 and 800°C in air [169]. The oxidation mass gains of these composites were lower than that of the cast  $\text{Ti}_3\text{Al}$  alloy (if the mass loss due to the generation of CO or  $\text{CO}_2$  from C in TiC is considered, the difference might be smaller). Particularly, the mechanical stabilities of the oxide scales on the cast alloy and the composites during thermal cycling were quite different. The oxide scale formed on the

cast Ti<sub>3</sub>Al was highly prone to cracking and spalling, while the oxide scales on the composites exhibited a very high stability and no cracking or spalling was observed. Microstructural studies indicated that the particle size of the oxide scale formed on the composites was much smaller than that of the scale formed on the cast alloy; and the interface between the oxide scale and the composite matrix was rugged. Obviously these two features are responsible for the improved oxidation and scale spallation resistances and are highly related to the structural features resulted from the incorporation of reinforcing particles into the alloy matrix. These particles and the high density grain boundaries could significantly accelerate the oxide nucleation on the surface, and then shorten the distance between the nuclei. This will limit the lateral growth of the oxide, resulting in fine oxide particles. Plastic deformation and creep of the scale are favoured by the small grain size; therefore, the growth and thermal stresses could be effectively released through scale deformation, decreasing the tendency to cracking and spallation. As the grain size of the substrate is rather small, preferential oxidation in grains or along grain boundaries and phase interfaces could take place, resulting in a rugged and rough interface on the composites. Some parts of the scale penetrate into the substrate, holding itself firmly to the matrix and keeping its integrity. In addition, some works on oxidation of TMCs with in-situ reinforcements of TiC or TiB also suggested that the strong interface cohesion and the clean interfacial microstructure between the reinforcement and the Ti matrix can act as barriers to solid-state diffusion, therefore decreasing the formation of non-protective TiO<sub>2</sub> scale [170,171].

On the other hand, some studies indicated that the beneficial effects endorsed by the secondary phase might only be limited to a low temperature range. At high temperatures, incorporation of particles having gas evaporation might deteriorate the scale integrity and then the oxidation resistance of the composites. Zhang *et al.* found that incorporation of in-situ TiB short fibres could decrease the oxidation resistance of Ti-6Al-1.2B alloy, especially when the oxidation temperature was high [172,173]. At temperatures lower than 700°C, the oxidation mass gain was limited and the oxide scale was thin. When the temperature was higher than 750°C, the increase in oxidation mass gain was significant, and the microstructures of the oxide scale and the interface were noticeably changed. Pores appeared in the metal matrix subsurface, and a porous layer was formed. At the same time, within and below this porous layer more pores were found at the interface between TiB short fibres and the matrix. The authors believed that this phenomenon was related to the gas formation and evaporation from the oxidation of TiB, i.e., the appearance of pores was due to the generation of B<sub>2</sub>O<sub>3</sub> at high temperature since B<sub>2</sub>O<sub>3</sub> evaporates considerably at 800°C and extensively above 1000°C. The evaporating temperature, 800°C, is quite close to the temperature at which the pores were observed at the Ti/TiB interface.

However, a comparison between this study and Lee's [167] study on TiB<sub>2</sub> particle-reinforced TiAl alloy at 800–1000°C might show that the morphology of the reinforcement is critical to the actual oxidation resistance of the composite system as well. In TiB<sub>2</sub> particle-incorporated TiAl, pores related to the formation of B<sub>2</sub>O<sub>3</sub> were not observed, and the composites with a higher volumetric fraction of TiB<sub>2</sub> showed a higher oxidation resistance. These results indicated that preferential transportation of oxygen along the interface between the reinforcement (especially long or chopped fibres) and the matrix was quite important to the whole oxidation resistance of the composite. In other words, the interface was acting as rapid short-circuit diffusion paths, so that oxygen could enter into the matrix alloy and reduce the oxidation resistance of the composite system [170,172].

Ductile reinforcements, including Nb, TiNb or Ti-6Al-4V particles, are incorporated into Ti<sub>3</sub>Al and TiAl to promote toughness [174–177]. By adding ~10 vol% of TiNb particles into  $\gamma$ -TiAl, the crack-initiation toughness can be increased to ~16 MPa·m<sup>1/2</sup>, nearly twice that of pure  $\gamma$ -TiAl (~8 MPa·m<sup>1/2</sup>). The beneficial effect of adding ductile TiNb reinforcements to enhance the room-temperature fracture and fatigue resistance of  $\gamma$ -TiAl alloys could be retained up to 800°C in air environments [178]. Kekare *et al.* studied the oxidation behaviours of TiNb-reinforced Ti-48Al (at%) composites in air and oxygen at temperatures ranging from 704 to 982°C. They concluded that TiNb particles are more oxidation resistant than the TiAl matrix; therefore, at these temperatures, these particles are not oxidised, only the outer boundaries are converted into TiO<sub>2</sub>. These ductile particles are also stable, and Nb does not diffuse out to contribute and influence the oxidation behaviour of the TiAl matrix. In addition, the interface between the particle and the matrix does not provide a faster diffusion path for the oxidation process, so that there is no preferential penetration of oxide at locations where TiNb is present [179].

### 12.9.3 Oxidation of titanium based in-situ composites

Development of metal-oxide composites using in-situ techniques has been attracting considerable attention. These metal-oxide in-situ composites are mainly Cu, Al, Fe and Ti based materials reinforced with alumina through the chemical reactions between Al, and oxide powders of CuO, Fe<sub>2</sub>O<sub>3</sub> or TiO<sub>2</sub>. The chemical reactions are actually thermite reactions, which is a type of aluminothermic reaction in which aluminium is oxidised by the oxide of another metal [180].

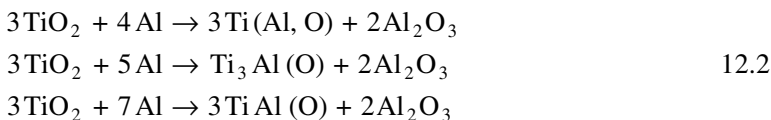
Recently, the reactions between TiO<sub>2</sub> and Al powders have been utilised by some research groups to fabricate Ti-based composites. From the Ellingham–Richardson diagram [181,182], the difference between the standard free energy changes for the formation of TiO<sub>2</sub> and Al<sub>2</sub>O<sub>3</sub> is small. However,

$\text{Al}_2\text{O}_3$  is still more thermodynamically stable than  $\text{TiO}_2$  under standard conditions, i.e., the reduction reaction of  $\text{TiO}_2$  by Al could still be thermodynamically possible according to the following equation:



$\text{Al}_2\text{O}_3$  particles, formed *in situ* within the reactions, could serve as an effective reinforcement to strengthen the composite and increase the hardness and wear resistance, since these particles have high strength and high hardness [183–188].

Since the reducing power of Al for  $\text{TiO}_2$  is limited, part of the oxygen will still dissolve into the Ti or the Ti-Al intermetallic phases formed [189]:



The oxygen content in the  $\text{Ti(Al)}$  and  $\text{Ti-Al}$  phases decreases with increasing Al content. For Ti-rich  $\text{Ti(Al)}$  solid solution and  $\text{Ti}_3\text{Al}$ , the dissolved oxygen content has been measured in the range of 15–20 at%. The high oxygen content in the Ti-based phases makes the materials brittle, but the low cost and other favourable features such as high hardness and high oxidation resistance would make these materials attractive for many applications. Researchers at the University of Waikato, the University of Auckland and Titanox Development Limited are focusing on understanding the correlations among processing, microstructure and property of these cost-effective Ti-based in-situ composites and on developing new processes for producing Ti-based intermetallic materials [190–198].

In these studies, the powders used to produce the in-situ composites were Al/ $\text{TiO}_2$  composite powders, which were produced by high energy mechanical milling of a mixture of Al and  $\text{TiO}_2$  source powders. The as-milled composite powders were pressed to prepare green compacts using cold isostatic pressing. These green compacts were then subjected to pressureless sintering or to further densification by hot isostatic pressing. With conventional sintering, the consolidation of the green compact is highly dependent on the temperature used. Increasing temperature could increase the density of the final composites. By sintering at 1650°C, a relative density of 95–97% can be achieved. HIPing at a lower temperature of 1300°C under a pressure of 200 MPa could obtain a fully dense  $\text{Ti(Al,O)}/\text{Al}_2\text{O}_3$  composite.

The distribution of the  $\text{Al}_2\text{O}_3$  particles in the composites is always homogeneous regardless of the sintering condition. The shape of the  $\text{Al}_2\text{O}_3$  particles becomes more faceted with increasing sintering temperature and as a result of HIPing. Conventional sintering and/or HIPing leads to the coarsening of the  $\text{Al}_2\text{O}_3$  particles. The coarsening rate increases in the order of  $\text{Ti(Al,O)}$ ,

$\text{Ti}_3\text{Al(O)}$  and  $\text{TiAl(O)}$ , being the matrix of the composite, respectively. This is due to the decrease of the solidus temperatures or melting points of the corresponding matrices in the same order. HIPing treatment of the pre-sintered green compact could, to a certain degree, decrease this detrimental effect associated with the use of high temperature, but coarsening could still be observed. The typical size of the  $\text{Al}_2\text{O}_3$  particles in the HIPed composite is around 3–10  $\mu\text{m}$ , as compared to the  $\text{Al}_2\text{O}_3$  particle size of 15–30  $\mu\text{m}$  in the pressureless sintered composites at temperatures above 1550°C [199].

Mechanical properties of these in-situ Ti-based composites were studied including hardness, bending strength and fracture toughness. The hardness of the  $\text{Ti(Al,O)/Al}_2\text{O}_3$  and  $\text{Ti}_3\text{Al(O)/Al}_2\text{O}_3$  composites is very high, in the range of 1000–1600 in Vickers Hardness Number (VHN). With increase of the Al content in the Ti-Al phases, the hardness decreases. The hardness of the  $\text{TiAl(O)/Al}_2\text{O}_3$  composites is substantially lower than that of the former two composites, in the range of 300–500 VHN, and it also increases with the fraction of  $\text{Al}_2\text{O}_3$  particles. The three-point bending strength of these composites is moderate, in the range of 180–300 MPa, and decreases almost linearly with the size and fraction of the  $\text{Al}_2\text{O}_3$  particles. With a given fraction of  $\text{Al}_2\text{O}_3$  particles, the bending strength increases in the order of  $\text{TiAl(O)/Al}_2\text{O}_3$ ,  $\text{Ti}_3\text{Al(O)/Al}_2\text{O}_3$  and  $\text{Ti(Al,O)/Al}_2\text{O}_3$  composites. When measured by using an indentation technique, the fracture toughness of the composites was found to be comparable to that of the engineering ceramics, in the range of 2–5  $\text{MPa}\cdot\text{m}^{1/2}$ , much lower than that of the Ti-based alloys and intermetallic compounds. The low fracture toughness could be attributed to the high oxygen content in the Ti and Ti-Al phases and the incorporation of large, brittle  $\text{Al}_2\text{O}_3$  particles.

These Ti-based materials, prepared by using cheap starting powders, are a relatively new type of in-situ composites, although mechanical testing has showed that they do not have excellent properties, especially bending strength and fracture toughness, which means they might be not good candidate materials for potential structural applications. The high hardness of these composite materials, possibly associated with their high content of oxygen and high fraction of stable alumina particles in the matrix, on the other hand, might indicate that they would have good oxidation resistance. Therefore these composites may find applications as less critical parts or as coating materials.

The well-known fact about the oxidation of Ti-based alloys and intermetallic compounds is that inward diffusion of oxygen is significant. The dissolution of oxygen into the unoxidised metal substrate is serious, and yields a notable proportion of the total mass gain during the oxidation of pure Ti [200]. Direct measurements on the oxidised specimens showed that 25–30% of the reacted oxygen dissolved in the metal at temperatures of 700–750°C and more than 50% at 900–950°C. Even for a Ti-24Al-11Nb alloy exposed for

24 h at 900°C, 37.7% of the total mass gain resulted from oxygen dissolution [201]. Therefore, the pre-incorporation of oxygen into the Ti-Al phase will, to a certain extent, decrease the inward diffusion and dissolution of oxygen, and hence increase the oxidation resistance of the composites.

Gao *et al.* studied the oxidation and scale spallation behaviours of these Ti-based in-situ composites [202–204]. They found that the scaling behaviour, especially the mechanical properties of the oxide scales, is quite different from that of the cast Ti-Al alloys under the same test conditions. For the  $\text{Ti}_3\text{Al}(\text{O})/\text{Al}_2\text{O}_3$  in-situ composite, the oxidation tests were carried out at 700–900°C in air. The isothermal oxidation tests were actually conducted in a discontinuous way, i.e., every 10 hours the mass gain and spallation of the samples were measured. Another set of tests was the fast cyclic oxidation (1 hour heating and 10 minutes cooling). Oxidation kinetics established with the cyclic and isothermal oxidation tests clearly showed that all the mass gains increased in a parabolic manner, and the kinetics obtained with cyclic and isothermal tests did not show any significant differences; the total mass gains after 100 h were almost the same. A comparison between this composite and other  $\text{Ti}_3\text{Al}$ -based alloys showed that this composite had a slightly lower oxidation mass gain [201,205,206]. The parabolic rate constants of this material stay between those of the pure  $\text{TiO}_2$  formers and Ti-49Al, although they are still much higher than those of the  $\text{Al}_2\text{O}_3$  formers.

The lower oxidation rate of the composite could partially be attributed to the incorporation of  $\alpha\text{-Al}_2\text{O}_3$  particles, which have a volumetric fraction of ~50%. These particles will not be further oxidised; oxygen and metal diffusion have to be conducted through a decreased cross-sectional area, resulting in a lower mass gain of the whole sample. On the other hand, the  $\text{Ti}_3\text{Al}$  matrix has pre-dissolved oxygen during preparation of ~10%; this will largely decrease the inward diffusion and dissolution of oxygen into the matrix. Additionally, the structures of the oxide scales formed on the cast alloy and the composite were quite different. The oxide scale on the cast alloy had many physical defects, such as cracks and pores, while the scale on the composite was quite dense and free of these defects. Obviously, a scale with dense, strong adherence and fewer cracking features can provide better protection to the underlying substrate against the aggressive environment, since the diffusion of reactants through this scale could be retarded. This is also true for the improved oxidation resistance observed with the  $\text{TiAl}(\text{O})/\text{Al}_2\text{O}_3$  in-situ composite [203].

Another group of Ti-based in-situ composites was prepared by using the starting powders of Al,  $\text{TiO}_2$  and C. The incorporation of carbon leads to the formation of carbides,  $\text{TiC}$  and  $\text{Ti}_2\text{AlC}$ , in the composites. It was observed that a thin oxide scale enriched with  $\alpha\text{-Al}_2\text{O}_3$  could always be developed on the sample surfaces, and the oxidation mass gain after 500–1000 cycles or 500–1000 hrs was less than ~0.3 mg/cm<sup>2</sup>, about two orders of magnitude lower than that of the cast TiAl alloys oxidised under the same conditions.

The superior oxidation resistance was attributed to the involvement of the ternary carbide  $Ti_2AlC$ , which has excellent oxidation resistance due to the different bonds between Ti-C and Ti-Al [207,208]. Due to the nature of this composite, oxide formation and growth on this ternary carbide will certainly influence the overall oxidation process of the composite, i.e., the  $Al_2O_3$ -rich scale formed on  $Ti_2AlC$  could extend to the surfaces of other phases through lateral diffusion and growth processes and eventually cover the whole surface, enhancing the oxidation resistance of the composite.

A notable feature is that during the thermal cyclic tests, no scale spallation was observed on these composites, indicating that the growth and thermal stresses have been effectively relieved in some way, and this is of great importance for the industrial applications of these composite materials. Generally, the stresses concentrated in oxide scales could be relieved through creep, deformation, cracking, detachment and/or spalling. The present composites did not show observable scale failures, indicating that the stress relief was mainly by means of creep and/or plastic deformation of the substrate and/or the scale.

The thermal stresses generated in the oxide scales are related to Young's modulus, the coefficient of thermal expansion (CTE), Poisson's ratio and the thickness of the oxide scale/matrix. Decreasing the CTE difference between the oxide scale and the alloy matrix, as a common approach, could effectively increase the spallation resistance. The CTEs of these composites were not measured; however, the CTE of the  $TiAl(O)/Al_2O_3$  composite could be roughly calculated by using the Turner equation. The value is calculated to be  $\sim 9.9 \times 10^{-6}/K$ , much lower than that of  $TiAl$ ,  $12.6 \times 10^{-6}/K$ , and close to that of  $\alpha-Al_2O_3$  and  $TiO_2$  ( $8.3 \times 10^{-6}$  and  $7.3 \times 10^{-6}/K$ , respectively). The CTEs of  $Ti_2AlC$  and  $TiC$  were reported to be  $\sim 9.0 \times 10^{-6}/K$  and  $7.4 \times 10^{-6}/K$  [209,210]. The CTE of these composites therefore might be around  $9.0 \times 10^{-6}/K$ . This means that the thermal stress in the oxide scales formed on these composites should be significantly lower than that on the  $TiAl$  matrix, leading to a smaller thermal mismatch and a lower tendency of scale failure.

The phase size in the matrix was relatively small, thus the phase boundaries were significantly increased, providing more sites for heterogeneous nucleation. A higher nucleation rate for oxides on the outer surface leads to the formation of a continuous oxide scale composed of very fine oxide particles [211,212]. It was believed that creep of the oxide and substrate could relieve part of the stresses generated, and the diffusion creep rate is related to the grain size. A finer grain size of the oxide would promote a higher creep rate, relieving the growth stress more effectively at temperature, thus improving the oxide scale spallation resistance.

Another microstructural feature of these composites is that  $\alpha-Al_2O_3$  formed through the in-situ chemical reactions between Al and  $TiO_2$  in the fine Al/ $TiO_2$  composite particles at high temperatures would tend to develop a three-

dimensional network in the matrix. It was also observed that these  $\alpha\text{-Al}_2\text{O}_3$  particles exhibit good adhesion with the alloy matrix through a thin interfacial area around their circumferences with a compositional gradient. After oxidation, they still have strong connections with the thermally grown oxides. It can be imagined that the three-dimensional alumina network can hold the matrix and the oxide together strongly, increase the adherence of the oxide scales and decrease the tendency of scale spallation.

Pores and cracks play an important role in the mechanical failure of the oxide scale, especially under rapid thermal cycling. The cracks tend to propagate laterally in the  $\text{TiO}_2$  scale, resulting in detachment of the scale. Alumina particles embedded into the oxide scale could stop the propagation of cracks and change the layered structure, therefore effectively inhibiting the development of cracks in the scale. Actually, the oxide scales grown on the composites were not completely covering the surface, since their lateral growth was blocked by the alumina particles. Under this condition, the defects developed in the oxide scale will be restricted to small areas, forming a relatively uniform oxide scale.

The composite powders of  $\text{Al}/\text{TiO}_2$  after mechanical milling were also thermally sprayed onto Ti plates. During the spraying process, reactions between Al and  $\text{TiO}_2$  could be initialised in the mechanically activated powders and result in the formation of  $\text{Ti}_3\text{Al(O)}/\text{Al}_2\text{O}_3$  in-situ composite coatings on the substrate [213]. The oxidation resistance of Ti with and without composite coatings was studied at 700–800°C in air. At 800°C, catastrophic oxidation occurred on Ti and resulted in an extremely thick rutile scale, in which cracking and spallation initialised after 10h of exposure. The coating, however, showed little difference after oxidation exposure. The scale consisted of rutile and  $\alpha\text{-Al}_2\text{O}_3$ , was dense and adhered to the substrate. The protection mechanisms of the  $\text{Ti}_3\text{Al(O)}/\text{Al}_2\text{O}_3$  composite coatings are similar to those of the  $\text{Ti}_3\text{Al(O)}/\text{Al}_2\text{O}_3$  in-situ composites. An adherent coating with higher oxidation and scale spallation resistance definitely could protect the underlying materials.

$\text{TiAl}_3$ -matrix composite layers containing  $\text{Al}_2\text{O}_3$  particles were also produced on Ti substrates by pulsed electric current sintering of mechanically alloyed powders [214]. The results showed that the oxidation and wear properties of  $\text{TiAl}_3$  coatings could be improved by the reinforcement of  $\text{Al}_2\text{O}_3$  particles.

These results are very encouraging. Due to the high content of oxygen dissolved in the Ti-Al phases, the materials are brittle and might not be suitable for many structural applications. If the oxygen content in the Ti-Al phases could not be effectively decreased to a low level, the production of Ti-based intermetallic materials from these cheap source materials ( $\text{TiO}_2$  and Al powders) will not be realised. However,  $\text{Ti}_3\text{Al(O)}/\text{Al}_2\text{O}_3$ ,  $\text{TiAl(O)}/\text{Al}_2\text{O}_3$  and  $\text{TiAl(O)}/\text{Ti}_2\text{AlC}/\text{TiC}/\text{Al}_2\text{O}_3$  produced from mechanically milled Al,  $\text{TiO}_2$

and/or C powders might represent a series of cost-effective composites possessing high hardness, excellent oxidation resistance and superior scale mechanical stability at high temperatures and could find applications as coating materials in areas requiring high-temperature corrosion and wear resistances.

## 12.10 Oxidation of iron aluminide based composites

Iron aluminides, including  $\text{Fe}_3\text{Al}$  and  $\text{FeAl}$ , are of interest for high-temperature structural applications since they have relatively high melting points, excellent oxidation, carburisation, sulfidation, and hot corrosion resistance, relatively low density and low material cost. The major advantages that can be derived from the use of iron aluminides include the following [215,216]:

1. Their density is lower than that of many stainless steels and therefore they offer better strength-to-weight ratio.
2. Their resistance to sulfidation in  $\text{H}_2\text{S}$  and  $\text{SO}_2$  gases is much better than that of any other iron- or nickel-based alloys.
3. They have a high electrical resistivity which increases with temperature.
4. They have good corrosion resistance in many aqueous environments.
5. They are cheap in material cost.

However, the ductility and fracture toughness of iron aluminides at room temperature and their creep strength at elevated temperatures are poor and should be overcome by suitable alloy design strategies such as element additions, grain size refinement and/or fine particle dispersions. Methods of improving the properties of iron aluminides through composite development are receiving great attention. Oxide (mainly  $\text{Al}_2\text{O}_3$  and  $\text{ZrO}_2$ ) [217–222] and non-oxide ceramics (such as  $\text{TiC}$ ,  $\text{WC}$ ,  $\text{TiB}_2$  and  $\text{ZrB}_2$ ) [223–229] have been incorporated into Fe-Al matrix using displacement reaction, mechanical alloying, hot pressing, liquid phase sintering, pressureless melt infiltration and pulse discharge sintering.

Oxides, especially  $\text{Al}_2\text{O}_3$ , are chemically stable and therefore do not degrade the inherent oxidation resistance of iron aluminides. This could be confirmed by Suganuma's work on the properties of  $\text{Fe}_3\text{Al}$  matrix composites reinforced with fine  $\text{Al}_2\text{O}_3$  particles (0–13 vol%) produced by hot pressing powder mixtures of Fe and Al [230]. The oxidation mass gain of the  $\text{Fe}_3\text{Al}/\text{Al}_2\text{O}_3$  composites was much lower than that of the Inconel 713 alloy at 1000°C, a representative high-temperature Ni-based superalloy, and the composites seemed to form an  $\text{Al}_2\text{O}_3$  protective layer on the surface. However, a direct comparison was not made between the reinforced and unreinforced  $\text{Fe}_3\text{Al}$  materials; therefore the exact influences of  $\text{Al}_2\text{O}_3$  particles on the oxidation performance of  $\text{Fe}_3\text{Al}$  was not revealed in this work. The isothermal oxidation

behaviour of atomised Fe-40Al intermetallic alloys doped with B and/or reinforced with  $\text{Al}_2\text{O}_3$  fibre was studied by Espinosa-Medina *et al.* at 800–1100°C [231]. All the samples had excellent oxidation performance and the mass gain data did not show that one special material has the best oxidation resistance at all temperatures.

Incorporation of less oxidation-resistant ceramic particles into iron aluminide matrices might, to a certain extent, degrade the overall oxidation performance of the composites. Few studies have been devoted to the oxidation properties of Fe-Al reinforced with  $\text{TiB}_2$ , TiC or WC particles. Work by Schneibel *et al.* showed that the oxidation mass gain of these composites was normally higher than that of the unreinforced iron aluminides [232,233].

## 12.11 Oxidation of nickel aluminide based composites

### 12.11.1 Nickel aluminides

As another group of important intermetallic compounds,  $\text{Ni}_3\text{Al}$  and  $\text{NiAl}$  have also long been considered as candidate materials for high temperature structural applications due to their merits of high melting point, high thermal conductivity and excellent oxidation resistance. The major advantages that can be derived from the use of  $\text{Ni}_3\text{Al}$  include the following [215,216]:

1. Resistance to oxidation and carburisation in both oxidising and reducing carburising atmospheres up to 1100°C.
2. Good tensile and compressive yield strengths at 650–1100°C, as opposed to many nickel-based superalloys.
3. Fatigue resistance superior to that of Ni-based superalloys.
4. Superior creep strength.
5. Excellent wear resistance at high temperatures ( $\geq 600^\circ\text{C}$ ).
6. The formation of  $\text{Al}_2\text{O}_3$  on the surface by pre-oxidation provides good chemical compatibility for many environments.

The superiorities of  $\text{NiAl}$  include the following [215,216,234]:

1. The melting point is as high as 1638°C, about 300°C higher than that of the Ni-based superalloys.
2. The density is about 5.95 g/cm<sup>3</sup>, about two-thirds that of Ni-based superalloys.
3.  $\text{NiAl}$  has excellent oxidation properties due to the formation of stable  $\text{Al}_2\text{O}_3$  scales at elevated temperatures.
4. The high thermal conductivity, 70–80 W/m·K (20–1100°C), is about five times of magnitude higher than that of Ni-based superalloys, leading to lower thermal stresses generated by temperature difference and lower temperature on blades.

5. Young's modulus at room temperature, 188 GPa, is only slightly lower than that of the Ni-based superalloys.
6. The material cost is low, so that it can be produced using conventional processes.

However, inadequate room-temperature toughness and poor tensile and creep strength have prevented the use of nickel aluminides. Although individual alloying strategies have successfully improved the ductility, fracture toughness, oxidation resistance and creep strength, no alloy composition has yet been developed that has an acceptable balance of properties. Thus far, alloys that show significant improvements in high temperature properties may have low toughness or ductility. Similarly, when attempts are made to optimise low temperature properties, creep strength is usually sacrificed. Development of composites can possibly circumvent these deficiencies.

### 12.11.2 Oxidation of fibre-reinforced nickel aluminide based composites

There are few fibre systems available for use in nickel aluminide based composites [235]. Strengthening in combination with toughening has been observed in NiAl composites reinforced with W or Mo [236–238]. However, the potential problems associated with them are large CTE mismatch (NiAl:  $16 \times 10^{-6}/\text{K}$ ; Mo:  $4.8 \times 10^{-6}/\text{K}$ ; W:  $4.5 \times 10^{-6}/\text{K}$ ), poor high temperature oxidation resistance, and high densities. SiC fibres have proven successful in Ti-based composite systems but are an unacceptable choice for nickel aluminides because of the large CTE mismatch (SiC:  $5.8 \times 10^{-6}/\text{K}$ ) and severe chemical incompatibility at high temperatures [239–241]. Significant toughening has been observed in NiAl composites reinforced with stainless steel fibres. The stainless steel fibre-reinforced system has proved the concept of using ductile reinforcements in a brittle matrix to improve toughness and tensile properties while maintaining a high fatigue limit. Nevertheless, this particular system would not be suitable for high temperature applications because of the extensive solubility of Fe in NiAl [242,243].

The choice of reinforcing fibre for nickel aluminide composites therefore is limited to  $\text{Al}_2\text{O}_3$  fibre due to its high modulus, low density and especially high strength at elevated temperatures. Furthermore, Ni-Al intermetallic compounds and  $\text{Al}_2\text{O}_3$  are thermodynamically compatible with each other. Polycrystalline and/or single-crystal  $\text{Al}_2\text{O}_3$  fibres have also been used to produce nickel aluminide matrix composites [244–251]. However, the large mismatch between the CTE of  $\text{Al}_2\text{O}_3$  fibres ( $8–9 \times 10^{-6}/\text{K}$ ) and that of the Ni-Al alloy matrix ( $16 \times 10^{-6}/\text{K}$ ) is still the major barrier for the development of Ni-Al based composites. This CTE mismatch will cause residual stresses to develop in the composite during thermal cycling [252]. The tensile residual

stresses in the matrix, if large enough in magnitude, can cause matrix cracking at room temperature. On the other hand, the interfacial debonding might be quite harmful for the oxidation performance of the composite system, since the physical defects along the fibre/matrix interface could act as the fast channels for inward transportation of oxygen.

Oxidation behaviours of  $\text{Al}_2\text{O}_3$  fibre-reinforced  $\text{Ni}_3\text{Al}$  and  $\text{NiAl}$  composites have been reported [253–255]. Monolithic  $\text{Ni}_3\text{Al}$  and  $\text{NiAl}$  alloys have good oxidation resistance at temperatures up to 1200°C, and  $\alpha\text{-Al}_2\text{O}_3$  has good high temperature stability. However, a composite with these two components does not always possess better or comparable oxidation performance. In the study of Doychak *et al.* [254], the monolithic  $\text{NiAl}$  and the composite without Ni coating on the fibre (Saphikon<sup>TM</sup>) have similar growth rates typical of other  $\text{Al}_2\text{O}_3$ -forming alloys, while the composite with Ni coating on the fibre shows relatively higher oxidation rates at all temperatures. Nourbakhsh's results showed that incorporation of  $\text{Al}_2\text{O}_3$  continuous fibres into  $\text{Ni}_3\text{Al}$  or  $\text{NiAl}$  decreased the oxidation resistance of the composites. Doychak *et al.* also found that a continuous oxide layer was present along the fibre length from the fibre ends towards the centre of the composite, and this layer was actually formed from oxidation of the matrix surrounding the fibres. They believed that Ni coating on the fibre would result in a high porosity around the fibre due to the diffusion of nickel into the matrix during processing. These pores could act as open channels for oxidation to occur along the entire length of the fibres. Nourbakhsh *et al.* suggested that the gaps between the fibres are not solely responsible for the rapid oxidation of their  $\text{Ni-Al}/\text{Al}_2\text{O}_3$  composites; the diffusion of oxygen in atomic form through the grain boundaries and the interface boundaries of the fibres is one of the factors responsible for the rapid oxidation of the composites [255].

Misra and Bowman studied the isothermal and cyclic oxidation behaviours of  $\text{NiAl}/\text{Al}_2\text{O}_3$  composites with interfacial Mo coating at 1100°C (Saphikon<sup>TM</sup> fibre) [256]. They found that the composites with interfacial Mo coatings had better oxidation resistance than the composites without Mo coating. Oxidation of an uncoated  $\text{NiAl}/\text{Al}_2\text{O}_3$  composite resulted in oxidation along the interface throughout the composite, with a thick interfacial oxide scale, starting from the fibre ends, while for the composites with Mo coating, oxidation is confined only to the fibre/matrix interface near the fibre ends. The interfacial oxidation products near the fibre ends, which were fairly dense and well bonded to the fibre, acted as a diffusion barrier for oxygen and prevented further oxidation inside the composite. The authors proposed that the presence of Mo probably accelerates oxidation of  $\text{NiAl}$  due to the formation of  $\text{MoO}_3$  melt which results in the formation of a thick oxide layer along the interface, strongly bonded to both the fibre and the matrix near the fibre ends.

### 12.11.3 Oxidation of particulate-reinforced nickel aluminide based composites

Particulate-reinforced nickel aluminide matrix composites have been fabricated with various techniques, including gas pressure infiltration, mechanical alloying, the exothermic dispersion (XD<sup>TM</sup>) process and solid-state reactive synthesis [257–270]. Oxide particles, such as Al<sub>2</sub>O<sub>3</sub>, Y<sub>2</sub>O<sub>3</sub> or ThO<sub>2</sub>, can improve the elastic limit and the creep properties of NiAl; TiB<sub>2</sub> dispersoids can increase toughness and compressive strength. Carbide containing NiAl shows continuous work-hardening behaviour at high temperatures.

Pregger *et al.* studied the short-term isothermal oxidation behaviours of NiAl matrix composites reinforced with TiB<sub>2</sub> particulates (0, 10 and 20 vol%) at temperatures ranging from 1000 to 1200°C [271]. Oxidation kinetics followed a parabolic rate law, and oxidation rate increased significantly with the amount of TiB<sub>2</sub> in the alloy. In this temperature range, an external protective α-Al<sub>2</sub>O<sub>3</sub> scale was developed on the NiAl surface, while on the NiAl/TiB<sub>2</sub> composites, a layer with Al<sub>2</sub>O<sub>3</sub> and TiO<sub>2</sub> was typically formed. The fraction of the surface covered by TiO<sub>2</sub> appeared qualitatively to be a function of TiB<sub>2</sub> concentration in the alloy. Formation of TiO<sub>2</sub> discrete crystallites on the oxide surface degrades the scale protective ability and increases the oxidation mass gain significantly. Addition of TiB<sub>2</sub> into the alloy matrix also accelerates void formation along the scale/matrix interface in comparison with unreinforced alloy. It was observed that after 48 h of oxidation, the void regions within NiAl/TiB<sub>2</sub> were so extensive that most of the oxide scale was out of physical contact with the substrate, producing a scale prone to spallation.

Air oxidation kinetics of Ni<sub>3</sub>Al matrix composites with high contents of TiC particles (75 and 88 vol%) were measured by Becher and Plucknett at 900°C for a duration of 24 h [272]. The results indicated that the mass gains of the composites were much higher than that of the unreinforced Ni<sub>3</sub>Al, whose oxidation normally involves the formation of a stable aluminium oxide scale. This finding is not surprising, since oxidation of TiC at high temperatures will lead to the formation of titanium oxide which grows very fast due to its high defect concentration.

## 12.12 Oxidation of niobium silicide-based in-situ composites

To achieve higher efficiency and performance of gas turbine engines, the inlet gas temperature should be increased. Currently, the operating temperature on high pressure turbine engines is approaching 1150°C, which is very close to the maximum melting point of the most advanced nickel-based superalloys (~1350°C). The service temperature of intermetallic compounds based on Ni-Al and Ti-Al cannot meet the requirements for use in the hot part of

aeroengines. New materials that have higher operating temperatures have therefore been under development [273–275]. Nb-based in-situ composites, including Nb-NbCr<sub>2</sub> [276–279], Nb-Nb<sub>3</sub>Al [280–283] and Nb-Nb<sub>5</sub>Si<sub>3</sub> [284–287], have been extensively studied as the candidates. Particularly, niobium silicide-based refractory metal–intermetallic in-situ composites (RMICs) are receiving the most attention.

Two-phase Nb-Nb<sub>5</sub>Si<sub>3</sub> alloys are the model material system in this type of composite materials, and have been subjected to extensive studies of the relationships between processing, microstructure and properties. The results obtained have demonstrated that they possess a useful range of mechanical properties, such as low-temperature toughness, reasonably good high-temperature strength and creep resistance [288]. However, a serious problem associated with these materials is their poor oxidation resistance, showing as very high metal recession rates, mechanical failure of oxide scales and structural disintegration [289]. Alloying with Ti, Al, Hf, Mo and/or Cr is currently under development to obtain multiphase and multicomponent Nb-Si materials with improved environmental resistance while retaining the structural properties [290–301].

The effects of alloying additions on the oxidation of Nb silicide-based in-situ composites have also been investigated and could be summarised as follows:

1. **Al** and **Cr** are commonly required for high-temperature alloys since they can form stable and slow-growing oxide scales, Al<sub>2</sub>O<sub>3</sub> and Cr<sub>2</sub>O<sub>3</sub>. In these composites, Al and Cr could improve the oxidation resistance of Nb solid solutions (Nb<sub>ss</sub>) and silicide [286]. Cr can also stabilise the Cr-rich Laves phase. It was believed that introduction of this phase could enhance the oxidation resistance of the composites [289,291]. However, at low to moderate temperatures, e.g. 800°C, higher oxidation rates and lower adherence of oxide scales were observed with increase of the Cr concentration in the Al-containing Nb-Ti-Si composites [298].
2. Addition of **Ti** can improve the oxidation resistance [286,291,292,299]. It is supposed that formation and distribution of fine Ti oxide particles in Nb<sub>ss</sub> and formation/segregation of Ti oxide along the phase boundary between the Nb<sub>ss</sub> and the intermetallics are responsible for the decreased oxidation mass gain [302]. Other researchers have also found that Ti could reduce the area fraction of Nb<sub>ss</sub> and then bring a reduction in the oxidation rate [303,304].
3. Addition of **Sn** could eliminate the pesting oxidation damage at low temperatures and further decrease oxidation rate by working together with Ti addition [292,303,305]. It was found that Sn has a significant effect on the niobium solid solution, leading to the formation of Sn-rich and Sn-poor parts in the solid solution in the as-cast microstructure. In the presence of Sn, the Si solubility in Nb<sub>ss</sub> increases considerably while

the Cr solubility decreases. As a result of the decrease of the Cr solubility in Nb<sub>ss</sub>, the Sn addition promotes the formation of NbCr<sub>2</sub> Laves phase and stabilises this phase [306]. The changes in microstructure and elemental solubility might contribute to the improved pesting resistance. However, the detailed mechanisms concerning the positive effects of Sn on the prevention of pesting are still not clear.

4. In the presence of Ti, Al, Cr and Mo, addition of **Hf** has no significant effect on the oxidation behaviour of Nb silicide-based in-situ composites at 800°C but is probably beneficial to oxidation at 1200°C [299,303].
5. **Mo** is detrimental to oxidation resistance. Geng *et al.* suggested that Mo content should not exceed 2 at% for oxidation resistance purposes [299].
6. Zelenitsas's oxidation studies at 800°C suggested that substitution of Nb by **Ta** does not decrease the oxidation rate [298].

## 12.13 Concluding remarks

Extensive experimental observations clearly show that the addition and presence of the reinforcing phases in the metal matrices exert various influences on the high temperature oxidation behaviours of the composite material systems. The real effects are highly dependent on their composition, distribution, morphology, stability and reaction with the matrix. The overall oxidation performance of a composite material is then not sufficiently controlled by the oxidation resistance of the reinforcement or the matrix, although their respective resistance is essential. For long and continuous fibre-reinforced composites, preferential oxidation attack in the interfacial area between the fibre and the matrix is often the prime reason for failure, especially when their thermal expansion coefficients are significantly different. Therefore, special attention must be given to ensure that the interface should remain intact and would not act as a fast diffusion path during exposure at elevated temperatures in aggressive atmospheres. For discontinuous phase (particulate or whisker) reinforced composite systems, fast oxygen diffusion might not be serious in comparison with long fibre-reinforced composites. This is particularly true when the reinforcing phases are fine and round particulates. Furthermore, addition of highly oxidation-resistant particulate or whisker into the alloy matrix could generally enhance the oxidation performance of the composite systems if the processing is well under control.

To reveal the mechanisms involved in the oxidation processes of composite materials, the oxidation properties of the reinforcing phases and the matrices must be well understood. At this stage, information on the oxidation of many applicable matrix materials under various environments is available. However, the response of the reinforcement to the environmental attack is lacking. Furthermore, the different processing routes used by different companies lead to the production of reinforcing phases with quite different compositions,

structures and properties. During composite production and utilisation at high temperatures, interdiffusion and chemical reaction may also occur between the reinforcement and matrix. These factors definitely make the characterisation of the oxidation properties of the composite material systems more complex and should be considered during design and fabrication of composite materials.

Protective coatings are widely developed and used for many high temperature materials. Development of coating systems seems to be the most viable method to overcome the interaction between the continuous fibre and the matrix and the degradation of composite materials in aggressive environments. However, current efforts on this aspect are not adequate for oxidation protection, though some surface treatment techniques have been established and applied to Al or Mg based metal matrix composites to protect them against corrosion attack in aqueous environments.

## 12.14 References

1. C.M. Ward-Close, R. Minor and P.J. Doorbar, *Intermetallics*, 4 (1996) 217.
2. L. Xiao, Y.S. Kim, R. Abbaschian and R.J. Hecht, *Mater. Sci. Eng. A*, 144 (1991) 277.
3. T.C. Lu, A.G. Evans, R.J. Hecht and R. Mehrabian, *Acta. Metall. Mater.*, 39 (1991) 1853.
4. R.A. MacKay, P.K. Brindley and F.H. Froes, *JOM*, 43 (1991) 23.
5. C. Korner, W. Schaff, M. Ottmuller and R.F. Singer, *Adv. Eng. Mater.*, 2 (2000) 327.
6. S.T. Mileiko, V.M. Kiiko, A.A. Kolchin, A.V. Serebryakov, V.P. Korzhov, M.Yu. Starostin and N.S. Sarkissyan, *Compos. Sci. Technol.*, 62 (2002) 167.
7. C. Leyens, J. Hausmann and J. Kumpfert, *Adv. Eng. Mater.*, 5 (2003) 399.
8. K.S. Ravi Chandran and K.B. Panda, *Adv. Mater. Process.*, 160 (2002) 59.
9. B.M. Parker, *Composites*, 5 (1974) 7.
10. A.C. van Maaren, O. Schob and W. Westerveld, *Philips Technical Review*, 35 (1975) 125.
11. J.O. Carlsson, *J. Mater. Sci.*, 14 (1979) 255.
12. J.O. Carlsson, *J. Mater. Sci.*, 14 (1979) 2726.
13. F.E. Wawner, Jr., Boron filaments, in *Comprehensive Composite Materials*, A. Kelly and C. Zweben (eds), Vol. 1: *Fibre Reinforcements and General Theory of Composites*, Elsevier Science, Amsterdam, 2000, p. 85.
14. N. Brack, A.N. Rider, B. Halstead and P.J. Pigram, *J. Adhes. Sci. Technol.*, 19 (2005) 857.
15. S. Yajima, K. Okamura, J. Hayashi and M. Omori, *J. Am. Ceram. Soc.*, 59 (1976) 324.
16. S. Yajima, J. Hayashi, M. Omori and K. Okamura, *Nature*, 261 (1976) 683.
17. Y. Hasegawa, M. Iimura and S. Yajima, *J. Mater. Sci.*, 15 (1980) 720.
18. Y. Hasegawa, *Compos. Sci. Technol.*, 37 (1990) 37.
19. Y.M. Yang, X.W. Liu, Z.L. Tan, S.J. Yang, Y. Lu and C.X. Feng, *J. Mater. Sci.*, 26 (1991) 5167.
20. D. Upadhyaya, F.H. Froes, J.F. Watts and C.M. Ward-Close, *J. Mater. Sci.*, 30 (1995) 3839.

21. O. Greck, J.P. Viricelle, D. Bahloul-Hourlier, P. Goursat, M. Dalbin, S. Thomin and A.M. Flank, *Key Eng. Mater.*, 136 (1997) 1950.
22. H. Ichikawa and T. Ishikawa, Silicon carbide fibres, in *Comprehensive Composite Materials*, A. Kelly and C. Zweben (eds), Vol. 1: *Fibre Reinforcements and Theory of Composites*, Elsevier Science, Amsterdam, 2000, p. 107.
23. A.C.D. Chaklader, H.H. Hawthorne and S.K. Bhattacharya, *Composites*, 12 (1981) 272.
24. T. Yogo and H. Iwahara, *J. Mater. Sci.*, 27 (1992) 1499.
25. Y.H. Chiou, M.T. Tsai and H.C. Shih, *J. Mater. Sci.*, 29 (1994) 2378.
26. M.H. Berger and A.R. Bunsell, Ceramic fibres, in *Comprehensive Composite Materials*, A. Kelly and C. Zweben (eds), Vol. 1: *Fibre Reinforcements and Theory of Composites*, Elsevier Science, Amsterdam, 2000, p. 147.
27. R. Venkatesh and S.R. Ramanan, *J. European Ceram. Soc.*, 20 (2000) 2543.
28. R. Venkatesh and S.R. Ramanan, *Mater. Lett.*, 55 (2002) 189.
29. M. Chatterjee, M.K. Naskar, P.K. Chakrabarty and D. Ganguli, *Mater. Lett.*, 57 (2002) 87.
30. S.T. Mileiko, *Compos. Sci. Technol.*, 65 (2005) 2500.
31. A. Parviz-Majid, Whiskers and particulates, in *Comprehensive Composite Materials*, A. Kelly and C. Zweben (eds), Vol. 1: *Fibre Reinforcements and Theory of Composites*, Elsevier Science, Amsterdam, 2000, p. 175.
32. J. Jiang, *Composites*, 26 (1995) 62.
33. M. Furukawa, J. Wang, Z. Horita, M. Nemoto, Y. Ma and T.G. Langdon, *Metall. Mater. Trans. A – Phys. Metall. Mater. Sci.*, 26 (1995) 633.
34. B.Q. Han and K.C. Chan, *Mater. Sci. Eng. A*, 212 (1996) 256.
35. M. Vedani and F. Gariboldi, *Acta Mater.*, 44 (1996) 3077.
36. J. Wadsworth and F.H. Froes, *JOM*, 41 (1989) 12.
37. H. Hu, *J. Mater. Sci.*, 33 (1998) 1579.
38. S. Kudela, *Int. J. Mater. Prod. Technol.*, 18 (2003) 91.
39. P.R. Smith and F.H. Froes, *JOM*, 36 (1984) 19.
40. X. Zhang, W. Lu, D. Zhang and R. Wu, *Scripta Mater.*, 41 (1999) 39.
41. S. Ragaran, P.B. Aswath and W.O. Soboyejo, *Scripta Mater.*, 35 (1996) 239.
42. Z.Y. Ma, S.C. Tjong and L. Geng, *Scripta Mater.*, 42 (2000) 367.
43. D.M. Liu and W.H. Tuan, *Acta Mater.*, 44 (1996) 813.
44. T. Parsonage, *Mater. Sci. Technol.*, 16 (2000) 732.
45. J. Zhang and C. Laird, *Mater. Sci. Eng. A*, 290 (2000) 155.
46. S.R. Dong, J.P. Tu and X.B. Zhang, *Mater. Sci. Eng. A*, 313 (2001) 83.
47. S.F. Moustafa, Z. Abdel-Hamid and A.M. Abd-Elhay, *Mater. Lett.*, 53 (2002) 244.
48. X.H. Zhang, C. Van and Z.Z. Yu, *J. Mater. Sci.*, 39 (2004) 4683.
49. Y.L. Chen, C.F. Yang, J.W. Yeh, S.S. Hung and S.W. Lee, *Metall. Mater. Trans. A – Phys. Metall. Mater. Sci.*, 36 (2005) 2441.
50. M. Loípez, J.A. Jiménez and D. Corredor, *Compos. Pt. A – Appl. Sci. Manuf.*, 38 (2007) 272.
51. E. Pagounis and V.K. Lindroos, *Mater. Sci. Eng. A*, 246 (1998) 221.
52. R.K. Galgali, H.S. Ray and A.K. Chakrabarti, *Mater. Sci. Technol.*, 15 (1999) 437.
53. S.C. Tjong and K.C. Lau, *Compos. Sci. Technol.*, 60 (2000) 1141.
54. H.Y. Wang, Q.C. Jiang, B.X. Ma, Y. Wang and F. Zhao, *Adv. Eng. Mater.*, 7 (2005) 58.
55. J.C. Rawers, W.R. Wrzesinski, E.K. Roub and R.R. Brown, *Mater. Sci. Technol.*, 6 (1990) 187.

56. F.H. Froes, C. Suryanarayana and D. Eliezer, *J. Mater. Sci.*, 27 (1992) 5113.
57. A. Hirose, M. Hasegawa and K.F. Kobayashi, *Mater. Sci. Eng. A*, 239–240 (1997) 46.
58. S. Djanarthany, J.C. Viala and J. Bouix, *Mater. Sci. Eng. A*, 300 (2001) 211.
59. A. Kakitsuji, J. Ramkumar, J. Kinose, H. Mabuchi, H. Tsuda and K. Morii, *Mater. Trans. JIM*, 43 (2002) 2589.
60. L.M. Peng and Z. Li, *Metall. Mater. Trans. A – Phys. Metall. Mater. Sci.*, 37 (2006) 500.
61. N.S. Stoloff and D.E. Alman, *Mater. Sci. Eng. A – Phys. Metall. Mater. Sci.*, 144 (1991) 51.
62. M.M. Moshksar, H. Doty and R. Abbaschian, *Intermetallics*, 5 (1997) 393.
63. S. Nourbakhsh, O. Sahin and H. Margolin, *Metall. Mater. Trans. A – Phys. Metall. Mater. Sci.*, 28 (1997) 1069.
64. C.K. Lin, S.S. Hong and P.Y. Lee, *Intermetallics*, 8 (2000) 1043.
65. J.H. Schneibel, C.A. Carmichael, E.D. Specht and R. Subramanian, *Intermetallics*, 5 (1997) 61.
66. R. Subramanian and J.H. Schneibel, *Mater. Sci. Eng. A*, 244 (1998) 103.
67. M.J. Crimp, *Mater. Sci. Eng. A*, 192–193 (1995) 633.
68. M. Krasnowski, A. Witek and T. Kulik, *Intermetallics*, 10 (2002) 371.
69. S. Gedevanishvili and Z.A. Munir, *Mater. Sci. Eng. A*, 242 (1998) 1.
70. P.V. Krakhmalev, E. Strom and C. Li, *Intermetallics*, 12 (2004) 225.
71. K.S. Kumar and J.D. Whittenberger, *Mater. Sci. Technol.*, 8 (1992) 317.
72. W.R. Wrzesinski and J.C. Rawers, *J. Mater. Sci. Lett.*, 9 (1990) 432.
73. S. Nourbakhsh, F.L. Liang and H. Margolin, *Metall. Trans. A*, 21 (1990) 213.
74. K. Ichikawa and Y. Kinoshita, *Mater. Sci. Eng. A*, 239–240 (1997) 493.
75. M. Heilmayer, H. Saage and J. Eckert, *Mater. Sci. Eng. A*, 239–240 (1997) 652.
76. J.M. Yang, W.H. Kao and C.T. Liu, *Mater. Sci. Eng. A*, 107 (1989) 81.
77. P.R. Subramanian, S. Krishnamurthy, S.T. Keller and M.G. Mendiratta, *Mater. Sci. Eng. A*, 244 (1998) 1.
78. E.A. Feest and J.H. Tweed, *Mater. Sci. Technol.*, 8 (1992) 308.
79. Z.X. Guo, *Mater. Sci. Technol.*, 14 (1998) 864.
80. N. Carrère, D. Boivin, R. Valle and A. Vassel, *Scripta Mater.*, 44 (2001) 867.
81. A. Chrysanthou, *Key Eng. Mater.*, 104–107 (1995) 381.
82. T.S. Srivatsan, T.S. Sudarshan and E.J. Lavernia, *Prog. Mater. Sci.*, 39 (1995) 317.
83. C.C. Koch and J.D. Whittenberger, *Intermetallics*, 4 (1996) 339.
84. C.C. Koch, *Mater. Sci. Eng. A*, 244 (1998) 39.
85. D.R. Johnson, *Curr. Opin. Solid State Mat. Sci.*, 4 (1999) 249.
86. C.M. Ward-Close, L. Chandrasekaran, J.G. Robertson, S.P. Godfrey and D.P. Murgatroyde, *Mater. Sci. Eng. A*, 263 (1999) 314.
87. J.W. Kaczmar, K. Pietrzak and W. Wlosinski, *J. Mater. Process. Technol.*, 106 (2000) 58.
88. S.C. Tjong and Z.Y. Ma, *Mater. Sci. Eng. R*, 29 (2000) 49.
89. K.I. Parashivamurthy, R.K. Kumar, S. Seetharamu and M.N. Chandrasekharaiah, *J. Mater. Sci.*, 36 (2001) 4519.
90. K. Das, T.K. Bandyopadhyay and S. Das, *J. Mater. Sci.*, 37 (2002) 3881.
91. D.L. Zhang, *Prog. Mater. Sci.*, 49 (2004) 537.
92. H.Z. Ye and X.Y. Liu, *J. Mater. Sci.*, 39 (2004) 6153.
93. D.B. Miracle, *Comp. Sci. Technol.*, 65 (2005) 2526.
94. R.A. MacKay, P.K. Brindley and F.H. Froes, *JOM*, 43 (1991) 23.

95. P.K. Brindley, S.L. Draper, J.I. Eldridge, M.V. Nathal and S.M. Arnold, *Metall. Trans. A*, 23 (1992) 2527.
96. S.L. Draper, P.K. Brindley and M.V. Nathal, *Metall. Trans. A*, 23 (1992) 2541.
97. P.R. Smith, J.A. Graves and C.G. Rhodes, *Metall. Trans. A*, 25 (1994) 1267.
98. S. Krishnamurthy, P.R. Smith and D.B. Miracle, *Mater. Sci. Eng. A*, 243 (1998) 285.
99. T.W. Chou and A. Kelly, *Annu. Rev. Mater. Sci.*, 19 (1980) 229.
100. P.C. Brennan, W.H. Kao and J.M. Yang, *Mater. Sci. Eng. A*, 153 (1992) 635.
101. S.Z. Zhu, Y.X. Lu, Z.G. Wang and J. Bi, *Mater. Lett.*, 13 (1992) 199.
102. Z. Fan, P. Tsakiroopoulos and A.P. Miodownik, *Mater. Sci. Technol.*, 8 (1992) 922.
103. R.M. Aikin, Jr., *JOM*, 49 (1997) 35.
104. S. Ranganath and R.S. Mishra, *Acta Mater.*, 44 (1996) 927.
105. S. Ranganath, *J. Mater. Sci.*, 32 (1997) 1.
106. T.M.T. Godfrey, P.S. Goodwin and C.M. Ward-Close, *Adv. Eng. Mater.*, 2 (2000) 85.
107. N. Chawla and Y.L. Shen, *Adv. Eng. Mater.*, 3 (2001) 357.
108. J. LLorca, *Prog. Mater. Sci.*, 47 (2002) 283.
109. M. Pahutova, V. Sklenicka, K. Kucharova and M. Svoboda, *Int. J. Mater. Prod. Technol.*, 18 (2003) 116.
110. L.H. Hihara and C. Tamirisa, *Mater. Sci. Eng. A*, 198 (1995) 119.
111. P.C.R. Nunes and L.V. Ramanathan, *Corrosion*, 51 (1995) 610.
112. H.M. Saffarian and G.W. Warren, *Corrosion*, 54 (1998) 877.
113. L. Bertolini, M.F. Brunella and S. Candiani, *Corrosion*, 55 (1999) 422.
114. A.S. Hamdy, A.M. Beccaria and P. Traverso, *Surf. Interface. Anal.*, 34 (2002) 171.
115. Z. Ahmad and B.J. Abdul Aleem, *Mater. Des.*, 23 (2002) 173.
116. A. Pardo, M.C. Merino, S. Merino, M.D. Lopez, F. Viejo and M. Carboneras, *Mater. Corros.*, 54 (2003) 311.
117. H.M. Wang and G. Duan, *Intermetallics*, 11 (2003) 755.
118. F. Winterhalter, V. Medri, A. Ruffini and A. Bellosi, *Appl. Surf. Sci.*, 225 (2004) 100.
119. F. Zucchi, G. Trabanelli, V. Grassi and A. Frignani, *Corrosion*, 60 (2004) 362.
120. J. Shankar, A. Upadhyaya and R. Balasubramaniam, *Corrosion Sci.*, 46 (2004) 487.
121. A. Pardo, M.C. Merino, R. Arrabal, S. Feliu Jr., F. Viejo and M. Carboneras, *Electrochim. Acta*, 51 (2006) 4367.
122. A. Neville, F. Reza, S. Chiovelli and T. Revega, *Corrosion*, 62 (2006) 657.
123. M. Gavgali, B. Dikici and C. Tekmen, *Corros. Rev.*, 24 (2006) 27.
124. I. Gurrappa and V.V. Bhanu Prasad, *Mater. Sci. Technol.*, 22 (2006) 115.
125. S. Tiwari, R. Balasubramaniam and M. Gupta, *Corrosion Sci.*, 49 (2007) 711.
126. P.J. Bania, *JOM*, 46 (1994) 16.
127. S. Naka, *Curr. Opin. Solid State Mat. Sci.*, 1 (1996) 333.
128. I. Weiss and S.L. Semiatin, *Mater. Sci. Eng. A*, 263 (1999) 243.
129. M. Peters, J. Kumpfert, C.H. Ward and C. Leyens, *Adv. Eng. Mater.*, 5 (2003) 419.
130. M. Yamaguchi, *Mater. Sci. Technol.*, 8 (1992) 299.
131. E.P. George, M. Yamaguchi, K.S. Kumar and C.T. Liu, *Annu. Rev. Mater. Sci.*, 24 (1994) 409.
132. Y.W. Kim, *JOM*, 46 (1994) 30.
133. H.M. Flower and J. Christodoulou, *Mater. Sci. Technol.*, 15 (1999) 45.
134. H. Clemens and H. Kestler, *Adv. Eng. Mater.*, 2 (2000) 551.

135. M. Yamaguchi, H. Inui and K. Ito, *Acta. Mater.*, 48 (2000) 307.
136. S. Djanarthany, J.C. Viala and J. Bouix, *Mater. Chem. Phys.*, 72 (2001) 301.
137. D. Banerjee, *Prog. Mater. Sci.*, 42 (1997) 135.
138. Y.W. Kim, *JOM*, 47 (1995) 39.
139. R.V. Ramanujan, *Int. Mater. Rev.*, 45 (2000) 217.
140. F. Appel, H. Clemens and M. Oehring, *Mat. Res. Soc. Symp. Proc.*, 646 (2001) N1.1.1.
141. Yu.V. Milman, D.B. Miracle, S.I. Chugunova, I.V. Voskoboinik, N.P. Korzhova, T.N. Legkaya and Yu.N. Podrezov, *Intermetallics*, 9 (2001) 839.
142. G.L. Chen and J.P. Lin, *Ordered Intermetallic Compounds as Structural Materials* (in Chinese), Metallurgical Industry Press, Beijing, 1999.
143. F.H. Stott, *Rep. Prog. Phys.*, 50 (1987) 861.
144. J. Li, P. Eveno and A.M. Huntz, *Werkstoffe und Korrosion*, 41 (1990) 716.
145. T. Narushima, T. Goto, T. Hirai and Y. Iguchi, *Mater. Trans. JIM*, 38 (1997) 821.
146. Y. Gogotsi and M. Yoshimura, *J. Mater. Sci. Lett.*, 13 (1994) 680.
147. P.W.M. Peters and J. Hempenmacher, *Compos. Pt. A – Appl. Sci. Manuf.*, 33 (2002) 1373.
148. D.Y. Song, N. Takeda and H. Kawamoto, *Mater. Sci. Eng. A*, 278 (2000) 82.
149. W. Wei, *J. Mater. Sci.*, 27 (1992) 1801.
150. L.A. Wittig and D.H. Allen, *J. Eng. Mater. Technol.*, 116 (1994) 412.
151. K.L. Choy, *Scripta Mater.*, 34 (1996) 1753.
152. J.F. Fromentin, K. Debray, Y.L. Petitcorps, E. Martin and J.M. Quenisset, *Compos. Sci. Technol.*, 56 (1996) 767.
153. R.A. Shatwell, *Mater. Sci. Eng. A*, 259 (1999) 162.
154. B.S. Maiumdar, *Mater. Sci. Eng. A*, 259 (1999) 171.
155. Y.W. Xun, M.J. Tan and J.T. Zhou, *J. Mater. Process. Technol.*, 102 (2000) 215.
156. E. Pippel, J. Woltersdorf, D. Dietrich, S. Stockel, K. Weise and G. Marx, *J. European Ceram. Soc.*, 20 (2000) 1837.
157. K.L. Choy, *Prog. Mater. Sci.*, 48 (2003) 57.
158. S. Nourbakhsh, F.L. Liang and H. Margolin, *J. Mater. Sci. Lett.*, 8 (1989) 1252.
159. V. Lavaste, M.H. Berger, A.R. Bunsell and J. Besson, *J. Mater. Sci.*, 30 (1995) 4215.
160. R. Venkatesh, P. K. Chakrabarty, B. Siladitya, M. Chatterjee and D. Ganguli, *Ceram. Int.*, 25 (1999) 539.
161. J.S. Fish and D.J. Duquette, *J. de Physique IV*, 3 (1993) 411.
162. S. Nourbakhsh, O. Sahin and H. Margolin, *Acta Metall. Mater.*, 43 (1995) 3035.
163. D.B. Lee, J.H. Park, Y.H. Park and Y.J. Kim, *Mater. Trans.*, 38 (1997) 306.
164. D.B. Lee, S.W. An and Y.J. Kim, *Mater. Trans.*, 40 (1999) 1050.
165. D.B. Lee, Y.C. Lee, Y.J. Kim and S.W. Park, *Oxid. Met.*, 54 (2000) 575.
166. S.K. Gong, H.B. Xu, Q.H. Yu and C.G. Zhou, *Surf. Coat. Technol.*, 130 (2000) 128.
167. D.B. Lee, M.H. Kim, C.W. Yang, S.H. Lee, M.H. Yang and Y.J. Kim, *Oxid. Met.*, 56 (2001) 215.
168. Y.X. Qin, W.J. Lu, D. Zhang, J.N. Qin and B. Ji, *Mater. Sci. Eng. A*, 404 (2005) 42.
169. Z.W. Li, W. Gao, J. Liang and D.L. Zhang, *Mater. Lett.*, 57 (2003) 1970.
170. Y.X. Qin, W.J. Lu, D. Xu and D. Zhang, *J. Mater. Sci.*, 40 (2005) 687.
171. Y.X. Qin, D. Zhang, W.J. Lu and W. Pan, *Oxid. Met.*, 66 (2006) 253.
172. E.L. Zhang, G. Zeng and S.Y. Zeng, *Scripta Mater.*, 46 (2002) 811.
173. E.L. Zhang, G. Zeng and S.Y. Zeng, *J. Mater. Sci.*, 37 (2002) 4063.

174. H.E. Deve, A.G. Evans, G.R. Odette, R. Mehrabian, M.L. Emiliani and R.J. Hecht, *Acta Metall. Mater.*, 38 (1990) 1491.
175. G.R. Odette, B.L. Chao, J.W. Scheckherd and G.E. Lucas, *Acta Metall. Mater.*, 40 (1992) 2381
176. K.T. Venkateswara Rao, G.R. Odette and R.O. Ritchie, *Acta Metall. Mater.*, 40 (1992) 353.
177. K.T. Venkateswara Rao, G.R. Odette and R.O. Ritchie, *Acta Metall. Mater.*, 42 (1994) 893.
178. K.T. Venkateswara Rao and R.O. Ritchie, *Acta Mater.*, 46 (1998) 4167.
179. S.A. Kekare, J.B. Toney and P.B. Aswath, *Metall. Mater. Trans. A – Phys. Metall. Mater. Sci.*, 26 (1995) 1835.
180. <http://en.wikipedia.org/wiki/Thermite>.
181. H. Ellingham, *J. Soc. Chem. Ind.*, 63 (1944) 125.
182. F.D. Richardson and E. Jeffes, *J. Iron. Steel. Inst.*, 160 (1948) 261.
183. D.Z. Wang, Z.R. Liu, C.K. Yao and M. Yao, *J. Mater. Sci. Lett.*, 12 (1993) 1420.
184. N.J. Welham, *Mater. Sci. Eng. A*, 255 (1998) 81.
185. N.J. Welham, *Intermetallics*, 6 (1998) 363.
186. F. Wagner, D.E. Garcia, A. Krupp and N. Claussen, *J. European Ceram. Soc.*, 19 (1999) 2449.
187. C.F. Feng and L. Froyen, *Compos. Pt. A – Appl. Sci. Manuf.*, 31 (2000) 385.
188. D. Horvitz, I. Gotman, E.Y. Gutmanas and N. Claussen, *J. European Ceram. Soc.*, 22 (2002) 947.
189. D.L. Zhang, Z.H. Cai and G. Adam, *JOM*, 56 (2004) 53.
190. D.L. Zhang and M. Newby, US Patent No: 6,264,719 B1, July 2001.
191. Z.H. Cai and D.L. Zhang, *Mater. Sci. Forum*, 437–438 (2003) 297.
192. D.L. Zhang and Z.H. Cai, *Mater. Sci. Forum*, 437–438 (2003) 451.
193. D.L. Zhang, W. Gao, D.Y. Ying, Z.W. Li, Z.H. Cai and J. Liang, US Patent No. 6,692,839, February 2004.
194. D.Y. Ying, D.L. Zhang and M. Newby, *Metall. Mater. Trans. A – Phys. Metall. Mater. Sci.*, 35 (2004) 2115.
195. D.L. Zhang, D.Y. Ying and P. Munroe, *J. Mater. Res.*, 20 (2005) 307.
196. C.Z. Han, D.L. Zhang and I. Brown, *Int. J. Mod. Phys. B*, 20 (2006) 3848.
197. D.L. Zhang, Z.H. Cai, A.J. Huang and R. Yang, *J. Am. Ceram. Soc.*, 89 (2006) 3325.
198. Z.G. Liu, S. Raynova and D.L. Zhang, *Metall. Mater. Trans. A – Phys. Metall. Mater. Sci.*, 37 (2006) 225.
199. Z.H. Cai and D.L. Zhang, *Mater. Sci. Eng. A*, 419 (2006) 310.
200. P. Kofstad, *High Temperature Corrosion*, Elsevier, London, 1988.
201. T.A. Wallace, R.K. Clark and K.E. Wiedemann, *Oxid. Met.*, 42 (1994) 451.
202. W. Gao, Z.W. Li and D.L. Zhang, *Oxid. Met.*, 57 (2002) 99.
203. Z.W. Li, W. Gao, D.L. Zhang and Z.H. Cai, *Corrosion Sci.*, 46 (2004) 1997.
204. Z.W. Li, W. Gao, D.L. Zhang and Z.H. Cai, *Oxid. Met.*, 61 (2004) 339.
205. G.H. Qiu, J.S. Wu, L.T. Zhang and T.L. Lin, *Scripta Metall. Mater.*, 33 (1995) 213.
206. P.E. Tortorelli and J.H. Devan, in *Oxidation and Corrosion of Intermetallic Alloys*, G. Welsch and P.D. Desai (eds), Purdue University, West Lafayette, IN, 1996, p. 300.
207. Y.C. Zhou and Z.M. Sun, *Phys. Rev. B*, 61 (2000) 12570.
208. X.H. Wang and Y.C. Zhou, *Corrosion Sci.*, 45, (2003) 891.
209. T. Saito, *Adv. Perform. Mater.*, 2 (1995) 121.

210. X.H. Wang and Y.C. Zhou, *Oxid. Met.*, 59 (2003) 303.
211. Y.D. He and F.H. Stott, *Corrosion Sci.*, 36 (1994) 1869.
212. Y.D. He, Z.W. Li, H.B. Qi and W. Gao, *Mater. Res. Innov.*, 1 (1997) 157.
213. Z.W. Li, W. Gao, D.Y. Ying and D.L. Zhang, *Scripta Mater.*, 48 (2003) 1649.
214. K. Uenishi, T. Matsubara, T. Shibusaki and K.F. Kobayashi, *Intermetallics*, 10 (2002) 105.
215. S.C. Deevi and V.K. Sikka, *Intermetallics*, 4 (1996) 357.
216. S.C. Deevi, V.K. Sikka and C.T. Liu, *Prog. Mater. Sci.*, 42 (1997) 177.
217. S.K. Mukherjee and S. Bandyopadhyay, *Mater. Sci. Eng. A*, 202 (1995) 123.
218. R. Subramanian, C.G. McKamey, L.R. Buck and J.H. Schneibel, *Mater. Sci. Eng. A*, 239–240 (1997) 640.
219. R. Subramanian, C.G. McKamey, J.H. Schneibel, L.R. Buck and P.A. Menchhofer, *Mater. Sci. Eng. A*, 254 (1998) 119.
220. M. Inoue, K. Saganuma and K. Niihara, *Mat. Res. Soc. Symp. Proc.*, 552 (1999) KK8.24.1.
221. H.Y. Gong, Y.S. Yin, X. Wang and Y.C. Liu, *Mater. Res. Bull.*, 39 (2004) 513.
222. J.H. Schneibel and S.C. Deevi, *Mater. Sci. Eng. A*, 364 (2004) 166.
223. R. Subramanian and J.H. Schneibel, *JOM*, 49(8) (1997) 50.
224. J.H. Schneibel, C.A. Carmichael, E.D. Specht and R. Subramanian, *Intermetallics*, 5 (1997) 61.
225. R. Subramanian and J.H. Schneibel, *Mater. Sci. Eng. A*, 244 (1998) 103.
226. J.H. Schneibel, *Mat. Res. Soc. Symp. Proc.*, 552 (1999) KK4.4.1.
227. B.G. Park, S.H. Ko and Y.H. Park, *Mat. Res. Soc. Symp. Proc.*, 646 (2001) N5. 19.1.
228. M.X. Gao, F.J. Oliveira, Y. Pan, L. Yang, J.L. Baptista and J.M. Vieira, *Intermetallics*, 13 (2005) 460.
229. A.Y. Mosbah, D. Wexler and A. Calka, *Wear*, 258 (2005) 1337.
230. K. Saganuma, *J. Alloy. Compd.*, 197 (1993) 29.
231. M.A. Espinosa-Medina, M. Casales, A. Martinez-Villafane, J. Porcayo-Calderon, G. Izquierdo, L. Martinez and J.G. Gonzalez-Rodriguez, *J. Mater. Eng. Perform.*, 9 (2000) 638.
232. J.H. Schneibel, R. Subramanian, K.B. Alexander and P.F. Becher, Processing and properties of FeAl-bonded composites, in *International Symposium on Nickel and Iron Aluminides*, S.C. Deevi (ed.), ASM International, Materials Park, OH, 1997, p. 329.
233. J.H. Schneibel and P.F. Becher, *J. Chin. Inst. Eng.*, 22 (1999) 1.
234. D.B. Miracle, *Acta Metall. Mater.*, 41 (1993) 649.
235. R.D. Noebe, R.R. Bowman and M.V. Nathal, The physical and mechanical metallurgy of NiAl, in *Physical Metallurgy and Processing of Intermetallic Compounds*, N.S. Stoloff and V.K. Sikka (eds), Chapman & Hall, New York, 1996.
236. S.Y. Chang and S.J. Lin, *Scripta Mater.*, 37 (1997) 23.
237. P. Ramasundaram, R. Bowman and W. Soboyejo, *Mater. Sci. Eng. A*, 248 (1998) 132.
238. T.A. Venkatesh and D.C. Dunand, *Metall. Mater. Trans. A – Phys. Metall. Mater. Sci.*, 31 (2000) 781.
239. J.M. Yang, W.H. Kao and C.T. Liu, *Metall. Trans. A*, 20 (1989) 2459.
240. T.C. Chou, *Scripta Metall. Mater.*, 24 (1990) 409.
241. D.J. Larkin, L.V. Interrante and A. Bose, *J. Mater. Res.*, 5 (1990) 2706.
242. R.B. Bhagat, *J. Mater. Sci.*, 24 (1989) 1496.

243. S.Y. Chang and S.J. Lin, *J. Mater. Sci.*, 32 (1997) 5127.
244. J.H. Schneibel, E.P. George, C.G. McKamey, E.K. Ohriner, M.L. Santella and C.A. Carmichael, *J. Mater. Res.*, 6 (1991) 1673.
245. S. Nourbakhsh, W.H. Rhee, O. Sahin and H. Margolin, *Metall. Trans. A*, 25 (1994) 1259.
246. W.C. Williams and G.C. Stangle, *J. Mater. Res.*, 10 (1995) 1736.
247. A.E. Murut and C.L. White, *Acta Mater.*, 45 (1997) 2547.
248. L. Wang, K. Xu, R.R. Bowman and R.J. Arsenault, *Metall. Mater. Trans. A – Phys. Metall. Mater. Sci.*, 28 (1997) 2755.
249. S. Yu and D.M. Elzey, *Mater. Sci. Eng. A*, 244 (1998) 67.
250. M. Rosefort, C. Dahmen, A. Bührig-Polaczek, W.P. Hu, H. Chen, Y.L. Zhong, G. Gottstein, D. Hajas and J.M. Schneider, *Adv. Eng. Mater.*, 8 (2006) 730.
251. W. Hu, T. Weirich, B. Hallstedt, H. Chen, Y. Zhong and G. Gottstein, *Acta Mater.*, 54 (2006) 2473.
252. S.M. Arnold, V.K. Arya and M.E. Melis, *J. Compos. Mater.*, 26 (1992) 1287.
253. O. Sahin, S. Nourbakhsh, W.H. Rhee and H. Margolin, *Metall. Trans. A*, 23 (1992) 3151.
254. J. Doychak, J.A. Nesbitt, R.D. Noebe and R.R. Bowman, *Oxid. Met.*, 38 (1992) 45.
255. S. Nourbakhsh, O. Sahin and H. Margolin, *Metall. Mater. Trans. A – Phys. Metall. Mater. Sci.*, 25 (1994) 1291.
256. A.K. Misra and R.R. Bowman, *Mater. Sci. Eng. A*, 196 (1995) 197.
257. S.M. Barinov, V.Yu. Evdokimov and V.Ya. Shevchenko, *J. Mater. Sci.*, 32 (1997) 5053.
258. K.P. Plucknett, P.F. Becher and S.B. Waters, *J. Am. Ceram. Soc.*, 81 (1998) 1839.
259. W.H. Tuan, W.B. Chou, H.C. You and S.T. Chang, *Mater. Chem. Phys.*, 56 (1998) 157.
260. S.K. Bhaumik, C. Divakar, L. Rangaraj and A.K. Singh, *Mater. Sci. Eng. A*, 257 (1998) 341.
261. C.S. Hwang and T.J. Liu, *J. Mater. Res.*, 14 (1999) 75.
262. A. Kitaoka, K. Hirota, M. Yoshinaka, Y. Miyamoto and O. Yamaguchi, *J. Am. Ceram. Soc.*, 83 (2000) 1311.
263. M. Li, H. Schaffer and W.O. Soboyejo, *J. Mater. Sci.*, 35 (2000) 1339.
264. K. Morsi, H.B. McShane and M. McLean, *Metall. Mater. Trans. A – Phys. Metall. Mater. Sci.*, 31 (2000) 1663.
265. P. La, Q. Xue and W. Liu, *Metall. Mater. Trans. A – Phys. Metall. Mater. Sci.*, 32 (2001) 1823.
266. C.T. Hu and W.C. Chiou, *Metall. Mater. Trans. A – Phys. Metall. Mater. Sci.*, 32 (2001) 407.
267. C. Curfs, I.G. Cano, G.B.M. Vaughan, X. Turrillas, A. Kvick and M.A. Rodriguez, *J. European Ceram. Soc.*, 22 (2002) 1039.
268. A. Michalski, J. Jaroszewicz, M. Rosinski and D. Siemiaszko, *Intermetallics*, 14 (2006) 603.
269. J. Meng, C.C. Jia and Q. He, *Mater. Sci. Eng. A*, 434 (2006) 246.
270. Y. Chen and H.M. Wang, *Intermetallics*, 14 (2006) 325.
271. B.A. Pregger, T. Kircher and A. Khan, *Mater. Sci. Eng. A*, 153 (1992) 567.
272. P.F. Becher and K.P. Plucknett, *J. European Ceram. Soc.*, 18 (1997) 395.
273. D.M. Shah, D.L. Anton, D.P. Pope and S. Chin, *Mater. Sci. Eng. A*, 192–193 (1995) 658.

274. M.R. Jackson, B.P. Bewlay, R.G. Rowe, D.W. Skelly and H.A. Lipsitt, JOM, 48(1) (1996) 39.
275. J.C. Zhao and J.H. Westbrook, MRS Bull., 28 (2003) 622.
276. D.L. Davidson, K.S. Chan and D.L. Anton, Metall. Mater. Trans. A – Phys. Metall. Mater. Sci., 27 (1996) 3007.
277. K.S. Chan, D.L. Davidson and D.L. Anton, Metall. Mater. Trans. A – Phys. Metall. Mater. Sci., 28 (1997) 1797.
278. M. Yoshida and T. Takasugi, Mater. Sci. Eng. A, 234–236 (1997) 873.
279. D.J. Thoma, F. Chu, P. Peralta, P.G. Kotula, K.C. Chen and T.E. Mitchell, Mater. Sci. Eng. A, 239–240 (1997) 251.
280. C.D. Bencher, A. Sakaida Rao, K.T. Venkateswara and R.O. Ritchie, Metall. Mater. Trans. A – Phys. Metall. Mater. Sci., 26 (1995) 2027.
281. T. Tabaru and S. Hanada, Intermetallics, 7 (1999) 807.
282. H. Ohno, T. Shinoda and Y. Oya-Seimiya, Mater. Trans., 44 (2003) 1729.
283. H. Ohno, T. Shinoda and Y. Oya-Seimiya, Mater. Trans., 44 (2003) 1736.
284. M.G. Mendiratta, J.J. Lewandowski and D.M. Dimiduk, Metall. Trans. A, 22 (1991) 1573.
285. M.G. Mendiratta and D.M. Dimiduk, Metall. Trans. A, 24 (1993) 501.
286. B.P. Bewlay, M.R. Jackson and H.A. Lipsitt, Metall. Mater. Trans. A – Phys. Metall. Mater. Sci., 27 (1996) 3801.
287. J.D. Rigney and J.J. Lewandowski, Metall. Mater. Trans. A – Phys. Metall. Mater. Sci., 27 (1996) 3292.
288. M.G. Mendiratta, J.J. Lewandowski and D.M. Dimiduk, Metall. Trans. A, 22 (1991) 1573.
289. P.R. Subramanian, M.G. Mendiratta, D.M. Dimiduk and M.A. Stucke, Mater. Sci. Eng. A, 239–240 (1997) 1.
290. B.P. Bewlay, J.J. Lewandowski and M.R. Jackson, JOM, 49(8) (1997) 44.
291. B.P. Bewlay, M.R. Jackson and M.F.X. Gigliotti, Niobium silicide high temperature in situ composites, in *Intermetallic Compounds: Vol. 3, Principles and Practice*, J.H. Westbrook and R.L. Fleischer (eds), John Wiley & Sons, 2002, p. 541.
292. B.P. Bewlay, M.R. Jackson, J.C. Zhao and P.R. Subramanian, Metall. Mater. Trans. A – Phys. Metall. Mater. Sci., 34 (2003) 2043.
293. B.P. Bewlay, M.R. Jackson, J.C. Zhao, P.R. Subramanian, M.G. Mendiratta and J.J. Lewandowski, MRS Bull., 28 (2003) 646.
294. J.H. Kim, T. Tabaru, M. Sakamoto and S. Hanada, Mater. Sci. Eng. A, 372 (2004) 137.
295. C.L. Ma, J.G. Li, Y. Tan, R. Tanaka and S. Hanada, Mater. Sci. Eng. A, 384 (2004) 377.
296. K.S. Chan, Mater. Sci. Eng. A, 409 (2005) 257.
297. K. Zelenitsas and P. Tsakiroopoulos, Intermetallics, 13 (2005) 1079.
298. K. Zelenitsas and P. Tsakiroopoulos, Mater. Sci. Eng. A, 416 (2006) 269.
299. J. Geng, P. Tsakiroopoulos and G.S. Shao, Mater. Sci. Eng. A, 441 (2006) 26.
300. J. Geng, P. Tsakiroopoulos and G.S. Shao, Intermetallics, 14 (2006) 227.
301. K. Zelenitsas and P. Tsakiroopoulos, Intermetallics, 14 (2006) 639.
302. Y. Murayama and S. Hanada, Sci. Technol. Adv. Mater., 3 (2002) 145.
303. J. Geng and P. Tsakiroopoulos, Intermetallics, 15 (2007) 382.
304. K.S. Chan, Metall. Mater. Trans. A – Phys. Metall. Mater. Sci., 35 (2004) 589.
305. J. Geng, P. Taskiropoulos and G.S. Shao, Intermetallics, 15 (2007) 270.
306. J. Geng, P. Tsakiroopoulos and G.S. Shao, Intermetallics, 15 (2007) 69.

# 13

## Design strategies for new oxidation-resistant high temperature alloys

B A PINT, Oak Ridge National Laboratory, USA

### 13.1 Introduction

There is always a need for new oxidation-resistant high-temperature alloys because of the continuous push for higher service temperatures and longer component lifetimes. While there is always the possibility of a revolutionary alloy development, the periodic table is finite and the more realistic near-term prospects for improved alloys focus on Fe- and Ni-base compositions which develop protective external oxides or scales of  $\text{Al}_2\text{O}_3$ ,  $\text{Cr}_2\text{O}_3$ , or  $\text{SiO}_2$ . Chromia-forming alloys are mentioned as they are used in a broad range of applications but their limitations also will be highlighted. The majority of this chapter will focus on alumina-forming alloys because alumina has a slower growth rate and better resists the detrimental effects of water vapor in exhaust or steam environments. The discussion of alumina-forming alloy development includes Al additions to NiCr and FeNiCr alloys and improving the performance of current alumina-forming alloys by slowing the consumption of Al (e.g. by optimized reactive element (RE) additions) or by increasing the Al reservoir. Typical of any alloy development, a recurring issue with Al additions is a balance of properties. Few alloys are needed only for oxidation resistance. Therefore, it is essential to maintain other properties, e.g. creep strength, for a structural alloy development process. Throughout the discussion, all of the compositions are given in atom% (which may be confusing in some instances) as this provides a better fundamental understanding of the role of composition.

### 13.2 Chromia-forming alloys

#### 13.2.1 Alloy development

The most widely used high temperature alloys are Fe- or Ni-base alloys that form protective chromia-scales during exposure. Because of the long history of research in this class of materials (Kofstad, 1988), the possibility of

developing new alloys is somewhat limited. A general concept in developing oxidation resistant alloys is to increase the concentration of the protective scale forming element, i.e. Cr. However, higher Cr contents often lead to problems with phase stability (e.g., formation of brittle, Cr-rich phase) or decrease in creep strength (e.g. type 310 stainless steel, Fe-27Cr-20Ni, compared to other 300 series compositions) (Maziasz *et al.*, 1999, 2007). For coating applications, Cr contents can go as high as 53% with the remainder Ni (similar to alloy 671).

One area where there is considerable current interest in chromia-forming alloys is for metallic interconnectors for solid oxide fuel cells (Quadakkers *et al.*, 2003; Brady *et al.*, 2006). For this application, a key figure of merit is the electrical conductivity of the external scale. This criterion excludes alumina and silica scales which are too insulating. Two examples are provided which show some of the potential alloy design strategies for this application.

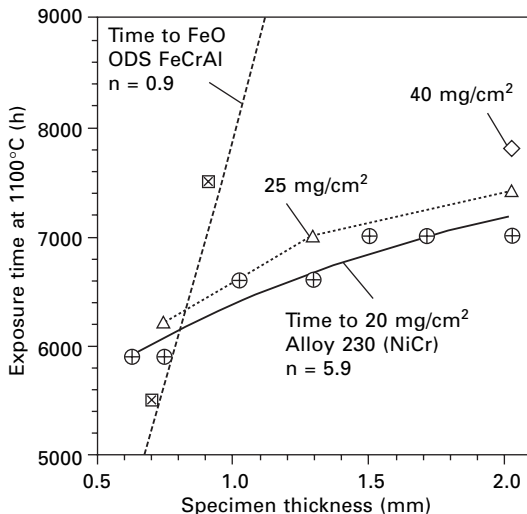
A commercial ferritic Fe-24Cr-0.4Mn-0.07Ti-0.004La (alloy 22APU) has been developed for fuel cells (Quadakkers *et al.*, 2003). The Cr content is likely restricted to 24% because of concern about embrittlement by sigma phase formation. However, the most critical design issue is the selection of the minor alloying additions of Mn, Ti and La. Lanthanum is a typical reactive element (RE) addition (Whittle and Stringer, 1980; Strawbridge and Hou, 1994; Pint, 1994; Pint *et al.*, 1995; Pint, 1996; Quadakkers and Singheiser, 2001; Pint, 2003a). It is favored in chromia-formers because of its higher solubility and larger ion size than Y (Quadakkers *et al.*, 2003; Pint, 2003a). The traditional RE role of La is to reduce the scale growth rate and improve scale adhesion (see Section 13.4). For this application, the addition of La has a slightly negative effect on scale electrical conductivity (Brady *et al.*, 2006). A proposed role of the Ti addition was to strengthen the alloy by creating a near-surface dispersion of internal oxides during oxidation (Quadakkers *et al.*, 2003). (This mechanism has not been proven but is a likely explanation.) A later study showed that Ti and Mn synergistically acted to increase the scale conductivity more than Mn additions alone (Brady *et al.*, 2006). Another role of the Mn addition was to form a Mn- and Cr-rich outer layer which is thought to inhibit the volatility of Cr containing compounds that poison the fuel cell performance. Poisoning of the cell by volatile Cr-containing compounds may be a critical impediment to developing durable solid oxide fuel cells with Cr-containing interconnectors. Another practical issue is maintaining low Al and Si impurities in the alloy to minimize the formation of insulating oxides that also can form internally. In general, the development of alloy 22APU is an excellent example of optimizing the alloy composition and dopants to maximize long-term alloy performance. At the temperatures of interest, 700–800°C, the oxidation-limited lifetime for this alloy (when the alloy is depleted in Cr and can no longer form chromia) can be quite

extensive (e.g. >100 kh for 0.3 mm thick material at 800°C) (Huczkowski *et al.*, 2004).

Another issue for interconnectors is matching the coefficient of thermal expansion (CTE) of the other fuel cell components (particularly the zirconia electrolyte). This subject was addressed by Ueda and Taimatsu (2000) for Fe-Cr-W alloys. The lowest CTE was observed for Fe-20Cr-3W which was studied in a later paper (Brady *et al.*, 2006). Additional work examined the CTE as well as the oxidation behavior of Fe-Cr-W and Fe-Cr-Mo alloys (Pint *et al.*, 2007a). This is another example of opportunities for development of chromia-forming alloys. However, alloy cost with 20Cr and 3W may be prohibitive.

### 13.2.2 Problems with chromia-forming alloys

Despite their current widespread use, it is difficult to imagine chromia-forming alloys being appropriate for future applications demanding higher temperatures and longer lifetimes. For example, as application temperatures push above 1000°C, the possibility of using chromia-forming alloys diminishes due to the rapid scale growth rate and volatilization of CrO<sub>3</sub> in air (Tedmon, 1966). A screening of ~15 commercial alloys at 1100°C for a heat exchanger application that required a minimum lifetime of 40kh showed that alloy 230 (Ni-27Cr-4W + La) had the slowest rate of mass gain in laboratory air among available, commercial chromia-forming alloys without Al additions (Pint and Keiser, 2006). To follow up, a series of alloy 230 specimens with different thicknesses was exposed at 1100°C with a cycle time of 100 h to determine the effect of specimen thickness on lifetime (see Section 13.5). This type of information is needed in order to design components. Figure 13.1 shows the time to a total mass gain (specimen mass gain + spalled oxide) (Pint *et al.*, 2002) of 20 mg/cm<sup>2</sup> as a function of specimen starting thickness. This mass gain is somewhat arbitrary, but this value is approximately where the rate of mass gain began to increase significantly. A second curve in Fig. 13.1 shows the time to 25 mg/cm<sup>2</sup> for the specimens that were not stopped sooner. While it took ~6 kh to reach 20 mg/cm<sup>2</sup>, it only took a few hundred more hours for the mass gain to increase 25% and, less than 1 kh later, the mass gain of a 2mm thick specimen doubled to 40mg/cm<sup>2</sup>. Therefore, at this point, a form of breakaway or accelerated oxidation began that showed no signs of stopping. The onset of this increased oxidation rate was not very sensitive to specimen thickness, suggesting that even very thick cross-sections of alloy 230 could not make the 40 kh lifetime goal. In contrast, some data points for an alumina-forming, oxide-dispersion strengthened (ODS) Fe-20Cr-9Al-0.4Ti-0.24Y alloy (alloy 956) also are shown in Fig. 13.1. These data correspond to the times at which the alloy began to form FeO and the entire cross-section was consumed (Pint and Keiser, 2006). For this alloy,



13.1 Time to accelerated attack as a function of specimen thickness for alloy 230 (Ni-27Cr-4W + La) and alloy 956 (ODS Fe-20Cr-9Al) for exposure in 100 h cycles at 1100°C in laboratory air. For alloy 956, the time is for the onset of FeO formation and increases significantly with thickness. For alloy 230, the times are to total mass gains of 20–40 mg/cm<sup>2</sup> that do not change significantly with thickness. The empirical  $n$  values relate the thickness to lifetime based on Equation 13.1 (see Section 13.5).

the lifetime is much more sensitive to specimen thickness and a ~4 mm thick alloy 956 component was predicted to meet the lifetime goal based on the current data. One reason for the difference between the two alloys is the rapid diffusion of Al in a ferritic alloy which does not result in significant composition gradients in the alloy. In contrast, the slower diffusion of Cr in the austenitic Ni-base alloy results in Cr depletion gradients (e.g. Evans and Lobb, 1984; Gleeson and Harper, 1998) independent of the total substrate thickness. Apparently, once these gradients achieve a critical value, the alloy can no longer form a protective chromia scale and enters a rapid degradation phase. Faster diffusion of Cr in ferritic (Fe-Cr) alloys appears to eliminate this problem at 800°–900°C (Huczkowski *et al.*, 2004) and likely results in longer lifetimes, but these alloys have not been investigated at 1100°C.

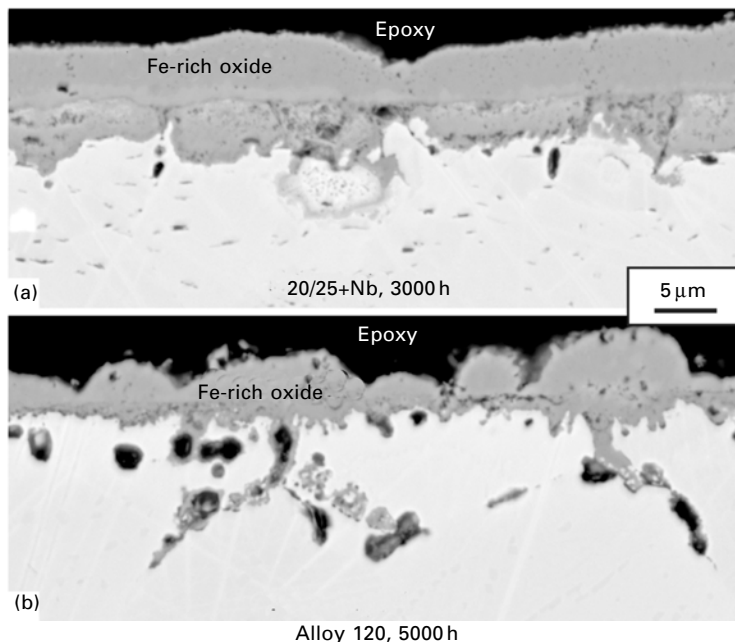
In addition to the temperature limitation, chromia-forming alloys suffer problems at lower temperatures due to the presence of water vapor in the environment (i.e. steam or combustion gas) (Opila, 2004). This is a significant issue as many high temperature applications involve these environments. The study of water vapor effects has been ongoing for many years (e.g. Caplan and Cohen, 1959; Fujii and Meussner, 1964) and is a very active area of current research (Otsuka *et al.*, 1989; Shen *et al.*, 1997; Nickel *et al.*,

1998; Asteman, *et al.*, 2000; Henry *et al.*, 2001; Zurek *et al.*, 2005; Ehlers *et al.*, 2006; Pint, 2006; Pint *et al.*, 2007b). However, there is not a comprehensive explanation for the role of water vapor on oxidation. The basic observation is that under time and temperature conditions that would normally form a thin protective Cr-rich scale, the addition of water vapor causes accelerated corrosion and the formation of thick duplex Fe-rich oxides on Fe-base alloys. Higher additions of Cr and Ni result in more resistance to this accelerated degradation (Peraldi and Pint, 2004). However, even for higher alloyed steels, it appears clear that prior to accelerated attack significant Cr depletion occurs in the alloy (Otsuka *et al.*, 2004; Pint, 2006; Young and Pint, 2006; Pint *et al.*, 2007b). This depletion has been quantified for thin (~100 µm) foils in laboratory tests in humid (10 vol%) air and occurs for both Fe- and Ni-base (alloy 625) materials, as shown in Table 13.1. It is believed to be due to the evaporation of  $\text{CrO}_2(\text{OH})_2$  (Asteman *et al.*, 2000; Young and Pint, 2006; Opila *et al.*, 2007) resulting in long-term linear kinetics for Cr consumption. For thin-section components, such as heat exchangers, the Cr loss restricts lifetime even at 650°C. Higher Cr content alloys, Ni-26Cr-5Mo-3Fe-0.2N (alloy 625) or 35Fe-35Ni-26Cr-0.8N-0.3C (alloy 120) will likely struggle to meet 40 kh lifetime goals in engine exhaust environments where the Cr consumption could approximately double due to higher gas velocities (Young and Pint, 2006). More rapid Cr consumption in engines has been confirmed in a natural gas-fired, microturbine (60 kW) test facility (Pint *et al.*, 2006a) where commercial fabricated foils of alloy 709 and alloy 120 formed Fe-rich oxides at ~735°C after only 3 and 5 kh exposures, respectively, Fig. 13.2

**Table 13.1** Residual Cr remaining (% of starting content) and amount consumed (at%) for various foil materials oxidized in humid air for 10 kh. The standard deviation for three EPMA composition profiles is shown (Pint, 2005; Pint *et al.*, 2007b)

Alloy	Starting (at%)				
	Cr	Mn	650°C	700°C	800°C
Alloy 709 (lab)	21.6	1.0	-1.7 ± 1.1 at% 92 ± 5%	-2.4 ± 0.9 at% 89 ± 4%	-10.5 ± 0.4 at%* 51 ± 2%
Alloy 120 (lab)	26.4	0.7	-1.6 ± 0.3% 94 ± 1%	-2.4 ± 0.5% 91 ± 2%	
Alloy 120 (comm)	26.4	0.7		-2.1 ± 1.1% 92 ± 4%	-12.4 ± 0.3 at% 53 ± 1%
Fe-22Cr-20Ni + Mn (lab)	22.2	3.8	-2.0 ± 0.2% 91 ± 1%	-3.3 ± 0.2% 85 ± 1%	
Alloy 625 (lab)	26.0	0.04	-1.6 ± 1.0% 94 ± 4%	-2.9 ± 0.5% 89 ± 2%	-6.0 ± 1.0 at%* 77 ± 4%

\*After only 6 kh.



13.2 Secondary electron images of polished cross-sections of foils exposed in the exhaust gas of a 60 kW microturbine at  $\sim 735^{\circ}\text{C}$ : (a) 130  $\mu\text{m}$  20/25 + Nb (Fe-22Cr-24Ni-1.1Mn-0.9Mo-0.5Si-0.24Nb-0.4C-0.4N) foil exposed for 3000 h; (b) 85  $\mu\text{m}$  alloy 120 (Fe-26Cr-35Ni-0.7Mn-0.2Mo-0.5Si-0.36Nb-0.3C-0.8N) foil exposed for 5000 h.

Adapted from Pint *et al.*, 2007c.

(Pint *et al.*, 2007c). Without the presence of 5–10 vol% water vapor, the scale after such exposures would be only 2–3  $\mu\text{m}$  thick. For thick-section components, the accelerated attack and Cr depletion will be less of a factor, but repeated shedding of thick oxides can affect flow in the tubes of steam plants (Nishimura *et al.*, 2005; Wright *et al.*, 2007).

### 13.3 Alumina-forming alloys

With the problems outlined above for chromia-forming alloys, oxidation-resistant alloy development tends to focus on alumina-forming alloys. A few examples will be given to illustrate some of the potential and a few of the problems with these alloys.

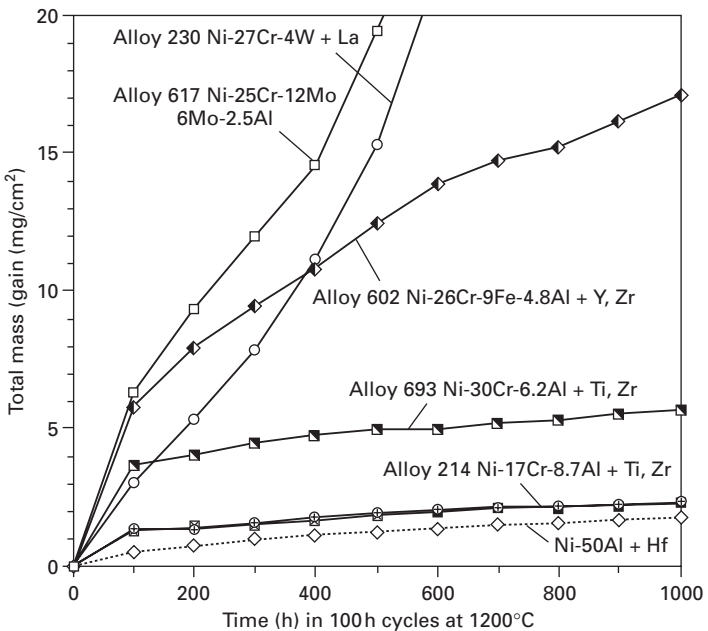
#### 13.3.1 Nickel-base alloys

For Ni-base alloys, the addition of Al to NiCr alloys has been done with a fair level of commercial success. Low levels of Al have been added to alloys

such as 617 (25Cr-12Co-6Mo-2.5Al-0.4Ti), 602 (26Cr-9Fe-4.8Al) and 693 (30Cr-6.2Al-5Fe) to maintain their fabricability, especially their weldability. Higher Al contents are found in alloy 214 (17Cr-8.7Al), superalloys like 142, N5 and 1484 (6–7Cr, 12–13Al) and in NiCrAlY and NiCoCrAlY coatings (10–20Cr, 10–20Al) (Goward, 1986; Wright *et al.*, 2000; Gleeson, 2006). In the case of sprayed or vapor deposited coatings, higher Al contents can be used, as ductility and weldability are not the major concern. Figure 13.3 gives a comparison of the total mass gain of some of the commercial NiCrAl alloys at 1200°C using 100 h cycle exposures in laboratory air. The addition of only 2.5Al to alloy 617 showed no benefit at this temperature compared to the high mass gain of alloy 230 (incidental 0.6Al). The addition of 4.8Al to alloy 602 had a more significant effect on reducing the total mass gain. However, alloy 602 primarily forms a chromia scale with some alumina formation, mostly as internal oxides. At 1200°C, the alloy becomes depleted in Al near the surface and significant spallation occurs despite the Y and Zr additions (Pint and Paul, 2007f). Increasing the Al content to 6.2Al, alloy 693 now shows a much lower total mass gain. Significant scale spallation occurred for this alloy, but the relatively low total mass gain suggests protective alumina formation. With 8.7Al, alloy 214 shows a reaction rate similar to one of the most oxidation-resistant alloys, Hf-doped NiAl (Doychak, 1994; Pint, 1998). After the first 100 h cycle, both alloy 693 and 214 showed a higher mass gain than NiAl due to the formation of a Ni-rich transient oxide, Fig. 13.3.

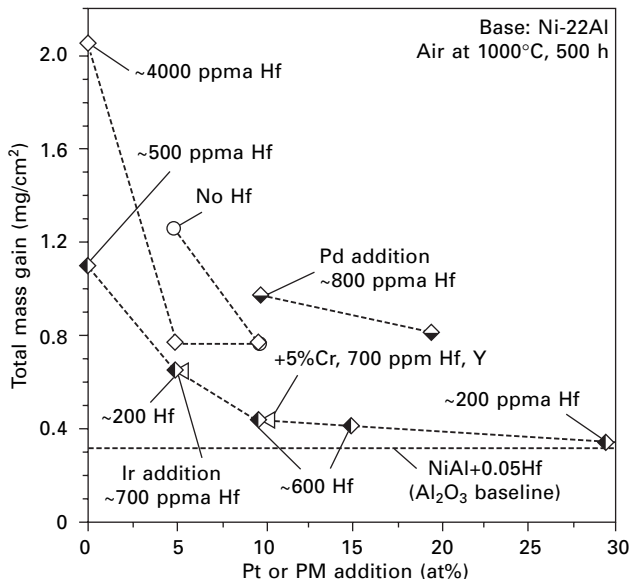
One application for Al-containing Ni-base alloys is cast tubing for steam cracking of ethanol where metal dusting, carburization and coking can be issues (Grabke, 1998). Because of the aggressive environment, NiCr cast alloys can lose strength as the Cr-rich carbide strengthening phase dissolves as the alloy becomes Cr depleted. Recent work has reported the successful addition of Al to Ni-base cast alloys, resulting in excellent oxidation resistance and little negative effect reported on creep properties (Kirchheimer *et al.*, 2005). Because mainly Al is depleted during oxidation, the Cr-rich carbides are relatively unaffected.

Another recent development has been in Ni-Pt-(16–22)Al alloys in the  $\gamma$ - $\gamma'$  phase field (Gleeson *et al.*, 2004; Pint, 2004; Izumi and Gleeson, 2005; Deodeshmukh *et al.*, 2006). The addition of a platinum group metal (PGM) such as Pt (or Ir, Pd, etc.) reduces the transient formation of Ni-rich oxide and makes the alloy into a primary alumina-former. (This method of improving oxidation resistance is revisiting a concept explored earlier: Tatlock and Hurd, 1984.) Nevertheless, a thin transient layer of Ni-rich oxide can be found even with Ni-30Pt-22Al (Pint *et al.*, 2007d). To show the effect on transient oxide formation, Fig. 13.4 shows the effect of PGM additions (Pt, Pd, Ir) and Hf on the mass gain after a 500 h isothermal exposure at 1000°C in air. As a (dashed) baseline, Ni-48Al + 0.05Hf sets a minimum in terms of



13.3 Total mass gain (specimen + spalled oxide) during 100 h cycles at 1200°C in laboratory air for various Ni-Cr-Al alloys. Generally, the mass gain decreases with Al content due to the formation of a protective alumina scale with NiAl + Hf having one of the slowest growth rates of any alumina-former. Two different specimens are shown for alloy 214 to indicate the reproducibility.

no Ni-rich oxide formation, minimal Hf internal oxidation and slow alumina growth. The alloys with only 22Al show higher mass gains primarily due to the transient formation of Ni-rich oxides, particularly the alloys with no PGM addition. (Internal oxidation of Hf can also add to the mass gain.) With higher PGM additions, the amount of transient oxide is reduced. Both Pt and Ir show similar benefits at the 5% level. Higher levels of Pd, which is significantly less expensive than Pt or Ir, are less effective. (Pint *et al.*, 2007d). The co-addition of 5Cr and 10Pt did not have much effect on the mass gain. However, this alloy contained both ~700 ppma Y and 700 ppma Hf, because of concerns that the alloying of Cr would increase the alloy S content and have a detrimental effect on scale adhesion. The addition of both Y and Hf increased the amount of internal oxidation which increased the mass gain. A primary reason for adding Cr is to increase the hot corrosion resistance of coatings based on these compositions (Deodeshmukh *et al.*, 2006). Because of the phase match of the  $\gamma$ - $\gamma'$  coating with the  $\gamma$ - $\gamma'$  superalloy substrate, the typical coating problem of Al loss due to interdiffusion into the substrate is minimized with these compositions (Gleeson *et al.*, 2004). However,



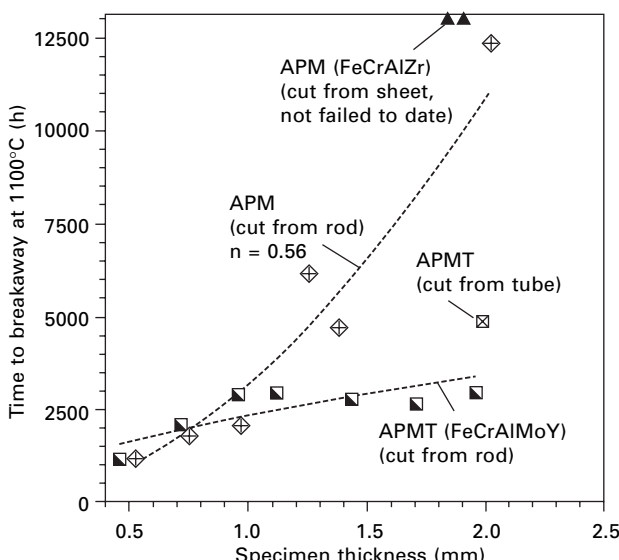
**13.4** Total mass gain (specimen + spalled oxide) after a 500 h isothermal exposure at 1000°C in laboratory air for various precious metal and Hf additions to alloys with 22% Al. NiAl + 0.05% Hf sets a (dashed) baseline in terms of no Ni-rich transient oxide, minimal Hf internal oxidation and slow alumina growth. The alloys with 22% Al primarily show higher mass gains due to the formation of Ni-rich oxide. Pd additions were not as effective as Pt or Ir. Internal oxidation of Hf also could cause increased mass gains. The addition of Cr did not have much effect with ~10% Pt, but Y, in addition to Hf, was added to this alloy, which may have resulted in additional internal oxidation. Adapted from Pint *et al.*, 2007d.

loss of Pt from the coating due to interdiffusion will likely limit their maximum use temperature (Zhang *et al.*, 2005). Because of the high cost of elements like Pt and Ir, these compositions are of more interest as coatings than as bulk alloys. However, they are being investigated for thin-walled ( $\sim 250 \mu\text{m}$ ) structures in advanced concept engines where creep strength and oxidation resistance are needed (Ballard *et al.*, 2007). Few data are currently available in the literature for the mechanical properties of these compositions.

### 13.3.2 Iron-base alloys

Alloys based on FeCrAl have been discussed for over 40 years (Wukusick and Collins, 1964). Intermetallics (Fe<sub>3</sub>Al, FeAl) also have been considered (Tortorelli and Natesan, 1998) but exhibit scale spallation problems due to their high CTE (Smialek *et al.*, 1990; Wright *et al.*, 2001a; Pint and Wright, 2004) which limit their lifetime and compatibility with other components

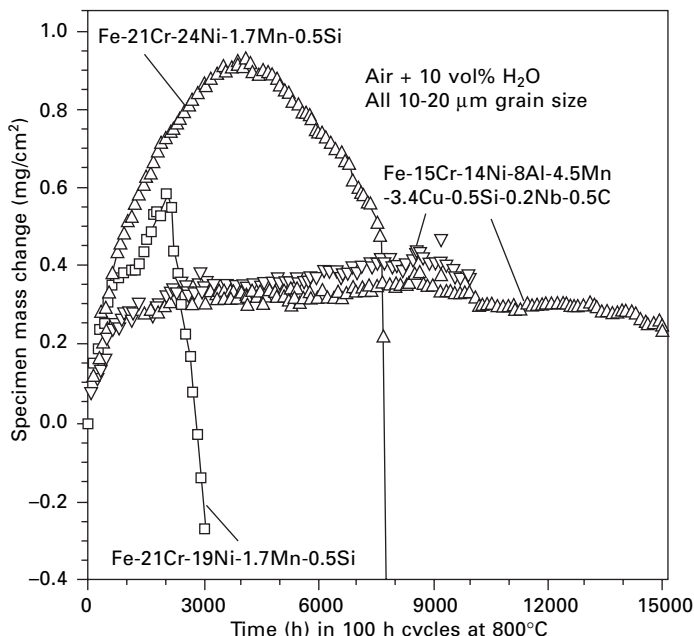
(see Section 13.5). One issue that has always limited ferritic alloys is poor creep strength, which can even limit their lifetime for applications where the strength requirements are minimal (like heating elements). ODS FeCrAl alloys are one solution to low strength ferritics (McColvin and Smith, 1985). However, the expense of powder processing makes ODS alloys expensive and joining issues limit their application. Quasi-dispersion-strengthened alloys, such as APM (Fe-20Cr-10.7Al-0.4Si-0.06Zr), which is a powder metallurgy FeCrAl (0.17O rather than 0.6–0.89O in ODS FeCrAl), have been successfully introduced (Pint *et al.*, 1995; Jönsson and Svedberg, 1997). A recent modification of this alloy, APMT (Fe-21Cr-9.8Al-1.6Mo-1Si-0.14Y-0.06Zr) (Jönsson *et al.*, 2004), highlights the trade-off in properties that is sometimes necessary. APMT has increased creep strength due to the addition of Mo. (The other primary change in composition is the addition of 0.14Y.) The increase in creep strength (along with the slightly lower Al content) has a negative effect on lifetime (time to breakaway oxidation) at 1250°C, Fig. 13.5. The same reduction in lifetime has been seen for comparisons of wrought and ODS FeCrAl (Wilber *et al.*, 2000; Pint and Wright, 2004). Thin (<1 mm)



13.5 Lifetime (time to breakaway oxidation) during 100 h cycles at 1250°C in laboratory air as a function of specimen thickness for two commercial powder metallurgy FeCrAl alloys (Kanthal alloys APM and APMT). Thicker specimens of the higher creep strength alloy, APMT (FeCrAlMoY), had a significantly shorter life in this test. APM (FeCrAlZr) had a nearly parabolic relationship ( $n = 0.5$ ) between lifetime and thickness. For both alloys, specimens cut from a rod specimen had shorter life than specimens cut from sheet (APM) or tube (APMT) product.

specimens of APMT have the same time to failure as the weaker APM alloy, Fig. 13.5. However, with thicker cross-sections, the inability of the stronger (ODS or APMT) substrate to accommodate stress (thermal and growth) from the alumina scale leads to increased scale spallation, which leads to a faster Al depletion (Evans, 1995; Evans *et al.*, 1995; Nicholls *et al.*, 1997). This lifetime penalty appears to be unavoidable.

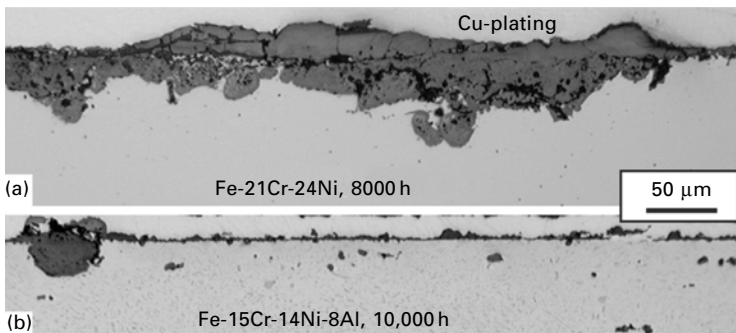
The development of an Fe-base, alumina-forming austenitic steel has long been sought for achieving creep strength and oxidation resistance at a reduced cost. As discussed in Section 13.2.2, the issue of Cr loss from thin-section components is a critical issue for the development of a durable, high temperature ( $>700^{\circ}\text{C}$ ) heat exchanger. A creep-resistant, alumina-forming Fe-base alloy would be ideal for that application. Initial work on Fe-15Cr-14Ni-8Al sheet material (~0.5–1 mm thickness) showed excellent oxidation resistance compared to chromia-forming alloys, Fig. 13.6 (Pint *et al.*, 2004a). The alloy variants without Al showed a higher initial mass gain because of the faster growth rate of the chromia scale compared to the alumina scale on



13.6 Specimen mass gains for various FeCrNi and FeCrNiAl alloys during 100 h cycles in air + 10 vol%  $\text{H}_2\text{O}$  at  $800^{\circ}\text{C}$ . The alloys without Al initially show a higher mass gain due to the formation of a Cr-rich oxide scale. The subsequent mass loss is a combination of scale spallation and evaporation of  $\text{CrO}_2(\text{OH})_2$  followed by breakaway oxidation. The specimens with Al show low mass changes for up to 15 kh. Adapted from Pint *et al.*, 2007c.

the alumina-containing alloys. Due to the presence of water vapor, the chromia-forming alloys began to lose weight, first due to evaporation of  $\text{CrO}_2(\text{OH})_2$  (Asteman *et al.*, 2000) and later due to accelerated oxidation when Cr was depleted in the underlying substrate. The specimens with 8Al showed relatively low mass gains for up to 15 kh (Pint *et al.*, 2007c). The reaction products of two of the specimens in Fig. 13.6 are shown in Fig. 13.7. The Fe-21Cr-24Ni-1.7Mn-0.5Si specimen (~1.2 mm thick) formed a thick Fe-rich oxide after 8 kh that spalled after each 100 h cycle, resulting in a continuous, large mass loss. The Fe-15Cr-14Ni-8Al alloy showed some Fe-rich nodule formation (likely explaining the initial mass gain), but most of the surface was covered with a thin, Al-rich oxide layer.

Adding Al to austenitic alloys has been done previously (Pivin *et al.*, 1980; Belen *et al.*, 1984; Ramakrishnan *et al.*, 1988). The problem with this strategy is that Al is a strong ferrite stabilizer, and the formation of a ferritic phase significantly reduces the creep strength compared to carbide-strengthened (Nb, Ti, and/or V) FeCrNi alloys. Table 13.2 gives some examples for conventional FeCrNi austenitic alloys and for Al-containing alloys. The addition of 8Al, as described above, resulted in a drastic reduction in the 750°C/100 MPa rupture life. A second series of alloys with 13–14Cr and 14–15Ni (higher Ni to reduce the amount of ferrite) also explored different strengthening mechanisms with modest success (Pint *et al.*, 2007c). The third generation of these alloys with 20Ni prevented the formation of ferrite and achieved significant 750°C creep strength while forming a protective alumina scale with only 5.3Al (Yamamoto *et al.*, 2007). A key issue that was identified was that of using only NbC strengthening. Additions of 0.9Nb did not interfere with alumina scale formation as did Ti and V additions and appeared to be slightly beneficial to alumina formation. This type of alloy has only recently



13.7 Light microscopy of polished cross-sections of sheet specimens exposed at 800°C in humid air: (a) Fe-20Cr-25Ni + Mn, Si after 8000 h; (b) Fe-15Cr-15Ni-4Al after 10 kh. The mass gain for these specimens is shown in Fig. 13.6. Adapted from Pint *et al.*, 2007c.

**Table 13.2** Room temperature tensile properties and 750°C/100 MPa creep properties of conventional and Al-containing austenitic steels. Comparative values (in italics) for conventional alloys are average values for various commercial and laboratory materials (Pint *et al.*, 2007c; Yamamoto *et al.*, 2007)

	Yield strength (MPa)	UTS (MPa)	Elongation (%)	Reduction of area (%)	750°C rupture life (h)
Fe-19Cr-9Ni (Type 347)	250	600	50	65	350
Fe-22Cr-23Ni+Nb (709)	325	700	45		2000
Fe-15Cr-14Ni+8Al	259	603	43	n.d.	20
Fe-14Cr-14Ni+8Al	203	568	56	35	172
Fe-14Cr-15Ni+7Al	201	573	52	20	234
Fe-14Cr-14Ni+9Al	199	505	41	17	77
Fe-13Cr-15Ni+7Al	281	767	41	30	94
Fe-16Cr-20Ni+5.3Al (with 10% cold work)	523	650	22	n.d.	2200

been developed, and its capabilities are still being evaluated. With only 5Al, the maximum use temperature is likely near 800°C. Nevertheless, it appears to be a promising composition class.

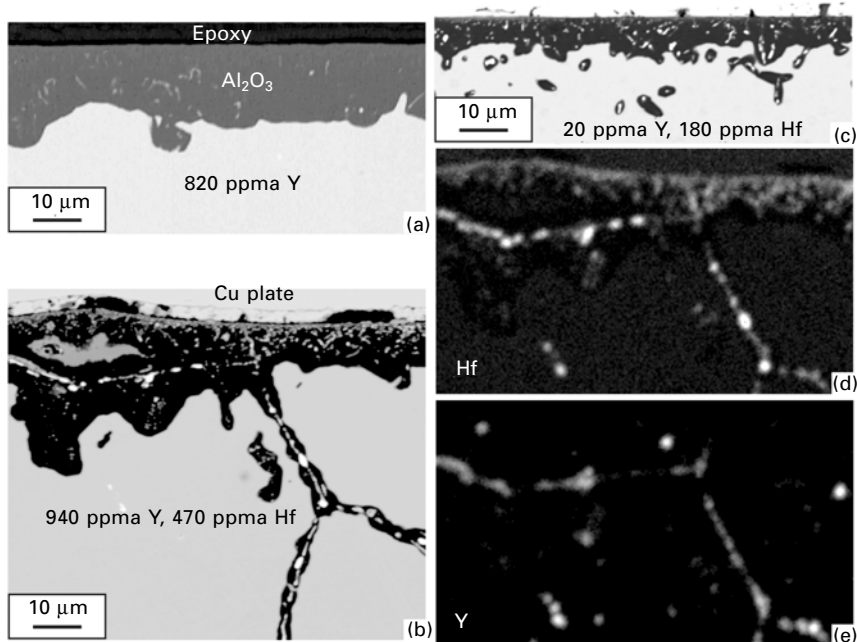
### 13.4 Reactive element (RE) optimization

One opportunity for the development of new high temperature materials is to maintain the base composition but consider strategies for optimizing the minor element additions, particularly RE additions. The effect of reactive element additions has been discussed for many years (Wukusick and Collins, 1964; Whittle and Stringer, 1980; Lang, 1989; King, 1989; Moon, 1989; Strawbridge and How, 1994; Pint *et al.*, 1995; Pint, 1996; Quadakkers and Singheiser, 2001; Pint, 2003a; Quadakkers *et al.*, 2003). The most significant RE effect in alumina-forming alloys is improved scale adhesion, which dramatically increases the oxidation-limited alloy lifetime (see examples later in this section). The improved adhesion has been attributed to the gettering of indigenous S by elements such as Y (Funkenbush *et al.*, 1985). However, more recent work (Hou, 1999) concluded that better alumina adhesion was observed with RE additions than could be obtained with low S (or desulfurized) undoped alloys (Smialek *et al.*, 1994). Additional RE effects include (1) changing the scale growth mechanism by inhibiting the outward diffusion of Al (or Cr in chromia scales) (Quadakkers *et al.*, 1989; Cotell *et al.*, 1990; Pint *et al.*, 1993). The change in the alumina growth mechanism leads to (2) a reduction by ~2–10 times in the parabolic growth rate constant, and (3) a change in the scale grain structure to a more columnar structure with smaller grains. A thinner scale has less strain energy (due to the scale–substrate CTE mismatch) and is less likely to spall (Przybylski and Yurek,

1989). The finer oxide grain structure initially was thought to result in a more plastic scale (Antill and Peakall, 1967). Ironically, more recent work on high-purity RE-doped bulk alumina discovered that RE dopants *increased* the scale creep strength (Cho *et al.*, 1997). Reported improvements in selective oxidation associated with RE additions can often be related to changes in alloy grain size and are not unique to RE additions (Pint, 1996). For example, finer alloy grain structures can produce improvements in selective oxidation (Liu *et al.*, 1997; Pint *et al.*, 1999b).

Particularly after the initial observations that RE ions segregated to scale grain boundaries (Ramanarayanan *et al.*, 1984; Przybylski *et al.*, 1987), it was widely recognized that this segregation behavior was most likely responsible for the RE effects, e.g., as suggested by Ecer *et al.* (1982) and Kofstad (1985). The additional observation that RE ions also segregated to the metal–oxide interface, first observed in 1987 but not published until later (Pint *et al.*, 1995), further emphasized the role of RE ionic segregation. However, a comprehensive segregation model was not proposed until Pint (1996) that covered RE effects in chromia and alumina scales as well as the different methods of RE addition (alloying, oxide dispersions and coatings or surface modifications). The unique aspect of the proposed dynamic segregation theory was that RE dopants were driven by the oxygen potential gradient to diffuse outward from the alloy into the scale. A change in interface energies due to the segregation of RE ions to the metal–scale interface likely explains the benefit of RE doping unrelated to any RE–S interaction.

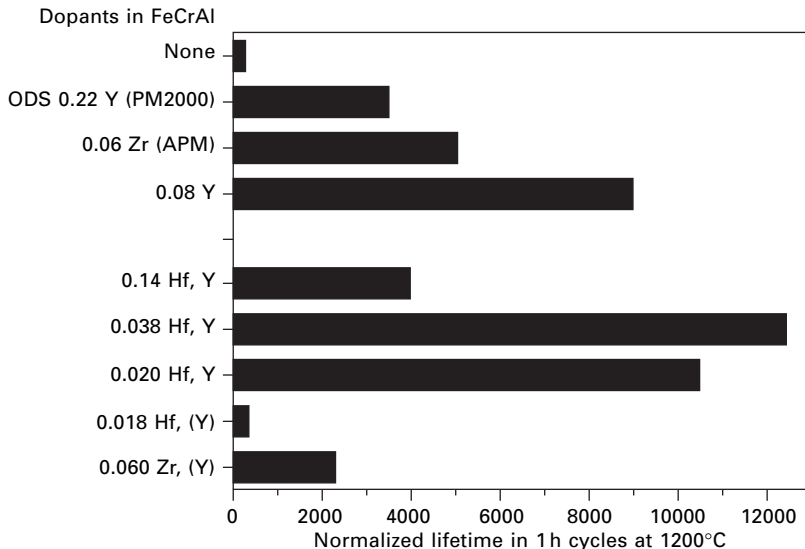
During the last 10 years, more RE-related research has been directed towards optimizing RE benefits. The type and amount of RE dopant addition is discussed elsewhere (Pint and Alexander, 1998; Quadakkers and Singheiser, 2001; Naumenko *et al.*, 2004). As mentioned above, there are a variety of ways to make RE additions but alloying is the most common, practical and effective (Pint, 1994, 1996). As alloying additions, RE dopants will have no appreciable effect on CTE (discussed in the next section) and, at low levels, will not affect the alloy mechanical properties, except, obviously, when added as an oxide dispersion. However, the type and amount of RE addition will strongly affect the rate of scale growth, which will strongly affect the rate at which Al is consumed. For example, Fig. 13.8 shows the scale formed on three different Fe-20Cr-10Al alloys after 2 kh (20 cycles each of 100 h) at 1100°C in laboratory air. Using backscattered (atomic number contrast) imaging, the RE-rich oxide precipitates are evident. An addition of 0.082Y resulted in some incorporation of Y-rich oxides, Fig. 13.8a. A thicker oxide with a large amount of internal oxidation was formed when 0.047Hf was added in addition to 0.094Y, Fig. 13.8b. Both Y and Hf formed oxide particles in the scale, and oxide pegs in the alloy, Figs 13.8d and 13.8e. However, when the amounts of Y and Hf were reduced to 0.002 and 0.018, respectively, a much thinner scale was formed with a parabolic rate constant one quarter



13.8 EPMA back-scattered electron images of the scale formed after 2000 h at 1100°C on (a) FeCrAl-0.082Y, (b) FeCrAl-0.094Y-0.047Hf and (c) FeCrAl-0.002Y-0.018Hf. X-ray maps from the upper portion of (b) are shown in (d) Hf and (e) Y.

that of FeCrAlY ( $1.5$  vs  $6.6 \times 10^{-13} \text{ g}^2/\text{cm}^4\text{s}$ ). The reduction in rate is likely because the RE-rich oxides are fast O diffusion paths that become permanent defects in the scale (Hindam and Whittle, 1982). By minimizing their size and density, a slower growth rate is achieved. The benefit of longer lifetime (time to breakaway oxidation of Fe) is illustrated for various FeCrAl alloys in Fig. 13.9, all with  $\sim 10\text{Al}$  and listed by the type and total amount of dopant addition. FeCrAlY is a common baseline used in many studies. This FeCrAlY had a lifetime of  $\sim 9000$  1-h cycles at  $1200^\circ\text{C}$  in dry  $\text{O}_2$ . For reference, two commercial FeCrAl alloys, PM2000 (ODS) and APM also are shown. Without a dopant, the lifetime of wrought FeCrAl (85 ppm S) was about 300 cycles. Single element additions of Zr or Hf did not have similar beneficial effects (Pint, 2003b). Using a co-doping strategy with Hf and Y, longer (20–38%) lifetimes were achieved due to a slower Al consumption rate (Pint *et al.*, 2003). However, there appears to be a critical dopant range for optimal lifetime. Too much dopant resulted in excessive internal oxidation which increased the rate of Al consumption, Fig. 13.8.

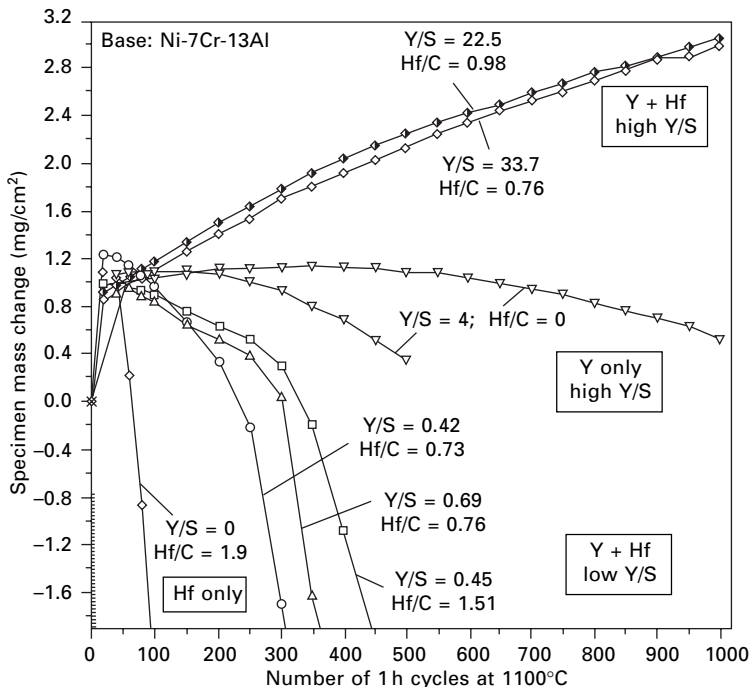
Too little dopant (0.018 Hf but no detectable Y) also produced little benefit, Fig. 13.9. Empirically, it has been observed that effective dopant levels are



13.9 Lifetime (time to FeO formation) for various FeCrAl alloys with ~10% Al and different dopant additions during 1 h cycles at 1200°C in dry O<sub>2</sub>. The highest lifetimes are with alloy additions with combinations of Hf and Y. However, adding too much or too little dopant results in reduced lifetime. For the alloys marked (Y), a Y addition was made but none was detected in the casting. Initial data from Pint (2003b).

related to the dopant–interstitial element ratios (Sigler, 1989), particularly Y/S and Hf/C or Zr/C, with ratios greater than unity being more effective (Wright *et al.*, 2000; Smialek and Pint, 2001; Pint and Schneibel, 2005). It has been suggested that this observation supports a ‘gettering’ mechanism (Funkenshush *et al.*, 1985) where, for example, Y prevents S from segregating to and weakening the metal–scale interface by forming a Y–S compound. However, the mechanism also could involve the activity and/or mobility of the dopant. For example, if Hf is tied up as HfC particles, it is less able to diffuse to the surface and dope the scale grain boundaries. When Hf/C > 1, there is free Hf in excess of that tied up as carbides. Figure 13.10 shows a variety of Ni-7Cr-13Al alloys with different Y/S and Hf/C ratios. The very poor spallation resistance observed for the Hf-only NiCrAl alloy with a Y/S ratio of 0 suggests that Hf alone is not adequate to improve scale adhesion in these alloys. Likewise, with Hf and low Y additions, the spallation resistance was not significantly better. Additions of Y alone improved the spallation resistance to some degree, but the best scale adhesion was observed for the alloy with both Y/S and Hf/C > 1 (Pint, 2003b).

A variety of alloys introduced in the past 20 years have excellent oxidation performance due to RE dopant optimization. Alloy 22APU, discussed in



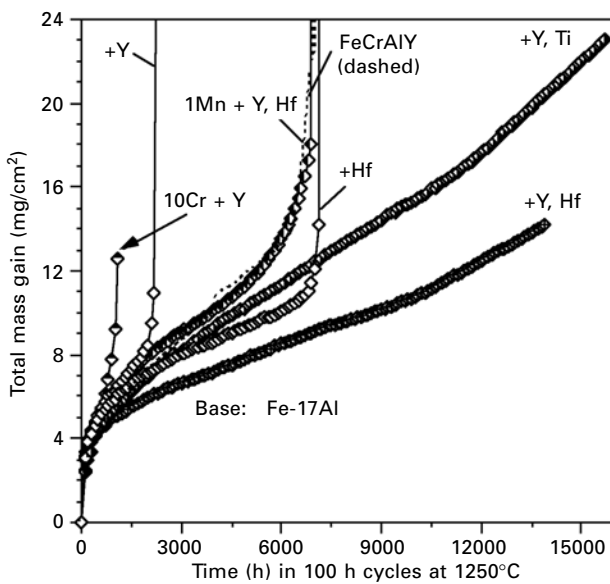
13.10 Specimen mass change during 1 h cycles at  $1100^\circ\text{C}$  in dry  $\text{O}_2$  for various Ni-7Cr-13Al alloys with various Hf/C and Y/S contents.  
Data from Pint (2003b).

Section 13.2.1 on chromia-formers, has been optimized with La and Ti additions. For FeCrAl foils, Aluchrom YHf has additions of 0.036Y, 0.028Zr and 0.009Hf and has a lifetime in 1 h cycles at  $1100^\circ\text{C}$  in dry  $\text{O}_2$  of 1200 h. This lifetime is similar to that of Durafoil, which is FeCrAl aluminized to increase the Al content to a higher level than typically found in rolled foils (Chang *et al.*, 2002; Dryepondt *et al.*, 2008). For NiCrAl, alloy 214 (Ni-17Cr-9Al-3Fe) contains 0.003Y and 0.012Zr, resulting in a very thin scale with very little internal oxidation (Pint *et al.*, 2003). Also, second generation nickel-base superalloys, e.g. General Electric's René N5+ and Pratt & Whitney PWA1487, contain a combination of Y and Hf that result in excellent inherent (uncoated) oxidation resistance (Wright *et al.*, 2000; Smialek and Pint, 2001; Pint *et al.*, 2006b). None of these superalloys has Hf/C or Zr/C ratio  $>1$ , suggesting that this ratio is not as critical as Y/S. Co-doping also has been used in NiCrAl coatings; Pratt & Whitney PWA286 is modified with Y, Hf and Si (Gupta and Duvall, 1984). No composition information is available on this proprietary coating (for which patent protection recently expired) but, based on the co-doping concept, the addition of the more-soluble Hf would allow a lower concentration of Y (with low solubility) to be used,

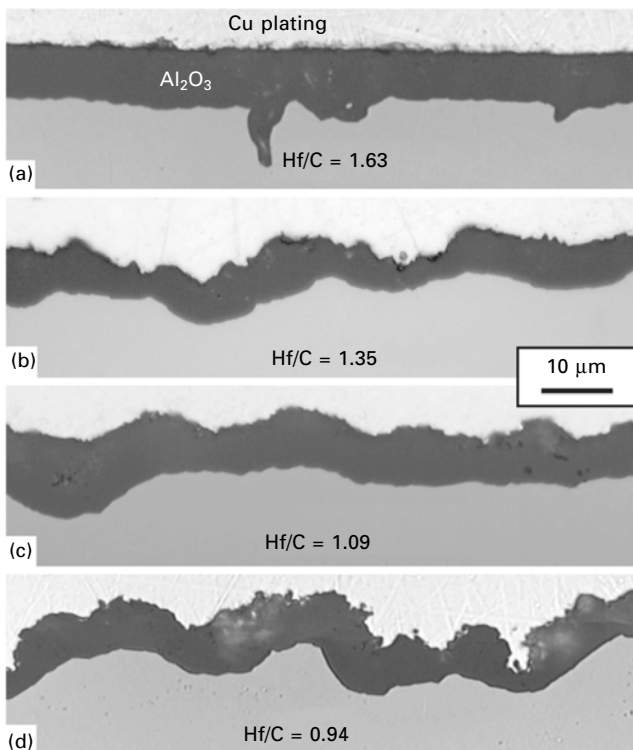
thereby reducing the amount of internal oxidation (as illustrated in Fig. 13.8). The role of Si on coating oxidation behavior has not been determined, but the Si addition may play a role during coating deposition.

Occasionally, RE optimization and co-doping are needed for other reasons. Ferritic alloys can suffer from a form of accelerated grain boundary attack at 1200–1300°C (sometimes called ‘broccoli’) that is thought to occur due to oxidation of Cr-rich grain boundary carbides (Kochubey *et al.*, 2006). This can reduce the lifetime of some commercial and experimental FeCrAl (Kochubey *et al.*, 2006),  $\text{Fe}_3\text{Al} + \text{Y}$  (Pint *et al.*, 1999a) and Fe(Al) alloys (Pint and Wright, 2004). For example, Fig. 13.11 shows the total mass gain for various Fe-(17–18)Al alloys at 1250°C in laboratory air, where those with only Y or 10Cr + Y additions show a much shorter time to breakaway oxidation than the alloy with a Hf addition. The addition of a carbide-former, Hf or Ti, in addition to Y, prevented the accelerated mass gain, leading to longer lifetimes (neither has failed to date) than any of the single RE additions.

As a final point, the mechanisms that govern these dopant-interstitial element effects are not fully understood. Figure 13.12 gives an example of the effect on scale morphology in Hf-doped Ni~50Al with different Hf/C ratios oxidized for 1000h (10 cycles each of 100h) at 1200°C in laboratory



13.11 Total mass gain (specimen + spalled oxide) during 100 h cycles at 1250°C in laboratory air for various ferritic Fe-(17–18)Al alloys. Additions of only Y showed relatively short times to breakaway oxidation due to ‘broccoli’ formation. Addition of Hf or Y and Hf or Ti prevent this form of attack. The co-doped alloy specimens have not reached breakaway oxidation to date.



13.12 Light microscopy of polished sections of NiAl + Hf after 1000 h (10 cycles each of 100 h) at 1200°C in laboratory air. The alloys shown in (a)–(d) differ in their Hf/C ratio. Adapted from Pint *et al.*, 2004b.

air. Metal–scale convolutions (and scale spallation) decreased with increasing Hf/C (Pint *et al.*, 2004b). Thermal or growth stresses are often used to explain convolutions, but these minor changes in Hf and C levels do not appear sufficient to have changed the stress or mechanical properties of the system. More fundamental work (particularly characterization) is needed to study the role of dopants and interstitials to better understand their role in the growth and maintenance of scales.

### 13.5 Strategies for increasing lifetime

In addition to developing alloys with higher temperature capabilities or for specific environments, another goal is to develop an alloy with a longer lifetime under the same conditions. For instance, a heat exchanger may be expensive to fabricate and require replacement every 40 kh of system operation. Thus, an alloy that could extend the heat exchanger lifetime to 60 or 80 kh

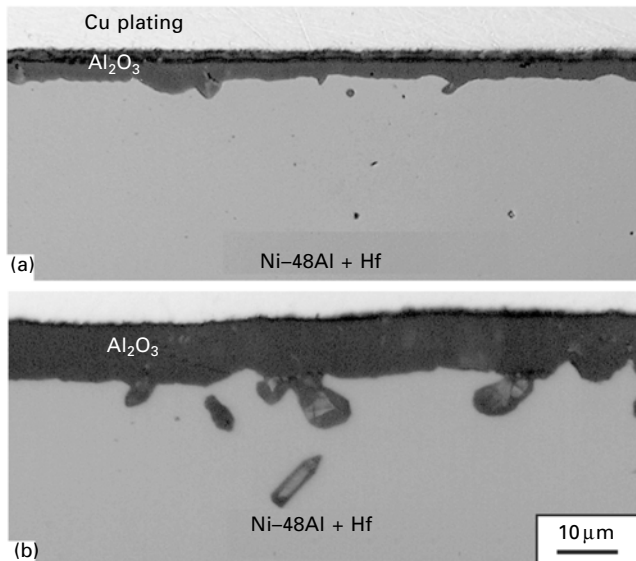
could reduce the long-term operating costs. Quadakkers and co-workers developed a simple reservoir-consumption model to predict the lifetime of FeCrAl alloys (Quadakkers and Bennett, 1994; Quadakkers and Bongartz, 1994). The model assumes uniform Al consumption from a substrate of thickness  $d$ , density  $\rho$  and starting Al content  $C_0$ . This information, along with the critical Al content,  $C_b$ , where the alloy can no longer form a protective alumina scale, are used to define the Al reservoir, which is then set equal to a consumption term:

$$(C_0 - C_b) \rho d = A k t_b^n \quad 13.1$$

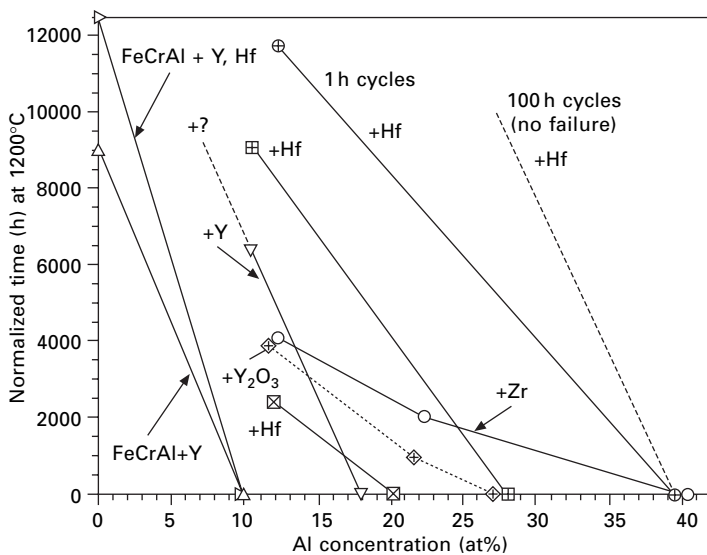
where  $A$  is a constant,  $k$  is a rate constant,  $t_b$  is the oxidation-limited lifetime, and  $n = 0.5$  for parabolic kinetics and  $n = 1$  for linear kinetics. The model is a simplification that does not consider the formation of Al gradients and other geometric factors which can affect lifetime (Wright *et al.*, 2004; Pint *et al.*, 2005). Also, it can be difficult to approximate Al consumption over long periods with only  $k$  and  $n$  as variables (Wright *et al.*, 2001a). However, Equation 13.1 is a good starting point to discuss lifetime issues and can also be used to discuss coating performance. As a note, while Equation 13.1 also applies to Ni-base alloys, the lifetime discussion focuses on Fe-base alloys because it is much easier to define and obtain failures in Fe-base alloys. In Ni-base alloys, the onset of  $t_b$  is less dramatic (e.g. the chromia-forming Ni-Cr alloy in Fig. 13.1) because the formation of Ni-rich oxides is slower than that of FeO and, for higher Al contents (e.g.  $\beta$ -NiAl), the lifetimes are incredibly long,  $>20$  kh at  $1250^\circ\text{C}$ . Even using a criterion such as number of cycles to zero mass change (i.e. when the specimen begins to lose weight due to spallation) can be difficult (Haynes *et al.*, 2004). Hf-doped NiAl does not reach zero mass gain after 10,000 1-h cycles at  $1150^\circ\text{C}$ . The scale is thin and protective, Fig. 13.13, with spallation only observed near the specimen edges.

Considering Equation 13.1 with the desire to increase  $t_b$ , one possibility is to increase the wall thickness,  $d$ , to increase the Al reservoir and extend lifetime. However, this would increase cost and could decrease the efficiency of the heat exchanger. Slowing the rate of Al consumption (determined by  $k$  and  $n$ ) is another strategy. Basically, that strategy was discussed in Section 13.4 on optimizing the RE dopants to slow the rate of growth and reduce scale spallation.

Another strategy is to increase the available Al reservoir,  $C_0 - C_b$ . For both Fe- and Ni-base alloys, increasing the starting Al content,  $C_0$ , leads to the formation of intermetallic phases which may or may not be desirable. One way to visualize reservoir data and the implication for the lifetime model is to plot time, particularly  $t_b$ , versus Al content for various Fe-Al alloys tested using 1 h cycles at  $1200^\circ\text{C}$ , Fig. 13.14. The use of 1 h cycles is to speed the Al consumption (scale spallation) rate. To illustrate the role of



13.13 Light microscopy of a polished cross-section of Ni-48Al + Hf ( $\text{Hf/C} = 1.63$ ) after exposure in 1 h cycles at 1150°C in dry  $\text{O}_2$  for (a) 1000 and (b) 10,000 cycles. Some internal oxidation of Hf occurred but the external alumina scale remained essentially flat.



13.14 Al concentration as a function of exposure time at 1200°C for various Fe-Al compositions with different RE dopants for 1 h cyclic testing at 1200°C in dry  $\text{O}_2$ . The lines connect the starting Al content ( $C_0$ ) at zero time to the breakaway Al content ( $C_b$ ) at time  $t_b$ . For comparison, the Al consumption rate in 100 h cycles is shown for Fe-40Al + Hf.

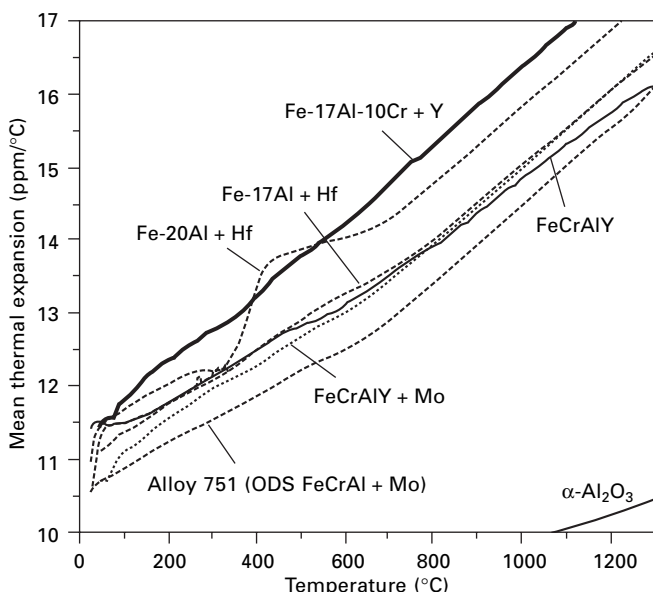
test cycle frequency, the slower rate of Al loss in 100 h cycles is shown for an Fe-40Al + Hf specimen that was stopped at 10 kh and had not reached breakaway. The lines in Fig. 13.14 connect the starting Al content ( $C_0$ ) symbol and the final Al content ( $C_b$ ) symbol but do not reflect the actual Al consumption as a function of time. Currently, additional specimens are being exposed and characterized to determine the shape of these curves. A few of the initial points are shown. Though not exact, the lines do give an indication of the average rate of Al consumption. The longest lives are for FeCrAlY type alloys (the same lifetimes listed in Fig. 13.9). These alloys start with the lowest values of  $C_0$  but, because of the slow Al consumption and low  $C_b$  (~0), their lifetime is very high. In contrast, Hf-doped  $\beta$ -FeAl begins with ~40Al, but the consumption rate is much higher. The reason is likely due to the very high CTE of the  $\beta$  phase, which results in higher thermal stresses due to the CTE mismatch between the metal and alumina scale, hence higher scale spallation rates (Smialek *et al.*, 1990; Pint and Wright, 2004). The Al consumption rate is even higher for Zr-doped Fe-40Al, even with  $Zr/C > 1$  (Pint and Schneibel, 2005). The FeAl lifetimes are further limited because, without the presence of 20Cr (as in FeCrAl),  $C_b$  is ~10–12% in binary Fe-Al alloys (Pint *et al.*, 1999a, 2005). This effect of Cr is typical of a third element effect (Stott *et al.*, 1995). A similar CTE-related spallation problem was observed in  $Fe_3Al$  alloys (Wright *et al.*, 2001b; Pint *et al.*, 2001), which are generally based on Fe-28Al-2Cr (Tortorelli and Natesan, 1998). Both FeAl and  $Fe_3Al$  specimens eventually lose enough Al and attain a ferritic structure after long exposures. Ferritic alloys (FeCrAl and Fe(Al)) have a lower CTE, and thus tend to have lower initial spallation rates than the Fe-base intermetallic phases. This phase change and the associated reduction in spallation behavior with time results in convex curves of Al content as a function of time in Fig. 13.14.

The spallation problems with intermetallic phases have led to more interest in the behavior of ferritic Fe(Al) compositions (Pint and Wright, 2004). While the intermetallic Fe-Al phases showed the longest lifetimes with Hf-doping (Pint *et al.*, 2001; Pint and Schneibel, 2005), the ferritic phases perform better with Y or Y + Hf doping, Figs 13.11 and 13.14. Under these conditions, the Al consumption rate (slope of the line) was similar in Fe-18Al + Y as in FeCrAlY. However, the lifetime was not as long for the former because of the much higher  $C_b$  compared to FeCrAlY. Thus, one potential alloy design goal is to look for ferritic compositions with lower  $C_b$ , represented by the dashed line in Fig. 13.14. Simply adding Cr to Fe-17Al initially has not shown promising results. Specimens of Fe-17Cr-10Al + Y failed quickly, due to the accelerated (broccoli) oxidation problem, Fig. 13.11. Adding Hf and Y to Fe-17Cr-10Al prevented this failure mechanism, but scale spallation has been higher than for Fe-17Al + Y. The increased spallation may be attributed to a measured increase in CTE compared to

Fe-17Al, Fig. 13.15. The CTE curves for Fe-17Al and Fe-20Al in Fig. 13.15 also demonstrate that increasing the Al content above 17–18Al will be problematic because the increased CTE results in more scale spallation and thus a faster Al consumption rate.

Additions of Mn also have been examined as a method to reduce  $C_b$  in Fe-17Al. However, specimens of Fe-17Al-1Mn + Y, Hf showed a higher scale growth rate, which limited lifetime at 1250°C, Fig. 13.11. Additions of 10 Mn had catastrophic effects at 1200–1250°C but showed more promising results at lower temperatures (1000°C). Thus one important criterion for additions to lower  $C_b$  is that they must not negatively affect the Al consumption rate (i.e.,  $k$  and  $n$ ), or their addition is counter-productive.

Another strategy for increasing lifetime suggested by Fig. 13.15 is to look for additions that reduce the alloy CTE, thereby improving scale adhesion. Among the formerly available ODS FeCrAl alloys is ODM751 (Fe-16Cr-9.6Al-0.8Mo-0.6Ti-0.24Y). The addition of Mo and reduced Cr appears to have reduced the CTE compared to wrought Fe20Cr10Al + Y, Fig. 13.15. However, recent work to reproduce this effect in wrought FeCrAlY + Mo did not produce the same CTE reduction. The strategy of CTE reduction also is relevant for Ni-base alloys because they have higher CTEs than Fe-base alloys (Haynes *et al.*, 2004) and has been explored for Ni-base bond coatings (Fritscher *et al.*, 1995).

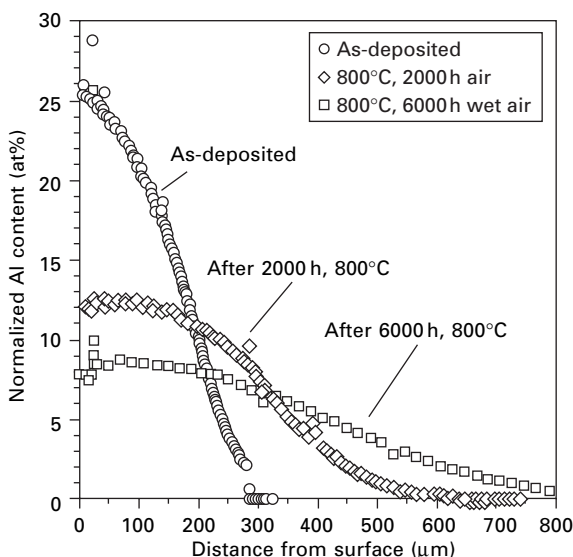


13.15 Mean thermal expansion coefficient as a function of temperature for various Fe-Cr-Al alloys.

As a final note, this section has not discussed other material properties, such as creep strength, joining or ductility, that might be negatively influenced by higher Al contents or other alloy additions. Those issues have been set aside while looking for a promising development direction for improving alloy lifetimes.

### 13.6 ‘Fantasy’ high temperature materials

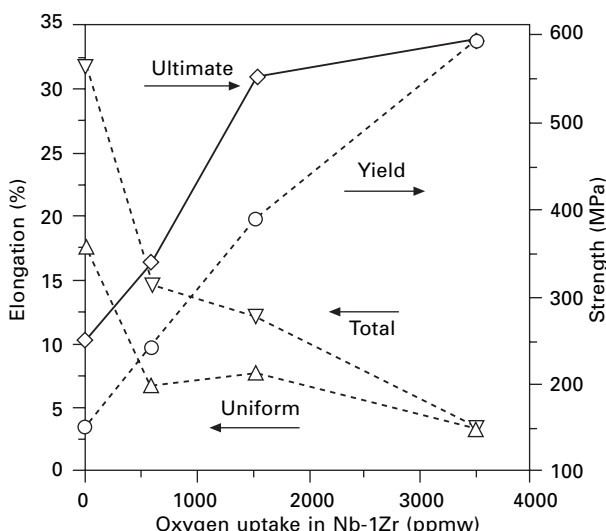
Some readers may consider this a very narrow discussion of alloy development, and there is no question that it has been narrowed to focus on oxidation resistance. However, when one considers the rest of the periodic table, there appear to be few opportunities (Pint *et al.*, 2006b). Many alloy development programs appear to pursue unusual and unlikely ‘fantasy’ compositions with the premise that an oxidation resistant coating will cure any oxidation resistance problem. However, coatings rich in Al have the problem of interdiffusion at high temperature. Figure 13.16 shows some Al diffusion profiles in Fe-9Cr-1Mo substrates for a relatively thick, chemical vapor deposited (CVD) diffusion aluminide coating. After only 2 kh at 800°C, a rather modest temperature, the surface Al content was reduced by ~50% (Zhang *et al.*, 2007). The surface



13.16 Electron probe microanalysis Al composition profiles of three chemical vapor deposited (CVD) aluminide coated Fe-9Cr-1Mo samples: as-deposited, after 2000 h at 700°C and after 2000 h at 800°C. Compared to the initial Al profile, significantly more Al interdiffusion occurred at 800°C than at 700°C. Results summarized from Zhang *et al.* (2004, 2007) and Pint *et al.* (2007e).

Al concentration was <10Al after only 6 kh at 800°C. Many power generation applications desire 40 kh minimum service lifetimes (Pint *et al.*, 2006b). In addition to interdiffusion and its effect on substrate mechanical properties (Dryepondt *et al.*, 2006), other coating compatibility problems must be addressed, such as the formation of undesirable phases and surface crack nucleation. Thus, the notion that coatings are universally available to protect non-oxidation resistant compositions is limited to short lifetime applications at best.

Among the alternative compositions that attract the most attention, refractory metals are investigated periodically (about every other decade or so) because of their high melting points (Shah *et al.*, 1992). What is often forgotten is that extensive prior effort has been devoted to improving the oxidation resistance of refractory alloys, particularly niobium-based alloys (Klopp, 1960). None of the numerous alloy additions investigated were able to solve the problem of high oxygen solubility in Nb (V- and Ta-based alloys have the same problem). This problem is ignored in many studies of oxidation where only mass gain or oxide thickness are examined after element X and/or Z is added. Figure 13.17 gives an example of how O uptake in the metal affects mechanical properties (DiStefano and Chitwood, 2001). Because of the high solubility of O in Nb, a significant amount of O will enter the alloy during exposure to oxidizing gases at high temperatures, resulting in solid solution strengthening but a major loss in ductility. Furthermore, it is a



13.17 The effect of oxygen uptake (i.e. internal oxidation) on the room temperature uniform and total elongation of Nb-1Zr as well as on the yield and ultimate tensile strength. Results summarized from DiStefano and Chitwood (2001).

mistake to assume that a surface oxide layer is protective as is the case for Fe- or Ni-base alloys. The high solubility of O in Nb (and V and Ta) means that a surface oxide acts as a source of O rather than a protective layer. This was demonstrated for V-4Cr-4Ti alloys, where a ductile specimen with a surface oxide was embrittled by annealing at 700°C in a quartz ampoule (Pint and DiStefano, 2005). The surface oxide layer dissolved into the V alloy substrate due to the lack of thermodynamic equilibrium in this metal–oxide system. Mo and W have low O solubilities, but their oxides are volatile at high temperatures in air. High levels of Al, Cr or Si additions (resulting in brittle phases) are generally required to form protective scales on refractory metal-based alloys. There has been recent interest in Mo-Si-B alloys (e.g. Dimiduk and Perepezko, 2003) but they have problems in some temperature ranges, and the boro-silicate scale is sensitive to water vapor effects at high temperatures (Opila, 2004). Any metal or ceramic that exclusively relies on the formation of silica will be hampered by this problem. In most alloys, the addition of Si, at the level needed to form a continuous silica scale, will have detrimental effects on other properties.

### 13.7 Future trends

As mentioned in the introduction, there will always be an incentive and/or an application which places new requirements on high temperature alloys, for either longer lifetimes, higher temperatures or a specialized environment or application. Another driver for alloy development, which is a critical current issue, is the cost of raw materials. The price of Ni has increased by a factor of ~10 in the past decade, and other key elements have increased to similar degrees. This has led to renewed interest in lower cost Fe-base compositions. It remains to be seen if the recently developed alumina-forming austenitic steels will have a commercial impact (Yamamoto *et al.*, 2007). Also, there has been recent interest in non-metallic alumina-formers, such as Ti<sub>2</sub>AlC (Wang and Zhou, 2003), which may find application as heating elements.

Another economic issue for alloy development is the production cost for high performance alloys, especially in industries where first cost is considered more important than lifetime costs. Such issues have led alloy manufacturers to cease production of low volume alloys. For example, Plansee and Special Metals recently dropped production of oxide dispersion strengthened (ODS) alloys. After years of research and development work, these alloys have failed to establish a sufficient market. However, with renewed interest in high temperature materials for power generation (both fossil and nuclear), a more substantial market may yet be found for materials that offer useful properties at temperatures unattainable by more conventional alloys.

Finally, aircraft turbine manufacturers often cite a US government report of about 1940 which could foresee no application for turbine engines in

aircraft. The current pessimism over new high temperature alloys based on precious metals, refractory metals, etc. may one day fall in the same category. However, the advent of turbine aircraft engines was largely due to innovative designs that significantly increased the thrust-to-weight ratio and only partially due to materials development. The limitations of some of the fantasy materials being investigated will be overcome only by a major shift in the current paradigm of materials science understanding of high temperature oxidation fundamentals or economics (in the case of precious metal-based alloys).

## 13.8 Summary

This chapter has focused on some practical examples and possibilities for designing high temperature, oxidation resistant alloys. The strategies are based on the fundamental concepts of high temperature oxidation that can be learned from textbooks but are often difficult to implement in practice. The fundamental goal is to encourage the formation of a slow-growing, dense and adherent oxide layer on the surface of the alloy. The oxides of practical interest are  $\text{Al}_2\text{O}_3$ ,  $\text{Cr}_2\text{O}_3$  and  $\text{SiO}_2$ , of which  $\text{Al}_2\text{O}_3$  is the most attractive because it has the highest thermodynamic stability. Unfortunately, adding Al to most alloys results in other problems that must be addressed. Therefore, an optimum composition will usually contain an Al concentration that is a trade-off between various properties. For alloys capable of forming alumina scales, controlling the minor dopants and interstitials usually is key to optimal performance. Further study of the mechanisms of oxidation, and especially dopant and interstitial effects, may shed light on new strategies for alloy development.

## 13.9 Sources of further information and advice

This chapter assumes a working knowledge of high temperature oxidation terminology and concepts. For more background in that area, consult one of the textbooks (Kofstad, 1988; Birks and Meier, 1983) or related proceedings on cyclic oxidation (Schütze and Quadakkers, 1999) or lifetime modeling (Schütze *et al.*, 2001). However, in recent years, many proceedings have been published in archival journals. Several recent book chapters have been written reviewing the oxidation behavior of various classes of alloys and intermetallics (Doychak, 1994; Natesan *et al.*, 1995; Grabke and Schütze, 1997; Brady *et al.*, 1999). Also, papers are periodically written on design principles (Brady and Tortorelli, 2004; Brady *et al.*, 2000) and reviewing high temperature materials applications (Gleeson, 2006).

Professional groups of interest for this topic would be the National Association of Corrosion Engineers ([www.nace.org](http://www.nace.org)) and the European

Federation of Corrosion or any of the materials societies (e.g. TMS or ASM International). All of these societies have websites that provide relevant information. Conferences on this topic are held almost annually. Some of the best attended are the Gordon Conference on High Temperature Oxidation (New London, NH, USA, every two years), European Federation of Corrosion workshops (held every one to two years), Microscopy of Oxidation (UK, every three years), the Les Embiez conferences (Les Embiez, France, every four years) and the Superalloys conferences (Seven Springs, PA, USA, every four years).

### 13.10 Acknowledgments

The author would like to thank J. Schneibel, M. P. Brady and I. G. Wright at ORNL for commenting on the manuscript. Also, a long list of collaborators contributed to the research upon which this chapter was written. K. Cooley, G. Garner, H. Longmire, J. Moser, W. Porter, J. Vought and L. Walker at ORNL assisted with the experimental work presented here. Commercial alloys were provided by B. Baker (Special Metals), M. Harper (while at Haynes International and at Special Metals), B. Jönsson (Kanthal), W. Matthews (Capstone), L. Paul (ThyssenKrupp VDM) and J. Rakowski (Allegheny Ludlum). The author also has been well educated by Professors G. J. Yurek and L. W. Hobbs at MIT and back to Mr Carlisle, Mr Swires and Mrs Kidder at Garfield High School. The writing was sponsored by the US Department of Energy, Fossil Energy Advanced Research Materials Program under contract DE-AC05-00OR22725 with UT-Battelle, LLC.

### 13.11 References

- Antill J E and Peakall K A (1967), 'Influence of an Alloy Addition of Y on the Oxidation Behaviour of an Austenitic and a Ferritic Stainless Steel in Carbon Dioxide,' *J Iron Steel Inst*, 205, 1136–1142.
- Asteman H, Svensson J-E, Norell M and Johansson L-G (2000), 'Influence of Water Vapor and Flow Rate on the High-Temperature Oxidation of 304L; Effect of Chromium Oxide Hydroxide Evaporation,' *Oxid Met*, 54, 11–26.
- Ballard D L, Martin P L, Gleeson B and Menon S (2007), 'Structure and Oxidation Behavior of PGM Modified Nickel-Base Alloys,' presentation at 18th AeroMat Conference and Expo, Baltimore, MD, ASM, June 2007.
- Belen N, Tomaszewicz P and Young D J (1984), 'Effects of Aluminum on the Oxidation of 25Cr-35Ni Cast Steels,' *Oxid Met*, 22, 227–245.
- Birks N and Meier G H (1983), *Introduction to High Temperature Oxidation of Metals*, London, Edward Arnold.
- Brady M P, Pint B A, Tortorelli P F, Wright I G and Hanrahan R J (1999), 'High-Temperature Oxidation and Corrosion of Intermetallics,' in *Materials Science and Technology: A Comprehensive Treatment*, Vol. 19B, *Corrosion and Environmental Degradation of Materials*, Weinheim, Wiley-VCH, 229–325.

- Brady M P, Gleeson B and Wright I G (2000), 'Alloy Design Strategies for Promoting Protective Oxide Scale Formation,' *JOM*, 52 (1), 16–21.
- Brady M P and Tortorelli P F (2004), 'Alloy Design of Intermetallics for Protective Scale Formation and For Use as Precursors for Complex Ceramic Phase Surfaces,' *Intermetallics* 12, 779–789.
- Brady M P, Pint B A, Lu Z G, Zhu J H, Milliken C E, Kreidler E D, Miller L, Armstrong T R and Walker L R (2006), 'Comparison of Oxidation Behavior and Electrical Properties of Doped NiO- and Cr<sub>2</sub>O<sub>3</sub>-forming Alloys for Solid Oxide Fuel Cell Metallic Interconnects,' *Oxid Met*, 65, 237–261.
- Caplan D and Cohen M (1959), 'High Temperature Oxidation of Chromium-Nickel Steels,' *Corr*, 15, 57–62.
- Chang C S, Chen L and Jha B (2002), 'Oxidation Induced Length Change of Thin Gauge Fe-Cr-Al Alloys,' in Bode H, *Materials Aspects in Automotive Catalytic Converters*, Weinheim, Wiley-VCH, 69–82.
- Cho J, Harmer M P, Chan H M, Rickman J M and Thompson A M (1997), 'Effect of Yttrium and Lanthanum on the Tensile Creep Behavior of Aluminum Oxide,' *J Am Ceram Soc*, 80 (1997) 1013–1017.
- Cotell C M, Yurek G J, Hussey R J, Mitchell D F and Graham M J (1990), 'The Influence of Grain Boundary Segregation of Y in Cr<sub>2</sub>O<sub>3</sub> on the Oxidation of Cr Metal,' *Oxid Met*, 34, 173–200, 201–216.
- Deodeshmukh V, Mu N, Li B and Gleeson B (2006), 'Hot Corrosion and Oxidation Behavior of a Novel Pt+Hf-modified  $\gamma'$ -Ni<sub>3</sub>Al +  $\gamma$ -Ni-based coating,' *Surf Coat Tech*, 201, 3836–3840.
- Dimiduk D M and Perepezko J H (2003), 'Mo-Si-B Alloys: Developing a Revolutionary Turbine Engine Material,' *Mater Res Soc Bull*, 28 (9), 639–645.
- DiStefano J R and Chitwood L D (2001), 'Oxidation and Its Effects on the Mechanical Properties of Nb-1Zr,' *J Nucl Mater*, 295, 42–48.
- Doychak J (1994), 'Oxidation Behavior of High Temperature Intermetallics,' in Westbrook J H and Fleischer R L, *Intermetallic Compounds, Vol. 1: Principles*, New York, John Wiley & Sons, 977–1016.
- Dryepondt S, Zhang Y and Pint B A (2006), 'Creep and Corrosion Testing of Aluminide Coatings on Ferritic Substrates,' *Surf Coat Tech*, 66, 3880–3884.
- Dryepondt S, Pint B A and Lara-Curcio E (2008), 'Creep- and Oxidation-Limited Lifetime of Commercial FeCrAl Foils,' in preparation for submission to *Acta Mater*.
- Ecer G M, Singh R B and Meier G H (1982), 'The Influence of Superficially Applied Oxide Powders on the High-Temperature Oxidation Behavior of Cr<sub>2</sub>O<sub>3</sub>-forming Alloys,' *Oxid Met*, 18, 55–81.
- Ehlers J, Young D J, Smaardijk E J, Tyagi A K, Penkalla H J, Singheiser L and Quadakkers W J (2006), 'Enhanced Oxidation of the 9%Cr Steel P91 in Water Vapour Containing Environments,' *Corr Sci*, 48, 3428–3454.
- Evans H E and Lobb R C (1984), 'Alloy Depletion Profiles During Non-Protective Oxidation,' *Corr Sci*, 24, 223–236.
- Evans H E (1995), 'Stress Effects in High Temperature Oxidation of Metals,' *Inter Mater Rev*, 40, 1–40.
- Evans H E, Nicholls J R and Saunders S R J (1995), 'The Influence of Diffusion-Related Mechanisms in Limiting Oxide-Scale Failure,' *Solid State Phenom*, 41, 137–156.
- Fritscher K, Leyens C and Peters M (1995), 'Development of a Low-Expansion Bond Coating for Ni-base Superalloys,' *Mater Sci Eng*, A190, 253–258.

- Fujii C T and Meussner R A (1964), 'The Mechanism of the High-Temperature Oxidation of Iron-Chromium Alloys in Water Vapor,' *J Electrochem Soc*, 111, 1215–1221.
- Funkenshuh A W, Smegill J G and Bornstein N S (1985), 'Reactive Element – Sulfur Interaction and Oxide Scale Adherence,' *Met Trans*, 16A, 1164–1166.
- Gleeson B and Harper M A (1998), 'The Long-Term, Cyclic-Oxidation Behavior of Selected Chromia-Forming Alloys,' *Oxid Met*, 49, 373–399.
- Gleeson B, Wang W, Hayashi S and Sordelet D (2004), 'Effects of Platinum on the Interdiffusion and Oxidation Behavior of Ni-Al-based Alloys,' *Mater Sci Forum*, 461–464, 213–222.
- Gleeson B (2006), 'Thermal Barrier Coatings for Aeroengine Applications,' *J Prop Power*, 22, 375–383.
- Goward G W (1986), 'Protective Coatings – Purpose, Role and Design,' *Mater Sci Tech*, 2, 194–200.
- Grabke H J and Schütze M (1997), eds, *Oxidation of Intermetallics*, Weinheim, VCH-Wiley.
- Grabke H J (1998), 'Thermodynamics, Mechanisms and Kinetics of Metal Dusting,' *Mater Corr*, 49, 303–308.
- Gupta D K and Duval D S (1984), 'A Silicon and Hafnium Modified Plasma Sprayed MCRAIY Coating for Single Crystal Superalloys,' in Gell M, et al., *Superalloys 1984*, Warrendale, PA, TMS, 711–720.
- Gurrappa I, Weinbruch S, Naumenko D and Quadakkers W J (2000), 'Factors Governing Breakaway Oxidation of FeCrAl-based Alloys,' *Mater Corr*, 51, 224–235.
- Haynes J A, Pint B A, Porter W D and Wright I G (2004), 'Comparison of Thermal Expansion and Oxidation Behavior of Various High-Temperature Coating Materials and Superalloys,' *Mater High Temp*, 21, 87–94.
- Henry S, Galerie A and Antoni L (2001), 'Abnormal Oxidation of Stabilized Ferritic Stainless Steels in Water Vapor,' *Mater Sci Forum*, 369–372, 353–360.
- Hindam H and Whittle D P (1982), 'Peg Formation by Short-Circuit Diffusion in  $\text{Al}_2\text{O}_3$  Scales Containing Oxide Dispersions,' *J Electrochem Soc*, 129, 1147–1149.
- Hou P Y (1999), 'Beyond the Sulfur Effect,' *Oxid Met*, 52, 337–351.
- Huczkowski P, Christiansen N, Shemet V, Piron-Abellan J, Singheiser L and Quadakkers W J (2004), 'Oxidation Limited Life Times of Chromia Forming Ferritic Steels,' *Mater Corr*, 55, 825–830.
- Izumi T and Gleeson B (2005), 'Oxidation Behavior of Pt plus Hf-modified  $\gamma$ -Ni +  $\gamma'$ - $\text{Ni}_3\text{Al}$  Alloys,' *Mater Sci Forum*, 522–523, 221–228.
- Jönsson B and Svedberg C (1997), 'Limiting Factors for Fe-Cr-Al and NiCr in Controlled Industrial Atmospheres,' *Mater Sci Forum*, 251–254, 551–558.
- Jönsson B, Berglund R, Magnusson J, Henning P and Hättestrand M (2004), 'High Temperature Properties of a New Powder Metallurgical FeCrAl Alloy,' *Mater Sci Forum*, 461–464, 455–462.
- King W E (1989), ed., 'The Reactive Element Effect on High Temperature Oxidation – After Fifty Years,' *Mater Sci Forum* 43, Switzerland, Trans Tech Publications.
- Kirchheimer R R, Becker P, Young D J and Durham R (2005), 'Improved Oxidation and Coking Resistance of a New Alumina Forming Alloy 60 HT for the Petrochemical Industry,' NACE Paper 05-428, Houston, TX, presented at NACE Corrosion 2005, Houston, TX, April 2005.
- Klopp W D (1960), 'Oxidation Behavior and Protective Coatings for Columbium and Columbium-Base Alloys,' DMIC Report 123, Columbus, OH, Battelle Memorial Institute.

- Kochubey V, Naumenko D, Wessel E, Le Coze J, Singheiser L, Al-Baidary H, Tatlock G J and Quadakkers W J (2006), 'Evidence of Cr-Carbide Formation at the Scale/Metal Interface During Oxidation of FeCrAl Alloys,' *Mater Lett*, 60, 1564–1568.
- Kofstad P (1985), 'On the Formation of Porosity and Microchannels in Growing Scales,' *Oxid Met*, 24, 265–276.
- Kofstad P (1988), *High Temperature Corrosion*, London, Elsevier Applied Science.
- Lang E (1989), ed., *The Role of Active Elements in the Oxidation Behavior of High Temperature Metals and Alloys*, London, Elsevier Applied Science.
- Liu Z Y, Gao W, Dahm K and Wang F H (1997), 'The Effect of Coating Grain Size on the Selective Oxidation Behaviour of Ni-Cr-Al Alloy,' *Scripta Mater*, 37, 1551–1558.
- Maziasz P J, Swindeman R W, Montague J P, Fitzpatrick M, Browning P F, Grubb J F and Klug R C (1999), 'Improved Creep-Resistance of Austenitic Stainless Steel for Compact Gas Turbine Recuperators,' *Mater High Temp*, 16, 207–212.
- Maziasz P J, Pint B A, Shingledecker J P, Evans N D, Yamamoto Y, More K L and Lara-Curcio E (2007), 'Advanced Alloys for Compact, High-Efficiency, High-Temperature Heat-Exchangers,' *International Journal of Hydrogen Energy*, 32, 3622–3630.
- McColvin G M and Smith G D (1985), 'Environmental Resistance of Incoloy Alloy MA956,' in Marriott J B, Merz M, Nihoul J and Ward J, *High Temperature Alloys, Their Exploitable Potential*, London, Elsevier, 139–153.
- Moon D P (1989) 'Role of Reactive Elements in Alloy Protection,' *Mater Sci Tech*, 5, 754–764.
- Natesan K, Ganeshan P and Lai G (1995), eds, *Heat Resistant Materials II*, Materials Park, OH, ASM International.
- Naumenko D, Kochubey V, Le Coze J, Wessel E, Singheiser L and Quadakkers W J (2004), 'Effect of Combined Y and Zr Additions on Protective Alumina Scale Formation on High Purity FeCrAl Alloys During Oxidation in the Temperature Range of 1200 to 1300°C,' *Mater Sci Forum*, 461–464, 489–495.
- Nicholls J R, Evans H E and Saunders S R J (1997), 'Fracture and Spallation of Oxides,' *Mater High Temp*, 14, 5–13.
- Nickel H, Wouters Y, Thiele M and Quadakkers W J (1998), 'The Effect of Water Vapor on the Oxidation Behavior of 9%Cr Steels in Simulated Combustion Gases,' *Fresenius J Anal Chem*, 361, 540–544.
- Nishimura N, Komai N, Hirayama Y and Masuyama F (2005), 'Japanese Experiences with Steam Oxidation on Advanced Heat-Resistant Steel Tubes in Power Boilers,' *Mater High Temp*, 22, 3–10.
- Opila E J (2004), 'Volatility of Common Protective Oxides in High-Temperature Water Vapor: Current Understanding and Unanswered Questions,' *Mater Sci Forum*, 461–464, 765–774.
- Opila E J, Myers D L, Jacobson N S, Nielsen I M B, Johnson D F, Olminsky J K and Allendorf M D (2007), 'Theoretical and Experimental Investigation of the Thermochemistry of  $\text{CrO}_2(\text{OH})_2(\text{g})$ ,' *J Phys Chem A*, 111, 1971–1980.
- Otsuka N, Shida Y and Fujikawa H (1989), 'Internal–External Transition for the Oxidation of Fe-Cr-Ni Austenitic Stainless Steels in Steam,' *Oxid Met*, 32, 13–45.
- Otsuka N, Nishiyama Y and Kudo T (2004), 'Breakaway Oxidation of TP310S Stainless-Steel Foil Initiated by Cr Depletion of the Entire Specimen in a Simulated Flue-Gas Atmosphere,' *Oxid Met*, 62, 121–139.
- Peraldi R and Pint B A (2004), 'Effect of Cr and Ni Contents on the Oxidation Behavior of Ferritic and Austenitic Model Alloys in Air with Water Vapor,' *Oxid Met*, 61, 463–483.

- Pint B A, Martin J R and Hobbs L W (1993),  $^{18}\text{O}/\text{SIMS}$  Characterization of the Growth Mechanism of Doped and Undoped  $\alpha\text{-Al}_2\text{O}_3$ , *Oxid Met*, 39, 167–195.
- Pint B A (1994), ‘Limitations on the Use of Surface Doping for Improving High-Temperature Oxidation Resistance,’ *Mater Res Soc Bull*, 19 (10), 26–30.
- Pint B A, Garratt-Reed A J and Hobbs L W (1995), ‘The Reactive Element Effect in Commercial ODS FeCrAl Alloys,’ *Mater High Temp*, 13, 3–16.
- Pint B A (1996), ‘Experimental Observations in Support of the Dynamic Segregation Theory to Explain the Reactive Element Effect,’ *Oxid Met*, 45, 1–37.
- Pint B A (1998), ‘The Oxidation Behavior of Oxide-Dispersed  $\beta\text{-NiAl}$ : I. Short-Term Cyclic Data and Scale Morphology,’ *Oxid Met*, 49, 531–560.
- Pint B A and Alexander K B (1998), ‘Grain Boundary Segregation of Cation Dopants in  $\alpha\text{-Al}_2\text{O}_3$  Scales,’ *J Electrochem Soc*, 145, 1819–1829.
- Pint B A, Tortorelli P F and Wright I G (1999a), ‘Long-Term Oxidation Performance of Ingot-Produced  $\text{Fe}_3\text{Al}$  Alloys,’ *Mater High Temp*, 16, 1–13.
- Pint B A, Leibowitz J and DeVan J H (1999b), ‘The Effect of an Oxide Dispersion on the Critical Al content in Fe-Al Alloys,’ *Oxid Met*, 51, 181–197.
- Pint B A, More K L, Tortorelli P F, Porter W D and Wright I G (2001), ‘Optimizing the Imperfect Oxidation Performance of Iron Aluminides,’ *Mater Sci Forum*, 369–372, 411–418.
- Pint B A, Tortorelli P F and Wright I G (2002), ‘Effect of Cycle Frequency on High Temperature Oxidation Behavior of Alumina-Forming Alloys,’ *Oxid Met*, 58, 73–101.
- Pint B A (2003a), ‘Progress in Understanding the Reactive Element Effect Since the Whittle and Stringer Literature Review,’ in Tortorelli P F, Wright I G, and Hou P Y, *Proc. John Stringer Symposium on High Temperature Corrosion*, Materials Park, OH, ASM International, 9–19.
- Pint B A (2003b), ‘Optimization of Reactive Element Additions to Improve Oxidation Performance of Alumina-Forming Alloys,’ *J Am Ceram Soc*, 86, 686–695.
- Pint B A, More K L and Wright I G (2003), ‘The Use of Two Reactive Elements to Optimize Oxidation Performance of Alumina-Forming Alloys’ *Mater High Temp*, 20, 375–386.
- Pint B A (2004), ‘The Role of Chemical Composition on the Oxidation Performance of Aluminide Coatings,’ *Surf Coat Tech*, 188–189, 71–78.
- Pint B A and Wright I G (2004), ‘The Oxidation Behavior of Fe-Al Alloys,’ *Mater Sci Forum*, 461–464, 799–806.
- Pint B A, Peraldi R and Maziasz P J (2004a), ‘The Use of Model Alloys to Develop Corrosion-Resistant Stainless Steels,’ *Mater Sci Forum*, 461–464, 815–822.
- Pint B A, Haynes J A, More K L and Wright I G (2004b), ‘The Use of Model Alloys to Understand and Improve the Performance of Pt-modified Aluminide Coatings,’ in Green K A, et al., *Superalloys 2004*, Warrendale, PA, TMS, 597–606.
- Pint B A (2005), ‘The Effect of Water Vapor on Cr Depletion in Advanced Recuperator Alloys,’ ASME Paper #GT2005-68495, presented at the International Gas Turbine and Aeroengine Congress and Exhibition, Reno-Tahoe, NV, 6–9 June 2005.
- Pint B A and DiStefano J R (2005), ‘The Role of Oxygen Uptake and Scale Formation on the Embrittlement of Vanadium Alloys,’ *Oxid Met*, 63, 33–55.
- Pint B A and Schneibel J H (2005), ‘The Effect of Carbon and Reactive Element Dopants on Oxidation Lifetime of FeAl,’ *Scripta Mater*, 52, 1199–1204.
- Pint B A, Walker L R and Wright I G (2005), ‘Characterization of the Breakaway Al Content in Alumina-Forming Alloys,’ *Mater High Temp*, 21, 175–185.

- Pint B A (2006), 'Stainless Steels with Improved Oxidation Resistance for Recuperators,' *Journal of Engineering for Gas Turbines and Power*, 128, 370–376.
- Pint B A and Keiser J R (2006), 'Alloy Selection for High Temperature Heat Exchangers,' NACE Paper 06-469, Houston, TX, presented at NACE Corrosion 2006, San Diego, CA, March 2006.
- Pint B A, More K L, Trejo R and Lara-Curzio E (2006a), 'Comparison of Recuperator Alloy Degradation in Laboratory and Engine Testing,' ASME Paper #GT2006-90194, presented at the International Gas Turbine and Aeroengine Congress and Exhibition, Barcelona, Spain, 8–11 May 2006.
- Pint B A, DiStefano J R and Wright I G (2006b), 'Oxidation Resistance: One Barrier to Moving Beyond Ni-Base Superalloys,' *Mater Sci Eng*, 415, 255–263.
- Pint B A, Brady M P and Armstrong T R (2007a), unpublished work, Oak Ridge, TN, Oak Ridge National Laboratory.
- Pint B A, Garner G W and Walker L R (2007b), 'Long-Term Behavior of Austenitic Stainless Steels in Air with Water Vapor,' submitted to *J Mater Sci*.
- Pint B A, Shingledecker J P, Brady M P and Maziasz P J (2007c), 'Alumina-Forming Austenitic Alloys for Advanced Recuperators,' ASME Paper #GT2007-27916, presented at the International Gas Turbine and Aeroengine Congress and Exhibition, Montreal, Canada, 14–17 May 2007.
- Pint B A, More K L and Wright I G (2007d), 'The Oxidation Behavior of Low Al Ni-Pt-Al Cast Alloys,' for submission to *Oxid Met*.
- Pint B A, Zhang Y, Walker L R and Wright I G (2007e), 'Long-Term Performance of Aluminide Coatings on Fe-Base Alloys,' *Surf Coat Tech*, 202, 637–642.
- Pint B A and Paul L D (2007f), 'Oxidation Behavior of Welded and Base Metal UNS N06025,' NACE Paper 07-470, Houston, TX, presented at NACE Corrosion 2007, Nashville, TN, March 2007.
- Pivin J C, Delaunay D, Roques-Carmes C, Huntz A M and Lacombe P (1980), 'Oxidation Mechanism of Fe-Ni-20-25Cr-5Al Alloys—Influence of Small Amounts of Y on Oxidation Kinetics and Oxide Adherence,' *Corr Sci*, 20, 351–373.
- Przybylski K, Garratt-Reed A J, Pint B A, Katz E P and Yurek G J (1987), 'Segregation of Y to Grain Boundaries in the  $\text{Al}_2\text{O}_3$  Scale Formed on an ODS Alloy,' *J Electrochem Soc*, 134, 3207–3208.
- Przybylski K and Yurek G J (1989), 'The Influence of Implanted Yttrium on the Mechanisms of Growth of Chromia Scales,' *Mater Sci Forum*, 43, 1–74.
- Quadakkers W J, Holzbrecher H, Briefs K G and Beske H (1989), 'Differences in Growth Mechanisms of Oxide Scales Formed on ODS and Conventional Wrought Alloys,' *Oxid Met*, 32, 67–88.
- Quadakkers W J and Bennett M J (1994), 'Oxidation Induced Lifetime Limits of Thin Walled, Iron Based, Alumina Forming, Oxide Dispersion Strengthened Alloy Components,' *Mater Sci Tech*, 10, 126–131.
- Quadakkers W J and Bongartz K (1994), 'The Prediction of Breakaway Oxidation for Alumina Forming ODS Alloys Using Oxidation Diagrams,' *Werkst Korros*, 45, 232–241.
- Quadakkers J and Singheiser L (2001), 'Practical Aspects of the Reactive Element Effect,' *Mater Sci Forum*, 369–372, 77–92.
- Quadakkers W J, Piron-Abellán J, Shemet V and Singheiser L (2003), 'Metallic Interconnectors for Solid Oxide Fuel Cells – A Review,' *Mater High Temp*, 20, 115–127.

- Ramakrishnan V, McGurty J A and Jayaraman N (1988), 'Oxidation of High-Aluminum Austenitic Stainless Steels,' *Oxid Met*, 30, 185–200.
- Ramanarayanan T A, Raghavan M and Petkovic-Luton R (1984), 'The Characteristics of Alumina Scales Formed on Fe-Based Yttria-Dispersed Alloys,' *J Electrochem Soc*, 131, 923–931.
- Schütze M and Quadakkers W J (1999), eds, *Cyclic Oxidation of High Temperature Materials*, London, Institute of Materials.
- Schütze M, Quadakkers W J and Nicholls J R (2001), eds, *Lifetime Modelling of High Temperature Corrosion Processes*, London, Maney.
- Shah D M, Berczik D, Anton D L and Hecht R (1992), 'Appraisal of Other Silicides as Structural Materials,' *Mater Sci Eng*, A155, 45–57.
- Shen J, Zhou L and Li T (1997), 'High-Temperature Oxidation of Fe-Cr Alloys in Wet Oxygen,' *Oxid Met*, 48, 347–356.
- Sigler D R (1989), 'Aluminum Oxide Adherence on Fe-Cr-Al Alloys Modified with Group IIIB, IVB, VB and VIB Elements,' *Oxid Met*, 32, 337–355.
- Smialek J L, Doychak J and Gaydosh D J (1990), 'Oxidation Behavior of FeAl + Hf, Zr, B,' *Oxid Met*, 4, 259–275.
- Smialek J L, Jayne D T, Schaeffer J C and Murphy W H (1994), 'Effects of Hydrogen Annealing, Sulfur Segregation and Diffusion on the Cyclic Oxidation Resistance of Superalloys: A Review,' *Thin Solid Films*, 253, 285–292.
- Smialek J L and Pint B A (2001), 'Optimizing Scale Adhesion for Single Crystal Superalloys,' *Mater Sci Forum*, 369–372, 459–466.
- Stott F H, Wood G C and Stringer J (1995), 'The Influence of Alloying Elements on the Development and Maintenance of Protective Scales,' *Oxid Met*, 44, 113–145.
- Strawbridge A and Hou P Y (1994), 'The Role of Reactive Elements in Oxide Scale Adhesion,' *Mater High Temp*, 12, 177–181.
- Tatlock G J and Hurd T J (1984), 'Platinum and the Oxidation Behavior of Nickel Based Superalloy,' *Oxid Met*, 22, 201–226.
- Tedmon C S (1966), 'The Effect of Oxide Volatilization on the Oxidation Kinetics of Cr and Fe-Cr Alloys,' *J Electrochem Soc*, 113, 766–768.
- Tortorelli P F and Natesan K (1998), 'Critical Factors Affecting the High-Temperature Corrosion Performance of Iron Aluminides,' *Mater Sci Eng*, A258, 115–125.
- Ueda M and Taimatsu H (2000), 'Thermal Expansivity and High-Temperature Oxidation Resistance of Fe-Cr-W Alloys Developed for a Metallic Separator of SOFC,' in McEvoy A J, *Proc. 4th Eur. Solid Oxide Fuel Cell Forum*, Vol. 2, Amsterdam, Elsevier, 837–843.
- Wang X H and Zhou Y C (2003), 'High-Temperature Oxidation Behavior of Ti<sub>2</sub>AlC in Air,' *Oxid Met*, 59, 303–320.
- Whittle D P and Stringer J (1980), 'Improvement in Properties: Additives in Oxidation Resistance,' *Phil Trans Roy Soc London*, Series A, 295, 309–329.
- Wilber J P, Bennett M J and Nicholls J R (2000), 'Life-time Extension of Alumina Forming FeCrAl-RE Alloys: Influence of Alloy Thickness,' *Mater High Temp*, 17, 125–132.
- Wright I G, Pint B A, Lee W Y, Alexander K B and Prüßner K (2000), 'Some Effects of Metallic Substrate Composition on Degradation of Thermal Barrier Coatings,' in Nicholls J and Rickerby D, *High Temperature Surface Engineering*, London, Institute of Materials, 95–113.
- Wright I G, Pint B A, Hall L M and Tortorelli P F (2001a), 'Experimental Results and Modeling Related to Oxidation Lifetimes,' in Schütze M, Quadakkers W J, Nicholls

- J R, *Lifetime Modelling of High Temperature Corrosion Processes*, London, Maney, 66–82.
- Wright I G, Pint B A and Tortorelli P F (2001b), ‘The High Temperature Oxidation Behavior of ODS Fe<sub>3</sub>Al,’ *Oxid Met*, 55, 333–357.
- Wright I G, Peraldi R and Pint B A (2004), ‘Influence of Aluminum Depletion Effects on the Calculation of the Oxidation Lifetimes of FeCrAl Alloys,’ *Mater Sci Forum*, 461–464, 579–590.
- Wright I G, Tortorelli P F and Schütze M (2007), ‘Oxide Growth and Exfoliation on Alloys Exposed to Steam,’ EPRI Report, Palo Alto, CA, Electric Power Research Institute, in press.
- Wukusick C S and Collins J F (1964), ‘An Iron-Chromium-Aluminum Alloy Containing Yttrium,’ *Mater Res Stndrd*, 4, 637–646.
- Yamamoto Y, Brady M P, Lu Z P, Maziasz P J, Liu C T, Pint B A, More K L, Meyer H M and Payzant E A (2007), ‘Creep-Resistant, Al<sub>2</sub>O<sub>3</sub>-Forming Austenitic Stainless Steels,’ *Science*, 316, 433–436.
- Young D J and Pint B A (2006), ‘Chromium Volatilization Rates from Cr<sub>2</sub>O<sub>3</sub> Scales into Flowing Gases Containing Water Vapor,’ *Oxid Met*, 66, 137–153.
- Zhang Y, Pint B A, Garner G W, Cooley K M and Haynes J A (2004), ‘Effect of Cycle Length on the Oxidation Performance of Iron Aluminide Coatings,’ *Surf Coat Tech*, 188–189, 35–40.
- Zhang Y, Haynes J A, Pint B A and Wright I G (2005), ‘A Platinum-Enriched γ + γ’ Two-Phase Bond Coat on Ni-Base Superalloys,’ *Surf Coat Tech*, 200, 1259–1263.
- Zhang Y, Liu A P and Pint B A (2007), ‘Interdiffusion Behavior of Aluminide Coatings on Fe-Base Alloys,’ *Mater Corr*, 58, 751–761.
- Zurek J, Michalik M, Schmitz F, Kern T U, Singheiser L and Quadakkers W J (2005), ‘The Effect of Water-Vapor Content and Gas Flow Rate on the Oxidation Mechanism of a 10%Cr-Ferritic Steel in Ar-H<sub>2</sub>O Mixtures,’ *Oxid Met*, 63, 401–422.

## Oxidation behavior of chemical vapor deposited silicon carbide

T G O T O, Tohoku University, Japan

### 14.1 Introduction

Silicon-based ceramics such as silicon carbide (SiC) and silicon nitride ( $\text{Si}_3\text{N}_4$ ) have been widely applied as high-temperature structural materials due to their high strength, high thermal shock resistance and excellent oxidation resistance.<sup>1</sup> SiC bodies are commonly fabricated by various kinds of sintering processes, but sintered SiC bodies contain additives which can cause serious degradation, particularly at high temperatures. Highly pure and dense SiC bodies are required in specific applications such as susceptors for semiconductor device fabrication, and for such applications, chemical vapor deposition (CVD) is available by using a wide variety of organo-metallic precursors containing Si and C sources.<sup>2</sup> CVD is more commonly used to obtain high-quality coatings, and CVD SiC coatings have been applied to carbon/carbon (C/C) composites and porous SiC sintered bodies as oxidation-protective coatings for spacecraft and combustion chambers. Since these coatings are exposed to extremely high-temperature environments, at most 2000 K in a wide range of oxygen partial pressures, the oxidation mechanism of CVD SiC and the limitation of its usage should be well understood.

Oxidation is a crucial issue for the degradation of SiC bodies, particularly at high temperatures.<sup>3</sup> The oxidation behavior of SiC can be primarily categorized into three types: ‘passive oxidation’ characterized by excellent oxidation resistance due to protective oxide layers, ‘active oxidation’ accompanied by a significant mass loss due to the formation of  $\text{SiO}$  and  $\text{CO}$  vapors, and ‘bubble formation’ caused by the high pressures of  $\text{SiO}$  and  $\text{CO}$  vapors at the  $\text{SiO}_2/\text{SiC}$  interface.<sup>4</sup>

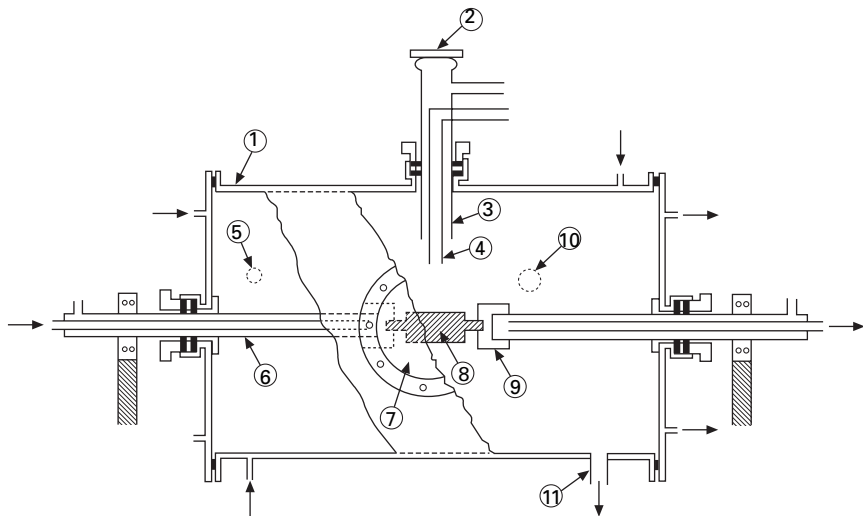
Passive oxidation has been studied using many forms of SiC, including powders, pressure-less and hot-pressed sintered bodies, pure CVD and single crystals. Since passive oxidation behavior is significantly sensitive to impurities and the microstructure, highly pure and dense SiC bodies with well-defined microstructures should be employed to understand the intrinsic oxidation mechanism.<sup>5</sup> Many studies have been conducted for highly pure CVD and

single crystal SiC; however, a number of issues such as the effect of crystallization of oxide scales on the oxidation rates, the difference of oxidation behavior between the Si-face and the C-face of a SiC single crystal, and the great difference of passive oxidation rate between SiC and  $\text{Si}_3\text{N}_4$  remain unsolved.<sup>6,7</sup> In the active oxidation and bubble formation regions, SiC bodies are no longer useful at high temperatures due to a significant loss of mass and non-protective  $\text{SiO}_2$  layer formation, respectively. Therefore, it is essential to understand the transition mechanisms operating in passive oxidation, active oxidation and bubble formation. In this chapter, the synthesis of CVD SiC is briefly mentioned and three typical oxidation features of SiC are reviewed.

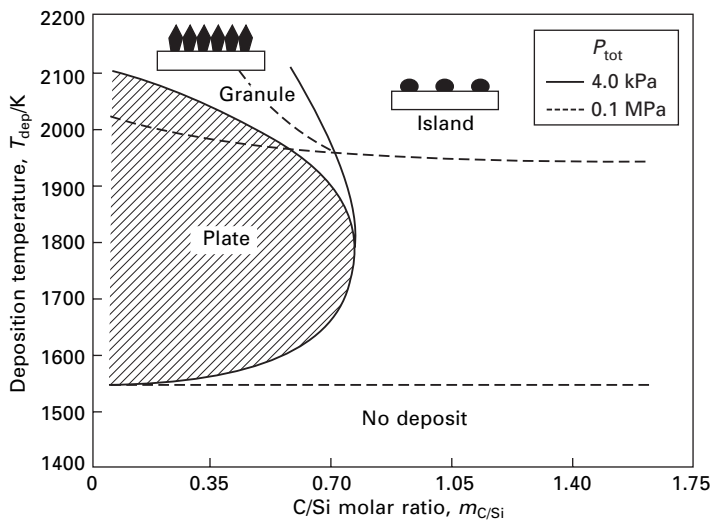
## 14.2 Synthesis of chemical vapor deposited (CVD) silicon carbide (SiC) thick plates

Since the deposition rate of CVD is rather small, commonly ranging from several to several tens  $\mu\text{m}/\text{h}$ , the form of deposits is usually limited to films. However, by choosing appropriate deposition conditions and experimental set-ups, thick plates or bulk forms of deposits can be synthesized by CVD. The authors have prepared thick Si-based ceramics ( $\text{SiC}^8$  and  $\text{Si}_3\text{N}_4^9$ ) and other non-oxide plates<sup>10,11</sup> by CVD. The deposition rate of CVD may be dominated by chemical reaction at low deposition temperatures ( $T_{\text{dep}}$ ) but by diffusion of source or product gases in a gas phase at high  $T_{\text{dep}}$ . In order to obtain thick plates by CVD, the substrate should be heated at a sufficiently high temperature with sufficient amounts of source gases supplied to the substrate zone. However, if the gases are heated too high or mixed too early, the formation of powder or intermediate products occurs in a gas phase, causing the decrease of deposition rates.<sup>12</sup> ‘Cold-wall type CVD’ can often be employed to increase the deposition rate by preventing such premature chemical reactions. The authors have constructed a cold-wall type CVD set-up as shown in Fig. 14.1, where a graphite substrate was directly heated by passing electric current, and precursor gases were supplied through a double tube nozzle without mixing before arriving at the substrate zone.<sup>13</sup> By optimizing the deposition conditions, CVD SiC and  $\text{Si}_3\text{N}_4$  thick plates were synthesized at significantly high deposition rates, around 2  $\text{mm}/\text{h}$ .<sup>8,9</sup>

$\text{CH}_3\text{SiCl}_3 + \text{H}_2$  gases have been widely used to prepare CVD SiC films, and relatively high deposition rates and a wide variety of morphologies have been reported.<sup>14</sup> Although the molar ratio of Si to C in  $\text{CH}_3\text{SiCl}_3$  is 1, the same as the stoichiometric ratio of SiC, the composition of deposits depends on deposition conditions, mainly Si-rich at  $T_{\text{dep}} < 1500$  K and C-rich at  $T_{\text{dep}} > 1700$  K. The precursors such as  $\text{SiCl}_4 + \text{CCl}_4 + \text{H}_2$  and  $\text{SiCl}_4 + \text{CH}_4 + \text{H}_2$  gases have also been used to prepare CVD SiC films.<sup>2</sup> The authors have employed  $\text{SiCl}_4 + \text{C}_3\text{H}_8 + \text{H}_2$  gases because  $\text{C}_3\text{H}_8$  was significantly active, probably due to the formation of hydrocarbon radicals in a gas phase.<sup>8</sup>



14.1 Cold-wall type CVD set-up: (1) water-cooled vacuum chamber; (2), (7) quartz glass windows; (3), (4) gas inlets; (5) pressure gauge; (6) water-cooled copper electrode; (8) graphite heater (substrate); (9) graphite socket; (10), (11) gas outlets.



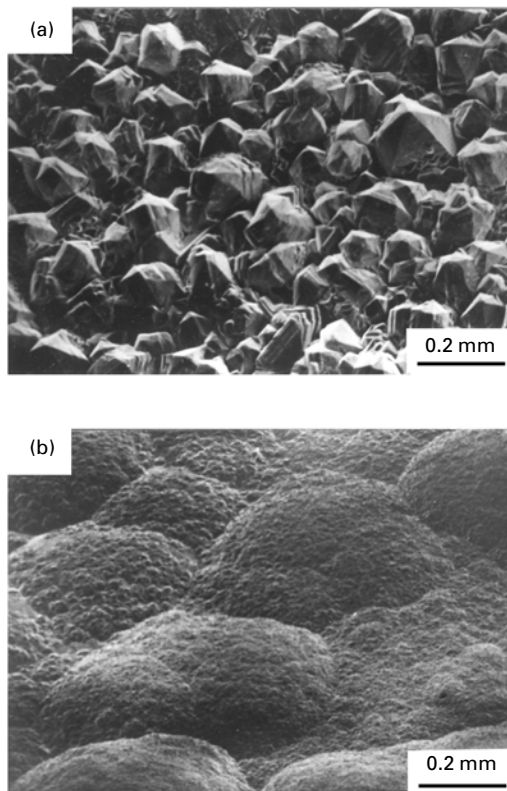
14.2 Effects of deposition temperature ( $T_{\text{dep}}$ ) and C/Si molar ratio ( $m_{\text{C/Si}}$ ) on the morphology of CVD SiC plates.

Figure 14.2 demonstrates the effects of deposition conditions ( $T_{\text{dep}}$  and C/Si molar ratio of  $m_{\text{C/Si}} = 3\text{CH}_3\text{Hg}/\text{SiCl}_4$ ) on the morphology of CVD SiC plates.<sup>8</sup> At a total pressure ( $P_{\text{tot}}$ ) of 4.0 kPa, plate-like deposits were obtained at  $m_{\text{C/Si}} < 0.7$  (hatched area in Fig. 14.2), while island- or granule-deposits

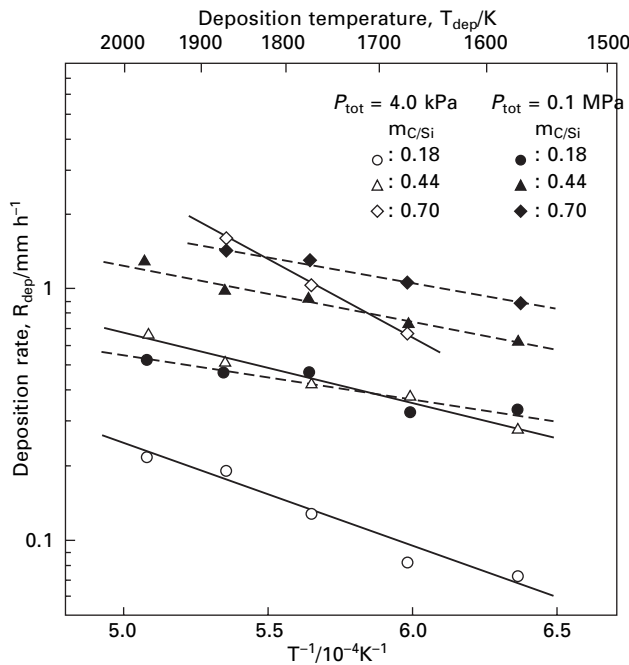
were obtained in other conditions. No deposits are obtained at  $T_{\text{dep}} < 1500$  K. At  $P_{\text{tot}} = 0.1$  MPa, the conditions for plate-like deposits extended to higher  $m_{\text{C/Si}}$  ratios.

Figure 14.3 shows typical morphologies of CVD SiC plates. Pyramid-like facets were well developed with significant (111) orientation at low  $P_{\text{tot}}$ , while a cone-like structure with (220) orientation was obtained at high  $P_{\text{tot}}$ . At  $m_{\text{C/Si}} > 1$ , the free-carbon content significantly increased accompanying a decrease in density. The density of the deposits at  $m_{\text{C/Si}} > 0.7$  was far smaller than that estimated from a mixture rule of pure SiC (density: 3.20 Mg/m<sup>3</sup>) and amorphous carbon (density: 1.38 Mg/m<sup>3</sup>), suggesting that a large amount of voids were formed with the co-deposition of free-carbon.

By combining the cold-wall type CVD set-up, local heating of a graphite substrate and reactive precursors, the deposition rate of CVD SiC plates was significantly enhanced compared to that of conventional thermal CVD. Figure 14.4 presents the temperature dependence of deposition rate of CVD SiC



14.3 Typical morphology of CVD SiC plates: (a) pyramid-like structure:  $T_{\text{dep}} = 1773$  K,  $P_{\text{tot}} = 4.0$  kPa,  $m_{\text{C/Si}} = 0.18$ ; (b) cone-like structure:  $T_{\text{dep}} = 1773$  K,  $P_{\text{tot}} = 0.1$  MPa,  $m_{\text{C/Si}} = 0.71$ .



14.4 Temperature dependence of deposition rate at  $P_{tot} = 4.0 \text{ kPa}$  and  $0.1 \text{ MPa}$ .

plates in the Arrhenius format at  $P_{tot} = 4.0 \text{ kPa}$  and  $0.1 \text{ MPa}$ . The highest deposition rate of dense CVD SiC plates was about  $2 \text{ mm/h}$ .<sup>8</sup> The appropriate conditions to obtain highly dense and pure CVD SiC plate were high  $T_{dep}$ , low  $P_{tot}$  and low  $m_{C/Si}$ , typically  $T_{dep} = 1773 \text{ K}$ ,  $P_{tot} = 0.3 \text{ kPa}$  and  $m_{C/Si} = 0.18$ , where well-faceted reddish translucent CVD SiC plates were obtained. The oxidation experiments have been conducted by using CVD SiC plates after mirror-polishing both surfaces. Highly pure and dense CVD SiC bulk forms and thick plates are now commercially available, and are applied to optics, wear parts, information storage and susceptors for semiconductor devise fabrication.<sup>15</sup> The authors have been collaborating with Admap Inc. (Japan) manufacturing CVD SiC products. Since then, CVD SiC plates translucent yellow in color with impurity level of ppb supplied from Admap have been used for the oxidation experiments.

### 14.3 Passive oxidation of silicon carbide

Oxidation resistance significantly depends on the defects of oxide layers. If the volume of an oxide layer is greater than that of the material, buckling of the oxide layer may take place, and if vice versa, the oxide layer becomes porous. Therefore, oxidation resistance may be primarily evaluated based on

the volume ratio of the oxide layer to the substrate material (called the Pilling–Bedworth ratio or PB ratio). Since the PB ratio of SiC is nearly 1 (almost no volume change by oxidation), a dense defect-free oxide ( $\text{SiO}_2$ ) layer can be expected to form on SiC. The increase in the thickness ( $x_O$ ) of the oxide layer during the oxidation process in such a situation is given by Eq. (14.1):<sup>16</sup>

$$x_O^2 + Ax_O = B(t + \tau) \quad 14.1$$

where  $A$ ,  $B$  and  $\tau$  are constants and  $t$  is oxidation time. This oxidation kinetics is termed ‘linear-parabolic,’ which can be approximated by a linear relationship and a subsequent parabolic relationship as given by Eqs (14.2) and (14.3), respectively:

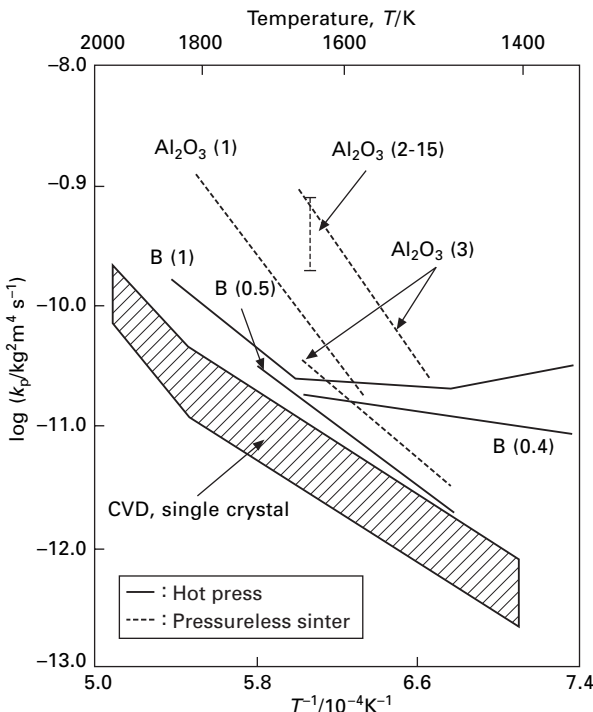
$$x_O = (B/A)(t + \tau) \quad 14.2$$

$$x_O^2 = B(t + \tau) \quad 14.3$$

where  $A$ ,  $B$  and  $\tau$  are constants, and  $B$  is often termed  $k_p$  (parabolic rate constant). The linear kinetics can be seen in the initial period, where the chemical reaction is rate-controlling. In a later period, the oxidation commonly obeys parabolic kinetics, where the diffusion process is rate-controlling.

Since SiC is one of the most promising high-temperature materials, the passive oxidation of various forms of SiC (hot-press, single crystal and CVD) has been investigated at high temperature. Figure 14.5 summarizes the temperature dependence of  $k_p$ , where the  $k_p$  of a highly pure, dense single crystal and CVD SiC is depicted by the hatched area.<sup>17</sup> Typical sintering additives ( $\text{Al}_2\text{O}_3$  and B) are indicated in Fig. 14.5 and the content of additives (in mass%) is shown in parentheses. The parabolic rate constants of sintered SiC bodies have been shown to be significantly greater than those of pure SiC, mainly due to high oxygen diffusion in the silicate phases formed by the reaction between  $\text{SiO}_2$  and sintering additives.<sup>18,19</sup> Therefore, highly pure, dense single crystals and CVD SiC should be employed to investigate the intrinsic oxidation mechanism of SiC. Single crystal SiC is also practically applicable to semiconductor devices, and so the oxidation behavior of single crystal SiC has been intensively studied to fabricate the gate dielectric  $\text{SiO}_2$  layer.<sup>19</sup>

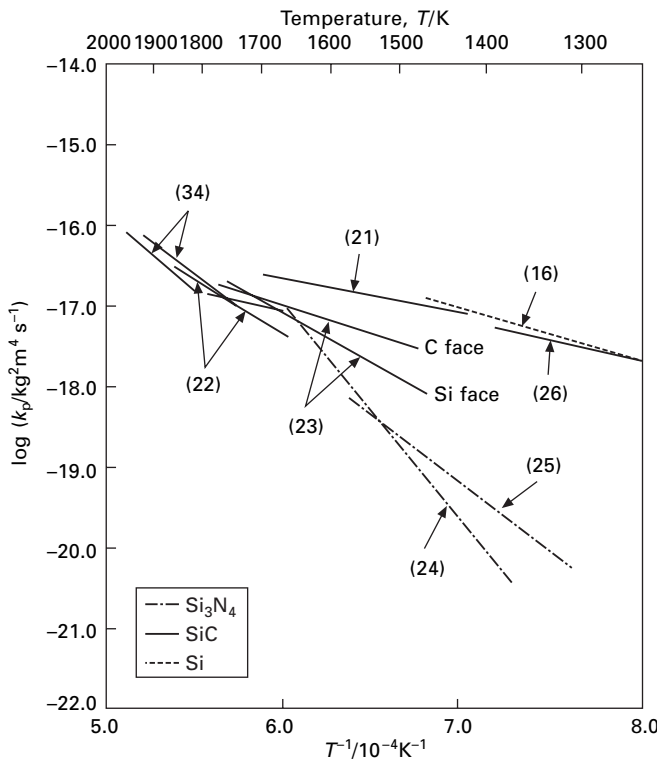
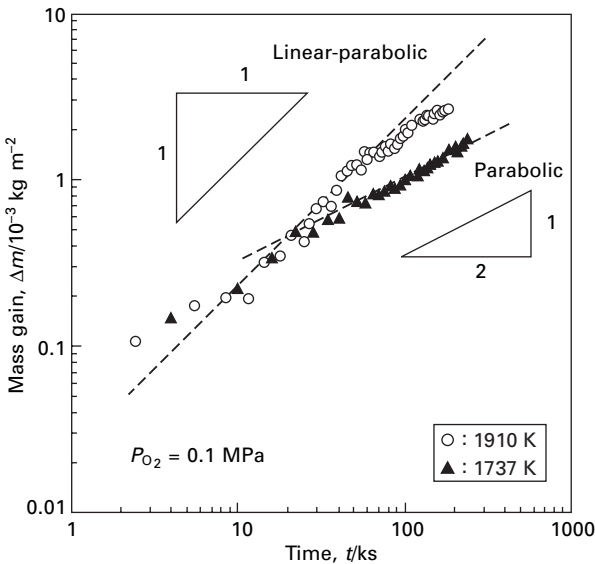
It is known that the oxidation rate of the  $(000\bar{1})$  face (C-face) of  $\alpha$ -SiC (ex. 4H or 6H type) is much greater than that of the  $(0001)$  face (Si-face), and the electrical properties of  $\text{SiO}_2$  layers have also been studied.<sup>20</sup> Figure 14.6 demonstrates the  $k_p$  of a single crystal and of CVD SiC so as to compare the calculated  $k_p$  from the oxygen diffusion (permeation) coefficients in vitreous  $\text{SiO}_2$ .<sup>1,6,21–26</sup> The  $k_p$  of SiC below 1500 K agreed with those of Si calculated from the permeation coefficient of  $\text{O}_2$  in amorphous  $\text{SiO}_2$ , and therefore it is well recognized that the oxidation kinetics of both Si and SiC can be controlled by the permeation of  $\text{O}_2$  in  $\text{SiO}_2$ . However, the  $\text{SiO}_2$  layers



14.5 Temperature dependence of  $k_p$  for various forms of SiC.

are always formed by the oxidation of silicon-based ceramics, including Si, SiC and  $\text{Si}_3\text{N}_4$ . If the rate-controlling step is the permeation of  $\text{O}_2$  in  $\text{SiO}_2$  for these materials, there should primarily be no difference of  $k_p$  between Si, SiC and  $\text{Si}_3\text{N}_4$ . On the contrary, anisotropy of  $k_p$  between the C-face and the Si-face of  $\alpha$ -SiC and a significant difference of  $k_p$  between SiC and  $\text{Si}_3\text{N}_4$  can be recognized in Fig. 14.6.<sup>27</sup> Some interfacial compound such as silicon oxynitride might be associated with the oxidation kinetics of  $\text{Si}_3\text{N}_4$ . Non-monotonous behavior of  $k_p$  over 1800 K has also been reported, suggesting the existence of different oxidation kinetics between low and high temperature ranges. In order to analyze the oxidation kinetics of SiC, the oxidation rate of highly pure and dense SiC should be measured continuously and precisely with time by using, for example, thermogravimetry.

Figure 14.7 demonstrates the relationship between mass gain and time of CVD SiC in logarithmic scales at 1737 and 1910 K at  $P_{\text{O}_2} = 10^5 \text{ Pa}$  in an Ar- $\text{O}_2$  atmosphere.<sup>28</sup> If the gradient of the line is 1, the oxidation kinetics is linear, and if the gradient is  $\frac{1}{2}$ , the oxidation kinetics is parabolic as given by Eqs (14.1) to (14.3). In Fig. 14.7, the mass gain increased linearly in the initial period, and parabolically in the latter period, satisfying the linear-parabolic kinetics. The  $k_p$  can be evaluated by extrapolating the values in the

14.6 Temperature dependence of  $k_p$  for  $\text{Si}_3\text{N}_4$ ,  $\text{SiC}$  and  $\text{Si}$ .

14.7 Relationship between mass gain and time of CVD SiC.

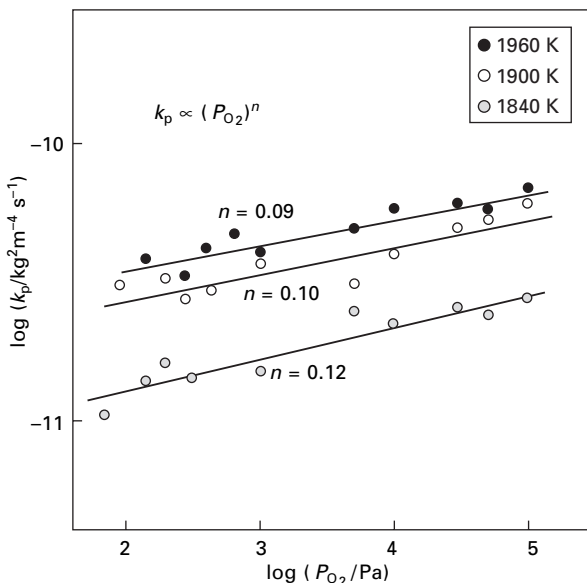
parabolic region of Fig. 14.7. The temperature and oxygen partial pressure dependences of  $k_p$  may obey Eqs (14.4) and (14.5), respectively:

$$k_p \propto \exp\left(\frac{E}{RT}\right) \quad 14.4$$

$$k_p \propto P_{O_2}^n \quad 14.5$$

where  $E$  is activation energy,  $R$  is the gas constant,  $P_{O_2}$  is the oxygen partial pressure and  $n$  is a constant. The values of  $E$  and  $n$  can be used to analyze the oxidation mechanism. In the case of low  $E$  and high  $n$ , the oxidation rate may be controlled by an inward diffusion of unionized species (ex. O<sub>2</sub> molecule), while for high  $E$  and  $n \approx 0$ , an outward diffusion of ionized species (ex. oxygen vacancy) is the dominant process of oxidation. The high or low  $E$  and low  $n$  may suggest a CO outward diffusion-limited process.

Figure 14.8 depicts the  $P_{O_2}^n$  dependence of  $k_p$  of CVD SiC from 1840 to 1960 K.<sup>28</sup> A linear relationship between  $k_p$  and  $P_{O_2}^n$  can be observed, where  $n = 0.09$  to 0.12 in Eq. (14.5). Table 14.1 summarizes the  $n$  values reported in the literature for the oxidation of SiC.<sup>28-34</sup> The reported  $n$  values are widely scattered from 0 to 0.6. Since experiments on the dependence of  $k_p$  on  $P_{O_2}^n$  are sensitive to impurities in SiC, it is difficult to obtain the rate-limiting process from these  $n$  values. However, it is noteworthy that the O<sub>2</sub> molecule or O<sup>2-</sup> ion diffusion is not the only possible rate-limiting process; CO outward diffusion is likely, particularly at high temperatures. Hot-pressed SiC may



14.8 Dependence of  $k_p$  of CVD SiC on  $P_{O_2}^n$ .

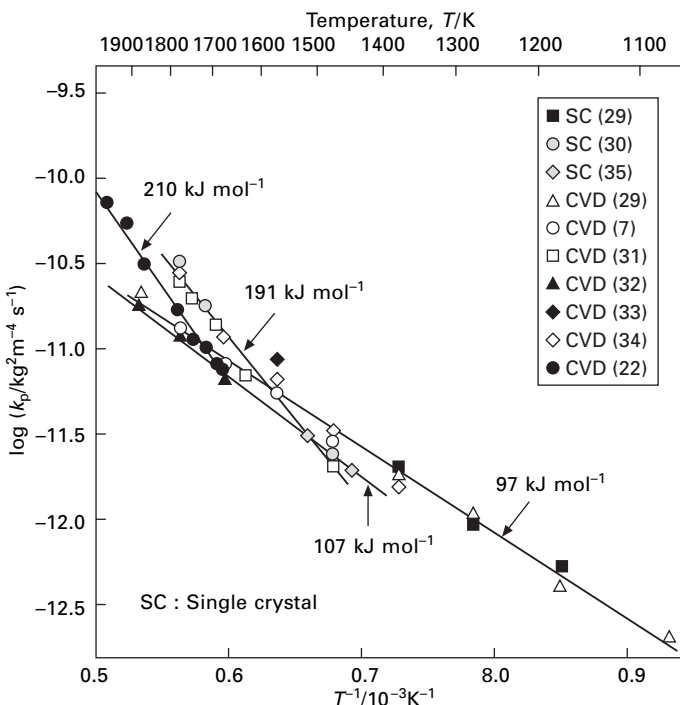
Table 14.1 Dependence of  $k_p$  on oxygen partial pressure,  $P_{O_2}^n$ 

Material	Value of $n$ in $P_{O_2}^n$	Rate-limiting process	Temperature (K)	Ref.
Powder SiC	0.5	O <sup>2-</sup> diffusion	1573–1823	29
Powder SiC	Independent	CO diffusion	1628–1718	30
Powder SiC	Dependent	O <sub>2</sub> diffusion	1273–1773	31
	Independent	CO diffusion	1773–1873	
SC SiC	0.3–0.6	Oxygen diffusion	1473–1773	32
HP SiC	0.55	O <sup>2-</sup> diffusion (interstitial)	1573	33
	0.03	O <sup>2-</sup> diffusion(vacancy)	1773	
CVD SiC	0.5	O <sup>2-</sup> diffusion	1823–1923	34
CVD SiC	0.09–0.12	CO diffusion	1670–1985	28

SC: single crystalline; HP: hot-press.

not be appropriate to investigate the intrinsic oxidation mechanism, because of the effect of impurities (sintering additives), where the inward diffusion of oxygen in the silicate phase through the grain boundary may be rate-controlling. Since powder SiC does not contain a high level of impurities, experimental results for powder SiC may be slightly more reliable than those of hot-pressed SiC to understand the intrinsic nature of oxidation. The small  $n$  values for powder and CVD may suggest the outward diffusion-limited process of oxygen vacancy or CO.

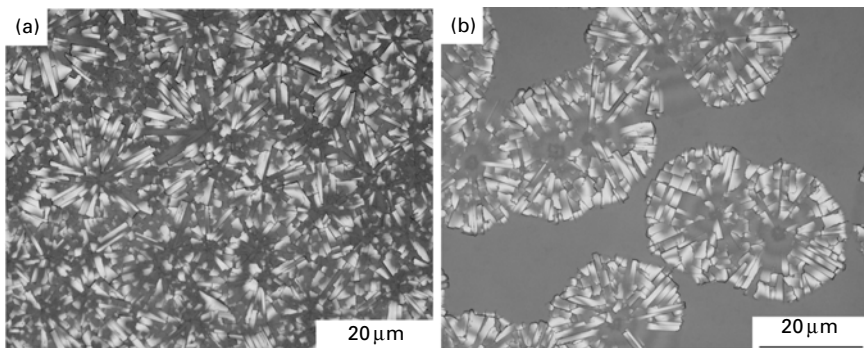
Figure 14.9 summarizes the temperature dependence of  $k_p$  in O<sub>2</sub> atmosphere for only pure SiC, i.e., single crystals and CVD SiC in the literature.<sup>7,28,23–41</sup> The  $E$  values below 1700 K were about 100 kJ/mol and well coincident with that of O<sub>2</sub> permeation in amorphous SiO<sub>2</sub>. However, the  $E$  value tends to increase to about 200 kJ/mol at temperatures higher than 1600 to 1700 K. This has been explained as being due to either (i) change of the oxidation mechanism, (ii) structural change of the oxide layer from β-cristobalite to vitreous (amorphous) SiO<sub>2</sub>, or (iii) acceleration of the oxidation rate by impurities (typically Na<sup>+</sup> and Al<sup>3+</sup> ions). Since the oxidation mechanism can be also discussed from the standpoint of the  $P_{O_2}^n$  dependence of  $k_p$  as depicted in Fig. 14.8, the weak  $P_{O_2}^n$  dependence of  $k_p$  ( $n \approx 0.09–0.12$ ) and the high  $E$  may suggest the existence of a rate-controlling step of outward diffusion of ionized species above 1600 K. The structure of the oxide layer is recognized to be amorphous (vitreous) SiO<sub>2</sub> below 1300 K, in the initial stage, and then β-cristobalite in a later stage around 1300 to 1500 K. Above 1600 K, the oxide layer may again become amorphous as the melting point of SiO<sub>2</sub> (about 2000 K) is approached. Since amorphous SiO<sub>2</sub> has a more open structure than β-cristobalite, which enables faster diffusion of chemical species, the oxidation rate may be accelerated with increasing temperature, resulting in a higher value of  $E$ . The  $k_p$  of hot-pressed SiC strongly depends on impurities



14.9 Temperature dependence of  $k_p$  for single crystal and CVD SiC.

and the structure of the oxide (usually silicate) layer as previously mentioned. However, it is not well understood whether the  $k_p$  values of highly pure and dense SiC are affected by the structure of the oxide layer.

A review of the effects of impurities and structure on  $k_p$  and  $E$  above 1600 K can be found in ref. (16). Since the structure of the oxide layer (either amorphous or crystalline) depends on the oxidation temperature, its effects can be hardly separated from those of temperature. However, we found that the structure of the oxide layer changed depending on the oxidant gas. Figure 14.10 demonstrates the surface morphology of oxide layers formed by oxidation of CVD SiC in atmospheres of Ar-O<sub>2</sub> and N<sub>2</sub>-O<sub>2</sub> at  $P_{\text{O}_2} = 1 \text{ kPa}$  and 1850 K after 8 h.<sup>28</sup> Since a significant volume change accompanies the phase transformation from the  $\beta$ - to the  $\alpha$ -cristobalite SiO<sub>2</sub> layer during the cooling process around 500 K, characteristic spherical features can be seen in crystallized SiO<sub>2</sub> layers while amorphous SiO<sub>2</sub> has a smooth, uniform morphology. The oxide layer was well crystallized after oxidation (Fig. 14.10(a)), whereas a significant amount of amorphous SiO<sub>2</sub> remained in N<sub>2</sub>-O<sub>2</sub> atmosphere (Fig. 14.10(b)).<sup>28</sup> However, there was no difference of  $k_p$  between these atmospheres. This suggests that the crystallization of the oxide layer is independent of  $k_p$ .



14.10 Surface morphology of oxide layers formed by oxidation of CVD SiC in (a) Ar-O<sub>2</sub> and (b) N<sub>2</sub>-O<sub>2</sub>.

It has often been reported that impurities, typically Al<sup>3+</sup> and Na<sup>+</sup> ions, significantly accelerate the oxidation rate of SiC.<sup>7</sup> Since Na<sup>+</sup> ions in the form of Na<sub>2</sub>O are commonly added to Al<sub>2</sub>O<sub>3</sub> sintered bodies as a sintering additive, we have sometimes observed an abnormally high  $k_p$  when using an Al<sub>2</sub>O<sub>3</sub> tube in experiments. Almost all researchers usually use Al<sub>2</sub>O<sub>3</sub> tubes for oxidation experiments. We always heat-treat Al<sub>2</sub>O<sub>3</sub> tubes for more than 24 h at a temperature higher than the experimental temperatures to eliminate Na<sup>+</sup> impurities. Another main source of contamination of the oxide layer is the tool used to hold the specimen during the experiments. In usual thermogravimetry, SiC specimens can be directly suspended by a hook, which is commonly fabricated of Al<sub>2</sub>O<sub>3</sub> (sometimes single crystal sapphire). Therefore, the material of the hook should be carefully chosen. The eutectic temperature of the Al<sub>2</sub>O<sub>3</sub>-SiO<sub>2</sub> system is 1719 K, whereas that of ZrO<sub>2</sub>-SiO<sub>2</sub> is 1956 K.<sup>42</sup> We have been using a ZrO<sub>2</sub> hook and ZrO<sub>2</sub> tubes for experiments to minimize the impurity effect, particularly at high temperatures. No impurities in SiO<sub>2</sub> layers were detected in our experiments. Therefore, impurities may also not be associated with the increase in  $E$  at high temperatures. The increase in  $E$  above 1600 K may not be associated with the change in structure of the SiO<sub>2</sub> layer, but related to the oxidation mechanism.

#### 14.4 Active oxidation of silicon carbide

The oxidation resistance of SiC obviously depends on the high temperature stability of the SiO<sub>2</sub> layer. The oxidation reaction of SiC may be expressed as Eq. (14.6):



The SiO<sub>2</sub> formation (rightward) reaction takes place at a certain  $P_{\text{O}_2}$ , which can be calculated from thermodynamic data, e.g.  $P_{\text{O}_2} > 10^{-15}$  Pa at 1600 K.

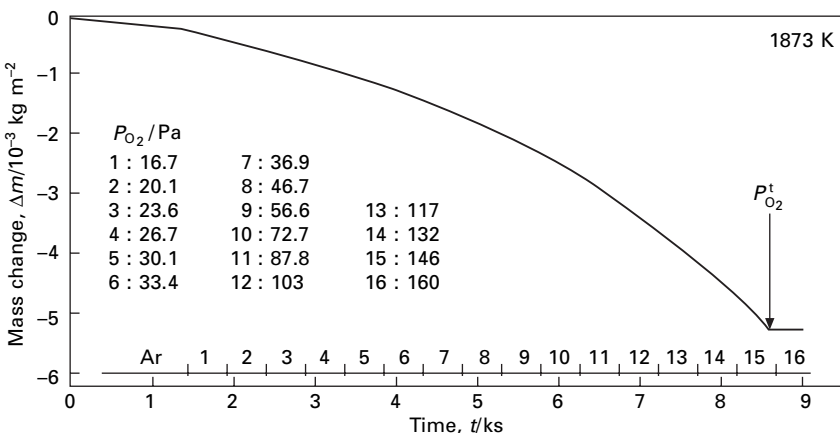
However, the protective  $\text{SiO}_2$  layer (passive oxidation) may not form under such conditions because  $\text{SiO}_2$  (s) is not stable and decomposes into  $\text{SiO}$  (g) and  $\text{CO}$  (g), i.e., the decomposition to  $\text{SiO}$  (g) and  $\text{CO}$  (g) is more significant than the formation of  $\text{SiO}_2$  (s) even at  $P_{\text{O}_2} > 10^{-15}$  Pa at 1600 K. Therefore, SiC will be severely degraded by  $\text{O}_2$  gas, and thus this oxidation mode is called ‘active oxidation’.<sup>4</sup>

Figure 14.11 demonstrates the relationship between mass change of CVD SiC and  $P_{\text{O}_2}$  at 1873 K in Ar- $\text{O}_2$ .<sup>43</sup>  $P_{\text{O}_2}$  increased step by step with time from 16.7 to 160 Pa. Mass loss (active oxidation) occurred up to  $P_{\text{O}_2} = 146$  Pa, and at  $P_{\text{O}_2} = 160$  Pa it drastically changed to slight gain of mass (passive oxidation). The  $P_{\text{O}_2}$  for the transition from active to passive oxidation ( $P_{\text{O}_2}^t$ ) is 160 Pa at 1873 K. This transition phenomenon can be commonly observed in the oxidation of Si-based ceramics and many kinds of metals.

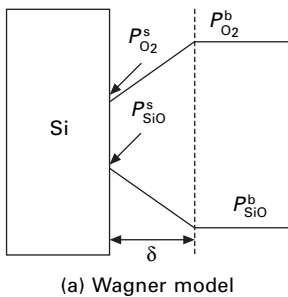
To understand this phenomenon, two kinds of models have been proposed: one is the Wagner model<sup>44</sup> and the other is the Turkdogan model as illustrated in Figs 14.12(a) and (b). The Wagner model was originally applied to explain the transition phenomenon for Si. Due to the high vapor pressure of  $\text{SiO}$  (g) ( $P_{\text{SiO}}$ ) at high temperature, the stability of  $\text{SiO}_2$  (s) is not determined by the dissociation pressure of  $\text{SiO}_2$  (s) but rather by the equilibrium  $P_{\text{SiO}}$  ( $P_{\text{SiO}}^{\text{eq}}$ ) given by Eq. (14.7):



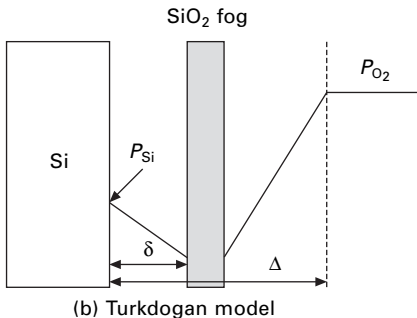
If  $P_{\text{SiO}}$  at the Si (s) surface is higher than  $P_{\text{SiO}}^{\text{eq}}$ ,  $\text{SiO}_2$  (s) will be stable at the Si (s) surface. The  $P_{\text{O}_2}^t$  is obtained from the  $\text{Si(s)-SiO(g)-O}_2\text{(g)}$  equilibrium. However,  $P_{\text{O}_2}$  at the Si (s) is significantly different from that in a bulk gas stream due to a gas boundary layer above the Si (s) surface. Therefore, Wagner proposed a model to estimate the  $P_{\text{O}_2}^t$  by assuming the steady state



14.11 Relationship between mass change of CVD SiC and  $P_{\text{O}_2}$ .



(a) Wagner model



(b) Turkdogan model

**14.12 Models for the active-to-passive transition:** (a) Wagner model, (b) Turkdogan model.

of  $O_2(g)$  and  $SiO(g)$  fluxes in the gas boundary layer at a thickness of  $\delta$ , as given by Eq. (14.8):

$$\frac{2D_{O_2}P_{O_2}^b}{\delta_{O_2}RT} = \frac{D_{SiO}P_{SiO}^s}{\delta_{SiO}RT} \quad 14.8$$

where  $D_x$  ( $x = SiO$  and  $O_2$ ) is the diffusion coefficient of  $x$  species,  $P_x^b$  is the vapor pressure of  $x$  in a bulk gas stream,  $\delta_x$  is the thickness of the gas boundary layer,  $R$  is the gas constant, and  $T$  is temperature. Since Eq. (14.9) can be assumed,  $P_{O_2}^t$  can be obtained by Eq. (14.10):

$$\delta_{SiO}/\delta_{O_2} = (D_{SiO}/D_{O_2})^{1/2} \quad 14.9$$

$$P_{O_2}^t = (D_{SiO}/D_{O_2})^{1/2} P_{SiO}^{eq} \quad 14.10$$

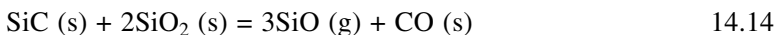
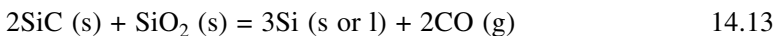
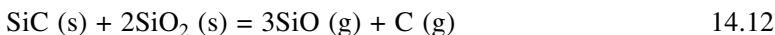
On the other hand, in the case of many metals such as Cu, Ni, Co, Fe, etc., active oxidation resulting in the formation of metal fumes takes place at low  $P_{O_2}$  and high temperatures and then becomes passive oxidation with increasing  $P_{O_2}$ . Turkdogan *et al.*<sup>45</sup> proposed a model to explain the transition behavior for these metals. As an example, for Fe, Fe (g) evaporates from the Fe (s)

surface and a gas boundary layer (thickness  $\delta$ ) for the diffusion of Fe (g) is formed. When Fe (g) encounters O<sub>2</sub> gas, FeO fumes are formed. The gas boundary layer (thickness  $\Delta$ ) is also formed between the bulk gas stream and the FeO fume zone. With increasing  $P_{O_2}$  in the bulk gas stream,  $\Delta$  increases and  $\delta$  decreases. The evaporation rate of Fe (g) from the Fe (s) surface is inversely proportional to the  $\delta$ . The evaporation rate of Fe (g) cannot exceed the Langmuir free evaporation rate in a vacuum. A further increase in  $P_{O_2}$  breaks the balance of the steady state, and then the direct oxidation would occur on the Fe (s) surface. Details of the Turkdogan model can be found in ref. (45). Since the highest vapor species from SiC is Si (g), Si (g) may react with O<sub>2</sub> gas, resulting in the formation of SiO<sub>2</sub> fumes.  $P_{O_2}^t$  in the Turkdogan model is given by Eq. (14.11) for the transition of SiC:

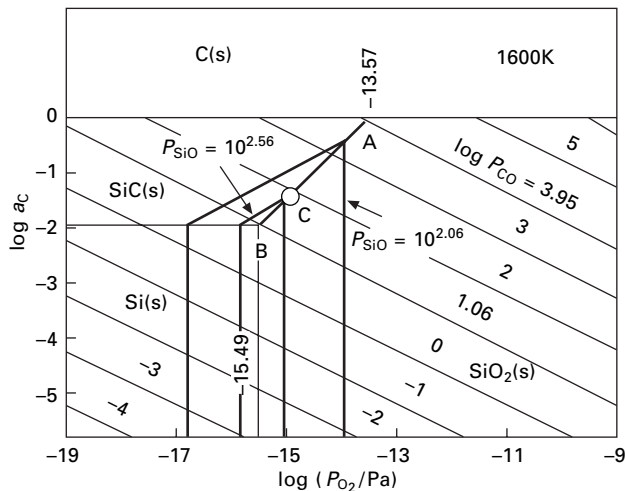
$$P_{O_2}^t = P_{Si}^* / h_{O_2} \sqrt{RT/2\pi M_{Si}} \quad 14.11$$

where  $h_{O_2}$  is the mass transport coefficient,  $P_{Si}^*$  is the equilibrium vapor pressure of Si, and  $M_{Si}$  is the atomic mass of Si. However, the  $P_{O_2}^t$  calculated using this model is several orders of magnitude smaller than that of experimental  $P_{O_2}^t$  for SiC. A significant amount of O was also experimentally detected on the SiC surface after active oxidation. In this model, the oxygen molecule should not arrive at the SiC surface, because Si gas evaporates from the SiC surface and the SiO vapors formed are only in contact with oxygen in the fume zone. Therefore, the Turkdogan model is not considered to be applicable to Si-based ceramic materials.

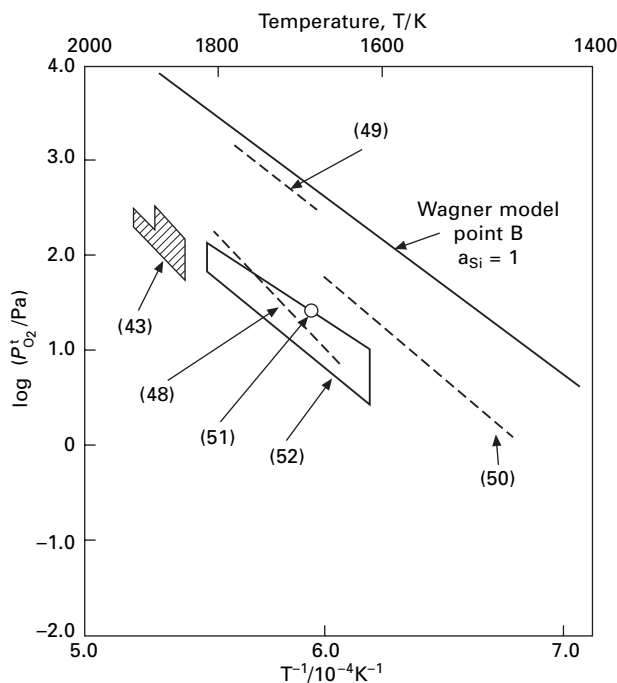
Since SiO and CO vapors can form during the active oxidation of SiC, application of the Wagner model to SiC becomes more complicated than that to Si.<sup>46</sup> Figure 14.13 demonstrates the phase stability diagram for the Si-C-O system at 1600 K as functions of carbon activity ( $a_C$ ) and oxygen partial pressure ( $P_{O_2}$ ).<sup>47</sup> In order to apply the Wagner model to SiC, the equilibrium vapor pressures of SiO and/or CO should be substituted in Eq. (14.8). SiO and CO equilibrium vapor pressures can be calculated from Eqs (14.12) to (14.14):<sup>48</sup>



The points A (carbon saturated,  $a_C = 1$ ) and B (silicon saturated,  $a_{Si} = 1$ ) in Fig. 14.13 correspond to Eqs (14.10) and (14.11), respectively. The point C satisfies the stoichiometric relationship of  $P_{SiO} = 3P_{CO}$ . Although there are one to two orders of difference between calculations from the model and the experiments, the Wagner model has been commonly considered to be applicable to explain the transition phenomenon for silicon-based ceramics such as SiC. Figure 14.14 summarizes the reported  $P_{O_2}^t$  for single crystal, sintered



14.13 Phase stability diagram for the Si-C-O system as functions of  $a_C$  and  $P_{O_2}$ .

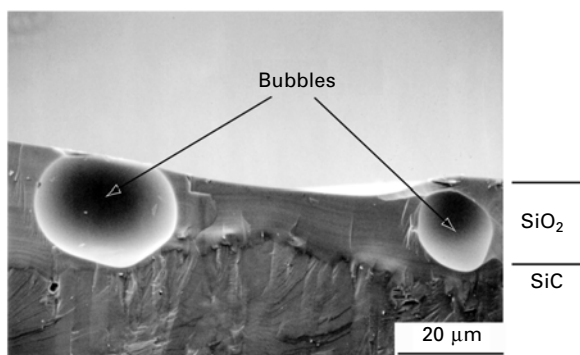


14.14 Temperature dependence of  $P_{O_2}^t$  for various forms of SiC.

SiC and CVD SiC.<sup>43,48–52</sup>  $P_{O_2}^t$  seems to be rather insensitive to impurities, and the temperature dependence of experimental  $P_{O_2}^t$  was generally in agreement with the values calculated using the Wagner model (at  $a_{Si} = 1$ ). The experimental  $P_{O_2}^t$  was only 1/10 to 1/100 of the values calculated using the Wagner model, and thus several assumptions in the Wagner model may be too simple. Various researchers have been attempting to modify the model to adjust the calculations.<sup>49</sup> The thermodynamic values and diffusion constants should be more accurately measured at high temperatures.

## 14.5 Bubble formation of silicon carbide

The bubble formation in SiC, particularly impure SiC such as that in SiC heating elements and hot-pressed SiC bodies, has often been observed at high temperatures. With the formation of SiO and CO vapors at the SiC/SiO<sub>2</sub> interface, the bubbles of SiO<sub>2</sub> emerge, grow and rupture. Figure 14.15 demonstrates typical bubbles formed during high temperature oxidation of CVD SiC at 1990 K. Bubbles with a much larger size of about 3 mm in diameter can be observed on the CVD SiC surface. Once bubbles form on the SiC surface, the SiO<sub>2</sub> layer on the SiC surface is no longer protective, and the SiC degrades significantly at high temperatures. Bubble formation can determine the limitation of high-temperature usage of SiC.<sup>1</sup> Table 14.2 summarizes data from the literature on bubble or pore formation in the oxidation of SiC, mainly for hot-pressed SiC.<sup>5,17,18,33,53–57</sup> A significant amount of sintering additives are contained in hot-pressed SiC, and silicate phases are formed by the reaction between SiO<sub>2</sub> and such additives. The bubbles or pores can appear at relatively low temperatures due to low melting points (or low viscosity) of silicate phases in hot-pressed SiC. The melting point of pure SiO<sub>2</sub> is the highest (~2000 K), the reported bubble formation temperature of highly pure CVD SiC being the highest at 1973 K.



14.15 Bubbles formed in SiO<sub>2</sub> layer at high temperature oxidation of CVD SiC at 1990 K.

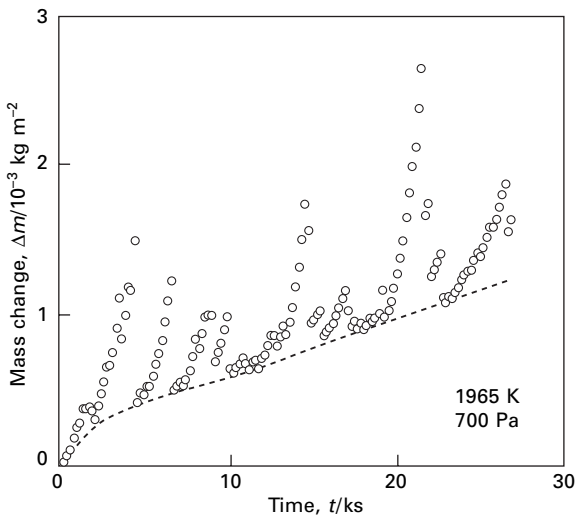
Table 14.2 Bubble formation in the oxidation of SiC

Material	Temperature (K)	Atmosphere	Feature	Ref.
HP SiC (several % Al <sub>2</sub> O <sub>3</sub> , 1% WC)	1673–1773	O <sub>2</sub>	Several µm bubbles in film	33
HP SiC (4%Al <sub>2</sub> O <sub>3</sub> + 4%W)	1578–1643	O <sub>2</sub>	10 µm bubbles near surface	18
HP SiC (0.5%Al)	1643–1773	Air	10 µm bubbles near surface	53
PLS SiC (B)	1673	Air	Several µm bubbles in film	17
PLS SiC	1573	O <sub>2</sub>	1–20 µm bubbles	54
CVD SiC	1973–2073	Air	3 mm bubbles	55
CVD SiC	1973	O <sub>2</sub>	A few µm bubbles	56
CVD SiC	2003	O <sub>2</sub>	Several µm bubbles on surface	57
CVD SiC	1910–2000	O <sub>2</sub>	A few mm bubbles on surface and several µm bubbles in film	5

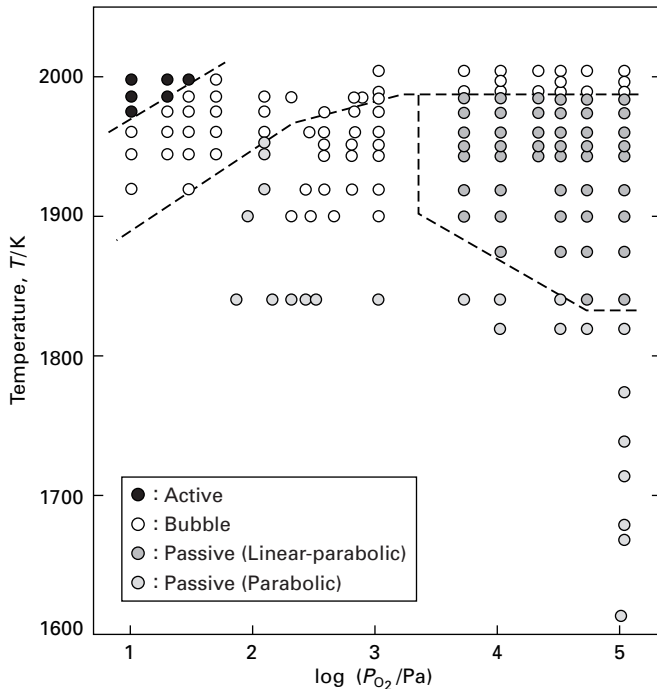
HP: hot-press; PLS: pressureless sinter.

Figure 14.16 demonstrates the time dependence of mass change of CVD SiC at 1965 K for  $P_{O_2} = 700$  Pa. The mass change fundamentally obeyed the parabolic law accompanying saw-shaped characteristics due to the sequence of formation and rupture of bubbles. The thermogravimetry is a sensitive tool for the identification of bubble formation. Figure 14.17 depicts the effects of temperature and  $P_{O_2}$  on the condition between passive oxidation and bubble formation.<sup>4</sup> The transition temperature from passive oxidation to bubble formation increased with increasing  $P_{O_2}$  at  $P_{O_2} < 10^3$  Pa and became almost constant (1985 K) at  $P_{O_2} = 10^3$  Pa. Bubbles form when total pressure of vapors ( $P_{tot}$ ) inside the bubbles exceeds the ambient pressure ( $10^5$  Pa). Therefore, the bubble formation temperature can be calculated from the equilibrium SiO and CO vapor pressures at the SiO<sub>2</sub>/SiC interface.

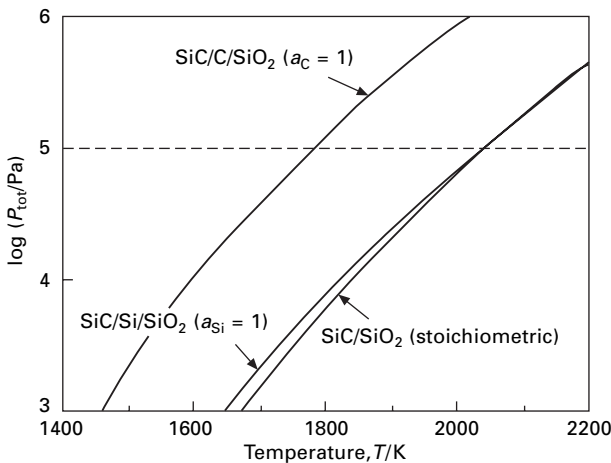
Figure 14.18 demonstrates the calculated equilibrium total pressure of SiO and CO vapors at the SiC/SiO<sub>2</sub> interface.<sup>4</sup> The equilibrium states at the SiC/SiO<sub>2</sub> interface can be expressed as either point A in Fig. 14.13 (SiC/C/SiO<sub>2</sub> equilibrium,  $a_C = 1$ ), point B (SiC/Si/SiO<sub>2</sub> equilibrium,  $a_{Si} = 1$ ) or point C (SiC/SiO<sub>2</sub> equilibrium with the stoichiometric gas composition of  $P_{SiO} = 3P_{CO}$ ). The vapor pressure at  $a_C = 1$  (point A) is the highest, more than  $10^5$  Pa at 1800 K. The vapor pressure exceeds  $10^5$  Pa at points B and C at more than 2000 K. On the other hand, the bubble formation temperature of CVD SiC was experimentally determined to be around 1950 K, indicating that the



14.16 Time dependence of mass gain for CVD SiC with bubble formation.



14.17 Effects of temperature and  $P_{\text{O}_2}$  on the condition between passive oxidation and bubble formation.



14.18 Equilibrium total pressure of SiO and CO vapors at the SiC/SiO<sub>2</sub> interface.

state at the SiC/SiO<sub>2</sub> interface is close to point A ( $a_C = 1$ ).<sup>57</sup> If the rate-controlling step of the passive oxidation of SiC is the inward diffusion of O<sub>2</sub> molecules or O ions into the SiO<sub>2</sub> layer, the  $P_{\text{O}_2}$  at the SiC/SiO<sub>2</sub> interface should be the lowest from the definition of the oxygen diffusion limited process, and the state of the SiC/SiO<sub>2</sub> should be expressed by point B ( $a_{\text{Si}} = 1$ ). On the other hand, the experimental results for the bubble formation temperature suggest a carbon saturated condition ( $a_C = 1$ ) at the SiC/SiO<sub>2</sub> interface, contrary to the O<sub>2</sub> (or O ion) inward diffusion limited process. Therefore, the passive oxidation mechanism of CVD SiC might possibly be CO outward diffusion-limited according to the bubble formation temperature.<sup>58</sup>

## 14.6 Summary

CVD SiC appears to be the best material to understand intrinsic oxidation behavior, i.e., passive oxidation, active oxidation and bubble formation. Although the oxidation behavior of CVD SiC has been studied mainly as basic research, many practical applications of CVD SiC as high-temperature oxidation-resistant coatings have been realized, particularly for carbon–carbon fiber composites and ceramic gas turbine blades. CVD SiC is a promising material for extremely harsh oxidizing conditions such as those in the re-entry of spacecraft. For these applications, the understanding of intrinsic oxidation behavior of SiC is essential. The passive oxidation kinetics of SiC may be dominated by the permeation of O<sub>2</sub> molecules at less than 1500 K, whereas the bubble formation temperature suggests that the oxidation is probably a CO outward diffusion-limited process. The active-to-passive transition is fundamentally explained by the Wagner model. However, more

precise thermodynamic data and the modification of the model are necessary to predict the active-to-passive transition more accurately.

## 14.7 References

1. Jacobson N S, 'Corrosion of silicon-based ceramics in combustion environments', *J Am Ceram Soc*, 1993 **76**(1) 3–28.
2. Schlichting J, 'Chemical vapor-deposition of silicon-carbide', *Powder Metall Int*, 1980 **12**(4) 196–200.
3. Narushima T, Goto T, Hirai T, Iguchi Y, 'High-temperature oxidation of silicon carbide and silicon nitride', *Mater Trans, JIM*, 1997 **38**(10) 821–835.
4. Goto T, 'High-temperature oxidation behavior of chemical vapor deposited silicon carbide', *J Ceram Soc Jpn*, 2002 **110**(10) 884–889.
5. Goto T, Homma H, 'High-temperature active/passive oxidation and bubble formation of CVD SiC in O<sub>2</sub> and CO<sub>2</sub> atmosphere', *J Eur Ceram Soc*, 2002 **22** 2749–2756.
6. Ramberg C E, Worrell W L, 'Oxygen transport in silica at high temperatures: implications of oxidation kinetics', *J Am Ceram Soc*, 2001 **84**(11) 2607–2616.
7. Ogbuji L U J T, Opila E J, 'A comparison of the oxidation kinetics of SiC and Si<sub>3</sub>N<sub>4</sub>', *J Electrochem Soc*, 1995 **142**(3) 925–930.
8. Hirai T, Goto T, Katji T, 'Preparation of silicon carbide by chemical vapor deposition', *J Ceram Soc Jpn*, 1983 **91**(11) 502–509.
9. Hirai T, Niihara K, Goto T, 'Rapid chemical vapour-deposition of Si<sub>3</sub>N<sub>4</sub>', *J Mater Sci*, 1977 **12**(33) 631–632.
10. Mukaida M, Goto T, Hirai T, 'Morphology and deposition rate of TiB<sub>2</sub> prepared by chemical vapour deposition of TiCl<sub>4</sub> + B<sub>2</sub>H<sub>6</sub> system', *J Mater Sci*, 1990 **25** 1069–1075.
11. Jiang C-C, Goto T, Hirai T, 'Preparation of titanium carbide plates by chemical vapour depositon', *J Mater Sci*, 1990 **25** 1086–1093.
12. Bryant W A, 'Fundamentals of chemical vapor-deposition', *J Mater Sci*, 1977 **12**(7) 1285–1306.
13. Niihara K, Hirai T, 'Chemical vapour-deposited silicon nitride, part 1. Preparation and some properties', *J Mater Sci*, 1976 **11** 593–603.
14. Weiss J R, Diefendroff R J, 'Chemically vapour deposited SiC for high temperature and structural applications', *Silicon Carbide-1973*, University of South Carolina Press, Columbia, SC, 1973, 80–91.
15. Pickering M A, Haigis W, 'CVD scaled up for commercial production of bulk SiC', *Amer Ceram Soc Bull*, 1993 **72**(3) 74–78.
16. Deal B E, Grove A S, 'General relationship for thermal oxidation of silicon', *J Appl Phys*, 1965 **36**(12) 3770–3778.
17. Costello J A, Tressler R E, 'Oxidation kinetics of hot-pressed and sintered  $\alpha$ -SiC', *J Am Ceram Soc*, 1981 **64**(6) 327–331.
18. Singhal S C, 'Oxidation kinetics of hot-pressed silicon carbide', *J Mater Sci*, 1976 **11** 1246–1253.
19. Costello J A, Tressler R E, Tsong I S T, 'Boron redistribution in sintered  $\alpha$ -SiC during thermal oxidation', *J Am Ceram Soc*, 1981 **64**(6) 332–335.
20. Ramberg C E, Cruciani G, Spear K E, Tressler R E, Ramberg Jr. C F, 'Passive-oxidation kinetics of high-purity silicon carbide from 800°C to 1100°C', *J Am Ceram Soc*, 1996 **79**(11) 2897–2911.

21. Muehlenbachs K, Schaeffer H A, 'Oxygen diffusion in vitreous silica—utilization of natural isotopic abundances', *Can Mineral*, 1977 **15** 179–184.
22. Shiroky G H, Price R J, Sheehan JE, 'Oxidation characteristics of CVD silicon carbide and silicon nitride', Rept No. GA-18696, GA Technologies, San Diego, CA, 1986.
23. Zheng Z, Tressler R E, Spear K E, 'Oxidation of single-crystal silicon carbide, part I. Experimental studies', *J Electrochem Soc*, 1990 **137**(3) 854–858.
24. Choi D J, Fischback D B, Scott W D, 'Oxidation of chemically-vapor-deposited silicon nitride and single-crystal silicon', *J Am Ceram Soc*, 1989 **72**(7) 1118–1123.
25. Du H, Tressler R E, Spear K E, Pantano C G, 'Oxidation studies of crystalline CVD silicon nitride', *J Electrochem Soc*, 1989 **136** 1527–1535.
26. Norton F J, 'Permeability of gaseous oxygen through vitreous silica', *Nature (London)*, 1961 **191** 701.
27. Persson J P, Käll P-O, Nygren M, 'Interpretation of the parabolic and non-parabolic oxidation behavior of silicon oxynitride', *J Am Ceram Soc*, 1992 **75**(12) 3377–3384.
28. Goto T, 'High temperature passive oxidation mechanism of CVD SiC', *Mater Sci Forum*, 2006 **522/523** 27–36.
29. Jorgensen P J, Wadsworth M E, Culter I B, 'Effects of oxygen partial pressure on the oxidation of silicon carbide', *J Am Ceram Soc*, 1960 **43**(4) 209–212.
30. Pultz W W, 'Temperature and oxygen pressure dependence of silicon carbide oxidation', *J Phys Chem*, 1967 **71**(13) 456–458.
31. Figzer E, Ebi R, 'Kinetic studies on the oxidation of silicon carbide', *Silicon Carbide – 1973*, University of South Carolina Press, Columbia, SC, 1973, 320–328.
32. Zheng Z, Tressler R E, Spear K E, 'Oxidation of single-crystal silicon carbide, part II. Kinetic model', *J Electrochem Soc*, 1990 **137**(9) 2812–2816.
33. Hinze J W, Tripp W C, Graham H C, 'The high-temperature oxidation of hot-pressed silicon carbide', *Mass Transport Phenomena in Ceramics*, Plenum, New York, 1975, 409–419.
34. Narushima T, Goto T, Hirai T, 'High-temperature passive oxidation of chemically vapor deposited silicon carbide', *J Am Ceram Soc*, 1989 **72**(8) 1386–1390.
35. Ramberg C E, Spear K E, Tressler R E, Chinone Y, 'Oxidation behavior of CVD and single crystal SiC at 1100°C', *J Electrochem Soc*, 1995 **142** (11) L214–216.
36. Costello J A, Tressler R E, 'Oxidation kinetics of silicon carbide crystals and ceramics: I, in dry oxygen', *J Am Ceram Soc*, 1986 **69**(9) 674–681.
37. Rodriguez-Viejo J, Sibiede F, Clavaguera-Mora M T, 'High temperature oxidation of CVD  $\beta$ -SiC, part 1. Experimental study', *J Eur Ceram Soc*, 1994 **13** 167–175.
38. Ramberg C E, Worrell W L, 'Thermogravimetric analysis of SiC oxidation', *Proc. 9th Int Conf High Temp Mater Chem*, vol. 97–99, Pennington, NJ, Electrochem Soc, Inc., 1997, 836–846.
39. Ogbuji L U, 'Development of oxide scale microstructure on single-crystal SiC', *J Mater Sci*, 1981 **16** 2753–2759.
40. Filippuzzi L, Naslain R, Jaussaud C, 'Oxidation kinetics of SiC deposited from  $\text{CH}_3\text{SiCl}_3/\text{H}_2$  under CVI conditions', *J Mater Sci*, 1992 **27** 3330–3334.
41. Harris R C A, 'Oxidation of 6H- $\alpha$  silicon carbide platelets', *J Am Ceram Soc*, 1975 **58**(1–2) 7–9.
42. Levin E M, Robbins C R, McMurtrie H F, *Phase Diagram for Ceramists*, Columbus, OH, Amer Ceram Soc, 1964.
43. Narushima T, Goto T, Iguchi Y, Hirai T, 'High-temperature active oxidation of chemically vapor-deposited silicon carbide in an Ar-O<sub>2</sub> atmosphere', *J Am Ceram Soc*, 1991 **74**(10) 2583–2586.

44. Wagner C, 'Passivity during the oxidation of silicon at elevated temperature', *J Appl Phys*, 1958 **29**(9) 1295–1297.
45. Turkdogan E T, Grieveson P, Darken L S, 'Enhancement of diffusion-limited rates of vaporization of metals', *J Phys Chem*, 1963 **67**(8) 1647–1654.
46. Nickel K G, 'The role of condensed silicon monoxide in the active-to-passive oxidation transition of silicon carbide', *J Eur Ceram Soc*, 1992 **9** 3–8.
47. Gulbransen E A, Jansson S A, 'The high-temperature oxidation, reduction, and volatilization reactions of silicon and silicon carbide', *Oxid Met*, 1972 **4**(3) 181–201.
48. Hinze J W, Graham H C, 'The active oxidation of Si and SiC in the viscous gas-flow regime', *J Electrochem Soc*, 1976 **123**(7) 1066–1073.
49. Balat M, Flamant G, Male G, Pichelin G, 'Active to passive transition in the oxidation of silicon carbide at high temperature and low pressure in molecular and atomic oxygen', *J Mater Sci*, 1992 **27** 697–703.
50. Gulbransen E A, Andrew K F, Brassart F A, 'The oxidation of silicon carbide at 1150°C to 1400°C and at  $9 \times 10^{-3}$  to  $5 \times 10^{-1}$  torr oxygen pressure', *J Electrochem Soc*, 1966 **113**(12) 1311–1314.
51. Kim H E, Moorhead A J, 'Effect of active oxidation on the flexural strength of  $\alpha$ -silicon carbide', *J Am Ceram Soc*, 1990 **73**(7) 1868–1872.
52. Vaughn W L, Maahs H G, 'Active-to-passive transition in the oxidation of silicon carbide and silicon nitride in air', *J Am Ceram Soc*, 1990 **73**(6) 1540–1543.
53. Schlichting J, Kriegesman J, 'Oxidation behavior of hot-pressed silicon carbide', *Ber Dt Keram Ges*, 1979 **56**(3–4) 72–75.
54. Mieskowski D M, Mitchell T E, Heuer A H, 'Bubble formation in oxide scales on SiC', *J Am Ceram Soc*, 1984 **67**(1) C17–18.
55. Schiroky G H, 'Oxidation behavior of chemically vapor-deposited silicon carbide', *Adv Ceram Mater*, 1987 **2**(2) 137–141.
56. Ogura Y, Morimoto T, 'Mass spectrometric study of oxidation of SiC in low-pressure oxygen', *J Electrochem Soc*, 2002 **149**(4) J47–J52.
57. Narushima T, Goto T, Yokoyama Y, Takeuchi Y, Iguchi Y, Hirai T, 'Active-to-passive transition and bubble formation for high-temperature oxidation of chemically vapor-deposited silicon carbide in CO-CO<sub>2</sub> atmosphere', *J Am Ceram Soc*, 1994 **77**(4) 1079–1082.
58. Luthra K L, 'Some new perspective on oxidation of silicon carbide and silicon nitride', *J Am Ceram Soc*, 1991 **74**(5) 1095–1103.

## Oxidation-resistant nanocrystalline coatings

X PENG and F WANG, Chinese Academy of Sciences, China

### 15.1 Nanocrystalline materials and coatings

Nanostructured materials have attracted considerable attention in the last two decades. Nanocrystalline materials are single- or multi-phase polycrystals with grain sizes in the nanometre range (typically below 100 nm in at least one dimension).<sup>1</sup> In nanocrystalline materials, a large fraction of atoms (up to ~50%) locate at grain boundaries or interphase boundaries. Because they possess numerous boundaries, the nanocrystalline materials with respect to conventional coarse-grained (normally micro-grained) polycrystalline counterparts are well known to display the unique and generally improved physical, chemical as well as mechanical properties. For example, nanocrystalline materials may exhibit higher thermal expansion coefficient, electrical resistivity and diffusivity, lower thermal conductivity, reduced density and elastic modulus, and increased hardness/strength, toughness/ductility and abrasion wear resistance, etc. Thus, nanocrystalline materials have a promising outlook for their applications in a wide variety of technological areas such as electronics, catalysis, ceramics, magnetic data storage, structural components, etc.<sup>1–5</sup>

Currently, the bulk metallic nanomaterials can only be synthesized at the laboratory scale, normally using the starting nanocrystalline powders which are consolidated in a chamber, through compaction techniques and severe plastic deformation processing.<sup>1–5</sup> The compaction techniques include hot pressing,<sup>6</sup> hot extrusion,<sup>7</sup> cold or hot isostatic pressing (HIP),<sup>8,9</sup> etc. However, consolidation of metallic nanopowders into bulk materials under high temperatures and pressures may considerably coarsen the grain size of nanocrystals. Besides, the nanocrystalline materials fabricated using these techniques may cause the formation of internal pores in a certain volume fraction. Nanocrystalline materials can also be manufactured through severe plastic deformation processing, which is divided into two major procedures: high pressure torsion (HPT) and equal-channel angular (ECA) pressing. HPT treatment usually results in the formation of materials with a mean grain size

of ~100 nm, while materials with a slightly larger grain size are produced using ECA pressing.<sup>10</sup>

Because of the current difficulty in industrial-scale fabrication of bulk nanocrystalline materials with desirable properties and a reasonable cost, surface nanocrystallization or nanocrystalline coatings have been regarded as a preferred choice to improve the service properties of many metal workpieces. Metal surface nanocrystallization is usually realized through techniques that can cause severe plastic deformation of the metals in the surface layer. The techniques commonly used include surface mechanical attrition (SMA),<sup>11</sup> shot peening,<sup>12,13</sup> particle impact,<sup>13,14</sup> circulation rolling,<sup>15</sup> etc. The effects of these surface modification treatments on the mechanical properties of various metals have been extensively investigated.<sup>3–5,11–15</sup> In addition, nanostructured surface layers can be produced using different coating and deposition techniques such as physical vapour deposition (PVD) including evaporation and sputtering,<sup>5,16,17</sup> chemical vapour deposition (CVD),<sup>5,18,19</sup> plasma spraying<sup>20,21</sup> and high velocity oxygen fuel (HVOF) deposition,<sup>22–24</sup> etc. PVD and CVD are well-established technologies for manufacturing the superhard (hardness > 40 GPa) or ultrahard (hardness > 80 GPa) transitional metal nitride coatings (such as TiN, TiCN, TiAlN, etc.) with grain sizes in the nanometre range. Hard nanostructured coatings manufactured by means of thermal spraying of feedstock nanoparticles of metals or ceramics are naturally not as hard as the PVD and CVD coatings. The aforementioned techniques are also applied to develop nanocrystalline coatings with superior oxidation resistance. The oxidation performance of these coatings strongly depends on their composition and structure.

## 15.2 Oxidation-resistant coatings

Once exposed to high temperature environments, almost all kinds of metals will spontaneously form a scale of thermally-grown oxides (TGO), which functions as a barrier isolating the metals from the environmental corrosive species. For a TGO scale with the desired protectivity, it should exhibit high thermal stability, good compactness and slow growth rate, as well as strong adhesion to the metal substrate. If a non-protective scale is formed, the oxidation would cause the rapid recession of metals, which profoundly reduces the mechanical properties and service lifetime of metal workpieces. Among the TGO oxides, chromia and alumina are two kinds of oxides kinetically and thermodynamically meeting the requirement of resisting high temperature oxidation. In general, chromia scale is the ideal scale against oxidation at temperatures below 1000°C and Type II hot corrosion (700–800°C), and alumina scale (particularly in its form of  $\alpha$  phase) is the best against Type I hot corrosion (800–950°C) and high temperature oxidation above 1000°C.

From the oxidation kinetic point of view, metals with ideal oxidation resistance should exclusively form an external scale of protective oxides such as chromia or alumina. Conventional commercial superalloys cannot, in most cases, guarantee the exclusive formation of the external scale, because of limitation of the content of chromium or/and aluminium (which would, if high, increase the alloys' brittleness and decrease their high-temperature strength and creep resistance). To increase the oxidation resistance at elevated temperatures, alloys are often pre-treated with a chromia- or alumina-forming coating which has a high content of chromium or/and aluminium. These coatings of the first generation are the well-known diffusional chromizing and aluminizing coatings, which are usually manufactured by chemical vapour deposition (CVD) or pack cementation.<sup>25,26</sup> The second generation coatings are so-called overlay coatings, the majority of which are of MCrAl type (M = Fe, Ni, Co, or their combinations) containing a small amount of yttrium. Compared to the diffusion coatings, overlay coatings have the advantage that their composition can be specifically designed and manufactured to match the particular environmental conditions required.<sup>27</sup> For an MCrAl coating with a desired property against high temperature oxidation, the content of chromium is normally in the range 16–24 wt% and that of aluminium in the range 13–18 wt%.<sup>27</sup> MCrAl overlay coatings have been fabricated by various techniques, such as electron beam physical vapour deposition,<sup>28</sup> magnetron sputtering,<sup>29,30</sup> plasma and HVOF spraying<sup>31–33</sup> and laser cladding.<sup>34</sup>

Another approach to oxidation-resistant coatings is to refine the grain structure, rather than to increase the content of chromium or/and aluminium. The phenomenon that the grain refinement of alloys promotes the formation of protective scale was first reported by Giggins and Pettit<sup>35,36</sup> and later by Merz.<sup>37</sup> Since then, publications on the study of grain refinement on the oxidation of metals, as well as on the development of oxidation-resistant protective coatings through grain refining, had been scarce until the late 1980s, when Wang and Lou found that the fine-grained Co-30Cr-5Al coating has an oxidation resistance better than the normal-grained alloy counterpart with a similar composition in air at 1100°C because of an increased ability to exclusively form an external scale of alumina.<sup>38</sup> Nanocrystalline coatings with superior oxidation resistance have been extensively reported in the last 10 years.<sup>30,39–48</sup>

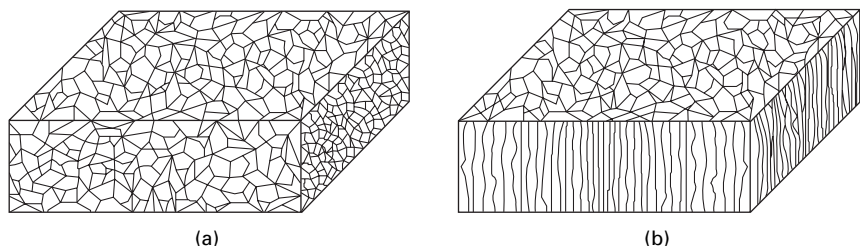
Compared to the conventional chromia- or alumina-forming coatings, nanocrystalline coatings exhibit an enhanced ability to fast-form chromia or alumina scales. Besides, nanocrystalline coatings have some unique advantages over conventional coatings. In particular, a nanocrystalline coating can be designed to have a composition similar to the metal matrix. This results in good compatibility of the coating with the matrix in its physical, chemical and mechanical parameters.

## 15.3 Oxidation-resistant nanocrystalline coatings

### 15.3.1 Selective formation of protective thermally grown oxides (TGO) scale

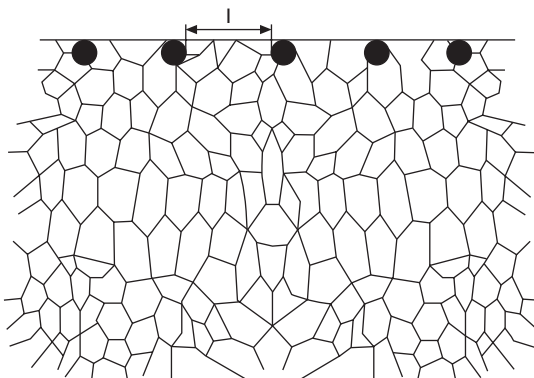
In recent years, much attention has been paid to the development of the oxidation-resistant coatings with a nano-grained structure.<sup>39-48</sup> Wang and co-workers found that many nanocrystallization coatings prepared using direct current magnetron sputtering exhibit a greatly enhanced oxidation/corrosion resistance, compared with conventional alloys with the same compositions.<sup>40,44,47,49</sup> The results suggest that oxidation resistance may be improved for many alloys through their surface nanocrystallization by various techniques.

Most investigators agree that the promotion of the selective formation of chromia or alumina scales is one of the primary reasons for the superior oxidation resistance of nanocrystalline coatings. So far, the intrinsic reason for the rapid formation of chromia or alumina scales during the initial oxidation stage has not been established experimentally. It is believed that the accelerated growth of chromia or alumina is mainly associated with the greatly enhanced diffusion of the corresponding oxide-forming component through the numerous grain boundaries in nanocrystalline coatings. Nanocrystalline coatings fabricated by different methods usually have different microstructures. Nanostructured coatings prepared using spraying, electrodeposition, etc., have a nano-grained structure in three dimensions, while nanostructured coatings produced by means of PVD methods like sputtering under certain controlled processing conditions<sup>5,29,39,47</sup> usually have a two-dimensional structure. That is, the planes normal to the deposition direction are composed of nanocrystals, whereas the planes parallel to the deposition direction consist of columnar crystals with a length over 100 nm. The two typical nano-coating structures are shown in Fig. 15.1.



15.1 The typical three-dimensional structure of nanocrystalline coatings: (a) consisting of nanocrystals in three dimensions; (b) consisting of nanocrystals in the plane normal to the coating growth direction and longer columnar grains in the plane along the growth direction.

Generally, the oxidation of alloys can be divided into two consecutive stages. They are the initial and transient stage (Stage I), in which a continuous layer of the most thermodynamically stable oxide is established, and the steady-state stage (Stage II), during which this oxide layer is thickened at a relatively low and constant oxidation rate. The initial and transient oxidation behaviour is crucial to the oxidation resistance of alloys. In most cases, the shorter the transient oxidation, the better the oxidation resistance of alloys. The initial and transient stage generally comprises four periods:<sup>50</sup> (1) adsorption of oxygen gas to the metal surface, (2) formation of individual oxide nuclei, (3) lateral growth to form a continuous oxide scale, and (4) growth of the oxide scale normal to the metal surface (the onset of Stage II). For the oxidation of nanocrystalline coatings, the numerous grain boundaries in the surface or near-surface zone would be the preferred sites for the nucleation of chromia or alumina, if they contain appropriate contents of chromium or/and aluminium. Consequently, the chromia or alumina nuclei have a close spacing with a mean value of  $l$ , as schematically shown in Fig. 15.2. The spacing is then easily filled by these oxides through their rapid lateral growth, because the abundant grain boundaries function as ‘short-circuit’ paths for the outward diffusion of chromium or/and aluminium from the interior of the coatings. As the oxide nuclei form a compact, continuous layer, the oxidation



15.2 Schematic showing numerous grain boundaries on the surface of nanocrystalline coatings probably functioning as the nucleation site of the desired oxides (filled circles), leading to a close inter-nuclei spacing with a mean value of  $l$ . The spacing is more easily filled by the same oxide through its rapid lateral growth, due to the fact that sufficient flux of the corresponding element to the oxidation front for the oxide growth can be supplied by the coating grain boundaries. (Note: the nucleation of non-protective oxides including the base-metal oxide is not considered here. These oxides initially formed will stop growing after the establishment of the desired protective scale, and then be engulfed by the thickened protective oxides and finally reduced from the scale-coating interface.)

rate is determined by the thickening rate of the oxide layer, which is dominated by the diffusion of cations and anions through the oxide layer.

As addressed above, a coating with excellent oxidation performance should exhibit a short initial and transient oxidation stage in which continuous chromia- or alumina-TGO scale can form. However, whether the initial and transient stage is short depends on the critical content of chromium or aluminium in the coating, below which less protective oxide scale forms. According to the classical Wagner theory,<sup>51</sup> external scale of chromia or alumina can be exclusively formed if the content of chromium or aluminium of an alloy reaches a critical value,  $N_m^*$ :

$$N_m^* = \left( \frac{\pi g^* N_O^S N_O D_O V_m}{2 \eta D_m V_{ox}} \right)^{1/2} \quad 15.1$$

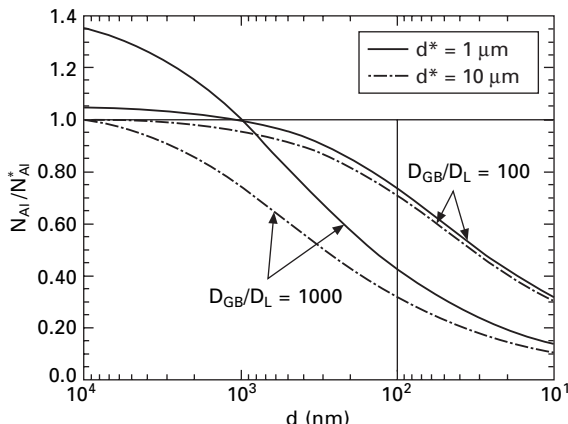
where  $g^*$  is a constant,  $N_O^S N_O$  are the concentrations of oxygen at the surface and in the alloy, respectively,  $\eta$  is a constant which is equal to  $y/x$  for the formed  $M_xO_y$ ,  $D_O$  and  $D_m$  are the diffusivities of oxygen and more active metal (chromium or aluminium in this case) in the alloy, and  $V_m$  and  $V_{ox}$  are molar volume of the alloy and the formed oxide (chromia or alumina), respectively. The concentration of chromium or aluminium should be not less than  $N_m^*$  for the formation of an external scale of the corresponding oxide. In the meantime, the increase of  $D_m$  will enable the decrease of the value for  $N_m^*$ . Actually, for a nanocrystalline coating,  $D_m$  can be substituted by an effective diffusion coefficient,  $D_{eff}$ , which is a summation of lattice diffusion ( $D_l$ ) and grain boundary diffusion ( $D_{gb}$ ) in the alloy:

$$D_{eff} = (1 - f)D_l + f D_{gb} \quad 15.2$$

where  $f$  is the area proportion of grain boundary. Assuming the alloy grains are cubic,  $f = 2\delta/d$  ( $\delta$  is the grain boundary width and  $d$  the grain size). Also, considering  $D_{gb} \gg D_l$ , Eq. (15.1) can be simplified as<sup>52</sup>

$$N^* = A \left( D_l + \frac{2\delta}{d} D_{gb} \right)^{-1/2} \quad 15.3$$

where  $A = (\pi g^* N_O D_O V_m / 2\eta V_{ox})^{1/2}$ . Thus, the smaller the grain size, the smaller value of  $N_m^*$  for the external scale formation is expected. Figure 15.3 shows the effect of the grain refinement on the ratio of the critical contents of Al ( $N_{Al}$ ) of finer-grained alumina-forming alloys to the critical value ( $N_{Al}^*$ ) of a reference alumina-forming alloy with grain size of 1  $\mu\text{m}$  and 10  $\mu\text{m}$ , respectively. It indicates that the critical content will be reduced by 30% if the grain size is reduced from 10  $\mu\text{m}$  to less than 10 nm when the grain boundary diffusivity of aluminium is 100 times larger than its lattice diffusivity, and by 70% when the grain boundary diffusivity is 1000 times larger. The theoretical calculation indicates that the grain refinement favours the selective

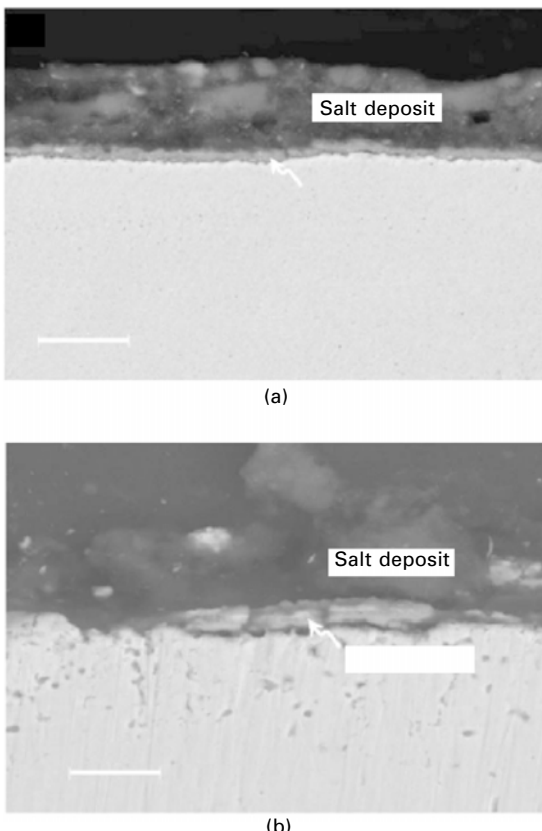


15.3 Dependence of the ratio of the critical aluminium contents ( $N_{Al}^*$ ) of an alumina-forming alloy to the critical value ( $N_{Al}^*$ ) of a reference alloy with grain size of 1  $\mu m$  and 10  $\mu m$ , respectively, on the decrease of the grain size,  $d$ . (Reprinted from reference [52] with permission from Elsevier.)

oxidation of chromium or aluminium to form a protective layer by reducing their critical content. This effect is more remarkable when the crystalline grains of coatings are in the nanometre range.

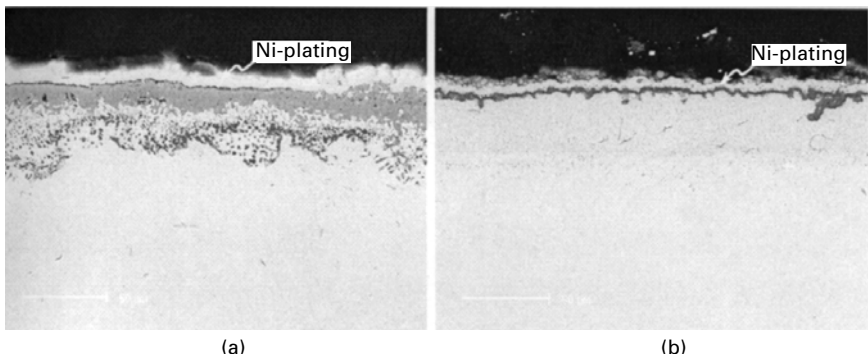
Currently, publications on the study of initial stage oxidation of nanocrystalline coatings are still lacking. However, effort to explore the theoretical and experimental evidence related to the promoted formation of protective scales on nanocrystalline coatings is in progress by the researchers in the authors' group. Recently, hot corrosion under molten  $Na_2SO_4-K_2SO_4-NaCl$  of a novel Ni-11Cr nanocomposite (by weight percentage) consisting of nanocrystalline Ni matrix and dispersed Cr nanoparticles was investigated, and compared to the arc-melted coarse-grained alloy with a higher Cr content (20 wt%).<sup>53</sup> It shows that the nanocomposite exhibited an excellent corrosion resistance because of the exclusive formation of an external chromia scale during a very short initial and transient stage (Fig. 15.4a), while during the same period no chromia scale was developed on the alloy counterpart, causing it to suffer a severe internal attack of sulfur-containing agents (Fig. 15.4b). The authors<sup>53</sup> proposed that the dispersed Cr nanoparticles, together with abundant Ni grain boundaries, provide sufficient sites for the nucleation and growth of chromia, which is crucial for the accelerated formation of a continuous chromia scale on the nanocomposite.

That nanocrystalline coatings promote the formation of protective scale is also supported by the indirect but credible results which show the exclusive formation of an external scale of chromia or alumina during various periods of oxidation.<sup>29–34,39–42</sup> Otherwise, the less protective oxides would be seen in



15.4 Cross-sectional morphologies of (a) the Ni-11Cr nanocomposite and (b) the arc-melted Ni-20Cr alloy after 30 min corrosion in air at 700°C under molten  $\text{Na}_2\text{SO}_4$ - $\text{K}_2\text{SO}_4$ - $\text{NaCl}$ . (Reprinted from reference [53] with permission from The Electrochemical Society.)

the scales. The promoted formation of protective scales can also be assumed by comparing the oxidation of cast nickel-base K52 alloy containing 21.8 wt% Cr and 2.9 wt% Al, and its corresponding sputtered nanocrystalline coating. Figure 15.5a shows the cross-section of the cast K52 after 100 h oxidation in air at 1000°C. The alloy formed an external chromia scale, below which internal oxidation of alumina occurred. In contrast, after the nanocrystallization of the alloy using the magnetron sputtering method, it only grew an extremely thin external scale of alumina in the same oxidation condition, as seen in Fig. 15.5b. The result clearly demonstrates that the nanocrystallization of some alloys may convert them from chromia formers into alumina formers, through profoundly reducing the critical content of aluminium for the formation of a continuous scale of its oxide. This consequently slows down the oxidation rate.



15.5 Cross-sectional morphologies of (a) cast K52 and (b) its corresponding sputtered nanocoating after 100 h oxidation in air at 1000°C.

The beneficial effect of the grain refinement on oxidation is correlated with the fact that the fine-grained structure favours the rapid selective formation of chromia or alumina scale. If a fine- or nano-grained alloy contains a very low content of chromium or/and aluminium, a protective scale of chromia or alumina cannot form. As a result, the oxidation rate is increased in reference to the conventionally coarse-grained counterpart with the similar composition.<sup>54–56</sup> This is because the non-protective scales formed on the fine-grained metals are finer-grained, leading to the diffusion-controlled scaling rate faster than that of the coarse-grained counterparts. This is also the reason that the grain refinement causes a faster oxidation rate of pure Fe and Ni.<sup>57,58</sup> On the contrary, if an alloy contains an appropriate content of chromium or aluminium (which should be lower than the values of conventional chromia- or alumina-formers), the grain-refining treatment probably causes the selective oxidation of chromium or aluminium. Therefore, for designing a nanocrystalline coating with ideal oxidation behaviour, optimization of composition is also a considerable factor.

### 15.3.2 Steady-state growth of protective thermally grown oxide scale

No sooner has the continuous scale of chromia or alumina become established than the steady-state growth of this oxide starts. For the constant, steady-state growth of the protective scale established, the nanocrystalline coatings should have the capability to continuously supply the flux of chromium or aluminium to the oxide/coating interface for balancing the consumption of the corresponding constituent by the scale growth. Assuming that the coating is single-phase, during oxidation the scale/coating interface is ‘stationary’, and the concentration profile of chromium or aluminium in the diffusion

zone below scale is linear, the minimum limit ( $N_m^{**}$ ) of chromium or aluminium for the exclusively growth of the corresponding oxide scale can, according to Wagner's treatment,<sup>59</sup> be given by

$$N_m^{**} = \frac{2V_m}{V_{ox}} \left( \frac{k_c}{D_m} \right)^{1/2} \quad 15.4$$

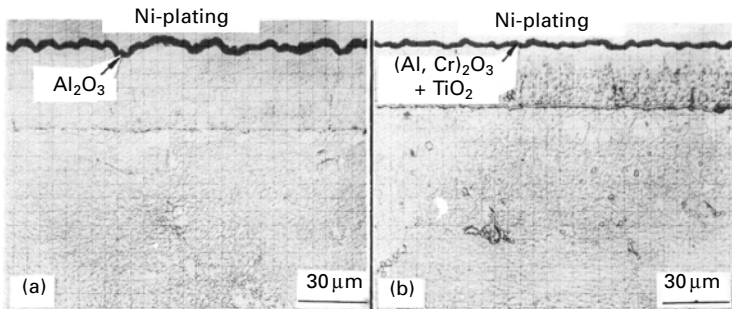
where  $k_c$  is the parabolic rate constant for the scale growth in terms of thickness. Gesmundo and Gleeson<sup>60</sup> further extended the treatment to the oxidation of two-phase alloys, where the second phase functions as a 'reservoir' for providing the amount of relative components needed for the stable growth of their corresponding oxide scales. In this case, Eq. (15.4) can be modified using

$$[N_m (2N_m^{**} - N_m)]^{1/2} = \frac{2V_m}{V_{ox}} \left( \frac{k_c}{D_m} \right)^{1/2} \quad 15.5$$

where  $N_m$  is the molar fraction of the oxide-forming element in the coating matrix. Most nanocrystalline coatings fabricated by PVD methods<sup>38–44,47–49</sup> or electrodeposition<sup>53,61–65</sup> are single- or two-phase coatings. Similarly,  $D_m$  in Eqs (15.3) and (15.4) can be expressed using  $D_{eff}$  (see Eq. (15.2)). Therefore, if the nano-grains of coatings are not significantly coarsened,  $D_{eff}$  may maintain a value which is high enough to support the steady-state growth of the protective scale, even though the coating possesses a content of chromium or aluminium lower than that of the corresponding element in the conventionally coarse-grained alloys. Although the thermal stability of nanocrystalline coatings has not so far been systematically investigated, it is assumed that they would remain an ultra-fine grained structure (<1 µm) because the coarsening kinetics would be restricted by the segregation of impurities and the precipitated phases during oxidation. For example, Lou *et al.*<sup>66</sup> found that after 100 h oxidation in air at 1000°C, the grains of the sputtered K38G nanocrystalline coating (containing ~14.8 wt% Cr and ~3.5 wt% Al) were coarsened but still ultrafine-grained, from 20–100 nm to 200–1000 nm. After the removal of the alumina scale formed, the ultrafine-grained coating continued to oxidize at this temperature for 500 h, and still grew a protective alumina scale similar to that formed on the nanograined coating without the pre-oxidation treatment. The comparative result is shown in Fig. 15.6, suggesting that if the alumina scale formed on the K38G nanocoating were exfoliated, a new alumina scale would re-form because the coarsened but ultrafine-grained coating still favours the rapid formation of the alumina scale.

### 15.3.3 Enhancement of scale adhesion

For an alloy or a coating with an ideal oxidation resistance, the TGO scale formed should not only grow slowly but also adhere well to the metal



15.6 Cross-sections of the K38G nanocrystalline coatings after 500 h oxidation in air at 1000°C: (a) without pre-oxidation treatment; (b) removal of the scale formed during the pre-oxidation treatment in air at 1000°C for 100 h [66].

substrate. Chromia or alumina scales usually experience heavy spallation during cooling from high temperatures. Once the scale exfoliates, the accelerated recession of metals will appear in the next oxidation cycles.

It is generally acknowledged that scale spallation is attributed to the synergistic effect of the stress build-up and release in the scale, and the intrinsic scale adhesion to the underlying metal. During oxidation, growth stress is developed in TGO scales due to a change in volume as the metal is converted into oxide, expressed by the Pilling–Bedworth ratio (PBR), whereas thermal stress is generated during heating and cooling due to the mismatched coefficients of thermal expansion (CTE) between the oxide and the metal substrate. The thermal stress is normally larger than the growth stress.  $\sigma_{ox}$  gives the equation for the thermal stress:<sup>67</sup>

$$\sigma_{ox} = \frac{E_{ox} \Delta T (\alpha_{ox} - \alpha_m)}{1 + 2 \left( \frac{E_{ox} t_{ox}}{E_\mu \xi_m} \right)} \quad 15.6$$

where  $E$  is the elastic modulus,  $\alpha$  is the coefficient of thermal expansion,  $\xi$  is the thickness, and the subscripts  $ox$  and  $m$  refer to the oxide and metal substrate, respectively. The stress level in the scale is a complex summation of the growth stress, thermal stress and stress relaxation. If the scale stress (usually compressive) is very large and its relaxation through creep is not adequate, scale damage takes place. Through-thickness cracking usually occurs in the scale–metal system where the interface adhesion is stronger than the cohesion within the scale (strong interface/weak oxide mode).<sup>68</sup> However, in many cases, the scale interface is not intrinsically strong, and is frequently weakened by void formation or segregation of trace elements such as sulphur (weak interface/strong oxide mode).<sup>68</sup> In this mode, spallation occurs as a result of progressive scale decohesion and bulking.

Schütze<sup>69</sup> gives an approach describing the critical strain ( $\varepsilon_c^i$ ) for the onset of decohesion of a more realistic interface, including interfacial roughness and the role of the physical defects. The equation is given by

$$\varepsilon_c^i = \frac{K_{IC}}{f \sqrt{\pi c_g}} \frac{\left(1 + \frac{r}{\xi}\right)(1 + \nu)}{E_{ox}} \quad 15.7$$

where  $K_{IC}$  is the interface fracture toughness,  $f$  a geometrical factor ( $\approx 1$ ),  $c_g$  half the length of the interfacial physical defect,  $r$  the roughness of interface height,  $\xi$  the scale thickness and  $\nu$  the Poisson ratio. During the growth of oxide scale, cation vacancies condense at the interface of scale and metal, normally forming interfacial cavities of various size. The growth of interfacial cavities can be stabilized by the segregated sulphur.<sup>70</sup> This, as can be seen from Eq. (15.7), will increase  $c_g$  and decrease  $\varepsilon_c^i$ .

It has been extensively reported that adding a small amount of rare earth or reactive elements such as Y, Ce or La (or their oxides) can greatly enhance the adhesion of TGO scales to metals. This phenomenon is referred to as the ‘reactive element effect (REE)’.<sup>71–73</sup> The following methods of improving scale adhesion using the REE have been proposed: (1) ‘pegging’ the scale to the underlying metal; (2) preventing coalescence of the vacancies at the interface; and (3) eliminating dissociated sulphur at the interface. These will increase  $r$  and decrease  $c_g$  and consequently increase  $\varepsilon_c^i$  (see Eq. (15.7)).

Generally, TGO scales formed on nanocrystalline coatings exhibit increased adhesion. The reasons can be summarized as follows. First, the nanocrystalline coating may form a scale with a lower thermal stress by decreasing the mismatch of the CTEs between the oxide and the coating. As there are numerous nucleating sites for the nanocoatings from the onset of oxidation (Fig. 15.2), the grain size of the oxide scale formed is much finer than that on the as-cast alloy.<sup>29</sup> The finer-grained oxide scale normally has a larger thermal expansion coefficient, because of the existence of numerous grain boundaries with a larger thermal expansion coefficient (about 2.5–5 times) than the crystal.<sup>74</sup> This naturally leads to a thermal stress lower than that in the scales on conventional alloys (Eq. (15.6)).

Second, it is easier to relax the scale stresses of the nanocrystalline coatings. According to the diffusional-creep theory, the deformation rate,  $\dot{\varepsilon}$ , of a polycrystalline material at a temperature at which grain-boundary diffusion predominates can be given as<sup>75</sup>

$$\dot{\varepsilon} = \frac{B\sigma\Omega\delta D_{gb}}{d^3KT} \quad 15.8$$

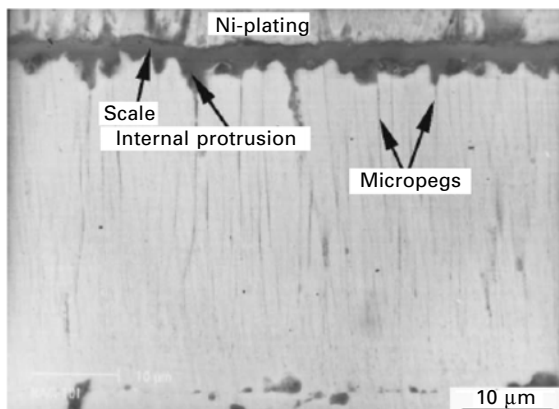
where  $B$  is a constant,  $\Omega$  the atomic volume,  $d$  the average crystal size,  $D_{gb}$  the grain boundary diffusivity,  $\delta$  the thickness of the boundary,  $K$  Boltzmann’s

constant and  $T$  the absolute temperature (K). The finer-grained oxides, together with the fine-grained coatings, can partially release the scale stresses generated during oxidation and cooling, through plastic formation such as diffusional creep, leading to a stress level in the scale below the limit at which scale decohesion occurs.

Third, the nanocrystalline coating can form a scale with an increased adhesion due to the formation of interfacial ‘oxide micropegs’. The sputtered nanocrystalline coatings usually exhibit a typical columnar microstructure in the plane normal to the deposition direction (Fig. 15.1b). The columnar boundaries act as ‘easy passages’ for oxygen when oxidation starts, leading to the formation of inward protrusions or micropegs along many columnar grain boundaries.<sup>29,39,44</sup> One example is presented in Fig. 15.7, where the internal protrusions or pegs are clearly seen in the nanocrystallized NiAl after 100 h cyclic oxidation in air at 1000°C.<sup>44</sup> The internal oxides can ‘peg’ the scale into the coating substrate.

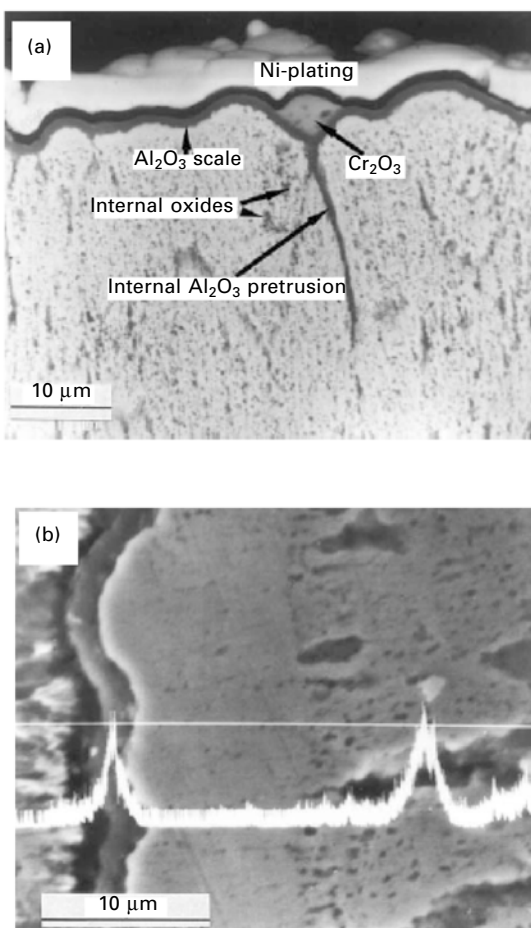
Fourth, the nanocrystalline coating may minimize the number of cation vacancies condensed at the scale–metal interface. Interfacial cavities usually form as a result of the condensation of cation vacancies during oxidation. When the cavity grows in size to reach a critical value, scale decohesion can occur (Eq. (15.7)). The nanocrystalline coatings, together with the fine-grained oxide scales, provide numerous additional grain boundaries to accommodate the vacancies, decreasing the number of vacancies annihilated at the interface area.

Fifth, the nanocrystalline coating may reduce the detrimental effect of sulphur on oxidation. In the 1980s a theory called the ‘sulphur effect’ was used to explain all questions regarding scale adhesion and the REE.<sup>76,77</sup>



15.7 Cross-section of NiAl nanocrystalline coating after 100 cycles oxidation in air at 1000°C. (Reprinted from reference [44] with permission from Elsevier.)

According to the theory, the bond between the oxide scale and the metal is basically strong. Sulphur, as a common impurity in metals, typically 1–10 ppm, segregates to the interface between the oxide scale and the metal, and weakens the interfacial bond. Reactive elements, having a strong affinity for sulphur, react with the sulphur and therefore prevent it from segregating to the interface.<sup>73</sup> However, Yang and Wang's recent work<sup>78</sup> shows that during 100 h cyclic oxidation at 1000°C in air, the scale (mainly alumina) formed on a cast Fe-25Cr-5Al-1S alloy (wt%) suffered heavy spallation, whereas the scale on the sputtered nanocrystalline coating with the same composition maintained good adhesion (see Fig. 15.8a). Line scanning of a sulphur X-ray



15.8 (a) Cross-section of the Fe-Cr-Al-1S nanocrystalline coating after 100 cycles oxidation in air at 1000°C, showing the good attachment of the scale to the coating; (b) the corresponding S X-ray line scanning across the section [78].

across the scale on the nanocoating reveals that sulphur was enriched in the scale (not the interface), as shown in Fig. 15.8b. This implies that the ‘sulphur effect’ on oxidation can be insignificant if the alloy has a nanocrystalline structure. The reason has not been explored in detail by the authors, but one reason might be that the numerous grain boundaries in the fine-grained scale and the coating are more preferred sites for sulphur segregation than the scale–metal interface. The minimized interfacial segregation will enhance the resistance to scale decohesion.

In addition, some nanocoatings with a specified composition have oxidation performance different in other ways from that of their conventionally coarse-grained alloy counterparts with the same composition. For example, it has been reported that there is a long period of typical phase transformation of the TGO alumina during the oxidation of NiAl intermetallics at 1000°C or below, from metastable  $\gamma$  and  $\theta$  to the most stable  $\alpha$ .<sup>79–81</sup> In contrast, the phase transformation is greatly promoted on the sputtered NiAl nanocrystalline coating.<sup>81</sup> The result suggests that the alloy nanocrystallization promotes the nucleation and growth of the most stable oxide. This is consistent with the observation that the alumina scale is more likely to form than the chromia scale on the nanocrystallized superalloys (see Fig. 15.5).

## 15.4 Concluding remarks

Based on our knowledge of the oxidation of nanocrystalline coatings, their excellent oxidation resistance primarily lies in two aspects: (1) fast formation of an external scale of chromia and/or alumina as a result of the existence of abundant grain boundaries, which function as the sites for nucleating chromia and alumina from the onset of oxidation, and thereafter provide sufficient flux of chromium or aluminium to the oxide–coating interface for the rapid lateral growth of these oxide nuclei to form a continuous layer; and (2) increased scale adhesion to the substrate, due to the modified mechanism for the relaxation of the scale stresses generated during oxidation and cooling, as well as to the retardation or prevention of vacancy condensation, or sulphur segregation at the scale–coating interface. Therefore, the oxidation resistance of some alloys may be greatly increased by nanocrystallization, without the necessity of increasing the content of chromium or/and aluminium in the alloys.

The service lifetime of a thin coating is controlled not only by oxidation but also by diffusion of the protective scale-forming element into the substrate. Although the coating may be oxidation resistant initially, it may not be able to form a continuous surface oxide layer during long-term exposure if the element content drops below a critical level. In this case, breakaway oxidation due to formation of non-protective oxides and significant internal oxidation attack may occur. Because it has a composition similar to the underlying

metal, the interdiffusion between the surface nanocrystallized layer (or nanostructured coatings such as those prepared by magnetron sputtering) and the substrate can be completely prevented. This is one of the main advantages of nanocrystalline coatings for high temperature applications.

## 15.5 Acknowledgements

We acknowledge financial support from the National Science Foundation of China (NSFC) project under Grant Nos 50571108 and 50671115.

## 15.6 References

1. Gleiter H, 'Nanocrystalline materials', *Prog Mater Sci*, 1989, 33, 223–315
2. Lu K, 'Nanocrystalline metals crystallized from amorphous solid: nanocrystallization, structure, and properties', *Mater Sci Eng*, 1996, R16, 161–221
3. Suryanarayana C, 'Nanocrystalline materials', *Int Mater Rev*, 1995, 44, 41–64
4. Gleiter H, 'Nanostructured materials: Basic concepts and microstructure', *Acta Mater*, 2000, 48(1), 1–29
5. Tjong S C, Chen H, 'Nanocrystalline materials and coatings', *Mater Sci Eng*, 2004, R45, 1–88
6. Rawers J, Slavens G, Krabbe P, 'Hot-press consolidation and tensile strength characterization of mechanically alloyed nanostructured Fe-Al and Fe-C powder', *Nanostruct Mater*, 1997, 9(1–8), 197–200
7. Liang G, Meng Q, Li Z, Wang E, 'Consolidation of nanocrystalline Al-Ti alloy powders synthesized by mechanical alloying', *Nanostruct Mater*, 1995, 5(6), 673–678
8. Haji-Mahmood M S, Chumbley L S, 'Processing and characterization of nanocrystalline molybdenum disilicide consolidated by hot isostatic pressing (HIP)', *Nanostruct Mater*, 1996, 7(1–2), 95–112
9. Lillo T M, Korth G E, 'Consolidation of nanocrystalline Fe-1.6 wt% C via low temperature hot isostatic pressing', *Nanostruct Mater*, 1998, 10(1), 35–43
10. Valiev R Z, Islamgaliev R K, Alexandrov I V, 'Bulk nanostructured materials from severe plastic deformation', *Prog Mater Sci*, 2000, 45(2), 103–189
11. Tao N, Wang Z, Tong W, Sui M, Lu J, Lu K, 'An investigation of surface nanocrystallization mechanism in Fe induced by surface mechanical attrition treatment', *Acta Mater*, 2002, 50(18), 4603–4616
12. Umemoto M, 'Nanocrystallization of steels by severe plastic deformation', *Mater Trans*, 2003, 44(10), 1900–1911
13. Liu G, Lu J, Lu K, 'Surface nanocrystallization of 316 L stainless steel induced by ultrasonic shot peening', *Mater Sci Eng*, 2000, 286(1), 91–95
14. Liu Y, Xiong T, Yang K, 'Thermal stability of 40Cr steel with surface nanocrystallization', *Mater Sci Forum*, 2006, 510–511, 434–437
15. Fan X, Zhou B, Zhu L, Wang H, Huang J, 'Surface nanocrystallization of low carbon steel induced by circulation rolling plastic deformation', 5th Pacific Rim Int Conf Advanced Materials and Processing, Parts 1–5, *Mater Sci Forum*, 2005, 475–479, 133–136
16. Hauert R, Patscheider J, 'From alloying to nanocomposites – improved performance of hard coatings', *Adv Eng Mater*, 2000, 2(5), 247–259

17. Mayrhofer P H, Mitterer C, Musil J, 'Structure–property relationships in single- and dual-phase nanocrystalline hard coatings', *Surf Coat Technol*, 2003, 174, 725–731
18. Veprek S, Haussmann M, Reiprich S, Shizhi L, Dian J, 'Novel thermodynamically stable and oxidation resistant superhard coating materials', *Surf Coat Technol*, 1996, 86(1–3), 394–401
19. Amaral M, Mohasseb F, Oliveira F J, Benedic F, Silva R F, Gicquel A, 'Nanocrystalline diamond coating of silicon nitride ceramics by microwave plasma-assisted CVD', *Thin Solid Films*, 2005, 482(1–2), 232–236
20. Lau M L, Strock E, Fabel A, Lavernia C J, Lavernia E J, 'Synthesis and characterization of nanocrystalline Co-Cr coatings by plasma spraying', *Nanostruct Mater*, 1998, 10(5), 723–730
21. Stover D, Pracht G, Lehmann H, Dietrich M, Doring J E, Vassen R, 'New material concepts for the next generation of plasma-sprayed thermal barrier coatings', *J Therm Spray Technol*, 2004, 13(1), 76–83
22. Tellkamp V L, Lau M L, Fabel A, Lavernia E J, 'Thermal spraying of nanocrystalline Inconel 718', *Nanostruct Mater*, 1997, 9(1–8), 489–492
23. He J, Schoenung J M, 'Nanostructured coatings', *Mater Sci Eng*, A, 2002, 336, 274–319
24. Picas J A, Forn A, Igartua A, Mendoza G, 'Mechanical and tribological properties of high velocity oxy-fuel thermal sprayed nanocrystalline CrC-NiCr coatings', *Surf Coat Technol*, 2003, 174(9/10), 1095–1100
25. Fitzer E, Maurer H J, *Materials and Coatings to Resist High Temperature Corrosion* (ed. Holmes D R, Rahmel A), London, Applied Science, 1978, 253
26. Restall J E, Malik M, Singheiser L, *Proceedings of High Temperature Alloys for Gas Turbines and Other Applications* (ed. Betz W), Dordrecht, D. Reidel Publishing, 1986, 357
27. Nicholls J R, Simms N J, Chan W Y, Evans H E, 'Smart overlay coatings – concept and practice', *Surf Coat Technol*, 2002, 149(2–3), 236–244
28. Nicholls J R, Hancock P, Al Yasiri L H, 'Optimising oxidation resistance of MCrAl coating systems using vapour phase alloy design', *Mater Sci Technol*, 1989, 5, 799–805
29. Wang F, Lou H, Zhu S, Wu W, 'The mechanism of scale adhesion on sputtered microcrystallized CoCrAl films', *Oxid Met*, 1996, 45(1–2), 39–51
30. Liu Z, Gao W, Dahm K L, Wang F, 'Oxidation behaviour of sputter-deposited Ni-Cr-Al micro-crystalline coatings', *Acta Mater*, 1998, 46(5), 1691–1700
31. Waki H, Kobayashi A, 'Development of lateral compression method of circular tube thin coating for mechanical properties of plasma sprayed CoNiCrAlY', *Mater Trans*, 2006, 47(7), 1626–1630
32. Brandl W, Toma D, Kruger J, Grabke H J, Matthaus G, 'The oxidation behaviour of HVOF thermal-sprayed MCrAlY coatings', *Surf Coat Technol*, 1997, 94–5(1–3), 21–26
33. Li C J, Li W Y, 'Effect of sprayed powder particle size on the oxidation behavior of MCrAlY materials during high velocity oxygen-fuel deposition', *Surf Coat Technol*, 2003, 162(1), 31–41
34. Hirose A, Kotani H, Kobayashik K, 'Surface modification by laser cladding of Ni-Cr-Al-Y alloy', *J. Iron Steel Inst Jpn*, 1993, 79(1), 105–112
35. Giggins C S, Pettit F S, 'Oxidation of Ni-Cr alloys between 800°C and 1200°C', *Trans. TMS-AIME*, 1969, 245, 2495–2507
36. Giggins C S, Pettit F S, 'The effect of alloy grain-size and surface deformation on the

- selective oxidation of chromium in Ni-Cr alloys at temperatures of 900°C and 1100°C', *Trans. TMS-AIME*, 1969, 245, 2509–2514
37. Merz M D, 'The oxidation resistance of fine-grained sputter-deposited 304 stainless steel', *Metall Trans A*, 1979, 10, 71–77
  38. Wang F, Lou H, 'Oxidation behaviour and scale morphology of normal-grained CoCrAl alloy and its sputtered microcrystalline coating', *Mater Sci Eng*, 1990, A43, 279–285
  39. Wang F, 'Oxidation resistance of sputtered Ni-3(AlCr) nanocrystalline coating', *Oxid Met*, 1997, 47(3/4), 247–258
  40. Wang F, Young D J, 'Effect of nanocrystallization on the corrosion resistance of K38G superalloy in CO + CO<sub>2</sub> atmospheres', *Oxid Met*, 1997, 48(5/6), 497–509
  41. Chen G, Lou H, 'Oxidation behavior of a sputtered Ni-5Cr-5Al nanocrystalline coating', *Oxid Met*, 1997, 53(5/6), 467–479
  42. Liu Z, Gao W, Dahm K L, Wang F, 'The effect of coating grain size on the selective oxidation behaviour of Ni-Cr-Al alloy', *Scripta Mater*, 37 (1997) 1551–1558
  43. Strauss D, Muller G, Schumacher G, Engelko V, Stamm W, Clemens D, Quadakkers W J, 'Oxide scale growth on MCrAlY bond coatings after pulsed electron beam treatment and deposition of EBPVD-TBC', *Surf Coat Technol*, 2001, 135(2–3), 196–201
  44. Yang S, Wang F, Sun Z, Zhu S, 'Influence of columnar microstructure of a sputtered NiAl coating on its oxidation behavior at 1000°C', *Intermetallics*, 2002, 10(5), 467–471
  45. Ajdelsztajn L, Picas J A, Kim G E, Bastian F L, Schoenung J, Provenzano V, 'Oxidation behavior of HVOF sprayed nanocrystalline NiCrAlY powder', *Mater Sci Eng A*, 2002, 338(1–2), 33–43
  46. Mrowec S, 'New generation of nanocrystalline coating materials resistant to high temperature corrosion', *High Temp Mater Proc*, 2003, 22(1), 1–24
  47. Peng X, Yan J, Zhou Y, Wang F, 'Effect of grain refinement on the resistance of 304 stainless steel to breakaway oxidation in wet air', *Acta Mater*, 2005, 53(19), 5079–5088
  48. Khanna A, Bhat D G, 'Nanocrystalline gamma alumina coatings by inverted cylindrical magnetron sputtering', *Surf Coat Technol*, 2006, 201(1–2), 168–173
  49. Wang F, Geng S, Zhu S, 'Corrosion behavior of a sputtered K38G nanocrystalline coating with a solid NaCl deposit in wet oxygen at 600 to 700°C', *Oxid Met*, 2002, 58(1–2), 185–195
  50. Kofstad P, *High Temperature Corrosion*, London, Elsiver Applied Science, 1988
  51. Wagner C, 'Reaktionstypen bei der oxydation von legierungen', *Z Elektrochem*, 1959, 63(7), 772–782
  52. Peng X, Wang F, 'Morphologic investigation and growth of the alumina scale on magnetron-sputtered CoCrAl nanocoatings with and without yttrium', *Corros Sci*, 2003, 45, 2293–2306
  53. Zhang C, Peng X, Zhao J, Wang F, 'Hot corrosion of an electrodeposited Ni-11 wt%Cr nanocomposite under molten Na<sub>2</sub>SO<sub>4</sub>-K<sub>2</sub>SO<sub>4</sub>-NaCl', *J Electrochem Soc*, 2005, 152, B321–B326
  54. Singh Raman R K, Khanna A S, Tiwari R K, Gnanamoorttys J B, 'Influence of grain size on the oxidation resistance of 2.25Cr-1Mo steel', *Oxid Met*, 1992, 37(1–2), 1–12
  55. Singh Raman R K, Gnanamoorttys J B, 'Influence of prior-austenite grain size on oxidation behavior of 9Cr-1Mo steel', *Oxid Met*, 1992, 38(5–6), 483–496

56. Singh Raman R K, Gnanamoorttys J B, Roy S K, 'Synergistic influence of alloy grain size and silicon content on oxidation behavior of 9Cr-1Mo steel', *Oxid Met*, 1994, 42(5–6), 335–355
57. Caplan D, Cohen M, 'Effect of cold work on the oxidation of iron from 400°C to 600°C', *Corros Sci*, 1966, 6(7), 321–335
58. Caplan D, Graham M J, Cohen M, 'Effect of cold work on oxidation of nickel at high temperature', *J Electrochem Soc*, 1972, 119(9), 1205–1215
59. Wagner C, 'Theoretical analysis of the diffusion processes determining the oxidation rate of alloys', *J Electrochem Soc*, 1952, 99, 369–380
60. Gesmundo F, Gleeson B, 'Oxidation of multicomponent two-phase alloys', *Oxid Met*, 1995, 44(1–2), 211–237
61. Peng X, Zhou Y, Zhang Y, Wang F, 'On the development and the oxidation of novel Ni-Cr and Ni-Al nanocoatings by composite electrodeposition', *MaterSci Forum*, 2004, 461–464, 409–416
62. Zhou Y, Peng X, Wang F, 'Oxidation of a novel electrodeposited Ni-Alnanocomposite film at 1050°C', *Scripta Mater*, 2004, 50(12), 1429–1433
63. Zhang Y, Peng X, Wang F, 'Development and oxidation at 800°C of a novel electrodeposited Ni-Cr nanocomposite film', *Mater Lett*, 2004, 58(6), 1134–1138
64. Yang X, Peng X, Wang F, 'Hot corrosion of a novel electrodeposited Ni-6Cr-7Al nanocomposite under molten (0.9Na, 0.1K)<sub>2</sub>SO<sub>4</sub> at 900°C', *Scripta Mater*, 2007, 56, 891–894
65. Peng X, Yang X, Zhang Y, Zhou Y, Wang F, 'Novel high-temperature oxidation-resistant nanocomposites developed by nanocomposite electrodeposition', *Mater Sci Forum*, 2007, 539–543, 1188–1195
66. Lou H, Zhu S, Wang F, 'Rehealing ability of oxide scales formed on microcrystalline K38G coatings', *Oxid Met*, 1995, 43(3–4), 317–328
67. Huntz A M, 'Stresses in NiO, Cr<sub>2</sub>O<sub>3</sub> and Al<sub>2</sub>O<sub>3</sub> oxide scales', *Mater Sci Eng*, 1995, A201, 211–228
68. Evans H E, 'Effects in high-temperature oxidation of metals', *Int Mater Rev*, 1995, 40(1), 1–40
69. Schütze M, *High Temperature Corrosion of Advanced Materials and Protective Coatings* (ed. Saito Y), Amsterdam, North-Holland, 1992
70. Grabke H J, Wiemer D, Viefhaus H, 'Segregation of sulfur during growth of oxide scales', *Appl Surf Sci*, 1991, 47, 243–250
71. Lang E, *The Role of Active Elements in the Oxidation Behavior of High Temperature Metals and Alloys*, Elsevier Applied Science, Belfast: printed in Northern Ireland at the University Press Ltd, 1989
72. Moon D P, 'Role of reactive elements in alloy protection', *Mater Sci Technol*, 1989, 5, 754–764
73. Hou P Y, Stringer J, 'The effect of reactive element additions on the selective oxidation, growth and adhesion of chromia scales', *Mater Sci Eng A*, 1995, 202, 1–10
74. Klam H J, Hahn H, Gleiter H, 'The thermal expansion of grain boundaries', *Acta Metall*, 1978, 35, 2101–2104
75. Karch J, Briant R C, Gleiter H, 'Ceramics ductile at low temperature', *Nature*, 1987, 330, 556–558
76. Smeguil J G, Funkenbusch A W, Bornstein N S, 'A relationship between indigenous impurity elements and protective oxide scale adherence characteristics', *Metall Trans*, 1986, A17, 923–932

77. Lees D G, 'On the reasons for the effects of dispersions of stable oxides and additions of reactive elements on the adhesion and growth-mechanisms of chromia and alumina scales – the “sulfur effect”', *Oxid Met*, 1987, 27(1–2), 75–81
78. Yang S, Wang F, 'Effect of nanocrystallization on sulfur segregation in Fe-Cr-Al alloy during oxidation at 1000°C', *Oxid Met*, 2006, 65(3–4), 195–205
79. Schumann E, 'The effect of Y-ion implantation on the oxidation of  $\beta$ -NiAl', *Oxid Met*, 2006, 43(1–2), 157–172
80. Yang J C, Schumann E, Levin I, Rühle M, 'Transient oxidation of NiAl', *Acta Mater*, 1998, 46(6), 2195–2210
81. Yang S, Wang F, Niu Y, Wu W, 'Isothermal oxidation of  $\beta$ -NiAl alloys and sputtered coating at 1000°C in air', *Mater Sci Forum*, 2001, 369–372, 361–368

H XU, H GUO and S GONG, Beijing University of Aeronautics and Astronautics, China

## 16.1 Introduction

Thermal barrier coatings (TBCs) made of low thermal conductivity ceramics have seen increasing application in gas turbine engines to provide thermal insulation to metallic components from hot gas in the engines used for aircraft propulsion, power generation, and marine propulsion [1–5]. The use of TBCs, along with internal cooling of the underlying superalloy components, provides a temperature reduction of up to 300 K in the surface of the superalloy component. This enables engines to operate at temperatures above the melting temperature of the superalloy, thereby improving the energy efficiency and performance of engines. On the other hand, TBCs contribute to reducing metal temperature, thus improving the duration capability of components.

Usually, a TBC system has a four-layered structure: the ceramic thermal barrier layer, the metallic bond coat layer, a thermally grown oxide (TGO) layer between the topcoat and bond coat, and substrate. Each layer has its own specific physical and chemical properties, which provide the required functions in TBC.

The ceramic thermal barrier layer provides thermal protection to the underlying materials. Also, this layer works as a shield to protect the underlying metallic parts from erosion and corrosion. The metallic bond coat is to protect the underlying superalloy substrate from oxidation, balance thermal mismatch between the topcoat and substrate, and prevent interdiffusion of elements in the substrate and bond coat.

The operating temperature for the bond coat often exceeds 1273 K. Due to oxidation of bond coat, a TGO layer is inevitably formed. The phase constituents of the TGO depend on the operating temperature, the thermal exposure time and the composition of the bond coat. In the initial stage, accompanying outward diffusion of elements from the bond coat and inward diffusion of oxygen from hot gas, the formation of TGO is dominated by a combined mechanism with external oxidation and internal oxidation. The TGO mainly consists of spinel phases, such as  $\text{NiAlO}_2$  and  $\text{NiCrO}_2$ , which are, however,

thermodynamically unstable and detrimental to oxidation resistance [6,7]. Subsequently, the growth of TGO is mainly governed by internal oxidation. As a result of selective oxidation, an  $\alpha\text{-Al}_2\text{O}_3$  is formed, replacing those spinel phases. In some cases, new spinel phases appear again after long-term thermal exposure when a continuous  $\alpha\text{-Al}_2\text{O}_3$  layer could not be maintained due to Al depletion in the bond coat. A continuous, defect-free TGO comprising  $\alpha\text{-Al}_2\text{O}_3$  is desirable to TBC, because  $\alpha\text{-Al}_2\text{O}_3$  has a very low oxygen ionic diffusivity and provides an excellent diffusion barrier, retarding further oxidation of the bond coat [8]. Additionally,  $\alpha\text{-Al}_2\text{O}_3$  is chemically stable, contributing to improved bonding between ceramic topcoat and bond coat.

The substrate materials in a TBC system are usually Ni- or Co-based superalloys, which include traditional polycrystalline, directionally solidified and single-crystal (SC) superalloys. At high operating temperatures, interdiffusion between substrate and bond coat occurs. The interdiffusion has a profound effect on the mechanical properties of the substrate and thermal cycling lifetime of TBCs [9]. For new generation SC alloys, additions of high concentrations of refractory elements can ensure superior high temperature capability; however, they leave the superalloys prone to microstructure instability. A well-known topologically close-packed (TCP) phase and a so-called secondary reaction zone (SRZ) are formed due to the interdiffusion, and have been found to degrade the mechanical properties of superalloys [10,11]. It then makes sense to consider the substrate and the TBC as an integrated system when designing a TBC for a specific superalloy substrate.

## 16.2 Manufacture of thermal barrier coatings (TBCs)

The two most important manufacturing techniques widely used for deposition of TBCs onto substrates are plasma spraying (PS) and electron beam physical vapor deposition (EB-PVD).

### 16.2.1 Plasma-sprayed thermal barrier coatings

Plasma-sprayed TBCs have been extensively used in hot sections of gas turbine engines. The coatings are formed by successive build-up of splats. The microstructure of the sprayed coatings is characterized by the existence of splats along with other microstructure features such as interlamellar and globular pores, intrasplat cracks and intersplat gaps. The lifetime, mechanical and thermal properties of the TBCs are closely related to the microstructure of the ceramic top coatings [12–14]. Generally, a certain amount of pores or microcracks is favorable in achieving a high level of thermal shock resistance,

because the microcracks and pores can serve as fields of stress concentration where the damage initiates and coalesces, as well as provide strain tolerance to the coating [15,16].

The orientation of most of the intersplat gaps and interlamellar pores is normal to the heat flow direction. The thermal conductivity of the plasma-sprayed TBCs usually ranges from 0.5 to  $2 \text{ W m}^{-1} \text{ K}^{-1}$ , lower than that of EB-PVD TBCs [17]. However, due to the relatively weaker bonding between lamellae and rougher interface morphologies, PS TBCs generally have shorter thermal cycling lifetime when compared to EB-PVD TBCs. This makes APS TBCs suitable only for less exacting applications in turbine engines, such as combustors, after-burner flame holders, and stator vanes.

In order to improve thermal cycling performance, microstructure modifications of PS TBCs have been conducted. TBCs with extremely high porosities have been produced by spraying of plastic–ceramic mixed powders. In addition, various gradient and layered structures have been studied [18–20]. The thermal shock resistance is greatly improved by the introduction of so-called segmentation cracks, in particular into the extremely thick thermal barrier coatings ( $>1 \text{ mm}$  thickness) [21–24]. These cracks can accommodate strains in the coatings during thermal shock testing, because opening of the cracks during tensile loading is possible in a similar manner to the mechanism attributed to EB-PVD coatings.

Recently, some innovative plasma-spray techniques have been employed to produce TBCs with lower thermal conductivities and more durable performance. The solution precursor plasma spray (SPPS) has been exploited to deposit TBCs, in which an aqueous chemical precursor feedstock, rather than YSZ powders, is injected into plasma jet [25,26]. The lack of large-scale ‘splat’ boundaries effectively toughens the TBCs, making SPPS TBCs highly durable relative to APS TBCs.

Functional structured YSZ coatings have been produced by using thermal plasma physical vapor deposition (TP-PVD) [27]. In this process, a peculiar layered structure composed of both powder-sprayed ‘splat’ and vapor-deposited nanoparticles or columns is achieved by PVD integrated with droplet deposition. The splats obtained by plasma spraying act as radiation shields, and the columns or nanoparticles with nanocracks and pores help to reduce both photon and phonon transportation and to release the stress that accompanies drastic temperature change.

### 16.2.2 Electron-beam physical-vapor deposited thermal barrier coatings

EB-PVD is an advanced method for TBC processing. It has been evidenced that EB-PVD TBCs are superior to PS TBCs in the following aspects [5,28]: (i) the possibility of achieving a columnar structure for the ceramic

coating, which exhibits a higher strain tolerance than the sprayed coatings, leading to a longer thermal cycling lifetime; (ii) the possibility of forming a smooth coating surface to avoid disturbing the aerodynamic flow around the turbine blades; (iii) significantly improved interfacial bonding between ceramic topcoat and metallic bond coat; and (iv) the ability to vary the microstructures of the deposited ceramics by adjusting deposition process parameters, such as substrate temperature and deposition rate. However, EB-PVD TBCs have higher thermal conductivities than the PS coatings since the orientation of the gaps between the columns is parallel to the direction of the heat flow, resulting in lower thermal insulation performance. Due to their excellent thermal shock resistance, EB-PVD TBCs are used primarily in the most severe applications, such as blades and vanes in aircraft engines.

Due to its feasibility of varying coating structure, EB-PVD has great potential to produce functionally graded TBCs. This technology is based on the known phenomenon of fractionation of multi-component systems during evaporation and subsequent condensation in vacuum. Such an approach, when applied to TBCs, allows replacing the flat interface between the metallic bond coat and the ceramic topcoat by a graded transition zone and achieving a good adhesion of the coating to the substrate by introducing components with different melting temperatures and vapor pressures into the composition of the mixture being evaporated. A successful example is the  $\text{Al}_2\text{O}_3$ -YSZ graded thermal barrier coating (GTBC) [29–31], which basically has the structure  $\text{MCrAlY-NiAl/NiAl+Al}_2\text{O}_3/\text{Al}_2\text{O}_3\text{-YSZ/YSZ}$ . The GTBC significantly improved the thermal cycling lifetime compared to the MCrAlY/YSZ TBC, because of the following microstructure features: (i) the formation of a pre-deposited  $\alpha\text{-Al}_2\text{O}_3$  thin film and a high concentration of Al in the surface layer of the bond coat, leading to improved oxidation resistance and hot-corrosion resistance; (ii) the formation of an ‘interlocking’ interface, contributing to the enhanced bonding between TGO and bond coat; and (iii) the formation of an  $\text{Al}_2\text{O}_3$ -YSZ graded transition zone, helping to reduce thermal stresses.

## 16.3 Thermal barrier coating materials

### 16.3.1 Ceramic topcoat materials

The primary function of the ceramic topcoat is to provide thermal insulation; consequently, the thermal conductivity is one of the most important factors when considering ceramic materials as TBC candidates. A 50% reduction in thermal conductivity reduces the surface temperature of metallic components by approximately 50 K [32], which corresponds to the accumulation of the increase in high temperature capability achieved over the decades by

development in single crystal (SC) Ni-based superalloys. Improved TBCs will enable future gas turbine engines to operate at higher gas temperatures, thus improving the efficiency and performance of engines.

Nowadays, considerable effort is being invested in seeking new ceramic materials even better than YSZ. The choice of TBC materials is based on several requirements: (i) low thermal conductivity; (ii) high temperature capability; (iii) phase stability during thermal cycling between room temperature and operation temperature; (iv) chemical inertness with TGO and metallic bond coat; (v) thermal expansion match with metallic substrate; (vi) good adherence to metallic bond coat; (vii) mechanical properties to sustain strength in high-pressure and high-temperature environments and resistant to erosion; and (viii) low sintering during high-temperature exposure.

A widely used TBC material for diesel engines and gas turbines is 6–8 wt% yttria stabilized zirconia (YSZ). It has one of the lowest thermal conductivities at 1273 K, because of its high concentration of point defects associated with the substitution of  $Zr^{4+}$  ions by  $Y^{3+}$  ions in the fluorite structure [33]. YSZ has a high coefficient of thermal expansion (CTE) ( $\sim 11 \times 10^{-6} \text{ K}^{-1}$ ), which is beneficial to the lower thermal stresses arising from thermal expansion mismatch between the ceramic topcoat and the underlying alloy. Furthermore, YSZ has been proved to be resistant to hot corrosion induced by  $Na_2SO_4$  and  $NaCl$ . A major disadvantage of YSZ is its limited temperature capability. YSZ cannot be used for long-term application above 1473 K due to the transformation of the metastable tetragonal phase to tetragonal and cubic phases and then to monoclinic phase [33]. Such transformation is accompanied by a volume change of up to 5%, which often results in spallation failure. To increase turbine inlet temperature at higher temperatures and to further reduce the thermal conductivity, some new candidate materials for TBC applications are under investigation, such as zirconate pyrochlore oxides [34–36], fluorite oxides [37–39], perovskite oxides [40], metal–glass composite [41,42], and nanocrystalline materials [43].

### *Zirconate pyrochlore oxides*

The pyrochlores,  $A_2^{3+}B_2^{4+}O_7$ , have received extensive attention, because some zirconate pyrochlores have lower thermal conductivities than YSZ. The pyrochlore unit cell can be considered as eight fluorite unit cells, each of which contains a single oxygen vacancy. The pyrochlore  $Y_2Zr_2O_7$  is actually unstable to heavily doped YSZ. However, the replacement of  $Y^{3+}$  ions with large ions such as  $La^{3+}$  or  $Gd^{3+}$  can stabilize the pyrochlore structure.  $La_2Zr_2O_7$  with the pyrochlore structure can be phase stabilized up to its melting point (2573 K), and is therefore proposed as a promising TBC material [34]. In addition,  $La_2Zr_2O_7$  has a lower thermal conductivity than YSZ. However,  $La_2Zr_2O_7$  coatings exhibited shorter thermal cycling lifetimes than YSZ

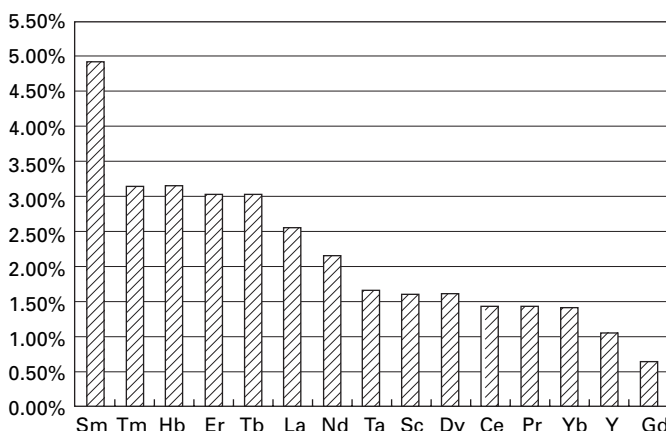
coatings, which may be explained by their relatively low CTE and poor toughness. A double  $\text{La}_2\text{Zr}_2\text{O}_7/\text{YSZ}$  layered TBC structure has been proposed to make full use of the advantages of  $\text{La}_2\text{Zr}_2\text{O}_7$  TBC.

### *Fluorite oxides*

Fluorite oxides for potential TBC applications include mainly  $\text{HfO}_2$ ,  $\text{CeO}_2$  and  $\text{ThO}_2$ .  $\text{CeO}_2$  cannot be used as a TBC material because of its volatilization at elevated temperatures, although it exhibits comparable thermal conductivity. The thermal conductivity of  $\text{HfO}_2$  is approximately  $2 \text{ W m}^{-1} \text{ K}^{-1}$  (373–773K), which is similar to that of YSZ. However,  $\text{HfO}_2$  is chemically reactive with metals and metal oxides.

Theoretically, thermal diffusivity of ceramics is proportional to the lattice oscillation frequency and lattice oscillation amplitude, both of which are affected by the distortion of the lattice. The addition of rare earth (RE) element oxides into zirconia could cause lattice distortion [33,44,45]. Simulation modeling results show that different RE element oxides cause different changes of lattice distortion of zirconia, as shown in Fig. 16.1. Based on this analysis, zirconia co-doped with different RE element oxides has been synthesized by high temperature solid phase sintering. Thermal conductivity of zirconia based TBCs is significantly lowered by adding the dopants of yttria and niobia [33].  $\text{La}_2\text{O}_3$  is also selected as an additive to YSZ since it has a significant influence on suppressing densification of YSZ.

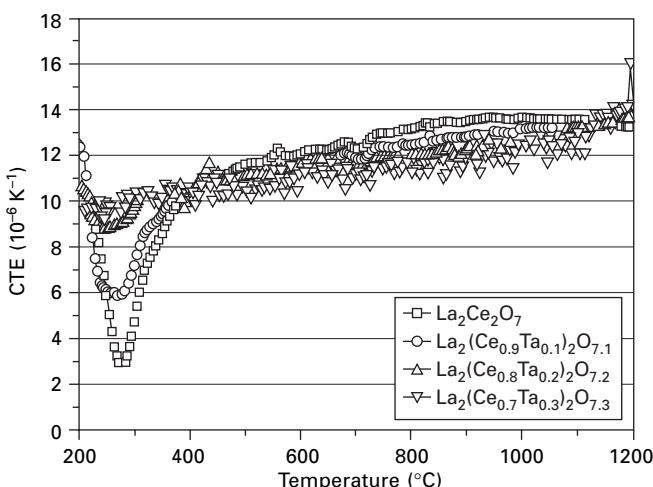
A  $\text{Gd}_2\text{O}_3\text{-Yb}_2\text{O}_3$  doped YSZ/YSZ double ceramic layered TBC is deposited by EB-PVD [46]. The undoped YSZ top layer is featured with clusters of columns with sub-grains growing around columns, while the doped YSZ



16.1 Changes of  $\text{ZrO}_2$  lattice distortions by rare earth element oxides addition.

bottom layer has a feather-like structure. The solidification, nucleation and growth of grains in the YSZ top layer are strongly affected by the surface morphology of the underlying doped YSZ layer. It should be noted that the porous structure has survived even after long-term exposure at 1473 K, evidence of its good resistance to sintering. It is believed that this type of structure could limit thermal transport processes and reduce thermal conductivity.

$\text{La}_2\text{Ce}_2\text{O}_7$  (LCO) has a cubic fluorite structure which consists of the corner-shared  $\text{CeO}_{7+x}$  hexahedrons forming the backbone of the network and  $\text{La}^{3+}$  ions substituting  $\text{Ce}^{4+}$  sites, where a big hole is formed by eight  $\text{CeO}_{7+x}$  hexahedrons [47]. It can largely tolerate vacancies at the  $\text{La}^{3+}$ ,  $\text{Ce}^{4+}$  and  $\text{O}^{2-}$  sites, without phase transformation.  $\text{La}_2\text{Ce}_2\text{O}_7$  has good phase stability up to 1673 K and a CTE close to that of MCrAlY bond coat in a temperature range of 573–1273 K. However, an abrupt reduction of CTE was observed between 473 K and 623 K, with a minimum value at 553 K, possibly due to the high concentration of oxygen vacancies in  $\text{La}_2\text{Ce}_2\text{O}_7$ . The doping of  $\text{Ta}_2\text{O}_5$  into  $\text{La}_2\text{Ce}_2\text{O}_7$  resulted in an increased CTE below 673 K (as shown in Fig. 16.2), and the thermal conductivity of the  $\text{La}_2\text{Ce}_{1.8}\text{Ta}_{0.2}\text{O}_{7.1}$  is  $0.52 \text{ W m}^{-1} \text{ K}^{-1}$  at 1273 K, only a quarter of that of 8YSZ [48]. However, the chemical reaction between  $\text{La}_2\text{Ce}_2\text{O}_7$  and  $\text{Al}_2\text{O}_3$  during thermal exposure produces  $\text{LaAlO}_3$ , which deteriorates the bonding between TBC and TGO. A YSZ/LCO double ceramic-layer TBC structure is proposed. Thermal cycling test results have shown that the thermal cycling lifetime of the double ceramic-layer TBC is nearly five times that of the single LCO-layer TBC, and is longer than that of 8YSZ TBC by around 30% [49]. It can be expected that the YSZ/LCO



16.2 Coefficients of thermal expansion (CTE) of La-Ce-O oxides.

double ceramic-layer TBC is a promising coating to substitute YSZ TBC for long-term application above 1473 K.

### *Mullite*

Mullite is a compound of  $\text{SiO}_2$  and  $\text{Al}_2\text{O}_3$ , with low density, high temperature stability, favorable strength and creep behavior [50]. In comparison with YSZ, mullite has a much lower CTE and better oxygen resistance. Mullite is more suitable than YSZ for application as TBC in diesel engines where the operating temperatures are lower than those in turbine engines while the temperature gradients across the coating thickness are larger. The mullite TBCs have exhibited longer thermal cycling lifetimes in diesel engines than YSZ TBCs. However, accelerated degradation often occurs when the temperature is higher than 1273 K. This is partially related to the crystallization of mullite at 1023–1273 K that causes volume contraction, leading to cracking and debonding [51, 52]. Recently, mullite materials have seen promising applications as environmental barrier coatings (EBCs) in  $\text{SiC}/\text{SiC}$  or  $\text{Si}_3\text{N}_4/\text{Si}_3\text{N}_4$  ceramic matrix composite (CMC) engines, in which they functioned as barriers to volatilization resulting in recession from water vapor and oxidation [53].

### *Metal–glass composite*

Metal–glass composite has recently become an attractive TBC candidate, based on three major advantages over other TBC materials: high CTE ( $12.3 \times 10^{-6} \text{ K}^{-1}$ ), good adherence to the underlying bond coat, and excellent oxidation resistance due to the absence of open porosity. The metal–glass composite consists of an ordinary glass and a MCrAlY alloy.

### *Nanocrystalline materials*

Nanocrystalline materials have more grain boundaries than other materials with larger grain size, therefore offering the potential of limiting thermal conductivity by incorporating grain boundary scattering with an extrinsic phonon-scattering effect. Nanocrystalline TBC exhibited a significant reduction in thermal conductivity when the grain size was smaller than 25 nm. However, the nanocrystalline materials rapidly coarsen at elevated temperatures and lose the initial advantages of being nanocrystalline. Despite this, some nanopores formed in EB-PVD TBCs can remain even after long-term heat treatment above 1473 K. For plasma-sprayed TBCs, the TBCs sprayed from the same materials could have different microstructural features due to different processing parameters and powder morphologies. The potential of nanocrystalline TBC has not yet been fully explored.

### 16.3.2 Bond coat materials

The bond coat is an oxidation-resistant metallic layer between the ceramic topcoat and the substrate. In most cases, failure of TBCs occurs at the interface between the bond coat and the TGO. The key to the durability of TBCs is the retentive strong bonding between the TGO and the bond coat. To accomplish this, it is necessary to create good bonding and to minimize the stress and strain energy during the coating process. A pre-formed  $\alpha$ -Al<sub>2</sub>O<sub>3</sub> scale during heat treatment in vacuum or deposited by EB-PVD is beneficial to provide strong bonding [54,55]. A defect-free and surface-flattened bond coat, which helps to eliminate out-of-plane stresses and strain energies, is desirable for TBCs as well. In addition, outward diffusion of some deleterious elements such as S, Mo and Ta from the substrate should be prevented during thermal exposure, because the presence of those elements or their oxides at the bond coat surface could cause cavities that weaken the bonding.

#### *MCrAlY*

MCrAlY coatings (where M = Co, Ni or Co/Ni) are widely applied to the first and second stage turbine blades and nozzle guide vanes, where they may be used as corrosion-resistant overlays or as bond coats for use with TBCs. Cr and Al are present in the MCrAlY composition because they form highly tenacious protective oxide scales, whilst Y promotes the formation of these stable oxides.

MCrAlY coatings can be manufactured by a number of processes including EB-PVD, low pressure plasma spraying (LPPS), vacuum plasma spraying (VPS), atmospheric plasma spraying (APS), and high velocity oxygen fuel (HVOF) spraying. PVD and VPS offer high quality in terms of minimal oxidation of the coating during deposition, but are the most expensive. Approvals have been granted for the use of APS and HVOF coatings on certain components with significant cost savings.

The diffusion of elements such as Mo, W, S and Ta into the MCrAlY layer has been recognized. Addition of a small amount of Si into MCrAlY can effectively prevent outward diffusion of Mo by increasing the diffusion activation energy [56–58]. However, the existence of Si on the surface of the bond coat deteriorates thermal cycling performance of TBCs, because silicon oxide is brittle at low temperatures and peristaltic at elevated temperatures. To circumvent this, a two-layered TBC with a Si gradient MCrAlY-Si bond coat was designed to block the outward diffusion of Mo from the substrate into the bond coat and to improve thermal cycling performance of TBCs [57].

Additions of reactive elements (RE), such as Y, Hf and Zr, to MCrAlY bond coats enhance the oxide adhesion. Y and Hf promote the formation of

fine alumina grains by acting as nucleation sites. In addition, these REs can form ‘oxide pegs’, the usefulness of which has been reported in the literature [59,60]. These pegs arrest crack propagation, while some researchers believe that these pegs do not relieve stress and could be a source of brittleness. The mechanism by which REs affect the lifetime of TBCs is still controversial.

### *NiAl coating*

For the next generation of advanced turbine engines, the turbine inlet temperature (TIT) could go up to 2100 K. In such case, the operating temperature of the MCrAlY bond coat will be much higher than it can endure. Therefore, it is important to develop new bond coat materials with high temperature capability, and to match them with the new ceramic topcoats and the new generation of single crystal superalloys.

Being a promising high temperature material with the potential capability of working at 1473 K, the ordered B2 type NiAl could be exploited as a bond coat material in TBC systems to replace the MCrAlY bond coats. To improve the oxide adhesion of NiAl, modifications of NiAl coatings have been conducted by adding elements such as Pt and Hf [61–63]. Hf-modified NiAl coatings were produced by co-deposition of NiAl and Hf using EB-PVD [64]. It has been shown that the Hf-doped NiAl coatings have several advantages over the undoped NiAl coatings, including: (i) refinement of grains; (ii) toughening of TGO layer; and (iii) enhancing the adherence of TGO to the bond coat. The thermal cycling lifetime of the Hf-doped TBCs is five times that of the undoped TBCs. It should be noted that the concentration of Hf plays an important role in affecting failure mechanisms of TBC. Failure of the 0.5 at% Hf doped TBC is shown as cracking at the interface between the YSZ topcoat and the bond coat, while the 1.5 at% Hf doped TBC cracked at the interface between the bond coat and the substrate.

### *Diffusion barrier coatings*

As the TBCs are applied onto advanced single crystal superalloy substrates, interdiffusion between the bond coat and the substrate has become a serious problem. The local concentration change caused by the interdiffusion would promote the precipitation of detrimental phases in the substrate. Outward diffusion of elements from the substrate, such as W, Mo and Cr, is detrimental to the interfacial bonding between TGO and bond coat, accompanied by volatilization of oxides of those elements at elevated temperatures. In addition, inward diffusion of Al into the substrate could result in Al depletion in the bond coat and finally degrade the oxidation resistance of the bond coat in long-term thermal exposure [7,65].

The low-activity pack cementation aluminizing process is a well-established

technique which has been widely used for the preparation of protective diffusion aluminide coatings. The Pt-aluminide bond coat alloys based on single-phase  $\beta$ -NiAl, with Pt substituting for Ni, have come into wide use. The addition of Pt gives the NiAl alloy excellent cyclic oxidation resistance, because: (i) Pt suppresses formation of spinel oxide phases which are usually brittle and may be a source of de-adhesion; and (ii) Pt would inhibit S segregation to the interface and the associated void formation. Despite these merits, the continued growth of an alumina scale and interdiffusion with the superalloy result in Al depletion from the  $\beta$ -NiAl coating, which in turn leads to the phase transformation of  $\beta$ -NiAl to martensite and  $\gamma'$ -Ni<sub>3</sub>Al [66,67]. The volume changes associated with these transformations result in undesirable surface undulations or ‘rumpling’ of the coating [68]. Rumpling of the  $\beta$ -(Ni,Pt)Al bond coat may cause delamination of the ceramic topcoat when used in a TBC system. To improve the performance of the Pt-modified aluminide coatings, Pt-based binary alloy coatings, such as Pt-Pd and Pt-Ir, have been proposed [69,70].

Narita *et al.* proposed a Re-based alloy diffusion barrier coating [71]. This diffusion barrier can effectively suppress the inward diffusion of Al to a single crystal superalloy and outward diffusion of Ta, Ti and Ni from the substrate.

High levels of alloying elements in nickel-based superalloys may leave them prone to different types of microstructural instabilities, and likely to have deleterious effects on their mechanical properties. This issue is particularly critical in the recent SC superalloys, in which the content of refractory elements, such as Mo, W, Ta, Re and Ru, has been progressively increased to improve the high temperature capability of superalloys. The best known type of microstructural instability is the precipitation from the supersaturated  $\gamma$  matrix of topologically close-packed (TCP) phases. A small amount of TCP phases would not degrade the mechanical properties of alloys. Recently, a new type of instability has been observed in the new-generation SC superalloys. This instability was observed beneath the diffusion zone of an aluminide coating and termed the secondary reaction zone (SRZ) [10,11]. The SRZ consists of a TCP phase containing the refractory elements such as Re, W and Ru, and a needle-like  $\gamma$  phase in a matrix of  $\gamma'$ . The formation of SRZ significantly degrades the mechanical properties of the SC superalloy. It is caused by inward diffusion of Al from the aluminide coating and outward diffusion of Re and Ru from the substrate.

RuAl is proved to be particularly effective on the reduction of SRZ. The possible mechanisms of SRZ reduction are as follows. First, the presence of a sufficient amount of Ru in the coating layer reduces the driving force for its outward diffusion from the substrate, thereby preventing the depletion of Ru content under the coating layer. Second, the formation of a secondary phase of Ru-Al compound in the coating layer keeps Al from diffusing into

the substrate. It restricts the increase of Al content under the coating layer, therefore SRZ formation is restricted. However, the single RuAl coating could not work as a bond coat in TBC due to its poor oxidation resistance. Cr-modified RuAl coating is proposed to improve oxidation resistance. To solve the problem, a two-layered NiAl/RuAl bond coat, in which NiAl works as the oxidation-resistant layer while RuAl acts as the diffusion-barrier layer, has been proposed.

Recently, a new bond coat system, ‘EQ coating’ (equilibrium coating), designed to be in thermodynamic equilibrium with the Ni-based superalloy substrate, has been proposed [72]. The composition of the ‘EQ coating’ is close to that in the Ni-based superalloy substrate. The interdiffusion between the coating and the substrate was effectively restricted.

## 16.4 Failure of thermal barrier coatings

TBCs work in the most demanding high-temperature environments of aircraft and industrial gas-turbine engines. The turbine blade service environment is very aggressive and complicated, such as high-temperature gas with high pressure, fast heating and cooling, corrosive atmosphere, deposition of deleterious combustion products, mechanical loading and so on. This wide variation of conditions is one of the main reasons why TBC failure mechanisms have not yet been completely understood. Despite this, some failure mechanisms are briefly discussed below.

### 16.4.1 High-temperature oxidation

Oxidation of the bond coat is the most important factor responsible for the spallation failure of TBCs. The formation and growth of TGO resulting from oxidation of the bond coat lead to constrained volume expansion, which causes TGO growth stress in the compressive state. On the other hand, residual compressive stress, resulting from thermal expansion mismatch between TGO and bond coat, is generated in the TGO upon cooling. The strain energy increases with thickening TGO and increasing TGO stress, and finally drives TGO fracture. For EB-PVD YSZ TBCs, the spallation failure of TBCs occurs in most cases by cracking at the interface between the TGO and the bond coat or within the TGO. For PS YSZ TBCs, the TBCs are often cracked in the first deposited YSZ lamella close to the TGO or along the interface between the TGO and the topcoat.

Above 1273–1473K, additional mechanisms, particularly sintering, can contribute to TBC failure. Sintering of TBCs results in densification of coating materials, reduction of porosity, and increase of micro-hardness and Young’s modulus. The less compliant coating resulting from sintering is less able to undergo strain relaxation to relieve the stresses developed in the coating due

to the mismatch in the thermal expansion coefficients between the coating and the substrate and in the sintering rate as well.

The majority of YSZ coatings prepared by EB-PVD and PS methods have a metastable tetragonal structure, denoted  $t'$ . The  $t'$  phase first transforms to the tetragonal phase ( $t$ ) with low yttria content during the high temperature stage, and then to the monoclinic phase ( $m$ ) during cooling. The phase transformation of  $t'$  to  $m$  is associated with a volume expansion of up to 5%, which will degrade the integrity of the YSZ topcoat and cause the degradation of TBCs.

#### 16.4.2 Hot corrosion

For industrial turbine engines or diesel engines burning low-quality fuel at 973–1273K, the YSZ TBC system cannot be successfully used due to the hot-corrosion problems caused by molten salts, such as Na, S and V, contained in the low-quality fuel. TBCs are also envisioned for military land or sea engines where they must be able to survive in low-quality fuel and corrosive environments in wartime emergencies. Volume destabilization of YSZ often occurs because  $\text{Y}_2\text{O}_3$  could be dissolved in molten salts, resulting in spallation of YSZ. On the other hand, molten salts diffuse into the bond coat through pores and cracks in the YSZ topcoat and lead to accelerated oxidation of the bond coat, with the TGO dissolving in molten salts by a fluxing mechanism.

#### 16.4.3 Deposition of deleterious combustion deposits

In-service erosion caused by the deposition of a significant amount of calcium-magnesium-alumina-silicate (CMAS) at high temperatures is found to be one of the most prevalent failure modes [73,74]. At temperatures above 1423 K, sand particles and debris ingested during operation become molten and adhere to the TBC surface. During this process, CMAS are incorporated in the molten phase, and the excellent wetting characteristics of CMAS enable the deposits to infiltrate the TBC. The addition of the CMAS layer changes the mechanical properties of the near-surface materials. The CMAS layer has a much lower CTE than the TBC and superalloy substrate. Consequently, large compressive stresses develop as the system cools, which elevate the energy release rate of the system, leading to delamination of the underlying TBC and materials removal.

### 16.5 Future trends

With the development of advanced gas-turbine engines towards higher efficiency and improved durability, the near-term focus will be on TBCs with improved durability and performance, which should be based on further

understanding of the failure mechanisms of TBCs. Also, there is a great motivation for developing TBC materials with improved properties. Considering this, some perspectives of TBCs can be summarized as follows:

1. For current YSZ-based TBCs, a strong and retentive bonding between the TGO and the bond coat is the key to determine the duration of TBCs, which can be greatly improved by controlling compositions and processing of the bond coat.
2. Great efforts have been invested in searching for new ceramic materials with better performance than the current YSZ. Investigation into new metallic bond coat materials, which will be oxidation-resistant at 1473 K and smartly adaptive to the environments, has been urged to keep in accordance with the new ceramic materials and the new-generation single crystal superalloys.
3. Innovative methods, along with new scientific techniques, should be developed for the assessment of TBC performance and the prediction of TBC lifetime more efficiently and accurately.

## 16.6 References

1. R.A. Miller, Surf. Coat. Technol. 30 (1987): p. 1.
2. S.M. Meier, D.K. Gupta and K.D. Sheffler, J. Met. 43 (1991): p. 50.
3. N.P. Padture, M. Gell and E.H. Jordan, Science 296 (2002): p. 280.
4. H.B. Xu, S.K. Gong and L. Deng, Thin Solid Films 334(1-2) (1998): p. 98.
5. T.E. Strangman, Thin Solid Films 127 (1985): p. 93.
6. E.Y. Lee, R.R. Biederman and R.D. Sisson, Mater. Sci. Eng. A 121 (1989): p. 467.
7. F.H. Stott and G.C. Wood, Mater. Sci. Eng. 87 (1987): p. 267.
8. D.R. Mumm and A.G. Evans, Acta Mater. 48 (2000): p. 1815.
9. U. Schulz, M. Menzebach, C. Leyens and Y.Q. Yang, Surf. Coat. Technol. 146–147 (2001): p. 117.
10. W.S. Walston, J.C. Schaefer and W.H. Murphy: *Superalloy 1996*, TMS, p. 9.
11. B. Tryon, T.M. Pollock, M.F.X. Gigliotti and K. Hemker, Scripta Mater. 50 (2004): p. 845.
12. H.B. Guo, S. Kuroda and H. Murakami, J. Am. Ceram. Soc. 89(4) (2006): p. 1432.
13. H.B. Guo, H. Murakami and S. Kuroda, J. Am. Ceram. Soc. 89(12) (2006): p. 3797.
14. A. Kulkarni, A. Goland, H. Herman, A.J. Allen, J. Ilavsky, G.G. Long, C.A. Johnson and J.A. Ruud, J. Am. Ceram. Soc. 87 (2004): p. 1294.
15. R. Morrell, *Handbook of Properties of Technical and Engineering Ceramics*, Part 1, Her Majesty's Stationery Office, 1989, pp. 151–158.
16. R. Vaßen, M. Ahrens, A.F. Waheed and D. Stöver, *Proceedings of International Thermal Spray Conference and Exposition*, Essen, Germany, 2002, p. 879.
17. D.M. Zhu and R.A. Miller, J. Therm. Spray Technol. 9(2) (2000): p. 175.
18. W.Y. Lee, D.P. Stinton, C.C. Berndt, F. Erdogan, Y.D. Lee and Z. Mutasin, J. Am. Ceram. Soc. 79 (12) (1996): p. 3003.
19. K. Kokini, J. DeJonge, S. Rangaraj and B. Beardsley, Surf. Coat. Technol. 154 (2-3) (2002): p. 223.

20. S. Rangaraj and K. Kokini, *Surf. Coat. Technol.* 173 (2–3) (2003): p. 201.
21. T.A. Taylor, D.L. Appleby, A.E. Weatherill and J. Griffiths, *Surf. Coat. Technol.* 43/44 (1990): p. 470.
22. P. Bengtsson, T. Ericsson and J. Wigren, *J. Therm. Spray. Technol.* 7 (3) (1998): p. 340.
23. D. Schwingel, R. Taylor, T. Haubold, J. Wigren and C. Gualco, *Surf. Coat. Technol.* 108–109 (1998): p. 99.
24. H.B. Guo, R. Vaßen and D. Stöver, *Surf. Coat. Technol.* 186 (2004): p. 353.
25. L.D. Xie, X.Q. Ma, E.H. Jordan, N.P. Padture, D.T. Xiao and M. Gell, *Surf. Coat. Technol.* 177–178 (2004): p. 103.
26. J. Karthikeyan, C.C. Berndt, S. Reddy, J.Y. Wang, A.H. King and H. Herman, *J. Am. Ceram. Soc.* 81 (1998): p. 121.
27. H.J. Huang, K. Eguchi, M. Kambara and T. Yoshida, *J. Therm. Spray Technol.* 15(1) (2006): p. 83.
28. R.L. Jones, in *Metallurgical and Ceramic Coatings*, K.H. Stern, ed., Chapman and Hall, London, 1996, p. 194.
29. H.B. Xu, H.B. Guo, F.S. Liu and S.K. Gong, *Surf. Coat. Technol.* 130 (2000): p. 133.
30. B.A. Movchan and K.Y. Yakovchuk, *Surf. Coat. Technol.* 188–189 (2004): p. 85.
31. H.B. Guo, H.B. Xu and S.K. Gong, *Mater. Eng. Sci. Eng. A* 325 (2002): p. 261.
32. M.J. Maloney, *Thermal Barrier Coatings Systems and Materials*, US Patent 6117560, 2000.
33. X.Q. Cao, R. Vassen and D. Stoever, *J. Euro. Ceram. Soc.* 24 (2004): p. 1.
34. R. Vassen, X.Q. Cao, F. Tietz, D. Basu and D. Strover, *J. Am. Ceram. Soc.* 83(8) (2000): p. 2023.
35. M.J. Maloney, US Patents 6117200 and 6231991, 2001.
36. H. Lehmann, D. Pitzer, G. Pracht, R. Vassen and D. Stover, *J. Am. Ceram. Soc.* 86 (8) (2003): p. 1338.
37. J. Wilden and A. Wank, *Materialwiss. Werkstofftech. (Mater. Sci. Eng. Technol.)* 32 (8) (2001): p. 654.
38. D.M. Zhu and R.A. Miller, *Ceram. Eng. Sci. Proc.* 23 (4) (2002): p. 457.
39. K.S. Murphy, US Patent 0118873 (2003) A1.
40. D.R. Clarke and S.R. Phillipot, *Materials Today*, June 2005: p. 22.
41. V. Verlotski, D. Stoever, P.H. Buchkremer and R. Vassen, German Patent 19852285 (2000).
42. M. Dietrich, V. Verlotski, R. Vassen and D. Strover, *Materialwiss. Werkstofftech.* 32 (8) (2001): p. 669.
43. H.S. Yang, G.R. Bai, L.J. Thompson and J.A. Eastman, *Acta Mater.* 50 (9) (2002): p. 2309.
44. X.J. Ji, Q.L. Wei, C.G. Zhou, S.K. Gong and H.B. Xu, *Int. J. Mod Phys. B* 20 (25–27) (2006): p. 4010.
45. C. Ding, In *2nd Plasma-technik-symposium*, ed. S. Sandmeier *et al.*, Plasma-Technik AG, Wohlen, Switzerland, 1997, p. 27.
46. Q.L. Wei, H.B. Guo and S.K. Gong, *Mater. Sci. Forum* 546–549 (2007): p. 1735.
47. X.Q. Cao, R. Vassen, W. Fischer, F. Tietz, W. Jungen and D. Strover, *Adv. Mater.* 15(17) (2003): p. 1438.
48. W. Ma, S.K. Gong, H.B. Xu and X.Q. Cao, *Scripta Mater.* 54 (2006): p. 1505.
49. W. Ma, S.K. Gong, H.B. Xu and X.Q. Cao, *Surf. Coat. Technol.* 200 (2006): p. 5113.
50. G. Brunauer, F. Frey, H. Boysen and H. Schneider, *J. Eur. Ceram. Soc.* 21 (2001): p. 2563.

51. P. Ramaswamy, S. Seetharamu, K.B.R. Varma and K.J. Rao, *J. Therm. Spray Technol.* 7 (4) (1999): p. 497.
52. T.M. Yonushonis, *J. Therm. Spray Technol.* 6 (1) (1997): p. 50.
53. K.N. Lee., R.A. Miller and N.S. Jacobson, *J. Am. Ceram. Soc.* 78 (3) (1995): p. 705.
54. W. Lih, E. Chang, C.H. Chao and M.L. Tsai, *Oxid. Met.*, 38 (1/2) (1992): p. 99.
55. W. Lih, E. Chang, B.C. Wu and C.H. Chao, *Oxid. Met.* 36 (3/4) (1991): p. 221.
56. D.B. Zhang, S.K. Gong, H.B. Xu and Y.F. Han, *Acta Metall. Sin. (English Letters)* 15 (2002): p. 45.
57. D.B. Zhang, S.K. Gong, H.B. Xu, H.T. Zhang and Y.F. Han, *Surf. Coat. Technol.* 168 (2003): p. 78.
58. X. Huo, J.S. Zhang, B.L. Wang, F.J. Wu and Y.F. Han, *Surf. Coat. Technol.* 144 (1999): p. 174.
59. N.M. Yanar, G.H. Meier and F.S. Petit, *Scripta Mater.* 46 (2002): p. 325.
60. T. Xu, S. Faulhaber, C. Mercer, M. Maloney and A. Evans, *Acta Mater.* 52 (2004): p. 1439.
61. R.E. Demaray, W.K. Halman and S. Shan, EPRI RD-2369-SR, 1982, p. 6.
62. G.W. Goward, *Surf. Coat. Technol.* 108–109 (1998): p. 73.
63. K.M. Carling and E.A. Carter, *Acta Mater.* 55 (2007): p. 2791.
64. L.D. Sun, H.B. Guo, H.F. Li and S.K. Gong, *Mater. Sci. Forum* 546–549 (2007): p. 1777.
65. M.J. Stiger, N.M. Yanar, M.G. Topping, F.S. Pettit and G.H. Meier, *Z. Metallkd* 90 (1999): p. 1069.
66. Y. Zhang, J.A. Haynes, B.A. Pint, I.G. Wright and W.Y. Lee, *Surf. Coat. Technol.* 163–164 (2003): p. 19.
67. S. Darzens, D.R. Mumm, D.R. Clarke and A.G. Evans, *Metall. Mater. Trans.* 34A (2003): p. 511.
68. V.K. Tolpygo and D.R. Clarke, *Acta Mater.* 48 (2000): p. 3283.
69. G. Lehnert and H.W. Meinhardt, *Electrodepos. Surf. Treat.* 1 (3) (1972–1973): p. 189.
70. F. Wu, H. Murakami, Y. Yamabe-Mitarai, H. Harada, H. Katayama and Y. Yamamoto, *Surf. Coat. Technol.* 184 (2004): p. 24.
71. F.Q. Lang and T. Narita, *Intermetallics* 15 (2007): p. 599.
72. A. Sato, H. Harada and K. Kawagishi, *Metall. Mater. Trans.* 37A (2006): p. 789.
73. M.P. Borom, C.A. Johnson and L.A. Peluso, *Surf. Coat. Technol.* 86–87 (1996): p. 116.
74. X. Chen, *Surf. Coat. Technol.* 200 (2006): p. 3418.



# **Part III**

Case studies

---



# High temperature corrosion problems in the petrochemical industry

Y HE and Z NING, University of Science and Technology  
Beijing, China and W GAO, The University of Auckland,  
New Zealand

## 17.1 Introduction

### 17.1.1 Importance of high temperature corrosion protection in the petrochemical industry

There are many high temperature, high pressure and highly corrosive media and environments associated with crude oil refining and chemical processes in the petrochemical industry. Research on high temperature corrosion and protection is critical to the long-term safe operation of petrochemical plants. Due to the applications of many new technologies and processes, the operating temperatures and pressures of the process units in the petrochemical industry are increasing gradually. For example, most of the petrochemical equipment is running at temperatures around 300°C. Some ethylene crackers are even operating at temperatures as high as 900°C, while the operating pressure in some hydrogenation reaction chambers is around 12 MPa. High temperature and high pressure require that the materials used should have better mechanical properties and a higher resistance against high temperature corrosion attacks. For high temperature and high pressure processing units, catastrophic consequences such as firing and/or explosion might be caused by the failures initialized by severe corrosion and oxidation attacks. Therefore it is extremely important to perform regular corrosion inspections and monitoring of the petrochemical equipment and to study the mechanisms involved in the high temperature corrosion and oxidation processes of the materials.

According to the source of crude oils, it can be seen that the proportion of the crude oils with a high sulfur content and a high total acid number (TAN) increases gradually. Large amounts of poor crude oils have also been exploited and sold on the market at relatively low prices. Some processing plants are trying to refine these low-quality crude oils due to the high profits to be made. Currently, poor crude oils with an acid number larger than 3.0 mg KOH/g and a sulfur content of 3.0% are being refined by some plants. Obviously, the refining process with poor crude oils makes high temperature

corrosion attack on the equipment more serious and challenges the present corrosion theories and experiences in material selection and field corrosion protection practice.

### 17.1.2 Main high temperature corrosion problems in the petrochemical industry

The major high temperature corrosion attacks in the petrochemical industry include high temperature oxidation, high temperature sulfidation, high temperature naphthenic acid corrosion and high temperature carburization. Due to the complexity of refining processes, working media and equipments used, many types of corrosion processes will occur and work together further to accelerate the progress of attack due to the synergetic effect. For instance, the outer wall of the radiant tubes of the heating furnaces will be in contact with sulfur-containing fuel gases, and suffer from a wide spectrum of high temperature corrosion problems such as high temperature oxidation, high temperature sulfidation and ash deposition. The inner wall of the radiant tubes meanwhile will be in contact with the processing media. If crude oils with a high content of sulfur and/or naphthenic acid were processed, serious high temperature sulfidation, high temperature naphthenic acid corrosion and/or high temperature carburization will occur. In addition, the furnace radiant tubes will probably deform if a large temperature difference exists between the two sides facing and not facing the burning flame. At the same time, processing media flowing in the tube with a high velocity may result in erosion attack to the inner wall of the tube. These corrosion and non-corrosion processes will work together to accelerate the failure of the furnace tubes. During failure analysis, the potential effects of these processes must be taken into account and discussed and their respective contributions to the failure must be distinguished carefully.

Extensive studies and tests on high temperature oxidation, high temperature sulfidation, high temperature naphthenic acid corrosion and high temperature carburization at a laboratory scale have been reported. These investigations are mainly focused on the influences of concentration, temperature, pressure and velocity of flow of the processing media on the high temperature corrosion behaviors of the materials used in petrochemical plants. However, these experimental results obtained in the laboratory are quite different from those measured directly from chemical process units [1]. Therefore, it is sometimes difficult to use knowledge acquired from laboratory studies to guide field corrosion protection practice. Few dynamic simulating apparatuses have been reported to study the corrosion behaviors of materials currently used or to be used in petrochemical plants. The reliability of the corrosion prediction and/or evaluation software established on the data collected in laboratory tests needs to be improved urgently.

Selection of proper corrosion-resistant materials is the most effective way to control high temperature corrosion problems in the petrochemical industry and is closely related to the mechanical properties, corrosion performance, economic feasibility and reliability of the materials. In addition, the potential influences of process engineering, operating conditions, construction and safe running of the materials to be used must be considered carefully and thoroughly. Since the design of petrochemical plants is mainly centred on the process engineering, the material selection should take the characteristics of these processes into account. Every processing plant may have its own unique processing techniques, which will sometimes result in a phenomenon that the same material may show a quite low corrosion rate in one plant while in another plant its corrosion rate might be quite high. Thus the rational selection of materials for the construction of processing units based on the analyses of the nature of the materials and their actual operating conditions is the key to controlling high temperature corrosion [2].

### 17.1.3 Main progress and prospects

Many models have been developed to explore the mechanisms involved in the high temperature corrosion processes found in the petrochemical industry, such as high temperature oxidation, sulfidation, naphthenic acid corrosion and carburization. The major focus of industrial application-oriented research has been on the following:

1. Many factors can affect high temperature corrosion processes in the petrochemical industry. Current investigations therefore aim to find the potential influences of some major factors on the corrosion processes and rates, such as temperature, velocity of flow and vacuum on high temperature naphthenic acid corrosion, and temperature and active sulfur content on high temperature sulfidation.
2. Because the data collected in laboratories are significantly different from those collected directly from the field corrosion inspection of the processing units, the pilot simulation apparatuses will bridge the gap between laboratory tests and field practices. For example, the dynamic simulation apparatuses for high temperature naphthenic acid corrosion can simulate the temperature, velocity of flow and acid number of the working media in industrial environments and can run continuously.
3. Proper surface modification can significantly enhance the resistance to high temperature oxidation. For example, aluminizing treatment can effectively decrease the high temperature sulfidation and oxidation rates.

## 17.2 High temperature sulfidation

Sulfidation is a type of accelerated corrosion of metals and alloys in sulfur-containing atmospheres and is usually identified both by the presence of sulfur and by the formation of sulfides within the materials. Sulfidation processes normally exhibit high scaling rates, since sulfides normally have quite high defect concentrations in their crystal lattices. On the other hand, some metallic components can form low melting point eutectics. These two characteristics of sulfidation lead to the formation of non-protective scales on and/or deeply in the substrate and cause rapid degradation of the processing equipment operating in the sulfur-containing environments. Sulfur is the most common contaminant present in the chemical and petrochemical processing industries, thus understandably, sulfidation related materials problems will be quite common in these industrial sectors.

### 17.2.1 Sources of sulfur in the petrochemical industry

Crude oil is mainly composed of two elements, H and C. In addition, crude oils may contain sulfides whose content may vary according to the place of production. The total amount of sulfur and sulfides is defined as the sulfur content of the crude oil. Normally the sulfur content can vary from 0.05% to 14%. The main sulfides in crude oil are organic, but small amounts of elemental sulfur and hydrogen sulfide ( $H_2S$ ) may exist. The organic sulfides include mercaptan, alkyl sulfide, bisulfide, sulfoxide, thiophene, etc.

The sulfur in crude oils can be categorized into two major groups, active sulfur and inactive sulfur. Elemental sulfur,  $H_2S$  and low-molecular mercaptan can react with metallic components and cause corrosion problems, so they are generally referred to as active sulfur, while alkyl sulfides, sulfoxide and thiophene will not react with metals directly and are then referred to as inactive sulfur. Although as molecular monomers, inactive sulfur cannot react with metals directly, they can decompose to form some highly corrosive sulfides (e.g.  $H_2S$ ) during petroleum refining processes such as catalytic cracking and hydrofining, to cause severe corrosion of the equipment.

### 17.2.2 Characteristics of sulfidation in the petrochemical industry

High temperature sulfidation can be found in primary, secondary and even downstream chemical processing units. Therefore, corrosion attack associated with sulfur is one of the major corrosion problems and can occur in the whole refining process. The total sulfur content in crude oils is not directly correlated with their corrosivity. Actually the corrosivity is mainly dependent

on the variety, content and stability of the sulfides in crude oils. If the inactive sulfur can be easily converted into active sulfur, crude oils with an extremely low sulfur content can still cause severe corrosion attack on the materials. The conversion processes can take place at both low and high temperature regions of the processing units. Thus, the corrosion problems associated with sulfur can be found in many units and environments. It is also quite difficult to conduct thermodynamic and kinetic studies of these corrosion processes, to find suitable corrosion protection methods and to select corrosion-resistant material, since the corrosive environments and the conversion between different sulfides are extremely complicated.

High temperature sulfidation normally occurs in regions where the temperature is higher than 240°C and sulfur, H<sub>2</sub>S and/or mercaptan can form. In essence, high temperature sulfidation in the petrochemical industry is the corrosion attack associated with active sulfur, such as H<sub>2</sub>S. At about 260°C, the organic sulfides in crude oils can decompose and generate elemental sulfur and H<sub>2</sub>S which can react directly with the metallic components, resulting in severe corrosion on the equipment surfaces [3]. The corrosion can be simply described as in the following formulae:



The low-molecular mercaptan can directly react with metals at temperatures ranging from 350 to 400°C as well. The reaction formula is:



The high temperature sulfidation environments in petroleum processing plants can be grouped mainly into two types: S + H<sub>2</sub>S + RSH and H<sub>2</sub> + H<sub>2</sub>S.

#### *S + H<sub>2</sub>S + RSH high temperature sulfidation environments*

At high temperatures, active sulfur can directly react with metals at any locations in contact with processing media. This sulfidation attack is a kind of uniform corrosion process. H<sub>2</sub>S is the most corrosive compound in these sulfides. The typical corrosive environments are located at the bottom of the towers of the atmospheric and vacuum distillation systems, pipelines, atmospheric heavy oil heat exchangers and vacuum residuum heat exchangers, the bottom of the main fractionating columns of catalytic cracking equipment and the coke retarding equipment.

The high temperature sulfidation rate is mainly dependent on the content of active sulfur in crude oils, and also on the total sulfur content. When the temperature is increased, the reactions between active sulfides and metallic components are accelerated, while at the same time the decomposition of

inactive sulfur increases. When the temperature is higher than 240°C, sulfidation becomes more and more severe with temperature. At temperatures ranging from 343 to 371°C, the decomposition rate of sulfides into H<sub>2</sub>S is the fastest. At 350 to 400°C, H<sub>2</sub>S can further decompose into S and H<sub>2</sub>. S has a stronger activity than H<sub>2</sub>S, leading to more severe attack to the metal surfaces. The corrosion rate may reach its maximum at around 430°C. When the temperature is higher than 480°C, the decomposition of sulfides almost finishes and the corrosion rate decreases.

In high temperature sulfidation, a progressive decrease in corrosion rate could be observed. At the beginning, the corrosion rate is quite high, while after a certain time it will decrease gradually to a constant value. This is related to the formation of FeS protective scales which can inhibit the corrosion processes. However, if the processing media are flowing with a high velocity, the protective scales are prone to detach from the substrate surface; corrosion will then continue on the fresh surface exposed to the highly corrosive environments.

Selection of proper materials is one of the main approaches used to prevent high temperature sulfidation. The materials used to build the bodies of the towers described above are composites of carbon steels with 410SS or 321SS, while the components in the towers should be fabricated with 410SS, 12AlMoV and/or aluminized carbon steels. The typical materials for pipelines are Cr5Mo alloys.

#### *H<sub>2</sub> + H<sub>2</sub>S high temperature sulfidation environments*

H<sub>2</sub> + H<sub>2</sub>S related corrosion normally occurs at temperatures higher than 240°C and can be found in hydrocracking and hydrofining units such as hydrocracking reactors, hydrodesulfurization reactors, catalytic reforming equipment and naphtha hydrofining reactors. About 90–98% of organic sulfur species can be converted into H<sub>2</sub>S in H<sub>2</sub>-rich environments. Therefore the presence of H<sub>2</sub> can accelerate the steel corrosion processes caused by H<sub>2</sub>S. The corrosion products are relatively porous and not similar to the dense and adherent scales formed in hydrogen-free environments. The reason is that in hydrogen-rich atmospheres, atomic hydrogen can penetrate into sulfide scales so that the corrosion processes can develop deeply into the metallic substrates.

In high temperature H<sub>2</sub> + H<sub>2</sub>S environments, temperature and concentration of H<sub>2</sub>S are the key factors affecting the corrosion rate. In engineering design, the corrosion rate is normally evaluated using A.S. Couper and J.W. Gormon charts and then used as the criterion for materials selection. In general, when the design temperature is not higher than 450°C, 18-8Ti stainless steel is acceptable for equipment fabrication.

### 17.2.3 Case studies

#### *Introduction*

Crude oils with low sulfur and low TAN were processed in Refinery A. The sulfur content was below 0.5% and the TAN was below 0.5 mg KOH/g. Two viscosity breaking towers were linked up to form the vacuum residuum viscosity breaking system. The materials used for the construction of pipelines and viscosity breaking towers were 1Cr-5Mo steel and carbon steel, respectively. The operating temperature of this system was around 360°C. According to the field investigation results, corrosion was found mainly on the parts fabricated by carbon steels. Serious thinning due to corrosion was observed on the body of the viscosity breaking towers, top connection pipelines and elbows at the bottom. The top connection pipeline of one viscosity breaking tower caught fire in December 2006 due to perforation on the wall caused by serious corrosion thinning (Fig. 17.1). The whole processing system had to be stopped immediately for repairs.

#### *Failure analysis*

According to the technological process and field investigation, high temperature sulfidation is the main corrosion form of the vacuum residuum viscosity

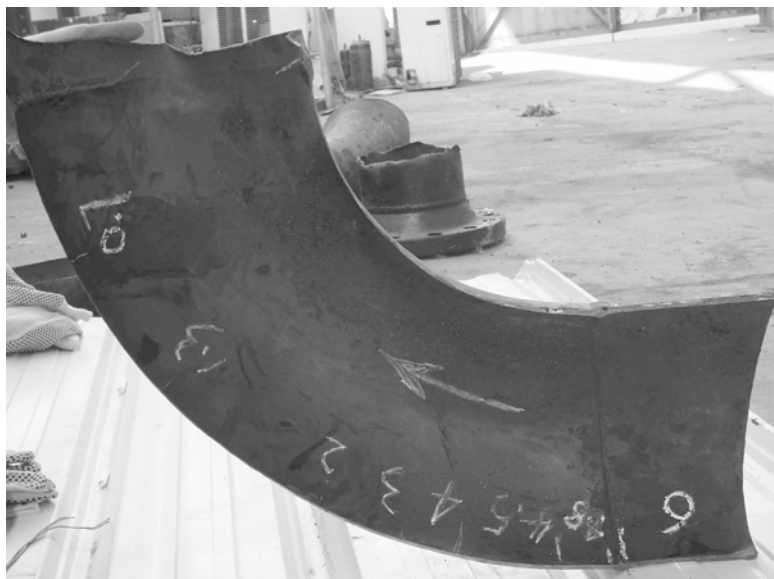


17.1 Corrosion thinning and firing location on top connection pipeline.

breaking system. During the viscosity breaking processes, the inactive sulfur can be converted into active sulfur, and this conversion can significantly increase the corrosivity of the processing media. In addition, the formation of light components and the velocity of flow will exert certain influences on the corrosion processes. It was found that the corrosion of 1Cr-5Mo alloy is slight, while corrosion of carbon steel is very severe (Fig. 17.2). Since 1Cr-5Mo is not resistant to high temperature naphthenic acid corrosion but has a high resistance to high temperature sulfidation, it is then concluded that high temperature sulfidation is the main corrosion form in the vacuum residuum viscosity breaking system. However, naphthenic acid does exist in the vacuum residuum and can still result in corrosion of the equipment.

#### *Corrosion control*

Based on the analysis of the field investigation results, it is suggested that the materials used to build the top connection pipelines and bottom elbows should be upgraded to 321SS and the inner wall of the towers be lined with 0Cr13 (410SS) plate 2–2.6 mm thick. The thickness of the carbon steel materials used to build high temperature oil-containing equipment (240°C, towers and heat exchangers), inlet and outlet of pumps (300°C) should be measured regularly during operation. The welding seams of the pipelines in which wet H<sub>2</sub>S might exist or the processing media are stagnant should be checked carefully.



17.2 Corrosion thinning of bottom elbow.

### 17.2.4 Techniques to control high temperature sulfidation

#### *Material selection*

Selection of candidate materials to be used in  $S + H_2S + RSH$  high temperature sulfidation environments and  $H_2 + H_2S$  high temperature sulfidation environments can be conducted using McConomy charts and A.S. Couper and J.W. Gormon charts, respectively. According to field practice, the high temperature parts ( $>240^\circ C$ ) of the towers can be fabricated using composite plates of carbon steel + 410 or 405 ferrite stainless steels. 410SS has a good corrosion resistance in high temperature sulfidation environments. Furthermore it has a similar coefficient of thermal expansion to carbon steel. So these two materials can be used easily to fabricate composite plates. The components in the towers can be fabricated using 410SS, 12AlMoV and/or aluminized carbon steels. 1Cr-5Mo steel and aluminized carbon steel can be selected to build the pipelines of the heat exchangers. 321SS with an excellent workability can be used as the body material for the towers since it has a better corrosion resistance than 410SS and 405SS. However, 321SS has a lower resistance to stress corrosion cracking than 410SS and 405SS, so it is important to control polythionic acid corrosion. 1Cr-5Mo is generally suitable for the construction of pipelines of the heat exchangers. However, this material might suffer serious erosion at the elbows of the oil transition lines, so that alternatively 316LSS can be used for these elbows. In high temperature  $H_2S + H_2$  environments, when the design temperature is not higher than  $450^\circ C$ , the corrosion rate of 18-8Ti austenite stainless steel is acceptable for industrial applications.

There are some disadvantages of using the above-mentioned charts to evaluate the corrosion rate of a special material used in industrial environments and to give guidance on field corrosion protection. For example, in a McConomy chart the corrosion rate is roughly calculated based on the total sulfur content and the temperature of the distillate oils and the nature of materials. The potential influences of the composition, the flowing state of the distillate oils, the active sulfur content, the composition of the sulfides, the decomposition of the organic sulfides and the total acid number on the high temperature sulfidation rate are not considered. If the flow velocity of the distillate oils is very high, the integrity of the protective FeS scales on the surface will be damaged and then corrosion will be accelerated, since fresh metallic surfaces will be continuously exposed to the corrosive media. The acid number will also affect the stability of the FeS scales. The content of the active sulfur is directly related to the content of corrosive media in crude oils. Some crude oils may have a high total sulfur content but a low content of active sulfur, and therefore the sulfidation rate is relatively low, while in other crude oils the total sulfur content is low but the active sulfur content is

quite high, leading to high corrosivity. As discussed above, the materials selection based on the engineering charts and field experiences may not always be reliable for the design and construction of industrial processing units. It is then important to monitor and inspect the corrosion of equipment during operation to prevent catastrophic consequences.

#### *Field monitoring and inspection of high temperature sulfidation*

Proper field monitoring and inspection techniques can be used to measure the real corrosion rate, to find safety risks on time and to avoid corrosion accidents. The field monitoring and inspection techniques normally include weight-loss coupons, electrical resistance probes, ultrasonic wall thickness measurements, infrared thermal imaging systems, etc. Ultrasonic wall thickness measurement is widely used to monitor the general and erosion corrosion rates of the equipment and pipelines in crude oil processing plants.

#### *Process control*

The location and rate of high temperature sulfidation can vary depending on changing technological processes and fluctuating operating conditions; therefore, it is possible to inhibit corrosion attacks by process control. For example, sulfidation of the high temperature parts could be inhibited by decreasing the total sulfur content in crude oils. In general, it is believed that when the sulfur content is lower than 0.5%, high temperature sulfidation will be very slight. Thus crude oils with a high sulfur content could be mixed with crude oils with a low sulfur content to obtain oils with a sulfur content lower than 0.5%. In addition, it is possible to confine the high temperature sulfidation problems within certain locations. In these regions, the building materials can be upgraded to those with a higher corrosion resistance to sulfidation, so that the total material costs can be significantly decreased.

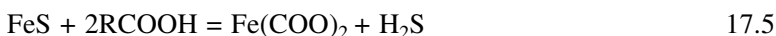
### **17.3 High temperature naphthenic acid corrosion**

#### **17.3.1 High temperature corrosion caused by naphthenic acid**

Naphthenic acid is a kind of organic acid in crude oils and has a saturated ring structure. Its content is typically measured and indirectly expressed by non-aqueous titration with potassium hydroxide (mg KOH per 100 ml for clean oils) or total acid number (TAN, as milligrams of KOH required to neutralize the acid in one gram of oil). Naphthenic acid in crude oils is a rather complex mixture. Its molecular weight ranges from 180 to 700, mainly from 300 to 400 [4].

### 17.3.2 Characteristics of high temperature naphthenic acid corrosion

During the refining processes, naphthenic acid will be heated, distilled, vaporized and condensed. It then can dissolve into the distillate oil which has a similar boiling point and result in corrosion problems. Naphthenic acid has the typical characteristics of monobasic aliphatic acid and the corrosion processes will mainly take place in liquid phases. In general, the naphthenic acid corrosion rate is relatively low when the temperature is lower than 240°C. At temperatures higher than 240°C, especially in water-free environments, corrosion becomes very serious. The reactions between naphthenic acid and metal can be described by the following equations:



Iron naphthenate, the product of naphthenic acid corrosion, is oleo-soluble; therefore, the corroded metal surfaces are normally clean and free of scales. In the regions with high temperature and high flow velocity, naphthenic acid corrosion will result in the formation of shape-edged streamline grooves along the flow direction. In the areas with low flow velocity, shape-edged pits will be formed. Since  $\text{Fe}(\text{COO})_2$  can dissolve into oils and then be removed easily by the flowing media, it is difficult to form protective scales on the metal surface. Even  $\text{FeS}$  formed on the surfaces can react with naphthenic acid: fresh metallic surfaces will be exposed to the corrosive media and corrosion can proceed continuously [5].

### 17.3.3 Major factors influencing high temperature naphthenic acid corrosion

#### *Total acid number (TAN)*

TANs of the crude oil and the distillate oil are the key factor in evaluating high temperature naphthenic acid corrosion. It is generally accepted that when the TAN is higher than 0.5 mg KOH/g, high temperature naphthenic acid corrosion will occur. Since naphthenic acid exists together with other oils that have similar boiling points, only the actual acid number of the distillate oils can determine the corrosivity and the corrosion rate. Under atmospheric distillation conditions, the highest acid number of the distillate oil will be shown in the temperature range of 371–426°C, and at 260°C in vacuum distillation towers [6].

### *Temperature*

High temperature naphthenic acid corrosion can normally be observed at temperatures ranging from 230°C to 400°C. Some of the literature has reported two peaks on the corrosion rate–temperature curves, the first peak at 270–280°C and the second at 350–400°C.

### *Vaporization and condensation*

TAN and corrosivity of the distillate oil can change during vaporization and condensation processes. Among the components in the distillate oils, naphthenic acid can vaporize and condense preferentially; this makes the TAN of the condensed oil increase significantly. The condensed liquid oil drops are flowing at high speed. Iron naphthenate formed on the surface will then be washed away quickly. As a result, shape-edged pits, holes and streamline grooves are formed on the clean surfaces.

### *Velocity and state of flow*

Velocity of the flowing media is one of the key factors in high temperature naphthenic acid corrosion. At a certain temperature, there appears to be a critical velocity for each particular material. The corrosion rate is very low when the velocity of flow is below this critical value. According to practical experience, high temperature naphthenic acid corrosion will be severe at the locations where the velocity of flowing media is high, or the flowing state is sharply changed, such as at elbows, pump barrels and locations where the protective cases of the thermocouples are installed [7].

### *Sulfur content*

The sulfur content in the oil influences the high temperature naphthenic acid corrosion process as well. At elevated temperatures, organic sulfides will decompose to release H<sub>2</sub>S which can react with metals to form FeS covering the surface. The presence of this scale can partially inhibit the corrosion caused by naphthenic acid but cannot provide full protection. It had been reported that alloys with a high Mo content are needed to build the equipment for processing the crude oils imported from the Gulf states into the USA. High Mo-containing alloys might not be needed for processing of the high sulfur-containing crude oils exploited from California. These results then demonstrated that a high sulfur content can inhibit the naphthenic acid corrosion, i.e., an increase of sulfur content may increase the critical acid number to initialize naphthenic acid corrosion.

## 17.4 Case studies in high temperature naphthenic acid corrosion

### 17.4.1 Crude oils with low sulfur and high total acid number (TAN)

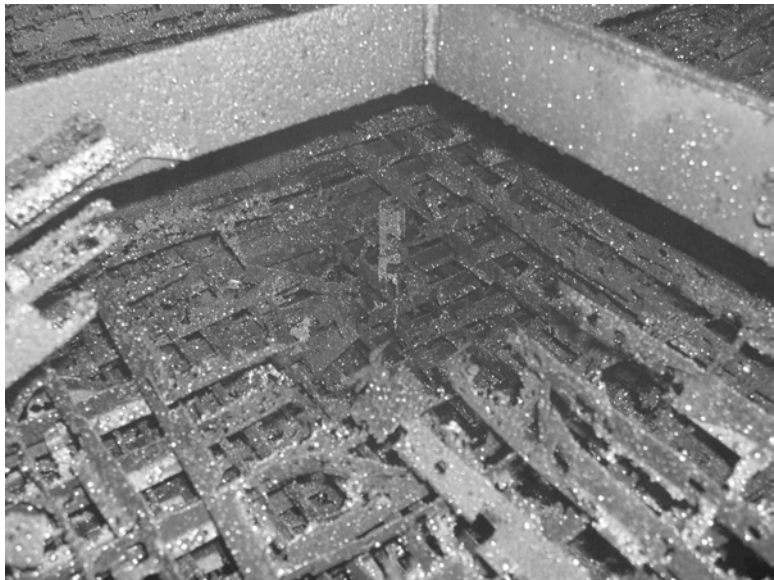
#### *Introduction*

Heavy crude oils with low sulfur and high TAN were processed within the atmospheric and vacuum units in Refinery B. The average TAN was about 3.0 mg KOH/g and the sulfur content was lower than 0.5%. It was found that severe corrosion occurred in the vacuum distillation systems during the inspection carried out in May 2006. The materials used to fabricate the wall of the third and fourth floors of the tower were carbon steel and 316L stainless steel. The inspection revealed that a lot of pits were formed on the inner wall as shown in Fig. 17.3.

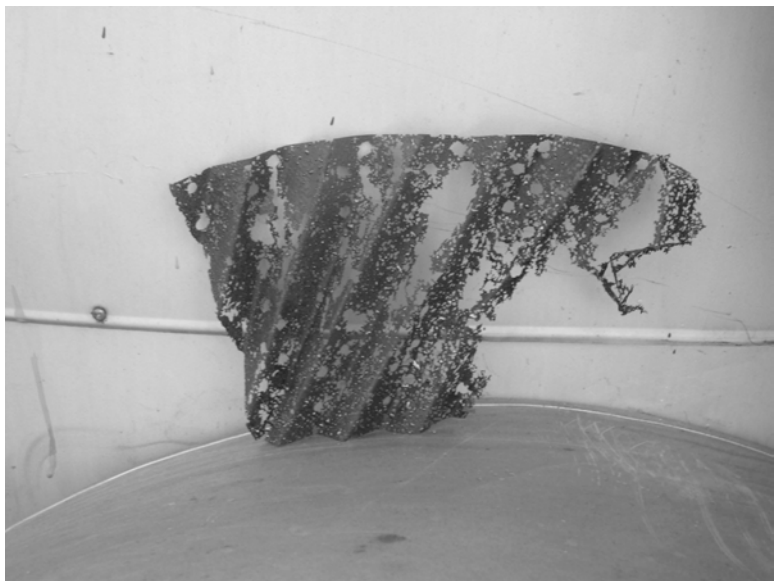
The packing materials (316LSS) of the third and fourth floors suffered severe corrosion attack. After one and a half years, a big hole (400 mm in diameter and 500mm in depth) was observed on the fourth floor of the tower due to the collapse of the packing materials (Figs 17.4 and 17.5). At the same time, corrosion of the oil collection tank on the third floor was severe as well (Fig. 17.6).



17.3 Corrosion pits on the inner wall of the tower wall on the third floor.



17.4 A big hole induced by severe corrosion on the fourth floor.



17.5 Corrosion thinning of 316LSS on the fourth floor.

#### *Failure analysis*

According to the field inspection, the high TAN of the crude oil is the main reason responsible for the severe corrosion of the vacuum distillation tower.



17.6 Corrosion of the oil collection tank on the third floor.

The average TAN of the crude oil is around 3.0 mg KOH/g and the density is 0.92 g/cm<sup>3</sup>, indicating that the TAN of the vacuum distillate oil might be quite high, resulting in an increase of the concentration of the corrosive medium and then an increase of naphthenic acid corrosion rate. Secondly, protective FeS scales cannot be formed on the metal surfaces since the sulfur content in the crude oil is relatively low. Thirdly, the vacuum distillation system is in the state of negative pressure operation; this will result in the right shift of the reaction equilibrium, leading to accelerated corrosion. Lastly, the electric desalting and alkali injecting processes might not work very well; therefore, the concentration of the corrosive media in the oil cannot be decreased to a low level to decrease the corrosion rate. The above-mentioned factors work together to induce severe corrosion attacks to the vacuum distillation system.

#### *Corrosion control*

The packing materials for the third and fourth floors and the oil collection tank on the third floor should be completely changed. The thickness of the wall of the third and fourth floors should be measured regularly using an ultrasonic technique. The desalting and alkali injection processes should be improved to decrease the content of the corrosive media in the oils to inhibit the corrosion process.

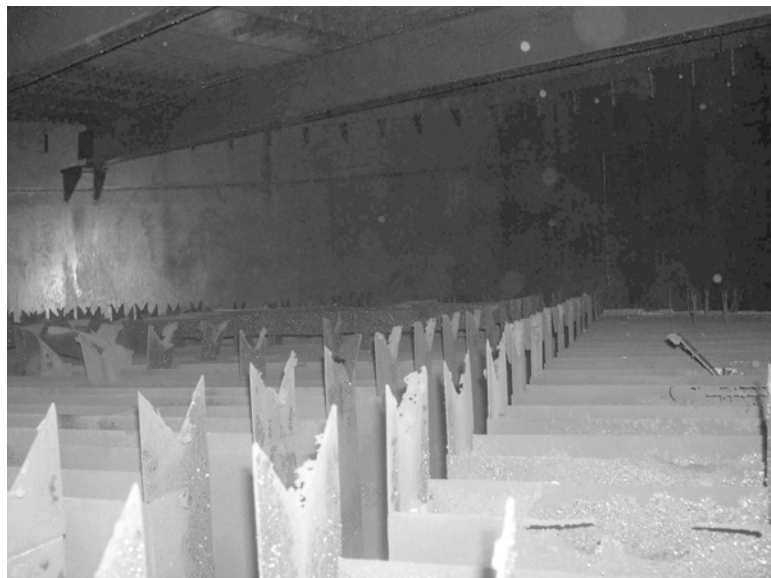
### 17.4.2 Crude oils with high sulfur and high total acid number (TAN)

#### *Introduction*

Heavy crude oils with high sulfur and high TAN were processed by Refinery C. The average TAN was 1.0 mg KOH/g, the sulfur content was 0.8% and the density was 0.9 g/cm<sup>3</sup>. It was found that severe corrosion had occurred in the vacuum distillation system during inspection in October 2006. The packing materials and components inside the tower are made of 304SS. Collapse of the packing materials on the second floor due to erosion was observed (Fig. 17.7). A lot of holes were formed on the bottom of the oil collection plates of the second floor. The packing materials on the third floor were completely corroded and washed away. Oil collection plates and supporting plates in the oil collection tank on the third floor suffered severe attack; actually only one plate was left, the others having been completely destroyed by corrosion (Fig. 17.8). The top of the gas rising tube suffered from severe erosion-corrosion and the tube wall looked like thin paper. About one half of the packing materials on the fourth floor were corroded away. No corrosion was found on the bottom and the feeding section of the vacuum distillation tower.



17.7 Packing materials remained on the second floor.



17.8 Corrosion of the oil collection tank on the third floor.

### *Failure analysis*

According to the field investigation, use of low grade materials is the main reason responsible for the severe corrosion attack which occurred in the vacuum distillation system in this processing plant. According to practical experience, 316LSS should be selected for the fabrication of the tower wall, packing materials and some oil collection tanks of the vacuum distillation system (especially the second, third and fourth floors) processing crude oils with high TANs. However, 304L stainless steel was used on these locations in Refinery C. Because 304L has a relative low resistance to these corrosion processes, severe attack occurred. In addition, the vacuum distillation system was running with loads higher than the design limitation, and the velocity of the processing media was very high. These two factors would also accelerate the corrosion processes.

### *Corrosion control*

All the packing materials on the second, third and fourth floors of the vacuum distillation system should be upgraded to 316LSS. The oil collection tank on the third floor should be changed. The load and the velocity of flow must be decreased by process control to decrease the corrosion rate.

### 17.4.3 Techniques to control high temperature naphthenic acid corrosion

#### *Material selection*

The corrosion rate of the materials used in high temperature naphthenic acid environments can be evaluated using API581. However, the influences of velocity and state of flow are not fully taken into account, leading to a large difference between the corrosion rates obtained from this method and from the field test. During operation therefore, corrosion rate of the equipment should be monitored regularly to ensure that the processing units can run safely [8].

Carbon steels can be used for parts where the operating temperature is lower than 220°C. Both Cr-5Mo and Cr-9Mo have a better corrosion resistance than carbon steels. However, when the velocity of flow is high, they will suffer serious corrosion attack. Thus they are normally the materials used for the radiant tubes in heating furnaces, pipelines and heat exchangers. Currently, Mo-containing 316SS and 317SS (>2.5% Mo) are the best materials against high temperature naphthenic acid corrosion. However, in the regions with high-speed flowing media or strong impacts, even 316SS will suffer severe attack [9, 10].

Surface modification is one of the effective ways to improve the resistance of carbon steels against high temperature naphthenic acid corrosion. A dense and protective Al<sub>2</sub>O<sub>3</sub> film can form on the surface of the aluminized carbon steels after thermal oxidation treatment. This alumina scale is stable and shows excellent resistance in many corrosive media. In addition, it has a high hardness and a high wear resistance. It had been proven that aluminized carbon steel tubes have good erosion resistance when used at locations with heavy oils at high temperatures. Therefore, some components in the vacuum distillation towers can be built by using carbon steels with suitable aluminizing treatments.

#### *Process control*

The total acid number (TAN) of crude oils can be decreased through suitable mixing processes, i.e., addition of crude oils with a low TAN into crude oils with a high TAN may obtain a mixed crude oil with a low TAN. If the TAN of this mixed crude oil is lower than the critical value for the initialization of high temperature naphthenic acid corrosion, the problems associated with this type of corrosion could be partially solved.

Addition of a small amount of dilute caustic solution into the oils can neutralize naphthenic acid and then is the most economical way to control high temperature naphthenic acid corrosion. However, a disadvantage of this method is that salt corrosion of furnace tubes may become serious. Furthermore,

this may deactivate the catalysts used in the hydrocracking equipments. Hence, the addition of caustic solution might be employed in crude oil processing plants which have no hydrocracking equipment.

The addition of oleo-soluble inhibitors can decrease the high temperature naphthenic acid corrosion rate at 316–400°C. These inhibitors can form adherent and protective thin films on the inner surfaces of the refinery process units to prevent the exposure of metallic surfaces to the corrosive media.

Extraction of naphthenic acid from the oils can completely solve the corrosion problems associated with this acid. It had been reported that naphthenic acid can be transferred into the water phase by using an aqueous solution of caustic soda. This is accomplished by converting the acid into basic salt that is preferentially soluble in water. At present, this method is successful only in the laboratory; practical application in crude oil processing plants has not been reported.

#### *Flow velocity and state control*

High velocity of flow and occurrence of turbulence should be avoided in engineering design and practical operation. The diameter of the tubes should be large enough to decrease the flowing velocity of the processing media. For example, the speed in the low velocity oil transition line should be controlled to be lower than 62 m/s, while in the high velocity oil transition line the speed should not be higher than 94 m/s.

### **17.5 High temperature corrosion of furnace radiant tubes**

#### 17.5.1 High temperature corrosion type of furnace radiant tubes

##### *Introduction*

Heating furnaces are commonly used in petrochemical plants. The working temperature of these heating furnaces ranges from 200 to 1000°C. The temperature of atmospheric and vacuum heating furnaces, coking furnaces and ethylene crackers is 300–400°C, 650°C and 900°C, respectively, and the radiant tubes used in these furnaces the typical examples suffering from various high temperature corrosion problems in refinery process units. The high temperature corrosion of furnace radiant tubes mainly includes high temperature oxidation, sulfidation, naphthenic acid corrosion, carburization and decarburization, coking and creep, etc.

Besides the high temperature corrosion processes (such as oxidation, sulfidation and ash deposition) that occur on the outer wall of furnace radiant tubes, high temperature sulfidation, naphthenic acid corrosion and coking on

the inner wall of the tubes should be considered as well. High temperature carburization and decarburization can occur on both the outer and inner walls of the furnace radiant tubes. The form and location of high temperature corrosion in the furnace radiant tubes may vary with temperature. For example, high temperature sulfidation and naphthenic acid corrosion on the inner wall of tubes are mainly responsible for the failure of atmospheric and vacuum heating furnaces. For coking furnaces, high temperature sulfidation on the inner wall of tubes and high temperature oxidation on the outer wall of tubes are the main corrosion processes observed, while for the ethylene crackers, high temperature coke deposition on the inner wall of tubes and oxidation of the outer tube wall are the main high temperature corrosion forms.

#### *High temperature oxidation*

At temperatures above 300°C, oxide scales are observable on the carbon steel surfaces. The oxidation rate increases greatly with temperature. When the temperature is higher than 570°C, the oxidation rate will be very high. The oxides formed are FeO, Fe<sub>3</sub>O<sub>4</sub> and Fe<sub>2</sub>O<sub>3</sub>, and their structures are highly dependent on the oxidation temperature. At temperatures lower than 570°C, the oxide scale does not have FeO and is composed of Fe<sub>3</sub>O<sub>4</sub> and Fe<sub>2</sub>O<sub>3</sub>. Fe<sub>3</sub>O<sub>4</sub> and Fe<sub>2</sub>O<sub>3</sub> have complex crystal structures and are relatively dense. Diffusion through this oxide scale is relatively difficult and slow. In addition, this oxide scale normally is adherent to the underlying substrate. Therefore, this oxide scale can, to a certain extent, protect the underlying substrate from oxidation. At temperatures higher than 570°C, the oxide scale will be a mixture of Fe<sub>3</sub>O<sub>4</sub>, Fe<sub>2</sub>O<sub>3</sub> and FeO, with FeO as the dominant oxide. FeO has a cubic crystal structure which has many vacancies. Oxygen atoms can easily transport through this porous oxide scale and arrive at the oxide scale/metal interface to form new oxides. The oxidation rate increases significantly with temperature. As the oxide scales become thicker, they are prone to cracking and spallation.

Formation of FeO therefore should be inhibited. Addition of Cr, Si and Al alloying elements can improve the high temperature oxidation resistance of steels. Cr-containing steels are widely used in petrochemical plants since a dense Cr<sub>2</sub>O<sub>3</sub> scale can effectively prevent the development of oxidation. For example, Cr25-Ni20 HK steel is selected for the converting tube, Cr25-Ni35 HP steel for the ethylene cracking tube and 2½ Cr-1Mo for the radiant tube in heat exchangers.

#### *High temperature sulfidation and naphthenic acid corrosion*

High temperature naphthenic acid corrosion can only happen at temperatures below 500°C since naphthenic acid will completely decompose when the

temperature is higher than 500°C. Corrosion associated with naphthenic acid is serious for the radiant tubes in the vacuum heating furnaces, while for the coking furnaces and ethylene crackers, this type of corrosion can be neglected. High temperature sulfidation on the radiant tubes in the coking furnace is more serious than that on the tubes in the atmospheric and vacuum heating furnaces. Coke deposition is quite serious on the inner wall of the cracking tubes in the ethylene crackers, thus it is not necessary to consider sulfidation attack.

### *High temperature carburization and decarburization*

Carburization is observed in petrochemical processes such as ethylene cracking. Carburization problems are common in equipment exposed to carbonaceous atmospheres. Free carbon is formed through the decomposition of carbides (such as CO or hydrocarbon) on steel surfaces at high temperatures. These free carbons can destroy oxide scales and penetrate into the steel substrate to form carbides. With the presence of oxygen in the atmosphere, pits will form on the surfaces. The corrosion products are oxides, carbides and graphite in the form of silk, plate and powder. These corrosion products can be blown off at areas with high gas velocities, resulting in severe corrosion. Carburization can also lead to cracking, creep fracture and fatigue of metallic components.

Decarburization of steel results from the reactions between the carbides in the steel and gaseous species in the atmosphere. Decarburization on the steel surface will decrease the surface hardness and fatigue strength. The reactions are as follows:



### *Coke deposition*

During the cracking processes of hydrocarbon, polymerization and condensation reactions may occur to form coke deposits on the inner surface of ethylene cracking tubes. The coking rate increases with the extent of pyrolysis reaction, the partial pressure of hydrocarbon and the mass of the source oil. Coke deposition will lead to many harmful consequences to the tubes: lower thermal conduction, higher wall temperature, higher energy consumption and shorter service life. In addition, the coke deposits will decrease the inner diameter of the tube and then increase the pressure difference. This will decrease the yielding efficiency of alkenes or shorten the cycle of operation.

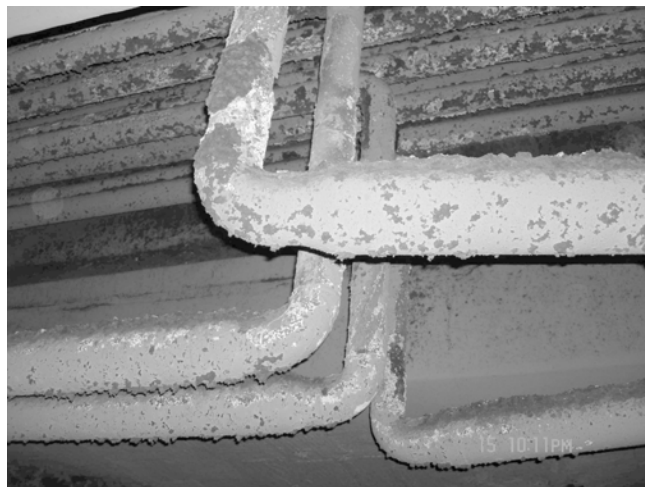
### 17.5.2 High temperature corrosion of furnaces in atmospheric and vacuum distillation systems (furnace radiant tubes work at about 300°C)

Heating furnaces in the atmospheric and vacuum distillation systems are normally working at temperatures ranging from 300°C to 400°C. The processing medium flowing in the radiant tubes is distillate oil. Since sulfur and naphthenic acid exist in this distillate oil, high temperature naphthenic acid corrosion and sulfidation become serious when the sulfur or naphthenic acid content is high. The fuel used for the heating of the tubes is heavy oil or gas with a trace amount of sulfur. During combustion, SO<sub>2</sub> and SO<sub>3</sub> will form due to the presence of oxygen. High temperature sulfidation then occurs on the outer wall of the furnace radiant tubes. The sulfides inside the furnace tube are H<sub>2</sub>S, S and mercaptan, all of which will contribute to the sulfidation attacks on the inner wall. The sulfides in the tube have a higher concentration than those outside the tube. Moreover H<sub>2</sub>S and mercaptan are more corrosive than SO<sub>2</sub> and SO<sub>3</sub>. Therefore, the inner wall of the tubes will suffer from more serious corrosion than the outer wall of the tubes. Furthermore, corrosion induced by the condensation of SO<sub>2</sub> and SO<sub>3</sub> at locations having a temperature close to the dewpoint should be considered as well.

More attention should be paid to high temperature naphthenic acid corrosion when sulfur and naphthenic acid exist together in the distillate oil, because the rate of high temperature naphthenic acid corrosion is much higher than that of sulfidation. High temperature naphthenic acid corrosion on the tubes in the irradiation chamber of the vacuum heating furnace is more serious than that on the tubes in the atmospheric heating furnace. Correspondingly, the materials used for the radiant tubes in the vacuum heating furnace should be carefully selected.

The operating temperature of the radiant tubes in the irradiation chambers of the atmospheric and vacuum heating furnaces is around 300–400°C. 1Cr-5Mo is used and shows a relatively low high temperature oxidation rate. Combustion products will adhere onto the tube surfaces to form an ash deposit which can decrease the heat transfer efficiency when the ash is quite thick (Fig. 17.9).

The candidate materials used for the tubes in the irradiation chamber of the atmospheric and vacuum heating furnaces can be carbon steel, 1Cr-5Mo, 1Cr-9Mo, 321SS and 316LSS. To select the suitable materials, the influences of corrosion attacks should be considered in the sequence of high temperature naphthenic acid corrosion, sulfidation and oxidation. Currently, carbon steel is still selected for the radiant tubes in the atmospheric heating furnaces used for the processing of low sulfur and low TAN crude oils. 1Cr-5Mo is widely used to fabricate radiant tubes in atmospheric and vacuum heating furnaces for the processing of high sulfur and low TAN crude oils, or in atmospheric



17.9 Ash deposition and oxidation in vacuum heating furnace.

heating furnaces for the processing of low sulfur and high TAN, or high sulfur and high TAN, crude oils. 1Cr-5Mo, 321SS and 316LSS are widely used in vacuum heating furnaces for the processing of crude oils with low sulfur and high TAN or with high sulfur and high TAN.

#### 17.5.3 High temperature oxidation of coking furnaces (furnace radiant tubes work at about 500°C)

The typical outlet temperature of the coking furnace is around 500°C and the medium flowing in the tube is vacuum residuum. High temperature naphthenic acid corrosion is slight, because naphthenic acid will decompose above 500°C, but sulfidation might occur on the inner wall of the radiant tubes and should be taken into account during material selection. 1Cr-5Mo is widely used for the tubes in the irradiation chamber of the coking furnace. The temperature on the outer wall of the tubes might be higher than 500°C, which is very close to the maximum applicable temperature of 1Cr-5Mo. During burning the coke deposits or when operation conditions fluctuate, the temperature on the outer wall of the tubes might be increased. If so, oxidation of the outer wall of the tubes might become more severe. This issue must be fully considered.

#### 17.5.4 High temperature corrosion of ethylene crackers (furnace radiant tubes work at about 900°C)

The outlet temperature of the ethylene crackers is typically around 900°C and naphtha oil is flowing inside the tubes. Ethylene cracker is the key

equipment of ethylene processing units. Coke is the by-product of the naphtha cracking process and coking is one of the main problems which prevent the long-term running of ethylene crackers. The ethylene crackers must be stopped to clean the coke deposits on the furnace radiant tubes after every 45–60 days, or even every month if the operating conditions are not well controlled. High temperature carburization can happen after coke deposition on the surfaces of the furnace tubes and will cause tube failure.

#### 17.5.5 Control of high temperature oxidation of furnace radiant tubes

Proper material selection is the key measure to control high temperature corrosion of the heating furnaces in the atmospheric and vacuum processing units. 1Cr-5Mo and 321SS should be selected to fabricate the furnace radiant tubes in the vacuum heating furnaces if the TAN of the crude oil is higher than 0.5 mg KOH/g. If the TAN is greater than 1.0 mg KOH/g, 316LSS can be used for the radiant tubes near the outlet of the furnace. Additionally, process control can be used to inhibit high temperature sulfidation and naphthenic acid corrosion of the radiant tubes in the atmospheric and vacuum heating furnaces. This can be done by mixing crude oils with different TANs or by adding caustic solutions to neutralize acidic components, etc.

1Cr-5Mo and 1Cr-9Mo can be used as the coking furnace tube materials. High temperature sulfidation on the inner wall of the furnace tubes and oxidation on the outer surface can be effectively decreased through proper surface treatment. Aluminizing treatment can effectively increase the sulfidation and oxidation resistance, and prolong the service life of the coking furnace tubes.

High temperature alloys, such as HK alloys and HP alloys, are normally selected for the radiant tubes in the ethylene crackers. High temperature coke deposition and carburization are the main factors responsible for the failure of radiant tubes. Four techniques are commonly used to increase coke deposition resistance:

1. After cleaning coke deposits, pretreatment solutions containing sulfur and/or phosphorus are added into the steam flowing through the radiant tubes before operation [11,12]. A protective sulfide layer can then be formed on the inner wall of the tubes to prevent catalytic coke formation.
2. During decoking treatment, decoking agents are added into the steam to shorten the decoking time period [13]. After this treatment, coking inhibitors are added into the flowing media containing hydrocarbon and steam. The inhibitor deposits onto the tube surface to form a protective coating to reduce coke deposition during normal operation.

3. Ceramic and/or glass-like coatings can be formed by heating the silicate pastes painted onto the inner wall of the tubes. These coatings can completely cover the metallic surfaces and then decrease the probability of formation of coke deposits. The main composition of the coating is  $K_2O$ ,  $SiO_2$  and  $Al_2O_3$ , etc.
4. An alloy layer can be formed on the tube surface through alloying treatment [14]. This alloy layer has low contents of Ni and Fe. Because Ni and Fe are the catalyst of coking reactions, the alloy layer with reduced contents of Ni and Fe can have a higher resistance to coke deposition on the tube surface.

## 17.6 References

1. Jorge L, 'The Iron Powder Test for Naphthenic Acid Corrosion Studies', *Corrosion 1999, The NACE International Annual Conference and Exposition*, Houston, TX, NACE International, 1999.
2. Brain E, Leonar E, Lagoven S A, Venezuela S A, 'Materials Upgrading History of an HDS Complex', *Corrosion 1996, The NACE International Annual Conference and Exposition*, Houston, TX, NACE International, 1996.
3. John R C, Young A L, 'New Understanding on Corrosion of Alloy in High-Temperature Sulfidizing Gases', *Corrosion 2002, The NACE International Annual Conference and Exposition*, Houston, TX, NACE International, 2002.
4. Nugent M J, Dobis J D, 'Experience with Naphthenic Acid Corrosion in Low TAN Crudes', *Corrosion 1998, The NACE International Annual Conference and Exposition*, Houston, TX, NACE International, 1998.
5. Saadedine T, 'Critical Review of Naphthenic Acid Corrosion', *Corrosion 1999, The NACE International Annual Conference and Exposition*, Houston, TX, NACE International, 1999.
6. Dove D, Messer B, Phillips T, 'An Austenitic Stainless Steel, Resistant to High Temperature Creep and Naphthenic Acid Attack in Refinery Environments', *Corrosion 2001, The NACE International Annual Conference and Exposition*, Houston, TX, NACE International, 2001.
7. Smart N R, Rance A P, 'Laboratory Investigation of Naphthenic Acid Corrosion under Flowing Conditions'. *Corrosion 2002, The NACE International Annual Conference and Exposition*, Houston, TX, NACE International, 2002.
8. Lagoven S A, 'Naphthenic Acid Corrosion by Venezuelan Crudes', *Corrosion 1997, The NACE International Annual Conference and Exposition*, Houston, TX, NACE International, 1997.
9. Reyes F A, Reyes H, Saucedo E, 'Effect of the Mexican Crude Oil Mixture (Heavy/Light) Corrosivity in 5%Cr, 9%Cr, 12%Cr-8%Ni, 18%Cr-8%Ni Stainless Steel', *Corrosion 2001, The NACE International Annual Conference and Exposition*, Houston, TX, NACE International, 2001.
10. Slavcheva E, Shone B, 'Factors Controlling Naphthenic Acid Corrosion', *Corrosion 1998, The NACE International Annual Conference and Exposition*, Houston, TX, NACE International, 1998.
11. Gandman Z, 'Method for Removing and Suppressing Coke Formation during Pyrolysis', *US patent 6,228,253*, 2001.

12. Greene M E, Morena R, 'Potassium Silicate Frits for Coating Metals', *US patent 6,423,415*, 2002.
13. Benum L W, Oballa M C, 'Process of Treating a Stainless Steel Matrix', *US patent 6,436,202*, 2002.
14. Petrone S S A, 'Surfaced Alloyed High Temperature Alloys', *US patent 6,268,067*, 2001.

## Oxidation processing of electronic materials

---

Z LI and W GAO, The University of Auckland,  
New Zealand

### 18.1 Introduction

Electronic materials are the materials used in electrical industries, electronics and microelectronics, and the substances for the building up of integrated circuits, circuit boards, packaging materials, communication cables, optical fibres, displays, and various controlling and monitoring devices. Discovery, development and application of new materials are the robust power for the development of human society. The history of human civilization, to a certain degree, could be regarded as a history of materials evolution. Modern society, especially since World War II, is enjoying the rapid development of novel electronic materials, which are the solid material bases of many creative and high-tech products and vastly change our lifestyle and vision. For example, extensive studies with GaN have allowed the development and commercialization of green and blue light emitting diodes (LEDs) with efficiency, brightness and longevity sufficient for displays, traffic lights and indicator lights in automobiles [1–3], while the continuous downscaling of electronic devices in communication systems allows us to enjoy the powerful and exquisite mobile phones in daily life.

Processing of electronic materials mainly includes crystal growth, epitaxy, lithography, deposition, annealing, doping (diffusion or ion implantation), etching (dry or wet) and metallization. For some of the processes, masks, insulating layers or diffusion barriers are needed, and these rely on the formation of oxides, nitrides or oxynitrides on the material surfaces. In integrated circuits, the fundamental electronic switching device is the (complementary) metal oxide semiconductor field effect transistor, which has at least three terminals – the gate, source and drain [4]. The gate electrode is separated electrically from the source and drain by a thin dielectric film, which is commonly SiO<sub>2</sub>. Formation of this film could be accomplished by using sputtering, evaporation, chemical vapour deposition or atomic layer deposition. Thermal oxidation is also used to grow the gate dielectric films due to its ease in processing control, though interactions of metals or alloys

with oxidizing species such as O<sub>2</sub>, H<sub>2</sub>O, CO/CO<sub>2</sub>, SO<sub>2</sub>/SO<sub>3</sub> or N-containing atmospheres will lead to the formation of oxides, carbides, sulphides and/or nitrides, resulting in many problems in association with material degradation at high temperatures [5]. However, oxidation processes under well-controlled conditions have been finding more and more applications in the modern electronics industry for surface cleaning, film growth, preparation of new materials and building up of novel structures for devices [6–9].

## 18.2 Oxidation processing in semiconductors

### 18.2.1 Oxidation of silicon, Si

To date, Si is still the backbone of the modern semiconductor industry. Its dominant role is the result of its fundamental advantages over its competitors: (i) availability in a wide variety of sizes and shapes; (ii) mature material preparation and property control; (iii) native oxide films on its surface; and (iv) compatibility to planar integrated circuit technology. In 2004 a grand total of about 4,000,000 m<sup>2</sup> of polished Si wafers was produced, equivalent to about  $1.25 \times 10^8$  200 mm wafers. This gives us a rough idea how big the industry is.

The Si surface (termination of the regular crystalline lattice) has a large number of unsatisfied chemical bonds, i.e., dangling bonds ( $\sim 10^{15}/\text{cm}^2$ ), which give rise to states within the forbidden gap of the semiconductor [10]. The unsatisfied orbitals could be filled from electrons on the semiconductor surface, thus the states act as acceptor states which when filled leave the surface in short supply of electrons and hence *p* type. Extensive studies show that both donor and acceptor states are found on the Si surface [11–13]. Because of the existence of these surface states, the electronic properties of devices (such as bipolar or field effect devices) are profoundly affected. To construct high quality electronic devices, it is therefore necessary to reduce and eliminate the surface states. A film of SiO<sub>2</sub> on the Si surface could tie up the dangling bonds and then decrease the density of the surface states [14]. In addition, SiO<sub>2</sub> has many other advantages such as low thermal expansion coefficient, high resistivity, excellent dielectric strength, large band gap and high melting point. It can act as a mask to common diffusing species, can be etched with HF leaving Si unaffected, is capable of forming a nearly perfect electrical interface with its substrate, and is stable down to 10<sup>-9</sup> torr at T > 900°C. These special characteristics of SiO<sub>2</sub> make it probably a more important material in Si technology than Si itself and also are in large part responsible for enabling the microelectronics revolution.

SiO<sub>2</sub> films could be applied onto the Si surface with many techniques to fulfil the surface electronic passivation purpose. However, a comparison of the different ways to prepare SiO<sub>2</sub> on Si (CVD, PVD and thermal oxidation)

showed that thermal oxidation resulted in the lowest surface state density [15]. The native oxide,  $\text{SiO}_2$ , of nanometre thickness, could grow on the clean Si surface in a few hours or days, depending on the real surface conditions. In the semiconductor industry, growth of  $\text{SiO}_2$  with superior electrical qualities relies largely on the thermally activated process, i.e., oxidation. Thermal oxidation growth of  $\text{SiO}_2$  on the Si substrate is carried out in dry or wet oxygen-containing (steam) atmospheres at elevated temperatures ( $>800^\circ\text{C}$ ) according to the following reactions:



The oxide growth rate is related to the oxidizing atmosphere and also the crystal orientation. For example, oxidation in a dry atmosphere at  $900^\circ\text{C}$  produces a  $\sim 20\text{ nm}$  thick oxide in 1 h, while oxidation in a wet atmosphere under the same conditions results in a much thicker oxide film,  $\sim 170\text{ nm}$ . The oxidation rate is orientation dependent, the order for the oxidation rate,  $R$ , being  $R(110) > R(111) > R(311) > R(511) > R(100)$ , and this order parallels the areal density of Si atoms [16–19]. An increase of temperature or the pressure of the reactant will increase the oxidation rate. Concentration of dopant in Si will influence the oxide growth process as well. Normally heavily doped materials oxidize faster than lightly doped ones.

$\text{SiO}_2$  films with different thicknesses are produced by oxidation (dry or wet) for different applications. Thick oxide films (0.1 to  $1\text{ }\mu\text{m}$ ), normally grown by wet oxidation, are used for device isolation and as masking layers; thin oxide layers ( $< 100\text{ nm}$ ) are finding applications as gate dielectrics, flash memory tunnel oxides and dynamic random access memory (DRAM) capacitor oxides. For reasons of space, only the literature on the fabrication of ultra-thin oxide films and the oxidation behaviour of low-dimensional Si nanostructures will be summarized in this chapter. Detailed discussions on the oxidation mechanisms and modelling of Si oxidation have been the subject of several excellent reviews [20–26].

### *Ultra-thin silicon dioxide films*

The utter simplicity of thermally growing  $\text{SiO}_2$  by exposing Si to oxygen-containing atmospheres at elevated temperatures is in large part responsible for the success of Si as the integrated circuit material. Currently almost all commercial  $\text{SiO}_2$  gate dielectrics are grown by thermal oxidation, using dry or wet oxidation processes, in conventional furnaces. However, the continuous downscaling of semiconductor devices according to Moore's Law (the exponential growth of chip complexity due to decreasing minimum feature size, accompanied by concurrent improvements in circuit speed, memory

capacity, and cost per bit) has put a strict requirement on the significant thickness reduction of insulating  $\text{SiO}_2$  films [27–29]. In the past few decades,  $\text{SiO}_2$  insulating films have decreased in thickness from hundreds of nanometres to less than 2 nm today, to maintain the high drive current and gate capacitance required of scaled MOSFETs. However, a further thickness reduction is required. For example, a  $\text{SiO}_2$  insulating film with a thickness of 1.2 nm is needed for 0.5 mm devices and of 0.5 nm for 0.12 mm ones. On the other hand, the continuous thickness reduction requires a higher quality of the insulating layers, such as integrity, density and insulating property.

The  $\text{SiO}_2$  films produced by conventional thermal oxidation growth may have difficulties in meeting these critical requirements since their sub-oxide transition layer is already 1–1.5 nm and their average density is much lower than that of the thick  $\text{SiO}_2$  films. Consequently the dielectric breakdown of thin thermally-grown  $\text{SiO}_2$  film is envisaged to be a significant possibility even at a typical operating voltage, hence such film cannot be used for construction of mini-semiconductor devices. Insulation layers with high- $k$  (dielectric constant) materials physically thicker than  $\text{SiO}_2$ , such as  $\text{Al}_2\text{O}_3$ ,  $\text{HfO}_2$ ,  $\text{La}_2\text{O}_3$ ,  $\text{Y}_2\text{O}_3$ ,  $\text{ZrO}_2$ , lanthanides and silicates, are capturing much attention [30–33]. However, high quality  $\text{SiO}_2$  films are still attracting great attention due to their high compatibility with Si. They have the potential as a unique buffer material filling the gap between the conventional oxide films and high- $k$  materials. Therefore, fabrication of ultra-thin  $\text{SiO}_2$  layers/films with superior performance using modified oxidation techniques, such as low-pressure and/or low-temperature oxidation, rapid thermal oxidation (RTO), in-situ steam generation (ISSG) oxidation, laser and plasma oxidation and VUV photo-oxidation [34–45], is still an active field in the semiconductor industry.

Rapid thermal oxidation (RTO) is currently one of the primary thermal techniques for growth of thin  $\text{SiO}_2$  films. In this process, the Si wafers are heated electrically by a current passing through them or heated by lamp radiation. This technique requires low thermal budget and the Si wafer can be heated and cooled quickly. RTO processes are generally conducted in a wide temperature range from 500 to 1100°C in various atmospheres, including  $\text{O}_2$ ,  $\text{O}_3$ ,  $\text{N}_2/\text{O}_2$ ,  $\text{N}_2\text{O}$  or NO.

Oxidation at low temperatures is another way to synthesize thin or ultra-thin  $\text{SiO}_2$  films since it can reduce the interface thickness and achieve a more precise process. However, in this case the oxidation process becomes too slow. Recently, it has been shown that oxidation of Si at low temperatures (<500°C) could be enhanced by UV or vacuum UV (VUV) radiation [40,46–49]. It was believed that if the photons released by the lamp have a higher energy than the bond energy of  $\text{O}_2$ ,  $\text{O}_2$  will be readily dissociated to generate excited state oxygen atoms which can react with Si to form  $\text{SiO}_2$  at low temperatures. Tinoco *et al.* employed plasma oxidation to produce ultra-thin

$\text{SiO}_2$  films in  $\text{O}_2$  and/or  $\text{N}_2\text{O}$  atmospheres at room temperature [50,51]. They believed that in plasma, various active oxygen ion species will be formed, leading to ionic transport through the growing film. The electric field, generated due to the different mobility of electron and ion, will accelerate the ions moving towards the Si surface and travel across the growing film through a combined drift-diffusion mechanism, resulting in a higher diffusion flux for reaction at the interface.

Ultra-thin  $\text{SiO}_2$  films, 1.2 to 5 nm, had been successfully prepared under well-controlled processing conditions using RTO, photo-assisted or plasma oxidation techniques. Extensive structural and electrical characterizations confirmed that these films possess high density, good wafer uniformity, excellent surface smoothness, high dielectric breakdown field strength and low leakage current density.

### *Oxidation of silicon nanostructures*

Low-dimensional (low-D) semiconductor nanostructures, such as nanorods, nanowires and nanobelts, are receiving more and more attention recently from the scientific community, since the construction of future nanoscale devices will greatly rely on these fundamental building blocks by using bottom-up paradigms. Accordingly, low-D nanostructures based on Si have been explored to build novel electronic devices such as field-effect transistors and sensors [52,53]. Similar to the processing of planar Si devices, thermal oxidation can create a high quality  $\text{SiO}_2$  scale fully surrounding the Si nanostructures for functional purposes. However, the oxide growth behaviours on these nanostructured Si are quite different from those on planar substrates due to the 2- or 3-D dimensional effects involved in these low-D structures.

Kao *et al.* [54,55] established a new experimental method and developed a model to investigate 2-D oxidation effects based on the oxidation of cylindrical Si structures of controlled radii of curvature with diameters larger than 1  $\mu\text{m}$ . This model proposed that the stress from 2-D oxide deformation affects the kinetic parameters in the Deal-Grove model [56]. In particular, the viscous stress associated with the non-uniform deformation of the oxide is identified as the fundamental force of oxidation retardation [57]. For the low-D nanostructures (nanowires or nanorods), the 2-D effects might be more significant. Liu *et al.* [58,59] studied the oxidation of Si nanocolumns fabricated by electron beam lithography (EBL) and reactive ion etching (RIE). The diameter of these columns is around 30 to 50 nm. Thermal oxidation progress of these Si nanowires was characterized over a temperature ranging from 800 to 1200°C in dry oxygen atmospheres. They found that the Si nanostructures with a smaller diameter oxidized more slowly than those with a larger diameter. Shir *et al.* [60] studied the oxidation behavior of Si nanowires with an average radius of 37 nm produced by Au-catalysed vapour-liquid-solid (VLS)

growth technique at temperatures ranging from 650 to 750°C in O<sub>2</sub>. The authors made an oxide thickness comparison between the scales formed on these nanowires and those formed on the planar Si wafer under the same oxidation conditions, and found that at the early stage of oxidation, the oxide growth rate of the Si nanowires is much higher than that of the Si wafer. As time increased, however, a marked slowing down of the oxidation of the Si nanowires was observed.

The mechanisms involved in the oxidation retardation are supposed to be related to the viscous stress normal to the Si/SiO<sub>2</sub> interface [58–63]. As new oxide grows at the interface, the old oxide expands due to the increase in volume of SiO<sub>2</sub> (0.045 nm<sup>3</sup>) compared to Si (0.02 nm<sup>3</sup>). At low oxidation temperatures, the high viscosity of SiO<sub>2</sub> makes this radial plastic deformation of the outer oxide layers difficult, resulting in a large stress normal to the interface that slows down the interfacial reaction between the oxidant and Si or limits the oxygen diffusion in the highly stressed oxides. Eventually, at a certain wire radius, oxidation will slow down to an insignificant rate, leaving behind an ultra-thin Si core. Obviously, the stress level is highly dependent on the curvature (diameter) and temperature. For a nanowire with a larger curvature (a smaller diameter), the old oxide layer has to expand more to accommodate a given increase in volume for subsequent oxidation. Therefore the observation is that the smaller in diameter, the slower in oxidation.

The deformation of oxide scale is also related to the temperature. At higher temperatures, the oxide can have a greater viscous relaxation, leading to a reduced stress for the same radius of curvature. This stress-related self-limiting oxidation can be used to prepare Si nanowires down to 5 nm in diameter with high reproducibility.

Oxidized Si islands and/or quantum dots (QDs) are basic components for single electron devices in silicon-on-insulator (SOI) materials, such as single hole/electron quantum dot transistors [64,65]. Oxidation of dots might be more complicated in comparison with the Si nanowires since this is a three-dimensional process, and detailed studies on the oxide scale growth processes and underlying mechanisms are very limited to date, though its applications to device fabrication have been reported. Single *et al.* [66,67] investigated the oxidation properties of Si dots on SiO<sub>2</sub> using energy filtering transmission electron microscopy. Si dots with an initial diameter of 9–81 nm were fabricated on silicon-on-insulator material through a standard lithographic route. The samples were then oxidized at 700, 850 and 1000°C in a dry oxygen atmosphere. The main experimental observations from these studies are summarized as follows:

1. A strong retardation of the oxidation process compared to the oxidation of a planar surface was observed.
2. The height of the remaining Si core increased with decreasing initial Si dot diameter.

3. The limiting lateral oxide thickness is independent of the initial diameter of the Si dots.
4. Oxidation of the dots depends significantly on their shape, i.e., this is a pattern dependent oxidation.

Therefore, it can be seen that the self-limiting oxidation behaviour of Si dots is different from that reported for the oxidation of Si nanowires. Researchers believe that this is due to the shape difference. The height of the Si dots is small, therefore top and bottom edges will influence the oxidation in the lateral direction, which interfere with vertical oxidation. The self-limiting oxidation process was only observed under critical temperatures. If the temperature is quite high (e.g. 1000°C), the Si dots will be fully oxidized and converted to oxide. A model was established to calculate the critical stress in  $\text{SiO}_2$  which causes the oxidation reaction to stop [67]:

$$\sigma_{\text{end}} = - \frac{k_b T}{\Delta\Omega} \ln \frac{R}{ab} \quad 18.3$$

where  $\sigma_{\text{end}}$ ,  $k_b T$ ,  $\Delta\Omega$  and  $R$  are stress, thermal energy, volume difference and oxidation rate, respectively. The average value for the critical stress that stops the oxidation is  $1.67 \times 10^9 \text{ Pa}$  at  $700^\circ\text{C}$  and  $2.59 \times 10^9 \text{ Pa}$  at  $850^\circ\text{C}$ .

### 18.2.2 Oxidation of gallium arsenide, GaAs

III-V semiconductors such as GaAs offer materials property advantages over Si, such as increased carrier mobility and direct band gap, and may be used for microwave and optoelectronic applications. Studies of the oxidation of GaAs started in the 1960s with an attempt to develop oxide-masked III-V semiconductors [68–71]. The experiments were conducted in a wide temperature range. Characterizations with extensive techniques, such as XPS, AES, SIMS and TEM, were focused on the analysis of the phase compositions of the thermally grown oxide scales. The main thermal oxidation product was found to be  $\text{Ga}_2\text{O}_3$  with a small amount of  $\text{GaAsO}_4$ ,  $\text{As}_2\text{O}_5$ ,  $\text{As}_2\text{O}_3$  or As at the oxide/GaAs interface, depending on the temperature [72–75]. These studies also indicated that the structure and orientation of the surfaces have a considerable influence on the quality and structure of the oxide layers.

The process of GaAs oxidation is so complex that even after many years of work there are important issues that are still a matter of controversy. Consequently, the GaAs metal insulator semiconductor field effect transistor (MISFET) technology did not develop very well since the electronic passivation of GaAs is not fully resolved. The challenges in the fabrication of high quality oxide layers on GaAs stimulate researchers to find out the most suitable techniques and conditions to solve the interface-related problems.

Lefebvre *et al.* [76–78] studied the compositional and electrical properties of the oxide layers formed on GaAs by thermal oxidation and electron cyclotron

resonance (ECR) plasma oxidation using XPS. They found that ECR-grown oxides are nearly stoichiometric and close to  $\text{GaAsO}_4$  while thermally grown oxides are closer to  $\text{Ga}_2\text{O}_3$  having a significant amount of  $\text{As}^{+3}$  oxidation states. Their capacitance–voltage measurements showed that the interfaces produced by thermal and ECR plasma oxidations of GaAs have similar electrical properties. Both interfaces were found to be equally unpassivated in terms of high levels of interface electronic states and Fermi level pinning. Wet oxidation using steam at 500 to 520°C was also tried by Oh *et al.* to grow native Ga oxide on GaAs surface. The results were not very promising since these films still suffered from a high GaAs–oxide interface recombination rate [79]. Takamiya *et al.* [80,81] developed a new method using ultraviolet and ozone oxidation–oxinitridation (plasma nitridation after oxidation) to produce nanometre-scale gate insulating layers on GaAs surfaces and then to fabricate depletion-type recessed gate GaAs-MISFETs. The devices exhibited a smaller leakage current than the simple oxide gate device and showed good pinch-off, no hysteresis, higher breakdown voltage and higher transconductance with no dip at the flatband voltage, suggesting the existence of very little interface charge. In addition, in-situ or ex-situ deposition of  $\text{Ga}_2\text{O}_3$  on GaAs using MBE might be one way to implement thermodynamically stable oxide–GaAs interfaces [82,83].

### 18.3 Oxidation of precursors for preparation of superconductors

Superconductors can be elements, intermetallic alloys or compounds that will conduct electricity without resistance below a certain temperature [84]. Discovery of superconducting materials could be dated back to 1911, when Heike Kamerlingh Onnes, a Dutch physicist on low temperature physics (and winner of the Nobel Prize in 1913), found that no resistance could be measured with mercury cooled by liquid helium. He said that when the temperature cooled to ~4.2 K, mercury has passed to a new state, which may be called the superconductive state. After that, superconductivity was also found in many pure metals such as Sn, Pb, V and Nb, though with very low transition temperatures.

Superconducting materials based on alloys and/or metallic/chemical compounds, including  $\text{V}_3\text{Si}$ ,  $\text{Nb}_3\text{Sn}$ ,  $\text{Nb}_3\text{Ge}$ ,  $\text{Nb}_3\text{Ti}$ ,  $\text{NbN}$ ,  $\text{PbMo}_6\text{S}_7$  and  $\text{MoC}$ , were discovered and developed from the 1950s. These materials possess much higher critical temperature ( $T_c$ ), current density ( $J_c$ ) and critical magnetic field ( $H_c$ ) than the elemental superconductors and were essential for providing high magnetic fields. In the late 1980s, scientists boosted development of superconducting materials with, the discovery of high temperature superconductors (HTS), which have much higher transition temperatures for coming into the superconducting state. In January 1986, Bednorz and Müller

at IBM Zürich found that the La-Ba-Cu-O system could exhibit superconductivity at ~30 K [85]; their findings were further confirmed by researchers from Tokyo University at the Fall Meeting of the Materials Research Society (MRS) in Boston. After this, superconducting oxide systems, including Y-Ba-Cu-O (YBCO), Bi-Sr-Ca-Cu-O (BSCCO) and Tl-Ba-Ca-Cu, with a transition temperature higher than the liquid nitrogen boiling point (77 K), were discovered and have generated great interest in the scientific and technological communities [86–89].

Processing is the key to industrial applications of all engineering materials. For high temperature superconductors, the development of appropriate processing techniques to yield desirable properties and shapes is essential to achieve their technological application [90–101]. For bulk high temperature superconducting materials, the most common techniques for engineering materials processing can be employed. For example, most HTS compounds could be synthesized by a sintering technique commonly used for ceramic processing. The techniques for growing single crystals of high temperature superconductors are similar to those commonly employed for other materials, such as flux growth, top-seeded solution growth, electrocrystallization, hydrothermal growth and floating zone growth methods [102–105].

One simple but efficient method for the synthesis of high temperature superconducting oxides is high temperature oxidation of a metallic precursor that contains the metallic constituents of the superconducting oxides. Metallic precursors of  $\text{EuBa}_2\text{Cu}_3$ ,  $\text{YBa}_2\text{Cu}_3$  and  $\text{HoBa}_2\text{Cu}_3$  made by melt-spinning were subjected to oxidation treatment to fabricate the high temperature superconducting oxide products [106–108]. This technique had been proven to be efficient for production of high temperature superconducting oxide materials in the form of ribbon or coating with a combination of good superconducting and mechanical properties [109–111], and provided a possible method to produce long superconducting wires. Metallic precursors were produced by melting the pure metals with the compositions that are thought to be favourable for the formation of the superconducting phase. To produce coatings, the ingots were then remelted, and the substrates were dipped into the melt several times to form metallic precursor coatings. To generate ribbons, coatings or other shapes, the ingots were melted quickly under an Ar atmosphere and the liquid alloy was ejected through a nozzle onto a suitable substrate by melt spinning (to yield long ribbons) [112], planar flow casting [113], melt dipping (to yield coatings on a substrate) [114–116] and melt writing (to yield long, continuous or irregularly shaped coatings) [117]. The general oxidation treatment for these metallic precursors proceeds in two steps in controlled atmospheres: (1) direct oxidation of metallic alloys in an oxidizing atmosphere at relatively low temperatures for a short time to fully oxidize the precursors [118]; and (2) annealing under lower oxygen partial pressures at relatively high temperatures for a long time to form superconducting phases.

The following three types of oxidation were observed in these experiments [112]:

1. Combustion oxidation: this is the fastest type of oxidation, in which the sample was combusted after a very short exposure depending upon the temperature, atmosphere, specimen composition, thickness and arrangement in the heating container. As a result, sample temperatures became very high during combustion. Therefore the oxidation products were highly deformed and non-uniform in colour, and had very rough surfaces.
2. Fast oxidation: in this type of oxidation, the samples did not combust, but oxidized very rapidly. After this type of oxidation, samples were buckled and had rough surfaces, but their colour was a rather uniform dull black.
3. Slow oxidation: this type of oxidation occurred in pure oxygen atmosphere when the temperature was relatively low. After oxidation treatment, the samples had a smooth, shiny surface and exhibited little distortion.

Microstructural observations and microanalysis performed with SEM, TEM, WDS and XRD confirmed the formation of superconducting phases in the system. BSCCO-Ag high- $T_c$  superconducting ribbons with  $T_{(R=0)} = 100\text{--}107$  K and  $J_c(77)$  as high as  $2000 \text{ A/cm}^2$  have been produced on many metallic substrates using this oxidation technique [115–118]. It was also found that the microstructure, especially the grain shape and orientation, has a very strong effect on the current carrying ability,  $J_c$ . BSCCO crystal grains grow in a plate-like shape and the super-current flows much easier along the plate planes than across the plates. It was found that multi-mechanical deformation followed by annealing can align the plate grains along the current flowing direction. A  $J_c$  record of  $10,000 \text{ A/cm}^2$  was reported in 1990–1991 with this method [119–121]. The BSCCO high temperature superconducting system has a weakness of sharply dropped  $J_c$  with increasing magnetic field. However, the multi-layer BSCCO-Ag composite ribbons treated with the method described above showed a much better magnetic field behaviour than those treated with ordinary methods [122].

## **18.4 Preparation of zinc oxide (ZnO) films and nanostructures by oxidation**

Zinc oxide (ZnO) is a cheap but important material with many unique properties and potential applications [123–125]. Firstly, it is a gas/pressure-sensing ceramic and can be used as non-linear varistors and sensors [126]. Secondly, piezoelectric ZnO can find applications in surface and bulk acoustic wave devices [127–129]. Thirdly, it is a semiconducting oxide with a wide band gap of 3.37 eV at room temperature and a large exciton energy of 60 meV,

thus it is an important functional oxide in optics and optoelectronics [130–134]. Highly transparent and conductive ZnO films are finding applications in solar cells and energy-efficient windows. ZnO exhibiting UV, green, blue or red colour emissions could be the candidate for the next generation of laser diodes (LDs) and light emitting diodes (LEDs).

#### 18.4.1 Preparation of zinc oxide films and nanostructures by traditional oxidation techniques

##### *Preparation of zinc oxide films*

ZnO films can be prepared by many techniques, including chemical vapour deposition (CVD) [135], electron beam evaporation [136], molecular beam epitaxy (MBE) [137], pulsed laser deposition (PLD) [138], sol-gel [139], spray pyrolysis [140], sputtering [141] and chemical bath deposition [142]. Thermal oxidation of metallic Zn [143–149], ZnS or ZnSe [150–153] films has been used to prepare ZnO films. The Zn precursor films were deposited onto the substrates (glass, sapphire or Si) by magnetron sputtering, thermal/electron-beam evaporation or filtered cathodic vacuum arc technique. Oxidation treatment was normally conducted in air or oxygen atmospheres in a wide temperature range typically from 300 to 1000°C.

Cho *et al.* [143] prepared ZnO films by oxidation of Zn films in an oxygen atmosphere and found that the particle size increased with increasing oxidation temperature, resulting in sharpened and enhanced X-ray diffraction peaks for ZnO. These samples have excellent emission properties; and the room-temperature photoluminescence (PL) spectra only show a strong UV peak around 383–390 nm. The oxidation temperature had a significant influence on the PL properties. As the temperature increased, the PL peak intensity increased and the peaks became sharper. The full width at half maximum (FWHM) of the PL peak was 107 and 23 meV for the samples grown at 700 and 1000°C, respectively, indicating a better optical quality when using a higher oxidation temperature. Similar phenomena had been observed by Chen [144] and Alivov [147]. In Cho and Chen's studies, the visible light emissions were very weak due to the low defect concentrations in these films.

Wang *et al.* [145], however, observed a different trend of PL vs. temperature in the ZnO films thermally grown in ambient air at temperatures ranging from 320 to 1000°C for 1 h. The UV peak of the sample oxidized at 410°C has the strongest PL intensity and the narrowest FWHM of the temperatures investigated, and the intensity ratios of UV emission to deep-level emission are 13 and 200 for the samples prepared at 700 and 410°C, respectively. When the oxidation temperature was higher than 800°C, the PL intensity increased again. Wang *et al.* also studied the correlations between the deep-

level emissions and the oxidation temperature and found that (i) the intensity of the broad visible band increases with increasing oxidation temperature; (ii) the visible band can be fitted well by two peaks located in the green and yellow energy range; and (iii) the position of the green peak depends strongly on the oxidation temperature. It red-shifts with an increase of temperature: a shift of 0.3 eV is observed for the sample grown at 1000°C compared to the 410°C oxidized sample. The yellow peak displays a weak temperature dependence. The intensity ratio of the green to yellow peak increases with the oxidation temperature, especially at temperatures higher than 900°C. Since the melting point of Zn is 419.5°C, the authors suggested that at lower temperatures ( $\leq 419^\circ\text{C}$ ) Zn stays in a solid state and can be oxidized at relative equilibrium conditions. When the temperature is higher than its melting point, oxidation is carried out at an unstable liquid state. More defects that are responsible for the non-radiative transition will be introduced into the films. However, a much higher oxidation temperature ( $\geq 900^\circ\text{C}$ ) facilitates the migration of grain boundaries and promotes the coalescence of small crystals, thus decreasing the concentration of nonradiative recombination centres. The complex relations between the formation and annihilation of defects and oxidation temperature lead to the complicated emission behaviours observed in thermally grown ZnO films.

In addition to the PL property characterizations, Alivov *et al.* [147] also studied the dependence of electrical properties on oxidation temperature and oxygen partial pressure. From Hall-effect measurements, they found that the resistivity of ZnO films increases with oxidation temperature from 381 Ω·cm at 400°C to  $6.02 \times 10^4$  Ω·cm at 900°C. At the same time, the carrier (electron) concentration decreases from  $4.56 \times 10^{15}$  to  $7.32 \times 10^{12}$  cm<sup>-3</sup>, and mobility increases from 3.6 to 14.2 cm<sup>2</sup>/V·s, providing evidence of improvement of crystal quality of ZnO films with temperature as the ZnO crystal lattice becomes more stoichiometric with high temperature annealing in oxygen. Alivov *et al.* also investigated the variation of the electrical properties as a function of the oxygen partial pressure. Resistivity and mobility increase by a factor of 2–4 when oxygen partial pressure is varied from  $1.01 \times 10^5$  to  $1.33 \times 10^{-3}$  Pa, indicating an improvement of film crystallinity. The authors believed that decreasing oxygen partial pressure can slow down the oxidation process of Zn and thus the best crystal quality can be expected at the lowest crystal formation rates.

As mentioned above, ZnO is a promising material for development of LEDs due to its high exciton binding energy (~60 meV). For these applications, however, *p*-type (hole) conduction must be realized. Though highly conductive *n*-type (electron) ZnO films have been created, progress in fabrication of *p*-type ZnO with low resistivity is very slow. Doping is the way to realize *p*-type conduction, and N is one of the candidates for *p*-type doping. Generally, doping of nitrogen in ZnO could be achieved by sputtering [154,155], CVD

[156,157], PLD [158], MBE [159], implantation [160], and/or solution approaches [161]. However, the chemical activity of O is higher than that of N; Zn preferentially combines with O rather than with N. As a result, it is difficult for N to be incorporated into ZnO films. Recently, it has been found that oxidation treatment of Zn-N ( $Zn_3N_2$ ) can directly incorporate N atoms into ZnO during the growth process to occupy oxygen positions, to partly compensate some donors (e.g. oxygen vacancy) and then to yield *p*-type conductivity during the course of thermal oxidation [162–165]. Nakano *et al.* [165] reported a significant improvement of *p*-type doping characteristics by oxidation at temperatures between 500 and 800°C, where more N acceptors are activated and the oxidation state is enhanced. However, other studies indicated that oxidation treatment at high temperatures (>500 or 600°C) might initialize a conduction-type transformation from *p* to *n* [162,163]. These different observations can be understood if one can see that the N-containing precursor films were prepared using different methods under different conditions.

#### *Preparation of zinc oxide nanostructures*

The semiconductor industry has been contributing to the progress of modern society with great accomplishments during the last 40 years or so using conventional top-down lithographic approaches. However, scientists believe that the strategy for developing future advanced devices with higher integration density, faster clock rate and lower power consumption will rely on the realization and utilization of novel low-D nanostructures with fascinating multi-functions through bottom-up paradigms [166–170]. ZnO has unique electronic, photonic and piezo-electric properties in one configuration and also the most diverse and abundant configurations of nanostructures. Low-D nanostructures, such as quantum dots, nanowires, nanobelts, nanosprings, nanobows, nanohelices and nanoprisms, are being exploited for future applications of sensors, transducers, field effect transistors, resonators and cantilevers at the nanometre level [171–173]. ZnO nanostructures could be prepared by many techniques, including electrochemical deposition with anodic alumina template [174], thermal evaporation-vapour transportation [175,176], MOCVD [177,179], MBE [180,181], PLD [182,183] and hydrothermal growth in solutions [184–186].

Besides these techniques, thermal oxidation of Zn (in the form of metal, film or powder) might gain popularity in the fabrication of ZnO low-dimensional structures due to its simplicity in processing control. To date, whiskers [187,188], nanowires [189–194], multi-layer nanosheets [195], tetrapod nanostructures [196,197], micro-rods [198], micro-belts/combs [199] and micro-spheres/cages [200] have been obtained by thermal oxidation in ambient atmospheres or in pure oxygen.

The growth mechanisms of these structures are very complicated and not clearly understood at this stage. Since the melting point of Zn is relatively low, only  $\sim 419.5^{\circ}\text{C}$ , and the processing temperature is high,  $500\text{--}1000^{\circ}\text{C}$ , the evaporation of Zn source materials will play an important role in the growth of these ZnO structures. It has been proposed that the growth mechanisms may follow a vapour–solid (VS) process; the vapour (Zn or ZnO; ZnO might be formed by reaction between Zn vapour and oxygen) leads to nucleation at energy-favoured positions, promoting the formation of low-D structures on the surfaces. As catalysts were not employed in these processes, the VS mechanism is slightly different from the vapour–liquid–solid (VLS) process using catalysts, such as Au, Sn or Fe [201–203].

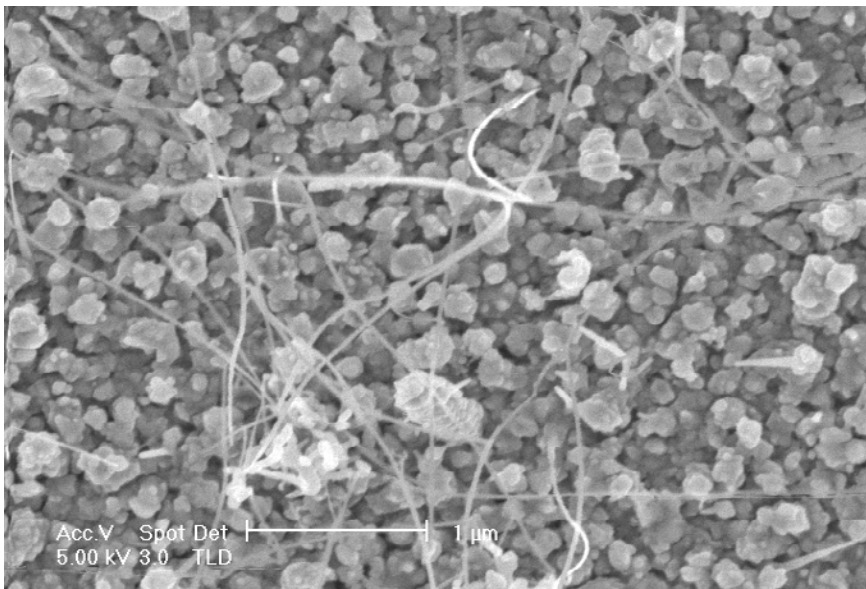
The room temperature photoluminescence properties of these samples were characterized. Their spectra normally consisted of two main peaks: one is the near band edge UV emission and the other is a broad peak located in the visible light region. The relative intensity ratio between these two peaks is dependent on the processing conditions, such as temperature and atmosphere. In general, the samples showed a quite strong green emission centred around  $500\text{--}530\text{ nm}$ , indicating that the defect concentrations (such as oxygen vacancy, zinc interstitial, or surface dislocations) of these samples are quite high [191,192,196,197,199].

#### 18.4.2 Preparation of zinc oxide films and nanostructures by wet oxidation

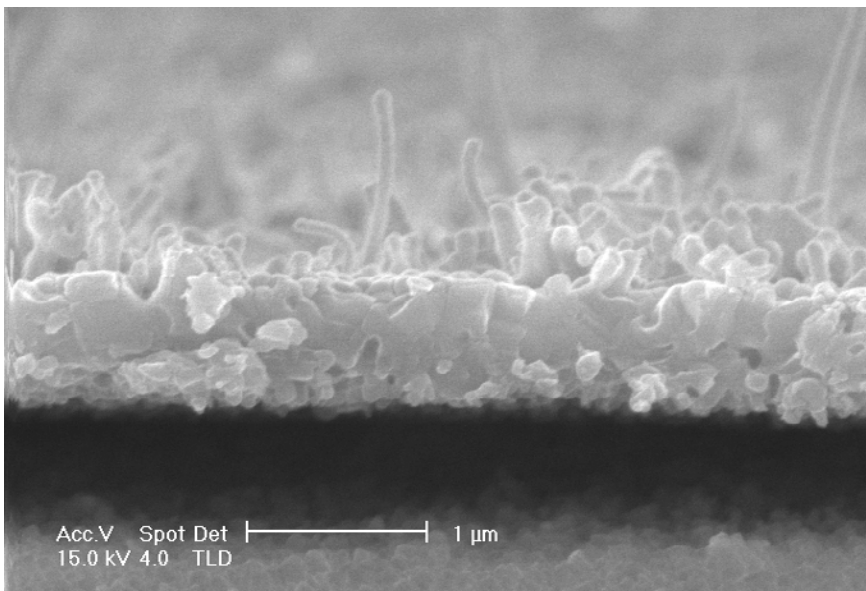
##### *Preparation of zinc oxide low-dimensional nanostructures*

In their studies on the preparation of ZnO by thermal oxidation, the present authors found that oxidation treatment in air will lead to the formation of ZnO films with a small amount of nanostructures, such as nanowires or nanorods, on their surfaces, as shown in Fig. 18.1(a). Treatment in pure oxygen may significantly decrease the formation of these structures, however leading to the formation of oxide films which are highly prone to cracking and spallation, as shown in Fig. 18.1(b). These results thus imply that in order to prepare mechanically strong ZnO films or nanostructures with well-defined dimension, shape and/or size, the oxidation conditions, including temperature, atmosphere and time, must be well under control.

A two-step method, sputtering deposition–wet oxidation, was therefore developed by the present authors in an attempt to prepare low-dimensional ZnO nanostructures. In this technique, Zn precursor films prepared by magnetron sputtering were used to grow ZnO nanostructures. During deposition, the sputtering conditions, such as gas pressure, power and time, were fully controlled. These precursor films were then subjected to oxidation treatment in which the temperature, time and atmosphere were under accurate



(a)



(b)

18.1 (a) ZnO nanowires on ZnO films formed by oxidation of Zn films in air; (b) ZnO films formed by oxidation of Zn films in oxygen, showing the poor interfacial adherence.

control. A special feature of this technique is that water vapour is introduced into the oxidizing atmosphere, since it was known that incorporation of water vapour into the oxidizing atmosphere could significantly affect the scaling behaviour of metals [204]. For example, oxide scales formed on pure metals in wet atmospheres would have significantly increased plasticity. Furthermore, whisker-type structures were often observed on some pure metals when water was added into the oxidizing atmospheres. It is then expected that wet oxidation under controlled conditions will produce ZnO with certain types of nanostructures.

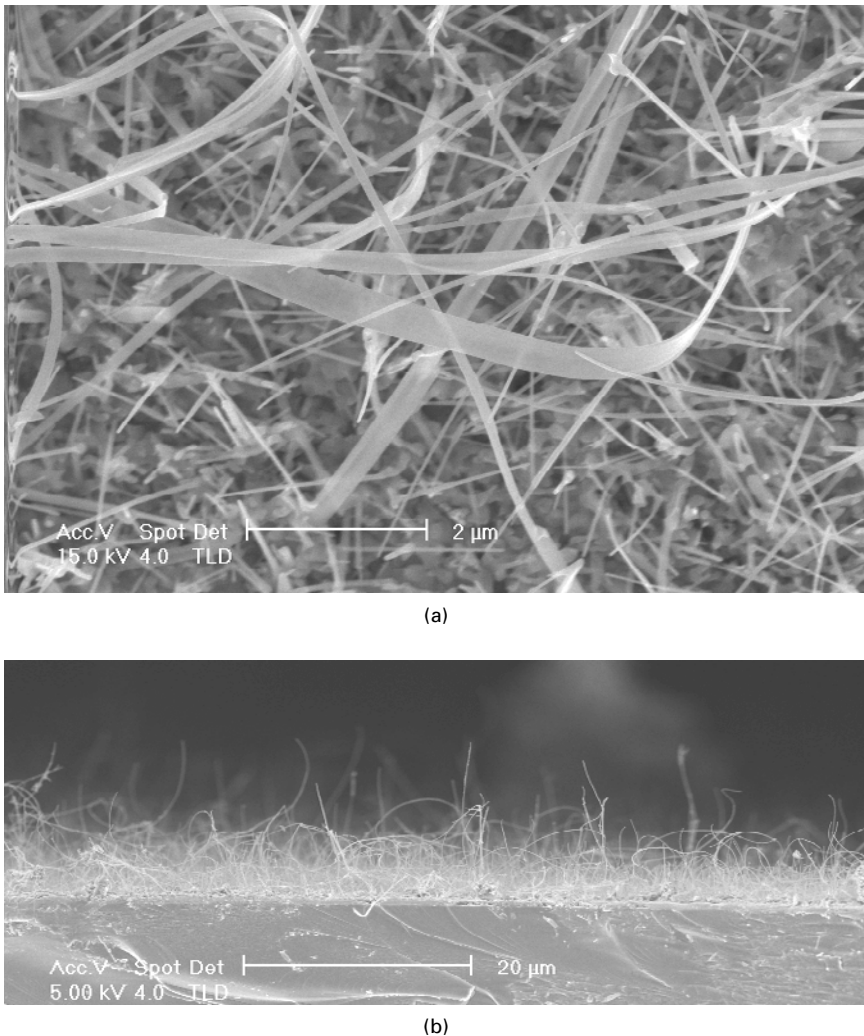
In our studies, the water vapour content was varied from 5 to 70% and the oxygen content was controlled by changing the carrier gas (argon, nitrogen and/or oxygen). The experimental observations confirmed that low-dimensional ZnO nanostructures could be thermally grown on the precursor surfaces. An adjustment of the oxidation temperature could change the growth of the nanostructure significantly, resulting in the formation of various nanostructures with high reproducibility [205]. At 350°C, oxidation in wet oxygen (10% water vapour) led to the formation of short blade-like whiskers with high distribution density on the sample surface. As the temperature increased to 375–400°C, nanowires 10–20 µm long formed on the surface. Nanobelts 150–480 nm wide and ~15 µm long were observed as well (Fig. 18.2(a)). The belts were very thin and were transparent to the electrons in scanning electron microscopy operating with low accelerating voltages. At 420°C, thin nanowires as long as 20–50 µm were grown on a dense ZnO layer. At this temperature, if water vapour content was decreased from 10 to ~5%, ZnO nanowires with a much larger length of 50–200 µm could form (Fig. 18.2(b)). A further increase of oxidation temperature would not favour the growth of nanostructures. A small amount of short nanorods formed on a dense ZnO film at 600°C. These observations then demonstrated that both temperature and water vapour content have significant effects on the growth behaviour of nanostructures and the growth processes for the non-planar nanostructures. The growth processes of the base planar oxide films and the low-dimensional nanostructures were competing against each other.

Pure Zn has high vapour phase pressures at high temperatures [206], 1.7, 10.9 and 1525 Pa at 350, 400 and 600°C, respectively, as calculated from the following equations [207]:

$$\log(p/\text{atm}) = 6.102 - \frac{6776}{T} (298^\circ\text{C} - \text{m.p.}) \quad 18.4$$

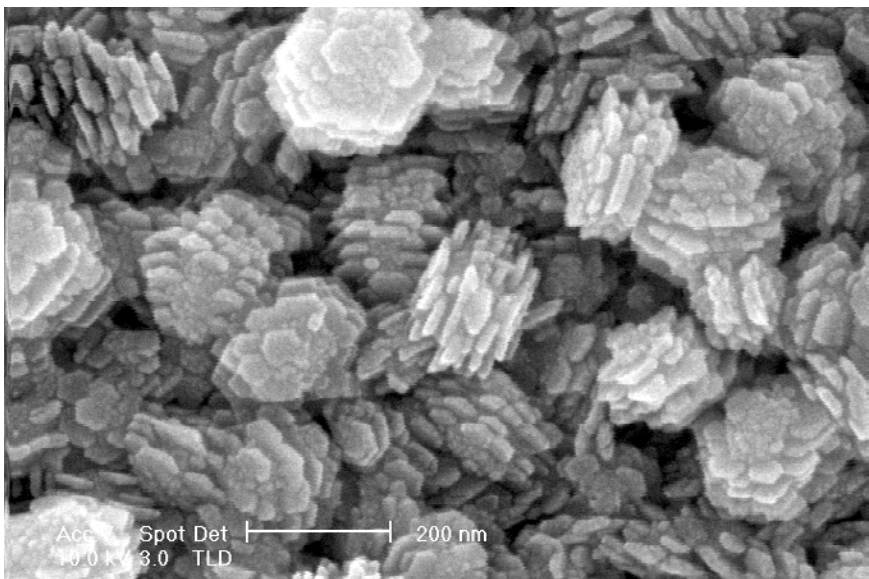
$$\log(p/\text{atm}) = 5.378 - \frac{6286}{T} (\text{m.p.} - 750^\circ\text{C}) \quad 18.5$$

The role of Zn vapour in the growth of ZnO nanostructures therefore could not be neglected. Thermal evaporation of metallic Zn will, to some extent, contribute to the nucleation and growth of low-dimensional nanostructures

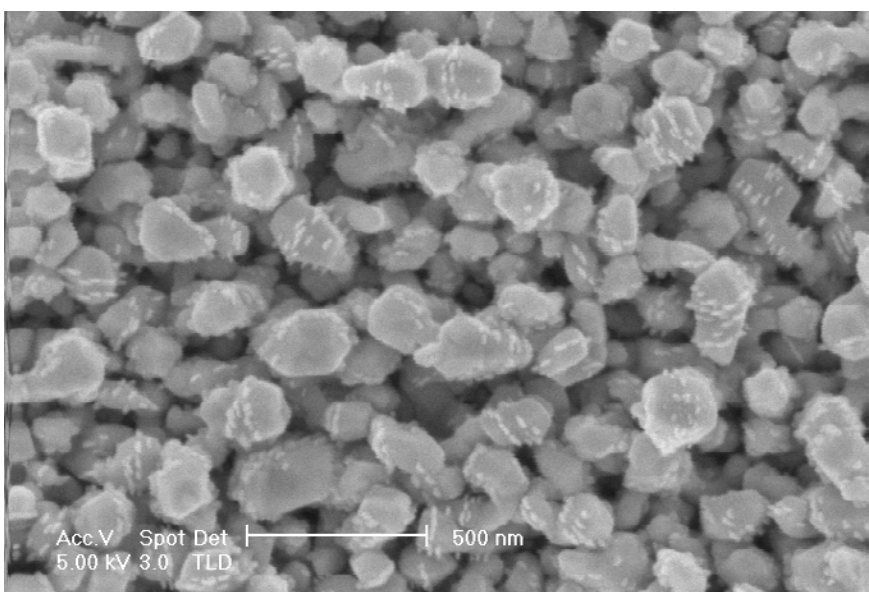


**18.2 (a)** ZnO nanobelts and **(b)** nanowires prepared by the sputtering deposition–wet oxidation technique.

through some similar mechanisms reported in the literature [192,200]. On the other hand, closer observation of the Zn precursor films revealed that they are composed of hexahedron-like particles, which have a multi-layered structure with thin platelets (Fig. 18.3(a)). These platelets, extruding out from the particles, will serve as the nucleation sites of the nanostructures. This is partially supported by the fact that no nanostructures were formed on Al-doped Zn precursor films, and morphological observations confirmed that no large platelets were presented on the Al-doped Zn particles (Fig. 18.3(b)). It is then suggested that at the very beginning of oxidation, Zn



(a)



(b)

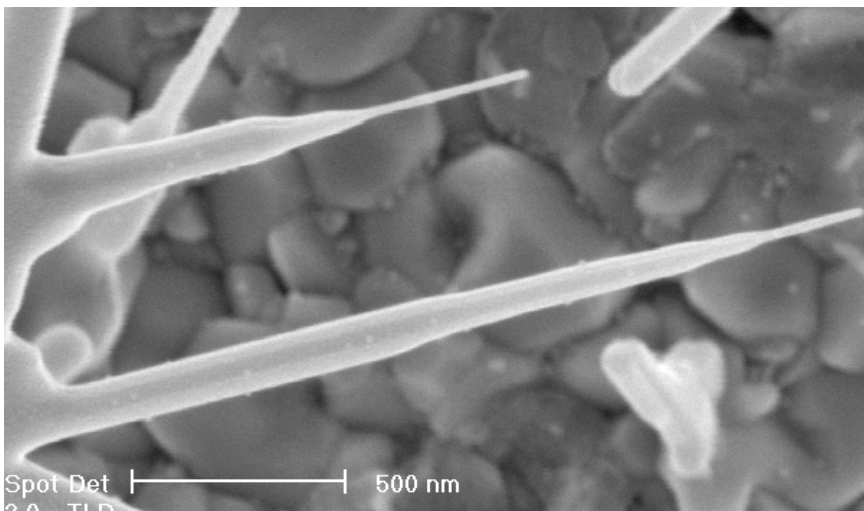
18.3 Typical surface morphologies of Zn precursor films prepared by magnetron sputtering: (a) pure Zn particles showing a multi-layered structure with platelets; (b) Al-doped Zn particles showing a smooth particle surface.

vapour was generated and then captured preferentially by the special structures on the Zn film surface to form Zn or ZnO nanostructures at small scales, which act as seeds for the growth of ZnO low-dimensional nanostructures into large dimensions through some mass transfer mechanisms.

Evaporation and oxidation of Zn compete with each other; an equilibrium state between them will determine the oxide growth behaviour. At low temperatures, oxidation is slow and most of the structural features on the Zn particles could survive, yielding more closely spaced whiskers with a suitable supersaturation. As the oxidation temperature increased, Zn vapour pressure increased, probably resulting in greater supersaturation. However, the oxide scale with a higher growth rate could completely cover the surface in a shorter time period and also destroy a larger amount of structural defects on the surface, leading to the formation of belts or wires with a lower surface distribution density. If the temperature was very high, oxidation would be dominant; the growth process was then fully governed by the diffusion through the oxide scale. Furthermore, as explained by Raynaud and Rapp [208], lattice, grain boundary and surface diffusion can contribute to oxide growth in metal oxidation. Because the activation energy for surface diffusion is significantly lower than that for lattice diffusion, the growth associated with steps created by a screw dislocation will lead to whisker growth at low temperatures. On the contrary, as the temperature increases, lateral lattice diffusion becomes more favourable, and oxide growth leads to a flatter morphology. However, some channels for growth of low-dimensional nanostructures might still be available in the base scale, leading to the formation of short rods on a dense oxide film.

Continuing growth of these ZnO nanostructures needs sustainable mass transfer through some mechanisms. It was generally believed that a fast diffusion path within the whisker should exist. TEM studies confirmed the existence of a central hollow tunnel within  $\alpha\text{-Fe}_2\text{O}_3$  blades or whiskers on iron [209]. The surface diffusion is larger than the lattice diffusion by a factor of  $10^4$  to  $10^6$ , so that the growth of whiskers could be maintained [210,211]. This mechanism cannot be excluded in the growth of ZnO whiskers or rods. Closer morphological observations also indicated that the diameter (or width) of some structures decreases as their length increases (Fig. 18.4), and their surface distribution density decreases with extended exposure. These results support a growth mechanism on the tip through a gradual decrease in mass supply that might be sourced from Zn evaporation and/or unstable ZnO nanostructures during heating. These vapours might be captured preferentially for the continuing growth of some stable ZnO structures.

Water also plays an important role in the growth of low-dimensional ZnO nanostructure, and co-existence of free oxygen and water is essential. It was believed that the easier break-up of water molecules in comparison with oxygen and the influence of water on the mechanical properties of oxides



18.4 ZnO nanorods showing a gradual decrease in diameter.

might accelerate this type of growth [208]. It is also suggested that water may enhance the sublimation of ZnO at temperatures, providing additional Zn species for the growth of low-dimensional nanostructures.

#### *Preparation of highly porous zinc oxide films*

Solids with well-controlled porosity are a rapidly developing class of materials with ever increasing applications, such as catalysts, electrochromic devices, ceramic membranes, batteries, sensors and solar cells. The sol-gel process with polymer alloying has been recognized as an efficient way to produce films with well-defined surface area, size distribution, homogeneity, porosity and film thickness. In these processes, however, complexing agents such as acetylacetone, diethanolamine and polyethylene glycol are needed. Samples with desired porosities could be obtained by removing the polymeric additives through firing at high temperatures [212–217].

A new two-step method, partial reactive sputtering deposition–wet oxidation, has been developed by the present authors. They found that modulation of precursors in the sputtering step can provide more opportunities for control of the structural and functional properties of the thermally grown oxides. This technique may also open a new way to fabricate porous ZnO films [205,218]. The innovative part of this processing is that a ‘partial reactive deposition’ is introduced.

In conventional reactive sputtering, the partial pressure of the reactive gas (oxygen or nitrogen) must be high enough to ensure the full reaction between the metallic and gaseous components. In the present technique, however, the

oxygen content in the sputtering atmosphere is strictly controlled, and is lower than the critical value for the full formation of ZnO through reactive sputtering [219]. As a result, the reaction between Zn and O is incomplete, thus a film containing Zn and ZnO is deposited onto the substrate. Due to the change in composition, the morphology of the precursor films is also modified. Microstructural observations showed that when 10% O<sub>2</sub> was added into the sputtering atmosphere, the large particles observed in sputtering with pure argon disappeared. Instead, fine particles (~90 nm) aggregated together to form small clusters or short chains. As the oxygen content increased, the particle size was further reduced (to about 50 and 30 nm for the films deposited with 20% and 30% O<sub>2</sub>, respectively). When oxygen content was higher than 20%, the peaks of (100), (002) and (101) for ZnO were clearly observed in the XRD spectra. Due to the co-existence of extremely fine Zn and ZnO particles, the continuous growth of one phase was no longer sustained. The discontinuous growth and preferential agglomeration then contribute to the pore generation in the growing precursor films.

The morphological change resulting from this partial reactive sputtering process is critical to the pore formation in the thermally grown ZnO films. Oxidation of these Zn-ZnO composite films in wet atmosphere leads to the formation of highly porous ZnO films. The oxide particle size and the porosity could be controlled by the oxygen content in the sputtering gas atmosphere. The crystal size of these porous films was calculated with the Scherrer formula:

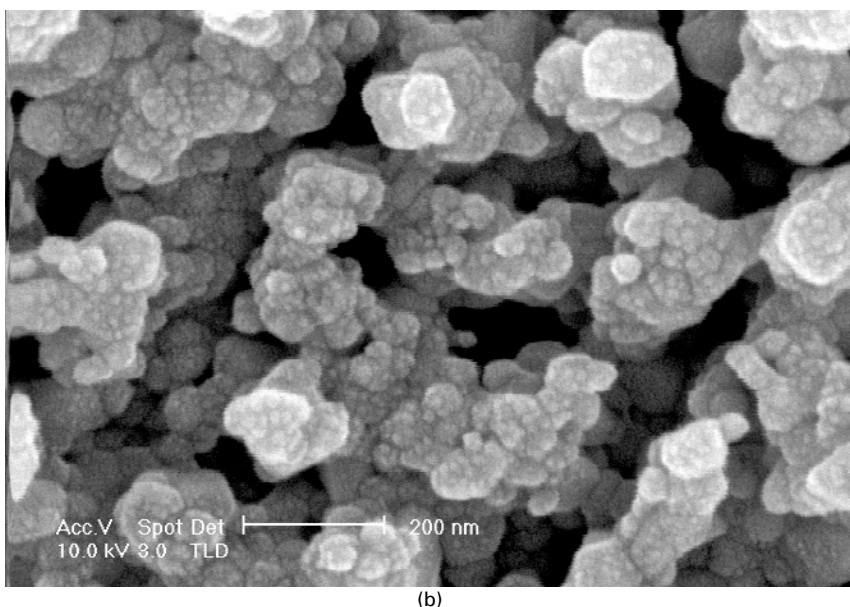
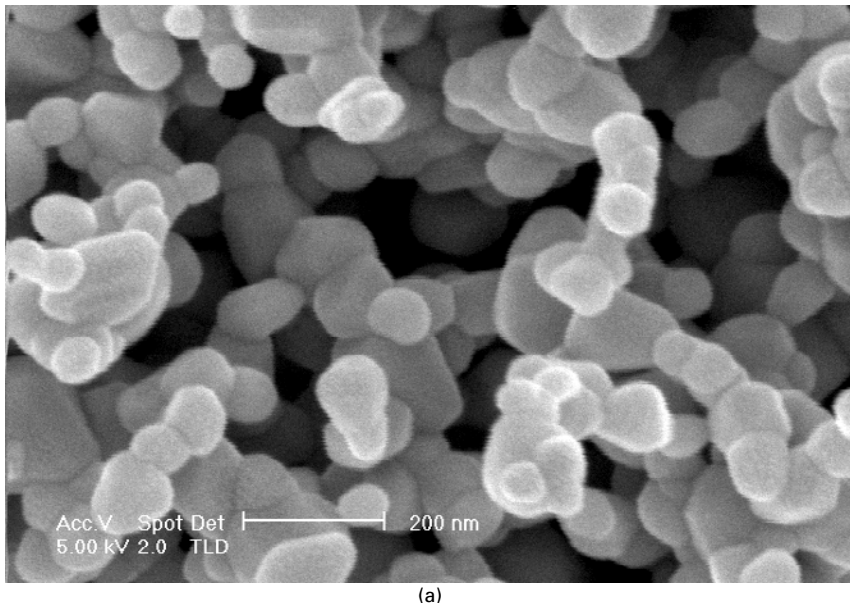
$$D = \frac{0.89\lambda}{\sqrt{B_M^2 - B_S^2} \cos(\theta_B)} \quad 18.6$$

where  $\lambda$ ,  $\theta_B$ ,  $B_M$  and  $B_S$  are the X-ray wavelength, the Bragg diffraction angle, and the full width at half maximum (FWHM) of the peaks measured from standard and present ZnO samples, respectively. The average crystal sizes are 55, 92 and 86 nm for the undoped ZnO films whose precursor films were deposited in the atmosphere with oxygen contents of 10, 20 and 30%, respectively, which are quite close to the average particle size measured with SEM (62, 98 and 79 nm, respectively; an average from 25 measurements). As the oxygen content in the sputtering atmosphere increased, the pore size and depth increased. Cross-sectional observations also showed that the pores are not concentrated in the surface or near-surface regions and are extended deeply down into the interfacial area. The films are also mechanically strong and adherent to their substrates.

A cerium-containing ultra-thin film was also applied onto the Zn-ZnO composite precursor film using electrochemical deposition in Ce(NO<sub>3</sub>)<sub>3</sub> ethanol solutions [220,221]. After oxidation, cerium oxide particles were incorporated to form Ce-doped ZnO films with a much smaller particle size. Doped porous

ZnO can also be achieved by oxidation of doped precursor films deposited by sputtering with composite targets [Fig. 18.5].

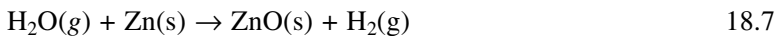
Fabrication of highly porous ZnO films mainly was conducted at 600°C. At this temperature, Zn vapour pressure is quite high, 1525 Pa. Therefore,



18.5 (a) Ce-doped and (b) Al-doped porous ZnO films.

loss of Zn through thermal evaporation will be significant, and this process will be further enhanced by the porous structures of the Zn–ZnO composite precursor films. Therefore, the particle size will be decreased and the pore size will be increased. The facts that ZnO films formed at lower temperatures are less porous, and those formed in pure water vapour atmospheres (N<sub>2</sub> or Ar as carrier gas) have larger and deeper pores, support the deduction that evaporation of Zn is an important factor in pore enlargement. Obviously a slower oxidation process occurring at a higher temperature would lead to more Zn mass loss within a longer time period. The mechanisms involved in the formation of small-sized Cr<sub>2</sub>O<sub>3</sub> films are also applicable to the formation of fine ZnO films doped with Ce [222–224].

Water vapour is also crucial to pore generation and enlargement as ZnO films formed in air or dry oxygen had a lower porosity than those formed in wet atmospheres [218]. It was reported that water could act as an active agent for pore generation and enlargement in the preparation of electrodes for fuel cells [225]. Water vapour might enhance the transportation of the Zn component out from the deep section. Hydrogen could be generated by the reactions between zinc and water at elevated temperatures. It is supposed that under certain conditions, hydrogen could react with ZnO to form Zn vapour, therefore leading to sublimation of ZnO [226]:



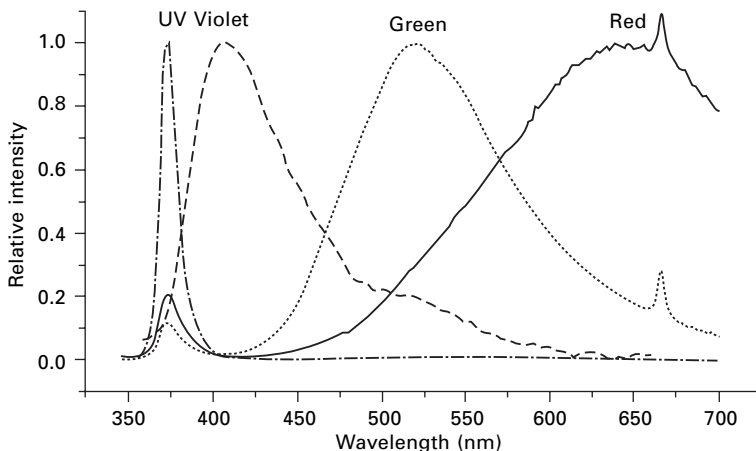
This process can enlarge the pore size and deepen the pores into the inner part of the film.

#### *Photoluminescence of zinc oxide films prepared by wet oxidation*

The room temperature photoluminescence (PL) properties of the ZnO films prepared by wet oxidation were characterized to explore the potential influences of processing conditions (sputtering/oxidizing atmospheres and oxidation temperature/duration). In general, the PL spectra consist of a near-band-edge UV peak and a wide peak in the visible light region. The relative intensity ratios between these two peaks and the position of the visible light emission are highly dependent on the deposition and oxidation conditions. Particularly, ZnO films with one dominant peak of UV, violet, green, or orange/red could be prepared, indicating that tuneable emissions could be obtained from undoped ZnO films with this technique (Fig. 18.6).

#### *Effect of sputtering and oxidizing atmospheres*

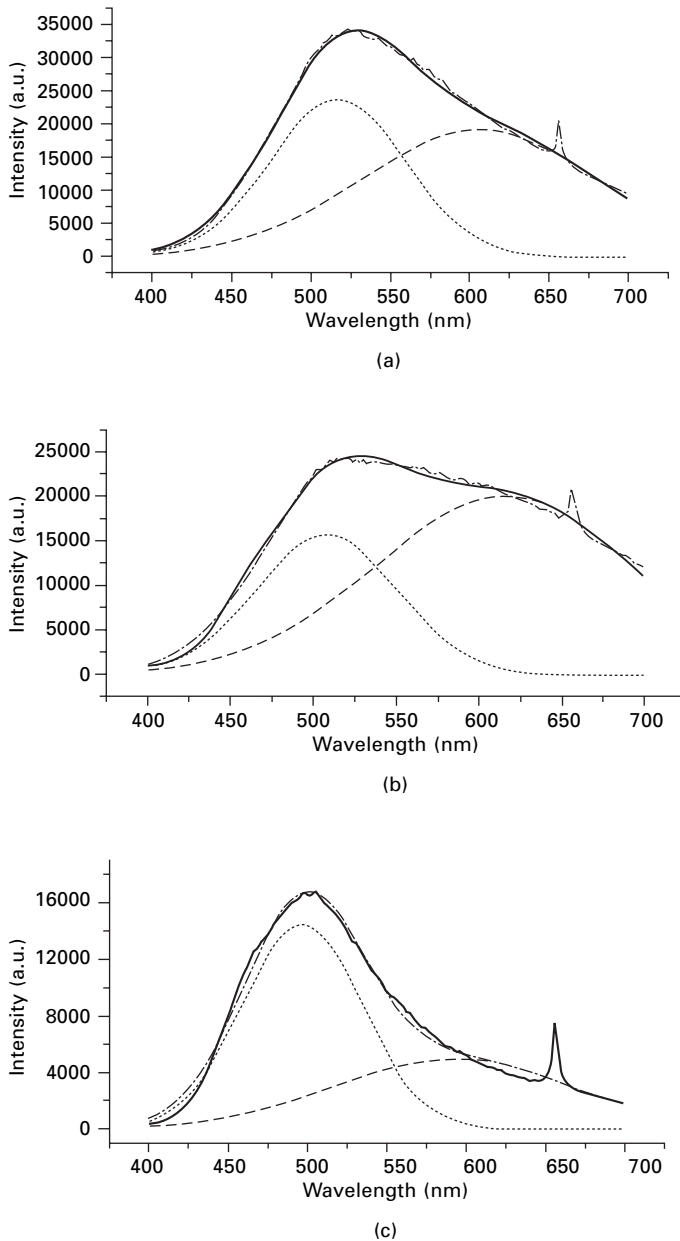
ZnO films grown from pure Zn films in different wet atmospheres (argon, nitrogen or oxygen) show different room temperature PL properties. The



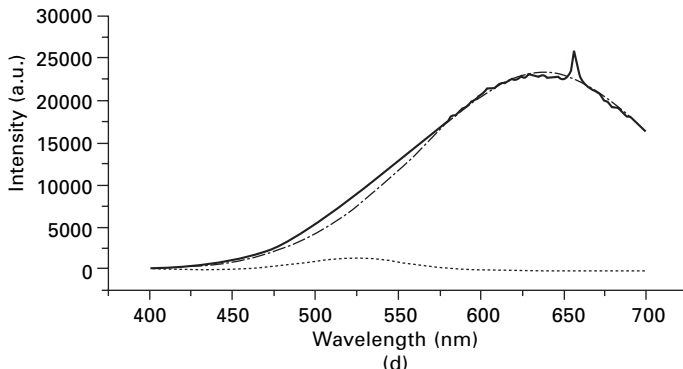
18.6 Typical photoluminescence spectra of ZnO films prepared by sputtering deposition–wet oxidation.

sample grown in wet oxygen has the strongest UV emission and the highest ratio of UV to visible light emission. It is supposed that in wet argon or nitrogen, the oxides formed may not have perfect crystallinity and/or stoichiometry and thus have a high defect concentration, leading to strong visible light emissions. On the contrary, oxidation in wet oxygen will supply the reaction with sufficient oxygen, and then grow oxide films with a better quality and fewer defects, leading to a stronger near band edge emission. Gaussian fitting analysis of the broad band in the visible light region revealed two peaks. For the oxide film grown in wet oxygen, the two peaks were positioned at 515 and 592 nm, and the integrated intensity ratio of  $E_{515}$  to  $E_{592}$  was 0.73. For the film grown in wet nitrogen, the peaks were centred at 504 and 569 nm; and the integrated intensity ratio of  $E_{504}$  to  $E_{569}$  was 1.95. This result showed that the defect species responsible for these two emissions (504/515 and 569/592 nm) should have some relation to the oxygen potential in the growth atmosphere. Oxidation treatment in oxygen-rich atmosphere favours the emission with a longer wavelength.

Stronger green and red/orange emissions could be observed in the ZnO films grown from the composite Zn-ZnO precursor films which were deposited in Ar with 10% and 20% oxygen. The broad defect-related emission was much stronger than the UV, and was fitted with two Gaussian peaks. One is located in the wavelength region of 518–534 nm (green); the other is shifted from 616 to 647 nm monotonically as the oxygen content increased (orange/red). The relative intensity ratios of green to red are 0.72, 0.37 and 0.024 for oxygen contents of 0, 10% and 20%, respectively (Fig. 18.7(a),(b) and (d)). For the specimen with 10% oxygen in sputtering atmosphere, when the carrier gas was changed from oxygen to argon, i.e., when the total oxygen



18.7 Effects of sputtering and oxidizing atmospheres on the visible light emissions from ZnO films thermally grown from Zn-ZnO composite precursor films: (a) sputtered in Ar and oxidized in wet oxygen; (b) sputtered in Ar + 10%O<sub>2</sub> and oxidized in wet oxygen; (c) sputtered in Ar + 10%O<sub>2</sub> and oxidized in wet argon; (d) sputtered in Ar + 20%O<sub>2</sub> and oxidized in wet oxygen.



18.7 (Continued)

content in the oxidizing atmosphere was decreased, the relative intensity ratio of green to red increased sharply from 0.37 to 1.44 (Fig. 18.7(c)).

The change in visible light emission properties of the ZnO films grown in different atmospheres implied that the defects were controlled by the oxygen content. ZnO particles in the precursor formed by this partial reactive deposition might have some defects due to the oxygen deficiency in the sputtering atmosphere. There are two types of intrinsic defects in undoped ZnO; one is oxygen vacancy ( $V_o$ ), and the other is interstitial zinc ( $Zn_i$ ) [227]. It was found that the formation enthalpy for  $Zn_i$  is low under both Zn-rich and O-rich conditions. However, some studies indicated that  $V_o$  may have the lowest formation energy [228–230]. It is then supposed that the original ZnO particles in the precursor films might have some defects, such as  $Zn_i$  and/or  $V_o$ . As the oxygen content in the sputtering atmosphere increases, the amount of imperfect ZnO particles in the composite precursor films increases, and/or the defect concentration in the imperfect ZnO decreases.

When exposed to high temperatures, these defects would be changed and new defects would be formed depending on the oxygen potential in the oxidizing atmosphere. For the oxidation process in wet oxygen, the excess Zn would tend to combine with oxygen to form oxide on the surface, generating extra spaces in the lattice. It is therefore possible to saturate the film with excess oxygen in the form of  $O_i$  [231]. However, if the oxygen in the oxidizing atmosphere is not sufficient, for example if the carrier gas was argon or nitrogen, the formation probability of  $O_i$  would be quite low. At the same time, the Zn particles in the precursor films will be transformed into ZnO. Under oxygen-rich conditions, Zn vacancy might be abundant in these oxide particles. Under certain conditions, oxygen would then be incorporated into the lattice and occupy the sites of Zn, forming antisite defects of  $O_{Zn}$ . In addition, hydrogen generated by the interaction between  $H_2O$  and Zn will enhance the sublimation of ZnO particles, i.e., the loss of Zn. This process

might also increase the formation of oxygen related defects, such as  $O_{Zn}$  and/or  $O_i$ .

It is therefore supposed that two types of defects will govern the colour emissions:  $O_{Zn}$  and/or  $Zn_i$  for green, and  $O_i$  for red/orange. They may co-exist in the ZnO films. Since both of them are generated by complex interactions with oxygen, they compete with each other. As the oxygen content in the sputtering atmosphere increases, the amount of original ZnO particles increases. After thermal oxidation, the concentration of  $O_i$  also increases, leading to a stronger red emission. In addition, the particle size, porosity and microstructures of these films are quite different. These differences may affect the PL, since the electronic structure of grain boundaries plays an important role in defect chemistry [232]. Further studies are needed in this direction.

#### *Effect of oxidation temperature*

It was reported that the PL properties of ZnO films formed by thermal oxidation were highly related to the processing temperature [143–145,147]. In the studies conducted by the present authors, the oxidation temperature was varied from 375 to 600°C. The results showed that the ZnO films grown from pure Zn films at 420°C had the strongest intensity of UV emission, followed by the films oxidized at 375, 500 and 600°C. This behaviour is similar to that reported in Ref. 145. The FWHM of the UV peak can be as low as 106 meV, which is comparable with the typical values (80–140 meV) from bulk and film of ZnO, indicating that the ZnO films grown by wet oxidation also had good optical qualities.

At 600°C, the intensity of the visible light emission is much higher than that of the UV emission. This wide band was analysed by Gaussian fitting, giving two peaks centred at ~520 nm (green) and ~620 nm (red). The integrated intensity ratio of red to green emission increased with increasing temperature from 0.63 at 420°C through 0.77 at 500°C to 1.25 at 600°C [233].

It is generally believed that the wide range of visible emissions are mainly due to intrinsic defects such as zinc/oxygen interstitials, zinc/oxygen vacancies, antisite oxygen and/or extrinsic impurities such as Cu [234–238]. Singly ionized oxygen vacancies, zinc interstitials and antisite oxygen might be responsible for the green emission in ZnO. Red/orange emission can be observed in undoped ZnO with surplus oxygen, and is attributed to oxygen interstitials ( $O_i$ ) [239,240]. Since these ZnO films were grown in oxygen-rich wet atmospheres, and the films oxidized at a higher temperature showed a stronger red emission, it is believed that oxygen-related defects, such as  $O_i$ , might be the origin. This is consistent with the experimental observations that annealing of ZnO in oxygen-rich atmospheres at temperatures higher than 600°C normally led to red emission [241,242]. Due to the competition between green and red emissions with oxidation temperature,

the defects governing the green emission could also be oxygen-related species.

#### *Effect of oxidation time*

The effect of oxidation time on the room temperature PL properties of ZnO films thermally grown from Zn precursor films was also studied. It can be clearly seen that the sample after 1 h exposure has the highest intensity ratio of UV to visible light emission, while longer oxidation significantly decreases the UV emission and increases the defect-related emission. Closer observation also reveals that a long exposure time slightly shifts the visible light emission to the longer wavelength region. As the duration of exposure increased from 0.5 to 2 h, the ratio of red to green emission increased from 0.68 to 1.25.

A short oxidation time may have two effects on the quality of the films. Firstly, the reaction between oxygen and zinc might not be completed. Secondly, the reaction is completed but many defects will be generated due to the fast growth process. This is especially true for oxidation of Zn at temperatures higher than its melting point. These defects could be partially annihilated during further annealing at elevated temperatures through diffusion and/or recrystallization processes. However, long-term annealing in wet oxygen atmospheres may have a negative influence on the structural and optical properties of the ZnO film since interactions between oxygen/hydrogen-related species with ZnO will lead to the formation of new defect species and/or a defect-rich layer in the near-surface region, resulting in new emission peaks and/or degradation of optical quality [236].

## **18.5 Concluding remarks**

Oxidation of metals normally leads to many undesirable consequences – materials loss, property degradation and structural damage – therefore it should be prevented by establishing a slow-growing stable oxide scale on the material surface to protect the underlying substrate. Oxidation reactions under well-defined conditions, however, are finding application in the processing of electronic materials. Thick SiO<sub>2</sub> films for diffusion barriers and electronic passivation are commonly prepared by dry or wet oxidation. Recent studies also indicated that modified oxidation techniques can be used to fabricate ultra-thin SiO<sub>2</sub> films and low-dimensional Si and ZnO nanostructures for the development of electronic devices with nanoscale dimensions. The electrical, mechanical, optical and photonic properties of these ultra-thin films and nanostructures are highly dependent on the oxidation processing conditions, especially atmosphere and temperature. Since most oxides and nitrides are excellent electronic materials, the capabilities of oxidation and nitridation should be fully explored with attempts to produce

thin films, composite layers and novel structures with well-controlled composition, dimension, shape, size and properties for various functional applications.

## 18.6 References

1. A. Nurmikkoy and R.L. Gunshorz, *Semicond. Sci. Technol.*, 12 (1997) 1337.
2. S.J. Pearton and F. Ren, *Adv. Mater.*, 12 (2000) 1571.
3. R.F. Davis, S. Einfeldt, E.A. Preble, A.M. Roskowski, Z.J. Reitmeier and P.Q. Miraglia, *Acta Mater.*, 51 (2003) 5961.
4. K. Seeger, *Semiconductor Physics: An Introduction*, Berlin, New York: Springer, 2002.
5. P. Kofstad, *High Temperature Corrosion*, London, New York: Elsevier, 1988.
6. G. Kamarinos and P. Felix, *J. Phys D – Appl. Phys.*, 29 (1996) 487.
7. S.M. Celik and M.C. Ozturk, *J. Electrochem. Soc.*, 145 (1998) 3602.
8. M. Nagase, S. Horiguchi, K. Shiraishi, A. Fujiwara and Y. Takahashi, *J. Electroanal. Chem.*, 559 (2003) 19.
9. I. Rapoport, P. Taylor, S.B. Kim, B. Orschel, J. Kearns and Y. Narendra, *ECS Transactions*, 1 (2005) 234.
10. W. Shockley, *Phys. Rev.*, 56 (1939) 317.
11. C.N. Berglund, *IEEE Trans. Electron. Dev.*, ED-IB (1966) 701.
12. P.V. Gray and D.M. Brown, *Appl. Phys. Lett.*, 8 (1966) 31.
13. R. Castagne and A. Vapaille, *Surf. Sci.*, 28 (1971) 557.
14. M.M. Atalla, E. Tannenbaum and E.J. Scheiber, *Bell Syst. Tech. J.*, 38 (1959) 749.
15. E.A. Irene, *Integrated Circuits*, ed. P. Stroeve, American Chemical Society, 1985.
16. H.Z. Massoud, J.D. Plummer and E.A. Irene, *J. Electrochem. Soc.*, 132 (1985) 1745.
17. H.Z. Massoud, J.D. Plummer and E.A. Irene, *J. Electrochem. Soc.*, 132 (1985) 2686.
18. H.Z. Massoud, J.D. Plummer and E.A. Irene, *J. Electrochem. Soc.*, 132 (1985) 2693.
19. E.A. Lewis and E.A. Irene, *J. Electrochem. Soc.*, 134 (1987) 2332.
20. A. Atkinson, *Rev. Mod. Phys.*, 57 (1985) 437.
21. E.A. Irene, *Crit. Rev. Solid State Mat. Sci.*, 14 (1988) 175.
22. T. Hattori, *Crit. Rev. Solid State Mat. Sci.*, 20 (1995) 339.
23. H.Z. Massoud, *Solid State Electron.*, 41 (1997) 929.
24. D.R. Wolters and A.T.A. Zegers-Van Duijnhoven, *Microelectron. Reliab.*, 38 (1998) 259.
25. K. Garikipati and V.S. Rao, *J. Comput. Phys.*, 174 (2001) 138.
26. A.G. Revesz and H.L. Hughes, *J. Non-Cryst. Solids*, 328 (2003) 48.
27. C.J. Sofield and A.M. Stoneham, *Semicond. Sci. Technol.*, 10 (1995) 215.
28. H.E. Maes, C. Claeys, R. Mertens, A. Campitelli, C. Van Hoof and J. De Boeck, *Adv. Eng. Mater.*, 3 (2001) 781.
29. R.W. Keyes, *Rep. Prog. Phys.*, 68 (2005) 2701.
30. J. Robertson, *Eur. Phys. J. Appl. Phys.*, 28 (2004) 265.
31. G.D. Wilk, R.M. Wallace and J.M. Anthony, *J. Appl. Phys.*, 87 (2000) 484.
32. J.P. Locquet, C. Marchiori, M. Sousa, J. Fompeyrine and J.W. Seo, *J. Appl. Phys.*, 100 (2006) 051610.

33. S.K. Ray, R. Mahapatra and S. Maikap, *J. Mater. Sci.: Mater. Electron.*, 17 (2006) 689.
34. M.M. Moslehi, S.C. Shatas and K.C. Saraswat, *Appl. Phys. Lett.*, 47 (1985) 1353.
35. T.Y. Luo, M. Laughery, G.A. Brown, H.N. Al-Shareef, V.H.C. Watt, A. Karamcheti, M.D. Jackson and H.R. Huff, *IEEE Electron Device Lett.*, 21 (2000) 430.
36. M.L. Green, E.P. Gusev, R. Degraeve and E.L. Garfunkel, *J. Appl. Phys.*, 90 (2001) 2057.
37. P. Mur, M.N. Semeria, M. Olivier, A.M. Pagon, C. Leroux, G. Reimbold, P. Gentile, N. Magnea, T. Baron, R. Clerc and G. Ghibaudo, *Appl. Surf. Sci.*, 175–176 (2001) 726.
38. V.K. Bhat, K.N. Bhat and A. Subrahmanyam, *Mater. Sci. Eng. B*, 98 (2003) 140.
39. A. Ludsteck, J. Schulze, I. Eisele, W. Dietl and Z. Nenyei, *J. Appl. Phys.*, 95 (2004) 2827.
40. A. Fukano and H. Oyanagi, *Mat. Res. Soc. Symp. Proc.*, 811 (2004) E1.3.1.
41. R. Singh, R. Paily, A. DasGupta, N. DasGupta, P. Misra and L.M. Kukreja, *Electron. Lett.*, 40 (2004) 1606.
42. P. Morgen, A. Bahari, U. Robenhagen, J.F. Andersen, J.K. Hansen, K. Pedersen, M.G. Rao and Z.S. Li, *J. Vac. Sci. Technol. A*, 23 (2005) 201.
43. P. Patzner, A.V. Osipov and P. Hess, *Appl. Phys. A*, 85 (2006) 145.
44. H.Z. Massoud, *ECS Transactions*, 2 (2006) 189.
45. A. Stadler, *IEEE Trans. Dielectr. Electr. Insul.*, 13 (2006) 394.
46. J.Y. Zhang and J.W. Boyd, *Appl. Phys. Lett.*, 71 (1997) 2964.
47. A. Fukano and H. Oyanagi, *Mat. Res. Soc. Symp. Proc.*, 751 (2003) Z3.19.1.
48. P. Patzner, A.V. Osipov and P. Hess, *Appl. Surf. Sci.*, 247 (2005) 204.
49. A.V. Osipov, P. Patzner and P. Hess, *Appl. Phys. A*, 82 (2005) 275.
50. J.C. Tinoco, M. Estrada and G. Romero, *Microelectron. Reliab.*, 43 (2003) 895.
51. J.C. Tinoco, M. Estrada, H. Baez and A. Cerdeira, *Thin Solid Films*, 496 (2006) 546.
52. Y. Cui and C.M. Lieber, *Science*, 291 (2001) 851.
53. Y. Cui, Q.Q. Wei, H.K. Park and C.M. Lieber, *Science*, 293 (2001) 1289.
54. D.B. Kao, J.P. McVittie, W.D. Nix and K.C. Saraswat, *IEEE Trans. Electron. Devices*, ED-34 (1987) 1008.
55. D.B. Kao, J.P. McVittie, W.D. Nix and K.C. Saraswat, *IEEE Trans. Electron. Devices*, ED-35 (1988) 25.
56. B.E. Deal and A.S. Grove, *J. Appl. Phys.*, 36 (1965) 3770.
57. E.A. Irene, E. Tierney and J. Angillelo, *J. Electrochem. Soc.*, 129 (1982) 2594.
58. H.I. Liu, D.K. Biegelsen, N.M. Johnson, F.A. Ponce and R.F.W. Pease, *J. Vac. Sci. Technol. B*, 11 (1993) 2532.
59. H.I. Liu, D.K. Biegelsen, F.A. Ponce, N.M. Johnson and R.F.W. Pease, *Appl. Phys. Lett.*, 64 (1994) 1383.
60. D. Shir, B.Z. Liu, A.M. Mohammad, K.K. Lew and S.E. Mohney, *J. Vac. Sci. Technol. B*, 24 (2006) 1333.
61. J. Kedzierski, J. Bokor and C. Kisielowski, *J. Vac. Sci. Technol. B*, 15 (1997) 2825.
62. J.L. Liu, Y. Shi, F. Wang, Y. Lu, S.L. Gu, R. Zhang and Y.D. Zheng, *Appl. Phys. Lett.*, 68 (1996) 352.
63. J.L. Liu, Y. Shi, F. Wang, Y. Lu, S.L. Gu, R. Zhang and Y.D. Zheng, *Appl. Phys. Lett.*, 69 (1996) 1761.
64. E. Leobandung, L.J. Guo and S.Y. Chou, *Appl. Phys. Lett.*, 67 (1995) 2338.

65. A. Fujiwara, Y. Takahashi, K. Murase and M. Tabe, *Appl. Phys. Lett.*, 67 (1995) 2957.
66. C. Single, F. Zhou, H. Heidemeyer, F.E. Prins, D.P. Kern and E. Piles, *J. Vac. Sci. Technol. B*, 16 (1998) 3938.
67. H. Heidemeyer, C. Single, F. Zhou, F.E. Prins, D.P. Kern and E. Piles, *J. Appl. Phys.*, 87 (2000) 4580.
68. B. Schwartz, *Crit. Rev. Solid State Mat. Sci.*, 5 (1975) 609.
69. S.P. Murarka, *Appl. Phys. Lett.*, 26 (1975) 180.
70. C.D. Thurmond, G.P. Schwartz, G.W. Kammlot and B. Schwartz, *J. Electrochem. Soc.*, 127 (1980) 1366.
71. C.W. Wilmsen, *J. Vac. Sci. Technol.*, 19 (1981) 279.
72. O.R. Monteiro and J.W. Evans, *J. Vac. Sci. Technol. A*, 7 (1989) 49.
73. T. Ishikawa and H. Ikoma, *Jpn. J. Appl. Phys.*, 31 (1992) 3981.
74. G. Hollinger, R. Skheyta-Kabbani and M. Gendry, *Phys. Rev. B*, 49 (1994) 11159.
75. Z.H. Lu, B. Bryskiewicz, J.P. McCaffrey, Z. Wasilewski and M.J. Graham, *J. Vac. Sci. Technol. B*, 11 (1993) 2033.
76. P.R. Lefebvre and E.A. Irene, *J. Vac. Sci. Technol. B*, 15 (1997) 1173.
77. P.R. Lefebvre, C. Zhao and E.A. Irene, *Thin Solid Films*, 313–314 (1998) 454.
78. P.R. Lefebvre, L. Lai and E.A. Irene, *J. Vac. Sci. Technol. B*, 16 (1998) 996.
79. T.H. Oh, D.L. Huffaker, L.A. Graham, H. Deng and D.G. Deppe, *Electron. Lett.*, 32 (1996) 2024.
80. T. Sugimura, T. Tsuzuku, T. Katsui, Y. Kasai, T. Inokuma, S. Hashimoto, K. Iiyama and S. Takamiya, *Solid State Electron.*, 43 (1999) 1571.
81. M. Takebe, K. Nakamura, N.C. Paul, K. Iiyama and S. Takamiya, *IEEE Trans. Electron. Devices*, 51 (2004) 311.
82. M. Passlack, M. Hong, J.P. Mannaerts, R.L. Opila, S.N.G. Chu, N. Moriya, F. Ren and J.R. Kwo, *IEEE Trans. Electron. Devices*, 44 (1997) 214.
83. M. Hong, M. Passlack, J.P. Mannaerts, T.D. Harris, M.C. Schnoes, R.L. Opila and H.W. Krautter, *Solid State Electron.*, 41 (1997) 643.
84. R.M. Scanlan, *Annu. Rev. Mater. Res.*, 10 (1980) 113.
85. J.G. Bednorz and K.A. Muller, *Z. Phys. B: Condens. Matter*, 64 (1986) 188.
86. R.J. Cava, *J. Am. Ceram. Soc.*, 83 (2000) 5.
87. D. Dew-Hughes, *Low Temp. Phys.*, 27 (2001) 713.
88. D.U. Gubser, *IEEE Trans. Appl. Supercond.*, 14 (2004) 2037.
89. L.C. Pathak and S.K. Mishra, *Supercond. Sci. Technol.*, 18 (2005) R67.
90. S. Jin and J.E. Graebner, *Mat. Sci. Eng. B*, 7 (1991) 243.
91. M. Schieber, *J. Cryst. Growth*, 109 (1991) 401.
92. K.H. Dahmen and T. Gerfin, *Prog. Cryst. Growth Charact. Mater.*, 27 (1993) 117.
93. A. Otto, L.J. Masur, J. Gannon, E. Podtburg, D. Daly, G.J. Yurek and A.P. Malozemoff, *IEEE Trans. Appl. Supercond.*, 3 (1993) 915.
94. M. Murakami, *Prog. Mater. Sci.*, 38 (1994) 311.
95. L.J. Masur, E.R. Podtburg, C.A. Craven, A. Otto, Z.L. Wang, D.M. Kroeger, J.Y. Coulter and M.P. Maley, *Physica C*, 230 (1994) 274.
96. J.N. Eckstein and I. Bozovic, *Annu. Rev. Mater. Res.*, 25 (1995) 679.
97. V. Matijasevic and I. Bozovict, *Curr. Opin. Solid State Mat. Sci.*, 1 (1996) 47.
98. S. Sengupta, *JOM*, 50 (1998) 19.
99. N.J. Long, R.G. Buckley, D. Pringle and A. Otto, *IEEE Trans. Appl. Supercond.*, 11 (2001) 2901.
100. P. Kuppusami and V.S. Raghunathan, *Int. Mater. Rev.*, 48 (2003) 1.

101. V. Pokropivny, Int. J. Nanotech., 1 (2004) 170.
102. W. Assmus and W. Schmidbauer, Supercond. Sci. Technol., 6 (1993) 555.
103. A. Revcolevschi and J. Jegoudez, Prog. Mater. Sci., 42 (1997) 321.
104. Y. Shiohara and A. Endo, Mater. Sci. Eng. R, 19 (1997) 1.
105. D.L. Kaiser and L.F. Schneemeyer, Growth of superconducting single crystals, in *Handbook of Superconducting Materials*, eds D.A. Cardwell and D.S. Ginley, Bristol and Philadelphia: Institute of Physics Publishing Ltd, 2003.
106. G.J. Yurek, J.B. Vander Sande, W.X. Wang, D.A. Rudman, Y. Zhang and M.M. Matthiesen, Metall. Trans. A, 18 (1987) 1813.
107. G.J. Yurek, J.B. Vander Sande, W.X. Wang and D.A. Rudman, J. Electrochem. Soc., 134 (1987) 2635.
108. R. Haldar, Y.Z. Lu and B.C. Giessen, Appl. Phys. Lett., 51 (1987) 538.
109. W. Gao, S.C. Li, D.A. Rudman and J.B. Vander Sande, Physica C, 167 (1990) 395.
110. W. Gao, D.A. Rudman and J.B. Vander Sande, J. Met., June 1990, 19.
111. K. Matsuzaki, Y. Kawamura, A. Inoue and T. Masumoto, J. Mater. Sci. Lett., 17 (1998) 939.
112. W. Gao, S.C. Li, D.A. Rudman, G.J. Yurek and J.B. Vander Sande, Physica C, 161 (1989) 71.
113. J.S. Luo, D. Michel and J.P. Chevalier, Appl. Phys. Lett., 55 (1989) 1448.
114. H.S. Chen, S.H. Liou, A.R. Kortan and L.C. Kimerling, Appl. Phys. Lett., 53 (1988) 705.
115. W. Gao, S.C. Li, D.A. Rudman, G.J. Yurek and J.B. Vander Sande, Appl. Phys. Lett., 55 (1989) 2227.
116. W. Gao and J.B. Vander Sande, Physica C, 171 (1990) 69.
117. W. Gao and J.B. Vander Sande, Mater. Sci. Eng. B, 8 (1991) 63.
118. W. Gao, S.C. Li, D.A. Rudman, G.J. Yurek and J.B. Vander Sande, J. Electrochem. Soc., 137 (1990) 1951.
119. W. Gao and J.B. Vander Sande, Physica C, 181 (1991) 105.
120. W. Gao and J.B. Vander Sande, Supercond. Sci. Technol. 5 (1992) 318.
121. W. Gao and J.B. Vander Sande, J. de Physique IV, 3 (1993) 187.
122. W. Gao, R. Parrella and J.B. Vander Sande, Physica C, 192 (1992) 173.
123. D.C. Look, J. Electron. Mater., 35 (2006) 1299.
124. Ü. Özgür, Ya.I. Alivov, C. Liu, A. Teke, M.A. Reshchikov, S. Dogan, V. Avrutin, S.J. Cho and H. Morkoç, J. Appl. Phys., 98 (2005) 041301.
125. S.J. Pearton, D.P. Norton, K. Ip, Y.W. Heo and T. Steiner, Prog. Mater. Sci., 50 (2005) 293.
126. D.R. Clarke, J. Am. Ceram. Soc., 82 (1999) 485.
127. C.R. Gorla, N.W. Emanetoglu, S. Liang, W.E. Mayo, Y. Lu, M. Wraback and H. Shen, J. Appl. Phys., 85 (1999) 2595.
128. H. Yamada, Y. Ushimi, M. Takeuchi, Y. Yoshino, T. Makino and S. Arai, Vacuum, 74 (2004) 689.
129. J.J. Chen, F. Zeng, D.M. Li, J.B. Niu and F. Pan, Thin Solid Films, 485 (2005) 257.
130. A. Waag, T. Gruber, C. Kirchner, D. Klärer, K. Thonke, R. Sauer, F. Forster, F. Bertram and J. Christen, ZnO metal organic vapor phase epitaxy: present state and prospective application in optoelectronics and spin electronics, in *Advances in Solid State Physics*, ed. B. Kramer, 42 (2002) 81.
131. H. Ohta, and H. Hosono, Materials Today, 7 (2004) 42.
132. K. Ramamoorthy, K. Kumar, R. Chandramohan and K. Sankaranarayanan, Mater. Sci. Eng. B, 126 (2006) 1.

133. Y. Ryu, T.S. Lee, J.A. Lubguban, H.W. White, B.J. Kim, Y.S. Park and C.J. Youn, *Appl. Phys. Lett.*, 88 (2006) 241108.
134. D.C. Look, *J. Electron. Mater.*, 35 (2006) 1299.
135. T. Gruber, C. Kirchner and A. Waag, *Phys. Stat. Sol. B*, 229 (2002) 841.
136. D.C. Agarwal, R.S. Chauhan, J.C. Pivin, M. Kumar, J. Ghatak and P.V. Satyam, *J. Appl. Phys.*, 99 (2006) 123105.
137. D.C. Look, D.C. Reynolds, C.W. Litton, R.L. Jones, D.B. Eason and G. Cantwell, *Appl. Phys. Lett.*, 81 (2002) 1830.
138. Y.R. Ryu, S. Zhu, J.D. Budai, H.R. Chandrasekhar, P.F. Miceli and H.W. White, *J. Appl. Phys.*, 88 (2000) 201.
139. N.I. Kovtyukhova, E.V. Buzaneva, C.C. Waraksa, B.R. Martin and T.E. Mallouk, *Chem. Mater.*, 12 (2000) 383.
140. S.A. Studenikin, N. Golego and M. Cocivera, *J. Appl. Phys.*, 83 (1998) 2104.
141. O. Kappertz, R. Drese and M. Wuttig, *J. Vac. Sci. Technol. A*, 20 (2002) 2084.
142. M. Ortega-Lopez, A. Avila-Garcia, M.L. Albor-Aguilera and V.M. Sanchez Resendiz, *Mater. Res. Bull.*, 38 (2003) 1241.
143. S.L. Cho, J. Ma, Y.K. Kim, Y. Sun, G.K.L. Wong and J.B. Ketterson, *Appl. Phys. Lett.*, 75(18) (1999) 2761.
144. S.J. Chen, Y.C. Liu, J.G. Ma, D.X. Zhao, Z.Z. Zhi, Y.M. Lu, J.Y. Zhang, D.Z. Shen and X.W. Fan, *J. Cryst. Growth*, 240 (2002) 467.
145. Y.G. Wang, S.P. Lau, H.W. Lee, S.F. Yu, B.K. Tay, X.H. Zhang and H.H. Hng, *J. Appl. Phys.*, 94 (2003) 354.
146. J. Zhao, L.Z. Hu, Z.Y. Wang, Y. Zhao, X.P. Liang and M.T. Wang, *Appl. Surf. Sci.*, 229 (2004) 311.
147. Ya.I. Alivov, A.V. Chernykh, M.V. Chukichev and R.Y. Korotkov, *Thin Solid Films*, 473 (2005) 241.
148. T.W. Kim, T. Kawazoe, S. Yamazaki and M. Ohtsu, *Appl. Phys. A*, 80 (2005) 1049.
149. W. Gao, Z.W. Li, R. Harikisun and S.S. Chang, *Mater. Lett.*, 57 (2003) 1435.
150. X.T. Zhang, Y.C. Liu, Z.Z. Zhi, J.Y. Zhang, Y.M. Lu, W. Xu, D.Z. Shen, G.Z. Zhong, X.W. Fan and X.G. Kong, *J. Cryst. Growth*, 240 (2002) 463.
151. P.P. Gorbik, A.A. Dadykin, I.V. Dubrovin, A.G. Naumovets, V.M. Ogenko and N.V. Parkhomovskii, *Inorg. Mater.*, 37(7) (2001) 817.
152. X.D. Gao, X.M. Li and W.D. Yu, *Mater. Sci. Eng. B*, 113 (2004) 274.
153. A. Miyake, H. Kominami, T. Aoki, N. Azuma, Y. Nakanish and Y. Hatanaka, *Phys. Stat. Sol. B*, 229(2) (2002) 829.
154. L.L. Chen, J.G. Lu, Z.Z. Ye, Y.M. Lin, B.H. Zhao, Y.M. Ye, J.S. Li and L.P. Zhu, *Appl. Phys. Lett.*, 87 (2005) 252106.
155. J.G. Lu, Z.Z. Ye, F. Zhuge, Y.J. Zeng, B.H. Zhao and L.P. Zhu, *Appl. Phys. Lett.*, 85 (2004) 3134.
156. G. Du, Y. Ma, Y. Zhang and T. Yang, *Appl. Phys. Lett.*, 87 (2005) 213103.
157. J.F. Rommeluère, L. Svob, F. Jomard, J. Mimila-Arroyo, A. Lusson and V. Sallet, *Appl. Phys. Lett.*, 83 (2003) 287.
158. A. Tsukazaki, A. Ohtomo, T. Onuma, M. Ohtani, T. Makino, M. Sumiya, K. Ohtani, S.F. Chichibu, S. Fuke, Y. Segawa, H. Ohno, H. Koinuma and M. Kawasaki, *Nat. Mater.*, 4 (2005) 42.
159. D.C. Oh, J.J. Kim, H. Makino, T. Hanada, M.W. Cho, T. Yao and H.J. Ko, *Appl. Phys. Lett.*, 86 (2005) 042110.
160. C.C. Lin, S.Y. Chen, S.Y. Cheng and H.Y. Lee, *Appl. Phys. Lett.*, 84 (2004) 5040.

161. J.M. Bian, X.M. Li, X.D. Gao, W.D. Yu and L.D. Chen, *Appl. Phys. Lett.*, 84 (2004) 541.
162. C. Wang, Z.G. Ji, K. Liu, Y. Xiang and Z.Z. Ye, *J. Cryst. Growth*, 259 (2003) 279.
163. Z.Y. Xiao, Y.C. Liu, J.Y. Zhang, D.X. Zhao, Y.M. Lu, D.Z. Shen and X.W. Fan, *Semicond. Sci. Technol.*, 20 (2005) 796.
164. E. Kaminska, A. Piotrowska, J. Kossut, A. Barcz, R. Butkute, W. Dobrowolski, E. Dynowska, R. Jakiela, E. Przezdziecka, R. Lukasiewicz, M. Aleszkiewicz, P. Wojnar and E. Kowalczyk, *Solid State Commun.*, 135 (2005) 11.
165. Y. Nakano, T. Morikawa, T. Ohwaki and Y. Taga, *Appl. Phys. Lett.*, 88 (2006) 172103.
166. C.M. Lieber, *MRS Bull.*, 28 (2003) 486.
167. Y.W. Heo, D.P. Norton, L.C. Tien, Y. Kwon, B.S. Kang, F. Ren, S.J. Pearton and J.R. LaRoche, *Mater. Sci. Eng. R*, 47 (2004) 1.
168. W.I. Park, J.S. Kim, G.C. Yi and H.J. Lee, *Adv. Mater.*, 17 (2005) 1393.
169. Z.L. Wang and J.H. Song, *Science*, 312 (2006) 242.
170. Y. Wu, J. Xiang, C. Yang, W. Lu and C.M. Lieber, *Nature*, 430 (2004) 61.
171. P.X. Gao, Y. Ding, W.J. Mai, W.L. Hughes, C.S. Lao, and Z.L. Wang, *Science*, 309 (2005) 1700.
172. Z.W. Pan, Z.R. Dai and Z.L. Wang, *Science*, 291 (2001) 1947.
173. Z.L. Wang, *J. Phys.: Condens. Matter*, 16 (2004) R829.
174. Y. Li, G.W. Meng, L.D. Zhang and F. Phillip, *Appl. Phys. Lett.*, 76 (2000) 2011.
175. Y.C. Kong, D.P. Yu, B. Zhang, W. Fang and S. Feng, *Appl. Phys. Lett.*, 78 (2001) 407.
176. Z.W. Pan, S. Dai, C.M. Rouleau and D.H. Lowndes, *Angew. Chem. Int. Edn. Engl.*, 44 (2005) 274.
177. W.I. Park, D.H. Kim, S.W. Jung and G.C. Yi, *Appl. Phys. Lett.*, 80 (2002) 4232.
178. S.W. Kim, S. Fujita and S. Fujita, *Appl. Phys. Lett.*, 86 (2005) 153119.
179. Y.J. Choi, J.H. Park and J.G. Park, *J. Mat. Res.*, 20 (2005) 959.
180. Y.W. Heo, V. Varadarajan, M. Kaufman, K. Kim, D.P. Norton, F. Ren and P.H. Fleming, *Appl. Phys. Lett.*, 81 (2002) 3046.
181. L.C. Tien, D.P. Norton, S.J. Pearton, H.T. Wang and F. Ren, *Appl. Surf. Sci.*, 253 (2007) 4620.
182. Z.W. Liu, C.K. Ong, T. Yu and Z.X. Shen, *Appl. Phys. Lett.*, 88 (2006) 053110.
183. A. Rahm, E.M. Kaidashev, H. Schmidt, M. Diaconu, A. Poppl, R. Bottcher, C. Meinecke, T. Butz, M. Lorenz and M. Grundmann, *Microchim. Acta*, 156 (2007) 21.
184. B. Liu and H.C. Zeng, *J. Am. Chem. Soc.*, 125 (2003) 4430.
185. M. Yang, G.S. Pang, L.F. Jiang and S.H. Feng, *Nanotechnology*, 17 (2006) 206.
186. Y. Sun, N.G. Ndifor-Angwafor, D.J. Riley and M.N.R. Ashfold, *Chem. Phys. Lett.*, 431 (2006) 352.
187. I.S. Kim and G.H. Lee, *Solid State Commun.*, 123 (2002) 191.
188. T. Gao, Y.H. Huang and T.H. Wang, *J. Phys.: Condens. Matter*, 16 (2004) 1115.
189. H.J. Fan, F. Bertram, A. Dadgar, J. Christen, A. Krost and M. Zacharias, *Nanotechnology*, 15 (2004) 1401.
190. G.H. Lee, H.D. Jeon, W.J. Lee, B.C. Shin and I.S. Kim, *J. Cryst. Growth*, 277 (2005) 1.
191. H.J. Fan, R. Scholz, F.M. Kolb and M. Zacharias, *Appl. Phys. Lett.*, 85 (2004) 4142.
192. A. Sekar, S.H. Kim, A. Umar and Y.B. Hahn, *J. Cryst. Growth*, 277 (2005) 471.
193. Y.H. Gui, C.S. Xie, Q.Y. Zhang, M.L. Hu, J. Yu and Z. Weng, *J. Cryst. Growth*, 289 (2006) 663.

194. H. Pan, J.Z. Luo, H. Sun, Y.P. Feng, C.K. Poh and J.Y. Lin, Nanotechnology, 17 (2006) 2963.
195. H.J. Fan, R. Scholz, F.M. Kolb, M. Zacharias, U. Gosele, F. Heyroth, C. Eisenschmidt, T. Hempel and J. Christen, Appl. Phys. A, 79 (2004) 1895.
196. L.W. Yang, X.L. Wu, G.S. Huang, T. Qiu and Y.M. Yang, J. Appl. Phys., 97 (2005) 014308.
197. Z.G. Chen, A.Z. Ni, F. Li, H.T. Cong, H.M. Cheng and G.Q. Lu, Chem. Phys. Lett., 434 (2007) 301.
198. D.X. Zhao, Y.C. Liu, D.Z. Shen, Y.M. Lu, L.G. Zhang and X.W. Fan, J. Appl. Phys., 94 (2003) 5605.
199. Y.Q. Chen, J. Jiang, Z.Y. He, Y. Su, D. Cai and L. Chen, Mater. Lett., 59 (2005) 3280.
200. A. Umar, S.H. Kim, Y.H. Im and Y.B. Hahn, Superlattices Microstruct., 39 (2006) 238.
201. R.S. Wagner and W.C. Ellis, Appl. Phys. Lett., 4 (1964) 89.
202. Y. Ding, P.X. Gao and Z.L. Wang, J. Am. Chem. Soc., 126 (2004) 2066.
203. Y.J. Li, M. Feneberg, A. Reiser, M. Schirra, R. Enchelmaier, A. Ladenburger, A. Langlois, R. Sauer, K. Thonke, J. Cai and H. Rauscher, J. Appl. Phys., 99 (2006) 054307.
204. A. Rahmel and J. Tobolski, Corrosion Sci., 5 (1965) 333.
205. Z.W. Li and W. Gao, Thin Solid Films, 515 (2007) 3323.
206. G.W. Sears, Acta Metall., 3 (1955) 367.
207. D.R. Lide, *CRC Handbook of Chemistry and Physics*, 82nd Edition, Boca Raton, FL: CRC Press, 2001/2, 4–134.
208. G.M. Raynaud and R.A. Rapp, Oxid. Met., 21 (1984) 89.
209. D.A. Voss, E.P. Butler and T.E. Mitchell, Metall. Trans. A, 13 (1982) 929.
210. A. Atkinson and R.I. Taylor, Phil. Mag. A, 43 (1981) 979.
211. M.L. Volpe and J. Reddy, J. Chem. Phys., 53 (1970) 1117.
212. K. Kajihara and T. Yao, J. Sol-Gel Sci. Technol., 19 (2000) 219.
213. S.J. Bu, Z.G. Jin, X.X. Liu, H.Y. Du and Z.J. Cheng, J. Sol-Gel. Sci. Technol., 30 (2004) 239.
214. B. Guo, Z.L. Liu, L. Hong and H.X. Jiang, Surf. Coat. Technol., 198 (2005) 24.
215. X.X. Liu, Z.G. Jin, S.J. Bu and T. Yin, J. Sol-Gel. Sci. Technol., 36 (2005) 103.
216. G. Frenzer and W.F. Maier, Annu. Rev. Mat. Res., 36 (2006) 281.
217. Z.F. Liu, Z.G. Jin, W. Li and J.J. Qiu, Mater. Lett., 59 (2005) 3620.
218. Z.W. Li, W. Gao and R.J. Reeves, Surf. Coat. Technol., 198 (2005) 319.
219. Z.W. Li and W. Gao, Mater. Lett., 58 (2004) 1363.
220. Y.D. He and F.H. Stott, Corro. Sci., 38 (1996) 1853.
221. Z.W. Li, W. Gao, S. Li, D. Zhang and Y.D. He, Oxid. Met., 56 (2001) 495.
222. F.H. Stott, G.C. Wood and J. Stringer, Oxid. Met., 44 (1995) 113.
223. Y.D. He and F.H. Stott, Corro. Sci., 36 (1994) 1869.
224. A. Ul-Hamid, Oxid. Met., 58 (2002) 23.
225. B.L. Yi, *Fuel Cells*, Beijing: Chemical Industrial Press, 2003.
226. D.F. Donald and A.W. Searcy, J. Phys. Chem., 68 (1964) 2335.
227. G.D. Mahan, J. Appl. Phys., 54 (1983) 3825.
228. F. Oba, S.R. Nishitani, S. Isotani, H. Adachi and I. Tanaka, J. Appl. Phys., 90 (2001) 824.
229. S.B. Zhang, S.H. Wei and A. Zunger, Phys. Rev. B., 63 (2001) 075205.
230. A.F. Kohan, G. Ceder, D. Morgan and C.G. Van de Walle, Phys. Rev. B., 61 (2000) 15019.

231. X.L. Wu, G.G. Siu, C.L. Fu and H.C. Ong, *Appl. Phys. Lett.*, 78 (2001) 2285.
232. D. Fernandez-Hevia, J. de Frutos, A.C. Caballero and J.F. Fernandez, *Appl. Phys. Lett.*, 83 (2003) 2692.
233. W. Gao and Z.W. Li, *J. Alloy Compd.*, doi:10.1016/j.jallcom. 2006. 02.107, 2006.
234. E.G. Bylander, *J. Appl. Phys.*, 49 (1978) 1188.
235. K. Vanheusden, C. Seager, W.L. Warren, D.R. Tallant and J.A. Voiget, *Appl. Phys. Lett.*, 68 (1996) 403.
236. M. Liu, A.H. Kitai and P. Mascher, *J. Lumin.*, 54 (1992) 35.
237. B.X. Lin, Z.X. Fu, Y.B. Jia and G.H. Liao, *J. Electrochem. Soc.*, 148 (2001) G110.
238. N.Y. Garces, L. Wang, L. Bai, N.C. Giles, L.E. Halliburton and G. Cantwell, *Appl. Phys. Lett.*, 81 (2002) 622.
239. H.C. Ong and G.T. Du, *J. Cryst. Growth*, 265 (2004) 471.
240. S.A. Studenikin, N. Golego and M. Cocivera, *J. Appl. Phys.*, 84 (1998) 2287.
241. X. Liu, X.H. Wu, H. Cao and R.P.H. Chang, *J. Appl. Phys.*, 95 (2004) 3141.
242. Y.W. Heo, K. Ip, S.J. Pearton and D.P. Norton, *Phys. Stat. Sol. A*, 201 (2004) 1500.

## Corrosion in modern incinerators

---

Y KAWAHARA, Mitsubishi Heavy  
Industries, Ltd, Japan

### 19.1 Introduction

Corrosion-resistant materials and coatings are key to increasing power generation efficiency and to reducing maintenance in waste-to-energy plants. The corrosion environment becomes more and more severe as steam temperatures increase. Steam with a temperature higher than 400°C and a pressure higher than 3.9 MPa becomes possible in waste-to-energy boilers by using highly durable corrosion-resistant materials and coatings, such as thermal spray of Al/80Ni20Cr alloy, HVOF-sprayed NiCrSiB alloy, Alloy 625 weld overlay for waterwall tubes, and 310S type stainless steels, high-Cr Mo-Ni base alloys and high Si-Cr-Ni-Fe alloys which have been widely used for superheater tubes. Furthermore, high durability coatings using cermet and ceramic materials have been applied to high temperature superheaters.

This chapter describes the major developments in corrosion-resistant materials and coating technologies and their application in the last 30 years in waste-to-energy plants, the corrosion mechanisms of alloys, the deterioration mechanisms of spray coating layers, and future prospects for the development of corrosion-resistant materials and coatings.

### 19.2 Recent trends in waste-to-energy plants and materials

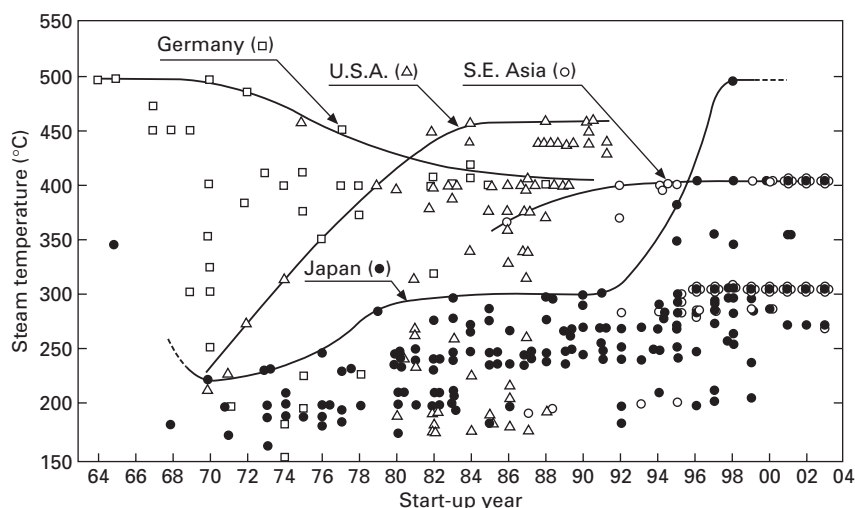
Promotion of waste recycling aims at a high level of material recirculation and reduction of environmental load such as CO<sub>2</sub> and dioxins. The concepts of highly efficient waste-to-energy (WTE) plants and waste gasification and ash melting power generation plants are positioned at the center of recycling by means of thermal processing. The steam condition for WTE boilers has increased from 300°C/2.9 MPa to 400°C/3.9 MPa and the first plant generating steam at 500°C/9.8 MPa has achieved continuous operation for over seven years in Japan.<sup>1</sup> In the past, the superheater tubes (SHTs) of the WTE boilers, where there is a severe high temperature corrosion (HTC) environment

containing a large amount of chlorides, were frequently replaced, as relatively inexpensive metal tubes were used. However, nowadays a high total cost performance is required by society, incurring minimal expenditure of public funds and low maintenance costs. Therefore, the development of low-cost and highly durable materials and application processes is essential to achieve high thermal efficiency and economy of WTE plants.

In recent years, SHTs made of corrosion-resistant materials (CRMs) have been progressively used for reduction of maintenance. For the waterwall tubes (WWTs), the application of corrosion-resistant coatings (CRCs), such as metal spray coating of highly corrosion-resistant Ni base alloys and weld overlay of Alloy 625, has been widespread in order to reduce maintenance. Furthermore, new combustion systems with reduced dioxins and waste recycling processes such as pyrolysis and gasification-melting furnaces have emerged. This chapter describes recent trends in the application of CRMs and CRCs in severe high temperature corrosion environments, on the corrosion mechanisms, tests and monitoring in the WTE boilers, and on the potential for further development.

### 19.3 Corrosion environment of waste-to-energy boilers

In most WTE plants, steam conditions of 300–450°C/2.9–5.8 MPa as shown in Fig. 19.1 are adopted to avoid corrosion damage to boiler tubes and to ensure stable operation. Due to increasing environmental concerns arising



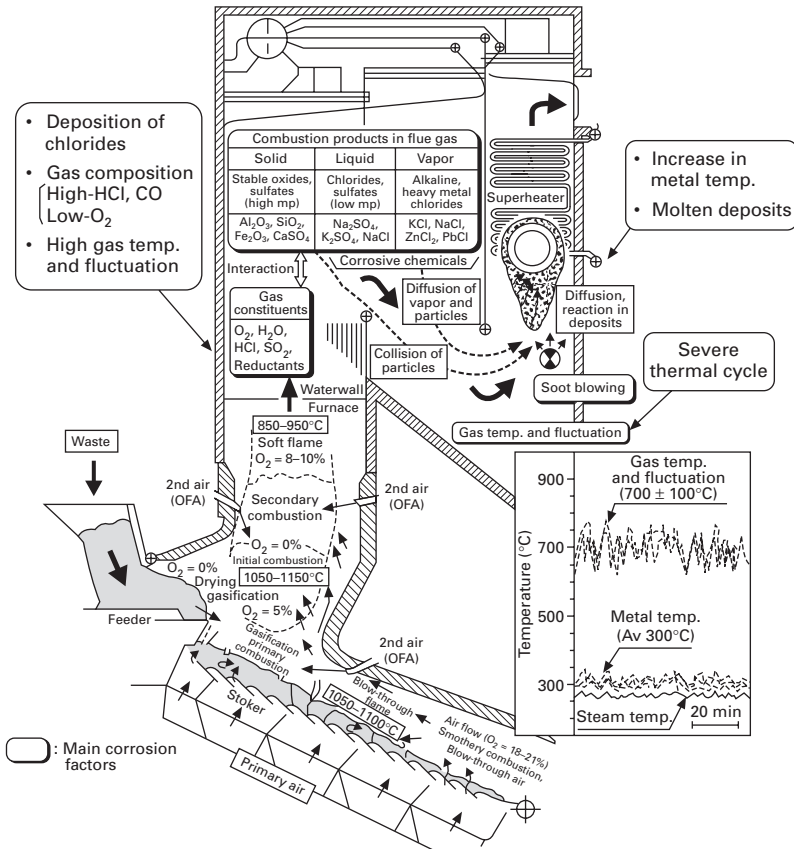
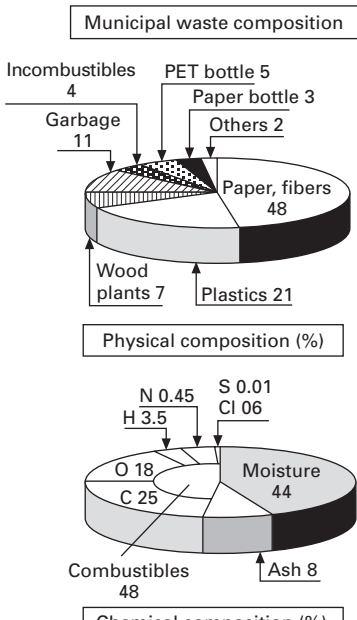
19.1 Trends in steam temperature of WTE boilers.

from technological and economic development, both the properties of the waste and the WTE plant operating conditions have changed:<sup>1</sup>

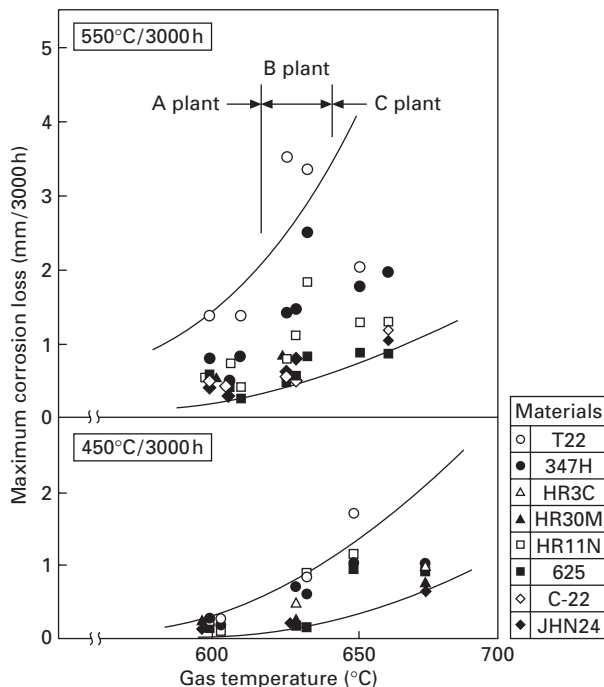
1. Strict pollution regulation: low O<sub>2</sub> operation, high temperature of combustion chamber, etc., to prevent generation of NO<sub>x</sub> and dioxins.
2. Energy saving and effective utilization of waste heat: severe corrosion environment due to improvement of heat efficiency such as high temperature and high pressure (400–500°C/3.9–9.8 MPa) of boilers, etc.
3. Minimization of waste products: need to reduce volume of ash and to produce non-polluting ash, leading to the development of next-generation plants, such as pyrolysis gasification-melting furnaces<sup>2</sup>, oxygen-enriched combustion, etc.
4. Improved cost performance: reducing cost of operation and advances in maintenance-free operation, such as advanced combustion control and monitoring technologies.

As various substances, including incombustibles as well as combustibles such as wood, paper, plastics, etc., are mixed in the waste, the gas temperature and composition fluctuate more than in boilers combusting fossil fuels; a lot of low melting point deposits containing high concentration of chlorides are also generated in the combustion gas. Figure 19.2 shows the explanatory drawing of factors of the HTC environment<sup>3</sup>. Dusts containing high concentrations of alkaline metals (Na, K, etc.), heavy metals (Pb, Zn, etc.), chlorides and sulfates adhere and deposit onto the material surfaces exposed in the combustion gas, and severe corrosion is caused on the high temperature components such as SHTs by ash deposits melting at 300–550°C. Furthermore, on the WWT surfaces where the gas temperature is very high (850°C or higher), the adherence of high concentration chlorides on the surface is promoted, and the corrosion damage is caused mainly by chlorination reactions. Also, since the temperature of superheater tubes is as high as 300–550°C, salt deposits are easily melted and corrosion rates as high as several mm per year or more are sometimes observed. Figure 19.3 shows the increase in corrosion rate of SHTs due to increase in the gas temperature<sup>3</sup>. The metals are attacked by general corrosion, intergranular corrosion, and localized corrosion when the molten adhering ash causes the breakdown of the protective oxide layer and attacks even highly corrosion-resistant alloys<sup>4</sup>.

Both the adherence of dust constituents, such as strongly corrosive chlorides and sulfates, and the temperature fluctuation can be reduced by lowering the temperature of the combustion gas introduced into the SHTs to less than 650°C. The reduction in gas temperature is effective for the stabilization of protective oxide layers on the metal surface. However, it is known that the soot blowers that are used for the purpose of dislodging deposits that decrease heat transfer may result in severe thermal cycling conditions and lead to breakdown of protective oxide layers.



19.2 Formation of corrosion environment in WTE boilers



19.3 Change in maximum corrosion thickness loss of superheater materials with gas temperature (metal temperature: 450°C, 550°C).

In response to the above-mentioned severe corrosive environments, the development and application of new CRMs and CRCs, corrosion resistance testing and evaluation methods, and methods for the analysis of corrosive environments have been advanced, as shown in Fig. 19.4 and described below.

#### 19.4 Progress of high temperature corrosion-resistant materials for superheaters

The alloy design of seamless tubes for use as SHTs takes into consideration both corrosion resistance and heat-resistant characteristics. Furthermore, excellent weldability, plastic workability, etc. are required for fabrication of the boilers. Generally, at temperatures of approximately 350°C or lower, carbon steel is used. In the high temperature region of 400°C or higher where high corrosion resistance is required, Fe base and Ni base austenitic materials (Tables 19.1 and 19.2) are tested and used. Field corrosion tests have shown that the addition of alloying elements such as Mo, Nb and Si to Ni-Cr-Fe alloys is effective for corrosion resistance<sup>5</sup>. The main corrosion-resistant alloys currently developed and applied are described below.

Materials	Application	'85	Process	'90	Year	'95	2000
Solid wall tubes	For superheater and waterwall  400°C/3.9MPa ↓ 500°C/9.8MPa			310HCbN			
			Ospray	HR11N	HR30M	QSX (Si)	
					Sanicro 28	Sanicro 65, 63 (Mod 625)	
				AC66		45TM (Si)	
					JHN24 (Mo)	MAC-N,F (Si)	
			Herical roll	HR160 (Co, W)	HC-2000 (Mo)	625	
					HC-22 (Mo)		
Weld overlays	For waterwall		Auto MIG		625		
	For superheater		PPW, PAW		625, 625M, C-276M		
Spray coatings	For waterwall		Flame, arc HVOF	Ni base alloy			
	For superheater		Plasma jet HVAF		Ni base alloy (DJ-1000, JP-5000)		
					Ni base alloy (inteli-jet)	ZrO <sub>2</sub> /Ni base alloy	
Refractory materials	For waterwall		Conventional castable (cement, phosphate bond)				
			Vibration, pressurized cast		Ceramic tile		
Corrosion testing and monitoring	Laboratory corrosion test			Coating test			
	Monitoring			Embedded test			
				Temperature gradient test			
			Electrochemical test	AC current			
					Noise		
					AC impedance		

— Studied, developed      — Increased application

#### 19.4 Development and application of WTE material technologies.

Table 19.1 Ni-Cr-Fe-(Mo) alloy tubings tested and applied to WTE boilers

Trade name	Shape of tubes (maker)	Chemical composition (mass%)												Tensile properties (RT)				Parts*	Reference
		C	Si	Mn	Cr	Ni	Mo	Fe	Nb+Ta	N	Al	Ti	Cu	Others	T.S. (kgf/mm <sup>2</sup> )	Y.S. (kgf/mm <sup>2</sup> )	E. (%)		
Alloy 825 (SB423)	Solid wall, composite (ASME)	≤0.05	≤0.5	≤1	19.5–23.5	38.0–46.0	2.5–3.5	bal.	–	–	≤0.2	0.6–1.0	1.5–3.0	–	≥67	≥30	30	SH (USA)	10
HR11N	Solid wall, composite (Sumitomo Metal)	≤0.03	≤0.6	≤2.0	27.0–30.0	38.0–42.0	0.5–1.5	bal.	–	0.1–0.2	–	–	–	–	≥60	≥25	≥35	Tested (Japan)	51
MAC-F	Mitsubishi Heavy Industries	0.010–0.020	3.40–4.20	≤0.50	21.0–25.0	36.0–40.0	–	bal.	0.20–0.40	0.05–0.09	≤0.10	≤0.10	–	–	≥62.2	≥24.5	≥30	SH (Japan)	18
Sanicro 38	Composite/ SA210A (Sandvik)	≤0.025	≤0.5	0.8	20	38	2.5	bal.	–	–	–	≤1.0	1.7	–	≥33	≥18	≥35	Tested (Europe)	13
NF 707	Solid wall (Nippon steel)	≤0.15	≤1.00	≤1.5	22.0–27.0	33.0–37.0	1.0–2.0	bal.	0.10–0.40	0.05–0.35	–	0.02–0.20	–	0.002–0.008B	≥58.2	≥20.4	≥30	Tested (Japan)	52
AC 66	Solid wall (Mannesman)	≤0.025	≤0.3	≤1.0	26.0–28.0	31.0–33.0	–	bal.	0.6–1.0	–	≤0.025	–	–	0.05–0.10Ce	≥51	≥18.9	35	SH (Europe)	53
Sanicro 28	Composite/ T22 (Sandvik)	≤0.02	≤0.7	≤2.0	26.0–28.0	29.0–32.0	3.5	bal.	–	–	–	–	0.6–1.4	–	≥56	≥22	≥40	SH (Europe)	11
HR 30M	Solid wall (Sumitomo Metal)	≤0.02	≤0.50	≤1.00	27.0–30.0	28.0–32.0	0.80–1.20	bal.	–	0.10–0.30	–	–	–	–	≥65	≥28	≥35	Tested (Japan)	7

Table 19.1 (Continued)

Trade name	Shape of tubes (maker)	Chemical composition (mass%)												Tensile properties (RT)				Parts*	Reference
		C	Si	Mn	Cr	Ni	Mo	Fe	Nb+Ta	N	Al	Ti	Cu	Others	T.S. (kgf/ mm <sup>2</sup> )	Y.S. (kgf/ mm <sup>2</sup> )	E. (%)		
NF 709 (310J2)	Solid wall (Nippon Steel)	≤0.1	≤0.75	≤1.5	19.0– 23.0	23.0– 27.0	1.0– 2.0	bal.	0.10– 0.40	1.10– 0.20	–	0.02– 0.20	–	0.002– 0.008B	≥65.3	≥27.6	≥30	SH (Japan)	8
QSX3	Solid wall (Sanyo Special Steel)	≤0.03	2.50– 3.50	≤1.00	24.0– 26.0	22.0– 25.0	–	bal.	0.10– 0.30	0.049	–	–	–	–	≥53	≥21	≥35	SH (Japan)	15
QSX5	Solid wall (Sanyo Special Steel)	≤0.03	2.50– 3.50	≤1.00	24.0– 26.0	22.0– 25.0	1.00– 2.00	bal.	1.10– 0.30	0.042	–	–	–	–	≥53	≥21	≥35	SH (Japan)	16
310S	Solid wall (JIS)	≤0.08	≤1.50	≤2.00	24.0– 26.0	19.0– 22.0	–	bal.	–	–	–	–	–	–	≥53	≥21	≥35	SH (Japan)	6
HR3C (310HCbN)	Solid wall (Sumitomo Metal)	≤0.10	≤1.50	≤2.00	23.0– 27.0	17.0– 23.0	–	bal.	0.20– 0.60	0.15– 0.35	–	–	–	–	≥67	≥30	≥30	SH (Japan)	7
MN25R (309J3L)	Solid wall (Nippon Steel)	≤0.025	≤0.70	≤2.00	23.0– 26.0	13.0– 16.0	0.5– 1.2	bal.	–	0.25– 0.40	–	–	–	–	≥70.4	≥35.2	≥30	SH (Japan)	52
HR2M (309J2)	Solid wall (Sumitomo Metal)	≤0.04	≤1.00	2.50– 3.50	21.0– 23.0	12.50– 15.50	1.00– 2.00	bal.	–	0.10– 0.25	–	–	–	–	≥60	≥25	≥35	SH (Japan)	55

\*SH = superheater.

Table 19.2 Ni-base alloy tubings tested and applied to WTE boilers

Trade name	Shape of tubes (maker)	Chemical composition (mass%)											Tensile properties (RT)				Parts*	Reference
		C	Si	Mn	Cr	Ni	Mo	Fe	Co	Nb+Ta	W	Ti	Others	T.S. (kgf/mm <sup>2</sup> )	Y.S. (kgf/mm <sup>2</sup> )	E. (%)		
Alloy 625 (SB 444)	Solid wall (ASME) Overlay (WSI, Daido)	≤0.1	≤0.5	≤0.5	20.0– 23.0	(bal. 10.0	8.0– 10.0	≤5	≤1.0	3.15– 4.15	–	≤0.4	AI≤0.04	≥84.4	≥42.2	≥30	SH (Japan)	7
Sanicro 63	Composite/ T22 (Sandvik)	≤0.025	≤0.5	≤0.5	21	bal.	8.5	3	–	3.4	–	–	–	≥66.3	≥25.5	≥50	WW,SH (Europe)	13
Sanicro 65	Composite/ T22 (Sandvik)	≤0.025	≤0.5	≤0.5	21	bal.	8.5	8	–	≤0.5	–	–	–	≥66.3	≥25.5	≥50	WW,SH (Europe)	12
Hastelloy C-22	Solid wall (Haynes Alloy) Composite/ 304H (Mitsubishi Materials)	≤0.015	≤0.08	≤0.5	20.0– 22.5	bal. 14.5	12.5– 14.5	2.0– 6.0	≤2.5	–	2.5– 3.5	–	V≤0.35	≥70.4	≥31.6	≥45	Tested (Japan)	14
HC-276M	Composite (Daido)	≤0.12	≤1.5	≤1.0	15.5– 21.0	bal.	12.0– 16.0	≤5.25	≤2.5	–	≤5.25	–	–	≥53	≥21	≥35	Tested (Japan)	36
Inconell 686	Solid wall (Special Metals)	≤0.01	≤0.08	≤0.75	19.0– 23.0	bal. 17.0	15.0– 17.0	≤5	–	–	3.0– 4.4	0.02– 0.25	–	79.4	53.1	56	Tested (USA)	54

Table 19.2 (Continued)

Trade name	Shape of tubes (maker)	Chemical composition (mass%)											Tensile properties (RT)				Parts*	Reference
		C	Si	Mn	Cr	Ni	Mo	Fe	Co	Nb+Ta	W	Ti	Others	T.S. (kgf/mm <sup>2</sup> )	Y.S. (kgf/mm <sup>2</sup> )	E. (%)		
JHN 24	Solid wall (Mitsubishi Materials)	≤0.015	≤0.08	≤0.50	19.0–21.0	bal.	17.0–19.0	0.5–6.0	≤2.5	0.5–1.2	–	–	V≤0.35 Hf≤0.3	≥73.4	≥33.6	≥30	Tested (Japan)	7
HR160™	Solid wall (Haynes Alloys)	≤0.15 3.0	2.4–3.0	0.5	26.0–30.0	bal.	≤1.0	≤3.5	27.0–33.0	≤1.0	≤1.0	0.20–0.80	–	≥66.8	≥24.7	≥40	SH (USA)	50
Nicrofer 45-TM	Solid wall (KTN)	0.05–0.12	25–0.3	≤1.0	26.0–29.0	≤45.0	–	21.0–25.0	–	–	–	–	Cu≤0.3 0.05–0.15REM	≥63.3	≥24.5	≥35	SH (Europe)	17
MAC-N	Mitsubishi Heavy Industries	0.010–0.025	3.20–3.80	0.20–0.60	24.0–28.0	bal.	–	9.0–13.0	–	0.20–0.40	–	–	Al≤0.35 N≤0.07	≥61.2	≥18.4	≥30	SH (Japan)	18

\*SH = Superheater, ww = waterwall.

#### 19.4.1 High Cr and high Ni-Fe base alloys

Austenitic stainless steels such as 309S and 310S of 25Cr-14–20Ni alloys,<sup>6</sup> or 310HCbN<sup>7</sup> and NF709<sup>8</sup> which are modified 310S alloys, are mainly used for 400°C/3.9 MPa boilers. Since the difference of the corrosion resistance in Ni-Cr-Fe alloys is small among the various materials under steam conditions below 450°C, as shown in Fig. 19.5,<sup>9</sup> 310S and modified 310S are selected because of their lower cost. Alloy 825, Sanicro 28 (composite tube) of 20–30Cr-30–40Ni alloys are sometimes used by high thermal efficiency plants in Europe, the United States and Southeast Asia.<sup>10,11</sup>

#### 19.4.2 High Cr and high Mo-Ni base alloys

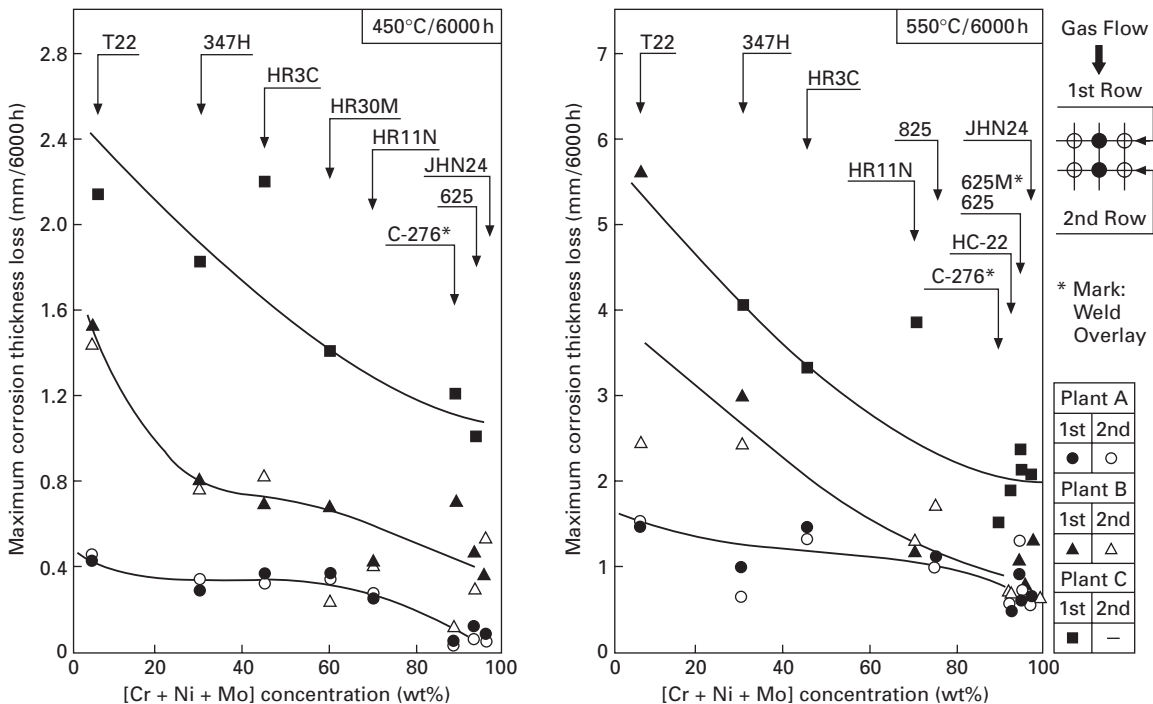
Alloy 625 and Sanicro 63 (composite tube) have excellent corrosion resistance under high temperature steam conditions of 450°C or higher.<sup>7,12,13</sup> Also, it is known that HC-22 and JHN24 alloys,<sup>7,9,14</sup> whose Mo content is higher than that of Alloy 625, show excellent corrosion resistance. For these high Mo-containing alloys, it is required to take into consideration in the material selection the fact that age deterioration of material may occur at high temperatures.

#### 19.4.3 High Si, high Cr and high Ni alloys

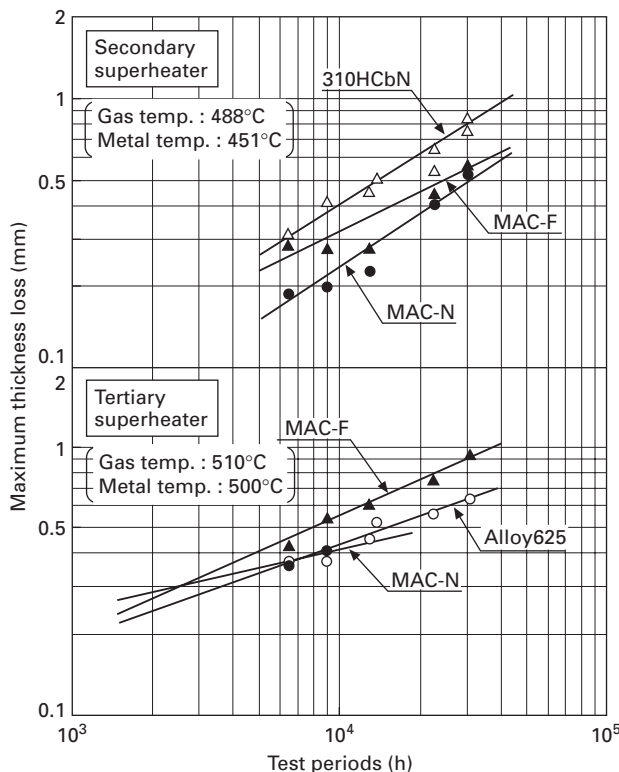
QSX3<sup>15</sup> and QSX5<sup>16</sup> are 310S alloys modified by adding Si of approximately 3%. It is known that Nicrofer 45TM<sup>17</sup> is used industrially and demonstrates good corrosion resistance. Furthermore, MAC-F and MAC-N alloys containing high Cr, high Ni, Fe and 4% Si have lasted for four years in the 500°C/9.8 MPa SHTs.<sup>18</sup> High Si alloys have some difficulties from the viewpoint of tube manufacturability, weldability and microstructural stability, but these MAC-F and N alloys have demonstrated good performance by optimization of the alloying elements for metals used in WTE boilers. Figure 19.6 shows an example of the corrosion rate of both Fe base and Ni base alloys containing high Si in field tests over four years.<sup>18</sup> The corrosion resistance of materials<sup>1</sup> varies according to the locations in the superheaters where corrosion environments are different. It is therefore necessary to make best use of the materials in accordance with the corrosion environment.

#### 19.4.4 Corrosion-resistant coatings for superheaters

In SHTs, the corrosion conditions are more severe than in WWTs due to higher metal temperatures and the presence of molten salts. Figure 19.7 shows the microstructures of the TiO<sub>2</sub>-Al<sub>2</sub>O<sub>3</sub>/625 cermet HVOF coating exposed for approximately two years in WTE superheaters result in remarkably



19.5 Change in maximum corrosion thickness loss with [Cr + Ni + Mo] concentration of alloys in 6000 hours of field tests.

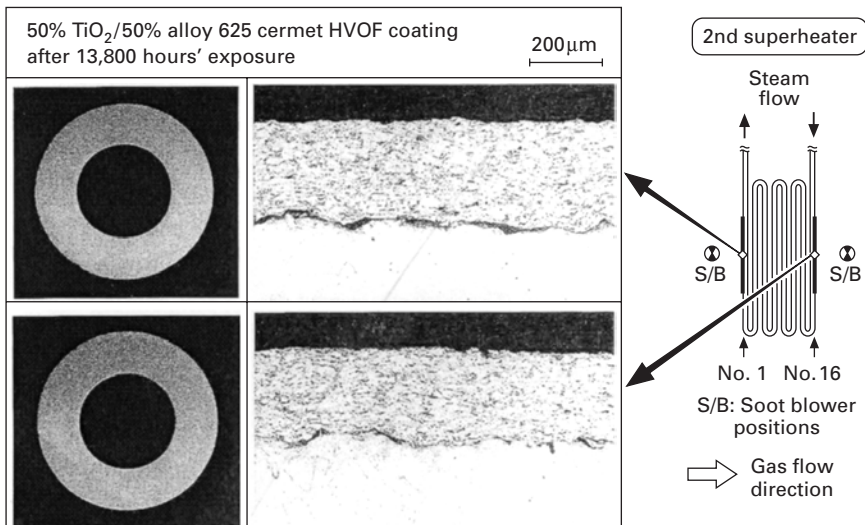


19.6 Change in maximum thickness loss with time in secondary and tertiary superheater steam outlet (soot blower not affected).

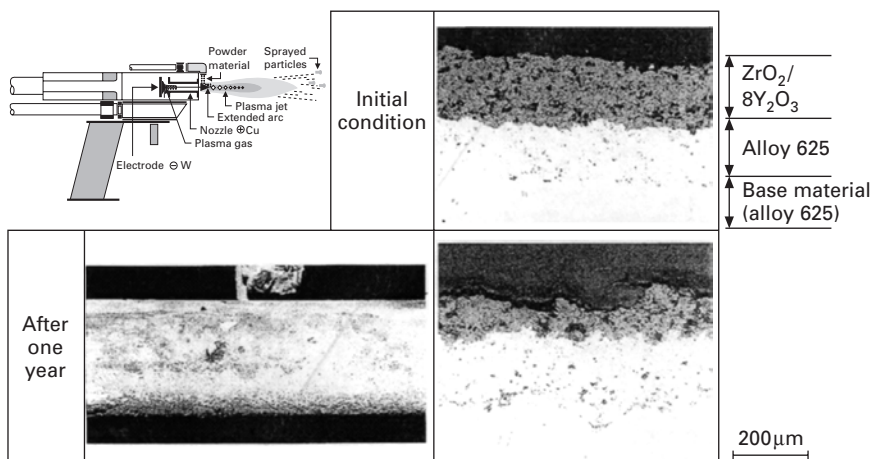
low thickness loss of coating layer and penetration of corrosive matter compared with conventional metal coatings.<sup>19</sup> Furthermore, the  $\text{ZrO}_2/625$  dual layer system applied by the plasma jet process also showed large bonding strength (Fig. 19.8) after two years' exposure in 500°C high temperature SHTs. Application of ceramics is considered to be effective to improve durability in spray coatings.<sup>20</sup>

## 19.5 Corrosion mechanisms of materials

The effect of the main factors governing the corrosion rate (CR) on the combustion gas side is described below.<sup>21</sup> Corrosion rates depend on the metal temperature and the gas temperature; these are considered to be the main factors determining the deposition rate and the composition of the deposits. As the temperature gradient ( $\Delta T = \text{gas temperature} - \text{metal temperature}$ ) is the driving force for condensation and deposition of the vapor components in the gas, the chloride concentration in the deposits is



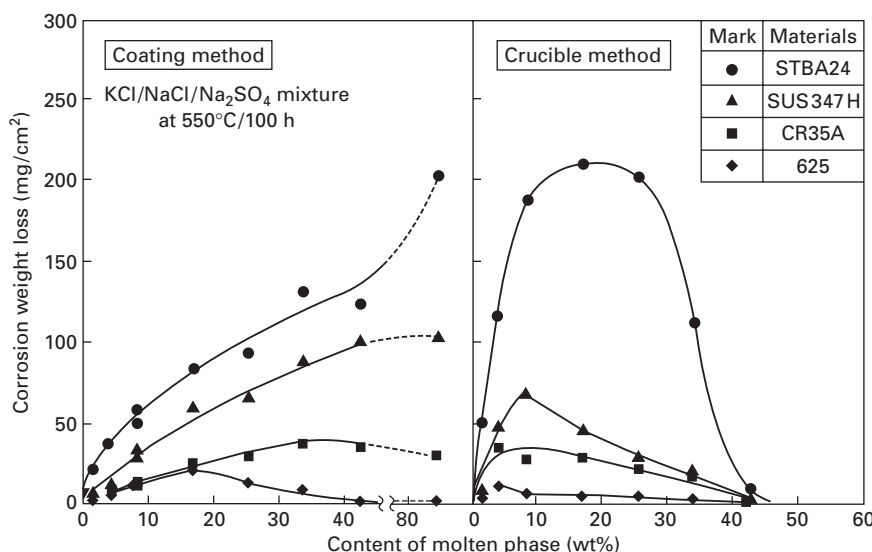
19.7 Cermet spray coating on 310HCbN superheater after 13,800 hours' exposure.



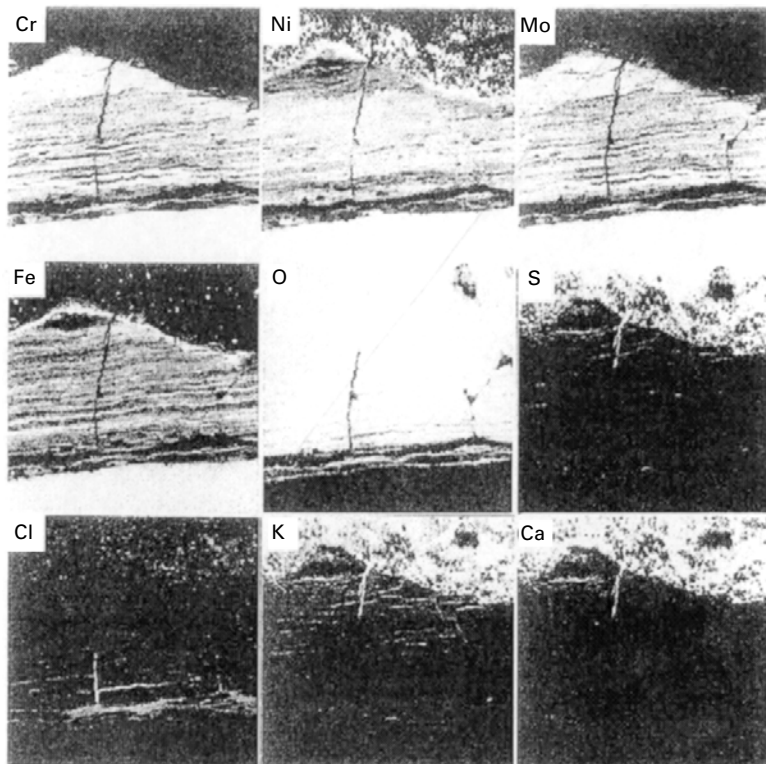
19.8  $\text{ZrO}_2/\text{Alloy 625}$  on-site 100 kW plasma-jet spray coating for 500°C superheaters.

high at locations where  $\Delta T$  is large and there is a tendency for the formation of low melting deposits. Furthermore, it is known that the amounts of Cl,  $\text{SO}_4$ , alkaline and heavy metals affect the physical properties of the deposits such as molten phase amount, permeability, etc.<sup>22</sup> The penetration of corrosive gas through the deposits and the presence of oxidizing constituents such as  $\text{O}_2$  are considered necessary for maintenance of the corrosion reaction, as the corrosion peak appears at around 10% of chloride concentration as shown

in Fig. 19.9. Moreover, rapid thermal cycling acts on the tube surface in the actual plants, due to gas temperature fluctuation and the use of soot blowers. The falling off and the regeneration of deposits and oxide layers are repeated. Figure 19.10 shows the example of crack generation of alloy 625 oxide layers due to the thermal fluctuation at the soot blow affected zone. The Cl and S partial pressures are considered to rise under the deposits due to penetration of Cl, S, etc. through the cracks onto the corrosion interface. Furthermore, if the protective oxide layer breaks down, direct reaction with molten chlorides may occur as shown in Fig. 19.11.<sup>5</sup> From the configuration of corrosion products distributed as chlorides, sulfides and oxides from the side nearest to the interface and their properties, the corrosion is considered to be a mixed high-temperature gaseous reaction in which chlorination, sulfidation and oxidation occur simultaneously. This type of corrosion is referred to as 'molten salt induced corrosion' because the corrosion reaction becomes active when the amount of deposits increases and part of the deposits melts.<sup>47</sup> On the other hand, it is considered also that molten salt corrosion occurs during the initial stage of corrosion when the oxide layer is thin. It is presumed that the corrosion by the direct reaction of molten salt changes gradually to the gas reaction as the oxide layer grows thicker. The influences of major factors such as temperature gradient, temperature fluctuation, molten ash amount, etc. on the CRs were examined quantitatively by recent research.<sup>24</sup> The factors causing characteristic intergranular corrosion include both material



19.9 Change in corrosion weight loss with molten phase content between coating test and crucible test.



19.10 Breakdown of protective oxide layer and penetration of corrosive species in Alloy 625 SHT influenced by soot blowing.

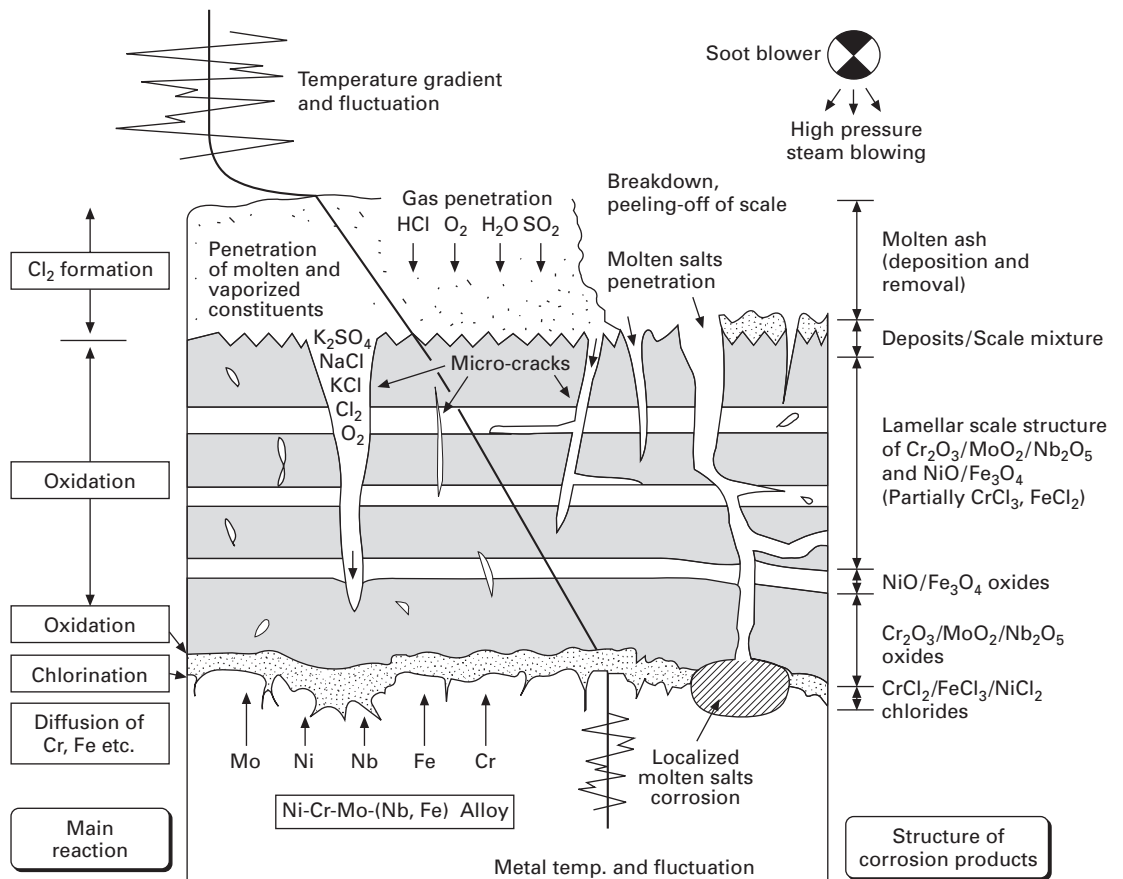
factors (impurities, grain boundary precipitates, etc.) and environmental factors (stress, molten salt, etc.).<sup>25</sup> This investigation will be continued.

## 19.6 Progress of corrosion-resistant coatings for waterwall tubes

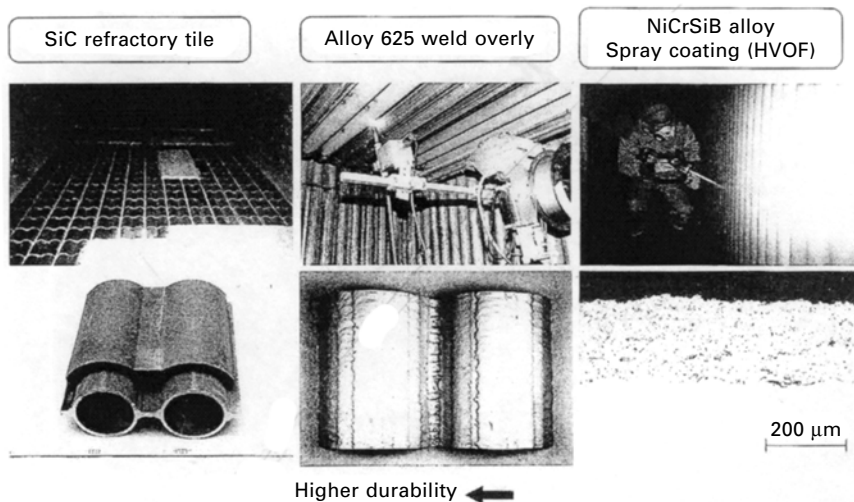
The metal temperatures of the waterwall tubes (WWTs) are relatively low, approximately 230–330°C, depending on the steam pressure (2.9–9.8 MPa). Here CRCs such as metal spray coatings, weld overlays, or claddings with high CRMs on the outer surface are applied onto the base material of carbon steel as shown in Fig. 19.12. Table 19.3 shows examples of the application of various CRCs to WTE boilers.

### 19.6.1 Spray coating

Metal spray coating of CRMs with a thickness of 150–500 µm can be applied on site quickly at low cost. The actual application of Al/80Ni20Cr alloy



19.11 Corrosion mechanisms in Ni-Cr-Mo-(Nb, Fe) alloy.



19.12 Application of CRCs to WWTs.

flame spray coating on WWTs started in 1985.<sup>26</sup> NiCrSiB alloy sprayed by the HVOF (High Velocity Oxygen Fuel) process with high durability was also developed.<sup>19,28</sup> Such HVOF coatings have been used in over 50 WTE plants in Japan. In Europe and the United States, testing in actual plants was conducted for WWTs and SHTs.<sup>29-34</sup> The spray coating systems (applied both on-shop and on-site) are selected in accordance with the workability, the severity of the corrosion environment, the required lifetime and the cost. The use of HVOF is prevalent. More recently, plasma jet coating systems of ZrO<sub>2</sub>/Ni base alloys have been developed and applied onto SHTs operated at 500°C/9.8 MPa in WTE boilers.<sup>20</sup>

### 19.6.2 Weld overlay

Since a dense coating layer that is chemically bonded with the base metal and as thick as several millimeters can be obtained by weld overlay, the durability of weld overlays is higher than that of thermal spray coatings. Alloy 625 weld overlays possess excellent corrosion resistance and welding workability. Application started in 1990 mainly on-site, and it is reported that the durability is 10 years or longer.<sup>35</sup> Table 19.3 lists the weld overlay materials and processes that are currently in use.<sup>7,36-39</sup> For many WWTs, MIG automatic welding and shielded arc welding are adopted for both in-shop and on-site applications. For the SHTs, MIG welding and PPW (plasma powder welding) are employed, and the tube bending processing can be done even after the application of weld overlays. For the 500°C/9.8 MPa high efficiency boiler WWTs, a maximum corrosion loss rate of approximately

Table 19.3 Durability of CRCs in WTE boilers

Coating process		Chemical composition (materials)	Applied condition (°C)			Durability (years)	Reference
			Parts*	Metal temp.	Gas temp.		
Weld overlay	MIG	21Cr-9Mo-3.5Nb-Al, Ti-Ni base (Alloy 625)	WW SH	270–330	700–1000	>10	35
	PPW	18Cr-14Mo-4W-Ni base (C-276M, 625M)	SH	470–510	510–650	(≈ Alloy 625)	36
	MIG	23Cr-16Mo-1.6Cu-Ni base (HC-2000)	WW SH	260–480	870–1730	(> Alloy 625, 0.52 mm/y)	38
	PAW	Alloy 625	SH	470–530	510–650	>1	37
	Laser cladding	625, HC-22, NiCr 309L, 686, etc.	WW	Coal fired black liquor		–	39
Spray coating	Flame	Al/80Ni20Cr	WW	230–300	700–900	>3	26
	Flame/fused	10Cr-Si, B-Ni base (12C)	SH	370–540	–	>1	29
Plasma	Plasma/fused	15Cr-Si, B, Fe-75Ni base	WW	230	700–800	4	27
HVOF	Hybride cap	18Cr-5Fe-5Nb-6Mo-Ni base (Diamalloy)	SH	370–540	–	>0.4	34
	DJ-1000	17Cr-4Fe-3.5B-4Si-Ni base (No-Fused)	WW SH	230–330	700–900	>3	28
	D-Gun	50TiO <sub>2</sub> -50 Alloy625	SH	430–460	500	>3	19
	DJ-1000 JP-5000	(Cermet)	WW	230	700–900	>3	–
	JP-5000	17Cr-4Fe-3.5B-4Si-Ni base	SH	430–500	510–650	>3	20
Plasma jet	Modified	ZrO <sub>2</sub> / Alloy 625,	SH				20
	PJ	NiCrSiB Alloy					

\* WW = waterwall, SH = superheater.

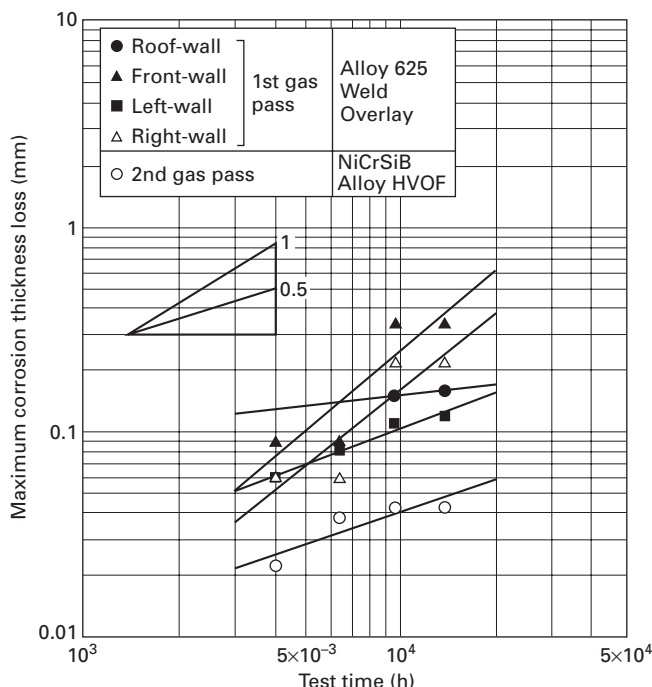
0.1–0.2 mm/year has been observed under metal temperatures of 330°C by the two-year field tests as shown in Fig. 19.13; the durability of these coatings for 15 years or longer has been verified.<sup>7</sup>

### 19.6.3 Composite tubing

Mainly in Europe, composite tubings with cladding of CRMs (outer tube) to carbon steel (inner tube) are used for WWTs and SHTs. There is extensive experience of the application of high Cr and high Mo-Ni base alloys including Alloy 625 (Sanicro 63); a detailed survey has been reported for the durability of these systems.<sup>11–13</sup>

### 19.6.4 Refractory materials

Refractory tiles with longer lifetime than conventional castable refractory materials have been developed and used; high-SiC tiles and/or high-Al<sub>2</sub>O<sub>3</sub> tiles are used in many cases. Basically, the tiles are installed by hanging or fixing to the outer surface of the WWTs, and the surface of the tile reaches



19.13 Maximum corrosion thickness loss of weld overlay and HVOF coating on WWTs of 500°C/9.8 MPa boiler.

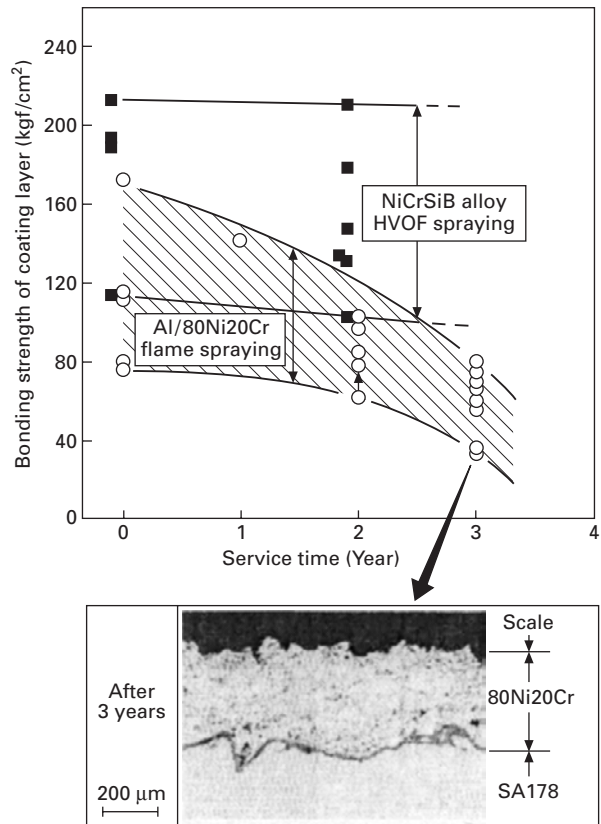
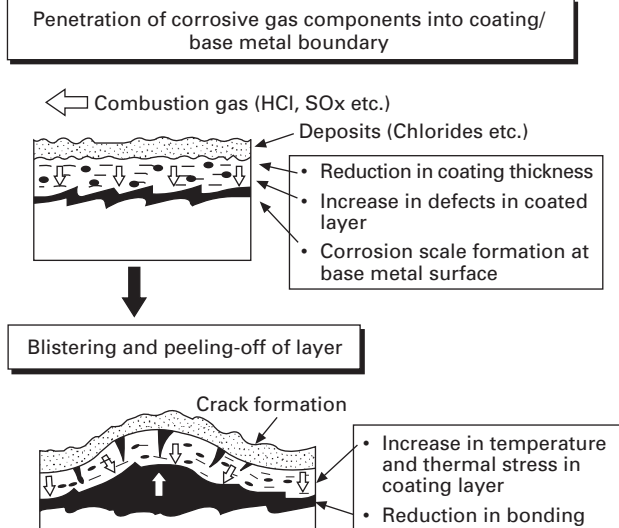
temperatures of approximately 900°C or lower. The materials, production method, shape and installation method are determined on the basis of evaluation of the oxidation resistance, thermal shock resistance, etc. in the high temperature combustion gas.

## 19.7 Deterioration mechanisms of spray coatings

Figure 19.14 shows the deterioration of the spray coating layer used for a long period. Corrosion of the base metal and deterioration of the coating occur due to the penetration of corrosive gases (HCl, etc.) to the interface of the base material/coating layer. Next, 'swelling' of the coating layer occurs, the reduction of adhesive strength is accelerated, and peeling of the layer occurs.<sup>26</sup> Accordingly, a dense coating is indispensable for improvement of lifetime. Supersonic flame spray coating (HVOF) in which the alloy powder in a semi-molten state is sprayed at supersonic speed is then preferable. The material factors that govern durability are the corrosion resistance of the coating materials, the adhesive strength with base materials, and the thermal properties including thermal expansion coefficient and the residual stress. As the physical properties of the coatings depend largely on the spraying conditions, a quantitative lifetime evaluation method for coating layers is required. Research and development of lifetime evaluation are expected in the future.

## 19.8 Corrosion testing and environmental monitoring methods

Information on the mechanism of corrosion must be intelligently used to establish a measure for evaluating corrosion, a method for corrosion testing, and a setting for the corrosion test. Among the various concise laboratory corrosion-simulation tests, researchers generally agree<sup>22</sup> that the ash-embedded test is the best to evaluate the order of corrosion resistance of materials with a satisfactory acceleration effect, and the temperature gradient test (TGT) with applied thermal load is best for evaluating the CRs in industrial plants. Refinements of these test procedures are helpful to the preparation of standards for integration in the JIS format that could also be compiled into international ISO standards.<sup>41</sup> There is an urgent need for reliable monitoring techniques to characterize the constantly fluctuating conditions of corrosion in waste incinerators in real time so that engineers can respond promptly to optimize plant operational parameters. This line of R&D is now very active. The advanced *in-situ* electrochemical monitoring (ECM) system is finally available. Advanced sensor systems of this kind will surely contribute to real-time determination of the melting temperature and deposition rate of the ash in waste incinerators.<sup>42</sup>



19.14 Deterioration mechanisms of spray coating layer and reduction in bonding strength in severe corrosive environment.

### 19.8.1 Corrosion test methods

In order to evaluate the corrosion resistance of materials in a laboratory, simplified laboratory HTC tests such as the ash-embedded or ash-coating method have been used, depending on the purpose. These simplified tests are effective for the purposes of comparing and evaluating the corrosion tendencies of materials over a short period of time, because they realize only some of the corrosion factors. However, they are difficult to use when evaluating the long-term corrosion lifetime of materials because they test only relatively moderate corrosion environments and it is difficult to exactly reproduce the CRs experienced in actual equipment.<sup>43</sup>

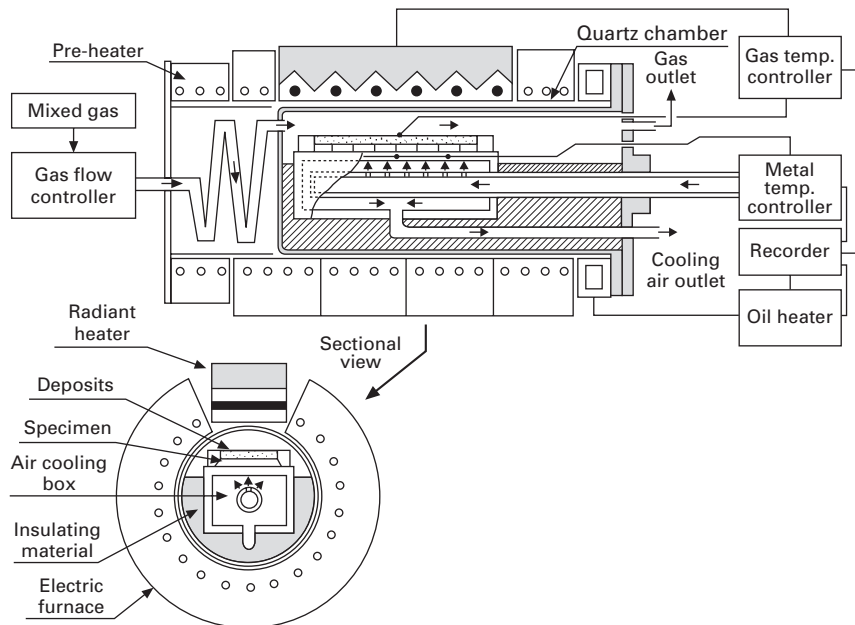
Factors that are difficult to reproduce in laboratories include such things as (i) various fluctuations such as in the temperature and the chemical composition of the combustion gas, and (ii) heat transfer rates and temperature gradients ( $\Delta T$ ) in boilers and heat exchangers. It is well known that these dynamic factors are closely implicated in the breakdown of the protective oxide scales that form on material surfaces and increases in CRs due to such breakdown. Therefore, the effect of these factors has been investigated in detail, particularly in the fields of high-temperature oxidation and gaseous corrosion.<sup>44</sup> On the other hand, in the field of HTC, investigations have been done only by using large-scale equipment such as burner-rig tests. In addition, it has been noted that the factors indicated in (ii) strongly influence the deposition behaviors and deposition rates of corrosive ash components contained in the combustion gas of fossil fuel or waste.<sup>45</sup> Accordingly, these factors are ranked as very important, because they relate closely to CRs.

Considering the above-mentioned conditions, and aiming at improving the accuracy of laboratory HTC tests and evaluating the corrosion lifetime of various materials more easily and quickly, a new temperature gradient test (TGT) with a thermal cycle component has been developed. The application of the TGT is mainly for waste combustion environments in which thermal cycles and  $\Delta Ts$  strongly influence corrosion.<sup>24,40</sup>

In order to clarify basic corrosion behaviors, especially with regard to the protective oxide layers of materials through TGTs with a thermal cycle component, a basic investigation is being made to study the influences of applied thermal parameters. Furthermore, long-term corrosion lifetimes are actually evaluated using the TGT results, and the corrosion lifetimes obtained through both the laboratory tests and practical WTE boilers are compared. In addition, the applicability of TGTs and the corrosion mechanisms of WTE boiler materials are being studied by integrating the above results.

#### *Procedure for conducting TGTs with a thermal cycle component*

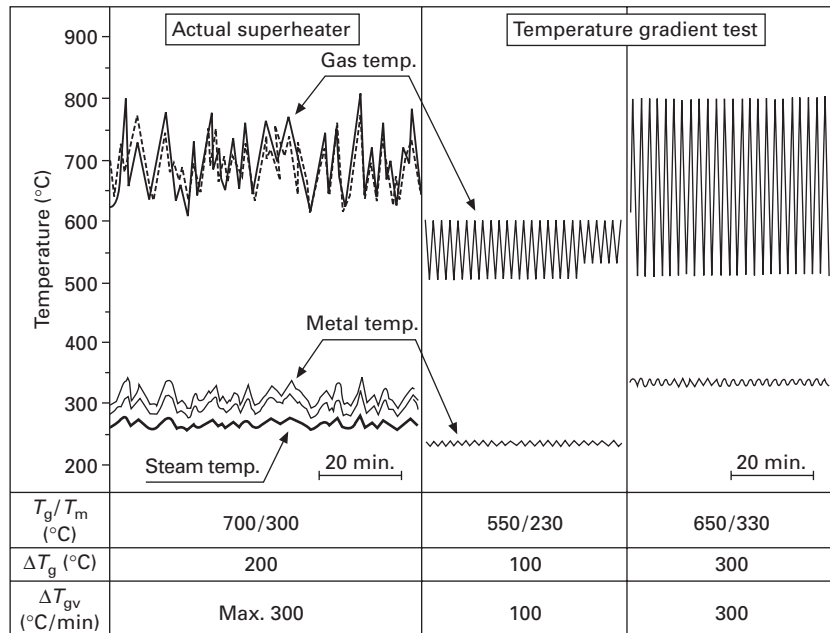
Figure 19.15 shows the configuration of the TGT equipment. The  $\Delta Ts$  and thermal cycles that characterize any given TGT are adjusted by controlling



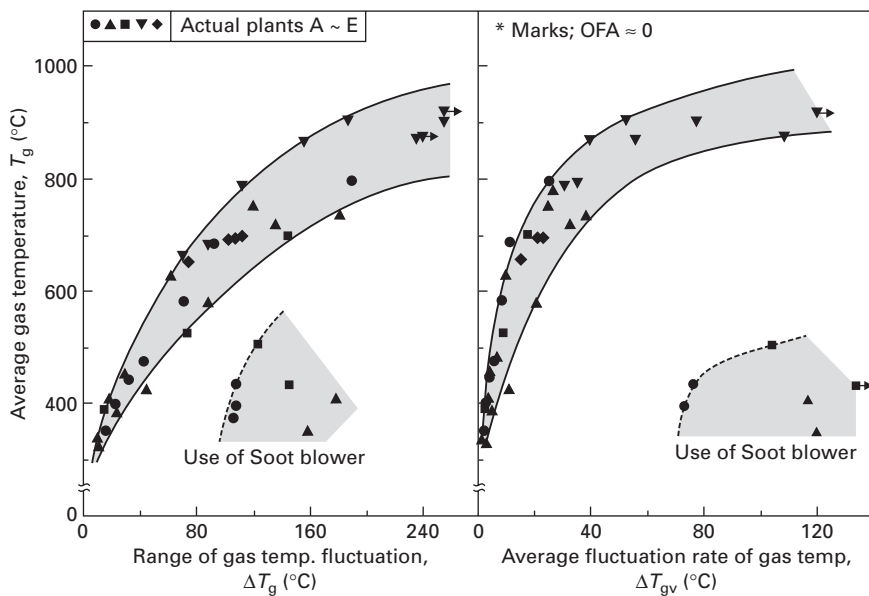
19.15 Schematic illustration of TGT apparatus.

the electrical resistance heater surrounding a silica furnace tube and the loading of the quick heating and cooling infrared radiant heater. The specimen bed is cooled by flowing air with a pressure of about  $10 \text{ kgf/cm}^2$  and a given  $\Delta T$ . The temperature of each sector is controlled separately in order to improve the accuracy of the metal temperature ( $T_m$ ). The gas temperature ( $T_g$ ) is measured at the surfaces of the corrosive deposit layers that adhere at a thickness of 3 mm to the upper surfaces of the specimens, and  $T_m$  values are measured individually by thermocouples mounted into each of the 10 specimens. Figure 19.16 compares the temperature fluctuations in both the laboratory tests and the WTE boiler. As can be seen in the figure, the metal temperature fluctuation range ( $\Delta T_m$ ),  $\Delta T$ , the gas temperature fluctuation range ( $\Delta T_g$ ) and the gas temperature fluctuation rate ( $\Delta T_{gv}$ ) can be set so as to simulate practical conditions. The testing period is usually 50 h. Furthermore, long-term tests (longer than 500 h) for measurement of long-term CRs have been conducted.

In various WTE boilers, changes in  $\Delta T_g$  and  $\Delta T_{gv}$  caused by variations in the properties of waste and combustion conditions were measured as shown in Fig. 19.17. These parameters naturally tend to increase with an increase of  $T_g$ . Moreover, large values of  $\Delta T_g$  and  $\Delta T_{gv}$  occur in boilers when a soot blower is used. It has been quantitatively confirmed that such gas temperature fluctuations ( $\Delta T_g$ ) cause  $\Delta T_m$  on material surfaces and strongly influence the



19.16 Comparison of thermal conditions in WTE boiler superheater and in TGTs.

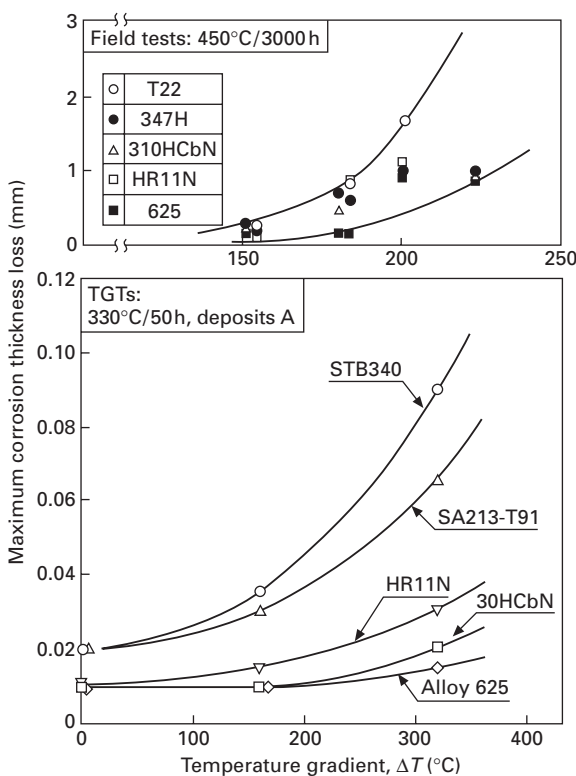


19.17 Correlation between average gas temperature and fluctuation range and fluctuation rate in WTE boilers.

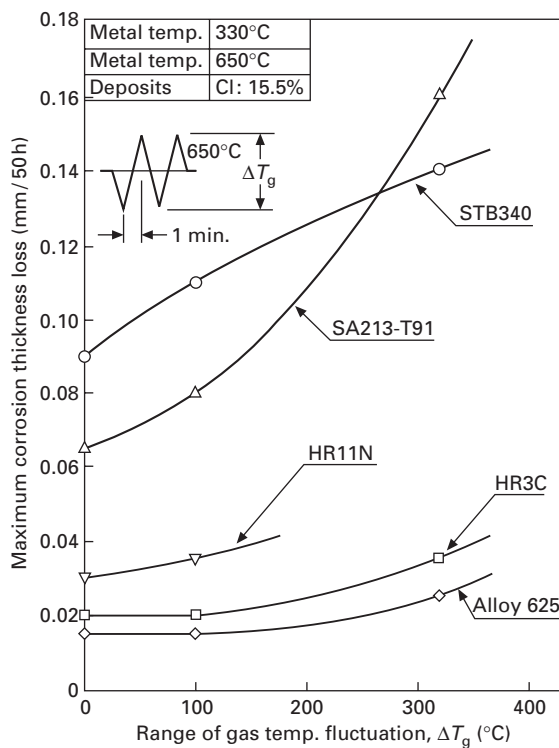
CRs and corrosion behaviors of the materials<sup>46</sup>. It is known that the CR in the area affected by soot blowing in a WTE boiler is about 1.5–3 times greater than that in non-affected areas. This indicates the magnitude of the impact of temperature fluctuations on CRs.

*Corrosion behavior with corrosive deposits in TGT with a thermal cycle component*

In the presence of corrosive deposits shown in Fig. 19.18 reported in a previous paper<sup>9</sup>, the penetration of corrosive components contained in the deposits is largely accelerated by  $\Delta T$ . On the other hand, the CR due to the thermal cycle is considered to be increased mainly by the breakdown of protective scales, as shown in Fig. 19.19. It can be concluded that  $\Delta T$  mainly contributes to the enhancement of environmental factors, and the temperature fluctuation relates strongly to the breakdown of the protective scales as material factors. It can be clearly seen that the TGT combined with a thermal



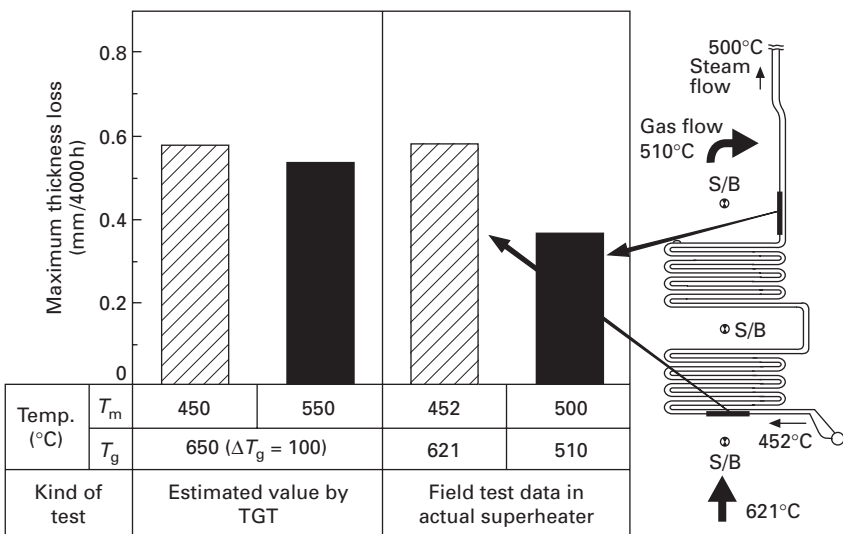
19.18 Comparison of maximum thickness loss in TGTs and in field tests.



19.19 Change in corrosion thickness loss with range of gas temperature fluctuation.

cycle component precisely reproduces corrosion mechanisms and phenomena experienced in practical WTE boilers.

As an example of reproducibility for TGTs, in order to investigate the corrosion resistance of weld-overlaid tubes using PAW, which is low in terms of both the amount of dilution of the base metal and the amount of heat input compared with conventional GMAW (MIG) welding, the corrosion lifetime was estimated using specimens of Alloy 625 overlay under the condition of a superheater operated at 500  $^{\circ}\text{C}$  and 9.8 MPa. Figure 19.20 compares the estimated thickness loss values where  $n = 0.5$  and the actual thickness losses after 4000 h of operation in a practical superheater after TGTs. Since the TGT was carried out under somewhat severer conditions than those in a practical superheater, the TGT results show a level equivalent to those obtained in practice, or slightly greater. In addition, V-shaped localized corrosion sometimes occurs in the vicinity of the bonding zone of SA178 contacted with Alloy 625 weld metal in actual plants. This type of localized corrosion is considered to be due to breakdown of protective oxides by



19.20 Estimated corrosion life and field data of 625 PAW overlaid SHT.

thermal stress arising where different materials are bonded, because this corrosion is observed even at the relatively low metal temperature at which deposited ash does not melt.<sup>46</sup>

By using TGTs with  $\Delta T$  and thermal cycle, localized corrosion can be reproduced clearly in a short test time.

#### *Role of protective oxide films and reproducibility of TGTs*

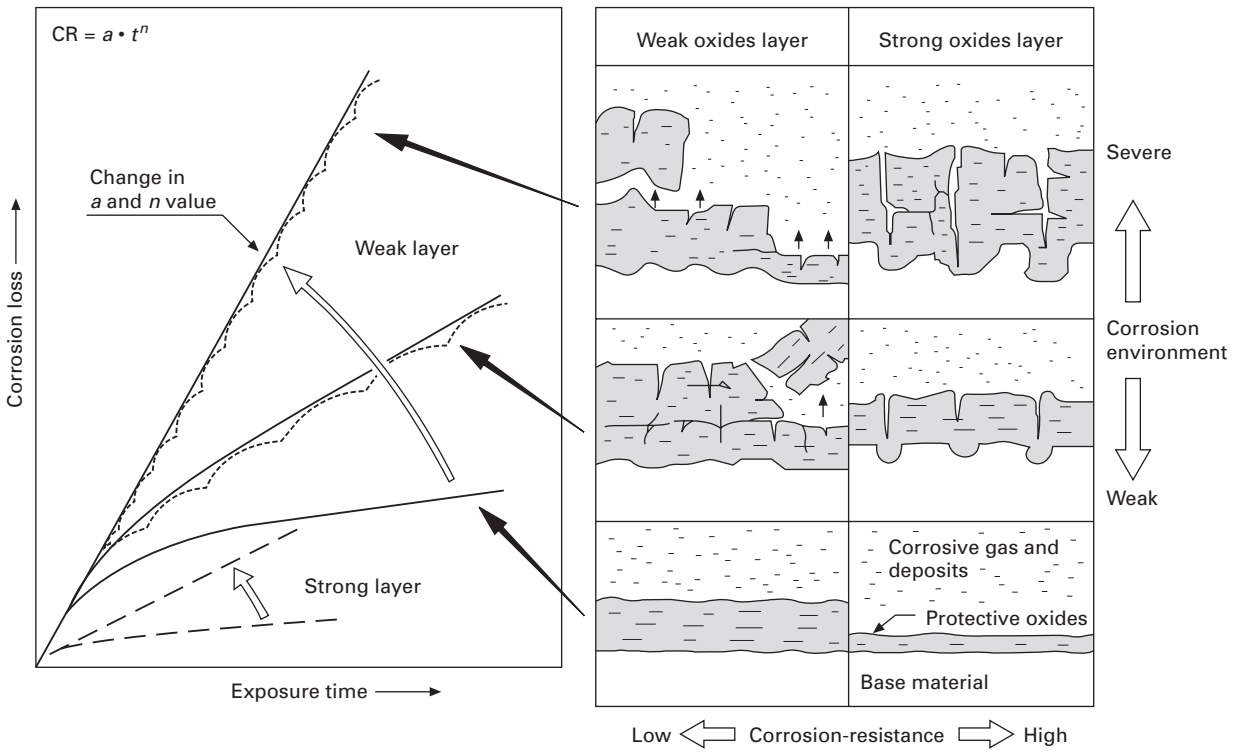
A low O<sub>2</sub> condition is produced at a corrosion interface in the presence of protective scales, and complex corrosion reactions such as chlorination, sulfidation and oxidation occur below the corrosive deposit layer. Thick scales have pores and cracks due to temperature fluctuations and the vaporization of chlorides.<sup>5</sup> As the thickness increases, the scales easily peel off from the surface. In particular, severe thermal cycles or increased gas velocities due to soot blowing accelerate the breakdown and spalling of the scale. Also, as a result of continuously repeated variations of gas conditions on the scales, the balance of chlorination, sulfidation and oxidation reactions at the corrosion interface and in the scales is forced to be changed by the penetration of O<sub>2</sub>. An increase of the partial pressure of O<sub>2</sub> ( $P_{O_2}$ ) temporarily halts the chlorination and sulfidation reactions. Therefore, a multi-layered scale structure is produced. The presence of multi-layered oxides formed by corrosion resistant elements such as chromium, nickel, aluminum, silicon and molybdenum increases the protective effect of the scales against the

attack of chlorine and sulfur and the penetration of corrosive species from outside.

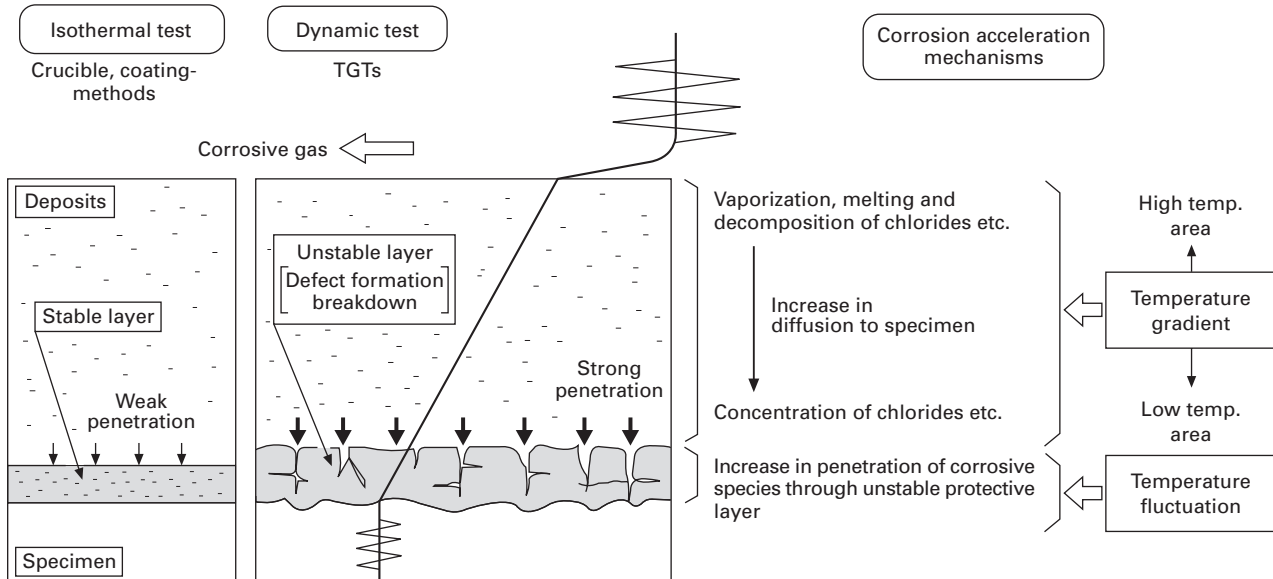
Such changes in corrosion reactions cause changes in the CR constant ( $a$ ) and index ( $n$ ), so that the index tends to change from 0.5 to 1 depending on the material used and the corrosive environment. In this situation, ferritic materials whose scales are naturally weak in terms of protectiveness have high CRs, and their thickness losses are comparatively uniform. On the other hand, the CRs of highly corrosion-resistant austenitic materials containing significant amounts of chromium, nickel, molybdenum, etc., which easily form protective multi-layered scales even in a low  $P_{O_2}$ , are very uneven, due to the stability of the scale layers. Therefore, the corrosion surfaces tend to be concave and convex in morphology.

The degree of penetration of the molten salts depends on the reactivity of the scales and salt components. It has been reported that the degree of penetration into oxides such as  $Cr_2O_3$ ,  $SiO_2$ ,  $Al_2O_3$  and  $Fe_3O_4$  is less than that into  $Fe_2O_3$ . Moreover, the degree of penetration is strongly influenced by the molten phase content in deposits.<sup>5</sup> In addition, localized corrosion is thought to be intensified when corrosive conditions that make it difficult for protective films to form at a low  $P_{O_2}$  are locally maintained for a long time. Accordingly, severe pitting corrosion as shown in Fig. 19.21 may occur in materials such as Alloy 625 that form a strong protective film.

From the phenomenon described above, in order to accurately reproduce CRs in WTE boilers, i.e. to obtain the CR constant ( $a$ ) and exponent ( $n$ ) equivalent to those in field data, the various fluctuations and deteriorating factors which the protective scales of material undergo during operation are needed in the laboratory. Such conditions are difficult to reproduce by conventional static ash-embedded or ash-coating methods. On the other hand, in the TGT with a thermal cycle component, CRs are considered to reach their steady state in a short time, since rapid thermal fluctuations can be reproduced at a frequency of more than one cycle per several minutes. Figure 19.22 shows corrosion acceleration mechanisms by  $\Delta T$  and fluctuation in dynamic TGTs. In the TGT, the corrosion factors for both the environment and the material are considered to act together in the same way as those in actual equipment. Depending on the environment, CRs that are even larger than those that occur in actual equipment can be produced. The TGTs can be concluded to be effective for determining corrosiveness and estimating CRs with a high accuracy from the perspective of the corrosion mechanism. From the application examples described above, it is clear that the TGTs have a high level of practicality. In order to reproduce corrosion phenomena with a high level of accuracy in a TGT, it is essential that not only the temperature conditions but also the corrosive environment such as deposited ash properties and gas conditions must be set up properly.



19.21 Change in CR with severity of environment and corrosion-resistance of materials.



19.22 Corrosion acceleration mechanisms by temperature gradient and fluctuation in dynamic TGTs.

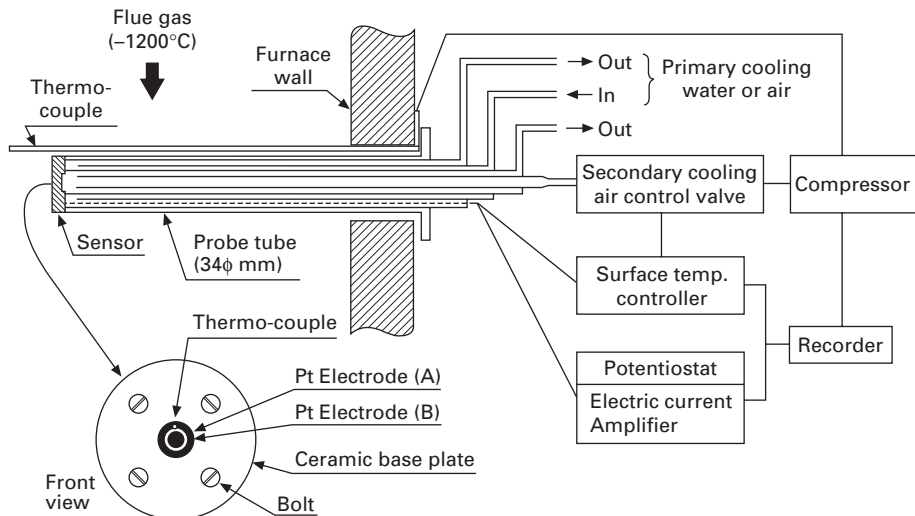
### 19.8.2 In-situ measurement of corrosion environment

Figure 19.23 gives a schematic diagram of ECM apparatus and an example of actual measurements of melting points. By raising and lowering the surface temperature, a sudden change in the electrode current with melting and solidification of deposits can be clearly distinguished. Figure 19.24 compares melting points measured *in situ* by ECS and measured in the laboratory by DTA ( $N_2$  gas atmosphere) in the deposits on the sensor surface. For deposits with a high content of heavy metals (Zn, Pb, etc.) and Cl both values are close, and also correspond to conventional data extracted from tube surfaces of actual boilers.<sup>42</sup>

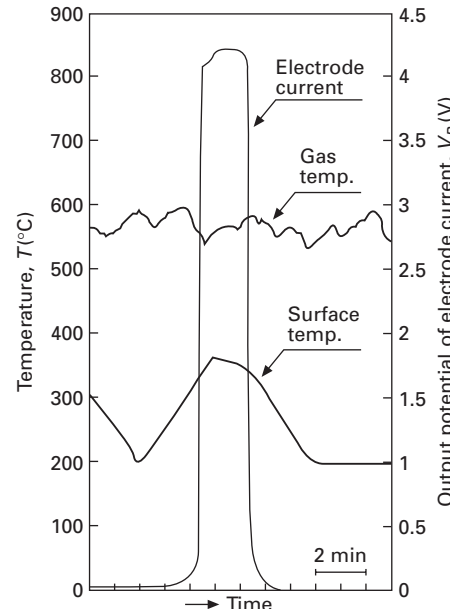
Melting points measured *in situ* were spread over a range of 290–340°C and are somewhat lower than the values measured with DTA (maximum difference of approximately 35°C). The reasons were considered to be (i) the composition of deposits on the surface of the sensor slightly differs from that of the manually sampled ones, especially in heavy metal chlorides with low melting points (such as  $ZnCl_2$  and  $PbCl_2$ ); and (ii) for the actual deposits, including a relatively smaller amount of molten phase, sensitivity to electrical conductivity change is greater than that to calorific change of DTA.

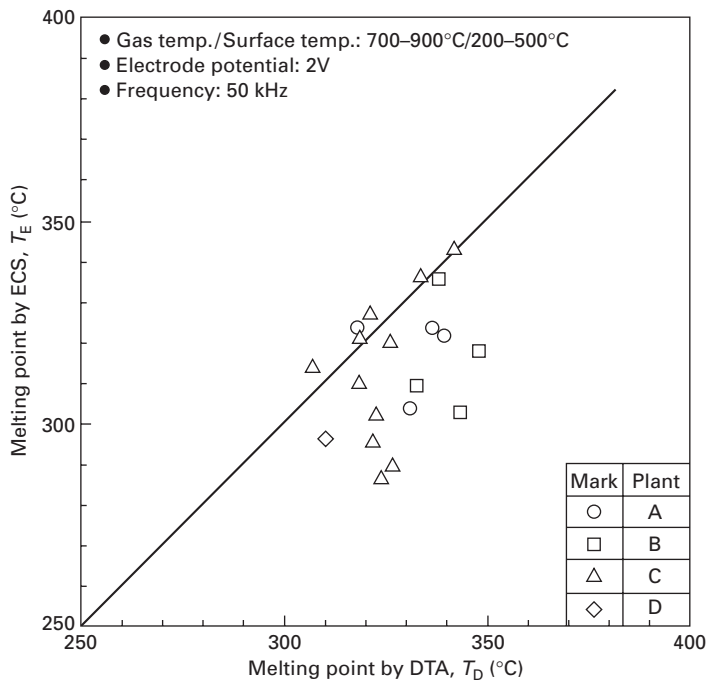
By using the ECM *in situ*, it is possible to measure the properties of deposits adjacent to the measuring surface, where the effect of corrosion is strong, free from the influence of moisture absorption and decomposition of deposits by manual sampling during shutdown periods. The presence of needle-like and cubic precipitate crystals was also confirmed. It is understood that when the surface temperature is low enough for this sort of deposition, the volatile constituents in the combustion gas around the surface area supersaturate and precipitation occurs by (i) vapor and (ii) particle diffusion mechanisms. Meanwhile, it is believed that the relatively large and lumpish particle depositions found are the result of (iii) collision of solid or liquid particles from the combustion gas. In the deposits, a relatively large amount of elements such as alkaline metals (Na, K) and heavy metal (Zn) as well as Cl, S and O was observed. Because the composition of the deposits on the sensor was the same as that of the deposits on the actual boiler tube surface, the ash deposition onto the surface of the sensor was believed to be similar to the actual ash deposition onto the boiler tubes.

Figures 19.25 and 19.26 show the relationship of the various gas and surface temperatures to the ash deposition rate. In Fig. 19.25, depending on the surface temperature of approximately 200–500°C, the ash deposition rate tends to increase largely as the gas temperature rises, which suggests that the above-mentioned deposition mechanisms (i) and (ii) operate especially in the earlier stages of deposition. In Fig. 19.26, the ash deposition rate increases along with the surface temperature and has a peak at approximately 450°C. Increasing the surface temperature, (a) the supersaturation of volatile

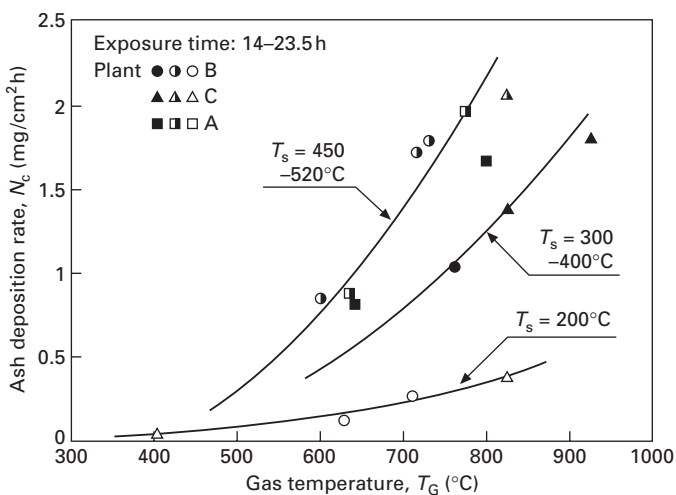


19.23 Schematic constitution of in-situ ECM system for corrosion environment.

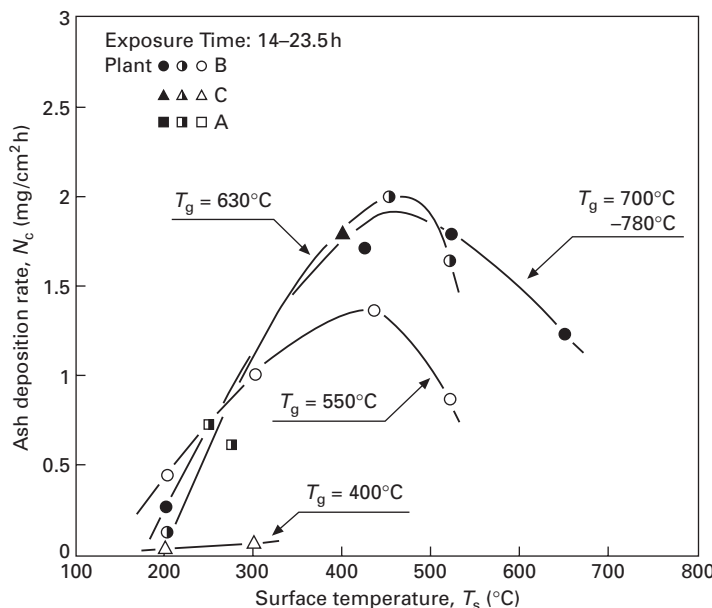




19.24 Correlation between melting point of deposits by in-situ electro-chemical sensor (ECS) and DTA in laboratory.



19.25 Changes in ash deposition rate with gas temperature.



19.26 Changes in ash deposition rate with surface temperature.

chlorides and sulfates decreases (phenomenon **a**), while since the molten phase content in deposits (melting point approximately 300°C) increases, the binder effect for colliding particles is thereby strengthened (phenomenon **b**). Furthermore, since the surface temperature exceeds the peak temperature, as part of phenomenon **b** the condensing constituents with low melting point from the vapor are largely reduced (particularly high vapor pressure constituents such as heavy metal chlorides) simultaneously, because  $\Delta T$  (the driving force of vapor diffusion) becomes smaller, and the overall rate of deposition decreases. Thus the peak is created through the combination of phenomena **a** and **b**. Investigations in three plants (A, B and C) having different characteristics of combustion gas showed the same tendency in ash deposition rates as described above. Consequently, it was found that the main factors affecting the deposition rate were considered to be the temperature condition and the direction of gas flow instead of the amount of vapor constituents in the combustion gas.

As mentioned above, the increase of the ash deposition rate due to increase of gas temperature in Fig. 19.25 agrees well with the actual thickness loss data<sup>9</sup> in relation to superheater CR in Fig. 19.3. An increase of gas temperature especially increases the deposition rate of chlorides which promote a higher CR. Also, the existence of a peak for the CR versus the tube surface temperature is similar to the peak of ash deposition rate. Therefore these two phenomena should be well correlated.

## 19.9 Corrosion lifetime evaluation of materials

It is generally assumed that HTC follows a linear rate law or a parabolic rate law as follows:

$$\Delta W = K_{p-l} t \quad 19.1$$

$$\Delta W^2 = K_{p-p} t \quad 19.2$$

where  $\Delta W$  is the corrosion loss (mm),  $K_{p-l}$  the linear CR constant,  $K_{p-p}$  the parabolic CR constant and  $t$  the time (h). In this study,  $K_{p-l}$  and  $K_{p-p}$  are assumed to be functions of five variables, i.e., gas temperature, metal temperature, HCl concentration of the flue gas, Cl concentration of the ash deposits on the tube surface, and the sum of Cr, Ni and Mo contents of test alloys. It was confirmed through field tests that these are the important variables for corrosion.<sup>3,4</sup>

To derive the least-square value of these constants, nonlinear regression analysis was performed using a statistical analysis program. A total of 185 field test data were used for the regression analysis. Air-cooled probes consisting of various alloys were exposed at three actual stoker-type WTE boilers for 700, 3000 and 6000 hours. Test conditions are summarized in Table 19.4. The metal temperature of the probes was controlled at 450 and 550°C. The obtained and derived regression equations for  $K_{p-l}$  and  $K_{p-p}$  are shown below:

$$K_{p-l} = 10^{-44.15} T_g^{10.17} T_m^{4.00} [\text{HCl}]^{0.61} [\text{Cl}]^{0.37} [\text{Cr} + \text{Ni} + \text{Mo}]^{-0.39} \quad 19.3$$

$$K_{p-p} = 10^{-86.91} T_g^{21.47} T_m^{7.47} [\text{HCl}]^{1.29} [\text{Cl}]^{0.58} [\text{Cr} + \text{Ni} + \text{Mo}]^{-0.76} \quad 19.4$$

where  $T_g$  is the gas temperature (°C),  $T_m$  the metal temperature (°C), [HCl] the HCl concentration in the flue gas (ppm), [Cl] the Cl concentration in the ash deposit (mass%) and [Cr + Ni + Mo] the sum of Cr, Ni and Mo content in the alloy (mass%).

According to Eqs (19.3) and (19.4),  $K_{p-l}$  and  $K_{p-p}$  increase with increasing  $T_g$ ,  $T_m$ , [HCl] and [Cl], and decrease with increasing [Cr + Ni + Mo]. The

Table 19.4 Operating conditions of test plants

	Plant		
	A	B	C
Type of furnace	Stoker	Stoker	Stoker
Capacity (t/day)	500	150	200
$T_m$ of the probe* (°C)	450/550	450/550	450/550
$T_g$ of the probe* (°C)	583–643	608–654	613–675
HCl in the flue gas (ppm)	690–1300	568–820	790–1420
Cl in the ash (wt%)	0.3–6.6	1.3–10.5	1.7–5.9

\*  $T_m$  = metal temperature,  $T_g$  = gas temperature.

value of the constant  $T_g$  is about three times larger than  $T_m$ . This means that the effect of the gas temperature on the CR is greater than that of the metal temperature in the field tests.

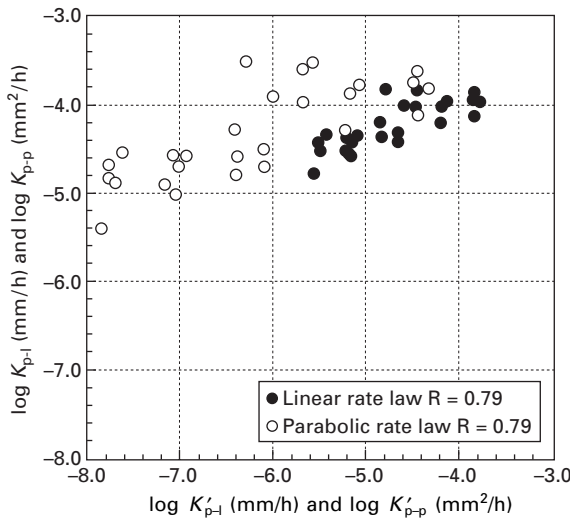
It is important to evaluate whether the CR constant corresponds to the linear  $K_{p-l}$  or to parabolic  $K_{p-p}$  in corrosion lifetime estimation, because the long time corrosion losses estimated are largely different from each other. According to field test results, the variation of corrosion loss with time could be fitted to a parabolic rate law for the three plants A, B and C, although the linear CR law approximation was suitable for the severe corrosive environment. The accuracy of the predictive equations, derived solely from the field corrosion test data, was evaluated by comparing the predicted values and the actual corrosion losses of superheater tube alloys in a 500°C 19.8 MPa high-efficiency WTE pilot plant.<sup>48</sup> Seven different locations for tertiary superheaters and secondary superheaters were measured after 13,800 hours of operation. Test alloys were Alloy 625, Alloy 825, JHN24, HR11N, HC-22, HR30M and 310CbN.  $T_g$ ,  $T_m$ , [HCl] and [Cl] data for each location are summarized in Table 19.5.

Figure 19.27 shows the relationship between the calculated and the measured values in the pilot plant for  $K_{p-l}$  and  $K_{p-p}$ . The agreement between the calculated and observed values was better for  $K_{p-l}$  than for  $K_{p-p}$ . However, more pronounced differences in  $K_p$  values were observed for low gas temperatures. The reason for these differences is that the gas temperature of the field test was higher than that of the pilot plant and the value of the constant  $b$  of  $T_g$  was much larger than that of constant  $c$  of  $T_m$  in Eqs (19.3) and (19.4). On the other hand, as shown in Table 19.6, the regression analysis results for the pilot plant data with the linear CR law assumption indicate that the effect of the variables on  $K_{p-l}$  is similar to the field test results, but the constant  $b$  of  $T_g$  is the same as the constant  $c$  of  $T_m$ . This means that the effect of gas temperature on  $K_{p-l}$  in the pilot plant was smaller than that in the field test. Therefore, Eq. (19.4) was modified in order to fit the calculated value to the observed value as follows:

$$K_{p-l} = 10^{-33.8} T_g^{5.65} T_m^{4.86} [\text{HCl}]^{0.61} [\text{Cl}]^{0.37} [\text{Cr} + \text{Ni} + \text{Mo}]^{-0.39} \quad 19.5$$

Table 19.5 Conditions at various SH locations in the pilot plant

Location	$T_g$ (°C)	$T_m$ (°C)	[HCl] (ppm)	[Cl] (%)
A	621	452	690	11.1
B	554	486	690	11.1
C	540	491	690	3.7
D	513	499	690	3.7
E	510	500	690	1.3
F	488	451	690	1.2
G	461	429	690	1.2



19.27 Comparison of the calculated values ( $K'_{p-l}$  and  $K'_{p-p}$ ) from Eqs (19.3) and (19.4) to observed values ( $K_{p-l}$  and  $K_{p-p}$ ).

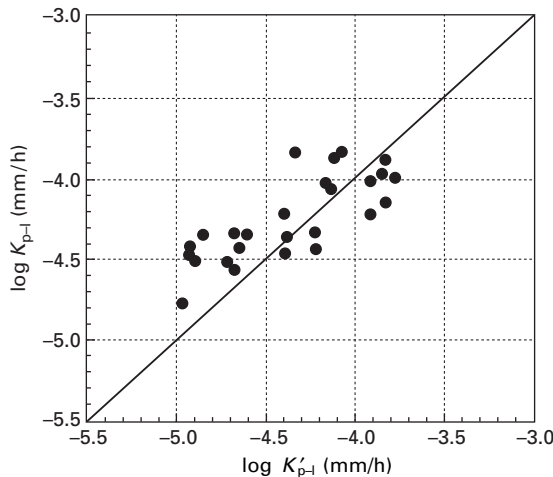
Table 19.6 Results of the regression analysis for  $K_{p-l}$  by using pilot plant data

Data number	95
Correlation coefficient	0.89
Standard deviation	0.15
Exponent of constant term	-31.14
Exponent $b$ for $T_g$	5.65
Exponent $c$ for $T_m$	4.86
Exponent $d$ for HCl	-
Exponent $e$ for [Cl]	0.1
Exponent $f$ for [Cr + Ni + Mo]	-0.72

In this equation, the constants for  $T_g$  and  $T_m$  are the values obtained in the regression analysis of Table 19.6 and the constants of the other variables are the same as in Eq. (19.4).<sup>49</sup> Figure 19.28 shows the relationship between the calculated  $K'_{p-l}$  from Eq. (19.5) and the observed  $K_{p-l}$  for the pilot plant data. Although a slight difference exists in both values, the correlation has been improved in comparison to the results shown in Fig. 19.20.

## 19.10 Summary

In recent years, WTE plants have been obliged to satisfy many additional requirements such as the suppression of pollutants, improvement of power generation efficiency, material recycling, etc. Various combustion methods and plant systems have been adopted, and the HTC environment of the



19.28 Comparison of the calculated values ( $K'_{p-I}$ ) from Eq. (19.5) to observed values ( $K_{p-I}$ ).

plants is becoming more complicated and diversified. It is believed that the development and application of corrosion prevention technologies should aim strongly to use the right material in the right place at a reasonable cost. Improvements in performance and lifetime of WTE plants have been supported by the development of CRM and CRC technologies. There are many subjects for future research, such as the development of software for effectively applying these corrosion prevention technologies to WTE boilers. It is expected that engineers and researchers in the field of CRMs and CRCs will meet these challenges.

## 19.11 References

1. Y. Kawahara, Recent Trends and Future Subjects on High-Temperature Corrosion-Prevention Technologies in High-Efficiency Waste-to-Energy Plants, *Corros. Eng.*, 2005, **54**, pp 213–235
2. Y. Kawahara and Y. Kaihara, Recent Trends in Corrosion-Resistant Tube Materials and Improvement of Corrosion Environments in the WTE Plants, *Corrosion/2001*, Paper No. 1173 (Houston, TX), NACE, 2001
3. Y. Kawahara, M. Nakamura, H. Tsuboi, and K. Yukawa, Evaluation of New Corrosion Resistant Superheater Tubings in High Efficiency Waste-to-Energy Plants, *Corrosion*, 1998, **54**(7), p 576
4. Y. Kawahara, N. Orita, M. Nakamura, S. Ayukawa, and T. Hosoda, Laboratory Corrosion Tests for Simulating Fireside Wastage of Superheater Materials in Waste Incinerators, *Corrosion/99*, Paper No. 89 (San Antonio, TX), NACE, 1999
5. Y. Kawahara, High Temperature Corrosion Mechanisms and Effect of Alloying Elements for Materials used in Waste Incineration Environment, *Corros. Sci.* 2002, **44**, p 223

6. M. Yokono, A. Matsumoto, M. Noguchi, H. Yakuwa, M. Miyasaka, K. Miyoshi, K. Kosaka, and Y. Fukuda, Corrosion/99, Paper No. 87 (San Antonio, TX), NACE, 1999
7. Y. Kawahara, N. Orita, K. Takahashi, and Y. Nakagawa, Demonstration Test of New Corrosion-Resistant Boiler Tube Materials in High Efficiency Waste Incineration Plant, *Tetsu-to-Hagane*, 2001, **87**(8), p 24
8. T. Ishizuka, H. Mimura, T. Takahashi, M. Kurita, N. Hirayama, and K. Mori, *Proceedings of High Temperature Corrosion and Protection/2000* (Lusutsu, Japan), 2000, p 9
9. Y. Kawahara, M. Nakamura, H. Tsuboi, and K. Yukawa, Evaluation of New Corrosion Resistant Superheater Tubings in High Efficiency Waste-to-Energy Plants, *Corrosion*, 1998, **54**, p 576
10. G.D. Smith and W.G. Lipscomb, Corrosion/89, Paper No. 201 (New Orleans, LA), NACE, 1989
11. E. Hagglom and L. Nylöf, in *Materials for Advanced Power Engineering, Part II, 1994*, D. Coutsouradis *et al.*, ed., Kluwer Academic Publishers, Netherlands, 1994, p 1597
12. A.B. Sandvik, Steel Technical Report
13. A. Wilson, U. Forsberg, M. Lunderg, and L. Nylöf, *Proceedings of Stainless Steel World/99* (Den Haag, Netherlands), November, 1999, p 669
14. T. Matsui, H. Takizawa, S. Wakita, Y. Kawahara, and T. Hosoda, Development of Ni-Cr-Mo Alloy for Superheater Tube Applications, Corrosion/2000, Paper No. 262 (Orlando, FL), NACE, 2000
15. A. Shiyo, T. Isomoto, M. Yoshioka, N. Hirayama, T. Urabe, and K. Nagashima, *Proceedings of the 10th Conference of The Japan Society of Waste Management Experts*, C5-3, 1999, p 749
16. A. Shiyo, T. Isomoto, K. Toyama, T. Urabe, and M. Yoshioka, *J. Japan Inst. Metals*, 2002, **66**(6), p 554
17. D.C. Agrawal, J. Klöwer, and G.K. Grossmann, Corrosion/97, Paper No. 155 (New Orleans, LA), NACE, 1997
18. Y. Kawahara, K. Sasaki, and Y. Nakagawa, Development and Application of High Cr-high Si-Fe-Ni base Alloys to High Efficiency Waste-to-Energy Boilers, *Proceedings of International Symposium on High-Temperature Oxidation and Corrosion 2005*, ISIJ/JSC (Nara, Japan), 2005, OP22
19. Y. Fukuda, Y. Kawahara, and T. Hosoda, Application of High Velocity Flame Sprayings for Superheater Tubes in Waste Incinerators, Corrosion/2000, Paper No. 264 (Orlando, FL), NACE, 2000
20. Y. Kawahara, Y. Nakagawa, M. Kira, T. Sakurada, H. Kamakura, and Y. Imaizumi, Life Evaluation of ZrO<sub>2</sub>/Ni Base Alloy Plasma-Jet Coating Systems in High Efficiency Waste-to-Energy Boiler Superheaters, Corrosion/2004, Paper No. 04535 (New Orleans, LA), NACE, 2004
21. Y. Kawahara, Basic Science and Application of High Temperature Corrosion and Protection in Energy Conversion and Environmental Equipments, JIM Seminar Text, 2001, p 39
22. Y. Kawahara and M. Kira, Effect of Physical Properties of Molten Deposits on High Temperature Corrosion of Alloys in Waste Incineration Environment, *Zairyo-to-Kankyo*, 1997, **46**(1), p 8
23. P.D. Miller, H.H. Krause, D.A. Vaughan, and W.K. Boyd, *Corrosion*, 1970, **28**, p 274

24. Y. Kawahara, Evaluation of High-Temperature Corrosion Life using Temperature Gradient Corrosion Test with Thermal Cycle Component in Waste Combustion Environment, *Mater. Corros.*, 2006, 57(1), pp 60–72
25. M. Uekado, Y. Kamei, and K. Hujii, *J. Japan Inst. Metals*, 2002, 66(6), p 576
26. Y. Kawahara and M. Kira, Corrosion Prevention of Waterwall Tube by Field Metal Spraying in Municipal Waste Incineration Plants, *Corrosion*, 1994, 53, p 241
27. Y. Yamada, M. Koyama, T. Otuka, M. Osawa, and K. Toyama, *Yosha-Gijyutu*, 1994, 14(3), p 30
28. Y. Kawahara, K. Sasaki, and Y. Nakagawa, Application of Flame Spray Coatings of Ni Base Alloy for Waste Incineration Boilers, *Proceedings of 43th Conference of JSCE Materials and Environments*, B-114, 1996, p 195
29. P.Z. Kubin, Corrosion/99, Paper No. 90 (San Antonio, TX), NACE, 1999
30. D.E. Burnham, D.R. Gibbs, J.S. Gitlinger, and H.E. Johnson, *Proceedings of 1989 Conference on Municipal Solid Waste as a Utility Fuel* (Springfield), October 1989, pp 10–12
31. H.H. Krause, Corrosion/92, Paper No. 140 (Nashville, TN), NACE, 1992
32. I.G. Wright, H.H. Krause, and R.B. Dooley, Corrosion/95, Paper No. 562 (Orlando, FL), NACE, 1995
33. T. Yoshikawa, Spray Coating and Weld Overlay in Circulating Fluidized Bed Boiler (CFB) and Waste-to-Energy (WTF) Boilers, *Proceedings of International Symposium on High Temperature Oxidation and Corrosion/2005* (Nara, Japan), 2005, p 27
34. P.L.F. Rademakers, R.W.A. Wetzel, and E. Kokmeijer, Materials for Advanced Power Engineering, *Proceedings of the 6th Liege Conference Part II*, 5, 1998, p 751
35. G. Lai and P. Hulsizer, *Proceedings of Stainless Steel World/99* (Den Haag, Netherlands), November, 1999, p 681
36. Y. Takeuchi, Y. Kawahara, and T. Hosoda, Application of Composite Tubes Plasma-Weld-Overlaid with Ni-Cr-Mo Alloy for Superheater in Waste Incinerators, *Corrosion/2000*, Paper No. 261 (Orlando, FL), NACE, 2000
37. Y. Kawahara, X. Li, Y. Nakagawa, H. Imaizumi, T. Katoh, and H. Nakajima, Laboratory Corrosion Tests of New Weldoverlay Materials in Simulated Environment of High Efficiency WTE Boilers, *Proceedings of 48th Conference of JSCE Materials and Environments*, C-308, 2001, p 431
38. Technical Report of Haynes Alloys International, Inc., 1998
39. M.S. Brennan and R.C. Gassmann, Corrosion/2000, Paper No. 235 (Orlando, FL), NACE, 2000
40. Y. Kawahara, M. Kira, and M. Ike, Corrosion/2001, Paper No. 01159 (Houston, TX), NACE, 2001
41. JSSA, 2003, Report on Standardization of High-Temperature Corrosion Test Method in Metallic Materials 2004
42. Y. Kawahara, *J. Japan Inst. Metals*, 2002, 66(6), p 583
43. Y. Kawahara, *J. High Temp. Soc. Japan*, 2002, 28(5), p 202
44. M. Schütze, in *Protective Oxide Scales and Their Breakdown*, D.R. Holmes, ed., John Wiley & Sons, Chichester, UK, 1991
45. Y. Harada, and T. Kawamura, Mitsubishi Technical Bulletin, 1980, p 139
46. Y. Kawahara, M. Kira, and M. Ike, *Mater. High Temp.*, 2001, 18, p 445
47. A. Zahs, M. Spiegel, and H. J. Grabke, *Mater. Corros.*, 1999, 50, p 561
48. Y. Kawahara, Y. Nakagawa, T. Hosoda, and T. Mizuko, Demonstration Test of New Corrosion-Resistance Superheater Tubing in a High-Efficiency Waste-to-Energy Plant, *Corrosion/2000*, Paper No. 265, Houston, TX, NACE, 2000

49. Y. Fukuda, Y. Kawahara, T. Shimada, M. Nakamura, and T. Hosoda, Prediction of Corrosion Rate for Superheater Tube Materials in Waste Incinerators by a Regression Analysis of Field Corrosion Test Data, Materials at High Temperatures, ROD, 118(s), pp 423–442
50. C.M. Antony, G.Y. Lai, J.W. Tackett, and E.J. Bickel, Pressure Vessels Pipe Div., ASME, 1993, **262**, p 57
51. S. Yamamoto, A. Natori, Y. Yamadera, N. Otsuka, T. Kubo, and K. Ogawa, *Karyoku-Gensiyoku-Hatsuden*, 1996, **47**(7), p 6
52. Nippon Steel's Tubes for Boiler and Heat Exchanger and Pipes for Piping, 1998
53. U. Brill, J. Klöwer, E. Maasen, H. Richter, W. Schwend, and J. Venkateswarlu, *Corrosion*, 1994, 53, p 1585
54. Technical Report of Special Metals, Inc., 1999
55. Technical Report of Sumitomo Metal Industries, Ltd, 1995

# 20

## Sulfidation of metallic materials

---

Z GRZESIK and K PRZYBYLSKI  
AGH University of Science and Technology, Poland

### 20.1 Introduction

In many branches of modern industry, metallic materials are exposed to sulfur containing atmospheres at high temperatures.<sup>1,2</sup> High temperature corrosion in such environments is well known to be much more severe than in purely oxidizing atmospheres. In fact, under sulfidizing conditions all common metals and conventional oxidation resistant alloys undergo very rapid, often catastrophic degradation. This is the reason why the kinetics and mechanism of sulfide corrosion of metallic materials and physicochemical properties of metal sulfides have been extensively studied for many years.<sup>1–6</sup> This information is necessary for designing novel materials resistant to degradation in sulfidizing environments. In spite of this, however, due to considerable experimental difficulties in studying high temperature reactions in sulfur containing atmospheres, the mechanism of sulfide corrosion, as well as the defect structure and transport properties of sulfides, are still less known than those of metal oxidation and physicochemical properties of the corresponding oxides.<sup>4,6</sup>

The present chapter is an attempt to summarize the current knowledge on the sulfidation processes of metals and alloys in relation to defect structure and transport properties of sulfides. In the first part, the physicochemical properties of sulfides important in high temperature corrosion are outlined. The second part contains selected results concerning the sulfidation kinetics and mechanism of pure metals and alloys, with additional considerations of analogies and differences between sulfidation and oxidation processes. On this basis some prospects for the development of a new generation of coating materials resistant to complex sulfidizing–oxidizing atmospheres are discussed.

## 20.2 Physicochemical properties of metal sulfides

### 20.2.1 Thermodynamic considerations

Metal sulfides are characterized by lower thermodynamic stabilities in comparison with those of corresponding oxides.<sup>2,7,8</sup> Thus, the dissociation pressures of sulfides are much higher and do not differ so significantly as in the case of metal oxides<sup>9</sup> (Table 20.1). Another feature of transition metal sulfides which distinguishes them from oxides is their lower melting points<sup>6,7,10</sup> (Table 20.2). In addition, metal sulfides are much more numerous than the

*Table 20.1* Gibbs free energy of formation and dissociation pressures for several metal sulfides and oxides

Sulfide	$\Delta G_{1273K}^0$ (kJ/mol S)	$p_{S_2}$ (Pa)	Oxide	$\Delta G_{1273K}^0$ (kJ/mol O)	$p_{O_2}$ (Pa)
Al <sub>2</sub> S <sub>3</sub>	-191	$2.4 \times 10^{-11}$	Al <sub>2</sub> O <sub>3</sub>	-424	$1.8 \times 10^{-30}$
CoS	-43.8	26	CoO	-145	$1.2 \times 10^{-7}$
Cu <sub>2</sub> S	-95.7	$1.4 \times 10^{-3}$	Cu <sub>2</sub> O	-77.7	$4.3 \times 10^{-2}$
CuS	63.6	$1.6 \times 10^{10}$	CuO	-11.6	$1.1 \times 10^4$
FeS	-78.9	$2.9 \times 10^{-2}$	FeO	-179	$2.3 \times 10^{-10}$
MnS	-196.9	$7.3 \times 10^{-12}$	MnO	-292	$1.2 \times 10^{-19}$
MoS <sub>2</sub>	-78.3	$3.8 \times 10^{-2}$	MoO <sub>2</sub>	-182	$1.3 \times 10^{-10}$
NiS	-50.4	7.5	NiO	-127	$3.8 \times 10^{-6}$
TiS	-228	$2.1 \times 10^{-14}$	TiO	-420	$3.9 \times 10^{-30}$

*Table 20.2* Melting points of selected sulfides and oxides

Sulfide	Melting point (K)	Oxide	Melting point (K)
Al <sub>2</sub> S <sub>3</sub>	1373	Al <sub>2</sub> O <sub>3</sub>	2288
CoS	1389	CoO	2068
Co <sub>3</sub> S <sub>4</sub>	?	Co <sub>3</sub> O <sub>4</sub>	1223
Cr <sub>2</sub> S <sub>3</sub>	1623	Cr <sub>2</sub> O <sub>3</sub>	2539
Cu <sub>2</sub> S	1373	Cu <sub>2</sub> O	1508
CuS	376	CuO	1599
FeS	1472	FeO	1642
MnS	1598	MnO	2058
MoS <sub>2</sub>	1458	MoO <sub>2</sub>	2200
NiS	1083	NiO	2230
TiS	2373	TiO	2023
TiS <sub>2</sub>	?	TiO <sub>2</sub>	2123
La <sub>2</sub> S <sub>3</sub>	2423	La <sub>2</sub> O <sub>3</sub>	2490
Ce <sub>2</sub> S <sub>3</sub>	2373	Ce <sub>2</sub> O <sub>3</sub>	1965
ThS <sub>2</sub>	2198	ThO <sub>2</sub>	3593
US <sub>2</sub>	1373	UO <sub>2</sub>	3151
Y <sub>2</sub> S <sub>3</sub>	1873	Y <sub>2</sub> O <sub>3</sub>	2683
InS	965	InO	1325
In <sub>2</sub> S <sub>3</sub>	1323	In <sub>2</sub> O <sub>3</sub>	2273

*Table 20.3 Sulfides and oxides in some metal-oxidant systems*

Metal	Sulfides	Oxides
Co	$\text{Co}_4\text{S}_3$	$\text{CoO}$
	$\text{Co}_9\text{S}_8$	$\text{Co}_3\text{O}_4$
	$\text{CoS}$	
	$\text{Co}_3\text{S}_4$	
	$\text{CoS}_2$	
Cr	$\text{CrS}$	$\text{Cr}_2\text{O}_3$
	$\text{Cr}_7\text{S}_8$	
	$\text{Cr}_5\text{S}_6$	
	$\text{Cr}_3\text{S}_4$	
	$\text{Cr}_2\text{S}_3$	
Ni	$\text{Ni}_3\text{S}_2$	$\text{NiO}$
	$\text{Ni}_7\text{S}_6$	
	$\text{NiS}$	
	$\text{Ni}_3\text{S}_4$	
	$\text{NiS}_2$	

corresponding oxides.<sup>4</sup> This important fact is well illustrated in Table 20.3, in which sulfides and oxides of selected common metals are listed.

### 20.2.2 Defect structure and transport properties of sulfides

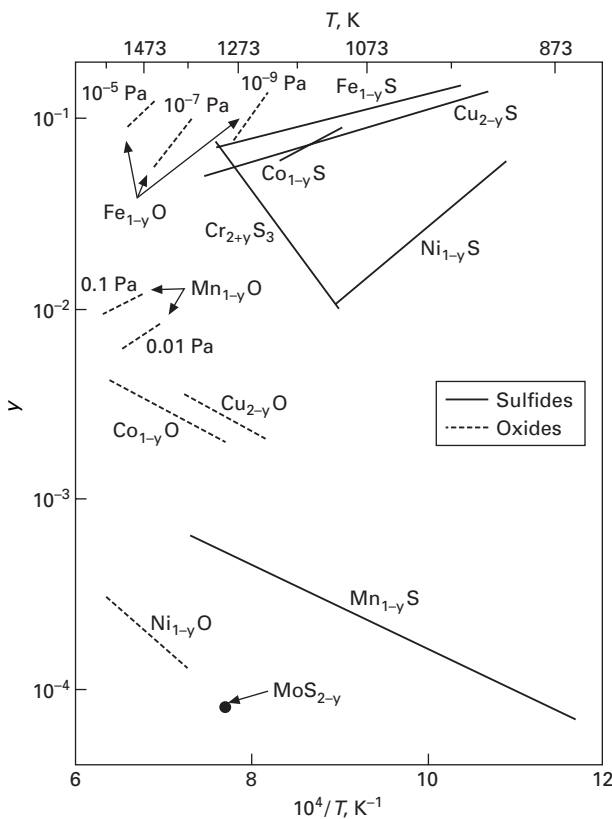
A number of important properties of transition metal sulfides and oxides are inherently related to atomic disorder in these compounds.<sup>3,5</sup> Point defects are responsible for lattice diffusion, which determines or strongly influences such important processes as mass transport, solid state reactions, high temperature creep, phase transformation, etc. From Wagner's theory of metal oxidation<sup>11</sup> it follows that at high temperatures, the parabolic rate constant of scale growth is the product of defect concentration and mobility. As a consequence, the defect structure and transport properties of metal sulfides and oxides have been studied for years in many scientific centers. In spite of this, however, these very important properties of sulfides are still less known than those of the corresponding oxides.<sup>4,6</sup> Such a situation results mainly from much greater experimental difficulties in studying high temperature heterogeneous reactions in sulfur containing atmospheres. Sulfur is not gaseous under normal conditions and its vapors are extremely aggressive at high temperatures, attacking all the metals, including gold and platinum. Consequently, all standard thermogravimetric devices and other equipment commonly used in oxidation studies are not applicable under such conditions. In the case of  $\text{H}_2\text{-H}_2\text{S}$  gas mixtures (in which sulfur partial pressure is

generally lower than 10 Pa) the situation is to some extent simpler than in pure sulfur vapors (where sulfur pressure can reach very high values, up to  $10^5$  Pa), because there is no danger of sulfur condensation on the cooler parts of the apparatus, and the sulfidation process can be performed under dynamic conditions, i.e. with the gas stream flowing through the reaction chamber at a suitable rate, maintaining a constant partial pressure of sulfur in the reaction zone. However, in H<sub>2</sub>-H<sub>2</sub>S environments only low sulfur pressures can be obtained. In addition, even more importantly, hydrogen may dissolve in the sulfide scale, changing its defect structure and, consequently, transport properties.<sup>12</sup> Thus, measurements in pure sulfur vapors are necessary and special equipment is required for such experiments. As a consequence, during the last 30 years several novel apparatus have been developed in many scientific centers active in this area of research,<sup>13-20</sup> which allow for the study of not only the mechanism and kinetics of metal sulfidation, but also point defect structure and transport properties of sulfides. In order to get a direct correlation between defect structure and mobility in investigated sulfides, the experiments are often carried out on scales obtained by completely sulfidized metals, i.e. on samples with defined texture.

It has been found that in contrast with the majority of transition metal oxides,<sup>5</sup> sulfides generally show many times higher deviation from stoichiometry and thereby significantly higher defect concentrations,<sup>4,6</sup> as illustrated in Table 20.4 and Fig. 20.1. It should be noted, however, that manganese sulfide,<sup>21</sup> Mn<sub>1-y</sub>S, and molybdenum disulfide,<sup>22,23</sup> MoS<sub>2+y</sub>, are important exceptions, showing much lower (by orders of magnitude) nonstoichiometry than the so-called common metal sulfides (Fe<sub>1-y</sub>S, Ni<sub>1-y</sub>S, Co<sub>1-y</sub>S, Co<sub>4-y</sub>S<sub>3</sub>). Unfortunately, deviations from stoichiometry and thereby defect structure in a number of sulfides have not yet been fully clarified. Good examples illustrating this situation are molybdenum and niobium sulfides. Since deviation from stoichiometry in molybdenum disulfide is extremely low,<sup>22,23</sup> there is still no agreement in the literature concerning the extrinsic disorder of this sulfide. Some authors<sup>24</sup> assume that the predominant defects are anion vacancies and quasi-free electrons, and others suggest that interstitial

*Table 20.4 Maximum nonstoichiometry of several metal sulfides and oxides at 1273 K*

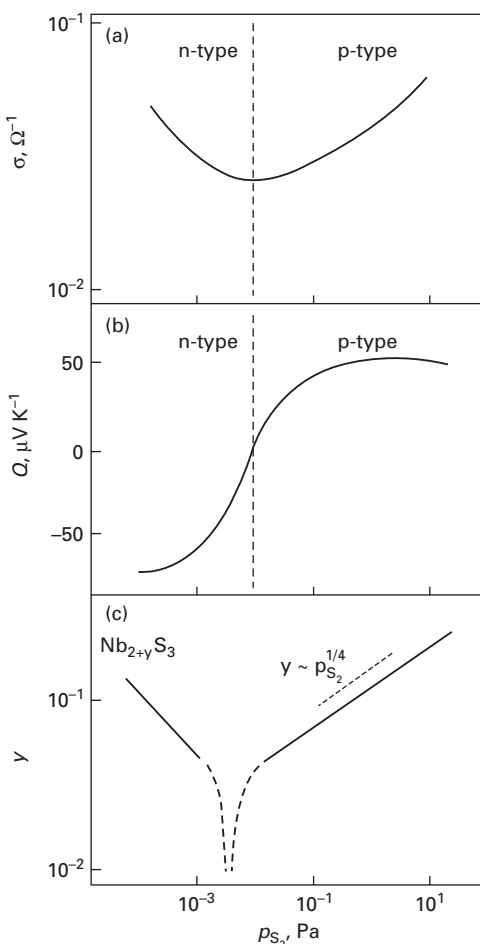
Sulfide	$\gamma$	Oxide	$\gamma$
Co <sub>1-y</sub> S	0.16	Co <sub>1-y</sub> O	0.009
Cr <sub>2+y</sub> S <sub>3</sub>	0.18	Cr <sub>2-y</sub> O <sub>3</sub>	0.00009
Cu <sub>2-y</sub> S	0.17	Cu <sub>2-y</sub> O	0.004
Fe <sub>1-y</sub> S	0.24	Fe <sub>1-y</sub> O	0.12
Mn <sub>1-y</sub> S	0.002	Mn <sub>1-y</sub> O	0.016
Ni <sub>1-y</sub> S	0.17	Ni <sub>1-y</sub> O	0.0006



20.1 Collective plot of maximum nonstoichiometry in several metal sulfides and oxides as a function of temperature.

anions and electron holes prevail.<sup>23,25</sup> Such a situation has made it difficult to satisfactorily describe the kinetics and mechanism of molybdenum sulfidation and, in particular, the influence of impurities on its sulfide corrosion. On the other hand, this information is very important since molybdenum, being highly resistant to sulfide corrosion, is considered to be one of the most important components in designing the new generation of alloys, resistant to sulfur attack at high temperatures. Extensive results of the Hall effect and electrical conductivity measurements,<sup>23,26,27</sup> as well as those of the kinetics and mechanism of molybdenum sulfidation<sup>25,28</sup> in He–S<sub>2</sub>, H<sub>2</sub>–H<sub>2</sub>S and He–S<sub>2</sub>–Li<sub>2</sub>S atmospheres, allow one to formulate the conclusion that the predominant defects in molybdenum disulfide are doubly ionized interstitial ions and electron holes. Thus, it is believed that this sulfide shows sulfur excess and not sulfur deficit and, consequently, that the proper chemical formula of this sulfide should be written as MoS<sub>2+y</sub>.

As far as the defect structure in niobium sulfide is concerned, the detailed experimental results and theoretical considerations<sup>29–32</sup> allow the conclusion that the correct formula of this sulfide scale on niobium should not be  $\text{Nb}_{1+x}\text{S}_2$  but rather  $\text{Nb}_{2\pm y}\text{S}_3$ . The assumption of a more complicated defect structure of this sulfide results directly from electrical conductivity, the Seebeck effect and nonstoichiometry data,<sup>29–32</sup> from which it follows that at low sulfur pressures this sulfide is n-type, and in the high pressure region it acts as a p-type semiconductor and the transition from n- to p-type behavior corresponds with the stoichiometric formula of  $\text{Nb}_2\text{S}_3$  (Fig 20.2). In addition, the minimum of nonstoichiometry corresponds with the n- to p-type transition behavior (see Fig. 20.2). All these data strongly suggest that interstitial cations and



20.2 Pressure dependence of (a) electrical conductivity, (b) the Seebeck effect, and (c) nonstoichiometry of  $\text{Nb}_{2+y}\text{S}_3$  at 1273 K.

quasi-free electrons are the predominant defects in the low pressure region, while cation vacancies and electron holes occur predominantly at high pressures, as suggested for the first time by Delmaire and Le Brusq,<sup>29</sup> as well as by Gesmundo *et al.*<sup>30</sup> It is important to note that detailed X-ray diffraction studies of niobium sulfides, reported by Kadijk and Jellinek,<sup>33</sup> have shown that the Nb<sub>2</sub>S<sub>3</sub> phase is not isotopic with the monoclinic phases Mo<sub>2</sub>S<sub>3</sub> and Nb<sub>2</sub>Se<sub>3</sub>, but belongs to the range of the phase 2s-Nb<sub>1+x</sub>S<sub>2</sub>, and this is probably the main reason why the discussed nonstoichiometric niobium sulfide was described in the literature as Nb<sub>1+x</sub>S<sub>2</sub> instead of Nb<sub>2±y</sub>S<sub>3</sub>.

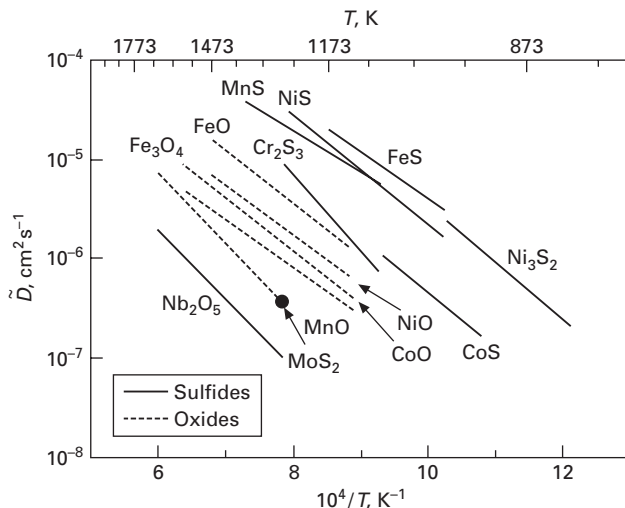
Transport properties of transition metal oxides and sulfides are characterized by two important parameters:<sup>3,5</sup> the self-diffusion coefficient of cations ( $D_{\text{Me}}$ ) or anions ( $D_X$ ), depending on whether the cation or anion sublattice is predominantly defected, and the defect diffusion coefficient ( $D_d$ ), being the direct measure of defect mobility. The self-diffusion coefficient can be determined experimentally using tracer methods, and in some cases it may also be calculated from the parabolic rate constant of scale formation, applying Wagner's theory of metal oxidation.<sup>11</sup> The defect diffusion coefficient, on the other hand, cannot be determined experimentally because it characterizes the random walk of defects in thermodynamic equilibrium.<sup>3,5</sup> It should be noted, however, that this coefficient can be calculated from chemical diffusion data, if only the degree of defect ionization is known. Chemical diffusion is the process of defect migration under a concentration gradient<sup>34–36</sup> and, consequently, the chemical diffusion coefficient ( $\tilde{D}$ ) is a direct measure of the rate of defect diffusion in a given solid under non-equilibrium conditions. Thus, the only difference between the rate of random walk of defects and their migration under a concentration gradient results from the accelerating effect of much more mobile electronic defects:<sup>3,5</sup>

$$\tilde{D} = (1 + |p|) \cdot D_d \quad 20.1$$

where  $p$  denotes the degree of defect ionization.

In contrast to oxides, the transport properties of metal sulfides are still less known. In a few cases only, the chemical and self-diffusion coefficients have been determined in direct measurements. However, the results of these experiments clearly indicate that chemical diffusion coefficients determined in sulfides do not differ significantly from those observed in oxides<sup>4</sup> (Fig. 20.3). In fact, the rate of chemical diffusion and thus the rate of defect mobility in the majority of transition metal sulfides is generally higher than in analogous oxides, but these differences do not exceed one order of magnitude.

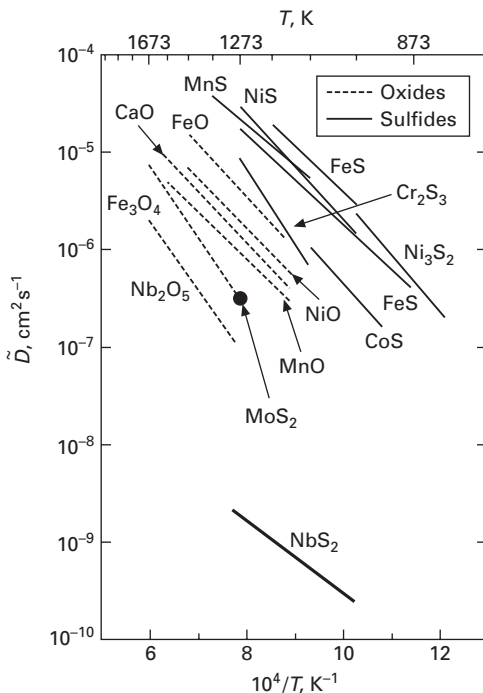
Some of the most important results concerning chemical diffusion in transition metal sulfides obtained recently<sup>31,37</sup> are the data describing the mobility of predominant defects in niobium sulfide, being the main product of niobium sulfidation. It has been shown in very accurate microthermogravimetric experiments that the mobility of these defects is



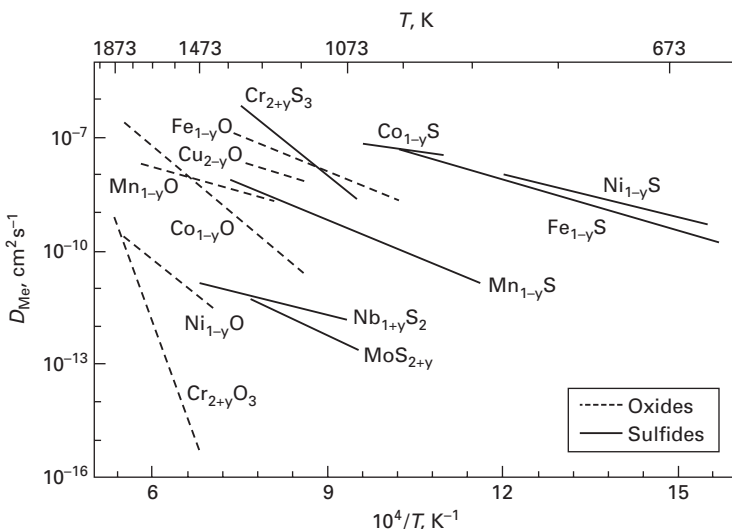
20.3 Comparison of chemical diffusion coefficients in several metal sulfides and oxides.

several orders of magnitude lower than that in all other metal sulfides and oxides (Fig. 20.4). It should be noted that one of the most fascinating problems in the case of niobium sulfidation is its extremely high resistance to sulfur attack at high temperatures, in spite of very high concentration of point defects in the growing scale on this metal. The only hypothetical explanation of this unexpected phenomenon, suggested for the first time by Gesmundo,<sup>30</sup> was based on the assumption that the mobility of defects in niobium sulfide scale is several orders of magnitude lower than in other transition metal sulfides. As pointed out previously, this theoretical hypothesis has been confirmed recently in studies on chemical diffusion in  $\text{Nb}_{2\pm y}\text{S}_3$  ( $\text{Nb}_{1+x}\text{S}_2$ ) using re-equilibration<sup>37</sup> and two-stage kinetic methods.<sup>38</sup> These results made it possible to explain the main reason for niobium's very high resistance to sulfide corrosion, despite a high defect concentration in niobium sulfide. Thus, in spite of a very high concentration of defects, the sulfide scale on niobium shows very good protective properties, comparable with those of the  $\text{Cr}_2\text{O}_3$  scale on chromium.

Other interesting results obtained recently – the first in the literature – concern chemical diffusion in molybdenum disulfide.<sup>39</sup> Figure 20.5 shows the collected data of self-diffusion coefficients in sulfides in relation to analogous results obtained for several metal oxides.<sup>4</sup> It follows clearly from this comparison that the rate of self-diffusion in metal sulfides is generally much higher than in the corresponding oxides. As chemical diffusion coefficients in metal oxides and sulfides are comparable (see Fig. 20.4), the significantly higher self-diffusion rates of cations in the majority of transition



20.4 Chemical diffusion coefficient in niobium sulfide on the background of analogous data obtained for several metal sulfides and oxides.

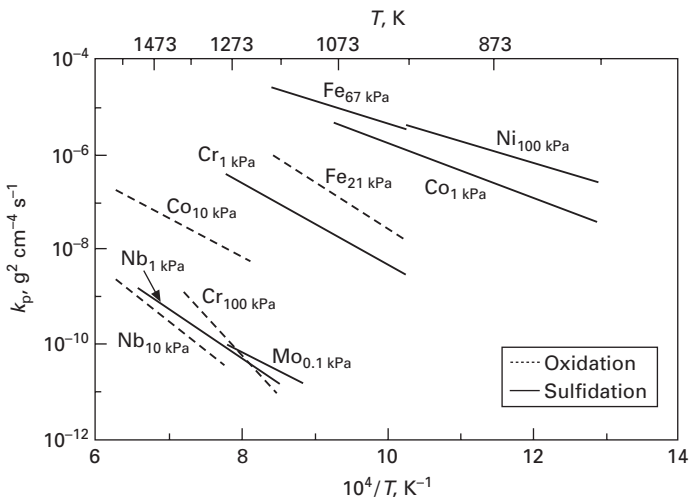


20.5 Comparison of self-diffusion coefficients in several metal sulfides and oxides.

metal sulfides result mainly from much higher defect concentration and not their mobilities. The only known exception is niobium sulfide.

### 20.3 Sulfidation of pure metals – a short review

In this section, the main similarities and differences between the kinetics and mechanisms of sulfidation and oxidation processes will be briefly discussed. One of the most important conclusions in this respect is that both sulfide and oxide scales on common metals grow by outward diffusion of cations. On the other hand, in the case of the sulfidation of some refractory metals, e.g. molybdenum, tantalum and tungsten, inert markers were found on the scale surface, strongly suggesting that the MoS<sub>2</sub>, TaS<sub>2</sub> and WS<sub>2</sub> scales, like the ZrO<sub>2</sub> scale, grow by inward diffusion of anions.<sup>4</sup> This important similarity in the growth mechanism of sulfide and oxide scales on metals results from the same type of predominant disorder in transition metal sulfides and oxides. It is interesting to note that the reactions of metals with sulfur are governed by the same basic principles as those for metal–oxygen reactions. However, the sulfidation rates of common metals are usually many times higher than their oxidation rates.<sup>4,6,40</sup> This is illustrated in Fig. 20.6, showing the collective plot of temperature dependence of sulfidation and oxidation rates of some metals. As the poor protective properties of sulfide scales on common metals result mainly from a very high concentration of point defects in their sulfides, it may then be concluded that the sulfidation rates are primarily determined by lattice diffusion. Consequently, grain boundary diffusion in sulfides is less important than in the case of metal oxidation. This is one of the reasons



20.6 Temperature dependence of sulfidation and oxidation rates of several metals.

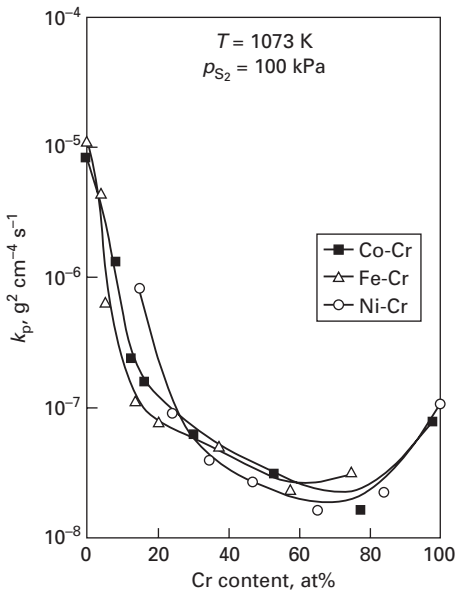
why the sulfidation reactions often follow ideal parabolic kinetics.<sup>2</sup> On the other hand, refractory metals are highly resistant to sulfide corrosion, their degradation rates being comparable to the oxidation rate of chromium, which is one of the metals most resistant to oxide corrosion. Low sulfidation rates of refractory metals, in turn, may result either from low defect concentration ( $\text{MoS}_{2+y}$ ) or low defect mobilities ( $\text{Nb}_{2\pm y}\text{S}_3$ ) in scales on these metals.

It is very important to note that the sulfur solubility in metals is much lower than in the case of oxygen.<sup>2</sup> The very small solubility of sulfur in metals as well as rapid scale formation make the formation of an internal sulfidation zone, which plays an important role in oxide corrosion, impossible.

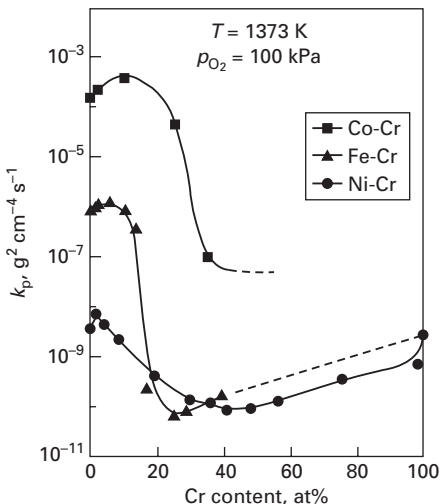
Finally, it should be noted that extensive experimental investigations have shown recently that small or even trace amounts of impurities may dramatically influence the rate of sulfide corrosion of metals due to the doping effect.<sup>41,42</sup> It has been found, for instance, that the rate of manganese sulfidation may be reduced by more than two orders of magnitude using very small amounts of lithium, incorporated into the scale growing on this metal.<sup>41</sup> On the other hand, the addition of small amounts of chromium increases the sulfidation rate of manganese by about one order of magnitude.<sup>42</sup> Both of these effects result from the influence of aliovalent dopants on the concentration of predominant defects in the growing scales. It may then be concluded that the doping effect may play a positive, but also a negative, role in high temperature sulfide corrosion of metals.

## 20.4 Sulfidation of selected alloys

Passing now to a discussion of alloy sulfidation, the similarities and differences between sulfide and oxide corrosion will briefly be considered. Following this concept Fig. 20.7 shows the sulfidation rate of Fe-Cr, Co-Cr and Ni-Cr alloys as a function of their composition. As can be seen, this dependence is analogous for all three alloy groups, being also very similar to the same dependence of the oxidation rate of these alloys<sup>2,43</sup> (Fig. 20.8). As in the case of oxidation, three composition ranges may be distinguished, differing in the influence of chromium concentration on the sulfidation rate and phase composition of scales, as shown schematically in Fig. 20.9. In the first, very narrow range (up to about 2% of chromium) the sulfidation rate is comparable with or even higher than that of the base metal, and the scale is homogeneous and consists of base-metal sulfide doped with chromium. In range II, which extends up to about 60% of chromium, the rate of sulfidation decreases abruptly with increasing chromium content in the alloy due to the formation in the scale of an inner barrier layer of sulfo-spinel. Finally, in range III, the scale is again homogeneous and consists of chromium sulfide doped with base metal, the sulfidation rate being considerably lower than that of pure chromium.



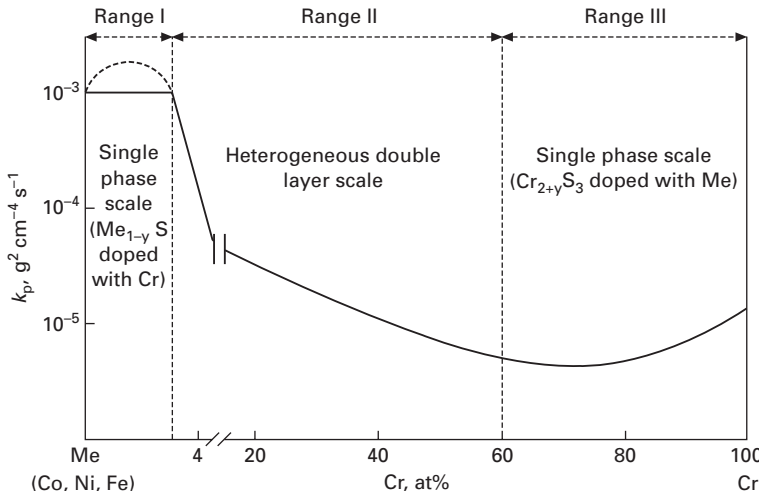
20.7 Dependence of the sulfidation rate of Fe-Cr, Co-Cr and Ni-Cr alloys on composition.



20.8 Dependence of the oxidation rate of Fe-Cr, Co-Cr and Ni-Cr alloys on composition.

#### 20.4.1 Dissociative mechanism of scale growth

As in the case of oxidation, the sulfide scales on the binary as well as on ternary and multicomponent alloys grow essentially by the outward diffusion

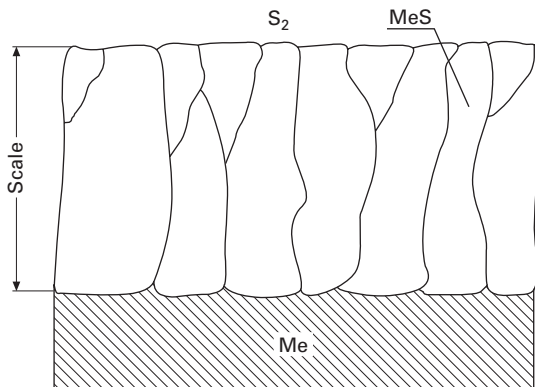


20.9 Schematic of the composition dependence of the sulfidation rate of Fe-Cr, Ni-Cr and Co-Cr alloys (for the  $p_{\text{S}_2}$  range = 10.13–1013 hPa).

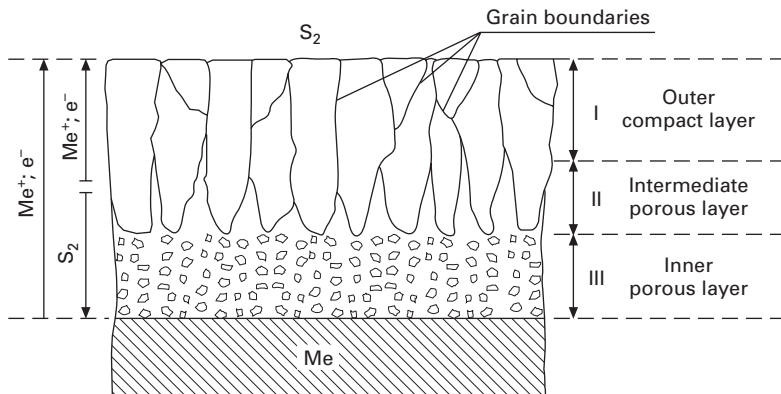
of cations,<sup>2,4,40</sup> because in the majority of transition metal sulfides and oxides the cation sublattice is predominantly disorders. These problems have been discussed in Section 20.3. It should be noted, however, that if the scale is heterogeneous and built of two layers, a dissociative mechanism may play an important role,<sup>44</sup> i.e. if full contact between the growing scale and the substrate is for any reason disturbed, hindering the transfer of cations from the metallic phase to the scale, the chemical potential of the oxidant (sulfur or oxygen) rises at the metal/scale interface, resulting in the increase of the oxidant pressure in the forming crack. As a consequence, a gradient of the oxidant pressure in the crack is established, resulting in the formation of the inner porous layer of the same phase composition. The loss of the oxidant in the crack due to this reaction is followed by gradual decomposition (dissociation) of the primary outer scale layer and ions and electrons liberated in this process diffuse outward.

However, it is well known that the scales growing by the outward diffusion of cations show highly developed growth texture, characterized by long columnar crystals, as illustrated schematically in Fig. 20.10. Such an anisotropic character of crystal growth clearly indicates that the reverse process of decomposition (dissociation) must proceed at the highest rate on crystal planes with the slowest growth rate, i.e., along the perpendicular-to-the-core grain boundaries, leading to the formation of dissociation fissures enabling the inward diffusion of the oxidant (Fig. 20.11).

In the case of pure metal sulfidation (oxidation), this mechanism starts to operate in later stages of the reaction, because the metal consumption zone may to some extent be compensated by the plastic flow of homogeneous

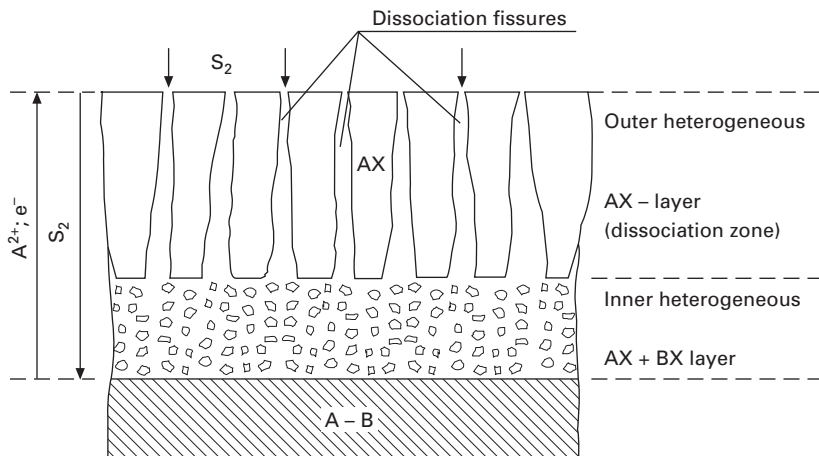


20.10 Scheme of the scale morphology formed on a flat metal sample by the outward volume diffusion of cations; Me = metal, S = oxidant.



20.11 Scheme of the growth mechanism of a single-phase, triple-layer sulfide scale on metals.

scales. As a consequence the dissociative mechanism leads to the formation of triple-layer scale of the same phase composition growing only by the outward diffusion of cations (Fig. 20.11). In the case of alloys, on the other hand, when heterogeneous scales are formed (Fig. 20.12), the dissociative mechanism starts to operate from the very beginning of the reaction.<sup>44</sup> The dispersed phase of slower growing sulfidation products of less noble metal accumulates in the inner scale layer, making the plastic flow of the scale impossible, which results in perforating dissociation of the primary, very thin scale layer and its further growth by simultaneous outward diffusion of more noble base metal and the inward diffusion of sulfur (Fig. 20.12). The scheme of such a mechanism of scale growth on binary alloys is presented in Fig. 20.12. It should be stressed that the mechanism of heterogeneous

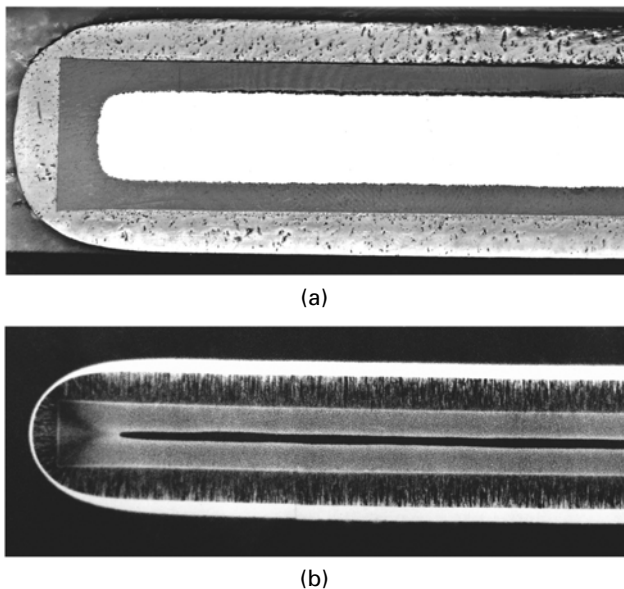


20.12 Scheme of the growth mechanism of a double-layer, heterogeneous sulfide scale on binary alloys; A = more noble base metal, B = less noble alloying component.

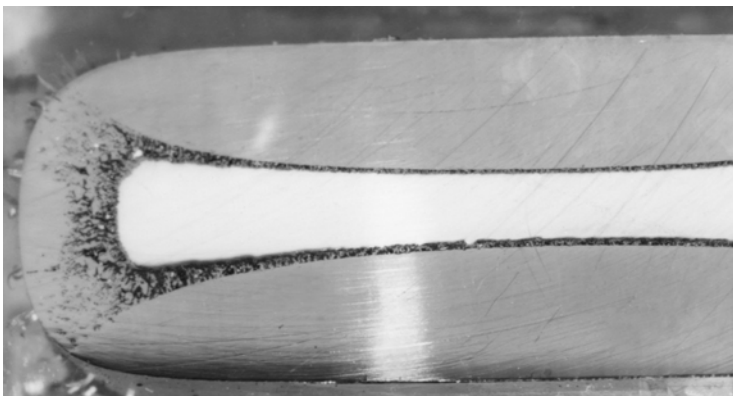
scale growth on alloys described above is equally valid in the case of sulfidation and oxidation. This has been proved in a number of works using the radioactive sulfur isotope  $^{35}\text{S}$  and oxygen  $^{18}\text{O}$  in two-stage sulfidation and oxidation experiments.<sup>45–48</sup> A spectacular illustration of dissociation fissures in the heterogeneous sulfide scale growing on Cu-Zn alloys is shown in Fig. 20.13. From the cross-section of the scale (Fig. 20.13(a)) formed on Cu-Zn alloy, it follows clearly that no plastic flow of the scale occurred, in contrast to the sulfidation observed in the case of pure copper or silver (Fig. 20.14). From the autoradiogram, in turn, presented in Fig. 20.13(b), it follows that due to perforating dissociation the radioactive sulfur isotope, introduced into the sulfidizing atmosphere in the second stage of the reaction, is present in the whole cross-section of the scale. In addition, it is clearly seen that the inward transport of sulfur through the outer scale layer proceeded along the favorable paths (dissociation fissures) both near the edges and in flat regions of the sulfidized sample.

#### 20.4.2 Sulfidation kinetics

However, despite great similarities in the growth mechanisms of oxide and sulfide scales, the sulfidation and oxidation *rates* of these alloys differ dramatically. This is illustrated in Fig. 20.15 by the dependence of oxidation and sulfidation rates of Fe-Cr alloys on their composition.<sup>40</sup> As can be seen, the oxidation rate of chromia formers (about 40% Cr) is more than four orders of magnitude lower than the sulfidation rate of alloys, on the surface of which a homogeneous  $\text{Cr}_2\text{S}_3$  scale is formed (about 60% Cr). These



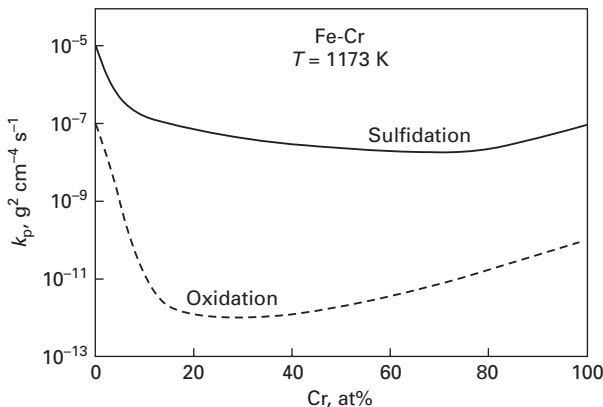
20.13 (a) Photograph and (b) autoradiogram of the cross-section of sulfide scale formed in two-stage sulfidation process on a flat Cu-9%Zn alloy sample; 60 min in non-radioactive and 60 min in radioactive sulfur.



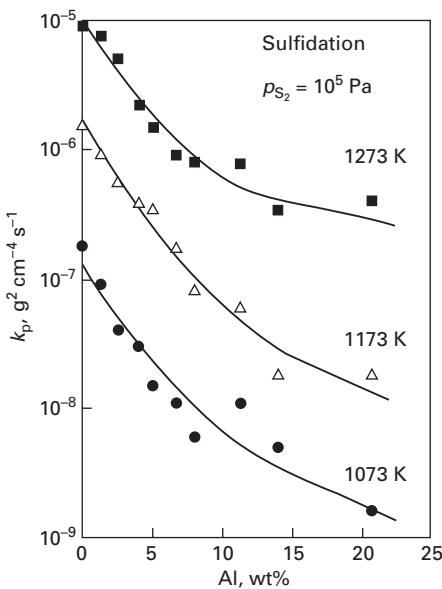
20.14 Cross-sections of sulfide scales formed on flat silver sample at 712 K, reaction time 10 min.

differences result from defect concentrations orders of magnitude higher in metal sulfides as compared to oxides.

Aluminum additions to the alloys under discussion improve their resistance to sulfide corrosion, but the effect is rather weak,<sup>49</sup> not exceeding two orders of magnitude even when the concentration of aluminum reaches 20 at% as



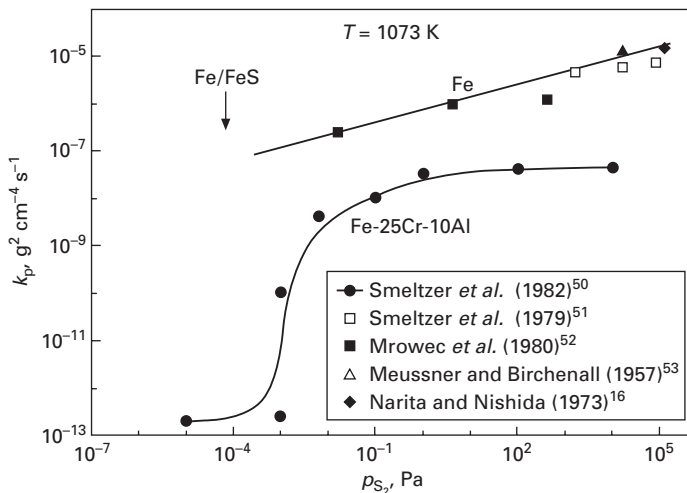
20.15 Dependence of the sulfidation and oxidation rates of Fe-Cr alloys on composition.



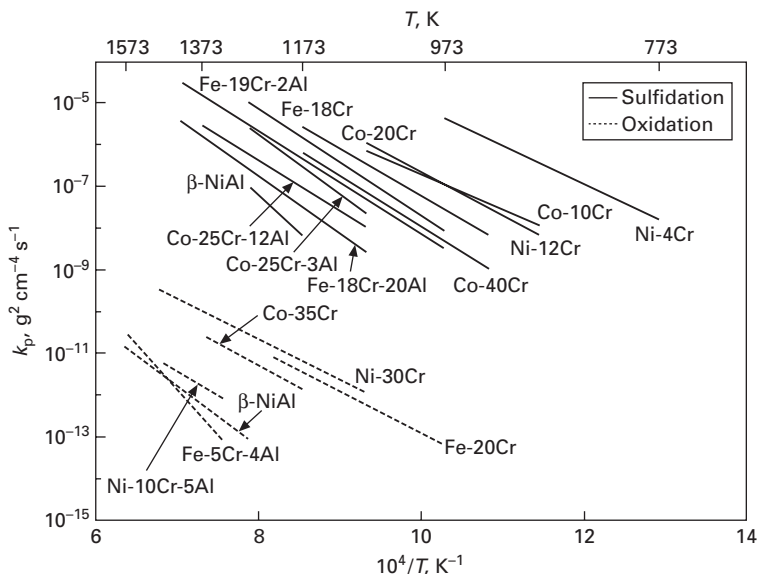
20.16 Influence of aluminum content in Fe-Cr-Al alloys on their sulfidation rate.

shown in Fig. 20.16. At very low sulfur pressure only, lower than the dissociation pressure of base-metal sulfide, a highly protective scale can form<sup>4</sup> (Fig. 20.17).

In order to illustrate the dramatic differences between sulfide and oxide corrosion of high-temperature alloys, Fig. 20.18 shows a collective plot of the temperature dependence of the sulfidation and oxidation rates for several



20.17 Influence of sulfur pressure on the sulfidation rate of iron and Fe-25Cr-10Al alloy.



20.18 Collective plot of the temperature dependence of the sulfidation and oxidation rates of several binary and ternary alloys and  $\beta$ -NiAl intermetallic.

binary and ternary alloys and  $\beta$ -NiAl intermetallic compound. It is clearly seen that all oxidation resistant alloys, including  $\beta$ -NiAl intermetallic compound,<sup>54,55</sup> corrode many orders of magnitude faster in a highly sulfidizing environment than in oxygen. Such a situation results mainly from the fact

that in oxidizing atmospheres highly protective chromia or alumina scale layers are formed on these alloys as a result of selective oxidation of chromium or aluminum. On the other hand, in sulfidizing environments even at much higher concentrations of chromium, and in particular aluminum, heterogeneous scales of poor protective properties are formed, containing sulfides of all alloying components.

This important difference results mainly from thermodynamic and kinetic reasons. In the case of oxidation, absolute values of free energies of formation of  $\text{Cr}_2\text{O}_3$  and  $\text{Al}_2\text{O}_3$  are much higher than those of base metal oxides ( $\text{FeO}$ ,  $\text{CoO}$ ,  $\text{NiO}$ ). Consequently, about 30 wt% of chromium and only 5–7 wt% of aluminum is high enough for selective oxidation of these alloying components. In addition, the growth rates of these oxide layers are so low that the rate of interdiffusion within the alloy is high enough to maintain the chromium and/or aluminum activity at the alloy scale interface for steady-state, selective oxidation. The situation is different in the case of sulfidation, because absolute values of free energies of formation of  $\text{CrS}$ ,  $\text{Cr}_2\text{S}_3$  and  $\text{Al}_2\text{S}_3$  are not much higher than those of iron, cobalt and nickel sulfides. Thus, selective sulfidation of chromium and/or aluminum is not favored, and heterogeneous scales are formed which have poor protective properties. In addition, the very high growth rates of base-metal sulfides impede the formation of a continuous chromium sulfide or aluminum sulfide layer.

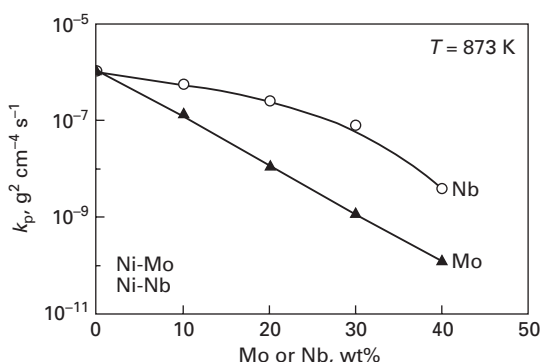
It should be stressed, however, that even if the chromium concentration in the alloy is high enough for selective sulfidation of this metal (60–70% Cr, see Figs 20.7 and 20.15) the rate of sulfidation of such an alloy is several orders of magnitude higher than that of oxidation because of defect concentration orders of magnitude higher in chromium sulfides.<sup>4,40</sup> Data concerning defect and transport properties of aluminum sulfide are still lacking, but the results of sulfidation of ternary Fe-Cr-Al<sup>49</sup> and Co-Cr-Al<sup>56</sup> alloys, as well as  $\beta$ -NiAl intermetallic compound,<sup>54,55</sup> clearly indicate that in highly sulfidizing environments selective sulfidation of aluminum is impossible even if its concentration exceeds 50 at%. Thus, from a practical point of view chromium and aluminum alone do not seem to be very promising in designing novel materials resistant to sulfide corrosion.

#### 20.4.3 Alloys containing refractory metals

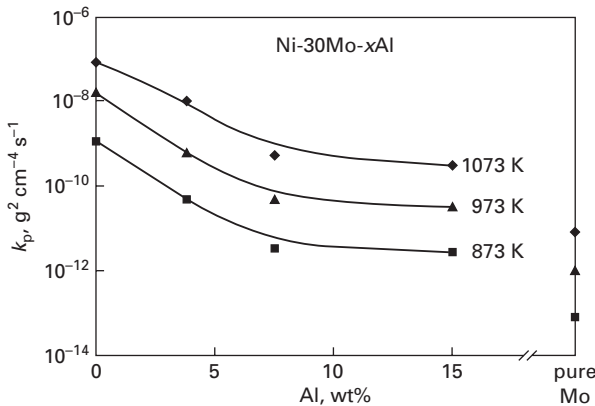
It has been found that there are a few metals highly resistant to sulfide corrosion, i.e. refractory metals and in particular molybdenum<sup>25,28</sup> and niobium.<sup>31,37</sup> The sulfidation rates of these metals are comparable with the oxidation rate of chromium, which is one of the most resistant metals to oxide corrosion. Taking into account this important observation, several years ago extensive research was undertaken in order to prove the possible role of refractory metals as alloying components in designing novel sulfidation-

resistant materials. The most interesting results have been obtained by Douglass *et al.*<sup>57–64</sup> in systematic studies of the influence of molybdenum, and subsequently of the combined effect of molybdenum and aluminum, on the sulfidation behavior of common metals (Fe, Ni, Co). Figure 20.19 shows, for illustration, the influence of niobium and molybdenum on the sulfidation rate of nickel. As can be seen, molybdenum is much more effective than niobium, but still the rate of sulfidation of highly alloyed nickel is about three orders of magnitude higher than that of pure molybdenum. Such a situation results from the fact that absolute values of the free energies of formation of refractory-metal sulfides are rather small, being comparable with those of common-metal sulfides. Selective sulfidation of niobium or molybdenum was, then, impossible and heterogeneous scales of moderate protective properties have been formed, even when the concentration of these metals in the alloy was relatively high (>30 wt%). The obvious conclusion was that refractory metals alone cannot improve satisfactory corrosion resistance of common metals against sulfur attack at high temperatures. The next step, then, was to study the combined effect of molybdenum *and* aluminum and the results seemed to be surprisingly promising.<sup>64</sup> Figure 20.20 illustrates the influence of aluminum addition on the sulfidation rate of Ni-30Mo alloys. It is clearly seen that the resistance against sulfur attack has been considerably improved, but the minimum sulfidation rate of such ternary Ni-30Mo-xAl alloys was still higher than that of pure molybdenum, as shown in Fig. 20.21. However, in the case of iron-base alloys the situation was much better. This is illustrated in Fig. 20.22 showing the effect of aluminum on the sulfidation rate of Fe-30Mo alloys.

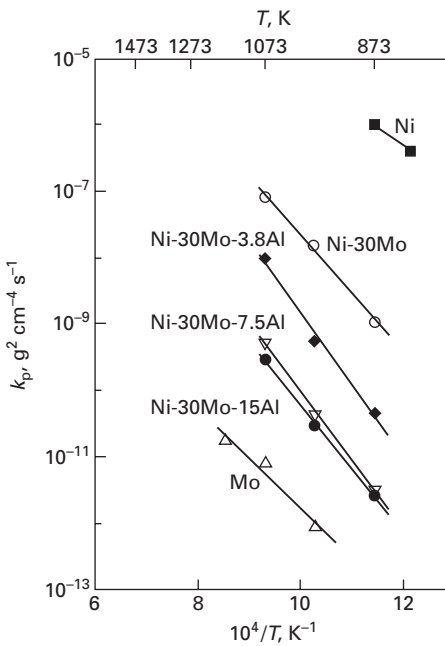
It follows clearly from this figure that the sulfidation rate of these ternary alloys decreased dramatically with increasing aluminum content and reached virtually the rate of pure molybdenum sulfidation with only 5 wt% of this



20.19 Influence of niobium and molybdenum on the sulfidation rate of nickel.

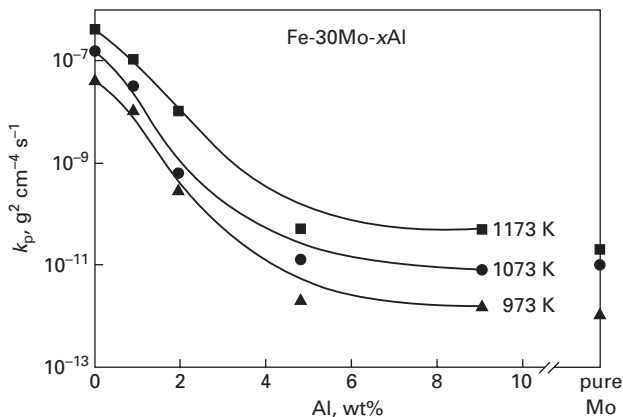


20.20 Influence of aluminum on the sulfidation rate of Ni-30Mo alloy for several temperatures.

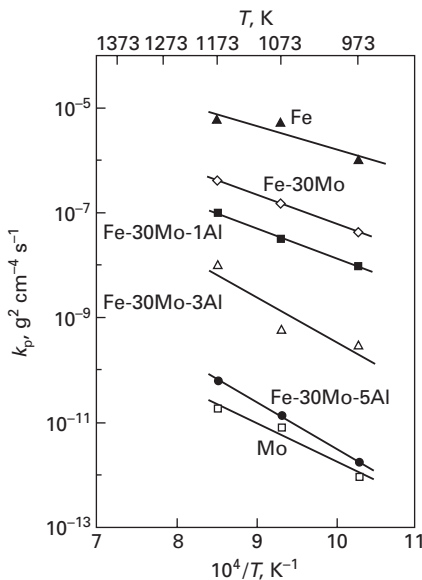


20.21 Temperature dependence of the sulfidation rate of binary Ni-30Mo and ternary Ni-30Mo-xAl alloys compared to the sulfidation rates of nickel and molybdenum.

alloying component. This combined effect of molybdenum and aluminum is better visualized in Fig. 20.23 showing the temperature dependence of the sulfidation rate of Fe-30Mo-5Al alloy on the background of the analogous dependence for pure iron and molybdenum.

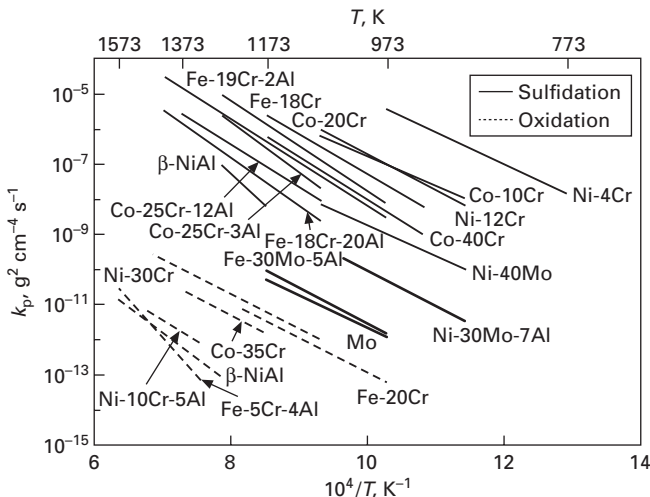


20.22 Influence of aluminum on the sulfidation rate of Fe-30Mo alloy for several temperatures.



20.23 Temperature dependence of the sulfidation rate of Fe-30Mo and Fe-30Mo-xAl alloys compared to the sulfidation rates of pure iron and molybdenum.

In order to stress further the importance of the results obtained by Douglass *et al.*,<sup>57–64</sup> Fig. 20.24 shows once again the temperature dependence of the sulfidation rate of Fe-30Mo-5Al alloy on the background of the sulfidation and oxidation rates of several binary and ternary high-temperature alloys. It follows clearly from this comparison that the rate of sulfide corrosion of the



20.24 Collective plot of the temperature dependence of the sulfidation and oxidation rates of binary and ternary alloys compared to the sulfidation rates of new Fe-Mo-Al and Ni-Mo-Al alloys and pure molybdenum (solid lines – sulfidation; dashed lines – oxidation).

alloy discussed is only slightly higher than the oxidation rate of chromia formers, being more than two orders of magnitude lower than the sulfidation rates of ternary Fe-Cr-Al alloys and  $\beta$ -NiAl intermetallic compound. Douglass *et al.*<sup>64</sup> have shown that excellent protective properties of the sulfide scale on this novel high-temperature material result from the formation of a double molybdenum–aluminum sulfide with spinel-like structure of formula  $\text{Al}_{0.5}\text{Mo}_2\text{S}_4$ . It may then be concluded that an important step forward has been made in creating a rational basis for designing new coating materials resistant to sulfide corrosion. It should be noted, however, that the Fe-30Mo-(5–9)Al alloys under discussion are heterogeneous and consist of two phases: iron-rich solid solution and a molybdenum-rich  $\beta$ -intermetallic compound. Because of the two-phase nature of these alloys the ‘pest’ phenomenon has been observed,<sup>64</sup> consisting of numerous cracks within the molybdenum-rich intermetallic regions. In addition, the oxidation resistance of this material is rather poor, because the aluminum activity at the alloy–scale interface is too low to suppress completely the formation of low-melting (1068 K) and highly volatile molybdenum oxide ( $\text{MoO}_3$ ).<sup>40</sup>

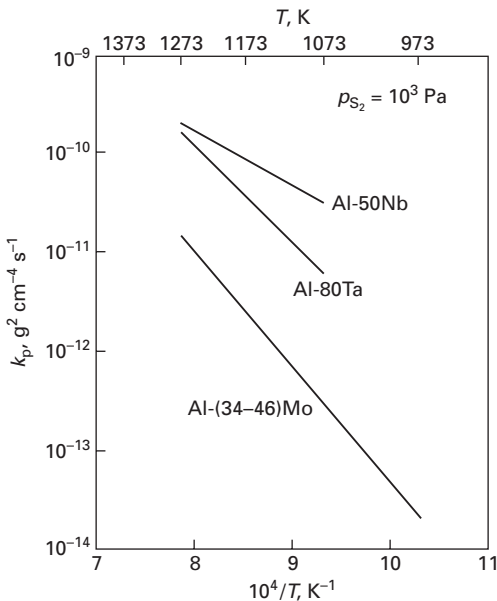
Considering this rather pessimistic situation, some 15 years ago Mrowec<sup>40</sup> arrived at the conclusion that it would be of interest to study binary aluminum base refractory metal alloys without any common-metal additions, because theoretical considerations strongly suggested that such materials of suitable composition and microstructure could create a promising basis for designing

novel coating materials resistant to both sulfidizing and oxidizing atmospheres.<sup>40,65</sup> However, Al-Re alloys (Re-refractory metal) are impossible to prepare by conventional metallurgical procedures because the boiling point of aluminum is lower than the melting point of all refractory metals. Nevertheless, a sputtering technique may be used successfully, because it does not rely on melting to mix alloying constituents.<sup>65,66</sup> Furthermore, sputtering allows high flexibility in the alloy composition, because of high vapor-quenching rates ( $10^{12}$  K s<sup>-1</sup>) enabling the deposition of highly super-saturated single-phase alloys in amorphous form. Finally, this method is well suited to modern coating applications, as amorphous alloys can be deposited over large areas, including complex shapes of industrial interest at relatively high deposition rates. Using this method a number of binary Al-(31–46)Mo and ternary Al-31Mo-(6–16)Si amorphous alloys have been sputter-deposited onto quartz substrates and their sulfidation and oxidation behavior has been studied using various thermogravimetric and other techniques.<sup>40,67–75</sup> The composition range was chosen in such a way that a single-phase, amorphous alloy could be formed and during thermal heating only intermetallic compounds could form without any traces of the separate Al-phase which would be liquid above 933 K.

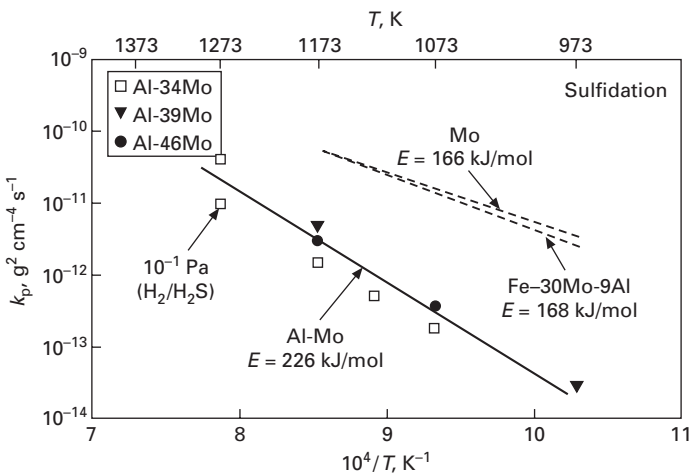
Preliminary investigations have demonstrated that all the materials studied crystallized immediately during heating to form a nanocrystalline mixture of Al-Re intermetallics in the form of a dense layer, and the sulfidation and oxidation processes of these layers followed familiar parabolic kinetics, being thus diffusion controlled.<sup>65</sup> However, the sulfidation rate of binary Al-Re alloys was strongly dependent on the kind of refractory metal, as illustrated in Fig. 20.25. It follows clearly from this plot that Al-Mo alloys show much better resistance to sulfide corrosion than those containing other refractory metals.

Figure 20.26 shows the temperature dependence of the sulfidation rate of several Al-Mo alloys on the background of analogous dependence for ternary Al-30Mo-9Al alloy and pure molybdenum. As can be seen, the rate of the reaction is virtually independent of alloy composition and, rather surprisingly, it is more than one order of magnitude lower than the sulfidation rate of pure molybdenum and ternary Fe-30Mo-9Al alloy developed by Douglass *et al.*<sup>64</sup> In addition, it has been found that even after prolonged sulfidation, exceeding hundreds of hours, the pest phenomenon was not observed and the scale remained compact and very well adherent to the substrate, even if thermal shocks were applied during sulfidation.

It is important to stress once again the fact that the sulfidation rate of the discussed Al-Mo alloys is more than one order of magnitude lower than that of pure molybdenum (Fig. 20.26). This rather unexpected situation results from the doping effect. The inner barrier scale layer on these alloys, constituting the main part of the scale, is composed mainly of the MoS<sub>2</sub> phase doped with



20.25 Temperature dependence of the sulfidation rates of binary Al-Mo, Al-Nb and Al-Ta alloys.



20.26 Temperature dependence of the sulfidation rate of Al-Mo and Al-30Mo-9Al alloys, as well as that for pure molybdenum.

trivalent aluminum ions, containing some inclusions of the second,  $\text{Al}_{0.5}\text{Mo}_2\text{S}_4$  sulfo-spinel phase.

It has been shown using the marker method<sup>65</sup> that the scale like that on pure molybdenum<sup>24,25</sup> grows by the inward diffusion of sulfur and consequently

that the rate-determining step of the overall growth process of the scale is the inward sulfur diffusion through the inner barrier layer, composed mainly of MoS<sub>2</sub> doped with aluminum.

It is interesting to explain the lower sulfidation rate of Al-Mo alloys as compared to pure molybdenum in terms of the doping effect. The predominant defects in MoS<sub>2</sub> scale growing on pure molybdenum are singly ionized interstitial sulfide ions and electron holes (MoS<sub>2+x</sub>).<sup>23,25</sup> The formation of these defects may be described by the following quasi-chemical reaction:



(the Kröger-Vink notation for defects is used throughout this chapter<sup>76</sup>). Applying to this defect equilibrium the mass action law

$$K = [\text{S}'_i][h^\bullet] p_{\text{S}_2}^{-1/2} \quad 20.3$$

and the appropriate electroneutrality condition

$$[\text{S}'_i] = [h^\bullet] \quad 20.4$$

one obtains the following dependence of defect concentration on sulfur pressure:

$$[\text{S}'_i] = [h^\bullet] = K^{1/2} p_{\text{S}_2}^{1/4} \quad 20.5$$

As the defect concentration in molybdenum disulfide is extremely low<sup>22</sup> it is reasonable to assume that the defect diffusion coefficient,  $D_i$ , being the direct measure of defect mobility,<sup>3,5</sup> is independent of their concentration and, consequently, the self-diffusion coefficient of sulfide ions,  $D_S$ , which is the product of  $D_i$  and  $[\text{S}'_i]$ , must depend on sulfur pressure in the same way as the concentration of defects:

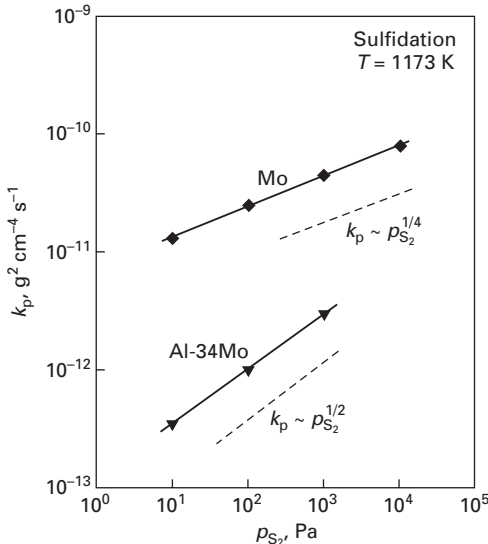
$$D_S = D_i [\text{S}'_i] = D_S^\circ p_{\text{S}_2}^{1/4} \quad 20.6$$

On the other hand, from Wagner's theory of metal oxidation it follows that, if the concentration of predominant defects in the growing scale on a given metal is low enough that their mobility is concentration independent, the self-diffusion coefficient of diffusing species depends in the same way on oxidant pressure as the parabolic rate constant of scale growth.<sup>2</sup> Thus, in the case of molybdenum sulfidation  $k_p$  should be the following function of sulfur pressure:

$$k_p = \text{const} \cdot D_S = \text{const} \cdot p_{\text{S}_2}^{1/4} \quad 20.7$$

which, in fact, has been found experimentally<sup>66</sup> (see also Fig. 20.27).

In the case of aluminum doped MoS<sub>2</sub>, not only lower defect concentration but also different pressure and temperature dependence are to be expected. If, namely, one assumes that the trivalent aluminum ions are dissolved

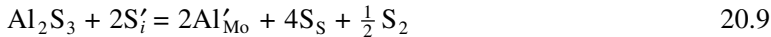


20.27 Dependence of the sulfidation rate of Al-34Mo alloy and pure molybdenum on sulfur pressure at 1173 K.

substitutionally on regular Mo sites, this process may be described by the following defect equilibria:



or



If other defects can be neglected the electroneutrality condition is given by:

$$[h^\bullet] = [\text{S}'_i] + [\text{Al}'_{\text{Mo}}] \quad 20.10$$

For such a doped molybdenum disulfide ( $\text{MoS}_2$ - $\text{Al}_2\text{S}_3$  solid solution) two limiting cases should be considered. If  $[\text{S}'_i] \gg [\text{Al}'_{\text{Mo}}]$ , the electroneutrality condition reduces to the following simplified form:

$$[\text{S}'_{\text{Mo}}] = [h^\bullet] \quad 20.11$$

This case corresponds to the defect situation for pure  $\text{MoS}_{2+y}$ , i.e., the concentration of foreign ions is too low to affect the native (intrinsic) defect equilibrium in the sulfide (Eq. (20.5)). If, on the other hand, the dopant concentration is much higher than that of native point defects,  $[\text{S}'_i] \ll [\text{Al}'_{\text{Mo}}]$ , the electroneutrality condition assumes the following simplified form:

$$[h^\bullet] = [\text{Al}'_{\text{Mo}}] \quad 20.12$$

In this case the foreign ions greatly influence the defect structure of the discussed sulfide, by the decreasing the point defect concentration and increasing that of electron holes, the latter being fixed by the dissolved amount of aluminum ions. In this limiting case the combination of Eqs (20.3) and (20.12) leads to the following relationship:

$$[S'_i] = \left( \frac{K}{[Al'_{Mo}]} \right) p_{S_2}^{1/2} \quad 20.13$$

As can be seen, under these conditions a very low point defect concentration in aluminum doped  $MoS_2$  increases more rapidly with increasing sulfur pressure than in the case of pure molybdenum disulfide (Eq. (20.5)). Thus, similarly to Eq. (20.7) the parabolic rate constant of alloy sulfidation should be the following function of sulfur activity:

$$k_p = \text{const} \cdot p_{S_2}^{1/2} \quad 20.14$$

From Eq. (20.13) it follows also that the effect of dopant depends not only on its concentration but also on sulfur activity. Concentration of native defects increases, with increasing sulfur pressure and consequently at any constant aluminum concentration both limiting cases (Eqs (20.11) and (20.12)) may theoretically be realized by appropriate changes of equilibrium sulfur pressure. At higher sulfur activities the concentration of dopant may be too low to affect the defect structure of  $MoS_2$  (Eq. (20.11)). With decreasing sulfur activity the concentration of point defects in the sulfide decreases and at sufficiently low sulfur pressure an extrinsic region may be reached, in which foreign ions determine the electron hole concentration (Eq. (20.12)). The lower the dopant concentration, the less sulfur pressure is needed to pass from the intrinsic to the extrinsic region.

In the case under discussion it has been found that the concentration of aluminum ions dissolved in  $MoS_2$ , constituting the main part of the inner, barrier scale layer on Al-Mo alloys, was in fact very low, not exceeding 0.01 wt%. However, the maximum concentration of predominant point defects (interstitial sulfide ions) in  $MoS_2$  is extremely low,<sup>22</sup> more than one order of magnitude lower than that of dopant. Thus, even at high sulfur pressures, of the order of  $10^4$  Pa, the intrinsic region is impossible to reach and Al dopant still controls the defect structure in  $MoS_2-Al_2S_3$  solid solution. This conclusion is in full agreement with experimental results shown in Fig. 20.27. As can be seen, the sulfidation rate of Al-Mo alloy is considerably lower than that of pure molybdenum and this rate increases more rapidly with increasing sulfur pressure, in agreement with Eq. (20.14). It should be noted that the higher activation energy of alloy sulfidation compared with that of pure molybdenum (Fig. 20.26) also confirms the doping effect. This conclusion follows from the fact that the activation energy of sulfidation, being equal to the activation

energy of sulfur self-diffusion in  $\text{MoS}_2$  scale, is the sum of the enthalpy of defect formation,  $\Delta H_f$ , and the activation enthalpy of defect migration,  $\Delta H_m$ .<sup>3,5</sup> Thus, in the case of pure molybdenum sulfidation, eliminating the equilibrium constant  $K$  from Eq. (20.5) and considering the fact that the defect diffusion coefficient,  $D_i$ , is the following function of temperature:

$$D_i = \text{const} \cdot \exp(-\Delta H_m) \quad 20.15$$

the combination of Eqs (20.5), (20.6) and (20.15) yields:

$$D_S = D_i [S'_i] = \text{const} \cdot p_{S_2}^{1/4} \exp\left(-\frac{\frac{1}{2} \Delta H_f + \Delta H_m}{RT}\right) \quad 20.16$$

(the entropy terms  $\Delta S_f$  in the modified Eq. (20.5) and  $\Delta H_m$  in Eq. (20.15) have been included in the constant term, because it could have been assumed that they are temperature independent).

As can be seen, the activation energy of sulfur self-diffusion in pure  $\text{MoS}_2$ ,  $E_D$ , and thereby the activation energy of molybdenum sulfidation,  $E_S$ , is given by:

$$E_D = E_S = \frac{1}{2} \Delta H_f + \Delta H_m \quad 20.17$$

It follows from this equation that in the case of molybdenum sulfidation one half of  $\Delta H_f$  participates in the activation energy of sulfur self-diffusion, because the concentration of both ionic and electronic defects increases with increasing temperature. In aluminum doped  $\text{MoS}_2$ , on the other hand, the concentration of electronic defects is fixed on the constant level (Eq. (20.12)) and consequently the whole value of  $\Delta H_f$  participates in  $E_D$ . Eliminating the equilibrium constant  $K$  from Eq. (20.13) and considering Eqs (20.6) and (20.15) yields:

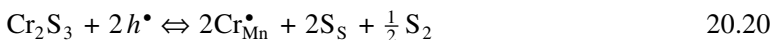
$$D'_S = \frac{\text{const}}{[\text{Al}'_{\text{Mo}}]} p_{S_2}^{1/2} \exp\left(-\frac{\Delta H_f + \Delta H_m}{RT}\right) \quad 20.18$$

where  $D'_S$  denotes the self-diffusion coefficient of sulfur in aluminum doped  $\text{MoS}_2$ . From the comparison of Eqs (20.16) and (20.18) it follows clearly that the activation energy of sulfur self-diffusion in Al-doped  $\text{MoS}_2$ , and thereby that of alloy sulfidation, must be higher than in the case of molybdenum sulfidation. It is important to note that the discussed Al-Mo alloys are also highly resistant to oxide corrosion,<sup>65</sup> though at temperatures not exceeding about 1000 K. Aluminum concentration at the alloy/scale interface is too low to suppress the formation of volatile  $\text{MoO}_3$  oxide, which destroys the compactness of the  $\text{Al}_2\text{O}_3$  scale, leading to catastrophic degradation of the Al-Mo alloys. It has been found, however, that the addition of small amounts of silicon reduces the activity of both molybdenum and oxygen at the alloy/scale interface, thus favoring the formation of molybdenum-free, highly

protective alumina scale. Consequently, ternary Al-31Mo-(6–9)Al alloys show excellent resistance not only to highly sulfidizing but also to highly oxidizing environments up to about 1273 K.

#### 20.4.4 Doping effect

In Section 20.3 it has been demonstrated that the doping effect may play an important role in improving protective properties of sulfide scales. It seems reasonable to discuss further examples of this phenomenon in order to demonstrate that the process of doping may not only improve but also considerably worsen the protective properties of scale, changing simultaneously the temperature and pressure dependence of the reaction. A good example of such a situation is observed in the case of Mn-Cr alloy sulfidation. The predominant defects in manganous sulfide ( $Mn_{1-y}S$ ) are doubly ionized cation vacancies and, consequently, three-valent foreign ions (for example chromium) incorporating substitutionally into the cation sublattice of the sulfide will increase the concentration of ionic defects and decrease electronic defects. These processes may be described by the following quasi-chemical defect reactions:<sup>77</sup>



It follows from these defect equilibria that the concentration of cation vacancies in chromium doped  $Mn_{1-y}S$  is higher than that in pure manganous sulfide, and the concentration of electron holes is lower. Consequently, the growth rate of  $Cr_2S_3\text{-}Mn_{1-y}S$  solid solution scale on Mn-Cr alloy should be higher than that of  $Mn_{1-y}S$  scale on pure manganese metal.

The electroneutrality condition for  $Cr_2S_3\text{-}Mn_{1-y}S$  solid solution is given by:

$$[Cr_{Mn}^{\bullet}] + [h^{\bullet}] = 2[V''_{Mn}] \quad 20.21$$

When the concentration of dopant is much higher than that of electronic defects ( $[Cr_{Mn}^{\bullet}] \gg [h^{\bullet}]$ ), as in the case discussed, the above electroneutrality condition reduces to the following simplified form:

$$[Cr_{Mn}^{\bullet}] = 2[V''_{Mn}] \quad 20.22$$

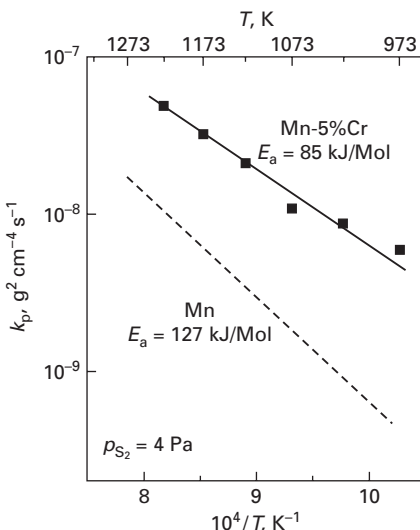
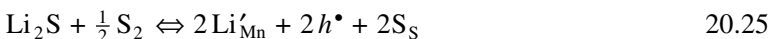
It follows from these considerations that in agreement with experimental results (Figs 20.28 and 20.29), the higher sulfidation rate of Mn-Cr alloy should be pressure independent and the activation energy of this reaction must be lower than that of pure manganese sulfidation. This last conclusion results from the fact that the activation energy of pure manganese sulfidation,

being equal to the activation energy of Mn self-diffusion in  $\text{Mn}_{1-y}\text{S}$ , is the sum of the enthalpy of defect formation and the activation enthalpy of defect migration in the crystal lattice:<sup>77</sup>

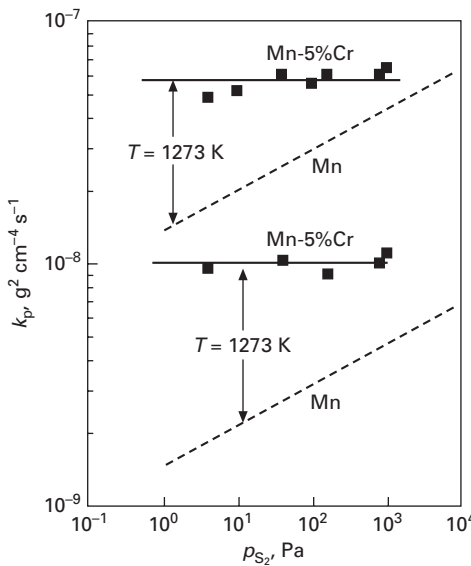
$$E_p = E_D = \frac{1}{3} \Delta H_f + \Delta H_m \quad 20.23$$

where  $E_p$  and  $E_D$  denote the activation energy of manganese sulfidation and that of cation self-diffusion in  $\text{Mn}_{1-y}\text{S}$ , respectively. In the case of alloy sulfidation,  $\Delta H_f$  is equal to zero because the concentration of cation vacancies is fixed by the presence of dopant in the scale (Eq. (20.22)). Thus, the activation energy of Mn-Cr alloy sulfidation should simply be equal to  $\Delta H_m$  only, i.e. the activation enthalpy of defect migration.

It follows from these considerations, confirmed by experimental results (Figs 20.28 and 20.29), that in the case under discussion the doping effect was negative. However, doping the same scale ( $\text{Mn}_{1-y}\text{S}$ ) by monovalent addition (for instance, lithium) may play a positive role. Assuming, therefore, that lithium ions are being substitutionally incorporated into the cation sublattice of the growing MnS scale on Mn-Li alloy, this process can be presented by the following quasi-chemical reversible reactions:<sup>41</sup>



20.28 Temperature dependence of the parabolic rate constant of Mn-5%Cr alloy sulfidation on the background of pure manganese sulfidation data.



20.29 Pressure dependence of the parabolic rate constant of Mn-5%Cr alloy sulfidation for several temperatures on the background of pure manganese sulfidation data.

From these equations it follows that the concentration of cation vacancies of lithium doped  $\text{Mn}_{1-y}\text{S}$  should be lower and the concentration of electron holes higher than that in pure manganous sulfide. As the rate-determining step of the overall sulfidation rate is the diffusional transport of cations through cation vacancies, the protective properties of lithium doped  $\text{Mn}_{1-y}\text{S}$  scale should be better than those of pure  $\text{Mn}_{1-y}\text{S}$  scale.

The electroneutrality condition for the case under discussion assumes the form:

$$[\text{Li}'_{\text{Mn}}] + 2 [\text{V}''_{\text{Mn}}] = [\text{h}^\bullet] \quad 20.26$$

Two limiting cases should be considered. If  $[\text{Li}'_{\text{Mn}}] \gg [\text{V}''_{\text{Mn}}]$ , the general electroneutrality condition described by Eq. (20.26) reduces to the following simplified form:

$$[\text{Li}'_{\text{Mn}}] = [\text{h}^\bullet] \quad 20.27$$

Under these conditions the very low concentration of cation vacancies in  $\text{Mn}_{1-y}\text{S}-\text{Li}_2\text{S}$  solid solution, and thereby the sulfidation rate of Mn-Li alloy, would increase much more rapidly with increasing sulfur pressure than that of pure manganese sulfidation. This conclusion results directly from replacing in the equilibrium constant  $K_v$  of the defect reaction of pure  $\text{Mn}_{1-y}\text{S}$ :



the electron hole concentration by that of dopant (Eq. (20.27)):

$$[V''_{Mn}] = \frac{K_V}{[Li'_{Mn}]^2} \cdot p_{S_2}^{1/2} \quad 20.29$$

On the other hand, when  $[Li'_{Mn}] \ll [V''_{Mn}]$  the general electroneutrality condition assumes the second simplified form:

$$2[V''_{Mn}] = [h^\bullet] \quad 20.30$$

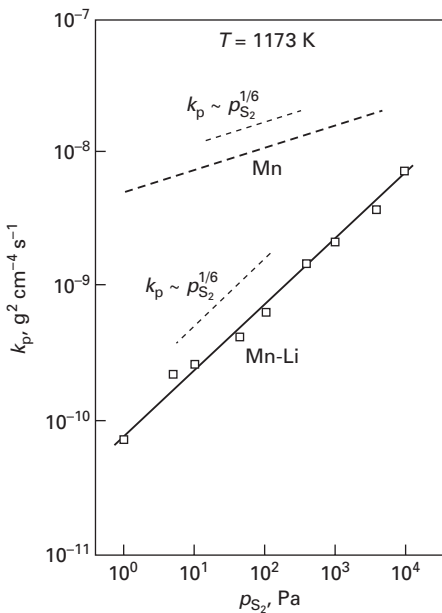
which implies that in this case the dopant concentration is too low to affect the intrinsic ionic and electronic disorder in  $Mn_{1-y}S$  and consequently the rate of sulfidation of such a very diluted Mn-Li alloy should be virtually the same as that of pure manganese sulfidation.

From these considerations it follows that if the concentration of monovalent dopant (lithium) is high enough to fix the concentration of electronic defects in the growing  $Mn_{1-y}S$  scale, the sulfidation rate of Mn-Li alloy should increase with increasing sulfur pressure with slope  $\frac{1}{2}$  (Eq. (20.29)) and the activation energy of this process should be higher than that of pure manganese sulfidation. This last conclusion follows from the fact that in the case of pure manganese sulfidation, the concentration of both ionic and electronic defects increase with increasing temperature and consequently only one third of  $\Delta H_f$  participates in the activation energy of cation self-diffusion and thereby in the activation energy of manganese self-diffusion. In lithium doped  $Mn_{1-y}S$  scale, on the other hand, if the dopant content is sufficiently high, the electron hole concentration is fixed at a constant level (Eq. (20.27)), and consequently the whole value of  $\Delta H_f$  participates in the activation energy of sulfidation. Eliminating the equilibrium constant  $K_V$  from Eq. (20.29) one obtains the following dependence of the concentration of cation vacancies in  $Mn_{1-y}S-Li_2S$  solid solution on sulfur pressure and temperature:

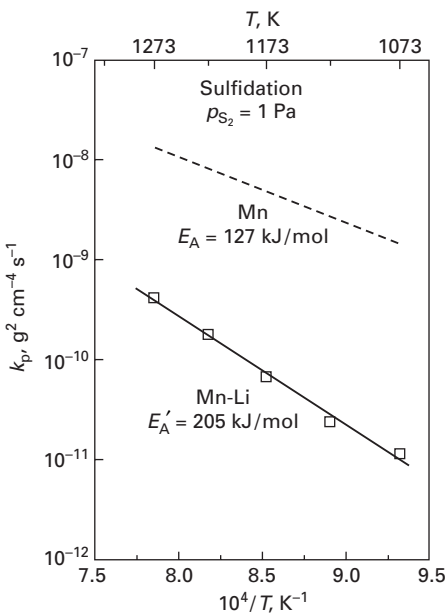
$$[V''_{Mn}] = \frac{1}{[Li'_{Mn}]^2} \cdot p_{S_2}^{1/2} \cdot \exp\left(\frac{\Delta S_f}{R}\right) \cdot \exp\left(\frac{\Delta H_f}{RT}\right) \quad 20.31$$

As can be seen, the concentration of cation vacancies in  $Mn_{1-y}S-Li_2S$  scale on Mn-Li alloy must increase more rapidly with increasing temperature than in pure  $Mn_{1-y}S$  and consequently the activation energy of alloy sulfidation should be higher.

These theoretical considerations are in full agreement with experimental results presented in Figs 20.30 and 20.31. As can be seen, the sulfidation rate of Mn-Li alloy increases more rapidly with increasing sulfur pressure than that of pure manganese sulfidation (Fig. 20.30) and the activation energy of the reaction is higher<sup>41</sup> (Fig. 20.31).

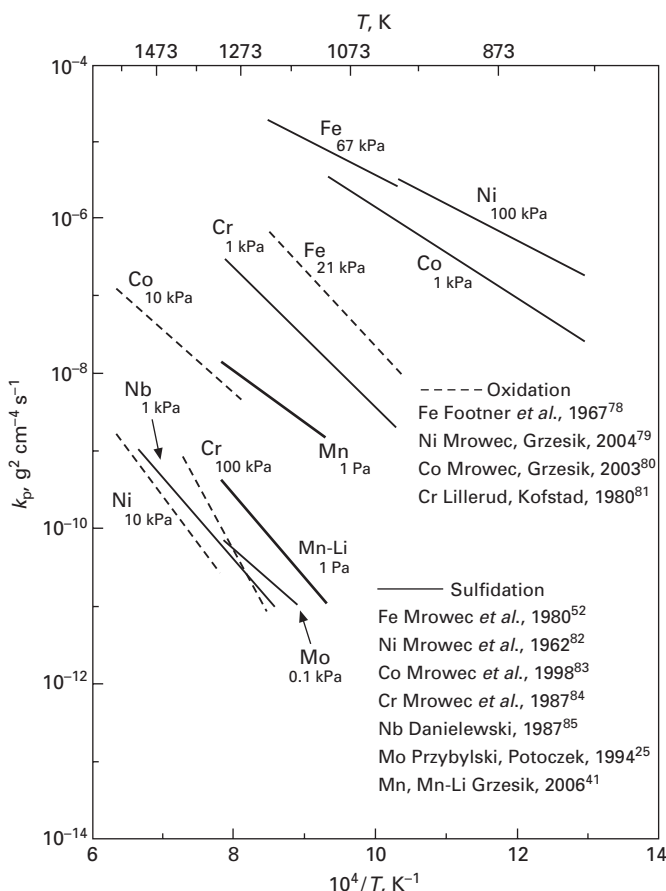


20.30 Pressure dependence of the parabolic rate constant of Mn sulfidation in pure sulfur vapor (dashed line) and in sulfur vapor containing Li<sub>2</sub>S (solid line), for several temperatures.



20.31 Temperature dependence of the parabolic rate constant of Mn sulfidation in pure sulfur vapor (dashed line) and in S<sub>2</sub> containing Li<sub>2</sub>S (solid line), at sulfur vapor pressure of 1 Pa.

If follows from these results that in agreement with Hauffe–Wagner theory,<sup>2,8</sup> the protective properties of the sulfide scale on Mn–Li alloy are considerably better then on pure manganese, due to the doping effect. In order to visualize the great role of this effect, the sulfidation rate of Mn–Li alloy is compared in Fig. 20.32 with the oxidation and sulfidation rates of several metals. As can be seen, the protective properties of lithium doped sulfide scale on manganese are comparable with those of the oxide scale on chromium and sulfide scales on niobium and molybdenum, three metals representing the highest resistance to oxide and sulfide corrosion, respectively. Thus, the



20.32 Comparison of the parabolic rate constant of Mn sulfidation in pure and  $\text{Li}_2\text{S}$ -containing sulfur vapor on the background of the sulfidation (solid lines) and oxidation (dotted lines) rates of several metals.

final conclusion is that in some cases the doping effect may play an important role in improving the corrosion resistance of metals and alloys to high temperature oxide and sulfide corrosion.

## 20.5 Concluding remarks

The main reason why common metals are rapidly attacked by sulfur results from the very high concentration of point defects in their sulfides. On the other hand, refractory metals are highly resistant to sulfide corrosion because of either low-defect concentration ( $\text{MoS}_2$ ) or low-defect mobility ( $\text{NbS}_2$ ) in the sulfides of these metals.

The mechanisms of sulfide and oxide corrosion of pure metals are very similar because of the same type of predominant disorder in transition-metal sulfides and oxides. However, despite great similarities in the growth mechanisms of oxide and sulfide scales, the sulfidation and oxidation rates of metals and consequently of conventional high temperature alloys differ dramatically. These differences result from defect concentrations orders of magnitude higher in common metal sulfides than in the corresponding oxides. As a consequence, all conventional oxidation-resistant alloys (chromia and alumina formers) undergo very rapid degradation in highly sulfidizing environments not only due to high defect concentration but also as a result of heterogeneous-scale formation of poor protective properties.

New prospects for the development of coating materials resistant to high-temperature sulfide corrosion have been created by combined alloying of common metals with molybdenum and aluminum and in particular by the development of novel nanocrystalline aluminum based refractory metal alloys containing silicon which are highly resistant to both sulfidizing and oxidizing environments.

## 20.6 Acknowledgement

The authors are very grateful to Professor S. Mrowec for his valuable and fruitful suggestions and final discussion during preparation of this chapter.

## 20.7 References

1. Meadowcroft D B, Manning M J, *Resistant Materials for Coal Gasification Systems*, London, Applied Science, 1993.
2. Kofstad P, *High Temperature Corrosion*, London and New York, Elsevier, 1988.
3. Mrowec S, *Defects and Diffusion in Solids*, Amsterdam–Oxford–New York, Elsevier, 1980.
4. Mrowec S, Przybylski K, ‘Defect and transport properties of sulfides and sulfidation of metals’, *High Temp Mater Processes*, 1984 **6**(1/2) 1–79.

5. Kofstad P, *Nonstoichiometry, Diffusion and Electrical Conductivity of Binary Metal Oxides*, New York, Wiley, 1972.
6. Mrowec S, Janowski J, 'Similarities and differences in defect dependent properties of transition metal sulphides and oxides', in Johannessen O, Andersen A G, *Selected Topics in High Temperature Chemistry*, Amsterdam, Elsevier, 1989, p. 55.
7. Schmalzried H, Navrotsky A, *Festkörperthermodynamik*, Weinheim, Verlag Chemie, 1975.
8. Mrowec S, *An Introduction to the Theory of Metal Oxidation*, Washington DC, National Bureau of Standards and National Science Foundation, 1982.
9. Barin I, Knacke O, *Thermochemical Properties of Inorganic Substances*, Berlin-Heidelberg-New York, Springer-Verlag, 1973.
10. Weast R C (editor-in-chief), *CRC Handbook of Chemistry and Physics*, Boca Raton, FL, CRC, 1985.
11. Wagner C, 'Beitrag zur Theorie des Anlaufvorgangs', *Z Physik Chem*, 1933 **B21** 25–41.
12. Norby T, 'Hydrogen defects in inorganic solids', in Johannessen O, Andersen A G, *Selected Topics in High Temperature Chemistry, Defect Chemistry of Solids*, Amsterdam, Elsevier, 1989.
13. Neunhöffer O, Hauffe K, 'Über die Umsetzung von Eisenarseniden mit Schwefeldampf', *Z Anorg Allg Chem*, 1950 **262** 300–308.
14. Geld PW, Krasowska A K, 'Mechanism sulfidnoy korozii zeleza', *Z Fiz Chim*, 1960 **34** 1585–1593.
15. Ge Wang R, Gesmundo F, Douglass D L, 'High temperature sulfidation of Mo–50 wt% Re', *Oxid Met*, 1989 **31** 453–478.
16. Narita T, Nishida K, 'On the sulfur distribution in FeS scale formed on pure iron at 700°C', *Trans Japan Inst Met*, 1973 **14** 439–456.
17. Danielewski M, Mrowec S, 'Microthermogravimetric studies of the kinetics and thermodynamics of heterogeneous reactions in sulfur-containing atmospheres', *J Therm Anal*, 1984 **29** 1025–1032.
18. Rusiecki R, Wójtowicz A, Mrowec S, Przybylski K, 'New thermobalance for studying the kinetics of high temperature reactions in sulphur atmospheres', *Solid State Ionics*, 1988 **21** 273–277.
19. Danielewski M, Mrowec S, Wojtowicz A, 'Defect and transport properties of nonstoichiometric cobaltous sulfide', *Oxid Met*, 1991 **35** 223–243.
20. Grzesik Z, Mrowec S, Walec T, Dabek J, 'New microthermogravimetric apparatus. Kinetics of metal sulphidation and transport properties of transition metal sulphides', *J Therm Anal Cal*, 2000 **59** 985–997.
21. Rau H, 'Defect energetics and range of homogeneity of  $\alpha$ -MnS', *J Phys Chem Solids*, 1978 **39** 339–343.
22. Rau H, 'Estimation of the homogeneity range of MoS<sub>2</sub>', *J Phys Chem Solids*, 1980 **41** 765–767.
23. Potoczek M, Przybylski K, Rekas M, 'Defect structure and electrical properties of molybdenum disulphide', *J Phys Chem Solids*, 2006 **67** 2528–2535.
24. Lee B S, Rapp R A, 'Gaseous sulfidation of pure molybdenum at 700°–950°C', *J Electrochem Soc*, 1984 **131** 2998–3005.
25. Przybylski K, Potoczek M, 'High temperature sulphidation of molybdenum', *Trans Mat Res Soc Jpn*, 1994 **14A** 169–174.
26. Fivaz R, Mooser E, 'Mobility of charge carriers in semiconducting layer structures', *Phys Rev A*, 1967 **163** 743–755.

27. El-Mahalawy S H, Evans B L, 'Temperature dependence of the electrical conductivity and Hall coefficient in 2H-MoS<sub>2</sub>, MoSe<sub>2</sub>, WSe<sub>2</sub> and MoTe<sub>2</sub>', *Phys Stat Sol (b)*, 1977 **79** 713–722.
28. Grzesik Z, Migdalska M, Mrowec S, 'The influence of lithium on the sulphidation behavior of molybdenum at high temperatures', *High Temp Mater Processes*, 2007 in press.
29. Delmaire J P, Le Brusq H, 'Relation entre la non-stoéchiométrie et les propriétés électriques du système niobium–soufre à l'équilibre thermodynamique à 1000°C', *Compt Rend Acad Sci Paris*, 1972 **275C** 889–891.
30. Gesmundo F, Viani F, Niu Y, 'The defect structure of 2s Nb<sub>1+x</sub>S<sub>2</sub> and the high temperature sulfidation of niobium', *Oxid Met*, 1992 **38** 465–482.
31. Grzesik Z and Mrowec S, 'Defect structure and transport properties of non-stoichiometric niobium sulphide', *High Temp Mater Processes*, 2006 **25** 209–216.
32. Tatsuki K, Wakihara M, Taniguchi M, 'Phase relations in the Nb–S system at high temperatures', *J Less-Common Met*, 1979 **68** 183–191.
33. Kadijk F, Jellinek F, 'The system niobium–sulfur', *J Less-Common Met*, 1969 **19** 421–430.
34. Wagner J B, 'Diffusion coefficients for some nonstoichiometric metal oxides', in *Mass Transport in Oxides*, NBS Special Publ. No. 296, 1967, p. 65.
35. Child P, Laub L B, Wagner J B, 'Chemical diffusion in nonstoichiometric compounds', *Mass Transport in Nonmetallic Solids*, *Proc Brit Ceram Soc*, 1971 **19** 29–34.
36. Child P, Wagner J B, *Heterogeneous Kinetics at Elevated Temperatures*, New York, Plenum Press, 1970.
37. Grzesik Z, Mrowec S, Dabek J, 'On the defect mobility in niobium disulphide', *Solid State Phenomena*, 2000 **72** 29–34.
38. Grzesik Z, 'Transport properties of sulphide scales formed in high temperature corrosion of metals', *Pol Ceram Bull, Ceramics*, 2005 **87** 8–124.
39. Potoczek M, Przybylski K, Rekas M, 'Chemical diffusion in molybdenum disulphide', *J Phys Chem Solids*, 2007 **68** 564–569.
40. Mrowec S, 'The problem of sulfur in high-temperature corrosion', *Oxid Met*, 1995 **44**(1/2) 177–209.
41. Grzesik Z, Mrowec S, 'The influence of lithium on the kinetics and mechanism of manganese sulphidation', *Corrosion Sci*, 2006 **48** 3186–3195.
42. Mrowec S, Grzesik S, 'The influence of chromium and lithium on the manganese sulphidation kinetics', *J Phys Chem Solids*, 2001 **62** 1171–1179.
43. Bénard J, *Oxydation des Métaux*, Paris, Gautier-Villars, 1964, pp. 150, 191.
44. Mrowec S, 'Dissociative mechanism of scales growth on metals and alloys', *High Temp Mater Processes*, 2005 **24** 375–394.
45. Brückman A, 'The mechanism of transport of matter through the scales during oxidation of metals and alloys', *Corrosion Sci*, 1967 **7** 51–59.
46. Brückman A, 'The use of autoradiography in studying the mechanism of oxidation of metals and alloys', *Rev Int Htes Temp Réfract*, 1978 **15** 63–68.
47. Brückman A, Emerich R, Mrowec S, 'Investigation of the high-temperature oxidation of Fe-Cr alloys by means of the isotope <sup>18</sup>O', *Oxid Met*, 1972 **5** 137–147.
48. Przybylski K, Szwagierczak D, 'Kinetics and mechanism of high-temperature oxidation of dilute cobalt–chromium alloys', *Oxid Met*, 1982 **17** 267–295.
49. Mrowec S, Wędrychowska M, 'High temperature sulphidation of iron–chromium aluminum alloys', *Bulletin de l'Académie Polonaise des Sciences, Série des Sciences Chimiques*, 1977 **25**(11) 877–883.

50. Smeltzer W W, Narita T and Przybylski K, 'High temperature sulfidation properties of iron-chromium-base alloys', in Proc. 'Corrosion-Erosion, Wear of Materials in Emerging Fossil Energy Systems', Ed. By Levy AV, NACE, Houston, 1982, pp 860–872.
51. Smeltzer W W, Fryt E, Bhide W S, Kirkaldy J S, 'Growth of the Iron Sulfide ( $Fe_{1-y}S$ ) Scale on Iron at Temperatures 600–1000°C', *J. Electrochem. Soc.* 1979, **126** 683–688.
52. Mrowec S, Danielewski M, Stoklosa A, 'Defect structure and diffusion in nonstoichiometric ferrous sulphide', *Solid State Ionics*, 1980 **1** 287–309.
53. Meussner R A and Birchenall C E, 'Growth of ferrous sulfide on iron', *Corrosion*, 1957 **13** 677–688.
54. Godlewska E, 'Sulphidation of NiAl-Cr materials at elevated temperatures', *High Temp Mater Processes*, 1999 **18** 363–386.
55. Godlewska E, 'Materials with the  $\beta$ -NiAl intermetallic phase – manufacturing and environmental resistance at high temperature', *Pol Ceram Bull, Ceramics*, 2001 **68** 1–92.
56. Biegun T, Brückman A, Mrowec S, 'High-temperature sulfide corrosion of cobalt–chromium alloys', *Oxid Met*, 1978 **12** 157–172.
57. Chen M F, Douglass D L, 'The effect of Mo on the high-temperature sulfidation of Ni', *Oxid Met*, 1989 **32** 185–206.
58. Carter R V, Douglass D L, Gesmundo F, 'Kinetics and mechanism of the sulfidation of Fe-Mo alloys', *Oxid Met*, 1989 **31** 341–367.
59. Glesson B, Douglass D L, Gesmundo F, 'Effect of Nb on the high-temperature sulfidation behavior of cobalt', *Oxid Met*, 1989 **31** 209–236.
60. Chen M F, Douglass D L, Gesmundo F, 'High-temperature sulfidation behavior of Ni-Nb alloys', *Oxid Met*, 1989 **31** 237–263.
61. Ge Wang R, Carter R V, Douglass D L, 'High-temperature sulfidation of Fe-Nb alloys', *Oxid Met*, 1989 **32** 273–294.
62. Glesson B, Douglass D L, Gesmundo F, 'A comprehensive investigation of the sulfidation behavior of binary Co-Mo alloys', *Oxid Met*, 1990 **33** 425–455.
63. Ge Wang R, Douglass D L, Gesmundo F, 'Effect of aluminum on the high-temperature sulfidation of Fe-30Nb alloys', *Oxid Met*, 1991 **35** 279–294.
64. Ge Wang R, Douglass D L, Gesmundo F, 'High-temperature sulfidation of Fe-30Mo alloys containing ternary additions of aluminum' *Oxid Met*, 1991 **35** 349–373.
65. Habazaki H, Dabek J, Hashimoto K, Mrowec S, Danielewski M, 'The sulphidation and oxidation behaviour of sputter-deposited amorphous Al-Mo alloys at high temperatures' *Corrosion Sci*, 1993 **34** 183–200.
66. Mrowec S, 'New generation of nanocrystalline coating materials resistant to high temperature corrosion', *High Temp Mater Processes*, 2003 **22** 1–22.
67. Grzesik Z, Habazaki H, Hashimoto K, Mrowec S, 'The sulphidation behavior of Mo-Al alloys with low aluminum contents', *Corrosion Sci*, 1994 **36** 1499–1511.
68. Habazaki H, Takahiro K, Yamaguchi S, Hashimoto K, Dąbek J, Mrowec S, 'New amorphous alloys resistant to high temperature corrosion', *Mater Sci Eng*, 1994 **A181/A182** 1099–1103.
69. Grzesik Z, Takahiro K, Yamaguchi S, Hashimoto K, Mrowec S, 'An RBS study of the sulphidation behavior of niobium and Nb-Al alloys', *Corrosion Sci*, 1995 **37** 801–810.
70. Grzesik Z, Mitsui H, Asami H, Hashimoto K, Mrowec S, 'The sulfidation of sputter-deposited niobium-base aluminum alloys', *Corrosion Sci*, 1995 **37** 1045–1058.

71. Hashimoto K, Mitsui H, Habazaki H, Asami K, Mrowec S, 'The sulfidation and oxidation behavior of sputter-deposited amorphous Al-Nb alloys at high temperatures', *Corrosion Sci*, 1996 **38** 1431–1447.
72. Mitsui H, Habazaki H, Akiyama E, Kawashima A, Asami K, Hashimoto K, Mrowec S, 'High temperature sulfidation and oxidation behavior of sputter-deposited Al-refractory metal alloys', *Mater Trans JIM (Japan)*, 1996 **37** 379–382.
73. Mitsui H, Habazaki H, Hashimoto K, Mrowec S, 'The sulfidation and oxidation behavior of sputter-deposited Al-Ta alloys at high temperatures', *Corrosion Sci*, 1997 **39** 59–76.
74. Mitsui H, Habazaki H, Hashimoto K, Mrowec S, 'The sulfidation and oxidation behavior of sputter-deposited amorphous Al-Nb-Si alloys at high temperatures', *Corrosion Sci*, 1996 **39** 9–26.
75. Mitsui H, Habazaki H, Hashimoto K, Mrowec S, 'The sulfidation and oxidation behavior of sputter-deposited Al-Ta-Si alloys at high temperatures', *Corrosion Sci*, 1997 **39** 1571–1583.
76. Kröger FA, *The Chemistry of Imperfect Crystals*, 1974, Amsterdam: North-Holland.
77. Mrowec S, Grzesik Z, 'The influence of aliovalent impurities on transport properties of nonstoichiometric manganous sulphide', *Bull Pol Acad Sci Chem*, 2002 **50** 37–49.
78. Footner D K, Holmes D R and Mortimer D, 'Oxidation of iron-chromium binary alloys', *Nature*, 1967 **216** 54–56.
79. Mrowec S and Grzesik Z, 'Oxidation of nickel and transport properties of nickel oxide', *J Phys Chem Solids*, 2004 **65** 1651–1657.
80. Mrowec S and Grzesik Z, 'The influence of chromium on the defect structure and their mobility in nonstoichiometric cobaltous oxide' *J Phys Chem Solids*, 2003 **64** 1387–1394.
81. Lillerud K P and Kofstad P, 'Oxidation of annealed, thermally etched chromium at 800–1100°C' *J Electrochem Soc*, 1980 **127** 2397–2410.
82. Mrowec S, Czerski L, Werber T, 'Kinetics and mechanism of nickel-sulfur reaction', *J Electrochem Soc*, 1962 **109** 273–278.
83. Mrowec S, Danielewski M, Wójtowicz A, 'Sulphidation of cobalt at high temperatures', *J Mater Sci*, 1998 **33** 2617–2628.
84. Mrowec S, Danielewski M, Dabek J, Sieminska G, 'Sulphidation of chromium at high temperatures', *Bull Acad Pol Sci Chem*, 1987 **35** 199–207.
85. Danielewski M, 'Sulphidation behaviour of niobium', in Proc. of European Corrosion Meeting Eurocorr'87, 1987 223–228.

# Index

---

- abrasive wear 118, 146–8, 158–9, 161  
effect of environment on wear rate 146, 147  
effect of temperature on wear rate 146, 147  
test facilities 124–6  
two-body and three-body abrasion at elevated temperature 146–8
- Abuluwefa group's studies 211–13
- acidic fluxing 169–71
- acoustic emission (AE) test 267
- activation energy  
alumina scale 292, 294  
effect of reactive elements 303
- oxidation of CVD silicon carbide 441, 442–3
- sulphidation of alloys containing refractory metals 627
- active oxidation (silicon carbide) 433, 434, 444–9
- active sulphur 498
- additives, chemical 107–8
- adhesion of scales  
effect of reactive elements on alumina scale 303–5  
enhancement and oxidation-resistant nanocrystalline coatings 465–70
- air, oxidation of iron and steel in  
air/gas ratio 212–13  
effects of water vapour addition 202–6  
excess air combustion 206–14  
low carbon, low silicon steel 199–202  
pure iron 198–9
- air jet erosion rigs 121–3
- alloy steels 197
- alloying elements *see* reactive elements
- alloys  
alloy layer for furnace radiant tubes 519  
analytical techniques 65–71, 72  
characteristics and erosion rate 144–5  
hot corrosion 172–9  
choice of alloy and prevention 179–81  
metal dusting 80, 81, 92–103, 104  
alloys with intrinsic metal dusting resistance 104–7  
oxidation *see* oxidation
- oxidation-resistant high temperature alloys *see* oxidation-resistant high temperature alloys
- sulphidation 609–34  
alloys containing refractory metals 617–28  
dissociative mechanism of scale growth 610–13, 614  
doping effect 622–3, 624–6, 628–34  
kinetics 613–17
- transition between external and internal oxidation *see* transition between external and internal oxidation of alloys
- $\alpha$ -alumina 477  
*in-situ* TMCs 379  
three-dimensional network 380–1
- alumina  
fibres 367  
nickel aluminide-based MMCs 384–5

- titanium matrix composites 373
- in-situ* MMCs 376–82
- scales *see* alumina scales
- tubes and oxidation experiments 444
- alumina-forming alloys 403–21
  - analytical techniques 66–71, 72
  - iron-based 68–71, 406–10
  - metal dusting 82, 85, 112–13
  - nickel-based 66–8, 403–6
  - reactive element optimisation 410–16
  - strategies for increasing lifetime 416–21
- alumina scales 3, 290–328, 457–8
  - growth and properties 291–301
    - growth mechanism 292–6, 297
    - kinetics 291–2, 293, 294
    - oxygen and cation diffusion coefficients 298–301
  - transient alumina formation and transformation 295–8
- influence of minor element addition 301–13
- adhesion 303–5
- influence of reactive elements in growth mechanism 309–13
- kinetics 302–3, 304
- location of reactive elements in
  - alumina scales 305–9
  - reactive elements 301–2
  - sulphur effect 313
- intermetallics 313–19
  - aluminide diffusion coating performance in oxidising atmospheres 316–19
  - microstructure and oxidation of iron aluminides 314–16, 317
- oxidation behaviour of titanium aluminium carbides 271–6
  - hot corrosion resistance 282–3
- oxidation-resistant nanocrystalline coatings 459–71
- oxidation of titanium aluminides 337, 338, 339, 340, 355–6
  - maintaining initially formed alumina scale 347
  - overlay coating 352
- see also* oxide scales
- alumina-YSZ graded TBC 479
- aluminides 313–19
  - coatings 421–2, 485–6
    - control of naphthenic acid corrosion 512
  - diffusion coating performance in oxidising atmospheres 316–19
  - nickel aluminide 112–13, 185–7
    - on titanium aluminides 349, 352, 356–7
  - iron aluminides *see* iron aluminides
  - nickel aluminides *see* nickel aluminides
  - titanium aluminides *see* titanium aluminides
- aluminium
  - aluminium content and mass gain due to oxidation of titanium-aluminium intermetallic compounds 343, 344
  - aluminium-doped porous zinc oxide films 542
  - diffusion and alumina scale growth 292–5, 296
    - aluminium diffusion coefficient 300–1
  - niobium silicide-based *in-situ* composites 387
  - sulphidation of alloys containing 614–15, 616, 617
    - alloys containing molybdenum and aluminium 618–21, 622–8
    - refractory metal alloys 621–2, 623
  - surface modification of titanium silicon carbide 268–9
  - titanium-aluminium-oxygen system 334–5, 336
- aluminium boron carbides 257, 258
  - processing 262, 263
- aluminium-killed steels 198, 203–4
- analytical techniques 1, 3, 59–79
  - metals and alloys 61–71
    - alumina-forming alloys 66–71, 72
    - chromia-forming alloys 65–6
    - chromium 62–4
    - nickel 61–2
  - semiconductors 71–5
    - silicon 71–3
  - III-V semiconductors 73–5, 76, 77
- anionic scale growth 19, 20, 22–3
- interface reactions and interface structure 27–8

- APM alloy 407  
 APMT alloy 407–8  
 applied load 131, 132  
 argon 543–7  
 artefact porosity 220, 221  
 ash-coating test 579  
 ash deposit 516, 517  
 ash deposition rate 588–91  
 ash-embedded test 577, 579  
 atmosphere/environment *see*  
     environment/atmosphere  
 atmospheric distillation systems 516–17  
 Auger electron spectroscopy (AES)  
     59–60, 71, 72, 74, 77  
 austenitic steels 408–10  
  
 balanced transport theory 206  
 basic fluxing 168–9, 170  
 bending strength 378  
 $\beta$  phase titanium aluminide 348–9  
 blisters 219  
 boilers, waste-to-energy 558–61  
 bond coat layer 476, 484–7, 489  
     *see also* thermal barrier coatings  
 boron fibres 366  
 brittle-ductile transition temperature 235,  
     238  
 brittle failure 237, 238  
 ‘broccoli’ formation 415  
 BSCCO superconducting system 529, 530  
 bubbles  
     oxidation of LTCs 264, 265  
     silicon carbide 433, 434, 449–52  
  
 calcium-magnesium-alumina-silicate  
     (CMAS) layer 488  
 carbide precipitates 93–4, 95, 96, 100–1,  
     102, 103  
 carbon  
     deposits *see* coking  
     metal dusting and suppressing the  
         carbon transfer reaction 107–9  
     silicon–carbon–oxygen system 447, 448  
 carbon dioxide  
     long-term oxidation of iron and steel  
         202–3, 207, 211–12, 213–14, 215  
     oxidation of titanium aluminides 342  
 carbon monoxide 83  
     diffusion and bubble formation on  
         silicon carbide 450–2  
  
 long-term oxidation of iron and steel  
     213–14, 215  
 carbon steels 197  
     control of naphthenic acid corrosion  
         512  
 carburisation 496  
     furnace radiant tubes 515, 518  
 carrier mobility 532  
 cast K52 alloy 463–4  
 Castrip process 195, 196–7, 226  
 cathodic protection 179, 180  
 cation diffusion coefficients 298–301, 312  
 cationic scale growth 19, 20, 21–2  
     interface reactions and interface  
         structure 26–7  
 caustic solution 512–13  
 ceramics  
     coatings 352  
         furnace radiant tubes 519  
         topcoat for thermal barrier layer 476,  
             479–83, 489  
         *see also* thermal barrier coatings  
 cerium-doped porous zinc oxide film  
     541–2, 543  
 cerium oxide 481  
 cermet coatings 567–9, 570  
 chemical additives 107–8  
 chemical diffusion coefficient 605–8  
 chemical vapour deposition (CVD) 182,  
     183, 457  
 silicon carbide 4, 433–55  
     synthesis of CVD silicon carbide  
         thick plates 434–7  
 chlorine 348  
     hot corrosion 178–9  
     waste-to-energy plants 570–1, 573  
 chromia-forming alloys 398–403  
     alloy development 398–400  
     analytical techniques 65–6  
     metal dusting 81, 82, 85, 92–4, 98,  
         102–3, 104  
         control 104–5, 106, 111–12  
         problems with 400–3  
 chromia scales 290, 457–8  
     oxidation-resistant nanocrystalline  
         coatings 459–71  
     parabolic rate constant 290, 291  
         *see also* oxide scales  
 chromium 399  
     analytical techniques 62–4

- control of metal dusting with pure chromium coating 110, 112
- corrosion-resistant materials for superheaters 563–4, 565–6, 567, 568, 569
- diffusion coefficient and alumina scale 300–1, 312
- effect of chromium content on erosion rate 144, 145
- niobium silicide-based *in-situ* composites 387
- sulphidation of alloys containing chromium 613–17
- chromium content 609, 610, 611
- chromium alloys
- coating to promote oxide film to control metal dusting 110, 112
  - model for transition from external to internal oxidation of alloys 54–5
  - experimental observations 43–50
  - metal nodules 44, 45, 47, 48, 55–6
- chromium–aluminium–carbon ceramics 284
- climb 26–8
- coatings 4
- control of metal dusting 112
  - metallic coatings 108–9
  - promotion of protective surface oxide films 109–10, 111
  - corrosion-resistant in WTE system
    - superheaters 567–9, 570
    - waterwall tubes 572–7  - diffusion coatings *see* diffusion coatings
  - interfacial coatings 373, 385, 389
  - nanocrystalline *see* nanocrystalline coatings
  - overlay coatings 352, 458
  - oxidation-resistant high temperature alloys 421–2
  - prevention of hot corrosion 179, 180, 181–7
  - coating-substrate system
    - requirements 184–7  - silicon carbide 4, 433–55
  - spray coatings *see* spray coatings
  - thermal barrier coatings *see* thermal barrier coatings
  - on titanium aluminides 352, 356–7
- titanium matrix composites 381
- cobalt 80–1, 88–92
- cobalt-based alloys
- hot corrosion 172–9
  - oxidation of cobalt–chromium alloys 43–50
  - Co-5Cr alloy 47, 48
  - Co-10Cr alloy 47, 49
- cobalt silicide scale 16, 17
- co-doping 414–15
- coefficient of thermal expansion (CTE) 184, 291
- alumina-forming alloys 419–20
- in-situ* TMCs 380
- interconnectors for solid oxide fuel cells 400
- mismatch and porosity 219–20
- coking (carbon deposition)
- furnace radiant tubes 515, 518
  - control of coking 518–19
  - metal dusting 81–2, 86
  - alloys 93, 94, 95–6, 100, 101, 102, 103
- coking furnaces 517
- coking inhibitors 518
- cold-wall type CVD 434–7
- columnar grains 16–17
- alumina scale 309, 311
- combustion deposits, deleterious 488
- combustion gases 341–3
- combustion oxidation 530
- compact strip process (CSP) 194–6
- complementary metal oxide semiconductor field effect transistor 521
- composite layer (sliding wear) 149, 150, 151
- composite oxide scale 37, 38, 39–40, 53
- composite tubings 576
- composites
- LTCs 269
  - metal matrix composites *see* metal matrix composites
- condensation 506
- conforming geometry sliding wear testing 119–20
- contaminants *see* impurities
- continuous reinforced MMCs 366–7, 371–3, 384–5
- copper 108–9, 218

- copper-zinc alloys 613, 614  
 corrosion acceleration mechanisms 585, 587  
 corrosion environment *see* environment/atmosphere  
 corrosion lifetime evaluation 592–4, 595  
 corrosion testing *see* testing  
 cracking-cracks  
     hot-rolled steel strips 230, 231, 232–3, 234, 236  
         finite element modelling 236–8, 239  
     *in-situ* TMCs 381  
     LTCs 266–7  
     segmentation cracks 478  
     WTE plant 571, 572, 573  
 creep 307, 467–8  
 critical concentration 38–9, 53, 461–2  
 critical strain 467  
 critical stress 527  
 critical thickness 236  
 critical volume fraction 38, 54  
 crude oils 495–6, 498  
     naphthenic acid corrosion  
         high sulphur and high TAN 510–11  
         low sulphur and high TAN 507–9  
     *see also* petrochemical industry  
 cryolite 280  
 crystallisation 443–4  
 crystallite size 314–16, 317  
 cyclic oxidation tests  
     alumina scales doped with reactive elements 303–5  
     LTCs 266–7  
 dangling bonds 522  
 decarburisation 515  
 decoking agents 518  
 defect diffusion coefficient 605–8, 627  
 defects  
     interface structure 24–5  
         and interface reactions 26–8  
         structure for metal sulphides 601–5  
     sulphidation of alloys containing  
         refractory metals 624–6  
         zinc oxide films 546–8  
 deformation of oxide scale 226–39  
     failure modes 230–1  
     laboratory simulation 231–6  
     numerical simulation 236–9  
 delamination 149, 151  
 deoxidation 197–8  
 dielectric films 521–2  
 diffusion 2–3, 9–35  
     aluminium-rich coatings and  
         interdiffusion problem 421–2  
     combined effects of interface reactions and interface structure 25–8  
     future trends 32–3  
     growth stresses and interfacial processes 28–32  
         experimental evidence of stresses associated with interdiffusion processes 29–30  
     interface reactions 21–3  
     interface structure 23–5  
     Kirkendall effect 11–16  
         specificity in two-phase diffusion couples 13–15  
     metal sulphides 605–8  
     mixed diffusion process and alumina scale growth 292, 294–5, 296  
     oxidation of chromium 63  
     role of oxide/metal interface during oxide scale growth 16–20  
     sulphidation of alloys 610–11, 612  
     thermal barrier coatings and  
         interdiffusion 477, 485  
 diffusion boundary 55  
 diffusion coatings 458  
     aluminide diffusion coating  
         performance in oxidising atmospheres 316–19  
     thermal barrier coatings 485–7  
     on titanium aluminides 349, 356–7  
 diffusion coefficients  
     aluminium 300–1  
     cation 298–301, 312  
     chromium 300–1, 312  
     defect 605–8, 627  
     oxygen 298–301, 309, 312  
     self-diffusion coefficients 605–8, 624, 627  
 diffusional creep 307, 467–8  
 disc on disc sliding wear testing 119, 120  
 disconnections 24, 25, 27–8  
 discontinuous reinforced MMCs 366, 367, 373–6, 386  
 dislocations  
     misfit 24–5, 26–7  
     misorientation 24–5, 26–8

- dissociation pressures 600  
 dissociative mechanism for scale growth 610–13, 614  
 dopant/interstitial element ratios 412–13, 414  
 doping effect  
   sulphidation of alloys 622–3, 624–6, 628–34  
   sulphidation of metals 609  
 dots, quantum 526–7  
 ductile failure 237, 238–9  
 ductility 357–8  
   brittle-ductile transition temperature 235, 238  
 duplex microstructure 16–17  
 dynamic segregation 307, 411
- electric arc furnace (EAF) 193, 194  
 electric steels 197  
 electro/electroless plating 182, 183  
 electrochemical monitoring (ECM) system 577, 588–91  
 electron backscatter diffraction (EBSD) 239–43  
 electron beam physical vapour deposition (EB-PVD) thermal barrier coatings 478–9  
 electron energy loss spectroscopy (EELS) 59, 60  
 electronic materials 5, 521–56  
   oxidation of precursors for preparation of superconductors 528–30  
   oxidation processing in semiconductors 522–8  
   preparation of zinc oxide films and nanostructures 530–48  
   traditional oxidation techniques 531–4  
   wet oxidation 534–48  
 embrittlement 355  
 energy dispersive X-ray spectroscopy (EDX) 60  
 engine valves 329, 330  
 environment/atmosphere  
   corrosion environment of WTE plant 558–61, 562  
   monitoring 577, 588–91  
   effect of sputtering and oxidising atmospheres on zinc oxide films 543–7  
 effect on wear rate  
   abrasive wear 146, 147  
   sliding wear 136–7  
 influence of gas species on oxidation of titanium aluminides 341–3  
 long-term oxidation of iron and steel 198–216  
   air or oxygen 198–202  
   reheat furnace atmospheres 206–16  
   water vapour addition 202–6  
 LTCs' interaction with 284  
 metal dusting 83–5  
 sulphidation environments in petrochemical industry 499–500  
 EQ coating (equilibrium coating) 487  
 equal-channel angular (ECA) pressing 456–7  
 equiaxial grains 16–17  
   alumina scale 309, 311  
 equilibrium constants 41  
 erosion oxidation interaction map 151–2, 153, 154, 161  
 erosive wear 117–18, 137–45, 158–9, 160–1  
   eroded material characteristics and erosion rate 144–5  
   impact angle and erosion rate 139–40, 141  
   impact velocity and erosion rate 137–9  
   particle feed rate and erosion rate 142–3  
   particle shape and erosion rate 142, 143  
   particle size and erosion rate 140–2  
   recent developments 151–8  
   enhanced oxidation kinetics due to erosion induced roughness 155–8  
   transition criteria for transition from metal erosion regime to oxide erosion regime 152–5  
   temperature and erosion rate 137, 138  
   test facilities 120–3  
 ethylene crackers 495  
   corrosion of furnace radiant tubes 517–18  
 eutectoid iron 240, 241  
 excess air combustion 206–14  
 external interface 9, 18–19

- external oxidation 36  
*see also* transition between external and internal oxidation of alloys
- failure  
 analysis and petrochemical industry  
 naphthenic acid corrosion 508–9, 511  
 sulphidation 501–2
- oxide scale during hot rolling 226–39  
 failure modes 230–1  
 laboratory simulation 231–6  
 numerical simulation 236–9
- thermal barrier coatings 487–8  
 CMAS deposits 488  
 hot corrosion 488  
 oxidation 487–8
- fast oxidation 530
- fayalite 217–18
- fibre-reinforced MMCs 366–7  
 nickel aluminide-based composites 384–5  
 titanium matrix composites 371–3
- Fick's laws of diffusion 299
- field monitoring and inspection  
 techniques 504
- filamentous carbon 95, 96, 97–8, 99, 101
- finishing rolling 192, 193, 226–7
- finite element (FE) modelling 236–9
- flow velocity and state 506  
 control 513
- fluorite oxides 481–3
- fluxing, salt 168–71
- four-point-bend method 227
- fractographic method 220
- fracture elongation 227–8
- fracture toughness 378
- free energy 41–3, 600
- friction coefficient 126–36
- fuel additives 181
- functionally graded thermal barrier  
 coatings 479
- furnace radiant tubes 496, 513–19  
 coking furnaces 517  
 control of high temperature oxidation 518–19
- corrosion in atmospheric and vacuum distillation systems 516–17
- ethylene crackers 517–18
- types of high temperature corrosion 513–15
- gallium arsenide 74, 75  
 oxidation 527–8
- gaps 237
- garnet phases 307
- gas temperature 580, 581  
*see also* temperature gradient; temperature gradient tests
- Gibbs free energy 41–3, 600
- GKN group 208–9
- gold 108
- graded thermal barrier coatings (GTBC) 479
- grain refinement 458  
 nanocrystalline oxidation-resistant coatings 461–2, 464
- grain size  
 iron aluminide 314–16, 317  
 and oxidation of titanium aluminides 353  
 oxide scales on steels 242–3
- graphite 86, 87–8, 89, 90, 95–6, 100
- growth stresses 28–32, 466  
 experimental evidence of stresses associated with interdiffusion processes 29–30  
 ideal stress-free growth of oxide scales 17–20  
 interfacial processes and growth stresses in scale growth 30–1  
 vacancy injection 31–2
- haematite 198, 216, 223, 225  
 EBSD analyses of structure 240, 241, 242–3  
 mechanical properties 227–8
- hafnium 344, 388  
 alumina-forming alloys 404–6, 411–16  
 hafnium-doped thermal barrier coatings 485
- hafnium oxide 481
- halogen effect 348
- hardness 378
- heat-resistant iron-based alloys 197
- high pressure torsion (HPT) 456–7
- high-strength low-alloy (HSLA) steels 197
- high stress abrasion testing 124, 125
- high temperature hot corrosion (HTHC) 165
- high temperature superconductors (HTS) 528–30

- high velocity oxygen fuel (HVOF) coatings 457, 574, 575, 576, 577
- Hochman mechanism 82, 86
- hot corrosion 3, 164–91  
     avoiding 179–82  
     coatings and prevention 179, 180, 181–7  
     degradation sequence 166–8  
     iron-, nickel- and cobalt-based alloys 172–9  
     mechanism for LTCs 279–83  
     salt chemistry 171–2, 173  
     salt fluxing 168–71  
     thermal barrier coatings 488  
     types of 165–6
- hot-forging simulation 235–6
- hot-rolled steel strips 3, 192–252  
     deformation and failure of oxide scale  
         during hot rolling 226–39  
     failure modes of oxide scale 230–1  
     laboratory simulation 231–6  
     mechanical properties of oxide scales 227–30  
     numerical simulation 236–9
- EBSD analyses of oxide scale structure 239–43
- long-term oxidation of iron and steel 198–221  
     effects of alloying elements 217–19  
     porosity in scale 203, 210–11, 219–21  
     pure iron in air or oxygen 198–9  
     reheat furnace atmospheres 206–16  
     steel in air or oxygen 199–202  
     water vapour addition 202–6
- production methods 192–7
- short-time oxidation of iron and steel 221–6
- hot ‘sandwich’ rolling studies 234–5
- hydraulic descaling 192, 193, 222, 226
- hydrogen 83  
     hydrogen and hydrogen sulphide gas mixtures 500, 601–2
- long-term oxidation of iron and steel 213–14, 215
- hydrogen permeability 205–6
- hydrogen sulphide 107–8, 499–500, 601–2
- impact angle 139–40, 141
- impact velocity 122–3  
     effect on erosion rate 137–9  
     enhanced oxidation kinetics due to erosion induced roughness 155–8
- impurities  
     and hot corrosion 176  
     oxidation of silicon carbide 444  
     sulphidation of metals 609  
         *see also* doping effect
- in-line strip process (ISP) 196
- in-situ* electrochemical monitoring (ECM) system 577, 588–91
- in-situ* MMCs  
     niobium silicide-based 386–8  
     titanium-based 376–82
- inactive sulphur 498
- incinerators *see* waste-to-energy (WTE)  
     incineration plants
- Inconel alloys 92–6
- incremental erosion rate 121–2
- indium aluminium phosphide 74, 76, 77
- indium phosphide 74, 75
- inert markers 11, 12, 19, 608  
     splitting 29–30
- inhibitors  
     hot corrosion 179, 180, 181  
     oleo-soluble 513
- initial and transient stage (oxidation) 459–64
- initiation stage (hot corrosion) 166, 167
- inspection 504
- integrated circuits 521
- interconnectors for solid oxide fuel cells 399–400
- interdiffusion *see* diffusion
- interface 2–3, 9–35  
     combined effects of interface  
         reactions and structure 25–8  
         elementary interface reactions 21–3  
         growth stresses and interfacial processes 28–32  
     Kirkendall effect and interface actions 11–16  
     role of oxide/metal interface during oxide scale growth 16–20  
     role in phase transformations 15–16  
     structure 23–5

- interface blocking 30–1  
 interfacial coatings 373, 385, 389  
 intermediate phases 9  
     similarity between growth of oxide scales and 16–17  
 intermetallic precipitates 103, 104, 105, 106–7  
 intermetallics *see* aluminides; iron aluminides; nickel aluminides; titanium aluminides  
 internal interface 9, 18–19  
 internal oxidation 36–7  
     *see also* transition between external and internal oxidation of alloys  
 internal oxides 355–6  
 interstitial-free (IF) steel 197, 203–4, 218–19  
 intrinsic metal dusting resistance 104–7  
 ion implantation 350–1  
 iridium 404–6  
 iron  
     metal dusting 80, 85–8  
         control 108  
     oxidation 3  
         in air or oxygen 198–9  
         effect of water vapour addition 202–6  
         long-term 198–221  
         reheat furnace atmospheres 206–16  
         short-time oxidation 221–6  
 iron aluminides 179  
     effect of microstructure on high temperature oxidation behaviour 314–16, 317  
     iron aluminide-based MMCs 382–3  
 iron-based alloys  
     alumina-forming alloys 406–10  
         strategies for increasing lifetime 417–20  
     hot corrosion 172–9  
     iron–chromium alloys 613–14, 615  
     iron–chromium–aluminium alloys 68–71, 72, 614–15, 616  
     iron–nickel-based alloys *see* nickel–iron-based alloys  
     metal dusting 102–3, 104  
     sulphidation 618–21  
 iron carbide 82, 86  
 iron naphthenate 505  
 iron oxides 227–30  
 iron sulphide 506  
 isothermal erosion rigs 121–3  
 jaw crusher test, lab scale 124  
 jet-type erosion rigs 121–3  
 Kikuchi diffraction pattern 239–40  
 kinks 25, 26  
 Kirkendall effect 11–16  
     basis 11–13  
     specificity of in two-phase diffusion couples 13–15  
 Kirkendall planes 11, 18–19, 29  
 Kirkendall voids 11–13, 14, 220  
 Krzyzanowski group's study 232–3  
 laboratory simulations  
     hot rolling tests 231–6  
     wear tests 118–26  
 lanthanum 399  
     surface modification of titanium silicon carbide 268–9  
 lanthanum cerium oxides 482–3  
 laser doppler velocimeter (LDV) 123  
 Laves phase 347–8  
 layered ternary ceramics (LTCs) 3, 255–89  
 future trends 283–4  
     developing new corrosion-resistant LTCs 284  
     interaction between LTCs and environment 284  
     selective oxidation 284  
 high-temperature oxidation mechanism 263–78  
     improvements to high-temperature oxidation behaviour of  $Ti_3SiC_2$  267–9  
      $Ti_3AlC_2$  and  $Ti_2AlC$  270–6  
      $Ti_3SiC_2$  263–7  
      $Zr_3Al_3C_5$  276–8  
 hot corrosion mechanism 279–83  
      $Ti_3AlC_2$  and  $Ti_2AlC$  against sodium sulphate 281–3  
      $Ti_3SiC_2$  against molten salts 279–80  
     microstructure 256–60  
     synthesis 260–3  
 ledges 24, 25, 26

- Lee and Choi's study 213  
 Li and Sellars' study 233  
 lifetime  
   chromia-forming alloys 400–1  
   corrosion lifetime evaluation of materials 592–4, 595  
   strategies for increasing lifetime of oxidation-resistant high temperature alloys 416–21  
 light emitting diodes (LEDs) 521  
 linear corrosion rate constant 592–4, 595  
 linear-parabolic oxidation kinetics  
   438–43  
 lithium 629–34  
 lithium carbonate 279–80  
 load, applied 131, 132  
 localised molten salt corrosion 571–2, 573, 583–4, 585, 586  
 long-term oxidation of iron and steel 198–221  
 low-dimensional nanostructures  
   silicon 525–7  
   zinc oxide 534–40  
 low stress abrasion testing 124–6  
 low temperature hot corrosion (LTHC)  
   165–6, 174  
 low temperature oxidation 524  
 low velocity erosion test facility 122, 123  
 magnetite 198, 200, 216, 223, 225  
   EBSD analyses of structure 240, 241, 242–3  
   mechanical properties 227–8  
 manganese 105–7, 399, 420  
   doping effect and sulphidation of alloys 628–34  
 manganese-chromium alloy 628–9, 630  
 Matano plane 11, 12, 14, 18–19  
 material selection 497  
   avoidance of hot corrosion 179–81  
   petrochemical industry  
     control of naphthenic acid corrosion 512  
     control of sulphidation 503–4  
     furnace radiant tubes 516–17, 518  
   mating surfaces, nature of 131–4  
 McEconomy charts 503  
 MCrAlY coatings 458, 484–5  
 mechanically mixed layer (MML) 149, 150, 151  
 melting points 588, 590  
   sulphides compared with oxides 600  
 mercaptan (RSH) 498, 499–500  
 metal dusting 3, 80–116  
   alloys 80, 81, 92–103  
     iron-based 102–3, 104  
     iron–nickel-based 97–101  
     nickel-based 92–6, 101  
   background 81–3  
   control of 103–10  
     alloys with intrinsic metal dusting resistance 104–7  
     coatings to promote protective oxide films 109–10, 111  
     suppressing the carbon transfer reaction 107–9  
   future trends 110–13  
   nature of metal dusting environment 83–5  
   pure metals 80–1, 85–92  
     iron 85–8  
     nickel and cobalt 88–92  
 metal erosion regime 152, 153  
   transition criteria from metal erosion regime to oxide erosion regime 152–5  
 metal extrusion 237  
 metal-glass composite 483  
 metal insulator semiconductor field effect transistor (MISFET) technology 527–8  
 metal matrix composites (MMCs) 4, 365–97  
   classification 365–6  
   corrosion 369  
   fabrication 368  
   matrix 367–8  
   mechanical properties 368  
   oxidation of iron–aluminide-based composites 382–3  
   oxidation of nickel aluminide-based composites 383–6  
   oxidation of niobium silicide-based *in-situ* composites 386–8  
   oxidation of titanium matrix composites 371–82  
     *in-situ* composites 376–82  
   reinforcing phase 366–7

- fibre 366–7, 371–3, 384–5  
 particulate 367, 373–6, 386  
 whisker 367, 373–6
- titanium alloys, titanium aluminides  
 and composites 369–71
- metal nodules 44, 45, 47, 48, 55–6
- metal oxides  
 compared with metal sulphides 600–1  
 transport properties 605, 606, 607
- metal sulphides 600–8  
 defect structure and transport  
 properties 601–8  
 thermodynamic properties 600–1
- metal temperature 580, 581  
*see also* temperature gradient;  
 temperature gradient tests
- metallic precursors, oxidation of 528–30
- metals  
 analytical techniques 61–4  
 characteristics and erosion rate 144–5  
 metal dusting 80–1, 85–92  
 metallic surface coatings to control  
 108–9  
 sulphidation 608–9
- minimill steel technology 194
- misfit dislocations 24–5, 26–7
- misorientation dislocations 24–5, 26–8
- molten salt induced corrosion 571–2,  
 573, 583–4, 585, 586
- molybdenum 173, 388, 423, 506  
 coating and nickel aluminide-based  
 MMCs 385  
 sulphidation 617  
 alloys containing molybdenum  
 618–28  
 WTE plant superheater tubes 565–6,  
 567
- molybdenum disulphide 602–3, 606,  
 607
- monitoring  
 environmental 577, 588–91  
 field monitoring and inspection  
 techniques in petrochemical  
 industry 504
- Moore's Law 523–4
- mullite 483
- nanobelts 536, 537
- nanocrystalline coatings 4, 456–75  
 oxidation-resistant 459–71
- enhancement of scale adhesion  
 465–70
- selective formation of protective  
 oxide scale 459–64
- steady-state growth of protective  
 oxide scale 460, 464–5, 466
- nanocrystalline materials 456–7, 483
- nanostructures  
 oxidation of silicon nanostructures  
 525–7
- preparation of zinc oxide  
 nanostructures  
 traditional oxidation techniques  
 533–4
- wet oxidation techniques 534–40
- nanowires  
 silicon 525–6  
 zinc oxide 534, 535, 536, 537
- naphthalene acid corrosion 496, 504–13  
 case studies 507–11  
 crude oils with high sulphur and  
 high TAN 510–11  
 crude oils with low sulphur and  
 high TAN 507–9
- characteristics 505  
 factors influencing 505–6  
 furnace radiant tubes 514–15, 516, 517  
 techniques to control 512–13
- naphthalene acid extraction 513
- nickel 218  
 analytical techniques 61–2  
 enhanced oxidation kinetics due to  
 erosion induced roughness  
 155–8  
 metal dusting 80–1, 88–92  
 nickel-titanium diffusion couple  
 29–30
- nickel aluminides  
 analytical techniques 66–8  
 bond coat in thermal barrier coating  
 systems 485  
 coatings  
 and hot corrosion 185–7  
 and control of metal dusting  
 112–13  
 MMCs based on 383–6  
 fibre-reinforced 384–5  
 particulate-reinforced 386  
 nanocrystallisation and growth of  
 oxide scales 470

- nickel-based alloys
- alumina-forming 403–6, 417, 420
  - hot corrosion 172–9
  - metal dusting 92–6, 101
    - chromia-forming nickel-based alloys and resistance to metal dusting 111
  - nickel-platinum-aluminium alloys 404–6
  - sulphidation 618, 619
  - WTE plant superheater tubes 563–4, 565–6, 567, 568, 569
- nickel-chromium alloys 158
- control of metal dusting 107–8
  - nickel-chromium-aluminium alloys 404, 405
  - Ni-20CR coating and hot corrosion 185–7
  - NiCrAlY coating and hot corrosion 185–7
  - oxidation 43–50
    - Ni-6Cr alloy 44, 45
    - Ni-8Cr alloy 44–7
- nickel-iron-based alloys 567
- metal dusting 97–101
    - control 109
    - intrinsic resistance 105–7
  - WTE plant 563–4, 567, 568
- nickel oxide scale 16, 17
- niobium 343–6, 347, 422–3
- ion implantation on titanium-aluminium intermetallics 350, 351
  - oxidation characteristics of Ti<sub>3</sub>Al-Nb alloys 353–7
  - sulphidation 617
  - alloys containing niobium 618
- niobium silicide-based *in-situ* MMCs 386–8
- niobium sulphide 604–6, 607, 608
- nitrogen
- long-term oxidation of iron and steel 209–12, 213, 215
  - oxidation of titanium-aluminium intermetallics 342
  - zinc oxide films
    - grown by sputtering and wet oxidation 543–7
    - nitrogen-doped zinc oxide films 532–3
- nodule formation 44, 45, 47, 48, 55–6
- non-conforming geometry sliding wear testing 119–20
- non-isothermal erosion rigs 121, 123
- nucleation 41–3
- numerical simulation 236–9
- ODS alloys 407, 423
- oil ash corrosion 181, 184
- oil collection plates 510, 511
- oil collection tank 507, 509, 510, 511
- Okada group's study 232
- oleo-soluble inhibitors 513
- overlay coatings 352, 458
- oxidation 159
- alloys 3, 36–58
    - compared with sulphidation 609, 610
  - model for transition from external to internal oxidation 43–56
  - oxidation rates compared with sulphidation rates 613–17
  - thermodynamics of chemical reactions 40–1, 42
  - thermodynamics of oxide nucleation at alloy surface and in alloy substrate 41–3
  - enhanced oxidation kinetics due to erosion induced roughness 155–8
- hot corrosion *see* hot corrosion
- iron *see* iron
- iron aluminide 314–16, 317
- LTCs 263–78
- selective oxidation 284
  - titanium aluminium carbides 270–6
  - titanium silicon carbide 263–9
  - zirconium aluminium carbide 276–8
- metal matrix composites 4, 371–88
- iron aluminide-based 382–3
  - nickel aluminide-based 383–6
  - niobium silicide-based *in-situ* composites 386–8
  - titanium matrix composites 371–82
- of metals compared with sulphidation 608–9
- petrochemical industry 496
- control of oxidation 518–19
  - furnace radiant tubes 514, 518–19

- processing of electronic materials *see* electronic materials
- silicon carbide 4, 433–55
- active 433, 434, 444–9
  - bubble formation 433, 434, 449–52
  - passive 433–4, 437–44
- steel *see* steel
- thermal barrier coatings 487–8
- thermodynamics of 40–3
- titanium aluminides *see* titanium aluminides
- tribology oxidation maps 151–2, 153, 154, 159, 161
- oxidation-affected erosion 152, 153
- oxidation-controlled erosion 152, 153
- oxidation-resistant coatings 457–8
- nanocrystalline 459–71
- oxidation-resistant high temperature alloys 4, 398–432
- alumina-forming alloys 403–21
  - chromia-forming alloys 398–403
  - ‘fantasy’ high temperature materials 421–3
- future trends 423–4
- reactive element optimisation 410–16
- strategies for increasing lifetime 416–21
- oxide dispersion strengthened (ODS) alloys 407, 423
- oxide erosion regime 152, 153
- transition criteria from metal erosion regime to oxide erosion regime 152–5
- oxide pegs 468, 485
- oxide scales 2, 36, 290, 457–8
- barrier of oxide of reactive element on titanium aluminides 347
  - EBSD analyses of structure 239–43
  - growth 2–3, 9–35
    - growth stresses and interfacial processes 28–32
    - ideal stress-free growth 17–20
    - interface reactions and interface structure 20–8
    - role of oxide/metal interface 16–20
    - similarity to intermediate phase growth 16–17
  - on hot-rolled steel strips *see* hot-rolled steel strips
  - mechanical properties 227–30
- metal dusting
- coatings to promote protective oxide films 109–10, 111
  - iron-based alloys 102–3
  - iron-nickel-based alloys 99, 100
  -
- oxidation-resistant nanocrystalline coatings 459–71
- enhancement of scale adhesion 465–70
  - selective formation of oxide scale 459–64
  - steady-state growth of protective scale 460, 464–5, 466
- role and reproducibility of TGTs 584–7
- silica 82, 85, 290, 347
- structure for titanium aluminides 337–8
- thermal barrier coatings and thermally grown oxides 476–7
- thickness 238, 239
- and wear 144–5, 159
- see also* alumina scales; chromia scales
- oxygen
- diffusion and alumina scale
  - growth mechanism 292, 294–5, 296
  - oxygen diffusion coefficient 298–301, 309, 312
  - reactive element doped alumina scale 309–11, 312
- long-term oxidation of iron and steel
- effects of water vapour addition 202–6
  - pure iron in oxygen 198–9
  - reheat furnace atmospheres 209–12, 213, 215, 216
  - steel in oxygen 199–202
- silicon–carbon–oxygen system 447, 448
- solubility in refractory metals 422–3
- titanium–aluminium–oxygen system 334–5, 336
- zinc oxide films grown by sputtering and wet oxidation 543–7
- oxygen interstitials 546–7
- oxygen partial pressure 441–2, 445–9, 450, 451
- oxygen vacancies 546

- pack cementation process 316–17  
 paddle wheel technique 123  
 palladium 404–6  
 parabolic rate constants 51, 54, 592–3, 594  
     alumina scale 290, 291, 292, 294  
         effect of reactive elements 304  
     aluminides 314, 315  
     comparison of oxide scales 290, 291  
     enhanced oxidation kinetics due to  
         erosion induced roughness  
         157–8  
     oxidation of low carbon, low silicon  
         steel 199, 200  
     oxidation of LTCs 263–4, 270  
     oxidation of pure iron 198–9  
     oxidation of silicon carbide 438–44  
     sulphidation of alloys 624–6  
 partial reactive sputtering deposition–wet  
     oxidation 540–3  
 particle feed rate 142–3  
 particle shape 142, 143  
 particle size 140–2  
 particulate-reinforced MMCs 367  
     nickel aluminide-based composites 386  
     titanium matrix composites 373–6  
 passive oxidation (silicon carbide) 433–4,  
     437–44  
 pegs 468, 485  
 ‘pest’ phenomenon 621  
 petrochemical industry 5, 495–520  
     corrosion of furnace radiant tubes  
         513–19  
         atmospheric and vacuum  
             distillation systems 516–17  
         coking furnaces 517  
         control of oxidation 518–19  
         ethylene crackers 517–18  
         types of corrosion 513–15  
     focus of application-oriented research  
         497  
     importance of high temperature  
         corrosion protection 495–6  
     main corrosion problems 496–7  
     naphthenic acid corrosion 496,  
         504–13, 514–15, 516, 517  
     sulphidation 496, 498–504, 514–15,  
         516, 517  
 phase transformations 15–16  
 photoemission spectroscopy (PES) 71–2, 73  
 photographic method for impact velocity  
     122–3  
 photoluminescence  
     zinc oxide films  
         prepared by traditional oxidation  
         531–2  
         prepared by wet oxidation 543–8  
     zinc oxide nanostructures 534  
 physical vapour deposition (PVD) 182,  
     183, 457  
     EB-PVD 478–9  
     TP-PVD 478  
 Pilling–Bedworth (PB) ratio 18, 437–8  
 Pilling–Bedworth-type equation 198  
 pin on disc sliding wear testing 119, 120  
 pits 97, 98, 99  
 plasma oxidation 524–5  
 plasma spray coatings 457  
     plasma jet spray coatings in WTE  
         plant 569, 570, 574, 575  
         thermal barrier coatings 477–8  
 plasticity of oxide scales 227–30  
 platelets 537, 538  
 platinum group metals (PGMs) 404–6  
 platinum-marker experiment 264–5  
 platinum-modified aluminide bond  
     coatings 486  
 porosity/pores  
     Kirkendall effect 12, 13  
     long-term oxidation of iron and steel  
         and porosity in scale 203,  
         210–11, 219–21  
     wet oxidation and highly porous zinc  
         oxide films 540–3  
 potassium carbonate 279–80  
 power plant steels 197  
 precursors, oxidation of 528–30  
 pre-oxidation treatment  
     LTCs 282–3  
     titanium aluminides 349–50  
 primary scale 192, 194  
 process control 497  
     naphthenic acid corrosion 512–13  
         sulphidation 504  
 propagation stage (hot corrosion) 166–8  
 pull-off tests 275–6  
 pyrochlores 480–1  
 quantum dots (QDs) 526–7

- rapid thermal oxidation (RTO) 524  
 Rapp–Goto precipitation criterion 169–70  
 rare earth element oxides 481  
 reaction layer 9  
     similarity between growth of oxide scales and 16–17  
 reactive elements (RE) 54–5, 484–5  
     effect on friction coefficient and wear rate in sliding wear 134–6  
     effects on long-term oxidation of iron and steel 217–19  
     influence on alumina scales 301–13  
         adhesion 303–5  
         growth mechanism 309–13  
         kinetics 302–3, 304  
         location of reactive elements in alumina scales 305–9  
         sulphur effect 313  
     RE optimisation and alumina-forming alloys 410–16  
     RE oxide film on aluminide diffusion coating 317–19  
     and scale adhesion 467  
     titanium aluminides 356  
         barrier of oxide of reactive element 347  
         oxidation 343–9  
 reflection high-energy electron diffraction (RHEED) 59, 60, 61–3  
 refractory metal alloys  
     oxidation-resistant high temperature alloys 422–3  
     sulphidation 617–28  
 refractory metals  
     coatings to induce oxide formation to prevent metal dusting 110, 111  
     sulphidation 608, 609  
     *see also under individual metals*  
 refractory tiles 574, 576–7  
 regression analysis 592–4, 595  
 reheat furnace atmospheres 206–16  
     Abuluwefa group's studies 211–13  
     carbon dioxide, carbon dioxide/carbon monoxide mixtures, water vapour and water vapour/hydrogen mixtures 213–14  
 GKN studies 208–9  
 Lee and Choi's study 213  
 Sheasby group's study 209–11  
     substoichiometric combustion gases 214–16  
     reproducibility of TGTs 584–7  
     reservoir-consumption model 417  
     resistivity 532  
     retained scale on strip 193–4  
     rotating disc method 123  
     roughing rolling 192–3, 194, 226–7  
     roughness, surface  
         erosion induced 155–8  
         roughening 353  
         sliding wear 149–50  
     ruthenium aluminide 486–7  
     salt fluxing 168–71  
         acidic fluxing mode 169–71  
         basic fluxing mode 168–9, 170  
     ‘sandwich’ rolling studies 234–5  
     scale adhesion *see adhesion of scales*  
     scale-free reheat furnaces 214–16  
     scanning electron microscopy (SEM) 66–7  
 Scherrer formula 541  
 secondary ion mass spectrometry (SIMS) 59, 60, 63–4, 65–9, 72–3, 74  
 secondary neutral mass spectrometry (SNMS) 69–71  
 secondary reaction zone (SRZ) 486–7  
 secondary scale 193, 194  
 segmentation cracks 478  
 selective oxidation 284, 617  
     nanocrystalline coatings 459–64  
 selective sulphidation 617  
 self-diffusion coefficients 605–8, 624, 627  
 self-healing coatings 184  
 semiconductors  
     analytical techniques 71–5, 76, 77  
     oxidation processing 522–8  
     III-V semiconductors 73–5, 76, 77, 527–8  
 Sheasby group's study 209–11  
 short-time oxidation 221–6  
 silica scales 82, 85, 290, 347  
 silicon  
     analytical techniques 71–3  
     effect on long-term oxidation of steel 217–18  
     oxidation 10, 522–7  
     nanostructures 525–7

- silicon–carbon–oxygen system 447,  
     448  
 surface modification of titanium  
     silicon carbide 268  
 in WTE plant superheater tubes  
     565–6, 567, 569  
 silicon carbide  
     chemical vapour deposited 4, 433–55  
         active oxidation 433, 434, 444–9  
         bubble formation 433, 434, 449–52  
         passive oxidation 433–4, 437–44  
         synthesis of CVD silicon carbide  
             thick plates 434–7  
     composites with LTCs 269  
     fibres 366, 372–3  
     particle-reinforced MMCs 374  
 silicon dioxide films 522–5  
     ultra-thin 523–5  
 silicon-killed steels 198, 203–4  
 silicon nitride 439, 440  
     particle-reinforced MMCs 374  
 silicon oxide vapour 450–2  
 silver 108, 347  
 sintering  
     silicon carbide 433  
     thermal barrier coatings 487–8  
 slab reheating 192  
 sliding velocity 128–30  
 sliding wear 117, 126–37, 158–9, 160  
     alloying addition and 134–6  
     applied load and 131, 132  
     atmosphere and 136–7  
     nature of mating surfaces and 131–4  
     recent developments 149–51  
     sliding velocity and 128–30  
     temperature and 126–8, 129  
     test facilities 119–20  
 slipping 230, 231  
 slow oxidation 530  
 sodium ions 444  
 sodium sulphate 164–5  
     deposit in salt fluxing 168–71  
     hot corrosion degradation sequence  
         166–8  
     hot corrosion of iron-, nickel- and  
         cobalt-based alloys 172–3,  
         174–5, 176–9  
     hot corrosion mechanism of LTCs  
         279, 280, 281–3  
     sulphate solution chemistry 171, 172
- solid oxide fuel cells metallic  
     interconnectors 399–400  
 solid particle erosion *see* erosive wear  
 solid solution treatment 269  
 solubility  
     oxygen in refractory metals 422–3  
     sulphur in metals 609  
 solution precursor plasma spray (SPPS)  
     478  
 solvent metal nodules 44, 45, 47, 48,  
     55–6  
 soot blowers 559, 580–2  
 spallation 291, 466  
     alumina-forming alloys and strategies  
         for increasing lifetime 417–20  
     thermal barrier coatings 487  
 spark plasma sintering (SPS) 314  
 specimen thickness 400–1  
 spinel 85, 105, 106, 476–7  
 spray coatings 181–2, 183, 184  
     deterioration mechanisms 577, 578  
     plasma spray coatings 457, 477–8,  
         569, 570, 574, 575  
     waterwall tubes 572–4, 575  
 sputtering 622  
     zinc oxide films  
         effect of sputtering atmosphere  
             543–7  
         partial reactive sputtering  
             deposition-wet oxidation 540–3  
     zinc oxide nanostructures 534, 537–9  
 stainless steels 197  
 steady-state growth of oxide scale 460,  
     464–5, 466  
 steel 3  
     global consumption 192  
     hot-rolled steel strips *see* hot-rolled  
         steel strips  
     long-term oxidation 199–221  
         effects of alloying elements  
             217–19  
         effects of water vapour addition  
             202–6  
     low carbon, low silicon steel in air  
         or oxygen 199–202  
     porosity in scale 203, 210–11,  
         219–21  
     reheat furnace atmospheres 206–16  
     short-time oxidation 221–6  
     types of 197

- Stellite-6 coating 185–7  
 strain rates 228, 229  
 stress-free oxide scale growth 17–20  
 stress-strain relationships 228, 229  
 stresses, growth *see* growth stresses  
 strip hot rolling *see* hot-rolled steel strips  
 substoichiometric combustion 207,  
     214–16
- sulphates  
     deposits in hot corrosion 164–5  
     solution chemistry 171, 172  
     *see also* sodium sulphate
- sulphidation 599–638  
     alloys 609–34  
         containing refractory metals  
             617–28  
         dissociative mechanism of scale  
             growth 610–13, 614  
         doping effect 622–3, 624–6,  
             628–34  
         sulphidation kinetics 613–17  
     petrochemical industry 496, 498–504  
         case studies 501–2  
         characteristics of sulphidation  
             498–500  
         furnace radiant tubes 514–15, 516,  
             517  
         hydrogen and hydrogen sulphide  
             sulphidation environments 500  
         sources of sulphur 498  
         sulphur and hydrogen sulphide and  
             mercaptan sulphidation  
             environments 499–500  
             techniques to control 503–4  
     physicochemical properties of metal  
         sulphides 600–8  
     pure metals 608–9  
     titanium aluminides 352–3
- sulphur  
     content of crude oils 495, 504  
         high sulphur and high TAN 510–11  
         low sulphur and high TAN 507–9  
         naphthenic acid corrosion 506–11  
     solubility in metals 609  
     sources for sulphidation in  
         petrochemical industry 498  
     sulphur effect on oxidation 468–70  
         role of reactive elements in  
             alumina scale 313  
     WTE plants 571
- superalloys  
     thermal barrier coatings and  
         interdiffusion 477  
     use in avoiding hot corrosion 179–81
- superconductors 528–30
- superheater tubes (SHTs) 557–8  
     corrosion-resistant materials 561–9  
         alloys high in chromium and  
             molybdenum-nickel 565–6, 567  
         alloys high in chromium and  
             nickel-iron 563–4, 567, 568  
         alloys high in silicon, chromium  
             and nickel 565–6, 567, 569  
         coatings 567–9, 570
- surface hot shortness 218
- surface modification 457  
     LTCs 268–9  
     roughening 353  
     titanium aluminides 349–53
- surface roughness *see* roughness, surface
- Tammann-type equation 198
- tangential strain 30
- tantalum 344–6, 388  
 tantalum aluminium carbide 257, 258,  
     259, 260
- tantalum-based alloys 422–3
- temperature  
     brittle-ductile transition temperature  
         235, 238  
     effect on wear  
         abrasive wear 146, 147  
         erosive wear 137, 138  
         sliding wear 126–8, 129  
     effect on zinc oxide films 547–8  
     metal dusting and  
         iron 87  
         iron-nickel-based alloys 98–9,  
             100  
         nickel-based alloys 94–6  
         nickel and cobalt 89, 90  
         naphthenic acid corrosion 506
- temperature gradient 569–70
- temperature gradient tests (TGTs) 577,  
     579–87  
     corrosion behaviour with corrosive  
         deposits 582–4  
     procedure for conducting TGTs with a  
         thermal cycle component  
         579–82

- role of protective oxide films and reproducibility 584–7
- tensile strength 227–8
- tertiary scale 193, 194
- testing
  - corrosion testing for WTE plant 577, 579–87
  - wear 118–26, 158
- thermal barrier coatings (TBCs) 4, 476–91
  - failure 487–8
  - deposition of CMAS 488
  - high temperature oxidation 487–8
  - hot corrosion 488
  - future trends 488–9
  - manufacture 477–9
  - materials 479–87
    - bond coat materials 484–7
    - ceramic topcoat materials 479–83
  - thermal conductivity 479–80
- thermal cycles 579–87
- thermal expansion coefficient *see* coefficient of thermal expansion (CTE)
- thermal plasma physical vapour deposition (TP-PVD) 478
- thermal spraying 181, 183
- thermal stress 466, 467
- thermally-grown oxides *see* oxide scales
- thermite reactions 376–7
- thermodynamic activity 41
- thin films
  - ultra-thin silicon dioxide films 523–5
  - zinc oxide
    - preparation by traditional oxidation techniques 531–3
    - preparation by wet oxidation 540–8
- thin slab casting 193, 194, 226
- three-body abrasion 118, 124, 146–8
  - testing 124, 125
- through-thickness cracks 230, 231, 232–3
- time, oxidation 548
- tin 218
  - niobium silicide-based *in-situ* composites 387–8
- titania 337, 338, 339, 340
  - slowing growth of 346
- titanium 110, 111, 399
  - nickel-titanium diffusion couple 29–30
  - niobium silicide-based *in-situ* composites 387
- Ti–IF steel 203–4, 218–19
- titanium–aluminium–oxygen system 334–5, 336
- titanium alloys 333, 369–71
- titanium aluminides 3–4, 329–64
  - advantages and potential applications of titanium aluminide-based alloys 329–30
  - future trends 358
  - metal matrix composites 368, 369–71
  - oxidation characteristics of TiAl-based alloys 334–53
  - improving oxidation resistance 346–9
  - influence of additional elements 343–9
  - influence of gas species 341–3
  - microstructure control and surface roughening 353
  - oxidation curves 336–7
  - oxidation sequences 338–40
  - phase relations 334–6
  - structure of oxide scale 337–8
  - surface treatments 349–53
  - Z phase 340–1
- oxidation characteristics of Ti<sub>3</sub>Al–Nb alloys 353–7
- properties 331–4
- Ti<sub>3</sub>Al 331, 332, 333
  - oxidation characteristics of Ti<sub>3</sub>Al alloys 353–6
- TiAl<sub>3</sub> 331–3
  - oxidation characteristics of TiAl<sub>3</sub>-based materials 357–8
- titanium aluminium carbides 259, 264
  - hot corrosion mechanism against sodium sulphate 281–3
- in-situ* titanium matrix composites 379–80
  - oxidation mechanism 270–6
- titanium borides
  - particle-reinforced nickel aluminide-based composites 386
  - particle-reinforced TMCs 374–6
- titanium carbide
  - impurity and oxidation of Ti<sub>3</sub>SiC<sub>2</sub> 266
- MMCs
  - in-situ* TMCs 379–80
  - particulate-reinforced nickel aluminide-based composites 386

- particle-reinforced TMCs 374–5
- titanium matrix composites (TMCs)
  - 369–82
  - oxidation 371–82
    - fibre-reinforced 371–3
    - in-situ* composites 376–82
    - particulate- or whisker-reinforced 373–6
- titanium niobide 376
- titanium silicon carbide 256, 257, 258, 259
  - hot corrosion
    - mechanism against various molten salts 279–80
    - pre-oxidation treatment 283
  - improvements to high temperature oxidation behaviour 267–9
  - oxidation mechanism 263–7
  - processing 260, 261–2, 263
- tool steels 197
- topologically close-packed (TCP) phases 486
- total acid number (TAN) 495
  - naphthenic acid corrosion 505, 507–11
    - crude oils with high sulphur and high TAN 510–11
    - crude oils with low sulphur and high TAN 507–9
- transfer layer 149–50, 151
- transient alumina phases 292
  - effect of reactive elements on transformation 311–13
  - formation and transformation 295–8
- transient oxidation 459–64
- transition between external and internal oxidation of alloys 3, 36–58
  - model 43–56
  - criterion for transition from permanent external oxidation to internal oxidation 50–5
  - experimental observations 43–50
  - formation of metal nodules 55–6
- transition criteria from metal erosion regime to oxide erosion regime 152–5
- translation factor  $T$  19–20, 30
- transmission electron microscopy (TEM) 59, 60, 74, 76
  - location of reactive elements in alumina scales 305, 306–7
- tribological degradation *see* wear
- tribology oxidation maps 151–2, 153, 154, 159, 161
- tungsten 343–6
- turbine aircraft engines 423–4
- turbocharger wheels 329, 330
- Turkdogan model of active-to-passive transition 446–7
- twin-roll caster 195, 196
- two-body abrasion 118, 124, 146–8
  - testing 124, 125
- two-phase diffusion couples 13–15
- ultra-thin silicon dioxide films 523–5
- vacancy injection 31–2
- vacancy sinks and sources 11–13, 14
- vacuum distillation systems
  - corrosion of furnace radiant tubes 516–17
  - naphthenic acid corrosion 507–11
- vacuum residuum viscosity breaking system 501–2
- vacuum UV (VUV) photo-oxidation 524
- valence-control rule 346
- vanadates
  - hot corrosion 175–9
  - solution chemistry 171, 173
- vanadium 110
- vanadium-based alloys 422–3
- vaporisation 506
- vapour pressure 450–2
- vapour-solid (VS) process 534
- viscosity breaking system 501–2
- void migration theory 203, 204–5
- Wagner's theory of oxidation 1, 601
  - active-to-passive transition for silicon carbide 445–6, 447–9
  - transition from internal to external oxidation 37–9, 43, 54
- waste-to-energy (WTE) incineration plants 5, 557–98
- corrosion environment of WTE boilers 558–61
- corrosion lifetime evaluation of materials 592–4, 595
- corrosion mechanisms of materials 569–72, 573
- corrosion-resistant coatings for waterwall tubes 572–7

- corrosion-resistant materials for superheaters 561–9, 570
- corrosion test methods 577, 579–87
- deterioration mechanisms of spray coatings 577, 578
- in-situ* measurement of corrosion environment 577, 588–91
- recent trends 557–8
- water vapour
- chromia-forming alloys 401–3
  - long-term oxidation of iron and steel 202–6
  - reheat surface atmospheres 207, 208, 209–12, 213–14, 215
  - oxidation of titanium aluminides 341–2
- waterwall tubes (WWTs) 558
- corrosion-resistant coatings 572–7
    - composite tubing 576
    - refractory materials 576–7
    - spray coating 572–4, 575
    - weld overlay 574–6
  - wear 3, 117–63
    - abrasive 118, 124–6, 146–8, 158–9, 161
    - erosive 117–18, 120–3, 137–45, 151–9, 160–1
    - future trends 158–9
    - recent developments 149–58
    - sliding 117, 119–20, 126–37, 149–51, 158–9, 160
  - test facilities for high temperature wear 118–26, 160
- weld overlays
- TGTs 583–4
  - waterwall tubes 574–6
- wet oxidation
- zinc oxide films 540–8
    - effect of oxidation temperature 547–8
    - effect of oxidation time 548
    - effect of sputtering and oxidising atmospheres 543–7
    - highly porous films 540–3
    - photoluminescence 543–8
  - zinc oxide low-dimensional nanostructures 534–40
- whirling arm erosion rig 122, 123
- whisker-reinforced MMCs 367
- titanium matrix composites 373–6
- work roll wear 237
- wustite 198, 199–200, 201, 202, 216
- EBSD analyses of structure 240, 241, 242–3
- mechanical properties 227–8
- porosity 210–11, 221
- short-time oxidation of iron and steel 223–6
- X-ray photoelectron spectroscopy (XPS) 59, 60, 71–3, 74, 75
- yttria stabilised zirconia (YSZ) 480, 489
- alumina-YSZ graded thermal barrier coating 479
  - failure of YSZ coatings 488
- yttrium 305, 307, 308
- alumina-forming alloys 411–15
  - reactive element-doped alumina scales 309
- Yu and Lenard's study 234
- Z phase 335–6, 337, 338–9, 340–1
- stabilisation of 346–7
- zinc-copper alloys 613, 614
- zinc interstitials 546–7
- zinc oxide 530–48
- applications 530–1
  - films
    - photoluminescence 531–2, 543–8
    - porosity 540–3
    - prepared by traditional oxidation 531–3
    - prepared by wet oxidation 540–8
  - nanostructures
    - prepared by traditional oxidation 533–4
    - wet oxidation and low-dimensional nanostructures 534–40
- zinc vacancies 546–7
- zirconate pyrochlore oxides 480–1
- zirconia 28
- hooks and tubes in silicon carbide oxidation experiments 444
- zirconium 67–8
- alumina-forming alloys 412–13
  - reactive element-doped alumina scales 308, 309
- zirconium aluminium carbides 255, 257, 258, 259
- oxidation mechanism 276–8
  - processing 262, 263